SCINT99

Proceedings of
The Fifth International Conference on

Inorganic Scintillators and Their Applications

August 16-20, 1999

Moscow State University, 119899 Moscow, Russia

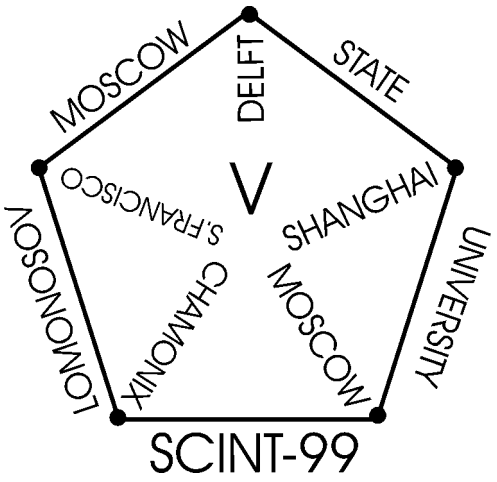

Edited by
Vitaly Mikhailin
Moscow State University

M.V.Lomonosov Moscow State University
Russian Academy of Sciences
Ministry of Education of the Russian Federation
Ministry of Science and Technologies of the Russian Federation
CERN
Euro-Asian Physical Society
Russian Physical Society

Sponsored by

Russian Foundation for Basic Research
CRISMATEC
SCIONIX Holland B.V.
Furukawa, Ltd.

International Scientific Committee

C.W.E. van Eijk (Netherlands)
A.V. Gektin (Ukraine)
H. Hofer (Switzerland)
T. Jones (UK)
M. Kobayashi (Japan)
M. Korzhik (Belarus)
M. Lebeau (Switzerland)
P. Lecoq (Switzerland)
J.A. Mares (Czech Republic)
C.L. Melcher (USA)
V. Mikhailin (Russia)
C. Morel (Switzerland)
W.W. Moses (USA)
F. de Notaristefani (Italy)
C. Pedrini (France)
P. Rodny (Russia)
B. Shulgin (Russia)
X.W. Tang (China)
S. Tavernier (Belgium)
T. Virdee (Switzerland)
M.J. Weber (USA)
R. Williams (USA)
A.J. Wojtowicz (Poland)
C. Woody (USA)
D.S. Yan (China)
W.M. Yen (USA)
Z.W. Yin (China)
G. Zimmerer (Germany)
R.Y. Zhu (USA)

Contents

Contents ..... ***iii***

Preface ..... ***xi***

Plenary presentations

P. Lecoq How high energy physics is driving R&D of new scintillators. *3*

W. Moses Scintillator requirements for medical imaging *11*

C. W. E. van Eijk Inorganic scintillators for the next generation of neutron beam facilities *22*

Ch. Lushchik, A. Lushchik and M. Kirm Separation of elementary mechanisms of photon multiplication in wide-gap crystals *33*

A. Vasil'ev Relaxation of hot electronic excitations in scintillators: account for scattering, track effects, complicated electronic structure *43*

S. E. Derenzo, M. Klintenberg, and M. J. Weber First Principle Calculations of Critical Scintillation Processes *53*

V. S. Kortov and I. I. Milman Storage and Dosimetric Properties of Oxides..... *61*

S. Schweizer, U. Rogulis, S. Assmann, and J.-M. Spaeth New materials for x-ray storage phosphors promising higher spatial resolution *70*

A. V. Gektin Halide scintillators: present status and prospects *79*

Ch. Pedrini Cerium-based and cerium-doped fluorescent and scintillating materials *89*

M. Korzhik Scintillators on a base of oxide crystals *97*

S. Baccaro, R. Dall'Igna, P. Fabeni, M. Martini, J.A. Mares, F. Meinardi, M. Nikl, K. Nitsch, G.P. Pazzi, P. Polato, A. Vedda, G. Zanella, R.Zannoni High Light Yield Ce^{3+}(Tb^{3+}) -doped phosphate and oxide scintillation glasses *106*

A.I. Nepomnyashikh, E.A.Radzhabov, A.V.Egranov, V.F.Ivashechkin, Yu. Kudenko, O. Mineev Fast scintillator BaF_2-LaF_3 ..... *113*

R. T. Williams, Y. C. Zhang, Yo. Abraham, and N. A. W. Holzwarth Electronic structure of pure and defective $PbWO_4$, $CaWO_4$, and $CdWO_4$ *118*

A. Hofstaetter, H. Alves, M. Bohm, D.M. Hofmann, O.V. Kondratiev, M.V. Korzhik, V.V. Laguta, M. Luh, V. Metag, B.K. Meyer, R. Novotny, N.G. Romanov, A. Scharmann, A. Vedda, A. Watterich Spectroscopic characterization of defects in tungstate scintillators *128*

M. Kobayashi, Y. Usuki, M. Ishii, N. Senguttuvan, K. Tanji, M. Chiba, K. Hara, H. Takano, M. Nikl, , P. Bohacek, S. Baccaro, A. Cecilia, M. Diemoz , A.Vedda, M. Martini Radiation hardness of doped $PbWO_4$..... *137*

X.D. Qu, L.Y. Zhang and R.Y. Zhu Radiation induced color centers and light monitoring for lead tungstate crystals *147*

A. Koch,P. Cloetens, W. Ludwig,, J. C. Labiche and B. Ferrand Reading thin-film scintillators with optical microscopes for X-ray imaging *157*

M.Balcerzyk, M. Moszynski, M. Kapusta Energy resolution of contemporary scintillators. Quest for high resolution, proportional detector *167*

W. Mengesha, J.D. Valentine A Technique for measuring scintillator electron energy resolution using the Compton coincidence technique *173*

Oral presentations

R. Novotny, R. Beck, W. Doering, V. Hejhy, A. Hofstaetter, M.V. Korzhik, V. Metag, H. Stroeher Electromagnetic calorimetry with $PbWO_4$ in the energy regime below 1 GeV *181*

BELLE calorimeter collaboration presented by B. Shwartz Electromagnetic calorimeter of the BELLE detector *186*

T. Inagaki, Y. Yoshimura, Y. Kanda, Y. Matsumoto and K. Minami Developement of CeF_3 crystal for high energy electromagnetic calorimetry *191*

N.Gendner, U.Holm, K.F. Johnson, A.Meyer-Larsen, S.Thies A PWO crystal calorimeter for high energy physics *195*

E. Auffray, G. Davies, P. Lecoq, R. Marcos, M. Schneegans P. Sempere, A. Annenkov, M. Korzhik Status on PWO crystals from Bogoroditsk after 1 year of preproduction for CMS-ECAL *201*

Z.W. Yin, Q. Deng, D.S. Yan Research and development on $PbWO_4$ crystals in Shanghai Institute of Ceramics *206*

E. Auffray, A.N. Annenkov, G.Yu. Drobychev, V.A. Evdokimov, A.A. Fedorov, M.V. Korzhik, V.L. Kostylev, P. Lecoq, O.V. Missevitch, A.V. Oskine, V.V. Panov, J.-P. Peigneux, M. Schneegans, R.F. Zouevski Methodology of certification of scintillators for large scale detectors *212*

P.A. Rodnyi, V.B. Mikhailik, A.S. Voloshinovskii, C.W.E. van Eijk, G.F. Zimmerer Search of Crystals for detection of Mixed Neutron-Gamma Flux *218*

M. Marsman, J. Andriessen, C.W.E van Eijk Charge compensation and lattice relaxation in $LiBaF_3:Ce^{3+}$ *224*

N. Shiran, A. Gektin, V. Komar, Yu. Nesterenko V. Voronova The role of oxygen in energy transfer processes in $LiBaF_3$ scintillators *230*

I. Tale , V. Tale , P. Kulis , M. Springis, U. Rogulis, J. Jansons, A. Veispals, H.-J. Fitting Mechanism of the recombination luminescence of $LiBaF_3$ crystals *236*

I.N. Ogorodnikov, V.A. Pustovarov, A.V. Kruzhalov, L.I. Isaenko, M. Kirm, G. Zimmerer A time-resolved spectroscopy study of fast luminescence in lithium borates *242*

A.B. Sobolev, A.Yu. Kuznetsov, A.N. Varaksin, Yu. L. Korol Electronic structure embedded cluster simulation of Ce^{n+} in fluorides and complex oxides *248*

A. Kuznetsov, A.B. Sobolev, J. Andriessen, Yu.L. Korol The choice of parameters in quantum - chemical simulation of the rare-earth ions electronic structure by a scattered waves cluster method *254*

Yu. Hizhnyi, M Bilyi, S. Nedelko Electron band structure and optical characteristics calculation of A_nBO_4 crystals *260*

V.A. Pustovarov, V.Yu., Ivanov, M.Kirm, A.V.Kruzhalov, G.N. Kulipanov, I.N. Ogorodnikov, G. Zimmerer,E.I. Zinin Time-resolved spectroscopy of self-trapped excitons in oriented BeO crystals under X-ray and VUV excitations *266*

P. Dorenbos Predictability of the 5d level positions of the triply ionized lanthanides in halogenides and chalcogenides *272*

W. Blanc, C. Dujardin, J.C. Gâcon, C. Pedrini, A.N. Belsky, I. Kamenskikh, C. Fouassier, S. Bourgeois Optical and scintillation properties of Ce^{3+}-doped fluorides *277*

O. Guillot-Noel, E.V.D. van Loef, P. Dorenbos, C.W.E. van Eijk, K.W. Kramer, H.U. Gudel Luminescence and scintillation properties in Ce^{3+} activated trihalide compounds *282*

V. A. Tarasov, E.V. Sysoeva, E.P. Sysoeva, O.V. Zelenskaya Modeling of detection systems on the base of scintillation materials *288*

Ya. A. Berdnikov, O. Ya. Berdnikova , V.F. Kosmach, V.M. Samsonov, A.P. Shishlo Optimization of scintillation light collection from $PbWO_4$ crystals *293*

N. Cocozzella, M. Lebeau, G. Majni, N. Paone, D. Rinaldi Quality inspection of anisotropic scintillating crystals through measurement of interferometric fringe pattern parameters *298*

S.Belogurov, G.Bressi, D.Iannuzzi, G.Carugno, E.Conti, A.T.Meneguzzo Infrared scintillation in crystals..... *304*

M. Martini, F. Meinardi, A. Vedda, M. Nikl, E. Mihokova, G.P. Pazzi, P. Fabeni, Y. Usuki, S. Baccaro Influence of dopant ions on traps and recombination centres in lead tungstate *309*

V. Nagirnyi, E. Feldbach, L. Joensson, M. Kirm, A. Kotlov, G. Svensson, M. Asberg-Dahlborg Relaxation of electronic excitations in $PbWO_4$ and $CaWO_4$:Bi crystals *315*

N. Klassen, S. Shmurak, V. Sinitsyn, B. Red'kin, S. Rybchenko, B. Ille, M. Lebeau, P. Lecoq, M. Schneegans Influence of surface particularities on scintillation light yield of lead tungstate *321*

I.A.Kamenskikh, M.Kirm, V.N.Kolobanov, V.V.Mikhailin, P.A.Orekhanov, I.N.Shpinkov, A.N.Vasil'ev, G.Zimmerer Luminescence and Electronic Structure of Calcium and Lead Tungstates and Sulphates *326*

H.F.Chen, C.Li, M. Shao, C.S. Shi, Z.M. Wang, C. Wu, Z.Z. Xu, Q. Deng, J.Y. Liao, Z.W. Yin Scintillation characteristics of Sb-doped $PbWO_4$ crystal *332*

R.T. Williams, H.M. Yochum, K.B. Ucer, D.K. Millers, L.G. Grigorjeva, S. Chernov Picosecond and nanosecond time-resolved study of luminescence and absorption of $CdWO_4$ and $PbWO_4$ *336*

J. Li; G. Chen; S. Ren; Y. Zhang; X. Chen Improvement in Scintillation Properties of PWO_4 crystals with different doping ions *342*

I. Dafinei, F. Cavallari, A. Cecilia, M. Diemoz, S. Guerra, E. Longo, G. Organtini, F. Pellegrino, S. Baccaro, M. Montecchi Measuring Technique for a large scale production of PWO scontillators *346*

S. Baccaro, A. Cecilia, R. Dall'Igna, M. Martini,, J. A. Mares, M. Montecchi, E. Mihokova, M. Nikl, K. Nitsch, P. Polato, A. Vedda, G. Zanella, R. Zannoni Radiation damage of Ce^{3+} (Tb^{3+})-doped phosphate and oxide scintillating glasses *352*

E.A. Radzhabov, A.I.Nepomnyashikh Slow components of decay in Ce-doped fluoride crystals *357*

A.N. Belsky, W. Blanc, C. Dujardin, C. Pedrini, A. Petrosyan, J. C. Gacon, E. Aufray, P. Lecoq Status of development of YAP-LuAP mixed scintillators. Optical, luminescence and light yield studies *363*

V.N. Makhov, J.Y. Gesland, N.M. Khaidukov, N.Yu. Kirikova, M. Kirm, J.C. Krupa, T.V. Ouvarova, G. Zimmerer VUV scintillators based on d-f transitions in rare earth ions *369*

C. Shi, J. Deng, D. Shen, G. Hu,Y. Wei, G. Zhang G.Zimmerer, J.Becker Channels of Energy Losses in CeF_3 crystals *375*

N. Garnier, C. Dujardin, A. Belsky, C. Pedrini, J.P. Moy, H. Wieczorek, P. Chevallier, A.Firsov Spectroscopy of CsI(Tl) Layers *379*

H. Wieczorek, M. Overdick Afterglow and Hysteresis in CsI:Tl *385*

G. Cho, K. S. Lee, D. K. Kim and K. S. Joo Annealing Effect on Optical Emission Properties of Pure and Na-doped CsI Thin Films for X-ray Radiographic Application *391*

Y.Q.Mao, Z. Yin Scintillating crystals in Shanghai institute of ceramics, Chinese Academy of Science *397*

M. Ishii, N. Senguttuvan, K. Tanji, T. Kittaka, Y. Usuki, M. Kobayashi, M. Nikl Effect of annealing on optical and scintillation characteristics of PWO crystals grown by Bridgman method *402*

A.G. Petrosyan, G.O. Shirinyan, K.L. Ovanesyan, T.I. Butaeva, C. Pedrini, C. Dujardin, A. Belsky Characterization of Bridgman and Czochralski grown LuAP and LuYAP single crystals *408*

Poster presentations

M. Kirm, A. Lushchik, Ch. Lushchik, S. Vielhauer, and G. Zimmerer Influence of uniaxial stress and external electric field on luminescence of KI crystals under selective VUV excitation *415*

V.A. Pustovarov, B.V.Shulgin, M.M. Kidibaev and A.A. Zhamangulov Luminescence excitation spectra and energy transfer in LiF-U,Cu and NaF-U,Cu scintillation crystals .. *421*

S.V. Gorbunov, K.V. Bautin, A.V. Kruzhalov, V.Y. Yakovlev New Features of Self-Trapped Exciton Luminescence in Beryllium Oxide..... *425*

M. Nikl, P.Bohacek, E.Mihokova, M. Kobayashi, M. Ishii, Y. Usuki, V.Babin, A.Stolovich, S.Zazubovich, M. Bacci Excitonic emission of scheelite tungstates AWO_4 (A=Pb, Ca, Ba, Sr) *429*

V.A. Pustovarov, A.V.Kruzhalov, V.L.Petrov, B.V.Shulgin, M.Kirm,G.Zimmerer and E.I.Zinin Optical and Luminescent VUV-Spectroscopy of $La_2Be_2O_5$ Single Crystals *435*

N.Yu.Kirikova, A.N.Belsky, B.Chassigneux, J.C.Krupa, V.N.Makhov, M.Queffelec Decay kinetics of d-f emission and thermoluminescence of $LiYF_4$ doped with rare earth ions (Ce^{3+}, Pr^{3+}, Nd^{3+})..... *440*

O.V. Ryaboukhin, V.Yu.Ivanov, A.V.Kruzhalov, F.G.Neshov Investigation of core-valence luminescence under the protons excitation..... *446*

R.A. Glukhov, C.Pedrini, A.N.Vasil'ev, A.Yakunin Track effects in crossluminescence ... *448*

O.I.Baum, A.N.Vasil'ev Modification of crossluminescence spectra due to localization of core hole: tight-bingding approximation *453*

V.Kisand, E.Gminder, M.Kirm, B.Steeg, S.Vielhauer, and G.Zimmerer Discrimination Between Different Free Exciton Creation Processes in Solid Krypton *458*

A.N. Vasil'ev, Y. Fang, V.V. Mikhailin The rates of exciton and electron-hole impact production in wide-gap insulators *464*

A.N. Belsky, C. Dujardin, I.A. Kamenskikh, A. Philippov, C. Guillot, N. Barrett, G. Dujardin, L. Hellner, G. Comtet, and C. Pedrini VUV-Photoelectron spectroscopy of scintillation materials *470*

Yu. Zorenko, V.Gorbenko, I. Konstankevych, M.Pashkovsky, M.Globus, B.Grinyov, V.Tarasov, P.Dorenbos, C.W.E. van Eijk, E. van Loef Scintillators on the base of single crystalline films of Al_20_3-Y_2O_3 system oxides *476*

E.N.Mel'chakov, A.N.Mishin, B.Moine, C.Pedrini, S.V.Petrov, P.A.Rodnyi, A.V.Sidorenko Emission Properties of Chloride Elpasolite *482*

V.G.Bondar', V.P.Gavrilyuk, K.A.Katrunov, V.S.Kanevskii, E.V.Krivonosov, V.P.Martynov GSO:Ce^{3+} scintillator with an energy resolution < 10% *487*

A.S. Voloshinovskii, V. B. Mikhailik, O. T. Antonyak, P. A. Rodnyi, P.Dorenbos, C. W. E. van Eijk, G. Zimmerer Luminescence of $CsGd_2Cl_7$:Ce^{3+} crystals *492*

S.Kh. Batygov, N.N. Vinogradova, Yu.K. Voronko, L.N. Dmitruk, L.V. Moiseeva Coactivation induced phosphorescence of $BaA_{l2}O_4$:Eu^{2+} *497*

R. Nakamura, M. Ishii Improvements in the X ray Characteristics of Gd_2O_2S:Pr Ceramic Scintillators *501*

C. Dujardin, M. Boudeulle, E. Galluci, C. Pedrini, A.G. Petrosyan, T. Hansen $LuAlO_3$, $YAlO_3$ and $LaLuO_3$ structure analysis with neutron diffraction *506*

B. Viana, D. Pauwels, N. Lemasson, A. Kahn-Harari, E.V.D. van Loef, P. Dorenbos, C.W.E. van Eijk Scintillation properties of $Lu_2Si_2O_7$:Ce^{3+} (LPS) crystals *511*

E.I. Gorokhova, Ananieva G. V., Demidenko V. A., Khristich O. A., Merkuliaeva T. I., Savostianov V. A. Doped Rare - Earth Oxysulfides Luminescent Ceramics *517*

O. Guillot-Noel, J.C. van't Spijker, P. Dorenbos, C.W.E van Eijk, K.W. Kramer, H.U. Gudel New results on the scintillation properties of $RbGd_2Br_7$:Ce and comparison with three other well-known scintillators: NaI:Tl, CsI:Tl and Lu_2SiO_5:Ce *523*

C. Dujardin, A. Garcia-Murillo, C. Madej, C. Pedrini, Goutaudier C., Petrosyan A.G., Ovanesyan K.L., Shirinyan G.O., A. Koch, M.J. Weber Synthesis and scintillation properties of some dense X-ray phosphors *527*

Yu. Zorenko, V. Gorbenko, I. Konstankevych, M. Batentschuk Scintillators with high Z_{eff} on the base of $Lu_3Al_5O_{12}$:Ce single crystalline films: growth, properties and applications *532*

L.N.Shpilinskaya, D.I.Zosim, L.V.Kovaleva, A.M.Kudin, A.I.Mitichkin, T.A.Charkina Radiation damage factors of CsI(Tl) crystals *538*

V. Babin, P. Fabeni, E. Mihokova, M. Nikl, A. Stolovich, G. P. Pazzi, S. Zazubovich Time-resolved spectroscopy of exciton states in undoped and doped CsI crystals *544*

K.V. Shakhova, A.N. Panova, V.I. Goriletsky, V.P. Gavrilyuk, N.N.Kosinov Photoinduced coloration of NaI(Tl) crystals: effect of the lead impurity trace concentration. *550*

M. Springis, P. Kulis1, I. Tale, A. Veispals, H.-J. Fitting Defect Luminescence of $LiBaF_3$ perovskites *555*

A. Shalaev and E. A. Radzhabov The Influence of Alkali Impurities on the $BaFBr:Eu^{2+}$ Photostimulated Luminescence..... *560*

V.D.Ryzhikov, L.L.Nagornaya, S.F.Burachas, E.A.Danshin. O.V.Zelenskaya, L.A.Litvinov, E.A.Losseva, V.V.Chernikov Detection of thermal and resonance neutrons using scintillators based on complex oxides *564*

B.V.Grinyov, L.A.Grin', E.F.Dolzhenkova, M.F.Dubovik, A.V.Tolmachev, V.A.Tarasov, V.N.Baumer Point defects in beta-irradiated $Li_2B_4O_7$..... *568*

M. Balcerzyk, W. Klamra, M. Moszynski, M. Kapusta, M. Szawlowski Nonproportionality and temporal response of ZnSe:Te scintillator studied by large area avalanche photodiodes and photomultipliers. *571*

P. Dorenbos, C.W.E. van Eijk, E.van Loef, M. Globus, B. Grinyov, M. Ratner, V. Tarasov, Yu. Zorenko Heavy oxyde scintillators: bulk crystals and thin films for radiation monitoring of environment and biological objects *577*

L. Limarenko, M. Pashkovsky, Z. Moroz, Yu. Zorenko, I. Konstankevych Impurity and intrinsic defects dependent scintillation properties of $PbWO_4$ single crystal *583*

L. Nagornaya, A. Apanasenko, Yu. Vostretsov, O. Zelenskaya, I. Tupitsyna, K. Katrunov, V. Ryzhikov Effect of gamma- and photoirradiation on radiation stability of scintillators based on $PbWO_4$ single crystals..... *589*

I.M. Soljskii, A.V. Gektin, M.V. Korzhik, R.V. Gamernyk, Z.A. Khapko, A.S. Voloshinovskii Influence of technology conditions on luminescence parameters of large-size $PbWO_4$ crystals..... *595*

V. Yevseyev, V. Samsonov Study of optical properties of $PbWO_4$ crystals irradiated by gamma-quantums, fast neutrons and 1GeV protons *599*

S. Burachas, V. Bondar, B. Grinev, K. Katrunov, V. Martinov, L. Nagornaya, V. Ryzhikov, G. Tamulaitis Lead tungstate scintillator crystals optimized for high-energy physics applications..... *604*

C. Shi, Y. Chen, X. Ye, D. Zhou, J. Liao, G. Hu, H.Chen On the green emission centers in $PbWO_4$ scintillator *609*

D. Millers, S. Chernov, L. Grigorjeva , V. Pankratov, M. Nikl, Y. Usuki Luminescence and transient absorption of doped PWO_4 scintillator crystals..... *613*

M. Boehm, A. Hofstaetter, M. Luh, B. Meyer, A. Scharmann,M. Korzhik, O. Kondratiev, A. Borisevich, V.V. Laguta, P. Lecoq, E. Auffray-Hillemans, Thermally stimulated luminescence properties of lead tungstate crystals *619*

L. Zheng; G. Chen, S. Ren, G. Sun; J. Wei; H. Yu, J. Li Study on macroscopic defect of $PbWO_4$ crystals grown by Bridgeman method *627*

R. Chipaux, M. Geleoc Optical anisotropy effects in lead tungstate crystals *629*

A. Cousson, W. Paulus, R. Chipaux Determination of the crystal structure of lead tungstate by neutron diffraction *636*

Remi Chipaux Light collection in the CMS lead tungstate crystals: relation between monitoring and calibration variations *639*

B.I. Zadneprovski, V.A. Nefedov, I.S. Bykov, E.V. Polyansky Spectral luminescent properties of molibden doped $PbWO_4$ *643*

M. Kirm, V. Kolobanov, V. Makhov, V. Mikhailin, D. Spassky, I. Shpinkov and G. Zimmerer Optical properties and luminescence of cadmium and zinc tungstate single crystals *648*

L. Nagornaya, I. Tupitsyna, A. Apanasenko, O. Zelenskaya Influence of admixture defects on scintillation and optical characteristics of cadmium tungstate single crystals..... *653*

P.I. Korenuk, Z. Moroz, S. Nedilko , M. Pashkovskii Influence of molybdenum ions impurities on the optical properties of lead tungstate single crystals..... *658*

B.G. Zaslavsky, A.M. Kudin, S.I. Vasetsky, V.S. Suzdal, J.A. Nesterenko, L.N. Shpilinskaya, L.V. Kovaleva, T.A. Charkina, A.I. Mitichkin, V.N. Zviagintsev Characteristic features of automated growth of large scintillation alkali halide single cristals free of oxygen-containing impurities..... *663*

N.V. Klassen, S.Z. Shmurak, A.P. Ivanov, S.I. Makhonin, A.A. Rogojin, A.E. Bakhur, A.O. Nikitin Manufacturing of scintillation elements by plastical deformation..... *668*

D. Z. Shen, G. H. Ren, S. H. Wang A Non-Vacuum Growth Technique for cubic PbF_2 Crystal with strong Cherenkov radiation effect *674*

O. Lebbou, C. Dujardin, C. Goutaudier, M.T. Cohen-Adad, C. Pedrini., B. Moine, A.N. Belsky Synthesis and scintillation properties of several borate oxydes *679*

E.E. Lomonova, S.Ch. Batygov, M.A. Borik, L.N. Dmitruk, Yu.K. Voron'ko, V.V. Osiko. The application of skull melting process for refractory scintillators production..... *684*

A.N. Shekhovtsov, M.F. Dubovik, A.V. Tolmachev, B.V. Grinyov, M.V. Dobrotvorskaya, T.I. Korshikova, E.F. Dolzhenkova, V.N. Baumer Growth and luminescence of LaB_3O_6 single crystals: pure and doped by Ce *689*

V.P. Martynov Interaction of melt with gas atmosphere at growing scintillation oxide crystals by the Czokhralski method *693*

A.N. Trukhin and L.A. Boatner Luminescence properties of $ScPO_4$ single crystal *697*

M.S. Pidzyrailo, O.M. Berdychevsky, V.V. Vistovsky, I.P. Pashuk Optical and spectral properties of the crystals $A_2ZnJ_4:Mn^{2+}$ (A = Cs, Rb)..... *703*

L.N. Dmitruk, S.H. Batygov, V.A. Balashov, N.N. Vinogradova, L.N. Moiseeva, E.G. Devitsin, V.A. Kozlov, Uy.N. Efimov, V.D. Fedorov Effect of impurites on the radiation hardness of the scintillating fluorohafnate glasses..... *708*

S. Schweizer, U. Rogulis, J.-M. Spaeth, L. Trinkler, and B. Berzina Magnetic resonance investigations on oxygen-related luminescence centres in $AlN:Y_2O_3$ ceramics... *715*

E.I. Gorokhova, Turin G. P., Permogorov S. A., Khristich O. A. Scintillation properties of monolithic polycrystalline ZnS-Te *720*

V.G. Volkov, V.P. Gavrilyuk, L.P. Gal'chinetskii, B.V. Grinyov, E.A. Danshin, K.A. Katrunov, V.Z. Kvitnitskaya, V.D. Ryzhikov Small-grained Detector of Ionizing Radiation Based on ZnSe(Te) *724*

Th. Benisch, S. Bernreuter, E. Devitsin, V. Kozlov S. Potashov, K. Rith, A. Terkulov, Ch. Weiskopf Luminosity monitor of the HERMES experiment at DESY..... *730*

V.R. Lyubynskiy, N.N. Smirnov, E.V. Sysoeva, E.P. Sysoeva, L.S. Zubenko Scintillation Assemblies Based on NaI(Tl) Crystals with α-radiation Reference Sources... *735*

V. Nekrasov, Yu. Borodenko, E. Selegenev, L. Piven', I. Solsky, Yu. Zorenko, L. Limarenko, Z. Moroz, M. Pashkovsky, I. Konstankevych Scintillation blocks of high sensitivity for detection of gamma-radiation based on cadmium tungstate *740*

K.Y. Nam, K.S. Joo, G. Cho, C.H. Lee Chemical Impurity Study on the Polyaniline by the Positron Annihilation *746*

Gu Mu, Tang Xuefeng, Tong Hongyong, Liang Ling, Chen Lingyan, Liao Jingying, Shen Dingzhong, Yin Zhiwen, Wang Jingcheng, Xu Weixin A study on point defects in lead tungstate with positron annihilation *753*

S.P.Chernov, D.N.Karimov, T.V.Ouvarova, E.O.Yankovskaya Fluoride systems $NaF-(R,Y)F_3$ as a new class of scintillators and active media for UV and VUV lasers *756*

Author Index *761*

Subject Index *766*

Material Index *771*

Preface

Series of international conferences devoted to various aspects of physics and chemistry of inorganic scintillators and their applications was launched by the International Workshop on Heavy Scintillators for Scientific and Industrial Applications, Crystal 2000 in Chamonix, France in 1992, continued by the Material Research Society meeting on Scintillator and Phosphor Materials in San Francisco in 1994, got its present name in Delft in 1995 at SCINT95 Conference, became a regular biannual meeting in Shanghai in 1997 and confirmed the lasting interest of scientific community to the field in Moscow in 1999 at SCINT99.

Novel scintillator application techniques, deeper insight in the physics of processes involved in scintillations, information on new materials and their properties as well as discussion of vital problems and questions of various origin were demonstrated in excellent talks and posters presented at SCINT99 by 250 participants.

The field is alive and booming. As a confirmation we present this book of Proceedings with 130 contributions. We would like to thank all the authors and referees for their cooperation.

Next is SCINT2001, Chamonix.

Vitaly Mikhailin,
November 1999

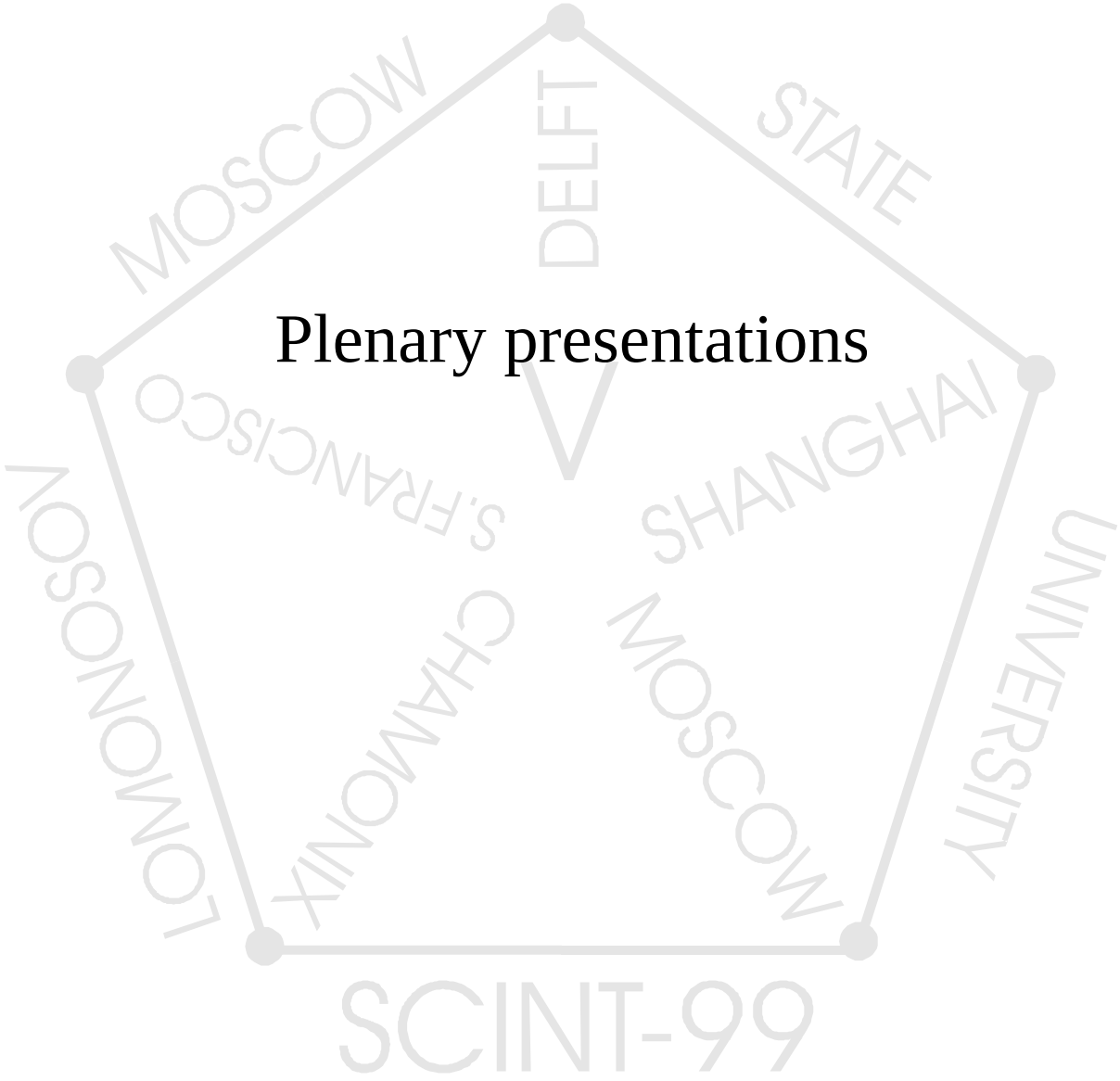

Plenary presentations

How High Energy Physics is driving the development of new scintillators

P. Lecoq

CERN, Geneva, Switzerland

Abstract: Scintillating crystals have been for a long time developed as a basic component in particle detectors with a strong spin-off in other fields like medical imaging. A typical example is BGO, which has become the main component of PET scanners since the large effort made by the L3 experiment at CERN to develop low cost production methods for this crystal. Systematic studies on basic mechanisms in inorganic scintillators was initiated by the Crystal Clear Collaboration at CERN 10 years ago, in the frame of a large R&D program to develop the detector technologies for the new CERN proton-proton collider, the LHC. This has contributed not to a small amount, to the development of new materials for a new generation of medical imaging devices with increased resolution and sensitivity. The role of Cerium as a very good activator for fast scintillators, and the very positive influence of Luthetium in many high density hosts, have been recognized early in this work. Heavy fluoride glasses, doped with Cerium, have shown an interesting potential in High Energy Physics, but will undoubtedly find several applications in several industrial applications, particularly when coupled to newly developed avalanche photodiodes. Examples will be given of recent large size High Energy Physics experiments like BELLE, BaBar, KteV, ALICE and CMS, to show the high demand on scintillator characteristics imposed by the severe working conditions of modern accelerators. These challenging developments will certainly result in important spin-off in several other fields.

Keywords: High Energy Physics, Crystal, Scintillator, Medical Imaging

1- Introduction

The discovery of α particles by Rutherford in 1899 was made possible because of the invention by Crookes a few years before of a device, called spinthariscope, which made use of the scintillating properties of Lead Sulfide. Indeed, scintillators were already involved in what can be considered as the first High Energy Physics experiment, and that was the beginning of a long common story.

When R. Hofstadter [1] introduced in 1948 Thallium doped Sodium Iodide, NaI(Tl), he probably did not realize that it was going to be the most popular scintillator for the next 35 years. The best example of the high discovery potential of scintillators in High Energy Physics was first given by the NaI (Tl) Crystal Ball experiment at SLAC [2] which allowed to reconstruct the precise spectroscopy of charmonium particles (Fig. 1).

But in the last two decades a new generation of HEP experiments has become a driving force for the development of new scintillators. This has started with Bismuth Germanate (BGO) for L3 [3] (Fig.2) and Caesium Iodide (CsI either Thallium doped or pure) for CleoII [4], Crystal Barrel [5], KTeV [6], Belle [7] and BaBar [8], which were already known but in small sizes and small quantities only.

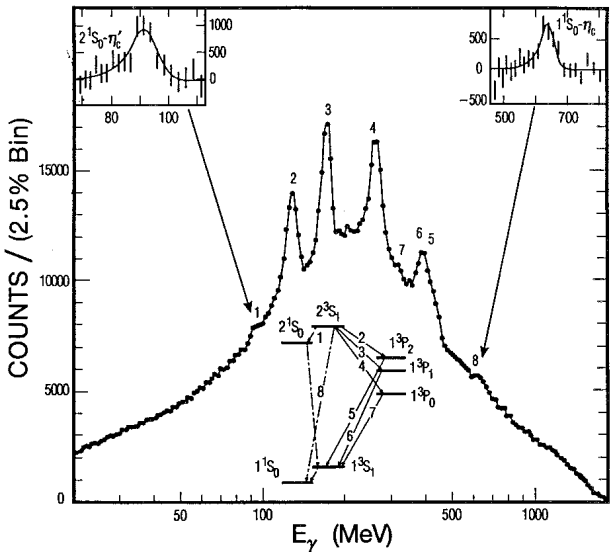

Figure 1: Charmonium spectroscopy with the Crystal Ball at SLAC

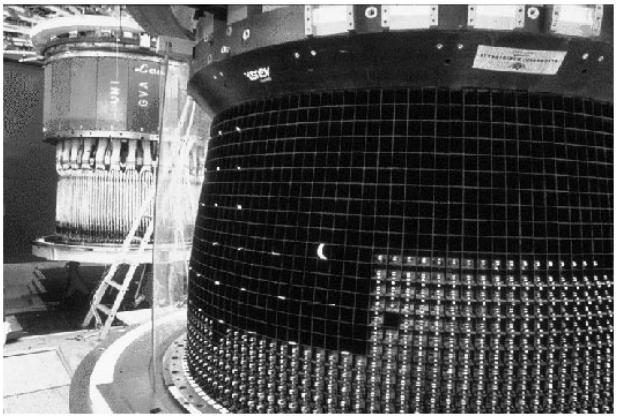
12000 BGO crystals
1.5 m^3, 11 tons
Figure 2: Construction of the L3 BGO detector at CERN

It became even more evident with Barium fluoride (BaF_2) for TAPS [9] and GEM [10], Cerium Fluoride (CeF_3) as a candidate for CMS [11] and L3P [12] and finally Lead Tungstate ($PbWO_4$) for CMS [11], which were essentially developed for HEP experiments. This paper will describe how the difficult physics constraints and harsh experimental conditions impose very tight specifications to modern detectors. The size of the experiments and the high quantitative demand allowed to organize the R&D effort on a large scale. This has been particularly illustrated by the work of the Crystal Clear Collaboration [13] which was able to create a multidisciplinary effort to make the best use of cross-fertilization between different categories of experts and industry to develop suitable scintillators at an industrial scale.

A better understanding of some basic mechanisms of energy relaxation, scintillation process, radiation damage is progressively being built through this common effort. The immediate consequence is to allow a much faster and much more efficient development of scintillators for other applications than High Energy Physics, and particularly for industrial and medical imaging devices. This paper will try to illustrate how present candidates for a new generation of low energy γ ray cameras can be developed if we can follow a similar methodology than the one used in High Energy Physics.

2- Physics requirements for High Energy Physics experiments

One of the main motivations for the construction of the CERN new proton collider LHC is the study of the symmetry breaking mechanism, which is supposed to be responsible for the generation of the masses of the particles in the electroweak theory. One or several scalar bosons (the Higgs bosons) are involved in this mechanism and can be detected through their leptonic and $\gamma\gamma$ decay modes. The main argument, generally used to stress the high level of performance required for the detectors, is the detection of 2γ resulting from the decay of the Standard Model Higgs boson, for which the natural width is completely dominated by the instrumental resolution below Higgs masses of $\approx$ 200 GeV/c^2. As this signal is associated with a very high backgrounds, generated by a combination of π° also decaying in 2γ, and the direct production of photons via the quark-quark, gluon-gluon and higher order diagrams, the signal to noise ratio is dominated by the photon detector energy resolution.

Usually electron and photon energies are measured in detectors called calorimeters, where they are stopped, producing a shower of secondary particles. In sampling calorimeters the photon energy is converted in high density absorber plates, and a small fraction of the energy is measured in a sensitive medium interleaved with the absorption medium. In a homogeneous detector, on the other hand, the electron or photon showers are fully contained in the sensitive medium. The energy is then revealed by scintillation or Cerenkov light, both collected in highly transparent media or by ionization in conductive liquids, where charges are collected.

Homogeneous detectors are well known to give excellent energy resolution that is usually parameterized in the following way:

$$\sigma(E)/E = a/\sqrt{E} \oplus b$$

where a is the statistical term (sampling or fluctuations of all sorts)
b is the constant term

High precision calorimetry at the future proton-proton machines requires an energy resolution of the order of 0.5% for 100 GeV photons.

An homogeneous calorimeter is not limited by sampling fluctuations and an energy dependant term of the resolution "a" as small as 2% has been currently achieved on several large size calorimeters. It is much more difficult to achieve a constant term "b" of $\approx$ 0.5%. On large systems like the L3 BGO calorimeter at CERN, one recognizes usually 3 contributions to the constant term:

$$b^2 = b_L^2 \oplus b_F^2 \oplus b_C^2$$

The b_L term represents the fluctuations due to the energy leakage. The front leakage due to backscattered particles has a negligible contribution above a few GeV. Having sufficient material for full longitudinal energy containment can easily control the rear leakage. For the photon energies up to 100 GeV, at least 25 radiation lengths are necessary to maintain the leakage term within reasonable limits (one radiation length is the mean distance over which a high-energy electron loses all but 1/e of its energy). The side leakage is more difficult to control. It is determined by the number of cells one has to sum-up to reconstruct the energy with sufficient precision. On the other hand this number is limited by the electronic noise and chiefly by the pile-up at LHC if the shower spreads too much laterally. Low noise electronics and high-density material will of course limit this contribution. A particular attention must be paid to all gaps, walls, and dead material in front, which may have an important contribution to the leakage term. All leakage contributions can be well reproduced by Monte-Carlo and a b_L term of $\approx$ 0.3% can be achieved with a crystal calorimeter.

The b_F term is associated to non-uniformity's. They can result from non-homogenous active material, like variation of doping concentration in non-intrinsic scintillators. Temperature gradient can be the dominant factor of non-uniformity when there is a strong dependence of the light yield with the temperature (Lead Tungstate for instance has a large temperature coefficient of - 1.9% / °C). Crystals like Cerium Fluoride (CeF_3), with a temperature coefficient as small as 1‰ / °C at room temperature will be insensitive to this effect. Other sources of non-uniformity are associated to the light collection. Pointing geometry implies cells of pyramidal shape. A strong non-uniformity is induced by the focussing effect of these cells, particularly if the refraction index of the medium is high; CeF_3, with an index of 1.6 is here again much better than BGO (n = 2.15) or PWO (n=2.3). Finally much attention should be paid to avoid large absorption of the light in the medium. This is perhaps the most important problem for crystals with an emission spectrum in the UV like BaF_2 and other cross-luminescent crystals, as well as for low density materials because of the long pathlength of the photons to reach the photodetector. For dense crystals with an emission spectrum in the visible, a b_F term as small as 0.25% should be possible.

The last contribution b_C corresponds to the intercalibration errors. Frequent calibrations with an efficient monitoring system are necessary to maintain this contribution below 0.3%. The L3 BGO has proven that a well-designed fiber monitoring system can maintain the intercalibration within 0.3% for long periods of time and more than 10000 crystals. The high luminosity pp machines will also provide excellent means for a continuous calibration of the detector. At LHC a rate of 10 Hz is expected for electron pairs from Z° decays in the central region, which should allow a weekly calibration with about 100 electrons per channel. If there is a good inner tracker, individual e^+ or e^- can be used (E/p matching) at a rate, which could be as high as 100 per channel and per day. Finally one should be able to take advantage of the copious number of minimum ionizing particles for an almost continuous intercalibration control of all the channels. The CMS PWO calorimeter is aiming at a precision of 0.2% for the determination of intercalibration constants.

Taking all these contributions together it seems that a constant term b = 0.5%, although difficult, is not out of reach for a well designed homogeneous calorimeter.

Fig. 3 shows the energy resolution in the required energy range for several already existing or proposed detectors.

3- Scintillator requirements for High Energy Physics experiments

The criteria for the choice of the scintillator are based on the density, the scintillation properties and the radiation hardness. The cost is also an important issue taking into consideration the very large volumes of several cubic meters considered for such detectors.

3.1 Density

The compactness of the calorimeter is essential in order to reduce the detector volume and cost. This is achieved by using high stopping power materials resulting in a small radiation length X0. A high-density material ($\rho > 5 g/cm^3$) is therefore needed, but not necessarily with very high Z components as it is often quoted. The density should be preferably based on a high compactness of the crystal lattice (a large number of atoms per unit volume), keeping the atomic number of the components not too large in order to reduce the lateral shower size (Moliere radius: $R_M \approx X_0 \times (Z+1.2) / 37.74$). A small Moliere radius will limit the contamination of the energy measurement by other particles from the same or other events (pile-up) and help for the position reconstruction as well as for the π^0 rejection which will be the dominant background at LHC. Finally a compact material will reduce the lateral spread of the shower in a high magnetic field.

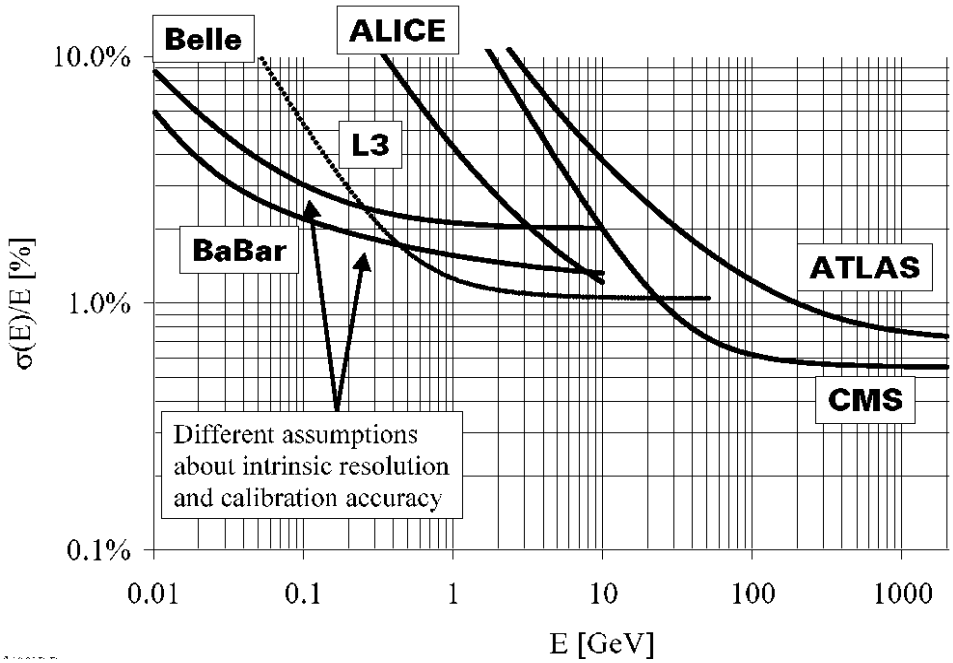

Figure 3: Energy Resolution of several HEP calorimeters

3.2 Scintillation properties

The pile-up will impose severe constraints to the readout, particularly at LHC. It is therefore essential to collect as much signal as possible within one bunch crossing (25 nsec), to keep a good signal to noise ratio in the electronics chain, and to reduce the fluctuations due to the timing jitter. Decay times of the order of the bunch crossing time or even less are necessary. Only crystals with optically allowed transitions (like the transition 5d $\rightarrow$ 4f for Ce^{3+}) can give rise to a fast scintillation. For some specific energy band configurations, more energetic excitations from the core states of the cation to the conduction band give rise to a recombination process from electrons of the anionic valence band. If the recombination energy is smaller than the gap between the valence and the conduction bands, Auger emission is impossible and the recombination is radiative. The induced luminescence (cross-luminescence) is intrinsically fast and temperature independent. This mechanism has been recognized as responsible for the emission of the fast component of BaF_2 [14,15]. It is likely that this cross-luminescence exists in many compounds and has not been discovered so far because of the high excitation energy required (typically above 15 eV).

As the electromagnetic calorimeter is usually installed in a magnetic field, readout by photodiodes is desired. This implies a sufficient light yield (a few 100 pe^- / MeV of deposited energy), and an emission wavelength above 250 to 300nm, where the quantum efficiency of the photodiodes is still high. A light emission in the visible spectrum will also ease the problems of light collection in long crystals.

The energy resolution of the calorimeter will strongly depend on all possible sources of non-uniformity. The light collection in a pointing geometry will introduce non-uniformity due to the focussing effect, which depends on the refractive index of the crystal. Fluoride crystals and glasses, with refractive index around 1.5, will limit this effect to a much smaller value (and therefore make it much easier to correct) than for the BGO (index 2.15) or PWO (index 2.3). The material can be intrinsically luminescent if it holds luminescent ions, or doped with a scintillating impurity. Intrinsic scintillators are generally preferred, as it is easier to control the light yield uniformity in long crystals. On the other hand, a controlled distribution of the doping could help correcting for the non-uniformity caused by the light collection in a pointing geometry. In addition the scintillation yield should be as independent as possible from the temperature. Large temperature coefficients increase the complexity of the detector

and of the software corrections, and temperature gradients between the front and back face of the crystals introduce non-uniformity's affecting the constant term of the resolution.

3.3 Radiation resistance

It is now well established that the most significant damage in inorganic scintillators results from the formation of color centers in the bulk of the material, which absorb part of the scintillation light on its path to the photodetector [16]. A short radiation length will therefore reduce the total attenuation for a given damage. In addition, as most of the color centers absorb mostly in the UV, crystals emitting light in the visible will be less severely damaged. Some surface effect may also occur but it is generally very small and saturates quickly with the dose.

The formation of color centers results from the trapping of electric charges by crystal defects and are therefore directly correlated with some impurities of the raw material A large effort should be made to purify the raw materials to the best quality. However, in some cases, a specific doping of the crystal has proved to be an efficient and economical way of significantly increasing the radiation hardness [17].

3.4 Cost considerations

The factors building-up the price of crystals must be identified and carefully analyzed. In some cases, the raw material of the desired purity can represent a substantial fraction of the cost. For this reason, all crystals based on the very rare Lutetium are discarded for applications were tons of crystals are needed, although a lot of them are very fast cross-luminescent materials ($KLuF_4$, K_2LuF_5) or very efficient scintillators (LSO). Cerium is much more favorable, as it is the most common of the rare-earth components. The purification of Cerium against the other rare-earth components may be difficult and expensive, but our first studies show that this is not a critical parameter. The growing technique and the crucible material are dominant parameters and crystals, which can be grown for instance by using the relatively cheap Bridgeman method in graphite crucibles, have obvious advantages. The cost of the energy plays also an important role, as a combination of the melting temperature and the pulling rate. From this point of view, the high melting point of GSO (1900 °C) and the high segregation factor of cerium in this matrix implying a low pulling rate (1 to 2mm / hour) may put some limits to the minimum obtainable price for such a crystal. On the other hand, the low melting point of PbF_2 (822°C) and the abundance of the raw material make it a potentially low cost material. A high crystal density, directly limiting the total volume for a calorimeter, but also the crystal dimensions and consequently the furnace and crucible sizes will be a major parameter of the total cost for a crystal based detector. Finally, the very good mechanical properties of PbF_2 or CeF_3 for instance, allow a high production yield of the mechanical processing, which will also reduce the final cost.

4- Crystal Calorimeters in the world

The continuous increase of the energy obtained in particle accelerators puts more and more emphasis on calorimetry as a tool to analyze the products of the collisions. As at the same time the proportion of interesting events is becoming smaller and smaller, the demand for high precision homogeneous calorimeters is continuously increasing. This is why the last 20 years have seen a dramatic boost in the development of scintillators and associated readout techniques, directly related to a dozen of projects of impressive dimensions. Table 1 gives a list of these projects and of their main characteristics. The properties of the crystals used in these calorimeters are listed in Table 2 where some qualitative figures of merit are also indicated.

Table 1: Crystal Calorimeters in the world

	Crystal Ball	CLEO II	L3	BaBar	Belle	*L** LoI	*GEM* EoI	*CMS* EoI	*L3P* EoI	ALICE	CMS
Where	SPEAR	CESR	LEP	SLAC	KEK	SSC	SSC	LHC	LHC	**LHC**	**LHC**
When	1972	Late 1980's		1999						**2005**	
Beam	e^+e^-	e^+e^-	e^+e^-	e^+e^-	e^+e^-	p p	p p	p p	p p	**ion ion**	**p p**
Beam Energy	4	6	100	9+3.1	8+3.5	20	20	8	8	**5.5·A**	**7**
	GeV					TeV					
Crystal	NaI(Tl)	CsI(Tl)	BGO	CsI(Tl)	CsI(Tl)	BaF_2	BaF_2	CeF_3	CeF_3	**$PbWO_4$**	**$PbWO_4$**
Number [k]	0.7	7.8	11.4	6.8	8.8	26	15	45	100	**36**	**82**
Length [X_0]	16	16	21.5	16	16	24.5	24.5	25	25	**22**	**25**
Photodetector	PMT	Si PD	Si PD	Si PD	Si PD	V4T	V4T	Si PD	VPD	**Si PD**	**APD/V3T**
B [T]	0	1.5	0.5	1	1	0.75	0.8	4	1	**≤ 0.5**	**4**
f_{BC} [MHz]	1.3	2.8	0.091	238	10-508	60	60	67	67	**8**	**40**
				New! asymmetric b-factory		Proposals				*New!* Large Hadron Collider	

Table 2: Scintillators used in HEP calorimeters (from P. Denes)

	NaI (1)	**BaF_2**	**CsI (1)**	**CeF_3**	**BGO ($Bi_4Ge_5O_{12}$)**	**PWO ($PbWO_4$)**
X [cm]	**2.59**	**2.03**	**1.86**	**1.66**	**1.12**	**0.92**
ρ [g/cm^3]	**3.67**	**4.89**	**4.53**	**6.16**	**7.13**	**8.2**
τ [ns]	**230**	**0.6 620**	**1050**	**30**	**340**	**15**
λ [nm]	**415**	**230 310**	**550**	**310 340**	**480**	**420**
n λ_{max}	**1.85**	**1.56**	**1.80**	**1.68**	**2.15**	**2.3**
L Y [%NaI-Tl]	**100**	**5 16**	**85**	**5**	**10**	**0/5**

5- Conclusions

Can other fields, like Medical Imaging benefit from this work? The answer is certainly yes if we can apply similar methods and take advantage of the large concerted effort which has been made for High Energy Physics developments. Clearly the impressive progress over the past 10 years in the understanding of fundamental mechanisms can be directly used to develop suitable scintillators for other applications. Several candidates are already actively studied by different groups with potential application in low energy γ ray imaging. Some of them are listed in Table 3 with their main properties.

Scintillator	*Density* ρ (g/cm3)	*Light Yield Ph/MeV*	Emission Peak λ (nm)	*Decay Time* λ (ns)	*Hygroscopic*
$YAlO_3$:Ce (YAP)	**5.55**	**16 000**	**350**	**30**	**No**
Gd_2SiO_5 :Ce (GSO)	**6.7**	**8 000/1 000**	**440**	**60 / 600**	**No**
Lu_2SiO_5 :Ce (LSO)	**7.4**	**27 000**	**420**	**40**	**No**
$LuPO_4$:Ce (LPO)	**6.2**	**13 000**	**360**	**24**	**No**
$Lu_3AL_5O_{12}$:Ce (LuAG :Ce)	**6.67**	**3 000/11 000**	**300 / 500**	**100**	**No**
$Lu_3AL_5O_{12}$:Sc (LuAG :Sc)	**6.67**	**22 400**	**275**	**610**	**No**
$LuAlO_3$:Ce (LuAP)	**8.34**	**9600**	**380**	**11/28**	**No**

Table 3: New Scintillators for Nuclear Medicine

A few prototype cameras are already under development for medical applications. High Energy Physics is acting as a driving force in the development of new scintillators because of the size of the projects and of the very challenging requirements imposed by the extreme difficulty of the physics to be done. The reasons for the success obtained so far are due to the interdisciplinary nature of the effort being made. A similar methodology needs to be used to develop Industrial and Medical Imaging techniques. The role of our community of scintillator experts is now to attract communities of potential user's and to work in close collaboration with them on the development of the instrumentation best suited to their needs.

References

1. Alkali halide scintillation counters, R. Hofstadter, Phys. Rev., Vol74, 1948, p100
2. M. Oreglia et al, Phys. Rev. D 25 2295 (1982)
3. L3 Collab., B. Adeva et al., Nucl. Inst. Meth. A289 (1990) 35
4. Y. Kubota et al., The CleoII detector, CLNS 91/1122, 1991
5. The Crystal Barrel collaboration
6. R.E Ray, The KTeV Pure CsI Calorimeter, Proc. Fifth International Conference on Calorimetry in High Energy Physics, World Scientific, New Jersey, Sept94, p110
7. The Belle Collaboration, Technical Design Report, KEK Report 95-1, April 95
8. The BaBar Collaboration, BaBar Technical Design Report, SLAC-R-95-457
9. R. Novotny et al., Nucl. Inst. Meth. A262 (1987) 340
10. GEM Letter of Intent, SSCL SR-1184, November 1991
11. CMS Technical Proposal, CERN/LHCC 94-38, December 1994
12. L3P Letter of Intent, CERN/LHCC 92-5 (1992)
13. R&D Proposal for the study of new fast and radiation hard scintillators for calorimetry at LHC: Crystal Clear Collaboration , CERN / DRDC P27 / 91-15, project RD-18
14. Y.Valbis et al, JETP Lett. 42 (1985) 172
15. S. Kubota et al, NIM A242 (1986) 291
16. P. Lecoq, P.J. Li, B. Rostaing, NIM A300 (1991) 240-258
17. A. Annenkov et al, NIM A426 (1999) 486-490

Scintillator Requirements for Medical Imaging*

William W. Moses

Lawrence Berkeley National Laboratory, University of California, Berkeley, CA 94720 USA

Abstract: Scintillating materials are used in a variety of medical imaging devices. This paper presents a description of four medical imaging modalities that make extensive use of scintillators: planar x-ray imaging, x-ray computed tomography (x-ray CT), SPECT (single photon emission computed tomography) and PET (positron emission tomography). The discussion concentrates on a description of the underlying physical principles by which the four modalities operate. The scintillator requirements for these systems are enumerated and the compromises that are made in order to maximize imaging performance utilizing existing scintillating materials are discussed, as is the potential for improving imaging performance by improving scintillator properties.

Keywords: Medical Imaging, Planar X-Ray, X-Ray CT, SPECT, PET

1. Introduction

The first medical image is arguably the x-ray image that Röntgen took of his wife's hand in 1895. While Röntgen used photographic film to convert the x-rays into a form observable by the human eye, within one year powdered phosphor materials such as $CaWO_4$ replaced photographic film as the x-ray conversion material [1, 2], and have been an integral part of medical imaging devices ever since. In fact, virtually all medical imaging modalities that require the detection of energetic photons (x- and γ- rays) use scintillators for their detection. These modalities include planar x-ray imaging, x-ray computed tomography (x-ray CT), SPECT (single photon emission computed tomography) and PET (positron emission tomography).

The volume of scintillator required each year for medical imaging devices is considerable. Table 1 estimates the number of medical imaging units sold annually and the typical amount of scintillator in each type of unit. All in all, about 175 metric tons of scintillator are required annually. The various medical imaging techniques that use scintillators all have different requirements. In principle, the ideal scintillator (one with high density, high effective atomic number, high luminous efficiency, short decay time, no afterglow, good spectral match to photodetectors, and low cost) could be used for each application. However, the ideal scintillator does not exist and so each modality must compromise, choosing from available materials the most suitable combination of properties. This paper describes the physical basis of the four medical imaging modalities listed in the paragraph above, the requirements for the scintillator in these modalities, the scintillators presently used by each of them, and the improvements in scintillator properties that would most benefit each application.

Modality	Annual Production	Scintillator Content	Annual Scint. Volume
Planar X-Ray	1,000,000 screens	50 cc / screen	50,000 liters
X-Ray CT	2,000 scanners	75 cc / scanner	150 liters
SPECT	2,000 scanners	3,000 cc / scanner	6,000 liters
PET	50 scanners	10,000 cc / scanner	500 liters

Table 1. Annual world-wide volume of scintillator required by medical imaging instruments.

* This work was supported in part by the U.S. Department of Energy under Contract No. DE-AC03-76SF00098, and in part by Public Health Service Grants No. R01-CA48002, R01-CA67911, & P01-HL25840 from the National Institutes of Health.

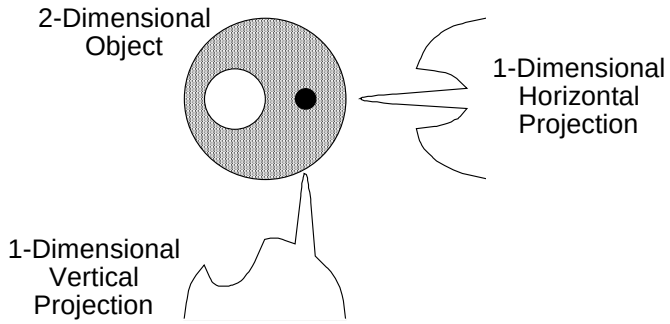

Figure 1. Computed Tomography. The 1-dimensional horizontal and vertical projections (the line integral of the density along parallel horizontal and vertical lines) are shown adjacent to the 2-dimensional object that they were taken of. Computed tomography is the process of reconstructing the 2-dimensional object given its 1-dimensional projections from all angles.

2. General Considerations

In all the systems considered in this paper, it is necessary to image photons whose energy is between 15 keV and 511 keV. The detection system must be very efficient, as safety concerns cause regulatory agencies to limit the total radiation dose that can be administered to a patient. Thus, reduced statistical noise cannot be obtained by increasing the source strength (*i.e.* the integrated x-ray flux or the injected activity), and so must be obtained by maximizing detection efficiency. At the 15–511 keV photon energies used for medical imaging, the attenuation length in tissue is 2–10 cm. This is similar to the distance that gamma rays need to travel to exit the body, so a significant fraction of the internally emitted gamma rays interact within the patient. Due to the low effective atomic number of tissue, most of these interactions result in Compton scatter, and most of the scattered photons continue to undergo Compton scattering until they leave the body. While the net radiation flux impinging upon the detector usually contains 10%–50% unscattered gammas (which can be used to form an accurate image), the majority are Compton photons that form a background. Thus, the detection system must be capable of reducing this Compton background, usually by physical collimation or by measuring the energy of each detected photon with 8%–20% full-width at half-maximum (fwhm) resolution.

X-ray CT, SPECT, and PET make use of the mathematical technique of computed tomography [3-5]. Briefly stated, computed tomography is a process where a 2-dimensional image of an object is formed using multiple 1-dimensional projections of that object, as demonstrated in Figure 1. The 2-dimensional object is a large circle of uniform density in which a medium circle of lower density and a small circle of higher density are embedded. The one dimensional projection of the object in the vertical direction is shown below the object. This projection is what would result if a planar x-ray of the object were taken, and represents the line integral of the 2-dimensional object's density along parallel, vertical lines that cross the object. The hemisphere corresponding to the large circle is clearly seen, modified by a dip due to the low density region and a spike due to the high density region. To the right of the object is its one dimensional projection in the horizontal direction. Again the hemisphere with the associated dip and spike are seen, but the positions of the dip and spike have changed because of the change in viewing angle. While the details are beyond the scope of this paper, taking one dimensional projections at all angles around an object (not just the two shown in Figure 1) provides enough information to reproduce a 2-dimensional image of the object.

3. Planar X-Ray Imaging

With planar x-ray imaging, x-rays are generated by accelerating an electron beam toward a metal cathode, where the impact creates bremsstrahlung photons. These x-ray photons have a broad range of energies, with a mean energy of approximately half that of the incident electron energy (which is determined by the accelerating voltage). Depending on the body part to be imaged, this voltage is from 25 kV to 300 kV, resulting in individual x-ray energies ranging from approximately 15 keV to 200 keV. The x-rays undergo differential absorption as they penetrate the body, and the emerging x-ray flux is measured to form an image. As the incident x-ray flux is not monochromatic, there is little additional information (such as the identification of Compton scattered photons) that can be obtained by measuring the energy. This, coupled with the high x-ray fluxes (10^{10} / sec / mm^2), dictate that individual quanta are not measured, and detectors that integrate the flux for the duration of the x-ray exposure are used.

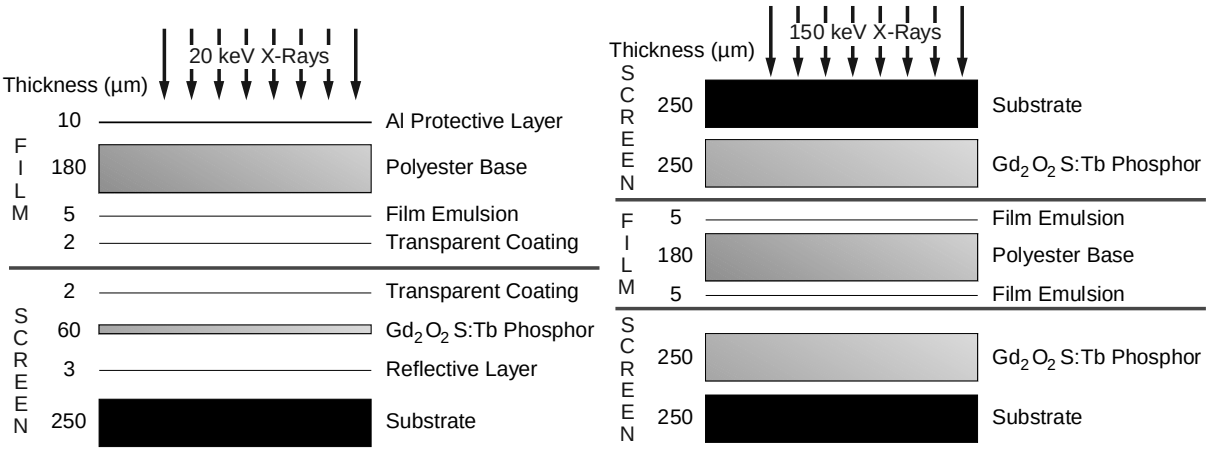

Figure 2. X-ray film / screen combination. The design at the left is for mammography, which requires extremely high spatial resolution. Specific resolution-enhancing features include thin scintillator screen and emulsion only on the side of the film substrate adjacent to the phosphor screen. The design at the right is for chest x-rays, which requires extremely high detection efficiency. Specific efficiency-enhancing features include dual, thick phosphor screens and emulsion on both sides of the film substrate.

Typical x-ray detector systems are shown in Figure 2 [6]. X-rays that penetrate the patient (and subsequent collimator) pass through a sheet of photographic film and strike a phosphor (powdered scintillator) screen. The subsequent scintillation photons expose the photographic film, which is mechanically separate from (but adjacent to) a phosphor screen. The film is then removed and chemically developed to form an image. Where possible, the x-rays are incident from the film side of the phosphor screen because of their exponential attenuation in the screen — with this geometry the maximum number of x-rays stop at the surface closest to the film. The scintillation photons undergo multiple scatters due to the powdered scintillator grains. This limits the lateral spread of the scintillation light (as compared to what would be obtained with a large, optically clear scintillator plate) and so enhances the spatial resolution. However, the lateral spread increases with increasing phosphor plate thickness, so applications that require high spatial resolution (such as mammography) use thin phosphor screens. In addition, spatial resolution can be degraded by scintillation photons that pass through the emulsion and are reflected at the back surface of the film substrate and then detected by the emulsion. This effect can be minimized either by an absorptive coating on the back surface of the film substrate or a dye in the film substrate that absorbs the scintillation light.

Material	Luminosity (photons/MeV)	Density (g/cm^3)	Wavelength (nm)	Shape
Gd_2O_2S:Tb	70,000	7.3	545	Good
LaOBr:Tb	67,000	6.3	425	Plate
Y_2O_2S:Tb	60,000	4.9	545	Good

Table 2. Materials used for planar x-ray imaging and their properties.

The left side of Figure 2 shows a film / screen system that is optimized for spatial resolution such as is used for mammography, which require high (~75 µm) spatial resolution when imaging low energy (~20 keV) x-rays. Such systems typically utilize a single, 60~µm thick phosphor screen and photographic film with emulsion on one side. The opposite trade-off is found in chest x-ray systems, as shown on the right side of Figure 2, which must be efficient for imaging higher energy (~150 keV) x-rays. These systems have thick (250 µm) phosphor screens placed on either side of the photographic film, which has emulsion on both sides.

The requirements for x-ray phosphors are, in order of decreasing importance, (1) high luminous efficiency (>60,000 photons/MeV), (2) high density (>7 g/cm^2), (3) emission wavelength well matched to the peak response wavelength of the photographic film (550 nm), (4) good particle shape (roughly spherical, 3–10 µm in diameter), and (5) good manufacturing properties (such as the ability to be made into a slurry without clumping). Table 2 lists the commonly used x-ray phosphors, as well as some of their relevant properties [7]. The Gd_2O_2S:Tb material is almost universally used due to its excellent combination of properties.

Opportunities for improving the scintillators used for planar x-ray imaging are somewhat limited as they are already near the theoretical limits. However, there is a need for higher x-ray "speed" in order to reduce the radiation dose to patients — many imaging procedures produce skin burns on the patient from the x-rays. In this context, "speed" does not refer to decay time, but is analogous to its definition for photographic film. That is, it refers to (the inverse of) the length of time necessary to achieve a proper exposure, given a fixed incident photon flux (and assuming a given image quality). A 10% increase in the speed is considered a very significant improvement. Such an increase could come from increased luminescent efficiency, decreased attenuation length, or development of microscopic scintillator structures (such as columnar CsI:Tl) that decrease the lateral light spread for a given screen thickness. It is also possible that development of phosphors whose emission wavelength is optimized for detection by silicon detectors (such as CCD's or amorphous silicon flat panel devices) would be useful. Electronic (as opposed to film based) readout of phosphors is an active area of research, and phosphors with 600–1000 nm emission wavelengths (and their higher number of emitted photons for a given energy conversion efficiency) would help these efforts.

4. X-Ray CT

Material	Luminosity (photons/MeV)	Density (g/cm^3)	Decay (µs)	Afterglow (@ 3 ms)	Form
$CdWO_4$	14,000	7.9	5, 20	<0.1%	Crystal
$(Y,Gd)_2O_3$:Eu,Pr	19,000	5.9	1000	3%	Ceramic
Gd_2O_2S:Pr,Ce,F	21,000	7.3	3	<0.1%	Ceramic

Table 3. Materials used for x-ray CT imaging and their properties.

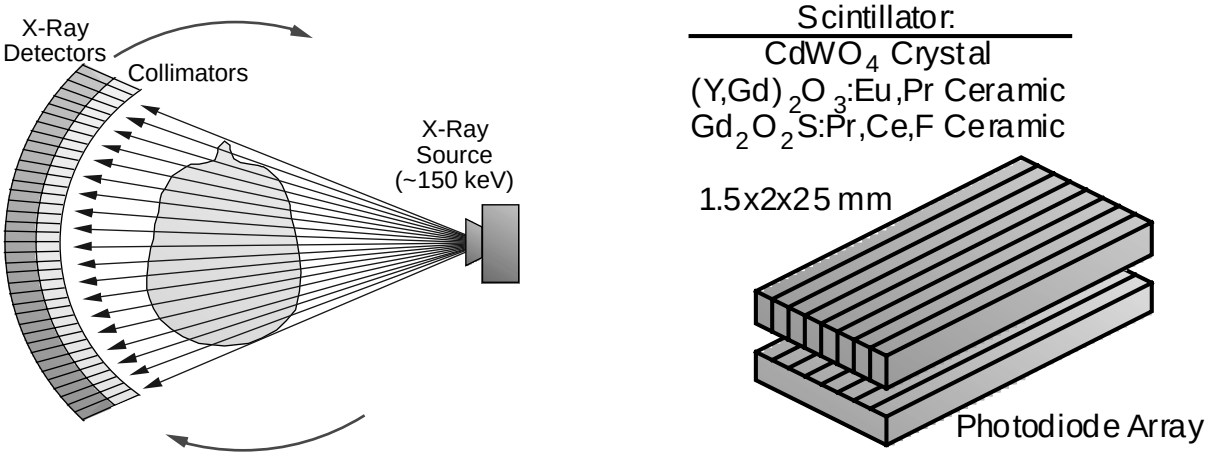

Figure 3. X-ray computed tomography system. On the left, an x-ray source illuminates the patient, while septa in front of the detectors reduce Compton scattered events. The source and detection system orbit around the patient. On the right is a typical detection system, consisting of scintillator crystals read out by photodiodes.

An x-ray CT system, as shown in Figure 3, consists of an x-ray source and an arc of individual x-ray detectors that monitor the transmitted x-ray flux [6]. As with planar x-ray imaging, the combination of the high x-ray photon flux and lack of a monochromatic source dictate that the energy of individual quanta are not measured, and so mechanical collimation is used to reduce Compton scatter. The entire assembly rotates around the patient (with a period of approximately 2 s), continuously moving but acquiring data in ~1 ms intervals. Typical x-ray detector elements, also shown in Figure 3, consist of crystalline or ceramic scintillator materials individually coupled to a photodiode. The photodiode output current is digitized with 20 bit dynamic range. Computed tomography converts this data into cross-sectional images that are stacked to form a 3-dimensional volumetric image.

The technique of computed tomography essentially makes use of the small systematic differences in nearly adjacent views to create an image. With x-ray imaging, these differences can be quite small, requiring that the transmitted flux be measured with 1–10 ppm (parts per million) accuracy. Such high accuracy implies that systematic errors must be rigorously controlled, both by minimizing the sources of error and by software corrections of the remaining errors. Such errors include beam hardening (the fact that the absorption coefficient μ is energy dependent and the x-ray beam is not monochromatic implies that the high energy portion of the x-ray spectrum is attenuated less than the low energy portion), x-ray tube drift (caused by x-ray tube acceleration voltage fluctuations and motion from cathode deformation caused by electron beam heating), and partial volume effect (the fact that each voxel in the patient does not contain material with a single, uniform μ value). Systematic effects from the scintillator that must be minimized include afterglow (decay components that extend beyond the 1 ms integration time), temperature dependence, and radiation damage (at the 10 rad level) [8]. Ceramic materials often show more uniformity than crystalline materials, as by nature they "average" the properties of many (very small) scintillator crystals.

The requirements for x-ray CT scintillators are, in order of decreasing importance, (1) low afterglow (<1% @ 3 ms), (2) high stability (chemical, temperature, and radiation damage), (3) high density (>6 g/cm^2), (4) emission wavelength well matched to photodiode readout (500–1000 nm), and (5) high luminous efficiency (>15,000 photons/MeV). Table 3 lists the commonly used scintillators for x-ray CT, as well as some of their relevant properties [9]. All three of the materials listed are presently used in commercial CT scanners. It is interesting to

note that several of the materials have more than one dopant. In general, the first dopant is a luminescent ion, while the subsequent dopants are used to reduce the afterglow.

There are opportunities for improving the scintillators used for x-ray CT imaging, as none of the properties (with the possible exception of the density) are already near fundamental theoretical limits. The most desired improvements are in the density and the stability, particularly with regards to radiation damage and temperature dependence of the luminous efficiency. Increase in the luminous efficiency is not deemed important, as the statistical noise is dominated by counting statistics of the incident flux, not the x-ray / photodetector response. Some of the materials could use improvement in specific areas. The $(Y,Gd)_2O_3$:Eu,Pr material would significantly benefit from a shorter decay time, while the Gd_2O_2S:Pr,Ce,F material would benefit from improved optical transparency. Finally, the fact that there are three commercially accepted materials (rather than one dominant material) suggests that the best properties of each material might be combined to create an improved material.

5. Spect

Nuclear medical imaging is a generic term that covers many imaging techniques, with the common theme being that ionizing radiation originating from within the body is detected and imaged in order to determine something about the physiology or anatomy of the subject [5, 6, 10-12]. With SPECT, a biologically active compound (*i.e.* a drug) is introduced into the body (in trace quantities) either by injection or inhalation. This compound then accumulates in the patient and the pattern of its subsequent radioactive emissions is used to estimate the distribution of the radioisotope and hence of the tracer compound. The radioisotopes used for SPECT are gamma ray emitters with monochromatic emissions between 60 keV and 511 keV, with the 140 keV emissions from ^{99m}Tc being the most common.

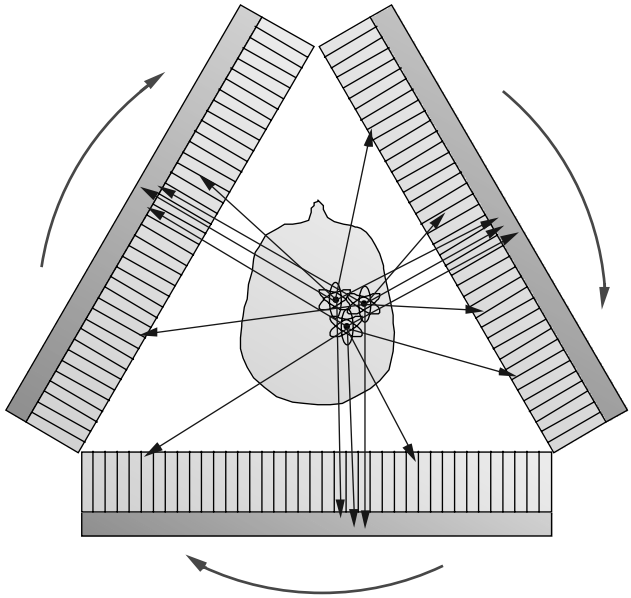

Figure 4. SPECT Camera Schematic. A collimator blocks gamma rays that are not traveling normal to its surface, and those gammas that pass through the collimator are detected with a planar position sensitive detector. The assembly rotates around the patient to provide the many projections necessary for computed tomography.

A typical SPECT camera is shown schematically in Figure 4. The emitted gamma rays are detected by two-dimensional position sensitive detectors. The direction of the gamma rays is determined by a collimator placed between the detector array and the patient — photons that are not traveling in the desired direction are absorbed by the collimator. The collimator and detector combination (and their associated electronics and mechanical support) form what is

known as a gamma camera “head”. While multiple heads increase the detection efficiency of a SPECT camera (and the cost), there is little efficiency gain above three heads, so most SPECT cameras have between one and three heads. Each head measures a planar projection of the activity in the patient, and by simultaneously rotating the heads, the requisite set of projections to perform computed tomography is obtained.

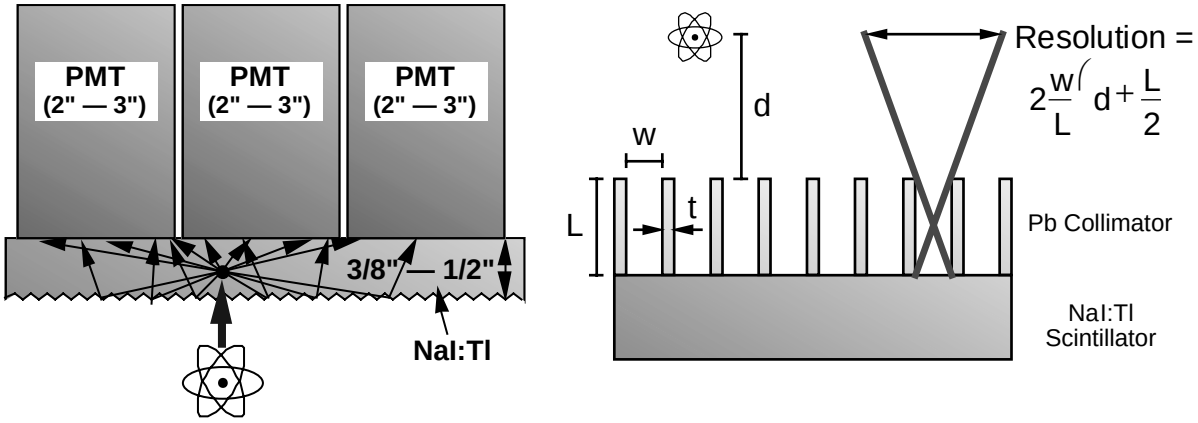

Figure 5. Anger Camera. Scintillation light from gamma ray interactions is detected by multiple photomultiplier tubes. The interaction position is determined by the ratio of the analog signals, and the energy by the analog sum of the signals.

The most commonly used gamma detector for SPECT is the Anger camera, which is named for its inventor [13]. A schematic of an Anger camera is shown in Figure 5. A plate of NaI:Tl scintillator crystal is optically coupled to many photomultiplier tubes. When a gamma ray interacts in the crystal, the resulting scintillation photons are emitted isotropically and are detected by several of the photomultiplier tubes. The position of the gamma ray interaction is then determined by the analog ratio of the photomultiplier tube output signals, and the gamma ray energy is determined by the sum of these signals. The accuracy of the position measurement is improved with increasing scintillator luminous efficiency.

The thickness of the NaI:Tl crystal determines the efficiency of the camera. As its attenuation length for 140 keV gamma rays is 4 mm, the 9–12 mm thick plates commonly used in SPECT systems provide nearly complete absorption. The scintillator surface not coupled to the photomultiplier tubes strongly affects the light distribution observed by the photomultiplier tubes and is often prepared with a proprietary surface treatment to optimize position and energy resolution. Care is needed near the edges of the scintillator crystal, as reflections from the crystal edges cause the dependence of the measured light distribution on the interaction position to be much weaker near the sides than near the middle. A typical Anger camera has 9% fwhm energy resolution and 3.5 mm fwhm position resolution for 140 keV gammas.

While the Anger camera is an important component of a SPECT imager, the performance of a SPECT camera is almost entirely determined by the collimator [14]. The collimator is usually made from cast lead with hexagonal cross section holes arranged in a honeycomb fashion. Each hole can be thought of as having a diameter w and a length L, separated from its neighbors by a lead septum of thickness t (typically 0.2 mm). The spatial resolution is determined by the collimator geometry and is given by

$$\text{Resolution} = 2\frac{w}{L}d + \frac{L}{2} \quad , \qquad (1)$$

where d is the distance from the collimator surface to the object being imaged. From Equation 1 we can see that the resolution scales linearly with the aspect ratio w/L of the collimator, and as L is typically 1–3 cm and d is typically tens of centimeters, increases

roughly linearly with the distance d from the collimator. While arbitrarily high spatial resolution can be achieved with a collimator by reducing w/L, more modest spatial resolution is usually obtained because this aspect ratio greatly affects the efficiency. The collimator transmission fraction is

$$\text{Efficiency} = \left(\frac{w}{2L} \right)^2 , \qquad (2)$$

so while the resolution improves linearly with w/L, the efficiency decreases quadratically. For a typical "all-purpose" collimator, the spatial resolution is 6.2 mm fwhm at a distance of 5 cm and the efficiency is 0.023%. Thus the spatial resolution of a SPECT image is determined by the collimator, not the Anger camera resolution (which is known as the intrinsic resolution).

The scintillator requirements for SPECT are, in order of decreasing importance, (1) high luminous efficiency (for good energy resolution and intrinsic spatial resolution), (2) high density (>3.5 g/cm^3), (3) low cost (<\$15/cm^2, where the area referred to is the surface area around the patient that must be surrounded with 3 attenuation lengths of scintillator), (4) an emission wavelength well matched to photomultiplier tube readout (300–500 nm), and (5) short decay time (<1 μs). Table 4 lists the commonly used scintillators for SPECT, as well as some of their relevant properties. Virtually the only material in use is NaI:Tl — CsI:Tl is only used in experimental devices using photodiode (rather than photomultiplier tube) readout.

Material	Luminosity (photons/MeV)	Density (g/cm^3)	Decay Time (ns)	Wavelength (nm)
NaI:Tl	38,000	3.7	230	415
CsI:Tl	60,000	4.5	1000	545

Table 4. Materials used for SPECT imaging and their properties.

There are some opportunities opportunities for improving the scintillators used for SPECT imaging. The most desirable improvements would be increased luminous efficiency. This would improve the energy resolution from its present 9% fwhm for 140 keV gamma rays, and also allow the same intrinsic resolution to be achieved with fewer (but larger) photomultiplier tubes.

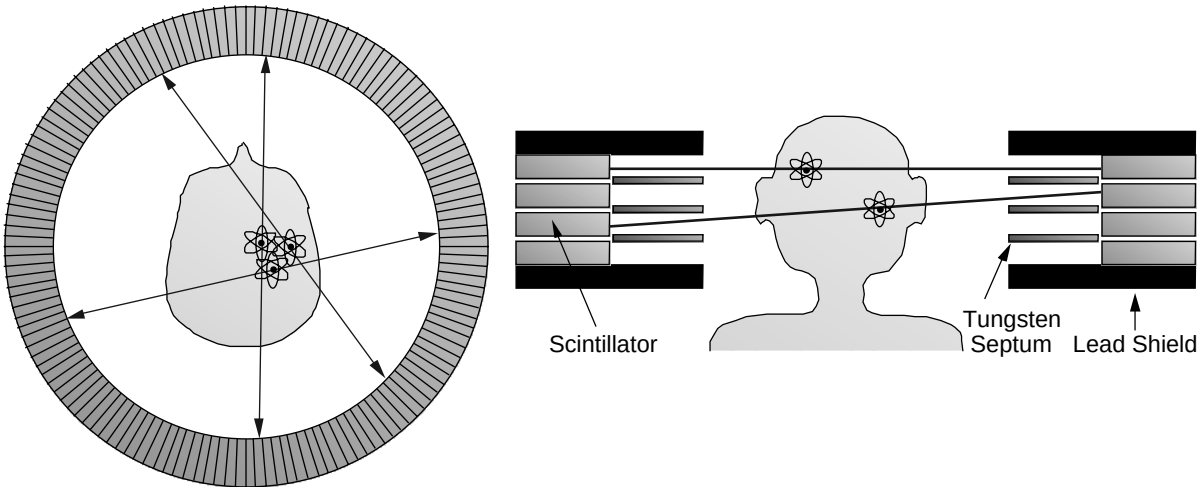

Figure 6. PET Camera Schematic. Positron annihilations yield back to back 511 keV photons, which are individually detected in a ring of photon detectors, shown on the left. Pairs are identified by time coincidence. Multiple rings are stacked up, as shown on the right, to create a 3-dimensional image.

6. Pet

PET (Positron Emission Tomography) [15] is similar to SPECT, in that a radioactively labeled drug is imaged, but PET employs positron emitting radioisotopes. The emitted positron rapidly thermalizes in the patient's tissue, attracts an electron, and annihilates to form back-to-back 511 keV photons. A typical PET camera, shown in Figure 6, consists of a planar ring of small photon detectors, with each photon detector placed in time coincidence with *each* of the individual photon detectors on the other side of the ring. When a pair of photon detectors simultaneously detect 511 keV photons, a positron annihilated somewhere on the line connecting the two detectors. The method of using time coincidence between two detectors (rather than a collimator and one detector) to restrict events to a line is known as electronic collimation, and is much more efficient than the mechanical collimation used in SPECT.

The set of all lines connecting detectors (known as chords) makes the requisite set of projections to perform computed tomography for a single plane. Multiple detector rings are stacked on top of each other to obtain images from multiple slices, and thus a three-dimensional image of the patient. Planes of tungsten septa placed between detector planes are often used to shield the detectors from Compton scattered photons emanating from other parts of the body, and images taken in this geometry are often known as "2-D PET" images. Coincidences between nearly adjacent "cross-plane" rings are usually added to the closest "direct plane" to increase detection efficiency. If the septa are removed, the efficiency is greatly increased (as coincidences from widely separated planes can be accepted), but the backgrounds also increase significantly. However, the signal to noise ratio improves in some situations, and this mode of operation is known as "3-D PET."

The most commonly used PET detector module is known as a block detector, and a schematic is shown in Figure 7 [16]. A block of BGO scintillator crystal is partially sawn through to make a group of quasi-independent crystals that are optically coupled to four photomultiplier tubes. When a gamma ray interacts in the crystal, the resulting scintillation photons are emitted isotropically but the saw cuts limit (but do not entirely prevent) their lateral spread as they travel toward the photomultiplier tubes. The position of the gamma ray interaction is then determined by the analog ratio of the photomultiplier tube output signals, and the gamma ray energy is determined and a timing pulse generated by the sum of these signals. The thickness of the BGO crystal determines the efficiency of the camera. As its attenuation length for 511 keV gamma rays is 1.2 cm, the 30 mm thick BGO crystals employed in PET systems provide nearly complete absorption. The coincidence timing efficiency is limited by the decay time of BGO — the photoelectron (p.e.) rate immediately after a 511 keV photon interaction is approximately 0.5 p.e./ns. A typical PET detector module has 20% fwhm energy resolution, 2 ns fwhm timing resolution and 5 mm fwhm position resolution for 511 keV gammas.

The scintillator requirements for PET are, in order of decreasing importance, (1) short attenuation length (<1.2 cm), (2) short decay time (<300 ns), (3) low cost (<\$100/cm^2, where the area again is that area surrounding the patient that must be covered with scintillator), (4) high luminous efficiency (>8,000 photons/MeV), and emission wavelength well matched to photomultiplier tube readout (300–500 nm). Table 5 lists the commonly used scintillators for PET, as well as some of their relevant properties [17]. The most common material in use is $Bi_4Ge_3O_{12}$ — Lu_2SiO_5:Ce is just beginning to be incorporated into PET scanners.

In contrast to the previously mentioned modalities, there are significant opportunities for improving the scintillators used for PET imaging. Substantial improvements in luminous efficiency (and hence energy resolution) and decay time (as compared to BGO) should be possible, as these are far from the theoretically possible limits. LSO goes a long way toward closing this gap, but improvements beyond those possible with LSO (such as the energy resolution) would also be valuable.

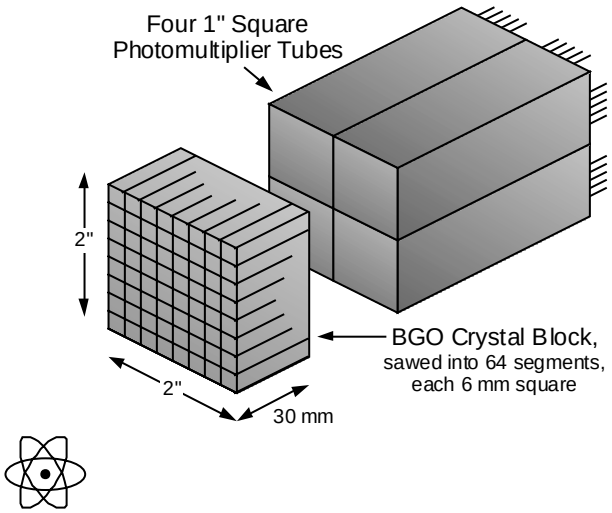

Figure 7. PET Detector Module. Scintillation light from gamma ray interactions is detected by multiple photomultiplier tubes. The interaction position is determined by the ratio of the analog signals, and the energy by the analog sum of the signals.

7. Conclusions

Material	Luminosity (photons/MeV)	Atten. Length (cm)	Decay Time (ns)	Wavelength (nm)
$Bi_4Ge_3O_{12}$	8,000	1.1	300	480
Lu_2SiO_5:Ce	25,000	1.2	40	420

Table 5. Materials used for PET imaging and their properties.

Scintillators have been used for over 100 years to non-invasively image the interior of the human body. Many techniques in use today involve imaging photons with energies of 15–511 keV, as these photons can be produced by x-ray sources or radioisotope decay, penetrate the body with reasonable probability, and be detected with high efficiency and good spatial resolution. Detectors for these applications have seen many years of development and refinement, and generally possess high detection efficiency (to maximize image quality for a given patient radiation dose), good energy resolution (to minimize background from Compton scatter in the patient), low cost (as there is a competitive commercial market for these devices), and good (75 μm–5 mm) spatial resolution. While the scintillator materials used for each imaging application are highly optimized, there is potential and desire for improvement (without violating theoretical or practical limits) for virtually applications.

8. Acknowledgments

I would like to acknowledge Dr. Stephen Derenzo, Dr. Thomas Budinger, and Dr. Ronald Huesman for many interesting conversations, Dr. Ruvin Deych for sharing his knowledge of x-ray CT, and Dr. James Colsher and Dr. Harold Kidd for their insights into the commercial aspects. This work supported in part by the Director, Office of Science, Office of Biological and Environmental Research, Medical Science Division of the U.S. Department of Energy under Contract No. DE-AC03-76SF00098, and in part by the National Institutes of Health, National Cancer Institute under grants No. R01-CA48002 and R01-CA67911, and National Institutes of Health, National Heart, Lung, and Blood Institute under grant No. P01-HL25840.

References

1. T.A. Edison. Nature (1896) 470.
2. M. Levy. Fortschr. auf dem Geb. d. Röntgenstrahlen 1 (1897) 75.
3. A.M. Cormack. J. Appl. Phys. 34 (1963) 2722–2727.
4. D.E. Kuhl and R.Q. Edwards. Radiology 80 (1963) 653–662.
5. A. Macovski. *Medical Imaging Systems* 1-256 (Prentice Hall, Englewood Cliffs, NJ, 1983).
6. E. Krestel. *Imaging Systems for Medical Diagnosis* 1-636 (Siemens Aktiengesellschaft, Berlin, 1990).
7. N. Miura. in *Phosphor Handbook* (eds. S. Shionoya & W. M. Yen) 521–537 (CRC Press, Boca Raton, FL, 1999).
8. R. Deych, J. Dobbs, S. Marcovici, *et al.* in *SCINT95: International Conference on Inorganic Scintillators and Their Applications* (eds. P. Dorenbos & C. W. E. van Eijk) 36–39 (Delft University Press, Delft, The Netherlands, 1995).
9. B.C. Grabmaier. in *Heavy Scintillators for Scientific and Industrial Applications* (eds. F. De Notaristefani, P. LeCoq & M. Schneegans) 65–74 (Editions Frontieres, Gif-sur-Yvette, France, 1993).
10. M.P. Sandler, R.E. Coleman, F.J.T. Wackers, *et al. Diagnostic Nuclear Medicine* 1-1549 (Williams & Wilkins, Baltimore, MD, 1996).
11. W.R. Hendee and R. Ritenour. *Medical Imaging Physics* 1-781 (Mosby Year Book, St. Louis, MO, 1992).
12. S. Webb. *The Physics of Medical Imaging* 1-633 (Institute of Physics Publishing, Bristol, 1993).
13. H.O. Anger. Rev. Sci. Instr. 29 (1958) 27–33.
14. B.M.W. Tsui, D.L. Gunter, R.N. Beck, *et al.* in *Diagnostic Nuclear Medicine* (eds. M. P. Sandler) 67–79 (Williams & Wilkins, Baltimore, MD, 1996).
15. S.R. Cherry and M.E. Phelps. in *Diagnostic Nuclear Medicine* (eds. M. P. Sandler) 139–159 (Williams & Wilkins, Baltimore, MD, 1996).
16. S.R. Cherry, M.P. Tornai, C.S. Levin, *et al.* IEEE Trans. Nucl. Sci. NS-42 (1995) 1064–1068.
17. W.W. Moses and S.E. Derenzo. in *Inorganic Scintillators and Their Applications* (eds. P. Dorenbos & C. W. E. van Eijk) 9–16 (Delft University Press, Delft, The Netherlands, 1996).

Inorganic scintillators for the next generation of neutron-beam facilities

Carel W.E. van Eijk

Radiation Technology Group, Interfaculty Reactor Institute
Delft University of Technology
Mekelweg 15, 2629 JB Delft, The Netherlands
vaneijk@iri.tudelft.nl

Abstract: A review will be presented of R&D for inorganic-scintillator application at new spallation neutron sources, particularly in (n,γ) reaction measurements at the anticipated TOF facility, CERN, and in neutron scattering experiments at the planned neutron sources ESS, SNS and N-arena.

Keywords: inorganic scintillators, gamma-ray detection, neutron detection, TOF, ESS, SNS, N-arena

Introduction

New or better neutron cross section information is important for modelling of stellar nucleosynthesis, development of accelerator driven systems (ADS), nuclear waste transmutation, dosimetry and therapy, and basic nuclear physics [1,2]. Almost exclusively for neutron cross section measurements a high-energy spallation neutron source, the Time-Of-Flight (TOF) system, will be constructed at the Proton Synchrotron of CERN [3]. TOF will supply neutrons in the energy range ~1 eV – 250 MeV. Energy selection is realized by time-of-flight selection over a 230 m long flight path. A testbeam is expected to be available in April 2000. The final beam (for specifications see Table 1) will be operational in 2002. A variety of detectors will be required to measure products of reactions such as (n,γ), (n,), (n, fission), and (n,xn'), where x 1. For (n,γ) reaction measurements application of an inorganic scintillator detection system with solid-angle coverage close to 4 is considered. The system should have an excellent gamma-ray sensitivity and be insensitive to neutrons.

Furthermore, neutrons (energy range ~ 1 meV – 1 eV) are used on a large scale in a variety of scattering measurements which provide basic microscopic information on the structure and dynamics of materials in materials science, chemistry, biology, the earth sciences and physics. New neutron sources are required to ensure that neutron beams of the highest quality are available for such measurements early next century. Therefore, at the same time, in Europe, USA and Japan R&D is under way for the introduction of a next generation of spallation neutron sources: respectively the European Spallation Source (ESS) [4], the Spallation Neutron Source (SNS, at Oak Ridge National Laboratory) [5] and the KEK-JAERI Joint Spallation Neutron Source – Neutron Arena (N-arena) [6]. For specifications see Table 1. Information on ISIS, UK, is given for comparison. For the instrumentation at the new facilities a next generation of neutron detectors is required as well: efficient, large-area, position-sensitive neutron detectors that can handle high count rates [7,8]. Inorganic scintillators will play an important role. Contrary to the application in TOF, these scintillators should have a high neutron sensitivity and be insensitive to gamma rays.

Table 1 Specifications neutron-spallation sources

Neutron Source (comm.)	**Proton Energy GeV**	**Beam Power MW**	**Current mA**	**Protons /pulse 10^{13}**	**Pulse Length**	**Rep Rate Hz**	**Target**	**n/p**	**n/s 10^{16}**	**Typical Flux n/cm^2 s**
TOF (2000)	24	0.05	0.002	3	4 x 7 ns at 0.1s	0.4	Pb	760	1.1	10^7-10^9 500 keV
ISIS (oper.)	0.8	0.2	0.2	2.5	2x0.1μs at 0.3μs	50	Ta	12	1.5	0.5 x10^{13} th
ESS (2010)	1.33	5 1	3.8 0.75	50 50	1 μs	50 10	Hg	20	50 10	5-50 x10^{13} th
SNS (~2005)	1	2	2	20	0.6 μs	60	Hg	15	18	2-20 x10^{13} th
N-arena (~2005)	3	1.2	0.4	10	~ 1 μs	25	Hg/ Solid	45	11	1-10 x10^{13} th

Gamma-ray scintillation calorimeter at TOF

We focus on cross-section measurements of (n,γ) reactions. There are two methods of measurement. Upon neutron capture a cascade of gamma rays is promptly emitted. We can

a) detect 1 gamma ray per cascade as indication of an (n,γ) reaction. This method is most suitable for stable isotopes and samples with low radioactivity. The detection efficiency has to be small to avoid detection of 2 or more gamma rays of the same neutron-capture reaction. Typical detectors are the Moxon-Rae detector (converter + plastic scintillator [9]) and the C_6D_6 liquid scintillator using pulse height weighting [10];
b) detect all emitted gamma rays of a cascade. This method is best for highly radioactive and fissile samples of sub-mg mass. A good energy resolution is required to reject the intrinsic gamma-ray background from the samples. Application of a 4 inorganic scintillator calorimeter is the best approach.

In this paper we limit the discussion to inorganic scintillator application, i.e. method b). The calorimeter system has to meet a number of requirements. It should be efficient for gamma-ray detection, insensitive to neutrons, be capable to distinguish between gammas from (n,γ) and (n,fission) reactions, have a time resolution of <10 ns, and be able to handle counting rates of 10^6 s^{-1}. In this case we do not need a new scintillator.

Some applicable scintillators are presented in Table 2. Of these BaF_2 appears to be well suited. At FZK Karlsruhe a 4 system is in operation existing of 30 hexagons and 12 pentagons with a total efficiency of > 90% [11]. The BaF_2 crystals, 15 cm deep, are read out by photomultiplier tubes (PMTs). A similar system is considered for TOF [2]. Simulations have shown that the background from scattered neutrons can be reduced sufficiently by application of shielding (^{6}LiH and ^{10}B) around the sample and between the crystals. The very fast 0.8 ns response facilitates discrimination between on the one hand the coincident gamma rays of a cascade and on the other hand gamma rays from the radioactive sample. Pulse shape analysis will further help to disentangle pile-up signals. In respect of this one should also realize that the total gamma-ray energy emitted in a cascade equals the neutron binding energy and is therefore fixed for each isotope (~ 10 MeV). Furthermore, segmentation into 162 crystals instead of 42 crystals is considered for handling of high counting rates.

Table 2. Properties of some scintillators of interest for calorimeter application

Scintill.	λ_{em} nm	ns	Light yield photons per MeV	Density g/cm^3	Z_{eff}^4 (x 10^{-6}) ‡	Neutron sensitivity relative	Accept. radioact. sample rel.	Ref.
BaF_2	~220/310	0.8/600	1500/11,000	4.88	38	4	400/1	11
CeF_3	285,305	5/31	4,000	6.16	50	1	20	12
BGO*	480	300	9,000	7.13	227	2	2	13
LXe	175	27	25,000	2.95	25		20	14

*$Bi_4Ge_3O_{12}$

‡As an indication of detection efficiency of scintillators by photoelectric effect Z_{eff}^4 values are presented. For a compound $B_pC_qD_r$ it is defined by $Z_{eff}^x = \sum w_i Z_i^x$, where Z_i is the atomic number of respectively B, C and D, and $w_i = k_i A_i / \sum m_j A_j$, with A_i, A_j the atomic mass of B, C or D, and k_i, m_j the corresponding p, q or r.

Neutron detector requirements for scattering measurements at new spallation sources

The new sources will produce very intense pulsed-neutron beams. In Table 3 a summary is presented of detector requirements for different kinds of neutron-beam-line instruments [7]. Large area position-sensitive detectors will be needed, in some cases with > 10^6 pixels. Although a time resolution of 1 s suffices for energy selection by means of time of flight measurement, a response time of 100 ns is required to handle the high rates. Occasionally local rates, i.e. approximately per pixel, will be as high as 10^6 s^{-1}. Global rates, i.e. over the whole detector, can go up to 10^7 s^{-1}. In a number of cases the stability has to be very high (VH). This means that observed intensity variations due to changes in detector efficiency and signal processing, e.g. by temperature changes, should not be more than 0.01% per day. The energy range to be covered is approximately from 1 meV to 1 eV, i.e. from cold to epithermal neutrons (wavelengths from ~ 9 Å – 0.3 Å). As will be seen below, particularly the epithermal part will pose a problem.

Several detector types are being considered to realize these neutron detectors. Inorganic scintillators are an important option, e.g. coupled to fibre arrays read out by means of PMTs or silicon sensors.

Principles, current scintillators

In Box 1 we summarize some interactions and related parameters important for thermal-neutron detection. In principle we need a material with ^{6}Li, ^{10}B or $^{155/157}$Gd nuclei because of their high thermal-neutron capture cross sections, , and the reaction products. From we find the linear absorption coefficient μ_n (Box 1). N_A is Avogadro's number, the density of the scintillator material, w the weight fraction of the neutron-sensitive nuclei, and A the atomic mass number of these nuclei. From the absorption length $=1/\mu_n$ we derive the scintillator thickness required for efficient neutron detection. In Fig. 1 is shown as a function of neutron energy E_n. In addition to the isotopes mentioned in Box 1 we show data for ^{3}He, used in gas filled neutron detectors, ^{113}Cd, a neutron absorber, and ^{235}U which gives energetic fission products and is used as a lining or foils in ionization chambers (natural abundance 0.7%). For the gadolinium isotopes drops rapidly with increasing E_n when entering the epithermal region. At 1 eV ^{3}He has the highest , followed by ^{10}B and ^{6}Li. In the cold-neutron region all 's show an $E_n^{-1/2}$ energy dependence.

Table 3. Neutron-detector requirements for the new spallation sources

	Sample to Detector Distance	**Angular Coverage/ Detector Size**	**Pixel Size**	**Rate (s^{-1}) Global/ Local**	**Stability**	**Energy Range**
Single-Crystal Diffraction	≤ 1m	2π	≤ 1 mm^2	$10^6/10^6$	H	0.3 - 5 Å
Powder Diff.	1 m	π	5 x 5 mm^2	10^5	M	0.3 - 5 Å
Disordered	≥ 1 m	π	5 x 50 mm^2	10^5	VH	0.1 - 5 Å
SANS (Small Angle Neutron Scattering)	2 – 10 m	1 m^2	1 x 1 – ~5 x 5 mm^2	10^6	H–VH	1 – 20 Å
Inelastic-Isotropic	2 – 6 m	10 m^2	20 x 20 mm^2	10^4	M	MeV – 1 eV
Inelastic Single Crystal	2 – 6 m	10 m^2	20 x 20 mm^2	$10^4/10^6$	M	MeV – 1 eV
Transmission	NA	50 x 50 mm^2	~ 100 μm	10^7	VH	0.1 – 20 Å

For efficient neutron detection the different reaction products and their energies are important. In applying ^{6}Li or ^{10}B heavy charged particles are produced with kinetic energies in the MeV range. Using crystals these particles will in general not be able to leave the scintillator. The full energy is deposited in it. For ^{6}Li this is 4.8 MeV. In the case of ^{10}B, in 93% of the reactions a 480 keV gamma ray is emitted. In general this gamma ray will escape from the scintillator so in this case we have energy deposition of either 2.8 MeV (7%) or 2.3 MeV (93%). It should be noticed that the escaping gamma ray can be observed in coincidence in a neutron-insensitive detector, thus providing a unique signature for neutron detection. Upon neutron capture in Gd a variety of high energy gamma rays is emitted. For a thin scintillator these will almost all escape. Only conversion electrons in the energy ranges indicated in Box 1 and, with a small probability, characteristic Gd X-rays and/or low energy gamma rays will be absorbed. There is a probability of ~ 25% that only gamma rays are produced which may all escape from the crystal [15]. For efficient detection of the electrons a scintillator thickness is required of ~0.1 mm. In the case of ^{157}Gd this is larger than the thickness needed for efficient neutron interaction.

When we discuss the pros and cons of the different cases it should be considered that there is in general a gamma-ray background near a neutron facility. Even at a spallation neutron source, where the neutrons are used for research in the intervals between the accelerator pulses, the gamma-ray background is a nuisance as gamma rays are not only produced during accelerator pulses but also in between by radioactive decay of neutron activated isotopes of the experimental setup and its surroundings. In most applications we want to discriminate the background signals in the detectors as much as possible, which in some cases implies reduction to a level of 10^{-8}.

Box 1

Nuclear neutron-capture reactions

cross sections at neutron wavelength of 1 Å

n + ^{6}**Li** (7.5%*) → ^{3}**H** (2.75 MeV) + ^{4}**He** (2.05 MeV)

σ = 520 b (absorption in ~3 mm enriched material)

n + ^{10}**B** (20%*) → ^{7}**Li** (1.0 MeV) + ^{4}**He** (1.8 MeV) BR 7%

→ ^{7}**Li** (0.83 MeV) + ^{4}**He** (1.47 MeV) + γ (0.48 MeV) BR 93%

σ = 2100 b (absorption in ~1 mm enriched material)

n + ^{157}**Gd** (16%*) → ^{158}**Gd** + **γ's** + **conversion el**. (29 keV - 182 keV; BR ~75%)

σ = 70,000 b (absorption in ~20 μm enriched material)

n + ^{155}**Gd** (15%*) → ^{156}**Gd** + **γ's** + **conversion el.** (39 keV - 199 keV; BR ~75%)

σ = 17,000 b (absorption in ~0.1 mm enriched material)

Linear neutron absorption coefficient (cm^{-1})

$$\mu_n = N_A \rho \sigma w/A$$

* natural abundance

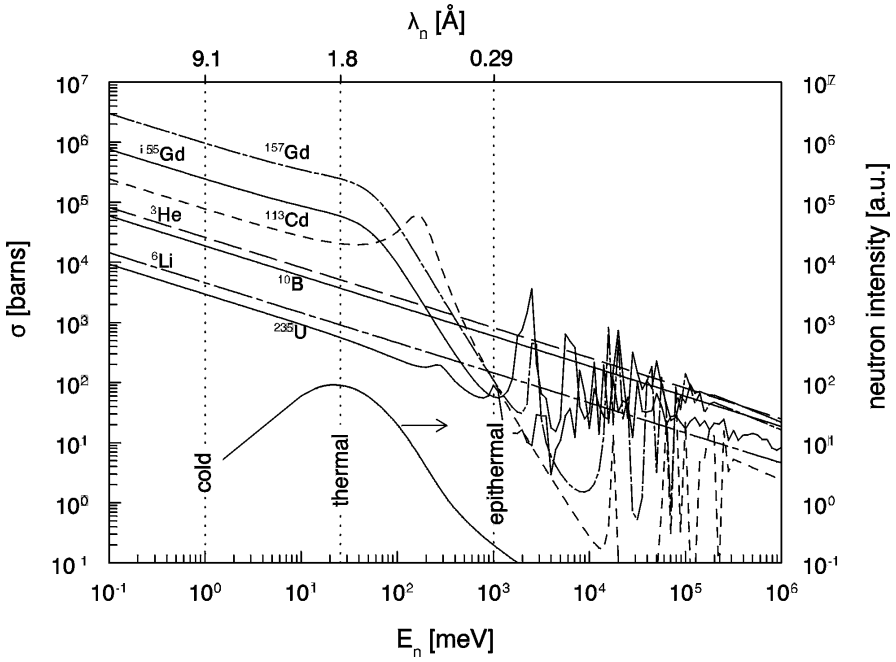

Fig. 1. Neutron capture cross sections of some isotopes important for neutron detectors as a function of neutron energy. The lowest curve shows a typical moderated-neutron spectrum of a nuclear reactor (right y-axis).

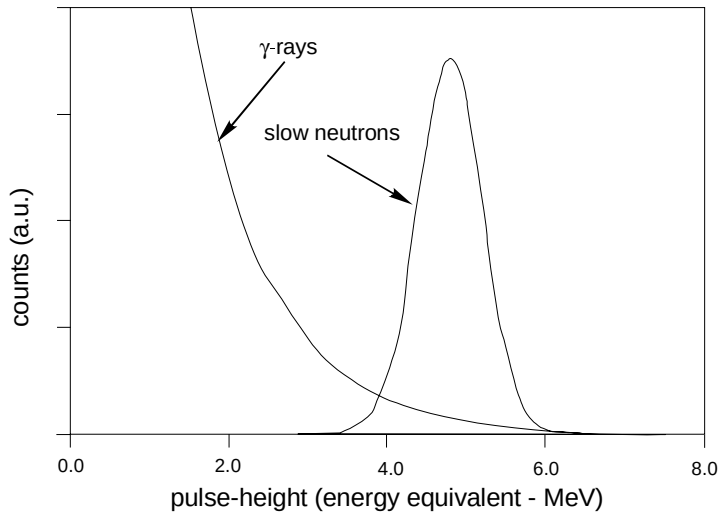

Fig. 2. Typical pulse-height spectrum recorded with a ^{6}Li glass scintillator-photomuptiplier detector.

Part of the method to realize this is the selection of a detector material with a small gamma-ray sensitivity. In principle this means a small density and a small Z. However, when we consider the $_{n}$ formula in Box 1 it is immediately clear that selecting a small to suppress the gamma background does not really help as the the neutron absorption coefficient is proportional to as well. Consequently, important requirements are a small Z_{eff}, a large weight fraction w and onbviously a high . Yet, even when these conditions are met, a gamma-ray background spectrum will show up in the neutron pulse-height spectrum. An example of such a spectrum is shown in Fig. 2. In this case gamma-ray discrimination is further optimized by selecting an energy band around the 4.8 MeV thermal-neutron peak. Considering the gamma and neutron-spectrum shapes in Fig. 2, it is clear that the best discrimination can be obtained if the neutron response is at a relatively high energy. This leads to the conclusion that Li is in principle the best material. In Table 4 we give some characteristics of commercially available thermal-neutron scintillators. They are Li based indeed.

Table 4
Traditional thermal–neutron scintillators

Scintill.	$_{em}$ nm	Light yield photons per neutron	Light yield photons per MeV gamma	ns	Density g/cm^3	Z_{eff}	Z_{eff}^4 (x 10^{-6})	Ref.
^{6}Li-glass:Ce	395	~6,000	~4,000	75				16,17
^{6}LiI:Eu	470	50,000	12,000	$1.4*10^3$	4.1	52.3	31	18
^{6}LiF/ZnS:Ag	450	160,000	~75,000	$\sim 1*10^3$				17,19

In considering the scintillator materials in Table 4 we can learn several things. First of all we notice the difference in light yield. A glass with an amorphous structure has more defects than a crystal. Consequently in the former there are many more non-radiative recombination channels. A second point is the difference in light yield per MeV for a neutron and a gamma ray. As stated before we need the highest neutron response relative to the gamma ray response. In the case of Li-glass a gamma ray of 1.5 MeV produces the same number of photons as the ^{3}H and ^{4}He nuclei which carry together 4.8 MeV. In the dense tracks of these

charged particles far less electron-hole pairs give rise to radiative recombination than in the tracks due to electrons produced by gamma-ray interaction.

In the case of LiI the difference in light yield is much smaller. The difference is difficult to predict and, notwithstanding the lower reaction energy, some B based scintillators may have a higher response than some Li based scintillators, even though the ^{7}Li nuclei give denser tracks than ^{3}H and ^{4}He, implying that B is in principle less favourable.

Another aspect is the response time. In the Ce doped glass the response is much faster than in the other two cases. This is characteristic for Ce with its allowed dipole 5d-4f transition with a decay time at the level of tens of ns. The long response times of the other materials set a limit to the count rates they can handle.

Considering the material properties, LiI is hygroscopic. The scintillator ZnS:Ag can only be obtained as a powder. LiF is admixed to it and the weight fraction of Li is much lower than in the case of LiI. This is also the case for Li-glass. The LiF/ZnS:Ag powder is mixed with an organic binder to form a scintillator layer. The scintillation light transport sets a limit to the layer thickness and this results in a relatively poor neutron detection efficiency [19]. On the other hand one should realize that particularly for ^{6}Li application of scintillation layers of larger thickness (crystals) for efficient neutron detection (Box 1) will result in a light spread which sets a limit to position resolution.

When we consider all these aspects that are far from optimal and the need for efficient neutron scintillators with a fast response to be applied at ESS, SNS and N-arena, it will be clear that better materials have to be developed. The main line of research is focused on ^{6}Li based scintillators. Because of the higher cross section development of ^{10}B based scintillators is also important, particularly for application in the epithermal region. The small amount of energy deposited when using Gd, its detection efficiency of 75% and its relatively high Z make Gd based neutron scintillators (phosphors) only of interest for special applications.

New thermal-neutron scintillators

We will confine ourselves mainly to developments in the field of Ce-doped thermal-neutron scintillators, which are the most promising because of their potentiality for a high light yield and a fast response. In Table 5 we summarize recently studied Ce-doped and a few undoped scintillation materials containing Li, B and/or Gd in the host compound. The Gd based scintillators, partly well known, are presented for the sake of completeness. Crystals have been studied of a limited number of compounds: $LiYF_4$:Ce, $LiLuF_4$:Ce, LiB_3O_5, $Li_2B_4O_7$, $Li_6Gd(BO_3)_3$:Ce, $LiBaF_3$, pure and doped, and the Gd compounds, with the exception of Gd_2O_2S which is available as powder and in ceramic form. Of the other compounds only powders have been studied. Of most of the materials we give only light yields under gamma-ray irradiation. If neutron responses have been measured this is indicated explicitly.

We will confine the discussion to a few cases only. An interesting material is $Li_6Gd(BO_3)_3$:Ce. It contains B, Li and Gd. Considering the different absorption lengths of these elements (Box 1), without special measures B and Li do hardly contribute to neutron detection. If we want to use Li we need material enriched in ^{6}Li and depleted in ^{10}B and ^{155,157}Gd. In this way we can select the optimal response. The reaction with ^{6}Li gives the highest signal per absorbed neutron (Table 5). The decay time of the fastest component of 200 ns is somewhat long. An advantage of the $Li_6Gd(BO_3)_3$ compound is its relatively low index of refraction of ~ 1.66 which makes efficient scintillation light transport in a scintillator powder – binder combination feasible. The powder-binder approach is attractive for covering large areas with a thin scintillator layer. A disadvantage is the high cost of ^{155,157}Gd depleted material. For this reason $Li_6Lu(BO_3)_3$ is also studied at present.

Table 5
Some Li, B and Gd containing Ce doped scintillators

Host	Dopant/ Ce conc-mol%	Λ Nm	Light yield Photons/MeV	τ ns	Density ρ g/cm^3	ρZ_{eff}^4 ($x10^{-6}$)	Ref.
$LiYF_4$	0.1	310,325	1,000/5,000	35/>10μs	4.0		20
$LiLuF_4$	0.1		4,000	>10μs	6.0		20
$LiBaF_3$	-	190-290	1,000-4,000	1/15μs	5.2		21-26
$LiBaF_3$	0.08	190-330	1,000-4,000	1/50/15μs			22-26
$LiBaF_3$	Ce-0.3; K	190-330	1,000-4,000	1/30/2.5μs			23,24
$LiBaF_3$	Ce-0.3;Rb	190-330	1,000-4,000	1/35/2.5μs			23,24
$Li_{1-x}Cs_xCl$	-	220-460		2/…			27
Cs_2LiYCl_6	0.5	372,400	20,000	600/6μs	3.3	15	28,29
$Cs_2LiLaCl_6$	1	220-400		1.4/36			30
Li_3YCl_6	0.2	360,385	6,000	250/2.5μs	2.45		28,29
$Li_6Y(BO_3)_3$	~1	390,420	~2,000		~2.8		31,32
$^6Li_6Gd(BO_3)_3$	1-4	385,415	14,000/(50,000/n)	200/800	3.5		32
$Li_6Lu(BO_3)_3$	~1	~400	~4,000				33
$LiYSiO_4$	5	410	10,000/(10,000/n)	38	3.8	4	34
$LiLuSiO_4$	~1	420	30,000	42/…	5.5	89	35
$ScBO_3$	1	385,420	10,000				31,36
YBO_3	1	385,415	10,000				31,36
$LaBO_3$	1	350,380	1,000				31,36
$GdBO_3$	1	410	10,000				31,36
$LuBO_3$ (calc)	1	380	10,000/10,000	~28/20μs	6.9	131	37-39
$LuBO_3$(vate)	0.1	410	~20,000	39/> μs	7.4	140	37-39
$CaYBO_4$	1	400	1,000				31,40
LiB_3O_5	-	310					41,42
LaB_3O_6	1	300,320	2,000				43
GdB_3O_6	1	305,325	200				31
$Li_2B_4O_7$	-	340					44
$YMgB_5O_{10}$	1	297,317	300				43
$LaMgB_5O_{10}$	1	300,320	300				43
$YAl_3B_4O_{12}$	1	345,365	10,000				31,36
$CaLaB_7O_{13}$	1	290-360	200				31
$RbGd_2Cl_7$	10	400	16,500/18,000/ 10,000	455/1.3μs+ 4.4μs/long	3.7	31	45
$RbGd_2Br_7$	10	420	42,000/18,000/ 2,000	43/0.4μs/ 20μs	4.7	31	45-47
Gd_2SiO_5	Ce	440	9,000/(800/n)	60/600	6.7	81	48
Gd_2O_2S	Tb			ms	7.3	101	
Gd_2O_2S	Pr,Ce,F	510	40,000	~μs			49,50

Another material that gives a good response upon thermal-neutron interaction is $LiYSiO_4$:Ce. The light yield is 10,000 photons per neutron and the response is fast, the decay time being 38 ns. In addition the sensitivity for gamma radiation is low ($Z_{eff}^4 = 4 \times 10^6$) which is important for application in mixed neutron/gamma-ray fields. Although only layers of ~3 mm of material are required for efficient neutron detection (Box 1) application of crystals instead of powders is important for efficient light collection. Therefore crystal growing of this material needs attention.

A special case is $LiBaF_3$. This compound shows both core-valence luminescence (CVL, = 1 ns) and self-trapped-exciton luminescence (STE, = 15 s). CVL is a very fast response mechanism. It results from filling of a hole in the outer core band by an electron of the valence band. CVL is fully quenched if excitation occurs by heavy, charged, particles such as ^3H and ^4He. Consequently, upon thermal-neutron interaction in $LiBaF_3$ we observe only the STE luminescence, while interaction with gamma rays results in both CVL and STE luminescence. Though the CVL intensity is only ~1000 photons/MeV, the signal is easy to recognize electronically as the whole luminescence occurs in ~1 ns. Thus we can efficiently veto gamma-radiation events [21]. See Fig. 3. The STE luminescence being rather slow, efforts have been made to speed up the response by cerium doping. It appeared difficult to obtain a cerium concentration above 0.08 mol%. To compensate for the 3+ cerium charge at a Ba^{2+} site co-doping of K^+ or Rb^+ was introduced, resulting in a higher concentration and both a reasonable 5d - 4f Ce signal of ~30 ns decay time and reduction of the STE-response time [23,24]. A peculiar phenomenon is that the neutron induced cerium signal occurs only after administering a significant radiation dose to the crystal. After this, the response is stable, at least for months. The mechanism is not yet fully understood. With the co-doped, irradiated crystals excellent gamma-ray backgrond suppression can be realized. Other compounds showing CVL that may have similar possibilities for neutron/gamma discrimination are $Li_{1-x}Cs_xCl$ and $Cs_2LiLaCl_6$. However, more research on these materials is required.

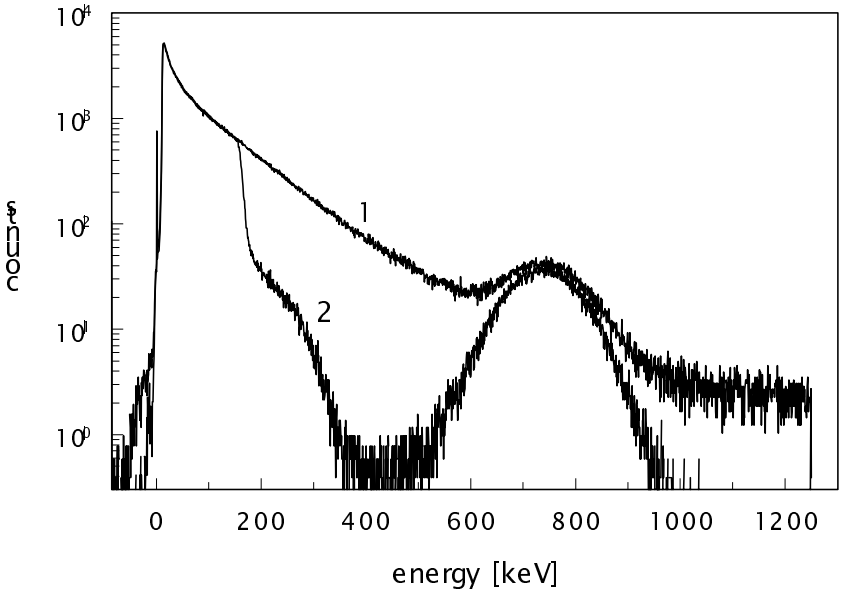

Fig. 3. Pulse height spectra of radiation emitted by a Pu-Be source shielded with paraffine and 6 cm of Pb recorded in $LiBaF_3$. Spectrum 1 is without discrimination and spectrum 2 with discrimination. The neutron peak at ~750 keV gamma-equivalent energy shows up almost free from the background.

Concluding remarks

Detector R&D for (n,γ) cross section measurements at the TOF facility is focused on gamma-ray detection system development using existing scintillators. For instrumentation at the planned spallation sources for neutron scattering measurements in the cold to epithermal region both fundamental neutron-scintillator research and system R&D are in progress. In this case position-sensitive detection is very important and consequently read-out schemes of large area detectors are a topic of research as well. E.g. see Hutchinson et al. in [7].

As for scintillator development, it should be noticed that in the case of application of scintillator powder-binder plates, which is in principle very attractive for large area detectors, efficient light collection is a crucial point. Without this we do not observe a neutron line as shown in Fig. 2 and 3, but a continuum. This would make neutron/gamma-ray discrimination more difficult.

In a number of scintillators background radiation is observed from intrinsic scintillator radioactivity. E.g. intrinsic alpha radiation is emitted in $LiBaF_3$ [23]. Considering the need of background reduction, in some cases even to a level of 10^{-8}, it will be obvious that intrinsic radioactivity is a point of attention. Considering the expected high rates, afterglow effects of scintillators should also be studied. These effects can easily extend over a period of time > ms.

In addition to research on crystals and powder-binder combinations more attention should be paid to development of new glass scintillator materials. If as fast as the traditional neutron glass scintillator (Table 4) but with a much higher light yield, a glass-plate scintillator would constitute an excellent large area detecor.

Acknowledgements

This work was made possible in part by grants from the Dutch Technology Foundation (STW), the Human Capital and Mobility project, "Search for new and better scintillators for radiation detection", and the Training and Mobility of Researchers project, "The 10 member European Network for Neutron Instrumentation, XENNI". Furthermore, the work was partly carried out in the framework of the "Crystal Clear Collaboration" and the "TOF Collaboration".

References

1. http://itumagill.fzk.de/ADS/whatsnew.html
2. TOF, Proposal of the European Collaboration for High-Resolution Measurements of Neutron Cross Sections between 1 eV and 250 MeV, CERN/SPSC 99-8, SPSC/P 310, 1999
3. http://home.cern.ch/~cgn/cgn_workshop.html
4. http://www.isis.rl.ac.uk/ess
5. http://www.ornl.gov/sns
6. http://neutron-www.kek.jp/N-arena/index.html
7. Proceedings of Workshop on Neutron Detectors for Spallation Sources, Brookhaven National Laboratory, September 24-26, 1998 (hastings@bnl.gov)
8. Proceedings of European Workshop on Thermal Neutron Detectors for the European Spallation Source, NEUDESS98, Delft University of Technology, October 27-28, 1998(ISO@iri.tudelft.nl)

9 M.C. Moxon and E.R. Rae, Nucl. Instr. Meth. 24 (1963) 445
10 F. Corvi et al., Nucl. Instr. Meth. A265 (1988) 475
11 K.Wisshak et al., Nucl. Instr. Meth. A292 (1990) 595
12 A. Giorni, ISN Grenoble, A CeF3 gamma detector, presented at first TOF collaboration meeting, CERN, 7-8 January 1999
13 P. Lecoq et al., Nucl. Instr. Meth. A300 (1999) 240
14 V. Chepel et al., Nucl. Instr. Meth. A367 (1995) 58, and A392 (1997) 427
15 C.R. Rausch, Detektoren für thermische Neutronen mit hoher Ortsauflösung, PhD-thesis, ch. 2-4, TU München, 1996
16 *Scintillation Detectors*, catalog, Crismatec (1991)
17 *Scintillation Materials*, catalog, Nuclear Enterprises Ltd. (1990)
18 J. Schenck, *Nature*, 171 (1953) 518

19 N.J. Rhodes and M.W. Johnson, in *Proc. SCINT95/1995*, P. Dorenbos, C.W.E. van Eijk, Editors, p. 73, Delft University Press, Delft (1996)
20 C.M. Combes et al., in *Proc. SCINT95/1995*, p. 396, loc. cit.
21 M.J. Knitel et al., *Nucl. Instr. Meth.* A374 (1996) 197
22 C.M. Combes et al., *Journal of Luminescence* 72-74 (1997) 753
23 C.M. Combes et al., in *Proc. SCINT97/1997*, Yin Zhiwen, Feng Xiqi, Li Peijun, Xue Zhilin, Editors, p. 349, CAS Shanghai Branch Press (1997)
24 C.M. Combes et al., in *Proc. SCINT97/1997*, p. 322, loc. cit.
25 A. Gektin et al., *IEEE Trans. Nucl. Sci*, 44 (1997) 857
26 A. Gektin et al., in *Proc. SCINT97/1997*, p. 121, loc. cit.
27 A.S. Voloshinovskii et al., *Journal of Luminescence* 79 (1998) 107
28 C.M. Combes, Scintillation Properties of ^{6}Li-based Materials for Thermal-Neutron Detection, PhD-thesis, TU Delft, 1999
29 C.M. Combes et al., *Journal of Luminescence*, 1999, tbp
30 P.A. Rodnyi et al., *Journal of Luminescence*, 1999, tbp
31 M.J. Knitel, New Inorganic Scintillators and Storage Phosphors for Detection of Thermal Neutrons, PhD-thesis, TU Delft, 1998
32 J.B. Czirr, A new class of neutron detectors. *Internal Report Photogenics Inc*. PGI-96-3 (1996)
33 N. Le Masson, ENSCP, France, private communication, 1999
34 M.J. Knitel et al., *Journal of Luminescence* 69 (1996) 325
35 J.C. van't Spijker et al., in *Proc. SCINT97/1997*, p. 326, loc. cit.
36 G. Blasse and A. Bril,. *J. Chem. Phys.* 47 (1967) 5139
37 W.W. Moses et al., in *Proc. SCINT97/1997*, p. 358, loc. cit.
38 L. Zhang et al., in *Proc. SCINT97/1997*, p. 303, loc. cit.
39 J.C. van't Spijker et al., in *Report Delft Univ. of Technology*, 1998
40 G. Blasse, *J. Inorg. Nucl. Chem.* 31 (1969) 1519
41 I.N. Ogorodnikov et al., *Journal of Luminescence* 72-74 (1997) 703
42 I.N. Ogorodnikov et al., in *Proc. SCINT97/1997*, p. 139, loc. cit.
43 M.J. Knitel et al., in *Proc. SCINT97/1997*, p. 318, loc. cit.
44 I.A. Kamenskikh et al., Luminescence properties and electron band parameters of $Li_2B_4O_7$. *Book of Abstracts SCINT97/97*, p. 64
45 J.C. van't Spijker et al., in *Proc. SCINT97/1997*, p. 330, loc. cit.
46 P. Dorenbos et al., *Nucl. Instr. and Meth.* B132 (1997) 728
47 O. Guillot-Noël et al. , *IEEE Trans. Nucl. Sci.* 46 (1999) tbp
48 H. Ishibashi et al., in *Proc. SCINT97/1997*, p. 295, loc. cit.
49 B.C. Grabmaier et al., in *Proc. SCINT95/1995*, p. 29, loc. cit.
50 W. Rossner et al., in *Electrochemical Society Proceedings* Volume 98-24 (1999) 187

Separation of elementary mechanisms of photon multiplication in wide-gap crystals

Ch. Lushchik[1], A. Lushchik[1] and M. Kirm[2]

[1]Institute of Physics, University of Tartu, Riia 142, 51014 Tartu, Estonia
[2]II. Institute of Experimental Physics, University of Hamburg, Luruper Chaussee 149, D-22761 Hamburg, Germany

Abstract: A complex experimental study of the excitation processes of intrinsic and impurity emissions by synchrotron radiation (5-40 eV) in wide-gap crystals at 8 K has been carried out. The creation processes of secondary electron-hole pairs, secondary excitons as well as the direct excitation of impurity centers by hot photoelectrons have been separated. The formation of groups of spatially correlated excitations or defects under conditions of the multiplication of electronic excitations has been revealed. Elementary creation mechanisms of secondary excitations are discussed.

Keywords: multiplication of excitations, VUV spectroscopy, alkali halides

Introduction

The effect of multiplication of electronic excitations (MEE), when one absorbed photon of $h\nu > (2\div4)E_g$ (E_g is the energy gap) creates two or three electron-hole pairs (e-h) in a crystal, was revealed for semiconductors (V. Vavilov, W. Shockley, et al. [1,2]) and luminescent dielectrics (E. Ilmas, Ch. Lushchik, et al [3,4]) many years ago. Photoluminescence with the quantum yield $\eta > 1$ is used in various discharge light sources [5,6]. Fast MEE processes play an important role in scintillators [7,8].

In 1964 the first paper titled 'Photon multiplication as the elementary act of scintillation process' was published [9]. In that paper the physicists of Tartu showed that one absorbed exciting photon in the region of fundamental absorption of doped alkali halide crystals (AHC) causes the appearance of two or even more emission quanta of impurity centers. The value of the quantum yield more than two was also obtained for the fast emission of NaI:Tl, that is for a photoscintillation [7-9].

Since that time the luminescence in visible and ultra-violet regions with η = 2-3 at the excitation by vacuum ultra-violet (VUV) radiation has been obtained in dozens of wide-gap single crystals and powder phosphors. At first, this phenomenon was called 'photon cutting', but later on the physicists of Tartu renamed it as 'photon multiplication'. As soon as the excitation spectra of the inertial recombination component of the luminescence were measured, it became clear that the main mechanism of photon multiplication is connected with the multiplication of e-h pairs that is similar to the processes in narrow-gap semiconductors. The excitonic mechanism of MEE, when hot photocarriers are able to create secondary excitons, was also revealed measuring the excitation spectra for fast luminescence ($\tau << 1$ s) in doped AHC [3,4].

In 1970 the spectral region of MEE investigation was extended up to 30 eV by means of the synchrotron facilities of the Institute of Physics in Moscow with an active participation of V.Mikhailin group and Tartu group (see, e.g. [10]). Since then, the action spectra of VUV radiation on wide-gap dielectrics have been widely studied. By the action spectra we mean the excitation spectra of impurity luminescence [10] and intrinsic luminescence [11,12], the quantum yield spectra of electron emission [13,14] and the spectra of radiation defect creation

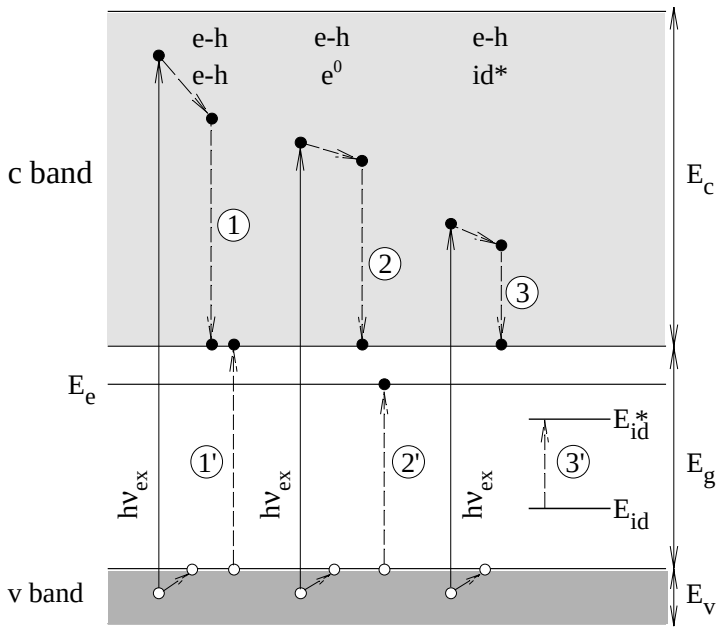

Figure 1. Schematic energy-level diagram of a wide-gap crystal and the processes of MEE following the absorption of a photon with the energy $h\nu_{ex}$. Formation of secondary e-h pairs, secondary excitons and excited impurity-defect centers (E_{id}*) at nonradiative Auger transitions 1 → 1', 2 → 2' and 3 → 3', respectively. Widths of conduction (E_c), valence (E_v) and forbidden energy bands (E_g) as well as the formation energy of anion excitons (E_e) are marked.

by VUV radiation [15,16]. These spectra are measured using synchrotron radiation (SR) as well as discharge laboratory sources. This study presents a number of results obtained using the synchrotron facilities of MAX-I Laboratory, Lund (Sweden) [17-19], SUPERLUMI station of HASYLAB at DESY (Germany) [20,22], and UVSOR in Okazaki (Japan) [18,21].

Fig. 1 illustrates in a simplified form the three main mechanisms of MEE in wide-gap crystals. Absorption of a photon with an energy of $h\nu_{ex}$ causes the formation of an electron in a conduction band (c-band) and a hole in a valence band (v-band). Secondary e-h pairs, secondary excitons and impurity-defect centers in the excited state arise due to isoenergetic nonradiative Auger transitions 1 → 1', 2 → 2' and 3 → 3'. By analogy with semiconductors these processes can be approximately considered, as an impact formation of secondary electronic excitations by hot photoelectrons.

Recently there has been a tendency toward the use of mainly luminescent methods for the investigation of MEE processes. However, it must be taken into account, that only the excitation spectrum of time-integrated emission alone measured in a wide region of exciting photon energy is insufficient for its valid interpretation. First of all, this excitation spectrum must be compared with the reflection and, in particular, with the absorption spectra of a matrix. The selective reflection of SR can be easily taken into account [17,23]. However, it is far more difficult to take into consideration a complicated absorption spectrum in a VUV region: in the region of fundamental absorption the value of absorption coefficient varies from about 10^6 to 10^3 cm^{-1}, or in other words, the penetration depth of exciting radiation ranges from 10^{-6} to 10^{-3} cm. In order to separate various MEE processes at the interpretation of the excitation spectrum, it is necessary to compare the emission efficiencies in the spectral regions with the absorption constant of approximately the same value. However, this

procedure alone is not enough. Our experience shows that a complex study of impurity and intrinsic emissions as well as other crystal characteristics is needed for a separation and detailed investigation of various elementary mechanisms of MEE.

Separation of the elementary mechanisms of MEE

Several experimental methods, conventional as well as the novel ones, are useful for the separation of the three main MEE mechanisms (the e-h mechanism, the excitonic and the impurity-defect mechanism):

- spectral-kinetic investigation of fast and inertial emissions [10,24-27],
- comparison of the excitation spectra for intrinsic and impurity emissions and the intensity ratio of two emissions as a function of incident photon energy [28-30],
- comparative study of luminescence excitation spectra and the quantum yield spectra of photoemission [18,21],
- comparative study of luminescence excitation spectra and the energy distribution of emitted electrons at various exciting photon energies [18,21],
- influence of an elastic uniaxial stress (EUS) on the optical properties of crystals under VUV excitation [19],
- influence of an external electric field on the luminescence properties of crystals under VUV excitation [22].

We used all the above-mentioned methods for the investigation of AHC. As a result of this complex study we can conclude that all the three main MEE mechanisms really take place in AHC. At the same time, we have found a variety of excitonic effects under conditions of multiplication in various wide-gap dielectrics. In semiconductors excitonic effects under such conditions have not been practically investigated because of a large effective radius of excitons and small values of an exciton absorption in respect to the absorption due to band-to-band transitions.

As the first example we discuss the data for a NaCl:Ag crystal. At 8 K, the emission of silver impurity centers (the maximum at 5.17 eV, $\tau \sim 100$ ns) is effectively excited by mobile

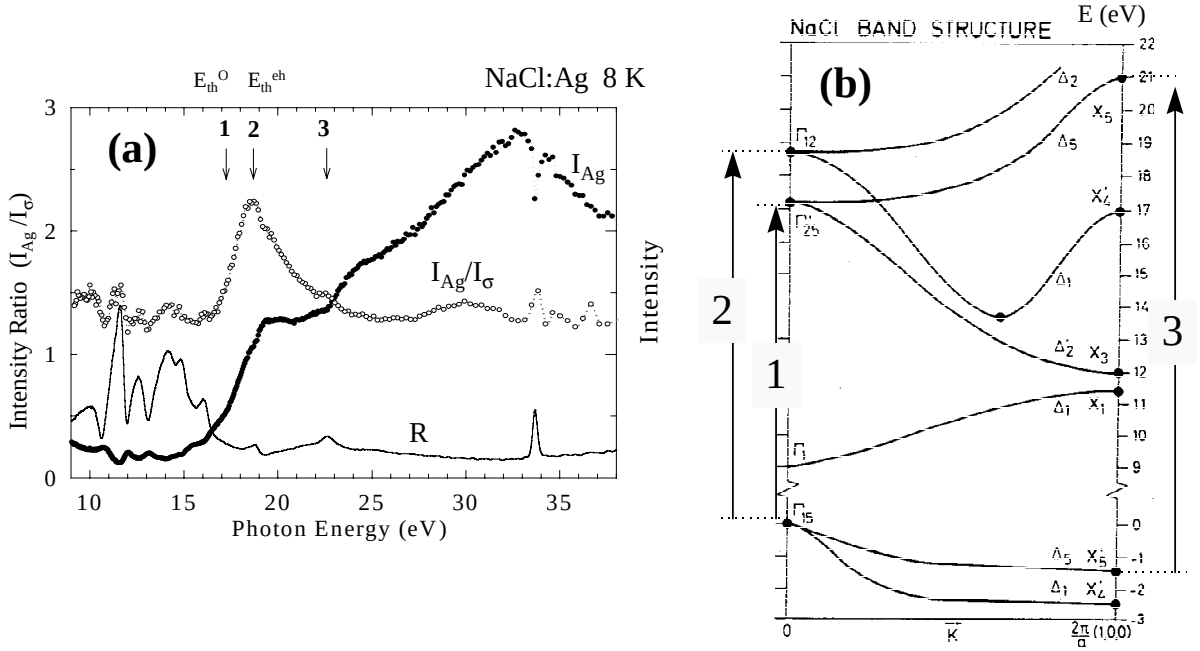

Figure 2. (**a)** -Reflection spectrum (solid line), excitation spectrum for Ag^+ emission (•) and the intensity ratio spectrum (o) for Ag^+ impurity emission (5.17 eV) and STE σ emission (5.4 eV) in NaCl:Ag at 8 K. (**b)** - A fragment of the band structure of NaCl [35].

excitons, while it can also be detected at the recombination of electrons and holes near Ag^+ centers [31]. The recombination of electrons with self-trapped holes (V_K centers) causes the appearance of σ emission (5.5 eV, $\tau \approx$ 2-3 ns) of self-trapped excitons (STE) [32]. Fig. 2*a* presents the excitation spectrum for Ag^+ emission in NaCl at 8 K. The luminescence efficiency is reduced in the region of high absorption coefficients, but it sharply increases at $h\nu_{ex} > 17$ eV, and there are several other steps of the efficiency increase up to the formation region of cation excitons (33.4 eV).

It is necessary to separate the near surface effects and the MEE process. In NaCl, the energy of direct photocreation of an exciton is E_e = 8 eV and the energy gap is about 9 eV. Therefore, the lowest photon energy for the creation of a secondary exciton equals $E_{th}^0 = E_g + E_e$ = 17 eV (if we do not take into account weak two-electron processes at $h\nu_{ex} = 2E_e$ [33]). For the e-h mechanism of MEE the lowest photon energy should be $E_{th}^{eh} = 2E_g$. Fig. 2*a* also shows the dependence of the intensity ratio for Ag^+ and σ emissions on the energy of exciting photons. This intensity ratio spectrum contains a lot of information. It is obvious that in the ratio spectrum the influence of a selective reflection of SR by a crystal surface is excluded. The value of I_{Ag}/I_σ ratio is approximately the same in the region of 9-17 eV, where one photon creates an e-h pair, and at 22.5-28 eV, where a photon is able to form two e-h pairs. However, there are the increased values of I_{Ag}/I_σ in the region of 17-22.5 eV. The increase of I_{Ag}/I_σ occurs in a relatively narrow region, less than 2 eV, that is comparable to the width of v-band in NaCl. Undoubtedly, this rise is connected with the excitonic processes at the first stage of MEE. The decrease of ratio takes place during 4 eV that significantly exceeds the binding energy of an exciton (≈ 1 eV).

Similar quasi-excitonic effects, obviously shifted toward the region of band-to-band transitions, were observed in Tartu long ago and interpreted as manifestations of e-h interaction in a pair of a spatially close electron and a hole formed at the absorption of the same photon (genetic e-h pair). The theory of such genetic effects was elaborated by Vasil'ev and Mikhailin [34]. We have observed the same excitonic effects in NaCl:Ag at 8 K. Ag^+ centers serve as effective electron traps, and**,** therefore, it is easy to detect the manifestations of genetic e-h pairs. However, it is significantly more difficult to observe these effects in a highly pure NaCl crystal.

Fig. 2*b* presents a fragment of a reliable band structure of NaCl. This diagram reflects well the sequence of the branches inside c- and v-band as well as the absolute values of E_g and E_v (width of a v-band). The measurements of the angular dependence of photoelectron emission from a (100) surface of NaCl have been interpreted on the basis of the band structure calculations [35]. According to this scheme, photons of 17 eV (number 1 in the Figure 2b) are already able to create photoelectrons with an energy sufficient for the creation (with the participation of phonons) of a secondary exciton with n = 1. Numbers 2 and 3 depict the energies of exciting photons that are able to create hot conduction electrons with an energy sufficient for the creation (again due to the Auger mechanism) of a secondary e-h pair at the Γ and X point of the Brillouin zone, respectively.

Elementary creation mechanisms of secondary excitations

Now we shall demonstrate the potential of the experimental method that involves an external action on a crystal with the aim to separate the excitonic and e-h mechanisms of MEE. Fig. 3 shows what we can expect for a system like NaI and KI, where the energy states of free and self-trapped excitons are separated by an activation barrier. The coexistence of free excitons (FE) and STE was revealed for the first time in 1975 in Tartu [36], and after that it was investigated in detail by Estonian and Japanese physicists (see [37] and references

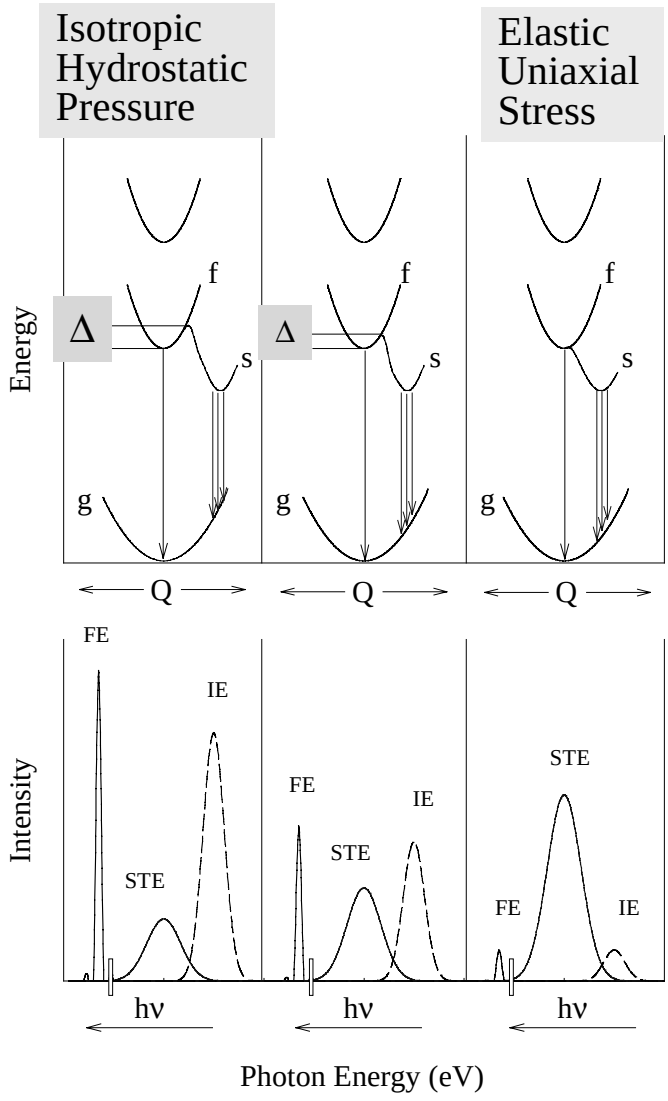

Figure 3. Influence of isotropic hydrostatic pressure (left column) and elastic uniaxial stress (right column) on the emission spectra of free and self-trapped excitons (FE and STE) as well as on the impurity emission (IE) at the direct optical formation of excitons in a KI-type crystal. Energy of a crystal without excitons (g) and with free (f) and self-trapped (s) excitons, as functions of the configuration coordinate of the ions.

therein). A high hydrostatic pressure draws together the neighboring anions, increases the width of the excitonic band and the height of the activation barrier and, as a result, reduces the intensity of STE emission and enhances the emission of impurities excited by FE [38]. On the other hand, an applied, relatively weak (~ 1 kg/mm^2) EUS only slightly changes the energy, but sharply reduces the crystal symmetry. According to modern theories [39,40], this should cause the disappearance of the activation barrier and facilitate the self-trapping of excitons. The EUS suppresses the FE emission as well as the impurity emissions connected with the energy transfer by FE, but increases the STE luminescence.

Just these results we obtained for the case of the creation of secondary excitons under the conditions of MEE in KI:Na [19,22]. We analyzed the behavior of the efficiency of the STE triplet emission (3.4 eV) and the emission of excitons localized near Na^+ impurity ions (2.95 eV). In the region of the creation of secondary excitons (13-16 eV) the applied EUS causes an enhancement of intrinsic emission and a weakening of the impurity emission excited by FE (see Fig.1 in [22]). EUS increases the probability of exciton self-trapping and reduces the excitation probability of impurity centers by FE. Theoretically, there is a very interesting situation at $h\nu_{ex} = 2E_e$, where the formation of two excitons by one absorbed photon is possible in the frame of two-electron approach. According to the theory, the probability of such an effect is at least an order of magnitude lower than for one-electron transitions [33]. Our experimental results in KI:Na do not manifest an efficient creation of two paraexcitons with J = 2 (11.5 eV) or two orthoexcitons with J = 1 (11.6 eV) by one photon. Nevertheless, we do not outrule a possible existence of these weak effects in KI:Na and NaCl:Ag.

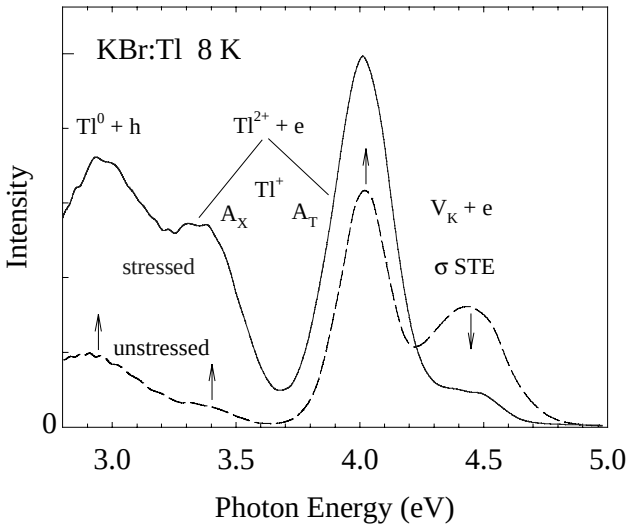

Figure 4. Emission spectra measured for the unstressed (dashed line) and stressed (solid line) sample of KBr:Tl (300 ppm) under excitation by 19 eV photons at 8 K.

The influence of EUS on the e-h processes in AHC was of our special interest. Fig. 4 depicts the emission spectra measured for an unstressed sample of KBr:Tl (300 ppm) at 8 K. A crystal excitation by photons, that create two e-h pairs each, provides an intense intrinsic recombination σ emission of STE (4.42 eV) as well as A_T and A_X Jahn-Teller components of the recombination luminescence of Tl^+ centers. The applied EUS changes drastically the emission spectrum - weakens the intrinsic STE emission and causes a significant enhancement of the intensity of recombination impurity emissions. So, the effect is quite opposite to the EUS influence on primary and secondary excitons. A possible reason for this difference is illustrated in Fig. 5. At 8 K, self-trapped holes are totally immobile but before the self-trapping free holes move in a crystal and can reach impurity Tl^+ centers, ionize them providing the appearance of an impurity emission due to the recombination of electrons with Tl^{2+} centers. The emission at 2.9 eV is caused by the interaction of hot holes with Tl^0 centers. In an unstressed sample there is a degeneracy of the energy states of light and heavy holes at the Γ point of the Brillouin zone. So, light holes quickly relax to the top of v-band and after conversion into heavy ones, undergo the self-trapping. The applied EUS reduces the crystal symmetry and removes the degeneracy for the states of heavy and light holes, and forms an energy gap between these states. This gap prevents the self-trapping of light holes with the formation of V_K centers resulting in the reduction of STE recombination emission. Simultaneously, the intensity of the recombination impurity emission increases due to the efficient interaction of hot holes with Tl^0 and Tl^{2+} centers. The investigation of EUS influence on the e-h processes is still in the beginning and should be continued.

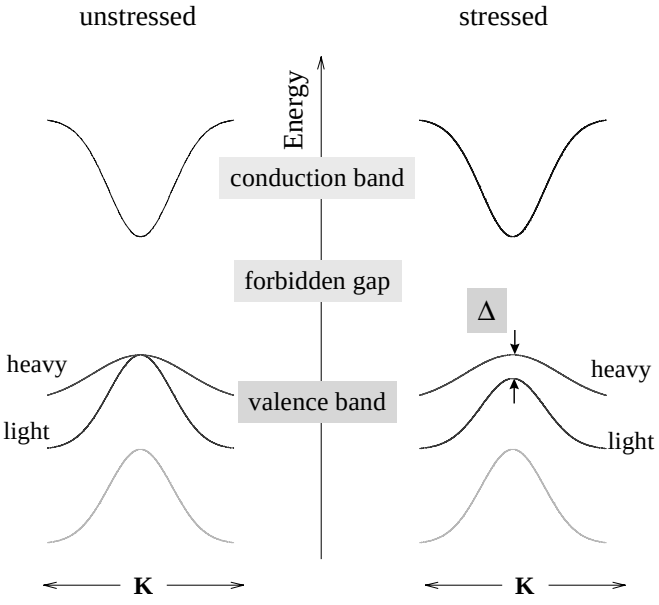

Figure 5. Schematic band structure for the stressed and unstressed sample of a face-centered alkali halide crystal.

The study of the influence of an external electric field on the creation of secondary e-h pairs in AHC at 5 K has been started as well. The first results are presented in [22]. It turned out that genetic

secondary e-h pairs in KI:Na can be destroyed by an external electric field. A similar effect for primary e-h pairs was observed earlier in KBr:In [41,42].

We had an obvious need for a comparison of the luminescent data and the energy distribution of electrons emitted from a crystal while studying the processes of impurity Tl^+ and Ag^+ center excitation by hot photoelectrons in AHC [18,21]. In a RbCl:Tl crystal, photons of 13-16 eV form photoelectrons with the kinetic energy of 5-7 eV, that is insufficient for a subsequent creation of secondary excitons or e-h pairs. However, such hot photoelectrons cause a direct excitation of Tl^+ centers. This fast process can be regarded as an analogue of the Frank-Hertz effect (resonant excitation of free atoms by slow electrons) in solids. The kinetic energies of photoelectrons were estimated by photoelectric methods in a thin film of RbCl [21].

Next, we discuss possible micromechanisms of the energy conversion from hot conduction electrons, formed in a matrix excited by VUV radiation to the creation of secondary excitons or e-h pairs. The following possibilities should be considered:

i. one-step process - an absorbed photon creates a two-electron excitation, e.g., two excitons or an e-h and an exciton [33,43];

ii. two-step process - one photon forms a hole and a hot conduction electron, that after some pathway in a lattice converts a part of its kinetic energy to the creation of a secondary e-h pair [2] or a secondary exciton [3,17] (the so-called impact mechanism of MEE);

iii. two-step process - again, a photon forms a hole and a hot conduction electron which after some pathway in a lattice participates in nonradiative Auger transition to a lower state in a c-band with the simultaneous creation of a secondary electronic excitation (Auger mechanism of MEE).

In semiconductors, the impact and Auger mechanisms of MEE are not equivalent [44]. However, the separation of these mechanisms is difficult even in well-studied wide-gap crystals (KI, KBr, NaCl, Xe, Kr). For a long time we have been trying to find differences between one-step and two-step mechanisms of the creation of secondary excitons, analyzing the effects that reflect the spatial correlation between the EE formed at MEE. A pathway of a photoelectron before the creation of a secondary EE is hundreds of interanion distances, that is why a primary photohole appears to be far away from the birth place of a secondary exciton and a slow electron. However, if a pathway of a hot photoelectron is only a few interanion distances, then in a crystal with an efficient self-trapping of holes we have a situation when a primary hole and a secondary exciton (or a hole) are spatially close to each other. It is just the situation that is realised in AHC.

A search for the manifestations of a high local density of electronic excitations under MEE conditions was started already in 1965. Some important peculiarities of the dependence of thallium impurity luminescence on the intensity of excitation have been found in KI:Tl [3]. The spatial proximity of primary and secondary self-trapped holes in the region of MEE can be clearly demonstrated while measuring the creation spectrum of the groups of spatially correlated defects in KBr at 8 K [45]. The efficiency of a defect triplet (V_K-F-I) creation is especially high in a spectral region where one absorbed photon ($h\nu_{ex}$ = 19 eV) causes the formation of two e-h pairs. This process can be explained the following way (see Fig. 6). At t_1, a photon creates a hole and a hot conduction electron, that (at t_2) forms a secondary e-h pair. A pair of Frenkel defects is created at the nonradiative recombination of an electron and a hole. According to our estimations, the distance between a primary self-trapped hole and an F does not exceed 4 interaction distances (see also [46,47]).

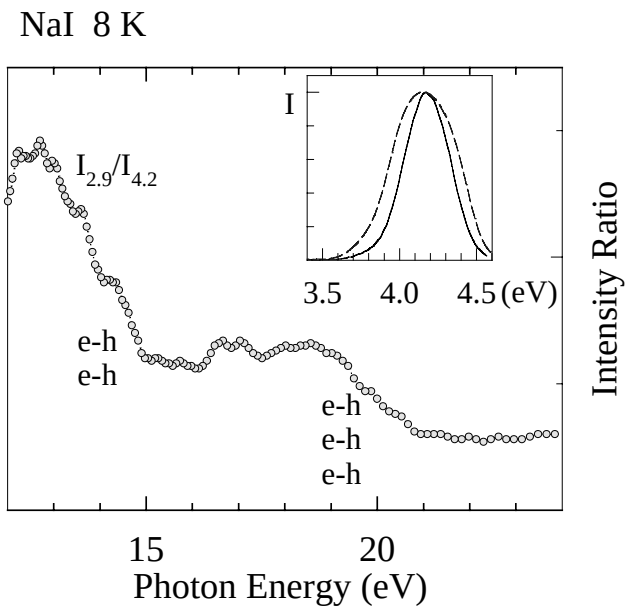

Figure 7. Intensity ratio spectrum (•) for the emission of STE (4.2 eV) and a Tl^+ impurity emission (2.9 eV) in NaI at 8 K. The inset shows the spectra of STE emission at the excitation by 6.05 eV (solid line) and 20 eV photons (dashed line) measured in a time window of 140 ns with a delay of 10 ns after excitation pulse.

We observed the manifestations of the groups of spatially correlated electronic excitations in NaI as well. The emission of STE (4.2 eV) dominates in NaI at 8 K, while a weak Tl^+ impurity emission at 2.9 eV is also observed. Fig. 7 demonstrates the intensity ratio spectrum for these two emissions. The value of ratio decreases in two stages: 13-15 and 19-21 eV. It is obvious that these two stages correspond to the formation of two and three e-h pairs, respectively (E_g = 6 eV). The presence of a group of close electronic excitations enhances the probability of electron recombination with V_K decreasing the intensity ratio for impurity and intrinsic emission in the region of MEE. Fig. 7 also shows the spectra of intrinsic emission at the excitation by 6.05 eV photons, able to form only a single e-h pair each and by 20 eV photons, when one photon forms three e-h pairs. In the latter case the STE emission is distorted by a field of a V_K center localized nearby. However, there is no distortion of STE emission in the case of NaI excitation by 13 eV photons (each of such photons can form two e-h pairs).

A contribution of the excitonic mechanism of MEE to the excitation of luminescent impurity centers is relatively small in case of a crystal excitation by high-energy particles or quanta. The e-h mechanism of MEE is responsible for the appearance of about 90 % of emission quanta in NaI:Tl. However, according to the spectra of electron energy losses in AHC, a part of the energy of electrons is spent for the formation of plasmons - longitudinal collective vibrations of valence electrons [49]. It was shown [50], that the formation efficiency of plasmons by fast δ-electrons is especially high in AHC with adjoining anions (e.g., in NaI where the effective radius of I^- is significantly bigger than that of Na^+). If the plasmon energy exceeds the value of $2E_g$, the decay of a plasmon into two e-h pairs occurs shortly after its creation.

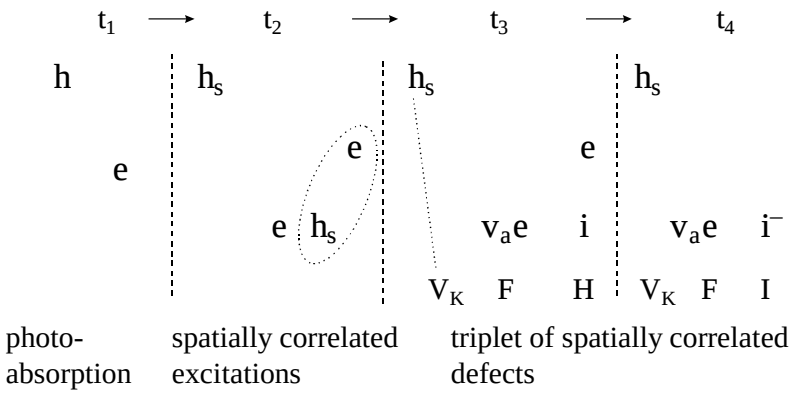

Figure 6. Formation of the groups of spatially correlated defects under conditions of MEE.

In our opinion, the elementary MEE processes in a NaI:Tl classical scintillator should be thoroughly studied in the region of exciting photons of 11-13 eV. Under conditions of high density of excitation (see, e.g., [8]) e-h recombinations in NaI:Tl occur during a shorter period that a lifetime of Tl^+ centers in the excited state providing a high efficiency of scintillations [7].

Conclusions

1. A complex use of luminescent and photoelectric methods is needed for the separation of elementary mechanisms of MEE. Important information on MEE mechanisms can be obtained by means of external action on a crystal under VUV irradiation.

2. Creation of secondary excitons and spatially correlated electrons and holes has been revealed using a complex of experimental methods. These effects must be taken into account in the theory of optical spectra in wide-gap crystals.

3. Direct manifestations of the groups of spatially correlated excitations or defects have been observed at VUV irradiation of crystals with self-trapped holes.

4. An analysis of the complicated structure of conduction bands in alkali halides allows to conclude that Auger processes with the participation of hot photoelectrons are essentially important for the creation of secondary e-h pairs or excitons. Impact mechanisms are also responsible for the excitation of impurity centers by hot photoelectrons

Acknowledgements

The authors are grateful to Prof. M. Kamada, Prof. I. Martinson and Prof. G. Zimmerer for valuable discussions and support during synchrotron measurements. This work was supported by the Estonian Science Foundation (grant No. 3868), the Craaford and the STINT Foundation (Sweden).

References

1. V. S. Vavilov, J. Phys. Chem. Solids **8** (1959) 223.
2. W. Schockley, Czech. J. Phys. **B 11** (1961) 81.
3. E. R. Ilmas, G. G. Liidya and Ch. B. Lushchik, Opt. Spectrosc. **18** (1965) 255, 359.
4. E. R. Ilmas, R. Kink, G. G. Liidya and Ch. B. Lushchik, Izv. Akad. Nauk SSR Ser. Fiz. **29** (1965) 27.
5. E. R. Ilmas and Ch. B. Lushchik, Trudy Inst. Fiz. Akad. Nauk Estonian SSR **40** (1972) 3.
6. M. Kirm, E. Feldbach, A. Lushchik, Ch. Lushchik, A. Maaroos, T. Savikhina, Proc. SPIE **2967** (1997) 18.
7. R. A. Kink, G. G. Liidja, Proc. 5th Conference on Scintillators, Kharkov (1969) 229.
8. V. Denks, Ch. Lushchik, T. Soovik, Sov. Phys. Sol. State **11** (1969) 3.
9. E. R. Ilmas, G. G. Liidja, and Ch. B. Lushchik, Trudy Inst. Fiz. Acad. Nauk Estonian SSR **26** (1964) 21.
10. S. N. Ivanov, E. R. Ilmas, Ch. B. Lushchik, and V. V. Mikhailin, Sov. Phys. Solid State **15** (1973) 1053.
11. N. S. Rooze, Sov. Phys. Solid State **17** (1975) 690.
12. J. K. Beaumont, A. J. Bourdilon, M. N. Kabler, J. Phys. C **9** (1976) 2961.
13. D. Blechschmidt, M. Skibovski and W. Steinman, Phys. Status Solidi **42** (1970) 61.
14. A. Ejiri, A. Hatano, and K. Nagakawa, J. Phys. Soc. Jpn. **63** (1994) 314.
15. Ch. B. Lushchik, and A. Ch. Lushchik, Decay of Electronic Excitations with Defect Formation in Solids (Nauka, Moscow 1989).
16. A. Lushchik, I. Kudryavtseva, Ch. Lushchik, E. Vasil'chenko, M. Kirm and I. Martinson, Phys. Rev. B **52** (1995) 10069.
17. A. Lushchik, E. Feldbach, R. Kink, Ch. Lushchik, M. Kirm, and I. Martinson, Phys. Rev. B **53** (1996) 5379.
18. E. Feldbach, M. Kamada, M. Kirm, A. Lushchik, Ch. Lushchik and I. Martinson, Phys. Rev. B **56** (1997) 13908.
19. M. Kirm, A. Lushchik, Ch. Lushchik and E. Vasil'chenko, in "Physics and Chemistry of Luminescent Materials" eds. C.W. Struck, K.C. Mishra and B. DiBartolo, PV 98-24, The Electrochemical Society Proceedings Series, Pennington, NJ (1999) 267.
20. G. Zimmerer, Nucl. Instrum. Methods Phys. Res. A **308** (1991) 178.
21. A. Lushchik, M. Kamada, M. Kirm, Ch. Lushchik, and I. Martinson, Radiat. Measur. **29** (1998) 229.

22. M. Kirm, A. Lushchik, Ch. Lushchik, S. Vielhauer and G. Zimmerer, Proc. Int. Conference Scintillators SCINT99 (1999) in this volume.
23. A. N. Vasil'ev, V. N. Kolobanov, I. L. Kuusmann, Ch. B. Lushchik and V.V. Mikhailin, Sov. Phys. Sol. State **27** (1985) 1616.
24. Yu. Aleksandrov, N. Lushchik, Ch. Lushchik, V. Makhov, M. Yakimenko, Trudy Inst. Fiz. Akad. Nauk Estonian SSR **55** (1984) 72.
25. Yu. M. Aleksandrov, I. L. Kuusmann, P. Kh. Liblik, Ch. B. Lushchik, V. N. Makhov, T. I. Syreishchikova, and M. N. Yakimenko, Sov. Phys. Solid State **29** (1987) 587.
26. B. Steeg, E. Gminder, M. Kirm, V. Kisand, S. Vielhauer, and G. Zimmerer, J. El. Spectr. and Rel. Phen. **101-103** (1999) 879.
27. M. Kirm, G. Zimmerer, E. Feldbach, A. Lushchik, Ch. Lushchik and F. Savikhin, Phys. Rev. B **60** (1999) 502.
28. A. Lushchik, E. Feldbach, Ch. Lushchik, M. Kirm and I. Martinson, Phys. Rev. B **50** (1994) 6500.
29. Ch. Lushchik, E. Feldbach, A. Frorip, M. Kirm, A. Lushchik, A. Maaroos and I. Martinson, J. Phys.: Condens. Matter **6** (1994) 11177.
30. M. Kirm, E. Feldbach, R. Kink, A. Lushchik, Ch. Lushchik, in "Excitonic Processes in Condensed Matter", Ed. M. Schreiber, Univ. Dresden, 1996, 179.
31. E. A. Vasil'chenko, N. E. Lushchik, Ch. B. Lushchik, Sov. Phys. Solid State **12** (1970) 167.
32. M. Kirm, A. Frorip, R. Kink, A. Lushchik, Ch. Lushchik and I. Martinson, Rad. Effects and Defects **135** (1995) 375.
33. D. L. Dexter, Phys. Rev. **126** (1962) 1962.
34. A. N. Vasil'ev, V. V. Mikhailin, Bull. Acad. Sci. USSR Fiz. Ser. **50** (1986) 113.
35. F. J. Himpsel and W. Steinmann, Phys. Rev. B **17** (1978) 2537.
36. Ch. Lushchik, I. Kuusmann, V. Plekhanov, J. Luminescence **18/19** (1979) 11.
37. Ch. B. Lushchik, in "Excitons", Eds. E. I. Rashba and M. D. Sturge, North-Holland Amsterdam, 1982, Chapter 12.
38. H. Nishimura, T. Oguri, T. Tsujimoto, M. Nakayama, H. Kurisu, T. Komatsu, S. Morita, and M. Kobayashi, Jpn. J. Appl. Phys. **32** (1993) 288.
39. E. I. Rashba, in "Excitons", Eds. E. I. Rashba and M. D. Sturge, North-Holland Amsterdam, 1982, Chapter 13.
40. A. Shelkan and G. Zavt, Bull. Estonian Akad. Sci. **39** (1990) 358.
41. V. P. Denks, V. I. Leimann, Sov. Phys. Solid State **10** (1968) 1426.
42. Ch. B. Lushchik, J. Luminescence **1/2** (1970) 594.
43. J. T. Devreese, A. B. Kunz, and T. C. Collins, Solid State Commun. **11** (1972) 673.
44. Yi Lu and Ching-Tang Sah, Phys. Rev. B **52** (1995) 5657.
45. M. Kirm, A. Lushchik, Ch. Lushchik, I. Martinson, V. Nagirnyi and E. Vasil'chenko, J. Phys. Condens. Matter **10** (1998) 3509.
46. A. Ch. Lushchik and Ch. B. Lushchik, Bull. Russ. Acad. Sci. Phys. **56** (1992) 201.
47. W. Meise, U. Rogulis, F. K. Koschnik, K. S. Song, J. M. Spaeth, J. Phys. Condens. Matter **6** (1994) 1815.
48. M. Creuzburg, Z. Physik **196** (1966) 433.
49. O. Pains, Elementary Excitations in Solids, W. A. Benjamin Inc. New-York- Amsterdam 1963.
50. Ch. Lushchik, T. Soovik and I. L. Kuusmann, Proc. 5th Conference on Scintillators (USSR), Kharkov (1969) 30, 200.

Relaxation of hot electronic excitations in scintillators: account for scattering, track effects, complicated electronic structure

A.N.Vasil'ev

Synchrotron Radiation Laboratory, Physics Faculty, Lomonosov Moscow State University, 119899 Moscow, Russia

Abstract: Analysis of relaxation scheme beyond the three-step model of scintillation is discussed. Two cases (crossluminescent crystals and crystals with 4f subband) are considered in details. The main attention is paid on the hot stage of relaxation, at which the relaxation is subdivided in two independent channels, and on interaction of thermalized excitations.

Keywords: Relaxation, scattering, track effects

Introduction

The contributions presented at the present Conference confirm the general tendency in the scintillator research: though the interest to alkali halide scintillators still exists, the expectations for improved properties required for novel applications such as higher yield, faster decay, higher atomic numbers, etc., are linked with more complicated compounds such as lutetium and gadolinium crystals, crossluminescent crystals, lead compounds, etc. However their performance often appears to be not as good as predicted by conventional theory. Thus, the comparison of the experimentally observed scintillation yields of various materials with the theoretical values predicted by empirical models for the evaluation of the number of electron-hole pairs presented in [1] reveals that the former ones are substantially smaller than the latter ones. The aim of the present paper is to consider the cases when this discrepancy cannot be removed by the perfection of the crystals and has a fundamental origin. The effect of the multiplicity of the energy relaxation pathways on the scintillation yield is discussed for the crystals with several types of electronic excitations when not all of them can participate in the scintillation process.

Often the scintillator light yield is expressed as (see e.g. [2–4]):

$$\eta = N_{eh} S Q , \qquad (1)$$

where N_{eh} is the conversion efficiency expressed as a number of electron-hole pairs or excitons created by the absorbed high-energy photon or a particle, S is the transfer efficiency of e-h pair energy to the luminescence center and Q is the quantum yield of luminescence. N_{eh} is normally expressed via the average energy E_{eh} required for the creation of a thermalized e-h pair in the following form: $N_{eh} = E_{inc}/E_{eh}$. Here E_{inc} is the energy of the quantum of absorbed radiation or the energy deposited by an ionizing particle. First estimations of E_{eh} being (2÷3) E_g (E_g is the forbidden energy bandgap) were made quite some time ago [5, 6] and refer to the case of a 'simple' insulator which can be characterized by electrons and holes (or excitons) as the only types of electronic excitations and E_g as the main and sufficient parameter of the energy band diagram, characterizing the conversion efficiency. However, if we consider for example crossluminescent crystals we can immediately see that the formula (1) requires modifications. Indeed, in this case 'scintillation-active' electronic excitations are the highest-lying core holes, i.e. E_g has to be substituted by E_{core}. Moreover, the number of the highest lying core holes created via the energy conversion process is not simply defined by the ratio of the high-photon energy and the energy of the highest-lying core level, as together with the core holes conduction band electrons and valence band holes are also created which

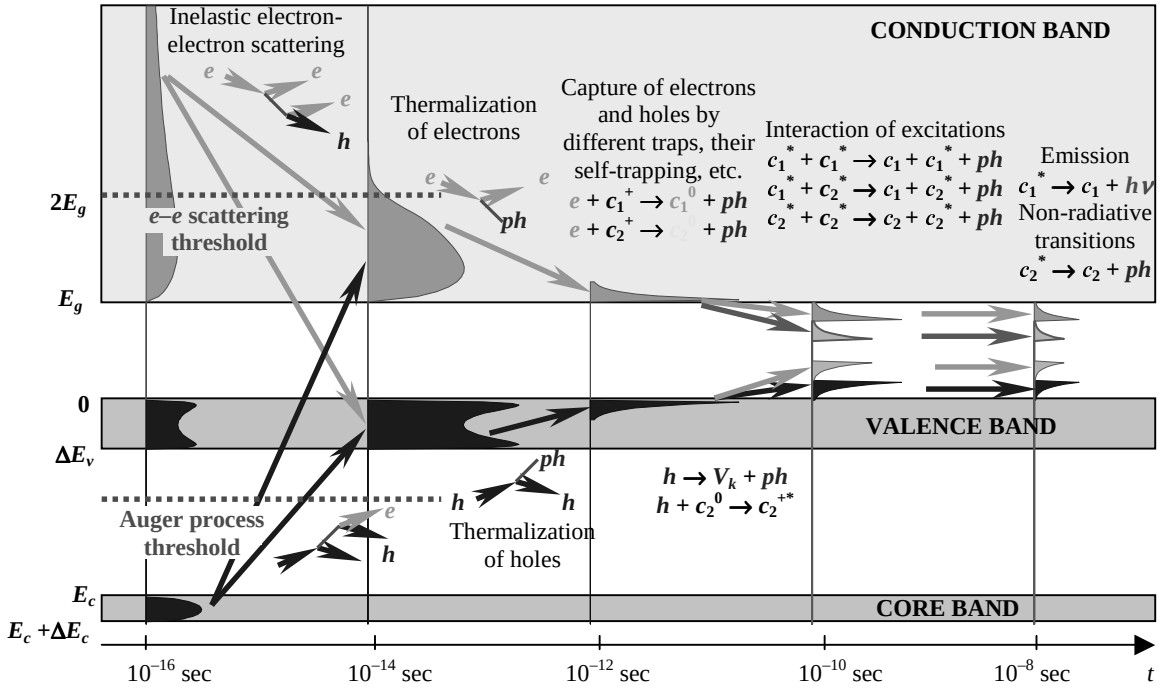

Figure 1. Scheme of relaxation of electron excitations in an insulator with two channels of relaxation

are not efficient in the crossluminescent process and thus we need to take into account the branching ratio between these two processes. Unfortunately, there is no simple way similar to the formula (1) to estimate the limiting scintillation yield of new compounds, however, investigations of the multiplicity of the energy relaxation pathways in the fundamental absorption range can provide information on the types of created electronic excitations and their partial distribution. In this paper we shall consider the cases of BaF_2 and CeF_3 for which (as it will be shown) the number of 'scintillation-active' excitations also cannot be defined by estimation (1).

Another process often omitted in the estimation of the expected scintillation yield is the interaction of the electronic excitations that after the hot relaxation stage and thermalization appear at the distances comparable to their interaction radius. This is the second question discussed here.

General scheme of relaxation of electronic excitations in crystals

Let us consider the well-known scheme of relaxation of excitations in ionic crystals paying attention on energy distribution and space correlation of excitations. First of all we discuss relaxation in ionic crystal with simple energy structure.

Propagation of an ionizing particle through a crystal results in the production of a large number of secondary electronic excitations, the relaxation of the excited crystal can be roughly subdivided into the following main stages (see Fig. 1):

a) emission and absorption of longitudinal photons (quanta of Coulomb field) by hot electrons and holes. These processes are also known as inelastic scattering of electrons and Auger decay of deep core holes. Their rates can be expressed in terms of integrals of energy loss function with the value of about 10^{15}–10^{16} s^{-1}. The number of electronic excitations increases only at this relaxation stage. The energy of the electronic subsystem is defined by the total ionization losses of the primary particle and does not decrease during this stage. Energy and spatial distribution of hot excitations can be described by the function $g_i^a(E,\mathbf{r})$, which is a convolution of elementary scattering events. This function

controls further stages of relaxation. The index *i* refers to different types of electronic excitations as has been discussed in the Introduction. From the relaxation point of view, different types of excitations are those, which do not undergo mutual transformations during the first stage of relaxation. Crystals with relatively simple electronic structure, such as alkali halides, have three types of such excitations: holes in the valence band, electrons in the conduction band (with the energies below the threshold of production of secondary excitations) and excitons.

b) The second stage is thermalization of electronic excitations with the emission of phonons. The duration of this stage is about 10^{-12} s, the number of electronic excitations does not change. This is the main stage for transferring the kinetic energy of excitations into heat due to phonon emission. During this stage the distribution of hot excitations $g_i^a(E,\mathbf{r})$ is convolved with distribution function $\lambda_i^b(E,\mathbf{r})$, which describes the thermalization of excitation of type *i* with energy *E*, into spatial distribution of thermalized excitations $g_i^b(\mathbf{r}) = \int\left(g_i^a(E,\mathbf{r}) \otimes \lambda_i^b(E,\mathbf{r})\right) dE$, symbol $\otimes$ denotes convolution over space coordinates.

c) During the next stage thermalized excitations are captured by traps, (self-trapped,) captured by emission and quenching centers, etc. The duration of this stage depends on the rates of different monomolecular (for self-trapping) and bimolecular (for capture by centers and traps) and can vary substantially. The spatial distribution of excitations $g_i^c(\mathbf{r})$ also depends on parameters of these reactions and is generated on the distribution at previous stage $g_i^b(\mathbf{r})$: $g_i^c(\mathbf{r}) = g_i^b(\mathbf{r}) \otimes \lambda_i^c(\mathbf{r})$. The excitation number conserves, and the total energy slightly decreases. This stage can be considered as interaction of excitations with stable defects and impurities.

d) The next stage is the migration of these relaxed excitations. Its time domain overlaps with stage (c), however here we take into account also the interaction with other excitations while in (c) we consider only interaction with crystal defects. Stage (d) can result in the decrease of the excitation number, or redistribution over the types of excitations. Since the interaction between excitations depends on the inter-excitation distances, this stage is controlled by the spatial distribution function $g_i^c(\mathbf{r})$. Therefore the intensity of interaction depends on the parameters of elementary scattering acts, which play the main role in stages (a) – (c). This stage is responsible for density effects, non-proportionality of energy response of scintillator and non-exponential decay kinetics.

e) The last stage is radiative and non-radiative decay of excitations. This is the final stage, and the main processes are local and carried out in the emission centers. Therefore this stage is hardly affected by the processes involved in the stages (a) – (d).

Peculiarities of cascade process

Cascade process (a) of inelastic scattering with production of secondary excitations is a sequence of elementary scattering acts. Each scattering act is characterized by its rate and distribution of secondary excitations over energy. The rate of scattering with production of new excitations is important for space distribution of secondary excitations (it defines the mean free path of an electron). In insulators such scattering has a prominent threshold. Simple parabolic model for conduction and valence dispersion laws results in threshold kinetic energy of 1 to 2 E_g. In systems with complicated dispersion laws the threshold is about E_g. The scattering rate is high enough for all energies of electronic excitations well above the threshold, and in this range the inelastic scattering with production of new excitations is the only way of relaxation. The competition between this channel and thermalization of excitations in the threshold region is discussed in [7–9].

Model of energy distribution	Number of scattering steps
(a) $E \Rightarrow (E_g)+(E-E_g)$	$N_1 = h\nu/E_g$
(b) $E \Rightarrow (E/2)+(E/2)$	$N_2 = \log_2(h\nu/E_g)$
(c) $E \Rightarrow (E')+(E-E')$ E' is random value between E_g and E–E_g	$N_3 = h\nu/1.4E_g$

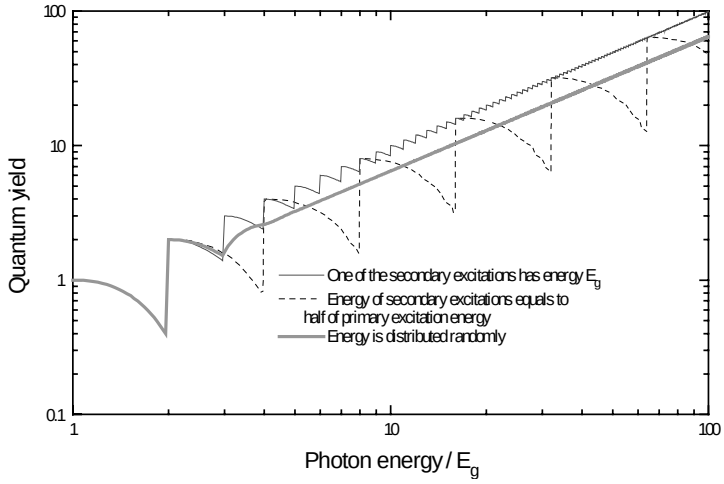

Fig. 2. Excitation yield versus photon energy for models of inelastic scattering, mentioned in the table [9]

The energy distribution of secondary excitations after the elementary scattering act defines the overall features of cascade process, e.g. number of steps in this process, photon energy dependence of excitation efficiency, etc. We will compare three types of this distribution for an oversimplified model of insulator without core levels and with narrow valence band, so the energy of any electron-hole pair is the sum of the forbidden gap energy E_g and the electron kinetic energy [9]. The efficiency of the luminescence excitation for this model is shown in Fig. 2. For clarity we suppose slight dependence of the luminescence excitation yield for energies below the threshold of electron-electron scattering with production of secondary excitation, which equals to $2E_g$ for this model. Three different types of energy distribution for secondary excitations are discussed: (i) one of the excitations has minimal possible energy; (ii) both secondary excitations have energy equal to half of the primary excitation energy; (iii) energy is randomly distributed between excitations. The oscillations of the quantum yield are observed in cases (i) and (ii), whereas in case of random distribution the quantum yield becomes smooth for energies higher than $4E_g$. In case (ii) the oscillations are not directly connected with details of electronic structure, but are very sensitive to the energy of excitations at the last-but-one step. It is obvious, that these models have no quantitative sense. Nevertheless, case (ii) illustrates the role of core levels, for which the energy distributions of secondary excitations for excitation energy below and above the edge strongly changes.

Relaxation in systems with complicated band structure

In crystals with more complicated electronic structure additional types of excitations exist. Here we discuss two examples. In crossluminescent crystals the highest lying core holes cannot decay via Auger processes due to energy conservation law and should be considered separately. In cerium compounds cerium 4*f* levels fall within the forbidden energy bandgap. Ce Frenkel excitons should be regarded as an additional type of excitations. Both in crossluminescent crystals and in cerium compounds additional types of excitations play a major role in the scintillation processes. In crystals with several types of relaxed excitations not all of them participate in scintillation process (e.g. uppermost core hole in crossluminescent crystal or Frenkel exciton in a crystal with rare-earth matrix), so one can use the notation of “useful” excitation. The presented scheme allows tracing the evolution of such “useful” excitations during each stage of relaxation.

Relaxation in a system with rare-earth ions

"Useful" excitations in crystals with rare-earth subband embedded into the forbidden gap can be produced through impact excitation only by electrons with kinetic energies in a rather narrow band (the kinetic energy should be higher than the rare-earth excitation energy but lower than the threshold of production of electron-hole pair with hole in the valence band, since the density of states in the valence band is much higher than that in rare-earth subband, see [10,11]). This configuration of thresholds reduces the number of "useful" excitations by the factor of about 5.

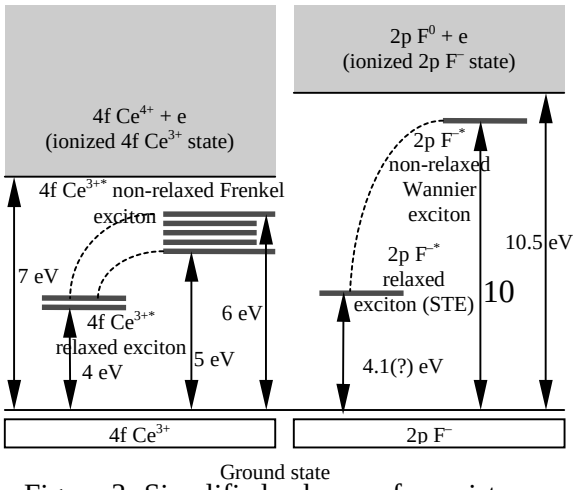

Figure 3. Simplified scheme of coexistence of two types of excitons in cerium fluoride [10, 11].

In some rare-earth halide crystals with possibility of coexistence of two types of excitons (e.g. CeF_3), anion excitons are not efficient in energy transfer to rare-earth excitons, so only the latter type of excitons is 'useful' for rare-earth emission. The final relaxation of these two types of excitons can be regarded as independent, since the energy of each relaxed exciton is insufficient for excitation of another type [10, 11]. Fig. 3 presents the simplified scheme of relaxation, which shows that energy transfer from fluorine subsystem to cerium subsystem can occur only at hot relaxation stage, and therefore has low probability.

Inelastic scattering with creation of new electronic excitations can be considered as emission of the longitudinal photons followed by their absorption with creation of new excitations. Therefore the distribution of secondary

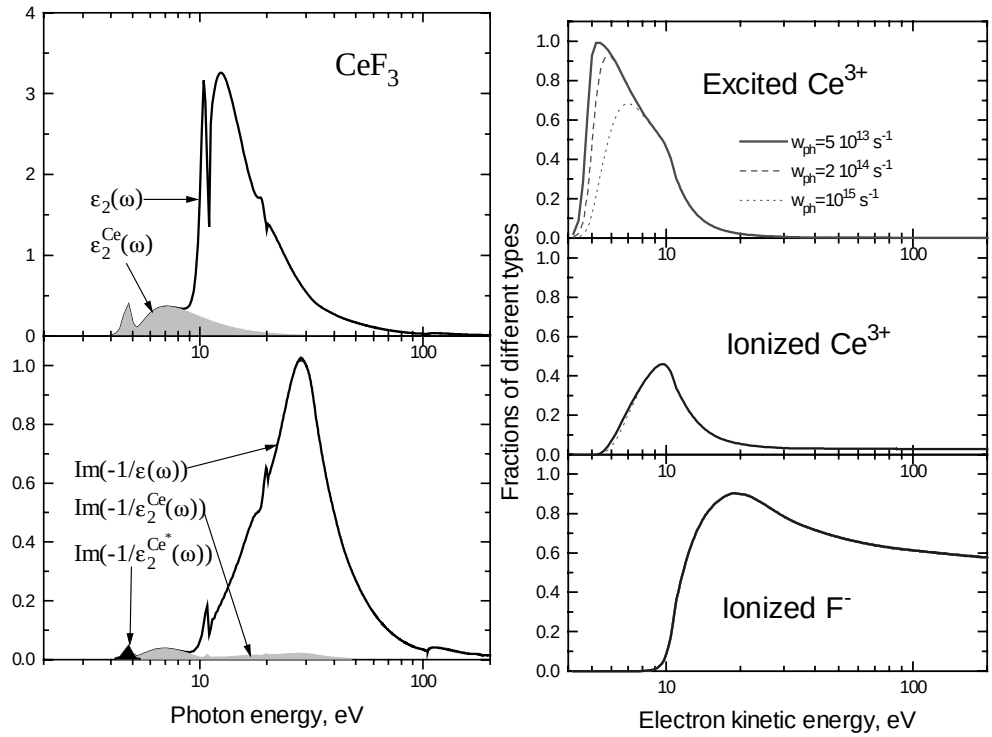

Fig 4. Simulated imaginary part of dielectric permittivity (upper left panel) and energy loss function (lower left panel) for CeF_3. Filled areas represent the addition due to 'useful' excitations (excited and ionized cerium states for CeF_3). Dependence of the fraction of ionized and excited ions and ionized ions produced by an electron, on electron kinetic energy for CeF_3 (right panel) [9].

excitations over types is proportional to the fraction of these types in the energy loss function [12] $\mathrm{Im}\left(-1/\varepsilon(\omega,\mathbf{k})\right)$. Since energy loss function is a sum over additives due to creation of different types of excitations, one can estimate the number of 'useful' excitations produced in each scattering event.

Fig. 4 presents the addition of Ce-transitions to imaginary part of dielectric function, which is responsible for the absorption, and to energy loss function. Cerium excitons are produced at final stages mainly by secondary excitations in rather narrow energy domain between the thresholds of inelastic scattering with production of different excitations. The secondary excitation should have energy above the threshold of the production of rare-earth excitation, but when its energy is higher then the threshold of the production of anion excitation, mainly the latter type of excitons are produced, since the oscillator strength for the production of excitations in anion sub-system is much higher than that for rare-earth sub-system. Therefore Ce ions can be excited only by electrons with kinetic energy from 5 to 15 eV (Fig. 4). This fact partially explains relatively low yield of CeF_3. This case is shown also in the general scheme of relaxation (Fig. 5).

These considerations allows us to perform the simulation of the excitation processes for photon energies from 5 eV to 120 eV [13, 14].

For energies below than 6 eV only direct excitation of 4f–5d transition occurs (process 1 in Fig. 6). The yield of excitons is equal to one.

In the region 6 eV < $h\nu$ < 9.8 eV ionization of cerium results in creation of separated electron-hole pairs (process 2). As the photon energy increasing the number of excitons diminishes while the number of separated electron-hole pairs increases. In the model under consideration it is mainly due to effect of potential barrier between 4f excitonic states and states of separated electron hole rather than binding of thermalized particles because of the relatively large separation between them.

Above 9.6 eV the primary electron has sufficient energy to excite 4f–5d transition (process 3). The number of excitons increases till 10.8 eV.

The abrupt decrease of the number of cerium excitons and holes at 11 eV is due to onset of the absorption of the photon on the valence band formed by 2p F states. This channel is strong

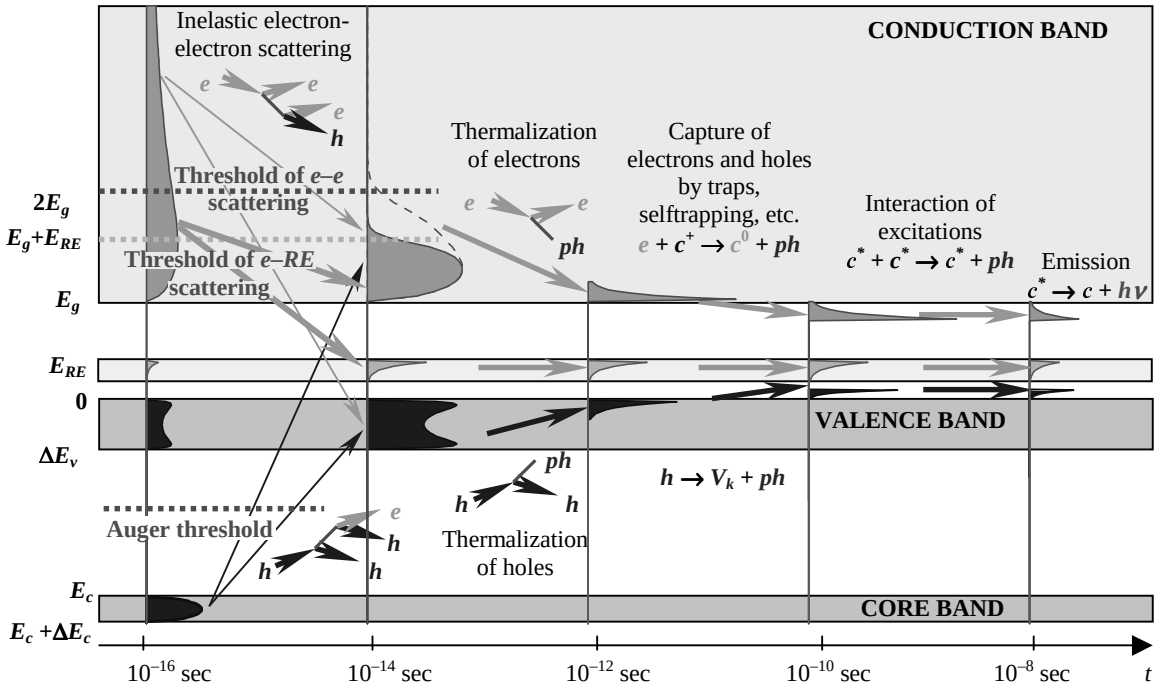

Figure 5. Scheme of relaxation of electronic excitations in rear-earth crystals

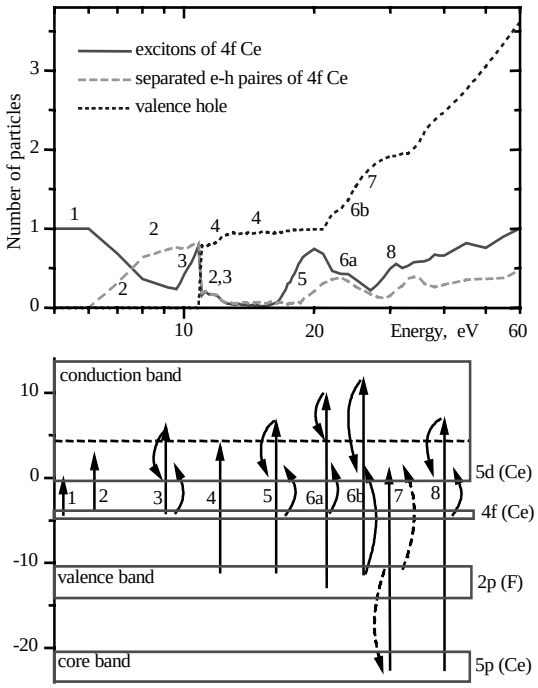

Fig. 6. The mean number of particles and the dominant relaxation processes occuring at various excitation enrgies in CeF_3. At the band structure scheme the straight full lines are for transitions of excitations, wavy lines show non-radiative relaxations [13].

because of the large number of electrons per elementary cell in 2p F band as compared with 4f Ce band (18:1). In spite of this fact near the edge of fundamental absorption (up to 13 eV) the contribution of 4f Ce into the dielectric permittivity may be comparable with that of 2p F. This contribution results in a small tail in the yield of cerium excitons in this region.

When $h\nu$ exceeds 15.6 eV ($E_g + E_{4f\text{-}5d}$) a part of electrons those are knocked out from the valence band (2p F) have an energy higher than the threshold of inelastic scattering, i.e. 4.8 eV. These electrons may loose their energy, creating additional excitons of 4f Ce (process 5).

Staring from 16.6 eV scattering of primary electron may leads to ionisation of cerium (process 6a). When primary electron arises from 4f cerium band the great part of the energy excess over the threshold of an inelastic scattering on cerium is acquired by the electron, but for width of 4f band is small enough. For the same magnitude of the energy excess the mean energy of the primary electron arising from the valence band is less than that in previous case because the width of the valence band is larger than that of 4f Ce and a considerable part of energy may be acquired by the hole. Therefore the increase of the number of excitons in the region above 16.6 eV is slower than for corresponding low energy region above 9.6 eV. Moreover the simultaneous rising of the mean number of excitons and 4f holes becomes possible and continues up to 20 eV.

The decrease of yield either cerium excitons or cerium holes in the region $h\nu > 21.2$ eV is related with the fact that strong competitive channel of multiplication of electronic excitations from valence band appears.

Starting from 40 eV the yield of particles become linear, the number of valence holes being 3-4 times larger than that of cerium excitons and 7 times larger than that of cerium holes.

In a wide energy region yield of cerium excitons is less than 1. Only at 60 eV it becomes equal to that of direct excitation of intracenter 4f-5d transitions. The yield of cerium excitons turns to be the same order of magnitude as experimental one of the fast luminescence in CeF_3.

Relaxation in a crossluminescent system

We would like to make to remarks concerning the relaxation process in crossluminescent crystals. Firstly, the mean energy required for the creation of the highest lying core hole (“useful” excitation in this case) is much higher than commonly used value of 2 to 3 forbidden energy bandgaps. The threshold of impact production of such excitations is about 2 times higher than that of the production of conduction-band-electron – valence-band-hole pairs, thus a large fraction of secondary excitations have energy insufficient to produce core holes (Fig. 7). Secondly, the radiative relaxation of the core hole is 5 orders of magnitude weaker than the allowed Auger process. Therefore Auger process should be strongly forbidden in order to make crossluminescence noticeable. Even small contribution of the

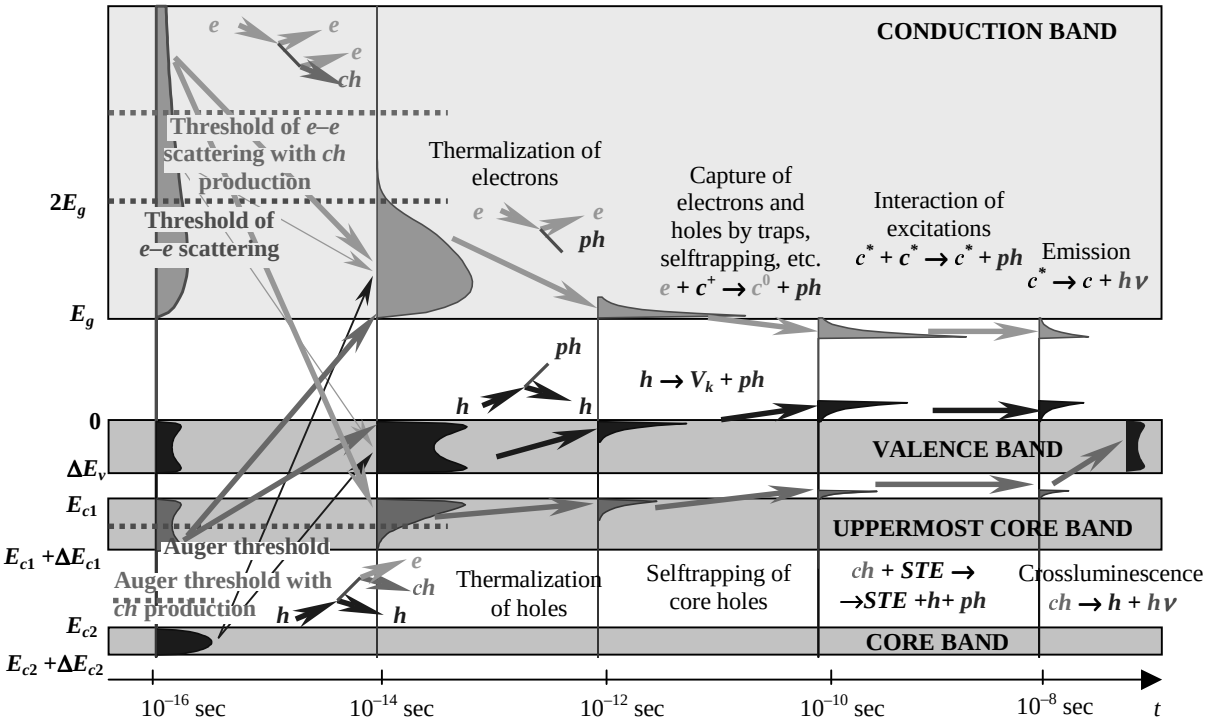

Figure 7. Scheme of relaxation of electronic excitations in crossluminescent crystals

Auger process (involving impurities or adjacent excitations) quenches this type of luminescence. So crossluminescence is very sensitive to track effects [15–18].

In crystals with two types of holes, i.e. valence band hole and outermost core band hole (e.g. 5pBa for BaF_2), only the latter type of holes is responsible for crossluminescence. Such holes can be produced only by high-energy excitations, since the threshold for the production

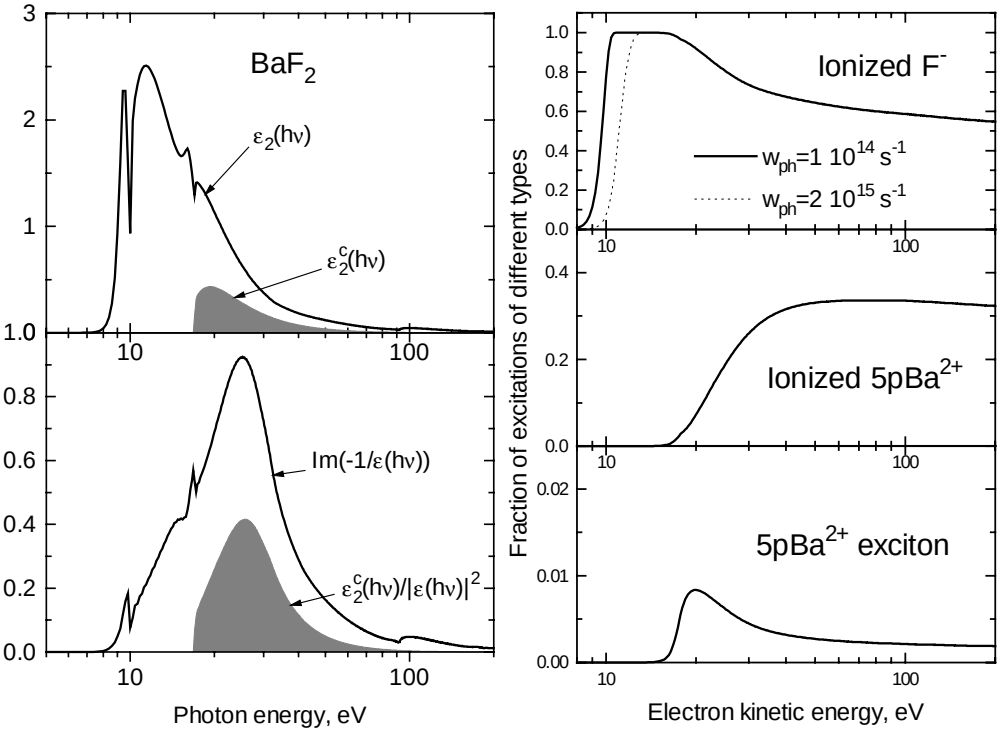

Fig. 8. Simulated imaginary part of dielectric permittivity (upper left panel) and energy loss function (lower left panel) for BaF_2. Filled areas represent the addition due to 'useful' excitations (outermost core holes for BaF_2). Dependence of the fraction of ionized and excited ions and ionized ions produced by an electron, on electron kinetic energy for BaF_2 (right panel) [9].

of core holes is higher than that for valence band holes and anion excitons. Fig. 8 shows the corresponding imaginary part of permittivity and energy loss function and displays the fractional composition of the secondary excitations.

In these substances two or more types of excitations can coexist during relatively long period (longer than 1 ns). For BaF_2 these are 5pBa holes, valence holes and anion excitons. Therefore one has to estimate only the number of "useful" excitations, which is less than the total number of secondary excitations. The corresponding mean energy for production of an "useful" excitation is well higher than typical values of 3 to 4 widths of forbidden gap. These values can be calculated only with account for energy distribution of secondary excitations in inelastic electron-electron scattering (secondary 5pBa holes only by high-energy electrons with energies above 18 eV). Therefore the number of new excitations depends not only on the most probable energy losses (which is about the energy of the main peak of energy loss function), but also by the rates of scattering in corresponding threshold regions.

The interaction between excitations produced by the same XUV photon result in specific kinetics of crossluminescence, which can be simulated after the calculation of space distributions of excitations (Fig. 9). This effect also modifies excitation spectra [15,17]. The most useful application of this quenching is the dependence of fast-to-slow emission ratio on the types of ionizing particle [19]. The simulation of this effect is presented elsewhere [18].

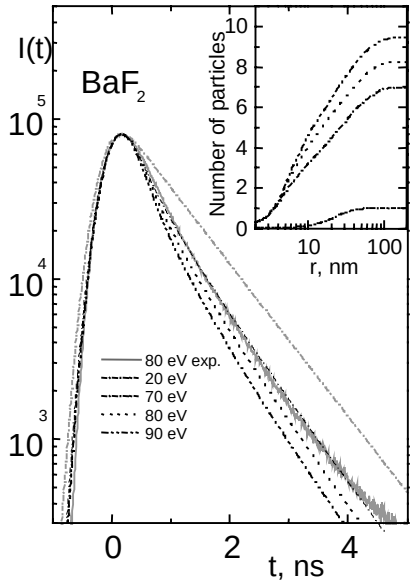

Figure 9. Simulation of BaF_2 crossluminescence decay kinetics after excitation by photons with different energy and the corresponding distribution of neighbor excitations (in the inset) [17].

Conclusions

Scintillation yield of insulators depends on numerous factors, which can be attributed to different stages of production of hot secondary excitations, evolution of their spatial distribution, and relaxation resulting in radiative and non-radiative processes. Three-step model is applicable for simple cases. The analysis of total scintillator efficiency is more sophisticated for crystals with complicated electronic structure, e.g. rare-earth crystals (CeF_3, etc.) and crossluminescent crystals (BaF_2, etc.).

References

1. C. van Eijk, Proc. Int. Conf. on Inorganic Scintillators and their Applications SCINT97, CAS, Shanghai Branch Press, China (1997) 3.
2. A.Lempicki, A.J.Wojtowicz, E.Berman, Nuclear Instruments and Methods in Physics Research **A333** (1993) 304.
3. D.J.Robbins, J. Electrochem. Soc. **127** (1980) 2694.
4. P.A.Rodny, P.Dorembos, C.W.E. van Eijk, Phys.Stat.Sol (b) **187** (1995) 15.
5. W.Shockley, Solid State Electon., **2** (1961) 35.
6. C.A.Klein, J. Appl.Phys. **39** (1968) 2029.
7. Vasil'ev, A.N., Fang,Y., Mikhailin,V.V, Phys. Rev. **B60** (1999) 5340
8. A.N. Vasil'ev, Y. Fang and V.V. Mikhailin, present volume
9. Vasil'ev A.N., Proceedings of the 13th International Conference on Defects in Insulating Materials, in Materials Science Forum, v. **239–241**, Trans Tech Publications, Switzerland (1997) 235.

10. Belsky A.N., Glukhov R.A., Martin P., Mikhailin V.V., Pedrini C., Vasil’ev A.N., Journal of Luminescence, **72–74** (1997) 96.
11. A.N.Belsky, I.A.Kamenskikh, V.V.Mikhailin, C.Pedrini, and A.N.Vasil'ev, Rad. Effects and Defects in Solids, **150** (1999) 1.
12. Vasil’ev A. N., Nuclear Instruments and Methods in Physics Research **B107** (1996) 165.
13. R.A.Glukhov, A.N.Belsky, C.Pedrini, A.N.Vasil’ev, Journal of Alloys and Compounds, **275–277** (1998) 488.
14. R.A.Glukhov, C.Pedrini, A.N.Vasil'ev, Proceedings of the International Conference SCINT97, Shanghai, CAS, Shanghai Branch Press (1997) 111.
15. Belsky A. N., Glukhov R.A., Kamenskikh I. A., Martin P., Mikhailin V. V., Munro I. H., Pedrini C., Shaw D. A., Shpinkov I.N., Vasil’ev A. N., Journal of Electron Spectroscopy and Related Phenomena **79** (1996) 147.
16. Terekhin M. A., Vasil'ev A. N., Kamada M., Nakamura E., Kubota S., Phys. Rev. **B52** (1995) 3117.
17. Glukhov R.A., Kamada M., Kubota S., Nakamura E., Ohara S., Terekhin M. A., Vasil’ev A. N., Proc. Int. Conf. on Inorganic Scintillators and Their Applications, SCINT95, Delft University Press, The Netherlands (1996) 204.
18. R.A. Glukhov, C.Pedrini, A.N.Vasil'ev, A.Yakunin, present volume
19. R. Novotny, Proc. Int. Conf. On Inorganic Scintillators and Their Applications, SCINT95, Delft University Press, The Netherlands (1996) 70.

Quantum Mechanical Cluster Calculations of Critical Scintillation Processes*

Stephen E. Derenzo, Mattias K. Klintenberg, and Marvin J. Weber

Lawrence Berkeley National Laboratory, Berkeley, CA 94720, U. S. A.

Abstract: This paper describes the use of commercial quantum chemistry codes to simulate several critical scintillation processes. The crystal is modeled as a cluster of typically 50 atoms embedded in an array of typically 5,000 point charges designed to reproduce the electrostatic field of the infinite crystal. The Schrödinger equation is solved for the ground, ionized, and excited states of the system to determine the energy and electron wavefunction. Computational methods for the following critical processes are described: (1) the formation and diffusion of relaxed holes, (2) the formation of excitons, (3) the trapping of electrons and holes by activator atoms, (4) the excitation of activator atoms, and (5) thermal quenching. Examples include hole diffusion in CsI, the exciton in CsI, the excited state of CsI:Tl, the energy barrier for the diffusion of relaxed holes in CaF_2 and PbF_2, and prompt hole trapping by activator atoms in CaF_2:Eu and CdS:Te leading to an ultra-fast (< 50 ps) scintillation risetime.

Keywords: Quantum mechanical calculations, Embedded cluster method, Hole diffusion, Prompt excitation, Thermal quenching, CsI, CsI:Tl, CaF_2:Eu, CdS:Te, PbF_2.

1. Introduction

This work is motivated by the need for a bright, fast, dense, heavy-atom scintillator for time-of-flight positron emission tomography in molecular nuclear medical imaging. It focuses on processes that quickly and efficiently convert ionization energy into useful optical photons. Since there are over 4,000 candidate host materials with good photoelectric stopping power and a suitable band gap, and each can be doped with many activators in different concentrations, a purely experimental search would involve synthesizing and testing an enormous number of samples! This is not practical, but fortunately the computational guidance that we need is now becoming accessible through modern quantum chemistry computer codes and faster computers.

The *theory* for these calculations is on solid mathematical footing, as almost all of solid state physics can be described by the Schrödinger equation, but numerical solutions of this equation for systems of realistic size are a serious challenge. Clearly, if computer speed continues to expand as it has in the recent past, it will be possible to model at the molecular level more and more of the processes important to a wide variety of technologies. This work is an attempt to see how well we can model known scintillators at the current time.

Section 2 describes processes critical for fast, efficient scintillation, computational procedures for modeling them, and the computer resources required. Section 3 shows some examples of how these methods can be applied to known scintillators and Section 4 discusses the possibilities for improvements in hardware and software and the use of quantum simulations to guide the search for new scintillators.

2. Scintillation Processes and Computational Methods

2.1 Scintillation Processes

Scintillation can be described in three stages [1, 2], with an overall luminous efficiency η (photons per MeV) given by

$$\eta = \gamma S q \qquad (1)$$

* U.S. DOE Contract DE-AC03-76SF00098 & U.S. NIH grant R01-CA48002

where γ is the number of electrons and holes produced per MeV of ionizing radiation, S is the efficiency with which the electrons and holes transfer their energy to the luminescent center, and q is the quantum efficiency of the excited state of the luminescent center.

The first stage is the production of separated electrons and holes by an energetic charged particle. This occurs in all crystals and the energy needed to create an electron-hole pair is typically three times the band gap of the crystal.

The second stage is the formation of an excited state. Here we distinguish four major types of scintillators: (1) the intrinsic scintillator, where the excitation occurs when an electron moves in the conduction band and becomes bound to a relaxed hole to create an exciton, (2) the self activated scintillator, where the electron and hole are both trapped on a luminous atom that is a major constituent of the crystal, (3) the scintillator with an electron-trapping activator atom that first traps an electron and then traps a relaxed hole to become excited, and (4) the scintillator with a hole-trapping activator atom that first traps a hole and then traps an electron to become excited.

The third stage is the return of the excited state to the ground state, either through the emission of a photon or through the production of phonons (heat). For a more complete treatment of these and many other scintillation mechanisms, see reference [2].

Of the many undoped and doped host crystals that have ever been tested, very few produce useful scintillation. The critical processes that distinguish these few include (1) the efficient excitation of activator atoms by the sequential trapping of electrons and holes, (2) for electron-trapping activators, the ability of relaxed holes to efficiently diffuse through the host crystal to an activator atom that has trapped an electron, and (3) minimal thermal quenching of the excited states.

2.2 The Embedded Quantum Mechanical Cluster Method

The embedded quantum mechanical cluster method is one of the most powerful methods for modeling solid state systems [3]. Among other features, it permits calculations of systems that have nonzero charge. It is compatible with commercial quantum chemistry programs even though they were generally designed for molecules rather than crystals.

In this method the crystal is modeled as a central cluster of typically 20 to 60 atoms embedded in a lattice of point charges designed to reproduce the electrostatic field of the infinite crystal. To explore scintillation processes, the Schrödinger equation is solved (at some level of approximation) to determine the energy and electronic configuration of the cluster (1) in the ground state, (2) with a missing electron, (3) with an extra electron, and (4) in an electronic excited state.

A large array of unit cells does not accurately reproduce the electrostatic potential of the infinite crystal field. As the number of unit cells in the array is increased, the potentials in the central volume of the array asymptotically reach limiting values that can disagree with the values given by the Ewald summation formula [4] by many eV. Even the Evjen method [5], which can eliminate the dipole moment for many crystals by using fractional charges at the edges of the unit cell, generates potentials with a large additive potential error. We have developed a method for optimizing point charge arrays for any crystal whose crystal structure is known [6]. It is more accurate and more automatic than previous methods [7, 8] and has errors less than 1 μV within the volume of a typical 50-atom cluster.

Crystal structure data can be obtained, for example, from the Inorganic Crystal Structure Database (Karlsruhe). This is one of most complete reference of its kind and is readily found on the internet by searching for ICSD.

2.3 The Schrödinger Equation

A quantum mechanical system is described by its wavefunction Ψ, which is a complex function (real and imaginary parts) of the three Cartesian coordinates of all of its particles.

$\Psi^*\Psi$ is the joint probability of all the particles in the system being at particular points in space. For N particles, the wavefunction is a function of $3N$ spatial coordinates, and for a stable (time invariant) system must obey the Schrödinger equation $H\,\Psi = E\,\Psi$, where H is a Hamiltonian operator that is the sum of a kinetic operator $\sum(1/m_i)(\ ^2/dx_i^2 + \ ^2/dy_i^2 + \ ^2/dz_i^2)$ and a potential term $\sum\sum q_i q_j / r_{ij}$ and E is the energy of the system. This equation has many solutions, and the ground state is the solution with the lowest energy.

In the Hartree-Fock method, each electron i is described by a molecular orbital ψ_i (a function of three spatial coordinates), and Ψ is the product of all orbitals summed over all antisymmetric permutations of electron assignment. This complication is necessary because the wavefunction must change sign if any two electrons are interchanged. Each molecular orbital ψ_i is approximated as a linear combination of basis functions, and each basis function ϕ_k is expanded by a linear combination of products of primitive Gaussian functions and polynomials that describe the s, p_x, p_y, p_z, etc. nature of the orbital.

$$\psi_i = \sum_{k=1}^{N} c_{ki}\,\phi_k \qquad (2)$$

The molecular orbital theory was a major step in the numerical solution of the Schrödinger equation (for which Mulliken won the Nobel prize in 1966). The Hartree-Fock method solves the Schrödinger equation by numerically optimizing one molecular orbital at a time, assuming at each step that the others are frozen. It ignores the dynamic electron correlation effects, which increase the strength of covalent bonds. On the other hand, it satisfies antisymmetric exchange perfectly, which decreases the strength of covalent bonds. As a result, the pure Hartree-Fock solution emphasizes ionic bonds and does not properly simulate the covalent bonds between two halogen atoms that share a hole to form a V_k center. Møller-Plesset second order correlation corrections (MP2) more properly show the bonding between the two halogen atoms in a V_k center. This was pointed out for the case of the NaCl crystal in reference [9]. Higher orders of correction (MP3 and MP4) are available, but the computational cost is so high that they are only useful for small (few atom) systems.

Another computational approach for including the correlation energy is the configuration interaction method, which describes the wavefunction as a linear combination of occupied and unoccupied Hartree-Fock solution orbitals. The lowest level of this method that includes a correlation correction is called configuration interaction doubles (CID), where all possible double substitutions of occupied with unoccupied orbitals are used. The inclusion of single substitutions produces CISD and the inclusion of triple substitutions produces CISDT. While this approach is effective for small (few atom) systems, the computational cost is so high for large systems that it has largely been replaced by Density Functional Theory (DFT).

DFT introduces approximate exchange and correlation functionals to the Hamiltonian and provides some correlation correction at the computational cost of a simple Hartree-Fock calculation. DFT is much more economical than Møller-Plesset and configuration interaction methods and has provided correlation corrections to much larger systems than were previously possible. (For the development of DFT, Kohn and Pople won the Nobel Prize in 1998.)

For heavy atoms, the inner electrons are relativistic and cannot be accurately modeled by the Schrödinger equation. However they do not play a direct role in chemical reactions and electronic excitations but rather an indirect role in defining a core potential that the outer electrons experience. In actual practice, the non-relativistic Schroedinger equation is solved for only the outermost electrons, and the inner electrons that are most strongly affected by relativity are handled by effective core potentials (ECPs) that were determined by solving the Dirac equation for the isolated atom. Quantum chemistry programs provide libraries of basis functions (called basis sets) and some of these include ECPs for atoms heavier than Ne. For atoms heavier than Ar only basis sets with ECPs are available and only the outermost valence electrons are treated quantum mechanically (typically 4 to 14 per atom).

For excited states and for excess electrons in the conduction band, diffuse basis functions must be added to the standard basis sets to describe the diffuse nature of the electrons involved. The addition of diffuse basis functions lowers the energy of the excited state relative to the ground state and results in more accurate molecular orbitals and excitation energies. See references [10] and [11] for more information on modern quantum chemistry.

2.4 The Configuration Space of Atomic Positions

When the cluster has an impurity atom, a non-zero charge, or is in an excited state the normal lattice positions of the atoms is not the configuration of lowest energy. To find the lowest energy, the forces dE/dx_i, dE/dy_i, dE/dz_i are computed for each moveable atom *i* and the atoms are moved to minimize those forces. One useful and realistic assumption is the Born-Oppenheimer approximation, which states that the electrons are much lighter and move much faster than the nuclei and as a result they move with the nuclei. A more mathematical description is that the Schrödinger equation does not need to include the velocities of the nuclei because they are moving relatively slowly, and a valid energy minimum can be found by computing the energies and forces at stationary points in the configuration space.

Figure 1 shows the energy of a system in the ground and excited states as a function of a generalized configuration coordinate. The system starts in the relaxed ground state, is excited, and then relaxes geometrically in an electronic excited state. After a photon is emitted, the system is in a distorted configuration of the ground state and quickly relaxes. This makes it plausible that the absorption edge energy (up arrow) is more energetic than the emission (down arrow) energy.

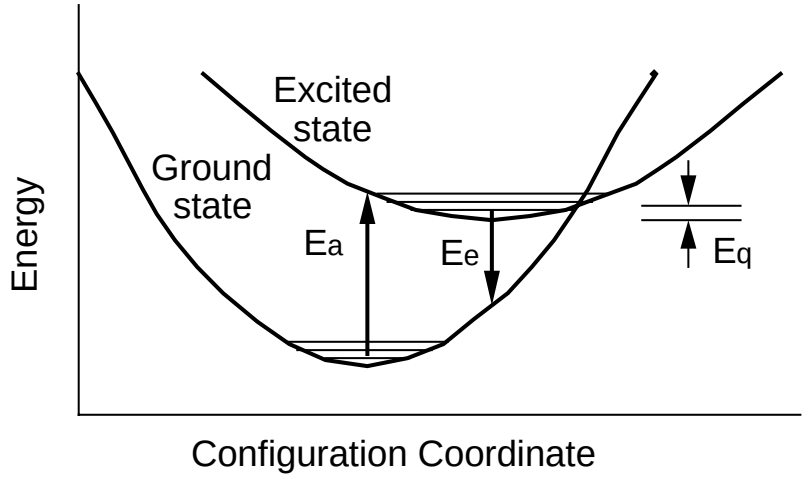

Figure 1. Configuration coordinate diagram (energy vs. atom positions) showing the absorption of a photon of energy E_a from the ground state, the emission of a photon of energy E_e from the relaxed excited state to a distorted ground state, and the thermal quenching energy E_q needed to distort the geometry of the excited state to a possible distorted ground state geometry.

Figure 1 also helps to explain thermal quenching, which occurs when the excited state configuration can be distorted by thermal vibrations to a possible ground state configuration. Here it is important to understand that the single horizontal axis coordinate shown is in reality a very large space of the spatial coordinates of all the atoms in the system. The overlap between the excited and ground states is not just the point where the curves cross in the figure, but a large subspace. One elegant way of solving for the quenching temperature is to use the Hessian matrix of second derivatives of the energy (a_{ij}) that is generated during the geometrical optimization. It can be used to parameterize the energy as a function of atom coordinates:

$$E = E_0 + \sum_{i=1}^{3N}\sum_{j=1}^{3N} a_{ij}(u_i - \bar{u}_i)(u_j - \bar{u}_j) \quad (3)$$

where the variable u_i stands for the *x*, *y*, and *z* Cartesian coordinates of the atoms. Usually this matrix is diagonalized to find the vibrational modes and frequencies but it also provides analytical expressions for the energy surface of the ground and excited states. In these terms the thermal energy required for quenching can be estimated as the difference between (1) the

minimum energy in the configuration space where the ground and excited state energies are equal (level crossing) and (2) the minimum energy of the excited state.

2.5 Computational Requirements

Let us consider a system of N_a atoms with N_e quantum electrons per atom and an average of N_b basis functions centered on each of the N_a atoms. There are then N_a x N_e molecular orbitals and each is expanded as a linear combination of N_b x N_a basis functions. This means that the Schrödinger equation determines the wavefunction Ψ by N_a^2 N_b N_e expansion coefficients, and that the Hamiltonian matrix consists of N_a^4 N_b^2 N_e^2 elements, which is one measure of the computational effort. Since the number of atoms N_a scales as the cube of the diameter *D* of the atomic cluster, the computational effort scales as the twelfth power of *D*! In practice, the scaling exponent is reduced somewhat by the use of molecular symmetry and the selective updating of matrix elements between iterations.

Considering a typical system described in this paper, we have N_a = 50, N_e = 10, and N_b = 10. The wavefunction is described by 250,000 expansion coefficients and the Hamiltonian matrix contains $250{,}000^2$ or over 6 x 10^{10} elements. Solving the Hartree-Fock equation takes approximately 50 hours on a Silicon Graphics, Inc. R10k processor which during this time is operating at typically 250 x 10^6 floating point operations/s for a total of 10^{15} floating point operations. Dividing these two numbers gives an indication that approximately 20,000 floating point operations are required per matrix element to solve the equation.

Geometrical optimizations require typically 10 to 20 iterations of atom coordinate changes, and each iteration requires the solution of the Hartree-Fock equation and the determination of the new Hessian matrix. Fortunately, as the process converges, the changes in the atom positions decrease, and the time required for each Hartree-Fock solution also decreases. As a general rule, a geometrical optimization takes about ten times longer than the initial energy solution of the Hartree-Fock equation.

For the examples described below, we have used both the Gaussian94 (a product of Gaussian, Inc., Pittsburgh, PA, U.S.A.) and the Jaguar (a product of Schrodinger, Inc., Portland, OR, U.S.A.) quantum chemistry codes on a local cluster of twelve R10k processors (Silicon Graphics, Inc.) and on the U.S. Department of Energy National Energy Research Supercomputer Center J-90 processors (Silicon Graphics, Inc.).

3. Examples

3.1 Hole Relaxation and Diffusion in CsI

A relatively small CsI cluster with a missing electron readily exhibits the V_k center, which is a hole shared by two covalently bonded I ions [12, 13, 14]. By making the cluster large enough to describe a V_k center at two equivalent nearest neighbor sites, the minimum energy path in atomic configuration space can be determined. In CsI the transition configuration between two V_k centers is a single-center hole. The energy difference between these two states is the barrier for relaxed hole diffusion in the 0° direction. Using a $Cs_{16}I_{29}$ cluster and MP2 correlation corrections, the barrier energy was predicted to be 0.15 eV [13]. A larger $Cs_{32}I_{33}$ cluster that allows a more complete relaxation gives a barrier of 0.23 eV, in excellent agreement with an experimental value of 0.23 eV, determined by measuring the risetime of CsI:Tl which varied from 890 ns to 13 ns from –60 to +50 °C [15].

3.2 Excitons in CsI

Plots of the two unpaired electron orbitals in excited (triplet) CsI show that the lower half-filled orbital has the same spatial distribution as the V_k center, and that the upper half-filled orbital is spatially diffuse. The excited state is the expected exciton, an e^--V_k center [16].

3.3 The excited state in CsI:Tl

The excited state of CsI:Tl was found to be localized entirely on the Tl atom both in a $TlCs_{19}I_{20}$ and a larger $TlCs_{31}I_{33}$ cluster. The slow risetime indicates that the Tl^+ ion first traps an electron and the relaxed hole diffuses to it to form the excited Tl^+ state [16].

3.4 Energy Barriers for Relaxed Hole Diffusion in CaF_2 and PbF_2

Calculations of relaxed hole transport in the $Ca_{16}F_{32}$ and $Pb_{16}F_{32}$ clusters using Hartree Fock and MP2 predict energy barriers of 0.21 eV and 1.1 eV [17], respectively. The barrier height for CaF_2 is in fair agreement with the experimental value of 0.31 eV [18].

3.5 Prompt Hole Trapping and Ultra-Fast Risetimes in CaF_2:Eu and CdS:Te

Using our 100-ps pulsed x-ray system [19, 20] we have deconvolved the impulse response and measured of the risetime of the luminous (24,000 photons/MeV) scintillator CaF_2:Eu to be less than 50 ps. This is incompatible with the diffusion time of relaxed holes in CaF_2, which we estimate to be longer than 1 µs at room temperature using the data of reference [18]. We are forced to conclude that the Eu^{2+} activator ions promptly trap almost all the available holes before they can relax and that the free electrons are then quickly trapped to rapidly and efficiently form the Eu^{2+} excited state.

To model this behavior, quantum calculations were performed on the ground and hole states of the clusters $Ca_{16}F_{32}$ and $EuCa_{15}F_{32}$ using three different sets of DFT exchange and correlation functionals. The ionization potential of Ca_5F_{10} ranged from 10.0 to 11.0 eV (average 10.4 eV) and the ionization potential of $EuCa_4F_{10}$ ranged from 8.2 to 10.0 eV (average 9.2 eV). From these energy values and the diagram in Figure 2 we see that the Eu atom has electrons whose energies are just above the top of the valence band and that it is plausible that holes transfer promptly to the Eu^{2+} activator ion.

The electron affinity for Ca_5F_{10} ranged from 1.2 to 1.4 eV (average 1.3 eV) and the electron affinity for $EuCa_4F_{10}$ ranged from 1.2 to 1.5 eV (average 1.4 eV). Thus it is plausible that the activator atoms have no electron affinity until they have trapped a hole.

Because CdS:Te is a luminous scintillator under electron beam excitation at temperatures as low as 1.6 K [21], it is unlikely that the diffusion of relaxed holes plays a role in the excitation of the activator. Moreover, our pulsed x-ray system measures the risetime to be less than 50 ps at room temperature.

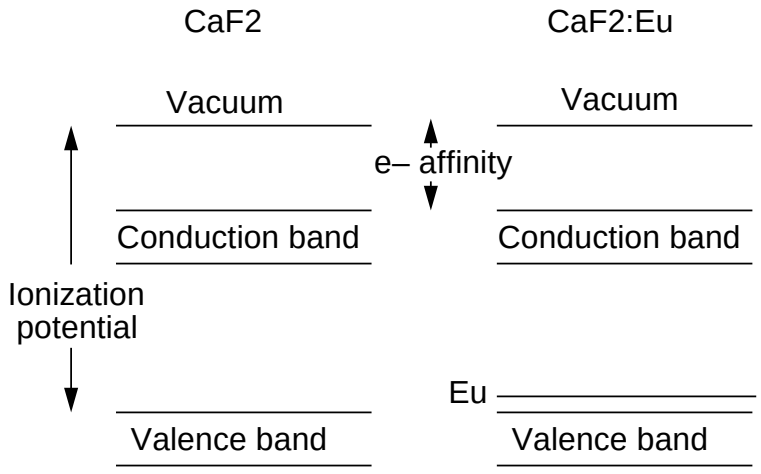

Figure 2 Band diagram for CaF_2 and CaF_2:Eu for the case where the ionization potential of CaF_2:Eu is slightly less than that of CaF_2.

To see if the quantum calculations support this interpretation, activator affinity calculations were performed on $Cd_{13}S_{13}$ and $Cd_{13}S_{12}Te$ clusters. The ionization potential for $Cd_{13}S_{13}$ ranged from 9.6 to 10.1 eV (average 9.8 eV) and the ionization potential for $Cd_{13}S_{12}Te$ ranged from 9.3 to 9.6 eV (average 9.5 eV). Here we see that Te has an electron whose energy is just above at the top of the valence band and that it is plausible that holes transfer promptly to the Te activator ion. The electron affinity for $Cd_{13}S_{13}$ ranged from 3.7 to 4.1 eV (average 3.9 eV) and the electron affinity for $Cd_{13}S_{12}Te$ ranged from 3.7 to 4.1 eV (average 3.9 eV).

Thus in this case too it is plausible that the activator atoms have no electron affinity until they have trapped a hole.

4. Discussion

This work shows that it is possible to use the embedded quantum mechanical cluster method to model a number of important scintillation mechanisms. Combining these results with experimental data can yield an improved understanding of scintillation mechanisms and the ability to simulate scintillation in families of host crystals and activator atoms and thus guide the experimental search Figure 3).

The experimental data showing the ultra-fast risetime of CaF_2:Eu and CdS:Te and the computational prediction of prompt hole trapping by the corresponding activator atoms is a good example of the combined power of experiment and simulation.

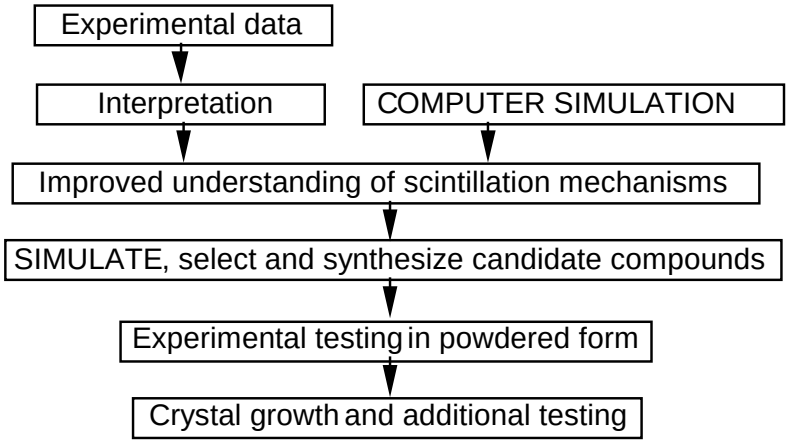

Figure 3. Role of quantum calculations in improving the understanding of scintillation mechanisms and in aiding the search for new scintillators.

The future of this work is limited by computational speed and the ability of the software to model crystal systems. While computer speed continues to increase at a spectacular rate, improvements in software are largely driven by applications in organic chemistry and for the catalysis of chemical reactions. More effort is needed to improve quantum chemistry codes to (1) increase the robustness of convergence for ionic systems and (2) support pseudo atoms that have the force properties of ground-state quantum atoms without having to include their electrons in the quantum calculation. Such improvements in software alone could speed the calculation by factors of 10 to 100 or improve the accuracy by allowing the use of more basis functions or a higher level of theory. The results described here represent only a small sampling of what will be possible in the future.

Acknowledgments

We thank W. Moses, K. Song, P. Gill, E. Heifets, R. Deich, J. Hay, and W. Goddard for helpful discussions and M. Ringnalda, G. Vacek, W. Pollard, J. Perry and R. Murphy for advice on the use of the Jaguar program. This work was supported in part by the Director, Office of Science, Office of Biological and Environmental Research, Medical Science Division of the U.S. Department of Energy under contract No. DE-AC03-76SF00098, in part by the U.S. Department of Energy National Energy Research Supercomputer Center, and in part by the National Institutes of Health, National Cancer Institute under grant No. R01-CA48002. Reference to a company or product name does not imply approval or recommendation by the University of California or the U.S. Department of Energy to the exclusion of others that may be suitable.

References

1. G. Blasse, Scintillator Materials, Chem Matter, **6** (1994), 1465-1475
2. P.A. Rodnyi. Physical Processes in Inorganic Scintillators. pp. 219, CRC Press (ISBN 0-8493-3788-7), Boca Raton, FL, 1997
3. R.W. Grimes, C.R.A. Catlow, and A.L. Shluger, Quantum mechanical cluster calculations in solid state studies, World Scientific, Singapore, 1992
4. P. Ewald, Die berechnung optischer und elektrostatischer gitterpotentiale, Ann Phys (Leiptzig), **64** (1921), 253-287
5. H.M. Evjen, Phys Rev, **39** (1932), 675
6. S.E. Derenzo, M.K. Klintenberg, and M.J. Weber, Determining point charge arrays that produce accurate ionic crystal fields for atomic cluster calculations, J Chem Phys (submitted), (1999),
7. C. Sousa, J. Casanovas, J. Rubio, and F. Illas, Madelung fields from optimized point charges for *ab initio* cluster model calculations on ionic systems, J Comp Chem, **14** (1993), 680-684
8. E.V. Stefanovich, and T.N. Thuong, A simple method for incorporating Madelung field effects into ab initio embedded cluster calculations of crystals and macromolecules, J Phys Chem B, **102** (1998), 3018-3022
9. V.E. Puchin, A.L. Shluger, and H. Itoh, Electron correlation in the self-trapped hole and exciton in the NaCl crystal, Phys Rev B, **52** (1995), 6254-6264
10. A. Szabo, and N.S. Ostlund. Modern Quantum Chemistry. pp. 466, Dover Publications, Inc., Mineola, NY, 1989
11. W.J. Hehre, L. Radom, P.v.R. Schleyer, and J.A. Pople. Ab Initio Molecular Orbital Theory. pp. 548, John Wiley & Sons, New York, 1986
12. S.E. Derenzo, and M.J. Weber, Ab-initio cluster calculations of hole transport and activator excitation in CsI:Tl and CsI:Na, IEEE Nuclear Science Symposium Conference Record (CD-ROM ISBN 0-7803-4261-5), (1997),
13. S.E. Derenzo, and M.J. Weber. Ab-initio calculations of hole transport and activator excitation in CsI:Tl and CsI:Na. Proceedings of The SCINT97: International Conference on Inorganic Scintillators and Their Applications, 103-106, (Edited by Y. Zhiwen, L. Peijun, F. Xiqi and X. Zhilin), Shanghi, P.R. China, 1997
14. S.E. Derenzo, and M.J. Weber, Prospects for first principle calculations of scintillator properties, Nucl Instr Meth A, **422** (1999), 111-118
15. J.D. Valentine, W.W. Moses, S.E. Derenzo, D.K. Wehe, and G.F. Knoll, Temperature dependence of CsI(Tl) gamma-ray scintillation decay time constants and emission spectrum, Nucl Instr Meth, **A325** (1993), 147-157
16. S.E. Derenzo, M. Klintenberg, and M.J. Weber. *Ab-initio* computations of hole transport and excitonic processes in inorganic scintillators. Proceedings of The Third International Conference on Excitonic Processes in Condensed Matter (EXCON '98), PV 98-25 (ISBN 1-56677-219-2), 391-402, (Edited by R. T. Williams and W. M. Yen), Boston, 1998
17. S.E. Derenzo, M. Klintenberg, and M.J. Weber, Ab-initio cluster calculations of hole trapping in PbF_2 and PbF_4, 1999 IEEE Trans Nucl Sci (submitted), **NS-46** (1998),
18. J.H. Beaumont, W. Hayes, D.L. Kirk, and G.P. Sommers, An investigation of trapped holes and trapped excitons in alkaline earth fluorides, Proc Roy Soc Lond, **A315** (1970), 69-97
19. S.E. Derenzo, W.W. Moses, S.C. Blankespoor, M. Ito, and K. Oba, Design of a pulsed x-ray system for fluorescent lifetime measurements with a timing resolution of 109 ps, IEEE Trans. Nucl. Sci., **NS-41** (1994), 629–631
20. S.C. Blankespoor, S.E. Derenzo, W.W. Moses, C.S. Rossington, M. Ito, and K. Oba, Characterization of a pulsed X-ray source for fluorescent lifetime measurements, IEEE Trans Nucl Sci, **NS-41** (1994), 698-702
21. J.D. Cuthbert, and D.G. Thomas, Optical properties of Tellurium as an isoelectonic trap in cadmium sulfide, J Appl Phys, **39** (1968), 1573-1580

Storage and dosimetric properties of oxides

V. S. Kortov, I. I. Milman

Ural State Technical University, 620002 Ekaterinburg, Russia

Abstract: General requirements imposed on storage phosphors, which are used in dosimetry of ionizing radiation, are discussed. Results of investigations into storage properties of some wide-band oxides (Al_2O_3, BeO, MgO) are reported. The role of oxygen vacancies and impurities in formation of storage properties of nonstoichiometric oxides is analyzed. Dosimetric properties of the said oxides are considered. It is shown that anion-defective wide-band oxides can serve as the basis for creation of radiation-sensitive media with high storage properties suitable for solid-state dosimetric applications.

Keywords: storage phosphors, thermoluminescence, thermostimulated exoelectron emission, electron spin resonance, storage and dosimetric properties.

In this report properties of storage phosphors (SP) based on wide-band oxides will be briefly analyzed. These phosphors show great promise for use in thermoluminescent (TL) and electron spin resonance (ESR) dosimetry.

Dose range of various dosimetric systems covers sixteen orders of magnitude and extends to temperatures up to 600^oC. Frequently one needs to measure doses in mixed radiation fields. The existing dosimetric methods cannot meet these requirements. Among them, luminescence of SP provides a relatively wide interval of registered doses, a high accuracy of measurements, and sensitivity to different types of radiation. Therefore we shall limit yourself to discussion of TL of SP.

Many materials possess storage properties, but only some of them can be used in radiation dosimetry. The main requirements imposed on TL SP dosimeters are known. They include a high sensitivity (ability to register small doses), a simple TL curve (it should be free of peaks overlapping the main dosimetric peak), low fading (ability to preserve the dosimetric information with minor losses), a wide range of measured doses, a narrow interval where the TL yield depends on energy, luminescence spectrum convenient for registration, a high radiation resistance, chemical inertness, mechanical strength, and transparency to the intrinsic radiation. The table below illustrates realization of these requirements taking some widely popular TL dosimeters as an example. It is seen that properties of even these dosimeters do not fully satisfy the requirements imposed on SP dosimeters [1].

However, a simplest model of TL imparts the physical sense to the set of the main requirements to SP. For example, sensitivity and the linear interval of registered doses are achieved at the expense of a high concentration of active luminescence centers. TL curves may have a simple shape (with one maximum) thanks to the presence of a dominant type of homogeneous active centers. Small fading is achieved when active traps in the forbidden band of the crystals are sufficiently deep. Energy levels of luminescence centers in the forbidden band determine the correlation between the TL spectrum and the spectral characteristic of the photoreceiver.

Table 1. Properties of commercially available SP.

Type	Materials	Sensitivity at ^{60}Co relative to LiF	Fading	Useful Range	Peak temperature, ^{o}C	Emission spectra, nm
TLD-100	LiF:Mg,Ti	1.0	5%/yr	10 μGy – 10 Gy	195	350-600 (400 max)
TLD-100H	LiF:Mg,Cu,P	15	Negligible	1 μGy – 10 Gy	220	400
TLD-200	CaF_2:Dy	30	16% in 2 wks	1 μGy – 10 Gy	180	483.5 max
TLD-400	CaF_2:Mn	10	12% in 3 months	1 μGy – 100 Gy	260	440-600 (500 max)
TLD-500K	Al_2O_3	30	5%/yr	0.5 μGy – 1 Gy	185	420 max
TLD-900	$CaSO_4$:Dy	20	8% in 6 months	1 μGy – 100 Gy	220	480, 570
DTG-4	LiF:Mg,Ti	2.5	5%/yr	50 μGy – 50 Gy	220	350-600 (410 max)

It is known that intrinsic and impurity defects are responsible for appearance of active and luminescence centers in SP. Therefore dosimetric properties can be formed through a purposeful modification of the defect structure of the phosphors. Until recently, effective SP were developed on the basis of alkali-halide and alkaline-earth crystals. Considerable study has been given lately to radiation-sensitive media based on wide-band oxides (Al_2O_3, BeO, MgO, SiO_2). These oxides are distinguished for stable chemical and mechanical properties and can contain deep trapping centers of charge carriers. Their defect structure is convenient to modify for creation of active centers. We examined SP of the said oxides by the methods of TL and thermally stimulated exoelectron emission (TSEE). Al_2O_3 was studied in most detail. Taking this material as an example, let us consider the major problems associated with SP based on wide-band oxides.

Investigations into storage properties of alkali-halide crystals show that the main active centers of thermoluminescence are anion vacancies producing F-centers. One might expect that defects in the anion sublattice could produce active centers of TL in oxides as well. This supposition also followed from investigations of alkaline-earth oxides (BaO, SiO_2, and CaO), which showed that oxygen vacancies were decisive for changes in electrical, optical, emission and other properties of the last oxides.

We analyzed two methods for producing vacancies in the oxygen sublattice of the oxides, which were realized in experiments: thermochemical coloring in strongly reducing conditions and radiation modification.

Figure 1 illustrates the dynamics of TL properties of an α-Al_2O_3 single crystal under different thermochemical treatment ( ) conditions. The TL intensity of the samples treated in strongly reducing conditions can be expected to increase as compared to its counterpart in the initial single crystal. When the crystal is held in vacuum at a high temperature, a TL peak appears at 273 K (curve 2). This peak, which is due to formation of oxygen vacancies, cannot serve dosimetric purposes, because it vanishes at room temperature. Under stronger reducing conditions (heating and holding of the sample in vacuum in the presence of graphite) an intensive peak is formed at 430 to 450 K. The intensity of this peak depends on the concentration of oxygen vacancies and changes over broad limits with the dose [2].

Analogous dependences were observed for TSEE. This effect, which frequently occurs simultaneously with TL, takes place in thin (up to 100 nm) layers and is very sensitive to changes in the concentration of electron centers. Figure 2 shows the kinetics of the TSEE flow in an α-Al_2O_3 single crystal before and after thermochemical treatment. When the crystal is treated in vacuum in the presence of graphite, the intensity of the peak is enhanced in the same temperature interval (430 to 450 K) as that of the TL dosimetric peak. One may think that TCT produces oxygen vacancies in the crystals and, thus, favors the increase in the concentration of active electron centers. Consequently, storage properties of the oxide are formed effectively.

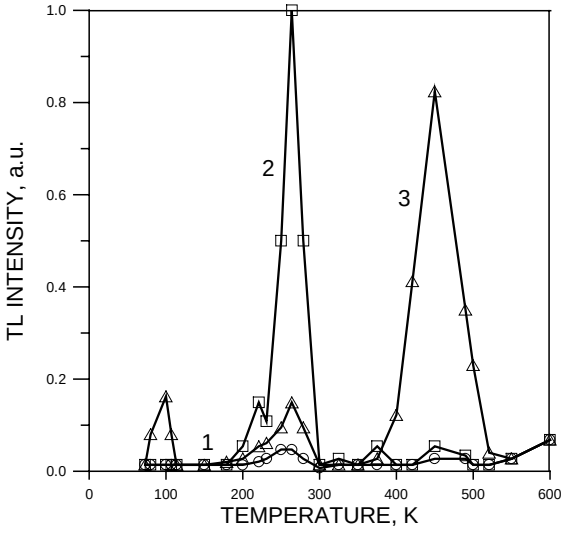

Figure 1. Dynamics of TL properties of α - Al_2O_3 depending on thermochemical treatment conditions. 1 - initial single crystals; 2 - vacuum of 10^{-3}, 1800 K, 10 hours; 3-vacuum of 10^{-3}, 1800K, 10 hours, graphite.

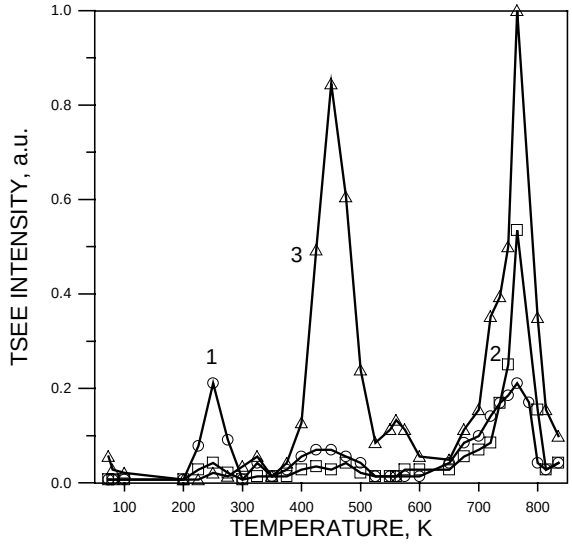

Figure 2. Dynamics of TSEE properties of α - Al_2O_3 depending on thermochemical treatment conditions. 1 - initial single crystals; 2 - vacuum of 10^{-3}, 1800 K, 10 hours; 3-vacuum of 10^{-3}, 1800K, 10 hours, graphite.

The improvement of storage properties during TCT represents a general feature of the wide-band oxides studied. TCT causes the increase in the TL intensity under X-ray and ultraviolet (UV) irradiation.

Storage properties of the oxides were formed best when anion defectness appeared during growth of crystals in strongly reducing conditions. A technique for growing shaped anion-defective single crystals of α-Al_2O_3 by Stepanov's method in the presence of graphite was developed. By this technique, it is possible to produce SP in quantities necessary for their commercial use as radiation detectors. These SP are uniform in properties and geometrical dimensions. The detectors were certified and were labeled TLD-500K. Anion-defective corundum grown in the presence of carbon was designated α-Al_2O_3:C. Initially carbon was assumed to be an active impurity and enter the oxide lattice as the C^{2+} ion forming hole centers. However, our investigations did not confirm that supposition. The formula α - Al_2O_3:C proved to be valid reflecting defectness of the anion sublattice of the oxide.

Let us consider briefly properties of this SP. Oxygen vacancies, which appear during the crystal growth, produce F-centers (two electrons in the anion vacancy) and F^+-centers (one electron captured by a vacancy). Optical and TL properties of the phosphor are determined by the presence and changes of these centers during heating and irradiation.

The optical absorption spectrum of anion-defective crystals of α-Al_2O_3 exhibits a band at 205 nm, which corresponds to absorption of F-centers. The spectrum also contains two bands at 230 nm and 250 nm, which are typical of absorption of F^+-centers. The absorption bands of F^+-centers appear only at concentrations exceeding 10^{15} cm^{-3}. The concentration of F-centers

calculated by Smakula's formula is $1.3 \cdot 10^{17}$ cm^{-3}. Annealing in outdoors at 2200 K for 5 hours eliminates F- and F^+-centers and inhibits TL sensitivity of the crystals.

The main contribution to TL of anion-defective single crystals of α -Al_2O_3 is made by F-centers. The luminescence spectrum of the crystal has a maximum at 420 nm (luminescence of F-centers), which correlates well with the maximum spectral sensitivity of photomultipliers. This is important for effective registration of TL by dosimetric equipment.

The TL curve has one peak near 460 K with the maximum half-width T = 60 K The dose can be determined from the peak intensity or integrally (from the peak area). The presence of an isolated peak meets the requirements of dosimetric storage properties. The low-temperature peak at 330 K is observed immediately after irradiation and vanishes at room temperature in a few minutes, incurring no error in the dose measurements.

The dose characteristic of the SP based on anion-defective α-Al_2O_3 crystals is given in Fig. 3. This characteristic remains linear while the dose changes by 6 orders of magnitude. The phosphor is highly sensitive (1 Gy).

It is worth noting that fading of the irradiated crystals at room temperature does not exceed 3% yearly. This is the smallest fading for the known TL dosimeters.

Storage properties of the oxides can also be improved by radiation treatment of the crystals. The main consequence of large threshold displacements of atoms in the oxide lattice is high radiation resistance of the oxides.

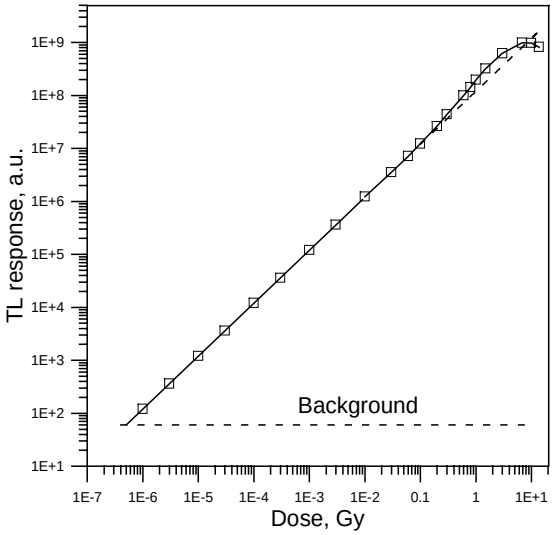

Figure 3. The dose characteristic of the anion-defective α-Al_2O_3 crystals

Intrinsic defects in the oxides can be produced only by corpuscular types of radiation: neutrons, fast electrons, or ions. X-ray and gamma types of radiation alter just the charge state of biographical defects and impurities. We used 16-MeV electrons from an electron accelerator to produce vacancies in the oxygen sublattice of the oxides.

Figure 4 shows TL curves for an anion-defective α-Al_2O_3 crystal before and after irradiation with fast electrons. As is seen, the intensity of the dosimetric peak at 440 K is diminished. Aluminum atoms are displaced to interstices under irradiation with fast electrons. One more optical absorption band at 305 nm, which is related to the interstitial aluminum ion (Al_i^+-center), was detected. TL and TSEE curves corresponded to the decay of the centers produced by the interstitial aluminum atom. Further investigations revealed that oxygen vacancies, which were produced in initial stoichiometric crystals as Frenkel defects exhibited new peaks near 515 K, which under irradiation, were less thermally stable than Schottky defects, which appeared during thermochemical coloring. Therefore thermochemical coloring was chosen as the main method for formation of storage properties in the oxides.

Impurities have a considerable effect on storage properties of the oxides. The chromium impurity is most active in α-Al_2O_3 crystals. The TL spectra always contained bands corresponding to luminescence of Cr^{3+} ions (693 nm). Luminescence of chromium ions is present, simultaneously with the dominating luminescence of F-centers, both in the peak at 575 K, which is due to the presence of this impurity in the crystal, and the main dosimetric peak at 430 K.

Among other impurities affecting storage properties of α-Al_2O_3 crystals, the Mg^{2+} impurity producing hole centers deserves mentioning. However, the TL peak associated with this center is located at the temperature of 230 K and does not present interest for practical dosimetry. Titanium impurities give weakly pronounced TL peaks in α-Al_2O_3 crystals. It may be stated that impurity defects are much less significant for improvement of storage properties of α-Al_2O_3 crystals as compared to defects in the anion sublattice.

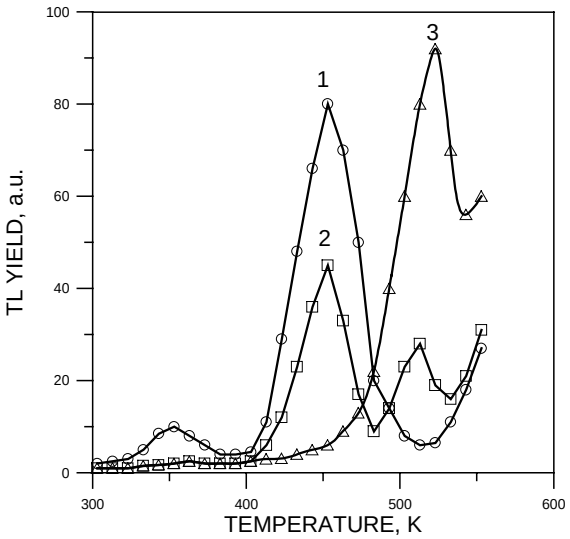

Figure 4. TL of anion-defective α-Al_2O_3 crystals irradiated with fast electrons and excited with X-ray radiation. 1 - initial, before irradiation; 2 - after irradiation at the fluence of $5 \cdot 10^{16}$ el. $\cdot$ cm^{-2}; 3 - $1 \cdot 10^{18}$ el. $\cdot$ cm^{-2}.

However, if impurities transform during thermochemical treatment, they can induce interesting and useful changes in storage properties. Take, for example, MgO crystals containing Mn^{2+} and Fe^{3+} impurities [3]. From Fig.5 (curve 2) it is seen that the ESR spectrum of the initial MgO:Mn,Fe crystal contains the line A related to impurity Fe^{3+} ions. This line disappears after TCT, because thermal treatment alters the charge of the iron ions: nonparamagnetic Fe^{2+} start dominating (curve 1). Iron ions return to the paramagnetic state (Fe^{3+}) upon irradiation and the ESR signal A appears again. Now the intensity of this signal is proportional to the irradiation dose. The aforementioned pro cess is confirmed by annealing curves obtained for the initial MgO crystal and the same crystal exposed to thermal treatment (the lower curve). The ESR signal of Mn^{2+} ions (1-6, g_4=1,981) does not change under irradiation and TCT. The sextet with separation of nearly 9 mT is associated

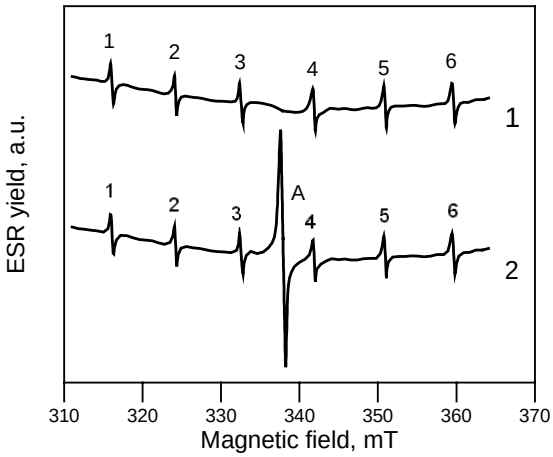

Figure 5. ESR spectra of virgin MgO:Mn,Fe single crystals (2) and crystals subjected to TCT (1) and after X-ray irradiation (2).

with the hiperfine spliting of Mn^{2+} having nuclear spin 5/2. It does not interfere with the regular features mentioned above. Noteworthy, a TL peak appears in the interval where the ESR signal of Fe^{3+} ions drops sharply in thermochemically treated crystals of MgO (T = 350 to 450K). This means that MgO:Fe,Mn crystals can be used for development of combination ESR-TL radiation detectors. Dose characteristics of these detectors are given in Fig. 6. As is seen, TL dosimetry provides a wider interval of doses and high sensitivity. However, the ESR channel can be used to measure doses at elevated temperatures (above 500 K) when the TL signal vanishes.

Storage properties of the BeO ceramic and films are very interesting [4]. This oxide possesses an extremely high intensity of the TSEE whose nature is unclear. Most probably, this phenomenon is explained by a favorable combination of electron centers produced by oxygen vacancies and hole centers formed by impurity lithium ions $[Li]^0$. As a result, emission processes are due to both ionization of electron centers and recombinations. $[Li]^0$ centers are paramagnetic [5] and the ESR signal (g=2,0095) increases in proportion to the dose (Fig.7).

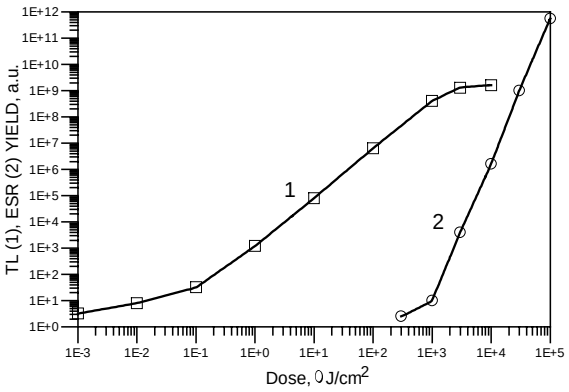

Figure 6. Dose dependences of the TL (1) and ESR (2) yield of MgO:Mn,Fe crystals subjected to TCT at UV irradiation.

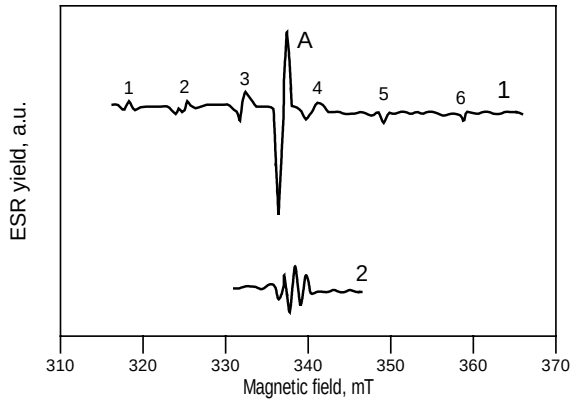

Figure 7. ESR spectra of BeO transparent ceramics (1) and L-α-alanine (2) after X irradiation; line 'A' is hole $[Li]^0$ centres, lines 'B' are Al^{2+} centres.

Significantly, paramagnetic centers decay intensively upon heating at temperatures from 350 to 450 K, that is, within the interval of the TL peak. The TSEE occurs at a higher temperature, i.e. TL and TSEE peaks do not overlap (Fig. 8). Thus, dosimetric information can be accumulated via three independent channels: ESR, TL, and TSEE. A combination TL-ESR-TSEE dosimeter based on the BeO:Li ceramic was proposed.

The investigations suggest that storage properties of the oxides can be strongly affected by deep traps whose ionization temperature is beyond the range of TL and TSEE involving anion and cation defects. We hit upon this fact for the first time while examining anomalies in storage properties of anion-defective corundum. The TL yield proved to drop with heating, whereas the peak intensity was enhanced. Moreover, examination by the method of fractional luminescence revealed the decrease in the activation energy within the dosimetric peak.

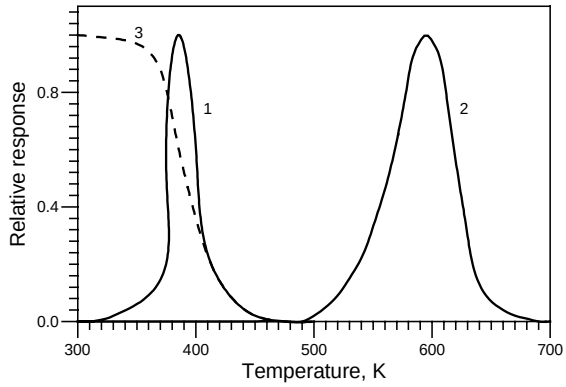

Figure 8. Thermostimulated processes in BeO:Li ceramic samples: 1- TL; 2- TSEE and 3- ESR signal after irradiated at room temperature.

The superlinear behavior of the dose dependence also called for explanation. The aforementioned features did not follow from the known models describing TL kinetics in crystals. The study of the temperature dependences of X-ray luminescence and photo-luminescence in the luminescence band of F-centers allowed relating the observed effects to temperature quenching. It was effectively realized in the range of the dosimetric peak. Thanks to the discovery of this relationship, the dependence of the TL yield on the heating rate and the anomalous behavior of the average activation energy could be formally described by a kinetic equation modified by the Mott factor. This factor allowed for temperature quenching. However, the origin of the observed specific features of TL was not understood. In this connection it was interesting to analyze the possible effect of the capture of carriers in deep traps. As is known, these traps can act as luminescence centers.

Indeed, we found deep traps experimentally [6]. Shown in Fig. 9 is the TL curve of an anion-defective α-Al_2O_3 crystal irradiated at 460 K (T_{irr}) (curve 1), 620 K (curve 2), and 720 K (curve 3). As is seen, two new high-temperature peaks (C at 730 K (T_m) and D at 880 K) appear in addition to the known peaks associated with oxygen vacancies (peak A) and the chromium impurity (peak B). Luminescence spectra of the peaks C and D also contained

bands typical of F- and F^+-centers. Moreover, the relative TL yield in the peaks C and D was found to depend considerably on the irradiation temperature. The peaks A and B dominated during irradiation at room temperature. The luminescence intensity in the peaks C and D increased with growing irradiation temperature when $T_{irr} < Tm$.

From these findings it follows that the proper control of the irradiation temperature may provide conditions when deep traps are filled and the traps associated with the dosimetric peak A remain empty. Therefore, when the crystal is subsequently irradiated at room temperature, it is possible to observe how the TL parameters of the dosimetric peak depend on preliminary occupancy of deep traps. Such experiments were performed for temperature quenching of radioluminescence (RL) (Fig. 10). Luminescence was registered in the luminescence band of F-centers for four states of deep traps:

* deep traps were not filled purposefully (state 1, initial);
* the deepest trap was occupied (state 2);
* both deep traps were occupied (state 3);
* both deep traps were filled and then emptied by thermal treatment at 1220K (state 4).

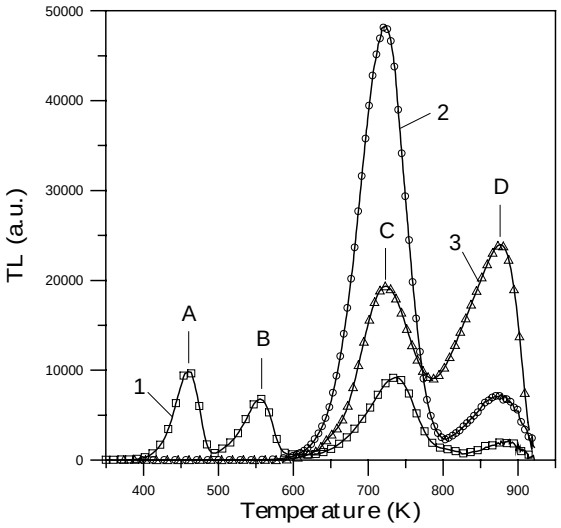

Figure 9. Glow curves of anion-defective α-Al_2O_3 crystals excited by the UV radiation at the heating rate of 2 $K \cdot s^{-1}$. The irradiation temperature: 1 - 460 K; 2 - 620K; 3 - 720K

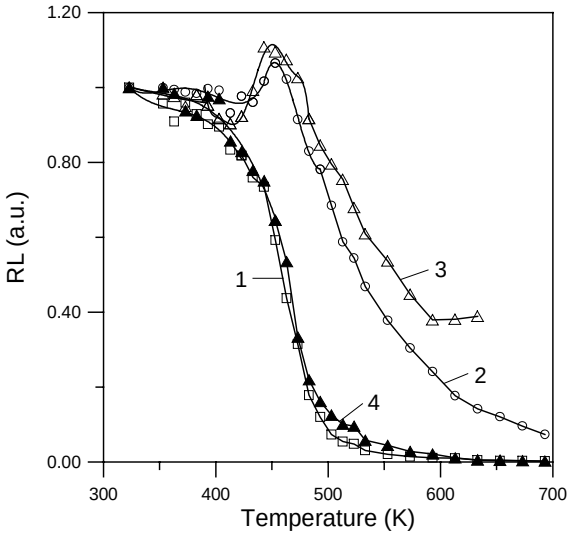

Figure 10. Temperature dependences of the RL yield in the luminescence band of F-centers for four states of deep traps: 1 - deep traps were not filled deliberately; 2 - deep trap D was filled at 775 K; 3 - both deep traps were filled at 620 K; 4 - both deep traps were emptied by thermal treatment at 1220 K for 15 minutes.

The trend of the luminescence quenching curves was found to depend on the occupancy of deep traps. Quenching was almost absent in the range of the dosimetric peak (450 K). The quenching interval shifted to higher temperatures, especially when both deep traps were filled. The examination of the effect of the heating rate on the TL yield led to a similar result. These regularities are illustrated in Fig. 11 for three main luminescence bands (330, 410, and 693 nm) depending on the occupancy of deep traps. As is seen, when the deep traps are filled, the heating rate has a much lesser effect on the TL yield. Analogous experiments proved that the other anomalies in storage properties of anion-defective crystals could also be attributed to the capture of charge carriers in deep traps during the dosimetric peak luminescence. The interactive process involved in the TL mechanism was analyzed for theoretical description of the observed regularities. We used the energy band scheme of the interaction between shallow traps, which are responsible for the dosimetric peak, and deep traps (Fig. 12). The system of equations corresponding to this scheme is well known.

However, it allowed for the temperature dependence of the probability that carriers are captured in deep traps [7] $\delta(T) = \delta_0 \frac{Cexp(-W / kT)}{1 + Cexp(-W / kT)}$, where δ_0 is the temperature-independent factor, *W* - quenching activation energy and C - the constant. Theoretical calculations fully described the observed anomalies in storage properties of anion-defective α-Al_2O_3 crystals. Experimental (curve 1) and calculated (curve 2) dependencies of the dosimetric peak intensity on the occupancy of deep traps are exemplified in Fig. 13. From the above data it follows that storage properties of the oxides are formed in complicated processes of formation and interaction of trapping centers produced by structural defects. A specific feature of the oxides is that defects caused by disturbance of their stoichiometry actively participate in the said processes.

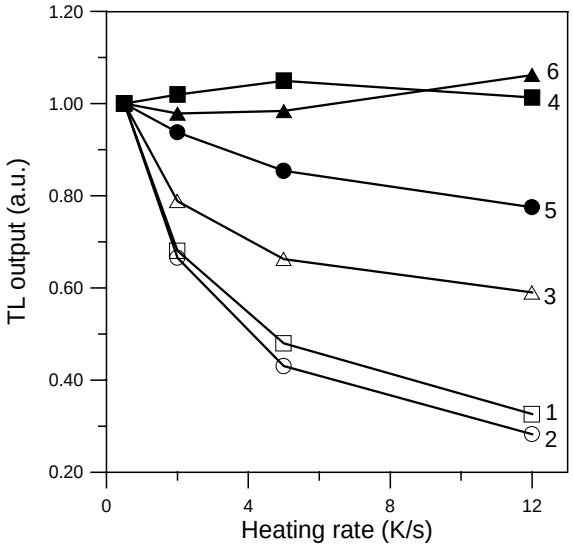

Figure 11. Heating rate dependences of the TL yield in the peak at 450 K in 330 nm (1, 4), 410 nm (2, 5) and 693 nm (3, 6) luminescence bands. Curves (1-3) and (4-6) were registered respectively before and after filling of deep traps at 620 K.

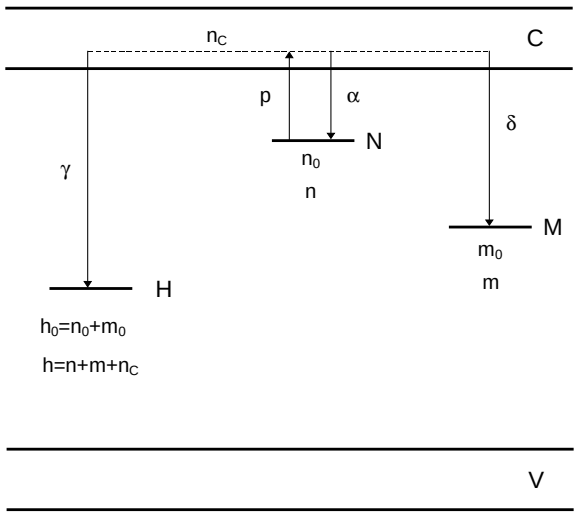

Figure 12. The energy band diagram of the interactive system of the traps. N - TL-active trap, M - deep trap, H - luminescence center. Transitions: γ - radiative recombination at the luminescence center H; δ - capture at deep traps M; α - capture at traps N; p - thermal emptying of shallow TL-active traps. For the other designations refer to the text.

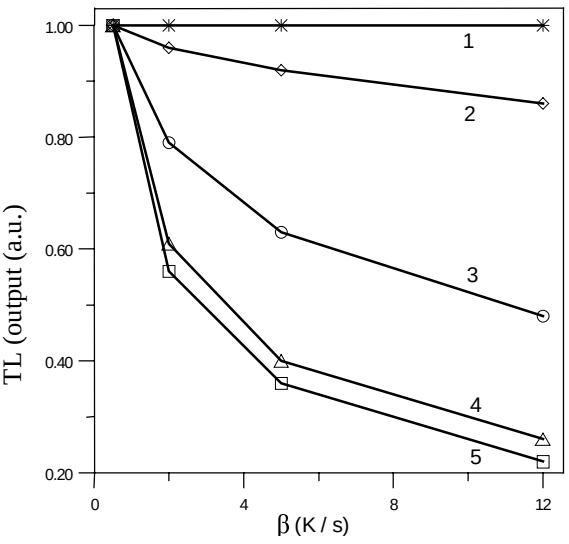

Figure 13. Theoretical dependences of the TL yield in the main peak on the heating rate and the occupancy of deep traps M: 1 - m_0/M = 1; 2 - m_0/M = 0.1; 3 - m_0/M = 0.01; 4 - m_0/M = 0.001; 5 - m_0/M = 0.0001.

Conclusions

1. When exposed to stimulating thermal and photo effects, wide-band oxides (Al_2O_3, BeO, MgO, SiO_2) may possess effective storage properties thanks to the presence of trapping centers with a relatively high ionization energy. Active storage centers are formed by oxygen vacancies. Thermochemical and radiation methods of producing oxygen vacancies in the oxides were proposed and realized. The former method is preferable in development of dosimetric materials, because Schottky defects have a greater thermal stability

2. The investigations into TL, TSEE, ESR, and optical absorption of the said oxides, which were performed in broad spectral and temperature intervals, showed that oxygen vacancies producing F- and F^+-centers play the decisive role in formation of storage and dosimetric properties of the oxides.

3. Impurity centers may play a large role in formation of defect associations including impurities and oxygen vacancies. Probably, such complex centers are decisive for formation of storage properties of the oxides.

4. Deep traps may considerably affect storage of the dosimetric information and the TL kinetics. A model of the interaction between traps, which are responsible for dosimetric TL peaks, and thermally stable deep traps was proposed and substantiated. The model explains the experimentally observed features of storage and dosimetric properties of the anion-defective aluminum oxide.

5. A principle was proposed for creation of radiation-sensitive storage media based on wide-band oxides through purposeful disturbance of stoichiometry in the anion sublattice. Using this principle, it was possible to develop highly sensitive TL dosimeters and working media for combination TL-TSEE-ESR dosimeters of ionizing radiation.

Acknowledgment

The authors are thankful to Dr. S. Nikiforov for his participation in the study of the role played by deep traps in formation of storage properties of anion-defective α-Al_2O_3 crystals.

References

1. S.W.S. McKeever, Thermoluminescence of Solids, Cambridge University Press, Cambridge, 1985, p. 376.
2. M.S. Akselrod, V.S. Kortov, and E.A. Gorelova, Radiat. Prot. Dosim. **47**, (1993) 159.
3. V.S. Kortov, I.I. Milman, Appl. Radiat. Isot. **47(11/12)**, (1996) 1551.
4. V.S. Kortov, and I.I. Milman, Radiat. Prot. Dosim. **65(1-4)**, (1996) 355.
5. Du Varney R.C.,Garrisson A.K., Phys Stat. Sol.(a).**42**, (1977) 609.
6. V.S. Kortov, I.I. Milman, and S.V. Nikiforov, Radiat. Prot. Dosim. **84(1-4)**, (1999) 35.
7. I..I. Milman, V.S. Kortov, and S.V. Nikiforov, Radiat. Meas. **29(3-4)**, (1998) 401.

New materials for X-ray storage phosphors promising higher spatial resolution

S. Schweizer, U. Rogulis, S. Assmann, and J.-M. Spaeth

University of Paderborn, Warburger Str. 100, D-33098 Paderborn, Germany

Abstract: Optically isotropic alkali halides such as RbBr and CsBr doped with Ga^+ are X-ray storage phosphors with a figure of merit comparable to that of the commercially used BaFBr:Eu^{2+}, promising higher spatial resolution. The paramagnetic centres generated upon X-irradiation and involved in the storage and read-out process were investigated by measuring the magnetic circular dichroism of the optical absorption (MCDA), the MCDA-detected electron paramagnetic resonance (EPR) and the photostimulated luminescence (PSL). It turned out that the electron centres are F centres and the hole trap centres are Ga^{2+} centres. In RbBr:Ga^+ we found two different Ga^{2+} centres with hyperfine interactions with ^{69}Ga of ^{69}A = 8.2 GHz and ^{69}A = 6.0 GHz, respectively, of which only the first one takes part in the PSL process. In CsBr:Ga^+ there is only one Ga^{2+} centre with ^{69}A = 6.5 GHz.

Keywords: Magnetic resonance, X-ray storage phosphor, RbBr:Ga^+, CsBr:Ga^+

1. Introduction

At present the photostimulable X-ray storage phosphor of first choice is powdered crystalline BaFBr doped with Eu^{2+} ions. Although digital radiography with such phosphor screens has many attractive features, it has one disadvantage compared to conventional X-ray films: the spatial resolution is still inferior. The reason for this is partially due to the matlockite structure of BaFBr. The crystal is birefringent and, therefore, there is too much light scattering from the statistical distribution of the crystallites in the film when the X-ray information is read out by a scanning laser beam. Consequently, one is interested in optically isotropic X-ray storage phosphor materials.

It has been shown in a preliminary study that RbBr and CsBr doped with Ga^+ are very promising X-ray storage phosphors [1] with a figure of merit as to sensitivity, X-ray conversion and read-out energy comparable to that of BaFBr:Eu^{2+}. Since these phosphors are optically isotropic, they are promising candidates for higher spatial resolution. In this article we present a comparison of the information storage process and the photostimulated luminescence (PSL) mechanism in RbBr and CsBr doped with Ga^+. RbBr had been studied in more detail previously [2]. The main results will be presented here again to enable comparison with CsBr:Ga^+.

2. Experiment

2.1. Sample preparation

RbBr was doped with 200 ppm Ga^+ in the melt and single crystals were grown by the Bridgman method. By using appropriate amounts of $GaBr_3$ and elementary gallium it was attempted to avoid the incorporation of trivalent gallium. The single crystal part grown first contains only a small Ga^+ concentration whereas the end part of the pulled crystal is doped with a much larger amount of Ga^+. In addition, the end part of the single crystal also contains

more other unavoidable impurities than the first part. A sample from the first part and one from the end part have been investigated. Henceforth, the two samples are referred to as “L” (low Ga^+ concentration) and “H” (high Ga^+ concentration). From optical absorption measurements the Ga^+ concentration ratio between the H and L samples was about 5:1.

In the case of CsBr the Ga^+ doping level was 200-3000 ppm. The crystal growth procedure was the same as for RbBr. For both systems the absolute Ga^+ concentration incorporated into the crystal was not determined. The maximum concentration is probably one order of magnitude less than the doping level.

2.2. Spectroscopy

Emission and excitation spectra of the photostimulated luminescence were measured with a single beam spectrometer, in which two 0.25 m double monochromators (Spex) were used. The samples were excited either with a halogen lamp for the visible spectral range or with a deuterium lamp for the ultraviolet range. The emission and excitation spectra were detected using a photomultiplier and single photon counting. The samples were X-irradiated (tungsten anode, 60 kV, 15 mA, 15 min) between 10 K and 300 K.

The magnetic circular dichroism of the optical absorption (MCDA), which is the differential absorption of right and left circularly polarised light in an external static magnetic field, and the MCDA-detected electron paramagnetic resonance (MCDA-EPR) were measured in a custom-built, computer-controlled spectrometer working at 24 GHz (K-Band). The samples could be X-irradiated between 4.2 K and 300 K in situ in the microwave cavity (tungsten anode, 60 kV, 15 mA, 30 min). For the optical bleaching experiments a HeNe laser (633 nm) was used.

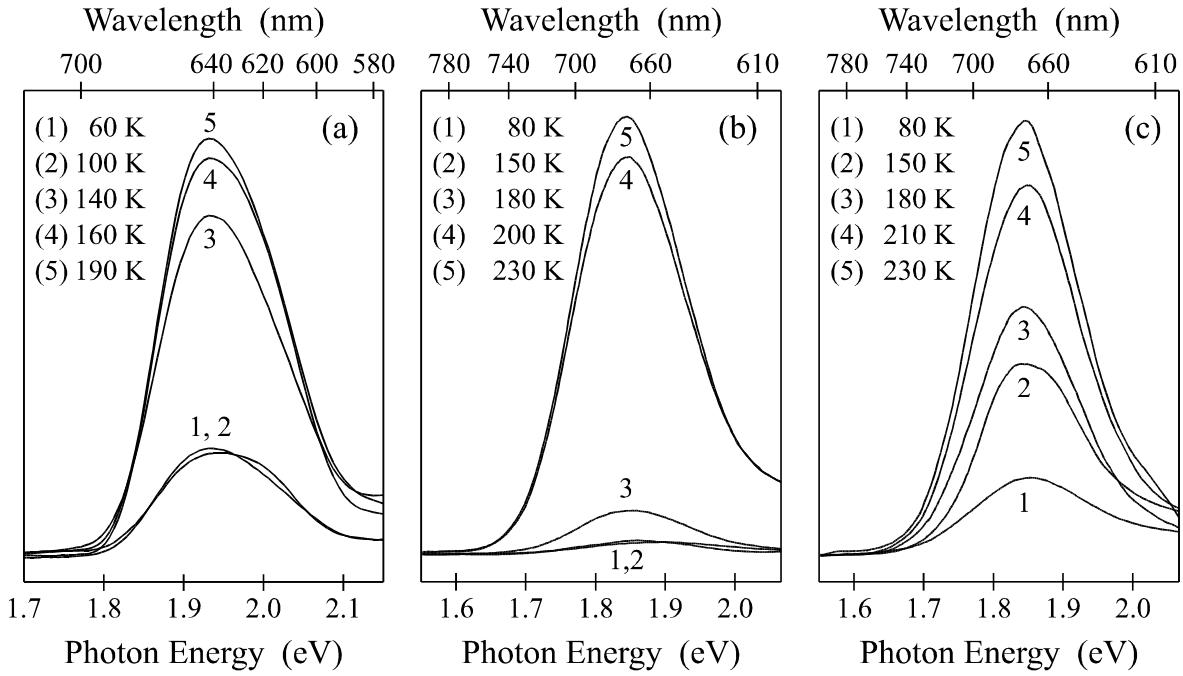

Figure 1 PSL excitation spectra of (a) CsBr:Ga^+, (b) RbBr:Ga^+, sample L, and (c) RbBr:Ga^+, sample H, for various subsequent temperature steps after X-irradiation at 60 K (CsBr:Ga^+) or at 80 K (RbBr:Ga^+). All spectra were recorded at 60 K (CsBr:Ga^+) or at 80 K (RbBr:Ga^+).

3. Experimental results

3.1. Luminescence properties

In order to obtain information about the electron and hole trap centres involved in the photostimulated luminescence (PSL) of X-irradiated RbBr:Ga^+ and CsBr:Ga^+, PSL excitation measurements were carried out as a function of temperature. At first, the samples were X-irradiated at 60 K (CsBr:Ga^+) or at 80 K (RbBr:Ga^+) for 15 min. Subsequently PSL excitation spectra were measured at 60 K (CsBr:Ga^+) or at 80 K (RbBr:Ga^+) after heating the sample first to a certain temperature and then cooling it down to 60 K or to 80 K again. This procedure was repeated for several temperatures. In all cases the Ga^+ luminescence at 2.41 eV (515 nm, CsBr:Ga^+) or at 2.21 eV (560 nm, RbBr:Ga^+) was detected. In Figure 1(a) the results for CsBr:Ga^+ are presented. While the spectrum measured after annealing to 100 K shows no considerable change in the weak Ga^+ luminescence, the temperature step to 140 K is followed by a strong increase of the PSL intensity. Further annealing to 160 K results again in a significant increase of the PSL intensity followed by only a small rise after the next step to 190 K.

Figure 1(b) shows the results for RbBr:Ga^+, sample L. While the spectra measured after annealing to 80 K, 130 K, and 150 K yield no considerable changes in the Ga^+ luminescence, the temperature step to 180 K is followed by a slight increase of the luminescence intensity. Further heating to 200 K results in a strong increase of the luminescence intensity followed by only a small rise after the next step to 230 K. This behaviour of the temperature-dependent luminescence spectra is different for RbBr:Ga^+, sample H, presented in figure 1(c). Besides the luminescence increase from 180 K to 210 K, similar to that of the other sample, a rise is also observed at the annealing step from 80 K to 150 K.

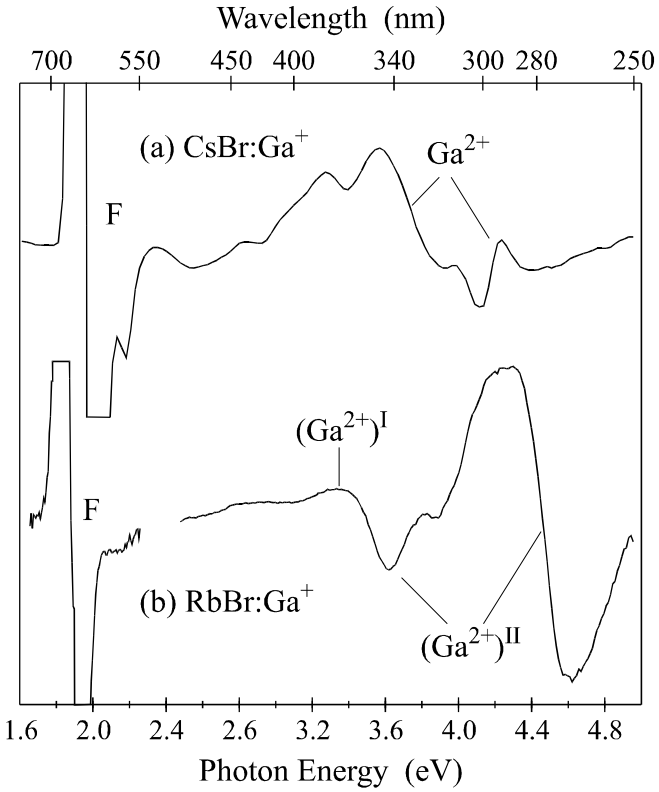

Figure 2 MCDA spectra of (a) CsBr:Ga^+ and (b) RbBr:Ga^+, sample L, after X-irradiation at RT. All spectra were recorded at 4.2 K.

3.2. MCDA and MCDA-detected EPR

The MCDA spectra of CsBr:Ga^+ and RbBr:Ga^+, measured after X-irradiation at RT, are shown in figures 2(a) and (b). The bands at 1.94 eV (640 nm, CsBr:Ga^+) and at 1.88 eV (660 nm, RbBr:Ga^+), having a derivative-like structure, belong to the F centres. Besides the F centre band, several MCDA bands were detected in the UV spectral range. Since the spectra are scaled up in favour of the UV bands, the F centre bands are cut off.

The MCDA-detected EPR spectra of the X-irradiated CsBr:Ga^+ and RbBr:Ga^+ samples are shown in figures 3(a) and (b). Several broad EPR lines appear in the magnetic field range up to 1300 mT. The line positions are isotropic within experimental error. They are due to one Ga^{2+} hole centre (CsBr:Ga^+) or two different Ga^{2+} hole centres (RbBr:Ga^+).

The EPR lines of each Ga^{2+} centre are split by a hyperfine (hf) interaction between the unpaired electron of the Ga^{2+} ($4s^1$ state) with $S = 1/2$ and the two magnetic isotopes ^{69}Ga (60.4% natural abundance) and ^{71}Ga (39.6% natural abundance), both with a nuclear spin of $I = 3/2$. The hf interaction leads to four "allowed" ($\Delta m_I = 0$) transitions marked with bars in figure 3. The transitions labelled with asterisks are due to "forbidden" ($\Delta m_I = \pm 1, \pm 2$) transitions. The allowed quartet lines for $I = 3/2$ have the same intensity. Since they are superimposed to forbidden transitions, the intensity pattern in figure 3 is different from the expectation for allowed transitions only.

Unfortunately, we did not observe any superhyperfine (shf) interactions with surrounding lattice neighbours. Therefore, we cannot establish the structural differences between the two Ga^{2+} centres found in RbBr:Ga^+ from the EPR spectra. The isotropic *g*-factors, the hf interaction parameters ^{69}A for ^{69}Ga, the wavelengths, at which the MCDA-detected EPR spectra were measured, as well as published data for NaCl:Ga^+ and KCl:Ga^+ are collected in table 1.

The excitation spectra of the MCDA-detected EPR ("tagged" MCDA, see [3]) are shown in figure 4(a) and 4(b) for the Ga^{2+} centre in CsBr:Ga^+ and the $(Ga^{2+})^{I}$ and the $(Ga^{2+})^{II}$ centre in RbBr:Ga^+, respectively. Figure 4(a) has the same spectral shape as the UV MCDA bands measured for CsBr:Ga^+ (figure 2(a)). Thus, the UV bands belong to Ga^{2+} centres. The spectrum for the $(Ga^{2+})^{I}$ centres in figure 4(b) shows that an energy of 3.35 eV (370 nm) is very suitable for measuring the MCDA-detected EPR spectrum of these centres, whereas 4.29 eV (289 nm) is suitable for the $(Ga^{2+})^{II}$ centres in RbBr:Ga^+ (figure 4(b), spectrum for the $(Ga^{2+})^{II}$ centres).

3.3. Production of $(Ga^{2+})^{I}$ and $(Ga^{2+})^{II}$ centres in RbBr:Ga^+

The relative intensities of the MCDA bands of $(Ga^{2+})^{I}$ and $(Ga^{2+})^{II}$ centres created upon X-irradiation were found to be dependent on the Ga^+ concentration and the irradiation temperature. In the sample L with low Ga^+ concentration after X-irradiation at RT a significant MCDA band of $(Ga^{2+})^{II}$ centres, but only a small band of $(Ga^{2+})^{I}$ centres was found (see figure 2(b)). In the sample H with high Ga^+ concentration after X-irradiation at RT the intensities of both MCDA bands are of the same order of magnitude with a smaller MCDA band of $(Ga^{2+})^{II}$ centres.

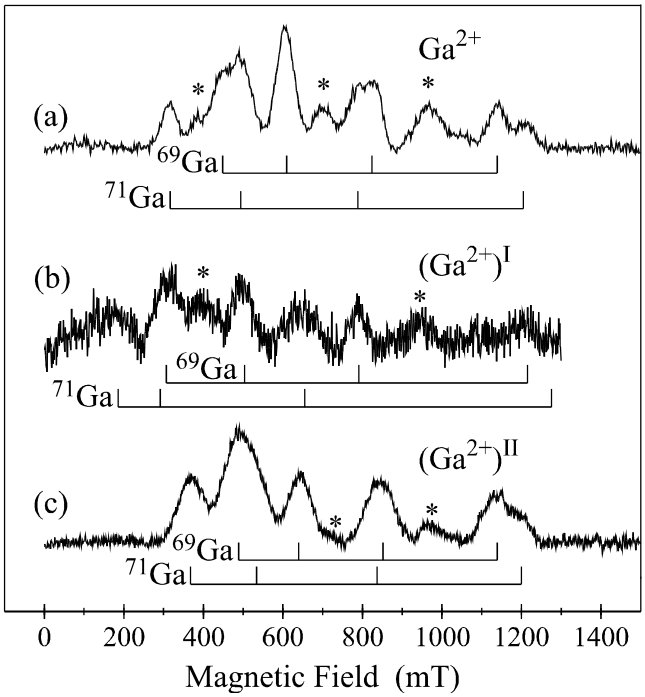

Figure 3 MCDA-detected EPR spectra of (a) Ga^{2+} centres in CsBr:Ga^{+}, detected at 300 nm, (b) $(Ga^{2+})^{I}$ centres in RbBr:Ga^{+}, sample L, detected at 370 nm, and (c) $(Ga^{2+})^{II}$ centres in RbBr:Ga^{+}, sample L, detected at 289 nm. All spectra were recorded in K-band (24 GHz) at 1.5 K.

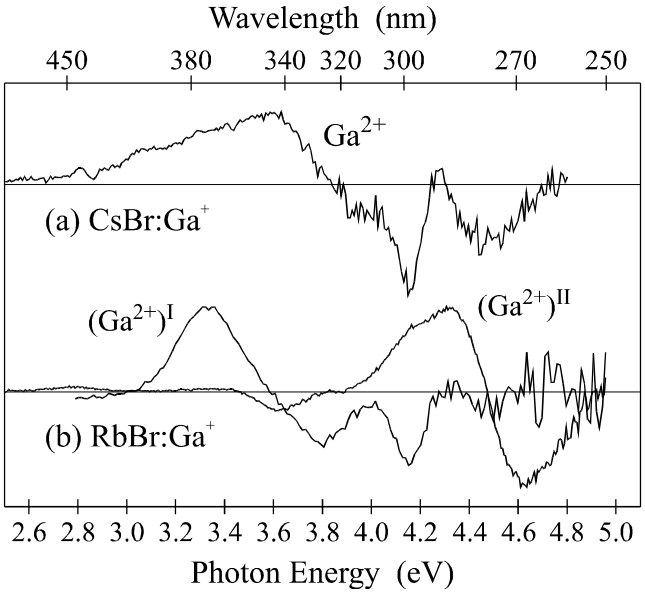

Figure 4 "Tagged" MCDA spectra of (a) Ga^{2+} centres in CsBr:Ga^{+} for B = 603 mT and (b) $(Ga^{2+})^{I}$ and $(Ga^{2+})^{II}$ centres in RbBr:Ga^{+}, sample L, for B = 300 mT and B = 500 mT, respectively. All spectra were recorded at 1.5 K.

When X-irradiating at 4.2 K, no Ga^{2+} centres appear, only F and V_K centres are observed. After annealing to about 180 K, where the V_K centres have begun to disappear, Ga^{2+} centres start to appear. In the sample L, the MCDA band of $(Ga^{2+})^I$ centres appears at 180 K and reaches its maximum value at 220 K. A weak MCDA band of the $(Ga^{2+})^{II}$ centres also appears at 180 K, reaches its maximum value when annealing further to 250 K and then remains unchanged to RT. Corresponding to the increase of the MCDA band of the $(Ga^{2+})^{II}$ centres the MCDA band of the $(Ga^{2+})^I$ centres decreases between 220 K and 250 K. At 250 K about half of $(Ga^{2+})^I$ centres are destroyed. In sample H, the MCDA band of $(Ga^{2+})^I$ centres appears at 180 K with a further increase to its maximum value at about 220 K. Only very few MCDA of $(Ga^{2+})^{II}$ centres is observed, even after annealing up to RT. In general, the MCDA of $(Ga^{2+})^I$ centres reaches its maximum value at about 220 K, i.e. by an annealing step above the decay temperature of the V_K centres, while the MCDA of $(Ga^{2+})^{II}$ centres reaches its maximum at 250 K.

Bleaching in the F centre absorption band at RT to stimulate the Ga^+ luminescence destroyed the Ga^{2+} MCDA signal in CsBr:Ga^+, whereas bleaching at 4.2 K did not change the Ga^{2+} MCDA band. In RbBr:Ga^+ bleaching could not destroy the $(Ga^{2+})^{II}$ MCDA signal, neither at RT nor at 4.2 K. However, the MCDA signal of the $(Ga^{2+})^I$ centres in RbBr:Ga^+ vanished after bleaching at RT as well as at 4.2 K.

3.4. Ga^+ aggregation

To investigate a conceivable tendency of the Ga^+ activator to form aggregates in CsBr and RbBr, which might negatively influence the phosphor properties, Ga^+ luminescence and PSL measurements were performed after annealing (and subsequent quenching) several Ga^+-doped samples. In RbBr we did not find any influence of Ga^+ aggregation on luminescence or PSL properties.

Crystal	Centre	Wavelength (nm)	^{69}A (GHz)	g
CsBr	Ga^{2+}	300	6.2 ± 0.05	2.04 ± 0.01
RbBr	$(Ga^{2+})^I$	370	8.2 ± 0.2	2.03 ± 0.01
	$(Ga^{2+})^{II}$	289	6.0 ± 0.05	2.005 ± 0.005
NaCl	Ga_c^{2+}		9.35	2.062
KCl	Ga_c^{2+}		8.86	2.012
	Ga^{2+}-V_c		6.33	2.01

Table 1 Isotropic *g*-factors, hf interaction parameters ^{69}A for ^{69}Ga, wavelengths, at which the MCDA-detected EPR spectra were measured, as well as published data for NaCl:Ga and KCl:Ga [5].

In CsBr:Ga^+ we investigated the UV excited Ga^+ luminescence as well as the PSL intensity before and after annealing up to 520 °C (melting temperature of CsBr: 632 °C). The luminescence and the PSL intensity increase by a factor of 2-3 (especially for Ga^+ doping levels above 3000 ppm), which demonstrate that Ga^+ aggregates were cracked at this annealing temperature.

4. Discussion

The MCDA and MCDA-detected EPR experiments have clearly shown that X-irradiation creates in CsBr:Ga^+ only one Ga^{2+} hole trap centre whereas in RbBr:Ga^+ two different Ga^{2+} hole trap centres are formed. In CsBr:Ga^+, Ga^{2+} centres are observed by MCDA after X-irradiation at 4.2 K and subsequent annealing up to 145 K (Note, that in CsBr V_K centres start to decay at 106 K for 0° jumps and at 130 K for 90° jumps [4]). Thus, we think that Ga^{2+} centres are formed upon hole capture by Ga^+ from a mobile V_K centre. The fact that also the PSL effect is correlated with the formation of Ga^{2+} centres in the described way is seen in its temperature dependence (figure 1(a)). After low temperature X-irradiation and annealing from 100 K to 140 K the PSL increases drastically while the MCDA of Ga^{2+} centres starts to appear.

Since the *g*-factor and the hyperfine interaction of the Ga^{2+} centres in CsBr:Ga^+ are isotropic within experimental error, we conclude that Ga^{2+} replaces Cs^+ on a regular lattice site without a nearest vacancy or defect present as in the case of RbBr:Ga^+ (see below).

The two different Ga^{2+} centres in RbBr:Ga^+ show no resolved shf interaction; nothing can be said about the structural differences from the EPR spectra alone. However, from the generation by X-irradiation at low temperature and subsequent annealing it can be concluded that $(Ga^{2+})^I$ centres are also formed upon hole capture by Ga^+ from a mobile V_K centre, while the formation of $(Ga^{2+})^{II}$ centres needs as well the mobility of another species, thought to be vacancies. $(Ga^{2+})^{II}$ centres are proposed to be Ga^{2+}-cation vacancy complexes, similarly to what was proposed by Baranov and Khramtsov [5] to occur upon X-irradiation in KCl and NaCl doped with Ga^+. When irradiating the sample at 4.2 K, only V_K and F centres are observed. At about 180 K, $(Ga^{2+})^I$ centres are observed (the V_K centres start to decay at about 170 K [6]). Thus, we think that mobile V_K centres are captured by Ga^+ centres forming $(Ga^{2+})^I$ centres. However, in sample L $(Ga^{2+})^{II}$ centres start to appear above 180 K, the maximum value is reached at about 250 K. The formation process of the $(Ga^{2+})^{II}$ centres is more complex than that proposed for $(Ga^{2+})^I$ centres. In KCl and RbCl cation vacancies become mobile at about 220 K [7-9]. A similar mobility temperature is also expected for RbBr since the migration energy of cation vacancies in RbBr (0.81 eV) is very close to that of KCl (0.84 eV) and RbCl (0.80 eV) [10]. The mobile cation vacancies can be captured by a Ga^{2+}, which attracts the negative cation vacancies due to its positive charge. The resulting complex is electrically neutral and stable. Apparently, the sample L contains cation vacancies in a considerable concentration, i.e. in the same order of magnitude as the concentration of Ga^+ in that sample. Possibly because of the doping method (see section 2.1.) Ga^{3+} centres are also incorporated causing the creation of cation vacancies. When following the formation of Ga^{2+} centres above 220 K in the sample L, the initial concentration of $(Ga^{2+})^I$ centres is found to decrease from 220 K to 250 K at the expense of the formation of more $(Ga^{2+})^{II}$ centres. Thus, cation vacancies are attracted by the positive $(Ga^{2+})^I$ centres and form $(Ga^{2+})^{II}$ centres. After X-irradiation at RT of

sample L we found a significant MCDA band of $(Ga^{2+})^{II}$ centres, but only a small band of $(Ga^{2+})^{I}$ centres. This corresponds to the X-irradiation at 4.2 K and subsequent annealing procedure. In sample H, we could observe $(Ga^{2+})^{II}$ centres after X-irradiation at RT. This is contrary to the fact that after X-irradiation at 4.2 K and subsequent annealing to room temperature very few $(Ga^{2+})^{II}$ centres were found. A very high mobility of the cation vacancies during the RT X-irradiation seems to favour the creation of the $(Ga^{2+})^{II}$ centres, while after low temperature X-irradiation and annealing to 220 K the V_K centres are preferentially trapped at Ga^+ to form $(Ga^{2+})^{I}$ centres and are not converted to $(Ga^{2+})^{II}$ centres. We think that the sample H contains less cation vacancies than sample L. This together with an enhanced vacancy mobility under RT X-irradiation may be the reason for the different ratio between $(Ga^{2+})^{I}$ and $(Ga^{2+})^{II}$ centres when produced by low temperature X-irradiation and annealing or by RT X-irradiation.

Ga^{2+} has a $4s^1$ configuration and therefore a large isotropic hf interaction. Both Ga^{2+} centres have, within experimental error, an isotropic *g* factor and isotropic hf interaction. However, due to the broad EPR lines and the superposition of many forbidden lines, a small *g* anisotropy would not be resolved. The observation that the larger hf interaction is observed for $(Ga^{2+})^{I}$ centres and the smaller one for the Ga^{2+}-V_c complex supports the assignments and is in agreement with the observation by Baranov and Khramtsov in KCl and NaCl [5].

The bleaching experiment showed that only the $(Ga^{2+})^{I}$ MCDA band disappears upon photostimulation of the F centres, i.e. only the $(Ga^{2+})^{I}$ centres are participating in the read-out process. From the centre models for the two Ga^{2+} centres this is understandable, since $(Ga^{2+})^{I}$ centres are positively charged attracting mobile electrons, while the neutral $(Ga^{2+})^{II}$ centres do not. The fact that the PSL effect is, indeed, correlated only with the $(Ga^{2+})^{I}$ centres is also seen in its temperature dependence (figure 1(b)). In the sample L after low temperature X-irradiation and annealing to 180 K, the PSL starts to increase and the MCDA of $(Ga^{2+})^{I}$ centres starts to appear. At 200 K the PSL increases drastically, while at this temperature $(Ga^{2+})^{II}$ centres are not yet formed. Thus, for the use of RbBr:Ga^+ as a storage phosphor, the generation of $(Ga^{2+})^{II}$ centres must be avoided, since they compete for primary holes but cannot be read-out. The generation of $(Ga^{2+})^{II}$ centres can be avoided in the higher doped sample after X-irradiation at low temperature with subsequent annealing, which is, of course, not a practical way to use a storage phosphor. Ways have to be exploited to suppress the generation of $(Ga^{2+})^{II}$ centres from a RT X-irradiation, possibly by an improved Ga^+ doping which avoids the formation of cation vacancies.

In contrast to RbBr:Ga^+, the information storage and read-out process is particularly simple in CsBr:Ga^+: The electron traps are F centres, the hole trap centres are Ga^{2+} centres. It has therefore less complications compared to RbBr:Ga^+ with Ga^+-vacancy complexes depending on the doping level (and possibly the way of Ga^+ doping). The peak of the F excitation band at 640 nm is at shorter wavelength compared to RbBr (675 nm). The X-ray stopping power of CsBr is higher. Due to the observed Ga^+ aggregation the upper Ga^+ doping level is limited to about 3000 ppm. Consequently, CsBr:Ga^+ seems a favourable candidate for a screen with higher spatial resolution than now possible with BaFBr:Eu^{2+}.

5. Acknowledgement

The co-operation and support by Dr P. Willems and Dr P. J. R. Leblans of Agfa-Gevaert company (Mortsel, Belgium) is gratefully acknowledged.

References

1. Th. Hangleiter, U. Rogulis, C. Dietze, J.-M. Spaeth, P. Willems, L. Struye, and P. J. R. Leblans, Proc. Int. Conf. on Inorganic Scintillators and Their Applications, SCINT95, Delft, Delft University Press, The Netherlands (1996), 452
2. U. Rogulis, S. Schweizer, S. Assmann, and J.-M. Spaeth, J. Appl. Phys. **84** (1998), 4537
3. J.-M. Spaeth, J. R. Niklas, and B. H. Bartram, Structural Analysis of Point Defects in Solids, Springer Series in Solid State Sciences **43** (Springer, Berlin, 1992)
4. J. J. Pilloud and C. Jaccard, Phys. Stat. Sol. (b) **92** (1979), 233
5. P. G. Baranov and V. A. Khramtsov, Sov. Phys. Solid State **20** (1978), 1080
6. D. Schoemaker, Phys. Rev. B **7** (2) (1973), 786
7. C. J. Delbecq, R. Hartford, D. Schoemaker, and P. H. Yuster, Phys. Rev. B **31** (1976), 3631
8. F. van Steen and D. Schoemaker, Phys. Rev. B **19** (1979), 55
9. E. Goovaerts, J. Andriessen, S. V. Nistor, and D. Schoemaker, Phys. Rev. B **24** (1981), 29
10. D. K. Rowell and M. J. L. Sangster, J. Phys. C: Solid State Phys. **14** (1981), 2909

Halide Scintillators. Present Status and Prospects

A.V.Gektin

Institute for Single Crystals, 60, Lenin Ave., 310001, Kharkov, Ukraine

Abstract: Halide scintillators are the most common used radiation detection materials during last decades. This paper presents a brief description of last alkali halide scintillator developments for nuclear medicine (SPECT, X-ray detectors, scintimammography and so on) and high energy physics (HEP). Examples will be given of recent design and developments like BELLE and BaBar in HEP, curve plates, cylindrical and matrix detectors in nuclear medicine, to show the high demand on scintillator parameters modification and improvement for new scientific experiments and industrial applications. The main physical aspects of ABX_3 halide scintillators and dosimeters R&D are also reported. Particular attention is paid to the last years search of new efficient halide scintillation crystals.

Keywords: halide scintillators, single crystals, ABX_3 structures, energy storage, dosimetry, medical imaging, high energy physics

1. Introduction

Halide scintillators is at present the most comprehensively used material for the registration of radiation. The first NaI(Tl) scintillator was described more than 50 years ago [1] and it is most commonly used so far. Later, a number of other scintillation materials were developed, i.e. there appeared a range of crystals for various applications and engineering solutions. Despite of rather long history of halide scintillators a search for new compounds, modernization and modification of detection principles, new applications are being continuously developed. The present paper is a brief review of such trends.

2. Halide scintillators for high- and medium-energy physics

High-energy physics is one of the reinforcing factors for search new and improvement of conventional scintillators in general and halide ones in particular [2,3]. Just owing to active development of methods for growing alkali halide scintillation crystals a number of big projects (BELLE [4], BaBar [5], KTeV [6], PeBeta [7]) have been recently implemented and are in the progress now. Last decade there were some partly successfully completed R&D for the development of BaF_2 for GEM [8] and CeF_3 for LHC [9] too.

The major part of the problems at the stage of R&D and crystal production is connected with: 1) a necessity to grow large-size crystals (from 300 mm for B-factories to 500 mm for KTeV); 2) requirements to the light output uniformity along the scintillator; 3) quenching of slow components of luminescence (afterglow problem); 4) radiation damage suppress.

While the first problem is related to the single crystal growth technology, the second one includes crystal performance and method of scintillator treatment. The light yield uniformity at every part of the crystal does not mean its total uniformity along the entire scintillator length. Fig.1 shows the distribution of light output at the radiation source scanning along one and the same CsI(Tl) crystal, only its surface being treated different ways. Actually, that means that the problem of light collection should be tuned for each scintillator from thousands of calorimeter elements [10]. Besides, stability of crystal surface treatment has to be provided with allowance for hygroscopicity of halides and aging of the crystal itself and its subsurface layers.

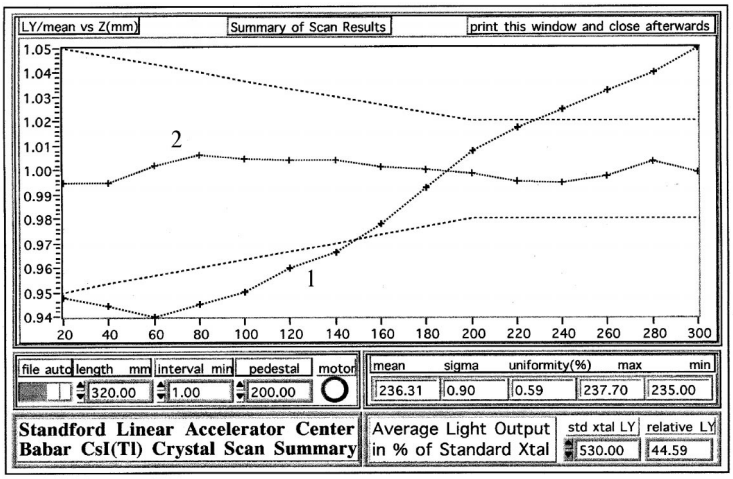

Fig.1. Light output uniformity tuning by proper crystal finishing. 1 – before tuning, 2 – after tuning.

The study of physical phenomena, which proceed during scintillation process, shows the variety of energy loss channels (see Fig.2). Reaching the maximum light yield for any crystal is connected with a realization of optimal conditions of energy transfer to the luminescence center. Any carriers capture by foreign traps result not only in the decrease of luminescence efficiency but also in the emergence of additional harmful effects. First of all, it is an additional absorption, energy storage and afterglow.

Therefore, investigations of such phenomena give a background for scintilaltion parameter improvement. The ways of suppression of either losses are different.

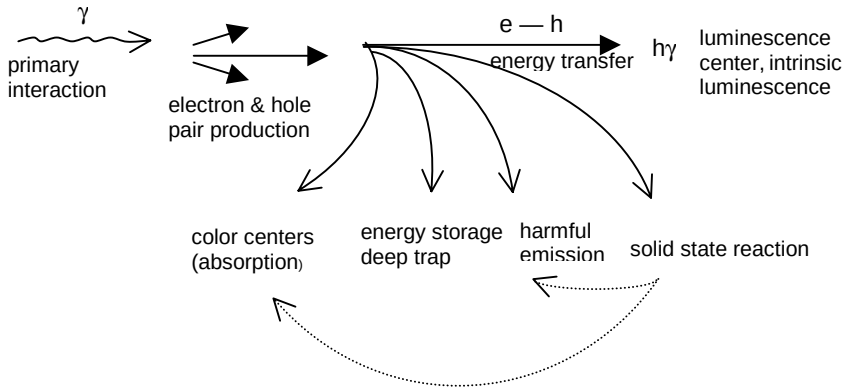

Fig.2. Schematic overview of scintillation efficiency losses.

Conventionally the experimental activity on scintillator improvement can be divided into three groups: crystal doping; intrinsic defects' equilibrium sustain; elimination of oxygen and hydroxyl impurities.

The first direction was the most actively developed regarding BaF_2 and CeF_3 [11]. Multiple experiments allowed to classify the impurities into harmless (Y, La, Lu), harmful (Ce, Rr, O, OH) and useful ones (Eu, Dy). However, later this was not included in the practice of growing scintillation crystals. Practically the only solution turned out to be important indeed – doping of BaF_2 with lanthanum. It was shown in [12] that such doping leads to a partial quenching of exciton luminescence. This became a core for the method of growing $Ba(La)F_2$ with the same as in BaF_2 a fast luminescence yield but with lower level of afterglow [13].

The most important turned out to be the study of a parasite role of the oxygen-containing impurities and finding out the sources of their emergence in crystals. It is known that the number of such kind impurities is large and their ratio depends on both – type of the crystal and its growth conditions. In practice, high purity of crystals cannot always be achieved by additional purification of raw material, therefore, scavengers are widely used.

In general, the oxygen-containing impurities are manifested in all alkali halide crystals primarily in the form of absorption bands that decrease transparency of crystals at the wavelength of scintillations. For long crystals these losses become critical. Variations of the absorption coefficient value only from 0.01 to 0.02 cm^{-1} result in the loss of light yield by 28 % [14].

The presence of oxygen-containing impurities in halides is the reason of additional slow decay luminescence[15]. Since such impurities are practically always available in crystals simultaneously in the form of different molecular complexes, it is difficult to discriminate the contribution of each. In this respect rather interesting are the results of [16,17] in which CsI crystals were deliberately doped with Cs_2CO_3. This resulted in the formation of two centers: O^{2-} and CO_3^{2-}, each having its intrinsic luminescence. The first one has the luminescence parameters 435 nm and τ=3.4 μs, the second, 394 nm and τ=1.4 μs, respectively. Such crystal is a good scintillator with comparative efficiency with respect to CsI(Na) 70% for ^{137}Cs and 130% for ^{241}Am and to NaI(Tl) 70% for ^{55}Fe. This efficiency is achieved at a dopant concentration 10 times lower than typical Tl or Na concentration in CsI crystals. This gives evidence to the fact that the efficient cross-section of carriers' trapping by oxygen-containing impurities is by an order higher than that of conventional dopants. Thus, it is clear that even an insignificant content of oxygen-containing impurities should result in afterglow. This effect becomes extremely important for making fast scintillators based on pure CsI. Even in the best samples of such scintillators the "Fast/Total ratio" rarely exceeds 0.7-0.8 [18], though theoretically it should approach 1.

Radiation damage is a particularly significant problem for halide scintillators applied in HEP. As the radiation doze becomes higher in modern electromagnetic calorimeters the requirements to scintillators become more severe. Consequently, the nature of radiation damage must be investigated. The traditional approach to the problem is usually reduced to the study of crystal transparency change before and after irradiation [19]. However, at a more thorough consideration it turns out that in the luminescence range of CsI(Tl) 540 nm there are no absorption bands of the intrinsic color centers. The absorption bands of color centers associated with hydroxyl impurity can be observed in this wavelength range [20]. This means that the problem of radiation resistance of such crystals is also connected with the presence of oxygen-containing impurities. Impurity color centers lower BaF_2 scintillation efficiency as well [21]. No doubt that radiation damage not only deteriorates scintillator transparency but also decreases the efficiency of luminescence due to the trapping of a part of carriers on the radiation-induced defects [22]

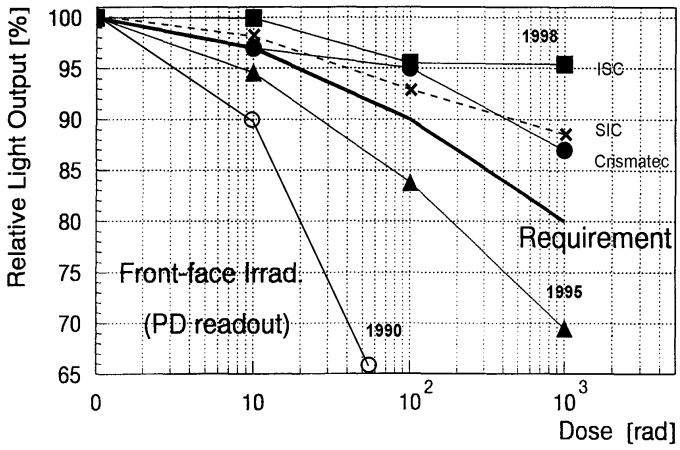

Fig.3. CsI(Tl) scintillator. Radiation damage improvement at last decade.

The recent years R&D were focused on the increase of radiation resistance of halide scintillators [20]. The final data for CsI(Tl) crystals are shown in Fig.3. One can see that after R&D connected with the development of the electromagnetic calorimeter for BELLE the ways of a partial radiation damage suppression have been found.

3. Halide scintillators in nuclear medicine

For the recent decades one of the widely used medical diagnostics is SPECT [23]. NaI(Tl) scintillation detector is the main element of gamma-camera. Several generations of gamma-cameras have superseded for these years (Fig.4), each next step forward resulting in a scintillator progress. Opportunities for improving the planar gamma camera resolution are limited as they already near theoretical limit. Up to 2000 of gamma-cameras are produced annually at present [23], but despite of this fact, modification of their design and principles of registration is being continued. The main efforts are concentrated around scintillator design [24,25].

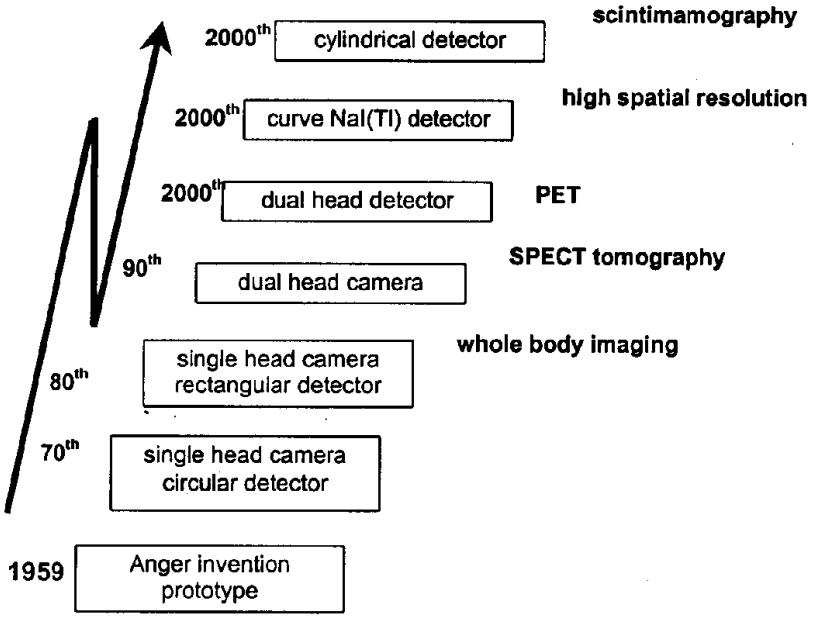

Fig.4. Schematic overview of the progress in medical gamma-cameras design and developments.

In this respect a change over from flat to curve detectors [26] is a principally new solution. This, as a minimum, improves 511 keV coincident detection performance and enhances SPECT performance with single head cameras without principal change of image reconstruction logic and technique. Decrease the distance from the collimator surface to the object allows to enhance the spatial resolution.

Such technical solutions have been already implemented and make a base for producing cameras of next generation.Even more important is detection using cylindrical detectors. As one can see from **Fig.5**, such geometry of detector allows to use alongside with Anger logic the elements of CT and even PET image reconstruction [27]. The first models of cylindrical detectors have been already made.

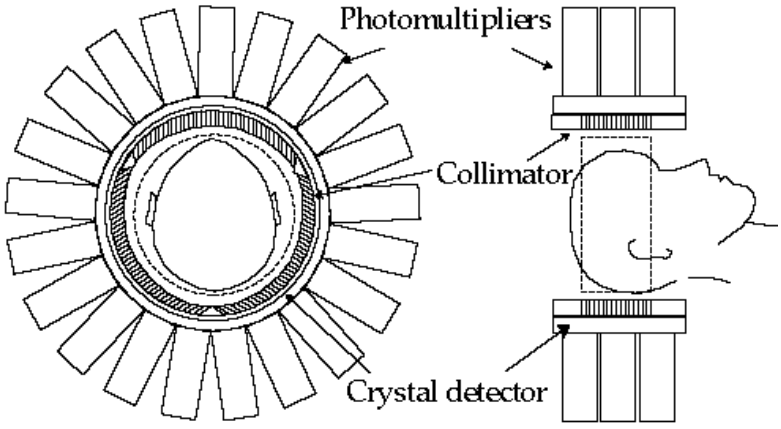

Fig.5. CERASPECT is an emission tomography imaging system designed for 3D imaging of brain using single-photon emitters. (In courtesy of Digital Scintigraphics, Inc.).

4. Pixelated detector methods

Practically full achievement of theoretical values of both energy and space resolution for the detection system is a significant restriction of the SPECT methods. One of the principal ways of breaking this barrier is elaboration of pixelated detectors [28]. In this case detection is realized owing to the development of both: semiconducting pixelated detectors (these are mainly matrixes based on CZT crystals [29]) and arrays –scintillation matrix-matrix of photodiodes. Such solutions are based, as a rule, on CsI(Tl) crystals, the emission wavelength of which is close to the optimal sensitivity of silicon photodiodes.

New generation X-ray sources have created a need for a detector that can provide multiple frames of detailed X-ray images. A new concept of a flat panel X-ray detector consists of an a-Si:H photodetector array with CsI(Tl) phosphor layer on top. Such digital system is based on the development of columnar structure evaporated CsI(Tl) scintillators [30,32]. Last CsI(Tl) layer spectroscopy studies shows different from single crystal spectral and kinetic characteristics and bring new features in the comprehension of scintillation process in this material [33]

5. ABX_3-type halide perovskites

For the recent years halide perovskites of the ABX_3-type (A - alkali, B - alkali-earth, X - halide ion) become not only objects for luminescence study, but also a subject for the development of radiation detectors [34,35] and laser media [36,37]. On one side, a variety of crystal nomenclature allows to select different energy gap and, on the other side, the crystal lattice gives prospects for finding a possibilities of their doping as compared to simple (two component) alkali and alkali-earth halides. Therefore, variation of the perovskite composition, selection of proper dopants and thermal treatment conditions make a basis for the sensor materials development.

5.1. Scintillation materials

The core-valence transitions with nanosecond luminescence are typical for some wide gap perovskites. Despite of the fact that this luminescence is significantly quenched and gives rather low yield it is yet important for the development of fast scintillators.

A restrictive factor regarding usage of such crystals is the presence of slow luminescent components. Physically this factor is explained by two groups of phenomena. Firstly, it is the intrinsic recombination luminescence. For instance, it is slow luminescence of self trapped excitons – STE (280-310 nm, decay time – hundreds of microseconds) that simultaneous presence with fast CV luminescence (the maxim at 130-220 nm, τ~1 ns). With this, $LiBaF_3$ crystals are used for n-γ-discrimination [35]. In this case the fact is used that two types of luminescence are manifested at γ-excitation and at n-excitation – only one (STE). There are some registration improvements in doped crystals [38]

Secondly, the restricting factors are connected with the presence of some impurities in crystals; those are primarily oxygen containing anions.

To modify emission parameters $KMgF_3$ and $LiBaF_3$ crystals were doped with Ce^{3+} ions. The investigations show that this activator allows to shift the spectrum of UV radiation towards the region convenient for registration, decrease the contribution of the slow exciton luminescence and partially bind the residual oxygen anions as well [39,40]. Thus, introduction of Ce^{3+} ions to $KMgF_3$ crystal results in the formation of some luminescence centers emitted at 350 nm and τ = 50 ns.

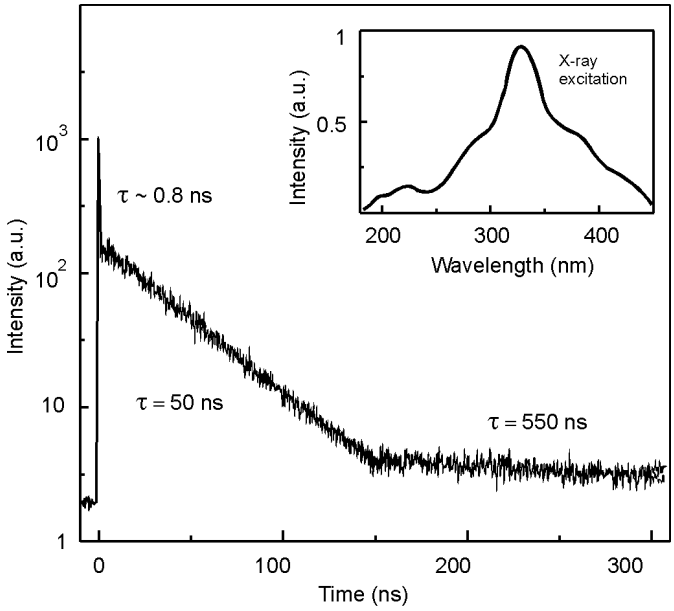

Fig. 6: X-ray excitated decay time spectrum of $LiBaF_3(Ce)$. Inset: X-ray luminescence spectrum.

Table 1. Some Li – based halide scintillators.

Material	Density g/cm^3	τ, ns	Light yield, ph/Mev	Ref.
$Li_3YCl_6:Ce^{3+}$	2.45	250/2300	3300	47
$LiYF_4:Ce^{3+}(Pr^{3+})$	3.97	~10/ ?	≤6000 (X)	48
$LiLuF_4:Ce^{3+}$	5.96		3800 (X)	48
$LiLuF_4:Pr^{3+}$	5.96		5100 (X)	48
$LiKYF_5$ (pure)	3.48		620	49
$LiKYF_5:Pr^{3+}$	3.48		4670	49
$LiBaF_3$(pure)	5.27	1 ns/2-30 μs	≤3600	35,41,50
$LiBaF_3:Ce^{3+}$	5.27	1/57/2-12 μs	≤7000	41,50
$LiBaF_3:Ce^{3+}K^+$	5.27	1/34/2 μs	5100	51
$LiBaF_3:Ce^{3+}Rb^+$	5.27	1/34/2 μs	4400	51
Cs_2LiYCl_6(pure)	3.31	6.6 μs	6500	47
$Cs_2LiYCl_6:Ce^{3+}$	3.31	0.6; 6 μs	9500	47
$LiYbF_4:Ce^{3+}$	6.09	<25 ns	?	52
$CsLiLaCl_6$		1.4/36		53
$CsLiYCl_6$	3.96	600/6 μs	9600	53
$Li_xCs_{1-x}Cl$				54

Their structure is considered in detail in [39]. Light yield of Ce^{3+} scintillation is in 2.5 times higher than fast CV scintillation one. $LiBaF_3$ doping by Ce^{3+} leads to the appearance of emission at 325 nm with τ ~ 50 ns at an X-ray and gamma excitation (Fig.6) and ~ 27 ns at a photoexcitation.

Spectral and kinetic parameters of the $LiBaF_3$(Ce) luminescence at synchrotron excitation in the range 40-300 nm at temperatures from 4 to 300 K was described in [41]. The obtained results allow to assume that energy transfer is realized not only by charge carriers but also by reabsorption of CV luminescence. The latter is connected with a significant overlapping of CV luminescence and excitation bands of Ce^{3+}.

The list of Li based hologenides includes other components too (Table 1). That are result of the thermal neutron scintillator search.

5.2 Storage and dosimetry materials

Crystal growth experiments show that usually halide single crystals and, particularly, fluorides are contaminated to some extent with oxygen containing impurities. These impurities are difficult to remove due to pyrohydrolysis effect.

Oxygen containing impurities are a parasite factor for ABX_3 scintillators the same way as for A^IB^{VII} ones. On the other hand, recent investigations showed that variation of the quantity and composition of oxygen containing impurities allows to change the efficiency of energy storage in such crystals [42]. Conventional range of crystal properties' variation at different doping of those is presented in Table 2.

Table 2. Efficiency of luminescence and energy storage in $LiBaF_3$.

Material	CV	STE	Ce^{3+}	O^{2-}	storage
$LiBaF_3$ pure	+++	+++	–	–	+
$LiBaF_3$(Ce)	++	++	+++	–	+
$LiBaF_3$(O)	++	++	–	++	++
$LiBaF_3$(Mg)	+–	–	–	–	+++
$LiBaF_3$(Mg,O)	+	+	–	++	+++
$LiBaF_3$(Ce,O)	++	++	++	+	+

The oxygen ions presence changes the sensitivity of the material to ionizing radiation and results in a significant energy storage. The latter is manifested in the intensification of coloration, variation of thermal stability of the intrinsic color centers and appearance of new centers. Thermostimulated luminescence (TSL) curves of the irradiated oxygen-enriched $KMgF_3$ crystals are given in Fig.7. One can see that together with TSL peaks at 80-220°C connected with thermal recombination of the radiation induced F_2^--color centers and accompanied by luminescence with λ_{max}=590 nm there appear intensive high temperature peaks (T>400°C) with a typical "oxygen" luminescence (~550 nm). Excitation of this luminescence in the irradiated samples can be realized at 415 nm and 315 nm. This luminescence and the corresponding absorption bands are absent in oxygen-free $KMgF_3$ crystals.

Co-doping of $KMgF_3$ by oxygen and Eu is the method for the dosimetry parameter improvement. As it shown in [42] $KMgF_3$(Eu) crystals possess a typical for f-f transition Eu^{2+} luminescence (the line 359 nm) revealing up to 600°C.

The TSL intensity of such crystals is much higher than of $KMgF_3$(O); note that apart from TSL peaks in the region of 480-570°C there appears an additional one at 395°C (Fig. 7). This means that an additional luminescence appears - typical for Eu^{2+}. Depending on the europium and oxygen content the ratio of the intrinsic (590 nm), "oxygen" (550 nm) and Eu^{2+} (359 nm) emissions are significantly redistributed. The optimal choice of the dopant' concentration allows to achieve the case when all the stored lightsum is revealed at heating in the form of a line with λ =359 nm.

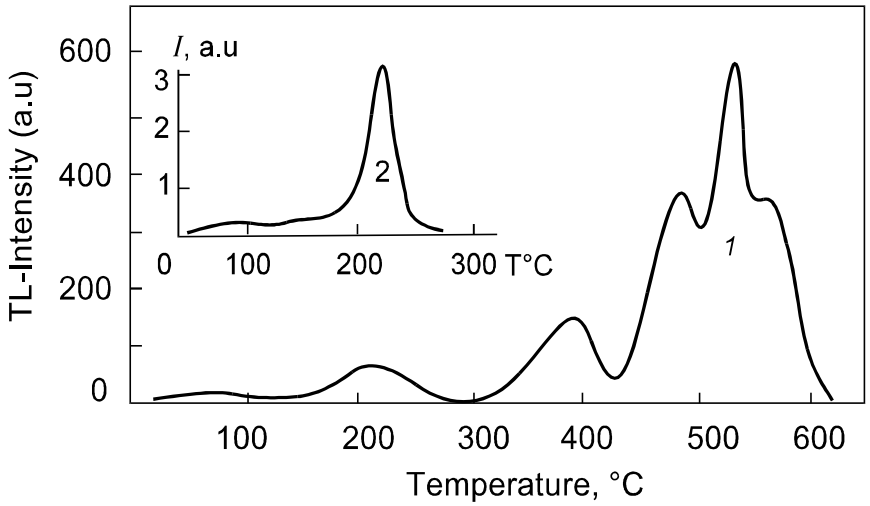

Fig.7. Glow curves of $KMgF_3(Eu_2O_3)$ (1) and LiF(Mg, Ti) (2) crystals after isodose γ-irradiation (^{241}Am, 60 keV, 0.03 Gy).

A $KMgF_3$(Eu,O) dosimeter is in the two orders of magnitude more efficient than classic dosimetric material LiF (Mg, Ti) [42].

The stored in the irradiated perovskites energy can be released not only by means of thermo- but also by the photostimulation (PS). The region of PS is 500-700 nm and the PS luminescence spectra are close to those at an intracenter excitation [43]. Photostimulation can be performed at room temperature by the visible and near IR laser. This gives evidence to a perspectivity of using these materials as memory media for digital radiography. Note that while the photostimulated luminescence of Eu^{2+} in $LiBaF_3$ is emitted slowly (in a millisecond range), the luminescence of Ce^{3+} has a nanosecond lifetime which is extremely important for application.

6. Search of new halide scintillators.

Search of new halide scintillators has been continued for the recent years. It was basically connected with the study of materials with high light yield. Table 3 shows the most essential results of such study. However, even the most promising from this point of view scintillators like $RbGd_2Br_7$:Ce [44], $RbGd_2Cl_7$:Ce [45], $LaCl_3$:Ce [46] have significant disadvantages limiting their practical application. These primarily are: high hygroscopicity, presence of slow components of luminescence, high intrinsic background of the material.

Table 3. High light yield halide scintillator studied since SCINT'95.

Material	Density g/cm^3	τ, ns	Ref.
$RbGd_2Br_7:Ce^{3+}$	4.8	66 ns	44
$RbGd_2Cl_7:Ce^{3+}$	3.74	>1 μs	45
$LaCl_3:Ce^{3+}$		20/333/2200	46
$LuBr:Ce^{3+}$		?	46
$K_2LaC_5:Ce^{3+}$	2.89	>1 μs	55
$Cs_2LiYCl_6:Ce^{3+}$	3.97		47
$CsGd_2F_7:Ce^{3+}$	5.74	2600	56

In general, one can state that despite of high activity of research traditional halide scintillators play the main role in all practical applications. With this, the intensity of engineer works focused on the improvement of systems and principles of radiation registration is continuously rising. Emergence of new technical solutions in its turn stimulates works on the improvement of halide scintillators' properties.

7. Conclusion

From the above we conclude that there is a need to continue of both halide scintillator performance improvement and a search of new efficient scintillation materials. As it was shown the main engineering efforts were concentrated on the traditional halide scintillators line NaI(Tl), CsI(Tl) and so on. So, we need to continue these works together with broadening of new scintillator engineering to adapt its to different applications.

References

1. R. Hofstadter, Phys.Rev. **75** (1949) 796
2. P. Lecog, this issue, p.
3. H.Newman, G.Gratta, R.Zhu, Scintillator and Phospor Materials, MRS Symposium Proc. **348** (1994) 3
4. BELLE Collaboration, Technical Design Report, KEK Report 95–1 (1995)
5. BaBar Technical Design Report, SLAC–R–95–457(1995)
6. K. Arisaka et.al. KTeV Design Report, FN–580(1992)
7. http://www.psi. ch
8. GEM letter of Intent., SSCL SR-1184, 1991
9. CMS Technical proposal, CERN/LHCC 34-38, 1994
10. B.Shwartz, this issue, p
11. S.Ren, G.Chen, F.Zhan et.al., Scintillator and Phospor Materials, MRS Symposium Proc. **348** (1994) 435; Yu.Gusev, E.Melchakov, I.Mironov, ibid p.463
12. See [11] p.277
13. E.Radzhabov, A.Shalaev, A.Nepomnyashickh, Proc. Int. Conf. Inorganic Scintillators and Their Applications (SCINT'97), Shanghaii, China, 1997, p.135
14. V.Gavryluk, Light collection in complex shape scintillators, PhD thesis, ISC, Kharkov,1999
15. A.Gektin, N.Shiran, T.Charkina et.al., Heavy scintillators for scientific and industrial application by F Nataristefany, P.Lecog, M.Schuegans Frontieres, France, 1992, p.493
16. V.I.Goriletsky, L.G.Eidelman, A.N.Panova, K.V.Shakhova, Nucl. Trasks Radiat. Meas. **21** (1993) 109
17. . . , . . , . . , . . , . . **75** (1993) 996
18. C.Woody, P.Levy, I.Kierstead et.al. IEEE Trans. Nucl. Sci. **37** (1990) 492
19. R.Zhu, see [13] p.73
20. A.Gektin, N.Shiran, see [13] p.115
21. L.Haliburton, G.Edvards see [11] p.423
22. A.Gektin, M.Globus, O.Shepelev et.al. Functional Materials, **4** (1997) N4 544
23. W.Moses, this issue, p
24. US Patent # 4, 584,478
25. US Patent # 5, 652,429
26. http://www.bicron.com
27. http://www.digitalscintigrahics.com
28. D.E. Kuhl, R.Q. Edwards. Radiology **80** 653, (1963) 80

29. J. Butler, S. Friesenhahn, C. lingreen et. al. IEEE NSS/MIC Conference records, **1** (1993) 565
30. T. Jing, C. Goodman, J. Drewery et. al. IEEE Trans. on Nucl. Sci. **41** (1994) 903
31. H. Wieczorek, G. Frings, P. Quadflieg, U. Schiebel. Proc. of Int. Conf. on Inorganic scintillators, SCINT'95, Delft, (1995) 547
32. V. Nagarkar, S. Tipinis, T. Gupta et.al. IEEE Trans. on Nucl. Sci. **46** (1999) 232
33. N. Garnier, C. Dujardiv, A.N. Belsky et. al., this issue, p
34. C. van Eijk in: Heavy scintillators for scientif. and industr. appl. Proc. "Crystal 2000", Int. Workshop. Chamonix, France. 1992. p.601
35. N.I.Knitel, P.Dorenbos, Haas I.T.M., C.W.E. van Eijk Proc. Int. Conf. SCINT'95, 1996, Delft, Netherlands, p.81
36. A.V.Gektin, I.M.Krasovitskaya, N.V.Shiran J. Lumin., **72-74** (1997) 664
37. F.Lohse, M.Fockele, J.M.Spaeth, Cryst. Latt. Defects, **16** (1987) 275
38. See [13] p.322
39. Shiran N., Komar V., Gektin A. et al. Proc. Int. Conf SCINT'95, 1996, Delft, Netherlands, p.352
40. A.Gektin, N.Shiran, V.Voronova IEEE Trans. Nucl. Sci. **44** (1997) 857
41. Gektin A., Shiran N., Voloshinovski A. et al. Int. Conf. SCINT'97, 1997, Abst., Shanghai, China, p.75
42. . . , . . , . . , - – -97, , 1997, .37
43. N.Shiran, V.V.Voronova Int. Conf. LUMDETR'97, 1997, Abstr., Ustron, Poland, p.112
44. P.Dorenbos, I. van Spijker, O.Frijns et.al., NIM (B) **132** (1997) 728
45. P.Dorenbos, I. van Spijker, O.Frijns et.al., see [13] p.330
46. O.Guillot-Noel, E van Loef, P.Dorenbos et.al., this issue p.
47. C.Combes, P.Dorenbos, C. van Eijk et.al., J.Luminescence, to be published
48. C.Combes, P.Dorenbos, C. van Eijk et.al., J.Luminescence, **71** (1997) 65
49. E.Devistin, N. Khaidukov, N.Kirikova et.al., Rad. Effects and Defects in Solids, 1995, p.133-134
50. A.Gektin, IEEE Trans. Nucl. Sci. **44** (1997) 857
51. C.Combes, see [13], p.349
52. P.Lecog, see [11], p.51
53. P.Rodnyi, V.Mikhailik, A.Voloshinovskii, this issue p.
54. A.Voloshinovskii, V.Mikhailik, Ya.Struk et.al. J.Luminescence, **79** (1998) 115
55. I. van Spijker, P.Dorenbos, I. de Haas et.al., Radation Measurements **24** (1995) 379
56. D.Schaart, P.Dorenbos, C. van Eijk et.al. Rad. Effects and Defects in Solids, **135** (1995) 329

Cerium-based and cerium-doped fluorescent and scintillating materials

C. Pédrini

Laboratoire de Physico-Chimie des Matériaux Luminescents,
Unité Mixte de Recherche 5620 CNRS – Université Lyon I
69622 Villeurbanne cedex

Abstract: Peculiarities of cerium ions and consequences for the fluorescence and scintillation properties of cerium-based and cerium-doped crystals are described and analyzed. In particular, it is shown that the electronic structure, the position of the Ce 4f level in the gap, the valence band width, the fact that cerium has two stable valence states Ce^{3+} and Ce^{4+}, can strongly influence the fluorescence and the scintillation efficiencies of the crystals. Particular attention is paid to Gd-based and Lu-based host lattices. Recent research on new dense cerium-doped systems are also reported.

Keywords : cerium, crystals, fluorescence, scintillation

I – Introduction

There is a strong interest for Ce^{3+} in ionic crystals because this ion very often exhibits an efficient and fast fluorescence in UV or visible region. Good laser materials, phosphors and scintillators are often cerium-based or cerium-doped compounds. Systems like CeF_3, cerium-doped YAG,(YSO, GSO, LSO), (YAP,LuAP), $LuPO_4$, borates are well-known scintillators and phosphors, and are used in many kinds of detectors and devices leading to applications in many fields.

This rare earth ion has special properties that it is important to investigate in order to understand the scintillation mechanisms and for a prospective research of optimized cerium-based or cerium-doped systems.

It is useful to recall that the scintillation efficiency η can be described by the product of three terms :

$$\eta = \beta S Q$$

β is the creation probability of electron-hole pairs.
S is the probability of transfer to emitting centers (Ce^{3+}). The donor centers can be excitons (correlated electron-hole pairs) which can transfer their energy non-radiatively, separated electron-hole pairs which can transfer their energy through a charge transfer process involving a sequential capture of a hole and of an electron or defect centers which can act as traps.
Q is the luminescence quantum efficiency.

Usually, in efficient scintillators, charge transfer process must be dominant, and the hole capture by cerium ions is of most importance.

II – Peculiarities of cerium ions and consequences for the fluorescence and scintillation properties of crystals.

II.1 Electronic configuration and band structure

Ce^{3+} ion has a very simple electronic ground configuration $4f^1$ with only one electron in the 4f level, resulting in two levels : $^2F_{5/2}$ (ground state) and $^2F_{7/2}$ separated by roughly 2000 cm^{-1} due to the spin-orbit coupling. The first excited configuration is $5d^1$. The excited states are very sensitive to the crystal field and to the point symmetry of Ce^{3+}. In case of low symmetry, the degeneracy is totally removed and five $^2F_{5/2}\rightarrow 5d$ absorption bands are observed while for cubic symmetry, only two states $5d(t_2)$ and 5d(e) are detected. Excitation in any of the 5d states is followed by a fast non-radiative relaxation to the lowest of 5d excited state that is the only emitting state. The radiative parity-allowed $5d\rightarrow 4f$ transition gives rise to an intense and fast fluorescence (typically few tens of nanoseconds). The emission spectrum exhibits two emission bands reflecting the transitions towards the two final states of the $4f^1$ configuration. Contrary to the other rare earth ions, the lack of $4f^n$ states between the 5d emitting level and the ground state leads to a very high fluorescence quantum efficiency close to 100%.

In Fig. 1 are represented the energy band structures of CeF_3 and of BaF_2 for comparison and the Auger hole cascade. After absorption of high energy photons, holes are created in deep core levels. These holes relax through Auger process between the states of the same ion because deep states of different ions do not overlap. This is not correct for the highest lying hole states such as Ce5p or Ba5p. The Ce hole relaxation channel ends at the 5p level ; the hole cannot reach the Ce 4f level because the $5p\rightarrow 4f$ Auger hole transition is forbidden since the 4f level is occupied by only one electron. The Auger process for the transition $Ce5p\rightarrow F2p$ is allowed and its high probability can be estimated to $10^{14}s^{-1}$ by assuming that the matrix elements for the Ba 5p-F 2p and Ce 5p-F 2p transitions are of the same order of magnitude [1]; the former matrix element can be calculated from the probability of radiative $Ba5p\rightarrow F2p$ transition (τ_R=0.9 ns). Therefore, the Auger cascade over Ce core levels is terminated by the transfer of the hole to the fluorine valence band. Finally, the Auger hole cascade along both Ce and F relaxation channels leads to relaxed holes only in the F 2p valence band. Cerium ions can be excited only through the capture of a hole, the probability of which strongly depends on the 2p-4f energy difference.

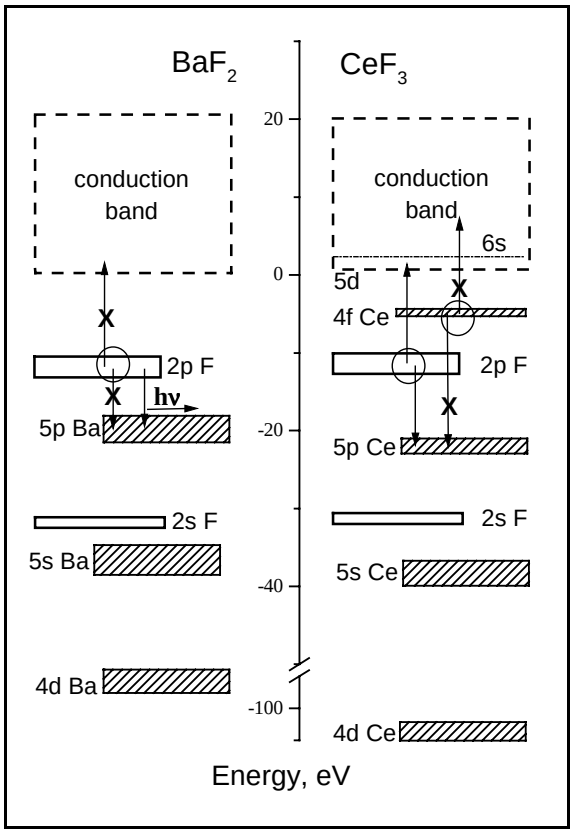

Fig.1:Energy band structure of BaF_2 and CeF_3 and Auger hole cascade.

II.2 Position of the Ce 4f level in the gap

Information on the position of the Ce 4f level in the gap can be obtained from X-ray or UV photoelectron spectroscopy [2]. In fluorides, the Ce 4f level is found to be around 4eV above the top of the F 2p valence band. This agrees with the absence of an increase of the CeF_3 luminescence excitation efficiency for photon energies in the region of the fundamental absorption edge of the lattice [3]. In oxides, the location of the Ce 4f level in the bandgap is very close (typically 1eV or less) to the top of the valence band. It is therefore expected that the capture of valence band hole by Ce 4f is then strongly probable, leading to a relatively high light yield in the region of the fundamental absorption edge of the crystal (see for example the case of LSO [3] or $LuBO_3$:Ce [4].

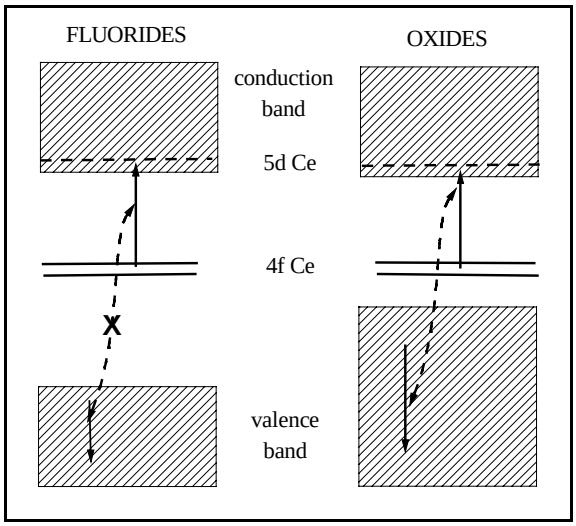

Fig. 2:Influence of the valence band width on the excitation efficiency of cerium in fluorides and oxides.

II.3 Influence of the valence band width

Another difference in the band structure of cerium-doped fluorides and oxides is the width of the valence band which is much larger for oxides than for fluorides (typically 10eV and 6eV, respectively). In addition, the Ce 4f-5d energy difference is larger in fluorides than in oxides. In Fig. 2, it is shown that the relaxation of the hole inside the valence band cannot excite efficiently cerium ions in fluorides while it is possible in oxides. Besides the valence band hole capture by Ce 4f, this additional process contributes to the difference of light output in cerium-doped fluorides and oxides.

II.4 Two stable valence states Ce^{3+} and Ce^{4+}

An important consequence of this situation is that charge transfer processes can occur between cerium ions and metallic ions M^{n+} with stable valence states, present in the lattice :

$$Ce^{3+} + M^{n+} \rightarrow Ce^{4+} + M^{(n-1)+}$$

For example, Yb-based and Yb-co-doped host lattices must be avoided because of the two stable divalent and trivalent valence states of ytterbium. Vanadates and tungstates also are not good host lattices for Ce^{3+} because of the 4+ and 5+ valence states of vanadium and the 5+ and 6+ ones of tungsten.

Another consequence is the propensity of cerium for the formation of cerium-bound exciton and for easy photoionization. Born cycle model can be used to represent the localized levels of Ce in the gap of the host by single configuration coordinate curves (Fig. 3). Photoionization and charge transfer processes are illustrated for Ce^{4+} and Ce^{3+} ions in the lattice. The final states describe these ions with an electron-hole pair nearby. The thermodynamic cycle for Ce^{4+} does not involve radiative process, but it generally does for Ce^{3+}, depending on the relative positions of the (Ce^{3+*} + lattice) and (Ce^{4+} + e_c) potential curves. Let us focus our attention on this point. The potential curve (Ce^{4+} + e_c) describes a

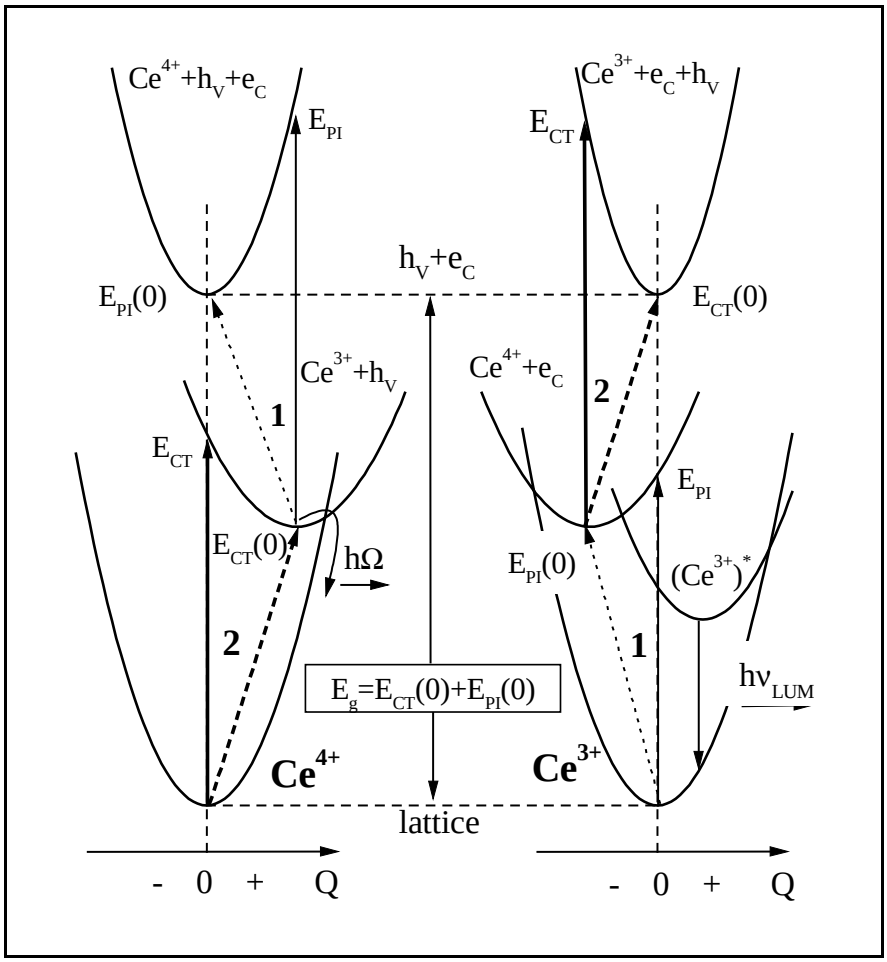

Fig.3: Photoionization (1) and charge transfer (2) mechanisms of Ce^{3+} and Ce^{4+} ions embedded in crystal lattice, illustrated through single configuration coordinate diagrams.

Ce^{4+} ion with an electron in the conduction band. This latter can be either bound to cerium forming a so-called cerium-bound exciton (Ce^{4+} + e_{bound}) where the hole is localized on cerium and the electron is delocalized in the neighbouring cations, or free in the conduction band and the potential curve (Ce^{4+} + e_{free}) describes the bottom of the conduction band.

The formation of impurity-bound exciton is strongly promoted when the impurity ion has two stable valence states. It was clearly demonstrated for europium and ytterbium ions in alkaline earth fluorides [5-7], and for titanium in sapphire [8]. The strong visible fluorescence of the well-known efficient CsI:Tl scintillator is probably originated from thallium-bound exciton as well [9].

The impurity-bound exciton can take part of the fluorescence process if the photoionization energy and the dopant ion emitting level energy are close. Such exciton can recombine radiatively or non-radiatively. It is characterized by a broad absorption band and when it emits, by a broad emission band as well, reflecting a more diffuse charge distribution, and by a large Stokes shift that accounts for the ion radii difference. Three scenarios are sketched in Fig. 4. Diagram (a) describes a fluorescence mechanism not influenced by the trapped exciton, while in (b) and (c), the exciton and the conduction band participate to the process.

Efficient phosphors and scintillators verify case (a), case (b) is where the Ce^{3+} fluorescence is partly quenched and case (c) is where it is totally quenched.

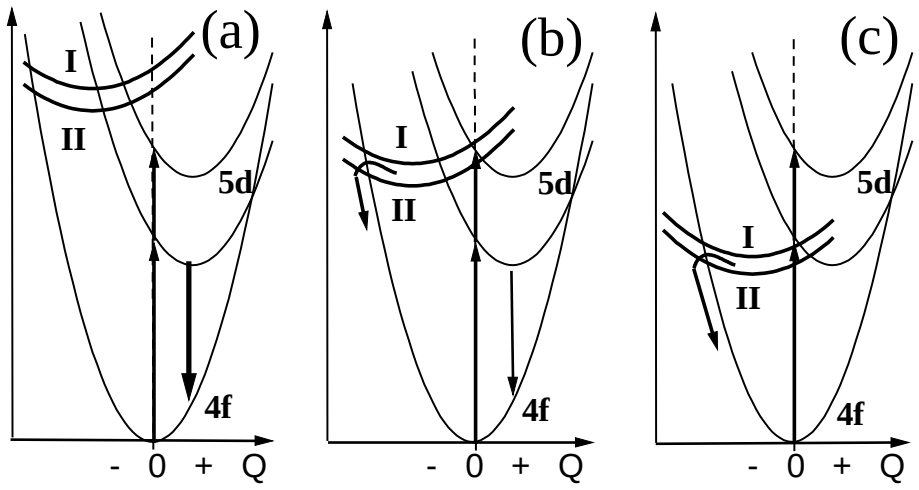

Fig.4 : Three scenarios for the fluorescence mechanisms of Ce^{3+} ions in crystals taking into account the states of the bottom of the conduction band (I) and cerium bound exciton (II): (a) – intense fluorescence of Ce^{3+}, (b) – partly quenched fluorescence of cerium and (c) – total quenching of the Ce^{3+} fluorescence.

In the frame of a search of new dense, fast and efficient scintillating materials, a new $LaLuO_3$:Ce cerium doped lutetium-based compound has been investigated [10]. It was shown that this system verifies case (b) while similar systems like $LuAlO_3$:Ce belongs to case (a) and Lu_2O_3:Ce to case (c). The Ce^{3+} fluorescence of $LaLuO_3$:Ce is strong when excited directly in the lowest 5d(t_2) level and very weak under excitation in the 5d(e) level or at higher energy. The temperature dependence of the fluorescence under the former excitation shows an usual behaviour with a decrease of the intensity above 200K which reflects a non-radiative relaxation towards the ground state (Fig. 5a). On the other hand, the fluorescence thermal variation is much more complex under higher energy excitation(Fig.5b). This behaviour can be described by taking into account the various channels of relaxation shown in Fig. 6.

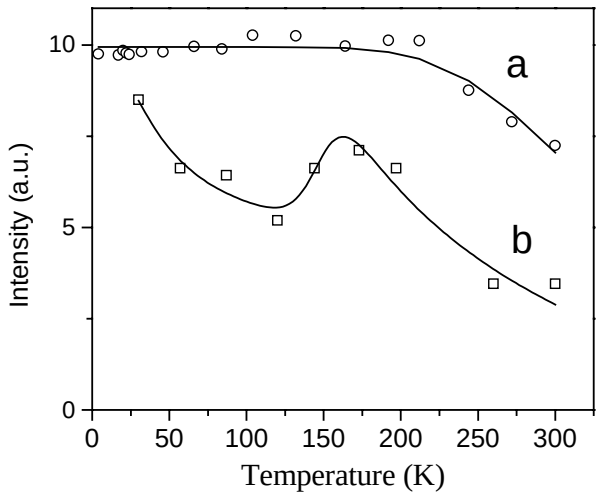

Fig.5 : Temperature dependence of Ce^{3+} fluorescence in $LaLuO_3$: (a) excitation at 340 nm in the 5d (t_2) levels ; (b) excitation at 250 nm in the 5d(e) levels. Solid lines are fitting curves using (a) the Mott and Seitz model and (b) a model involving relaxation processes (see fig.6)

III – Peculiarities of Gd-based host lattices

The lowest ^6P excited state of Gd^{3+} $4f^7$ configuration usually absorbs and emits around 310nm in the region of absorption and emission of Ce^{3+} that depends on the crystal field strength. Energy transfer between Gd^{3+} and Ce^{3+} can therefore occur. The best condition for an efficient and fast scintillation of Ce^{3+} is when the electron-hole pairs can efficiently transfer their energy to Gd^{3+} ions among which a fast $Gd^{3+} \rightarrow Gd^{3+}$ energy diffusion can be

established, followed by an efficient $Gd^{3+} \rightarrow Ce^{3+}$ energy transfer. For that, three conditions are required : (i) the Ce^{3+} emission must occur at wavelengths long enough (>350nm) in order to prevent $Ce^{3+} \rightarrow Gd^{3+}$ back transfer ; (ii) the Gd^{3+} 4f-4f emission and Ce^{3+} 4f-5d absorption bands must overlap for an efficient $Gd^{3+} \rightarrow Ce^{3+}$ energy transfer ; (iii) Gd^{3+} ions must be separated in the Gd-based lattices by a short distance (<0.5nm) for a fast $Gd^{3+} \rightarrow Gd^{3+}$ energy diffusion. P. Dorenbos et al. [11] in Fig. 1 and Table 2 have presented three cases where (a) Ce→Gd energy transfer and Gd^{3+} emission are dominant ;(b) Ce→Gd and Gd→Ce energy transfers co-exist ; (c) Gd→Ce only occurs giving rise usually to efficient and fast scintillation. It is clear that high crystal field Gd-based host lattices are more favourable.

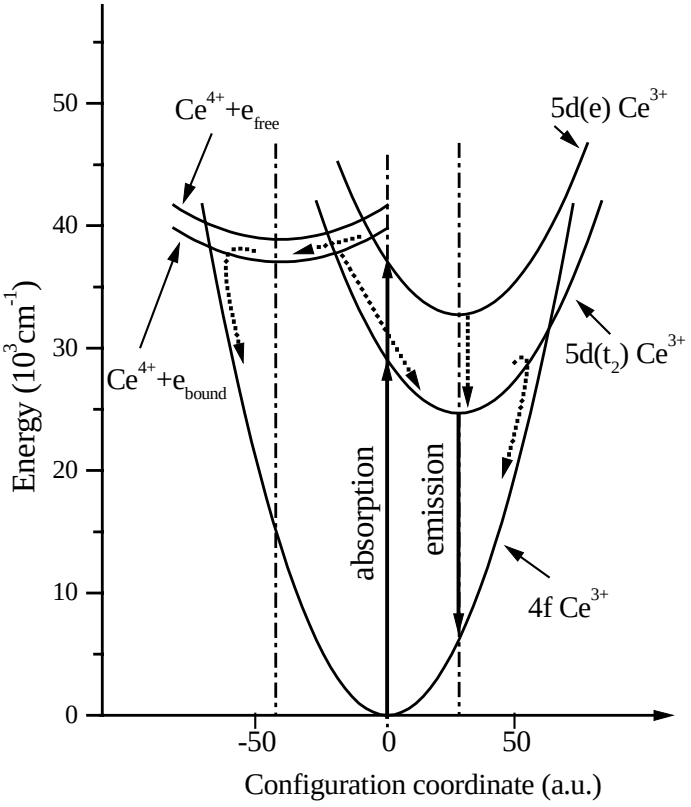

Fig.6 : Semi-quantitative configuration coordinate curve diagram for $LaLuO_3$:Ce illustrating the quenching of the Ce^{3+} fluorescence via the cerium-bound exciton. The principal non-radiative relaxation process are marked by pointed arrows.

IV – Peculiarities of Lu-based host lattices

The main peculiarity of the electronic structure of Lu-based host lattices is the presence of the full Lu 4f shell in the energy region of the O or F 2p band. In both cases of fluorides and oxides, the Lu 4f and 2p bands overlap giving rise to a broader valence band. This may influence the probability of valence band hole capture by cerium ions, and as a result the light yield of the system.

The effect has been studied in details in the case of fluorides [12], in which the Lu 4f level is above the F 2p level. The energy difference between the top of the valence band and the Ce 4f level is therefore reduced and this is favourable to a more efficient hole capture by Ce^{3+} and a higher light yield, as observed [12].

In oxides, the Lu 4f level is deeper than the O 2p band so that it is not expected improvement of hole capture cross-section. More studies are in progress in order to know more about the role played by the Lu 4f band in the scintillation mechanism.

V – Research of new dense cerium-doped systems

Such a research is very active and tries to answer to requirements of users of γ scintillators and X-ray phosphors. It is mostly carried out on polycrystalline compounds and sometimes on single crystals when the crystal growth problems are solved.

An important family of cerium-doped systems are borates. They usually exhibit a very strong fluorescence related to the small Stokes shift and other properties that make them attractive for use in optical systems [13,4,14]. The relatively high melting point of some borates, in particular $LuBO_3$ orthoborates (~1600°C) which is among the most dense borates, is a serious difficulty for crystal growth owing to the low temperature vaporization of boron ions.

Lanthanide tantalates are of interest because of their very high density close to 10. Cerium-doped tantalates have been recently investigated [15,16], but unfortunately, these systems usually exhibited very weak cerium fluorescence.

It has been demonstrated that sulfides are appropriate host lattices for cerium ions. Recently, a new dense red luminescing scintillator, $Lu_2S_3:Ce^{3+}$, has been discovered [17]. Other lutetium-based chalcogenides like selenides and may be tellurides, deserve further attention in the search of new dense cerium-doped scintillators if their bandgap is wide enough to allow 5d→4f emission of cerium.

Many Ce doped Cl and Br scintillators have been studied mainly by the Delft group [18]. Some systems like $RbGd_2Br_7$:Ce and $RbGd_2Cl_7$:Ce show light yields comparable to those of best scintillators. However, in general, chlorides and bromides are low density compounds and their hygroscopicity may limit practical use.

VI – Conclusions

Ce^{3+} ion is usually a very efficient luminescent center due to its particular electronic configuration.

However, the scintillation efficiency of cerium-doped materials strongly depends on the host lattice.

In fluorides, the Ce^{3+} scintillation is generally not very efficient. The fluorescence excitation is mainly due to the direct excitation of the 4f(Ce^{3+}) electron (impact excitation), after the relaxation of hot electron and core hole. The capture of 2p(F^-) hole has negligible probability since 4f(Ce^{3+}) level is situated at rather too high energy related to the top of the valence band. The efficiency of CeF_3 is the result of the high concentration of Ce ions since the probability of the direct excitation of the 4f(Ce) electron after the inelastic scattering is high.

In other compounds, in particular in oxides, the Ce^{3+} scintillation can be very high because Ce^{3+} can be efficiently excited through sequential capture of hole and electron.

Description of successive photoionization and charge transfer processes using potential curves allows to explain the non-radiative and radiative channels of relaxation in Ce^{4+} and Ce^{3+} ions, respectively. But the efficiency of the Ce^{3+} fluorescence depends on the energy of the cerium-bound exciton state which can partly or completely quench the Ce^{3+} fluorescence if it is low enough.

In Gd compounds, the Ce^{3+} fluorescence can be sensitized or quenched by Gd^{3+} ions depending upon the relative energy of the lowest emitting states of Gd^{3+} and Ce^{3+}.

In Lu compounds, it is clear that the Lu 4f full level plays a role in the scintillation process and influences the high yield of the scintillator.

The search of new fast and dense cerium-doped scintillators is very active. Lu_2SiO_5:Ce(LSO) is certainly the reference at the present time, but it has serious drawbacks (reproducibility of quality, strong non-linearity, not very fast response) and the improvement of other known systems and the discovery of better ones are important challenges to take up.

Acknowledgments

The author wishes to express his warm thanks to the collaborators of his laboratory and of other institutes for their contribution to this research.

This work was performed in the frame of “Crystal Clear” collaboration with CERN and was supported in part by NATO grant HTECH.LG.971230.

References

1. A.N. Vasil'ev, Nucl. Instr. and Math. in Phys. Res. B 107 (1996) 165
2. D. Bouttet, C. Dujardin, C. Pédrini, W. Brunet, D. Tran Minh Duc and J.Y. Gesland, Proc. Int. Conf. on Inorganic Scintillators and Their Applications, SCINT 95, 1996, Delft University Press, The Netherlands, p. 111
3. C. Pédrini, A.N. Belsky, A.N. Vasil'ev, D. Bouttet, C. Dujardin, B. Moine, P. Martin and M.J. Weber, Mater. Res. Soc. Symp. Proc. 348 (1994) 225
4. L. Zhang, C. Madej, C. Pédrini, C. Dujardin, J.C. Gâcon, B. Moine, I. Kamenskikh, A.N. Belsky, D.A. Shaw, M.A. Mac Donald, , Proc. Int. Conf. on Inorganic Scintillators and Their Applications, SCINT 97, 1997, CAS, Shanghai Branch Press, p. 303
5. D.S. McClure and C. Pédrini, Phys. Rev. B 32 (1985) 8465
6. B. Moine, B. Courtois and C. Pédrini, J. Phys. France 50 (1989) 2105
7. B. Moine, C. Pédrini and B. Courtois, J. of Lum. 50 (1991) 31
8. W.C. Wong, D.S. McClure, S.A. Basun and M.R. Kokta, Phys. Rev. B51 (1995) 5682
9. N. Garnier, C. Dujardin, A.N. Belsky, C. Pédrini, J.P. Moy, H. Wieczorek, P. Chevallier, A. Firsov, this proceeding.
10. C. Pédrini, L. Zhang, C. madej, C. Dujardin, A. Petrosyan, I.A. Kamenskikh, A.N. Belsky, D.A. Shaw, M.A. Mac Donald, Proc. Int. Conf. on Inorganic Scintillators and Their Applications, SCINT 97, 1997, CAS, Shanghai Branch Press, p. 343
11. P. Dorenbos, J.C. van't Spijker, C.W.E. van Eijk, Proc. Int. Conf. on Inorganic Scintillators and Their Applications, SCINT 97, 1997, CAS, Shanghai Branch Press, p. 307
12. W. Blanc, C. Dujardin, J.C. Gâcon, C. Pédrini, A.N. Belsky, I. Kamenskikh, C. Fouassier and S. Bourgeois, this proceeding.
13. M.J. Knitel, Ph. D. Thesis, Delft University Press, 1998
14. O. Lebbou, C. Dujardin, C. Goutaudier, M.-Th. Cohen-Adad, C. Pédrini, B. Moine, A.N. Belsky, this proceeding
15. E. Zych, A. Lempicki, M.J. Downey, Materials Science Forum, vols 239-241 (1997) p. 267
16. C. Dujardin, A. Garcia-Murillo, C. Pédrini, C. Madej, C. Goutaudier, A. Koch, A.G. Petrosyan, M.J. Weber, this proceeding
17. J.C. van’t Spijker,P.Dorenbos,C.P.Allier,C.W.E. van Eijk,A.E.Ettema, , Proc. Int. Conf. on Inorganic Scintillators and Their Applications, SCINT 97, 1997, CAS, Shanghai Branch Press, p. 311.
18. C.W.E. van Eijk, Proc. Int. Conf. on Inorganic Scintillators and Their Applications, SCINT 97, 1997, CAS, Shanghai Branch Press, p. 3.

Scintillators on a base of oxide crystals

M.Korzhik

Institute for Nuclear Problems, 220050, 11 Bobryiskaya, Minsk, Belarus

Abstract: In this paper we accent mainly on the physical aspect of the scintillator research, development and properties of the synthetic oxide crystals. Ce- doped and lead tungstate scintillators have been discussed.

Keywords:Scintillator, synthetic single crystal, crystal doping, crystal structure, energy transfer, point structure defects, light yield, scintillation kinetics.

1. Status and prospects of oxide scintillation materials

Inorganic scintillation materials fascinate us, both from the point of view of application for ionizing radiation detectors and as instrumental of the material science development. Although its fraction in crystal's industrial and experimental production does not exceed of some percents, they have a stable growing demand in industry, nuclear medicine and scientific research. Oxide crystals have a great potential to construct new advanced scintillation materials [1]. Some of them have been developed for the last decade and they are rear-earth (RE) oxiorthosilicate (RE_2SiO_5) and perovskite ($REAlO_3$) crystals doped with Ce ions. The crystals are dense, fast, high light yield scintillators and are produced by the well developed crystal growth methods. Among recently developed materials the lead tungstate (PWO) scintillator becomes the most used scintillation material in high energy physics experiments due to its application in experiments at LHC [2]. Lead tungstate single crystals possess a number of unique properties. Recently it was shown that PWO scintillation crystals demonstrate good energy and time resolutions (σ_E=1.54%/ E+0.3%, σ_T=130 ps) which were achieved with mono-energetic photons and electrons with energies from 50 to 850 MeV [3]. Moreover, further improvement of the PWO crystal light yield makes it promising to be applied not only in high energy physics, but also in nuclear medicine, detection of illicit drugs and explosives and nuclear materials control systems. Especially, it seems to be promising in application in so-called "active" methods of non-destructive characterization, based on media irradiation with consequent detection of transmitted or emitted gamma quanta. Our estimation shows that after improvement of the PWO crystal scintillation light yield up to 100 phe/MeV with PMT readout corresponding to statistical limit the energy resolution will be **σ**=3% at 10 MeV, which will ensure success of its application in the relatively low energy range. Besides, lead tungstate crystal due to its radiation hardness [4] becomes promising material for the control of the luminosity of therapeutic particle beams. Use of the particle beams with energy 10-100MeV in the cancer therapy is one of the prospective methods which is under development in several laboratories worldwide. Bithmut germanate BGO scintillation material is widely used in Positron Emission Tomograph (PET) diagnostic technique now. However, it will be replaced by Lu based materials in new generation of PET scanners with use of the TOF registration systems in nearest future. Fast and bright scintillation materials on a base of oxide crystals become a favorites at the development of new intra-operation probes and small animal SPECT and PET scanners. Some properties of the already developed and used scintillation materials on a base of oxide crystals are summarized in the Table 1.

2. Peculiarities of the synthetic oxide crystal materials

Main advantage of the synthetic single crystal materials is possibility to control their properties by the adjustment of the crystal synthesis conditions. However, relatively fast rate

of the melt transformation in the crystal mass due to crystal growth, limited purity of the raw materials cause creation of the specific defects in crystals which affect scintillation parameters. Here we review three typical phenomena which influence on scintillation properties: isomorphic impurity ions in the crystal, not isomorphic impurity ions in the crystal, new modifications of the crystal structure to be appeared just in the synthetic crystals. The lead tungstate crystal is a good example to demonstrate all of them.

Presence of isomorphic Mo impurity ion which replace W ion in the host generates slow components in the scintillations and afterglow [5]. At small concentrations of order of some ppm the Mo ions form in PWO crystals shallow electron centers of type $(MoO_4)^{3-}$ and their properties are described in [6]. Such centers affect scintillation parameters of PWO crystals strongly influencing on distribution of the emitted light among scintillation and afterglow. They appear due to MoO_4^{2-} oxicomplexes which are stable electron trap centers. Although raw material is cleaned from Mo before crystal growth, molybdenum ion is chemically very close to the tungsten ion and is rather hard to separate at the raw material production level. We never observed lead tungstate crystals without Mo traces. The first excited energy level of molybdenum oxicomplex is found lower than the tungstate complex one. Consequently, in the crystals with presence of Mo the luminescence quenching of the regular tungstate groups due to multipole Coulomb interaction is observed. Thus, giving the rise of slow components in the kinetics of scintillations, Mo impurity also decrease the fraction of the fast components in the total scintillations. Influence of the Mo impurity on the scintillation properties of the crystal is strongly dependent from the concentration. At small Mo impurity concentration a significant afterglow is detected in the scintillations. This afterglow level in the scintillation is decreased with increasing of Mo concentration and slow components having decay times within a range of some hundreds of ns show up in the scintillation kinetics.

The doping of PWO crystals by specified not isomorphic impurities like La, Lu, Y, Nb sufficiently improve radiation hardness of the scintillation elements [7,8]. An impressive suppression of the irradiation induced absorption of full size scintillation elements was observed for the doping level of some tens of ppm. La^{3+} type ion with stable valent state at its localization in Pb^{2+} site introduces in the crystal an extra positive uncompensated charge, so they will compete to the creation of V_o anion vacancies giving some decrease of anion vacancy and dramatically fall of di-vacancy concentrations respectively. On the contrary, Nb^{5+} doping ion localizing in W^{6+} site introduces in the crystal an extra negative uncompensated charge and does not affect sufficiently on the anion vacancy concentration or based defects. Nb doping influences the amount of the cation vacancies V_c giving decrease of its amount.

However, incorporation in the crystals of another not isomorphic impurities such as Yb or Eu caused fall down the crystals radiation hardness [9]. Such impurities are heterovalent. They change the valent state under irradiation and creates the divalent ion states with strong interconfiguration d-f absorption transitions. At such doping concentration level of 100 ppm an irradiation induced absorption coefficient in the crystal scintillation region becomes larger than 100 m^{-1} as shown in [7].

A leakage of Pb ions from the melt naturally occurs due to the high vapor pressure of PbO when grown by Czochralski method. The new structure found for Pb-deficient synthetic stolzite, $Pb_{7.5}W_8O_{32}$ is a superstructure of a sheelite type [10]. The presence of the superstructure was observed in the crystals have been grown with lead deficiency as well as in crystals made from stoichiometric raw materials when free surface-to-volume ratio is large. The superstructure appears due to partial deficiency of lead in one, Pb(3), of the four lead sites. In fact, lead tungstate crystal is a solid solution of the pure sheelite and the sheelite like type crystals and fraction of each phase depends from the technological conditions.

Table1. Properties of some oxide crystal scintillators

SCINTILLATOR	Density, g/cm^3	LightYield, Photon/Mev	Decay time, ns	Emission, nm	Method of the crystal growth
BGO ($Bi_4Ge_3O_{12}$)	7,13	8000	300	480	Czochralski Brigeman
$CdWO_4$	7,9	10000	20000	470/540	Czochralski
GSO (Gd_2SiO_5: Ce)	6,71	12500	60 (fast)	430	Czochralski
YAP ($YAlO_3$: Ce)	5,55	14000	28 ±0,2	350	Czochralski Bagdasarov
LSO (Lu_2SiO_5: Ce)	7,1	25000	40 ±2	420	Czochralski
LuAP ($LuAlO_3$: Ce)	8.34	14000	~10	350	Czochralski Brigeman
(Lu-Y)AP ($Lu_{05}Y_{05}AlO_3$: Ce)	6.3	14200	24(average)	350	Bagdasarov Czochralski Brigeman
PWO ($PbWO_4$)	8,28	200	10 (average)	420	Czochralski Modified Brigeman

3.Ce-activated scintillation materials

Among a variety of doped oxide materials we discuss here those which deliver fast and bright scintillations. The scintillation effect in these crystals of compound structure oxides is attributed to the isomorphic additional impurities of some rare-earth ions, emitting fast decaying $d \rightarrow f$ luminescence in the near-ultra violet (u.v.) range. Among trivalent rare-earth ions only Ce^{3+}, Pr^{3+}, Nd^{3+} and Yb^{3+} have luminescent interconfiguration $d \rightarrow f$ transitions. However, $d \rightarrow f$ luminescence bands of Nd^{3+} and Yb^{3+} ions are localized in the range v>40000 cm^{-1}; moreover, interconfiguration luminescence of Nd^{3+} ions has additional quenching owing to non-radiative transitions to the numerous *f*-levels. Ce^{3+} and Pr^{3+} ions can be used as satisfactory activators [11]. Comparison of the Ce^{3+} and Pr^{3+}ions luminescence kinetics shown that luminescence decay time of Pr^{3+} is shorter in the same crystals [12,13]. Moreover, *d*-energy levels of the Pr^{3+} ions are very sensitive to the strength and symmetry of crystalline field. The use of the matrices with relatively large local crystalline field leads to a considerable shift in the $d \rightarrow f$ luminescence band to the deep u.v. range, and to the superimposition of the one with absorption $^3H_4 \rightarrow {}^1S_0$ (f^2- configuration) transition and, as a consequence, to the appearance of an additional quenching channel. For this reason, the $d \rightarrow f$ luminescence of Pr^{3+} ions is not observed for the majority of fluoride matrices at T=300 K.

The most attractive activator is Ce^{3+} ion and its high quantum yield $5d^1(^2T_2) \rightarrow 4f^1(^2F_{5/2,7/2})$ luminescence is a final stage in the creation of the scintilations in Ce doped crystals. A simple mechanism of scintillation arising in Ce doped crystals consisted from two stages: $Ce^{3+} + h \rightarrow Ce^{4+}$ and $Ce^{4+} + e \rightarrow (Ce^{3+})^* \rightarrow Ce^{3+} + h\nu$, where h and e are created by ionizing radiation

termalized valence band hole and conducting zone electron, hv is radiating photon, has been proposed [14]. This model has been augmented with a simple single configuration diagram [15]. Nevertheless, it was determined that the scintillations in Ce doped crystals arise mainly due to Coulomb interaction of excited matrix states (self trapped excitons) and Ce^{3+} ions. From the study of the scintillations in Ce doped oxide crystals we identified two general properties. Bright scintillations are associated with complex structure oxide crystals (1) which when undoped have intrinsic luminescence from relaxed excited matrix states; and (2) which when doped have a resonance between the intrinsic matrix luminescence bands and the activator absorption interconfiguration bands. Some details of general properties are described in [16]. YAP:Ce scintillation crystal is good confirmation of these properties. From a variety of the undoped crystals grown in USSR during 20 year we selected one which had a small amount of the defects and trace impurities. The light yield of the intrinsic excitonic luminescence in this crystal at room temperature was about 12000 ph/Mev [17] which is close to the light yield value of the Ce doped YAP crystal with optimal concentration of the activator (see Table1). Thus, sensitizing process of the trivalent Ce luminescence by excitons is important contributor to the total light yield of the scintilations. The fact that the rise times of several of Ce doped crystals have now been measured to be some hundreds of picoseconds [18] has been testified in favor of such mechanism of the scintillations.

In fact, scintillation is the result of two independent processes in the crystals with relatively small concentration of Ce ions. In the first, the relaxed excited matrix states are created beginning with the entry of the ionizing radiation into the crystal continuing through the creation of thermalized electrons and holes and the subsequent localization of these states. The typical time $_1$ here is in the ps region. In the second, the excited radiating doping ions are created in typical time $_2$ which is comparable with an activator radiating time of not less than ~10 ns. Since $_1 << _2$, casual distribution of relaxed excited matrix states in the first stage establishes the initial conditions for the second stage. It indicates that system can be described in donor –acceptor approximation by the kinetics equations as it shown in the case of GSO:Ce [19]. Within this model it is shown that light yield and scintillation kinetics depend on concentration of the activator in Ce doped scintillation materials. This is in good agreement with data observed for YAP:Ce crystals obtained by horizontal oriented crystalization method [20]. Fig.1(a,b) presents data of the YAP:Ce scintillator light yield and scintillation kinetics measurements, and numerical calculations in frame of the model. These dependencies are observed in many oxide crystals, however they susceptible to corruption by additional impurities very often, especially at low activator concentration.

Analysis of rare-earth ions energy spectra shows that Y, Ce, Gd, and Lu can be used as matrix-forming elements. These ions in trivalent state, except Gd^{3+}, have no energy *f*-levels with energies in the visible and near-u.v. range and, hence, they will have no quenching effect on the activators, radioactive transitions.

The most known cerium-doped gadolinium based scintillator is oxyorthosilicate, Gd_2SiO_5 [21] while more recently, cerium-activated gadolinium perovskite, $GdAlO_3$:Ce (GAP), has also been shown to be a promising scintillator [22]. Both crystals have a bright, fast scintillation and slow components whose decay time constants depend on cerium activator content [23-27]. Gd^{3+} ion energy levels are formed in a narrow sub-zone between the valence and conduction bands, so that the excited will always relax to this Gd^{3+} excited state. Gd-based crystals are similar in their energy structure formed by Gd^{3+} ions, at the same time, those being doped with Ce^{3+} ions differ in the energy difference between the sub-zone formed by Gd^{3+} excited state $^6P_{7/2.5/2}$ and $5d^1(^2T_2)$ energy level of the Ce^{3+} ions. Although well known, GSO and GAP, having this difference δE equal to 1000 and 200 cm^{-1}, respectively, both have some fraction of the slow scintillation component. Otherwise, gadolinium-based scintillators will always have a slow component whose minimum

contribution to the total light yield occurs when $\delta E \sim kT$ [19]. This situation is very close to that realized in gadolinium perovskite crystal.

La^{3+} , Yb^{3+} have no energy *f*-levels with energies in the visible and near-u.v. range, however, majority of the crystals on a base of these elements have strongly suppressed scintillations or even photo- luminescence of the trivalent cerium ions. In ytterbium-based crystals, Yb^{3+} ions are formed at an energy of $\approx 10^4$ cm^{-1} above the $^2F_{7/2}$ ground state in a narrow $^2F_{5/2}$ subzone in the forbidden zone. Thus, non-radiative quenching of the Ce^{3+}-activator luminescence which is observed usually in the oxide crystals above 17000 cm^{-1} is negligible. However, strong quenching of the Ce^{3+} luminescence is occurred due to spontaneous $Ce^{3+} \rightarrow Yb^{3+}$ electron tunneling [28] when electron donors, here the Ce^{3+} ions, are in an excited state. Similar tunneling ionization, first observed in chemical reactions [29]. Moreover, in ytterbium-based crystals, scintillations can be quenched by two additional mechanisms. In the first of these, Yb^{3+} destroys the relaxed excited matrix states. Yb^{3+} ions, as a rule, have a f→d interconfiguration transition of 50000 cm^{-1} [30] and therefore overlap or form the bottom of conduction band in oxide crystals. The captured electrons from the conduction band produce excited $(Yb^{3+})^-$, hence, in ytterbium-based crystals, relaxed excited states interacting with Ce^{3+} ions will increasingly be suppressed, reducing the Ce^{3+} luminescence yield. In the second, the formation of $(Yb^{3+})^-$ ions in a matrix is similar to having an additional Ce^{3+} quenching channel with $Ce^{3+} \rightarrow (Yb^{3+})^-$ energy transfer. The role of the La ions in the strong quenching of Ce^{3+} scintillations is still debated. Recently [31], properties of new Ce doped scintillation materials on a base of borate crystals have been manifested. These crystals are not too dense, however, they show very bright and fast scintillations.

Among oxide crystals the rare earth perovskite crystal family delivered a set of the promising scintillation materials during last several years [32-35]. Single crystals of rare-earth aluminum oxide perovskites ($REAlO_3$), have a number of advantages in comparison with other oxide crystals. Availability of crystal growth technology for laser use, good physical and chemical characteristics, relatively strong crystalline field in the site of Ce ion localization providing scintillation luminescense in near u.v. region with decay times τ_{sc}<30 ns, good transparency in the scintillation luminescence spectral region make these crystals promising for use in modern ionizing detection systems.

A common goal for $REAlO_3$ scintillation crystals technology is cerium stabilization in the trivalent state during the crystal growth process. It was determined [36] that presence of Ce^{4+} ions in the tested crystals leads to quenching of the Ce^{3+} $d \rightarrow f$ luminescence; hence it must has influence on single crystal scintillation efficiency. Ce^{4+} ions have not optically active transitions in visible or near u.v. region, however, they generate hole centers in the crystal when replaced trivalent matrix forming ions. Such hole centers quench excited matrix states decreasing the light yield of the scintillations. Also they cause wide absorption band in the u.v. region which overlaps interconfiguration transition of the Ce^{3+} ions in perovskites.

The cerium doped lutetium aluminum perovskite $LuAlO_3$ is the lutetium analog of YAP. LuAP has been suggested as a scintillation material [11] and its scintillation properties have been reported [37-39]. The material properties of LuAP make it quite attractive as a gamma detection scintillator. Its density is 8.34 g/cc - higher than that one of LSO (7.1 g/cc) [40] , $Lu_3Al_5O_{12}$ (6.9 g/cc) [1], or $LuPO_4$ (6.2 g/cc) [41]. Its melting point of 1960 ^OC is similar to that of $LuPO_4$ (1947 ^OC) and significantly lower than that of LSO (2150 ^OC), and is sufficiently low that it can be grown in molybdenum crucibles rather than the more expensive iridium crucibles. Although YAP and LuAP have very similar spectroscopic properties, LuAP scintillation kinetic is faster than the decay under photoexcitation.

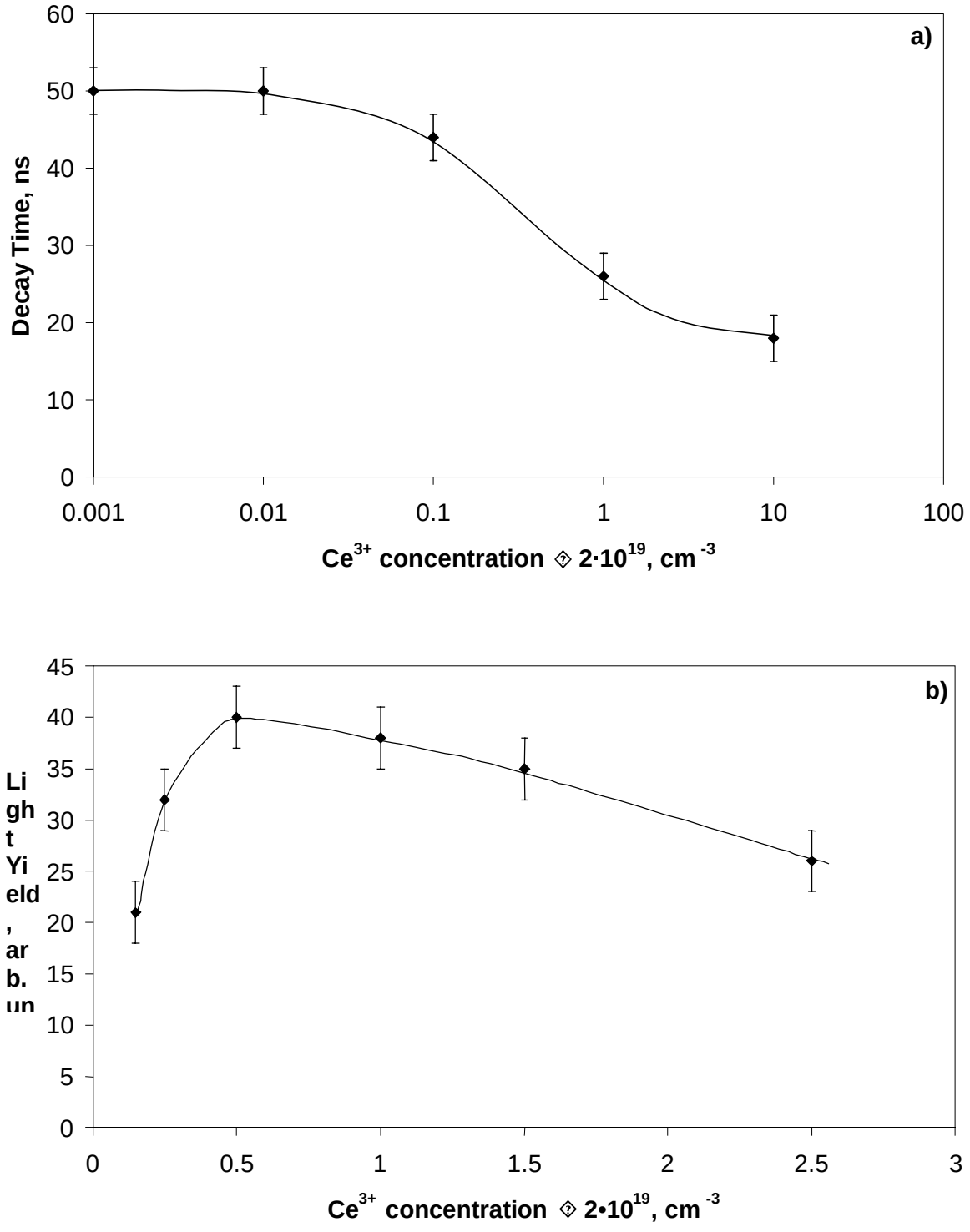

Fig.1 Decay time (a) and light yield (b) of YAP:Ce scintillator versus Ce concentration.

The production technology of LuAP cerium doped crystals is still not developed. The reason of LuAP crystal growth problems lies in the difficulty of obtaining its single crystal state from Lu_2O_3-Al_2O_3 oxide. To overcome this difficulty the lutetium crystal with a perovskite structure by growing solid solutions of $(Lu_x$-$Y_{1-x})AlO_3$ crystals have been grown and studied [42]. Yttrium aluminum perovskite has a wider stability region in the Y_2O_3-Al_2O_3 phase diagram than LuAP. The Y^{3+} ion radius is very close to that of lutetium. Both perovskites have similar melting points and so dissolve into each other. The luminescence

excitation spectra of YAP, $(Lu_{0.5}\text{-}Y_{0.5})AlO_3$, and LuAP, are similar, however, in the Ce^{3+} luminescence band in (Lu-Y)AP there is a shift to a short wavelength region. Adjusting the crystal growth parameters, $(Lu_{0.5}\text{-}Y_{0.5})AlO_3$:Ce scintillation crystals with a density of 6.3 g/cm^3, a luminescence band maximum at 342 nm, a light yield of 14,200 photons/MeV, and decay times of 4.6 (33%), 22(52%), and 83(15%) ns were obtained.

4. $PbWO_4$ lead tungstate scintillator

Engineering of lead tungstate scintillator by the community of technologists, solid state physics specialists and high energy physicists shown us an impressive example how fast scintillation material may be developed if it needed for mass application. First time it was reported for high energy physics application some years ago [43] but now scintillation elements found application in electromagnetic calorimetry of CMS and ALICE experiments at Large Hadron Collider at CERN. Use of the accelerators with high luminosity require scintillation elements able to keep their stability under long-term exposure to ionizing radiation.

Lead tungstate crystal occurs in nature as tetragonal stolzite [44], sheelite type and monoclinic raspite [45]. A high pressure form has also been prepared under high temperature [44]. The $PbWO_4$ has been determined as sheelite-type crystal of tetragonal symmetry with space group $I4_1/a$ and parameters of the unit cell a=b=5.456(2)Å, c= 12.020(2) Å. At the growth of the large PWO crystals by Czochralski method a dominating lead evaporation from the melt is occurring. With Pb deficiency in the melt, crystallization occurred with a new atomic arrangement, which has tetroganal symmetry with space group $P\bar{4}$. Such composition is $Pb_{7.5}W_8O_{32}$ and has a=b=7.719(2) Å, c= 12.018(2)Å [10]. Usually, crystals grown at the conditions when ratio of free surface-to-value is large are solid solution of pure sheelite and sheelite–like type crystal is occured. The luminescence in lead tungstate crystals appeared to be due to charge transfer transitions in anionic molecular complexes WO_4^{2-} and WO_3. Pb^{2+} ions do not show luminescence in the crystals, but play a considerable role in the scintillation creation through sensitization [46,47] . Details of the PWO spectroscopy and radiation damage mechanism are given in [5,7,8]. Lead tungstate crystal is an exception with respect to the other tungstate crystals and analogies with other crystals of the tungstate family for spectroscopy and defects identification are not adequate. Such exceptionality appears to be due to a combination of three factors, which are: the presence of the lead ions in the crystal, relatively narrow band gap and existence of the superstructure of sheelite-type in synthetic stolzite. All these factors have to be taken into account at the production of defect free high quality crystals. For the moment a mass production technology of the crystal ingots with diameter 42 mm and length 270 mm in installed at Bogoroditsk Techno- Cmemical Plant in Russia. Currently, more than 600 ingots are pulled every month to produce scintillation elements for CMS electromagnetic calorimeter.

References

1. C.W.E. van Eijk, J. Andriessen, P. Dorenbos, R.Visser, Nucl.Instr.Methods, **A348**(1994)546
2. CMS TDR, The Electromagnetic Calorimeter Technical Design Report, CERN/LHCC 97-33, CMS TDR4, 15 December 1997
3. R. Novotny, W. Döring, K. Mengel, V. Metag, In the Proceeding of SCINT'97 International Conference on Inorganic Scintillators and Their Applications, Edt. By Yin Zhiwen, L.Peijin, F.Xiqi, X. Zhilin. Shanghai Branch Press (1997) 187

4. A.N.Annenkov, M.V.Korzhik, V.L.Kostilev, P.Lecoq, V.D.Ligun. (1997) In the Proceeding of SCINT'97 International Conference on Inorganic Scintillators and Their Applications, Shanghi, Edt. By Yin Zhiwen, L.Peijin, F.Xiqi, X. Zhilin. Shanghai Branch Press (1997)362
5. M.Böhm, A.E.Borisevich, G.Yu.Drobychev, A.Hofstaetter, O.V.Kondratiev, M.V.Korzhik, M.Luh,, B.K.Meyer, J.-P.Peigneux, A.Scharmann, Phys. Stat. Sol. A. **167(**1998)243
6. A.Hofstaetter, A.Sharmann, D.Scharmann, D.Schwabe, B.Vitt, Z.Phys. **30**(1978)305
7. A.N.Annenkov, E.Auffray, R.Chipaux, G.Yu.Drobychev, A.A.Fedorov, M.Geleoc, N.A.Golubev, M.V.Korzhik, P.Lecoq, A.A.Lednev, A.B.Ligun, O.V.Missevitch, V.B.Pavlenko, J.-P.Peigneux, A.V.Singovski, Radiation Measurements, **29**(1998)27
8. A.Annenkov, E. Auffray, M. Korzhik, P. Lecoq, J.-P. Peigneux**,** Phys. Stat. Sol.(a), **170(**1998)47
9. A.N. Annenkov, A.A. Fedorov, Ph. Galez, V.A. Kachanov, M.V. Korzhik V.D. Ligun, J.M. Moreau, V.N. Nefedov, V.B. Pavlenko, J.P. Peigneux, T.N. Timoshchenko, B.A. Zadneprovskii, Phys. Stat. Sol.(a), **156**(1996)493
10. J.M.Moreau, R.E.Gladyshevskii, Ph.Galez, J.P.Peigneux, M.V.Korzhik**.** Journal of Alloys and Compounds, **284**(1999)104
11. V.G.Baryshevsky, D.M.Kondratiev, M.V.Korzhik, A.A. Fyodorov, V.I. Moroz, V.I. Kachanov and B.I. Minkov, Nucl. Tracks Radiat. Meas., **21**(1993)111
12. E.G Gumanskayia, S.A.Smirnova, M.V.Korzhik, V.B.Pavlenko, A.A. Fyodorov, Optica i Spectroscopia, **72**(1992)155(in Russian).
13. P. Dorenbos, R.Visser, C.W.E. van Eijk, N.M. Khaidukov, M.V.Korzhik, IEEE Trans. On Nucl. Sci., **40**(1993)388
14. V.V.Averkiev, J.A.Valbis, Luminescence of crystals and convertors of ionizing radiation. Nauka, Novosibirsk, (1985)(in Russian)
15. A.J.Woitowicz, A.Lempicki, D.Wishnevski, M.Balcerzyk, C.Brecher. (1994) IEEE Nucl. Sci. Conf. Rec. 134
16. M. V. Korzhik and W. P. Trower, Appl. Phys. Letters, **66**(1995)2327
17. P.Dorenbos (privat communication)
18. S.E.Derenzo (privat communication)
19. D. M. Kondratiev, M. V. Korzhik, A. A. Fyodorov and V. B. Pavlenko, Phys. Stat. Sol.(b), **197**(1996)251
20. V.G.Baryshevsky, M.V. Korzhik, V.I.Moroz, V.B.Pavlenko, A.A.Fyodorov, S.A.Smirnova, O.A.Egorycheva, V.A. Kachanov, Nucl. Instrum. Meth. **B58**(1991)291
21. H.Ishibashi, K. Shimizu, K. Susa and S. Kubota, Nuclear Instrum. And Methods, **A294**(1990)271
22. M. V. Korzhik, V.G. Baryshevsky, G.Yu. Drobyshev, A. A. Fyodorov, V.I. Moroz, V.B. Pavlenko, S.A. Smirnova, O.A. Egorytcheva, O.G. Savinova, V.A. Kachanov, C. W. E. van Eijk, and P. Dorenbos, In Heavy Scintillators for scientific and industrial applications. Ed. P. Lecoq, F. De Natarestifani, and M. Shneegans, Editions Frontiers, Gif-sur-Yvette, 1993, p. 196
23. H.Ishibashi, K. Shimizu, K. Susa, and S. Kubota, IEEE Trans. Nuclear Sci., **36**(1989)170
24. V.G. Baryshevsky, M. V. Korzhik, B.I Minkov, A.A. Fyodorov, A.S. Lobko, and V.A. Voloshin, Phys. Energy Sci, **4**(1991)114 (in Russian).
25. V.A. Voloshin, M.V. Korzhik, M.B. Kosmyna, M.L. Meilman, B.I Minkov, V.I. Moroz, A.A. Fyodorov, and V.B. Pavlenko. Spectroscopic and scintillation characteristics of cerium doped gadolinium orthosilicate single crystals. Preprint Inst. Single Crystals. Kharkov ISC-91-8,1991 (in Russian)
26. C. L. Melcher, J. S. Schweitzer, H.Suzuki, T.A.Tombrello, J. Lum., **60/61**(1994)948
27. V.G. Baryshevsky, D. M. Kondratiev, M. V. Korzhik, V. B. Pavlenko, and A. A. Fyodorov, J. Lumin., **60&61**(1994)956

28. M. V. Korzhik, G. Yu. Drobyshev, D. M. Kondratiev, A. E. Borisevich, V. A. Pavlenko, and T. N. Timochenko, Phys. Stat. Sol., (b) **197**(1996)495
29. R. B. Zutkovskii and R. F. Chairutdinov, Chimia Vysokih Energii, **7**(1973)558 (in Russian)
30. M. L. Meilman, A. I. Kolomitsev, and Z. M. Baskakova, Zh. Prikl. Spektroskopii **42**(1985)781 (in Russian)
31. Inorganic scintilators and their applications. Ed. Yin Zhiwen, Li Peijun, Feng Xiqi, Xue Zhilin, Shanghai, P.R.China, 1997
32. M.J. Weber, J. appl. Phys. **44(**1973)3205
33. R.Autrata, P.Schouer, Jiri Kvapil and Jos. Kvapil, Scanning, **5**(1983)91
34. V.G. Baryshevsky, R.F.Zouevski, M.V.Korzhik, A.S.Lobko, V.I.Moroz, S.A.Smirnova, V.B.Pavlenko, A.A.Fyodorov. Pis'ma v JTP, **V17**(1991)82 (in Russian)
35. M. V. Korzhik, , V.I. Moroz, V.B. Pavlenko, A. A. Fyodorov and S.A. Smirnova, Nucl. Tracks Radiat. Meas., **21**(1993)113
36. V.G. Baryshevsky, M.V. Korzhik, B.I. Minkov, S.A. Smirnova, A. A. Fyodorov, P. Dorenbos and C W E van Eijk, J. Phys.: Condens. Matter **5**(1995)7893
37. B. I. Minkov, Functional Materials, **1**(1994)103 (In Russian)
38. A. Lempicki, M. H. Randles, D. Wisniewski, M. Balcerzyk, C. Brecher, and A.J. Wojtowicz, IEEE Trans. Nucl. Sci., **42**(1995)N4
39. W.W. Moses, S. E. Derenzo, A. Fyodorov, M. Korzhik, A. Gektin, B. Minkov, and V. Aslanov, IEEE Trans. Nucl. Sci., **42**(1995)No.4.
40. C. L. Melcher and J. S. Schweitzer, IEEE Trans. Nucl. Sci., **NS-39**(1992)502
41. A. Lempicki, E. Berman, A. J. Wojtowicz, IEEE Trans. Nucl. Sci., **NS-40**(1993)384
42. M.V.Korzhik, W.P. Trower, A.A.Fyodorov, S.A.Smirnova, V.A.Aslanov, In Proc. of SCINT'95 Inorganic scintillators and their applications. Ed. P.Dorenbos, C.W.E. van Eijk. Delft Univ. Press, 1995 p.355
43. V.G. Baryshevsky, M. V. Korzhik, V.I.Moroz, V.B.Pavlenko, A. S. Lobko, A. A. Fyodorov,V.A. Kachanov, V.L. Solovianov, B.I. Zadneprovsky, V.A. Nefyodov, B.A. Dorogovin, L.L. Nagornaja, Nucl. Instr. Meth. in Phys. Res. **A322**(1992)231
44. P.W. Ritcher, G.J.Kruger, C.W.F.T.Pistorius. Acta Cryst., **B32**(1976)928
45. T. Fujita, I. Kawada, K. Kato. Acta Cryst., **B33**(1977)162
46. M. V. Korzhik, V.B. Pavlenko, T.N. Timoshchenko, V.A. Kachanov, A.V.Singovskii, A.N. Annenkov, V.A. Ligun, I.M. Solskii, J.-P. Peigneux, Phys. Stat. Sol.(a), **154**(1996)779
47. A.N. Belski, S.M.Klimov, V.V.Mikhailin, A.N.Vasilev, E.Auffray, P.Lecoq, C.Pedrini, M.V. Korzhik, A.N. Annenkov, P.Chevallier, P.Martin, J.S.Krupa. Chem. Phys. Lett. **277**(1997)65

High light yield Ce^{3+}(Tb^{3+})-doped phosphate and oxide scintillation glasses

S. Baccaro[1], R. Dall'Igna[2], P. Fabeni[3], M. Martini[4], J.A. Mares[5], F. Meinardi[4], E.Mihokova[5], [a] M. Nikl[5], K. Nitsch[5], G.P. Pazzi[3], P. Polato[2], A. Vedda[4], G. Zanella[6] and R. Zannoni[6]

[1]*ENEA, INN/TEC, via Anguillarese 301, 00060 S.Maria di Galeria, Rome, Italy*
[2]*Stazione Sperimentale del Vetro, via Briati 10, 30141 Murano-Venezia, Italy*
[3]*IROE del CNR, via Panciatichi 64, 50 127 Florence, Italy*
[4]*INFM&Dept.of Material Sci., University of Milano, via Cozzi 53, Milano, Italy*
[5]*Institute of Physics AS CR, Cukrovarnicka 10, 162 53 Prague, Czech Republic*
[6]*INFN&Dept. of Physics, University of Padova, via Marzolo 8, 35131 Padova, Italy*

Abstract: Photo- and radioluminescence, decay kinetics and thermoluminescence are reported for the set of Ce-doped phosphate glasses and Tb-doped silicate ones. Presence of Gd^{3+} ions in the glass host matrix at concentrations above 20 % enhances the energy transfer towards the Ce^{3+} and Tb^{3+} emission centres, which results in the enhancement of the radioluminescence light output. Energy transfer between $Gd^{3+}\leftrightarrow Ce^{3+}$ ions and $Gd^{3+}\rightarrow Tb^{3+}$ ions in phosphate and silicate glass matrices, respectively, was evidenced from the decay kinetics of Gd^{3+}, Ce^{3+} and Tb^{3+} emission centres as well.

Keywords: scintillation glasses, Ce^{3+} and Tb^{3+} emission centres, luminescence, energy transfer

1. Introduction

Scintillation glasses can be used in the bulk or fibre forms for the detection of X-rays and γ-rays or neutrons [1,2]. They are less expensive with respect to single crystal materials, but suffer from rather low transfer efficiency resulting in low light yield [3]. Inefficient transfer of thermalized electrons and holes towards the emission centres is caused by the presence of many trapping sites in the glass matrix, which may serve as the centres of nonradiative recombination. Noticeable influence of the host matrix composition was reported as for this aspect [4].

Glass scintillator materials are investigated comparatively less with respect to single crystal scintillators. In high energy physics field dense Ce^{3+}-doped fluoride glasses were investigated as possible (cheaper) alternative material for electromagnetic calorimeters [3,5]. At higher concentrations of Ce^{3+} ions an unfavourable combination of low transfer efficiency and quenching of Ce^{3+} scintillation due to interaction between closely occurring elementary excitations was noted. The latter effect was noticed by several authors in CeF_3 single crystal scintillators [6,7,8]. Also a negative impact of oxygen ion presence for the light yield values obtained was stated [5].

Within Ce^{3+}-doped glasses the silicate matrix-based ones seem to provide the highest LY [9], the values about 6 ph/keV were reported for the Ce20 composition [1,10]. Li-enriched silicate glass was optimised in the same technological laboratory for Tb^{3+}-doping (Tb10Mg4 composition) and achieved similar light yield [2,10]. While Ce^{3+}-doped silicate glasses are developed for the X-ray detection, the Tb^{3+}-doped (Li-enriched) ones are interesting for the

[a] corresponding author, electronic mail: nikl@fzu.cz

neutron detection. Emission properties of these materials were described in [10,11]. Ce^{3+}-doped silicate glass shows the dominant emission round 400-410 nm with leading decay time about 40-45 ns under 337 nm excitation, while shorter decay time about 18 ns was obtained under ^{22}Na excitation. Both kinds of excitations caused also slower components in the decay, which were noted by other authors for similar Ce^{3+}-doped commercial glass (GS1) down to ms time scale [12]. Scintillation spectrum of Tb10Mg4 glass shows typical four line emission spectrum peaking at 482, 542, 585 and 621 nm. Decay kinetics is governed by parity forbidden 4f-4f transition between Tb^{3+} levels, which shows about 2.7 ms decay time.

The problem of low transfer efficiency could be solved either by higher dopant concentration or by sensitisation of energy transfer to the emission centres. The latter concept is used in many phosphors, scintillation or laser crystals. Higher doping levels are difficult to reach due to devitrification of the glass matrix during the preparation procedure [1,2]. We have developed new concept of energy transfer sensitisation in scintillation glass based on nearly resonant energy migration through a rare earth ion subsystem in the glass matrix followed by a single step transfer to an emission centre. More specifically, Gd^{3+} ions at sufficiently high concentration enabled effective energy migration in the phosphate and oxide -based glass matrices followed by single-step energy transfer towards emission centres created by Ce^{3+} or Tb^{3+} doping. For Ce^{3+} doping, such energy transfer processes are similar to those described e.g. for $GdAlO_3:Ce^{3+}$[13] or $Lu_xGd_{1-x}AlO_3:Ce^{3+}$[14]. Efficient energy transfer $Gd^{3+} \rightarrow Tb^{3+}$ is known in many matrices, see e.g. in [15]. An interesting point is that Gd-Gd energy migration works well even for Gd-diluted systems, see e.g. in ref. 16 for mixed (Y,Ce,Gd,Tb) fluorides where Tb^{3+} centres are efficiently emitting already for Gd^{3+} concentration round 30%.

In this paper a complete optical characterisation of Ce^{3+}-doped phosphate and Tb^{3+}-doped silicate glasses with substantial percentage of Gd^{3+} ions in the glassy matrix (above 20%) will be given. Also the thermoluminescence and radioluminescence measurements are included. The influence of concentration of important constituents (Ce^{3+} and Tb^{3+} ions) will be reported as well.

2. Experimental

Luminescence and scintillation characteristics were obtained by Spectrofluorometer 199S (Edinburgh Instrument) equipped with hydrogen and X-ray (35 kV, Mo anticathode) lamps and ^{22}Na radioisotope as the excitation sources and using photon counting detection, see e.g. [7]. TSL measurements after X-ray irradiation (Machlett OEG 50 X-ray tube) were performed by means of an apparatus described elsewhere [17]. Luminescence decays obtained in an extended dynamical and time scales were measured using the excitation by excimer laser (N_2 (337nm) and XeCl (308 nm) lines) and detection by photomultiplier coupled with the digital oscilloscope Tektronix TDS 680B, see e.g. [7]. Slow decays in ms time scale were measured with Xe microsecond flashlamp and multichannel analyser in a scanning regime at mentioned Spectrofluorometer 199S. All the spectra are corrected for experimental distortions, decay times are extracted from decay curves using deconvolution procedures, i.e. removing thus distortions due to finite width of the excitation pulse (essential mainly in the ns time scale).

The starting terbium doped silicate glass (Gd-free Tb10Mg4 sample) had the following composition (in melt, wt.%): SiO_2 (58%), Al_2O_3 (16%), Tb_2O_3 (11.5%), Li_2O (10.5%), MgO(4%) [2]. Another three samples with modified composition containing about 22-30% of Gd (samples Tb0Gd25, Tb3Gd30 and Tb10Gd22) were prepared for evaluation of Gd effect in energy transfer processes and transfer efficiency enhancement. Similarly, four samples of Ce-doped phosphate glass were prepared using $NaPO_3$, $GdPO_4$ and $CePO_4$ starting materials.

The samples are further noted as Na74Gd25Ce1, Na99Ce1, Na75Gd25 and Na52Gd45Ce3, where the number denote the molar percentage of the starting materials in the melt. Mixed constituents were melted in a quartz ampoule at around 1200 ^{0}C and then poured into a graphite crucible. Appropriate annealing had to be applied for both silicate and phosphate glasses to remove thermal stresses before cutting and polishing procedures.

3. Experimental Results And Discussion

3.1 Ce-doped phosphate glasses

The absorption spectra of Na75Gd25 and Na74Gd25Ce1 samples are given in Fig.1 at room temperature (RT). The transitions related to Ce^{3+} and Gd^{3+} energy levels are marked in the figure. According to classification of ref. 18, this is the case of intermediate crystal field, in which the lowest $4f^1$-$5d^0$ transition of Ce^{3+} is of about the same energy as the lowest $4f^1$-$4f^1$ transition round 312 nm belonging to Gd^{3+} ion. In such a situation, at elevated temperatures bi-directional energy transfer should occur between Gd^{3+} and Ce^{3+} ions. In Fig. 2 excitation and emission spectra related to Ce^{3+} emission centres are given together with X-ray excited emission for the Na74Gd25Ce1 sample. In the latter emission spectrum, also the Gd^{3+} emission peak is clearly visible round 312 nm, which is in perfect overlap with the lowest part of Ce^{3+} excitation spectrum. Such overlap is an evidence that efficient energy transfer $Gd^{3+}\rightarrow Ce^{3+}$ can occur. In Fig.3 X-ray excited emission spectra of all the four phosphate glass samples are given. The samples are about the same shape and all the measurements were performed in comparable conditions, so that the spectra can be compared in an absolute way. Strongly increasing efficiency of Ce^{3+} emission can be seen for Gd-containing (Na74Gd25Ce1, Na52Gd45Ce3) samples with respect to Gd-free Na99Ce1 one. Also strongly decreasing intensity of Gd^{3+} emission line at 312 nm is noticed with increasing Ce^{3+} concentration in the samples.

The energy transfer $Gd^{3+}\rightarrow Ce^{3+}$ can be evidenced also from Gd^{3+} emission decay in Fig.4. While Ce-free Na75Gd25 sample show undistorted Gd^{3+} decay kinetics of single exponential shape and decay time about 6.5 ms, substantial shortening and non-exponential shape (mean decay time about 0.52 ms) is evident for Na74Gd25Ce1 sample. Such behaviour can be explained by efficient energy transfer from the Gd-subsystem towards Ce^{3+} emission centres. Photoluminescence decay kinetics of Ce^{3+} centres themselves is characterised by leading fast component about 29 ns (inset of Fig.5) with a slow non-exponential tail, which is increasing in the amplitude with elevating temperature - Fig. 5. The latter phenomenon is a consequence of the $Ce^{3+}\rightarrow Gd^{3+}$ back energy transfer, which can be expected according to the mutual position of the Gd^{3+} and Ce^{3+} absorption bands (Fig.1).

Thermoluminescence glow curves of all the four samples after irradiation at 10 K is given in Fig.6. Smooth and rather structureless shape of the curves is related to the glass nature of the host matrix. Spectral composition matches very well the Ce^{3+} emission peak round 340-350 nm in the samples with non-zero Ce concentration, while Gd-like emission pattern is observed in Na75Gd25 sample. Such situation can be understood under expected hypothesis that the rare earth ions serve as the centres of radiative recombination, while electron are stored in the traps related to the host matrix. The electron traps are rather shallow (with the exception of Na52Gd45Ce3 sample, which was visibly of worse quality) as very low TSL signal was present above 150 K. Such situation is favourable for timing characteristics of scintillation emission at RT, because de-trapping times can be expected in μs time scale and no substantial delayed recombination due to the host matrix traps can be expected.

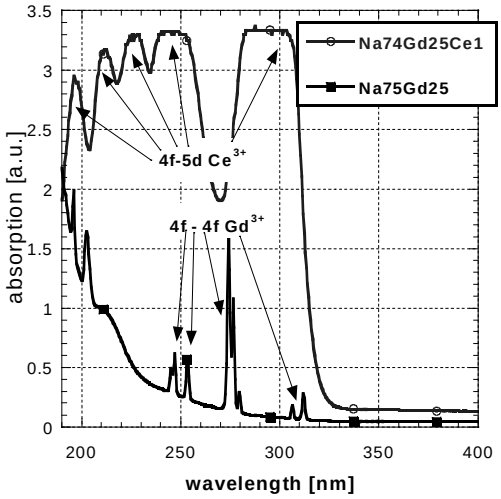

Fig. 1 The absorption spectra of phosphate glasses at RT. The absorption bands belonging to Ce^{3+} and Gd^{3+} transitions are marked.

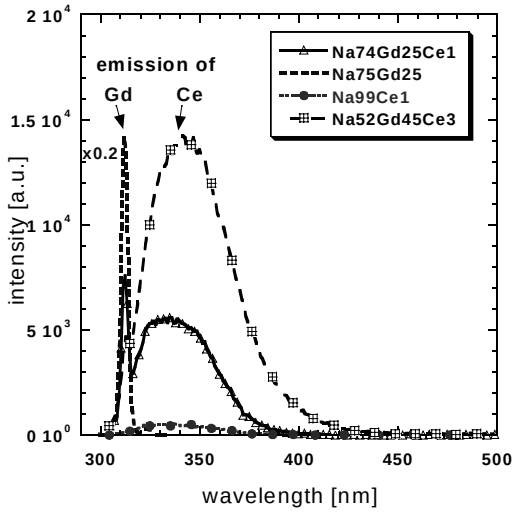

Fig.3 X-ray excited emission spectra of four phosphate glass samples at RT. Spectra are mutually comparable in an absolute scale.

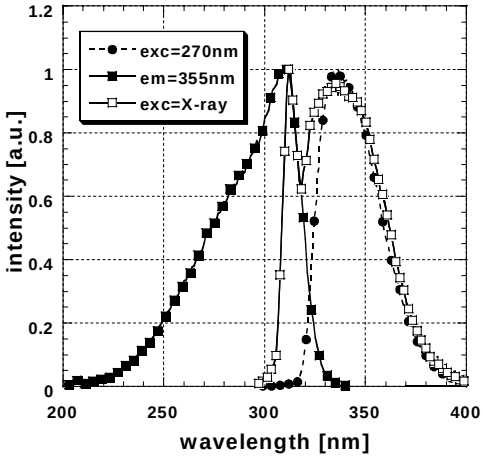

Fig. 2 Excitation (em.= 355 nm) and emission (ex=270nm and X-ray) spectra of Na75Gd24Ce1 sample at RT.

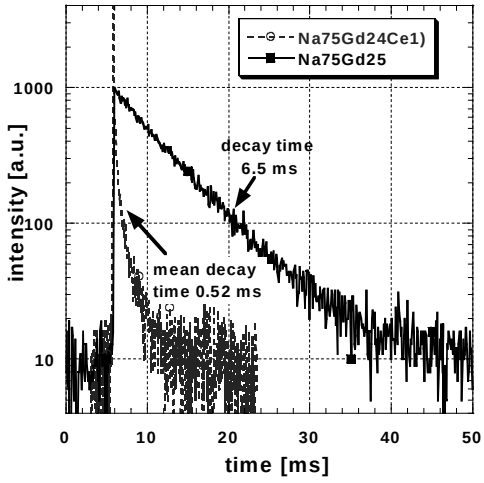

Fig. 4 Photoluminescence decay of Gd^{3+} centres (exc.=275 nm, em.=312 nm) at RT.

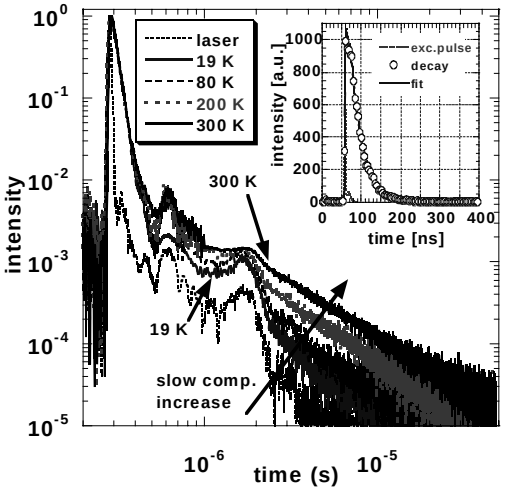

Fig. 5 Photoluminescence decay of Na52Gd45Ce3 phosphate glass (exc.=308 nm, em=345 nm). The arrow shows the enhancement of the slow decay components in the μs time scale with elevated temperature. In the inset the fast decay component related to 5d→4f transition of Ce^{3+} is given, which is fitted by one exponential of 29 ns decay time.

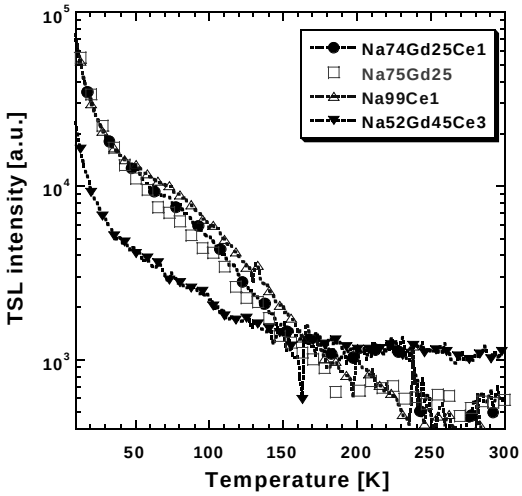

Fig. 6 Thermoluminescence of all the four phosphate glasses after irradiation at 10 K.

3.2 Tb-doped silicate glasses

Gd^{3+} presence in the silicate glass matrix gives rise to the same absorption peaks round 310 nm as in the phosphate matrix. Silicate matrix however, shows an absorption tail down to 340-350 nm, which obscures a bit mentioned Gd^{3+}-related absorption feature. Essential excitation and emission spectra of Tb0Gd25 and Tb10Gd22 samples are given in Fig.7. Emission spectrum of Tb10Gd22 shows four leading narrow bands at 485 nm, 545 nm, 585 nm and 620 nm, which are broadened due to fluctuating crystal field in the glassy environment. No Gd^{3+} emission is present in Tb10Gd22 sample round 312 nm, while it is clearly visible in Tb0Gd25 one. In the excitation spectra of Tb^{3+} emission (leading 545 nm band of Tb10Gd22 sample) enhanced excitation is evident in the position of Gd^{3+} excited states round 275 and 312 nm. Such a feature gives a good evidence of $Gd^{3+}\rightarrow Tb^{3+}$ energy transfer. Under X-ray excitation, enhanced Tb^{3+} emission was obtained with respect to the Gd-free sample with the same level of Tb^{3+} doping (10%) - Fig. 8. Tb-free sample Tb0Gd25 shows efficient Gd^{3+} emission under X-ray excitation as well, but also noticeable Tb^{3+} emission was observed (Fig.8), which is explained by trace concentration of Tb^{3+} in the material and efficient $Gd^{3+}\rightarrow Tb^{3+}$ energy transfer due to Gd-Gd energy migration process.

Another evidence about $Gd^{3+}\rightarrow Tb^{3+}$ energy transfer can be again obtained from the decay kinetics of Gd^{3+} and Tb^{3+} emission centres. Gd^{3+} decay in Tb0Gd25 sample shows nearly single exponential decay with the decay time about 2.1 ms, see Fig. 9. In Tb-doped samples, noticeable shortening of Gd^{3+} decay is obtained, which is increasing with Tb concentration - Fig.9. Under excitation round 275 or 312 nm, rising part is clearly obtained in Tb^{3+} emission decay at 544 nm, which can be fitted with approximately the same two characteristic times obtained in the fit of Gd^{3+} decay in Fig.9. Decaying part of 545 nm Tb^{3+} emission is fitted well with 2.7 ms decay time obtained earlier at older samples like the Tb10Mg4 one.

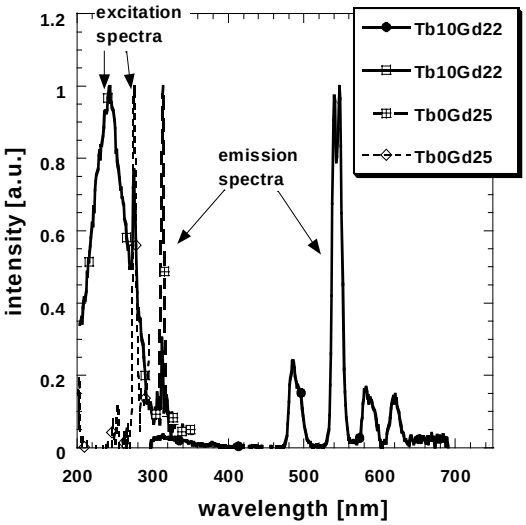

Fig.7 Excitation (em.= 544 nm) and emission (ex.= 275 nm) spectra of Tb10Gd22 silicate glass. Emission (ex.=275 nm) and excitation(em.= 312 nm) spectra of Tb0Gd25 glass (all at RT).

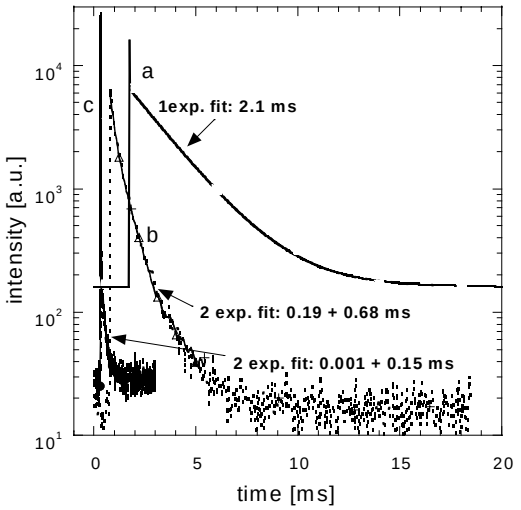

Fig.9 Photoluminescence decays of Gd^{3+} 312 nm emission line in: (a) Tb0Gg22; (b) Tb3Gd30 and (c) Tb10Gd22 under exc.= 275 nm and at RT.Two exponential fits are given by solid lines with the decay times indicated in the figure.

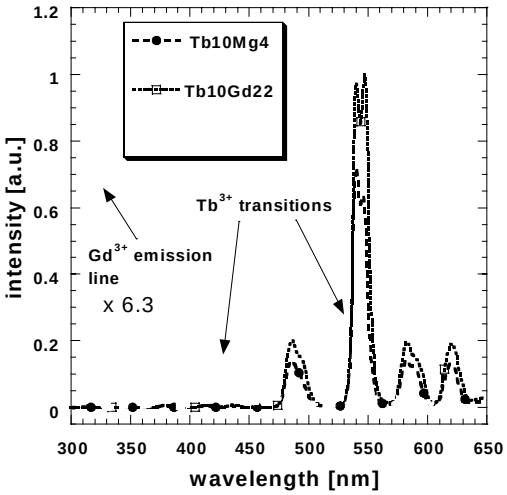

Fig. 8 X-ray excited emission spectra of silicate glasses at RT. Spectra are comparable in an absolute scale.

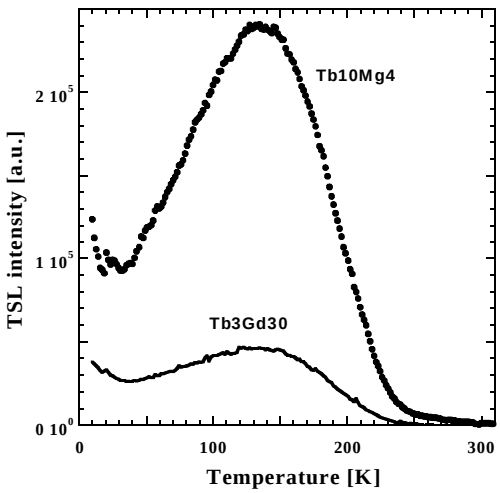

Fig. 10 Thermoluminescence of Tb-doped silicate glasses after irradiation at 10 K.

Thermoluminescence glow curves indicate deeper trapping states with respect to the phosphate systems reported above, see Fig. 10. Presence of Gd^{3+} ions in the host matrix clearly lowers the amplitude of TSL signal, which might be related to more efficient energy transfer from the glass matrix to the Gd-subsystem, where it is promptly delivered towards Tb^{3+} emission centres.

4. Conclusions

The measurements of excitation and emission spectra under UV and X-ray excitations evidenced well the $Gd^{3+} \rightarrow Ce^{3+}$ energy transfer in the phosphate glass matrices and

$Gd^{3+} \rightarrow Tb^{3+}$ energy transfer in the silicate ones. In both cases this interpretation is supported also by observed Gd^{3+} decay kinetics in its 312 nm emission band. Thus Gd-enriched and Ce-doped phosphate glasses provided several times enhanced light output with respect to Gd-free and equivalently doped system. In a similar, but less expressed manner, the emission of Tb^{3+} centres is enhanced in Gd-enriched silicate glasses. Participation of Gd^{3+} ions in the energy transfer processes in the Ce-doped phosphate glasses brings necessarily the slow components in the photoluminescence decay, which are increasing in amplitude with elevated temperature due to the back $Ce^{3+} \rightarrow Gd^{3+}$ energy transfer. Due to long decay time of Tb^{3+} centres in silicate glass, no additional delay is introduced due to Gd-Gd energy migration in this system.

Acknowledgement

This research was supported by NEWLUMEN project of INFN in Italy.

References

1. G. Zanella et al, NIM A **345**, (1994), 198.
2. G. Zanella et al, NIM A **359** (1995), 547.
3. E. Auffray et al (Crystal Clear collaboration) NIM **A380** (1996) 524.
4. M.J.Weber, M.Bliss, R.A.Craig, and D.S. Sunberg, Rad. Eff. Def. in Solids **134**, (1995) 23.
5. E.G.Devitsin et al., NIM A **405**, (1998) 418.
6. C. Pedrini et al., Chem. Phys. Lett. **206**, (1993) 470.
7. M.Nikl et al., J.Phys.Cond.Mat. **7**, (1995) 6355.
8. M.A. Terekhin et al., J.Phys.Cond.Mat. **8**, (1996) 497.
9. M.J. Weber, "Scintillator materials for calorimetry", Proc. of 5th IC on Calorimetry in High Energy Physics, ed. by H.A, Gordon, D. Rueger, World Scientific 1995, p. 17.
10. M.Betinelli et al, Phys.Chem.Glasses **37** (1996), 4.
11. S.Baccaro et al., Proceedings of 5th ESG conference, Prague, June 21-24 (1999), p.C1-23.
12. C.Angelini et al., NIM **A281** (1989) 50.
13. J.A.Mareš et al, Rad. Eff. and Def. **135**, (1995) 867.
14. J.A.Mareš et al, J.Lumin. **72-74**, (1997) 737.
15. G.Blasse, J.All. and Compounds **192** (1993) 17.
16. G. Blasse, phys.stat.sol. (a) **73**, (1982) 205.
17. M.Martini et al., Chem.Phys.Lett. **260**, (1996) 418.
18. P.Dorenbos, J.C.Spijker and C.W.E. van Eijk, Proc. of SCINT97, Shanghai, China. Sept. 22-25, p.307.

Fast scintillator BaF_2-LaF_3

A.I.Nepomnyashchikh[1] , E.A.Radzhabov[1] , A.V.Egranov, [1] V.F.Ivashechkin, [1] A.P.Ivashkin [2], Yu.G. Kudenko [2], O.V. Mineev [2]

1 Vinogradov Institute of Geochemistry, Russian Academy of Sciences
Favorskii street 1a, P.O.Box 4019, 664033 Irkutsk, Russia
2 Institute for Nuclear Research, Russian Academy of Sciences
60-th October Anniversary prosp. 7a, 117312 Moscow, Russia

Abstract: The scintillation properties of BaF_2-xLaF_3 single crystals have been investigated for La concentrations up to 10 mol %. The luminescence spectra of the crystals have been recorded during x-ray excitation. The slow component of BaF_2-10% LaF_3 is reduced by a factor of 25, whereas the yield of the fast component remains almost constant.

Keywords: scintillators, rare-earth ion, fast decay time, emission

Introduction

The BaF_2 crystals are known as fast scintillators. The fast ultraviolet emission under x-ray or particle excitation is due to cross-luminescence transitions. This emission has an extremely fast decay time (600-800 ps) and the intensity is independent of temperature. However, the disadvantage of BaF_2 scintillators is an intensive slow exciton luminescence, which has lower photon energy than cross-luminescence.

The high precision electromagnetic calorimetry in high energy physics requires radiation resistant, fast scintillating crystals with a short radiation length. For experiments which work in high radiation environment and need very good time resolution BaF_2 would be a good choice in case of suppression of dominating slow component. For example, the BNL E926 experiment "Measurement of the decay $K_L^0 \to \pi^0 \nu \bar{\nu}$ " needs a good performance electromagnetic calorimeter with time resolution of about 200 psec in the range of photon energies 50 – 1000 MeV to measure the momentum of neutral kaons with high accuracy. To efficiently use this calorimeter as photon veto system the intensity of slow component must be reduced by a factor of 10-20. The energy resolution of 1.5-2.0% at 1 GeV using only fast component is also very desirable.

The slow component can be suppressed considerably by doping with La [1], Cd [2], Mg, or Sr [3]. The reason of this is not clear yet. The migration of exciton to impurity followed by nonradiative quenching of exciton was proposed [1].

One can suggest that the impurities, in particular oxygen, contribute to the decrease of the cross-luminescence. Thus, the application of pure lanthanum fluoride is of great importance for the production of fast scintillators, based on solid solutions of barium and lanthanum fluoride crystals.

Although there have been several attempts to reduce the slow component by introduction of LaF_3 into the BaF_2 crystal [1,4], further study of the suppression of the slow component is needed. We reexamine the effects of La doping on decay characteristics of BaF_2 crystals aiming to develop a large size fast scintillator, suitable for fast electromagnetic calorimeters in high counting rate experiments.

Experimental methods

The desired crystals are to possess a high radiation stability and transparency in the area of cross-luminescence bands. A high crystal homogeneity is needed for obtaining a good energy resolution. The fast scintillator detectors as prisms (35*35*300 mm) of BaF_2 with the slow component suppressed are required for a new project on BNL collider in Brookhaven.

Raw materials preparation

The industrial technology for the production of super pure BaF_2 for crystal has been developed at the Angarsk Electrolysis Chemical Complex (AECC). This technology produced about 1600-2000 kg of BaF_2 per year. Pure $BaCO_3$ from Donetsk city chemical enterprises and pure hydrofluoric acid from AECC are used as initial raw materials. The processes of BaF_2 production consists of three main stages:

(i) The synthesis of barium hydrofluoride at the interaction of the $BaCO_3$ and hydrofluoric acid, thus:

$$BaCO_3 + 3HF = BaF_2*HF + CO_2 + H_2O \qquad (1)$$

(ii) Production of the barium fluoride by the barium hydrofluoride thermal decomposition:

$$BaF_2*HF = BaF_2 + HF \qquad (2)$$

(iii) Drying, annealing and melting the BaF_2in an anhydrous HF atmosphere.

The quality of thus grown BaF_2 is demonstrated in table 1.

NN	Impurity	Concentration, $*10^{-4}$%	NN	Impurity	Concentration, $*10^{-4}$%
1	Mn	< 0,5	7	Co	< 5
2	Mg	< 8	8	Ni	< 5
3	Pb	< 0,8	9	O	< 1
4	Si	< 6	10	Ti	< 7
5	Cr	< 5	11	Mo	< 5
6	Fe	< 8	12	Cu	< 7

Table 1. The contents of inadvertent impurities in BaF_2.

The synthesis of the super pure lanthanum fluoride consists of three main stages as:

- The synthesis of the LaF_3 from the pure “Lao-Lum” lanthanum oxide and HF acid

$$La_2O_3 + 6HF = 2LaF_3 + 3H_2O \qquad (3)$$

- The deposition after filtering, drying and annealing with the excess ammonium fluoride.
- Melting LaF_3 in an anhydrous HF atmosphere.

Crystal preparation

Combined Shteber-Stockbarger method was used to grow $Ba_{1-x}La_xF_{2+x}$ crystals. The application of this method is necessary to produce crystals free of defects. The crystals were grown under high vacuum conditions with the reduction of the melt by lead and cadmium fluorides. The crystals, characterized by a wide range of transparency from 10,5 eV to infrared range, were grown from the lanthanum fluoride using the above procedure [6].

Having in mind that elasticity of vapors of barium and lanthanum fluorides is significantly dependent on the temperature, overheating of the melt surface should be avoided. At the same time, the conditions for the intensive connective mixing of melt are essential to complete and purification. A special technology of heating and cooling allowing melting of all loaded material, effective mixing and prevention of melt evaporation has been developed.

We studied the influence of the crystallization front shape on the crystal structure and crystal quality. The effect of “loose crust” formed on the crystal surface is found when the crystallization front is concave. The conditions to keep flat-convex crystallization front along the total length of the crystal to be grown are revealed. A method was developed for purpose

growing special crystals with a given size and shape. The scintillation detectors as quadrangular prism (35x 35 x300 mm) are created. The intensity of the fast emission is homogenous for entire length of crystals and the slow self-trapped exciton emission is significantly diminished.

Several highly transparent crystals LaF_3 doped with concentration up to 30% were prepared. The crystals with sell structure was usually obtained within 0.5-20% LaF_3 concentration range (see also [5]).

The quality of BaF_2 – 5 mol% LaF_3 is shown in table 2.

NN	Impurity	Concentration, $*10^{-4}$%	NN	Impurity	Concentration, $*10^{-4}$%
1	Mn	<1	7	Al	20
2	Mg	10	8	Ni	3
3	Pb	1	9	Ca	2
4	Si	10	10	Ti	1
5	Fe	15	11	V	<3

Table 2. The concentrations of impurities in BaF_2 – 5 mol% LaF_3

Measurements

Decay of luminescence was measured by single photon counting technique using CAMAC time-to-digital converter. Samples ∅17 mm x 15 mm were irradiated with ^{137}Cs γ- source or ^{90}Str-^{90}Y - β sources. Photomultipliers FEU 100 were used as start and stop ones.

The emission spectra were measured using grating vacuum monochromator VM4 and FEU39A. The spectra were not corrected for spectral response of spectrometer, but the sensitivity in 4-6 eV region is not significantly varied. The x-ray tube (W, 25 kV, 10 mA) was mounted apart from entrance slit of monochromator. Such type of measurement geometry allows to obtain a minimal variation of emission intensity from sample to sample.

Results

Cross-luminescence of pure BaF_2 consists of two bands at 6.3 and 5.7 eV. The LaF_3 doping does not affect cross-luminescence intensity excited by x-rays (within the experimental error of 10-20%). As the La concentration increases to about 10 %, the intensity of the slow component decreases by the factor of 25, whereas the yield of the fast component remains almost constant.

The emission spectrum of the cross-luminescence broadened to low-energy side and both bands become less resolved with increasing LaF_3 concentration above 1 %, while the decay time and the intensity is unchanged (Fig.1).

As in the previous works [1,4] there are unexplained sample to sample differences of the cross-luminescence characteristics. Thus the intensity of the fast component of BaF_2-0.1%LaF_3 is smaller than that of BaF_2-5%LaF_3 (Fig.1). The large scatter of the points may be due to the variations in the quality of the crystals (Fig.2).

Obviously the fluorine 2p valence band broadens in solid solution and core-valence luminescence spectrum slightly changes. In LaF_3 the valence band is larger then in BaF_2 due to the existence of two different fluorine sites with different Madelung potentials. Contrary to the previous results [4] we found a larger continuous decrease of exciton emission above 1 % of LaF_3. For concentrations of La larger than 0.3% the logarithm of intensity versus the concentration of LaF_3 can be approximated by a straight line (Fig.2).

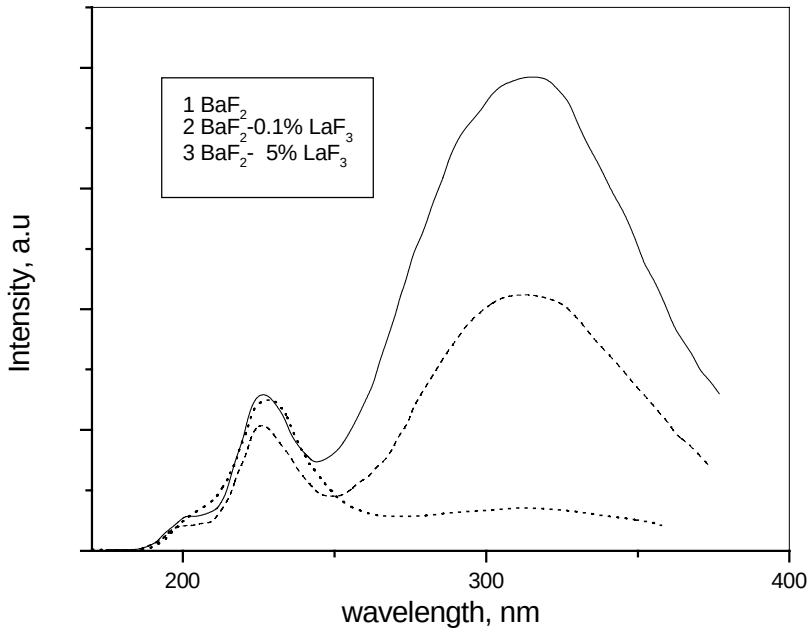

Fig.1. X-ray excited luminescence spectra at room temperature of La-doped BaF_2 crystals.

Decay time measurements of the luminescence have been performed for some of the crystals. Compared to undoped BaF_2, no change was found in the decay time of the cross-luminescence for all the studied La-doped crystals. The decay time of the exciton emission decreases with the LaF_3 concentration, however, faster as compared with results derived from Schotanus et.al. [1]. As the intensities, the decrease of the decay time can be represented by a two-exponential function (Fig.2).

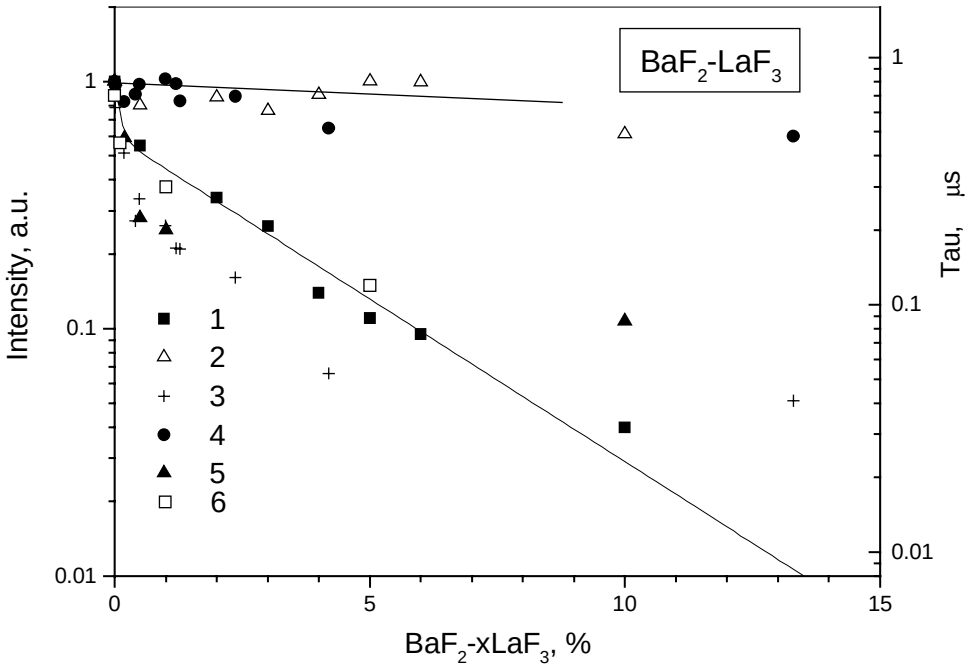

Fig. 2. Intensities of x-ray emission of the slow (1) and fast component (2) and the decay time of the slow component (6) of La-doped BaF_2 crystals. For comparison we include the results derived from Schotanus et.al. (3,4) [1] and from Sobolev et.al (5) [4]

Conclusion

- BaF_2 and LaF_3 produced in AECC are good quality raw materials for growing of the crystals for high energy physics.
- The method of large size BaF_2, LaF_3 and solid solution $Ba_{1-X}La_XF_{2+X}$ crystals growth have been developed at the Institute of Geochemistry.
- The effect of "loose crust" formed on the crystal surface is found when the crystallisation front is concave.

It is the authors' opinion that the crystals BaF_2-xLaF_3 of a good quality could yield a material with nearly total suppression of the slow component without quenching the fast cross-luminescence.

References

1. Schotanus P., et.al.. Nucl. Instr. And Meth. **A281** (1989) 162
2. Springis M., et.al Proceedings of SCINT95, 1996, Netherlands, 403
3. Hamada, M.M., et.al. Nucl. Instrum. and Meth. in Phys. Res. **A353** (1994) 33
4. Sobolev B.P., et. al. Scintillator and Phosphor materials, Materials Research Society Symposium Proceedings V. 348, Pittsburgh, Pennsylvania (1994) 277
5. Multicomponent crystal based on heavy metal fluorides for radiation detectors. Sobolev B.P. (edi-tor), Barcelona (1994) 153-162
6. E.Radzhabov and A.I.Nepomnyaschikh. Exciton Emission in LaF_3 Crystals. Materials Science Forum Vols. 239-241, 1997, p.p. 275-278. © 1997 Trans Tech Publication, Switzerland

Electronic structure of pure and defective $PbWO_4$, $CaWO_4$, and $CdWO_4$

R. T. Williams, Y. C. Zhang, Y. Abraham, and N. A. W. Holzwarth

Department of Physics, Wake Forest University
Winston-Salem, NC 27109 USA

Abstract: Within the framework of density functional theory, we have studied the electronic ground-state properties and approximated the optical dielectric constants and reflectivity of $PbWO_4$ as well as $CaWO_4$ and $CdWO_4$. The band structure also provides insight into the transport properties of excitons, electrons, and holes in these materials. A supercell adaptation of our calculation method which was previously applied to $CaWO_4$:Pb at 50% concentration has now been used to study Pb vacancies, Bi impurities, and La impurities in $PbWO_4$. Preliminary results of electronic structure calculations for $CdWO_4$, having the wolframite structure, are presented for comparison.

Keywords: $PbWO_4$, $CaWO_4$, $CdWO_4$, electronic structure, defects

Introduction

Lead tungstate ($PbWO_4$) and cadmium tungstate ($CdWO_4$) are dense, fast scintillator crystals which have achieved technological importance for high energy radiation detectors and medical imaging, respectively. Calcium tungstate ($CaWO_4$, the mineral scheelite) is an important phosphor for lighting and displays. We recently compared the electronic structures of the four scheelite-structure materials $CaWO_4$, $PbWO_4$, $CaMoO_4$, and $PbMoO_4$ [1]. The present paper discusses further aspects of the electronic properties of the first two of these crystals and presents new electronic structure results for $CdWO_4$ using the same calculation method. Furthermore, a supercell adaptation of the method has been employed to study chemical impurities and vacancies at effective 50% concentrations. Results for Pb impurities in $CaWO_4$ were reported in Ref. [2]. Additional results on Pb vacancies, La impurities, and Bi impurities in $PbWO_4$ are reported here. Comparisons to experimental data on photoelectron spectroscopy, reflectivity [3], electronic transport, EPR, and luminescence spectroscopy will be discussed.

The density functional calculations were performed using the Linearized Augmented Plane Wave (LAPW) technique using the WIEN97 code[4]. The calculational and convergence parameters were detailed in our previous work[1-3].

One electron energy spectrum of $PbWO_4$

The density of states (*N(E)*) distribution for $PbWO_4$ from -20 to +15 eV is presented in Fig. 1. The labels appearing above the peaks indicate the dominant atomic and molecular attributes of each band, determined by analyzing the partial densities of states and contour maps of the electron densities for specific energy ranges [1] as will be discussed below. Recently, Hofstaetter, Meyer, Niessner, and Oesterreicher[5] have measured the ultraviolet photoelectron spectrum (UPS) of $PbWO_4$ which is also shown in Fig. 1. The energy scale of the UPS has been translated rigidly for best agreement of major features of the calculation. In particular, the spectrum can be made to align simultaneously with the "Pb6s-O2p" peak, the bottom of the valence band, the two main groups of oxygen states in the valence bands, and

the valence band edge. This alignment of energy scales corresponds to a value of photoelectron threshold energy (from top of valence band to vacuum energy) of 5 eV. This is a reasonable value corresponding to the sum of the 4.2 eV band gap and a small positive electron affinity. On the other hand, photoelectron spectra measured by Shpinkov et al show at most a small bump in the place expected for the Pb6s-O2pσ band below the valence band. [6]

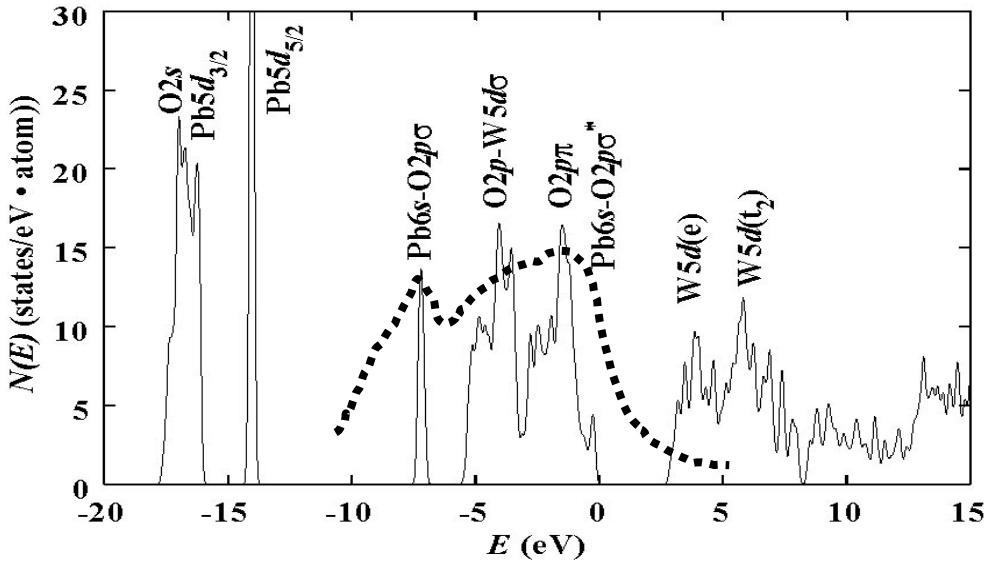

Fig. 1 -- Total density of states for the upper core, valence, and conduction bands of $PbWO_4$ calculated with a Gaussian smearing function (Ref. [1,3]). The zero of energy is taken at the top of the last occupied band. The labels indicate the dominant atomic and molecular attributes of each band. The broken curve is an experimental ultraviolet photoelectron spectrum from Hofstaetter et al [5] as discussed in the text.

For the scheelite materials, the structure of *N(E)* in the vicinity of the band gap is primarily associated with the WO_4 group which has approximately tetrahedral symmetry. A molecular orbital diagram for these states, based on the work of Ballhausen [7] and from analysis of the electronic structure results, is shown in Fig. 2. The W^{6+} ions split the 2*p* states of the nearest neighbor O^{2-} ions into σ and π orbitals. These states then form linear combinations appropriate for the tetrahedral symmetry of the WO_4 site to compose the main contribution to the valence bands. The 5*d* states of the W^{6+} ions also hybridize with the O 2*p* states and the tetrahedral crystal field splits the *5d* orbitals into "e" states which dominate the bottom of the conduction band and the "t_2" states which dominate the upper conduction band. This basic structure is also seen in the density of states for $CaWO_4$. In addition, the valence band of $PbWO_4$ is also strongly affected by the Pb 6*s* states which hybridize with the O 2*p* states in an approximately octahedral environment, as also diagrammed in Fig. 2. The "Pb6*s*—O2*p*σ" hybrid forms a bonding state *below* the bottom of the valence band while the "Pb6*s*—O2*p*σ*" antibonding hybrid contributes to the density of states at the top of the valence band of $PbWO_4$.

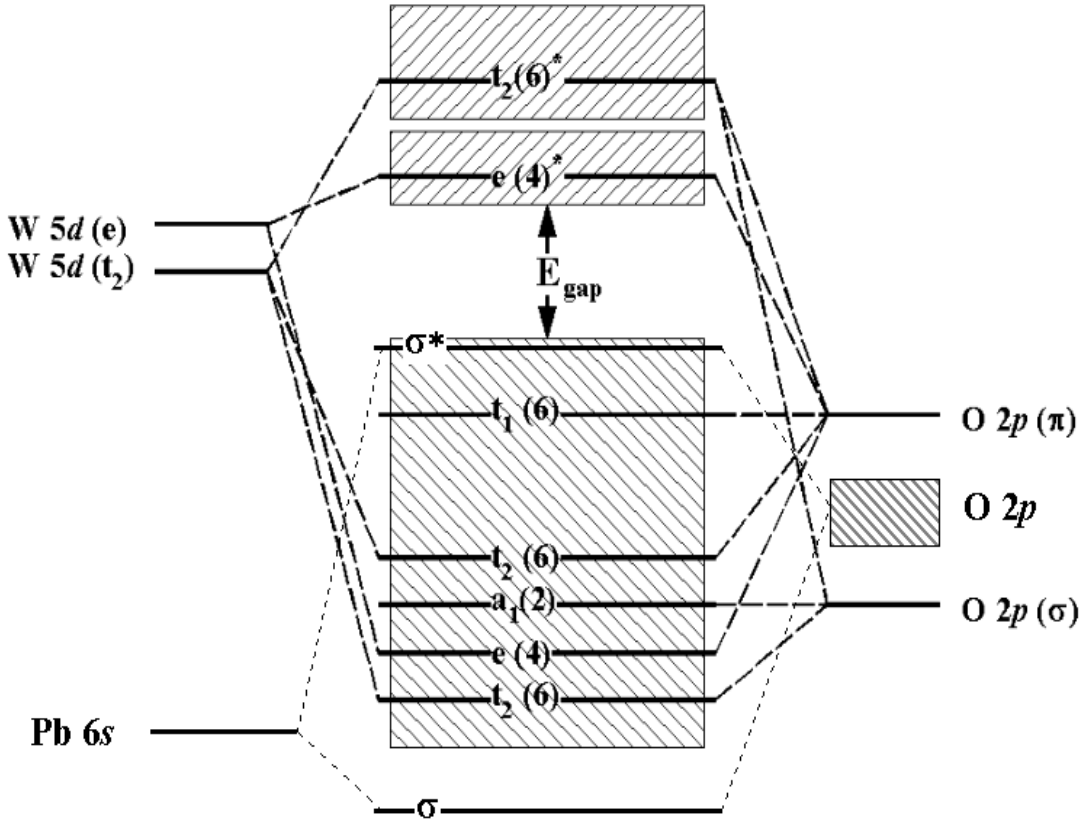

Figure 2. Schematic molecular orbital diagram for W-O and Pb-O interactions superimposed on blocks representing calculated $PbWO_4$ valence and conduction bands.

Experimental confirmation of the Pb6s-O2p character of states at the top of the valence band of $PbWO_4$ can be inferred from consideration of EPR studies of Pb impurity states in $CaWO_4$ by Born, Hofstaetter, and Scharmann [8]. Analysis of the EPR hyperfine analysis showed that $CaWO_4$:Pb exhibits a shallow hole state centered on Pb with approximately 50/50 sharing of the hole between Pb6*s* and the O2*p* ligands [8]. This is in qualitative agreement with the calculated partial densities of states found in a supercell simulation of $CaWO_4$: $PbWO_4$ alloy (at 50% concentration) by the present method [2]. Thus, there are several experimental results which are consistent with our analysis of the role of bonding and antibonding Pb6*s*--O2*p* states in pure $PbWO_4$.

Band dispersion, self-trapping, geminate recombination

The energy dispersion curves of $PbWO_4$ and $CaWO_4$ are compared in Fig. 3. The minimum band gap in $CaWO_4$ is at Γ, whereas in $PbWO_4$ the minimum gap is definitely away from Γ, apparently indirect from Δ to Σ with direct gaps at Δ and Σ lying only slightly higher.[1] The main reason for this difference in the nature of the two band gaps is the highly dispersing band at the top of the valence bands, derived from the Pb6*s*—O2*p* antibonding state discussed above. The band structures in Fig. 3 provide a reasonable basis for understanding what has heretofore been a puzzling mixture of experimental differences and similarities between the two scheelite-structure tungstates $CaWO_4$ and $PbWO_4$, namely:

(a) Self-trapped holes in $CaWO_4$ are observable by EPR with stability up to 150K [9], whereas no EPR of self-trapped holes has been observed in $PbWO_4$ at any temperature.[10] The data in $CaWO_4$ show that the hole autolocalizes on a relaxed pair of (WO_4^{2-}) tungstate groups.[9]

(b) In fact, no significant concentrations of trapped holes in any paramagnetic sites are found in $PbWO_4$ irradiated at low temperature. Yet trapped electron centers including intrinsic self-trapped electrons (see below) are found in $PbWO_4$, so holes reside somewhere, presumably in nonparamagnetic pairings. [11]

(c) Electrons self-trap on an intrinsic tungstate group as WO_4^{3-} in $PbWO_4$, observed by EPR with stability up to 50 K.[12,13] In $CaWO_4$, electrons localize on a tungstate group perturbed by a defect on the neighbor cation site.[9]

(d) The intrinsic blue recombination luminescence in both $CaWO_4$ and $PbWO_4$ has many experimental similarities, and is attributed in both cases to electron-hole recombination on a local tungstate group of the perfect crystal, i.e. a self-trapped exciton on the tungstate sublattice. [14] This similarity of the recombination event in the two materials contrasts with the difference in hole trapping.

Considering the $CaWO_4$ band structure in Fig. 3 and the previous accompanying discussion, we see that the W-O2pπ states at the top of the valence band, to which holes would relax before self-trapping, have narrow dispersion width of about 0.5 eV per band.

The empirical fact that holes self-trap in $CaWO_4$ is at least consistent with the narrow dispersion of the topmost valence band. As discussed by Toyozawa [15], a carrier in a band will self-trap if the local lattice relaxation energy it induces, E_{LR}, exceeds the localization energy equal to half the dispersion width of the band, W/2. Their difference is the thermal trap depth, E_T, of the autolocalized carrier. Herget et al [9] determined that E_T = 0.42 eV for self-trapped holes in $CaWO_4$.

In $PbWO_4$, the similar narrow tungstate energy bands are present near the top of the valence bands, but the dispersive Pb-O band extends 1 eV higher than the tungstate bands. A hole will move from the tungstate groups up into the Pb-O band on a time scale much shorter than needed for self-trapping. Because of the 1-eV width of the Pb-O band, the cost of hole localization from that band is approximately a factor of two higher than in the topmost tungstate valence band. Thus, the single-particle band-structure supports the empirical observation that individual holes in $PbWO_4$ are mobile whereas holes autolocalize in $CaWO_4$. The mobile holes in $PbWO_4$ may find diamagnetic trapping centers or possibly pair into 2-hole singlet self-trapped states of unknown structure.

In view of this difference of hole-trapping in the two materials, what can we understand of the strong similarity of blue recombination luminescence attributed to an exciton autolocalized on the tungstate group in both crystals? It suggests that excitons but not holes self-trap on the tungstate sublattice in $PbWO_4$. There is a well documented precedent for just this behavior in alpha quartz (SiO_2), where excitons are well known to self-trap, but stable self-trapped holes are not found.[16] The fact that the electron self-traps in $PbWO_4$ implies that its interaction with the lattice will contribute to exciton localization. The fact that the electron is known to autolocalize on a tungstate group, not on Pb-O bonds, suggests how it may "anchor" the exciton to a particular tungstate group and so prevent dissipation of the hole wavefunction along the Pb-O valence states.

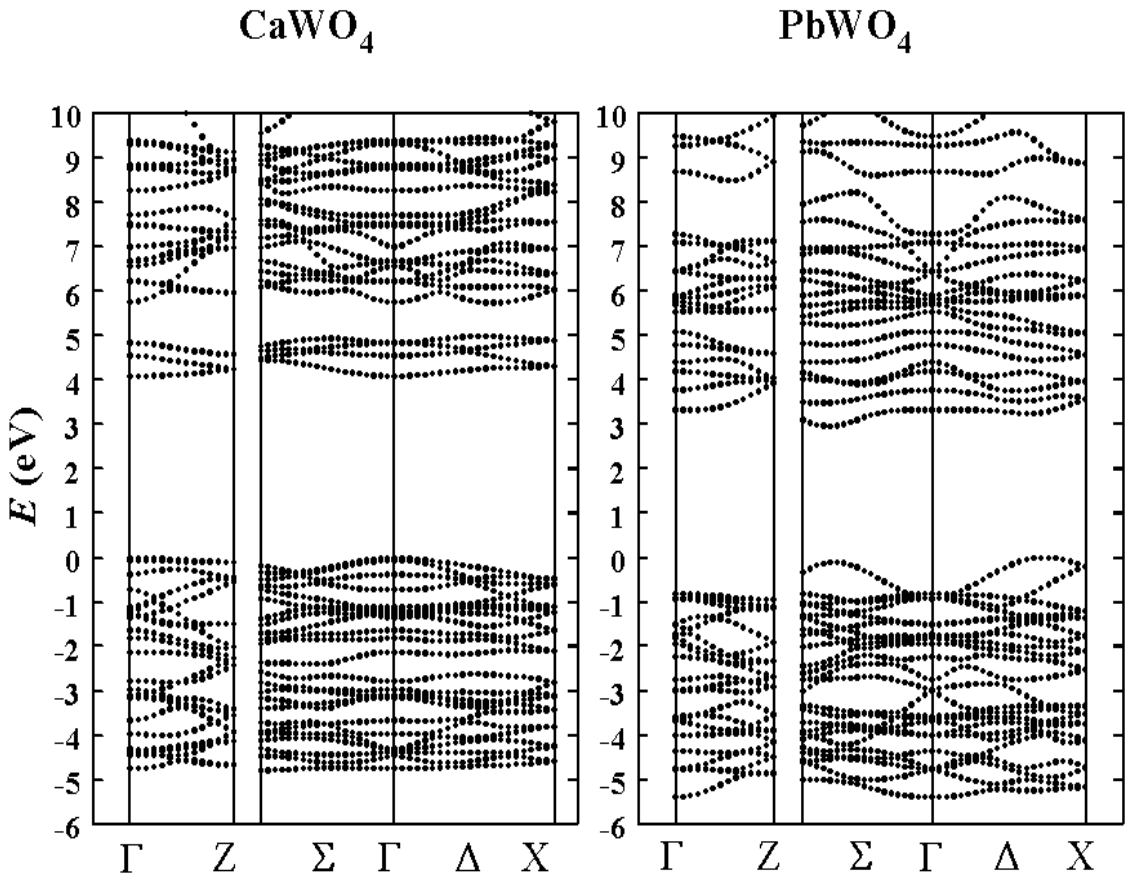

Figure 3. Energy dispersion curves for $CaWO_4$ and $PbWO_4$.

Another difference in the band structures of $CaWO_4$ and $PbWO_4$ which is noticeable in Fig. 3 is that the conduction bands of $CaWO_4$ clearly divide into two groups with a gap of nearly 1 eV between, whereas there is not such a clear division nor a gap in the $PbWO_4$ conduction bands. The lower conduction bands in $CaWO_4$ are composed mainly of W states, whereas the upper group of conduction bands has strong Ca3d character, as previously noted. The conduction bands of $PbWO_4$ have strong W character throughout, with weak hybridization of Pb states. The conduction band character of $CaWO_4$ provides a reasonable basis for understanding the unusually large 2.2 eV difference between the band gap of $CaWO_4$ and the threshold for excitation of thermoluminescence (i.e. production of free carriers which escape geminate recombinaton). [17, 18] Electrons excited to the lower conduction band and holes in the valence band quickly relax to self-trapped excitons and undergo geminate recombination, yielding intrinsic blue luminescence in pure crystals. This route successfully competes with the escape of carriers to defect traps that can be seen in thermoluminescence; hence, the absence of thermoluminescence excitation in the corresponding photon energy range.[17,18] However, photons of energy 2 or 3 eV higher than the band edge can excite electrons into the Ca3d conduction band. Existence of the 1-eV gap retards their scattering into the lower conduction states that contribute to bound exciton states, allowing free-electron transport to charge traps and corresponding thermoluminescence, as observed.

In $PbWO_4$, the offset between the band gap (actually the lowest reflectivity peak) and the threshold of thermoluminescence excitation is smaller, about 0.7 eV. However, this is much larger than the probable exciton binding energy (< 0.1 eV, see below). In Ref. [3], we described a model in which the geminate recombination yield is greatest for excitation of carriers just to the band edges, where electrons are known to autolocalize in $PbWO_4$. Under

the reasonable assumption that polaron mobility becomes higher in states farther from the band edges, non-geminate carrier processes eventually become dominant as the band-to-band excitation energy is raised. The threshold of their dominance is the threshold for thermoluminescence excitation.

Optical constants, reflectivity, and exciton binding energy

Although density functional theory is rigorously a ground-state formalism, there has recently been considerable progress in developing methods to calculate optical properties using density functional results as the starting point [19]. As a first step toward investigating the optical properties, we have calculated the imaginary part of the dielectric constant from the self-consistent LAPW wavefunctions $\psi_{nk}(\boldsymbol{r})$ and one-electron eigenvalues E_{nk}, using the code developed by Abt and Ambrosch-Draxl [20]. There are of course no excitonic effects included in these calculations. Taking the Kramers-Kronig transform of ε_2, we obtain the calculated spectrum of ε_1 after adjusting the calculated band gap and calculated visible refractive index to agree with experiment. [21] Our calculated reflectivity was compared to the experimental measurement by Shpinkov *et al* [22] in Refs. [2,3]. The agreement between the measured and calculated reflectivity for $PbWO_4$ is surprisingly good. The sharp peak in the calculated spectrum at the band edge is due to a near singularity in the joint density of single-particle states. Since no lower-energy discrete features are found in the experimental spectrum, we conclude that whatever exciton discrete states are observable in the absorption spectrum should have a low binding energy compared to the ~0.3 eV width of the experimental reflectivity peak. The suggestion of a small exciton binding energy in $PbWO_4$ was supported by consideration in Ref. [3] of the measured optical and static dielectric constants for $PbWO_4$ which are quite large -- $\varepsilon_1(1.9\text{ eV}) \equiv \varepsilon_{opt} = 5.06$ [21] and $\varepsilon_1(0\text{ eV}) \equiv \varepsilon_{static} = 23.6$, respectively, for a-axis polarization.

Defects and dopants

Defects and dopants in the tungstate crystals have been studied using the present calculation method adapted for a supercell of two normal unit cells, in one of which the imperfection is introduced. The defects studied in this way are effectively at 50% alloy composition. The method and results for $CaWO_4$:Pb were described in Ref. [2]. In the present paper, we report results obtained in this way for Pb vacancies, Bi impurity substituting for Pb, and La impurity substituting for Pb in the $PbWO_4$ crystal. Figure 4 shows the valence and conduction band partial density of states curves for each of the three defects alongside the partial DOS for perfect $PbWO_4$. Lattice relaxation around the defects has not yet been included in these results.

Pb vacancy -- Pb vacancies in $PbWO_4$ are hole traps considered important in radiation damage and charge transport. [10,11] In the case illustrated in Fig. 4, removal of 50% of the neutral Pb atoms from the crystal leaves it noticeably electron deficient, with the Fermi level moving about 0.5 eV below the top of the valence band. There are no new states introduced deep in the gap. The conduction band edge states seem somewhat more separated from the main conduction band in the crystal with vacancies, but it is not clear that a gap state has split off from the conduction band. As expected from doubling of the unit cell size, the bands are narrower in the crystal with periodic vacancies, and charge becomes more localized on the Pb6s-O2p bonding state. The top of the valence band has a stronger Pb-O character in the defective than in the perfect crystal, implying that holes will exist largely on oxygen and on the Pb ions neighboring the Pb vacancy. The calculation confirms the experimental evidence [10,11] that Pb vacancies do not introduce a deep mid-gap trap, but rather a shallow acceptor level.

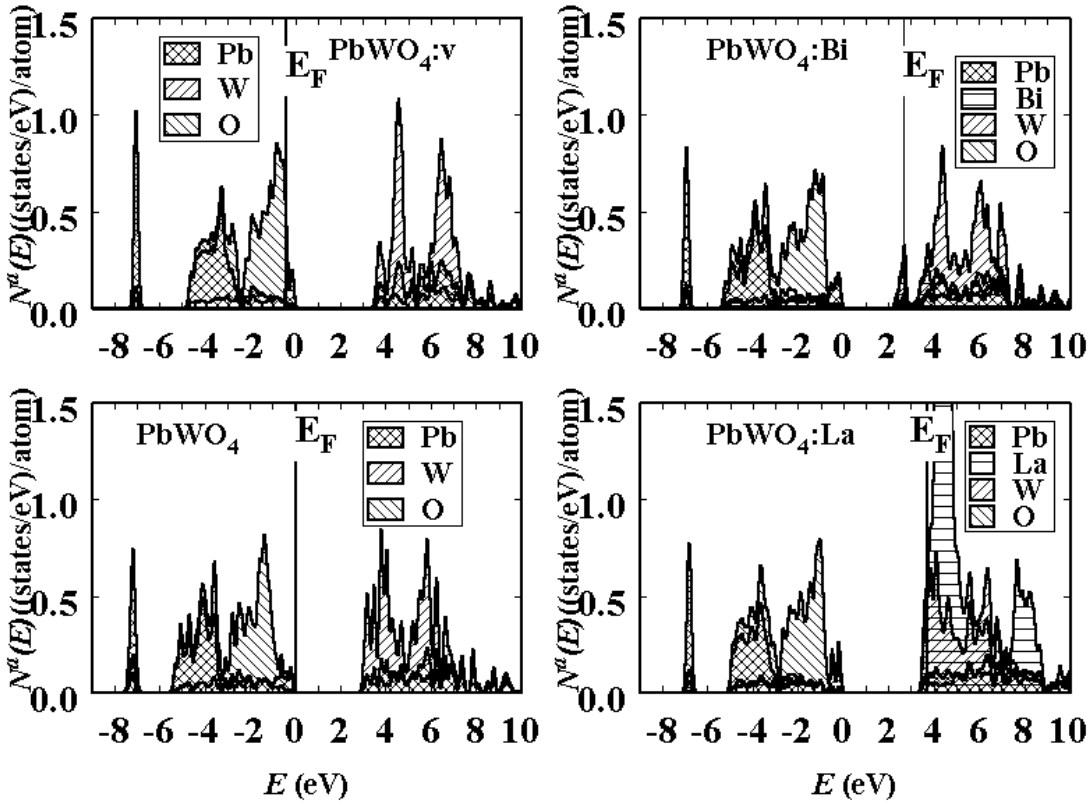

Figure 4. Partial densities of states data calculated for pure $PbWO_4$, Pb vacancies "$PbWO_4$:v", and Bi and La substitutional impurities ("$PbWO_4$:Bi" and "$PbWO_4$:La", respectively). The defects are effectively at 50% concentration, calculated in a supercell adaptation of the LAPW method used for pure $PbWO_4$. The Fermi levels are marked as E_F and the zero of energy is taken to be at the top of the oxygen bands.

$PbWO_4$:Bi --Bismuth has one higher atomic number than Pb, and so should act as a donor when substitutionally incorporated in $PbWO_4$. Using the same supercell approach, every alternate Pb was replaced by Bi. The partial DOS plot is shown in Fig.4. A distinct, partially filled band occurs in the upper band gap. It is not simply composed of Bi states, but has a nearly equal contribution from W ions, forming the localized gap state.

$PbWO_4$:La -- Lanthanum ionizes to La^{3+} when substituted for Pb in the $PbWO_4$ host, contributing an extra electron per La atom incorporated. The Fermi level lies in the bottom of the conduction band for this 50% alloy composition. The DOS shoulder at the top of the valence band in Fig. 4 seems enhanced with La incorporated. There is a very strong DOS contribution from La in the lower conduction band states. Note that in contrast to Bi, the La dopant acts as an electron donor without simultaneously introducing a new state in the band gap. This agrees with experimental observations on the role of La dopant in $PbWO_4$, which is that it has the beneficial effect of donating electrons to fill potential hole traps and thus improve post-radiation transparency, without itself introducing absorption bands that adversely affect transparency. The La contribution to the valence bands is f-like in the intense lower peaks, and d-like in the peaks at higher energy.

Cadmium tungstate, $CdWO_4$

Band structure calculations for $CdWO_4$ (having wolframite structure) and $CdMoO_4$ (having scheelite structure) have recently been undertaken using the same calculation method. The detailed results will be presented in a future publication, but because of the importance of

cadmium tungstate as a medical imaging scintillator and basic interest in comparing a tungstate crystal having wolframite structure with results on scheelite structure discussed above, we would like to briefly present some of the preliminary results here. In the wolframite structure, oxygen ions are arranged with 3 different bond lengths in approximately octahedral symmetry around the tungsten ions, in contrast to the 4 equal bond lengths in nearly tetrahedral symmetry of oxygens around tungsten in the scheelite materials such as $CaWO_4$ and $PbWO_4$. Oxygen has an approximate octahedral arrangement around Cd sites in $CdWO_4$, roughly as it does around Ca and Pb in the respective scheelite tungstates.

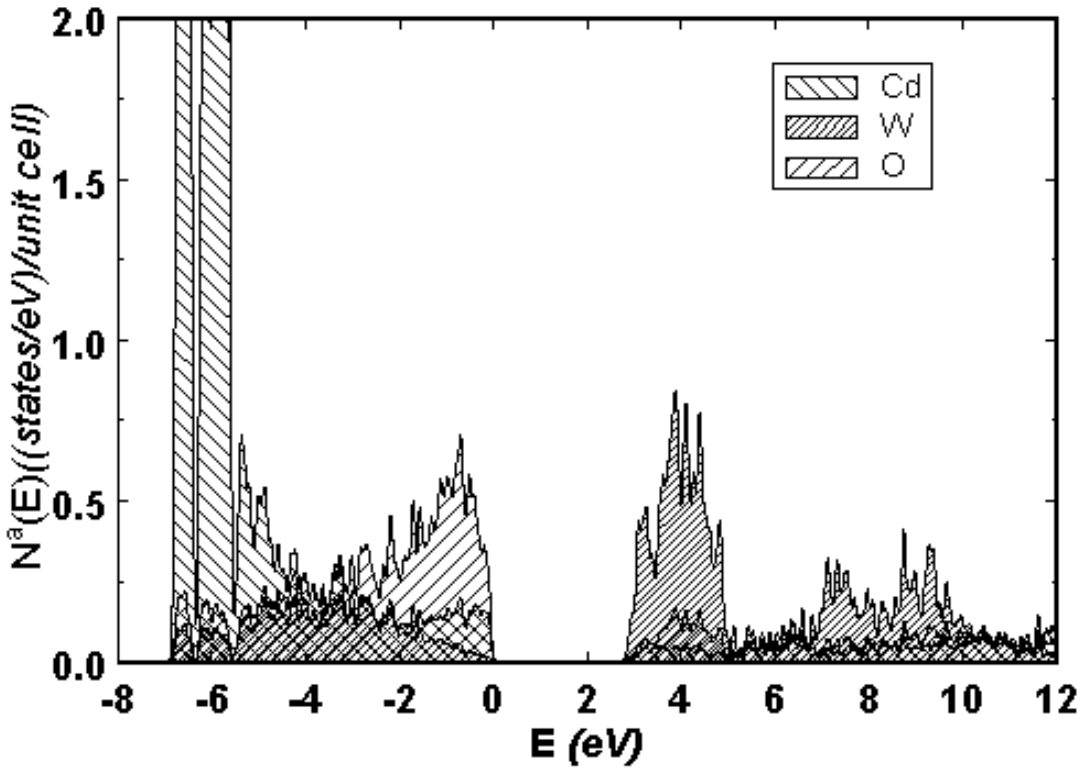

Figure 5. $CdWO_4$ partial densities of states.

The partial density of states plot for the valence and conduction bands is shown in Fig. 5. Oxygen 2*p* states dominate the top of the valence band, with some contribution from Cd, but very little from W. The bottom of the valence bands is dominated by Cd 4*d* states, while the middle of the valence band has some W 5*d* contribution. It is noticeable that the valence bands do not exhibit the clear grouping into O2*p*σ bonding and O2*p*π nonbonding combinations with tungsten as was seen in $CaWO_4$ and $PbWO_4$. That basic structure still characterizes the valence band to be sure, but perhaps because of the lower symmetry, the notch of demarcation between the two groups is not evident for $CdWO_4$. While Cd-O orbitals are dominant at the top of the valence band, there is no indication of a Cd-O band isolated from the W-O bands as was found in $PbWO_4$.

The conduction bands group into two regions derived primarily from the W 5*d* states, the lower band is derived from "t_2" molecular orbitals while the upper band is derived from "e" orbitals. It is interesting that this is the reverse of the ordering of conduction band states found in the scheelite crystals studied previously. That is, in $CaWO_4$ and $PbWO_4$, the "e" states comprise the lower conduction bands and the t_2 states the upper. This reversal can be explained by the following symmetry considerations. In both the wolframite and scheelite tungstates, the conduction band is dominated by the crystal field split W 5*d* orbitals with the

weakly bonding state forming the lower conduction band and the more strongly antibonding state forming the upper conduction band. In the octahedral geometry (wolframite structure) the "t_2" orbitals are approximately directed *between* the bond directions while "e" orbitals are approximately directed *along* the bond directions. In the tetrahedral geometry (scheelite structure), the "e" orbitals are approximately directed *between* the bond directions while "t_2" orbitals are approximately directed *along* the bond directions. Nagirnyi has also concluded from polarization of the intrinsic luminescence that the ordering of the e and t_2 conduction states is reversed in $CdWO_4$ relative to $PbWO_4$.[23]

The energy dispersion curves calculated for $CdWO_4$ cannot be presented here for lack of space. They show that the minimum band gap does not occur at Γ but at Y, which is at the zone face center along the b crystal axis. The top of the valence band has narrow dispersion. The lowest conduction band has relatively wide dispersion relative to the tungstate crystals considered previously. The preliminary calculated reflectivity spectrum of $CdWO_4$ has only a broad peak above the band edge, in contrast to the sharp structure of $PbWO_4$ reflectivity, but in approximate agreement with the experimental observation of only very weak reflectivity structure above the band edge of $CdWO_4$.[18]

Acknowledgments

We acknowledge support by NSF grants # DMR-9403009, -9706575, and -9732023. We would like to thank A. Hofstaetter, M. Nikl, and N. Nagirnyi for helpful discussions and sharing of unpublished data.

References

1. Y. Zhang, N. A. W. Holzwarth, and R. T. Williams, Phys. Rev. B **57**, 12738 (1998).
2. N. A. W. Holzwarth, Y. Zhang, and R. T. Williams, International Workshop on Tungstate Crystals, Roma, October 12-14, 1998.
3. Y. C. Zhang, N. A. W. Holzwarth, R. T. Williams, and M. Nikl, Proc. 3rd Int'l Conf. on Excitonic Processes in Condensed Matter, ed. by R. T. Williams and W. M. Yen (The Electrochemical Society, Pennington, N. J., 1999) p. 420.
4. P. Blaha, K. Schwarz, and J. Luitz, WIEN97, Vienna University of Technology, 1997 [Improved and updated Unix version of the orginal copyrighted WIEN code, which was published by P. Blaha, K. Schwarz, P. Sorantin, and S. B. Trickey, Comput. Phys. Commun. **59**, 399 (1990)].
5. A. Hofstaetter, B. K. Meyer, W. Niessner, and I. Oesterreicher, private communication.
6. I. A. Shpinkov, I. A. Kamenskikh, V. N. Kolobanov, and V. V. Mikhailin, CMS Document 1996-213, 2nd Annual RDMS CMS Collaboration Meeting, CERN, Dec. 16-17, 1996 (unpublished).
7. C. J. Ballhausen and A. D. Liehr, J. Mol. Spectrosc. **2**, 342 (1958).
8. G. Born, A. Hofstaetter, and A. Scharmann, Z. Physik **245**, 333 (1971).
9. M. Herget, A. Hofstaetter, T. Nickel, and A Scharmann, Phys. State. Sol. (b) **141**, 523 (1987).
10. S. Baccaro et al, Proc. Intl. Workshop on Tungstate Crystals, Rome, Oct. 1998.
11. A. Annenkov, E. Auffray, M. Korzhik, P. Lecoq, and J. –P. Peigneux, phys. stat. sol. (a) **170**, 47 (1998).
12. V. V. Laguta, J. Rosa, M. I. Zaritskii, M. Nikl, and Y. Usuki, J. Phys. Cond. Matter **10**, 7293 (1998).

13. Böhm, F. Henecker, A. Hofstaetter, M. Luh, B. K. Meyer, O. V. Kondratiev, and M. V. Korzhik, Proc. of European Conference on Defects in Insulating Materials, EURODIM98, Keele, UK, July 6-11, 1998.
14. S. G. Nedel'ko et al, in Proc. of SCINT95 (Delft University Press, Delft, 1996) 263.
15. Y. Toyozawa: Electrons, holes, and excitons in deformable lattice, in *Relaxation of Excitations*, Springer Ser. Solid State Sci., Vol. 18, ed. By R. Kubo, E. Hanamura (Springer, Berlin, Heidelberg, 1980), p. 3.
16. W. Hayes, M. H. Kane, O. Salminen, R. L. Wood, and S. P. Doherty, J. Phys. C **17**, 2943 (1984); W. Hayes and T. J. L. Jenkin, J. Phys. C **19**, 6211 (1986); K. S. Song and R. T. Williams, Self-Trapped Excitons, Springer Ser. In Solid State Sci., Vol 105 (Springer, Berlin, Heidelberg, 1993) p. 293.
17. V. Mürk, M. Nikl, E. Mihokova, and K. Nitsch, J. Phys.: Condens. Matter 9, 249 (1997).
18. V. Nagirnyi, E. Feldbach, L. Jönsson, M. Kirm, A. Kotlov, A. Lushchik, L.L. Nagornaya, V. D. Ryzhikov, G. Svensson, I. A. Tupitsina, M. Åberg-Dahl, Proc. Workshop on $PbWO_4$, Rome, Oct. 12-15 (1998).
19. R. Del Sole and R. Girlanda, Phys. Rev. B **48**, 11789 (1993); M. Rohlfing and S. G. Louie, Phys. Rev. Lett. **81**, 2312 (1998).
20. R. Abt, C. Ambrosch-Draxl, and P. Knoll, Physica B **194-195**, 1451 (1994).
21. G.F.Bakhshieva and A.M.Morozov, Sov.I.Opt.Technol. **44**(9), 542 (1977).
22. I. N. Shpinkov, I. A. Kamenskikh, M. Kirm, V. N. Kolobanov, V. V. Mikhailin, A. N. Vasil'ev, and G. Zimmerer, phys. stat. sol. (a) **170**, 167 (1998).
23. V. Nagirnyi, International Conference on Luminescence, Osaka, August 23-27, 1999.

Spectroscopic characterization of defects in tungstate scintillators

A. Hofstaetter[1], H. Alves[1], M. Böhm[1], D.M. Hofmann[1], O.V. Kondratiev[2], M.V. Korzhik[2], V.V. Laguta[3], M. Luh[1], V. Metag[4], B.K. Meyer[1], R. Novotny[4], N.G. Romanov[5], A. Scharmann[1], A. Vedda[6], A. Watterich[7]

[1] *1st Physics Institute, University of Giessen, H.-Buff-Ring 16, D35392 Giessen, Germany*
[2] *Institute for Nuclear Problems, 11 Bobruiskaya, 220050 Minsk, Belarus*
[3] *Frantsevich Institute (IPMS), 3 Krzhizhanovsaya, 252180 Kiev, Ukraine*
[4] *2nd Physics Institute, University of Giessen, H.-Buff-Ring 16, D35392 Giessen, Germany*
[5] *A.F. Ioffe Institute, 26 Polytekhnicheskaya, 194021 Sankt Petersburg, Russia*
[6] *Dipt. di Scienza dei Materiali, Univ. di Milano, via R. Cozzi 53, 20125 Milano, Italy*
[7] *Res. Inst. Sol. St. Phys. & Optics, Konkoly-Thege M. út 29 – 33, Budapest H-1121, Hungary*

Abstract: Various electron centres analyzed by Electron Paramagnetic Resonance play an important role in radiation-induced processes like Thermally Stimulated Luminescence in lead tungstate (PWO). Among them an intrinsic $(WO_4)^{3-}$ centre contributing to the characteristic glow peak near 50 K gives also valuable hints with respect to the electronic structure of PWO and its luminescence. In slightly disturbed form - with a threevalent ion nearby - this trap is responsible for TSL emission near 100 K. Other more deep centres are localized at cationic sites, some of them being metastable at room temperature. Charge state of several impurities including such used as dopants has been shown to depend on annealing procedures and IR illumination. No paramagnetic hole type centres have been observed until now. This is accompanied by the fact that in PWO the trapped electrons become mobile at elevated temperatures, whereas in other tungstates like $BaWO_4$ and $ZnWO_4$ (self)trapped holes are the mobile species initiating similar TSL emissions. First results of Optically Detected Magnetic Resonance on the luminescence of PWO give hope for a quantitative understanding of its nature in the near future.

Keywords: $PbWO_4$, $BaWO_4$, $ZnWO_4$, magnetic resonance, defect centres

Introduction

A thorough understanding of its defect structure is essential for any scintillator material since during application it always will be exposed to ionizing radiation. For more complicated ternary compounds like the tungstates this is an extensive task as can be seen e.g. from the numerous investigations on lead tungstate published after it has been selected for the CMS detector at CERN. Inspite of great progress in growing large crystals of reproducible high quality some models for centres responsible for the radiation damage in $PbWO_4$ are still far from being proved. One of the exceptions is an intrinsic $(WO_4)^{3-}$ centre created by ionizing radiation at low temperatures [1]. EPR results prove for this paramagnetic defect the regular axial symmetry of the tungsten site and the complete neighbourhood of eight lead cations to be preserved. From this and from the characteristic structure of the g tensor describing the resonances it is evident that the molecular character of the tungstate group is very pronounced in PWO, too, as also revealed by band structure calculations [2]. It explains the large superhyperfine interaction with the ^{207}Pb nuclei showing up in the spectra [3] and the stabilization by a Jahn-Teller effect acting on the ^{2}E state of the $(WO_4)^{3-}$ complex. Following the thermal decay of the centre its trap depth was determined to be 50 meV [1]. With this value and the frequency factors derived from the decay curves a nearly perfect fit of the TSL

glow peak near 50 K is possible proving that electrons stemming from $(WO_4)^{3-}$ centres are responsible for this emission [4].

Disturbed $(WO_4)^{3-}$ centres: $(WO_4)^{3-}$ - La^{3+}

In some crystals doped with threevalent ions (Y, La, Lu) part of the electrons released from the intrinsic centre are retrapped at $(WO_4)^{2-}$ sites with slightly different surrounding, one of the lead neighbours in the (001) plane being replaced by the impurity. The additional electrical field along a [110] direction caused by the surplus charge splits the resonances of this paramagnetic species under a rotation around [001] into two branches [3], the lacking Pb neighbour changes the superhyperfine pattern in a characteristic way. This is observed very nicely for $(WO_4)^{3-}$ - Y^{3+}, in case of Lu [3] and La (Fig. 1) it is masked by the hyperfine lines due to the interacton with these I = 7/2 nuclei.

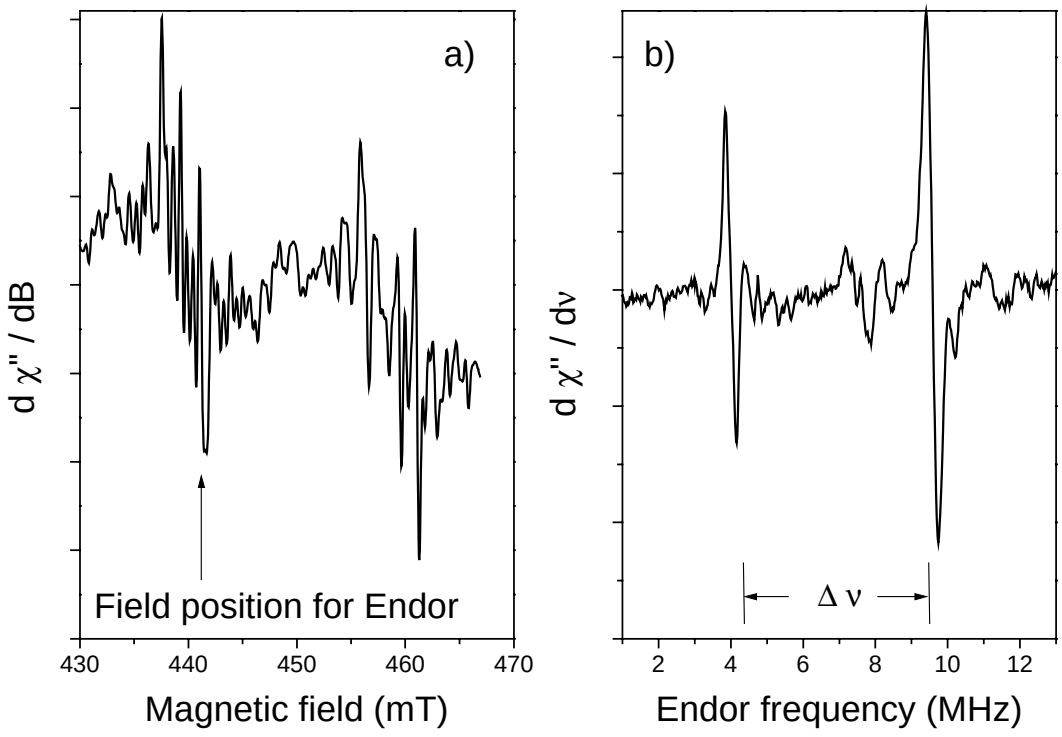

Fig. 1: a) EPR spectrum of PWO: 80 ppm La after X-irrad. at T = 4 K and heating to 75 K
B II [110], ν = 9.5 GHz, T_{Meas} = 20 K
b) Endor resonances measured on the EPR line at B = 442 mT; T_{Meas} = 10 K

Endor measurements performed on this centre unambiguously prove that the new manifold of lines is really due to the interaction with ^{139}La since the frequency separation $\Delta\nu$ = 5.32 MHz between the Endor doublet exactly corresponds to the difference in nuclear Zeeman splitting for this nucleus at the external field used. For the sake of completeness it should be mentioned that quadrupole interaction makes the Endor spectra much more complicated in other regions of the EPR spectra.

As can be seen by their creation when heating the samples to 75 K thermal stability of the disturbed centres is higher than that of the intrinsic ones. Unfortunately their decay cannot be followed directly because of strong line broadening as result of faster spin-lattice relaxation with increasing temperature. We therefore used another approach: First the crystal was

irradiated and heated to 75 K in order to create $(WO_4)^{3-}$ - La^{3+}. Its EPR spectrum was then recorded under identical conditions at T = 20 K before and after a two minutes anneal at elevated temperatures. The experimental results are shown in Fig. 2 by the squares.

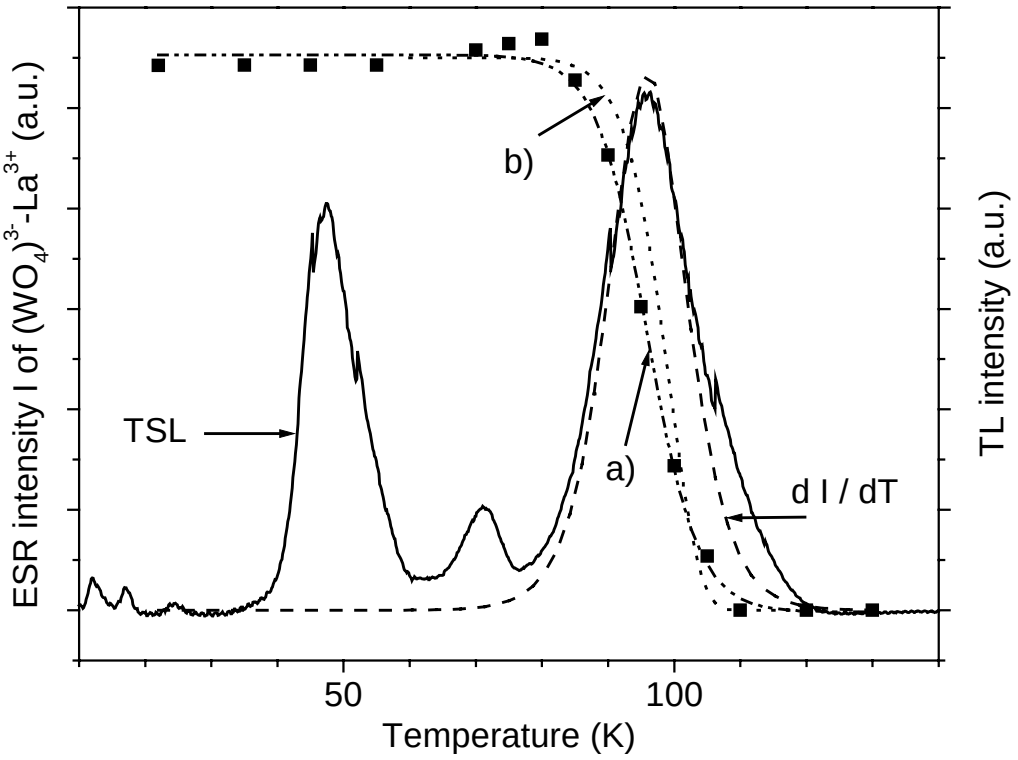

Fig. 2: Comparison of TSL emitted by a PWO: 80 ppm La crystal X-irr. at T = 4 K (50 kV, 20 mA, appr. 50 Gy) and thermal stability of $(WO_4)^{3-}$ - La^{3+} centres

Temperature dependence of the EPR intensity I was then fitted by a Boltzmann equation

$$I = \frac{I_{Start} - I_{End}}{1 + e^{(T - T_0)/\Delta T}} + I_{End} \qquad \text{(curve a)}$$

resulting in T_0 = 96 K. Decay rate of centres as function of temperature given by the first derivative dI/dT of this dependence runs practically parallel to the glow peak at 97 K, beside a small high temperature shoulder on the latter. This second unambiguous prove for a direct correlation between a TSL peak in PWO and a well-defined electron centre identified by EPR is further supported by a theoretical calculation of the decay using trap parameters derived from an analysis of the TSL curves: Within a systematic study of TSL emissions of a variety of PWO crystals [5] in Y- and La-doped samples this 97 K peak was shown to be characterized by a thermal activation energy of 190 meV and a frequency factor S of about 10^9 s^{-1}. Using these data together with the calculated heating rate of the experiment curve b was obtained which very well fits the data measured.

The correlation to the $(WO_4)^{3-}$ - La^{3+} centre becomes nicely clear also from another fact: If the electron trapped at the W site is neighboured by one triply positive ion 0.386 nm apart it will feel the attractive force of one additional elementary charge. Taking into account the dielectric constant ε = 23.6 [6] of PWO this results in an electrostatic energy of 0.158 eV which accounts in very good approximation for the difference in thermal activation energies for the intrinsic and for the disturbed centre.

The recombination partners for the electrons released from both traps are still unknown. It is, however, obvious that there is not only one recombination process responsible for the TSL peaks near 50 and 100 K since the maxima of their spectral composition vary in different crystals from 444 to 484 nm (2.79 to 2.56 eV) for emissions connected to the 50 meV trap and from 443 to 477 nm (2.8 to 2.6 eV) for those connected to the 190 meV one [5]. At the first glance that points to a situation where the electrons are ionized into the conduction band and then recombine at different acceptor sites. On the other hand overall situation with PWO seems to be more complicated as indicated by the onset of photoconductivity under excitation in the spectral range between 250 and 350 nm only above 150 K [3] and the finding of Mürk et al. [7] that free electrons and holes are not created below this temperature. This could mean that the thermal activation at lower temperatures takes place only into an upper localized level with much higher probability for hopping to neighbouring sites. Only at higher temperatures the lattice vibrations then compete successfully with the localization mechanisms as evidenced e.g. by thermal quenching of the luminescence. In any case a charge transport occurs as seen by the thermally stimulated currents observed parallel to both TSL glow peaks and by the retrapping increasing the occupation number of other electron traps like $(MoO_4)^{2-}$.

Another complication with respect to the TSL of PWO lies in the fact that near 50 K as well as near 100 K not only one trap gets emptied. Our analysis [5] showed there to contribute also such with a thermal activation energy of 70 meV respectively 270 meV. So often one has an overlapping of several peaks as indicated by the shoulder in Fig. 2, and it makes no sense to speak of “the 100 K peak”.

Paramagnetic centres of type X_{Pb} - V_O

Our knowledge concerning these centres is still rather restricted compared to that on the species mentioned above. The assumption of a neighbouring oxygen vacancy is motivated by the typical site splitting observed in their spectra (Fig. 3) since for W and Pb only one magnetically nonequivalent site exists, for the oxygen ligands, however, four.

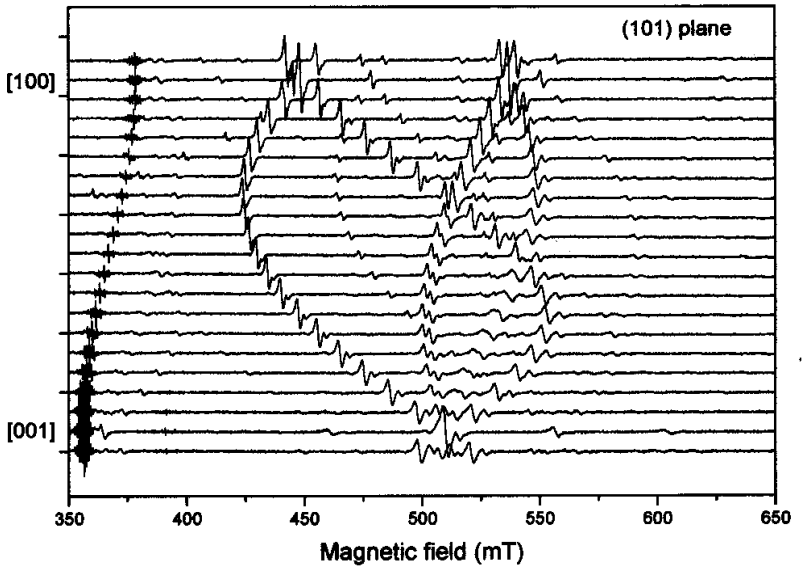

Fig. 3: Angular dependence of Pb^+(?) - V_O for an [010] rotation

The tentative assignment of these resonances to Pb^+ is based on the observation of two hyperfine lines accompanying each EPR line - best seen in the spectrum taken at orientation [001] - having the intensity ratio expected for ^{207}Pb. In addition, g and hyperfine values are in the typical range of Pb^+ [8]. On the other hand the overall hyperfine splitting of this centre is

rather complicated and might be influenced by saturation effects. So for a final proof of this assignment further experiments are necessary.

Altogether we observed at least five centres of this type, most of them having g values smaller than the value $g_e = 2(.0023)$ of the free electron, but one also with a larger one. In all cases the g shift, that means the deviation from g_e, is rather large. This excludes that the resonances are due directly to oxygen vacancies since in that case the spin-orbit coupling responsible for the g shift would be to small. So we attribute at this stage of the investigations the unknown species X mainly to metal ions like Cd or Ni replacing Pb cations. Thermal stability of the X_{Pb} - V_O species we checked only qualitatively until now. The Pb^+(?) related defect is destroyed when heating to 200 K, others can be created at room temperature and are metastable there. By this those are of course of special interest with respect to the application of PWO under CMS conditions. Since the existence and intensity of this type of centres differs from sample to sample and is strongly influenced by annealing processes a systematic study is a very wide task and far from being completed.

Influences of external treatments

Changes in presence and intensity of paramagnetic species as well as of TSL peaks due to annealing or illumination have been observed by us quite often showing that many experimental findings in PWO depend very much on the history of the sample used. So for instance annealing the lanthanum doped sample discussed in Figs. 1 and 2 at 850 ^{0}C in oxygen inverts the intensity ratio of the TSL peaks near 70 and 100 K and leaves the 50 K peak unchanged. In parallel the number of $(WO_4)^{3-}$ - La^{3+} centres created by the procedure described earlier is much smaller in the annealed sample. The most logical explanation for that is a conversion of La^{3+} into another charge state since a threevalent neighbour is necessary to stabilize this centre.

Unfortunately La^{3+} is not paramagnetic, so we cannot monitor it directly by EPR. This is, however, possible with Eu^{2+} which we observed in PWO for the first time [9]. Its paramagnetic resonance is unambiguously identified via its hyperfine structure due to the interaction with ^{151}Eu and ^{153}Eu nuclei and has an angular dependence characteristic for axial symmetry. This shows that Eu^{2+} is incorporated at regular cationic Pb^{2+} sites. By annealing in oxygen at 850 ^{0}C the EPR intensity of Eu^{2+} is reduced by a factor 20, and in TSL the same changes are observed as for PWO:La. That the situation is not so simple and straightforward can be seen from the fact that a following annealing in Ar using the same conditions brings the EPR intensity of Eu^{2+} back to the initial value but leaves the TSL nearly unchanged compared to the oxidized situation.

Further evidence that the annealing process does not just cause conversion of Eu_{Pb} from 2+ to 3+ and back can be found from luminescence spectroscopy since in the as received crystal as well as after annealing in oxygen respectively argon we see always the same intensity of the characteristic $^5D \rightarrow {}^7F$ transition of Eu^{3+} in S_4 symmetry. This implies that for Eu^{2+} and its changes a more complex defect structure is responsible, probably including close pairs of Eu^{3+}-e^-. Finally it should be mentioned that the regular PWO luminescence also drastically changed, increasing under oxygen and decreasing under subsequent argon annealing, which shows the importance of the overall defect structure for the performance of PWO.

Changes in charge state or electronic configuration following high temperature treatments in different atmospheres we have observed until now for Eu, Gd, La (indirectly), Mn and Cu. This means that such processes obviously play some role in PWO and one has to take into account the possibility that dopants are present in the crystal in another valency than planned.

As an especially interesting example the results for a nominally pure crystal shall be presented. This sample showed in the as grown state a very poor luminescence with unusual strong emission in the red. After annealing part of it in oxygen at 980 ^{0}C the usual PWO luminescence was restored. When we compared both samples in EPR we found in the as grown one some amount of Eu^{2+} which was absent in the annealed one, as expected. Instead now rather strong resonances due to Mn^{2+} and Cu^{2+} were observed [10]. These impurities certainly did not enter during the treatment but were present before, copper most probably in 1+ state. Partly it exists in this state in form of a complex Cu^{+}-X^{3+} with a suitable neighbour nearby also in the annealed sample. This gives rise to an interesting photostimulated phenomenon: By excitation with IR light (1080 nm, E = 1.15 eV) the electron is transferred to the neighbour and another Cu^{2+} centre appears. In contrast to the first one it is not stable but decays near 23 K when the electron thermally activated moves back to the neighbour. More details will be given elsewhere [10]. With respect to the discussion about different phases of PWO like raspite it should be noted here that this complex is formed only at rather high temperatures. Annealing the as grown sample at 850 ^{0}C only creates normal Cu^{2+} and Mn^{2+}. This might indicate that very high diffusion and reorientation rates are necessary, including perhaps even local structural changes.

EPR and TSL of $BaWO_4$ and $ZnWO_4$

Like in many other tungstates 11], (self)trapped holes of O^- type can easily be created in both materials by X-irradiation at sufficiently low temperatures. They become mobile above 50 K and give rise to characteristic TSL emissions (Fig. 4).

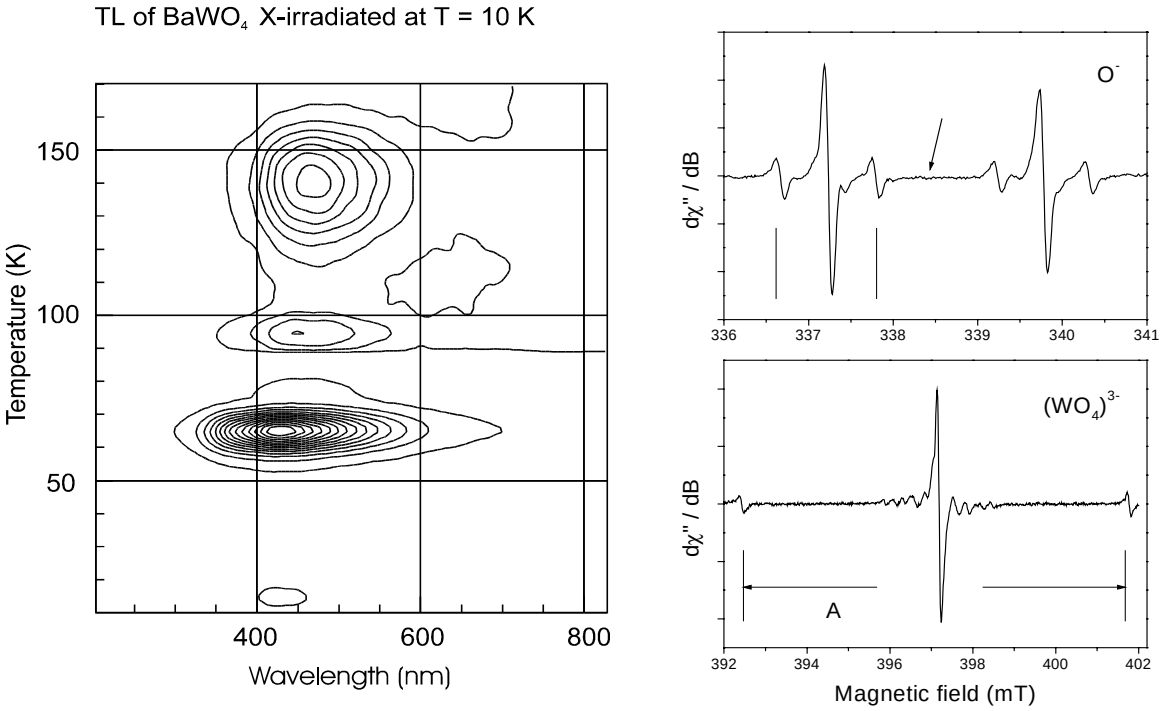

Fig. 4: TSL of $BaWO_4$ after X-irrad. at 10 K and paramagnetic centres created by this irradiation

While in $ZnWO_4$ the intrinsic hole due to the monoclinic symmetry of the crystal with different W - O bond lengths experiences at low temperatures inequivalent hyperfine interaction with two tungsten neighbours which averages out with raising temperature as result of thermally activated hopping between two oxygen sites [12] it is characterized in the

scheelite $BaWO_4$ by an equivalent one. This manifests on one hand in the higher intensity of the hyperfine lines stemming from the situation that now both W neighbours have the 14.3 % probability to be ^{183}W, on the other hand also the case that both belong to this isotope resulting in total nuclear spin I = 1 can be seen in form of the small lines indicated by an arrow.

In both materials in the temperature range between 50 and 70 K the holes recombine yielding blue TSL for $BaWO_4$, blue-green for $ZnWO_4$, close to the intrinsic luminescence of these crystals. Partly they convert into extrinsic hole centres like OH^-, $(PO_4)^{2-}$ or $(NbO_4)^{2-}$. This together with the fact that the electron centres present in the samples do not completely vanish during this process gives clear evidence that in these tungstates the intrinsic holes are the mobile species, in contrast to electrons in PWO.

Some electron traps observed in $BaWO_4$ and $ZnWO_4$ are related to tungstate or molybdate complexes, too. In zinc tungstate, as in $CaWO_4$, $(WO_4)^{3-}$ type centres can be stabilized only by some defect in the neighbourhood like in case of $(WO_4)^{3-}$ - La^{3+}. In $BaWO_4$, however, the puzzling situation occurs that a $(WO_4)^{3-}$ centre is found which preserves the full axial symmetry of the W site and by that resembles very much the intrinsic electron centre in PWO. To be sure that we really deal with centres related to tungsten we performed again Endor experiments on the hole as well as on the electron resonances. They unambiguously prove that we observe in both species a hyperfine interaction with a ^{183}W nucleus. The reason for this apparently simultaneous existence of intrinsic hole and electron centres has still to be found out, not at last by theoretical calculations of the band structure for $BaWO_4$. Maybe this compound with its moderate compression of the tungstate tetrahedra is something like a link between PWO and the scheelites with more compressed oxocomplexes. In any case $(WO_4)^{3-}$ is a deeper trap in $BaWO_4$ than in PWO. This results in much higher thermal stability, a bigger hyperfine splitting A from the interaction with ^{183}W and a relatively smaller one with the Ba neighbours (seen as group of tiny lines on both sides of the central EPR line) due to a stronger localization of the wave function of the trapped electron on the tungsten site.

Results of optically detected magnetic resonance

Under excitation with a He-Cd laser (λ = 325 nm, P ≈ 10 mW) at T = 1.7 K all samples studied in our ODMR setup showed a broad luminescence peaking near 505 nm (Fig. 5, left part). In two crystals (one doped with Nb, the other with Eu) we could detect on this emission magnetic resonance signals via a resonant increase of the luminescence intensity (Fig. 5, right part) under the action of 24 GHz microwave quanta.

As in the case of $CaMoO_4$ and $CaWO_4$:Mo [13] the results are typical for the emission from a triplet state of an anionic complex which undergoes a distortion along one of the four X - O bonds most probably caused by a (Pseudo-) Jahn-Teller effect. Due to this structural change four orientations fixed in the crystal lattice exist for the fine structure tensor splitting the triplet sublevels already in zero field. For orientations of of an applied external magnetic field closest to these distinguished directions the resonance positions run through a minimum as seen in the right part of Fig. 5. This experimental situation repeats in the (001) plane every 90^0 showing that the luminescence really stems from a XO_4 unit.

The angle of $36(+n\cdot 90)^0$ with respect to [100] corresponding to these turning points clearly reflects the respective rotation of the anionic tetrahedra about the [001] axis typically for the scheelites. Unfortunately we could not resolve until now any hyperfine structure on the signals, so the question for the nature of the central ion in the emitting complex remains open at the moment. In addition, not in all crystals we were able to detect such ODMR signals. This points strongly to the situation known from $CaWO_4$ where different sources exist for broad green luminescence bands with nearly the same wavelength of the emission maximum.

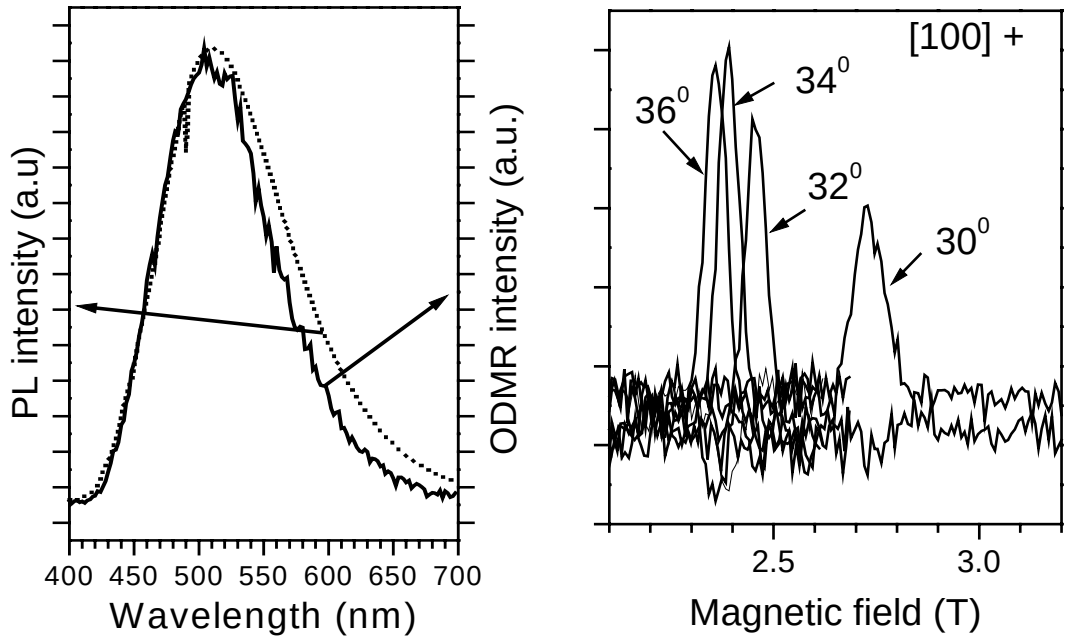

Fig. 5: Luminescence (dotted) and spectral dependence of ODMR signals (left)
Angular dependence of resonances for [001] rotation (right) in PWO:Nb

Conclusions

As result of a large amount of magnetic resonance studies several classes of paramagnetic defects could be identified. They can be grouped into

a) electrons trapped at regular W lattice sites. Among them an intrinsic $(WO_4)^{3-}$ centre stabilized by a Jahn-Teller distortion is found which contributes to the characteristic glow peak of the thermally stimulated luminescence (TSL) near 50 K.
b) $(WO_4)^{3-}$ centres with a nearby three-valent ion, e.g. La, Lu or Y contributing to a TSL peak near 100 K
c) electron traps connected to impurity metals at cation sites with a disturbed oxygen surrounding
d) foreign atoms on cation sites. They can be further divided into those like Ce^{3+}, Er^{3+} and Nd^{3+} being not affected by any of the treatments used and others, which thereby change their charge state.

Thermal stability of some of the centres of type c) and d) is correlated to glow peaks, too. The differences observed from sample to sample in the spectral composition of the TSL and its sensitivity to annealing procedures shows, however, that creation of centres and their thermally stimulated recombination in $PbWO_4$ depend strongly on the overall defect structure of the particular crystal. This puts additional importance to the open question for the hole counterparts of the trapped electrons. In this respect interesting hints have been found from other tungstate scintillators like $BaWO_4$ and $ZnWO_4$. For both materials in contrast to $PbWO_4$ no contribution of cation states to the valence band is expected. Consequently, typical (self)trapped holes at one of the oxygen ligands are created by X-irradiation. There recombination with trapped electrons of types a) respectivley b) (see above) gives rise to TSL

peaks in the range 50 to 70 K, too, with spectral compositions close to those in $PbWO_4$. In contrast to the latter, however, in both other tungstates the holes are the species becoming mobile at this temperature shedding once more some light on the exceptional status of PWO.

First ODMR results prove that at least in some cases the green emission originates from anionic oxocomplexes and that Jahn-Teller distortions play a significant role in PWO and other scheelites, as claimed from investigations of the polarization of the luminescence many years ago [14] and evident also from the stabilization of $(WO_4)^{3-}$.

Acknowledgements

We would like to thank P. Bohacek (Prague) for growing the $BaWO_4$ crystal. This work was supported by Deutsche Forschungsgemeinschaft (DFG) as project ME 852/4-1. One of us (V.V.L.) thanks DFG for a personal grant.

References

1. V.V. Laguta, J. Rosa, M.I. Zaritski, M. Nikl, and Y. Usuki, J. Phys. Cond. Matter **10** (1998), 7293
2. Y. Zhang, N.A.W. Holzwarth, and R.T. Williams, Phys. Rev. **B 57** (1998), 12738
3. M. Boehm, F. Henecker, A. Hofstaetter, M. Luh, B.K. Meyer, A. Scharmann. O.V. Kondratiev, and M.V. Korzhik, Rad. Effects and Defects in Solids (1999), in press
4. M. Boehm, F. Henecker, A. Hofstaetter, M. Luh, B.K. Meyer, A. Scharmann. V. Metag, R. Novotny, O.V. Kondratiev, and M.V. Korzhik, in "Tungstate Crystals"; Proc. Intern. Workshop on Tungstate Crystals, Rome - October 12-14, 1998 (eds. S. Baccaro, B. Borgia, I. Dafinei, E. Longo), 141
5. M. Boehm, A. Hofstaetter, M. Luh, B.K. Meyer, A. Scharmann, M.V. Korzhik, O.V. Kondratiev, A.E. Borisevich, V.V. Laguta, P. Lecoq, and E. Auffray-Hillemans, to be published
6. W.S. Brower and P.H. Fang, J. Appl. Phys. **40** (1967), 2391
7. V. Mürk, M. Nikl, E. Mihokova, and K. Nitsch, J. Phys. Cond. Matter **9** (1997), 249
8. E. Goovaerts, S.V. Nistor, and D. Schoemaker, Phys. Rev. **B 28** (1983), 3712
9. M. Boehm, A. Hofstaetter, M. Luh, B.K. Meyer, A. Scharmann, M.V. Korzhik, O.V. Kondratiev, and V.V. Laguta, to be published
10. A. Hofstaetter, V.V. Laguta, B.K. Meyer, and R.Y. Zhu, to be published
11. B. Cord, A. Hofstaetter, and A. Scharmann, phys. stat. sol. (b) **106** (1981), 499
12. A. Hofstaetter, K. Raksanyi, A. Scharmann, F. Schön, and A. Watterich, Proc. XII Int. Conf. "Defects in insulating materials", Nordkirchen (Germany) - August 16-22, 1992 (eds. O. Kanert, J.-M. Spaeth: World Scientific, Singapore 1993), 700
13. P.G. Baranov, V.V. Dyakonov, A. Hofstaetter, N.G. Romanov, A. Scharmann, and F. Schön, Proc. 24th Congress Ampere (Poznan 1988), 997
14. E.G. Reut, Izv. Acad. Nauk SSSR, Ser. Fiz. **43** (1979), 1186

Radiation hardness of doped $PbWO_4$

M. Kobayashi,[a] Y. Usuki,[b] M. Ishii,[c] N. Senguttuvan,[c] K. Tanji,[c]
M. Chiba,[d] K. Hara,[e] H. Takano,[e] M. Nikl,[f], P. Bohacek,[f]
S. Baccaro,[g] A. Cecilia,[g] M. Diemoz[h], A. Vedda,[i] M. Martini[i]

[a] *KEK, High Energy Accelerator Research Organization, Tsukuba 305-0801, Japan,*
[b] *Furukawa Co., Kamiyoshima, Yoshima, Iwaki 970-1153, Japan.*
[c] *SIT, Shonan Institute of Technology, Fujisawa 251-8511, Japan,*
[d] *Department of Physics, Tokyo Metropolitan University, Hachioji 192-0364, Japan,*
e) Institute of Physics, University of Tsukuba, Tsukuba 305-8571, Japan,
f) Institute of Physics, Cukrovarnicka 10, 16200 Prague, Czech Republic,
[g] *ENEA, INN/TEC, Via Anguillarese 301, S.Maria di Galeria, 00060 Roma, Italy,*
[h] *INFN, Sez. di Roma & Universita di Roma "La Sapienza", Roma, Italy,*
[i] *INFM and Dip. di Scienze dei Materiali, Universita di Milano, Milano, Italy*

Abstract: We confirmed that not only La^{3+} but also the other trivalent-ions such as Lu^{3+}, Gd^{3+}, Y^{3+} give significant improvement in optical transmittance and radiation hardness of $PbWO_4$. According to the hypothesis of Pb^{2+} deficiency in grown crystals and charge compensation by trivalent ions for the observed improvements, tetravalent ions may be as efficient as or even more efficient than trivalent ions. We have extended the dopants to tetravalent ions (Zr^{4+}, Th^{4+}), ions with two different charge states ($Ce^{3+,4+}$, $Sb^{3+,5+}$), etc. We found that Th^{4+} gives a similar improvement to that given by typical trivalent ions. $Ce^{3+,4+}$ and $Sb^{3+,5+}$ gave both an improvement and a degradation at the same time. We will describe the obtained result of 2+, 3+, 4+ and 5+ ion dopings on radiation hardness, transmittance at short wavelengths, etc.

Keywords: $PbWO_4$, Radiation damage, Doping

1. Introduction

In these years, doping of various ions into lead tungstate ($PbWO_4$ or PWO) has been extensively studied to improve the transmittance in the short wavelength region (330-450 nm), radiation hardness, decay time, etc.(see papers in [1]). In order to understand the mechanism for the dramatic improvement by La^{3+} doping [2-4] and thereby to improve PWO further, we have studied different trivalent ions (La^{3+}, Y^{3+}, Gd^{3+}, Lu^{3+}, Sc^{3+}) in comparison with non-doping and divalent (Cd^{2+}) and pentavalent (Nb^{5+}) ions. We confirmed [5] that not only La^{3+} but also Lu^{3+}, Gd^{3+}, Y^{3+} significantly improve the transmittance and radiation hardness. The obtained improvements have been successfully explained in terms of the following hypothesis[6]: The two absorption bands at 350 and 420 nm can be due to the defects related to Pb^{3+} and O^- colour centres, respectively, which should be created as a result of Pb^{2+} deficiency during crystal growth and/or annealing process in order to recover the total charge balance. Introduction of trivalent ions could compensate the Pb^{2+} deficiency, thereby reducing the densities of the Pb^{3+}/O^--related defects. Doping with various ions of different charges has also been studied in several institutes (for example, see [7-9]). Doping with Nb^{5+} was intensively studied by CMS with an intention to cause oxygen leakage thereby reducing the densities of the Pb^{3+}/O^--related defects, and was found [8] to give an apparently similar improvement to that with trivalent ions. $Sb^{3+,5+}$ doping was first studied in Shanghai [9] and claimed to give an improvement.

The smallness of the assumed Pb^{2+} deficiency (as small as or even smaller than 1000 at. ppm [10-12]) makes difficult to detect it directly through the study of the microstructure of grown crystals. Recently, a rather clear evidence of the Pb^{2+} deficiency has been obtained by Han et al. [13] from an observation of dielectric relaxation in PWO:La^{3+} crystals. They confirmed that the density of mobile defects in undoped PWO is reduced as the concentration of La^{3+} is increased. The observed polarization is most probably due to the creation of [$2(La_{Pb}^{3+})^{\square}$-$V_{Pb}$"] dipole complexes, and indicates the existence of Pb^{2+} deficiency (as mobile defects) in undoped PWO. The improvement brought by La^{3+} doping can be understood well if the mobile Pb^{2+} vacancies, which should degrade transmission and radiation hardness, should be caught within the dipole complexes to become immobile. However, the failure to detect ESR signal for Pb^{3+} [14] indicates that the defects related with the Pb^{2+} deficiency may not be of a simple (point defect-like) nature.

If the above-mentioned hypothesis should be the dominant mechanism for the observed improvement by trivalent-ion doping, tetravalent-ion doping may be as efficient as or even more efficient than trivalent-ion doping. With this expectation we have recently extended the dopant ions to tetravalent ions (Zr^{4+}, Th^{4+}), ions with two charge states($Ce^{3+,4+}$, $Sb^{3+,5+}$), etc. We will report the obtained results for these 2+, 3+, 4+, and 5+ ions mainly with respect to radiation hardness, optical transmission and light yield, since the other properties (excitation-emission spectra, decay time, etc.) did not change much.

Table 1 List of doped PWO samples studied in the present work. The thickness across which the transmittance was measured is underlined. Dopant concentration in crystal was measured by ICP analysis, unless otherwise indicated.

Sample	Dopant (at.ppm) (in melt/in crystal)	Size (mm)	Notes
PWO:La,#4	La^{3+}(135/202)	10x10x20	From the same ingot as La2[2]. k=2.5
PWO:Lu	Lu^{3+}(135/43)	10x10x45.2	k=0.31
PWO:Gd(135)	Gd^{3+}(135/208)	10x10x25.5	k=1.55
PWO:Gd(80)	Gd^{3+}(80/ 123(a))	10x10x20	
PWO:Gd(60)	Gd^{3+}(60/ 92(a))	10x10x40	
PWO:Y	Y^{3+}(135/108)	10x10x20.5	k=0.8
PWO:Sc	Sc^{2+}(135/7)	10x10x20.2	k=0.06
PWO:Ce	$Ce^{3+,4+}$(135/29)	10x10x20	k=0.21
PWO:Sb	$Sb^{3+,5+}$(135/<33)	10x10x20	k<0.1
PWO:Zr	Zr^{4+}(135/<13)	10x10x40	
PWO:Th	Th^{4+}(135/35)	10x10x20	k=0.26
PWO:Pb	Pb^{2+}(135)	10x10x20	Very close to undoped crystal
PWO:Cd	Cd^{2+}(135/41)	10x10x20.3	k=0.3
PWO:Mn	Mn^{2+}(135/5.5)	10x10x20	k=0.04
PWO:Nb	Nb^{5+}(1350/670)	10x10x21	
PWO:La,Nb	La^{3+}(135/220(a)) Nb^{5+}(1350/650(a))	10x10x30	Clouded locally (about 5%).

a) Calculated for segregation coefficient k=1.55(Gd), 0.4(Nb^{5+}).

2. Test Samples and Measurement

All the test samples (see Table 1) were grown by Furukawa Co. in the same way (3-times crystallization [15] in air by Cz. method using a Pt crucible and annealing at 600 ^{o}C in the air for 6h) by using raw material with a nominal purity of 99.99% from the same source. The test samples were cut from an ingot with 35 mm in diameter and 80 mm in length. Most of the dopants were added into the melt by 135 at. ppm. Nb^{5+} was added by 1350 at. ppm because 135 at. ppm did not give sizable effects. True concentration in the crystal (see Table 1) was measured by ICP in most samples, or calculated by using the known segregation coefficient in a few samples. The impurities remaining in grown crystals were analyzed by GDMS. Although not all the samples were measured, we can expect from the results for more than 10 present and past samples measured so far that the impurities were well controlled to be at similar level in all the samples. Typically [4], most of the impurities are below 0.1 at. ppm level (Mo impurity[16,17] less than 0.02 at. ppm level) with no ones above 1 at. ppm level.

Transmission was measured with a spectrophotometer (Hitachi 220 or U-2310), and photoluminescence (excitation and emission) with a fluorescence spectrophotometer (Hitachi F4500). We measured the scintillation intensity for ^{60}Co γ-rays by mounting the sample on a 2-in. PMT (Hamamatsu R2259) with a bialkali photocathode and a silica window. The pulse height was analyzed with a PHA in the charge mode within 1 μs gate and compared with the single photoelectron peak. We measured the decay time spectra with a Lecroy qVt using a conventional single photoelectron technique and a fast 2-in. PMT (Hamamatsu H3177) with a bialkali photocathode and a silica window. Radiation damage was measured by irradiating the samples with ^{60}Co γ-rays at JAERI for the accumulated dose from 10^4 to 10^8 rad (10^2 to 10^6 Gy). The irradiation period was roughly 1h, 1h, 3h, 22h, and 100h for 10^4, 10^5, 10^6, 10^7, and 10^8 rad, respectively. Transmittance measurement was carried out in 30-50h after irradiation. Recovery of the damages was also measured in a few to 200d after the 10^8 rad irradiation. We calculated the induced absorption coefficient $\mu_{ir} = (1/d)ln(T_o/T)$, where d is the thickness across which the transmittance T_o (before irradiation) and T (after irradiation) were measured.

3. Results

3.1 Trivalent-ion doping

As shown in Fig. 1, all the tested trivalent ions (except Sc^{3+}) significantly improve the transmittance in the short wavelength region (330-450 nm). Excitation-emission spectra are not much affected by doping (see Table 2). The main blue emission occurs at 420 nm for the excitation at 310-320 nm. A second broad peak, which was seen at around 600 nm in the undoped or divalent-ion doped samples, almost vanished by the doping with trivalent-ions (except Sc^{3+}); see Fig. 2 for an example. At the same time, the weak phosphorescence (τ_{decay} ~ 4-9 ms), which was observed at around 600 nm in undoped, Cd-, Mn-, Sc-, and Sb-doped PWO, was reduced to an undetectable level by doping with trivalent ions (except Sc^{3+}). As for decay time, the main component was as short as a few to several ns for all the samples. While the decay time of undoped PWO usually consists of three components, the slowest component vanished when trivalent ions (except Sc^{3+}) were doped; see Table 2. The light yield was 36-41 p.e./MeV (see Table 2) for most of the samples with the exception of Ce-, Mn-doped and rather heavily La-, Nb-doped ones. Light yield should be reduced due to new nonradiative traps induced by high dopant concentration[18].

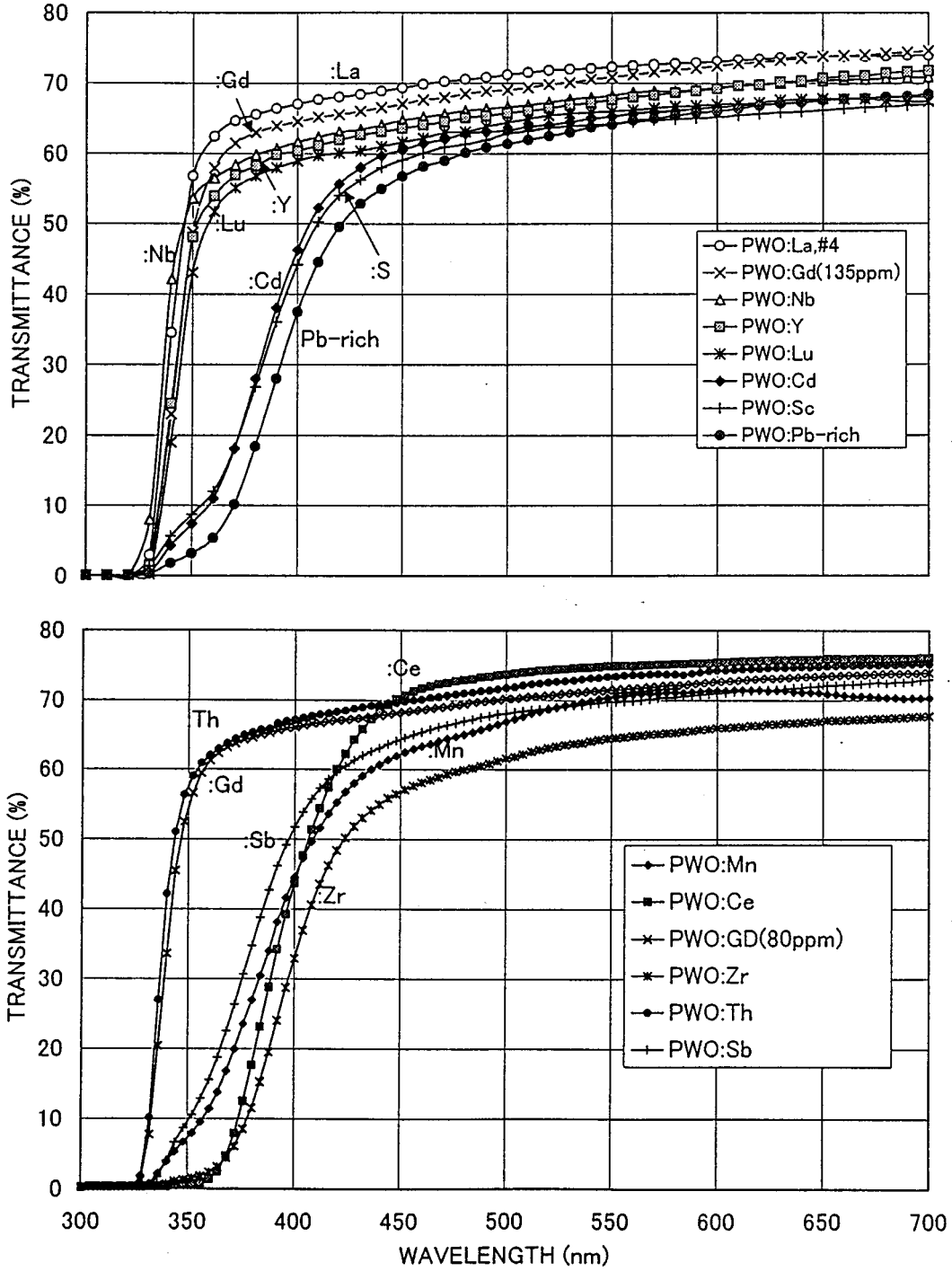

Fig. 1 Transmission spectra before irradiation. The thickness (see Table 1) for transmission measurement was 20 mm except for PWO:Lu^{3+} (45 mm).

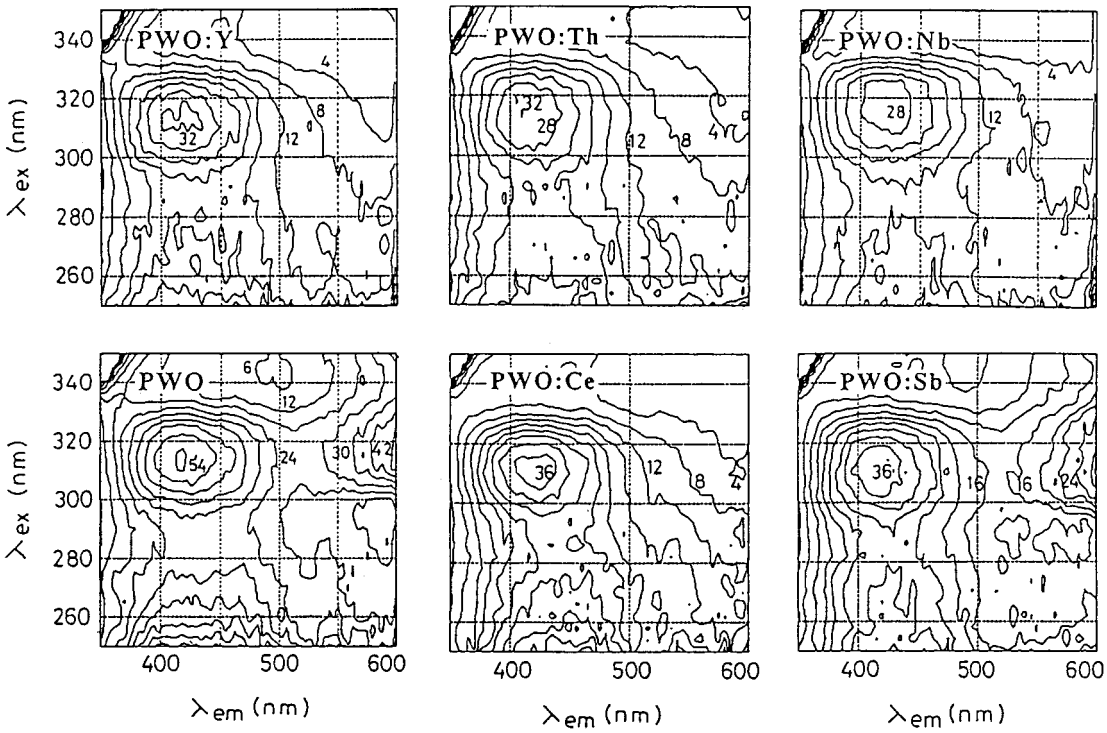

Fig. 2 Excitation and emission (from crystal surface) spectra for UV excitation in typical samples. The contour of emission intensity is plotted with attached numbers giving rough relative intensity.

Table 2 Obtained result. λ_{ex} and λ_{em} denote the excitation and emission peak wavelengths, respectively, and LY the scintillation light intensity for ^{60}Co γ-rays (see text). The i-th decay constant and its intensity (in percentage of the total intensity) are denoted as τ_i and I_i, respectively. $<\tau>_{av}$ is the weighted sum of $\tau_i I_i$.

Sample	$\lambda_{ex}/\lambda_{em}$ (nm)	LY p.e./MeV	Decay constants (ns) $\tau_1(I_1)$ $\tau_2(I_2)$ $\tau_3(I_3)$	$<\tau>_{av}$
PWO:La,#4	308/410	31	2.5(79%) 14(21%)	4.9
PWO:Lu	315/422	37	4.1(75%) 9.7(25%)	5.5
PWO:Gd	315/418	33	3.3(81%) 22(19%)	6.9
PWO:Gd(80)	315/415	39	1.3(49%) 6.5(51%)	3.9
PWO:Gd(60)	315/415	39	5.6(100%)	5.6
PWO:Y	315/418	40	3.3(75%) 11(25%)	5.2
PWO:Sc	312/410	37	1.4(54%) 5.5(24%) 20(22%)	6.5
PWO:Ce	310/420	15	2.0(68%) 6.6(32%)	3.5
PWO:Sb	310/420	41	2.9(59%) 8.5(23%) 22(18%)	7.6
PWO:Zr	315/420	36	2.9(52%) 12(48%)	7.1
PWO:Th	315/415	40	3.1(41%) 8.2(59%)	6.1
PWO:Pb-rich	315/418	37	1.5(61%) 8.9(26%) 29(13%)	7.0
PWO:Cd	315/418	41	1.6(60%) 8.2(26%) 26(14%)	6.7
PWO:Mn	312/415	26	1.7(51%) 9.6(38%) 46(11%)	9.5
PWO:Nb	318/422	26	2.1(80%) 8.3(14%) 42(6%)	5.4
PWO:La,Nb	314/405	27	2.2(72%) 16(28%)	6.1

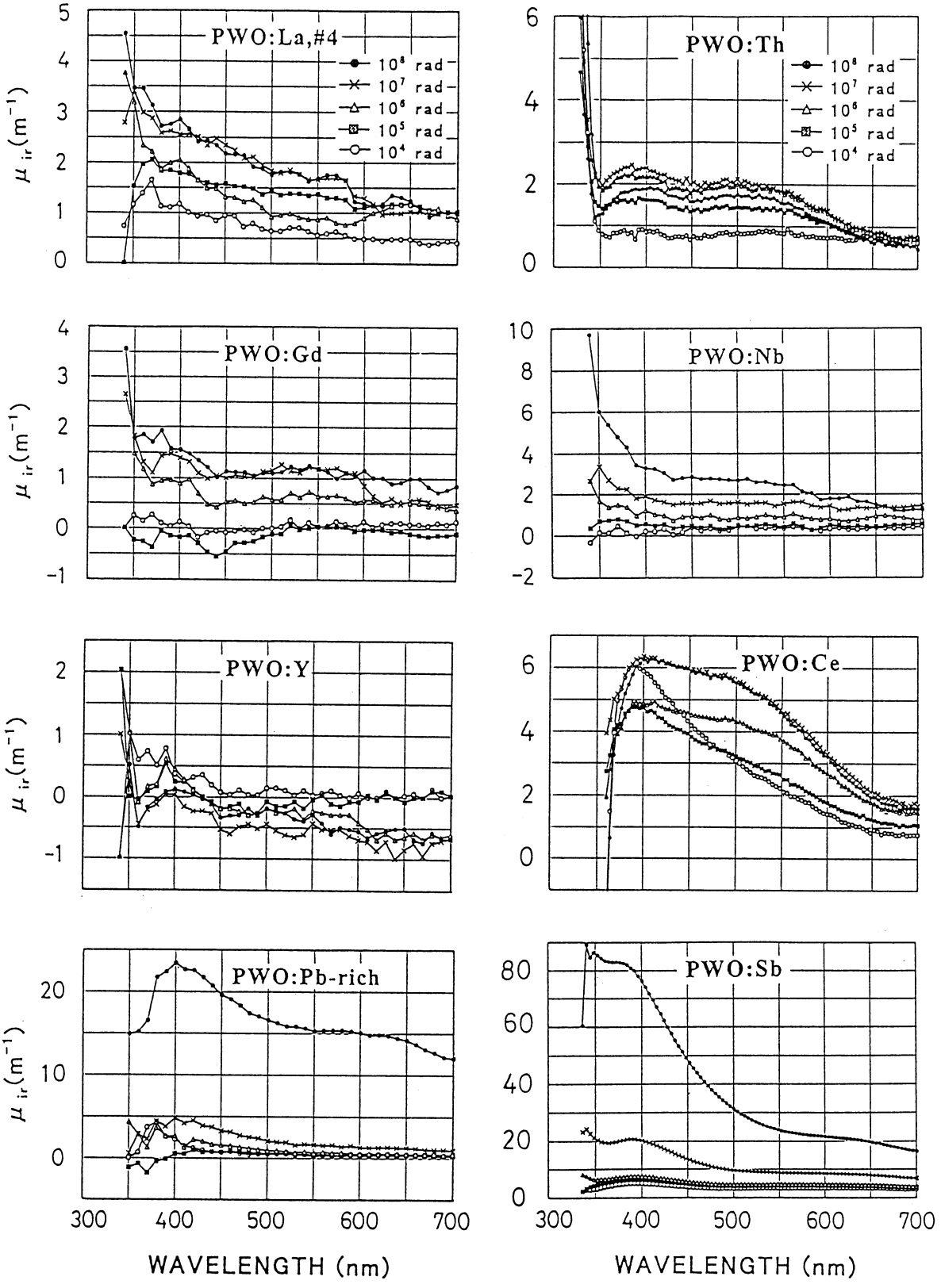

Fig. 3 Radiation-induced absorption coefficient μ_{ir} versus wavelength at different doses in some samples (see Table 1).

The $\mu_{ir}(\lambda)$ spectra are given in Fig. 3 for typical samples. The μ_{ir} at 420 nm, the emission peak wavelength, versus accumulated dose is given in Figs. 4 and 5. These figures show that the doping with trivalent ions (except Sc^{3+}) significantly improves the radiation hardness. The

recovery after 10^8rad irradiation, also shown in Figs. 4 and 5, seems to continue for a period as long as 200 days. PWO:Y^{3+} shows "recovery" although it had no significant damage upon irradiation. This apparent "recovery" needs more study with more samples. This may be related to the initial transmittance (before irradiation) which was a little lower among the present test samples.

3.2 Tetravalent-ion doping

Th^{4+} significantly improves both the transmittance in the short wavelength region (see Fig. 1) and the radiation hardness (see Figs. 3-5), similarly to trivalent ions. The wavelengths of the excitation and emission peaks, decay time, and light yield of PWO:Th were almost the same as for the trivalent-ion-doped samples (see Table 2 and Fig. 2). Absence of clear effect of Zr^{4+} doping in transmittance may be due to either entrance of Zr^{4+} not into Pb^{2+} lattice but as interstitial because of much smaller ion radius of Zr^{4+}~ 0.79A (compared with Pb^{2+}~1.20A) or negligible entrance into the lattice (see Table 1). The former case may be more probable since the radiation hardness was sizably degraded by Zr^{4+} doping.

3.3 Doping of $Ce^{3+,4+}$, $Sb^{3+,5+}$ having two charge states

For $Ce^{3+,4+}$ doping, we saw no big improvement in the transmittance in the short wavelength region (see Fig. 1). The reason for the absence of big improvements by $Ce^{3+,4+}$ doping is not clear. The Ce concentration in crystal is not large (18 at. ppm) but sizable. Ce should surely exist in the lattice, since the ion radius (Ce^{3+}~1.03A, Ce^{4+}~0.92A) is not very different from Pb^{2+} (1.20A) and since the TSL glow curve (Fig. 6) is different from the case of undoped PWO. The radiation hardness is between the (good) trivalent-ion-doped samples and (poor) undoped ones (see Figs. 3-5). Another distinctive difference of Ce doping from the trivalent-ion dopings is a reduction by half in light yield (see Table 2).

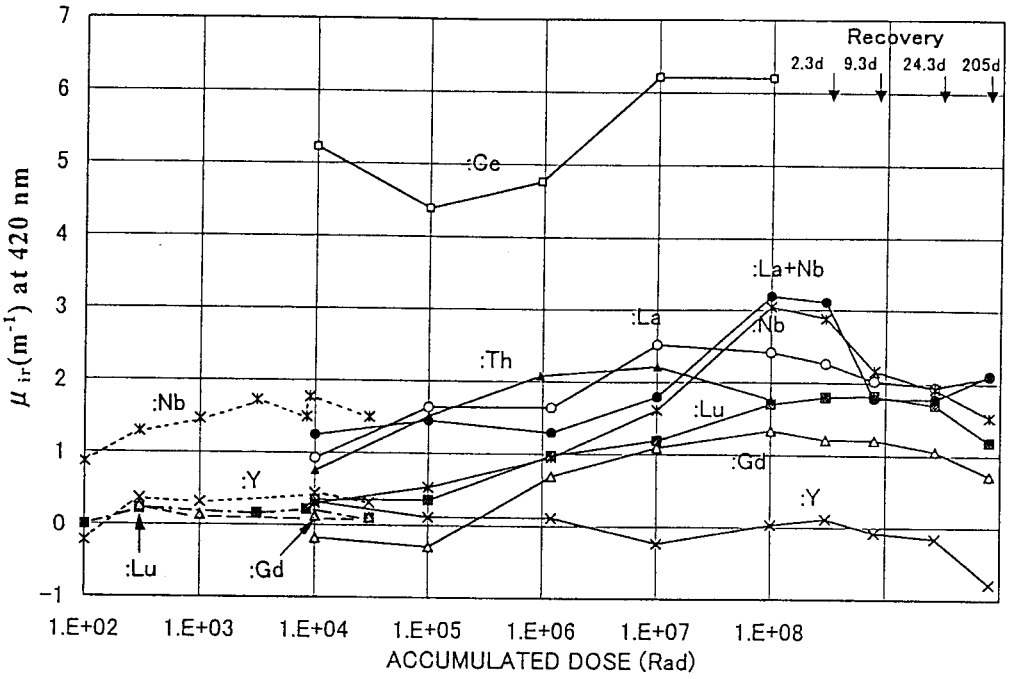

Fig. 4 Radiation-induced absorption coefficient μ_{ir} at 420 nm (the emission peak) versus accumulated dose. The results obtained in Italy below about $3x10^4$ rad are also shown by connecting the data points with dotted lines. The recovery after 10^8 rad irradiation is also given for some samples.

The reason for the absence of big improvement either by $Sb^{3+,5+}$ doping (135 at.ppm in the melt) may be different from that for $Ce^{3+,4+}$ doping. The concentration of Sb in the lattice may be too small due to possible evaporation of Sb due to large vapour pressure. According to the work in Shanghai[19], the seed/tail part of Sb in a Br. grown PWO:Sb was 30.7/48.6 at. ppm when the Sb concentration in the melt was 900 at. ppm. An improvement in transmittance similar to the case of 3+ ion doping was found [19] for the doping of 900 at. ppm. In the Cz. growth, evaporation may be even larger than in Br. growth. Then, the Sb concentration in the present sample may be much smaller than 10 at. ppm. This may be the reason for the absence of improvement. Our concentration study requires some 40-60 at. ppm doping level at least. However, the radiation hardness was degraded by Sb-doping by 135 at. ppm. The reason for this is not yet clear. The light yield of PWO:Sb was as large as or a little larger than that of the trivalent-ion-doped samples (see Table 2 and Fig. 2).

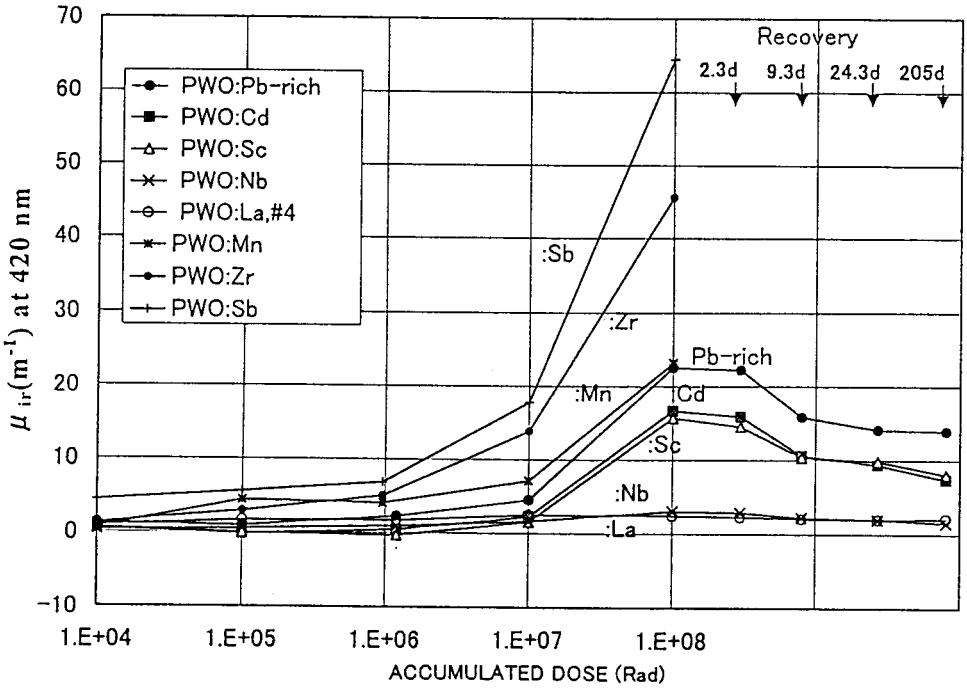

Fig. 5 Radiation-induced absorption coefficient μ_{ir} at 420 nm versus accumulated dose for typical samples which showed significant degradation. The results of PWO:La^{3+} and PWO:Nb^{5+}, given in Fig. 4, are reproduced for comparison. The recovery after 10^8 rad irradiation is also given for some samples.

4. Summary and discussions

(1) All the trivalent ions (La^{3+}. Lu^{3+}, Gd^{3+}, Y^{3+}) except Sc^{3+} gave similar and significant improvement in transmittance in the short wavelength region (330-450 nm) and in radiation hardness. Among the trivalent ions, Y^{3+} showed the best radiation hardness in consistency with Ref. [7]. Sc^{3+} ions have a much smaller ion radius (0.81A) than Pb^{2+}(1.20 A), and may not have entered into Pb^{2+} sites but as interstitial.

(2) Among tetravalent ions, Th^{4+} gave a significant improvement similar to the trivalent ions. Zr^{4+} gave no improvements but degraded the radiation hardness. Zr^{4+} probably did not occupy the Pb^{2+} site but stayed as interstitial like an impurity.

(3) $Ce^{3+,4+}$ gave no improvement in transmittance, a limitted improvement in radiation hardness, and reduction in light yield by half. Absence of big improvements may be due to that the oscillation of Ce between 3+ and 4+ charge states may give rise to new hole trapping sites,

and/or hinder formation of stable dipole complex [2(Ce_{Pb}^{3+})$^{\square}$-V_{Pb}"] thereby failing in making Pb^{2+} vacancy immobile. Ce^{3+} ions are known[20] to play a role of catalyst to help recombination of the positive holes and the ionized electrons, which may be produced by irradiation, through a chain of reactions, $Ce^{3+}+A^{+}$(ionized atom)--> $Ce^{4+}+A$, Ce^{4+}+F-centre-->Ce^{3+}, to reduce radiation damages in glasses Complicated role of Ce ions in PWO is reflected also in enhanced TSL signal around 100C, i.e. some new rather stable nonradiative traps may be introduced. Observed light yield loss may be related to these traps at Ce sites, taking into account the absence of any Ce^{3+} luminescence even at low temperatures.

(4) $Sb^{3+,5+}$ doping by 135 at.ppm (in the melt) gave no improvement. When the concentration was increased to 900 at.ppm (31-49 at.ppm in crystal), significant improvement was observed in Shanghai [19] in the transmittance at short wavelengths. Large vapour pressure of Sb probably caused evaporation loss of the dopant. TSL spectrum (for 135 at.ppm Sb doping) has a similar shape as for trivalent ion doping in consistency with the partial improvement in transmittance, although the 50C TSL peak is suppressed in much lesser extent. However, the reason for the degradation in radiation hardness (observed already for 135 at.ppm of Sb) is not yet clear.

(5) As for the improvement in radiation hardness, Nb^{5+} was found to be as good as La^{3+}, but a little poorer than Y^{3+}, Gd^{3+} and Lu^{3+}. Co-doping of La^{3+} and Nb^{5+} did not make any big difference from the single doping of either La^{3+} or Nb^{5+}.

(6) The TSL results obtained in Italy after irradiation at room temperature are in good consistency with the result of radiation hardness. A large TSL peak is usually seen at 50 ^{o}C for undoped and divalent-ion-doped samples. It was absent in all the trivalent-ion (except Sc^{3+}) doped samples, leading to low intensity and structureless TSL glow curves spectra [21].

(7) All the undoped (PWO:Pb-rich), divalent-ion (Cd^{2+}, Mn^{2+}), Sc^{3+}, and Zr^{4+}-doped samples got a tint of black upon 10^8 rad irradiation. PWO:$Sb^{3+,5+}$ got a tint of yellowish brown.

(8)As shown in Fig. 3. the $\mu_{ir}(\lambda)$ spectrum has two maxima at around 400 and 550-600 nm in undoped (PWO:Pb-rich), Cd^{2+}, Mn^{2+}, Sc^{3+}, $Ce^{3+,4+}$, and Zr^{4+}-doped samples. In the other samples, the $\mu_{ir}(\lambda)$ spectrum is almost flat, indicating a good compensation of well-defined colour centres by trivalent- or tetravalent or pentavalent-ion dopings.

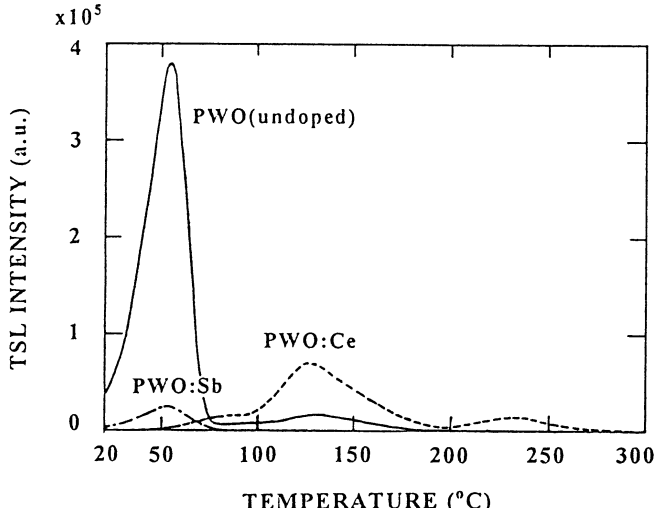

Fig. 6 TSL spectra of PWO(undoped), PWO:Ce and PWO:Sb after irradiation at room temperature. In Nb-(La-, Y-, Gd-, Lu-) doped PWO, the 50C peak is suppressed by a few orders of magnitudes [21] with the peak intensity as small $5x10^2$ ($1x10^2$), and not shown in the figure.

Obtained experimental data show that even several tens at. ppm of (La^{3+}, Lu^{3+}, Y^{3+}, Gd^{3+}, Th^{4+}) is enough to give significant improvement by charge compensation of the Pb^{2+} deficiency. The obtained result for Th^{4+} doping supports the hypothesis worked out by Nikl et al.[6], Han et al.[13], etc. sketched in Introduction. $Ce^{3+,4+}$, and $Sb^{3+,5+}$ give both an improvement and a degradation at the same time. This complicated nature is different from the case of the other dopant ions having a stable unique charge state, and may be due to the presence of two charge states. For further improvement of PWO scintillators, it should be demanding to understand in which part of the technological process the Pb^{2+} deficiency is introduced and what is its true level, and to make clearer the nature of the resultant defects and colour centers.

References

1. Proc. International Workshop on Tungstate Crystals, Rome, October, 1998.
2. M. Kobayashi et al., Nucl. Instr. Meth. A399(1997)261; A404(1998)149.
3. S. Baccaro et al., Phys. Stat. Sol. (a)160(1997)R5.
4. K. Hara et al., Nucl. Instr. Meth. A414(1998)325.
5. M. Kobayashi et al., Ref.[1], p.161; Nucl. Instr. Meth. A (in press).
6. M. Nikl et al., J. Appl. Phys. 82(1997)1.
7. S. Baccaro et al., phys. stat. sol. (a)164(1997)R9.
   S. Baccaro et al., Proc. SCINT97 held in Shanghai, 1997, p.203
8. E. Auffray et al., Nucl. Instr. Meth. A402(1998)75. Lecoq, Ref.[1], p.23.
9. D.S. Yan: Ref.[1], p.7.
10. M. Ishii et al., Ref.[1], p.61.
11. Y. Usuki et al., KEK Preprint 97-194, 1997.
12. P. Bohacek et al., Ref.[1], p.55.
13. B. Han, X. Feng, G. Hu, P.Wang, Zh.Yin, J. Appl. Phys. 84(1998) 2831.
14. V.V. Laguta et al., J. Phys. Cond. Mat. 10(1998)7293.
15. Y. Usuki et al., Proc. Workshop on Scintillating Crystals, KEK Proc. 97-9, p.207.
16. M. Kobayashi et al., Nucl. Instr. Meth. A373(1996)333.
17. R.Y. Zhu et al., Nucl. Instr. Meth. A376(1996)319.
18. M. Nikl et al., Appl. Phys. Lett. 71(1997)3755.
19. L. Xian-cai, et al., Chin. Phys. Lett. 1999 (in press).
20. N. Soga and M. Tashiro, J. Ceram. Assoc. Japan 70(1962)143
21. S. Baccaro et al., Rad. Eff. Def. 1999 (in press).

Radiation Induced Color Centers and Light Monitoring for Lead Tugstate Crystals[1]

Xiangdong Qu, Liyuaii Zhang and Ren-yuan Zhu

California Institute of Technology, Pasadena, CA 91125, USA

Abstract: In this paper, we present result of a study on undoped as well as various doped lead tungstate crystals. Radiation induced color center density was compared to radio luminescence. Light output degradation for crystals under irradiation was measured. Correlations between variations of crystal transmittance and light output were investigated. Finally, monitoring wavelength was determined so that adequate sensitivity and good linearity may be achieved.

Keywords. Lead, Tungstate, Color Center, Monitoring, Radiation Induced

Introduction

Because of its high density and fast decay time, lead tungstate ($PbWO_4$) crystal was chosen by the Compact Muon Solenoid (CMS) experiment to construct a precision electromagnetic calorimeter (ECAL) at the Large Hadronic Collider (LHC) [1]. The crystal, however, is subject to the radiation damage [2], which has been extensively studied in the last several years [3, 4, 5, 6, 7, 8]. Our previous studies on PbW04 samples concluded that although most $PbWO_4$ crystals suffer from non-negligible radiation damage the scintillation mechanism in $PbWO_4$ is not affected by radiation, i.e. the loss of light output is due only to absorption by radiation induced color centers [8]. Following a kinetic model [9], we also proposed that the level of the radiation damage in $PbWO_4$ crystals should be dose rate dependent because of the damage recovery observed, which was later confirmed by experimental measurements [8].

Since the loss of transmittance, or the increase of radiation induced color center density, can be measured by a light monitoring system, we can use variations of transmittance data to estimate variations of light output. This makes possible to use a light monitoring system as inter calibration *in situ* at LHC, and thus makes a precision calorimeter possible by using $PbWO_4$ crystals which suffer from some radiation damage. In this paper, we report result of a study on undoped as well as doped $PbWO_4$ crystals, including photo and radio luminescence spectra (Section 2), radiation induced color density (Section 3), light output degradation (Section 4), and correlations between variations of light output and transmittance (Section 5), leading to a conclusion of monitoring wavelength.

Photo and Radio Luminescence

Table 1 lists peak wavelength of Photo (λ_{pho}) Radio (λ_{rad}) luminescence for six pairs PbW04 crystals samples of different types. All samples, except SIC 274 which has a rectangular shape, are full size with CMS tapered geometry. Also listed in the table are date these samples were received and dopant in the crystal. Samples denoted with SIC were grown at Shanghai Institute of Ceramics by Bridgman method. Samples denoted with BTCP were grown at Bogoroditsk Techno-Chemical Plant by Czochralski method.

[1] Work supported in part by U.S. Department of Energy Grant No. DE-FG03-92-ER40701

Table 1. PbW04 Crystal Samples Measured at Caltech

ID	Dimension (cm)	Date	Dopant	λ_{pho} (nm)	λ_{rad} (nm)
SIC 167	2.1×**23**×2.3	10/97	No	495	510
SIC 210	2.1×**23**×2.3	5/98	No	495	510
SIC 274	2.5×**21**×2.5	10/98	Sb	510	450
SIC 275	2.2×**23**×2.6	10/98	Sb	510	450
BTCP-1965	2.1×**23**×2.3	10/97	La	420	435
BTCP-1971	2.1×**23**×2.3	5/98	La	420	435
BTCP-2133	2.2×**23**×2.5	4/99	Y/Nb	420	—
BTCP-2162	2.2×**23**×2.5	4/99	Y/Nb	420	—
SIC S301	2.2×**23**×2.6	6/99	Y/Sb	420	445
SIC S347	2.2×**23**×2.6	6/99	Y/Sb	420	445
SIC S392	2.2×**23**×2.6	6/99	Y	420	445
SIC S412	2.2×**23**×2.6	6/99	Y	420	445

Photo luminescence was measured by using a Hitachi F-4500 fluorescence spectrophotometer. A schematic of the measurement setup is shown in Figure 1, where UV excitation light was shot to a bare surface of the sample and the photo luminescence, without passing through sample, was measured by a photo multiplier tube (PMT) through a monochromator. The setup used to measure radio luminescence is shown in Figure 2, where whole body of a wrapped sample was irradiated by a ^{60}Co γ-ray source at a dose rate of about 1,000 rad/h, and the radio luminescence, passing through sample, was focused and measured.

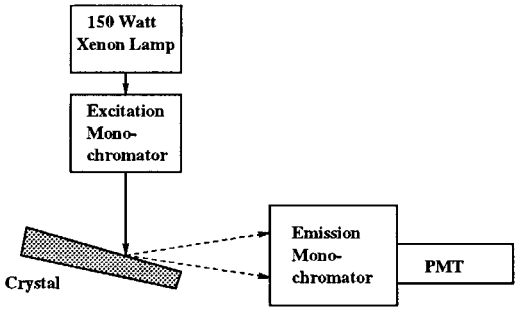

Figure 1. A schematic of setup used to measure photo luminescence

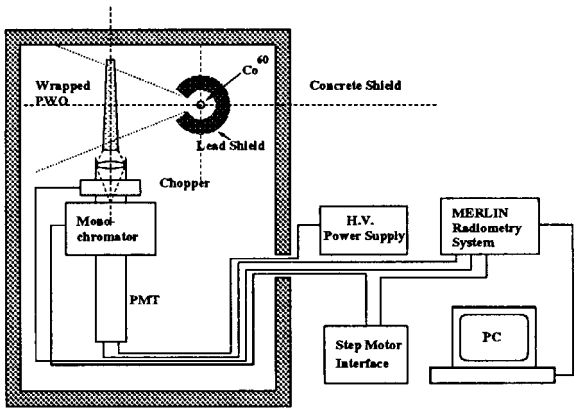

Figure 2. A schematic of setup used to measure radio luminescence

A comparison of photo (solid) and radio (dashed) luminescence spectra for undoped (SIC-210), La doped (BTCP-1971), Y/Sb double doped (SIC-S301) and Y doped (SIC-S412) samples is shown in Figure 3. All spectra were corrected by monochromator efficiency and

PMT quantum efficiency. The vertical axis "Intensity" refers to photon numbers, and its scale is arbitrary. As seen from the figure the peak of radio luminescence is 15 to 25 nm red shifted as compared to the photo luminescence. This red shift can be explained by internal absorption since $PbWO_4$ transmittance at shorter wavelength is poorer than that at longer wavelength. A cross check of photo luminescence with a modified setup, where luminescence light passed through sample, showed similar red shift, and thus confirmed this explanation.

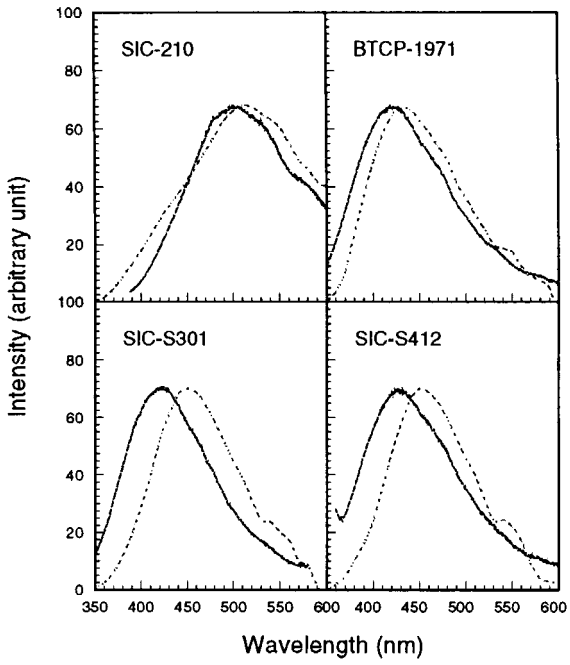

Figure 3. A comparison of photo (solid) and radio (dashed) luminescence spectra for four $PbW0_4$ samples

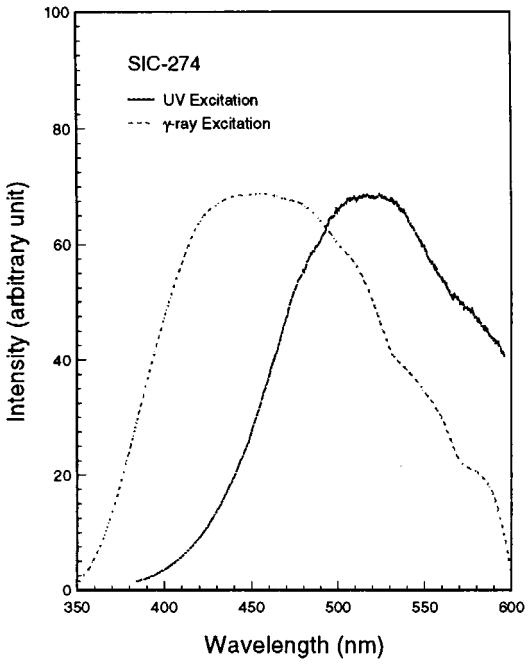

Figure 4. A comparison of photo (solid) and radio (dashed) luminescence spectra for a Sb doped sample SIC-274

The Sb doped samples is significantly different, however. Figure 4 shows a comparison of photo (solid) and radio (dashed) luminescence spectra for a Sb doped sample SIC-274. The peak of radio luminescence is blue shifted by 60 nm as compared to the photo luminescence. The origin of this blue shift is suspected due to that the UV photon is not energetic enough to excite the scintillation centers in Sb doped sample. This was confirmed by an X-ray luminescence spectrum with a peak consistent with radio luminescence.

Since the photo luminescence spectrum measured with setup in Figure 1 is not affected by internal absorption, it can be seen as the intrinsic emission spectrum in general, while the radio luminescence spectrum is a convolution of intrinsic emission and internal absorption with later depends on the light path. For $PbW0_4$ monitoring, however, the photo detector quantum efficiency weighted radio luminescence spectrum is more relevant since scintillation light propagates through the crystal then reaches the photo detector. Measurement on the other sample of the same type in Table I provided consistent result. The photo luminescence spectrum of Y/Nb double doped samples was measured to be identical to that of La doped sample. We, however, did not have chance to measure its radio luminescence since the Y/Nb doped sample pair was in our possession only for limited time.

Radiation Induced Color Centers

It is known that color centers are created in $PbW0_4$ crystals under irradiation. It is also known that radiation induced color centers may annihilate under room temperature. During irradiation, both annihilation and creation coexist, the color center density will reach an

equilibrium at a level depending on the dose rate applied. Assuming the annihilation speed of color center *i* is proportional to a constant a_i and its creation speed is proportional to a constant b_i and the dose rate (*R*), the differential variation of color center density when both processes coexist can be written as [9]

$$dD = \sum_{i=1}^{n} \{-a_i D_i + (D_i^{all} - D_i) b_i R\} dt \,, \tag{1}$$

where D_i is the density of the color center *i* in the crystal and the summation goes through all centers. The solution of Equation 1 is

$$D = \sum_{i=1}^{n} \frac{b_i R D_i^{all}}{a_i + b_i R} \left[1 - e^{-(a_i + b_i R)t}\right] + D_i^0 e^{-(a_i + b_i R)t} \Big], \tag{2}$$

where D_i^{all} is the total density of the trap related to the center *i* and D_i^0 is its initial density. The color center density in equilibrium (D_{eq}) thus depends on the dose rate (*R*):

$$D = \sum_{i=1}^{n} \frac{b_i R D_i^{all}}{a_i + b_i R}, \tag{3}$$

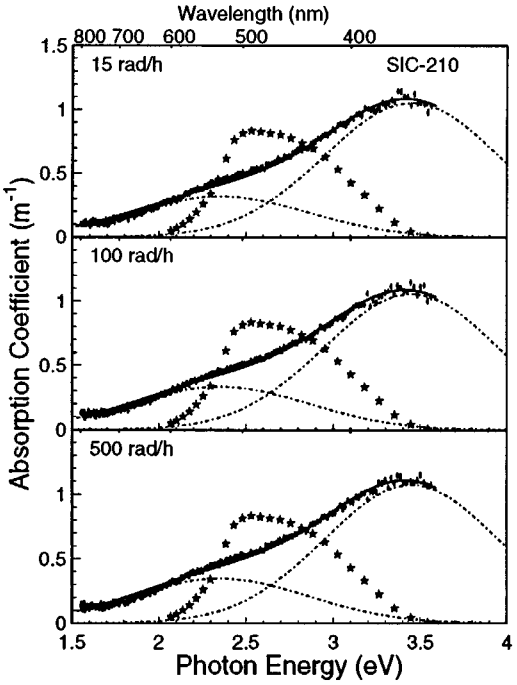

Figure 5. Radiation induced color center density for a undoped sample SIC-210

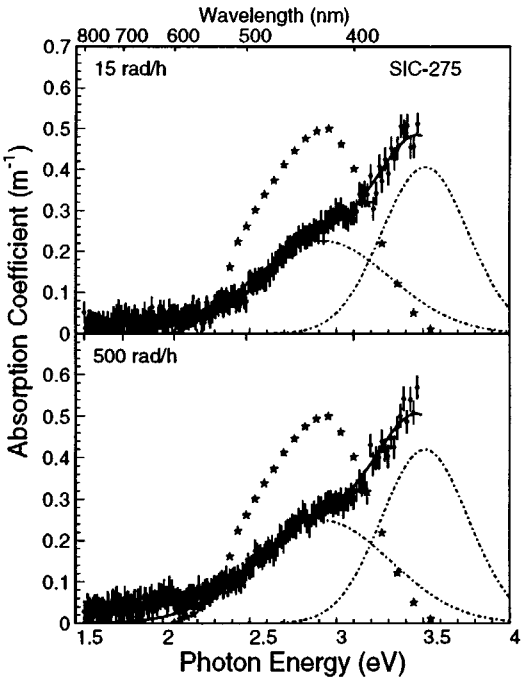

Figure 6. Radiation induced color center density for a Sb doped sample SIC-275

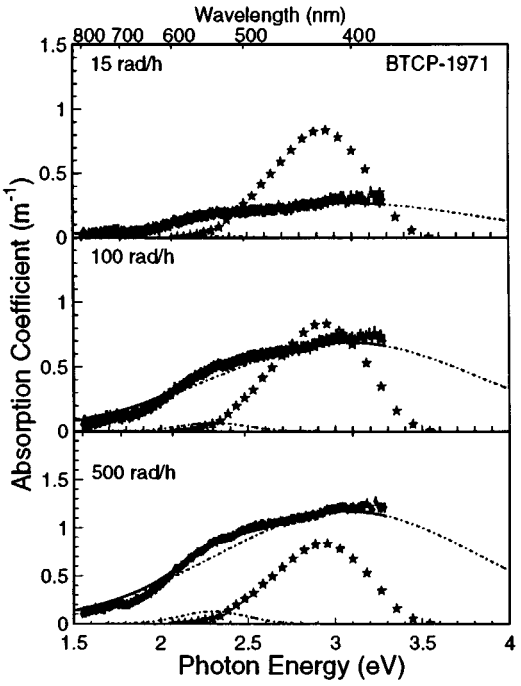

Figure 7. Radiation induced color center density for a La doped sample BTCP-1971

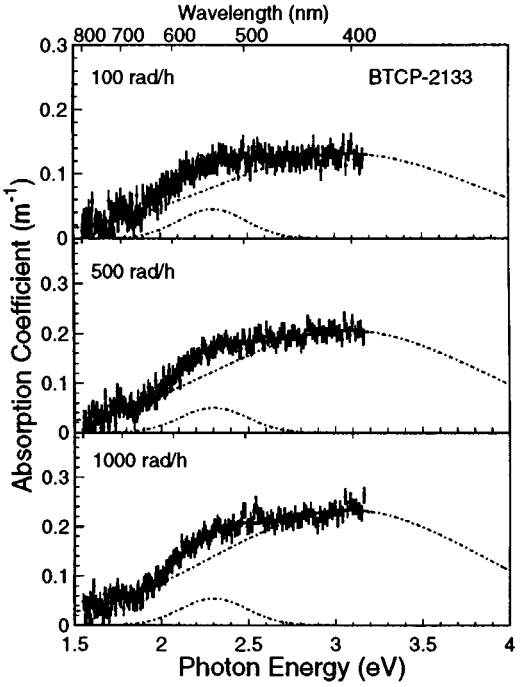

Figure 8. Radiation induced color center density for a Y/Nb doped sample BTCP-2133

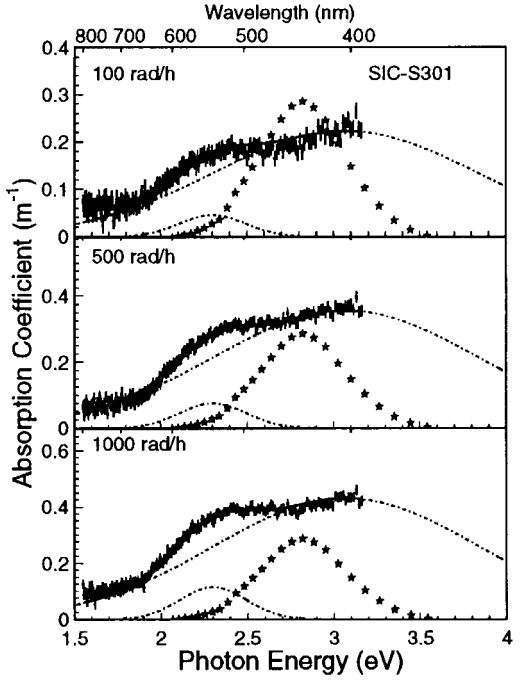

Figure 9. Radiation induced color center density for a Y/Sb doped sample SIC-S301

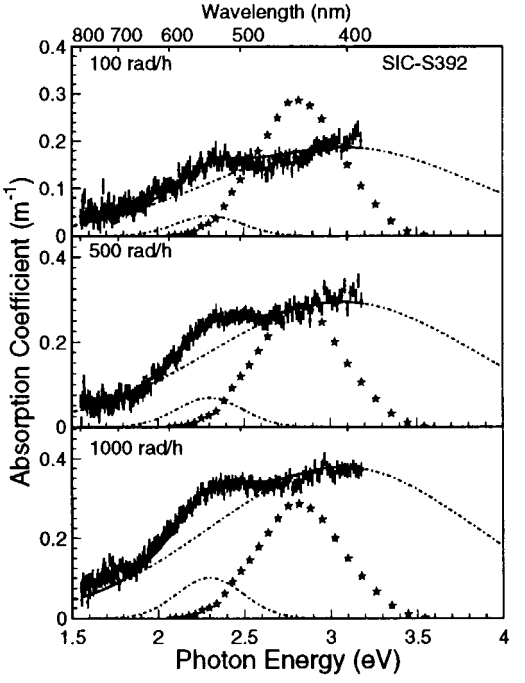

Figure 10. Radiation induced color center density for a Y doped sample SIC-S392

Figures 5,6,7,8,9 and 10 show radiation induced color center density as function of photon energy for six types of $PbWO_4$ crystals in equilibrium at different dose rates. The stars in these figures represent corresponding radio luminescence spectra weighted with quantum efficiency of the PMT used in monitoring test bench, which is described in Section 5. Since we have not yet measured radio luminescence spectrum for Y/Nb double doped crystals, the corresponding PMT quantum efficiency weighted radio luminescence spectrum is not shown in Figure 8. It, however, is expected to be similar to the radio luminescence spectra in all other tri-valent doped $PbWO_4$ samples, e.g. in Figure 7. The points with error bars in these figures are radiation induced color center density (D), or absorption coefficient, measured in equilibrium under dose rates specified. It was calculated according to equation

$$D = 1/LAL_{equalibrium} - 1/LAL_{before}. \quad (4)$$

where LAL is light attenuation length calculated by using longitudinal transmittance according to Equation I of reference [10], and the subscript "equilibrium" and "before" refer to "in equilibrium" and "before irradiation" respectively. For all these samples, the radiation induced color center density was decomposed to a sum (solid line) of two color centers with Gaussian shape in photon energy (dashed lines):

$$D = \sum A_i e^{-\frac{(E-E_i)^2}{2\sigma_i^2}} \quad (5)$$

where E_i, σ_i and A_i denote the energy, width and amplitude of the color center *i*, and *E* is photon energy. As seen from these figures, the two center fit provides a rather good description of the radiation induced color center data with χ^2 / DoF much less than one.

Table 2. Summary of Radiation Induced Color Centers

ID	E_1/σ_1 eV/eV	A_1^a m^{-1}	A_1^b m^{-1}	A_1^c m^{-1}	A_1^d m^{-1}	E_2/σ_2 eV/eV	A_2^a m^{-1}	A_2^b m^{-1}	A_2^c m^{-1}	A_2^d m^{-1}
S-167	2.35/0.51	0.23	0.39	0.47	—	3.45/0.50	0.99	0.88	1.07	—
S-210	2.35/0.51	0.20	0.21	0.22	—	3.45/0.50	0.91	0.91	0.93	—
S-274	2.92/0.39	0.33	—	0.38	—	3.51/0.25	0.88	—	0.90	—
S-275	2.92/0.39	0.22	—	0.24	—	3.51/0.25	0.40	—	0.41	—
B-1965	2.30/0.19	0.00	0.04	0.05	—	3.07/0.76	0.10	0.22	0.46	—
B-1971	2.30/0.19	0.01	0.06	0.12	—	3.07/0.76	0.26	0.69	1.16	—
B-2133	2.30/0.19	0.00	0.04	0.05	0.05	3.07/0.76	0.10	0.13	0.20	0.23
B-2162	2.30/0.19	0.01	0.03	0.06	0.06	3.07/0.76	0.10	0.19	0.30	0.30
S-S301	2.30/0.19	0.00	0.04	0.07	0.11	3.07/0.76	0.10	0.22	0.35	0.42
S-S347	2.30/0.19	0.00	0.00	0.03	0.07	3.07/0.76	0.10	0.13	0.14	0.38
S-S392	2.30/0.19	0.00	0.04	0.06	0.10	3.07/0.76	0.10	0.18	0.29	0.37
S-S412	2.30/0.19	0.00	0.03	0.04	0.06	3.07/0.76	0.10	0.15	0.19	0.24

^{a,b,c,d} represent 15, 100, 500, 1000 rad/h respectively.

Table 2 lists numerical result of the fit for all 12 samples listed in Table I, where S and B represent SIC and BTCP respectively. Consistent fit result was found for the same type of two samples in general. It is also interesting to note that all tri-valent (La, Y/Nb, Y/Sb and Y) doped samples have two common radiation induced color centers at the same energy and with the same width. One broad center is at wavelength of 400 nm (3.07 eV) with a width of 0.76 eV, and other narrow center is at a longer wavelength of 540 nm (2.30 eV) with a width of 0.19 eV. The radiation induced color centers in undoped and Sb doped samples, however, are rather different.

It is also interesting to note that these two color centers are peaked well apart at two sides of the peak of radio luminescence, and they have different damage and annihilation constants. This indicates that $PbWO_4$ monitoring light wavelength must be carefully chosen so that variations of crystal light output may be adequately estimated by using variations of transmittance.

Light Output Degradation Under Radiation

Spectroscopically speaking, crystal light output is a convolution of radio luminescence, trans- mittance and quantum efficiency of photo detector. Following Equation 3, $PbWO_4$ light output degradation under irradiation is also dose rate dependent since luminescence and photo detector quantum efficiency are not affected by radiation, or at least not in the same time scale. Figure 11 shows light output normalized to before irradiation (solid dots with error bars) as function of time for six $PbWO_4$ crystals under lateral irradiation by a ^{60}Co γ-ray source. Also shown in the figure is the dose rate applied. Once again, the dose rate dependence of light output is clearly observed.

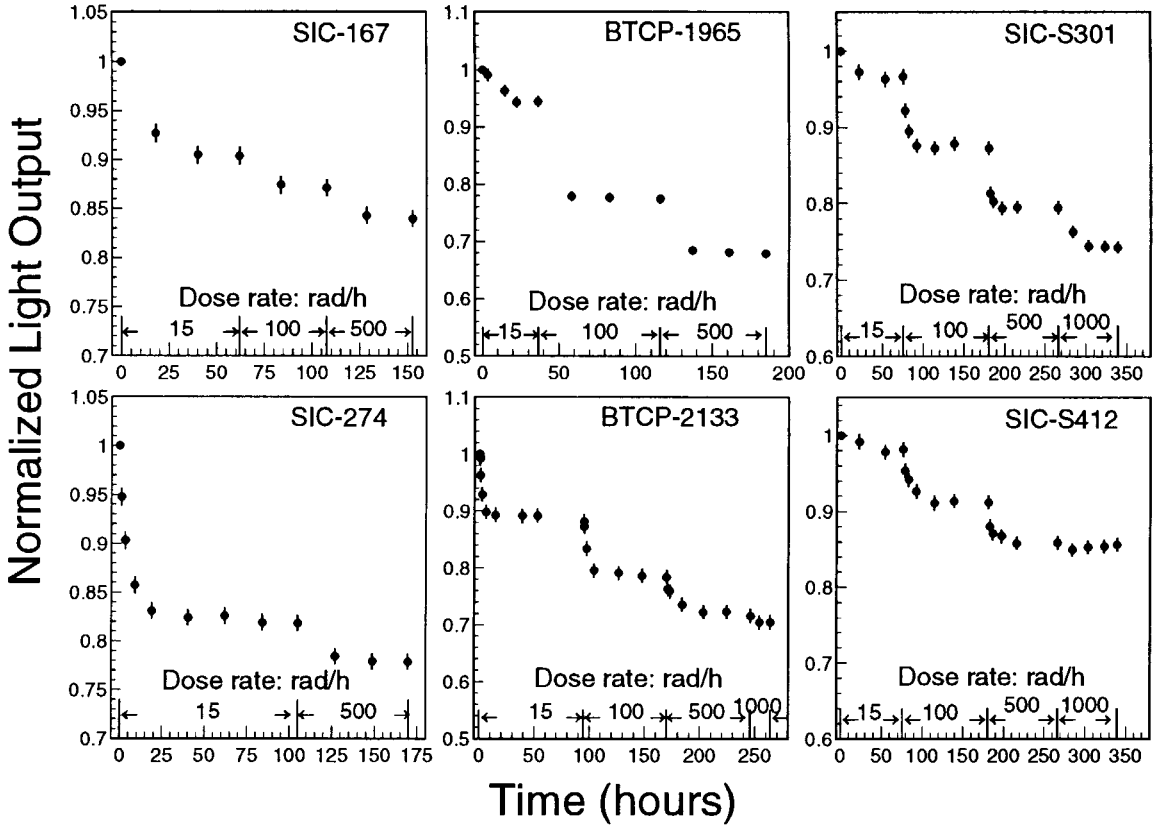

Figure 11. Normalized light output is shown as function of time after irradiation for six $PbW0_4$ crystals

Table 3 lists the normalized light output in equilibrium under different dose rate for all 12 samples, where R, S and B represent Dose Rate, SIC and BTCP respectively. The improvement of radiation hardness for crystals produced recently is clearly shown in this table.

Table 3. Summary of Light Output Degradation in Equilibrium under Irradiation

R	S	S	S	S	B	B	B	B	S	S	S	S
rad/h	167	210	274	275	1965	1971	2133	2162	S301	S347	S392	S412
15	90.4	80.0	82.0	83.6	94.5	72.2	89.2	86.1	96.6	95.1	98.2	98.2
100	87.1	77.0			77.9	47.2	78.6	76.8	87.3	88.6	91.3	91.2
500	84.0	—	78.0	80.0	83.6	—	72.3	70.3	79.5	82.1	78.0	85.9
1.000							70.5	68.2	74.3	78.0	80.2	85.3

$PbW0_4$ Crystal Monitoring

As discussed in Section I, the crucial inter calibration *in situ* at LHC for CMS $PbWO_4$ ECAL is to be provided by a light monitoring system [2], which uses relative variations of transmittance to estimate relative variations of light output for each individual crystal. Figure 12 is a schematic showing a monitoring test bench at Caltech. Monitoring light from a Xenon lamp went through a monochromator and injected to an integrating sphere. The light from one output of the sphere was coupled to the front end of sample through a quartz fiber and an air gap. The light from other output of the sphere was measured by a photo detector as reference. The sample was wrapped with Tyvek paper and optically coupled to a PMT. The output of the PMT is coupled to either a Merlin from ORIEL through a lock-in amplifier for transmittance measurement (position 1), or a LeCroy QVT multichannel analyzer for light output measurement (position 2). When the switch is in position 2, the shutter at the input of monochromator is closed so that there is no interference between scintillation light and monitoring light source. For absolute light output measurement the sample was shot by a small ^{137}Cs source. To simulate radiation environment *in situ* at LHC, the sample was either irradiated by a ^{60}Co source under 15 to 1,000 rad/h or under recovery after irradiation.

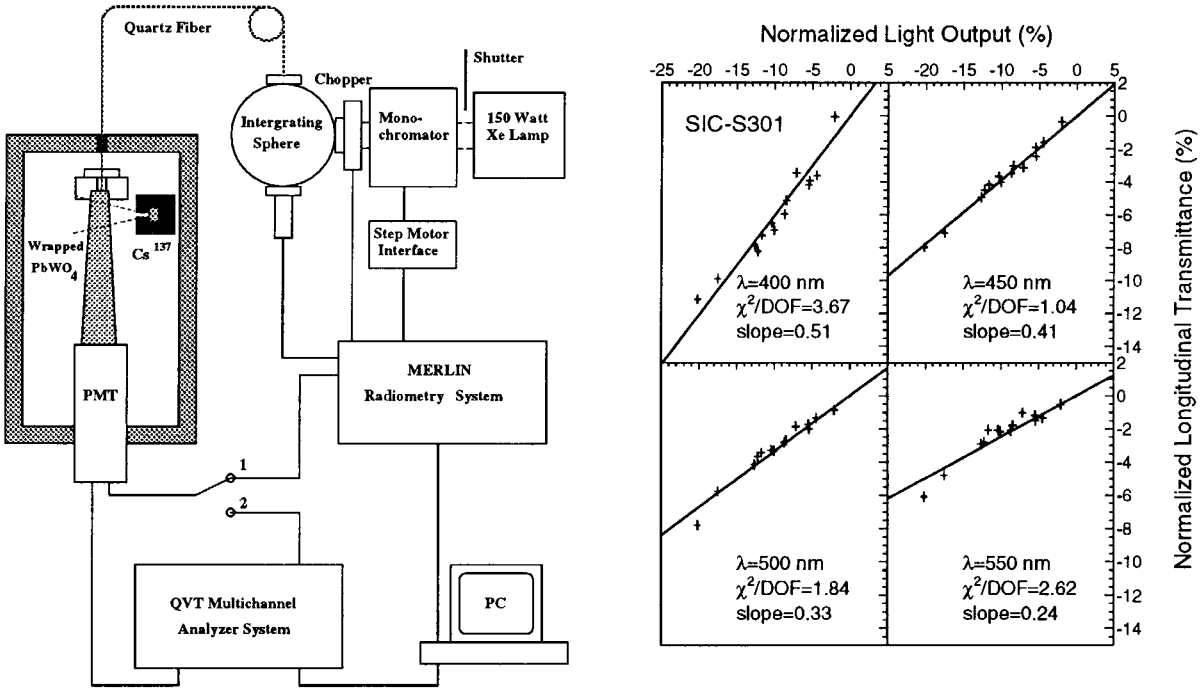

Figure 12. The monitoring test bench for light

Figure 13 shows correlations between relative variations of transmittance ($\Delta T/T$) and light output (ALY/LY) for monitoring light at four different wavelengths: 400,450,500 and 550 nm for a Y/Sb double doped sample SIC-S301. The correlation was fit to a linear function:

$$\frac{\Delta T}{T} = slope \times \frac{\Delta LY}{LY}. \qquad (6)$$

The result of the fit, the χ^2/DoF and the slope, is also listed in the figure. While the slope represents the sensitivity for $PbWO_4$ monitoring, the χ^2/DoF represents the linearity of the fit.

From the figure it is clear that the linearity is generally good when light output loss is less than 15%, and some systematic deviations exist for monitoring light of 400, 500 and 500 nm,

as compared to 450 nm, since not all wavelengths are adequate for the monitoring. Figure 14 shows monitoring sensitivity (solid dots), or slope, defined as $\frac{\Delta T}{T} = \frac{\Delta LY}{LY}$ and linearity (open dots), defined as χ^2/DoF, as function of monitoring wavelength for sample SIC-S301. Also shown in the figure is the PMT quantum efficiency weighted radio luminescence (dashed line). While a shorter monitoring wavelength is preferred for a better sensitivity, the best linearity is achieved at around 445 nm which coincides with the peak of radio luminescence.

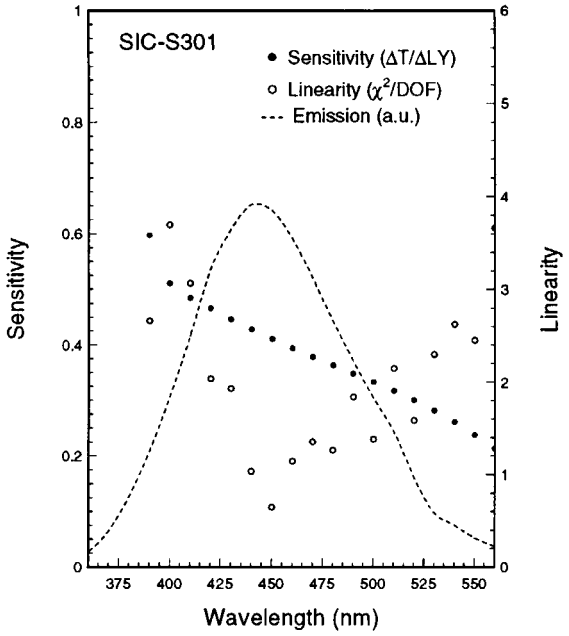

Figure 14. Monitoring sensitivity and linearity are shown as function of wavelength together with radio luminescence for a Y/Sb double doped sample SIC-S301

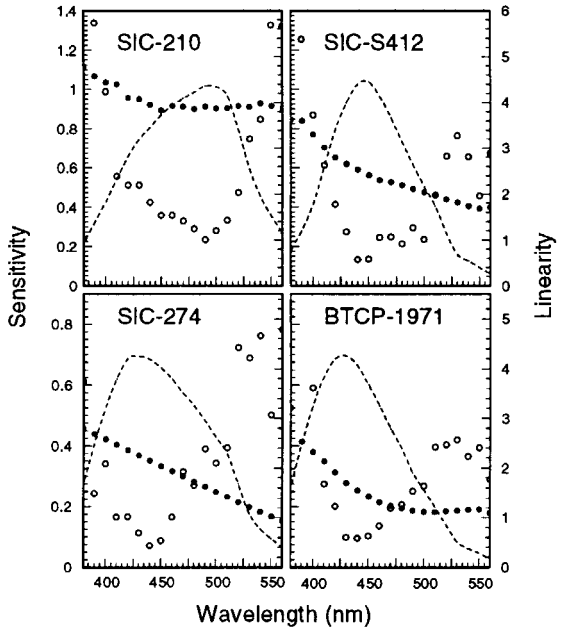

Figure 15. Monitoring sensitivity and linearity are shown as function of wavelength for four $PbW0_4$ samples

Figure 15 shows monitoring sensitivity (solid dots) and linearity (open dots) and PMT quantum efficiency weighted radio luminescence (dashed lines) for undoped (SIC-210), Y doped (SIC- S412), Sb doped (SIC-274) and La doped (BTCP-1971) $PbW0_4$ samples. All these samples have a better monitoring sensitivity at shorter wavelength and the best linearity around the peak of PMT quantum efficiency weighted radio luminescence. The better monitoring sensitivity at shorter wavelength is understood because of the poorer initial transmittance as compared to that at longer wavelength. The best linearity around the peak of radio luminescence is caused by two radiation induced color centers discussed in Section 3. Since we did not have enough time to systematically measure Y/Nb double doped sample in our test bench, its monitoring sensitivity and linearity are not shown in this report. However, preliminary result with few data points indicates that it is similar to all other tri-valent doped samples.

Summary

We measured photo and radio luminescence, radiation induced color centers, light output degradation and monitoring sensitivity and linearity for six types of $PbWO_4$ crystals: undoped. La doped, Sb doped, Y/Nb double doped, Y/Sb double doped, and Y doped. All tri-valent doped samples, including La, Y/Nb, Y/Sb and Y doped samples, have consistent intrinsic photo lu- minescence peaked at 420 nm. Because of internal absorption, their radio luminescence is 15 to 25 nm red shifted. Similarly, the peak of radio luminescence of undoped $PbW0_4$ crystal is 15 nm red shifted from the photo luminescence (495 nm). The only exception is Sb doped $PbWO_4$ Its peak of radio luminescence is 60 nm blue shifted from

photo luminescence (510 nm), explained by not energetic enough photons of the UV excitation light.

Radiation induced color center density in all samples can be decomposed to two color centers. All tri-valent doped samples have two common radiation induced color centers peaked at 400 and 540 nm. The peaks of radiation induced color centers for undoped samples are at 360 and 530 nm, and that of Sb doped samples are at 350 and 430 nm. These two centers are located at two sides of luminescence and with different damage and recovery constant. The physical nature of these color centers are not yet identified.

Because it is less transparent at short wavelengths, the monitoring sensitivity for PbW04 crystal is better at short wavelength. The best linearity, however, can only be achieved with monitoring light wavelength around the peak of radio luminescence weighted with quantum efficiency of photo detector. Since $PbWO_4$ photo detector used in CMS ECAL is Si avalanche photo diode, which has a flat quantum efficiency as compared to that of the PMT with bi-alkali photo cathode used in this investigation, it is expected that the monitoring wavelength of choice is around 450 nm for all tri-valent or Sb doped $PbWO_4$ crystals. The undoped crystal, however, would require a monitoring wavelength around 510 nm.

Acknowledgements

Prof. Z.W.Yin and P. Lecoq provided samples in this report. Dr. Q.Deng measured sample SIC-167 and BTCP-1965 when he was at Caltech. Many interesting discussions with Drs. F.Nessi, P.Lecornte, J.Y.Liao, D.Z.Shen, D.S.Yan and Z.W. Yin are acknowledged.

References

1. *Compact Muon Solenoid Technical Proposal*, **CERN/LHCC 94-38,** LHCC/PI (1994).
2. CMS Collaboration, The *Electromagnetic Calorimeter Technical Design Report*, **CERN/LHCC 97-33** (1997).
3. H.F.Chenf *et al., Nucl. Instr. and Meth.* **A414** (1998) 149.
4. P.Lecoq *et al., Nucl. Instr. and Meth.* **A403** (1998) 302, *Nucl. Instr. and Meth.* **A402** (1998) 75 *Nucl. Instr. and Meth*. **A365** (1995) 291.
5. M.Kobayashi *et al., Nucl. Instr. and Meth.* **A406** (1998) 442, *Nucl. Instr. and Meth.* A404 (1998) 149, *Nucl. Instr. and Meth.* A399 (1997) 261, *Nucl. Instr. and Meth.* **A373** (1996) 333.
6. M.Korzhik *et al., Rad. Meas.* **29**(1) (1998) *27, J. Allo. & Comp,* **238** (1996) 46, *Phys. Stat. SoL* **a156** (1996) 493 *and Phys. Stat. Sol*. **A154** (1996) 779.
7. M.Niki *et al., Phys. Stat. Sol*. **A164** (1997) R9, *J. Appl. Phys. Lett.* **82**(11) (1997) 5758, J. *Appl. Phys. Lett.* **71**(26) (1997) 3755, *Phys. Stat. Sol.* **bl96** (1996) *K7 and Phys. Stat. Sol.* **bl95** (1996) 311.
8. R.Y.Zhu *et al., Nucl. Instr. and Meth.* **A413** (1998) 297, IEEE *Trans. Nucl. Sci***. NS-45** (1998) 686, *IEEE Trans. Nucl. Sci*. **NS-44** (1997) 468, *Nucl. Instr. and Meth.* **A376** (1996) 319, *IEEE-NUCL-S* **V43** (1996) 1585.
9. D.Ma and R.Y.Zhu, *Nucl. Instr. and Meth.* **A332** 113 (1993).
10. R.Y.Zhu *et al., Nucl. Instr. and Meth.* **A376** (1996) 319.

Reading thin-film scintillators with optical microscopes for x-ray imaging

A. Koch[1], P. Cloetens[1], W. Ludwig[1], J. C. Labiche[1] and B. Ferrand[2]

[1]*European Synchrotron Radiation Facility (ESRF), B.P. 220, 38043 Grenoble Cedex, France*
[2]*LETI/DOPT, CEA-Grenoble, 17 rue des Martyrs, 38054 Grenoble Cedex 09, France*

Thin-film scintillators are used to detect high-resolution x-ray images and to convert them into visible-light images that are projected by microscope optics onto a CCD camera. Several components of the detection system have been improved: $Lu_3Al_5O_{12}$ scintillators activated by Tb or Eu have been deposited by liquid phase epitaxy. These scintillators increase x-ray absorption compared to the previous used $Y_3Al_5O_{12}$. Optics and scintillator have been optimised for highest spatial resolution. A specially developed x-ray slit allowed the characterisation of the camera down to a resolution of 0.5 µm fwhm. A CCD camera having a dynamic range of 14 bit at a readout rate of 20 Mpixels/s provides a more efficient use of synchrotron radiation at the ESRF.

Keywords: scintillator, thin film, x-ray imaging, microscopy, microtomography, CCD

Introduction

X-ray radiography and tomography with micrometer resolution gains increasing interest in science and industry [1,2]. High resolution requires intense x-ray sources since the absorbed dose for a given signal-to-noise ratio (SNR) is inversely proportional to the pixel surface of the detection system. Third-generation synchrotron sources that are operational for a few years provide the necessary intensity and monochromaticity with exposure times below 1 s.

Thin-film scintillators are used to detect high-resolution x-ray images and to convert them into visible light that is projected by microscope optics onto a charge-coupled-device camera (CCD camera). This detection scheme has prooved to be very flexible and economic [3].

The detection system will be discussed from a system engineering point of view. The essential components are the scintillator, the optics and the CCD camera. The characteristics of these components have to be adapted to eachother. High x-ray absorption requires thick layers of well absorbing scintillators. High resolution on the other hand demands thin layers adapted to the depth of focus of the optics. Recent progress on liquid phase epitaxy of $Lu_3Al_5O_{12}$ (LAG) scintillators activated by Tb or Eu and their properties are reported. A high luminescence efficiency improves the SNR up to a certain limit. A high numerical aperture (NA) of the optics increases the light collection but reduces depth of focus and hence demands for thin layers. The spectral emission and time response of the scintillator has to be matched to the characteristics of the CCD. A CCD camera providing a dynamic range of 14 bit at a readout rate of 20 Mpixels/s has been developed for that purpose. The best system design is a compromise between these parameters, for a required spatial resolution, SNR, dynamic range and x-ray intensity [4]. Different techniques to characterize submicrometer spatial resolution have been established. A special developed tungsten-carbide slit (WC slit) allows a characterisation of the imaging system down to 0.5 µm fwhm. This paper adresses recent progress on several components of the detection system.

This kind of high-resolution on-line detector is a versatile tool for three types of imaging applications: (a) computed microtomography, (b) real-time radiography of the kinetics of a

system and (c) quantitative imaging to perform, for example, phase retrieval in coherent imaging. In the case of high-resolution tomography a large number, of the order of 1000, radiographs have to be recorded to reconstruct the three-dimensional distribution in the sample. The efficiency of the scintillator together with the short readout time and low-noise level of the camera allow to exploit more effectively the valuable synchrotron beams. A complete tomographic scan can now be performed with a high spatial resolution in less then 9 minutes. Results of 'fast' microtomography performed on metallurgical samples illustrate the possibilities. The detector allows to study a larger number of samples in the limited time available at third-generation synchrotrons and it opens the possibility to perform in-situ high-resolution tomography during for example the application of strain or during an annealing process.

2. X-ray imaging with thin-film scintillators

To achieve high-resolution x-ray imaging, scintillators are combined with diffraction-limited microscope objectives. The scintillator converts the x-ray image into a visible-light image that is magnified onto a CCD camera. The imaging problem is the following (Fig. 1). A low divergent x-ray beam is partially absorbed by the scintillator and generates a visible-light image. The light image (object plane of the optical system) is projected onto the CCD (image plane). In practice, the x-ray beam can be considered to be parallel w.r.t. the experimental conditions. Therefore, the light intensity distributions across arbitrary planes in the scintillator are identical, apart from amplitude changes as a result of the attenuation of the x-ray beam. These intensity distributions are imaged and summed at the CCD. The CCD will be focused onto a specific object plane within the scintillator.

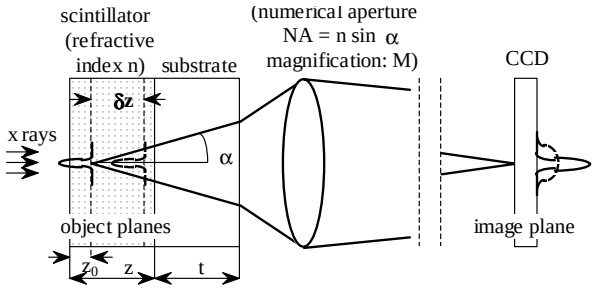

Fig. 1. X-ray imaging with scintillators. Identical visible-light images are created by the x-ray beam in different planes of the scintillator. An image in plane z_0 is focused onto the CCD (solid curves). An image in plane $z_0+\delta z$ is out of focus at the CCD (dashed curves).

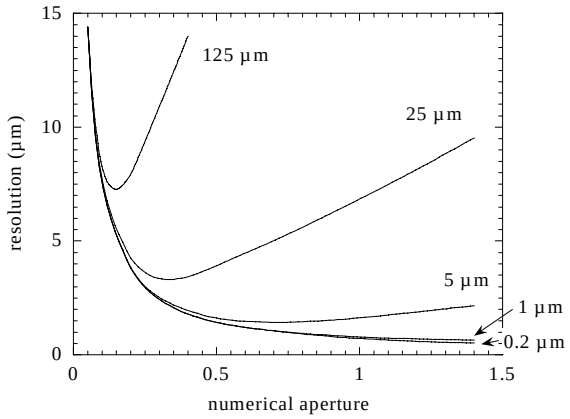

Fig. 2. Spatial resolution R vs. numerical aperture NA of an optical system for different thicknesses z of a scintillator. The left wing is degraded by diffraction, the right one by defect of focus. Parameters used for computation: n = 1.95, $z_0 = z/2 = \delta z_{max}$, λ = 550 nm, R in (fw90%int of LSF).

The planes before and behind this plane will be out of focus at the CCD but will nevertheless contribute to the total signal distribution.

The image resolution, therefore, is determined by the amount of defect of focus of the image distributions before and behind the focal plane. Further degradation of the image occurs due to diffraction and spherical aberrations arising from the thickness of the scintillator and the substrate. Parallax by misalignment, i.e. an angle between x rays and optical axis, may also degrade the image quality.

The frequency response of an imaging system suffering from a defect of focus and diffraction has been derived by Hopkins under the assumption of a circular aperture [5]. We applied his formula to compute the resolution of our optical system [3]. The spatial resolution R is expressed in terms of full width, which covers 90% of the integrated line spread function (fw90%int of LSF). This is done since the LSF changes significantly its shape if resolution is determined by defect of focus. The fwhm of LSF is therefore no longer an unambiguous measure of resolution. In the diffraction-limited case $R_{fw90\%int} = 2.6\ R_{fwhm}$. Fig. 2 shows numerical simulations of optical systems as a function of NA, using: refractive index $n = 1.95$ for YAG ($Y_3Al_5O_{12}$), wavelength $\lambda = 550$ nm and $z_0 = z/2 = \delta z_{max}$. Highest spatial resolution is obtained with a thickness of the scintillator between 1 - 5 µm and adequate NA of the optics. If the x-ray energy is low absorption takes place in the first micrometers of the scintillator and a thin layer is not necessary. Lee et al. for example [6] achieved a contrast of 10% for periodic structures of 1 µm using a 60 µm thick $CdWO_4$ crystal and optics with a NA of 0.5. The energy applied was 20 keV; 50% is absorbed in the first 20 µm. Assuming a Gaussian modulation transfer function (MTF) this corresponds to 1.4 µm fwhm of LSF. A similar result is obtained from Fig. 2.

Combining this type of detector with magnifying x-ray optics, e.g. compound-refractive lenses, improves the resolution to 0.3 µm fwhm [7].

3. Improved performance of the imaging system

Initially, commercially available components had been used for the imaging system: YAG:Ce scintillators epitaxially grown on undoped YAG substrates of 170 µm thickness (Crismatec, Nemours, France), microscope optics (Olympus, Japan) and slow-scan, high-dynamic range cameras (Photometrics or Princeton, USA) [3]. A substrate thickness of 170 µm was chosen because this corresponds to the thickness of microscope cover slides. High aperture microscope objectives usually correct for spherical aberrations arising from this plate thickness.

Several improvements have been achieved: (a) an increase in absorption by using scintillators with higher atomic number and higher density, (b) a more appropriate method to characterize the camera resolution, (c) higher resolution with thinner scintillators and optics with higher NA, and (d) a faster, high-dynamic range CCD camera.

3.1 $Lu_3Al_5O_{12}$ scintillators increase the x-ray absorption compared to $Y_3Al_5O_{12}$

LAG scintillators activated by Eu or Tb have been grown by liquid phase epitaxy on YAG substrates. The growth process is described in Ref. [8,9]. The lattice adjustment between LAG and YAG has been achieved with Sc that substitutes Al. The stoicheiometric composition of LAG as referred to in this paper is: $Lu_3Al_{5-x}Sc_xO_{12}$ with $x \approx 0.5$. The concentration of Eu and Tb has been varied to optimize the light yield. Fig. 3 and Fig. 4 show the results as a function of the activator concentration in atom% of Lu. Layers of different thickness have been measured with a frontside-illuminated CCD (EEV05-30). The data is referred to the signal response of YAG:Ce (supplier: Crismatec). Although the efficiency of LAG:Eu is slightly

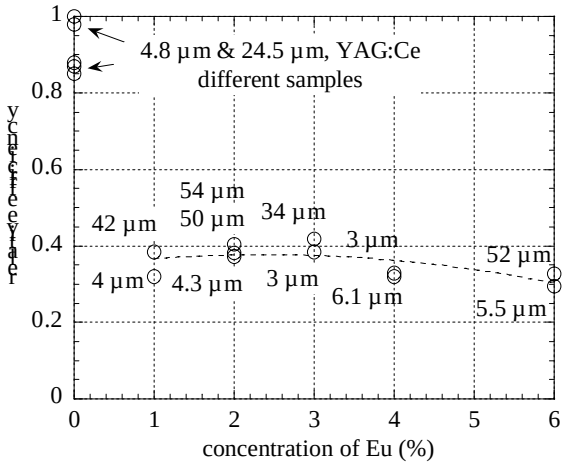

Fig. 3. Luminescence efficiency of thin films of LAG:Eu deposited by liquid phase epitaxy on YAG as a function of the Eu concentration in atom% of Lu.

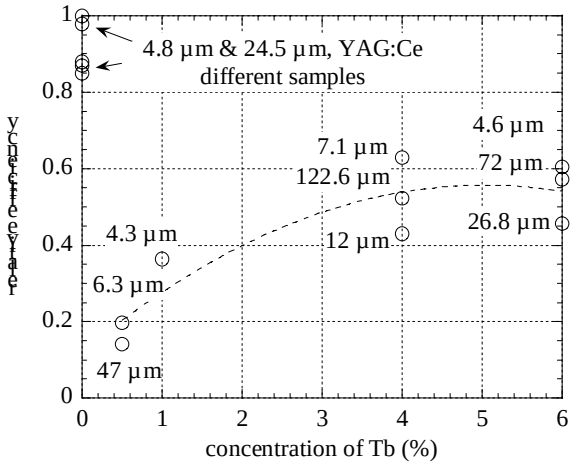

Fig. 4. Luminescence efficiency of thin films of LAG:Tb deposited by liquid phase epitaxy on YAG as a function of the Eu concentration in atom% of Lu.

lower than LAG:Tb, it is preferred as a result of its reduced afterglow in the exposure range between 100 ms to 1s that is mostly used [8].

Compared to YAG:Ce (≈ 21000 ph/MeV), absorption increases and luminescence efficiency decreases. A net gain in signal of approximately a factor of 3.3 before the absorption edge of Y (17 keV) and a factor of 1.2 for energies > 17 keV has been obtained. However, the SNR may not be affected by the reduced efficiency of LAG if the NA of the optics is sufficiently large. Noise analysis showed [4] that for NA's > 0.5 the SNR is limited by x-ray photon statistics. Then, SNR^2 is expected to increase proportional to absorption. Fig. 5 shows the absorption (total energy transfer) for a 5 µm thick layer of YAG, LAG and Lu_2O_3. Lu_2O_3 may further increase the signal response. It can be prepared with a sol-gel method that does not require a specific substrate material for crystal growth. With this technique it is however difficult to achieve the required film thickness. The light yield is ≈ 50000 ph/MeV for a cristalline powder [10] which is a factor of two higher than for the YAG:Ce films.

Undesired luminescence from the YAG substrates contributes to the total signal detected by the CCD. Its cause is not yet fully understood. Different substrates from different manufacturers have been tested and the efficiency relative to YAG:Ce varies between 1.4 - 6%. As mentioned above the optics usually require a substrate thickness of 170 µm. Hence the signal contribution from the substrate can be relatively important especially for thin layers of the scintillator and high x-ray energies. The image quality is reduced since the depth of focus of the optics in general is too small to assure that the signal from the substrate is in focus. The spectral emission of the substrate has been measured and it is almost identical with that of Ce. Hence Ce impurities in the order of 10 ppm are believed to be the reason. Beside an improvement in purity of the YAG crystal other methods can be applied: It is expected that spectral filtering of the emission of a LAG:Eu/YAG crystal reduces the recorded substrate luminescence by a factor 2. If the LSF is precisely known resolution enhancement by two-dimensional deconvolution has been demonstrated [11].

3.2 X-ray slit for characterisation and alignment of submicrometer resolution

To measure submicrometer resolution different techniques have been used so far: (a) A coherent method [3]. Interference fringes of a boron fiber with tungsten core have been used as a test target.

The theoretical interferogram is compared with the measured one, yielding the spatial resolution of the camera especially the MTF. This method relies on the precise knowledge of the object and the coherence properties of the x-ray beam in order to calculate the theoretical interferogram. (b) A slit has been manufactured out of two tungsten blocks with an evaporated aluminum spacer [3]. The spacer was etched away in the center of the slit. This method gives directly the LSF, however, the mounting is difficult; any dust particles may change the distance between the two blocks. The minimum slit width achieved was 1.2 µm, i.e. the gap between two W blocks of 10 x 1 mm^2. (c) Another method uses a GaAs edge. A 600 µm thick GaAs wafer was cleaved along its crystal planes perpendicular to its surface. This method probes the edge response of a detector. In general, a slit measurement has the advantage of being a 'conservative' method, i.e. any mistake in the measurement or set up gives results which are worse than the camera resolution. This is not the case for the other methods. For example, total reflections at an edge may artificially sharpen the response.

Therefore, an improved slit based on gauge blocks and flexure hinges has been used to characterise the detector, developed by M. R. Howells (Lawrence Berkeley Laboratory, USA). The actual slit is formed by two commercially available gauge blocks of tungsten carbide. The gauge blocks are 2.5 mm thick and have a 45 degree slope toward the slit edge; the width of the flat end surface, the contact surface, is 20 µm. The flexure hinges have been realized in stainless steel by electroerosion.

3.3 Optical system with a numerical aperture of 0.95

To explore the limits of resolution, an objective with a NA of 0.95 (Olympus SPlanApo 40x/0.95) and a scintillator with a layer thickness of 1 µm have been chosen. According to Fig. 2 the system should be diffraction limited with a spatial resolution of R_{fwhm} = 0.3 µm.

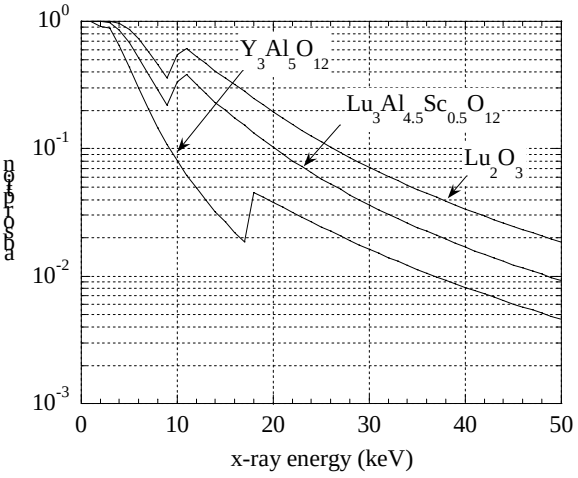

Fig. 5. Absorption for 5 µm thick layers of different scintillators: $Y_3Al_5O_{12}$ (4.55 g/cm^3), $Lu_3Al_{4.5}Sc_{0.5}O_{12}$ (6.62 g/cm^3) and Lu_3O_3 (9.42 g/cm^3).

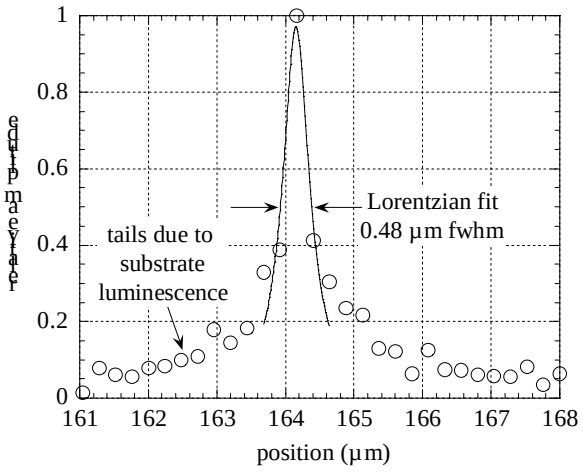

Fig. 6. Line spread function of 1 µm thick layer of LAG:Eu. Optical system: NA = 0.95, 40x, 2.5x eyepiece, input pixel size 0.24 µm. X-ray energy: 11.5 keV.

Fig. 6 shows the results. After an initial high slope, tails appear which are interpreted to result from the substrate luminescence. The Lorentzian fit therefore is only done for the 5 central data points. At 11.5 keV 75% of the light is expected to be emitted from the 1 µm thick layer and 25% from the 170 µm thick substrate, i.e. a ratio of 3.

Dividing the integral of the LSF at its central peak by that around its blurred part confirms this ratio. The data has been binned 30 times in the direction perpendicular to the slit.

3.4 Fast-readout, low-noise CCD camera (FRELON camera)

A detection system has to compromise between dynamic range and acquisation rate. A high acquisation rate requires a high bandwidth of the electronic circuits which in turn increases the noise and reduces the dynamic range. Futhermore, for a given SNR the necessary exposure time is proportional to the pixel surface. The synchrotron beams at the ESRF are sufficiently intense to obtain exposure times of 50 ms with pixel sizes at the input of the detector of 1 µm. A dynamic range of 14 bit in a single image is often required. A fast readout, compared to the exposure time, is especially important in tomography experiments where up to one thousand images have to be taken for a single 3D reconstruction.

A CCD camera has been developed in-house for such applications. It is based on Thomson chips of 1024^2 or 2048^2 pixels. These chips offer high readout speed at four parallel outputs with low-noise operation. The CCD is cooled to -20 °C to reduce the dark current and to allow exposure times of several minutes without significant excess noise. Extreme care was taken concerning electromagnetic compatibility to prevent crosstalk between the 4 channels that are read in parallel. This was a prerequisite to cope with the fast rise time, high current clock speeds and low-level, wide-bandwidth signals.

The result is a family of cameras with a readout speed of 20 Mpixels/s at a true dynamic range of 14 bit. A multi-pinned-phase (MPP) chip technology has also been implemented which provides lower dark current at a reduced full well capacity. Table 1 summarizes the characteristics of the cameras developed. Fig. 7 shows the non-linearity residual w.r.t. a linear fit for each of the 4 readout channels. The remaining non-linearity is low and especially similar for each output. Also the parameters offset, gain and crosstalk for each channel are matched to eachother to achieve a single uniform image.

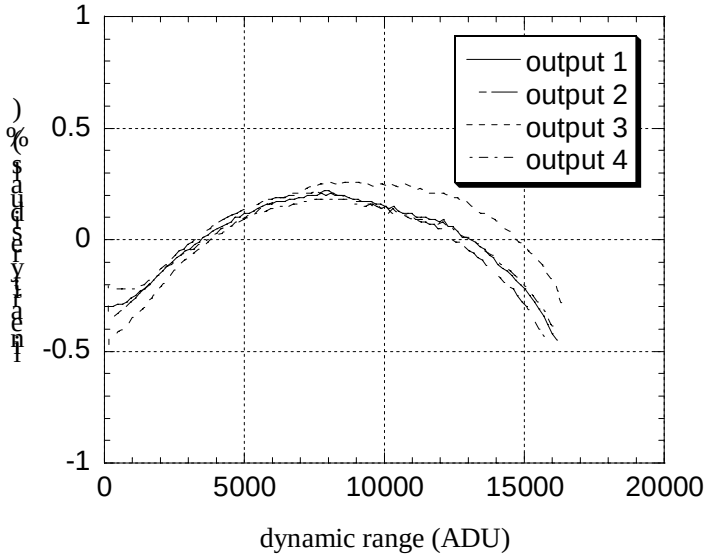

Fig. 7. Non-linearity residuals for the 4 readout channels of the Frelon camera. All 4 output signals are combined to a single uniform image with identical image quality.

	Camera 1024	MPP Camera	MPP Camera
CCD chip	Th7896A	Th7896M	Th7899M
number of pixels	1024^2	1024^2	2048^2
pixel size	$(19\ \mu m)^2$	$(19\ \mu m)^2$	$(14\ \mu m)^2$
readout speed	$20 \cdot 10^6$ pixels/s	$20 \cdot 10^6$ pixels/s	$20 \cdot 10^6$ pixels/s
sensitivity	40 e^-/ADU	22 e^-/ADU	20 e^-/ADU
readout noise	44 e^- rms	31 e^- rms	20 e^- rms
full-well capacity	$600 \cdot 10^3$ e^-	$350 \cdot 10^3$ e^-	$320 \cdot 10^3$ e^-
dynamic range	13600	11300	16000
dark current	200 e^-/s/pixel	3 e^-/s/pixel	3 e^-/s/pixel
non-linearity (integral)	± 0.2%	± 0.4%	± 0.3%

Table 1. Fast-readout and low-noise CCD camera (Frelon camera). Further characteristics: full frame transfer, 4 outputs for readout, normal and MPP mode, anti blooming, binning, region of interest readout, Peltier cooling to -20 °C, AIA computer interface, fibre optic link.

5. Applications

The advent of third-generation synchrotron radiation sources is proving better than anticipated for the development of imaging techniques. The high photon flux available, even in a monochromatised beam, makes high-resolution imaging with good photon statistics possible. The coherence of the synchrotron beams allows a trivial form of phase imaging with an improved sensitivity compared to absorption imaging. However, few detection systems were initially available to fully exploit these new possibilities. The improvements described above contribute to make up for this retardation. Transparent luminescent screens coupled to a high quality CCD by light optics are now daily used at different experimental stations performing X-ray imaging at synchrotron sources. The major technique for which this device is used, is microtomography but other applications are also interesting.

Real-time radiography allows to track rapidly varying bulk phenomena if the sample is not too thick in order to avoid confusing superposition by the projection over the sample thickness. Using the full-frame size (1024×1024) of the Frelon camera it is in principle possible to record 20 images per second. With an exposure time equal to the read-out time a figure of 10 images/s seems reasonable. This speed was demonstrated at the experimental station ID19 at the ESRF when imaging the growth and motion of gas bubbles in beer [12]. These real-time imaging possibilities are presently used to investigate the mechanism of liquid metal embrittlement [13]. The penetration of the liquid metal gallium into the grain boundaries of aluminum was imaged in-situ and the kinetics of the penetration process was measured. Many other applications can be considered such as the observation of processes involving solidification, plastic deformation, combustion or phase transitions.

Quantitative imaging, where the recorded image is a two-dimensional map of the X-ray intensity distribution, is crucial in techniques involving computer processing such as tomography and phase retrieval. The digital output format and excellent linearity of CCD-based detectors are important advantages. A poor MTF of the system results in a spoiled resolution but also in artefacts if the computer processing does not consider and correct for the convolution with the detector response. Correction is possible [11] but the useful SNR will be reduced compared to the case of a better MTF. Reduction of the tails in the LSF, due to substrate fluorescence as discussed earlier, is thus an important issue.

The phase-sensitive imaging method developed at ESRF [14,15] based on simple propagation has the advantage of being extremely simple from an experimental point of view. However, there is no straightforward relationship between the image intensity and the optical phase. A phase retrieval scheme must be used to disentangle the phase information from the recorded Fresnel diffraction patterns. Such a scheme was implemented based on four images recorded at different distances with respect to the sample. The detector used consists of a YAG:Ce converter screen coupled to the Frelon camera by an optical system with a magnification of 20 times. The computer processing for the determination of the quantitative phase maps includes correction for the detector response. Combined with tomography this technique results in quantitative 3D mapping of the density in the sample [15]. A total of about 3000 images must be recorded, hence a short readout time is again crucial.

Computed tomography involves recording a large number of radiographs corresponding to slightly ($\approx 0.2°$) different angular positions. Using the high-resolution detector original results were obtained in the field of materials science [13] and biology [8], both in absorption mode and in a phase contrast mode sensitive to the edges in the specimen. The experimental conditions were improved together with the detector in order to reduce the time to record a complete tomographic scan. This time gain is important to increase the number of samples that can be investigated but also to avoid any drift during the scan compared to the spatial resolution. Finally, this makes it possible to perform tomography in a nearly real-time way.

The white synchrotron beam is monochromatised by a multilayer rather than the more usual perfect silicon crystals. This increases the incident flux by two orders of magnitude to about 10^{12} photons/s/mm^2 at an x-ray energy of 20 keV. The multilayer used consists of 100 Ru/B_4C layers with a period of 4.2 nm deposited on a high-quality substrate. The tasks to be performed during a tomographic scan are: exposing the detector, reading the image, storing the image to disk and moving the rotation stage. The acquisition was optimized in the following way: exposure of the new image and storing the previous one are done in parallel and reading the image and moving the stage are also parallelized. The dead time per image, i.e. the time which is not used to expose the CCD, is reduced in this way to 0.3 s while reading the camera at 5 Mpixels/s. This value can be further reduced by reading the four channels in parallel.

As an example we discuss the investigation of metal alloys casted in the semi-solid state. This material is brought at a temperature where the eutectic is a liquid whereas the primary phase remains solid. The material is quenched from the high temperature so as to freeze the semi-solid state. The knowledge of the three-dimensional connectivity of the primary phase is crucial in order to understand the plastic deformation of this material. For the investigation an effective pixel size at the input of the detector of 1.9 µm was chosen as a compromise between spatial resolution and field of view. The x-ray energy was set to 17.5 keV. A 25 µm thick YAG:Ce layer grown on a 500 µm thick YAG substrate was used as a converter. The NA of the optics was 0.3, well adapted to the thickness of the sensitive layer (c.f. Fig. 2). The exposure time for a single projection was 0.3 s using the full well capacity of the Frelon camera. Recording about 900 images took less than 9 minutes. This includes recording 800 projections and also flatfield and dark images without sample and without x-ray illumination.

Fig. 8a shows an example of absorption tomography of an aluminum alloy with 10% of copper in mass. In this slice through the reconstructed volume the primary phase appears in dark whereas the eutectic is white. A 3D study of the volume indicates that the primary phase is highly connected. The good SNR makes binarization of the volume and determination of the microstructure straightforward. Fig. 8b is a result of tomography obtained in a phase-sensitive mode. The sample is an industrial A356 alloy (Al-7 % Si-1 % Mg) and in this case the attenuation coefficient of the primary phase and the eutectic can not be distinguished.

Therefore edge enhancement was used and the detector was set at a distance of 0.6 m with respect to the sample. The primary phase is in this case delineated by a white/black fringe. The short acquisition time allowed to study a large number of samples differing in their composition, annealing history or casting process. Also the microstructure of a given sample could be followed at different stages of the annealing process.

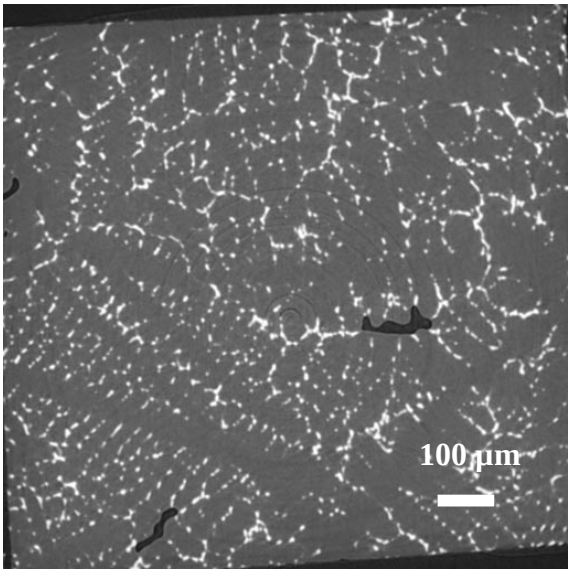

Fig. 8a Reconstructed slice obtained by absorption tomography of a semi-solid Al/Cu alloy. The primary phase is gray and the eutectic is white (courtesy of L. Salvo).

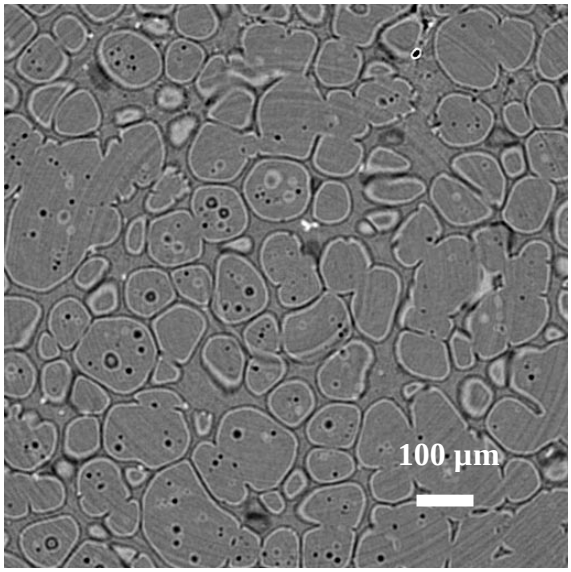

Fig. 8b Tomography in a phase-sensitive mode of an alloy A356 (Al-Si). The primary phase is delineated by a white/black fringe.

6. Conclusions

Thin-film scintillators have found applications in x-ray imaging with micrometer resolution, especially at synchrotron radiation sources. Recent development efforts have increased the x-ray absorption by employing scintillators with higher atomic number and higher density. Potentially, improvements are still expected with e.g. Lu_2O_3 films. The image quality presently is limited by undesired luminescence from the substrate. Either the purity of YAG can be improved or other non-epitaxial methods, like sol-gel deposition, may be used which leave a wider choice of substrate materials. This type of detection system together with the high photon flux of synchrotron x-ray sources allows real-time radiography and fast tomography with micrometer resolution. To achieve this it was necessary to improve several components of the acquisition system, including its software.

Acknowledgements

We thank M. R. Howells (Lawrence Berkeley Laboratory, USA) for providing the x-ray slit for the high-resolution measurements and we acknowledge the help of the members of the Topography Group at the ESRF. We are grateful to L. Salvo and collaborators (GPM2, ENSPG (INPG), Grenoble) for providing the tomographic data of metal alloys.

References

1. P. Cloetens, M. Pateyron-Salomé, J.Y. Buffière, G. Peix, J. Baruchel, F. Peyrin, M. Schlenker, “Observation of microstructure and damage in materials by phase sensitive radiography and tomography”, J. Appl. Phys. **81**, 5878-5886 (1997).
2. A. Sasov and D. Van Dyck, "Desktop x-ray microscopy and microtomography", J. Microsc. **191**, 151-158 (1998).
3. A. Koch, C. Raven, P. Spanne, and A. Snigirev, "X-ray imaging with submicrometer resolution employing transparent luminescent screens", J. Opt. Soc. Am. **A15**, 1940-1951 (1998).
4. A. Koch and C. Raven, "Scintillators for high resolution x-ray imaging", in *Proc. of the Int. Conf. on Inorganic Scinillators and Their Applications SCINT97*, Y. Zhiwen, F. Xiqi, L. Peijun, and X. Zhilin, eds. (CAS, Shanghai Branch Press, Shanghai, 1997), pp. 28-31.
5. H. H. Hopkins, "The frequency response of a defocused optical system", Proc. Roy. Soc. **A231**, 91-103 (1955).
6. H. R. Lee, B. Lai, W. Yun, D. C. Mancini, and Z. Cai, "X-ray microtomography as a fast three-dimensional imaging technology using a CCD camera coupled with a $CdWO_4$ single-crystal scintillator", in *Developments in X-Ray Tomography*, U. Bonse, ed., Proc. SPIE **3149**, 257-264 (1997).
7. B. Lengeler, C. G. Schroer, M. Richwin, and J. Tümmler, "A microscope for hard x rays based on parabolic compound refractive lenses", Appl. Phys. Lett. **74**, 3924-3926 (1999).
8. A. Koch, F. Peyrin, P. Heurtier, B. Ferrand, B. Chambaz, W. Ludwig, and M. Couchaud, "X-ray camera for computed microtomography of biological samples with micrometer resolution using $Lu_3Al_5O_{12}$ and $Y_3Al_5O_{12}$ scintillators", in *Physics of Medical Imaging*, J. M. Boone and J. T. Dobbins, eds., Proc. SPIE **3659**, 170-179 (1999).
9. B. Ferrand, D. Pelenc, I. Chartier, and C. Wyon, "Growth by LPE of Nd:YAG single crystal latters for waveguide laser applications", J. Crystal Growth **128**, 966-969 (1993).
10. C. Dujardin, A. Garcia-Murillo, C. Pedrini, C. Madej, C. Goutaudier, A. Koch, A. G. Petrosyan, M. J. Weber, "Synthesis and scintillation properties of some dense X-ray phosphors", submitted to this *Proc. of the Int. Conf. on Inorganic Scinillators and Their Applications SCINT99.*
11. H. Graafsma and R. Y. de Vries, "Deconvolution of two dimensional point-spread-function of area detectors using the maximum entropy algorithm", to be published in: J. Appl. Crystallogr. 1999.
12. P. Cloetens, J. I. Speso, and F. Sever, "Real-time phase-contrast imaging", ESRF Newsletter **30**, 53 (1998).
13. W. Ludwig and D. Bellet, "Penetration of liquid gallium into the grain boundaries of aluminium: a synchrotron radiation microtomographic investigation", submitted to J. Mater. Science Eng. 1999.
14. A. Snigirev, I. Snigireva, V. Kohn, S. Kuznetsov and I. Schelokov, "On the possibilities of x-ray phase contrast microimaging by coherent high-energy synchrotron radiation", Rev. Sci. Instrum. **66**, 5486-5492 (1995).
15. P. Cloetens, W. Ludwig, J. Baruchel, D. Van Dyck, J. Van Landuyt, J.P. Guigay, and M. Schlenker, "Holotomography: quantitative phase tomography with micrometer resolution using hard synchrotron radiation X-rays", submitted to Appl. Phys. Lett. 1999.

Energy resolution of contemporary scintillators. Quest for high resolution, proportional detector.

M. Balcerzyk, M. Moszyński and M. Kapusta

Soltan Institute for Nuclear Studies, PL-05-400 Otwock, Poland

Abstract: We have measured nonproportionality in response to γ-radiation and intrinsic energy resolution of several groups of scintillators - NaI(Tl) and CsI(Tl); GSO:Ce, YSO:Ce and LSO:Ce; YAP:Ce and LuAP:Ce; YAG:Ce and LuAG:Ce. The basic questions we address are **1.** For scintillators different only by substitution of lutetium by yttrium or gadolinium (like YAP and LuAP; YAG and LuAG; LSO, YSO and GSO) how are nonproportionality and intrinsic energy resolution different in such a group? **2.** For scintillators of type $X_kZ_lO_m$ different in proportions of X and Z ions (like YAP ($YAlO_3$:Ce) and YAG ($Y_3Al_5O_{12}$:Ce); LuAP ($LuAlO_3$:Ce) and LuAG ($Lu_3Al_5O_{12}$:Ce) how are nonproportionality and intrinsic energy resolution different in such a pair? **3.** How is nonproportionality different among scintillators containing only light elements as constituents: YAP, YSO and YAG?

Keywords: nonproportionality, energy resolution, gamma detector

Introduction

In recent years the problem of nonproportional response to γ-radiation and energy resolution recalled the attention of scintillator researchers community [1,2,3]. Nonproportionality is the convolution of γ response and electron response defined as the ratio of photoelectron yield at specific energy to the photoelectron yield at 662 keV and is given in % [4]. There is still no convincing theory accounting for the observed nonproportionality and energy resolution. Valentine *et al.* [3] pointed out to electron response function as a more fundamental measure of nonproportionality of a scintillator. He developed a formula for calculation of γ-photon response function (a measure of nonproportionality) as a convolution of electron response function with the electron energy distribution caused by the deposition of full energy of γ-photon in a crystal. Calculations of Valentine *et al.* showed that several double oxide scintillators (BGO, LSO, GSO) have increasing nonproportionality (i.e. electron response function) while lowering energy.

Another interesting case are iodine scintillators: NaI, NaI(Tl), CsI, CsI(Na) and CsI(Tl). According to Mengesha *et al.*[5], electron response functions for NaI(Tl), CsI(Na) and CsI(Tl) are similar in shape but different in magnitude. They are flat down to 100 keV, then increase up to 118% at 10 keV and decrease down to 110% at 2 keV for NaI(Tl). The maximum at 10 keV is 140% for CsI(Na) and at 8 keV 120% for CsI(Tl) [5]. It shows that the choice of dopant for particular scintillator affects the nonproportionality curve.

Zerby gave the first suggestion that energy resolution is connected with nonproportional response to electrons [6]. Nonproportionality and intrinsic energy resolution curves based on e-h pair density distribution spectrum were calculated by Dorenbos *et al.* for NaI(Tl) [1]. The calculation correctly predicted the energy resolution for 662 keV.

Table 1. **Scintillators used in this study**

Crystal	Ce conc., mol%	Size (mm)	Manufacturer	Sur-face finish	Light output (ph/MeV) for 662 keV γ	Wavelength of emission maximum (nm)	Sh aping time (μs)
NaI(Tl)	-	∅10x10 ∅76x76	Amcrys-H Ukraine	G	38000[c)]	415[c)]	3
CsI(Tl)	-	∅9x9	Bicron	G	61000±3000[a)]	550[c)]	6
GSO:Ce	?	5x10x10	Russia	P	7600±380[a)]	430[d)]	3
YSO:Ce	0.068	disk ∅60x10	CTI	G		440	
LSO:Ce	0.22 in melt 0.044	3x3x20 half disk ∅60x10	Ramet CTI	P G	27300±1400[a)]	440[d)]	2
YAP:Ce	0.5	3x3x20	Preciosa	P	18000±900[a)]	365[b)]	3; 1.5
LuAP:Ce	0.105	quarter of disc, ∅20x1	Litton Airtron	P	11300±450[a)]	365[b)]	1. 5
YAG:Ce	1.08	2x10x10	*Preciosa*	P	16700±660[a)]	520[b)]	2
LuAG:Ce	?	irregular ∅10x5	Russia	P	5600[b)]	510; 300[b)]	6

a) Ref. [7], b) Ref. [8] c) Ref. [9], d) Ref. [10], G – ground, P - polished

In this framework we have decided to measure nonproportionality and intrinsic energy resolution *Dsc* of several groups of scintillators (NaI(Tl) and CsI(Tl); GSO, YSO and LSO; YAP and LuAP; YAG and LuAG). The basic questions we wanted to address are:

1. For scintillators different only by substitution of lutetium by yttrium or gadolinium (like YAP and LuAP; YAG and LuAG; LSO, YSO and GSO) how are nonproportionality and *Dsc* different for such a group?

2. For scintillators of type $X_kZ_lO_m$ different in proportions of X and Z ions {like YAP ($YAlO_3$:Ce) and YAG ($Y_3Al_5O_{12}$:Ce); LuAP ($LuAlO_3$:Ce) and LuAG ($Lu_3Al_5O_{12}$:Ce)}, how are nonproportionality and *Dsc* different in such a pair?

3. How is nonproportionality different among scintillators containing only light elements: YAP:Ce, YSO:Ce and YAG:Ce?

4. Having answers to questions 1, 2 and 3 we inquire about fundamental reasons for the shape of nonproportionality and *Dsc* curves.

5. Is it possible to obtain a dense scintillator with flat nonproportionality curve down to 5 keV? Will such an ultimate scintillator have energy resolution below 5% for 511 keV?

Experiment

All the measurements were carried out with the highest light output crystals. The main characteristics of the crystals are summarized in Table 1. NaI(Tl) crystal was assembled by the manufacturer. Other crystals were wrapped in several layers of Teflon tape. Teflon from one flat side of a packet was removed. This side was glued to factory-calibrated, front-end, 2" Philips XP2020Q photomultiplier. XP2020Q is a standard bialkali PMT with quantum effi-

ciency (QE) of 25% at 400 nm, 5% at 550 nm and 1% at 600 nm. In measurements of YAG and LuAG crystals we tested also ADIT 2" B51D01 PMT with extended bialkali photocathode. ADIT PMT has QE of 25% at 400 nm, 10% at 550 nm and 1% at 670 nm. For measurements of 3" NaI(Tl), YSO and LSO (CTI) we have used Philips 3" bialkali XP3312 PMT with glass window. It has 30% QE at 400 nm. The measurements were carried out with PMT connected to preamplifier and EG&G ORTEC Spectroscopy Amplifier model 672. PC-based multichannel analyzer Tukan produced at SINS was used to record energy spectra. For all crystals the shaping time was chosen as the shortest to get 90% of maximum light output.

Results

Number of photoelectrons and proportionality

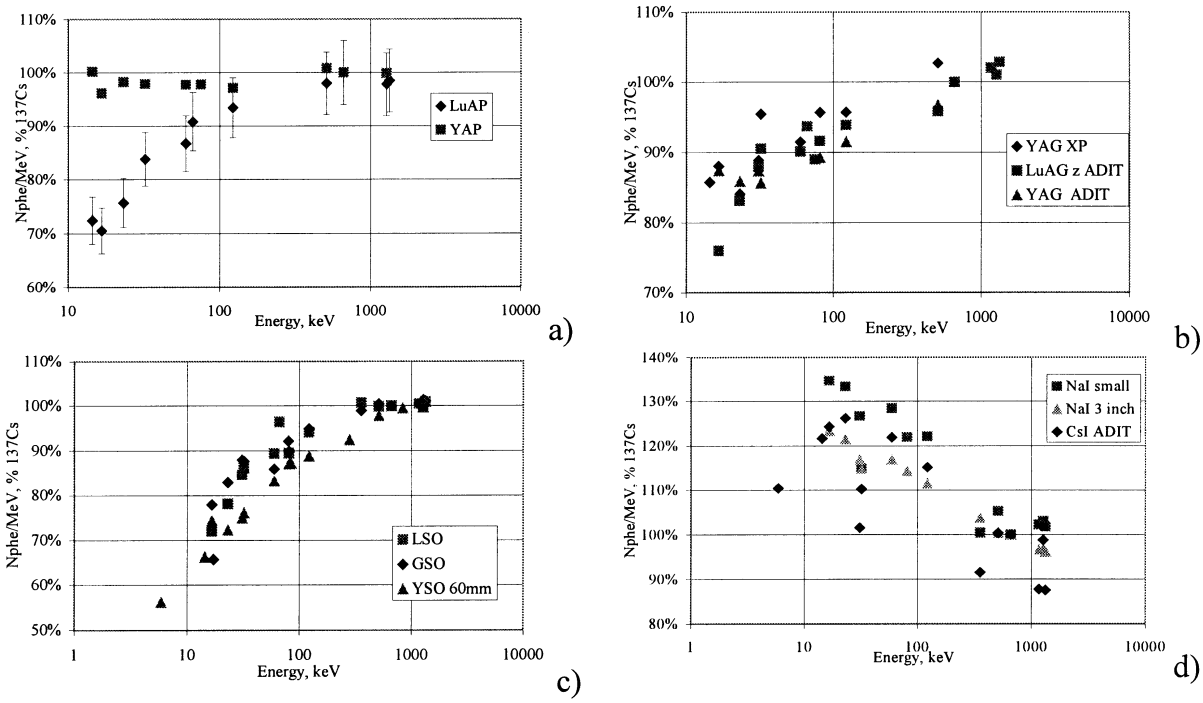

Fig. 1 Proportionality of scintillators a) YAP:Ce and LuAP:Ce, b) YAG:Ce and LuAG:Ce, c) GSO:Ce, YSO:Ce and LSO:Ce and d) NaI(Tl) and CsI(Tl) in % of number of photoelectrons for 662 keV of ^{137}Cs. Error bars are representative for all measurements.

We report first measurement of proportionality and *Dsc* over a wide range of energies for LuAP:Ce, LuAG:Ce and YSO:Ce. Proportionality of LuAG:Sc was measured by Dorenbos *et al.* [2]. The proportionality and photoelectron yield data for LuAP:Ce and YAP:Ce are presented in Fig. 1a). The proportionality is presented as photoelectron yield versus energy given as a percentage of photoelectron yield at 662 keV. As recently reported by Kapusta *et al.* [11] and other authors [5], YAP:Ce is exceptionally proportional within 6% of 662 keV photoelectron yield in the range 5 – 1300 keV. For most of the scintillators at energies of K and L X-ray absorption edges, there is a drop in proportionality curves. For YAP, for which K line of yttrium is at 17 keV, we do not observe such a feature. For LuAP:Ce proportionality drops down to 70% at 16 keV. After excellent results of YAP:Ce we expected much better proportionality for LuAP:Ce. A drop in proportionality at K line 63 keV of lutetium is seen.

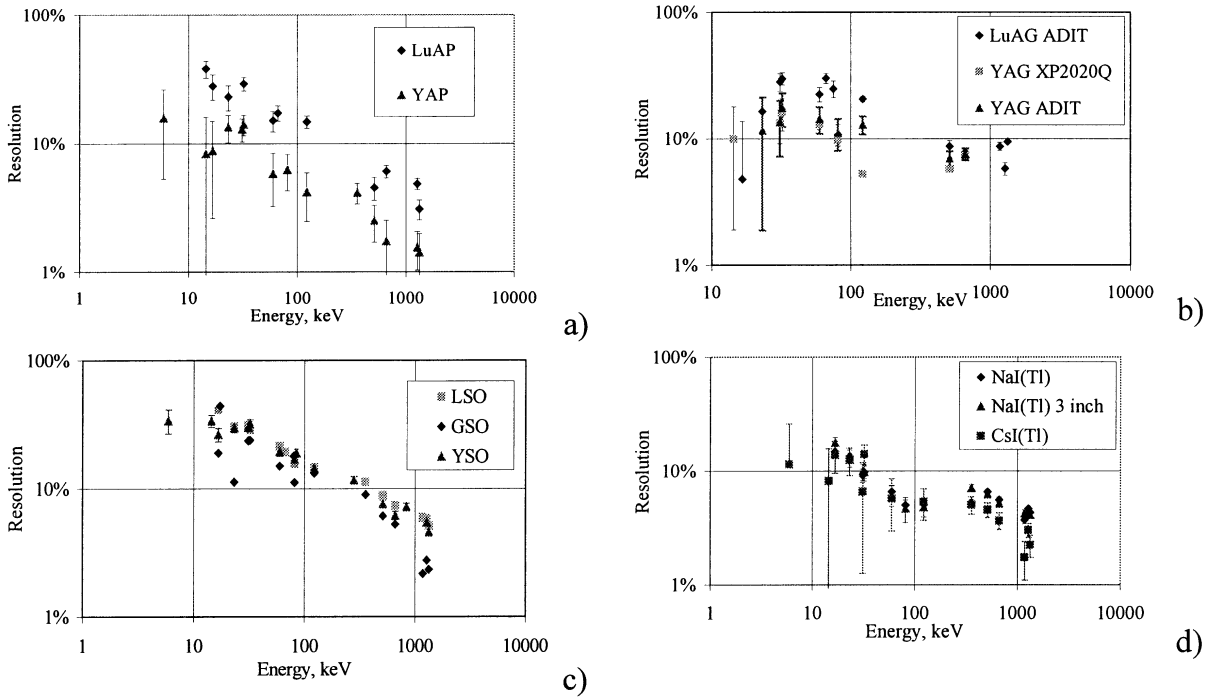

Fig. 2 Intrinsic energy resolution *Dsc* of scintillators a) YAP:Ce and LuAP:Ce, b) YAG:Ce (with XP2020Q and ADIT B51D01) and LuAG:Ce, c) GSO:Ce, YSO:Ce and LSO:Ce and d) NaI(Tl) and CsI(Tl)

Quite surprisingly, YAG:Ce (Fig. 1b) is not similarly proportional to YAP:Ce. For YAG:Ce we see continuous drop in proportionality with lowering energy down to 86% at 14 keV. This suggests that there are other properties than only the properties of constituent elements of scintillator, which determine the proportionality of the crystal. Shapes of proportionality curves for GSO:Ce and LSO:Ce presented in Fig. 1c are similar in shape to the one for LuAP:Ce – a slow drop in proportionality with lowering energy. Again as for LuAP:Ce, for YSO:Ce the proportionality result is disappointing. In Fig. 1d we present the proportionality data for NaI(Tl) and CsI(Tl). The shape of the curves agrees well with the data of Aitken *et al.* [12]. The percentage values are probably different because of the different crystal thickness' used in both studies. We have kept 3" NaI(Tl) crystal for a day in the darkness. For ∅10x10mm and ∅76x76mm crystals we have essentially the same proportionality results. Note that for both iodides the photoelectron yield is the highest for ca. 20 keV and drops for both lower and higher energies. Photoelectron yield for 662 keV γ together with PMT types are given in Table 2.

Table 2. Photoelectrons yield for 662 keV γ (in photoelectrons/MeV). Error is 3%. PMT types are given.

NaI(Tl) XP3312	CsI(Tl)-XP2020Q	GSO:Ce XP2020Q	YSO:Ce XP3312	LSO:Ce XP3312	YAP:Ce XP2020Q	LuAP:Ce XP2020Q	YAG:Ce ADIT	LuAG:Ce ADIT
10700	3840	1630	6950	6900	5290	2510	1480	1630

Overall and intrinsic energy resolution

The energy resolution, intrinsic energy resolution *Dsc* [13], gain variance ν of PMT [2] are defined elsewhere. Using the method described in Ref. 2 we have measured gain variance for PMT's used in this study. For XP2020Q ν is equal 0.09, for ADIT B51D01 ν is equal 0.15, for XP3312 ν is equal 0.19. Therefore we assume that everything except photoelectron statistical distribution contributes to *Dsc*.

Dsc for the measured scintillators is shown in Fig. 2. On log-log plots *Dsc* versus energy data form an inclined curve with the plateau between roughly 100 keV and 300 keV. Note that for energies lower than about K line of heaviest element in a compound, *Dsc* is approximately constant (LuAG, YAG and YAP). *Dsc* for lutetium containing compounds is higher than for corresponding yttrium containing compound (see YAP and LuAP and YAG and LuAG pairs in Fig. 2a and Fig.2b. That may be caused by lower crystal quality for lutetium containing crystals.

Here we must note excellent overall and intrinsic energy resolution of YAP:Ce. For 662 keV with XP2020Q PMT overall resolution is 4.18±0.04% and *Dsc* is only 1.3±0.5% the lowest one ever observed for scintillators [11].

Discussion

1. In pairs of compounds: YSO:Ce – LSO:Ce and YAG:Ce – LuAG:Ce nonproportionality and *Dsc* curves are practically the same. That indicates that crystal structure is the most important factor, which determines nonproportionality and hence *Dsc*. The case of excellently proportional YAP and nonproportional LuAP may be caused by low quality of LuAP crystal. It is characteristic to nonproportionality curves, that one can easily see positions of K and sometimes L lines of the heaviest elements. In Fig. 1a) for LuAP we can see them in 60 – 66 keV range. Lempicki *et al.* [14] determined parasitic absorption at the emission wavelength region of LuAP:Ce to be 2.3 cm^{-1} at 343 nm – the maximum of absorbed light spectrum. For 32 keV X-rays, 95% of the flux is absorbed at 250 μm. Therefore when emission light is observed from the other side of the sample, the mean path of light is 750 μm for 1 mm thick sample and that light is attenuated to $\exp\left(-2.3\,\mathrm{cm}^{-1}\times 0.075\,\mathrm{cm}\right)=84\%$, the value we have observed. Similar calculation for 122 keV gives 87%, while we observe 93±6% proportionality. Parasitic absorption can also influence intrinsic energy resolution, since it increases uncertainty of full-energy-peak width by additional variation of scintillation pulse height. However that should be checked by the direct measurement of electron response.
2. YAP and YAG from compositional point of view are similar. The electronic properties of the Y-Al-O system cannot be simply scaled according to cation ratio, and any of the fundamental properties cannot be transferred from one crystal to another [15]. Again, proportions of component elements, even at the high-energy interaction as γ absorption, are secondary to electronic properties of the crystal. Nonproportionality curves are specific to crystal structure. It would be interesting to check for proportionality differences due to different dopants in the same host, especially Ce, Tb and Eu. Mengesha *et al.* have shown that for CsI(Na) and CsI(Tl) nonproportionality curves (precisely, electron response) are of similar shape with different values of maxima at 10 keV and 12 keV respectively [5]. The pair of LuAG:Ce and LuAG:Sc [2] is not different in nonproportionality. That suggests that dopant choice is not important for nonproportionality or *Dsc*.
3. Assuming that nonproportionality is determined by crystal structure, no predictions can be given on nonproportionality of light-element-containing scintillators. Of them YAP:Ce is proportional and ZnSe:Te almost proportional [16].
4. *Dsc* is determined by (i) nonproportionality curve and (ii) quality of the crystal. (i) can be seen in YAP:Ce, YSO:Ce and LSO:Ce cases. For (ii), if we compare CsI(Tl) and YAG:Ce, we see, that YAG:Ce proportionality curve varies in a smaller range than for CsI(Tl), however *Dsc* curve has lower values for the latter scintillator.
5. Electron response curves without maximum (e.g. LSO, YAP, CaF_2, BGO etc. [5]) can be fitted to the relation of the type $1-\beta\left(E/E_g\right)^{(-\alpha)}$, where E_g is some arbitrary, low energy,

for example energy gap of a scintillator, E is energy of electron and α, β are positive constants. For iodides (curves with maximum) this formula has to be extended to $1-\beta\left(E/E_g\right)^{(-\alpha)}+\delta\left(E/E_g\right)^{(-\gamma)}$, where δ and γ are positive constants [17]. K_2LaCl_5:Ce is proportional down to 12 keV, LuAG:Sc down to 8 keV [2], LuAG:Ce slightly worse. Based on YAP:Ce curve, LuAP:Ce is expected to have a better proportionality curve with improved technology. There are above-mentioned candidates for proportional *and* high-resolution scintillators, but, by now, the search for the new ones is based on trial and error.

Acknowledgements

This work was supported in part by Polish Committee for Scientific Research (KBN) grants 8 T11E 025 15 and 8T 10C 005 15.

References

1. P. Dorenbos, M. Marsman, C.W.E. van Eijk "Energy resolution, non-proportionality, and absolute light yield of scintillation crystals" , SCINT95 Proceedings (1995) 148
2. P. Dorenbos, J.T.M de Haas and C.W.E. van Eijk "Non-proportionality in the scintillation response and the energy resolution obtainable with scintillation crystals." IEEE Trans. Nucl. Sci. **42** (1995) 2190
3. J.D. Valentine, B.D. Rooney and J.Li "The Light Yield Nonproportionality Component of Scintillator Energy resolution" IEEE Trans. Nucl. Sci. **45** (1998) 512
4. J.D. Valentine, B.D. Rooney and P. Dorenbos "More on Scintillation Response of NaI(Tl)" IEEE Trans. Nucl. Sci. **45** (1998) 1750
5. W. Mengesha, T.D. Taulbee, B.D. Rooney and J.D. Valentine "Light Yield Nonproportionality of CsI(Tl), CsI(Na) and YAP" IEEE Trans. Nucl. Sci. **45** (1998) 456
6. C.D. Zerby, A. Meyer and R.B. Murray "Intrinsic line broadening in NaI(Tl) gamma-ray spectrometers", Nucl. Instr. Meth., **12** (1961) 115
7. M. Moszyński, M. Kapusta, M. Mayhugh, D. Wolski and S.O. Flyckt "Absolute Light Output of Scintillators", IEEE Trans. Nucl. Sci. **44** (1997) 1052
8. A. Lempicki, M.H. Randles, D. Wi niewski, M. Balcerzyk, C. Brecher, and A.J. Wojtowicz"$LuAlO_3$:Ce and Other Aluminate Scintillators", IEEE Trans. Nuc. Sci., **42** (1995) 280
9. Scintillation Detectors the catalog of Saint-Gobain Ceramiques Industrielles.
10. C.L. Melcher, J.S. Schweitzer, C.A. Peterson, R.A. Manente, H. Suzuki,"Crystal growth and scintillation properties of the rare earth oxyorthosilicates", SCINT95 Proceedings, (1996) 309
11. M. Kapusta, M. Balcerzyk, M. Moszyński, J. Pawelke "A high energy resolution observed from a YAP:Ce scintillator", Nucl. Instr. Meth. A **421** (1999) 610.
12. D.W. Aitken, B.L. Beron, G. Yenicay, H.R. Zulliger, "The fluorescent response of NaI(Tl), CsI(Tl), CsI(Na) and CaF_2(Eu) to X/rays and low energy gamma rays", IEEE Trans. Nucl. Sci. **NS-14** (1967) 468
13. M. Moszyński, M. Kapusta, D. Wolski, M. Szawlowski, W. Klamra, IEEE Trans. Nucl. Sci. **45** (1998) 472
14. A. Lempicki, C. Brecher, D. Wisniewski, E. Zych, A.J. Wojtowicz, IEEE Trans. Nucl. Sci. **43** (1996) 1316
15. W. Y. Ching, Yong-Nian Xu, "Nonscalability and nontransferability in the electronic properties of the Y-Al-O system" Phys. Rev. B **59** (1999) 12 815
16. M. Balcerzyk, W. Klamra, M. Moszyński, M. Kapusta, D. Wolski, M. Szawlowski in this Proceedings
17. M. Balcerzyk, M. Moszyński, M. Kapusta in preparation

A Technique for Measuring Scintillator Electron Energy Resolution using the Compton Coincidence Technique

W. Mengesha and J.D. Valentine

Neely Nuclear Research Center, Nuclear and Radiological Engineering Program, Georgia Institute of Technology

Abstract: A technique for determining scintillator total electron energy resolution $\eta_{e,tot}$ has been described. The technique is based on slight modification of the compton coincidence technique previously used for scintillator electron response measurement. Considerations have been made on important factors which may result in measurement complications. MCNP4B together with algorithms written to simulate the CCT were used to determine the total electron energy resolution $\eta_{e,tot.}$ In addition, algorithms have been developed to convolve the resulting $\eta_{e,tot}$ with the electron spectrum produced by full energy gamma-ray events to calculate total photon energy resolution.

Keywords: Nonproportionality, total photon energy resolution, scintillators.

Introduction

Scintillation detector pulses due to gamma-ray interactions are produced through a chain of cascade processes, which result in blurring of the incident gamma-ray energy information. For scintillators coupled to photomultiplier tubes(PMTs), five major processes can be identified as follows: 1) scintillation photon or light production 2) light collection at PMT photocathode 3) photoelectrons production by the photocathode due to light absorption 4) photoelectron collection at the first dynode of the PMT and 5) multiplication by the PMT dynodes. The separate processes outlined above each result in some degree of broadening of the recorded photopeak. Several previous studies have characterized the different processes and evaluated their significance in photopeak broadening[1-3]. If the broadening due to process 1) is termed intrinsic energy resolution $\eta_{\gamma,int}$, or the contribution due to statistical variations in the number of scintillation photons produced when a photon (gamma ray or x ray) deposits all of its energy in the scintillation crystal, two sub-processes can be further identified as broadening components: a) intrinsic electron energy resolution $\eta_{e,int}$, and b) the component of photon energy resolution due to light yield nonproportionality $\eta_{\gamma,non}$. The later component is due to variations in the number of primary and secondary electrons produced when a photon is fully absorbed in a scintillator and will vary to some degree with scintillator crystal size. While $\eta_{e,int}$ is size independent, light yield nonproportionality will contribute to this component due to delta rays.

Recently, $\eta_{\gamma,non}$ was characterized based on results from Compton coincidence technique (CCT) shown in Figure 1, which was developed to characterize light yield nonproportionality [4-6]. In this study, an experimental technique for determining $\eta_{e,int}$ is described. This technique is based on slightly modifying the CCT such that the total electron energy resolution $\eta_{e,tot}$, for monoenergetic electrons can be estimated.

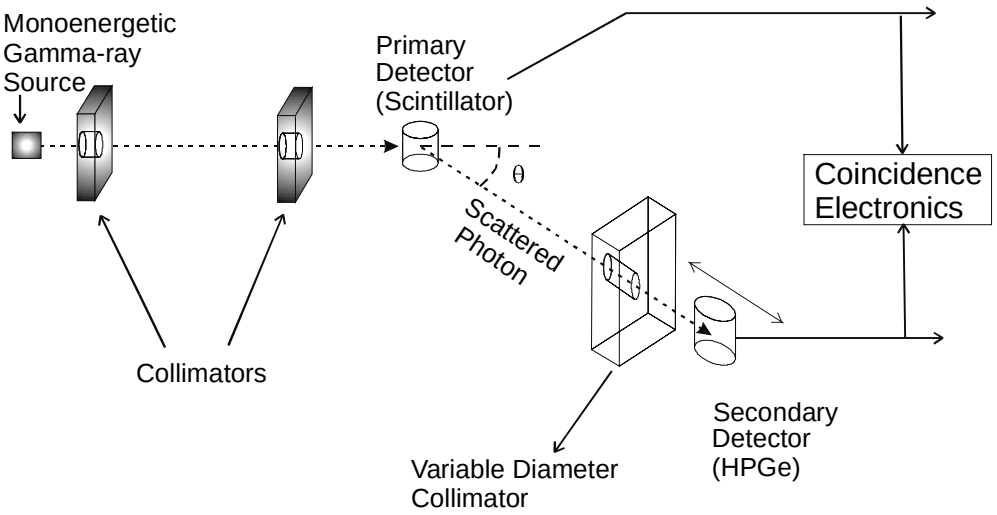

Figure 1. Schematic of modified the Compton Coincidence Technique. Where solid angle subtended by secondary detector Ω can be varied either by changing the collimator diameter or varying the distance between the primary and secondary detectors.

Based on the measured $\eta_{e,tot}$, the energy resolution contributions from processes 2)-5) above must be decoupled to determine $\eta_{e,int}$. However, by convolving $\eta_{e,tot}$ with $\eta_{\gamma,non}$, the total photon energy resolution $\eta_{\gamma,tot}$ can be determined. Consequently, these calculated $\eta_{\gamma,tot}$ results can be compared with measured results to validate the $\eta_{e,tot}$ measurements and convolution process. Furthermore, the same convolution algorithms will be used to convolve $\eta_{e,int}$ with $\eta_{\gamma,non}$ to determine $\eta_{\gamma,int}$. The following sections thus describe the modified CCT for determining $\eta_{e,tot}$, special considerations associated with the modified CCT, and the convolution algorithm mentioned above.

Experimental Technique

In the CCT, which has been described in detail previously [5-6], a collimated beam of photons is incident on the scintillation detector being studied, as seen in Figure 1. A secondary high purity germanium (HPGe) detector is located at an angle θ from the axis of the collimated beam. The CCT records scintillator pulses only when a coincident pulse is recorded by the secondary HPGe detector. In this manner, most pulses recorded by the CCT are the result of events in which a gamma ray Compton scatters once in the scintillator and then interacts in HPGe detector. The Compton electrons within the primary detector approximate a monoenergetic internal electron source and can thus be used to characterize the nonproportional behavior of scintillator light yield as a function of electron energy by using θ. In this study, the CCT was modified such that a variable solid angle Ω could be subtended by the secondary detector. With variable Ω, the modified CCT further enhances the ability to estimate scintillator response to monoenergetic electrons, and thus characterize $\eta_{e,tot}$. Variation of Ω can be achieved by either varying the collimator diameter or varying the distance between the primary and secondary detector. In implementing the modified CCT, there are two significant considerations: 1) accounting for the finite solid angle subtended by the secondary detector; 2) effects of multiple scattering within the scintillator on the measured $\eta_{e,tot}$. These two considerations both complicate measurement of monoenergetic electrons within the primary detector and the latter results in an electron energy continuum on which the single scatter pulses are superimposed at a specific angle θ, respectively. However, the former is the basis for the modified CCT.

It is evident from Klein-Nishina formula that the solid angle limits the number of scattered photons that are incident on the HPGe detector. Therefore variation of the solid angle will clearly have influence on the range of scattered photon energies (or coincidence energy spectrum recorded by the primary detector) by limiting the recoil electron energy distribution. The electron energy resolution $\eta_{e,tot}$ measured plotted as a function of solid angle, when extrapolated to zero solid angle provides an estimate of $\eta_{e,tot}$ which is free from the solid angle effect, and thus approximates the response to monoenergetic electrons. In this study, the principle of solid angle variation (modified CCT) has been demonstrated using MCNP4B simulation by varying collimator diameter. A 1 cm diameter by 2 cm height right cylinderical NaI(Tl) detector together with 4.1 cm diameter by 6.4 cm height HPGe detector simulated the experimental equipment to be used. As shown in Figure 2, analysis of coincidence events for lead collimators of variable size and a pencil beam 662 keV source provides an example of how the modified CCT is implemented.

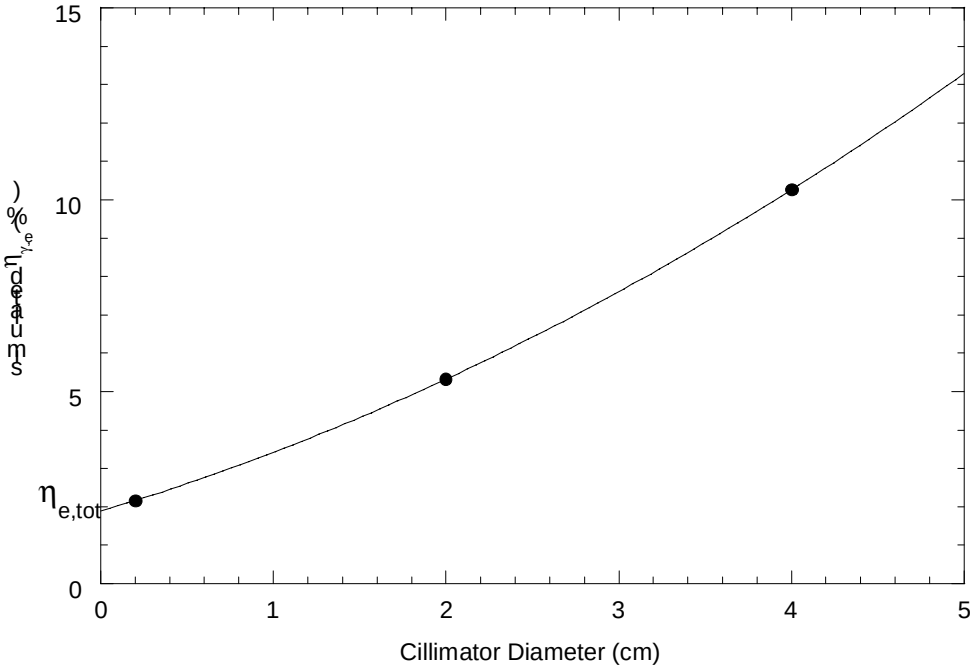

Figure 2. Simulated results from modified CCT experiment showing extrapolation to $\eta_{e,tot}$.

The effect of multiple scattering in the scintillator has also been addressed using modified CCT simulations. Multiple scattering is primarily dependent on the size of the primary detector. As mentioned previously, multiple scattering produces a continuum on which single scatter pulses are superimposed, and thus there is some potential for complicating $\eta_{e,tot}$ estimation. By distinguishing between single and multiple scatters in the simulations, any complications in subsequent analyses could be identified and characterized. Figure 3 and 4 show typical coincidence spectra recorded by the NaI(Tl) primary detector and HPGe secondary detector.

Figure 3 shows the entire coincidence spectrum, as well as the spectrum recorded when only considering events in which the energy deposited in the HPGe was within an "energy window" centered about the energies associated with single scatter events. Using this "energy window" most multiple scatter events are eliminated. Furthermore, results indicate that measured η_e values are unbiased estimates of the value determined for single-scatter only data. Consequently, it was concluded that multiple scatter effects will not affect the modified CCT results. To be able to utilize $\eta_{e,tot}$ results from the modified CCT, algorithms were

developed to convolve these results with $\eta_{\gamma,non}$ results to determine $\eta_{\gamma,tot}$. These results can then be compared to measured $\eta_{\gamma,tot}$ values to verify the modified CCT results. In addition, the same algorithms can be used to analyze intrinsic energy resolution results. Calculation of $\eta_{\gamma,tot}$ was based on MCNP4B simulations of 2.54 × 2.54 cm right cylinderical NaI(Tl) crystal in which only full energy events within the NaI(Tl) were considered.

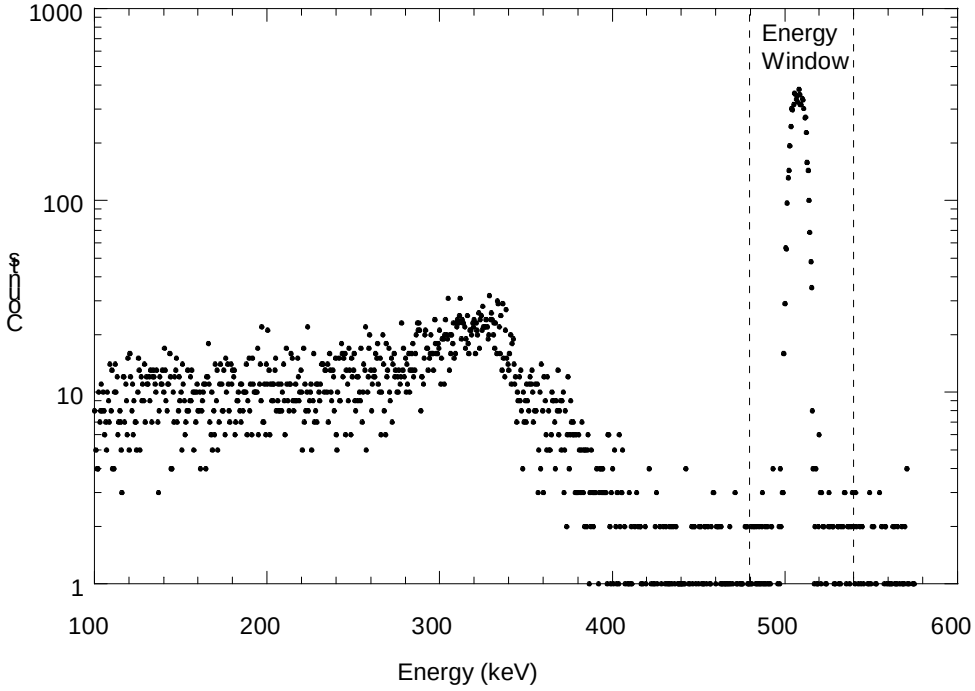

Figure 3. Typical NaI(Tl) coincidence spectrum for all coincidence(Total) and for coincidences resulting full energy deposition in HPGe detector (Energy window)- see Figure 4.

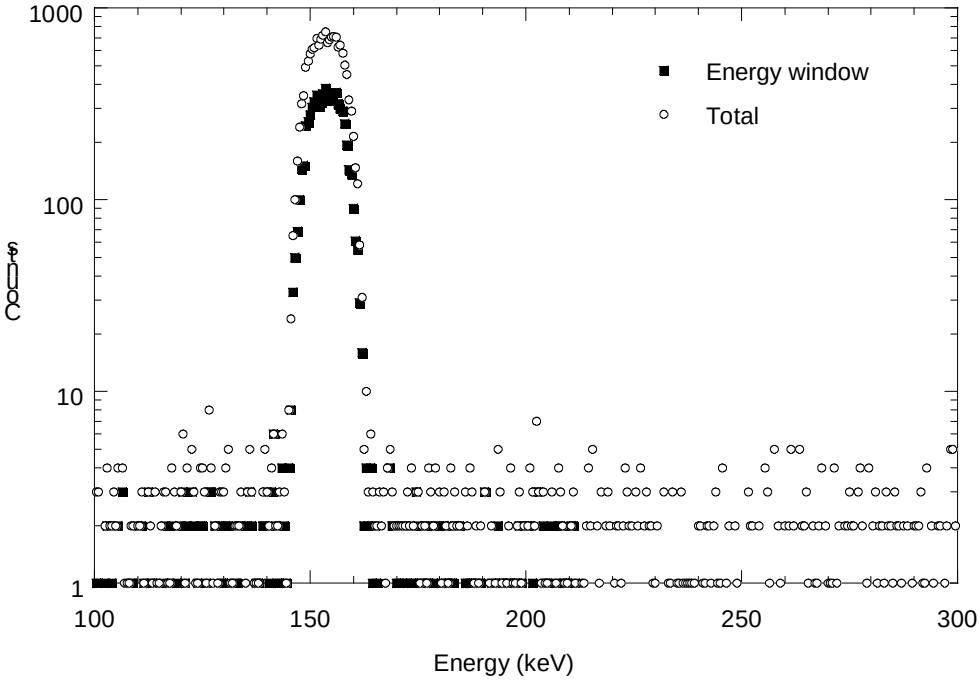

Figure 4. Typical HPGe coincidence spectrum with "energy window" bracketing single scatter events in which scattered photon deposited full energy.

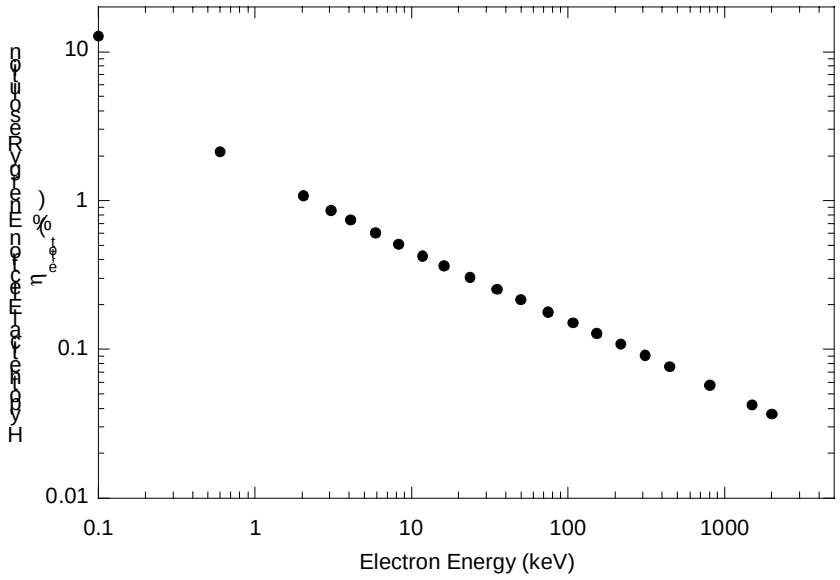

Figure 5. Hypothetical total electron energy resolution $\eta_{e,tot}$

The simulations were used to determine primary electron energies due to photoelectric and Compton interactions. Secondary electron energies produced following photoelectric absorption were accounted for by sampling a simplified cascade sequence for NaI(Tl) [7]. The light yield for a particular full energy deposition event was then calculated by convolving the electron energy distribution (primary plus secondary electrons) from each full energy event with previously measured electron response for NaI(Tl) detector[5]. In a similar manner, the energy resolution associated with each of the primary and secondary electrons is determined using the previously measured $\eta_{e,tot}$ results from the modified CCT. It was then assumed that $\eta_{e,tot}$ was representative of a Gaussian shape, such that the $\eta_{e,tot}$ associated with each electron could be summed in quadrature with that from all other electrons associated with particular gamma-ray event. Subsequently, the light yield from a single gamma-ray event was integrated into appropriate bins based on the sum of light yields and $\eta_{e,tot}$ values for all electrons. By repeating this procedure for a large number of gamma rays, a photopeak was generated, the centroid of which determines the photon response and the variance of which determines $\eta_{\gamma,tot}$.

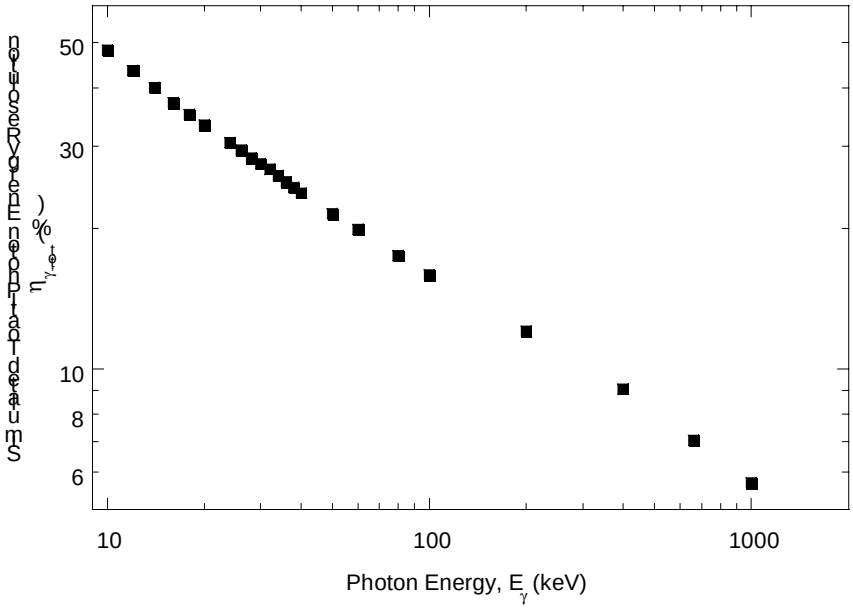

Figure 6. Simulated total photon energy resolution $\eta_{\gamma,tot}$.

Since measured $\eta_{e,tot}$ values were not available values consistent with the electron response and normalized such that $\eta_{\gamma,tot}$ value of 7% FWHM at 662 keV were used (see Figure 5). Assuming this hypothetical $\eta_{e,tot}$ values, a range of gamma ray energies were analyzed and the results are shown in Figure 6.

Discussion

A method for determining scintillator total electron resolution $\eta_{e,tot}$ has been described. This method is based on modifying the CCT and uses electron energy resolution measurements from variable solid angle experiments to estimate $\eta_{e,tot}$ for monoenergetic electrons. In addition, algorithms have been developed to convolve either the intrinsic energy resolution $\eta_{e,int}$ or $\eta_{e,tot}$ with $\eta_{\gamma,non}$ to yield either $\eta_{\gamma,int}$ or $\eta_{\gamma,tot}$. While $\eta_{\gamma,int}$ results determined in this manner will indicate the importance of intrinsic energy resolution to total energy resolution, $\eta_{\gamma,tot}$ results provide a means of verifying measured $\eta_{e,tot}$ results. The modified CCT will be implemented at several different angles to determine $\eta_{e,tot}$ as a function of energy and subsequently convolved with $\eta_{\gamma,non}$ and compared to measured $\eta_{\gamma,tot}$ values. Finally, techniques will be developed to deconvolve the light collection quantum efficiency, photoelectron, and multiplication components of energy resolution such that $\eta_{e,int}$ can be determined.

References

1. P.M. Woodward, *Proc. Comb. Phil. Soc*. 44(1948)404.
2. G.F.J. Garlick and G.T. Wright, *Proc. Phys. Soc*.,B65(1952)415.
3. P. Dorenbos, J.T.M. de Haas, C. W. E. van Eijk, *IEEE Trans. Nucl. Sci*., 42(1995)2190.
4. J.D. Valentine, B.D. Rooney, and J. Li, *IEEE Trans. Nucl. Sci*., 45(1998)512.
5. J.D. Valentine and B.D. Rooney, *Nucl. Instr. Meth*., A353(1994)37.
6. B.D. Rooney and J.D. Valentine, *IEEE Trans. Nucl. Sci*. 43(1996)1271.
7. B.D. Rooney and J.D. Valentine, *IEEE. Trans. Nucl. Sci.*, 44(1997)509.

Oral presentations

Electromagnetic Calorimetry with $PbWO_4$ in the Energy Regime below 1 GeV

R. Novotny[1], R. Beck[3], W. Döring[1], V. Hejny[4], A. Hofstaetter[2], M. V. Korzhik[5], V. Metag[1], H. Ströher[4]

[1] *2nd Physics Institute, University Giessen, D - 35392 Giessen, Germany*
[2] *1st Physics Institute, University Giessen, D - 35392 Giessen, Germany*
[3] *Institute for Nuclear Physics, University Mainz, D – 55128 Mainz, Germany*
[4] *Institute for Nuclear Physics, KFA Jülich, D – 52425 Jülich, Germany*
[5] *Institute for Nuclear Problems, BY – 22050 Minsk, Belarus*

Abstract: The investigation of the performance and application of $PbWO_4$ in electromagnetic calorimetry at energies below 1 GeV has been continued. The significantly improved optical and scintillation properties of recently produced 15 cm long La+Nb- or Sb-doped crystals are documented. The lineshape, energy and time response of a 5x5 matrix to monoenergetic photons between 66 and 790 MeV energy are compared to previous measurements. The proposed concept for a compact photon spectrometer implemented into the *ANKE* magnetic spectrometer at COSY (KFA Jülich) is illustrated.

Keywords*:* $PbWO_4$, Electromagnetic Calorimetry, Tagged Photons, Photon Detection

Introduction and Motivation

$PbWO_4$ has been selected as the most appropriate scintillator material for the new generation of homogeneous high energy electromagnetic calorimeters as under construction for the *CMS* or *ALICE* [1] detectors at the future *LHC*. Due to the thermal quenching at room temperature, one has to cope with a very fast but low intensity scintillator material. Nevertheless, in a series of previous experiments using electrons [2] and energy marked photons [3,4] between 50 and 855 MeV, respectively, the applicability of $PbWO_4$ as a radiation detector in the energy regime even far below 1 GeV has been proven. Very promising energy ($\sigma/\mathbf{E} = 1.54\%/\sqrt{\mathbf{E}} + 0.30\%$, E given in GeV) and time ($\sigma \le 200\,ps$) resolutions have been achieved with a 5x5 matrix, however, consisting of crystals with inhomogeneous and not optimum optical and scintillation quality. From the comparison to the high resolution BaF_2-spectrometer TAPS [5] one can conclude that the achievable energy resolution below 200 MeV is significantly limited by the low photon statistics of $PbWO_4$. Therefore, any further improvements will strongly rely on scintillation crystals with high optical transparency and an enhanced yield of luminescence.

The New $PbWO_4$-Crystals

In order to assemble a new test matrix consisting of 5x5 detector modules La+Nb-doped crystals of slightly tapered shape have been manufactured and pre-selected by RI&NC (Minsk, Republic of Belarus) and Bogoroditsk Techno Chemical Plant (Russia). The optically polished crystals of 150 mm length (~ 16 radiation lengths X_0) have a quadratic front surface (20.5 x 20.5 mm^2) and a tapering angle of ~ 0.4^o. The value and the homogeneity of the optical quality is determined by measuring the transmission perpendicular to the crystal axis at various positions within the relevant wavelength regime between 300 and 900 nm, respectively. Fig. 1 illustrates the distributions for two typical samples. In some cases a weak absorption band centered near λ ~ 420 nm becomes visible. The transparency region towards

the natural absorption edge can be characterized by that particular wavelength where the absolute value of the optical transmission drops down to T = 50%. On average, that wavelength amounts to $\lambda(T=50\%)$ = 350.9 nm with a variation of less than 2 nm along the crystal axis.

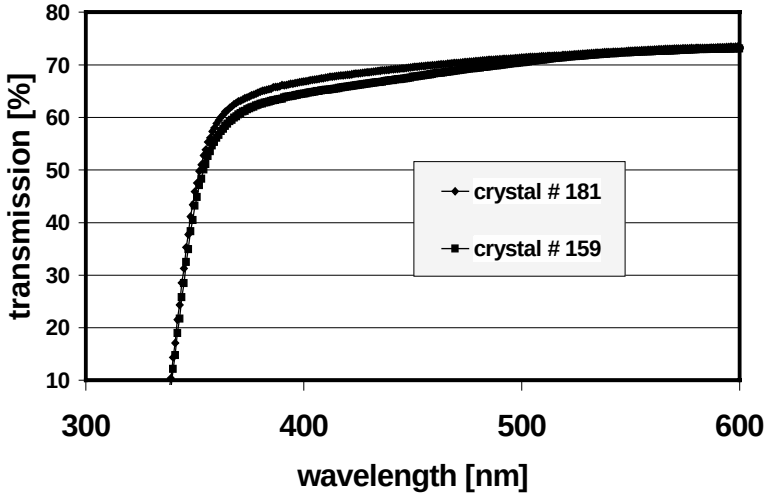

Figure 1: Optical transmission as a function of wavelength for two typical tapered La+Nb-doped $PbWO_4$ samples measured perpendicular to the crystal axis.

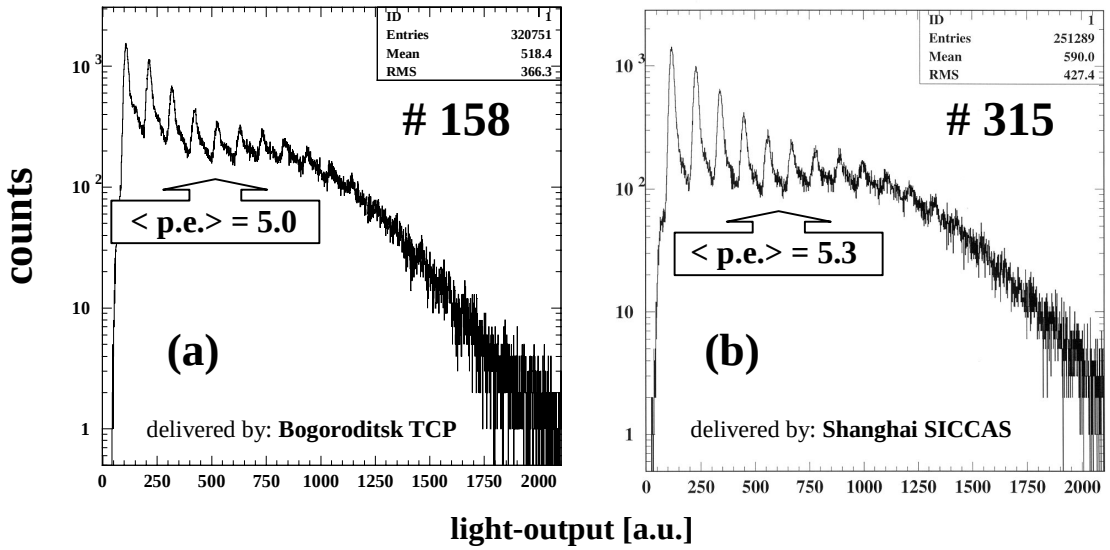

Figure 2: Response of $PbWO_4$-crystals to a ^{60}Co γ-source measured with a HPD for one of the tapered crystals # 158 (a) and a sample of rectangular shape provided by SICCAS #315 (b). The mean number of photo-electrons is indicated.

Exploiting the excellent single photo-electron response of hybrid photodiode tubes (HPD) the luminescence yield has been measured using a ^{60}Co γ-source (E_γ= 1.17, 1.33 MeV). Fig. 2 shows on a logarithmic scale spectra of the observed light-output of two high quality crystals. The number of detected photo-electrons (PE) can be counted directly. Fig. 2a illustrates the distribution for one of the best tapered crystals, Fig. 2b the corresponding spectrum of a Sb-doped rectangular sample (20 x 20 x 150 mm^3) provided by Shanghai SICCAS High Technology Corporation (Shanghai, China).

The significant improvement in the scintillation performance of 150 mm long crystals is illustrated in Fig. 3 in a comparison of the measured light-output of the present samples to the crystals used in previous experiments. The obtained mean light-output of <LO> = 4.6 PE

corresponds to an increase of 33% with respect to the value of first generation crystals (<LO> = 3.4 PE). In addition, the narrow distribution reflects the improved reproducibility in crystal production. By coupling sample #158 to a photomultiplier tube (Hamamatsu R2059-01), energy resolutions of σ/E = 30% and σ/E = 25% have been obtained for the photopeak of ^{137}Cs (E_γ = 662 keV) and ^{60}Co (E_γ ~ 1.25 MeV) γ-sources, respectively.

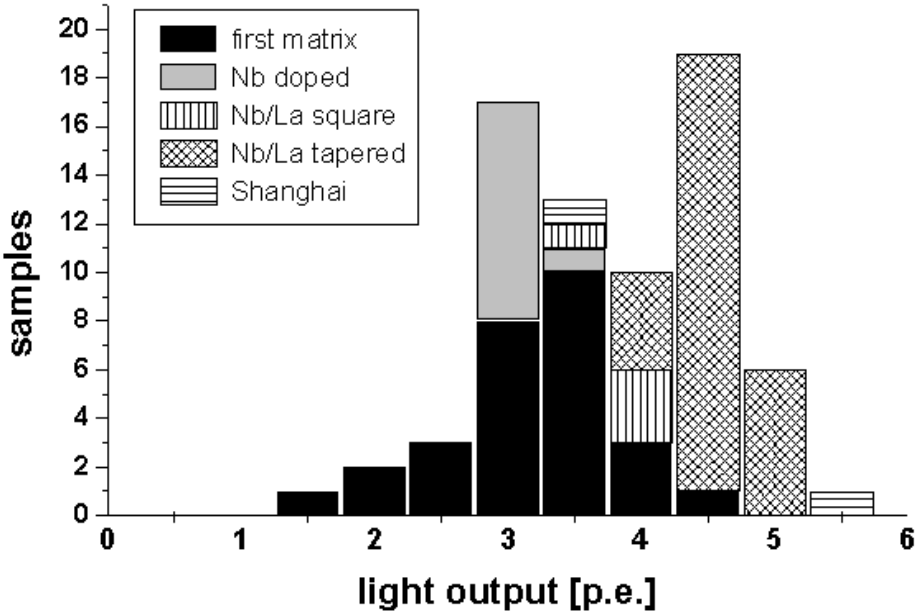

Figure 3: Distribution of the mean number of photo-electrons measured by means of a HPD using a ^{60}Co γ-source. The quality of the present La+Nb-doped samples is compared to those from previous deliveries and two selected crystals provided by SICCAS.

Response to High Energy Photons

According to the specification tests reported above a sufficient number of excellent crystals was available to set-up a matrix of 5x5 detectors in order to repeat the measurement of the response to energy marked photons between 66 and 790 MeV energy at the tagging facility of MAMI (University Mainz, Germany). The crystals, individually wrapped in PTFE-foil, are coupled with optical grease to fast photomultiplier tubes (Hamamatsu R3478, base: E2253-06, ∅ = 19 mm – covers 35% of the crystal end face) and stacked into a light-tight box, which was temperature stabilized at t = 5.5°C. The detector block can be moved by remote control to illuminate directly each crystal with the collimated photon beam (< 10 mm$^{\varnothing}$) for calibration purposes. A plastic scintillator in front of the crystal matrix serves as a charged particle veto-detector. The detector signals are transferred via long coaxial cables (~ 50 m RG58) to the data acquisition system to deduce energy and time information using commercial electronics.

The inspection of the lineshape by means of a digital scope (500 MHz bandwidth) indicates no significant slow scintillation components in agreement to measurements by the supplier which stated that more than 96.5% of the total light-output (1 µs integration width) are emitted within the first 100 ns.

Affected by the chosen photomultiplier/base combination an unexpected non-linear energy calibration had to be applied to correct for saturation effects, which has limited the finally achieved resolution after the reconstruction of the electromagnetic shower deposited within the detector array. In spite of that complication, the response for the central detector measured in previous tests can be reproduced and is shown in Fig. 4 in comparison to GEANT4 simulations, which consider only fluctuations of the shower containment and do not take into

account the influence due to photon statistics or collection of the scintillation light, respectively. Due to uncertainties in the calibration procedure, the preliminary energy resolution of $\sigma / \mathbf{E} = 2.58\% / \sqrt{\mathbf{E}} + 0.60\%$ (E given in GeV) does not reach the former excellent results. Providing similar pulse height spectra in two adjacent detector elements by directing the photon beam in between an intrinsic resolution for each module of $\sigma \leq 160$ ps can be deduced from the distribution of the relative time between these responding detectors.

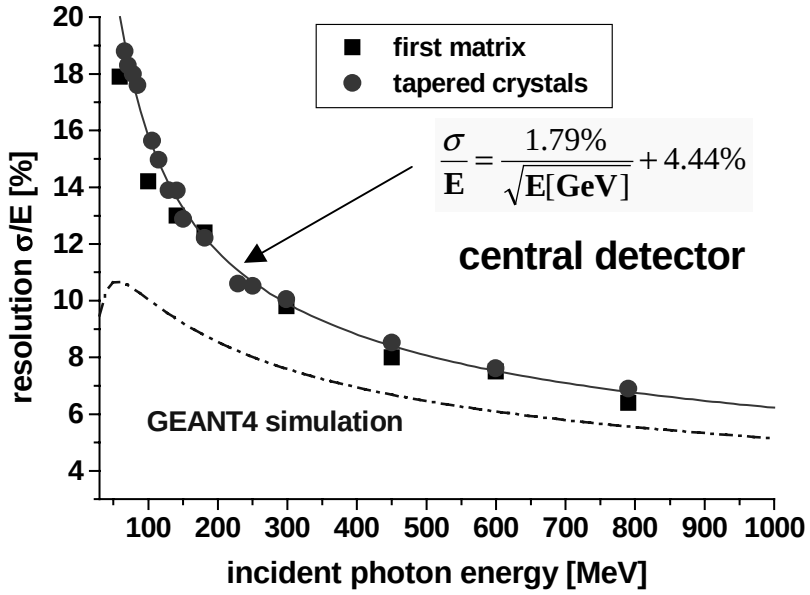

Figure 4: Energy resolution of the central detector module for high energy photons in comparison to previous results and a shower simulation using the GEANT4 code, which does not consider the contributions due to photon statistics or the collection of the scintillation light.

Conclusions and Outlook

Based on the obtained optical and scintillation properties of the present generation of 150 mm long La+Nb- or Sb-doped crystals from various suppliers an optimum quality of fast $PbWO_4$-crystals for low and medium energy applications appears to be reached. In spite of the superior quality of the test matrix - in particular with respect to light-output and homogeneity - an expected improvement of the energy resolution of the reconstructed electromagnetic shower induced by photons below 1 GeV can not be reported here due to electronical read-out limitations. However, success can be expected in a re-measurement in the near future. Further significant improvements of the photon statistics at low energies below 200 MeV will rely on an increase of the luminescence yield hopefully achievable by adding specific dopants. In that case one might have to cope with slower scintillation components or a reduced radiation hardness, compromises which might not cause a severe limiting factor for nuclear physics applications at low and intermediate energies. A specific research program has started in close collaboration with RI&NC (Minsk, Republic of Belarus).

Initiated by the promising detector parameters of $PbWO_4$ a first technical proposal for a nuclear physics application at intermediate energies is in preparation. A compact photon detector with nearly 4π-coverage in solid angle has been suggested as an upgrade of the charged particle magnetic spectrometer ANKE - ***A**pparatus for studies of **N**ucleon and **K**aon **E**jectiles* - at the synchroton COSY (KFA Jülich, Germany).

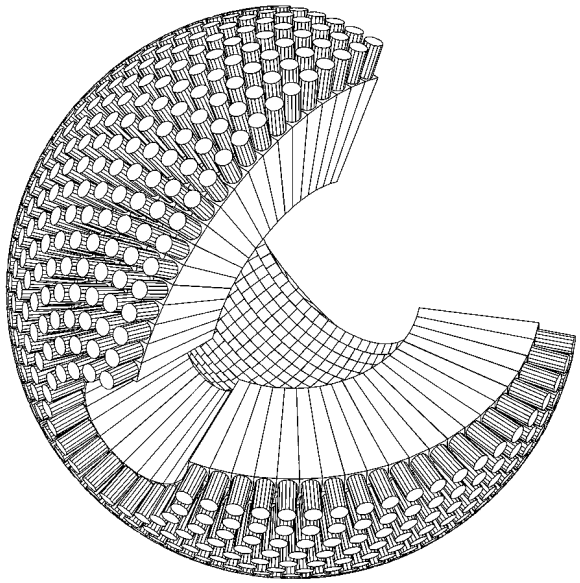

Figure 5: Schematic view of the proposed photon detector for *ANKE* at *COSY* (KFA Jülich).

The physics program, which is concentrating so far on charged meson production in nucleon-nucleon and nucleon-nucleus collisions, could be completed by the direct identification of neutral mesons emitted in coincidence based on an invariant mass analysis of the detected decay photons. Due to geometrical constraints (∅ ~ 60-70 cm) a very compact, spherical arrangement with high granularity (~ 1000 scintillator elements), sufficient time- (particle discrimination) and energy resolution (photon energy < 2 GeV) is needed. Due to the strong strayfield of the magnetic spectrometer a fast read-out in a magnetic field (< 0.5 T) has to be guaranteed. Fig. 5 gives a first impression of the envisaged geometrical arrangement.

At the moment, $PbWO_4$ appears to be the only scintillator material to fulfill all the essential experimental requirements. The project would strongly benefit from a further increase of the luminescence yield as proposed by appropriate doping.

References

1. CMS, CERN/LHCC 94-38; ALICE, CERN/LHCC 95-71
2. R.Novotny et al., IEEE Trans. on Nucl. Sc. 44 (1977) 477
3. R.Novotny et al., Proceedings of SCINT97, p. 187
4. K.Mengel et al., IEEE Trans. on Nucl. Sc. 45 (1998) 681
5. A.Gabler et al., Nucl. Instr. and Meth. in Phys. Res. A346 (1994) 168

This work has been supported by BMBF, DFG, SFB 201 and GSI.

Electromagnetic calorimeter of the BELLE detector

BELLE calorimeter collaboration
presented by B.Shwartz

Budker Institute of Nuclear physics, Novosibirsk

Abstract: The electromagnetic calorimeter of the BELLE detector built for experiments on B-meson physics is described. The energy resolution measured with prototype ranges from about 3% at 20 MeV to 1.6% at 1 GeV. The calorimeter consisting of 8736 CsI(Tl) crystals was installed to the detector and demonstrates its good performance in the experiment.

Keywords: Electromagnetic calorimeter, CsI(Tl) crystals, energy resolution.

The BELLE detector for experiments at the KEKB, an energy asymmetric B-Factory with high luminosity, has been constructed at KEK, Japan [1] to study CP violation in B meson decays. Since one-third of these decay products are π^0's and other neutral particles providing photons in a wide range from 20 MeV to 4 GeV, a high resolution calorimeter appears to be a very important part of the detector. This calorimeter based on CsI(Tl) scintillating crystals was developed and constructed by the BELLE ECL collaboration [2] including researchers from 12 universities and institutes.

The CsI(Tl) crystals were chosen as a material for the calorimeter due to its high light output, short radiation length, good mechanical properties and moderate price. The schematic view of the calorimeter is shown in Fig.1.

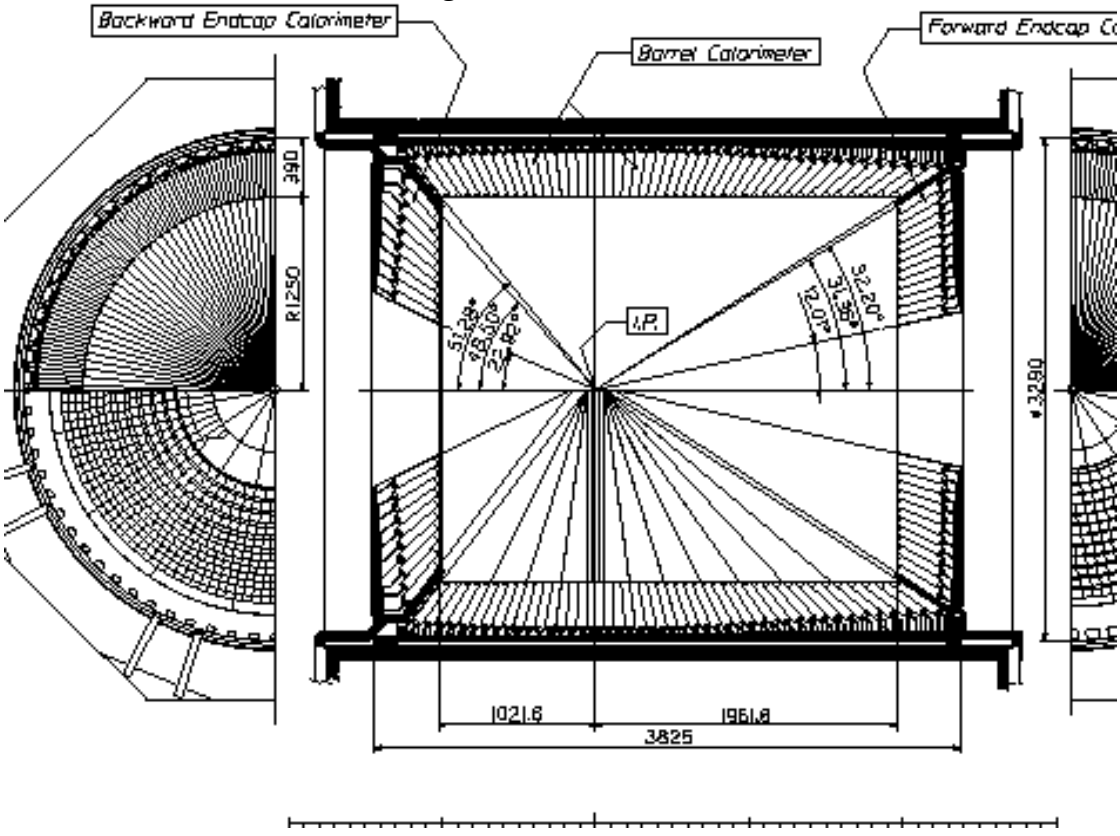

Fig.1. Electromagnetic calorimeter of the BELLE detector.

The barrel part contains 6624 CsI(Tl) elements of 29 types. Each crystal is a truncated pyramid of the average size about 6×6 cm^2 in cross section and 30 cm (16.2 X_0) in length. The end caps contain altogether 2112 CsI crystals of 69 types. The total number of the crystals is 8736 with total mass of about 43 tons. The calorimeter covers the polar angle region of $17° < \theta < 150°$, corresponding to a total solid angle acceptance 91% of 4π.

The production of the crystals had been continuing for about four years. Together with spare the 8851 crystals were produced and delivered to KEK by three manufacturers: Budker Institute of Nuclear Physics (Russia) in co-operation with the Institute of Single Crystals (Ukraine) – 5946 pieces, Shanghai Institute of Ceramics (Chine) – 1890 pieces and Crismatec (France) – 1017 pieces. To control the quality of the large number of crystals special devices for the measurement of the sizes as well as scintillation properties were developed and constructed. These devices were installed both at the vendor's sites and at KEK.

The scintillation characteristics of each crystal are measured by irradiating with collimated ^{137}Cs γ-source (Eg=662 keV) at nine points along the crystal while the light was detected by the standard bialkali phototube (Hamamatsu R1847S). The light output of the counter was defined as the average of the nine measurements with respect to that from small, ∅2.5×2.5 reference crystal. The nonuniformity was defined by G=(maximum−minimum)/average. Fig.2,a shows the average light output and its spread for the crystal shipments from BINP, Novosibirsk. The same for nonuniformity is presented in Fig.2,b. As it is seen from figures the light output of the crystals is well above the specifications (0.29 for at least 90% of counters and not less than 0.27 for the remaining). The nonuniformity of the crystals is also satisfied the requirements which were better than 9%.

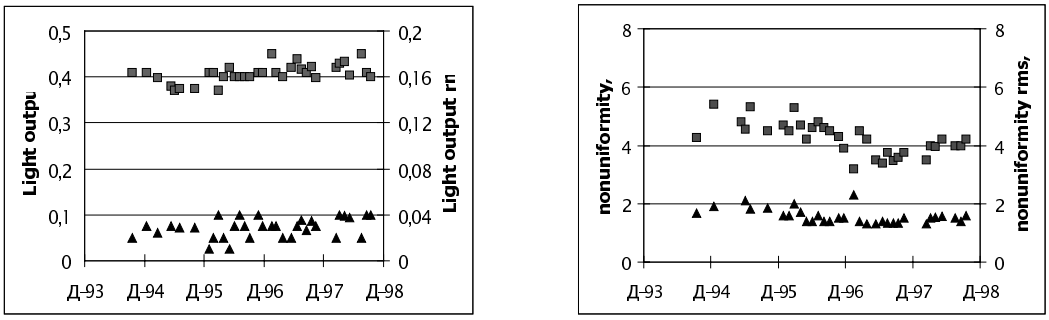

a b

Fig.2 . Average light output (a) and nonuniformity (b) for each shipment from BINP is shown by (□) and corresponding rms of this values are marked with (Δ).

Each crystal is wrapped with a layer of 200 μm thick Gore-Tex porous teflon and covered by the 40 mm thick aluminised polyethylene. For light read out two 10×20 mm^2 Hamamatsu S2744-08 photodiodes are glued to the rear surface of the crystal via an intervening 1 mm thick acrylite plate. The LED attached to the plate can inject the light pulses to the crystal volume to control the optical condition stability. Two preamplifiers are attached to the photodiodes. For the electronics channel control the test pulses are fed to the inputs of the preamplifier.

Before the assembly all counters were tested with cosmic rays using the special set-up containing the scintillation trigger counters and drift chambers for cosmic particles track reconstruction. Using the average energy deposition of cosmic muons taken from the simulation the light collection efficiency of the described counters were measured to be 5000 photoelectrons/MeV in average while a noise level was about 250 keV.

The barrel crystals were installed in a honeycomb-like structure formed by 0.5 mm thick aluminium septum walls stretched between the inner and outer cylinders. Eight crystals, four rows in ϑ and two columns in φ, were inserted in each cell and fixed in position by screws at the back. The overall support structure is gas tight and flushed with dry air to provide a low humidity (5%) environment for crystals. The preamplifier generated heat (about 3 kW in total) is absorbed by the liquid cooling system. The end cap support structure is similar to the barrel one.

The special study of the calorimeter prototype was performed using the tagged photon beam of the VEPP-4 storage ring at BINP [3]. This facility provided a possibility to test the performance of the calorimeter in the energy range from 30 to 900 MeV with precisely (about 1%) known photon energy which is measured by the special tagging system [4]. The prototype contained 36 barrel crystals arranged in 6×6 matrix. The best energy resolution is obtained when the measured energy is defined as a sum of 5×5 channels around that hitted by the incident photon at the condition that the energy deposition in each crystal exceeds the threshold of 0.5 MeV. The results are presented in Fig.3. The data above 900 MeV were obtained with the bremsstrahlung photons produced by the beam electrons at the nuclei of the remaining gas in the vacuum pipe.

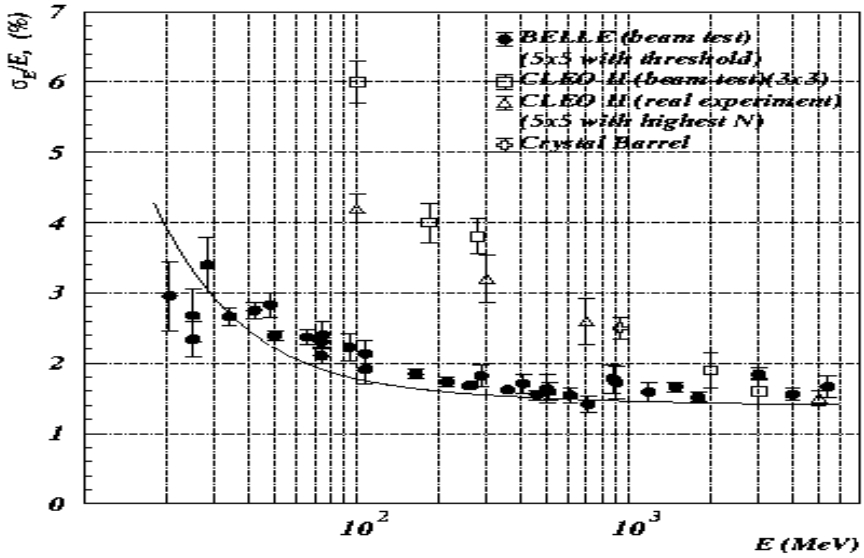

Fig3.Energy resolution as a function of the incident photon energy for 5×5 cluster. The solid line is the smooth approximation of the Monte Carlo simulation.

As it is seen from figures the energy resolution at 1 GeV range determined mostly by the rear energy leakage is about 1.6% which is in a good agreement with the results of other detectors. At low photon energy the resolution dominated by the electronics noise is better than 3% which is the best result for the detectors of this type. The equivalent electronics noise was measured to be 200 keV/channel (incoherent part) and 50 keV/channel (coherent part).

A good position resolution had been also obtained and the high calorimeter performance was confirmed.

Since BELLE will work at high intensity collider the radiation hardness of the crystals was carefully studied. At the first stage tests with several full-size crystals from each producer were made with ^{60}Co source at Tokyo Institute of Technology [4].

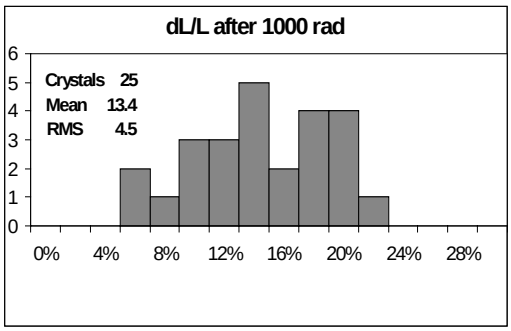

Fig.4. The light output loss for full size crystals after irradiation with 1 krad.

Later the large set of 55 crystals produced by Amcrys-H, Institute of Single Crystals, Kharkov, was tested with the gamma beam provided by the 1.4 MeV electron accelerator at the Budker Institute of Nuclear Physics. This study is presented by the separate report in this Conference. The light output deterioration, ΔL/L, for the set of 25 crystals of the same shape and sizes as used for the BELLE calorimeter irradiated by 1 krad dose is presented in Fig.4. All of the crystals meet the requirements and can be used for the calorimeter. It should be noted also that ΔL/L distribution it very wide in spite of all crystals were grown by the same method and with the same source of the raw material. The best crystal looses 4% only while the reduction for the worst one is 24%.

In the autumn of 1998 the calorimeter was integrated to the BELLE detector. The last spring the detector started the operation at the KEKB collider. Several procedures have been using for the stability control as well as for the relative and absolute calibration. One of these uses cosmic rays selecting by the special trigger. Variations of calibration constants determined by the cosmic calibration, averaged over barrel calorimeter is shown in Fig.5. As it is seen the long term stability of the calorimeter response is not worse then 1%.

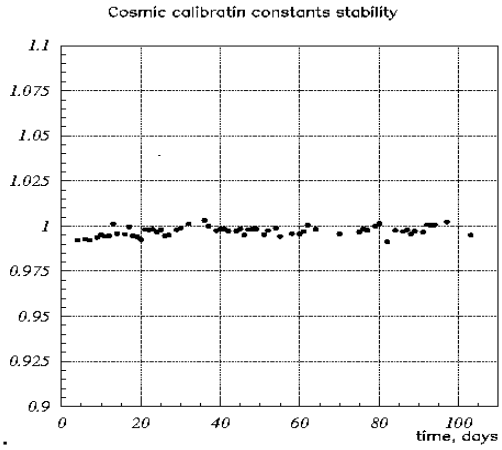

Fig.5. Stability of the cosmic calibration.

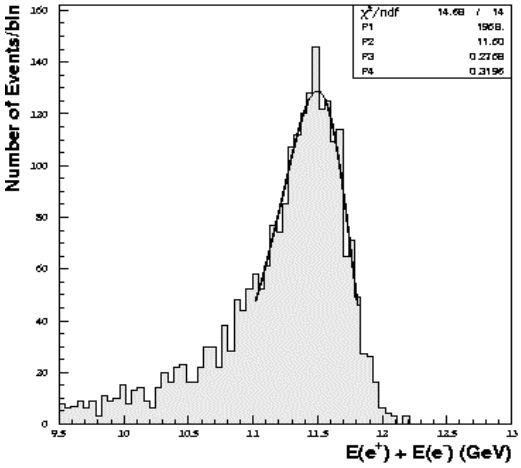

Fig.6. The total energy distribution for the $e^+e^- \to e^+e^-$ events.

For accurate calorimeter calibration the following processes are used: $e^+e^- \to e^+e^-$, $e^+e^- \to \gamma\gamma$, $e^+e^- \to e^+e^-\gamma$ as well as $\pi^0 \to \gamma\gamma$ and $\eta \to \gamma\gamma$ decays. The distribution of the total energy for e^+e^- events is presented in Fig.6. The experimental value of the energy resolution in comparison to the simulation result is referred in the Table.1

Table 1. The total energy and the energy resolution for e^+e^- elastic scattering events.

	Calibration by Cosmic rays	**Calibration by e^+e^- events**	**M.C. simulation**
E_{peak}, GeV	11.38	11.37	11.37
σ_E, GeV	0.31	0.26	0.28
σ_E/E, %	2.7	2.3	2.5

The table shows a good agreement of the experimental result to the simulation.

Fig.7 shows the inclusive $\gamma\gamma$-pair invariant mass distribution in hadronic events. The π^0 peak is clearly seen with the $M_{\gamma\gamma,peak} = (134.2 \pm 0.3)$ MeV/c^2 and $\sigma_{M\gamma\gamma} = (5.7 \pm 0.2)$ MeV/c^2.

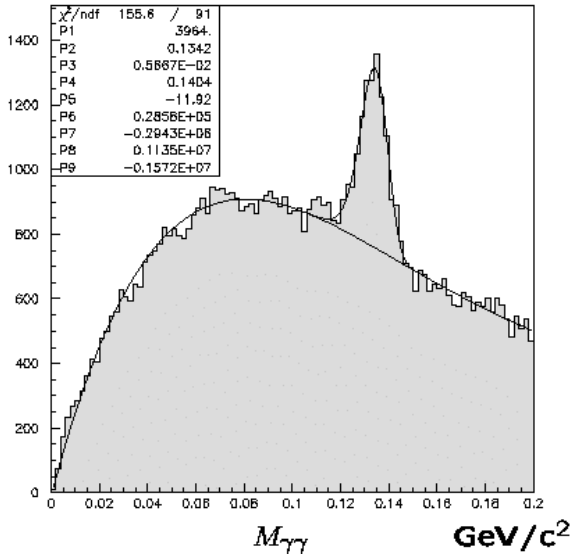

Fig.7. The $\gamma\gamma$-pair invariant mass distribution in hadronic events, E_γ>20 MeV.

In conclusion the main results of this work can be listed:

- The largest calorimeter based on CsI(Tl) crystals was constructed and put into operation, all 8736 crystals are working;
- Energy resolution measured with real events is in a good agreement with the simulation;
- During the calorimeter development the careful study of the energy and position resolution had been performed with the prototype at the gamma test beam. The energy resolution better than 3% had been obtained even at E_γ=20 MeV;

References:

1. BELLE TDR, KEK report 95-1, April 1995.
2. http://bsunsrv1.kek.jp/~ecl/
3. H.S.Ahn, et al., Nucl.Instr.&Meth, A410 (1998) 179;
   H.Ikeda, et al., A detailed beam test of CsI(Tl) calorimeter for BELLE with photon beams of energy between 20 MeV and 5.4 GeV., submitted to Nucl.Instr.& Meth.
4. V.M.Aulchenko, et al., Nucl.Instr.&Meth, A355 (1995) 261.
5. K.Kazui, et al., Nucl.Instr.&Meth., A394 (1997) 46.

Development of CeF_3 Crystal for High Energy Electromagnetic Calorimetry

T. Inagaki, Y. Yoshimura and Y. Kanda [1]
Y. Matsumoto and K. Minami[2]

[1]*High Energy Accelerator Research Organization, KEK, 1-1 Oho, Tsukuba, Ibaraki 305-0801, Japan*
[2]Ohyo Koken Kogyo Co., Ltd, OKEN, 88-77 Shingou, Higashimatsuyama, Saitama 355-0071, Japan

Abstract: The R&D study for a long CeF_3 crystal has been performed by a small collaboration of KEK and OKEN since 1992 and a significant progress has been achieved recently. Transparent crystals of more than 10-cm long are stably grown with a high yield-rate using Bridgeman-Stockbarger method in a vacuum furnace by reducing the oxygen effects at high temperature. The main point is to maintain the fluorine atmosphere supplied by two scavengers with a pump control. No significant difference in the crystal qualities is observed between several commercial CeF_3 powders. The crystals are transparent down to the wave-length of 280 nm without any red-shift. However, they still show some problems such as a radiation damage and a high sensitivity for temperature control of furnace. We will continue further studies and start a production for application to the high-energy physics experiments not-having high demand for radiation hardness.

Keywords: crystal growth, CeF_3

Introduction

CeF_3 is one of the heavy and fast scintillators suitable for various high energy physics experiments. The properties are better than those of undoped-CsI, which is commonly used as a fast scintillator, in various points as shown in Table. Another promising fact for CeF_3 is that it is possibly cheaper than CsI, when a cheap and stably-grown method is established, because Ce is abundant on the earth.

However, the stable growth of long crystals has not been easily achieved through many attempts [1] since the discovery of the good properties in 1989 [2]. The long crystals frequently become cloudy and the yield rate is low. We found that it is due to the facts of the directional difference of the thermal expansion rate of CeF_3 crystal and the special behavior of CeF_3 at high temperature.

Our studies [3]

The thermal expansion rate is quite different in three directions in reference to the crystal axis as shown in Fig.1. Unless a crystal is grown as a single one, it must break up during cool-down. Although the optimization of the furnace for single crystal is not yet finished, several trials increase the yield rate for long crystals (>10 cm) up to 50 %.

Fig.2 shows a result of a thermo-gravimetry test for a CeF_3 powder. Large mass deficiencies appear at two temperatures, a few hundred ^oC and 1000 ^oC. The out gases from these mass deficiencies are identified as H_2O^+ (combined water) and SF_3^+ by a simultaneous mass spectrometry test.

Although a large amount of oxygen supplied from the combined water at the relatively low temperature made the crystal using this powder turn black at first, a scavenger which decomposes around the temperature changed the crystal to be colorless.

The rapid mass decrease, which starts at very high temperature near the melting point, is considered as decomposition of CeF_3, because there are many evidences of fluorine liberation from CeF_3. Fig.3 shows a result of thermo-gravimetry tests in different atmosphere. This clearly shows an oxygen effect at the high temperature. Since no single-step reaction for decomposition explains the huge mass deficiency consistently, a kind of chain reaction has to occur at the high temperature using the oxygen contained in the powder. Fluorine excess will block the reaction, however, another scavenger, which covers the temperature, is not effective to remove perfectly the cloudiness of crystals. Eventually we found a method to keep the fluorine emitted from the two scavengers (for the low and high temperatures) by a control of vacuum pump. The crystals made by the method show the good properties consistent with short samples, and they are well reproduced.

Radiation hardness is one of the charm points which have been expected for CeF_3, and the study on the radiation damage provides a critical check on the crystal quality. Our crystals show some damage below 1kGy exposure of ^{60}Co with a segregation behavior by a preliminary test. Two prominent absorption bands are observed at 320 and 500nm. Fig.4 shows the measured photo-peak for ^{137}Cs gamma rays in various exposures. It indicates saturation with the dose below 100kGy and some difference above it.

Further step

We are trying to enlarge our group for more extensive studies of CeF_3 crystals and several universities in Japan have already joined after a small meeting in June. We would also start a production to supply crystals for high-energy physics experiments which do not highly demand the radiation-hardness. Since the growth of long crystals needs the works for long time with high cost, that not matches to many-times trials for further improvement. The production for application will stimulate workers and play an important role to get a valuable know-how for further improvement.

Table Properties of CeF_3 and undoped-CsI

	CeF_3	CsI
Density (gr/cm^3)	6.16	4.53
Radiation Length (cm)	1.7	1.9
Moliere Radius (cm)	2.6	3.8
Light Yield (in ratio with NaI, %)	4–5	3–4
Temperature Dep. Of Light Yield (%/°C)	0.05	–1.5
Deacay Time (ns)	5, 30	10, 30, > 1000
Refraction Index at 400nm	1.62	1.75
Hygroscopicity	none	slight
Tensil Strength (dyn/cm^2)	3.1×10^9	–
Young Modulus (dyn/cm^2)	1.1×10^{12}	$< 2 \times 10^{10}$
Thermal Expansion Coefficient (/°C)	1.3×10^{-5}	4.8×10^{-5}
Thermal-Neutron Cross-Section (barn)	0.65	35

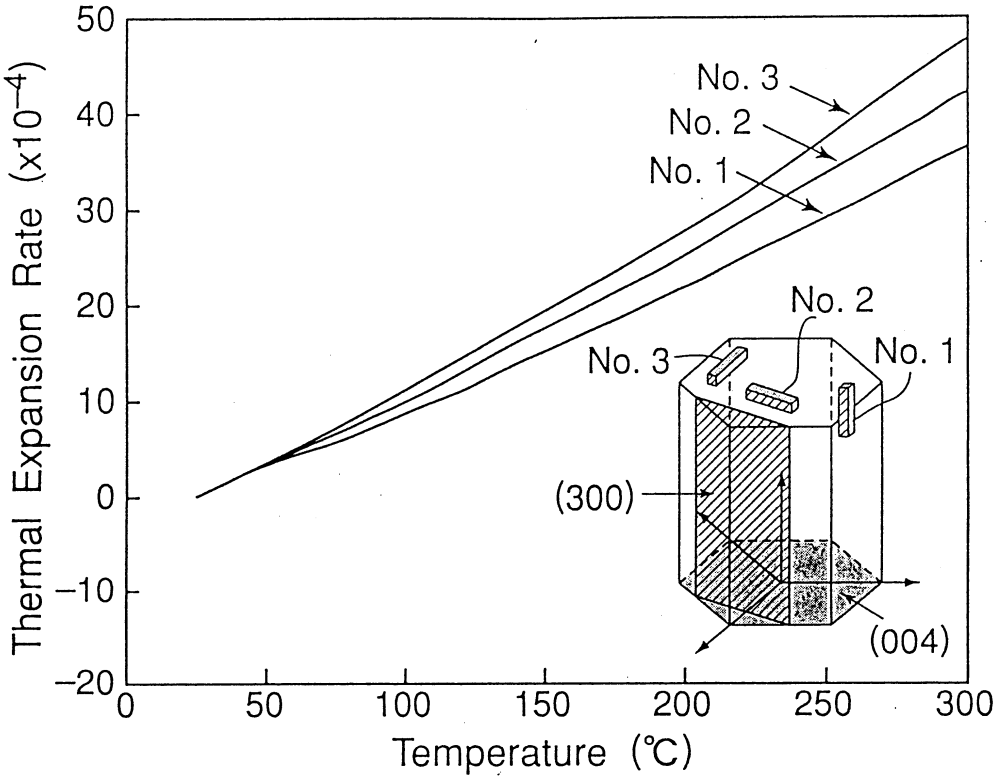

Fig.1 Temperature Dependence of the linear thermal expansion rate.

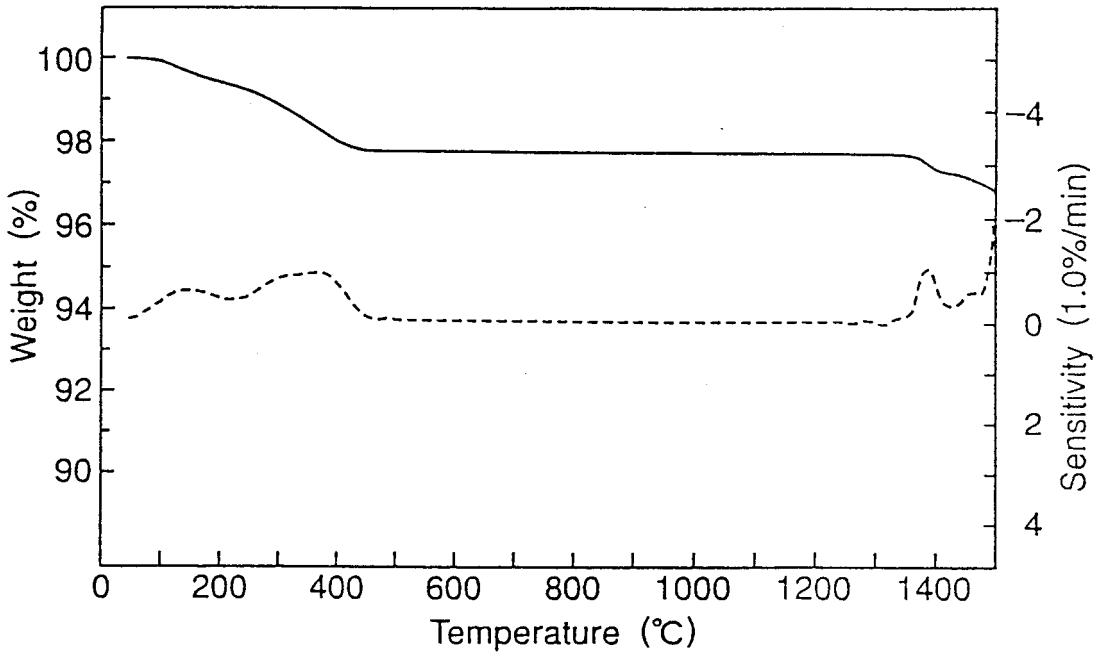

Fig.2 Mass deficiency with temperature (solid) and its derivative (dashed).

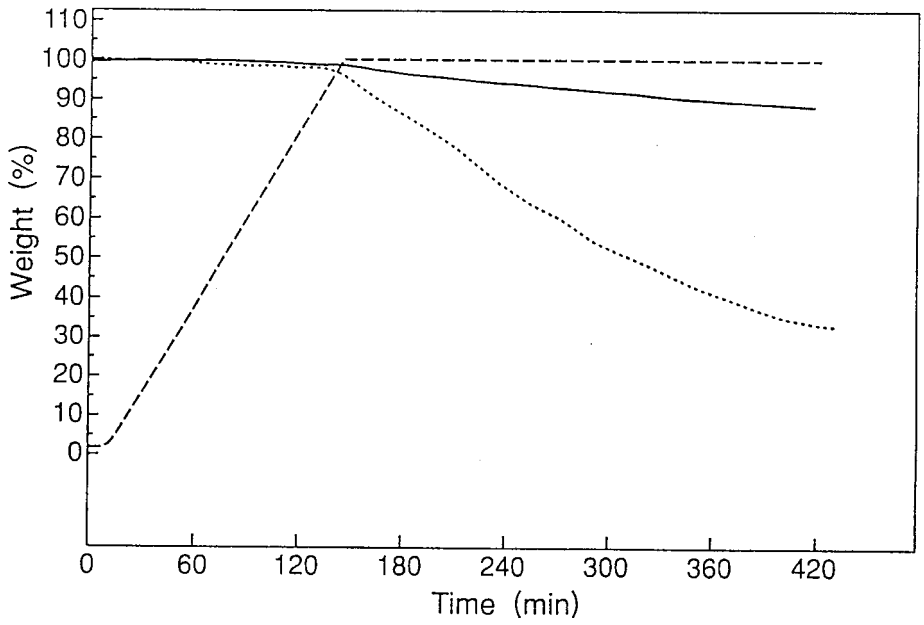

Fig.3 Mass deficiency with the temperature-rise (dashed) in two different atmosphere of pure helium (solid) and a mixture of helium (80%) and oxygen (20%) (dotted).
The temperature is hold constant at 1350 °C after raised by 10 °C/min.

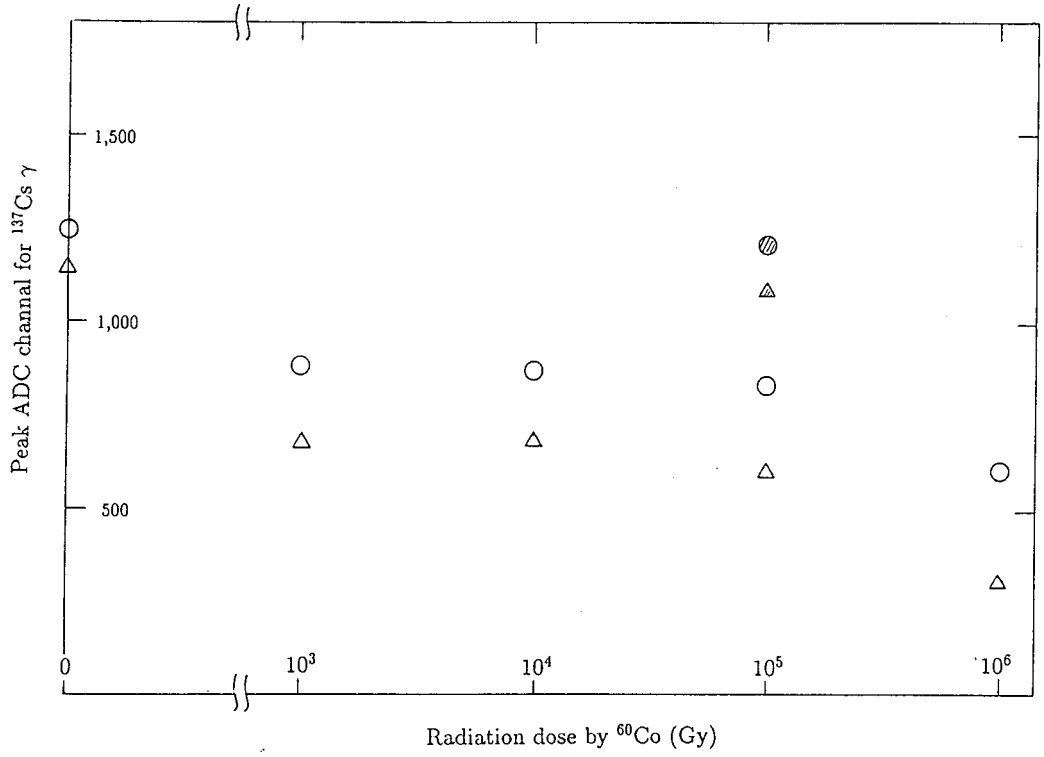

Fig.4 Dependence of light-yield for ^{137}Cs photo-peak on the exposure of ^{60}Co radiation, for samples taken from a 150mm ingot made by Bridgeman–Stockbarger method: upper (circle) and lower (triangle). UV-light are illuminated for 12-hours after the 10 kGy exposure (shaded).

References

1. E. Auffray *et al.*, Nucl. Instr. and Meth. A 383 (1996) 367.
2. D. F. Anderson, IEEE Trans. Nucl Sci. NS-36 (1989) 137; Nucl. Instr. and Meth. A 287 (1990) 606. W. W. Moses and S. E. Derenzo, IEEE Trans. NS-36 (1989) 173.
3. T. Inagaki et al., KEK Preprint **98-191** (1998); to be published in NIM A.

A PWO crystal calorimeter for high energy physics

N.Gendner[1], U.Holm, A. Meyer-Larsen, S.Thies

I. Institut für Experimentalphysik, Universität Hamburg,
Luruper Chaussee 149, D-22761 Hamburg, Germany

K.F. Johnson

High Energy Physics, Florida State University, Tallahassee, Florida 32306, USA

Abstract: A compact homogenous electromagnetic calorimeter with an energy resolution of $5\% \sqrt{E/GeV}$ made out of lead tungstate crystals, has been built for use in the ZEUS detector. 4 x 4 crystals, each of dimensions 23.8 x 23.8 x 200 mm^3, are placed in a water-cooled copper box and read out by small photomultipliers Hamamatsu R5600-U03. The whole device fits into a space of 12 x 12 x 27cm^3. The Lanthanum doped crystals from BTCP, Bogoroditsk, Russia were delivered in autumn 1997.

Bench tests have been performed concerning light yield, signal decay and radiation stability: A maximum of 1240 photoelectrons/GeV was reached with our setup, 90% of the scintillation light pulse decays within 50 ns, and the radiation induced absorption reaches saturation after a few 10 Gy with a relatively fast recovery. For 20 cm length the transmission is reduced to 80% at saturation level.

Beam tests with electrons from 3 to 100 GeV showed an energy resolution of $4.75\%/\sqrt{E/GeV}$ and a linearity of better than 1%. EGS4 Monte Carlo simulations reproduce the results very well.

1 Overview

HERA is the electron/proton collider located in Hamburg, Germany. It collides electrons or positrons of approximately 30 GeV on protons at 820 GeV. The ZEUS detector is a large, general purpose detector. A detailed description of ZEUS can be found in [1].

The beampipe calorimeter (BPC) is a ZEUS subsystem which intercepts electrons emanating from the interaction point at small angles (15-34 mrad). A description can be found in [2]. The beampipe tracker (BPT) is a small silicon tracker in front of the BPC with a position resolution of 0.1 mm.

The so-called Crystal BPC is the third in a series of BPCs, each with improving energy resolutions. The lead tungstate ($PbWO_4$) crystals used are a development of BTCP, Bogoroditsk and CMS [3]. Their excellent properties seem to make possible a compact calorimeter with an energy resolution of $5\%/\sqrt{E/GeV}$.

2 Results of Bench Tests of $PbWO_4$ Crystals

Several bench tests were performed on two batches of crystals produced by BTCP, Bogoroditsk, Russia and delivered in summer 1995 resp. november 1997. The quality of the crystals has increased a lot from 1995 to 1997 due to improvements in the growth process (stoichiometric ratio of the elements, removal of impurities, doping) and post-growth annealing [3].

[1]corresponding author. Tel.: +49 40 8998 2167; FAX: +49 40 8998 2101; email: nils@maren.desy.de

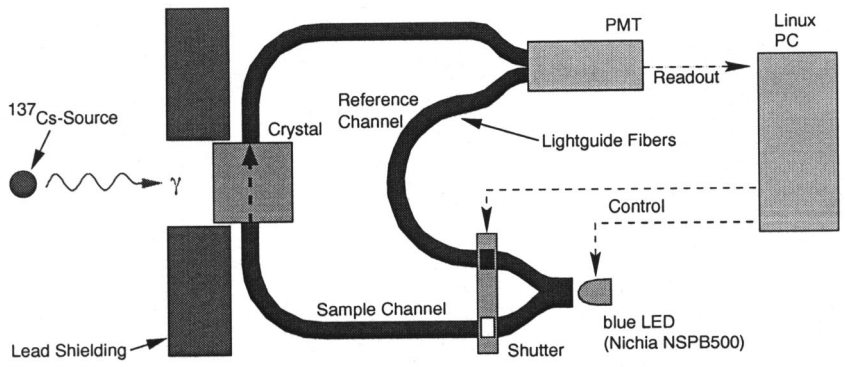

Figure 1: The setup used for online measurements of the transmission during irradiation.

2.1 Light Yield

Measurements have shown that the light yield of the 1997 crystals, compared to the 1995 crystals, has almost doubled [4].

To attain the required energy resolution with the Crystal BPC, at least 400 photoelectrons (p.e.) from the photomultiplier (PMT) cathode per GeV of energy deposit in the crystal, the stochastic minimum, are necessary. To optimize the photon collection optics, several measurements with single crystals, different wrappings and different light guide shapes (tapered, cylindrical) using cosmics were performed. Best results (1040 p.e./GeV) were achieved with a setup described in chapter 3.

Lately, Hamamatsu released a new PMT (R7400U) with an improved dynode design. Measurements using this PMT show a p.e. yield of 1240 p.e. per GeV under optimal conditions [5]. This would result in an even better energy resolution of the Crystal BPC as compared to our design goal.

2.2 Radiation Damage Effects

We have performed irradiation tests of $PbWO_4$ crystals at a ^{137}Cs source (150 GBq). The optical transmission through the width of 23.8mm was measured during irradiation with a mean dose rate of 3.6Gyh^{-1}. The crystal is placed upstanding at a distance of 5 cm from the ^{137}Cs source (Fig. 1). The blue light from a LED (Nichia NSPB500, 470 nm) travels through the center of the crystal vertically to the irradiation direction. It is detected by a PMT. Changes in the LED or PMT performance are corrected by a reference channel. The measurements are performed "online" once per minute during irradiation and annealing phases.

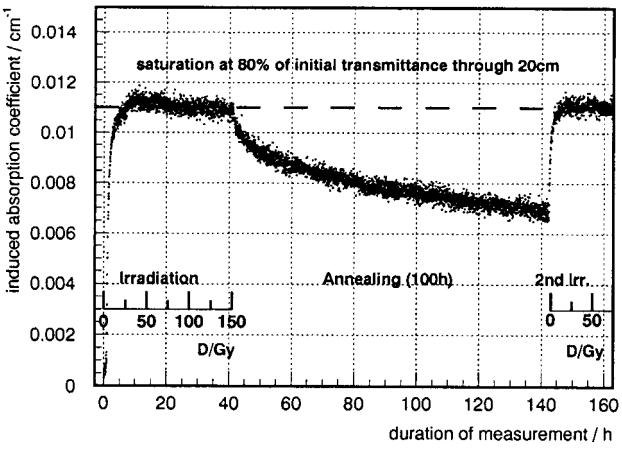

Figure 2: Online transmission measurement

In Fig. 2 a cycle of irradiation, annealing and re-irradiation of a 1997 crystal is shown. The induced absorption coefficient is plotted versus time resp. total absorbed dose.

During the initial irradiation a dose of 150 Gy is applied. The radiation damage of the crystal already reaches saturation after a few 10 Gy.

After blocking the irradiation, annealing of the radiation damage can be observed. After 100 h of annealing, the induced absorption coefficient has fallen by 36%. Finally, a second irradiation is applied at the same dose rate as the first irradiation. Similar to the first irradiation, the radiation damage reaches saturation again after a few 10 Gy.

At saturation level the induced absorption coefficient is $0.011cm^{-1}$ corresponding to a decrease in transmittance to 80% through one crystal length (20cm), which is still sufficient to guarantee proper operation of the Crystal BPC.

3 Design of the Crystal BPC

The Crystal BPC will be installed in a place deep inside the ZEUS detector where there is very little free volume. Thus compactness is a major constraint of the calorimeter's design.

The Crystal BPC consists of a 4 x 4 matrix of crystals of $200x23.8x23.8mm^3$, where the long dimension is parallel to the beampipe. The whole device fits into a space of $12x12x27\ cm^3$.

The crystals are each wrapped with Tyvek (Dupont) diffuse reflective paper. At the back of each crystal there is an 8mm diameter, 10mm long lightguide (GS218, UV transparent) glued to the crystal which connects it to a Hamamatsu R5600U-03 PMT, a miniature PMT of only 12mm length and 16mm overall diameter. At the rear of each crystal two lightguide fibers are attached which bring the light from the LED-based calibration system to the crystal (see section 4.5) resp. directly to the PMT for monitoring purposes.

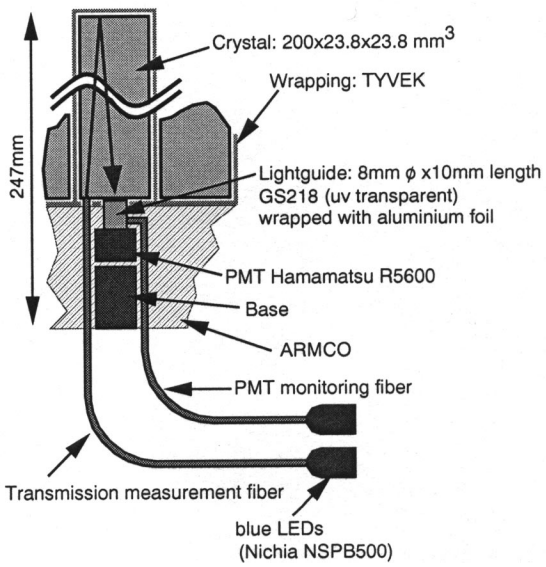

Figure 3: The design of the Crystal BPC.

The Crystal BPC is thermally stabilized by water cooling pipes attached to the calorimeter housing.

4 Results of the CERN SPS Beam Test

The beam test was performed in May, 1998 at the X5 beam line of the CERN SPS. A detailed description of the beam test setup can be found in [6] and [7].

4.1 Energy Resolution

A good energy resolution is the major constraint of the Crystal BPC. In Fig. 4 the result of a test beam measurement is shown. A 30 GeV electron beam was injected into the center of an inner crystal. Taking into account the known beam energy spread of 1%, the energy resolution results in $4.75\%/\sqrt{E/GeV}$.

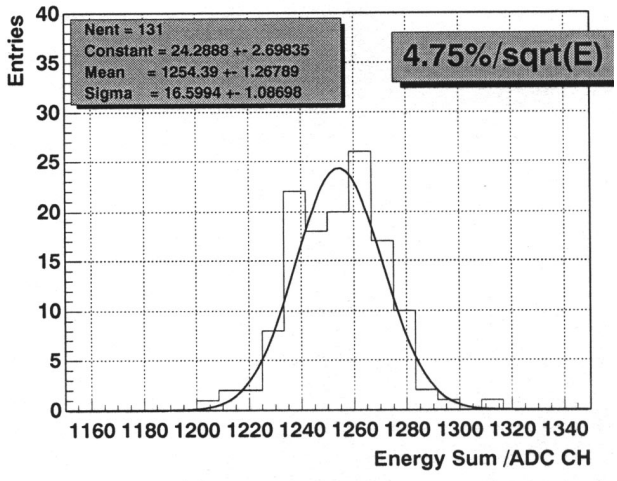

Figure 4: Energy resolution of the Crystal BPC.

The mean value corresponds to about 420 p.e. per GeV of energy deposit. This is only 40% of the p.e. yield which was observed in the bench tests. Those measurements were performed with optimal optical couplings of the lightguide to the single crystal and to the PMT whereas apparently the optical couplings are worse in the full Crystal BPC. Although the light yield is sufficient, it can still be improved by optimizing the assembly procedure.

4.2 Linearity

The linearity of the Crystal BPC was tested using electrons with energies of 5 to 30 GeV. The beam was injected into an inner crystal. Longitudinal shower leakage losses are taken into account by applying correction factors determined by Monte Carlo simulations.

A linear fit is applied to the data. Fig. 5 shows the deviation of the measured data from the fitted line. The deviation is smaller than ±1% for energies equal to or greater than 10 GeV. Only the 5 GeV data, measured with a low intensity beam and poor statistics, shows a larger deviation of 3.8%. Without the 5 GeV data, the largest deviation of the other points from the fit improves to 0.65%.

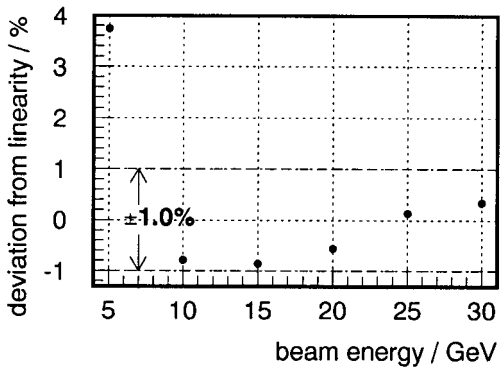

Figure 5: Linearity of the Crystal BPC.

4.3 Uniformity

The response of the Crystal BPC will suffer from non-uniformities due to leakage effects at the calorimeter edges and the cracks between the crystals.

This is shown in Fig. 6, where the calorimeter response to a 15 GeV electron beam is plotted versus horizontal electron impact position. The results are shown for one half of the calorimeter (two adjacent crystals).

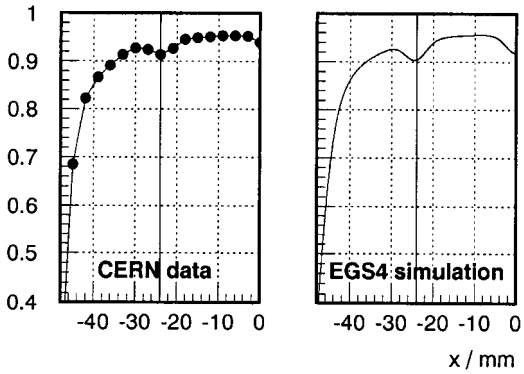

Figure 6: Uniformity of the Crystal BPC.

The beam test data is compared to an EGS4 Monte Carlo simulation. The Monte Carlo describes the real geometry of the Crystal BPC including the cracks between the crystals. The behaviour of the calorimeter response at the calorimeter edges and the cracks is in very good agreement with the Monte Carlo.

A ray tracing Monte Carlo simulation showed that the light collection using small lightguides covering only 9% of the crystal surface causes a negligible non-uniformity [6].

Measurements concerning energy resolution show a uniform resolution over 80% of the calorimeter width, deteriorating at the calorimeter's edges due to shower fluctuations.

4.4 Temperature Effect

During the CERN beam test, the Crystal BPC, packed into a box for thermal insulation, was exposed to the temperature changes in the test beam area. It was equipped with several temperature sensors which recorded the temperature very precisely. A cooling system was not installed.

The temperature of the calorimeter housing varied periodically with a period of 24 hours according to the time of day.

In order to examine the consequences of these temperature changes, a special measurement was performed after the beam test. One inner crystal of the Crystal BPC was replaced by a plastic dummy equipped with several sensors measuring the temperatures of the neighbouring crystals. The housing of the crystal BPC was equipped with water cooling pipes.

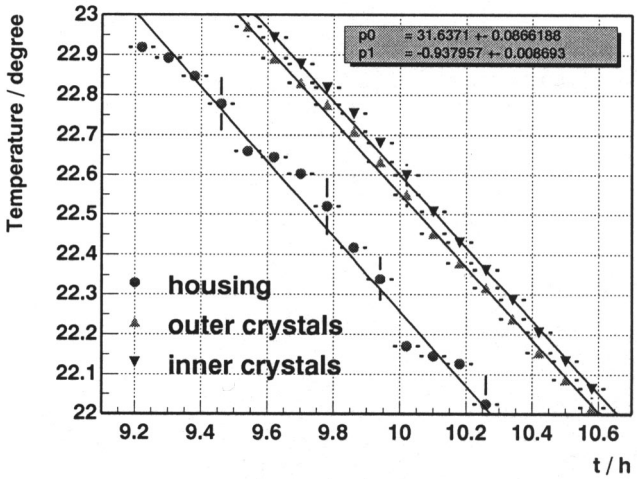

Figure 7: Temperature curves measured at the Crystal BPC housing resp. the crystals.

The temperature of the cooling water was changed periodically while measuring the housing and crystal temperatures.

We observed a phase difference between the housing temperature change and the crystals' temperature changes of (17±2) minutes. This delay is taken into account for the temperature correction of the data to extrapolate from the measured housing temperature to the crystal temperature.

From the test beam data, a change in light yield of -2%/K is obtained, which reproduces previous measurements. Using this information, the data is corrected for the temperature effect.

4.5 Radiation Damage Monitoring System

The calorimeter's energy calibration will change continuously due to appearance and annealing of radiation damage of the crystals. To compensate this effect, the Crystal BPC has to be re-calibrated continuously.

The absolute energy calibration in situ is possible by using kinematic peak (KP) events. Small angle, elastic scattering of electrons off protons produces a narrow peak at the accurately known beam energy called the "kinematic peak", which can be used as an energy calibration point.

A Monte Carlo simulation showed that an absolute calibration of the Crystal BPC to better than the required 0.5% could be performed in reasonable time intervals about once a day under nominal HERA beam conditions.

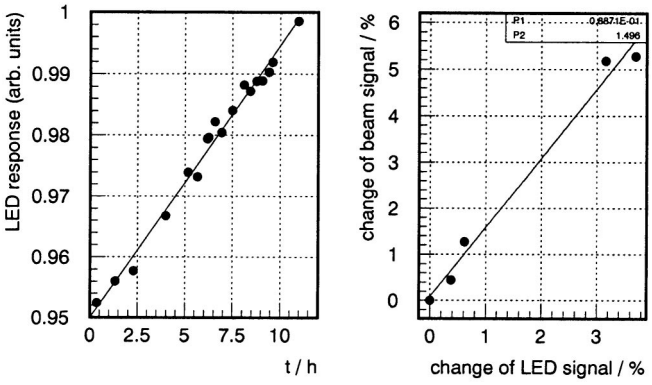

Figure 8: Recovery of the irradiated crystal. The increasing signal of the LED system (left) and the correlation between LED system and beam response (right) are shown.

For the time between absolute calibrations, variations in the crystals[5] transmissions are monitored by an LED system. A bright, blue LED (Nichia NSPB500, 470 nm) injects light into each crystal from the back using a bundle oflightguide fibers. The light traverses the length of the crystals and is reflected off the front face back to the PMT where it is detected.

The LED system proved its functionality when two crystals were interchanged with irradiated crystals and the recovery was tracked. In Fig. 8 a nearly linear rise of the LED signal of one recovering irradiated crystal with time can be observed. The correlation between the rise of the LED signal and of the crystal response to a 30 GeV electron beam is also shown.

5 Conclusions

The measurements show that $PbWO_4$ crystals have reached a high quality level which makes it possible to use them for high precision calorimetry.

The Crystal BPC has been built in its final dimensions and proved its functionality during a CERN SPS beam test. The results show that the high demands concerning the calorimeter performance, especially energy resolution, uniformity, handling of temperature changes and correction for the radiation damage and recovery in a real beam environment, can be satisfied.

Detailed descriptions of the project can be found in [6] and [7].

6 Acknowledgements

This work has been supported by the German Bundesminister fur Bildung und Forschung (BMBF) under contract 057HH19P.

We would like to thank the ZEUS BPC group, especially A. Pellegrino and R. Klanner, for useful discussions and support. We would also like to thank P.Lecoq for useful discussions and E. Auffray for her help in irradiating the crystals and measuring light yields of crystals.

References

1. ZEUS Collaboration, The ZEUS Detector, Status Report, ed. U. Holm, DESY, Hamburg (1993)
2. B. Surrow, Measurement of the Proton Structure Function F_2 at Low Q^2 and very Low x with the ZEUS Beam Pipe Calorimeter at HERA, DESY, Hamburg (1998)
3. CMS EMC Group, The EMC Project, Technical Design Report, CERN/LHCC 97-33, CERN, Geneva (1997)
4. M. Moritz, Voruntersuchungen zum Bau ernes Kalorimeters aus Bleiwolframat-($PbWO_4$)-Kristallen, Diploma Thesis, Hamburg (1998)
5. S. Thies, Untersuchungen an Komponenten des strahlrohrnahen Bleiwolframatkalorimeters BPC-III, Diploma Thesis, Hamburg (in preparation)
6. A. Meyer-Larsen, Konstruktion, Aufbau und Kalibration ernes strahlrohrnahen Blei-wolframatkalorimeters, Ph.D. Thesis, Hamburg (in preparation)
7. N. Gendner, Ph.D. Thesis, Hamburg (in preparation)

Status on PWO crystals from Bogoroditsk after one year of preproduction for CMS-ECAL

E.Auffray[1], G.Davies[1], P.Lecoq[1], R.Marcos[1], P.Sempere[1],
M. Schneegans[2], A. Annenkov[3], M. Korzhik[4]

[1]*CERN, Geneva, Switzerland*
[2] *LAPP, Annecy, France*
[3] *Bogoroditsk Techno-Chemical Plant, Bogoroditsk, Russia*
[4] *INP, Minsk, Belarus*

Abstract: IN September 1998, the CMS electromagnetic calorimeter entered into its construction phase. Since that time, 1500 crystals have been produced by Bogoroditsk Techno-Chemical Plant (BTCP) in Russia and analysed at CERN. An overview about mechanical and optical properties as well as radiation hardness characteristics of these crystals will be presented.

1. Introduction

After a long period of R&D on PWO in close collaboration with the producers [1, 2] for improvement of optical properties and radiation hardness, crystals meeting the very tight requirements for their use in the electromagnetic calorimeter of the CMS experiment at the future LHC at CERN have been produced since the beginning of 1998. The properties of these first crystals allowed us to enter in the preproduction phase at BTCP (Bogoroditsk Techno Chemical Plant) in September 1998. Since then, 1500 crystals have been produced and delivered, from which 1000 were fully characterised in the CERN regional centre (Fig.1).

For all crystals, it was checked whether they are within the specifications defined so far [3]. After a visual inspection to check for all posible visible defects, different parameters of these crystals have been measured: dimension, transmission, light yield and decay time. In addition, a few of these crystals have been irradiated. The main results of those tests are outlined in the following sections. The results have been obtained for 1000 crystals received in 5 batches. Apart from radiation hardness tests, all results were obtained using the ACCOS machine (Automatic Crystal COntrol System), which is designed to allow for automatic mechanical and optical characterisation of a large amount of crystals in a short time. The design principle and the set-up of this machine are reported elsewhere [4, 5].

Fig. 1: Some of 1000 crystals characterised in CERN regional centre

2. Dimension measurements

In a first step after the visual inspection, the crystal dimensions are measured using a 3-dimensional precision measurement instrument, which is part of the ACCOS system [4,5]. We observe that for the 1st batches the range of the dimension compared to nominal value was slightly too large (-200μ +50μ) compared to the specifications (–100μ +0μ) see Fig 2. This was mainly due to the fact that the automatic cutting procedure developped at CERN [6] to obtain the very strict tolerance required for CMS-ECAL crystals was not yet installed in BTCP. Now this new procedure has been partially installed and we thus observe a significant progress on crystal dimensions for the last 2 batches, as it can be seen in Fig. 3.

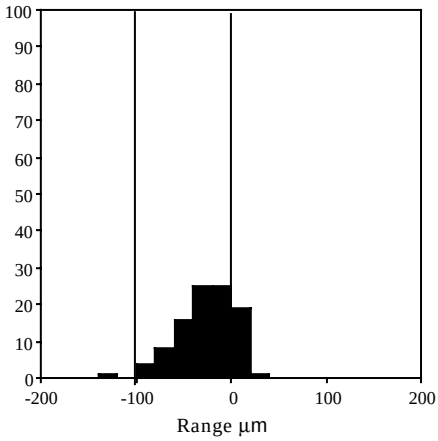

Fig. 2 : distribution of the AR dimensions compared to the theoretical value for batch 1

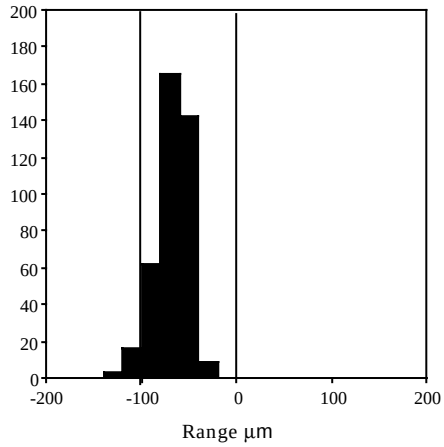

Fig. 3 : distribution of the AR dimensions compared to the theoretical value for batch 5

3. Optical measurements

3.1 Transmission

The transmission measurements on the ACCOS machine are performed with a compact spectrophotometer using a halogen lamp and a set of 11 interference filters with wavelengths between 330nm & 700nm.

In Figures 4, 5, 6, the transmission measurements at 350nm, 420nm, 620nm for the 1000 crystals are displayed. For each of those 3 wavelengths, transmission specifications have been defined [3].

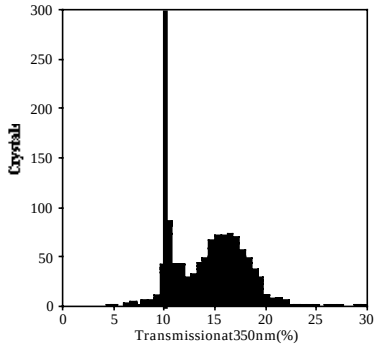

Fig. 4 :Transmission at 350nm for 1000 crystals

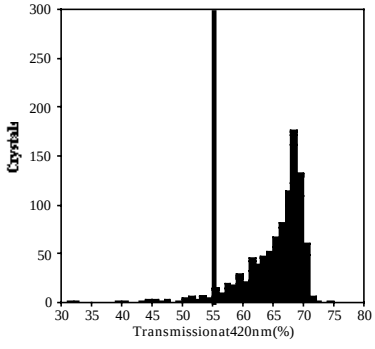

Fig. 5 :Transmission at 420nm for 1000 crystals

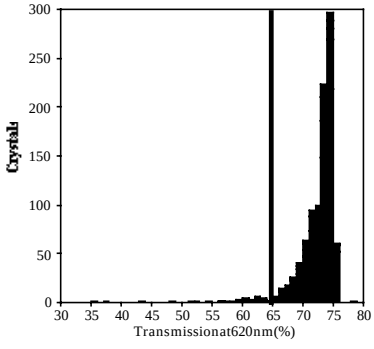

Fig. 6 :Transmission at 620nm for 1000 crystals

As it can be observed in figures 4, 5, 6, only a small fraction (~4%) of the crystals is below the specificied transmissions.

The first crystals received were La doped, and progressively the doping of the crystals has changed to a double doping (Y,Nb), which has been identified to improve the radiation hardness of these crystals [7]. As a consequence, the band edge is shifted to higher wavelengths of few nanometers, which slightly reduces the optical transmission at 350nm as can been seen on Figure 4.

The rejection at 420nm and 620nm is mainly caused by core defects in the crystals. In the first 2 batches, a significant part of the crystals (~11 %) showed core defects, but progressively the crystals became more and more transparent. Finally, for the 2 last batches (total of 600 crystals), no crystal was rejected due to core defects.

3.2 Light yield & non-uniformity

Fig.7 shows the light yield distribution measured for the 1000 crystals. Almost all of the crystals have a sufficiently high light yield with a mean value of about 10 pe/MeV. Only 2% of the crystals have a light yield slightly below 8 pe/Mev. No crystal with very poor Light yield has been identified so far.

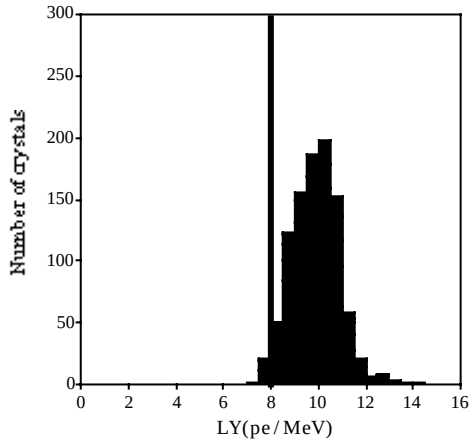

Fig. 7 : Light yield distribution for 1000 crystals

Another important parameter for the use of PWO in the CMS-Ecal is the longitudinal light collection uniformity. The tapered shape of the crystals leads to an intrinsic non uniformity (NUF), which has to be corrected. The best and most convenient treatment was found to be the depolishing of one lateral face with a proper roughness, a treatment which can be performed directly by the producers [8]. With a surface roughness of about 0.2 μm for the crystals received, one obtains a adequate NUF for most crystals. The crystals outside specifications were retreated in our laboratory for having NUF values within the specification.

3.3 Decay time

The decay time of all crystals is also measured with the ACCOS machine [4,5]. Most of the crystals were found to emit as much as 97% of the light within 100ns.

4 Radiation hardness &Band edge slope

For practical reasons, the radiation hardness can not be verified on all crystals. Nevertheless, we found a correlation between the radiation hardness and the slope of the band-edge parameter, which can be easily measured for all crystals [3].

This can be verified on Figure 8, in which the light yield loss after an irradiation of 1.5Gy at a dose rate of 0.15Gy/h for 141 crystals out of a sample of 1000 crystals is plotted. The distribution peaks at 2.5% with only two crystals having a loss slightly higher than 6%, which also don’t fulfil the slope specification.

86 crystals among the 1000 have been also irradiated at high dose rate and high dose (3Gy/min, 500Gy). All crystals irradiated have an induced absorption coefficient at 420nm below the specification value of $1.5m^{-1}$, except 3 for which the value is between $1.5m^{-1}$ & $1.7m^{-1}$ (see Figure 9).

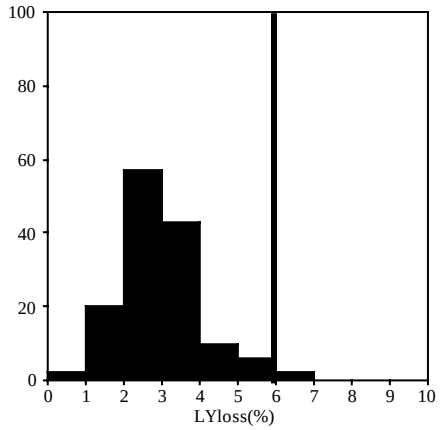

Fig. 8 : Distribution of the light yield loss after 1.5Gy at 0.15Gy/h

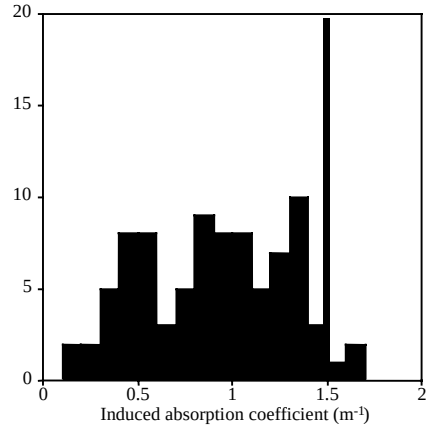

Fig. 9 : Distribution of Induced absorption at 420nm after 500Gy at 240Gy/h

The results of radiation test obtained confirm the significant progress in radiation hardness achieved for PWO crystals from BTCP.

5. Conclusion :

After a long R&D period, 1500 crystals have been produced in the BTCP since September 1998, from which 1000 have been fully characterised at the regional centre at CERN. Encouraging results and significant progress have been observed concerning the production yield, crystal parameters and rejection rate. The production yield has now reached a level of 500 crystals / month with a rejection rate around 10% (see Figure 10). The crystal parameters are more and more stabilised with a good transparency, a light yield of about 10 pe/MeV and with a light yield loss of less than 6% under 1.5 Gy irradiation. All results obtained so far correspond well to the planning towards the final production quality level.

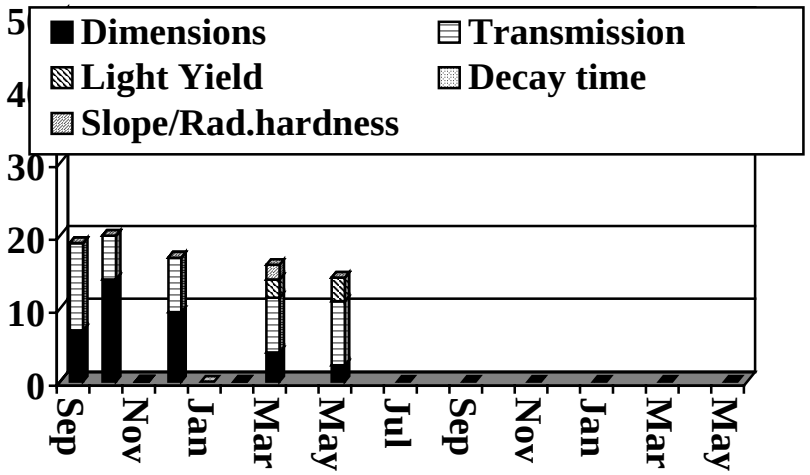

Fig. 10 : percentage of rejected crystals batch per batch

Acknowledgement

The authors wish to thank the people from BTCP for the procurement of the crystals, and all the members of the CMS-ECAL group. They are particularly grateful to J. Bourges and T. Otto from the group TIS-RP who helped us for irradiation studies and to the lab27 team : B. Buisson, H. Cabel, A. Deforni, R. Morino for their invaluable help in running ACCOS at CERN. We are also indebted to our Software team for providing the very powerful CRISTAL system, particularly to G. Chevenier, C. Koch, Z. Kovacs, J. M. Le Goff, and A. Samar.

Reference :

1. A. N. Annenkov et al,: Systematic study of the short term instability of PbWO4 scintillator parameter under irradiation, Radiation measurements, Vol 29, n 1, 27-38 (1998), CMS Note 1997-055
2. E. Auffray et al.: Improvement of several properties of lead tungstate crystals with different doping ions, Nuclear Instruments and Methods in Physics, A402 75-84 (1998), CMS Note 1997-054
3. E. Auffray et al.: Specifications for lead tungstate crystals preproduction, CMS Note 1998-038.
4. G. Drobychev et al, Studies and Proposals for an Automatic Crystal COntrol System (ACCOS), CMS-note 1997/036
5. E. Auffray et al, Performance of ACCOS, an automatic system for PWO crystal quality control, submitted for a CMS Note and to NIM
6. M. Lebeau : Precision mechanical processing of lead tungstate crystals for the CMS experiment at CERN-LHC, Proceeding of International Workshop on tungstate Crystals, 12-14 October 1998, (1999), 69.
7. A. Annenkov et al. : Suppression of the radiation damage in lead tungstate scintillation crystals, Nuclear instruments and Methods in Physics A 426 (1999) 486-490
8. E. Auffray et al. : Light Collection in $PbWO_4$ crystals, Proceeding of International Workshop on tungstate Crystals, Roma, 12-14 October 1998, (1999), 275.

Research and Development Works on $PbWO_4$ Crystals in Shanghai Institute of Ceramics

Z.W. Yin, Q. Deng, D.S. Yan

Laboratory of Functional Inorganic Materials, Shanghai Institute of Ceramics
Chinese Academy of Sciences
1295 Dingxi Road, Shanghai 200050, P.R. China

Abstracts: An overview of the latest research and development works on $PbWO_4$ crystals in Shanghai Institute of Ceramics are presented. Big progress both in quantity and quality of the full size crystals has been achieved. Crystal growth parameters on 28-crystal furnace have been optimized. Raw materials production has also been scaled up and their quality have got improved. Doping and annealing studies are carried out to optimize the light yield and radiation hardness of lead tungstate crystals. Y doping shows the best performance for the large size crystal due to its adequate segregation coefficient. It was found Y doped crystal is more sensitive to its bleaching temperature compared to other doped lead tungstate crystals, overheat (more than 100□) would create color centers (more absorption) at 420 nm in the crystal. This kind of absorption can be removed by low dose rate irradiation.

Keywords: Lead tungstate; Bridgman method; Light yield; Radiation hardness

1. Introduction

Shanghai Institute of ceramics began its R&D works on $PbWO_4$ crystals since 1994 when lead tungstate crystal was chosen as scintillation material in electro-magnetic calorimeter for CMS at CERN[1]. Since then intensive research works on its raw material, growth technology, crystal processing and scintillation properties were carried out. Modified Bridgman method was being used for $PbWO_4$ crystal growth in SIC, multi-crystal growth furnace was designed to meet the requirement of mass production. From the very beginning, one furnace can only grow 3 crystals at one time, up to now, a 28-crystal furnace has been well designed and used for $PbWO_4$ preproduction. The capability of raw material production has also been scaled up to 800 kg per month. On the quality assurance study, SIC took a strategy to improve crystal quality step by step from small crystal size to larger size, first to make good small crystals with 5 cm length, then 10 cm crystals, finally full size crystals. In 1997, SIC had successfully produced radiation hard 5 cm samples with fine tuned post treatment method [2]. In early 1998, SIC transferred her good experience to longer crystals, 10 cm length crystals were made and meet quality requirement of CMS. Since later 1998, SIC concentrated her study strength on full size crystal research and development.

As we have known, $PbWO_4$ is a rather complicated crystal, its scintillation and radiation damage mechanisms have been intensively studied [3,4,5], but so far still are not very clear. On several years experimental practice, we understand that the quality of PWO crystals mainly depends on the purity of raw material, optimum stoichiometry tuning, correct growth technology and post crystal treatments. In this paper, the main results of the latest research and development works on $PbWO_4$ crystals in SIC will be presented.

2. Improvement of Raw Material

Table 1 shows the quality progress of raw material since 1998. Table 2 shows the GDMS analysis results of four $PbWO_4$ crystal samples. Raw material analysis results show that most impurities in WO_3 have been reduced in 1999 as compared to that of 1998, while PbO raw material kept its purity. Four crystal samples taken from top and bottom parts of the crystal were analyzed. These crystals are all Y doped. Table 2 shows that in the different parts of the crystal Y concentration is uniform, which means its segregation coefficient is close to 1.

Table 1 GDMS analysis results of raw material (by Shiva Technology West)

Sample	WO_3	WO_3	PbO	PbO
Date	03/99	04/98	03/99	04/98
Fe	0.35	0.89	0.09	0.07
Mn	<0.01	0.02	<0.01	<0.01
Cr	<0.01	0.11	0.05	0.03
Cu	<0.01	0.08	0.09	0.10
Ca	<0.07	0.36	0.22	<0.05
Mg	<0.01	0.04	0.05	0.01
Al	0.30	0.22	0.85	0.70
K	0.11	0.23	<0.05	0.15
Na	0.07	0.15	0.02	0.08
Mo	0.20	0.61	<0.01	0.01
Si	0.25	0.15	0.27	0.15
Cl	0.32	1.0	0.5	0.60
As	<1	1.9	<0.01	<0.01
Y	<0.01	<0.01	<0.01	<0.01
Sb	<0.05	0.20	<0.05	<0.05
La	<0.005	0.01	<0.005	<0.005

Table 2 GDMS analysis results of four Y doped PWO samples

Sample	Top 1	Top 2	Bottom 1	Bottom 2
Na	0.5	0.3	0.26	0.3
K	2.5	2.0	0.27	0.46
Ca	<0.05	0.12	1.8	2.3
As	1.8	0.5	0.13	0.19
Y	60	80	60	65
Nb	<0.05	<0.05	<0.05	<0.05
Mo	1.8	1.5	1.5	1.1
Sb	0.1	0.05	<0.05	<0.05
La	<0.01	<0.01	<0.01	<0.01

Now SIC has completed her first stage on scaling up PbO and WO_3 raw material production.

In this stage, the raw material produced by SIC can guarantee impurity contents within allowable limits for 1000 pcs crystals in the preproduction period. In the mean time SIC will continue her effort on scaling up raw material production capability to meet the requirement of mass production and to lower the production cost.

3. Crystal Growth Technology

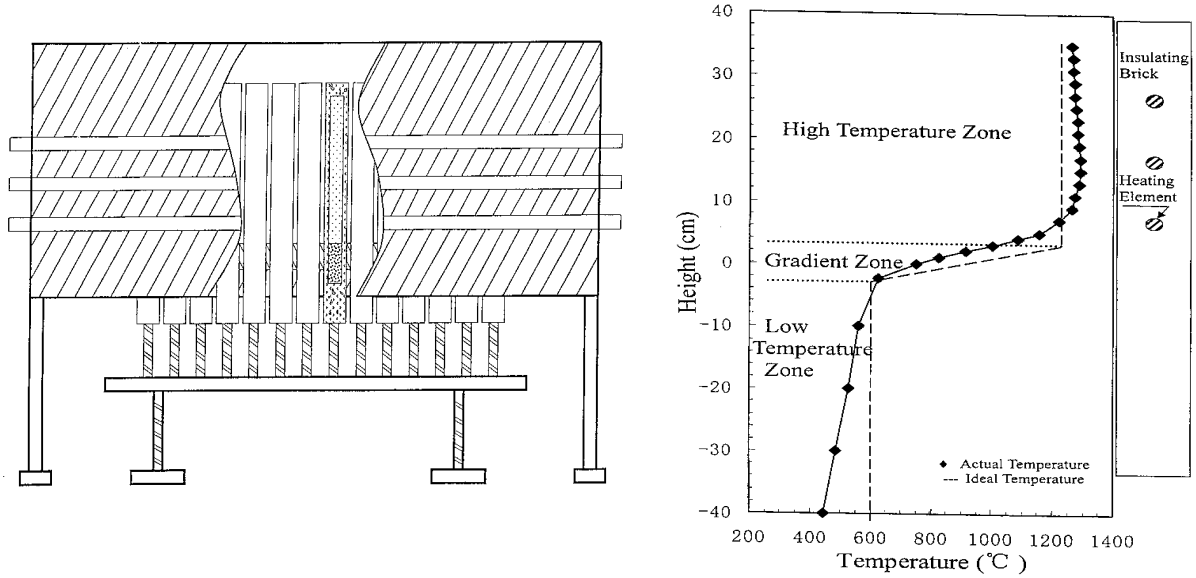

Fig. 1 Schematic representation and temperature profile of multi-crystal growth furnace

A set of computer controlled multi-crystal growth furnace which can grow 28 pcs crystals at one time has been designed and constructed in SIC. The layout of the furnace and its temperature profile are shown in Fig. 1. Experiments on optimizing crystal growth parameters have been carried out in last several months. Up to now, all round growth parameters have been well settled. More than 60% yield has been achieved on growing defect free full size crystals. And by using these multi-crystal growth furnace, SIC has succeed to reach a production capability of more than 150 crystals per month. In the near future, more furnaces will be constructed to meet mass production requirement.

4. Quality Assurance

It is well known that $PbWO_4$ crystal usually has intrinsic defects due to its two main components PbO and WO3 having different evaporating rate in the melt [6]. And the analysis results reveal these intrinsic defects are mainly lead and oxygen related defects [7, 8]. These defects spoil the scintillation properties of PWO crystals. There are two approaches to overcome these intrinsic structure defects to improve the crystal quality. One approach is to reduce the impurities and defects in the crystal by raw material purification and growth technology optimization. Another approach is to compensate these intrinsic defects by intentional doping [9, 10, 11]. SIC is using both approaches to improve the crystal quality.

Table 3 shows the quality progress of $PbWO_4$ crystals produced in SIC, test results shown in the table were done in Caltech, U.S.A.. The big progress on full size crystals was achieved in the period of 1998 to 1999. Both quality and quantity of full size crystals got improved in this period.

Table 3 Full size $PbWO_4$ crystal samples investigated at Caltech, U.S.A.

Year	Sample ID	L.O. @200 ns (p.e./MeV)	Fraction(%) 100ns/1μs	L.O. Loss (%)@R(rad/h)		
				15	100	480
1997	SIC 167	9.2	93.2	90.4	87.1	84.0
1998	SIC 210	8.0	75.7	80.0	77.0	----
1999	SIC S249	9.1	99.1	94.5	85.7	78.0
	SIC S392	8.4	97.3	98.2	91.3	83.6
	SIC S412	8.3	98.6	98.2	91.2	85.9
	SIC S301	9.4	96.6	96.6	87.3	79.5
	SIC S347	9.9	97.8	95.1	88.6	82.1

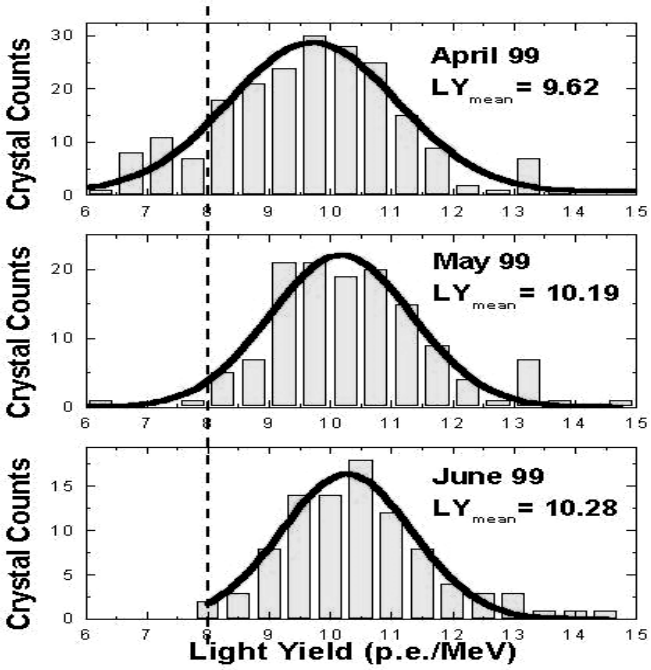

Fig. 2 Statistics on light yield of PWO crystals produced in SIC

Fig.2 presents the light yield statistics on $PbWO_4$ crystals produced in April to June in SIC. The statistics were carried out on all Y doped crystals. The light yield is defined as the number of photons extracted from the crystal and coupling on the photocathode of a quartz window XP2262B Philips photomultiplier, when excited by a Cs^{137} γ source. As shown in the figure, the mean values of light yield are improved month by month, and their distributions are becoming narrower monthly. In June, nearly all measured crystals have a light yield higher than 8 p.e./MeV.

During radiation hardness study on Y doped crystals, we found that 250°C thermal bleaching which we usually used before any scintillation properties measurements to eliminate pre-existing color centers in the crystals would create color centers (more absorption) at 420 nm region. Their transmission curves before and after 250°C bleaching are shown in Fig.3. However this kind of damage can be recovered by low dose rate irradiation or optical bleaching [12, 13, 14].

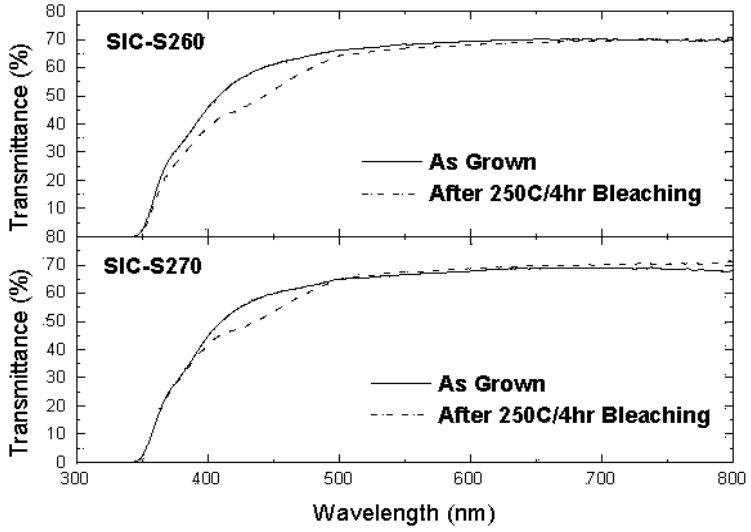

Fig. 3 Transmission curves of Y doped PWO crystals before and after 250°C bleaching

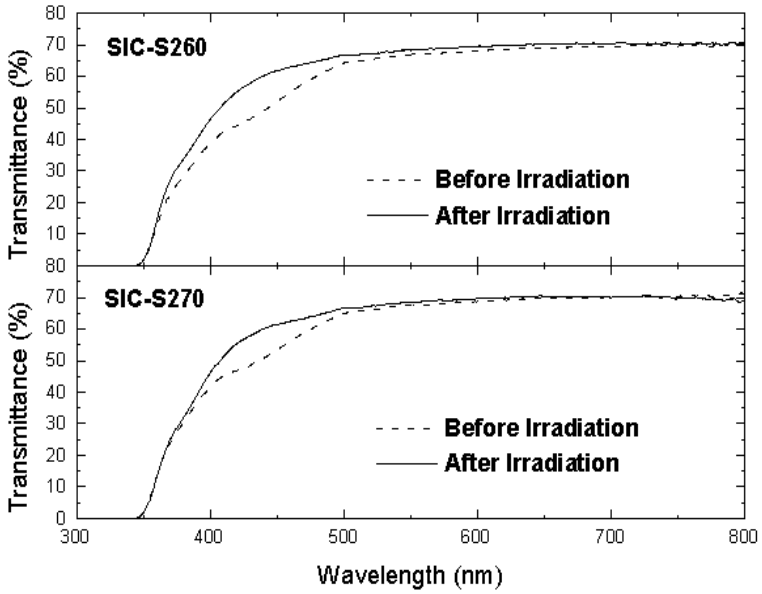

Fig. 4 Transmission curves of Y doped PWO crystals before and after irradiation

Fig. 4 shows transmission curves of Y doped PWO crystals before and after irradiation. Irradiation test were carried out in Shanghai, dose rate is 35 rad/hr and total dosage is 2450 rad. In the figure, two samples show transmission increase at 420 nm region after irradiation. Their light yields are also increased about 10%. This phenomenon can be explained by the kinetic model of color centers creation and annihilation established by Renyuan Zhu *et al*. in [5]. Before irradiation, these Y doped crystals have pre-existing color centers caused by unsuitable thermal treatment. During the irradiation, both color centers creation and annihilation co-exist. Since Y doped crystal emits blue light which is peaked at 420 nm, optical bleaching process originated from PWO(Y) scintillation has a high efficiency for 420 nm center. Then color centers recovery becomes dominant compared to the damage process caused by low dose rate irradiation. The combined effects of a low dose rate irradiation thus cause an improvement on transmission at 420 nm while optically bleachable center density is not zero at the beginning. When the dose rate increases, damage process becomes dominant, thus a loss in both light yield and transmission will be observed as shown in Fig. 5.

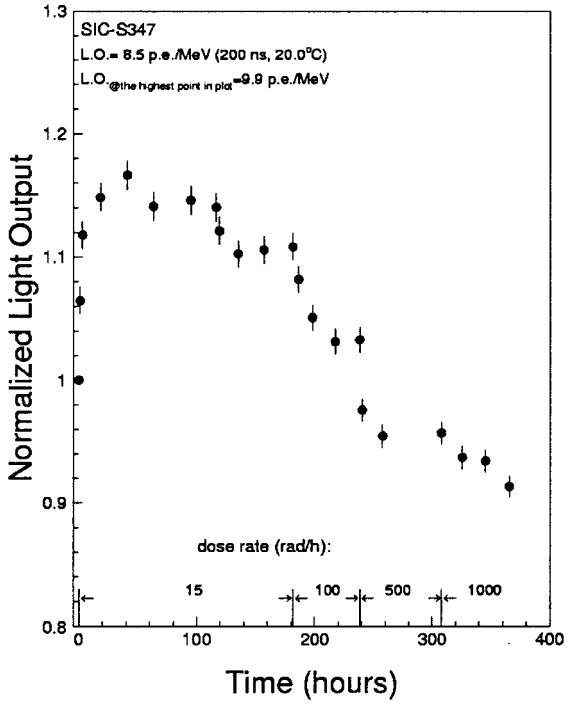

Fig. 5 The normalized light output of SIC-S347 as a function of irradiation time and dose rate (Test results provided by Dr. Renyuan Zhu at Caltech)

A serial of experiments on bleaching temperatures were carried out to find the ground state of Y doped PWO crystals. Up to now 50°C and 48 hours seems to be adequate bleaching condition to make Y doped

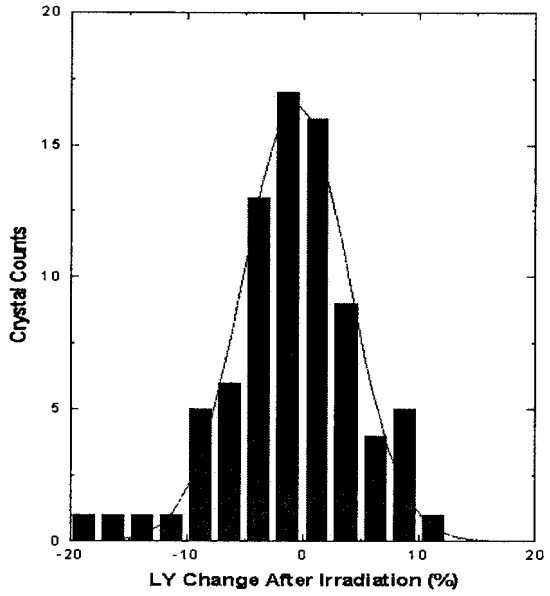

Fig.6 Irradiation results of Y doped PWO crystals produced in June in SIC

PWO crystals most close to its ground state. More experiments on thermal and optical bleaching are needed to understand and cure the stability of Y doped PWO crystals.

Fig. 6 shows the irradiation results of Y doped crystals made in June in SIC. All these crystals received 50°C and 48 hours thermal bleaching before irradiation. The irradiation condition is 35 rad/h and a total dose of 2450 rad with side irradiation. The figure shows that more than 90% crystals their light yields change before and after irradiation are within ±10%, which meet the requirement of CMS.

5. Summary

In this paper, the latest results of research and development work on PWO crystals in SIC are presented. It can be summarized as following points:

1. Raw material production capability and their qualities can meet the preproduction stage requirement, and keep the impurity contents within allowable limits.
2. Several 28-crystal growth furnaces have been constructed, all round parameters have been well settled, more than 60% growth yield was achieved.
3. The light yield and radiation hardness of Y doped PWO crystals have been improved steadily. Most full size crystals can meet the CMS requirements.
4. Y doped PWO crystals are sensitive to thermal and optical bleaching. 250°C annealing would spoil the transmission at 420 nm and light yield. Thermal bleaching parameters should be carefully selected to solve this problem.

References

1. CMS Technical Proposal, CERN/LHCC 94-38, LHCC/P1 Dec 15 1994.
2. R.Y. Zhu, et al., IEEE Trans. Nucl. Sci. 45(3), (1998)686.
3. P. Lecoq, et al., Nucl. Instr. Meth., A365, (1995)291.
4. A. N. Annenkov, et al., CMS NOTE 1998/041, CERN. July 20, 1998, Phys. Stat. Sol. (a), (1998)170.
5. R.Y. Zhu, et al. IEEE Trans. Nucl. Sci. NS44, (1997) 468.
6. A. N. Annenkov, et al., Radiation Measurements, Vol 29, (1998)27.
7. J.Y. Liao, et al. Wuji Cailiao Xuebao, 12(3), (1997) 286.
8. M. Nikil, et al., Phys. Stat. Sol. (a), 156, (1996)493.
9. E. Auffray et al., Nucl. Instr. Meth. A402(1998)75.
10. A. N. Annenkov et al., Nucl. Instr. Meth. A426(1999)484.
11. M. Kobayashi et al., Nucl. Instr. Meth. A399(1997)261.
12. R.Y. Zhu, et al., PWO Internal Meeting, Shanghai, July, 1999.
13. P. Lecomte, et al., PWO Internal Meeting, Shanghai, July, 1999.
14. H.F. Chen, et al., PWO Internal Meeting, Shanghai, July, 1999.

Methodology of Certification of Scintillators for Large Scale Detectors

E. Auffray[1], A.N. Annenkov[2], G.Yu. Drobychev[3], V.A. Evdokimov[3], A.A. Fedorov[3], M.V. Korzhik[3], V.L. Kostylev[2], P. Lecoq[1], O.V. Missevitch[3], A.V. Oskine[3], V.V. Panov[3], J.-P. Peigneux[4], M. Schneegans[4], R.F. Zouevski[3]

[1]*CERN, CH-1211 Geneva, Switzerland*
[2]*BTCP (Bogoroditsk Techno-Chemical plant), 301800 Tula region, Bogoroditsk-4, Russia*
[3]*INP (Institute for Nuclear Problems), 11 Bobruiskaya st., 220050 Minsk, Belarus*
[4]*LAPP-IN2P3, chemin de Bellevue – BP-110, F-74941 Annecy le Vieux, CEDEX France*

Keywords: light yield, uniformity, optical transmission, radiation hardness

Abstract: The building up of the large scale detectors for high-energy physics experiments in coming millenium such as CMS electromagnetic calorimeter requires the production of tens of thousands of scintillating crystal. The high-performance target of such detectors impose strict requirements on parameters of crystals, such as sufficient light yield, acceptable light yield uniformity, short decay time free of slow components, and very limited light yield loss under irradiation, precise dimensions. The challenge is to provide a high production rate and appropriate quality control for such a large scale project. The certifying procedure approach developed for the production centers and CERN is presented here. Multilevel quality control scheme is proposed. The equipment built for the automatic measurement of the optical and scintillation properties and the associated software tools as well as the method and tools for the radiation hardness tests are presented.

Qualifying crystal Parameters

CMS (Compact Muon Solenoid) electromagnetic calorimeter (ECAL) requires the production of $PbWO_4$ scintillating crystal elements of 23 cm length in 34 different shapes over several years, 80000 elements in total [1]. To fit the calorimeter precision requirements, each element has to pass through a certifying procedure before delivery. In the past, similar calorimeter projects have required at least one order of magnitude fewer measurements [2]. The specifications for the PWO crystal pre-production are summarized below [3]:

- LY threshold of 8 photoelectrons per MeV is applied (as detected by a Philips PM 2262B covering the full crystal output area with a $n = 1.5$ coupling grease, using the ^{60}Co photopeak position determination by classical pulse-height spectra analysis).
- In order to keep the contribution of light yield non-uniformity (LYN) in energy resolution below 0.2%, a LYN slope smaller than $\pm 0.35\%/X_0$ (PWO radiation length X_0=0.89 cm) in the first half of the crystal length must be achieved.
- To be compatible with LHC high luminosity, the contribution of the fast component to the scintillation decay defined as LY(100 ns)/LY(1 μs) should exceed 90%.
- For the longitudinal optical transmission:
  ≥ 10% at 350 nm and a slope of the band edge measured between 340 and 380 nm
  S>1.5%/nm – indicates an acceptable radiation hardness;
  ≥ 55% at 420 nm – guarantees a minimum absorption length of ~80 cm in order not to affect the light collection uniformity of the crystal;
  ≥ 65% at 600 nm – guarantees the absence of large core defects;

- For the transversal optical transmission:
  the dispersion of the intercept point of transmission spectra with a line of T=50% should not exceed 6 nm full range when measured at 6 points every 4 cm along the crystal starting at 1.5 cm from the front face.
- Radiation hardness is a parameter for which systematic and direct measurements are difficult. Crystals will be studied on a sampling basis at irradiation facilities at CERN and special irradiation facilities near producer. Crystals should have the following characteristics:
  induced absorption for full saturation of the crystal $\mu \leq 1.5$ m^{-1} at 420 nm after a lateral ^{60}Co irradiation with a total absorbed dose > 50 krad and a dose rate > 10 krad/h;
  light yield loss < 6% after front ^{60}Co irradiation with a total absorbed dose of 200 rad and a dose rate of 15 rad/h corresponding to the LHC irradiation environment; no recovery time constant shorter than one hour.
- Dimensions tolerances 0 ÷ -100 μm referring to nominal values defined in [1] and the planarity of faces must be better than 20 μm.

The Automatic Crystal Control System (ACCOS)

The conventional laboratory methods used for crystal measurements cannot provide the necessary productivity. Therefore a high-productivity industrial system has been constructed [4] and installed at both the crystal production facilities and at CERN. It is automated in order to reduce the influence of the human factor and provide an output of at least 30 crystals per day. The PWO crystal is fragile mechanically and can easily be damaged by contact with hard materials of equipment parts. Therefore frequent handling of crystals should be strictly avoided. The adopted solution is to keep crystals lying on special supports during all measurements and to move the spectrometers along them. Consequently, special compact spectrometers have been designed. The overall set-up including the associated 3D machine is installed in a temperature-controlled and light-tight room. A bar-code reader identifies each crystal from the bar-coded label glued on the small end-face at the production stage.

Light Yield and Light Yield Non-uniformity Measurements

A 'start-stop' or delayed coincidence method is used for both scintillation decay time and light yield measurement. The proportionality between the stop channel count-rate and scintillator light yield for small quantities of light is used to determine the LY by integration of the decay time spectrum. It means that scintillation decay times and the LY of a scintillator can be measured simultaneously. In this case, neither optical coupling between scintillator and PM nor scintillator wrapping are needed in contrast to the very widely used method of pulse-height spectrum measurement with uses the radioactive γ-source (usually ^{60}Co) with consequent total absorption peak position determination. The start-stop method puts two constraints on event rates, which limits the productivity. One is the limitation on the annihilation source activity. It should not exceed ~10^5 Bq. At higher activity the probability of random coincidence of two γ-quanta from different decays (background) becomes too high. The second is the limitation on the probability of detecting light photons in the stop channel per single excitation. A conventional TDC requires an average number of detected photons to be not more than 0.1 per single excitation; otherwise, the measured scintillation decay curve will be distorted, especially in the slow component region. The use of multi-hit TDC allows this problem to be avoided. Stop-channel detector dead time can also cause distortion, but especially in the fast component region when the fastest component in scintillation is less than or comparable to the stop channel dead time that takes place for PWO scintillators. A one-hit TDC (or TDC with multi-stop rejection [5]) was implemented to overcome the distortion

problem. The most comprehensive analysis of TDC with multi-stop rejection is made in [6]. The start-channel detector consists of a Hamamatsu UV-extended R5900 type PM coupled to a 20×20×20 mm^3 BaF_2 scintillator. The ^{22}Na annihilation source with an activity of 200 kBq is mounted as close as possible to the scintillator and delivers about $2 \bullet 10^4$ cps of starts. The start PM with scintillator and source is mounted on a moving platform together with the transversal transmission spectrophotometer for scanning along the crystal. The stop-channel is based on a Hamamatsu R5900 PM with a low dark pulses count rate. The average number of stop signals (detected scintillation photons) is about 0.3 per single excitation for the most luminous PWO scintillators. The count rate of the useful events (scintillation photons produced by scintillation decay in PWO collected in decay time spectrum) is about $1 \bullet 10^3$ cps, and a spectrum with acceptable statistics can be acquired in one minute.

Optical Measurements

Longitudinal transmission can be reconstructed using transversal transmission data. However, it is impossible to obtain the required precision in case of PWO scintillation elements because of uncertainties in the Fresnel reflection level from crystal to crystal. This uncertainties are caused by the deviation of the crystal growth axis from crystallographic axis *a* by ±5°. Therefore both types of transmission measurements should be performed. As PWO is a birefringent crystal and the shape of the scintillation elements varies, a wide-aperture photodetector is required. This prevents from the use of spectrometers based on photodiode arrays with a light dispersing prism. On the other hand, the PWO transmission spectrum has no narrow absorption bands, so it is not necessary to measure PWO transmission spectrum at many wavelengths. It can be measured only at several well-chosen wavelengths with subsequent reconstruction of the total spectrum to speed up the measurements. For this purpose, a set of 11 interference filters was used. Two dedicated compact spectrophotometers for optical transmission measurement have been designed and built. The optical part of each spectrophotometer includes a 20 W halogen lamp, a four-lens collimator, three objective lenses, a rotating changer with interference filters, collecting mirrors, a 20×20 mm^2 UV-extended photodiode Hamamatsu S6337 and readout electronics. The spectrometer dimensions are 70×80×220 mm^3. The compact design of spectrometers allows the fast movement of the spectrometer from the measurement zone to the calibration position (air measurement). During measurements, the rotating wheel with interference filters crosses the light beam sequentially. Such a system provides a fast switching (0.5 s) of the light wavelength. The time necessary to measure a transmission spectrum in the range 330…700 nm is less than 10 s for one spatial point.

Dimension Measurements

All dimension measurements are carried out with the standard three-dimensional machine TOPAZ 7 supplied by Johansson AB (Sweden) which provides three coordinates of several points on each crystal face with a precision of ±5 μm and subsequent calculation of the crystal dimensions and face planarity.

Software

Software provides a user interface, acquisition, data processing, results storage and presentation. It also supports communication with C.R.I.S.T.A.L. software [7] and 3D-machine. Software components are implemented in LabVIEW™ graphical programming system and Microsoft™ Visual C++ and runs on an IBM-compatible PC under Microsoft™

Windows NT operating system. A special algorithm was developed for scintillation kinetics data processing [8]. Instead of non-linear iterative fitting procedure usually used for multi-exponential functions and giving sometimes unstable results due to inherent convergence problem, new approach is based on non-iterative 3-step integrating/subtraction procedure working without user intervention.

Radiation Hardness Test

An irradiation set-up for full size crystals that has been installed near BTCP consists of irradiation shaft with ^{60}Co source and a specialized 4-channel spectrophotometer. Optical transmission variation is measured before and immediately after the irradiation at 3 different wavelengths. Dose rate is about 10 krad per hour. Productivity - 4 crystals per hour. Set-up provides safe handle of four crystals in special container during irradiation and measurement. Optical scheme of the spectrophotometer provides illumination of the crystal by wide divergence probe light beam emulating light collection geometry close to electromagnetic shower case. This increases sensitivity to induced absorption by factor of ~5 in comparison with narrow parallel beam geometry due to increased effective light path length. Cross-check with irradiation facility on X5 beam at CERN has shown agreement in transmission measurements within sub per cent level.

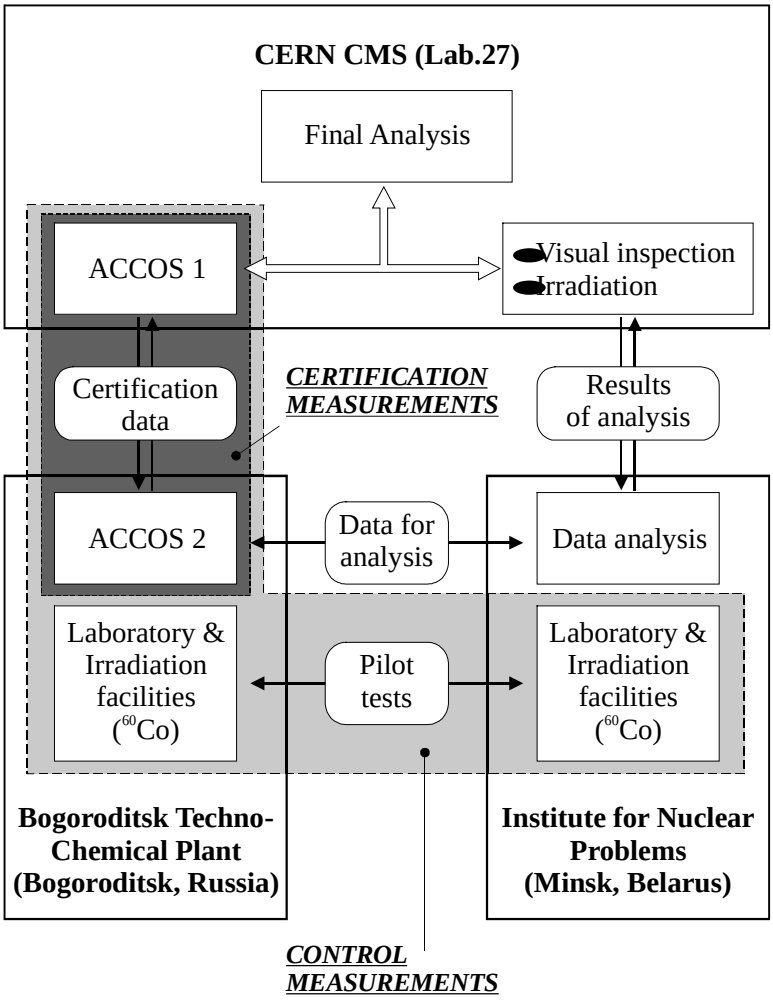

Fig. 1. PWO Crystal Quality Control scheme

Control measurements

To provide the stability of the technology and minimize a number of reclamation a set of control measurements should be carried out in addition to certification:

- Raw material quality check provided by pilot crystal growth and measurements (1 per 100 crystals) – the only acceptable method in terms of time and expenses;
- Technology discipline check:
  analysis of average crystals parameters per lot;
  analysis of average crystals parameters during some period for each growing machine
  analysis of rejected crystals
- Radiation hardness characterization on the sampling basis:
  measurement of radiation induced absorption in top parts of crystals (10 top parts per 100 crystals);
  measurement of radiation induced absorption in full-size crystals in case of previous check gives marginal results;
- Tracking of crystals properties change during detector exploitation:
  light pulse monitoring of crystals transparency inside the detector;
  exchange of damaged or degraded crystals.

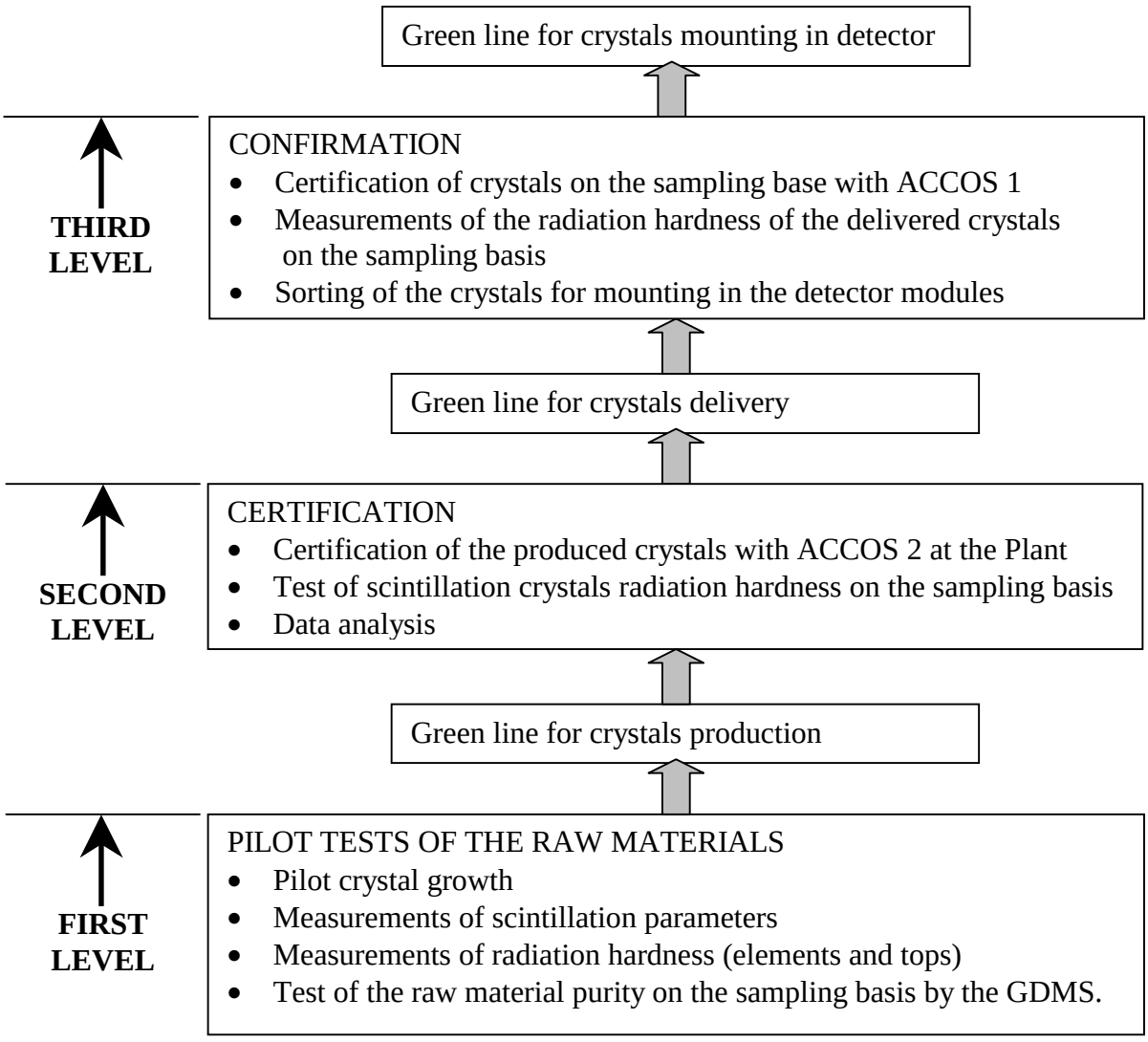

Fig. 2. Decision making hierarchy

Pilot crystals along with top parts of regular crystals are analyzed in details in INP (Minsk) using the same methods and laboratory equipment as were exploited during PWO scintillation crystal technology development. All necessary measurements can be performed within following quality control scheme (Fig.1). This structure assumes both crystal producer and user participation. Certification process is already applied to pre-production stage of PWO crystals by BTCP. All equipment and method used have shown adequate stability and productivity. All rejected crystals were investigated by independent laboratory methods with full confirmation of results. Crystals passed through certification procedure also were checked by laboratory methods on the sampling basis with full agreement. Interaction between all participants of crystal production and certification shown in Fig.1 allows to formalize decision making levels during PWO mass-production (Fig.2). On the first level BTCP and INP provide pilot crystal growth and test with appropriate decision on the acceptance of specific raw material batch for crystal production. On the second level produced crystals go through certification procedure on ACCOS2 system and radiation hardness check at BTCP with data analysis at INP with appropriate decision on crystals delivery to CERN. On the third level Lab 27 at CERN carries out visual inspection, certification on the sampling basis on ACCOS 1, radiation hardness test on X5 beam with appropriate decision on crystal mounting into detector.

Conclusions

Large-scale detectors for new experiments in high-energy physics require radically increased amount of measurements of significantly extended set of parameters with increased precision

To meet the requirements of CMS ECAL in terms of amount, productivity and precision of certification measurements specialized equipment and methods were developed and implemented in Automatic Crystal COntrol System (ACCOS) To provide the stability of mass-production technology parameters the multilevel quality control scheme is developed (including both certification and additional control measurements).

References

1 The Electromagnetic Calorimeter Project, Technical Design Report, CERN/LHCC 97-33.

2 M. Schneegans, Progress of the L3/BGO Calorimeter, Nucl. Instrum. Meth. Phys. Res., vol. A257, pp. 528-537, 1987.

3 E. Auffray et al., Specifications for Lead Tungstate Crystal Preproduction, CMS Note 1998/038.

4 G. Drobychev et al., Studies and proposals for an Automatic Crystal Control System, CMS Note 1997-036.

5 W.W. Moses, A method to increase optical timing spectra measurement rates using a multi-hit TDC, Nucl. Instrum. Methods Phys. Res., vol. A336, pp. 253-61, 1993.

6 A.F. Cherniavskii et al., Statisticeskie metody analiza sluchainyh signalov v iaderno-fizicheskom experimente, Pod. red. A.N. Pisarevskogo, M., Atomizdat, 1974, 352 p. in Russian.

7 J-M. Le Goff et al., C. R. I. S. T. A. L./ Concurrent Repository & Information System for Tracking Assembly and production Lifecycles – A data capture and production management tool for the assembly and construction of the CMS ECAL detector, CMS Note 1996-003.

8 O.V.Missevich, G.Yu.Drobychev, M.V.Korzhik, A.V.Oskine, R.F.Zouevski. Fast Method of PWO Scintillation Light Collection Time Calculation. // Nucl. Instrum. Meth. A – in print

PSearch of Crystals for Detection of Mixed Neutron-Gamma Flux

P.A. Rodnyi[1], V.B. Mikhailik[2], A.S .Voloshinovskii[2],
C.W.E. van Eijk[3], G. F. Zimmerer[4]

[1] St.Petersburg State Technical University, Polytekhnicheskaya 29, 195251 St.Petersburg, Russian Federation
[2] Lviv Franko State University, Kirilo i Mefodii 8, 290005 Lviv, Ukraine
[3] Delft University of Technology, IRI, Mekelweg 15, 2629 JB Delft, The Netherlands
[4] II Institute of Experimental Physics, Hamburg University, Luruper Chaussee 149, 22761 Hamburg, Germany

Abstract: Main requirements to perspective compounds for original method of thermal-neutron pulse-shape discrimination in mixed neutron-gamma fluxes have been determined. Time-resolved emission spectra, luminescence excitation spectra, and decay curves of LiCl-CsCl and $Cs_2LiLaCl_6$:Ce compounds measured under VUV and X-ray excitations are presented. The crystals offer two kinds of emission, which are well separated in spectral and temporal scales. One band peaking at 4.4 eV with a decay constant about 2ns is observed only under excitation by photons with energy above 14 eV, the emission related to core-valence luminescence. Another band belongs to excitonic luminescence (~ 1 μs) in LiCl-CsCl and to d-f transitions of Ce^{3+} (~ 36 ns) in $Cs_2LiLaCl_6$:Ce.

Keywords**:** core-valence luminescence, Ce^{3+} emission, neutron-gamma discrimination, LiCl-CsCl**,** $Cs_2LiLaCl_6$

1. Introduction

Neutrons and gamma-rays coming in mixed flux can be detected by one scintillator detector through decay-time separation of output signals produced by two types of radiation [1]. The scintillation crystal in such detector must contain two kinds of luminescence centres with different decay constants. If one centre is insensitive to heavy ionizing particles and another one is efficiently excited by any ionizing radiation, the output signal of the detector may be separated by electronics. It is well known that core-valence luminescence (CVL) is almost insensitive to the heavy ionizing particles such as neutrons or alpha particles [2]. This type of luminescence, which exhibit very short decay time (~ 1 ns) at gamma-ray excitation, may be applied in detector with neutron-gamma (n-γ) discrimination. CVL is observed only in some fluorides, chlorides and bromides, so a choice of the materials is limited by these three kinds of halides. Besides, only Cs, Rb, Ba and K are active regarding to CVL [3].

Another type of luminescence centres must be sensitive to the heavy particles as well as to other kinds of ionizig radiation and offers a feasible for fast scintillator decay time. One way to do this is to use interconfiguration (d-f) transitions in Ce^{3+} and Pr^{3+} ions, which exhibit decay constants of tens nanoseconds [4]. In addition, the scintillation crystal must contain atoms (e.g., ^{6}Li isotope) with large capture cross-section for neutrons.

A possibility of decay-time discrimination of neutrons and gamma-rays has been first demonstrated in pure [5] and Ce-doped [1,6] $BaLiF_3$ crystals. The investigations have revealed some problems. Ba ions, which are replaced by Ce^{3+} in $BaLiF_3$, have coordination number 12 and it is difficult to obtain a crystal with a large concentration of Ce^{3+} (> 0.1 mol.%). Besides, the CVL band overlaps with absorption spectrum of the Ce^{3+} ions in $BaLiF_3$. Consequently, search of new hosts for detection of mixed n-γ flux is called for.

Position of CVL band shifts to long-wavelength region in the raw: K → Ba → Rb → Cs cations, therefore Cs-based crystals are preferable for the n-γ detectors. The long-wavelength emission (visible or near ultraviolet) is needed to avoid the reabsorption in crystal and to match better the scintillator with photomultiplier tube. Considering above general requirements, we can propose two types of Cs-based compounds for the n-γ detectors:

1. The lithium-caesium halides with intrinsic (excitonic) or/and extrinsic (impurity) luminescence centres.
2. The compounds containing trivalent metal M (M ≡ Y, La, Gd etc.), which can be replaced by Ce^{3+} and Pr^{3+} ions. The chemical formulas of such crystals can be: $LiCsMX_5$, Cs_2LiMX_6, $Li_2Cs_5MX_{10}$, $Li_3Cs_3M_2X_{12}$ (X ≡ F, Cl, Br) etc.

In this work we present results of investigation of two potential candidates for the n-γ discrimination: LiCl-CsCl mixed compounds and the Ce-doped elpasolite-structure crystals $Cs_2LiLaCl_6$. Time-resolved emission spectra, luminescence excitation spectra, and decay curves of the crystals have been measured under X-ray and VUV excitations at 300 and 7 K. In LiCl-CsCl we have observed a fast (2 ns) wide-band emission peaking at 4.4 eV (CVL) and long-lived luminescence band 2.9 eV attributed to radiative decay of self-trapped excitons. The $Cs_2LiLaCl_6:Ce^{3+}$ crystal exhibits two basic emission bands: a 4.4 eV band with a decay constant of 1.4 ns related to CVL, and a 3.3 eV band with a decay constant of about 36 ns, which belongs to interconfiguration (5d → 4f) transitions of Ce^{3+} ions.

2. Experimental

The samples of LiCl-0.27CsCl and LiCl-0.05CsCl were synthesized in quartz tubes from the proper mixtures of LiCl and CsCl single crystals. Pure and Ce-doped $Cs_2LiLaCl_6$ have been prepared from the melts of proper mixtures of single crystalline CsCl, LiCl and $LaCl_3$ compounds using the Bridgeman technique. Taking into account that the initial materials are hygroscopic, the preparation procedures have been performed in dry atmosphere.

The preliminary measurements of the luminescence spectra were performed under pulsed (FWHM ~ 1 ns, repetition frequency 20 kHz) X-ray (40 kV) excitation [7]. A grating MDR-2 monochromator, FEU-100 photomultiplier and a single photon counting technique were used for the emission detection.

The studies of the luminescence characteristics under excitation by VUV-synchrotron radiation were carried out at the SUPERLUMI station of HASYLAB (DESY). The emission was analyzed by means of visible a 0.5 m Czerny-Turner-type monochromator and a XP2020Q photomultiplier. The facility enables low-temperature measurements of the excitation and emission spectra at different stages of the luminescence decay using appropriate delay and time gates.

3. Results and discussion

Fig.1 shows the emission spectra of the LiCl·0.27CsCl compound obtained with different time gates under excitation with 21 eV photons at 300K. The decay profile of the emission is illustrated in inset of the figure, the curve contains two decay constants: 2.0 ± 0.1 ns and about 1 μs. A wide emission band (FWHM about 1.6 eV) peaking at 4.4 eV belongs to fast luminescence (curve 2, fig.1), because the spectrum has been measured at zero delay and 10-ns time gate. A narrow low-energy band with a maximum at 2.9 eV (curve 3, fig. 1) has been detected at 40-ns delay and 50-ns time gate, so, it manifests essentially a slow emission.

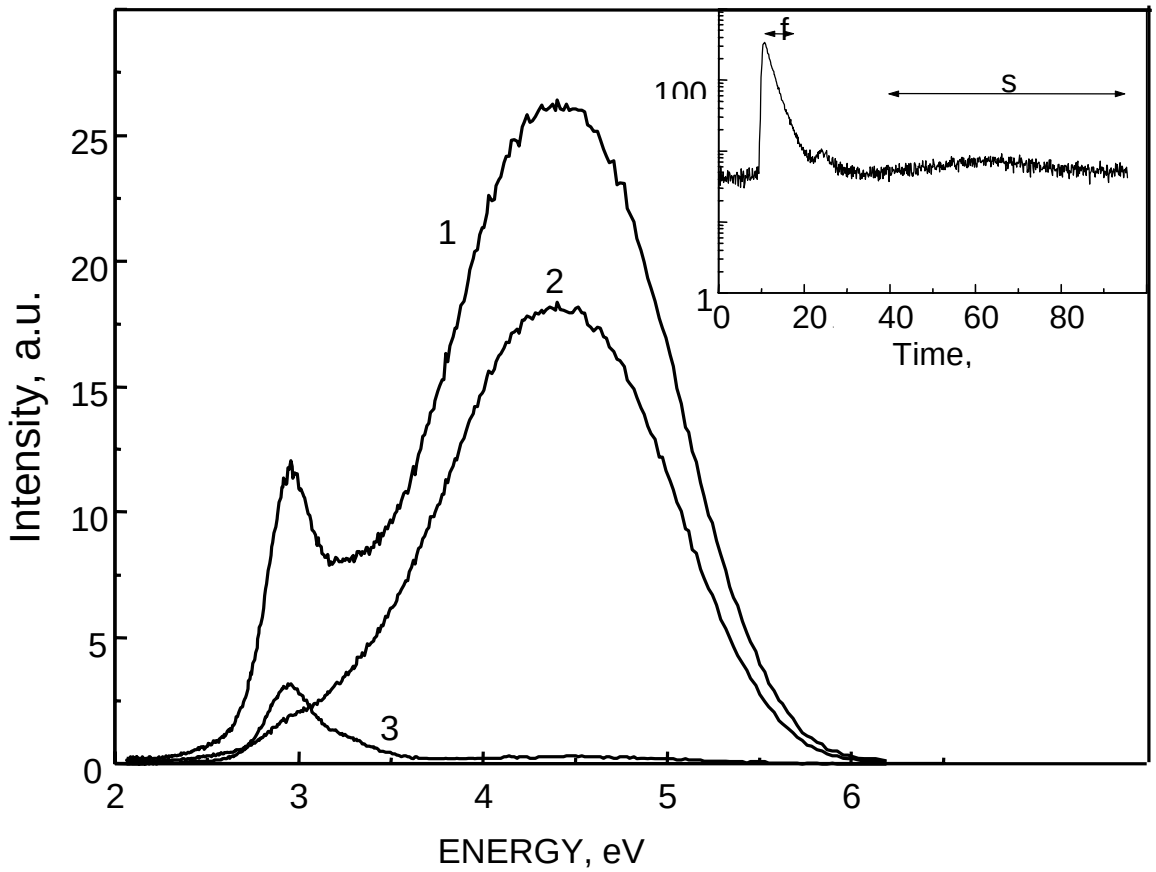

Fig.1. Emission spectra of the LiCl-0.27CsCl compound measured at 300 K under excitation by 16.1-eV quanta: 1- integral spectrum, 2- fast, and 3 – slow components; insert – decay time profile of the 4.4-eV emission band (segments f and s display the time gates used for measuring the fast and slow-emission components, respectively.

The 4.4-eV emission band of the lithium-caesium chloride belongs to CVL that confirms by the following experimental results:

1. The short decay time is typical for CVL.

2. The spectral position of the emission band conforms to that for CVL in CsCl [8,9] and Cs-based alkali halides [10,11].

3. The luminescence excitation spectrum exhibit a characteristic for Cs-based and Cs-doped crystals threshold at 14.1 eV (generation of core 5pCs holes occurs at energy of incident photons in excess of 14 eV).

4. The spectrum shape and intensity of the band remains almost the same at 7 and at 300 K.

Recent results for KCl-CsCl [10] and RbCl-CsCl [11] compounds let us choose an optimal concentration of CsCl in LiCl. The LiCl-0.27CsCl possesses properties of pure CsCl: it has high intensity of CVL and excitonic luminescence. Although, some details of emission and excitation spectra in the mixed crystal differ from that in pure CsCl. For instance, LiCl-CsCl dos not exhibit a 5.1-eV emission band, while CsCl possesses two CVL bands: 4.4 and 5.1 eV [8,12]. A single emission band is typical for six-fold cooordination, the intensity of the 5,1-eV band reflects the quantity of $CsCl_8$ clusters in a face-centred cubic crystal [10,11]. For example, in $Rb_{1-x}Cs_xCl$, the $CsCl_8$ clusters are created at $x > 0.38$ [10].

In line with assumption of work [8], we can consider that the long-living 2.9-eV band of the LiCl-CsCl belongs to the π-emission of self-trapped excitons. Thus, the LiCl-CsCl compound exhibit two emission bands with good spectral and temporal separation. Assuming that the 4.4-eV emission is not excited by neutrons, one can consider the lithium-caesium chloride as a feasible scintillator material for n/γ discrimination. The drawbacks of the compound are: (i) high hygroscopisity, (ii) it is impossible to change the characteristics of the excitonic luminescence. In principle, the characteristics (intensity and decay time) of the slow component can be changed by incorporation an activator in the compound, e. g., thallium.

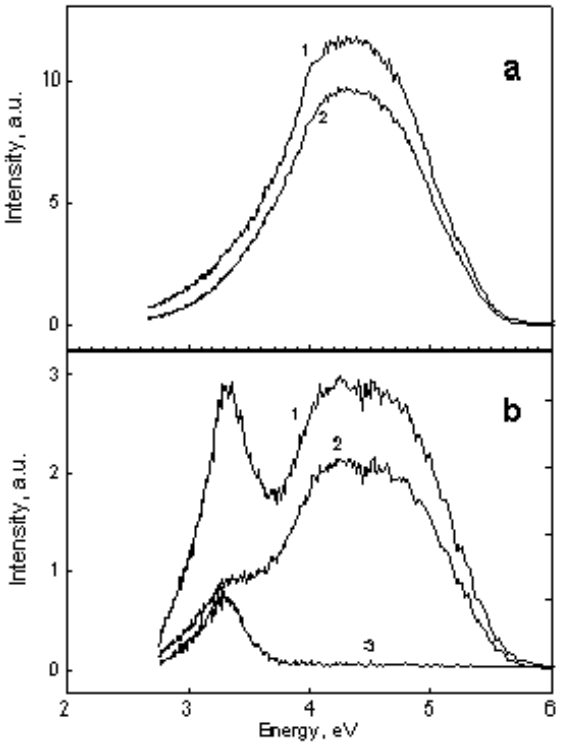

Fig.2. Emission spectra of pure (a) and Ce-doped (b) $Cs_2LiLaCl_6$ excited by 16.1-eV quanta at 300 K: 1 – integral spectra; 2 – fast, and 3 – slow components

The next step was investigation of Ce-doped and pure elpasolite-structure $Cs_2LiLaCl_6$ crystals. The rare-earth site has perfect octahedral coordination in the cubic elpasolites and La^{3+} can be easily replaced by Ce^{3+} ions in $Cs_2LiLaCl_6$ [13]. The preliminary measurements at X-ray excitation allow us to choose an optimum concentration of Ce^{3+} (~ 1 mol.%) in the crystal. Typical emission spectra of pure and Ce-doped $Cs_2LiLaCl_6$:Ce, recorded at 300 K under vacuum ultraviolet (VUV) excitation, are shown in fig. 2. The integral spectrum (curve 1) involving full decay pulse exhibits two emission bands peaking at 4.4 and 3.3 eV of almost equal maximum intensities. The shape of the slow-emission spectrum of $Cs_2LiLaCl_6$:Ce (curve 3, fig.2b) correlates with Ce^{3+} emission in pure $CeCl_3$ [14], it means that this emission is related to the interconfiguration transitions. Comparison of fast-emission spectra of $Cs_2LiLaCl_6$:Ce (curve 2, fig.2b) and pure $Cs_2LiLaCl_6$ (curve 2, fig.2a) crystals shows that the high energy band belongs to intrinsic luminescence.

The 4.4-eV emission of $Cs_2LiLaCl_6$:Ce exhibits an exponential decay with constant $\tau = 1.4$ ns over at least three orders of magnitude, which is characteristic of CV luminescence in Cs-based chlorides. The slow component of the VUV-excited 3.3-eV band with $\tau = 36.4 \pm 0.3$ ns (curve 1, fig.3) indubitably belongs to d-f transitions of Ce^{3+} ions in $Cs_2LiLaCl_6$. This emission displays also a fast component (curve 1, fig.3) which can be related to CV transitions, as observed in the emission spectrum of the pure crystal (curve 2, fig.2a). The d-f transitions of Ce^{3+} cannot give so fast (~ 1.5 ns) luminescence. At direct excitation of Ce^{3+} centres (in range 4 to 7 eV), the fast component is not detected and decay constant is equal to 35.5 ± 0.3 ns (curve 2, fig.3). So, the Ce^{3+} ions in $Cs_2LiLaCl_6$ exhibit almost the same decay constants at UV and VUV excitations.

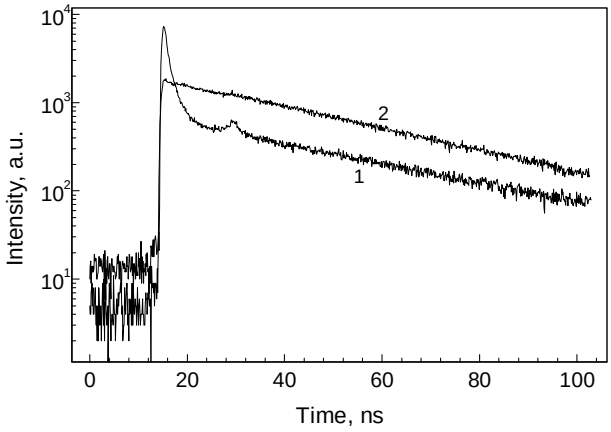

Fig.3 Decay curves of the 3.3-eV emission band in $Cs_2LiLaCl_6$:Ce excited by 19-eV (1) and 4.43-eV photons (2), T = 300 K.

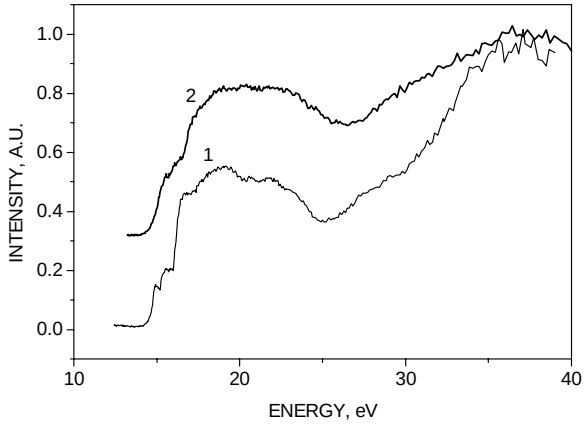

Fig. 4 Excitation spectra of emission near 4.4 eV in $Cs_2LiLaCl_6$:Ce (1) and pure $Cs_2LiLaCl_6$ (2), T = 7 K.

The excitation spectra of the 4.4-eV emission band of the Ce-doped and pure $Cs_2LiLaCl_6$ are presented in fig.4. The spectra are typical for Cs-based chlorides and a threshold at 14 eV uniquely shows that the 4.4-eV band belongs to 5pCs → 3pCl transitions (CVL). The core-exciton related structure in the 14 to 20 eV range, which is usually detected in binary compounds like RbCl:Cs [11], does not show up in $Cs_2LiLaCl_6$ and in similar system $Cs_2NaLaCl_6$ [15]. The two-step threshold of the excitation spectrum near 15 eV (fig. 4) is observed in all elpasolites but this is not explained yet. It is felt that the upper core band of $Cs_2LiLaCl_6$ is formed not only by 5pCs but also by 5pLa states. A difference in the threshold shapes of the excitation spectra for $Cs_2LiLaCl_6$:Ce (curve 1, fig.4) and pure $Cs_2LiLaCl_6$ (curve 2, fig.4) points to an influence CVL on Ce^{3+} emission (in case of simple reabsorption these spectra would be similar).

4. Conclusions

Two features of core-valence luminescence: insensitivity to neutron excitation and ultra-fast decay can be used for separation of the ionzing radiations. The primary results indicate that the both studied compounds exhibit two kinds of emission with well spectral and temporal separation. A slow component in LiCl-CsCl is not too efficient and decay time is very long at room temperature, then, it is necessary to choose an activator in order to improve the scintillation properties of the compound.

The presence of Li ions, efficient CVL and Ce^{3+} luminescence, and the difference between the decay constants (1.4 and 36 ns) of these two emissions allow us to consider $Cs_2LiLaCl_6:Ce^{3+}$ as a promising material for thermal-neutron detection with efficient neutron-gamma discrimination.

References

1. C.M. Combes, P. Dorenbos, R.W. Hollander, and C.W.E. van Eijk, Nucl. Instrum. Methods Phys. Res., **A 416** (1998) 364.
2. S. Kubota , M. Suzuki, J. Ruan (Gen), F. Shiraishi, and Y. Takami, Nucl. Instr. and Meth. **A 242** (1986) 291.

3. P.A. Rodnyi, Sov. Phys. Solid State, **34** (1992) 1053.
4. E.D. Thoma, H. Shields, Y. Zhang, B.C. McCollum, and R.T. Williams, J. Luminesc., **71** (1997) 93.
5. M.J. Knitel, P. Dorenbos, J.T.M. de Haas, and C.W.E. van Eijk, Nucl. Instrum. Methods Phys. Res., **A 374** (1996) 197.
6. C.M. Combes, P. Dorenbos, C.W.E. van Eijk, J.Y. Gesland, and P.A. Rodnyi, J. Luminesc., **72-74** (1997) 753.
7. E.N. Mel'chakov, P.A. Rodnyi, A.V. Rozhkov, and F.Yu. Soldatenkov, 12th International Conference on High-Power Particle Beams, BEAMS'98, Program, Haifa, Israel, 1998, p.242.
8. A. Lushchik, E. Feldbakh, A. Frorip, K. Ibragimov, I. Kuusmann, and Ch. Lushchik, J. Phys. Condens Matter, **6** (1994) 2357.
9. M. Itoh, S. Kubota , J. Ruan (Gen), and S. Hashimoto, Rev. Solid State Science, **4** (1990) 467.
10. A.S. Voloshinovskii, V.B.Mikhailik, M.S. Mikhailik, P.A. Rodnyi, E.N. Mel'chakov, I.H. Munro, C. Muthen, D. Shaw, G. Zimmerer, J. Bekcker, and M. Runne, Solid State Comm., **103** (1997) 689.
11. A.S. Voloshinovskii, M.S. Mikhailik, V.B. Mikhailik, E.N. Mel'chakov, P.A. Rodnyi, C.W.E. van Eijk, and G. Zimmerer, J. Lumines., **79** (1998) 107.
12. A.N. Belsky, I.A. Kamenskikh, V.V. Mikhailin, and A.N. Vasil'ev, J. Electr. Spectr. and Related Phenom., **79** (1996) 111.
13. M. Karbowiak, E. Simoni, J. Drozdzynski, and S. Hubert, Acta Physika Polonica, **A 90** (1996) 367.
14. A.S. Voloshinovskii, P.A. Rodnyi, O.T. Antonyak, N.S. Pidzyrailo, Phys. Solid State, **36** (1994) 339.
15. E.N. Mel'chakov, A.N. Mishin, B. Moine, C. Pedrini, S.V. Petrov, P.A. Rodnyi, and A.V. Sidorenko, "Emission Properties of Chloride Elpasolites", 1999 (this conference).

Charge compensation and lattice relaxation in $LiBaF_3:Ce^{3+}$

M. Marsman, J. Andriessen and C.W.E. van Eijk

Radiation Technology Group, Interfaculty Reactor Institute, Delft University of Technology, Mekelweg 15, 2629 JB Delft, The Netherlands

Abstract: The electronic properties and the structure of a luminescence center in $LiBaF_3:Ce^{3+}$, consisting of a Ce^{3+} substitution at a Ba site *plus* a charge compensating Li^+ substitution at a nearest Ba site, were investigated. Using a planewave pseudopotential molecular dynamics code, we determined the equilibrium structure of this defect complex, both for Ce^{3+} in the $[Xe]4f^1$ ground state configuration, as well as for Ce^{3+} in its $[Xe]5d^1$ excited state configuration. These calculations show an excessive relaxation, induced by a $4f \rightarrow 5d$ excitation of the Ce^{3+} ion. We also performed quantum chemical cluster calculations at the Hartree-Fock level, to determine the energy of the *4f* and *5d* levels of Ce^{3+} in both these equilibrium structures. From these calculations we find the $4f \rightarrow 5d$ absorption lines, and the $5d_Z^2 \rightarrow 4f$ emission line of Ce^{3+} in $LiBaF_3$. From the ΔSCF energy between the $4f \rightarrow 5d_Z^2$ absorption line and the $5d_Z^2 \rightarrow 4f$ emission line we find a Stokes shift of 0.61 eV, compared to 1 eV found experimentally. The origin of this large Stokes shift is identified as a strong coupling of the crystal field splitting of the Ce^{3+} *5d*-manifold with the displacement of four of its F nearest neighbours.

Keywords: $LiBaF_3:Ce^{3+}$, Stokes shift, Lattice relaxation, Hartree-Fock, Ab initio molecular dynamics

Introduction

In our group, Combes *et al.*[1] studied the optical and scintillation properties of $LiBaF_3:Ce^{3+}$, in light of its possible use as a scintillation detector for thermal neutrons. The X-ray induced emission spectra of pure $LiBaF_3$ show a cross luminescence (CL) contribution, with two peaks, at 190 and 225 nm, and a broad band attributed to self-trapped exciton (STE) luminescence, centered around 290 nm. When doped with Ce^{3+}, $LiBaF_3$ shows in addition to the CL and STE emission, Ce^{3+} luminescence between 300 and 400 nm. Optical absorption measurements on $LiBaF_3:Ce^{3+}$, show four bands, at 204, 218, 240 and 250 nm (6.078, 5.688, 5.166 and 4.960 eV), attributed to *4f-5d* transitions of Ce^{3+}.

The above-mentioned experimental results reveal two remarkable aspects of Ce^{3+} in $LiBaF_3$; i) The Ce^{3+} *5d*-manifold is splitted fourfold -essentially a perturbed cubic splitting-, which is noteworthy since $LiBaF_3$ is a cubic system, and ii) $LiBaF_3:Ce^{3+}$ shows a Stokes shift, of around 9000 cm^{-1} ($\approx$1 eV), between the maximum of the Ce^{3+} emission band at 320 nm, and the absorption band at 250 nm, which is unusually large compared to for instance $BaF_2:Ce^{3+}$, where it is around 2000 cm^{-1}.

The explanation of these properties of Ce^{3+} in $LiBaF_3$ constitutes quite a challenge for computational physicists, and has prompted us to study the geometry and electronic structure of the luminescence center in $LiBaF_3:Ce^{3+}$, by means of ab initio methods.

Crystalline $LiBaF_3$ has the inverse perovskite structure (simple cubic), and one formula unit in the unit cell (a_0=3.988 Å)[2]. When Ce^{3+} is incorporated in the $LiBaF_3$ lattice, on a regular lattice site, it must be accompanied by a charge compensating defect. We have considered as possible sites for Ce^{3+} in $LiBaF_3$, the Li site and the Ba site, which leave

respectively excess charges of 2+ and 1+ to be compensated. In pure $LiBaF_3$ both sites have O_h pointgroup symmetry. However the perturbed cubic splitting of the Ce^{3+} *5d*-manifold, observed in experiment, clearly points at a lowering of symmetry at the Ce site, most probably caused by the charge compensating defect. The extent to which the cubic splitting is perturbed, indicates that the charge compensating defect is likely to be located within next-next nearest neighbour distance of the Ce^{3+} ion. In the following we will indicate the complex of a Ce^{3+} ion on a regular lattice site with an associated charge compensation by the term *luminescence center*.

Recently Andriessen *et al.*[3] used the HF-LCAO method with gaussian type orbitals, on a cluster of ions, consisting of the Ce ion surrounded by one or more shells of its nearest neighbours plus the charge compensation defect, to calculate the splitting of the Ce^{3+} *5d*-manifold in a number of possible luminescence center configurations: i) Ce^{3+} on a Ba site plus an O^{2-} ion at a nearest F site, ii) Ce^{3+} on a Ba site plus an interstitial F^- ion in the nearest neighbour region, iii) Ce^{3+} on a Ba site plus a vacancy at a nearest Li site, iv) Ce^{3+} on a Ba site plus a Li^+ at a nearest Ba site, v) a Ba vacancy compensating for two Ce^{3+} substitutions at Ba sites, and vi) Ce^{3+} on a Li site, plus a vacancy at a nearest Ba site.

Qualitative comparison of the calculated splittings, with the position of the Ce^{3+} bands found in the optical absorption measurements, led to the conclusion that the configuration of the luminescence center in $LiBaF_3:Ce^{3+}$, most likely consists of Ce^{3+} at a Ba site, charge compensated by a Li^+ ion at a nearest Ba site.

The previously mentioned study however, did not include the influence of lattice relaxation on the position of the Ce^{3+} energy levels. The motivation to take lattice relaxation into account, is twofold: 1) It is necessary in order to reach quantitative agreement between the energy of the Ce^{3+} *4f→5d* absorption lines predicted by calculations, and the lines found in experiment, and 2) The large Stokes shift of Ce^{3+} in $LiBaF_3$, indicates that a Ce^{3+} *4f→5d* excitation is followed by a strong lattice relaxation.

In this paper we calculate the relaxation of the $LiBaF_3$ lattice, in case it contains a luminescence center consisting of a Ce^{3+} on a Ba site plus a Li^+ at a nearest Ba site. We use the relaxed geometry to redo the calculations of Andriessen *et al.*, and determine the energy differences between the Ce^{3+} *4f* groundstate and the levels of its *5d* configuration. We perform separate calculations on $LiBaF_3$ containing Ce^{3+} in its $[Xe]4f^1$ ground state configuration, and Ce^{3+} in the $[Xe]5d^1$ excited state configuration, to find both the *4f→5d* absorption lines, as well as the *5d→4f* emission line, and to study the origin of the large Stokes shift in $LiBaF_3:Ce^{3+}$.

1. Method

Lattice relaxation. For calculations of the lattice relaxation we used the Vienna Ab-initio Simulation Package (VASP)[4,5]. The VASP program calculates the electronic ground state of a periodic system and the Hellmann-Feynman forces acting on the nuclei in its unit cell, within the framework of the DFT, using a plane-wave basis set to represent the electronic wave functions, and Vanderbilt-type[6] ultrasoft pseudopotentials to describe the electron-ion interaction. The Hellmann-Feynman forces acting on the pseudoatoms in the unit cell are then used to minimize the free energy with respect to the ionic coordinates.

To approximate the case of an isolated luminescence center in an otherwise pure $LiBaF_3$ host lattice, we used the so-called supercell approach. The relaxation studies presented here were all done on a simple cubic supercell made up of 3×3×3 unit cells of $LiBaF_3$, in which one Li ion was substituted by a Ce ion, and one of the Ba ions nearest to the Ce substitution was removed. Optimizing the geometry of a supercell of this size, containing around 135

atoms, is computationally very demanding. Therefore the sampling of the Brillouin zone (BZ) was limited to a single point, the Γ-point, and convergence with respect to supercell size could not be checked by comparison with calculations on supercells larger than 3×3×3 unit cells. And even then a single optimization requires around 50 hrs. CPU-time on 64 nodes of the T3E Cray supercomputer of the HPαC center of the Delft University of Technology.

Energy levels. To determine the electronic structure, and investigate the spectroscopic properties of the luminescence center in $LiBaF_3:Ce^{3+}$, we have performed ab initio quantum chemical calculations, at the Hartree-Fock level, using the Gaussian^{TM} G94 program[7].

To model the luminescence center, we take a cluster of atoms out of the crystal, consisting of the Ce ion, its first, second, and third shell of neighbours (respectively 12 F, 8 Li, and 17 Ba ions), and the substitutional Li ion. This cluster is treated as if it were a molecule, and the Hartree-Fock equations are solved only for this limited part of the crystal. To represent the interaction of the cluster with the rest of the lattice, it is surrounded with point charges, which are fitted to ensure the correct Madelung potential at the cluster sites.

In the G94 code, the Hartree-Fock formalism is formulated in the LCAO form with a fixed gaussian basis set, which can be found in Ref. 8. For Ce^{3+}, we used the scalar relativistic effective core potential (ECP) of Stevens *et al.*[9,10], with a [$Kr4d^{10}$] core, to describe the electron-ion interactions.

On embedding Ce^{3+} in a solid, the *LS* term ^2D will be splitted by the crystal field, and the five-fold degeneracy will be lifted in accordance with the symmetry of the site the ion occupies. To find the crystal field splitting of the Ce^{3+} *5d* configuration, we calculate the HF total energy of each of the *5d* crystal field states in our cluster of choice. The energy of the *4f→5d* absorption or *5d→4f* emission lines of Ce^{3+} in a given cluster, is found as the ΔSCF energy between the *5d* crystal field states and the $^2F_{5/2}$ ground state of Ce^{3+}.

2. Results

Ce^{3+} ground state. Fig. 1A shows a part of the supercell containing the Ce ([Xe]$4f^1$) and Li substitutions, before optimization of the geometry. The resulting geometry after relaxation, Q_{01}, is depicted in Fig. 1B. The Ce ion has moved along the *z* axis, towards the Li substitution, by ≈0.23 Å. Its movement is a result of the electric field in this defect configuration, which is oriented in the +*z* direction.

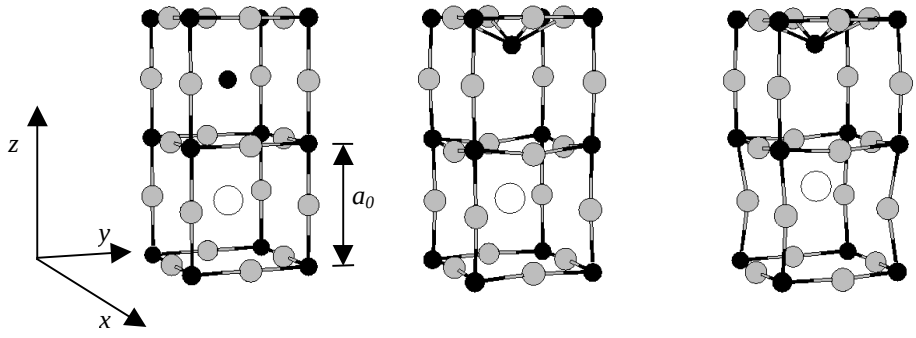

Fig. 1A-C: Part of the $LiBaF_3$ supercell, containing the substitutional Ce and Li ions. $LiBaF_3$ has a simple cubic lattice, with Li ions (black) at the corners, F ions (grey) at the midpoints of the ribs, and a Ba ion (not shown) at the center of the cube. The Ba sites depicted here are occupied by a Ce (white) and a Li ion. Shown above are, (A) part of an unperturbed $LiBaF_3$ lattice with a Ce and a Li ion on two neighbouring Ba sites , (B) Q_{01} the optimized configuration containing Ce^{3+} in its ground state, and (C) Q_{02} the configuration after lattice relaxation induced by the $4f\rightarrow5d_{z^2}$ excitation of Ce^{3+}.

The Li ion has moved upwards along the *z* axis ≈1.1 Å (!), and ends up nested against the four F ions in the plane above it. This is a result of the attractive forces from the F^- ions in the $z=2a_0$ plane and the repulsive electrostatic interaction with the Ce^{3+} ion.

The F ions in the $z=0$ and $z=a_0/2$ planes have moved ≈0.13 Å inwards, in the direction of the Ce ion. This results both from the attractive electrostatic force between the negative charge of the F ions and the positive effective charge of the Ce^{3+} substitution at a Ba^{2+} site, as well as from the smaller size of the Ce^{3+} compared to Ba^{2+}.

The four F ions in the $z=a_0$ plane, between the substitutional Li ion and the Ce ion, have moved away from the charge compensating defect towards the Ce ion by ≈0.22 Å, most likely as a result of the electric field, mentioned earlier.

Movement away from the Li substitution is also shown by the other F ions which surround it, in the $z=3a_0/2$ and $z=2a_0$ planes. These displacements are a result of the repulsive electrostatic forces between the negatively charged F ions and the negative effective charge of the Li^+ substitution at a Ba^{2+} site.

From the supercell geometry Q_{01}, we take a cluster of atoms and calculate the Ce^{3+} *4f→5d* absorption lines, as outlined in Sec. II. The results of these calcultations are listed in Table I.

Calc. [eV]	Exp. [eV]
Ce^{3+} 4f→5d	
4.886	4.960
5.241	5.166
5.492	5.688
5.878	6.078
Ce^{3+} $5d_Z^2$→4f	
4.279	3.875

Table I: The Ce^{3+} 4f→5d absorption lines, and $5d_Z^2$→4f emission line in $LiBaF_3$, as found from molecular cluster calculations with G94, and from experiment.

Ce^{3+} excited state. The lattice relaxation following the Ce^{3+} *4f→5d* excitation, starts from the geometry Q_{01} (see Fig. 1B). The resulting geometry after relaxation, Q_{02}, is shown in Fig. 1C. This relaxation is dominated by the movement of the Ce substitution ($[Xe]5d^1$) and its nearest neighbouring F ions in the $z≈a_0/2$ plane. The Ce ion moves along the *z* axis, towards the substitutional Li ion, by ≈0.38 Å. (Note that the Ce ion now ends up at a distance of more than 0.6 Å from the regular Ba lattice site on which it was substituted!) The F ions in the $z≈a_0/2$ plane move inwards ≈0.25 Å, along ⟨110 directions to within 2.67 Å of the Ce ion, while the F ions in the $z≈a_0$ plane move outwards ≈0.15 Å, in the direction of their nominal

positions in unperturbed $LiBaF_3$. The extend of this $Q_{01} \rightarrow Q_{02}$ relaxation is quite remarkable if we take into consideration that the Ce^{3+} $4f \rightarrow 5d$ excitation hardly affects the completely filled Ce *5p*-shell, which is responsible for the bulk of the repulsive forces between Ce and its neighbours.

From the supercell geometry Q_{02}, we again take the cluster of atoms described in Sec. II, and calculate the energy differences between the $^2F_{5/2}$ groundstate of Ce^{3+}, and the levels of its crystal field splitted *5d*-manifold. The lowest Ce^{3+} *5d* crystal field state is found to be dominantly made up of the $5d_Z^2$ orbital. The Ce^{3+} $5d \rightarrow 4f$ emission line is found as the energy difference between this crystal field state and the Ce^{3+} groundstate (see Table I).

3. Discussion and conclusions

As can be seen from Table I, the calculated Ce^{3+} $4f \rightarrow 5d$ absorption lines show good agreement with experiment. The energy of the $5d_Z^2 \rightarrow 4f$ emission line however, comes out ≈0.4 eV too large. The energy difference of 0.61 eV, between the first absorption line and the emission line, i.e. the Stokes shift we find from calculations, therefore shows the same discrepancy with experiment.

In geometry Q_{01} (Fig. 1B) the Ce substitution ($[Xe]4f^1$) has more or less the same twelve-coordination of F^- ions, it would have in the unrelaxed inverse perovskite structure of Fig. 1A. This geometry gives rise to a relatively small crystal field at the Ce site, and consequently to a modest splitting of the *5d*-manifold. However in this structure the derivative of the crystal field at the Ce site, with respect to the displacements shown in the relaxation from $Q_{01} \rightarrow Q_{02}$ by the F nearest neighbours in the $z \approx a_0/2$ plane, is quite large. Any $4f \rightarrow 5d$ excitation of Ce^{3+} will rapidly undergo a nonradiative transition to the lowest Ce^{3+} crystal field state ($5d_Z^2$). The before mentioned displacements ($Q_{01} \rightarrow Q_{02}$), which cause an increase of the crystal field at the Ce site, almost double the overall crystal field splitting of the Ce^{3+} *5d*-manifold, from 1.07 eV in geometry Q_{01} to 1.70 eV in Q_{02}. The ΔSCF between the $^2F_{5/2}$ ground state and the *5d*-centroid position decreases minimally, by 0.04 eV. The ΔSCF between the $5d_Z^2$ crystal field state and the *5d*-centroid however, increases by 0.57 eV. (This increase accounts for 93% of the Stokes shift we find in our calculations.) These observations show that when the $5d_Z^2$ state is occupied, the increase in crystal field splitting of the *5d*-manifold results directly in a lowering of the total energy of the system, thus providing the driving force behind the $Q_{01} \rightarrow Q_{02}$ relaxation.

The discrepancy of 0.4 eV, between the calculated energy of $5d_Z^2 \rightarrow 4f$ emission line and the experimentally observed Ce^{3+} emission, can be attributed to several flaws in our calculational approach;

1) Our HF-LCAO cluster calculations –and those of Ref. [3] as well- do not allow the ions to polarize. (We did not include polarization functions in the basisset used in the cluster calculations. Therefore the polarizability of the atoms is much too small.) The change in polarization of the ions in the cluster, as a result of the $Q_{01} \rightarrow Q_{02}$ relaxation, is likely to be quite substantial, and could conceivably lower the energy of the predicted emission line.

2) The supercell calculation of the lattice relaxation induced by the $4f \rightarrow 5d$ excitation, can not optimize the structure beyond the next-nearest neighbours of the Ce ion. This limit is imposed by the size of the $LiBaF_3$ supercell (3×3×3 unit cells). Calculations on for instance a 4×4×4 supercell would include the relaxation of the third and fourth shell of atoms around the Ce ion, and this could very well affect the immediate surroundings of the Ce ion, and consequently the cluster calculation on the $5d_Z^2 \rightarrow 4f$ emission line. Unfortunately calculations on a larger supercell exceed our computer resources.

3) The spatially extended defect structure we are considering introduces a large dipole moment within the supercell. The field of this dipole can not correctly establish itself if the size of the supercell is insufficient to contain it completely. This results from the application of the periodic boundary conditions, which does not allow for a gradual change of the eletrostatic potential over a distance greater than the size of the supercell. This error can be reduced by increasing the size of the supercell.

4) The sampling of the BZ in our supercell calculations was limited to the Γ-point only, which introduces an unknown error in the results. Applying a more extensive sampling of the BZ however, would be computationally to demanding.

Despite the apparent failure to fully reproduce the Stokes shift of $LiBaF_3:Ce^{3+}$ in our calculations, we consider our method of combining supercell calculations to determine the lattice relaxation, with cluster calculations to find the Ce^{3+} energy levels, to be a great success. All previous efforts in this direction, underestimated the Stokes shift by at least a factor of five. In addition to this we feel confident that we have identified the origin of the large Stokes shift of Ce^{3+} in $LiBaF_3$.

References

1. C.M. Combes, P. Dorenbos, C.W.E van Eijk, *et al.*, J. Lum. **72-74**, 753 (1997).
2. C.E. Messer, J. Sol. Stat. Chem. **2**, 144 (1970).
3. J. Andriessen, H. Merenga, *et al.*, Proc. Int. Conf. on Inorganic Scintillators and Their Applications, SCINT95, 1996, Delft University Press, The Netherlands.
4. G. Kresse and J. Furthmüller, Comput. Mater. Sci. **6**, 15 (1996).
5. G. Kresse and J. Furthmüller, Phys. Rev. B **54**, 11169 (1996).
6. D. Vanderbilt, Phys. Rev. B **41**, 7892 (1990).
7. M.J. Frisch, *et al.*, *Gaussian 94 (Revision C.3)*, Gaussian, Inc.: Pittsburgh, PA, (1995).
8. J. Andriessen, P. Dorenbos and C.W.E. van Eijk, Mat. Res. Soc. Symp. Proc. **348**, 355 (1994).
9. W.J. Stevens, H. Basch and M. Kraus, J. Chem. Phys. **81**, 6026 (1984).
10. T.R. Cundari and W.J. Stevens, J. Chem. Phys. **98**, 5555 (1993).

The role of oxygen in energy transfer processes in $LiBaF_3$ scintillators

N. Shiran, A. Gektin, N. Ivanov, V. Komar, Yu. Nesterenko, V. Voronova

Institute for Single Crystals, 60 Lenin Ave., 310001, Kharkov, Ukraine

Abstract: It is shown that both radiative and nonradiative energy losses in $LiBaF_3$ based scintillators as well as radiation damage are defined by the presence of oxygen and magnesium ions. The Mg^{2+} doping converts $LiBaF_3$ crystals into storage phosphor perspective for thermoluminescent dosimetry.

Keywords: $LiBaF_3$, scintillator, energy losses, colour centres, thermoluminescent dosimeter, oxygen, magnesium.

1. Introduction

$LiBaF_3$ crystals are the perspective material for scintillation [1-6]. This material is crystallized into inverse perovskite structure (density 5.27 g/cm^3, Z ~ 56). The core-valence (CV) luminescence appear in this matrix due to a radiative recombination of the electron from the F^- 2p-valence band with a hole in the Ba^{2+} 2p-core band. This fast component (0.8 ns) emits at 195, 225 nm. Besides, there is a wide emission band at 300 nm with microsecond decay time related to self-trapped exciton (STE) [1-4].

At γ-excitation the light yields of CV and STE emissions are less than 1200 and ~ 1600 ph/MeV, accordingly. The absence of CV luminescence at alpha particle or thermal neutron capture is the most remarkable scintillation property of $LiBaF_3$, allowing to discriminate thermal neutron and γ-quanta [3].

It was shown that Ce^{3+} emission in $LiBaF_3$(Ce) is manifested at 325 nm with a decay time ~ 30 ns [4]. Upon γ-excitation the light yield of different origin crystals $LiBaF_3$(Ce) varies from 1300 to 2200 ph/MeV [3, 5, 6].

Our preliminary investigation showed that the luminescence characteristics of $LiBaF_3$ based scintillators depend on the oxygen impurity [4]. X- or γ-irradiation leads to colouration of $LiBaF_3$ crystals. The reasons of colouration and poor radiation resistance of pure and Ce doped $LiBaF_3$ were studied by several authors [7-9]. It may be suggested that radiation damage of $LiBaF_3$ samples of different origin depends on some unknown impurities. One of them most likely is oxygen. Since obtaining the oxygen free fluoride compound is an extremely complicated task, traces of this impurity are always available in fluoroperovskites. It can be also magnesium because it usually occurs in lithium compounds due to their isomorphism. Moreover, Mg^{2+} is generally recognized as an ion responsible for the creation of new traps and for thermal stabilization of the intrinsic colour centres [10].

Thus, main purpose of this work was to investigate the role of oxygen and magnesium in the energy transfer processes and radiation damage of $LiBaF_3$ based scintillators.

2. Experimental

Pure and doped $LiBaF_3$ crystals were grown by the Bridgman method in graphite crucibles in reactive atmosphere from the specially synthesized and purified raw material of stoichiometric composition. Five types of single crystals were investigated: pure, doped with CeF_3, Li_2O, MgF_2 and co-doped with MgF_2 and Li_2O. Oxygen containing anions were determined by IR and UV absorption spectroscopy. The techniques for the registration of optical absorption, excitation, photo- and radioluminescence and thermostimulated luminescence were described in [9].

3. Results

3.1. Luminescence and excitation spectra

Emission and excitation spectra of pure and Ce doped $LiBaF_3$ crystals at synchrotron pulse (τ=0.8 ns) irradiation are shown in Fig. 1. One can see that the Ce luminescence at 325 nm is excited not only in Ce absorption bands (196, 214, 237, 247 nm) but also in the range of e-p (115 nm) and STE (132 nm) transitions as well as in the band at 74 nm close to the CV excitation. It is noteworthy that at the e-p excitation along with the main Ce^{3+} emission an insignificant contribution of 400 nm emission is observed. We consider that this slow luminescence is connected with the presence oxygen containing impurities. Traces of oxygen anions were found in even nominally pure crystals.

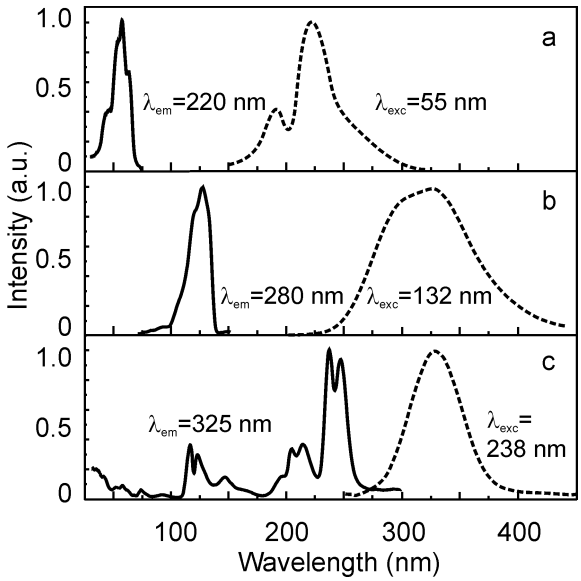

Fig. 1. Excitation (solid lines) and emission (dashed lines) spectra of pure (a, b) and Ce doped (c) $LiBaF_3$ crystals measured at synchrotron pulse (0.8 ns) irradiation.
Time gates: 2 ns (a), 500 ns (b), 50 ns (c) [9].

Pure and MgF_2 doped crystals do not absorb in the region of 200 - 300 nm and show no luminescence at photoexcitation in this range. In absorption spectra of Li_2O doped crystals some additional bands with the maxima at 208 - 280 nm were observed. They overlap the region of CV and STE luminescence. Excitation in the maxima of the oxygen induced absorption bands results in appearance of emission in the blue region of spectrum (Fig. 2). The intensity of oxygen luminescence (λ_{ex}=255 nm, λ_{em}=420 nm) is low in Li_2O doped samples and is higher in Li_2O and MgF_2 co-doped crystals (λ_{ex}=230 nm, λ_{em}=380 nm). These oxygen induced excitation bands are overlapped with CV and STE luminescence bands.

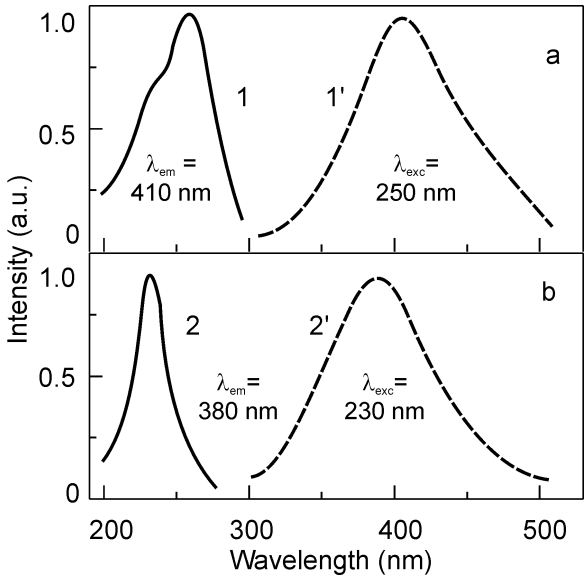

Fig. 2. Excitation (1, 2) and photoluminescence (1′, 2′) spectra of doped with Li_2O (a) and co-doped with Li_2O and MgF_2 (b) $LiBaF_3$ crystals.

At a pulse X-ray excitation (Fig. 3) the spectra of CV, STE and Ce^{3+} luminescence are noticeably overlapped but can be separated by varying the time gate. Decay times of CV, STE and Ce^{3+} emission are 0.8 ns, 0.6 μs and 50 ns, respectively.

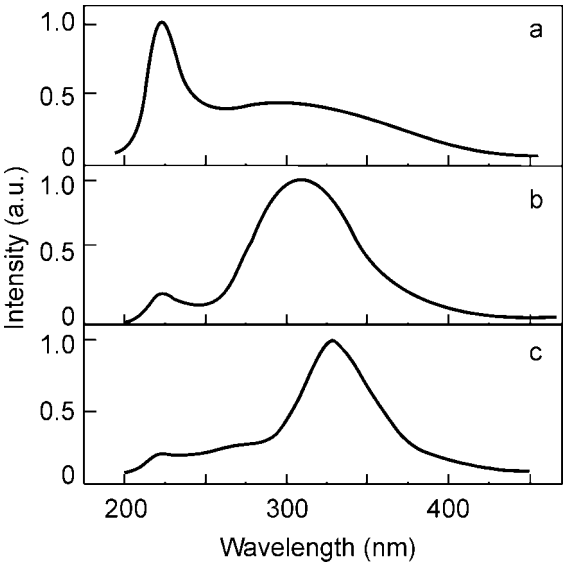

Fig. 3. Luminescence of pure (a, b) and Ce doped (c) $LiBaF_3$ crystals at X-ray pulse (2 ns) excitation. Time gates: 2 ns (a), 1 μs (b), 50 ns (c).

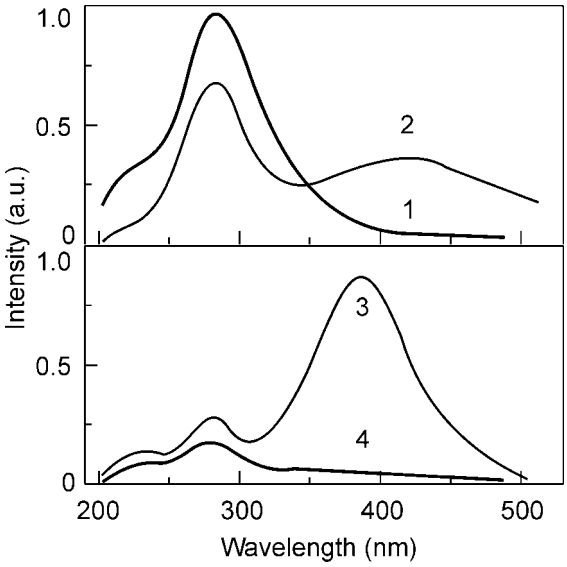

Fig. 4. Gamma-luminescence spectra of $LiBaF_3$ crystals: pure (1); doped with Li_2O (2); Li_2O and MgF_2 (3); MgF_2 (4).

As it is seen in Fig. 4 doping with oxygen gives not only insignificant rise of radioluminescence intensity in the long wavelength tail of STE emission, but also suppresses the latter as compared to that of pure crystal. In Mg^{2+} and O^{2-} co-doped crystals the STE luminescence is noticeably quenched and an additional band at 380 nm appears. The decay time of blue emission connected with O^{2-} ions is about 300 μs.

3.2. Radiation damage

Gamma-induced optical absorption spectra of pure and oxygen doped crystals are similar except the additional band at 330 nm in $LiBaF_3$(O) (Fig. 5, curves 1, 2). Transparency recovery in Li_2O doped crystals occurs at their heating to 300°C instead of 200°C as it is for pure one. Note, that oxygen induced colour centres absorb straight in the maximum of Ce^{3+} luminescence.

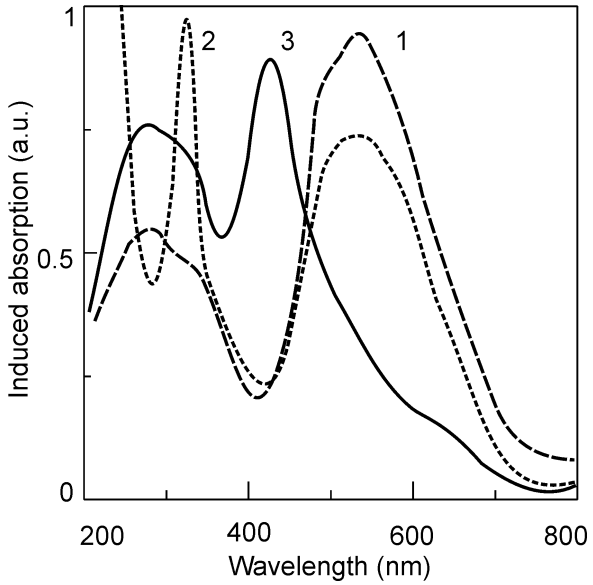

Fig.5. Gamma-induced absorption spectra of pure (1) and doped with Li_2O (2), and MgF_2 (3) $LiBaF_3$ crystals. ^{60}Co, 10^4 rad, 20°C.

If the concentration of Mg^{2+} ions exceeds 10^{-3} %, the crystals become green-yellow under ionized irradiation (Fig. 5, curve 3). The Mg^{2+} ions are responsible for a wide absorption band with the maximum at 420 nm and suppression of longer wavelength bands. Thermal annealing of $LiBaF_3$(Mg) colour centres occurs only at 450°C.

Heating of the irradiated crystals leads to the appearance of thermostimulated luminescence (TSL). The shapes and intensities of glow curves depend on the crystal purity and kind of the dopant (Fig. 6).

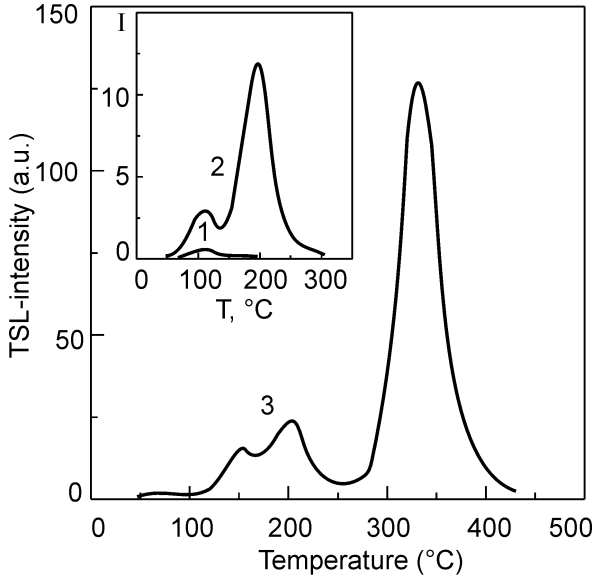

Fig. 6. Glow curves of γ-irradiated $LiBaF_3$ crystals: pure (1), Li_2O doped (2), MgF_2 doped (3). ^{60}Co, 100 rad, 20°C, heating rate 0.2°C s^{-1}.

In the case of pure samples the stored energy is released in TSL peaks at 110°C and 170°C (curve 1). In Li_2O doped crystal the main peak is at 200°C (curve 2). In $LiBaF_3$(Mg,O) the TSL intensity is higher and the peaks are at 200°C and 350°C. In Mg^{2+} doped crystals with an extremely low oxygen concentration all the lightsum is released in the high intensity peak at 350°C (curve 3). In this case the recombination emission is revealed in the region of 550 - 610 nm instead of ~ 400 nm as it is in oxygen containing crystals.

4. Discussion

First of all it is necessary to note that oxygen impurity in $LiBaF_3$ crystals promotes origination of both emission centres and charge carrier traps. It can be assumed that oxygen luminescence centres are $O^{2-}v_a^+$ type dipoles. The excess positive charge compensation in Ce^{3+} and Mg^{2+} doped crystals can be realized either by the oxygen ion or by the cation vacancy (Ce^{3+} - in the lattice site of Ba^{2+}, Mg^{2+}- in that of Li^+). Formation of the dipoles: $Ce_{Ba}^{3+}v_{Li}^-$ and $Ce_{Ba}^{3+}O^{2-}$ is possible in $LiBaF_3$(Ce) crystals containing the oxygen traces. In $LiBaF_3$(Mg,O) the dipoles $Mg_{Li}^{2+}v_{Li}^-$ and $Mg_{Li}^{2+}O^{2-}$ can be formed. The theoretical calculations show that compensation of the charge of the cation impurity by substitution of Ba^{2+} by Li^+ in $LiBaF_3$ matrix is favourable [11]. Which kinds of dipoles are the most probable is not clear so far. But it is clear that the oxygen containing dipoles can play the role of the luminescence centres. With this, the spectral characteristics depend on the structure of the dipole. In crystals doped with Li_2O oxygen excitation and luminescence spectra are shifted a bit as compared with those in crystals containing oxygen and magnesium together. However in both cases the decay times are very long (τ ~ 300 μs).

Overlapping of the oxygen centres absorption with CV and STE luminescence bands and with of Ce^{3+} luminescence excitation region points to the fact that the presence of O^{2-} causes losses in the energy transfer and increase afterglow level. Afterglow is connected with long decay times of $O^{2-}v_a^+$ centre emission. Perhaps, it is just these losses explain a significant variance of literature data on the value of scintillation yield and decay times in $LiBaF_3$ and $LiBaF_3$(Ce) crystals of different origin [3, 5, 6].

The study of the radiation induced absorption, bleaching and TSL showed that oxygen and magnesium ions are responsible for the formation of new traps. Oxygen stimulates the colour centre creation (absorption at 330 nm, stability ~ 200°C). Note that this band is superimposed on that of Ce^{3+} -ion emission. Naturally, such type colour centres have to decrease the scintillation output of $LiBaF_3$(Ce) crystals as a result of reabsorption of fast Ce^{3+} luminescence.

Mg^{2+}-ions presence in $LiBaF_3$ leads to appearance of more deep traps. CV and STE luminescence turn to be practically quenched. In irradiated crystals an additional absorption band at 420 nm appears. It is just its presence that defines the "green-yellow" colouration of samples, the latter being related to F-centres in [8]. These colour centres are stable up to 300°C. A TSL curve with a narrow intensive peak at 350°C demonstrates radiative recombination of captured carriers (Fig. 6).

Thus, two facts can be emphasized. Primarily, the presence of O^{2-} and Mg^{2+} ions leads not only to radiative but nonradiative as well losses at energy transfer in scintillators. Consequently, for the achievement of maximum scintillation efficiency of $LiBaF_3$ the concentration of these ions should be lowered to minimum. On the other hand introduction of Mg^{2+} ions turns $LiBaF_3$ from a fast scintillation material to an energy storage phosphor and even to thermoluminescent dosimetric material.

5. Conclusion

It is shown that both radiative and nonradiative energy losses as well as radiation damage in $LiBaF_3$ based scintillators are defined by the presence of oxygen and magnesium ions.

At doping with magnesium $LiBaF_3$ crystal losses the fast scintillator properties and turns to a storage phosphor, perspective for thermoluminescent dosimetry.

References

1. E. Melchakov, M. Petrova, J. Podkolzina et al., Opt. and Spect. **69** (1990) 807
2. J. Janson, Z. Rachko, J. Valbis et al., J. Phys. Cond. Mat. **5** (1993) 1589
3. M. Knitel, P. Dorenbos, I. de Haas, C. van Eijk, Rad.Meas. **24** (1995) 361
4. A. Gektin, N. Shiran, V. Voronova et al., Proc. Int. Conf., SCINT'97, Schangai, China, 121
5. C. Combes, P. Dorenbos, C. van Eijk et al., ibid., 322
6. C. Combes, P. Dorenbos, R. Hollander et al., Nucl. Inst. Meth. **A 416** (1998) 364
7. I. Tale, P. Kulis, U. Rogulis et al., J. Lumin. **72-74** (1997) 722
8. I. Tale, M. Springis, P. Kulis et al., Radiat. Meas. **29** (1998) 279
9. A. Gektin, N. Shiran, A.Voloschinovski et al., Rad. Meas. **29** (1998) 295
10. S. Mc. Keever, J. Phys. D: Appl. Phys. **24** (1991) 988
11. R. Jackson, M.Valerio, J. de Lima, J. Phys. Cond. Mat. **8** (1996) 10931

Mechanism of the Recombination Luminescence of $LiBaF_3$ crystals

I.Tale[1] , V.Tale[1] , P.Kulis[1] , M.Springis[1] , U.Rogulis[1], J.Jansons[1] A.Veispals[1], H.-J.Fitting[2]

[1]*Institute of Solid State Physics, University of Latvia, Kengaraga str.8,1063 Riga, Latvia*
[2]*Physics Department, University of Rostock, Universitätsplatz 3, D-18051 Rostock, Germany*

Abstract: The radiation energy storage and read-out processes are discussed, resulting from investigation of the EPR, luminescence afterglow and thermostimulated luminescence (TSL) in undoped $LiBaF_3$ crystals. X- irradiation below 170 K results in creation of a long-time-temperature-independent afterglow due to the tunneling recombination between close electron and hole centres. The F-type electron centres and the V_K as well as probably O^{2-} centres are the tunneling recombination partners, responsible for the 4.1 eV and 3.15 eV luminescence bands respectively. It is shown that observed diffusion-controlled tunneling recombination kinetics is caused by thermoactivated migration of the V_K centres via reorientation hops of the molecular bound resulting in the tunneling recombination with close F-type centres. The formation of the self-trapped exciton in the course of electron resonance transfer from F-type centres to V_K centres is discussed.

Keywords: $LiBaF_3$; Color Centres, Hole-Self-Trapping; Diffusion-Controlled-Tunneling Luminescence

Introduction

$LiBaF_3$ represents a group of materials, prospective as scintillators and as radiation memory materials for dosemetric purpose. Well-known cross luminescence bands in ultraviolet have been found in the $LiBaF_3$ crystals by the X-ray and electron beam irradiation [1-3]. In the undoped crystals we have recently observed several additional luminecsence bands of unknown origin. The broad luminescence band between 250 and 400 nm is proposed to be due to the self-trapped excitons [4]. It can be expected, that intrinsic defects can cause other radiative electron transitions. The F–type color centres are the main radiation defects created by X- irradiation at room temperatures [4,5]. Recently the EPR of V_k – centre in undoped crystals has been reported after X –irradiation at liquid nitrogen temperature [6].

In the present paper the origin of the recombination luminescence due to the intrinsic color centres is investigated. Radiation energy storage and read-out processes are discussed, resulting from the investigation of the luminescence afterglow and thermostimulated luminescence (TSL) spectra in crystals, X-irradiated at temperatures from LNT up to RT.

Experimental

$LiBaF_3$ samples under investigation were crystals grown using monocrystalline LiF and BaF_2 as a raw material. X-ray structure analysis showed that $LiBaF_3$ samples tend to grow in a mosaic-type polycrystalline blocks. For EPR meaurements monocrystalline $LiBaF_3$ blocks was split off from the as grown crystall. The samples was X- irradiated using W-anticathode X-ray tupe operated at 45 kV, 10 mA. The thermostimulated luminescence was recoreded at heating rate 0.1 K/s. EPR measuremens was performed by RE-1306 spectrometer.

Results

The electron paramagnetic resonance (EPR) spectrum of the x-irradiated $LiBaF_3$ crystals shows spectral patterns corresponding to axial centres oriented along the [110] axis (Figure 1). Splitting in the spectrum can be explained by a hyperfine (*hf*) interaction of the unpaired spin S = 1/2 with two fluorine nuclei (I = 1/2 with a natural abundance 100%). The F^{19} *hf* interaction parameters from the EPR angular dependencies (A_{II} = 2550 MHz, $A_{\perp}$ = 300 MHz) are in good agreement with the parameters for V_K (fluorine F_2^-) centres found in other perowskite crystals [7-9]. Figure 2 shows the orientation of the V_K centre in $LiBaF_3$ lattice. No EPR signal of V_K centres was observed after x-irradiation at room temperature, therefore such centres are not stable in $LiBaF_3$ at room temperature.

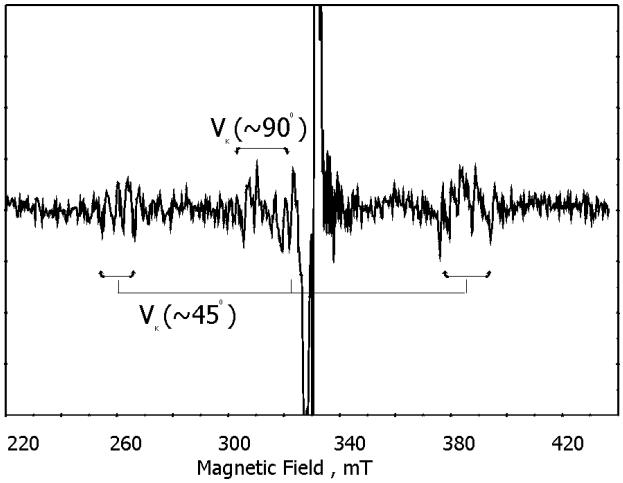

Figure 1. The EPR spectrum at 80 K of the $LiBaF_3$ crystal after x-irradiation at 80 K. Microwave frequency 9.18 GHz. The orientation of the crystal is approximately 5° deviated from the B ‖ [100]. ~45° and ~90° oriented V_K centres are shown, the lines are split due to the crystal disorientation. Central strong lines belong to unidentified radiation defects.

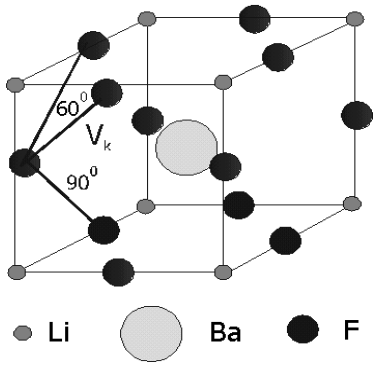

Figure 2. The V_k centre in $LiBaF_3$. Eventual reorientation hops of the molecular bound are shown.

The thermostimulated motion of the V_K centres shall manifest the recombination luminescence in $LiBaF_3$. We investigated thermostimulated luminescence (TSL) of various undoped $LiBaF_3$ crystals X-irradiated at 80 K. In the temperature region below RT the TSL curve in the samples containing F-type centres is represented by 4 peaks at about 125 K, 140 K, 185 K and 210 K (Figure 3).

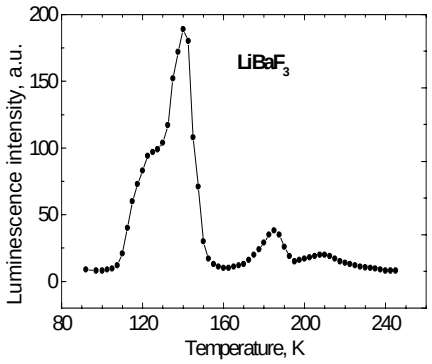

Figure 3. TSL of $LiBaF_3$ crystal X-irradiated at 80 K.
Heating rate 0.1 K/s.

X-irradiation in the temperature region of 125 K and 140 K TSL peaks results in creation of the long-term temperature-independent afterglow, i.e. the tunnelling luminescence (TL) appears [10]. The TL was observed at 80 K after cooling of the X- irradiated sample down to 80 K (cooling rate 2 – 3 K/s). The TSL curve below 100 K shows decay of the glow intensity even in the course of heating of sample indicating that at LNT the TL prevails even directly after stop of excitation (Figure 3). Because TL arises due to the radiative charge-transfer-recombination between the electron and hole centres being randomly distributed in pair separation, the characteristic hyperbolic afterglow kinetics of TL was observed at 80 K in $LiBaF_3$ samples after X- irradiation at various temperatures below 200 K.

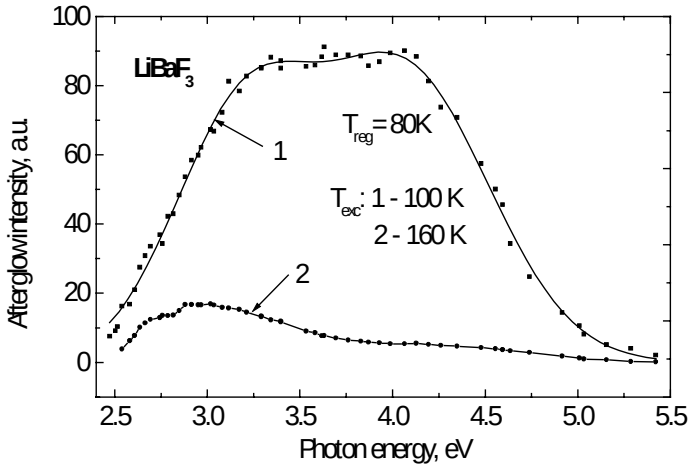

Figure 4. TL luminescence spectra of $LiBaF_3$ crystal recorded at 80 K after cooling down from various X-irradiation temperatures: 1: 80 K; 2: 160 K

The TL spectrum sufficiently depends on the X- irradiation temperature (Figure 4). In the whole temperature interval the composite band represents the TL indicating that several radiative transitions are involved in the TL. In Figure 4 two typical TL spectra obtained after X- irradiation at 100 K and 160 K are presented. Increase of the X- irradiation temperature results both in the decrease of the TL intensity as well as the change of shape of the TL spectra.

Similar continuous diminish of the TL intensity occurs by the heating of the preliminary X-irradiated at 80 K sample to various temperatures followed by cooling down to LNT too. The TL completely vanishes above the 170 K. It corresponds to the complete emptying of traps responsible for 140 K TSL peak (Figure 3).

Figures 5 and 6 represent the results of decomposition of complex TL spectra obtained using curve fit by Gaussians. The best fit of the TL spectrum created at 100 K was achieved assuming presence of two elementary TL bands.

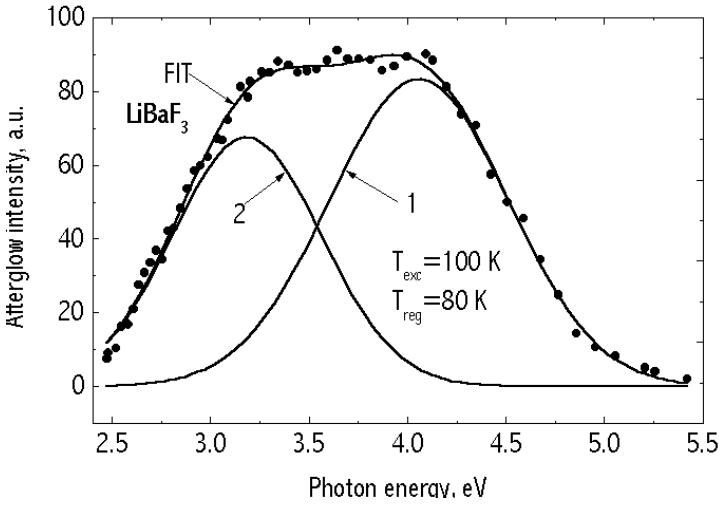

Figure 5. Curve fit by Gaussians of the TL spectrum observed at 80 K after cooling down from the excitation temperature at 100.

1: TL band at hν =4.05+-0.04 eV, FWHM=0.91+-0.04 eV.

2: TL band at hν =3.18+-0.03 eV, FWHM=0.76+-0.03 eV.

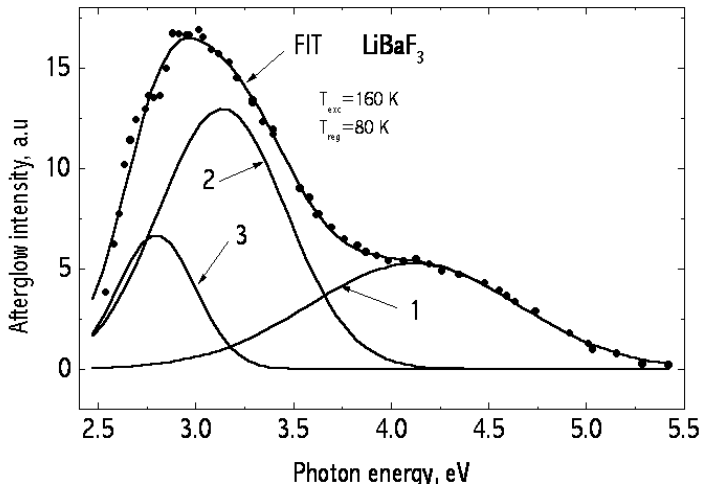

Figure 6. Curve fit by Gaussians of the TL spectrum observed at 80 K after cooling down from the excitation temperature at 100.

1: TL band at hν =4.11+-0.14 eV, FWHM=1.06+-0.17 eV;

2: TL band at hν =3.13+-0.24 eV, FWHM=0.65+-0.27 eV;

3: Tl band at hν =2.8+-0.02 eV, FWHM=0.4 +-0.2 eV.

Because the TL spectrum in this case corresponds to the early stage of the first 125 K TSL peak, all the radiation defects created can contribute in TL. The main TL band peaks at $h\nu$=4.05+-0.04 eV having FWHM=0.91+-0.04 eV. The slightly less TL band is found at $h\nu$=3.18+-0.03 eV and has FWHM=0.76+-0.03 eV. The TL spectrum created at 160 K corresponds to the latter stage of the 140 K TSL peak. Similar decomposition shows that at least three elementary TL bands peaking at $h\nu$=4.11+-0.14 eV (FWHM=1.06+-0.17 eV), $h\nu$=3.13+-0.24 eV (FWHM=0.65+-0.27 eV) and $h\nu$=2.8+-0.02 eV (FWHM=0.4 +-0.2 eV) are present. Taking into account the inaccuracy of curve fit it can conclude that two TL bands are present in the whole temperature region.

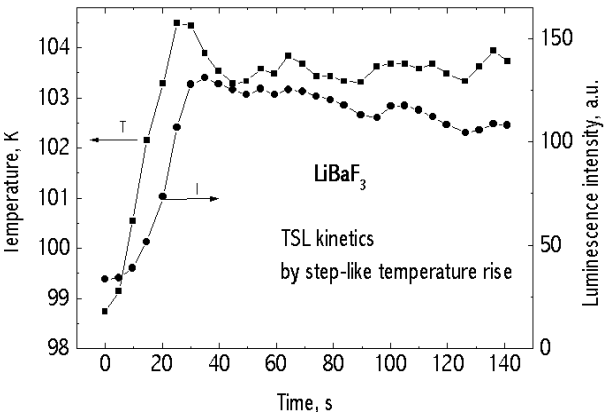

Figure 7

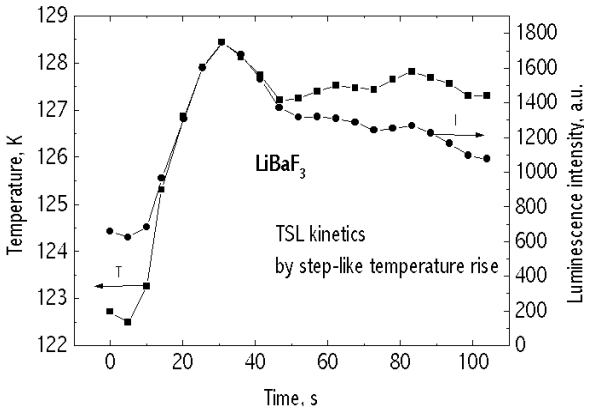

Figure 8

The simultaneous records of the temperature (T) and TSL intensity (I) by step-like heating of the $LiBaF_3$ sample X-irradiated at 80 K in the early stagesnof the 120 K TSL peak (Figure 7) and close to the maximum intensity of the 120 K TSL peak (Figure8).

In the early stages of the 130-140 K TSL peak the diffusion-controlled-tunnelling-recombination kinetics occurs, as discussed in the case of halide crystals in [9]. A small step-like (2-5 K) increase of the stimulation temperature leads to the long-term-increase of the recombination luminescence to the quasi-stationary value. Figures 7 and 8 represent the simultaneous records of the time dependence of both the temperature and the TSL intensity increase. At early stage of the 120 K peak (Figure 7) the increase of the TSL intensity is delayed with respect to the increase of temperature. The transition time to the new quasi-stationary recombination decreases with increased stimulation temperature. Figure 8 represents the similar records of temperature and TSL intensity at temperatures close to the 125 K TSL peak temperature. The TSL intensity without any delay follows the temperature changes simultaneous reaching the maximum values of temperature and TSL intensity. The conclusion can be drawn that the recombination process responsible for the 125 K TSL peak involves the random walk of one of the reaction partners. Decrease of the reaction partner separation leads to radiative charge-transfer between close pairs with a probability exponentially increasing with decreasing pair separation [9]. For the given diffusion rate the recombination rate and corresponding pair separation distribution function can be characterised by corresponding mean recombination radius, which decreases by increase of the diffusion rate constant, i.e. temperature. Step-like increase of temperature causes redistribution of the pair separation function. Thus, the new mean recombination radius and corresponding quasi-stationary recombination rate will be reached having some time delay.

Discussion

The diffusion-controlled-tunnelling-recombination kinetics in $LiBaF_3$ crystals indicates that the thermoactivated migration of the V_K centres occurs starting from ~100 K via reorientation hops, without breaking the molecular bound. Either the 60^0 or the 90^0 hops can occur in $LiBaF_3$ lattice (Figure 2). Above 130 K the V_K centres are thermally destroyed. The F–type centres are the main electron centres created by ionising radiation simultaneously with the V_K centres. It is reasonably to propose that the 125 K TSL peak is due to the radiative diffusion-controlled-tunneling-recombination of V_K-centre and F-type centre pairs. Spontaneous electron transfer from F-type to V_K centre results in the photon emission. The radiative transitions can be either a direct ones between the ground states of the electron and hole centres or two step processes via excited state of V_K centres. In the latter case the luminescence of self-trapped excitons will occur. Energy of the TL band coincides with the self-trapped exciton emission energy reported in [4]. We have investigated the decay kinetics of luminescence at 4.58 eV (spectral region of TL due to the F-V_K recombination) excited by electron beam pulses (Figure 9). At 300 K sufficiently exceeding the temperature of hole self-trapping, a non-exponential decay of luminescence due to the diffusion-controlled recombination is accompanied by the fast decay component. Presence of fast decay supports the exciton mechanism of the TL via V_K centres. Presence of the F-V_K recombination band in TL spectra by excitation of sample above the V_K localisation temperature can be explained taking into account, that in the course of cooling of the sample to 80 K part of released V_K centres are self trapped.

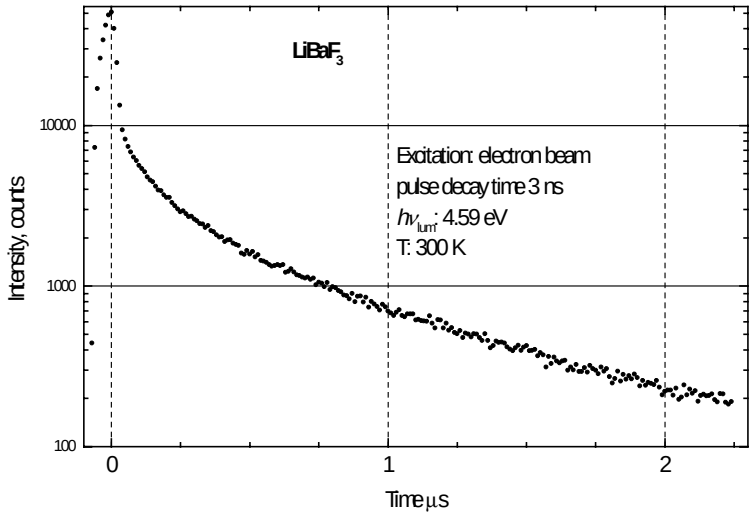

Figure 9. The decay kinetics of $LiBaF_3$ luminescence at $h\nu$ = 4.58 eV (spectral region of TL due to the F-V_K recombination) excited by electron beam pulses, (duration 6 ns, decay time 3 ns) at 300 K.

We propose that the TL band at 3.18 eV origins due to the electron-tunneling transfer between F-type centers and trace impurity centers. The spectral position of these centers is close to the blue luminescence band discussed in [11]. The spectral position of the blue luminescence band and its excitation is similar to those, caused by oxygen in other fluorides [12]. O^{2-} incorporated in F^- site without charge compensation will act as acceptor.

Conclusions

1. In $LiBaF_3$ crystals self-trapping of holes occurs in the form of fluorine F_2^- molecular V_K centres occupying the fluorine site and oriented along [110] direction.

2. The thermoactivated migration of the V_K centre occurs starting from ~100 K via reorientation hops, without breaking the molecular bound. Above 130 K the V_K centres are thermally destroyed.
3. The main radiation defects in undoped $LiBaF_3$ crystals below 100 K are F-type electron centres and self trapped holes (V_K-centres).
4. The luminescence band at ~4.1 eV (~302 nm) is caused by charge-transfer transitions between F-type and V_K centres. The preferable mechanism is two step processes via formation of the self-trapped exciton.
5. The luminescence band at ~ 3.15 eV (~393 nm) is caused by charge-transfer transition between F-type and impurity centres. The eventual trace impurities involved are oxygen ions substituting fluorine.

References

1. M.J. Knittel, P. Dorenbos, J.T.M. de Haas and C. V. E. van Eijk, Nucl. Instr. And Meth. A **374**, 197 (1996).
2. E.N. Melchakov, M. A. Petrova, I. G. Podklozina, P. A. Rodnyi and M. A. Terekhin, Opt. Spectrosc. **69**, 481 (1990).
3. P. A. Rodnyi, M. A. Terekhin and E. N. Melchakov, J. Lumin. **47**, 281 (1991).
4. I. Tale, P. Kulis, U. Rogulis, V. Tale, J. Trokss, A. Veispals, M. Barboza-Flores and H. -J. Fitting, J. Lumin. **72-74**, 722 (1997)
5. P. Kulis, I. Tale, M. Springis, U. Rogulis, J. Trokss, A. Veispals and H.-J. Fitting, Rad. Effects and Defects in Solids. (1999), (in press).
6. I. Tale, H. -J. Fitting, P. Kulis, V. Ogorodnik, U. Rogulis, M. Springis, V. Tale, J. Trokss, A. Veispals, Rad. Effects and Defects in Solids. (1999), (in press).
7. J.J. Rosseau and J.C. Fayet, *Phys. Stat. Sol. (b)* **77**, 195 (1976)
8. L.E. Halliburton and E. Sonder, *Solid state Communications* **21**, 445 (1969)
9. T.P.P. Hall, *Brit. J. Appl. Phys.* **17**, 1011 (1966)
10. E. Kotomin, I. Tale, V. Tale, P. Butlers, and P. Kulis, J. Phys. Condensed Matter., **1**, 6777 (1989).
11. M. Springis, P. Kulis, I. Tale, A. Veispals, and H. –J. Fitting, Proc. SCINT'99, (1999).
12. P. W. M. Jacobs and S. H. Song, J. Phys. Chem. Sol. **41**, 437 (1980).

A time-resolved spectroscopy study of fast luminescence in lithium borates

I.N. Ogorodnikov[1], V.A. Pustovarov[1], A.V. Kruzhalov[1], L.I. Isaenko[2], M. Kirm[3] and G. Zimmerer[3]

[1]*Experimental Physics Dept., Urals State Technical University, Mira Street 19, 620002 Ekaterinburg, Russia*
[2]*Design and Technological Institute of Monocrystals, RAS, Russkaya Street 3, 630058 Novosibirsk, Russia*
[3]*II. Institut für Experimentalphysik der Universität Hamburg, Luruper Chaussee 149, D-22761 Hamburg, Germany*

Abstract. The paper presents the results of a complex study of electronic excitation dynamics for single crystals LiB_3O_5 and $Li_2B_4O_7$ carried out by the use of the low-temperature luminescent VUV spectroscopy with sub-nanosecond time-resolution under photoexcitation by synchrotron radiation. The decay kinetics of the photoluminescence, reflectivity, time-resolved emission and luminescence excitation spectra were measured at 9.6 K and 295 K. The intrinsic origin of luminescence in both crystals was attributed to radiative annihilation of self-trapped exciton (STE). The σ- and π-emission bands of the STE's singlet and triplet transitions were revealed. The creation and decay of the relaxed and non-relaxed excitons in lithium borates are discussed.

Keywords: lithium borates (LiB_3O_5 and $Li_2B_4O_7$), self-trapped exciton, time-resolved VUV - spectroscopy, synchrotron radiation

1. Introduction

In Ref. [1,2] we have presented preliminary results of a study of the fast intrinsic UV-luminescence in LiB_3O_5 (LBO). This luminescence can be applied to scintillation technique, especially for the ^{6}Li-based thermal neutron detection. Since the bright ultraviolet luminescence of LBO was revealed, it has been the subject of extensive research. The current state of the art for this luminescence was given in [1,2]. Similar luminescence has been found also for $Li_2B_4O_7$ (LTB). However, the origin of the fast luminescence for both crystals has been insufficiently studied.

2. Experimental Details

In this work we present the results of a study of the time-resolved photo-luminescence (PL) spectra in the energy region from 2 eV to 8.2 eV, time-resolved PL excitation spectra over the broad energy range from 4 eV to 40 eV, and reflectivity of single crystals of lithium borates LBO and LTB at 9.6 K and RT carried out at the SUPERLUMI experimental station of HASYLAB by the use of synchrotron radiation. Time-resolved spectra were recorded within a time window (length Δt) correlated with the arrival of SR pulses (delayed δt). In the present experiments the delay and length were δt_1=1.2 ns, Δt_1=5.9 ns for a fast component, and δt_2=23.5 ns, Δt_2=111 ns for a slow component. Simultaneously with the excitation, the reflection spectra were recorded at an angle of incidence 17.5° by a XP2230B photomultiplier from a sodium salycylate coated window (see other experimental details in Ref. [3]). Characterization of the specimens was made in our previous work [2].

3. Results and Discussion

The broad band PL at 2.5-4.5 eV was observed for LTB and LBO crystals under photon excitation above 7.5 eV. Decay of the LTB and LBO luminescence consists of two fast exponential components with time-constants τ_1<1 ns and τ_2~8.5 ns, and of a slow component in microsecond time-range (Fig. 1). The fast component with τ_1 can be effectively excited over all the 7.5-40 eV energy region as shown by the excitation spectrum of the fast component. In contrary, the fast component with τ_2 can be excited in the selected range of 9.5-10.5 eV only. Spectra of PL of LBO and LTB were measured at various exciting photon energies 7-40 eV (Fig. 2,3). The PL exhibits a clearly defined excitation band peaking at 8.0 eV (Fig. 4,5). Its long-wavelength slope is represented as a steeply rising curve at 7.5-7.9 eV correlated with the fundamental absorption edge (FAE) of LBO [2] and LTB, respectively. However, the PL excitation spectra of LBO for the fast and slow components are quite different, having maxima at 7.9 eV, and 8.8 eV, respectively.

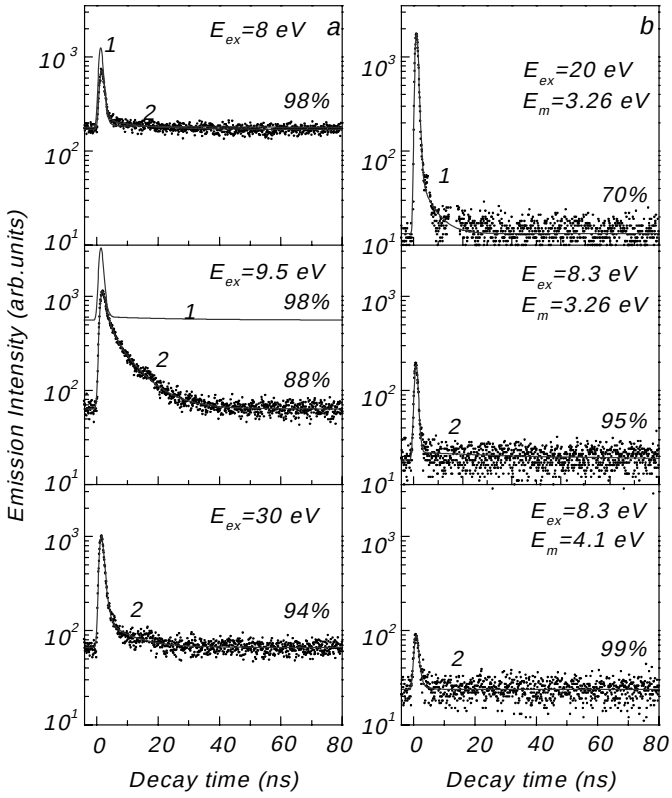

Figure 1. Decay kinetics of the LBO (*a*) and LTB (*b*) PL at 295 K (1) and 9.6 K (2) for various excitation (E_{ex}) and emission (E_m) energies (for LBO E_m= 3.87 eV). Persents indicate a contribution of the slow component to the total light-yield.

A complex emission band of the LBO PL consists of three subbands at 3.1-3.2 eV (I), 3.6-3.8 eV (II), and 4.2-4.4 eV (III). The slow components and steady-state luminescence peak mainly at the central subband (II), contribution of the other subbands are insignificant. The subband (III) becomes pronounced at the excitation in the energy range of 9.5-10 eV. The most plausible model developed from these results is as described further. We attribute PL in LTB as well as subband (I-II) in LBO to radiative annihilation of self-trapped excitons (STE), whereas subband (III) in LBO was associated with the recombination luminescence.

Let us to discuss this model using the obtained experimental data. From our model it follows that the excitation of LTB and LBO by photons around FAE creates the non-relaxed excitons e^o, which decay several ways: including migration, self-trapping, and dissociation into the separated components. In fact, the peak of the LTB reflectivity at 8 eV coincides with the narrow intense PL excitation band. This peak of reflectivity has been earlier attributed to a creation of excitons in LTB [4]. The LBO reflectivity spectrum demonstrates a 'hump' at 8.0-8.3 eV and a peak at 9 eV. This structure also match the LBO PL excitation band, and we associate this 'hump' at 8.0-8.3 eV with creation of excitons in LBO. The excitonic peculiarities in the complex oxides usually coincide with the region of the most effective excitation of the intrinsic emission in spite of the fact that the excitonic absorption in them appears often only slightly as a shoulder or 'hump' on the long-wavelength FAE [5].

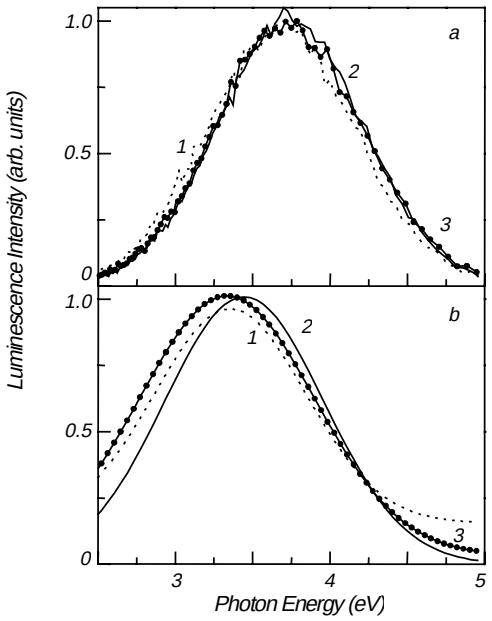

Figure 2. The time-resolved PL spectra of LTB measured for the slow (*a*) and fast (*b*) components at 9.6 K (1,2) and 295 K (3) at E_{ex}=30 eV (1), 8.3 eV (2) and 10 eV (3).

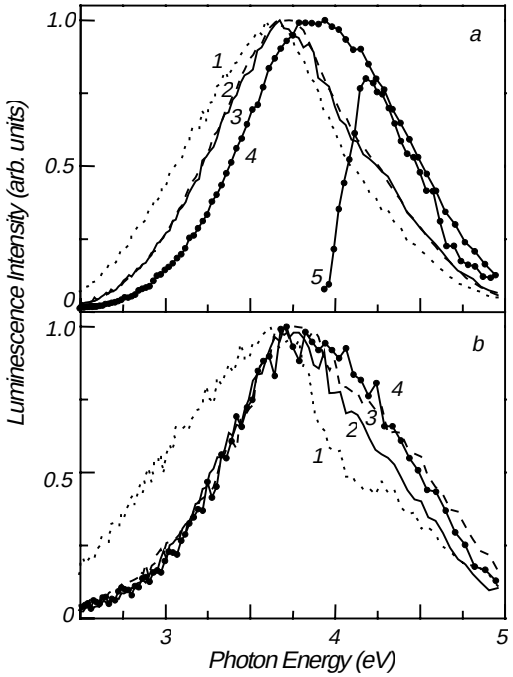

Figure 3. The time-resolved PL spectra of LBO measured for the slow (*a*) and fast (*b*) components at 9.6 K (1-3) and 295 K (4) at E_{ex}=30 eV (1), 9.5 eV (2), 8.1 eV (3) and 7.75 eV (4). Plot (5) is a difference between (4) and (3).

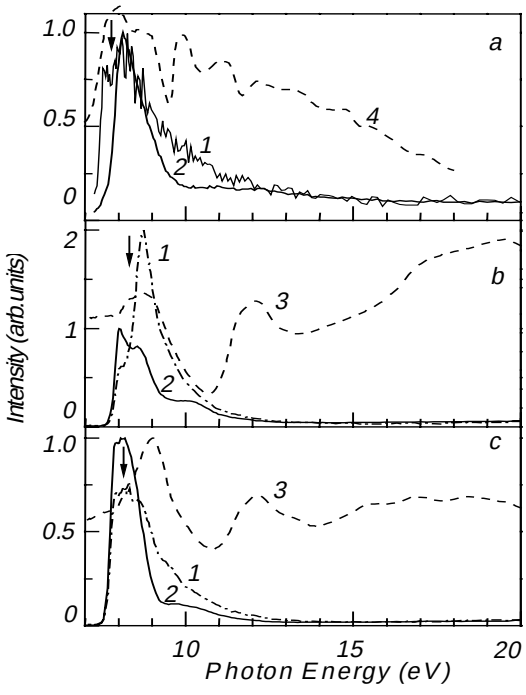

Figure 4. The PL excitation spectra of the fast (1) and slow (2) components measured at E_m= 3.87 eV for LTB (*a*), LBO⊥*Z* (*b*) and LBO⊥*X* (*c*) at 9.6 K and reflectivity of LBO at 9.6 K (3). The reflectivity spectrum of LTB is taken from Ref.[15] (4). The arrows point the positions of the long-wavelength maxima in the corresponding $\varepsilon_2(E)$ spectra.

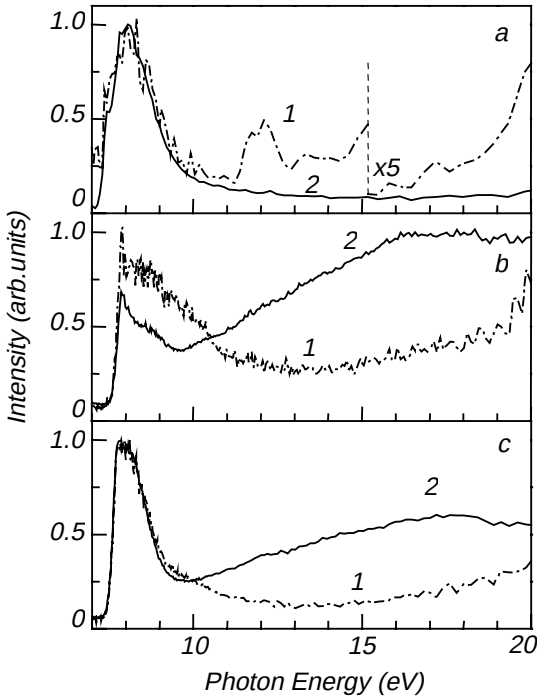

Figure 5. The PL excitation spectra of the fast (1) and slow (2) components measured at E_m= 3.87 eV for LTB (*a*), LBO⊥*Z* (*b*) and LBO⊥*X* (*c*) at 295 K

Migration of excitons and their non-radiative decay on the surface are responsible for the surface energy losses (SEL). The profile of the PL excitation spectra is evidence for the excitonic mechanism of the energy transport in LTB and LBO.

Such spectra are inherent either in system with an excitonic emission, or in system with an excitonic transport of energy to the activator emission centres. The LTB and LBO luminescence at 9.6 K is preferably excited in the exciton creation region associated with a clearly pronounced peak on the PL excitation spectra (Fig. 5). In this case, the drop of the excitation efficiency above 10-12 eV can be explained by SEL on account of the dramatic increase of the optical absorption coefficient. Notably, the increase of reflectivity above 8 eV correlates with this peak of the PL excitation (Fig.5).

The second channel of the exciton decay is self-trapping with following radiative annihilation of STE. The presented results together with the previously obtained data for LTB [6,4] and LBO [2,7] revealed the specific features of the broad band short-wavelength luminescence of these crystals: namely, a fairly high quantum yield, a large Stokes shift (≈4 eV), absence of the PL excitation bands over all the optical transparency region, presence of an exponential component in the luminescence decay kinetics, an effective PL excitation over the assumed excitonic optical absorption region, the 'freezing' of the effective energy transport towards the lattice defects. Such features are typical for STE in alkali halide crystals (AHC) [8], or in the low-symmetry oxides, *e.g.* BeO [9] and Al_2O_3 [10]. This suggests that the broad luminescence band at 3.6 eV in both, LTB and LBO is due to the radiative annihilation of the relaxed electronic excitation - self-trapped excitons. The effective excitation of this luminescence over the FAE spectral region points to a creation of this STE through relaxation of exciton e^o. In the selective creation of exciton e^o, the quantum yield of the STE's emission in LTB and LBO remains nearly constant during the cooling from RT to 9.6 K. This is supported by the direct measurements of the temperature behaviour of the steady-state PL over the 8-500 K temperature region [2]. The absence of 'freezing' of the STE's luminescence at 9.6 K indicates that there is no potential barrier for self-trapping, or this barrier should be very low. Such picture is typical for a large class of the low-symmetry oxides with complex lattice, *e.g.* Al_2O_3 [10].

The exciton dissociation ($e^o \rightarrow e^- + h^+$) can proceed through the autoionization at low temperatures as well as through the thermally stimulated process at elevated temperatures. The autoionization of e^o at low temperatures is due to the mixed origin of the excitonic states, causing usually the dynamical instability of the exciton and its decay with creation of an electron and hole. On the further stages, these separated charge carriers either can be trapped on the appropriate trapping centres, or they can recombine on the suitable recombination centres. This process does not require any activation energy and can take place even at low-temperature. In contrary, the thermally stimulation dissociation requires an activation energy E_d and results in an increase of intensity of the recombination luminescence, adhering to the Arrhenius low: $I \sim \exp(-E_d/ k_B T)$. The PL excitation spectra of LTB and LBO at RT are typical for that of an excitation for the recombination processes with participation of the lattice defects [8]. Manifestation of the excitonic peak at the long-wavelength slope of the PL excitation spectra at RT is due to the thermally stimulated dissociation of the created exciton into the separated electron an hole, which can contribute to the appropriate recombination process. It is of fundamental importance that the short-wavelength part of the PL spectra of LBO is observed also in the thermally stimulated luminescence (TL) spectra. In other words, this part of PL can effectively be excited through the electron and hole recombination process with participation of the lattice defects: the trapped hole (O^-) and electron (B^{2+}) centres. The corresponding TL peaks associated with a decay of these centres appear at 240 K and 130 K, respectively [7]. More over, upon heating from 130 K to 240 K, the quantum yield of the X-ray luminescence (XRL) of LBO increases by 20-25 times with an activation energy of 65 meV [7].

Below 130 K these defects act only as the effective electron and hole traps, the XRL yield at these temperatures is fairly low. In the view of the developed model, the activation energy of 65 meV can be associated with E_d. The PL excitation spectra of LTB show no recombination type band, because of the insufficient concentration of the relevant lattice defects as well as because of their higher temperature stability. The TL intensity of the undoped LTB crystals is fairly low [11], and the temperature quenching of XRL starts above 320 K [6].

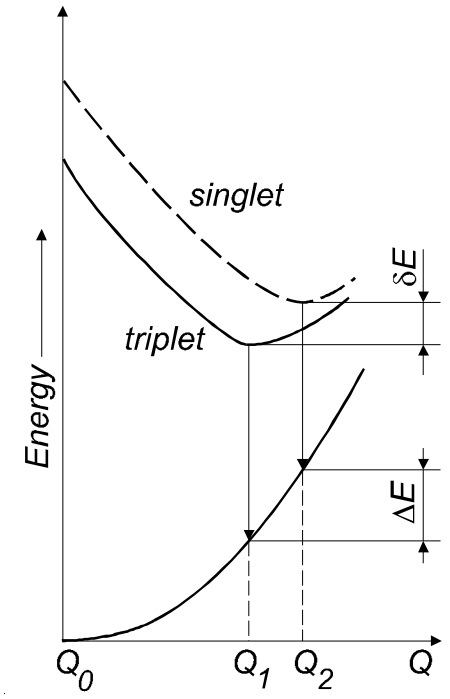

Figure 6. Adiabatic potential energy curves for the lowest singlet and triplet transitions in lithium borates LTB and LBO.

Figure 6 shows the assumed adiabatic configurational coordinate diagram of the potential energy for the two lowest levels of STE in lithium borates, which are responsible for the singlet and triplet radiative transitions. This diagram demonstrates that the singlet level of STE has the minimum at Q_2, which exceeds Q_1, indicating the triplet minimum. The difference between positions of the singlet and triplet emission band maxima is governed by $\Delta E_m = \delta E - \Delta E$ (see Fig.6 for details). This means that ΔE_m for each crystal is determined by δE and ΔE, and it can be either positive or negative. The estimated value of ΔE_m=–(300÷400 meV) is for LTB and +(50÷60 meV) for LBO. In case of AHC, the splitting value δE is several tens of meV [12], comparable with ΔE_m for LBO.

The ΔE in LBO is supposed to be very small, and both the singlet and triplet STEs should differ little in the lattice relaxation.

Notably, the decay kinetics of the STE's luminescence for LTB and LBO is similar to that for NaBr, NaI and molecular crystals of the noble gases. At the same time, in LTB as well as in NaBr and NaI [12], the maximum of the σ-emission band falls on more long-wavelength region than that for the π-emission band, whereas in LBO as in molecular crystals [13], the situation is reversed.

The second fast component τ_2 = 8.5 ns is effectively excited at 8.8 eV, and it was attributed to manifestation of another type of non-relaxed exciton in LBO. The emission spectrum of that remains the same, so the final stages of the radiative relaxation are also identical. The τ_2 is determined by the process of transformation of energy of the 8.8 eV exciton. Such situation is not surprising for the low-symmetry oxides, for example, there were revealed at least three kinds of excitons in SiO_2, differentiated by the excitation energy as well as by their mobility [14].

4. Conclusion

In present work the time-resolved PL spectra in the energy region from 2 eV to 8.2 eV, time-resolved PL excitation spectra over the broad energy range from 4 eV to 40 eV, decay kinetics of PL and reflectivity of single crystals of lithium borates LiB_3O_5 and $Li_2B_4O_7$ at 9.6 K and 295 K were measured. It was revealed that the short-wavelength UV luminescence of both crystals at 3.5 eV has intrinsic origin due to radiative annihilation of self-trapped

exciton. In both crystals we found the σ and π emission bands, resulting from the singlet and triplet transitions of the STE. The long-wavelength (LTB) and short-wavelength (LBO) shifts between spectral positions of the σ and π emission band maxima were explained in the framework of a model of the adiabatic potential energy surfaces. For LBO it was revealed also a recombination type emission band as well as an existence of another non-relaxed exciton, excited at 8.8 eV.

The work was partially supported by the European Commission (ERBIC15CT960721).

References

1. I. Ogorodnikov, A. Porotnikov, A. Kruzhalov, and V. Pustovarov, In 'Proc. of Intern. Confer. SCINT97', Z. Yin, P. Li, X. Feng and Z. Xue, Eds., p.139-142, Shanghai, 1997
2. I. Ogorodnikov, E. Radzhabov, L. Isaenko, A. Kruzhalov, In 'Excitonic Processes in Condensed Matter', R. Williams and W. Yen, Eds, PV 98-25, p. 426-431, The Electrochem. Soc. Proc. Series, Pennington, NJ, 1998
3. G. Zimmerer, Nucl. Instr. And Meth. **A 308 (**1991**)** 178
4. I. Kamenskikh, V. Kolobanov, V. Mikhailin, I. Spinkov et al., Abstracts of SCINT97, Shanghai, 1997. p.64.
5. V. Mürk, B. Namozov, N. Yaroshevich, Radiat. Measurem. **24**(4) (1995) 371
6. O. Antonyak, Y. Burak, I. Lyseiko, N. Pidzyrailo, Z. Khapko. Opt. Spectrosk. **61**(3) (1986) 550
7. I. Ogorodnikov, E. Radzhabov, L. Isaenko et al., Fiz. tverd. Tela, **41**(2) (1999) 223
8. Ch. Lushchik, In 'Excitons', E. Rashba and M. Sturge, Eds., p. 505, North-Holland, Publ. Conf., Amsterdam, 1982
9. I. Ogorodnikov, A. Kruzhalov, Material Science Forum, **239-241** (1997) 51
10. B. Namozov, M. Fominich, V. Mürk, R. Zakharchenya, Fiz. tverd. Tela, **40**(5) (1998) 910
11. R. Komatsu, T. Sugawara, K. Sassa et al., Appl. Phys. Lett. **70**(26) (1997) 3492
12. T. Matsumoto, T. Kawata, A. Miyamoto et al., J. Phys. Soc. Jpn. **61**(11) (1992) 4229
13. G. Zimmerer, In 'Proc. Int. Scool of Phys. "Enrico Fermi"; course 96, Verenna. 1985', M. Grassano and N. Terzi, Eds., p.37, North-Holland, Amsterdam, 1987
14. A. Silin', A. Trukhin, Point defects and elementary excitations in glassy and crystalline SiO_2, Zinatne, Riga, 1985
15. Ya. Burak, Ya. Dovgyi and I. Kityk, Fiz. Tverd. Tela (in Russian), **31**(9) (1989) 275

PElectronic Structure Embedded Cluster Simulation of Ce^{n+} in Fluorides and Complex Oxides

A.B.Sobolev, A.Yu.Kuznetsov, A.N.Varaksin, Yu.L.Korol

Experimental Physics Department, Urals State Technical University, 620002, Ekaterinburg, Russia

We present results of an investigation of the electronic structure of Ce^{3+} impurity in CaF_2, Lu_2SiO_5 crystals. The effects of lattice polarisation and relaxation were considered. The calculations were performed using embedded cluster technique based on synthesis of the scattered wave method and the molecular statics method.

Keywords: Electronic structure, clusters, relaxation

1. Introduction

The doping of wide sets of crystals with cerium has been found to provide a scintillation crystal with fast light pulses on gamma-ray irradiation. Therefore, the accurate calculations of electronic structure of cerium ions in ionic crystals may be useful for understanding of the process of transfer of irradiated energy to the cerium center. In this paper we present the calculation results obtained by the embedded cluster Johnson's scattered-wave method [1]. The aim of the investigation was estimation of the position of impurity levels in the forbidden gap of perfect crystals and the values of the 5d orbital splitting (10Dq in cubic field). Similar investigations had been carried out earlier by the group of Prof. C.W.E. van Eijk with the participation of Dr. Andriessen J. using Hartry Fock approach [2, 3]. We conducted similar investigations for crystals SrF_2, $SrC1_2$, LSO (Lu_2SiO_5) using local potential [4-5]. Recently we have revised our understanding of the possibilities of the local density functional method in describing the electronic structure of rare-earth ions [6]. The results obtained in the above-mentioned investigation relate to describing Ce ion in crystals CaF_2 and LSO with account for the results shown in [6].

2. Description of the Model

One of the model features was involvement of Ce (5dn4f0) electronic state in self-consistency, as was proposed in [6]. In the model, molecular orbital MO corresponding to Ce5dn state (e.g., in octahedral clusters $-e_g$) was populated with n electrons, while MO's corresponding to 4f states remained vacant. In the given approach, the value of energy 4f cannot be estimated, and need be derived either from the experimental data, or from other calculations. Another important model feature was that the cluster Coulomb potential was created as in supercell approach.

3. Electronic Cluster Simulation Clusters in CaF_2

The CaF_2 crystals belong to spatial group O_h^5. We used a supercell with translation vectors **a** = (2,0,0), **b** = (0,2,0), **c** = (0,0,2), in units A_o = 2.725 Å, which included ions 4Ca, 8F, 4V and presented a four-fold standard elementary cell; here, V stands for hollow "muffin-tin" spheres occupying the octahedron interstitial sites. It was established from the experimental data that type CaF_2 (also SrF_2, BaF_2) crystals doping with trivalent metal cations Me^{3+} leads to emergence of interstitial ions Fe_{i-} compensating for the cation excessive charge [7].

It was shown experimentally that at small concentration of the doping trivalent cations (less than 1 mole %), dipoles with distances $R_{12} = A_o$ and $R_{12} = A\sqrt{3}$ between the dipole components prevail (they are designated as nearest neighbour NN, and next nearest neighbour NNN configurations, respectively). In this connection, in our calculations we considered the clusters presenting ideal crystal CaF_2 fragments corresponding to the described defects:

- Ce^{n+}(n = 2, 3) – selection of origin of coordinates at Ca; cluster [CaV_6F_8] (O_h symmetry);
- CeF_{nn} – selection of origin of coordinates at Ca; cluster [CaV(Fi)V5F_4F_4] (C_{4v});
- CeF_{nnn} – selection of origin of coordinates at F [FCaV(Fi)V3F6F6] (C_{3v}).

Calculations show that the valence band is formed mainly by F2*p* orbitals, and the conduction band, by Ca3s states, which correlates with the known calculation and experimental data for CaF_2 [8]. The E_g bandgap width is 8.6 eV. The respective value obtained by the LMTO method equals $E_g \sim 6.11$ [8] (Eg exp = 12.1 eV [8]). The calculated value of the self-interaction correction (SIC) to E_g value for F2p states equals 7.3 eV (SrF_2 – 7.4 eV [4]).

4. Simulation of Ce^{n+} ion in CaF_2

4.1. Calculations of spatial structure of cerium defects in CAF_2 crystal by the molecular statics (MS) method

The MS method was used to calculate the energies of formation and spatial structure of defects due to calcium ion substitution for trivalent cerium ion in CaF_2 crystal. The following situations were simulated: 1) bivalent calcium ion substitution for trivalent cerium ion (isolated defect); 2) fluorine ion occupying an interstitial site of anion sublattice (isolated defect); 3) dipoles [Ce+ – F_{i-}] being nearest (NN) and next nearest (NNN) neighbours to each other (isolated and periodic defects). Our calculations point to NN complexes being energetically favourable for the CaF_2 crystal; the difference between the NN and NNN complexes in the isolated defect model was 0.79 eV. In the periodic defect model, the calculated energies difference between NN and NNN complexes equals 2.64 eV; such a big discrepancy is explained by the strong interaction between the defects, since the elementary cell in the periodic defect model comprises 13 ions only. According to the experimental data [7], the difference between the bond energies of NN and NNN cerium complexes in CaF_2 crystals, at small cerium ions concentration (isolated defects approximation), is 0.886 eV.

Let us consider briefly the character and amount of lattice relaxation near the (Ce^{3+} – F_i) dipoles in the CaF_2 crystal. The NN and NNN complexes present neutral defects of the crystal lattice; however, since they are formed by a pair of charged defects (Ce^{3+} and F_i ions), they cause rather strong lattice distortion in the immediate neighbourhood. In an isolated NN dipole, due to defect symmetry, the coordination spheres that comprise the ions surrounding the NN dipole present dumb-bells with the centers on these ions. The first coordination sphere comprises 12 fluorine ions surrounding Ce^{3+} and F_- ions. Fluorine ions located between Ce3+ and F_- are subjected to maximum, in absolute value, displacements of 6.5 % of the lattice parameter A_o. Other ions in the first coordination sphere undergo displacements of the order of 3–4 % A_o. Here we should note the rather big displacements of ions forming the dipole proper: the Ce^{3+} ion is displaced towards the fluorine interstitial ion by 4.9 %, and the fluorine interstitial ion is displaced towards the Ce^{3+} ion by 7.8 % of A_o. A somewhat different displacements pattern is present in the periodic defects model. For the 13-ion unit cell, in cases of both the NN and NNN dipoles, due to symmetry, the calcium and cerium ions (i.e., all cations) undergo no displacements. At that, the amount of all anions displacement is found to be the same: For the NN dipole, fluorine ions displacement is 4.9 %, for the NNN dipole, it is equal to 2.2 % of the lattice constant.

4.2. Electronic structure calculation of Ce^{n+} ion in CAF_2 crystal bycluster method

Figure 1 shows changes in the one-electron spectrum of clusters simulating CeF_{nn} defects versus relaxation in the fluorine ions surrounding the cerium ion. In case of cluster $[CeV_8B_8]$ (Ce^{n+}), we deal with symmetric arrangement of fluorine ions relative to the Ce position. In case of CeF_{nn} defect, the surrounding equatorial fluorine ions are moved away relative to the cerium ion – interstitial fluorine axis. As it follows from the presented data, the general tendency of the relaxation effect is decrease in the value of orbital splitting of Ce5d states by the octahedral crystalline field (e_g-t_{2g}) – 10Dq. Such calculation result is easy to grasp, if we bear in mind that the value of splitting of delocalized 5d-states is roughly inversely proportional to r^5, where r is the metal – ligand distance. The Figure central part illustrates the effect of relaxation in case of type CeFnn defect. As distinct from the previous case, there is observed orbital splitting $e_g \rightarrow b_1+a_1$ and t_{2g}-b_2+e by tetragonal field.

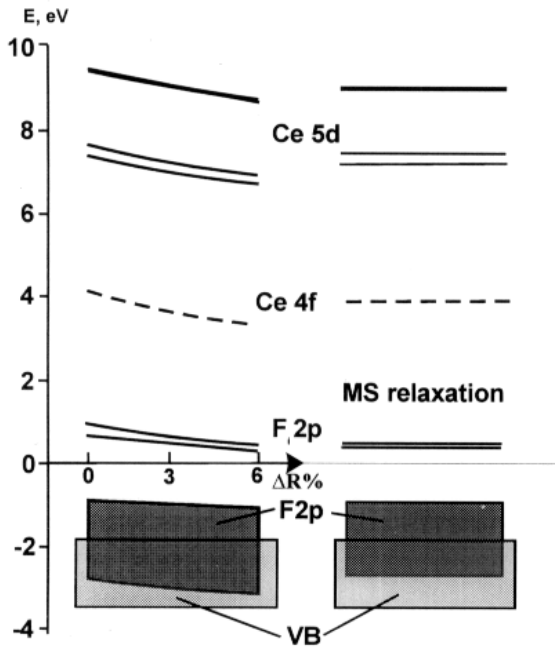

Fig.1. Cluster's one-electron diagrams for CeF_{nn} defects

For comparison, Fig. 1 in its right part gives the calculation for the relaxed geometry. It may be seen that the one-electron spectrum occupies an intermediate position between the calculation for the experimental lattice and calculation for the symmetric relaxation of the order of 5 %.

Our calculations were made without account for spin-orbital splitting (SL). For tetragonal and trigonal cases, SL-interaction in 5d shell must lead to splitting of symmetry levels **e** to two sublevels. Thus, for our case, with account for crystalline and SL-splittings, there must exist five absorption bands, which fact is in agreement with the experimental results interpretation offered in [9]. Estimate of the SL-splitting [4] yields, for cerium, ξ_{5d} = 0.11 eV, which results in that level e corresponding to 5d-state in $\boldsymbol{Ce}^{3+}$ must split to two sublevels e and e . Oour results and the experimental data are given in Table 1 and Fig. 2. The energy of Ce4f state is taken from the experimental data for CaF_2 crystal. The calculated SIC to value E_g is 7.3 eV. Since, as was shown in [6], SIC to Ce5d states amounts to about 4.5 eV, the position of Ce4f states may appear overestimated relative to the experiment to a value of about 3 eV.

Table 1 One-electron 5d- energies (in eV) of CaF_2-Ce for Ce^{2+}, CeFnn and CeFnnn centers

Ce^{2+} (O_h)	CeFnn(C_{4v})			CeFnnn (C_{3v})	
A	A	B	C	B	
5.4 (t_{2g})	5.59 (e)	6.63	5.29	6.08 (e)	–
5.23 (t_{2g})	5.67 (e)	6.36	4.70	5.91 (e)	–
3.65 (e_g)	5.50 (b2)	6.13	4.54	4.99 (a1)	–
	4.18 (a1)	–	4.19	3.97 (e)	3.97
	3.89 (b1)	3.89	3.89		

A – our results, B – experimental data of absorption for Ce^{3+} in CaF_2 [7],
C – HF Ce5d energies for CeF_{11} cluster in CeF_3 crystal corrected by value 3.89 eV (this is the difference between 5d-4f energies for Ce^{3+} in CaF_2) – Table 5.2.10 [10].

5. Simulation of the Ce^{3+} Ion in LSO

5.1. Molecular Status Simulation of the Ce^{3+} Ion in LSO

Formation energies and the spatial structure of defects due to the substitution of a trivalent cerium ion for the lutetium ion in the LSO crystal were calculated by the molecular statics method with the use of a MOLSTAT computer program [11]. As we had no chance of implementing the "genuine" potential fitting procedure, the values of the constants for the potentials were chosen from considerations of "similitude" (e.g., the interaction between the Si^{4+} and O^{2-} ions in the LSO crystal was set equal to that for the SiO_2 crystal).

A further step in our research was carrying out MS calculations of the energies for substitution of a cerium ion for lutetium ions, as well as calculating the relaxation of oxygen ions closest to Lu1 and Lu2, and the variations of the Madelung potentials across these ions. Calculations show that energetically the substitution of the Lu1 position for a cerium ion is the more favorable. The Ce^{3+} Lu1 substitution energy equals +6.90 eV, while the Ce^{3+} Lu2 substitution energy is equal to +7.5 eV, i.e., 0.35 eV greater. In both cases the substitution energy is positive as the ionic radius of a cerium ion is greater than that of a lutetium ion. The results obtained correlate with experimental data and bear out the conjecture [12] as to the replacement of the Ce^{3+} ion by lutetium in position 1. This hypothesis rests on the following simple considerations: The mean Lu-O spacing in the LuO_7 coordination polyhedron is 2.32 Å, while that in the LuO_6 octahedron measures 2.23 Å; a comparison of the ionic radii R_{Lu}^{ion} = 0.84 Å and R_{Lu}^{ion} = 1.03 Å permits the assertion that the Ce^{3+} ion replaces the lutetium ion chiefly in position 1.

5.2. Calculating the Electron Structure of Perfect LSO Crystal

The initial stage of our investigation consisted in simulating a perfect crystal in terms of cluster techniques and drawing a comparison with other calculation data and experimental evidence. A study was made of the $[SiO_4]^{4-}$, $[Lu1O_7]^{11-}$ and $[Lu2O_6]^{9-}$ clusters, which are structural fragments of the LSO crystal. Energy diagrams for $[Lu2O_6]^{9-}$ and $[Lu1O_7]^{11-}$ clusters versus XPS data are presented in [11]. On the whole, the results are in unsatisfactory agreement with the experimental data.

5.3. Calculating the Electron Structure of the Ce^{3+} Impurity in the LSO Crystal

It has been shown in the foregoing that Ce^{3+} ions replace Lu^{2+} ion in the Lu1 position, which has seven-fold coordination. The local symmetry of the center in hand is C_1, a circumstance that adds complexity to calculations.

The dependences of the one-electron spectrum of clusters simulating impurity Ce^{3+} in LSO on relaxation of the oxygen ions surrounding Ce^{3+} are illustrated in Fig. 2. Similar to fluorine systems, increase in the impurity – anion mutual spacing decreases the value of orbital splitting between 5d states. It is worth notice that in case of six-fold coordination, the value of splitting is greater, and the splitting pattern in somewhat different from that in case of the seven-fold coordination. Where for equilibrium states the group of two states is lower, and the group of 3 states (corresponding, in the case of an ideal octahedron, to eg and t2g states) is higher in energy, at increase in mutual impurity – anion spacing, the group of 3 states goes lower in energy. This is explained by the fact that the mean interionic Lu-O spacing in the $Lu1O_7$ polyhedron is 0.1 Å greater than that in the $Lu2O_6$ octahedron. Hence, the splitting values should be higher for the cluster with six-fold coordination.

The Figure presents one-electron diagrams of clusters simulating Ce^{3+} impurity in positions Lu1 and Lu2 with account for lattice relaxation as compared with the ideal crystal data.

The results analysis shows that relaxation has a much weaker effect on the one-electron spectrum of the respective clusters compared to the fluoride systems case. The value of

splitting varies inappreciably with the increase in the cerium – oxygen distance. The position of 5d states undergoes major changes relative to the VB of the ideal crystal. The relaxation average value is 5–8 % outward for Lu1 and Lu2 position.

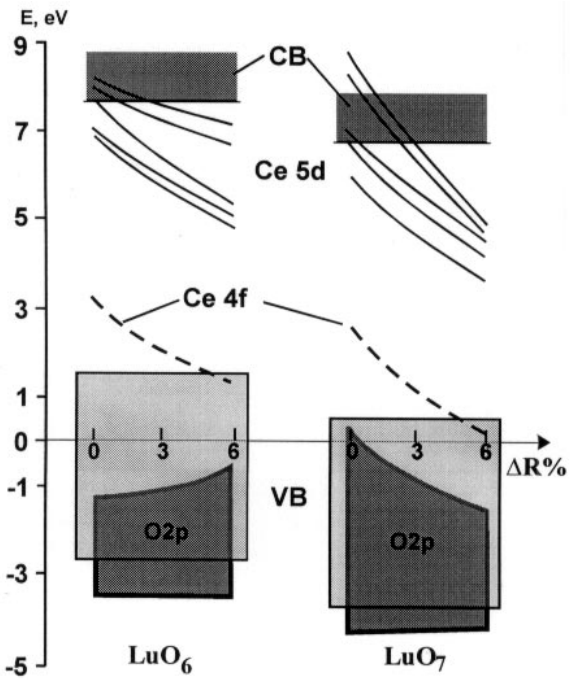

Fig.2. Electronic structure Ce^{3+} in LSO with relaxation

Assuming the errors introduced by the use of the local potential into the relative position of one-electron states belonging to different ions to be inappreciable (SIC for Ce5d .5 eV for O^{2-} it is about 4Ev [13]), we can correlate defect and crystal level positions. Basically, all methods of such correlation are controversial, by virtue of the approximate nature of the cluster model itself. As a rule, defect levels are measured relative to the states of the nearest ions, and the value thus obtained is viewed as an estimate with respect to crystal bands. Yet, as the cluster is small here, the electron states of the nearest neighbors, viz., oxygen ions, that surround the impurity ion are highly distorted owing to the interaction with Ce^{3+}. From this standpoint, the defect in the object being simulated is the cluster in its entirety, and it is therefore more rightful to estimate the defect states with respect to the oxygen states in a nondistorted lattice. Table 2 furnishes results of calculations of the electron structure of the $[CeO_6]^{9-}$ and $[CeO_7]^{11-}$ clusters simulating the substitution of a Ce^{3+} ion for the Lu2 and Lu1 ions with allowance for the relaxation and polarization of the ions in the remainder of the crystal. The energies of the one-electron states are reckoned from the 4f states of the Ce^{3+} ion. By defect position symmetry, we have 7 molecular states for the 4f shell and 5 states for the 5d shell. The Ce5d-state energies given in Table 2 are reduced by 2 eV, for considerations discussed in detail in Section 2 of the present paper. Inspection of the tabulated data shows that the widths of the O2p, Ce4f, and Ce5d bands for the $[CeO_7]^{11-}$ cluster are less than the counterparts for the $[CeO_6]^{9-}$ cluster. Apparently, this result stems from the fact that by virtue of the proximity of the ionic radius of the Ce^{3+} ion to that of Lu1, the amount of distortion in the present case is much less than the counterpart for the Ce^{3+} Lu2 substitution (the main interionic Lu-O spacing in the $Lu1O_7$ polyhedron is 0.1 Å greater than that in the $Lu2O_6$ octahedron).

Table 2 One-electron energies (in eV) of clusters of $[CeO_6]^{9-}$ (O_h symmetry point group), $[CeO_6]^{9-}$ (C_1) and $[CeO_7]^{11-}$ (C_1) simulating the Ce^{3+} center in LSO crystals. (A)

Energy levels		$[CeO_6]^{9-}$		$[CeO_7]^{11-}$		Exp.[14]
		A	B	A	B	
5d levels	$4e_1$	6.24		5.41	5.81	-
	$3e_1$	5.64		4.67	4.85	5.63
	$2e_1$	4.49	3.91	4.47	4.52	4.7
	$1e_2$	4.25	3.89	3.62	4.05	4.2
	$1e_1$	3.48	3.48	3.48	3.48	3.48
Cluster's O2p states		-2.76	-	-4.08	-	-
Top of valence band		-1.76	-0.59	-4.1	1.45	-

A-our resuls; B-HF Ce5d energies for cluster in LSO crystal corrected on value 3.48 eV (this is the difference between 5d-4f energies for Ce3+ in LSO[14] – tabl.6.3.6 [10].)

6. Conclusions and Summary

Obtained estimations of Ce5d-levels positions in the bandgap of LSO and CaF_2 and values of orbital 5d splitting look reasonable in comparison with experimental and known HF clusters data. A satisfactory agreement with the data available for fluorides and complex oxides points to the usefulness of the embedded cluster model in cerium defect simulations.

Acknowledgements

This work was supported by NWO 96/801 grant of Russian-Dutch research cooperation.

References

1. K.H. Johnson, Adv. Quant. Chem. **7** (1973) 143
2. R. Visser, J. Andriessen, P. Dorenbos, and C.W.E. van Eijk, J. Phys.: Condens. Matter. **5** (1993)5887
3. H.Meringa, J. Andriessen, and C.W.E. van Eijk, Proc. Int. Conf. on Inorganic Scintillators and Their Applications, SCINT95. Delft University Press, The Netherlands (1996) 138
4. A.B. Sobolev, A.N. Varaksin, and A.Yu. Kuznetsov, Fiz. Tverd. Tela. **38** (1996) 2729 (In Russian)
5. A.Yu. Kuznetsov, A.B. Sobolev, A.N. Varaksin, and O.A. Keda, Zhurn. Struktur. Khimii. **38** (1997) 1046 (In Russian)
6. A.Yu.Kuznetsov, A.B Sobolev, J.Andriessen, Yu.L.Korol, The choice of parameters in quantum-chemical simulation of the rare-earth ions electronic structure by a scattered waves cluster method., Proc. Int. Conf. on Inorganic Scintillators and Their Applications, SCINT99. Moscow (to be published)
7. W.J. Manthey, Phys. Rev. **B 8** (1973) 4086
8. V.P. Zhukov, and V.M. Zaynullina, Fiz. Tverdogo Tela. **40** (1998) 2019
9. Yu. N. Kolmogorov, and A.N. Varaksin, Zhurn. Struktur. Khimii. **32**(1991)162
10. H. Merenga, Electronic Structure Calculation on Cerium-Containing Crystals: Towards a Better Understanding of Scintillation in Ionic Crystals, Delft: Delft University Press. - III. Thesis Delft University of Technology, 1997
11. A.Yu. Kuznetsov, A.B. Sobolev, A.N. Varaksin, and O.A. Keda, Phys. Stat. Sol. (b) **204** (1997)701
12. J. Andriessen, A. Sobolev, A. Kuznetsov, H. Merenga, P. Dorenbos, and C.W.E. van Eijk, Proc. Int. Conf. On Inorganic Scintillators and Their Applications - SCINT95, Delft University Press, The Netherlands (1996) 130
13. A.B. Sobolev, Fiz. Tverdogo Tela. **35** (1993) 2509 (In Russian)
14. P. Dorenbos, C.W.E. van Eijk, A.J.J. Boss, and C.L. Melcher, J. Phys.: Condens. Matter **6** (1994)4167

The Choice of Parameters in Quantum-Chemical Simulation of the Rare-Earth Ions Electronic Structure by a Scattered Waves Cluster Method

A.Yu.Kuznetsov[1], A.B.Sobolev[1], J.Andriessen[1], Yu.L.Korol[1]

[1]*Experimental Physics Department, USTU, 620002, Ekaterinburg, Russia*
[2]*Faculty of Applied Physics, Delft University of Technology c/o IRI, Mekelweg 15, 2629 JB Delft, The Netherlands*

Abstract: Results are presented of an investigation of the electron structure of the Ce^{3+} ion. The calculations were performed using the molecular cluster model in quasirelativistic approximation. The effect on calculation results of the MT-parameters variation and making a self-interaction correction are discussed. A variant of estimate of the energy of $4f \rightarrow 5d$ transition for cerium ion in the formalism of the Jonson's Scattered Wave method is proposed.

Keywords: Electronic structure; cluster method; rare-earth ions

Introduction

In calculations of the electron structure of quantum-chemical systems, cluster methods are most universal due to their relative simplicity and the possibility, within the framework of single approach, to describe both an ideal crystal and a crystal with defects. At the same time, cluster models employed in the practical calculations, based on the self-consistent Jonson's Scattered Wave (SW) method [1], make use of a number of approximations: muffin-tin (MT) approximation; local density functional approximation; relativistic effects reference method; boundary conditions reference method. Depending on the concrete structure of ion electron shells, the above approximations may affect the spectrum in different directions, which renders ambiguous the final calculation result. For this reason, finding out the order of error brought in the calculation with each an approximation, i.e., establishing a strict hierarchy of approximations for each type of physical and chemical problems presents a vital issue in the computational solid-state physics. This problem is particularly important in case of rare-earth (RE) ions, in view of the specific nature (shape, length, fast-oscillating type) of the f-electrons wave functions. The purpose of the present paper is to find out the order of errors introduced in cluster calculations by the scattered wave method of the electron structure of 4f ions on an example of Ce^{3+} ions.

Computation parameters

One of the problems addressed in this paper was the investigation of the effect of muffin-tin approximation parameters on one-electron energy spectrum of clusters in simulation of rare- earth ions. In our calculations, a cluster presents a molecule comprising a central sphere with an ion skeleton, and a number of empty spheres (vacancies V) on the cluster periphery. Here, "cluster" is a conditional term, not related to absence of an ion in a cluster. The ion—hollow sphere approximation allows us to consider the results of cluster calculations as pseudo-atomic (ionic), and compare the obtained data with the results of calculating the isolated ions using a Desclaux code [2].

Self-consistent molecular calculations with account for relativistic effects were carried out for cluster $[CeV_6]^{3+}$. Self-consistency was established for the 5d- and 4f- states (other states were considered "frozen"); at that, molecular orbitals e_g and t_{2g} corresponded to the 5d-, and

t_u, t_{2u} and a_{2u}, to the 4f-states. Calculations were made for three configurations: the ones with vacant 5d-state ($4f^15d^0$ configuration), vacant 4f-state ($4f^05d^1$ configuration), and for Slater transition state [3] ($4^{0.5}5d^{0.5}$ configuration). Tangent MT-spheres were selected. Calculations were conducted for three values of vacancy radii (R_v): 0.5, 0.7 and 0.9Å. Cerium ion MT-radii (R_{Ce}) varied within the range of 1.2÷1.5Å. By virtue of the tangency condition, the cerium radius change is connected with the modification of the inter-ionic distance Ce—V. Relativistic effects were taken into account in quasi-relativistic approximation [4], with introduction in the scheme of the self-consistent SW-method.

Results and discussion

The results of calculation for a molecular cluster $[CeV_6]^{3+}$ simulating the Ce^{3+} ion for different configurations are shown in Fig.1. The observed variations reflect the influence of the cluster geometry parameters which are directly linked with the error of the MT potential approximation by form. The results are presented in absolute units, i.e., with account for the position of the MT-zero level relative to vacuum. The energy status of 4f-level for the $4f^15d^0$ configuration (E_{4f}^{occ}) in the case of non-relativistic calculations (Fig.1, a) for different R_v values varies insignificantly (0.3÷0.4 eV) over the entire investigated range of cerium MT-radii variation, staying in the region of 31.3 2 eV. This value is in satisfactory agreement with the results of atomic non-relativistic calculations carried out in the formalism of the local density functional approach (LDA) method for Ce^{3+} ion (-30.6 eV) [5]. The Desclaux code calculation yields the value of E_{4f}^{occ} =37.87 eV. The insignificant change in one-electron energy of the 4f-level at MT-radii variation is connected with a high degree of 4f-wave function localization in the vicinity of Ce^{3+} ion position. According to paper [6], the average valu e for the 4f-wave function $(\langle r^2_{\ 4f})^{1/2}$ is 0.6Å.

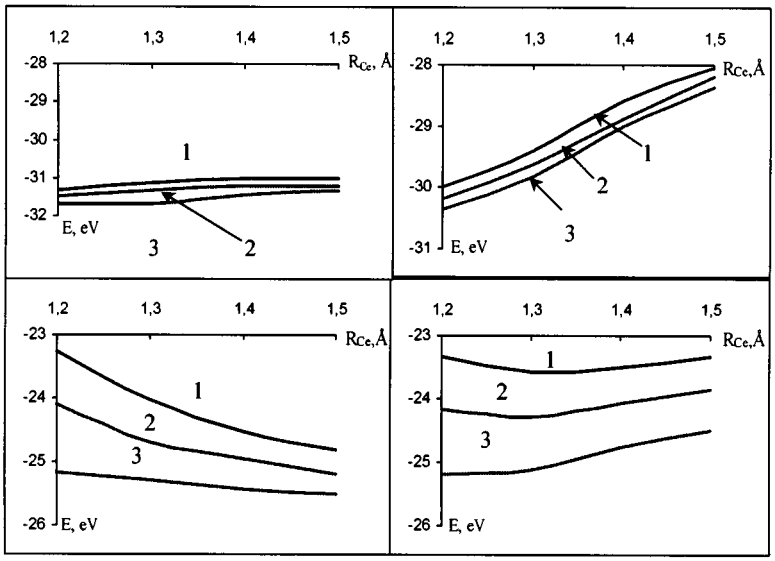

Fig.1. One-electron energies E_{4f}^{occ} (a, b) и E_{5d}^{occ} (c, d) Ce^{3+} ion in nonrelativistic (a, c) and relativistic (b, d) cases for others values of R_v: 1—0.9; 2—0.7; 3—0.5Å

In simulating the cerium ions excited states use is normally made of the $4f^05d^1$ configuration. At that, self-consistency establishment changes the degree of 4f and 5d functions localization as compared with the case of Ce^{3+} ($4f^15d^0$). The general tendency consists in that the functions corresponding to 5d (occupied) states become more localized, while 4f (vacant) functions get de-localized. The nature of the dependence of one-electron energy of the 5d-state (E_{5d}^{occ}) (Fig.1, c) differs from the above-discussed case for the 4f-level. The causes of such spectrum behavior become clear from Fig.2, where the dependences of

radial solutions for 4f- and 5d-wave functions are shown for the case of atomic calculation of an isolated Ce^{3+} ion. Since the wave function for the 5d-state ($4f^0 5d^1$ configuration) is more de-localized for 4f, the change in the geometry parameters of the problem noticeably influences the change in position of E_{5d}^{occ} with the increase in R_{Ce} The change in the level of one-electron energy (ΔE_{5d}) with increase of R_{Ce} is considerable, the maximum value of AE5d (-1.7 eV) being observed for R_V = 0.9Å (Fig.1, c, curve 1).

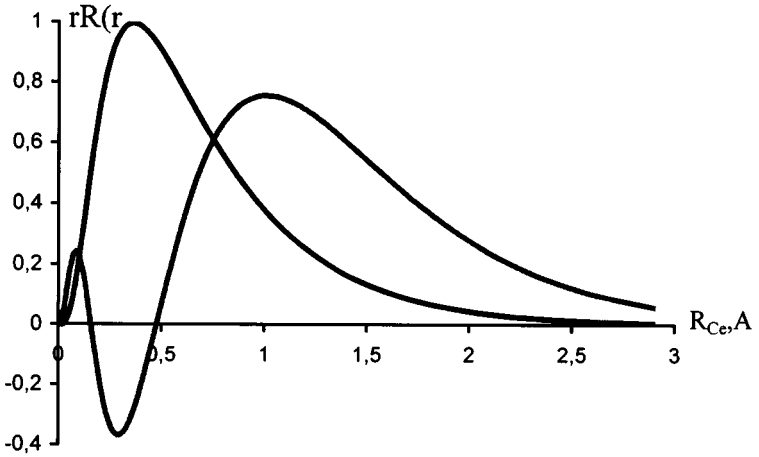

Fig.2. Radial 4f- (1) and 5d- (2) wave functions Ce^{3+} ion obtained by Desclaux code (nonrelativistic case)

The obtained results offer practical methods of cluster simulation of rare-earth ions in crystals by the methods involving use of the MT-approximation. Since there is but a weak dependence of the value of one-electron energy for the 4f-state ($4f^1 5d^0$ configuration) on distance, this brings us to a conclusion that the MT-averaging is responsible for insignificant errors in describing the electronic density of the ground state of a 4f type. At the same time, the error introduced by the MT-approximation is too large for the spectral region related to the excited states (5d-level for $4f^0 5d^1$configuration). Evidently, there are no simple recipes to correct the situation, yet the investigations made establish the order of the error which will always be present in cluster simulation of rare-earth elements by the SW-method, irrespective of other causes.

Let us consider in more detail the relativistic effects influence on the calculation results. Obviously, it is impossible to discriminate the effects from the relativistic and the MT-parameters. Fact is that, with the relativistic corrections being included in the potential construction, the degree of localization of the wave functions decreases, which, in its turn, changes the magnitude of MT-contributions from the given group of states to the overall potential. The dependence of E_{4f}^{occ} on cerium MT-radius in the relativistic case is illustrated in Fig.l, b. With R_{Ce} variation, the value of the relativistic shift lies within 1.3÷3.03 eV, while in the limiting case (R_{Ce} = 1.5Å and R_V = 0.9Å) it is close to such for the atomic LDA-calculations for Ce^{3+} ion: 3.1 eV [5]. The value of E_{4f}^{occ} in our relativistic calculation (-28.05 eV) for this limiting case is also in good agreement with the results given in [5] (-27.54 eV). In case of the $4f^0 5d^1$ configuration (Fig.1, d), the relativistic shift for E_{5d}^{occ} changes its value from 0 to 1.4 eV with Rce varying from 1.32 to 1.5 A, and is directed in the sense opposite to the way it would change with E_{5d}^{occ} variation in the non-relativistic case due to MT-averaging with the increase in Ce MT-radius. In case R_V = 0.9Å (Fig.1, d, curve 1), the value of E_{5d}^{occ} remains practically unchanged with change of R_{Ce}, staying at ~-23.3 eV, and with R_V = 0.5Å (Fig.1, d, curve 3), it varies within -25.2÷-24.5 eV, which is quite close to our result for Ce^{3+} ion obtained using the Declaux relativistic atomic program (-26.095 eV).

The most important parameters in the quantum-chemical calculations of the electronic structure of defects in dielectrics are the position of defect levels relative to crystal zones and estimate of the optical transition energy: excitation or absorption. Normally such estimates may be made with varying degrees of accuracy, depending on the approximations used. Let us consider the possibilities of estimation by the scattered wave method and compare the results with the literature data of atomic calculations performed by the Hartree-Fock (HF) method. All the results that follow (Table) relate to the relativistic case. One-electron energies E_{4f}^{occ} (occupied state) and E_{5d}^{occ} (vacant state) relate to the $4f^15d^0$-, and E_{4f}^{occ} and E_{5d}^{occ}, to the $4f^05d^1$ configurations. The MT-parameters for the SW calculations were selected in view of obtaining the results being ultimately close to the data of atomic calculations by the Declaux program (column D in Table) or those cited in [5] (see above). Through such an approach we had the opportunity to juxtapose the results we had obtained in applying the molecular cluster model with the data of the isolated ions calculation.

Let us compare the absolute values of energies of 5d- and 4f-levels obtained by the SW method with the HF calculation literature data (see Table, columns A and C). The essential differences arise from the known problem of taking in calculation of the self-interaction correction (SIC), which is inherent to any computational method making use of the local form of the exchange-correlation potential [7]. We resorted to the scheme of taking the self-interaction into account for the SW method, disregarding non-orthogonality, earlier in [8]. The above-mentioned problem is missing in the Hartree-Fock theory [9]. We obtained, with account for the above correction, the values for one-electron energies, E_{4f}^{occ} = 39.89 eV and E_{5d}^{occ} = 29.02 eV, our results being in reasonable agreement with the HF calculations data (see Table, columns A and B). Note that the SIC value depends weakly on the MT-parameters, the scope of its change over the entire range of MT-radii R_V and R_{Ce} variation stays within ~3%. In estimating the defect levels position in Ce^{3+}, several approaches may apply: via the total energies difference; the procedure for Slater transition state; the difference of one-electron energies E_{4f}^{occ} and E_{5d}^{occ}; the difference of one-electron energies E_{5d}^{occ} and E_{4f}^{occ}; the difference $E_{5d}^{occ} - E_{4f}^{occ}$. The difference between the energy positions of the f- and d-levels (E_{5d-4f}^{total}) of an atom, as derived by the Declaux program from the total energies difference, was -7.489 eV, and, for the same case, the transition state procedure ($E_{5d-4f}^{0.5}$) yielded -7.527 eV. The value for $E_{5d-4f}^{0.5}$ obtained from the HF calculations was 5.37 eV [10], which likewise poorly agrees with the experimentally found value of6.2 eV [II]. The SW method calculation yielded the values of $E_{5d-4f}^{0.5}$ equal to -9.40 and -19.69 eV, ignoring and including SIC, respectively (see Table). One fact is worth notice: on the one hand, the SW calculation results, accounting for SIC, yield reasonable values for the one-electron energies as compared with the HF calculations; on the other hand, our data for $E_{5d-4f}^{0.5}$ very poorly correlate with the experimental data for the $4f \rightarrow 5d$ transition energy. Thus, while obtaining adequate results for one-electron energies, no feasible way to reasonably estimate the energy of Ce^{3+} ion excitation proceeding from the one-electron energies of the SW calculations may be offered (the same being true for the HF data). The reason is that SIC accounts for the error of incomplete self-interaction compensation in Coulomb energy, leaving out the problem of accounting for the correlation effects. At the same time, no fairly simple methods of accounting for the correlation in using the local potential are available. Through use of fractions for the occupied 4f- and 5d-states, as offered in paper [6], the degree of occupancy may by expressed in terms of the total energy minimum. This is a promising approach; nevertheless is application has been limited so far to calculations of isolated atoms or ions.

One-electron energies and energies of $4f \rightarrow 5d$ transition for Ce^{3+} ion (eV)

Energy Parameters	A	B	C	D
E_{4f}^{occ}	-28.05	-39.89	-37.495	-29.495
E_{5d}^{virt}	-21.04	-21.04	-18.044	-24.265
E_{4f}^{virt}	-37.38	-37.38	—	-36.154
E_{5d}^{occ}	-24.49	-29,02	-29.602	-26.095
$E_{5d-4f}^{0.5}$	9.40	17.68	—	7.527
E_{5d-4f}^{total}	—	—	5.37	7.489

A—our results wit lout SIC; B—our results with SIC;
C—HF date from []; D—results due to Desclaux program.

A more reasonable method of simulation in cluster or molecular calculations may be the calculation of $4f^0 5d^1$ configuration, since in the latter case the correlation effects contribution is considerably smaller than that in case of the $4f^1 5d^0$ configuration. Further estimation of the 4f-level position may be made proceeding from either the experimental, or the calculated data for the $4f \rightarrow 5d$ transition energy. Here we should take notice of an additional circumstance in relation to the calculation of Ce^{3+} impurity in oxides. Since the 5d-state position in energy gap of an oxide crystal may be defined relative to the oxygen 2p-state only, the SIC for states 5d of Ce^{3+} and 2p of oxygen need not be made simultaneously. It was shown in paper [12] on simulation of defects in MgO that SIC for the states in charge of the valence band upper limit value (oxygen p-state) amounts to ~4 eV. According to the present paper, SIC for the 5d-state was found to be close in value. By generalizing these results for the case of cluster simulation of rare-earth ions in oxides, we may assert that the $4f^0 5d^1$ configuration calculations may be made without bringing in the SIC. The thus obtained results, namely: the 5d-level position relative to crystal axis; 5d-level orbital splitting in crystal field; other estimates related to electron density distribution, should be regarded as "non-empirical". A similar approach was applied in interpreting the HF-calculation results [13], where the authors were compelled to make an empirical adjustment in the one-electron energies calculation. In general, our data show that the methods based on LDA approximation, in their classical formulation, fail to define the absolute position of the 4f-shell energy and the absorption energy due to a strong influence of the 4f-electrons correlation.

Conclusions and summary

The hereby presented investigations establish the order of the effect of MT-approximation parameters on the one-electron spectrum of rare-earth elements for the SW method. The results closest to the isolated ions calculations were obtained at maximum values of cerium MT-radii and minimum "vacancy" radii. In real crystals, such a set of parameters is physically impossible due to the crystal lattice structure. The simplest solution to the given situation might be an a posteriori adjustment of the results relative to the one-electron spectrum, based on comparison with the model calculation data. The values of respective corrections to one-electron levels are construed proceeding from analysis of the dependences of the values of one-electron energies on the MT-radii variation, and their comparison with the atomic calculations. It was shown that use of the $4f^1 5d^0$ configuration does not allow to estimate the ground state absolute energy and the rate-earth ions absorption energy. On the basis of a numerical experiment, a method of cluster simulation of a rare-earth ion was proposed, consisting in the $4f^0 5d^1$configuration calculation followed by an a posteriori estimation of the absorption energy.

Acknowledgements.

The work was carried out with the support of the NWO program (grant 96/801) and the Russian Foundation for Fundamental Research, grant 98-03-33195a.

References

1. K.H.Johnson, *Adv. Quant. Chem*. 7 (1973) 143.
2. J.P.Desclaux, *Comp. Phys. Commun*. **9** (1975) 31.
3. J.C.Slater, *The Self-Consistent Field for Molecules and Solid.* McGraw-Hill Publ. Inc., New-York 1974.
4. J.H.Wood, and A.M.Boring, *Phys. Rev*.—**B 18** (1978) 2701.
5. P.Cortona, S.Doniach, and C.Sommers, *Phys. Rev*. **A 31** (1985) 2842.
6. M.-A.Perrin, and E.Wimmer, *Phys. Rev*. **B 54** (1996) 2428.
7. S.Lundqvist, and N.H.March (Ed.), *Theory of Inhomogeneous* Electron Gas, Plenum Press, New-York, 1983.
8. A.B.Sobolev, *Fiz. Tverd. Tela,* **35** (1993) 2509.
9. R.A.Heaton, J.G.Harrison, and C.C.Lin, *Phys. Rev*. **B 31** (1985) 1077.
10. R.Visser, J.Andriessen, P.Dorenbos, and C.W.E.Van Eijk, *J. Phys.: Condens. Matter*. **5** (1993) 5887.
11. W.C.Martin, R.Zalubas,and L.Hagan, *Atomic Energy Levels*—The Rare-Earth Elements, NBS, Washington, 1978.
12. A.B.Sobolev, *Fiz. Tverd. Tela,* **36** (1994) 2926.
13. H.Merenga, *Electronic Structure Calculation on Cerium-Containing Crystals*: *Towards a Better Understanding of Scintillation in Ionic Crystals,* Delft: Delft University Press.—III. Thesis Delft University of Technology, 1997.

Electron band structure and optical characteristics calculation of A_nBO_4 crystals

Yu. A. Hizhnyi, M. U. Bilyi, S. G. Nedelko

Optics department of the Physics faculty ,Taras Shevchenko Kyiv University
6, acad. Glushkova av., Kyiv, Ukraine

Abstract: The results of semiempirical LCAO calculations of electron band-structure and optical constants for potassium sulfate K_2SO_4, potassium chromate K_2CrO_4 and two crystal modifications of lead tungstate $PbWO_4$ are presented. Semiempirical parameters of the method are determined from experimental data by means of fitting of the calculated energy levels of molecular oxyanion CrO_4^{2-} to experimental absorption spectrum of potassium sulfate. Calculated spectral dependence of the imaginary part of dielectric constant $\varepsilon_2(\omega)$ is compared to experimental reflection in optical and UV-region. Assumptions concerning the applicability of chosen computational approach to the explanation of optical features of complex ion-covalent crystals are made.

Keywords: electron, band-structure, calculation, oxide, crystals.

1. Method of calculations

Effective electron band-structure calculations for oxide crystals like lead tungstate are complicated by several factors: their crystal composition is nontrivial (up to 24 atoms per unit cell), hard atoms with large number of core electrons are present (Pb, W), both ion and covalent types of electron bonds are available. Only in recent years the power of computational technique afforded an opportunity to carry out suchlike zone calculations by *ab-initio* methods [1]. The majority of these methods were elaborated and tested earlier on considerably simpler compounds. But in the case of oxide crystals the rapidity of modern computers still forbids a full adaptation of those approximations in electron structure evaluation that form the basis of prevailing computational methods. Almost all of nevertheless adjusted calculational models require expensive computational resources (up to necessity for a «parallel supercomputers»). On the contrary, the semiempirical methods are greatly less critical for computer time. Therefore they have not yet lost the relevance when being applied to a complicated crystals like $PbWO_4$.

In this work we present the results of semiempirical LCAO (Linear Combination of Atomic Orbitals) calculations of the optical constants for A_nBO_4 (A = Pb, K; B = W, S, Cr) oxide crystals. In this method a solution $\Psi(\vec{k})$ of one-electron Shrödinger equation for a crystal is composed as a linear combination $\Psi(\vec{k}) = \sum_\alpha c_\alpha \chi_\alpha(\vec{k})$ of Bloch wavefunctions $\left|\chi_\alpha(\vec{k})\right\rangle = \sum_i e^{i\vec{k}\vec{r}_i}\left|b_\alpha(\vec{r}-\vec{r}_i)\right\rangle / \sqrt{N_p}$ where α denotes the number of atomic orbital, $\vec{r}_i$ - position of the atom, b_α - atomic wavefunction, N_p - the amount of atoms involved into summation. Using the variation procedure, one can obtain the system of equations $\sum_\alpha \langle\beta|\hat{H}|\alpha\rangle c_\alpha - Ec_\beta = 0$ that yields steady-state one-electron energy levels for a given wave vector $\vec{k}$. Hamiltonian matrix elements are: $H_{\alpha\beta}(\vec{k}) = \sum_{i,j}\exp\left(i\vec{k}\left(\vec{r}_i - \vec{r}_j\right)\right)\langle j,\beta|H|i,\alpha\rangle / N_p$ where $\langle j,\beta|\hat{H}|i,\alpha\rangle$ - interatomic matrix elements.

In the original formulation of the method, made by Harrison [2], diagonal matrix elements $H_{\alpha\alpha}(\vec{k})$ were substituted by ionization potentials of appropriate atomic states, while off-diagonal ones - by semiempirical parameters, that were obtained from experimental data for ordinary crystals like Ge, Si, etc. In our calculations we use the set of parameters, that were determined via fitting of the calculated energy levels of molecular oxyanion CrO_4^{2-} to experimental absorption spectrum of K_2CrO_4 in aqueous solution. Potassium chromate crystals are characterized by meaningful spectral bands, which are insensitive to crystalline defects. This fact gainfully distinguishes them from a heavier representatives of given class of compounds. According to a widely-spread viewpoint, such molecular anions XO_4^{2-} (X = W, Cr, S, etc.) basically form spectral properties of oxide crystals in the region of fundamental absorption.

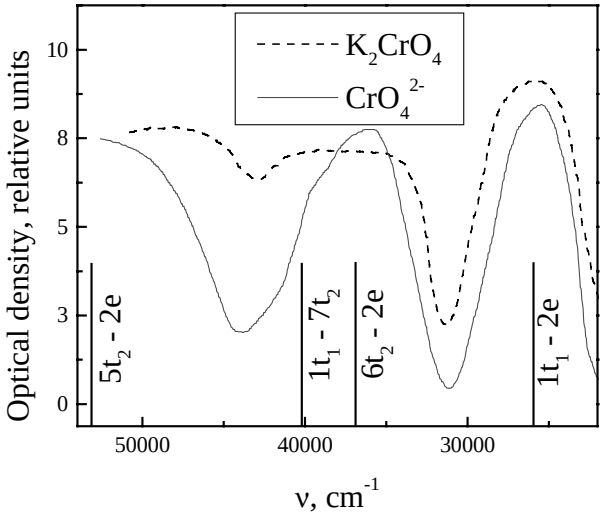

Fig. 1. Absorption of K_2CrO_4 (dashed line) and CrO_4^{2-} anion in saturated solution of K_2CrO_4 (solid line). Calculated transitions in anion are indicated by vertical lines.

We have applied the present method to the energy calculations of CrO_4^{2-} molecular cluster (regular tetrahedron with interatomic distance Cr-O equal to averaged length of corresponding bond in K_2CrO_4 crystal [3]) replacing appropriate variables by definite values for particular molecule. Semiempirical parameters of the method, validated by Harrison, we used only as a first approximation. Via variation procedure we obtained a set of coefficients and basis orbitals energies that ensured the best agreement between cluster energy levels and experimental absorption of CrO_4^{2-} anions in K_2CrO_4 aqueous solution (fig. 1).

2. Calculations of the optical properties of oxide crystals

Spectral dependence of the imaginary part of dielectric constant $\varepsilon_2(\omega)$ was calculated using the expression [4]:

$$\varepsilon_2(\omega) = \frac{4\pi^2 e^2 \hbar}{3m^2\omega^2} \sum_{n,s} \int_{BZ} \frac{2}{(2\pi)^3} \delta(\omega_{ns}(k) - \omega) \left| M_{ns}(k) \right|^2 d^3k \qquad (1)$$

where indexes n and s correspond to filled and unfilled bands respectfully,

$$\omega_{ns}(\vec{k}) = (E_s(\vec{k}) - E_n(\vec{k}))/\hbar \ , \qquad \left| M_{ns}(\vec{k}) \right|^2 = \left| (\Psi_n(\vec{k}) \left| \vec{\nabla} \right| \Psi_s(\vec{k})) \right|^2 .$$

I order to obtain $\varepsilon_2(\omega)$ from experimental absorption spectra we used Kramers-Kronig relation in approximations of [5]. All calculations were done for single polarization along $\vec{a}$ crystallographic axis. In the calculations of density of states (DOS) for K_2CrO_4, $\varepsilon_2(\omega)$ and DOS for K_2SO_4 we account 2s and 2p orbitals for oxygen, 3s and 3p - for sulfur, 4s and 3d for chromium, 4s - for potassium. On the integration over Brillouin zone $E(\vec{k})$ was calculated in 343 points of it's irreducible part. Radial parts of atomic wavefunctions $b_\alpha(|\vec{r} - \vec{r}_i|)$ were taken for neutral atoms according to [6]. The results of DOS calculations for potassium chromate and sulfate are shown in Fig. 2 and comparison between DOS and experimental reflection R(E) is presented in Fig. 3.

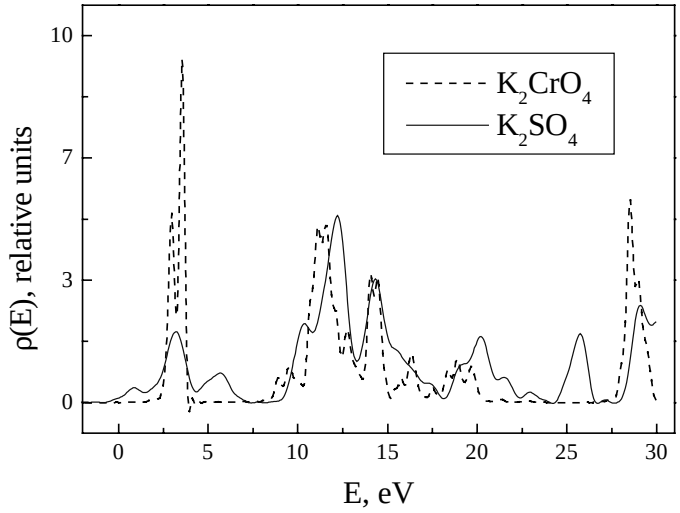

Fig. 2 Calculated density of states for potassium sulfate K_2SO_4 (solid) and potassium chromate K_2CrO_4 (dashed).

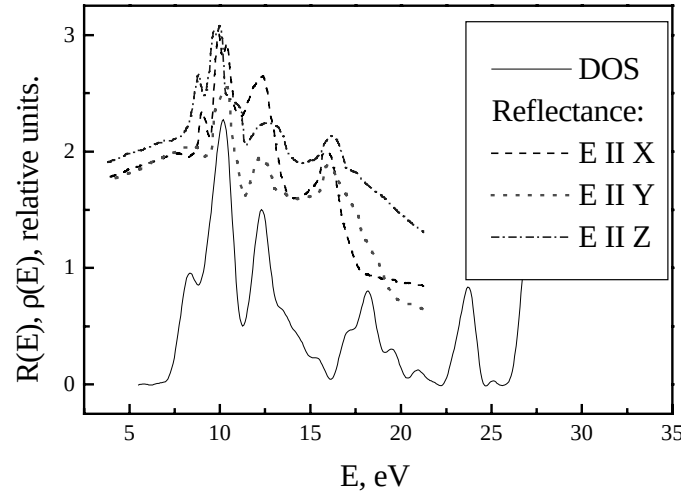

Fig. 3 Calculated DOS (solid) and experimental reflectance according to [9] (dashed) for K_2SO_4.

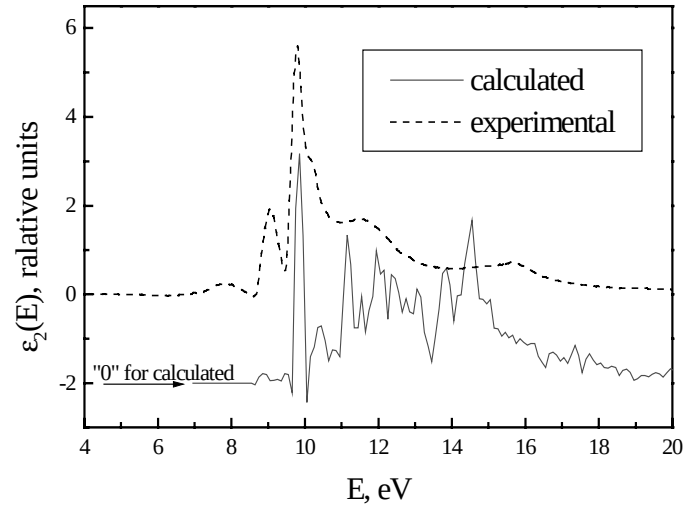

Fig. 4 The imaginary part of dielectric constant for K_2SO_4: theoretically calculated (solid) and obtained from experimental data [7] (dashed).

We can discern from Fig. 3 the energy region 5 - 15 eV, where spectral distribution of ρ(E) and R(E) are quite similar, up to the coincidence of three bands with maxima at 7, 10.5 and 12.5 eV. Calculated and experimentally obtained $\varepsilon_2(E)$ spectra for K_2SO_4 are presented in Fig. 4.

Theoretical calculation of $\varepsilon_2(E)$ for lead tungstate $PbWO_4$ in two crystal modifications - sheelite (tetragonal) and raspite (monoclinic) - was carried out by the same method and approximations as for potassium chromate. Some details of band-structure evaluation for these compounds one could find in our previous work [8]. 2s and 2p orbitals were taken into account for oxygen, 6s and 6p - for lead and 6s, 5d - for tungsten. There was only one significant dissimilarity between lead tungstate calculations and those for K_2CrO_4: we had used Slater-type radial atomic wavefunctions [9].

Experimental reflection spectra of lead tungstate (Fig. 5) were employed for determination of experimental $\varepsilon_2(E)$ - Fig. 6. Considerable discrepancies in spectral distribution of reflectance are obvious for different experiments. This feature is often attributed to the diversity of growing conditions. Theoretical spectrum of $\varepsilon_2(E)$ bears analogy to the curve 6a (see Fig. 7) for raspite and to 6c or 6d (see Fig. 8) for sheelite.

The correlation in spectral peculiarities between theoretical and experimental curves shown at Fig. 2 and Fig. 8 is evident. Therefore we are eligible to assert the presented semiempirical method to be substantially applicable for the calculation of optical constants of complex oxide crystals.

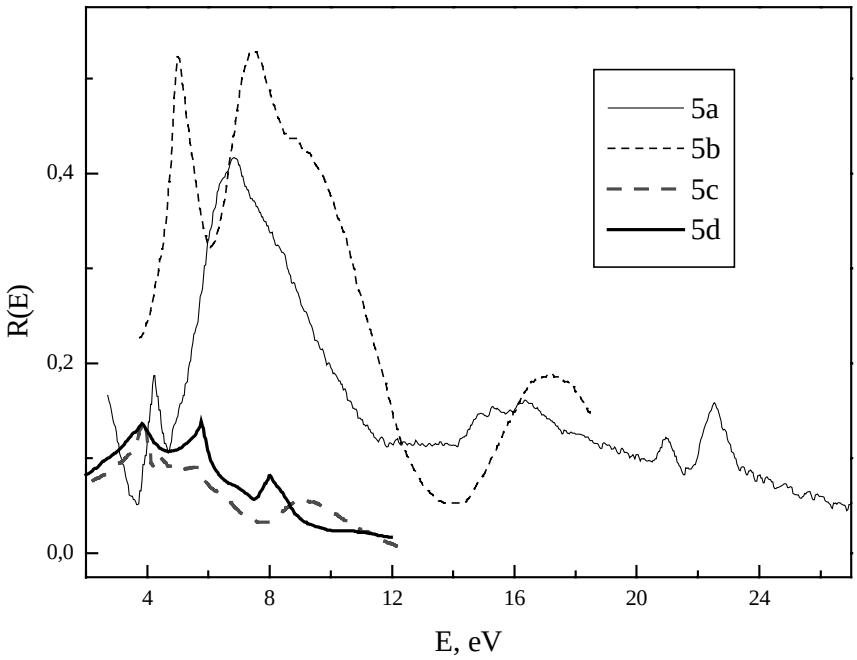

Fig. 5 Reflectance of «pure» (5a, 5b, 5c) and Mo-doped (5g) $PbWO_4$ crystals. 5a and 5b were taken from [10] and [11]; 5c, 5d - own data.

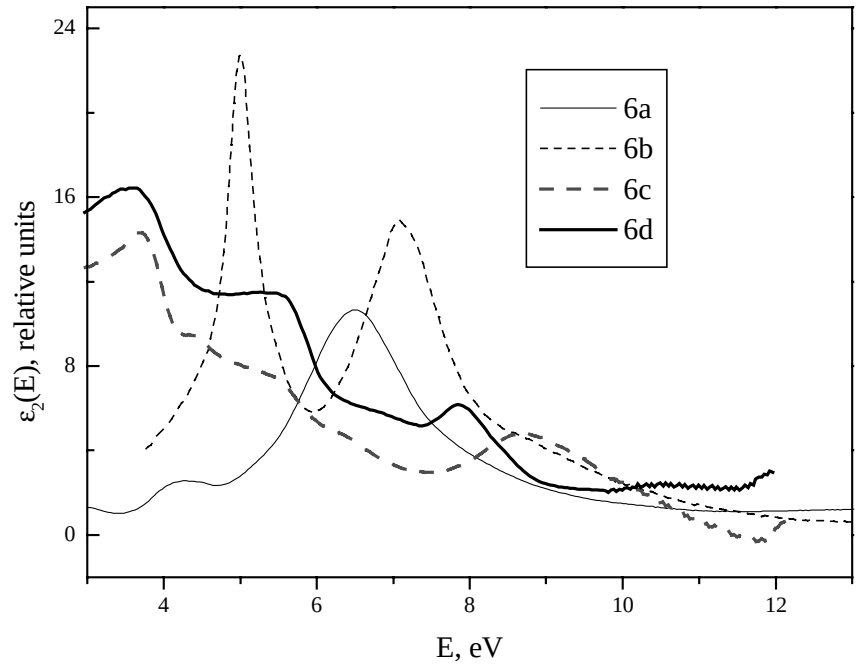

Fig. 6 The imaginary part of dielectric constant for $PbWO_4$ obtained from experimental reflectance. 6a, 6b, 6c - correspond to «pure» crystals, 6d - to Mo-doped

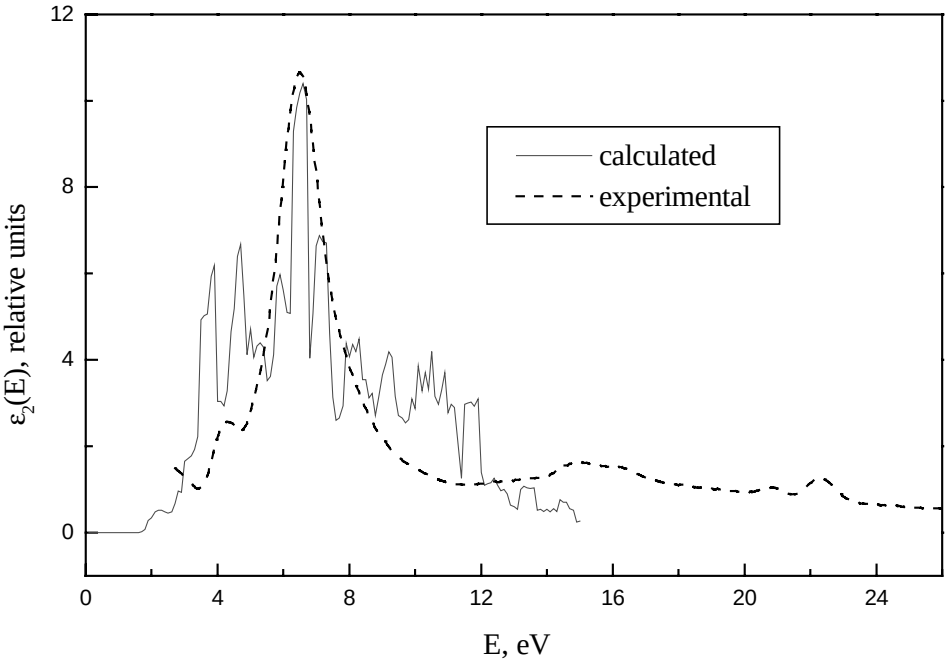

Fig. 7 The imaginary part of dielectric constant $\varepsilon_2(E)$ for monoclinic crystal modification of $PbWO_4$: theoretically calculated (solid) and obtained from experiment (dashed).

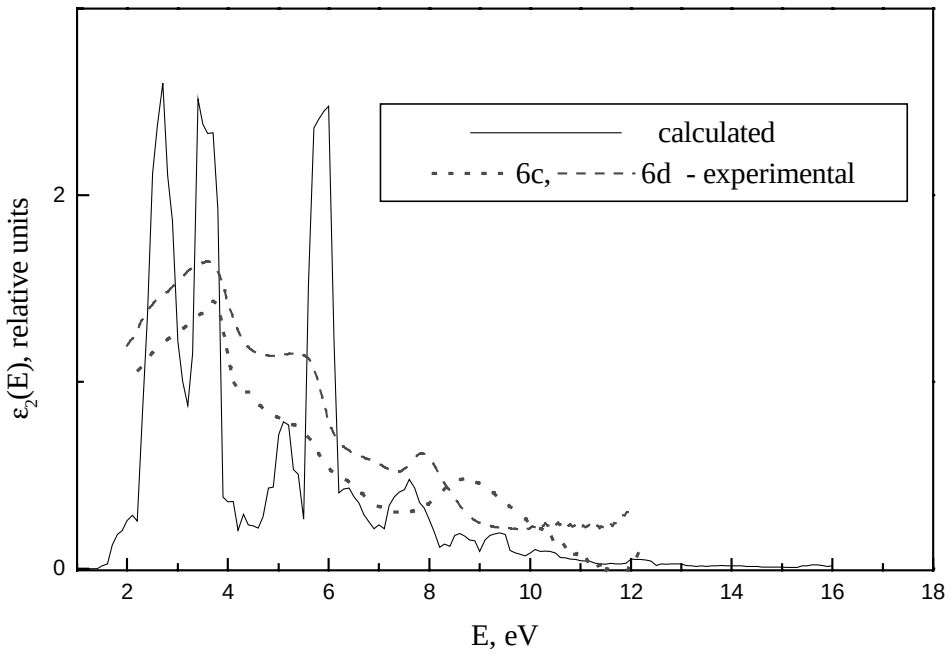

Fig. 8 The imaginary part of dielectric constant $\varepsilon_2(E)$ for orthogonal crystal modification of $PbWO_4$: theoretically calculated (solid) and obtained from experiment (dashed).

3. Conclusions

1. Comparison between calculations of the imaginary part of dielectric constant $\varepsilon_2(\omega)$, compared with appropriate experimental data for complex oxide crystals, prove a sufficient effectiveness of semiempirical LCAO method used.
2. The best agreement between theory and experiment in the description of electronic properties takes place in the energy region, that corresponds to the upper part of a valent band.

3. The obtainment of semiempirical parameters from clearly interpretable experimental absorption of potassium chromate K_2CrO_4 can be accounted as a well-chosen approach in the electron band-structure calculations for lead tungstate $PbWO_4$ and other oxide crystals.

References

1. Y. Zhang, N. A. W. Holzwarth, and R. T. Williams, Phys. Rev. **B 57** (1998) 12738
2. W. A. Harrison, Electronic structure and properties of solid state (in Russian), Mir, Moscow, 1983
3. J. A. Mc.Ginnety, Acta Cryst. **B28** (1972) 162
4. D. Brust, Phys. Rev. **134** (1964) A1337
5. Ya. O. Dovhyj, I. V. Kityk, The electronic structure and optics of the nonlinear crystals (in Ukrainian), Svit, Lviv, 1996
6. C. F Bunge, J. A. Barrientos, A. V. Bunge, Atomic Data and Nuclear Data Tables **53** (1993) 113
7. I. V. Kityk, B. V. Andriyevskyj, V. O. Yuvshenko, Phys. Stat. Sol. (b) **182** (1994) K79
8. S. G. Nedelko, Yu. A. Hizhnii, Ukrainian Phys. J. **42** (1997) 101
9. P. Gombash, The multiparticle problem in quantum mechanics, Izdatiniit, Moscow, 1953
10. V. Kolobanov, J. Becker, M. Runne, A. Schroeder, and others, Proc. Intern. Conf. SCINT'95, Delft, the Netherlands (1996) 249
11. E. G. Reut, Proc. Intern. Conf. PhYSCI'94, Delft, the Netherlands (1995) 147

Time-resolved spectroscopy of self-trapped excitons in oriented BeO crystals under X-ray and VUV excitations

V.A. Pustovarov[1], V.Yu. Ivanov[1], A.V. Kruzhalov[1], I.N. Ogorodnikov[1], G.N. Kulipanov[2], É.I. Zinin[2], M. Kirm[3] and G. Zimmerer[3]

[1]*Experimental Physics Dept., Urals State Technical University, Mira Street 19, 620002 Ekaterinburg, Russia*
[2]*Budker Institute of Nuclear Physics, RAS, Lavrentiev Ave. 11, 630090 Novosibirsk, Russia*
[3]*II. Institute of Experimentalphysics of the Hamburg University, Luruper Chaussee 149, D-22761 Hamburg, Germany*

Abstract: The paper presents the results of a complex study of electronic excitation dynamics for single crystal BeO carried out by the use of the low-temperature optical and luminescent VUV spectroscopy with sub-nanosecond time-resolution under photoexcitation by synchrotron radiation. The decay kinetics (1 ns -500 ns) of the photoluminescence, reflectivity (8-35 eV), time-resolved emission (2.5-10.4 eV) and luminescence excitation (6-35 eV) spectra were measured at 9.6 K and 295 K for the oriented BeO crystals . A large variety of radiative relaxation channels of the electronic excitations, as well as the multiplicity of the excited states of self-trapped excitons, depending on the crystal orientation, exciting photon energy and temperature were revealed and are discussed.

Keywords: beryllium oxide (BeO), luminescence, self-trapped exciton, time-resolved VUV - spectroscopy, synchrotron radiation

1. Introduction

It is known, that self-trapped excitons (STE) in broad band-gap oxides were discovered more than twenty years ago. However, all the suggested models for these STE as well as the channels of the STE formation are still under discussion. To date it was found that these STE are inherent in the oxides with a low local symmetry of the anion positions (*e.g.* SiO_2, Al_2O_3, $YAlO_3$, $Y_3Al_5O_{12}$) [1]. As a rule, these compounds demonstrate only slightly the typical excitonic structure of the optical constant spectra in the photon energy range around the fundamental absorption edge (FAE). On the contrary, the high-symmetry oxides (*e.g.* MgO, CaO) exhibit usually a well-resolved excitonic features in the optical constant spectra, despite the fact that STE is not realized in these crystals.

Hexagonal beryllium oxide crystal BeO (E_g=10.63 eV) is formed by the anion tetrahedra distorted along the optical axis ***C***. Because of this, the local symmetry of BeO is reduced to C_{3v}, and there are both the ‘base’ and ‘axial’ configurations of the BeO lattice defects. In the case of the trapped hole centres the ‘base’ configuration is associated either with a hole localized on the orbital of one of the three equivalent off-axis oxygens in the anion tetrahedron or with a hole, tunneling between these three equivalent positions. The axial configuration of the defect is usually attributed to a hole localized at the axial oxygen in the same tetrahedron [2-4].

Our first investigations of the photoluminescence (PL) excitation spectra over the 8-35 eV energy and 77-300K temperature regions for the BeO emission bands at 4.9 и 6.7 eV have been made at the Nuclear Physics Institute in Novosibirsk by the use of the synchrotron radiation (SR) of the VEPP-2M storage ring. For the energy ranges of both the excitonic and interband transitions we have revealed not only the main features of the 4.9 eV and 6.7 eV PL

excitation spectra, but the principle differences between them as well. From these results we have developed a model of two kinds of STE in beryllium oxide crystal [2,3].

The next step in this field was made through the use of the time-resolved luminescent spectroscopy of BeO under excitation by the non-filtered X-ray synchrotron radiation (XSR) in the range from 3 eV to 62 keV (Φ =(0.1÷6)×10^{16} photons·s^{-1}·cm^{-2}) from the VEPP-3 storage ring. For the first time we revealed a premeditated population of some states not only for the optical centres in BeO, but for the excitonic states as well. The results of a study of both the luminescence decay kinetics and orientation effects allowed us to put forward a hypothesis about splitting of the multiplet excitonic states and radiative transitions from the singlet states in BeO [5].

The main goal of the present paper is not only a further investigation of the relaxation processes for the electronic excitations (EE) in , but a study of the channels of a creation of the excited states of STE as well. The work was made by the use of the time-resolved luminescent spectroscopy with sub-nanosecond time-resolution over the UV- and VUV-emission ranges under selective photoexcitation of PL for the oriented BeO crystals at 9.6 and 295 .

2. Experimental Details

All the examined BeO crystals were grown by V.A. Maslov through the use of the advanced flux method [6]. The content of impurities in the BeO samples was analysed using a laser mass-spectrography method [4,7]. The samples of the BeO single crystals were produced in the form of a prism or a plane-parallel plate with the naturally occurring facets oriented either parallel or perpendicular, regarding to the main optical **C**-axes.

The experiments were performed at the SUPERLUMI station of HASYLAB at DESY [8]. The luminescence in the 2.5-6.0 eV region was analyzed by a Czerny-Turner mounting monochromator equipped with a photomultiplier (PM) R2059 (Hamamatsu). For the emission in the VUV range was usd a 0.5 m vacuum monochromator equipped with PM R1460 (Hamamatsu). Two in situ interchangeble gratings of the 2 m primary monochromator, Al and Pt coated, were applied in measurements of the PL excitation spectra over the 6-35 eV energy range. A typical spectral resolution was 0.25 nm. The PL excitation spectra were corrected for the equal number of the exciting photons for each energy region, but the emission spectra are presented as they are measured. Time-resolved spectra were recorded within a time window (Δt) correlated with the arrival of SR pulses (delay δt). In present experiments the delay and width were δt_1=2.2 ns, Δt_1=8.2 ns for the fast component, and δt_2=23 ns, Δt_2=111 ns for the slow component. Simultaneously with the excitation, the reflection spectra were recorded at the angle of incidence of 17.5° by a XP2230B PM (Valvo) with a help ofa sodium salycylate coated window.

3. Experimental Results

We revealed that the crystallographic orientatation of BeO, relative to the electrical vector of the exciting radiation ***E***, may have a dramatic effect on both the PL emission and PL excitation time-resolved spectra. For example, the fast component of PL for BeO at ***E*** **||** ***C*** exhibits at least two emission bands at 4.0 eV and 5.0 eV with FWHM of ~1.0 eV (Figure 1*a*,*b*). The emission spectrum of the fast component is shifted in its spectral position towards the long-wavelength side as the energy of the exciting photons increases from the FAE to the range of interband transitions. From the PL excitation spectrum for the fast component it follows that the 4.0 eV emission band is more effectively excited in the energy range around the $E_{n=2,\ 3}$ maxima of the excitonic absorption, whereas the 5.0 eV emission band is effectively excited in the energy range adjacent to the first excitonic maximum (Figure 2*a*).

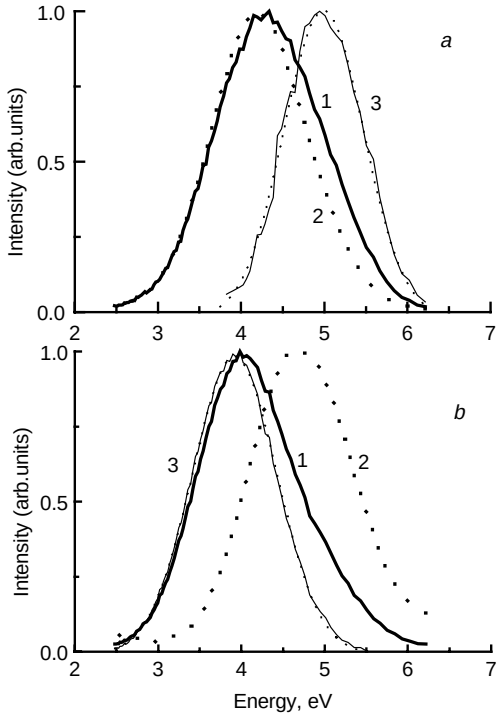

Figure1. Time-resolved photoluminescence spectra of BeO (T=9,6K) at the orientation ***E*** ‖ ***C*** and the excitation energies 10.25 eV (a) and 10.7 eV (b): 1- the spectrum in 'fast' time window; 2 - the spectrum in 'slow' time window; 3 – the spectrum of their difference and its fitting by Gaussian.

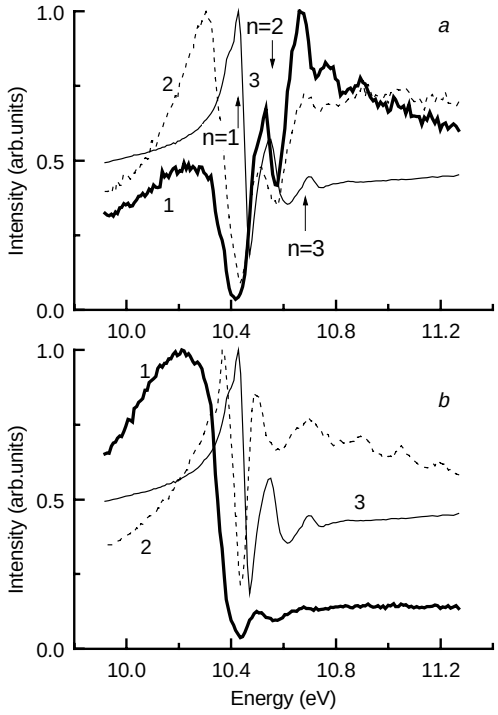

Figure2. The excitation spectra of ultraviolet luminescence 3.35 eV (1) and 4.75 eV (2) of BeO (T=9.6K) measured in 'fast' (a) and 'slow' (b) time windows at the orientation ***E*** ‖ ***C*** in comparison with reflection spectra (3).

The fast component of the 4.0 eV emission band on photoexcitation around $E_{n=2}$ at 9.6 K demonstrates a decay time equal to 2.2 ns, whereas that for the 5.0 eV emission band at photoexcitation around $E_{n=1}$ exhibit τ=4.4 ns (Figure 3). It should be noted that we have previously revealed the 4.0 eV emission band with τ=2 ns on excitation by XSR, however the second fast component (5.0 eV) was not observed there because of its fairly narrow the effective excitation energy range around $E_{n=1}$. A slow stage of the decay kinetics in BeO at ***E*** ‖ ***C*** is represented by two emission bands at 4.2 eV and 4.7 eV (Figure 1*a*,*b*). First of them is more effectively excited in the 9.5-10.2 eV energy range, below $E_{n=1}$. In this connection, the 4.2 eV emission band was attributed to a radiative relaxation of the electronic excitations localized on the impurity or lattice defects (Figure 2*b*). Notably, on excitation by the 9.5 eV photons at 9.6 K, the initial stage of a decay kinetics of the 4.2 eV luminescence is characterized by two components with τ=2.7 ns and 34 ns. At the same time, the 4.7 eV emission band is characterized by a decay kinetics with τ_1=54 ns and τ_2=36 ms. In doing so, the τ_2 component covers up to 95% of the total light yield.The PL excitation spectrum of the slow component of the 4.7 eV emission band is comparable with that for the 'fast' component of the 5.0 eV emission band, namely, the 4.7 eV luminescence is more effectively excited in the energy region adjacent to $E_{n=1}$ (Figure 2*a*,*b*).

The fast component of the 4.0 eV luminescence at a different orientation of the BeO crystal (***E*** ⊥ ***C***) is only slightly pronounced (Figure 3). Almost the same result was obtained in our previous work with the use of the XSR-excitation [5]. However, we have never observed the fast component of the 5.0 eV luminescence at the ***E*** ⊥ ***C*** orientation, even though the energy of the exciting photons was varied over all the 6-40 eV energy range. The

slow component (τ=52 ns) at this orientation is concentrated at the 4.6 eV emission band (Figure 4) and its PL excitation spectrum differs from that for the fast component of the 4.0 eV emission band only by a more effective excitation around $E_{n=1}$ (Figure 5). On photoexcitation at 9.6 K we have observed no fast components for the 6.7 eV emission band. The main component of the VUV-luminescence decay kinetics is fitted by an exponentian with τ=340 μs. This was in a full agreement with our previous results [2,5]. The VUV-luminescence of BeO at the ***E*** || ***C*** orientation is effectively excited around $E_{n=2,3}$ as well as in the region of creation of separated electron-hole pairs (Figure 6). However, this luminescence is more effectively excited in the range of interband transitions ($E > E_g$) than in the excitonic region. It should be noted that the profile of the VUV PL excitation spectrum for ***E*** || ***C*** looks like that for a fast component of the 4.0 eV emission band. At the ***E*** ⊥ ***C*** orientation, the VUV PL excitation spectrum varies over a wide range. The VUV luminescence is more effectively excited around $E_{n=1}$, whereas the excitation efficiency in the range of the interband transitions ($E > E_g$) is considerably less pronounced (Figure 6). Figure 7 demonstrates the steady-state PL excitation spectra for both the UV- and VUV-emission bands of BeO (***E*** || ***C***) at 9.6 K. One can see significant differences between these two PL excitation spectra not only in the exciton energy range, but in the range of the electronic excitation multiplication (EEM) at $E >$ 20 eV. The energy threshold for the EEM effect is equal to $2E_{n=1}$ for the 6.7 eV emission band, and ~$2E_g$ for the 4.8 eV emission band.

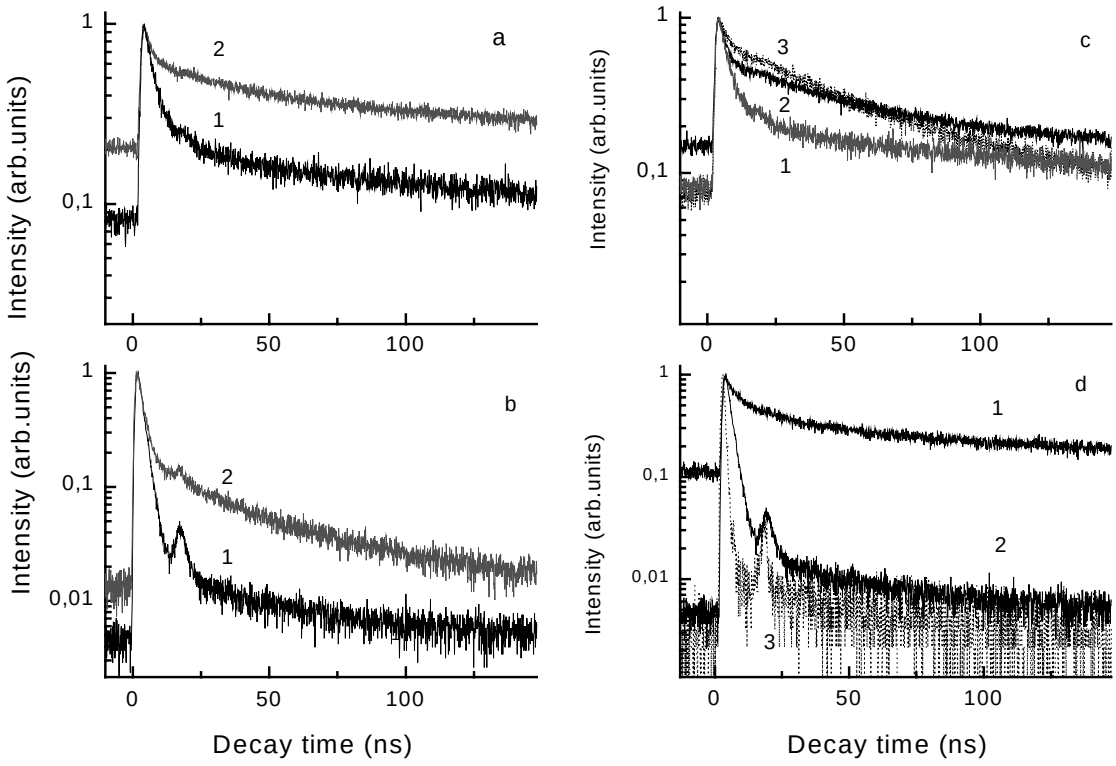

Figure 3. The PL decay kinetics for BeO at 9.6 K: (*a*) - E_m=5.0 eV, E_{ex}=10.24 eV, ***E*** || ***C*** (1), ***E*** ⊥ ***C*** (2)**;** (*b*) - E_m=3.35 eV, E_{ex}=10.67 eV, ***E*** || ***C*** (1), ***E*** ⊥ ***C*** (2); (*c*) - ***E*** || ***C***, E_m=5.0 eV, E_{ex}=10.24 eV (1), 10.67 eV (2) and 11.27 eV (3); (*d*) - ***E*** || ***C***, E_m=3.35 eV, E_{ex}=10.24 eV (1), 10.67 eV (2)**;** the excitation pulse recorded using the registration system (3).

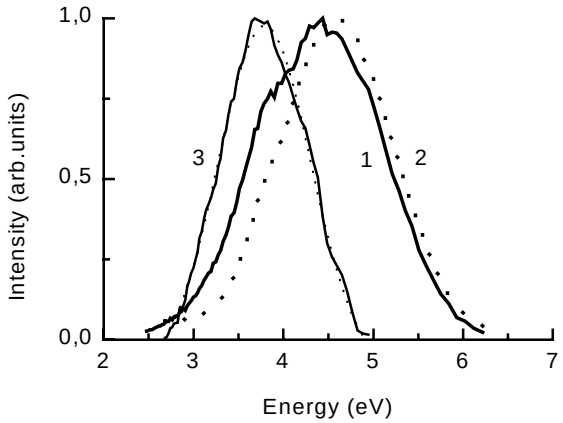

Figure 4. Time-resolved photoluminescence spectra of BeO (T=9,6K) at the orientation $\boldsymbol{E} \perp \boldsymbol{C}$ and the excitation energy 10.25 eV: 1- the spectrum in 'fast' time window; 2 - the spectrum in 'slow' time window; 3 –the spectrum of their difference and its fitting by Gaussian.

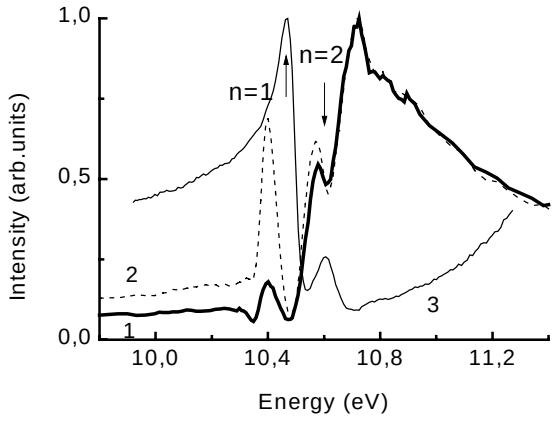

Figure 5. The excitation spectra of ultraviolet luminescence 3.35 eV (1) and 4.75 eV (2) of BeO (T=9.6K) measured in 'fast' (1) and 'fast' (2) time windows at the orientation $\boldsymbol{E} \perp \boldsymbol{C}$ in comparison with reflection spectra (3).

4. Discussion

Presented experimental results demonstrate that fast BeO luminescence at 4.0 eV exhibits fairly specific spectral, kinetic, orientation and polarization features, which set the 4.0 eV emission band apart from the previously studied luminescence of the triplet STE in BeO. In addition, the 4.0 eV luminescence band can not be associated with any of the impurity or lattice defects in BeO. From the BeO electronic structure it can not be associated with the core-valence transitions, resulting usually in a typical fast emission in some crystals. The profile of the PL excitation spectra for the 4.0 eV emission band directly specifies its intrinsic origin and supports our previous hypothesis [2,3] concerning its association with the singlet STE. It should be noted that the relaxation of an exciton onto the lowest radiative singlet level proceeds from the $E_{n\,=\,2,3}$ excitonic states as in alkaline iodides [9]. However, BeO exhibits more pronounced red-shift of the singlet level, and this fact points on a substantial lattice relaxation. The fast luminescence at 5.0 eV should be considered in a similar manner. In fact, from the profile of the excitation spectrum of the 5.0 eV emission band it follows its intrinsic origin, however the relaxation of an exciton proceeds from the $E_{n=1}$ excitonic level. The analysis of the experimental results allowed us to put forward the picture of relaxation of the intrinsic EE in BeO at 9.6 K. From this picture it follows that at the $\boldsymbol{E} \parallel \boldsymbol{C}$ orientation, the 5.0 eV and 4.7 eV emission bands (the characteristic time-constants of 4.4 ns and 54 ns, respectively) are effectively excited on creation of the excitons in a ground state $E_{n=1}$. The creation of the excitonic states $E_{n=2,3}$ results in more effective excitation of a fast 4.0 eV luminescence (τ=2.2 ns) and the 6.7 eV luminescence (τ = 340 μs). The picture considerably changes for the opposite orientation ($\boldsymbol{E} \perp \boldsymbol{C}$): the 6.7 eV luminescence can be effectively excited only around $E_{n=1}$, whereas the fast 4.0 eV luminescence at this orientation is considerably suppressed even at excitation in the $E_{n=2,3}$ energy range. At the same time, the fast 5.0 eV luminescence is not observed, and a slow component (τ~52 ns) of a luminescence decay kinetics is represented by an intensive band at 4.6 eV. The UV- and VUV PL excitation spectra differ noticiably in profile over the photon energy range of creation of electron-hole pairs, starting above 11 eV. In terms of theory of hot scattering of electron-hole pairs, this suggests that the UV and VUV emission bands differ also in respect to the migration energy losses. In fact, the formation of radiative state for the 6.7 eV emission band takes place without energy losses, i.e. the place of self-trapping practically coincides with the birthplace

of the non-relaxed EE, but a creation of that for the 4.8 eV emission band occurs after a sufficient migration of the initial EE. The high value of σ_0 = 0.60 in the Urbach's rule for BeO suggests a strong exciton-phonon interaction as well.

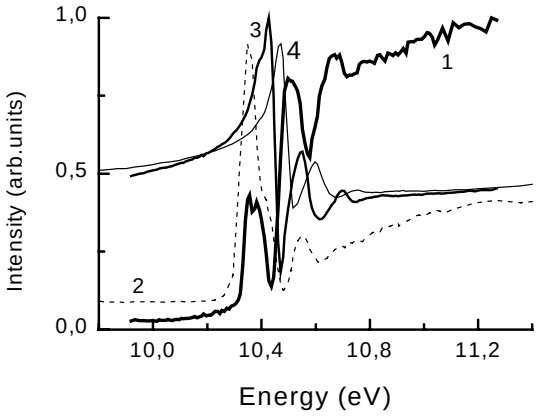

Figure 6. The excitation spectra of VUV-luminescence 6.7 eV of BeO (1,2) in comparison with reflection spectra (3,4) at the orientation ***E*** **||** ***C*** (1,3) or **E** ⊥ **C** (2,4), T=9.6K.

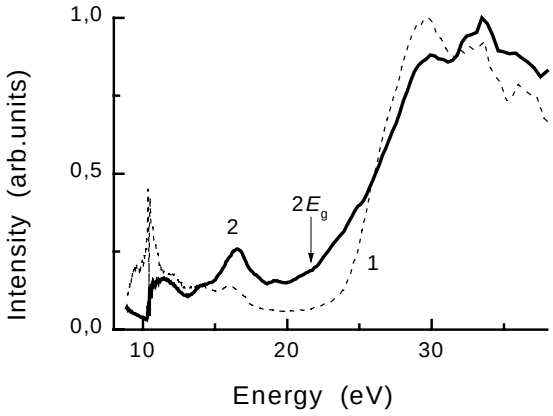

Figure 7. The excitation spectra of UV-luminescence 4.8 eV (1) and VUV-luminescence 6.7 eV (2) at the orientation ***E*** **||** ***C***, T=9,6K.

5. Conclusion

In present work the time-resolved PL spectra in the energy region from 2.5 eV to 10.4 eV, time-resolved PL excitation spectra over the broad energy range from 6 eV to 35 eV, decay kinetics of PL and reflectivity of the oriented single crystals of BeO at 9.6 K and 295 K were measured. We have revealed a number of the different channels of radiative relaxation of EE in BeO using a low-temperature VUV-spectroscopy. This method allowed us not only to separate with confidence the intrinsic and extrinsic emission bands, but to proof experimentally the various multipletisy of the relaxed excitonic states. A general picture of the EE relaxation in BeO looks fairly complicate. The EE relaxations from the basic and excited excitonic states result in creation of various emission centres. Their population depend on orientation and temperature of a crystal.

References

1. Ch. Lushchik, In 'Excitons', E. Rashba and M. Sturge, Eds., p. 505, North-Holland, Publ. Conf., Amsterdam, 1982
2. V. Ivanov, V. Pustovarov, S. Gorbunov, A. Kruzhalov, Fiz. tverd. Tela, **36**(9) (1994) 2634
3. V. Ivanov, V. Pustovarov, S. Gorbunov, et al., Fiz. tverd. Tela, **38**(11) (1996) 3333
4. I. Ogorodnikov, A. Kruzhalov, Material Science Forum, **239-241** (1997) 51
5. V. Pustovarov, V. Ivanov, A. Kruzhalov, É. Zinin, Fiz. tverd. Tela, **36**(5) (1994) 1523
6. V. Maslov et al., Proc. 6th Intern. Confer. On Cryst. Growth, p 268, Moscow, 1980
7. S. Gorbunov, A. Kruzhalov, M. Springis, Phys. Stat. Solidi (b) **141** (1987) 293
8. G. Zimmerer, Nucl. Instr. And Meth. **A 308 (**1991**)** 178
8. T. Matsumoto, M. Shirai, K. Kan'no. J. Phys. Soc. Japan **64**(3) (1995) 987

Predictability of 5d level positions of the triply ionized lanthanides in halogenides and chalcogenides.

Pieter Dorenbos

Radiation Technology Group, Interfaculty Reactor Institute, Delft University of Technology, Mekelweg 15, 2629 JB Delft, The Netherlands

Abstract: Information on 4f-5d transition energies of the triply ionized lanthanides (Ce3+, Pr3+ ,..., Lu3+) in over 300 different halogen and chalcogen compounds has been gathered, analyzed and occasionally re-interpreted. Some of the main results will be presented. From clear patterns that emerge from the data, the position of 5d levels of yet uninvestigated lanthanide doped materials can be predicted.

Keywords*:* lanthanides; 5d-4f transitions; crystal field depression.

Introduction

Transitions between the $4f^n$ ground state and low lying $4f^{n-1}$-5d levels of the triply ionized lanthanides play an important role in many luminescent devices. Figure 1 shows that the wavelength of absorption and emission depends both on the type of lanthanide ion and the type of host crystal. The typical doublet 5d→4f ($^2F_{5/2}$,$^2F_{7/2}$) emission of Ce^{3+} in for example $LiYF_3$ is located in the ultra violet near 310 nm, whereas in Lu_2S_3, the luminescence is located in the red part of the spectrum. The 4f5d→$4f^2$ transitions of Pr^{3+} is at considerably shorter wavelength than if Ce^{3+} is the dopant. The Nd^{3+} $4f^25d→4f^3$ luminescence is usually located in the vacuum ultra violet below 200 nm.

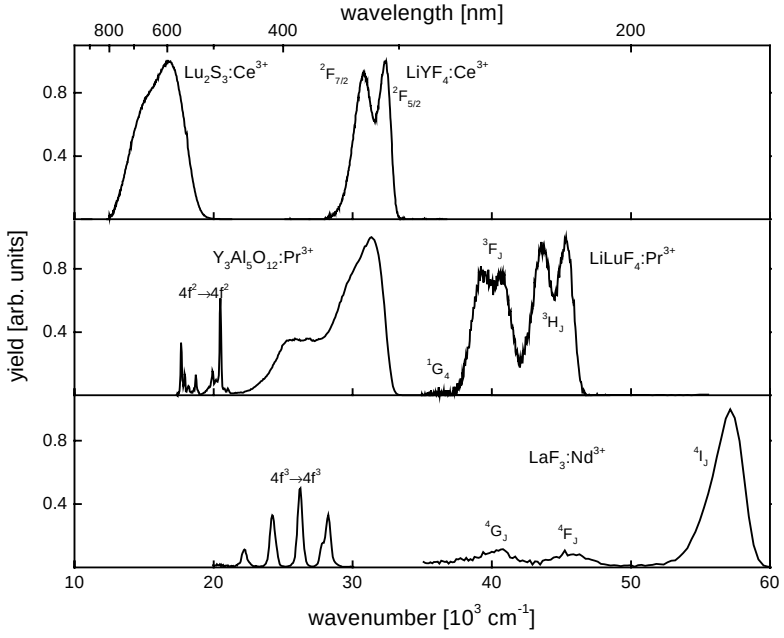

Figure 1: X-ray excited emission spectra of: Ce^{3+} in Lu_2S_3 and $LiYF_4$, Pr^{3+} in $Y_3Al_5O_{12}$ and $LiLuF_4$ and Nd^{3+} in LaF_3.

It is well known that from the 5d level energy of Ce^{3+} in a specific compound, the 5d level energy of other lanthanides in that compound can be predicted fairly well. The first electric dipole allowed transition in Pr^{3+} is usually found at 12,500 cm^{-1} higher energy [1,2,3]. Nd^{3+} and Tb^{3+} are usually found at 22,000 and 14,000 cm^{-1} higher energy [1]. The aim of this work is to study these energy differences in more detail. What are the values of these energy differences for the other lanthanides, and are they really constant irrespective the type (fluorides, chlorides, bromides, iodides, oxides, sulfides, selenides) of compound. For that and other purposes, a research has been performed on the literature on 4f-5d transitions of the lanthanide ions. Information has been gathered, critically analyzed and occasionally re-interpreted, comprising about 330 different compounds and 13 different Ln^{3+} dopants (Ce^{3+}, Pr^{3+}, Nd^{3+}, ..., Yb^{3+}, Lu^{3+}).

Data on $4f^n \rightarrow 4f^{n-1}5d$ transitions

The gathered information on the first electric dipole allowed *fd* absorption in Ce, Pr, Nd, Sm, Eu, and Gd is shown in Figure 2. The *fd* energy difference of Ln^{3+} in compound *A* denoted as $\Delta E(Ln,A)$, is plotted against the energy of the first electric dipole allowed *fd* transition, $\Delta E(Ce,A)$ of Ce^{3+} in that same compound. The data for Pr^{3+} and Nd^{3+} show a constant energy difference with those of Ce^{3+} despite the fact that the absolute variation in *fd* energy of Ce^{3+} amounts more than 30,000 cm^{-1}. Although information on Sm^{3+} and Eu^{3+} is only known for a few fluoride host crystals, they also show a constant energy difference with Ce^{3+}. What can be observed for the energy of the *fd* absorption transition in Ce, Pr and Nd does also hold for the energy of the *df* emission to the ground state. This is illustrated by the full data symbols in Figure 2. Actually this implies that there is no significant difference of Stokes shift between these three lanthanides. The situation for the lanthanides with more than half filled 4f shell is slightly different in a sense that the first electric dipole allowed transition is not the *fd* transition of lowest energy. There are always spin forbidden 5d levels located at lower energy [4]. Both the electric dipole allowed transition and the most intense spin forbidden transition in Tb^{3+}, Dy^{3+},..., Yb^{3+} show the same behavior. Whether the lanthanide ions are in free space, doped in fluoride crystals, in oxides, chlorides or sulfides and despite the fact that the absolute value of $\Delta E(Ln,A)$ may change by more than 30,000 cm^{-1} from compound to compound, $\Delta E(Ln_1,A) - \Delta E(Ln_2,A)$ remains surprisingly constant.

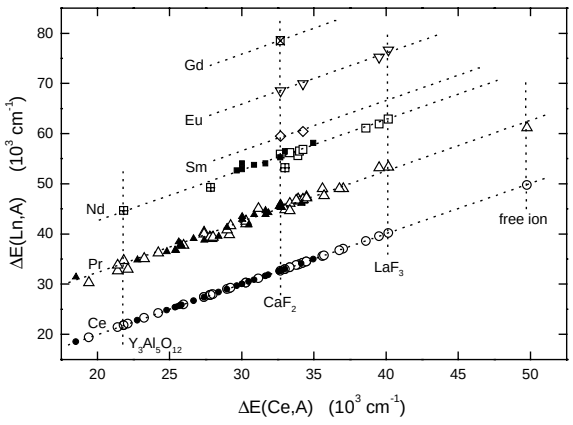

Figure 2. $\Delta E(Ln,A)$ plotted against $\Delta E(Ce,A)$ for different compounds *A*. Solid data symbols pertain to information derived from emission wavelengths.

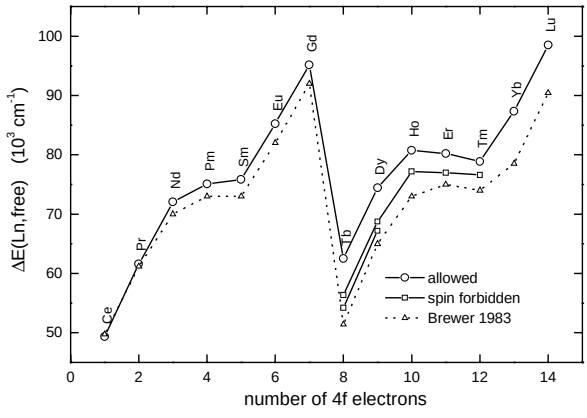

Figure 3. Predicted values for $\Delta E(Ln,free)$ also values predicted by Brewer [5] are shown.

Having established this, it is now possible to predict the *fd* transition energy of all lanthanides in a compound with an accuracy of typically ±600 cm^{-1} once the *fd* transition energy of only one of the lanthanides in that compound is known. This corresponds with a wavelength accuracy of ±5 nm which is smaller than the typical FWHM of *fd* absorption bands. Since most information in literature is available on $\Delta E(Ce,A)$, it is convenient to introduce the following expression

$$\Delta E(Ln, A) = \Delta E(Ce, free) - D(A) + \Delta E^{Ln,Ce} \quad (1)$$

$D(A)$ is the so-called depression value of the 5d levels in compound A. It expresses the amount by which the *fd* energy is lowered when the lanthanide is doped in a crystalline environment. $\Delta E^{Ln,Ce}$ is a short hand notation for the average value of $\Delta E(Ln, A) - \Delta E(Ce, A)$. The values for $\Delta E^{Ln,Ce}$ as function of *Ln* together with the standard deviation and the number of data points used in the averaging procedure are compiled in Table 1. By putting $D(A) = 0$, one obtains estimates for the $\Delta E(Ce,A)$ values of the gaseous Ln^{3+} ions. The thus estimated energies of both the lowest energy electric dipole allowed and the most intense spin forbidden $4f^{n-1}5d$ transition for all free trivalent lanthanides $\Delta E(Ln,free)$ are compiled in Table 1 and displayed in Figure 3.

Table 1. Values for $\Delta E^{Ln,Ce}$ averaged over N different host crystals together with its standard deviation. If Ln=Tb,..., Tm then in addition $\Delta E^{Ln,Ce}$ values for the most intense spin forbidden *fd* transition are compiled. $\Delta E(Ln,free)$ is the value predicted for the free lanthanides. Values for Pm^{3+} are estimations based on interpolation. All energy values are in cm^{-1}.

Ln	$\Delta E^{Ln,Ce}$				$\Delta E(Ln,free)$	
	allowed *fd*	N	forb. *fd*	N	allowed *fd*	forb. *fd*
Ce	0	--	--	--	49340	--
Pr	12240±750	64	--	--	61580	--
Nd	22720±650	18	--	--	72060	--
Pm	(25740)	0	--	--	(75080)	--
Sm	26500±455	2	--	--	75840	--
Eu	35910±380	4	--	--	85250	--
Gd	45820	1	--	--	95160	--
Tb	13160±950	28	7010±860	22	62500	56350
Tb[a)]	--	--	4870±300	4	--	54210
Dy	25100±610	4	19400	1	74440	68740
Dy[a)]	--	--	17840	1	--	67180
Ho	31800±1400	5	27830±220	2	81140	77170
Er	30880±540	7	27650±400	9	80220	76990
Tm	29540±370	8	27260±210	6	78880	76600
Yb	38010±570	3	--	--	87350	--
Lu	49170	1	--	--	98510	--

[a)] for Tb^{3+} and Dy^{3+} two values are compiled for the spin forbidden transitions observed at energies lower than the spin allowed transition.

The main result of this study is that the influence of the compound on the *fd* transition energy of all lanthanides can be expressed in one single parameter, i.e. the depression value *D(A)*. Since also the Stokes shift appears in first approximation independent on the type of lanthanide ion, it can also be regarded as a property of the host crystal. From all data collected, values for *D(A)* and $\Delta S(A)$ has been calculated. The values for *D(A)* pertaining to about 330 different compounds are displayed in Figure 4. The compounds are grouped into the fluorides, chlorides, bromides, iodides, oxides, sulfides and selenides. For the special case that the lanthanide ion is Ce^{3+}, the right side y-axis shows the absorption wavelength of the first electric dipole allowed *fd* transition. The depression values of LaF_3, $LaCl_3$, $LaBr_3$, La_2O_3, La_2O_2S, and La_2S_3 have been connected by dashed line segments. Figure 4 demonstrates that the increase of covalency between the lanthanide ion and the anion ligands yields an increasing depression value and a red shift of the absorption and luminescence bands. It is outside the scope of this paper to further discuss the relation between the crystallographic, physical or chemical properties of the host and the values for the depression.

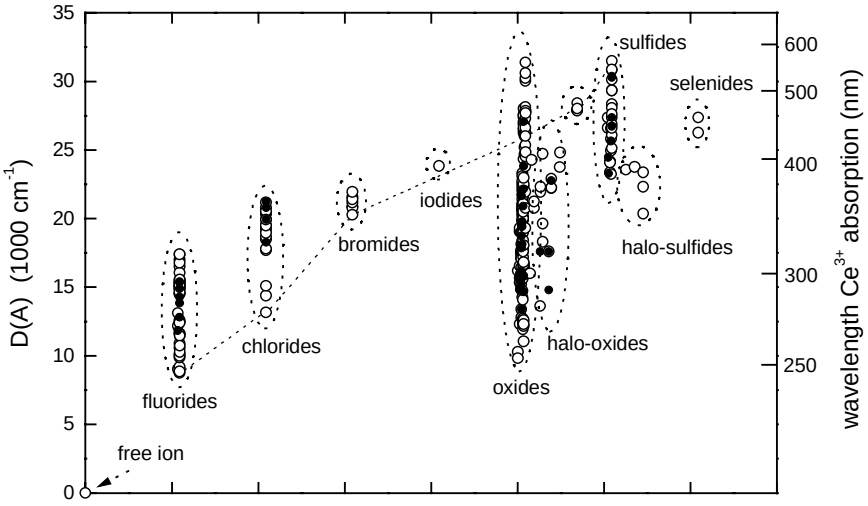

Figure 4: Open symbols, depression values of the triply ionized lanthanides determined from *fd* absorption data. Closed symbols, data estimated from *df* emission spectra. The right side axis shows the wavelength of the first electric dipole allowed *fd* transition in case that Ce^{3+} is the dopant. The dashed line connects the depression values for LaF_3, $LaCl_3$, $LaBr_3$, La_2O_3, La_2O_2S and La_2S_3.

Figure 3 shows that the *fd* energy difference varies irregularly through the lanthanide series. Experimentally it is well known that this variation is quite similar for the neutral, singly and doubly ionized lanthanides [6]. Based on these known variations and the experimentally known values for *ΔE(Ln,free)* of Ce^{3+}, Pr^{3+} and Yb^{3+} Brewer in 1971 [6] and based on the values for Ce^{3+}, Pr^{3+} and Lu^{3+} Sugar et al. in 1973 [7] predicted the *ΔE(Ln,free)* values for the other gaseous triply ionized lanthanides. Later in 1983 Brewer [5] presented new estimates based on new experimental data. These new estimates are also displayed in Figure 3. According to Brewer [5], the large variation of *ΔE(Ln,free)* through the lanthanide series is almost entirely determined by the ionization energy of the $4f^n$-shell. This ionization energy is large for the half filled and the fully filled 4f-shells of Gd^{3+} and Lu^{3+} resulting in large values for *ΔE(Ln,free)*. The values *ΔE(Ln,free)* for Ce^{3+} and Tb^{3+} are about 40,000 cm^{-1} lower. These ions have ground state configurations $4f^1$ and $4f^8$, and the ionization energy of the 4f-core is relatively low.

Even up until today the *ΔE(Ln,free)* values of Nd, Pm, Sm, Gd, Dy, Ho, Er, and Tm have not been established experimentally, and the values by Brewer [5] are the most reliable predictions available. The values predicted in this work have an entirely different origin. They are based on values extrapolated from data on the triply ionized lanthanides whereas the values by Brewer are based on extrapolations from lanthanide ions with lower charge state.

Implications for scintillator research

If one is interested in fast scintillators with a decay time shorter than 100 ns, the optical transitions involved should be electric dipole allowed. For the triply ionized lanthanides starting with Tb^{3+} until Yb^{3+} having more than half filled 4f-shell this is usually not the case. The first electric dipole allowed transition starting from the ground state multiplet of these lanthanides is always located at higher energy than several of the spin forbidden $4f^n \rightarrow 4f^{n-1}5d$ transitions. Multiphonon relaxation from the higher lying state to the lower spin forbidden states will then result in spin forbidden transitions with consequently long decay times. For efficient and fast scintillators the lanthanides with less than half filled 4f shell are the only candidates. Figure 2 and 3 show that Sm^{3+}, Eu^{3+} and Gd^{3+} will have the first electric dipole allowed transition at very high energy, deep into the vacuum ultra violet. 5d-4f luminescence has never been observed for these ions because $4f^{n-1}5d$ states always relax to high lying $4f^n$ states. Since Pm^{3+} is radioactive the only remaining lanthanides for fast scintillators are Ce^{3+}, Pr^{3+} and Nd^{3+}.

From the gathered information on *df* transitions, *D(A)* and *ΔS(A)* values of about 330 different halogen and chalcogen compounds are available [8], see Figure 4. With the help of Eq. (1) the wavelength of the first electric dipole allowed *fd* absorption and *df* emission to the ground state for Ce^{3+}, Pr^{3+} and Nd^{3+}, but also for the other lanthanides, can then be predicted with typically 5 nm accuracy.

References

1. G. Blasse, J.P.M. van Vliet, J.W.M. Verwey, R. Hoogendam, M. Wiegel, J. Phys. Chem. Solids, 50(6) (1989) p.583.
2. A.J. de Vries, G. Blasse, Mat. Res. Bull., 21 (1986) p.683.
3. G. Blasse, Chemical Physics Letters, 146(3,4) (1988)p.343.
4. L.J. Nugent, R.D. Baybarz, J.L. Bernett, The Journal of Physical Chemistry, 77(12) (1973) p.1528.
5. L. Brewer, "Systematics and the Properties of the Lanthanides", edited by S.P. Sinha, D.Reidel Publishing Company, Dordrecht, The Netherlands (1983) p.17.
6. L. Brewer, Journal of the Optical Society of America, 61(12) (1971) p.1666.
7. J. Sugar, J. Reader, The Journal of Chemical Physics,59(4) (1973) 2083.
8. P. Dorenbos, to be published.

Optical and scintillation properties of Ce^{3+}-doped fluorides

[1]Dujardin C. , [1]Blanc W., [1]Gâcon J.C., [1]Pedrini C., [1,2]Belsky A.N., [2]Kamenskikh I., [3]Fouassier C. and [4]Bourgeois S.

[1]Laboratoire de Physico-Chimie des Matériaux Luminescents, U.M.R. CNRS 5620, Université Lyon1
[2]Synchrotron Radiation Laboratory, Physics Faculty, Moscow State University
[3]Institut de Chimie de la Matière Condensée de Bordeaux, U.P.R 9048 CNRS, Université Bordeaux I
[4]Laboratoire de Recherches sur la réactivité des Solides, U.M.R. 5613 CNRS, Université de Bourgogne

Abstract: Influence of lutetium in scintillation processes is presented in fluorides materials. Comparative study of LaF_3-LuF_3 and $LiYF_4$-$LiLuF_4$ doped with Ce^{3+} is performed. X-ray photoelectron spectroscopy measurement on $LiYF_4$ and $LiYF_4$:5%Lu allow to draw an energy band scheme. Major information is that Lu 4f band is above the top of F 2p generally considered as the valence band. Vacuum ultra-violet spectroscopy shows how lutetium influences the energy transfer from free electrons and holes to cerium. Scintillation processes of compounds appear to be very different.

Keywords***:*** lutetium, fluorides, LuF_3,LaF_3,$LiLuF_4$,$LiYF_4$, Ce^{3+}

Introduction

Research of fast and dense scintillators with high light output promotes studies of lutetium based cerium doped materials. A lot of oxides have been studied while few lutetium based fluorides have been investigated. LuF_3:Ce^{3+} seems to have a very good light yield contrary to LaF_3:Ce^{3+}. From handbook of X-ray and UV photoelectron spectroscopy, we can get the binding energy in the range of the valence band: Lu4f: 12-13 eV; F2p: 17.4 eV; O2p: 13.6 eV (for free ions) . In crystals, these energies can be shifted slightly. One can note that Lu4f should give rise to a band which overlaps the valence band. Since all the holes created by high-energy excitation relax toward the top of the valence band before transferring to the activator, lutetium may play an important role in the energy transfer processes. We propose a comparative study of LuF_3, LaF_3, $LiLuF_4$, $LiYF_4$ doped with Ce^{3+}.

Light yield

Light yield of single crystals have been measured: 440 Ph/Mev for LaF_3 [1], 8000 Ph/MeV for LuF_3 [2], from 2180 to 6290 Ph/Mev for $LiYF_4$ and 3780 Ph/Mev for $LiLuF_4$ [3] all doped with Ce^{3+}. Nevertheless, light yield is cerium concentration dependent and the distribution coefficient in Lu-based samples is very important. The crystal shape may influence the light yield as well. We measured then emission spectrum from powders under x-ray excitation under the same conditions to obtain comparative light yield on these materials with the same cerium concentration (0.5at.%). In powders, the concentration is much easier to control than in single crystals. The x-ray tube high voltage was set at 40kV and the sample holder was carefully oriented in the same position for all samples. 2 mm thick powder was deposited to ensure the full absorption of x-rays (broad energy distribution maximum around 30 keV). As a result, LuF_3:0.5%Ce gives 50 times more light than LaF_3:0.5%Ce, and $LiYF_4$:0.5%Ce and $LiLuF_4$:0.5%Ce exhibit a slightly lower light yield than LuF_3:0.5%Ce. Of course, these results are not fully accurate since penetration depth of x-rays is not the same from sample to sample

due to the changes of density. Nevertheless, it gives the order of magnitude and the difference between LuF_3:0.5%Ce and LaF_3:0.5%Ce is remarkable. Even LuF_3:0.5%Ce light yield is better than CeF_3, suggesting changes in terms of energy transfer processes.

X-ray photoelectron spectroscopy (XPS)

In ref. [4], we performed XPS measurements on several samples including LaF_3:Ce, $LuAlO_3$:Ce, Lu_2SiO_5 (LSO) and $LiLuF_4$. First, it was shown that in fluoride compounds doped with cerium, the energy difference between Ce4f and the valence band (F2p) is more important than in oxides. This plays an important role for hole capture by Ce^{3+} and then for electron-hole pair transfer to cerium [5,6]. Second, in the region of the valence band, a very intense peak assigned to the 14 4f electrons of Lu, overlaps the O 2p or F 2p in LSO and $LiLuF_4$ spectrum. But in LSO, a tail appears on the low energy part of the 4fLu band. This tail does not appear in fluorides. We suspected that the top of Lu4f lies above the top of F2p and below O2p. To avoid the very intense band from lutetium, we compare XPS spectrum of $LiYF_4$ and $LiYF_4$:5%Lu (fig. 1)

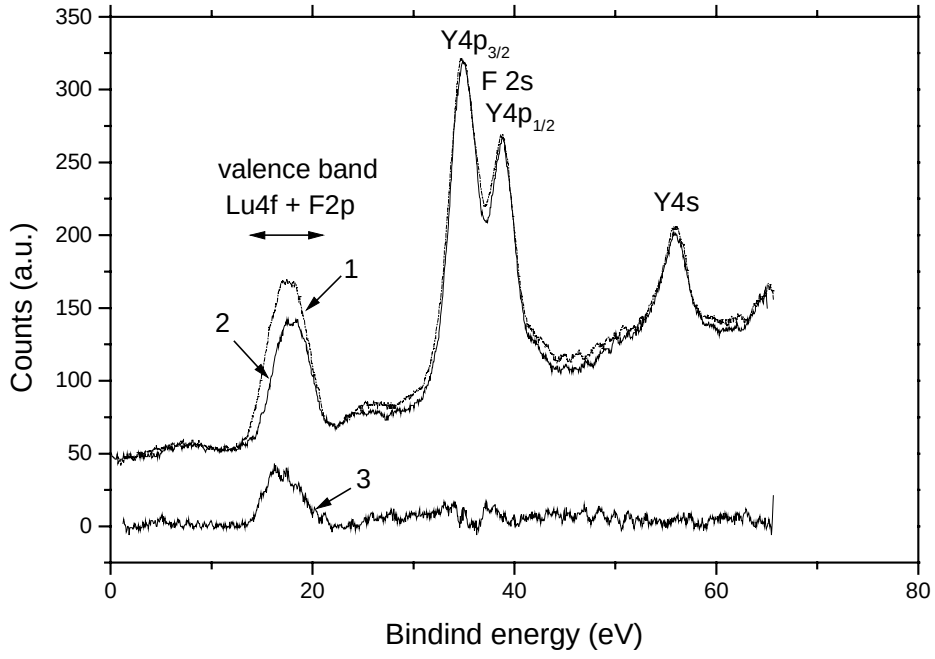

Figure 1. XPS measurements performed on powders (1) $LiYF_4$:5%Lu, (2) $LiYF_4$. (3) is the difference between (1) and (2).

Difference between both spectra show clearly that Lu4f is lying at 1-2 eV above the top of F2p in lutetium based materials. It is always hard to define precisely the onset and the end of each band, because the edge is not sharp.

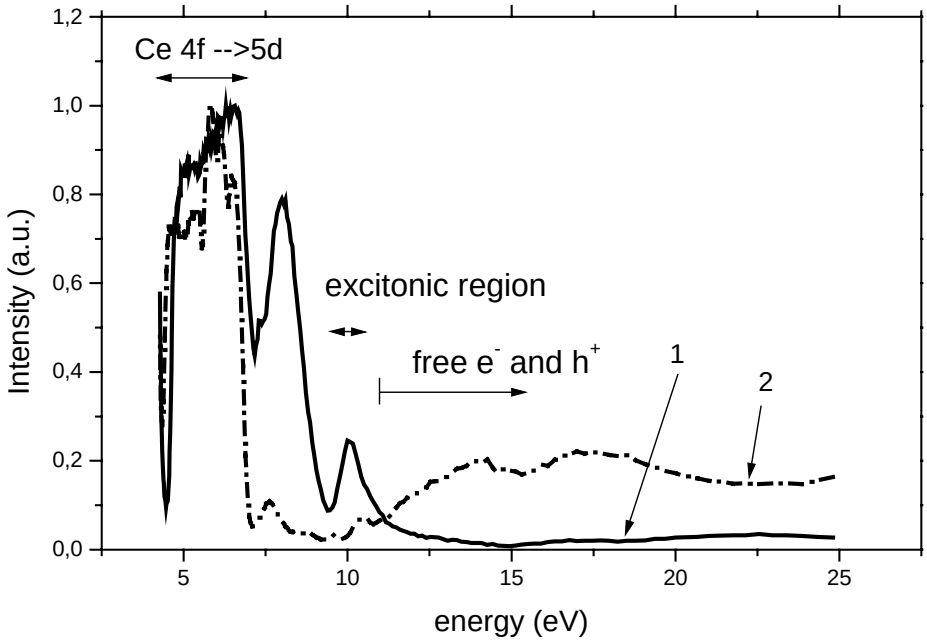

Figure 2. VUV excitation spectra at room temperature of (1) $LaF_3:Ce^{3+}$ and (2) $LuF_3:Ce^{3+}$. The fluorescence wavelength is set on the Ce^{3+} emission (310nm)

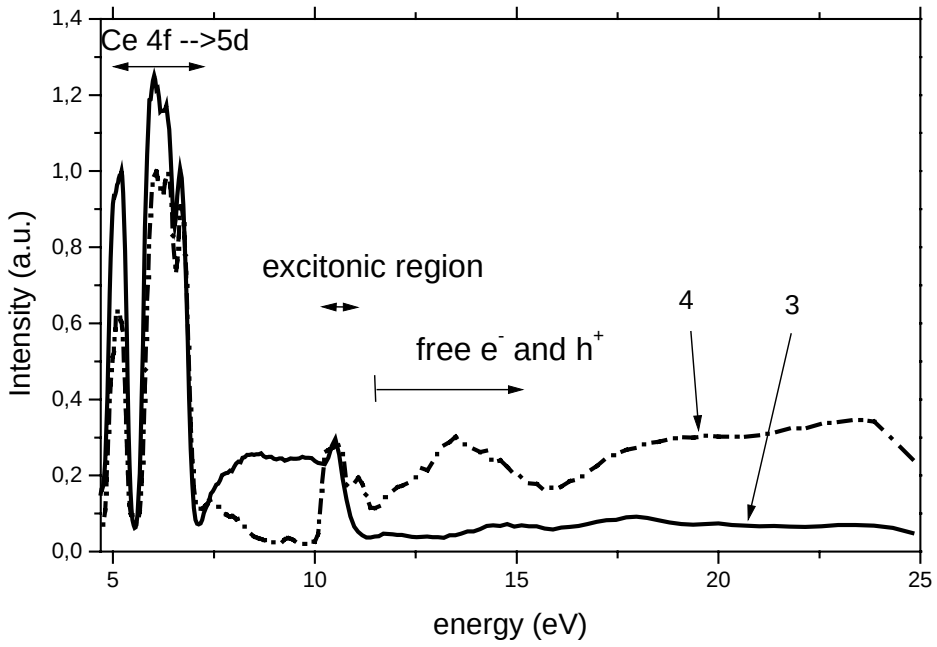

Figure 3. VUV excitation spectra at room temperature of (3) $LiYF_4:Ce^{3+}$ and (4) $LiLuF_4:Ce^{3+}$. The fluorescence wavelength is set on the Ce^{3+} emission at 310nm.

VUV spectroscopy

VUV spectroscopy is presented in figures 2 and 3. Since in this energy region, the absorption coefficient is extremely high, the spectra shape is very sensitive to the surface defects. All measurements were performed on freshly cleaved samples.

Both Lu based compounds exhibit the same behavior for energy excitation over the fundamental absorption edge. Above 11 eV, the tendency in the fluorescence yield is different from two other materials. We cannot argue for Lu4f absorption increase since the photoionization cross section is not very important at low energy for Lu4f orbitals. In figure 4, the photoionization cross section of Lu4f and F2p (free ions) versus the excitation energy are plotted. These values were taken from reference [7]. In materials, the relative intensity remains in the same order of magnitude. Recent UPS measurements from 30 to 130 eV performed on $LuAlO_3$ led to spectra where the relative intensity of Lu4f and O2p bands reproduces exactly the theoretical prediction for free ions [8].

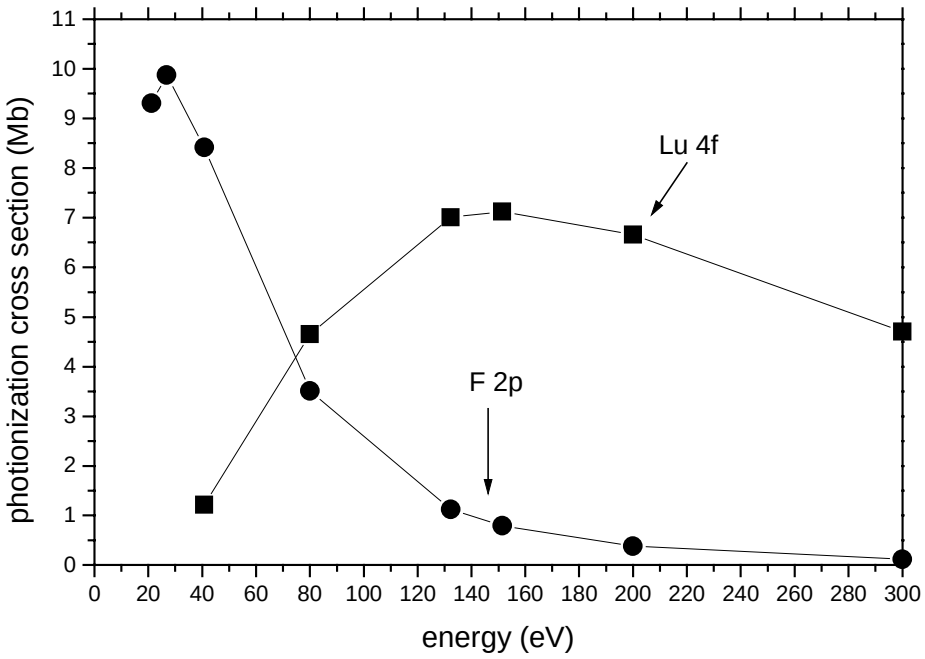

Figure 4. Photoionization cross section of F2p and Lu4f subshell versus energy excitation from reference [7]

It means that differences in the excitation spectra originate essentially from changes in the energy transfer processes. For excitation energy above 11 eV, free electrons and holes are created. Since the energy difference Lu 4f - Ce 4f is smaller than F2p - Ce 4f, we suspect that hole capture by cerium in lutetium based compounds is easier. Other key point is the same nature of orbitals Lu4f and Ce4f. Due to the same symmetry mixing between Lu4f and Ce4f is easier as well.

Nevertheless, light yield of $LiLuF_4$:Ce is not one order of magnitude larger than $LiYF_4$:Ce, contrary to the case LuF_3:Ce versus LaF_3:Ce. In reference [5], the poor light yield of LaF_3:Ce was explained by the low probability of hole capture by cerium. In $LiYF_4$:Ce, the situation is pretty different since self-trapped exciton (STE) emission appears under energy excitation above the fundamental absorption [3]; it is even detected it in the x-ray induce emission of powders. This kind of materials is very favorable for the STE formation. On the contrary, such emission is not so easy to detect in LaF_3:Ce. It was mentioned in reference [9] an STE

emission around 254 nm in LaF_3. We do not detect such emission. Even if it does exist, this emission does not match with the cerium absorption bands and STE transfer to Ce^{3+} cannot occur. Influence of lutetium in LuF_3:Ce seems to be manifested in energy transfer processes: it can facilitate the hole trapping by cerium. For $LiLuF_4$:Ce, since the light yield is not significantly improved, the role of lutetium can be to help hole transfer to cerium as well. However since STE transfer efficiency is already good, it does not remain a lot of free electrons and holes to be trapped. Other solution is the replacement of the STE transfer by free electron hole pair transfer to cerium. We suppose that the latter possibility dominates. First we do not detect a so intense STE emission in $LiLuF_4:Ce^{3+}$. Second, kinetic behaviors of lutetium based compounds are very similar. Under 10 eV excitation, these material do not exhibit any rise (up to the detection limit of 0.5 ns). At 10.5 eV excitation, a rise time appears and is removed under higher energy excitation. On the contrary, $LaF_3:Ce^{3+}$ does not exhibit any rise time, but some slow components and a decay acceleration due to some quenching [5] and $LiYF_4:Ce^{3+}$ presents rise time under most of energy excitation except for 10.5 eV excitation. The similarities of the lutetium based compounds suggest that cerium doped LuF_3 and $LiLuF_4$ have the same kind of energy transfer: $Ce^{3+} + h^+ \rightarrow Ce^{4+}$; $Ce^{4+} + e^- \rightarrow Ce^{3+ *} \rightarrow Ce^{3+} + h\nu$, this transfer being helped by Lu orbitals.

Conclusion

Comparatives studies (XPS, VUV spectroscopy, kinetics) of LaF_3 – LuF_3 and $LiYF_4$ – $LiLuF_4$ doped with cerium point out that lutetium plays a major role in the energy transfer from free electron hole pairs to cerium. Since the Lu 4f bands overlaps the F 2p valence band and is even 1-2 eV above the top of the valence band, the hole trapping by the cerium ion is easier. Then, $LuF_3:Ce^{3+}$ has a good light yield contrary to $LaF_3:Ce^{3+}$. In the case of $LiYF_4:Ce^{3+}$ which has already a pretty good light yield due to a good STE to cerium transfer, when Y is replaced by lutetium, we suspect that sequential electron hole trapping by cerium, as described above, is the dominant process which is very sensitive to cerium concentration. To our knowledge, the scintillation efficiency of only one crystal of $LuF_3:Ce^{3+}$ has been reported. In this material, cerium distribution coefficient is pretty high, and effective cerium concentration is roughly from 0.05 to 0.1 at.%. Nevertheless, a good light yield has been measured. If good quality crystal containing between 0.5 and 1 at.% could be grown, be significantly improved.

References

1. W.W.Moses and S.E.Derenzo, Nucl.Instr.meth. **A299**, 51 (1990)
2. B.Moine et al. Material Science Forum, **239-241** (1997) 245-248
3. C.M.Combes, P.Dorenbos, C.W.E. van Eijk, C.Pedrini, J.Y.Gesland, Proc. Int. Conf. On Inorganic Scintillators and Their Applications, SCINT95, 1996, Delft University Press, The Netherlands, 396-398
4. D.Bouttet, C.Dujardin, C.Pedrini, W.Brunat, D.Tran Minh Duc and J.Y.Gesland, Proc. Int. Conf. On Inorganic Scintillators and Their Applications, SCINT95, 1996, Delft University Press, The Netherlands, 111-113
5. C.Pedrini et al., Mat. Res. Symp. Proc. **Vol.348** (1994) Material Research Society
6. A.J.Wojtowicz, Proc. Int. Conf. On Inorganic Scintillators and Their Applications, SCINT95, 1996, Delft University Press, The Netherlands, 396-398
7. J.J.Yen, I.Lindeau, Atomic Data and Nuclear Data Table 32, 1-155 (1985)
8. A.N.Belsky this conference
9. R.T.Willams, E.D.Thomas and P.H.Bunton, Mat. Res. Symp. Proc. **Vol.348** (1994) Material Research Society

Luminescence and scintillation properties in Ce^{3+} activated trihalide compounds

O. Guillot-Noël[1], E. V. D. van Loef[1], P. Dorenbos[1], C. W. E. van Eijk[1], K. W. Krämer[2] and H. U. Güdel[2]

[1]*Radiation Technology Group, Interfaculty Reactor Institute, Delft University of Technology, Mekelweg 15, 2629 JB Delft, The Netherlands*
[2]*Department of Chemistry and Biochemistry, University of Bern, Freiestrasse 3, 3000 Bern 9, Switzerland*

Abstract: In the present study, we investigated the optical and scintillation properties of the cerium-doped lanthanide trihalide: $LaCl_3$, $LuBr_3$ and $LuCl_3$, under optical, X-ray and γ-ray excitation. Emission and excitation spectra, X-ray induced emission spectra, pulse height measurements and scintillation decay time spectra are reported. A first simple mechanism of the scintillation process is proposed.

Keywords*:* Scintillation crystals; rare-earth trihalides; γ-detection; Energy resolution.

Introduction

In the family of rare-earth trihalides, only CeF_3 [1, 2], LaF_3:Ce [3, 4] and $CeCl_3$ [5] compounds have been extensively studied. Crystals of $LaCl_3$:Ce, $LuBr_3$:Ce and $LuCl_3$:Ce were grown by the Bridgman technique. Optical and excitation spectra in the 240-800 nm wavelength range were recorded using the spectrophotometer Quanta master QM1 of Photon Technology International (PTI). Excitation spectra in the 150-300 nm wavelength range were recorded using a Vacuum Ultra Violet (VUV) setup. Transmission spectra were measured with a Cary 5-Varian spectrometer operating in the 200-800 nm wavelength range. X-ray induced emission spectra were performed with an X-ray tube with a Cu anode operating at 35 kV and 25 mA, an EMI 9462 photomultiplier tube (PMT) and an ARC VM504 monochromator. Measurements were performed between 130 K and 400 K. Pulse height spectra were recorded with a Hamamatsu R1791 PMT. Light yields, expressed in photoelectrons per MeV (phe/MeV) were deduced from the measurements of the peak position of the photopeak compared with that of the single electron spectrum [6] and were converted into photons/MeV (ph/MeV) using the procedure described in [7]. Scintillation decay time spectra were performed using the multi-hit method [8], employing XP2020Q PMTs as 'start' and 'stop' tubes and using γ-rays of a ^{137}Cs source.

Results

At 300 K, the Ce^{3+} luminescence in $LaCl_3$ consists of a double peaked band between 300 nm and 400 nm (Fig. 1), due to the transitions from the lowest level of the 5d configuration to the two $^2F_{5/2}$, $^2F_{7/2}$ multiplets of the $4f^1$ configuration. The peak positions are located at 337 nm and 358 nm (Table 1). The excitation spectrum is composed of two saturated broad bands: one between 237 nm and 294 nm attributed to 4f→5d absorption of Ce^{3+} and the other peaking around 200 nm due to the exciton absorption band which transfers its energy to the Ce^{3+} ion. Based on the C_{3h} symmetry of the rare earth site, five peaks are expected to occur in the 4f→5d absorption spectra. This is in agreement with the measurements of Rodnyi et al. [9]: the broad band splits in five 4f → 5d absorption bands peaking at 281, 274, 263, 250 and 243 nm. From these results, the Stokes shift amounts to about 5900 cm^{-1} (Table 1).

Table 1. Optical properties of $LaCl_3$:Ce, $LuBr_3$:Ce and $LuCl_3$: Ce compounds.

Host	[Ce^{3+}] in %	Ce emission in nm	Ce absorption in nm	Stokes Shift in cm^{-1}	STE max. emission in nm	Exciton Absorption in nm
$LaCl_3$	0.57	337,358	237-294	~5900	~405	200
$LuBr_3$	0.021-0.76	408,448	230, 310-400	~3600	~440	225
$LuCl_3$	0.45	374,400	215, 335	~3100	~400	/

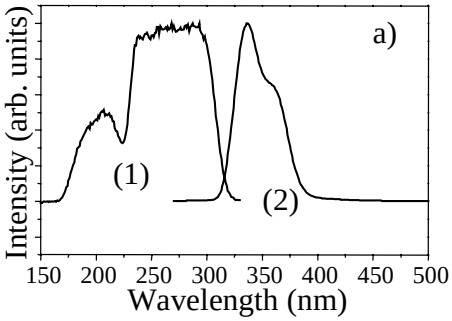

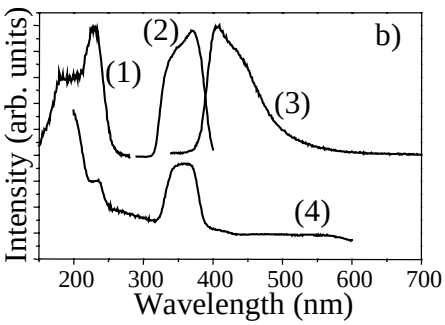

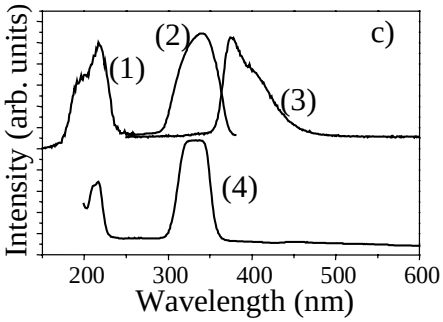

Fig. 1. a) (1) Excitation spectrum of the 350 nm emission and (2) emission spectrum under excitation at 250 nm in $LaCl_3$:0.57% Ce at 300 K. b) (1) and (2) Excitation spectra of the 410 nm emission, (3) emission spectrum under excitation at 220 nm and (4) optical absorption spectrum in $LuBr_3$:0.76% Ce at 300 K. c) (1) and (2) Excitation spectra of the 400 nm emission, (3) emission spectrum under excitation at 220 nm and (4) optical absorption spectrum in $LuCl_3$:0.45% Ce at 300 K.

For the $LuBr_3$:0.76% Ce compound, the two Ce^{3+} emissions (Fig. 1b) (3)) are located at 408 nm, 448 nm. A long tail is seen on the right side of the Ce^{3+} emission due to a broad luminescent band peaking around 440 nm attributed to the self trapped exciton (STE) luminescence. Excitation spectra of the Ce^{3+} emission (Figs. 1b) (1) and (2)) reveal the existence of two excitation bands: one peaking around 355 nm due to 4f→5d absorption of Ce^{3+} and the other extending from 150 nm to 250 nm.

The second one consists of the exciton absorption band characteristic of the $LuBr_3$ host but also of another absorption band peaking around the same wavelength at 230 nm which can be attributed to another 4f→5d absorption of Ce^{3+}. The Stokes shift amounts to about 3600 cm^{-1} (Table 1).

The two Ce^{3+} 5d-4f emissions in the $LuCl_3$:0.45% Ce compound (Fig. 1c) (3)) are located at 374 nm and 400 nm. Two broad 4f→5d absorption bands of Ce^{3+} are seen in Figs. 1c) (1), (2) and (4) peaking at 335 nm and 215 nm. The Stokes shift amounts to about 3100 cm^{-1} (Table 1).

For $LaCl_3$:0.57% Ce at 300 K, the Ce^{3+} luminescence shows up under X-ray excitation (Fig. 2 a)). Moreover, a broad band, extending to 500 nm and peaking around 405 nm is seen on the right side of the Ce^{3+} emission, which is not present under optical excitation (Fig. 1a)). This band is due to self-trapped exciton (STE) luminescence. From 135 K to 400 K, the total light yield of $LaCl_3$:Ce remains almost constant. As the temperature rises, the Ce^{3+} luminescence intensity is enhanced at the expense of the STE luminescence intensity (see Fig. 3 a)), revealing an anti-correlation between these two types of emissions. Of the X-ray

induced $LuBr_3$ emission spectra recorded at 300 K, the one of $LuBr_3$ shown in Fig. 2a) with very low Ce^{3+} concentration (0.021%) is dominated by the very broad STE luminescence already seen under optical excitation at 220 nm (Fig. 1b)). When the Ce concentration rises, the contribution of the Ce^{3+} emission is enhanced whereas the contribution of the STE emission decreases drastically compared to the quasi-pure crystal (Fig. 2a)). The total light yield (Fig. 3b)) increases from 135 K to 300 K and decreases from 300 K to 400 K. Between 135 K and 300 K, the Ce^{3+} luminescence intensity increases and the STE intensity decreases.

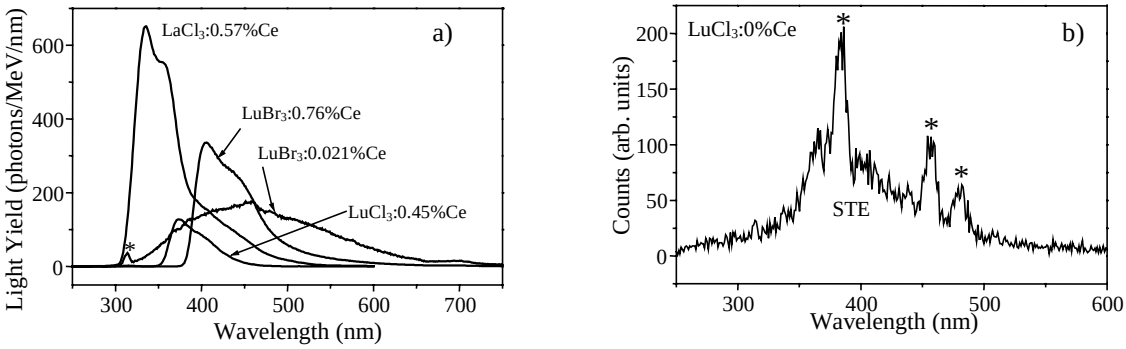

Fig. 2. a) X-ray induced emission spectra at 300 K of $LaCl_3$:0.57% Ce, $LuBr_3$:0.021%, 0.76% Ce and $LuCl_3$:0.45% Ce. The star indicates Gd impurity. b) X-ray induced emission spectra at 300 K of $LaCl_3$:0.57% Ce. The stars indicate Tb impurity. For Fig 2a) the y-axis has been calibrated using the light yields derived from the pulse height measurements.

Under X-ray excitation of the $LuCl_3$ compounds, STE emission peaking around 400 nm is seen for the pure compound (Fig. 2b)) and the two Ce^{3+} 5d-4f emissions are seen for the $LuCl_3$:0.45%Ce compound. The total light yield under X-ray excitation (Fig. 3c)), decreases by about 10% from 135 K to 170 K, then increases by 30% from 170 K to 225 K, and finally decreases by 20% from 300 K to 400 K.

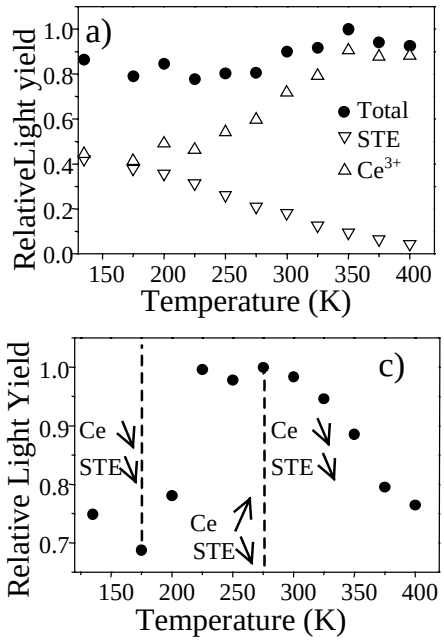

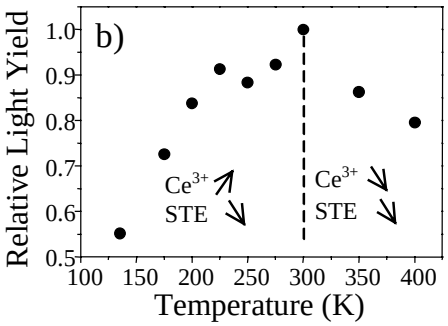

Fig. 3. Temperature dependence a) of the light yields of Ce^{3+}, STE, and total luminescence in $LaCl_3$:0.57%Ce, b) of the total light yield in $LuBr_3$:0.76%Ce. The data are derived from X-ray induced emission spectra. In Fig. 3 b) temperature dependence of Ce^{3+} and STE components are indicated by arrows. c) Temperature dependence of the total light yield in $LuCl_3$:0.45%Ce. The data are derived from X-ray induced emission spectra. Temperature dependence of Ce^{3+} and STE components are indicated by arrows.

Light yields derived from pulse height spectra under ^{137}Cs 662 keV gamma, expressed in photons per MeV of absorbed γ-ray energy are compiled in Table 2. From all the studied compounds, the $LaCl_3$:0.57% Ce possesses the highest light yield with 40000±4000 ph/MeV obtained with a shaping time of 10 μs. For the $LuBr_3$ compounds (Table 2), as the Ce

concentration increases from 0.021% to 0.46%, the light yield decreases from 32000±3000 ph/MeV to 18000±2000 ph/MeV.

A further increase from 0.46% to 0.76% Ce content results in a light yield increase from 18000±2000 ph/MeV to 24000±2000 ph/MeV. The $LuCl_3$:0.45% Ce compound shows the lowest light yield with 5700±500 ph/MeV at a shaping time of 10 μs.

The results of decay measurements performed on all the compounds are gathered in Table 2. The decay curves were analyzed by assuming three decay components. We indicate whether these contributions are exponential or non-exponential. The decay curve of $LaCl_3$:0.57% Ce under ^{137}Cs γ-ray excitation is composed of three components: a short exponential component of 20±2 ns which represents 10% of the total light yield, a second non-exponential component of 330±30 ns (20% of the total light yield) and a long exponential component of 2.2±0.2 μs which represents the main component of the decay curve with 70% of the total light yield. With a filter transmitting the Ce^{3+} luminescence (at 330 nm), the contribution of the first two components is enhanced compared to the long one (see Table 2). With a filter transmitting the STE luminescence (at 430 nm), the decay curve is mainly composed of the long component (95%).

Table 2. Light yields derived from pulse height spectra, characteristic components of the scintillation decay time of $LaCl_3$:0.57% Ce, $LuBr_3$:0.021%, 0.46%, 0.76% Ce and $LuCl_3$:0.45% Ce compounds. The light yields and the decay time are obtained under 662 keV γ-ray excitation.

Host	**[Ce^{3+}] in %**	**Photon Yield in 10^3 ph/MeV 10 μs**	**Decay time components Short(ns)/2nd(ns)/Long(μs) {% to the total light yield}**		
$LaCl_3$	0.57	40±4	20±2 exp {10%}[1] {20%}[2] {0%}[3]	330±30 non-exp {20%}[1] {30%}[2] {5%}[3]	2.2±0.2 exp {70%}[1] {50%}[2] {95%}[3]
$LuBr_3$	0.021	32±3	/ {0%}	900±100 non-exp {5%}	>8 non-exp {95%}
$LuBr_3$	0.46	18±2	32±3 exp {10%}	450-550 non-exp {20%}	>5 non-exp {70%}
$LuBr_3$	0.76	24±2			
$LuCl_3$	0.45	5.7±0.5	50±5 exp {25%}	250-350 non-exp {45%}	>4 non-exp {30%}

exp=exponential, non-exp= non-exponential, [1]without filter, [2]with 330 nm interference filter, [3]with 430 nm interference filter.

For all the trihalide compounds, the decay curve can be described by three components (Table 2): a short exponential around few tens of ns, a 2nd non exponential around few hundreds of ns and a long non- or exponential around few μs.

Discussion

The previous studies allow us to propose three different mechanisms.

i) *Energy transfer by direct electron-hole capture on Ce^{3+}*. After absorption of a γ-ray, free electrons and free holes are created in the conduction band and the valence band respectively. These free electrons and holes can be trapped within 1 ns by a Ce^{3+} ion. The decay associated to this mechanism is characteristic of the lifetime of the excited state of Ce^{3+}. For all the compounds, a very fast decay, which can be attributed to this process, has been observed in the decay curve under γ-ray excitation.

ii) *Energy transfer by binary electron-hole recombination*. After ionization, the hole may become self-trapped forming a V_k center within a few ps [10]. The electron may be trapped in shallow meta-stable states possibly associated to the Ce^{3+} ion or other defects in the lattice. Next, the mobile V_k center can be trapped on or close to a Ce^{3+} ion. The recombination of the electron with the V_k center trapped near a Ce^{3+} ion will eventually excite the Ce^{3+} center. Alternatively, it is also possible that the electron is trapped first by a Ce ion and next the diffusing V_k center is trapped at the $[Ce^{3+} + e^-]$ center. If one assumes that i) the $[V_k + e^-]$ distribution is random and ii) the electron diffusion migration is random, theoretically the decay is described by a $(1+at)^{-2}$ dependence. For all the trihalide compounds, a non-exponential intermediate component has been observed in the decay curve under γ-ray excitation (Table 2). This component could be due to this type of energy transfer. This attribution has to be confirmed because fit of this intermediate component by a t^{-2} dependence was not very accurate.

iii) *Energy transfer by diffusion of STE*. In the trihalide compounds, after creation of free holes and free electrons the main process is probably the formation of STEs. Indeed, under X-ray excitation, STE emission is seen in the spectra of $LaCl_3$ and $LuBr_3$ (Fig. 2a)). Moreover, for all the compounds, the decay curves show a component in the range of a few microseconds (Table 2) which can be attributed to processes involving STE luminescence and energy transfer via STE to Ce. The STE can transfer its energy by different mechanisms. A radiative transfer from STE to Ce can occur. In this process, an overlap between STE emission and Ce^{3+} absorption is necessary. For $LaCl_3$ and $LuBr_3$, such an overlap occurs as we learn from the positions of the Ce^{3+} 4f→5d absorption and of the STE emission (Figs. 1, 2). However, for this type of radiative transfer a strong temperature dependence is not expected. Consequently the results of the X-ray excitation (Fig. 3) have to be explained by another mechanism. The transfer from STE to Ce^{3+} can also occur by an STE diffusion process which is thermally activated. In $LaCl_3$:0.57% Ce, at 135 K under X-ray excitation, the total luminescence is due to both STE and Ce^{3+} luminescence (Fig. 3a)). When the temperature rises, the STE mobility increases, and the STE transfers its energy to Ce^{3+} centers. This mechanism can be described by a set of two coupled differential equations that predict an anti-correlation of STE and Ce^{3+} luminescence yields [11] as is also observed in Fig. 3a). By this process, we expect a decay component for the Ce^{3+} ions which is determined by the lifetime of the STE [11]. This process can be associated to the slow component (few μs, Table 2) of the scintillation decay curve of $LaCl_3$:0.57% Ce. For $LaCl_3$, the first two components of the scintillation decay represent 30% of the total light yield at room temperature (Table 2). From the X-ray excitation measurements at 300 K, 80% of the total light yield is due to Ce^{3+} luminescence (Fig. 3a)). It means that 80%-30% = 50% of the long 2.2 μs component is probably due to the Ce^{3+} luminescence induced by diffusion of STE and transfer from STE to Ce. This 50 % is exactly what we obtained for the long component (Table 3), when we study only the Ce^{3+} luminescence by using a filter at 330 nm. For the two other studied compounds ($LuBr_3$ and $LuCl_3$), the experiments presented in this work are not sufficient to discuss accurately the mechanism involved in the transfer for these two compounds.

References

1. W. W. Moses, and S. E. Derenzo, IEEE Trans. on Nucl. Sci. **36** (1989) 173
2. D. F. Anderson, IEEE Trans. on Nucl. Sci. **NS-36** (1989) 137
3. W. W. Moses and S. E. Derenzo, Nucl. Instr. and Meth. in Phys. Res. **A 299** (1990) 51
4. A. J. Wojtowicz, M. Balcerzyk, E. Berman, and A. Lempicki, Phys. Rev. **B 49(21)** (1994) 14880

5. S. E. Derenzo, and W. W. Moses, Proc. of the "Crystal 2000" Int. Workshop, in "Heavy Scintillators for Scientific and Industrial Application, Eds F. De Notaristefani, P. Lecoq, and M. Schneegans, Edition Frontieres, Gif-sur-Yvette, France (1993) 125
6. M. Bertolaccini, S. Cova, and C. Bussolatti, Proc. Nucl. Electr. Symp. Versailles, France, 1968
7. L. H. Luthjens, P. Dorenbos, J. T. M. de Haas, A. Hummel, and C. W. E. van Eijk, Rad. Phys. and Chem. **55 (3)** (1999) 255
8. W. W. Moses, Nucl. Instr. and Meth. **A 336** (1993) 253
9. P. A. Rodnyi and A. S. Voloshinovskii, private communication, December 1998
10. K. S. Song, and R. T. Williams, "Self-Trapped Excitons, " Springer Series on Solid-State Sciences 105, Ed. M. Cardona, Springer-Verlag, Heidelberg **chap. 4 and 5** (1993)
11. K. Tanimura, N. Itoh, J. Phys. Chem. Sol. **42** (1981) 901

Modeling of the detection systems on the base of scintillation materials

V.A,Tarasov, E.V.Sysoeva, E.P.Sysoeva, O.V.Zelenskaya

Institute for Single Crystals, Lenin Ave.60, Kharkov,Ukraine

Abstract: The main stages of the detection system modeling are considered. The advantages and disadvantages of the different approach to detection system modeling are discussed (modeling of the individual stages, modeling the detection system as a whole, sequential modeling of all stages). The results of the Monte Carlo sequential modeling of the scintillation gamma- and beta- spectrometers are presented.

Keywords*:* scintillation detector, detection system, spectra simulation, Monte Carlo method, scintillation spectrometer.

Introduction

The range of problems solved using scintillation technique is at present wide enough. There are new scintillation materials, materials for elements of detectors and photodetectors now. This creates a problem of optimal choice of materials and design of detecting systems (DS). The mathematical modeling permits to decrease the time and means for DS optimization.

Approach to modeling the scintillation detection systems

DS-modeling is generally understood as the calculated prediction of DS parameters based on some mathematical model. For example the model of scintillation spectrometer-most informative instrument- may be described with Fredholm equation:

$$F(V) = \int_{E1}^{E2} f(V,E)\,k(E)\,dE \qquad (1)$$

where $k(E)$ — spectrum of acting particles

$f(V,E)$ — response function

$F(V)$ — instrument spectrum

This equation reproduces formally the spectrometer operation and at the known spectrum of acting particles and response function gives the instrument spectrum. As a result we may predict parameters of spectrometer, for example resolution, effectiveness, pulse magnitude etc. The main problem for that model consists of construction the response function in an evident form. This is practically unreal because of numerous acting factors.

The powerful tool for DS modeling is Monte Carlo method. This method works with success at probability description of the processes, which take place during ionizing radiation detection. The following basic stages of ionizing radiation detection with scintillation DS are:

interaction of radiation with objects on the way to the detector,

interaction of radiation with the detector elements,

conversion of the ionizing radiation to the light,

light passage through scintillator and collection on the photodetector,

light conversion to the electrons at the output of the photodetector,
grading the electron pulses (analysis of pulses).

Monte Carlo calculations of individual phases of ionizing radiation detection are well known. Calculations of interaction of radiation with objects on the way to the detector and interaction of radiation with the elements of detector belong to classical Monte Carlo problems of radiation transport in the matter [1-4]. These problems are solved by modeling the particles trajectories [1,5,6]. The modeling passage of scintillation light from scintillator volume to photodetector is a usual stage in designing scintillation detectors. Light collection process in scintillation counters is described in literature in detail. The calculations are based on the laws of geometric optics and photometry [7,8]. Mirror reflection is usually simulated using Fresnel laws. The diffuse surface is very often considered as Lambert source. Photodetector has an essential influence on the spectrometer signal formation. It is known that distribution of photoelectrons ejected from photocathode is described using Poisson distribution. But as it was noted in [9] is better to use normal distribution for modeling of photomultiplier. The modeling of pulse-height analyzer is reduced to simple grading the pulses by number of electrons in each pulse.

The modeling of individual phases may be described the same way as the scintillation spectrometer operation with equation (1). But in these cases the functions $k(E)$ and $F(V)$ will mean:

Phase	***k*(*E*)**	***F*(*V*)**
Way to the detector	initial spectrum of the source	spectrum of radiation falling into detector
Interaction with detector	spectrum of radiation falling into detector	spectrum of radiation absorbed within scintillator
Conversion of radiation to light	spectrum of radiation absorbed within scintillator	coordinate and magnitude spectrum of appearing scintillations
Light collection	coordinate and magnitude spectrum of appearing scintillations	coordinate and magnitude spectrum of scintillations falling into photodetector
Process in photodetector	coordinate and magnitude spectrum of scintillations falling into photodetector	magnitude spectrum of the electron pulses at the output of the photodetector

The advantage of Monte Carlo calculations of individual stages consist of the possibility to study in detail the influence of the factors emphasized at individual stage on the formation of individual response. The main disadvantage consist of the absence a priori of information about real acting spectra $k(E)$ for individual stages, except for stage 1 (way to detector). Therefore at modeling the individual stages of ionizing radiation detection some simplifications are introduced: point source (stage 2), uniform volume distribution of places of scintillations (stages 3 and 4), uniform illumination of photocatode surface (stage 5) etc. The obtained information gives no idea of mutual influence of the main factors on the formation of the real spectrometer response.

It is typical for modeling the spectrometer as a whole [10] to retrace the chain of signal formation at one acting particle. The main advantage of this consist of the maximal approach to the work of real DS. The main disadvantage is the absence of the information about spectral distributions at intermediate stages and a long time required for a repeated simulation of the spectra with modification of parameters.

We popularize the approach for modeling the scintillation DS based on the sequential execution of individual stages of work. At then modeling the spectral distribution obtained at each stage is both an object for independent research and a starting point for getting next spectral distribution right up to the instrumental spectrum. The modeling of individual stages is realized with algorithms known from literature. The arising additional problems consist of the search appropriate information mode about spectral distributions on intermediate stages.

Monte Carlo sequential modeling of the scintillation spectrometers

We used such approach to simulate DS spectra for the solution of radioecological problems. The systems are as follows:

1) scintillation gamma-spectrometer on the base NaI(Tl) scintillator (scintillator ∅63x63 mm diffuse surface, Al-housing 1mm, diffuse reflector MgO 3mm, optical coupling with photodetector) designed for determination of ^{137}Cs in water solutions in 1 liter Marinelli vessel;
2) scintillation beta-spectrometer on base of plastic scintillator (scintillator ∅100x10 mm, polished surface, input Al-window 0.01mm, mirror reflector, optical coupling with photodetector) designed for determination of ^{90}Sr in disk form specimens ∅100x10mm .

Figures 1 to 5 present simulated spectra obtained at the individual stages of modeling. Figures 1a and 2a give initial spectra of particles radiated from ^{137}Cs and ^{90}Sr sources, accordingly. Figures 1b and 2b give spectra of particles of these radionuclides, emergent from volume sources. Figure 3 gives spectral distribution obtained after modeling the interaction of radiation in detectors. Figure 4 gives spectral distribution obtained after modeling of light collection in scintillators. Figure 5 gives spectral distribution of pulses obtained at the output windows.

Conclusion

Compared below are the parameters of some DS on the base of scintillators measured and obtained at modeling the spectrometer sensitivity by full absorption peak for ^{137}Cs in Marinelli vessel geometry (see Table). In all cases we can observe a good conformity of the calculated and experimental results.

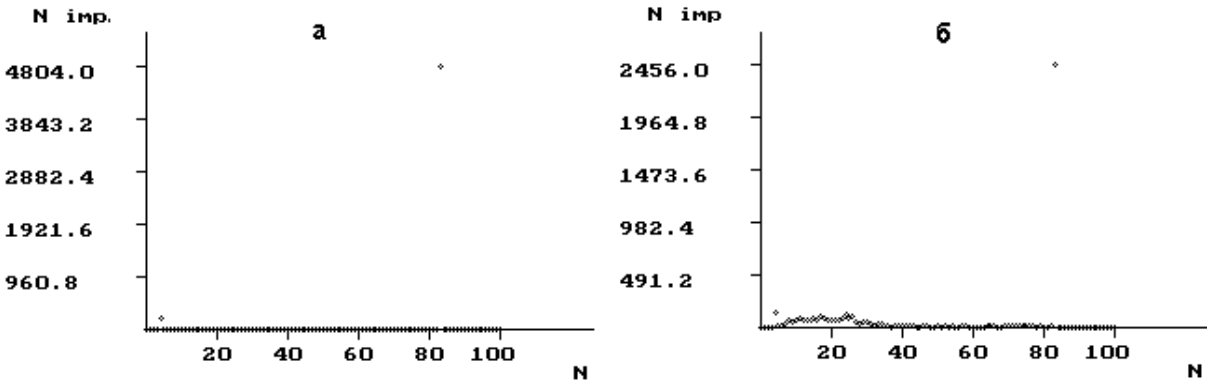

Figure 1. Spectra of gamma - radiation of ^{137}Cs sources: a) point source; b) Marinelli vessel.

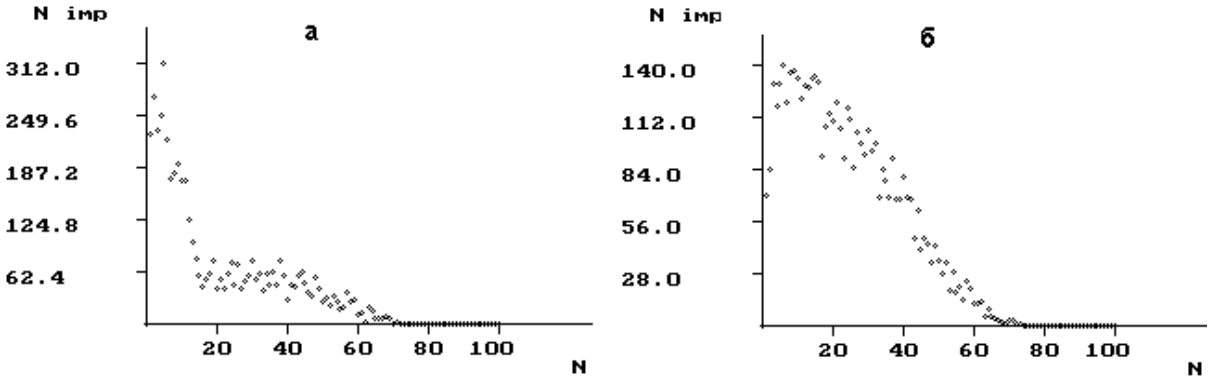

Figure 2. Spectra of beta-radiation of ^{90}Sr sources: a) point source; b) plastic disk.

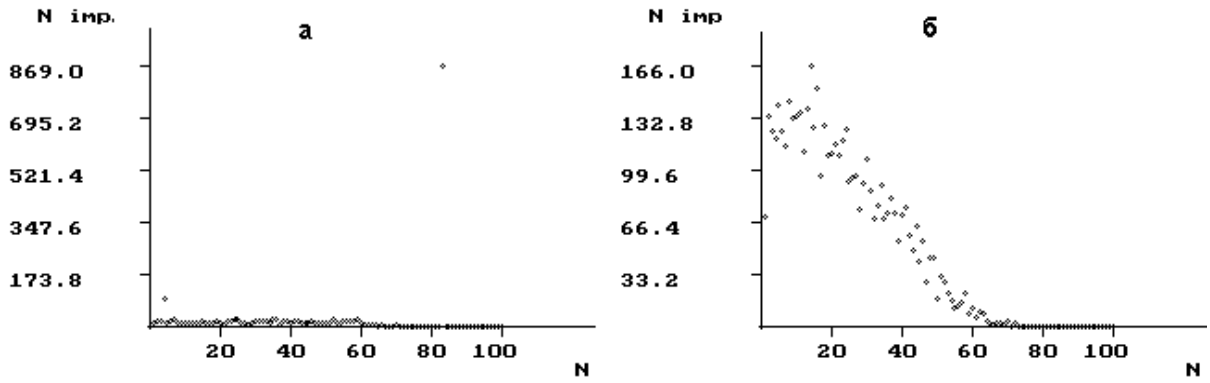

Figure 3. Energy loss spectra in scintillators: a) gamma-spectrometer; b) beta-spectrometer.

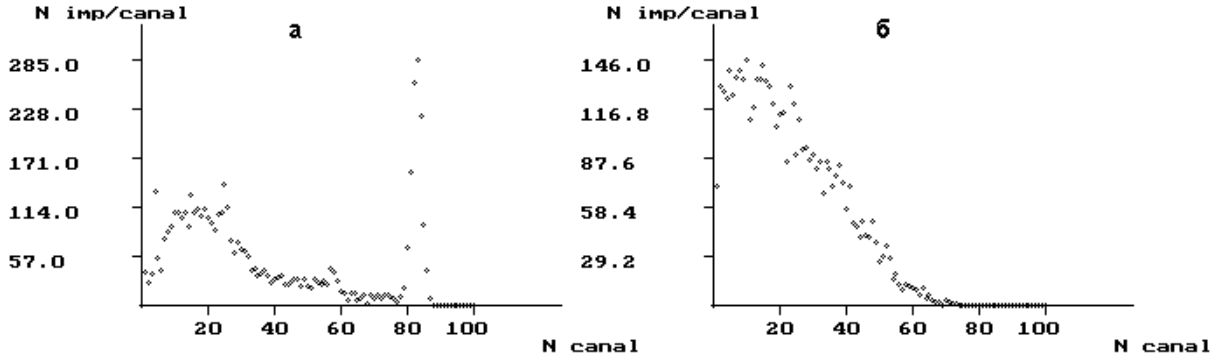

Figure 4. Spectral distribution of the light pulses magnitudes at the output windows of the detectors: a) gamma-spectrometer; b) beta-spectrometer.

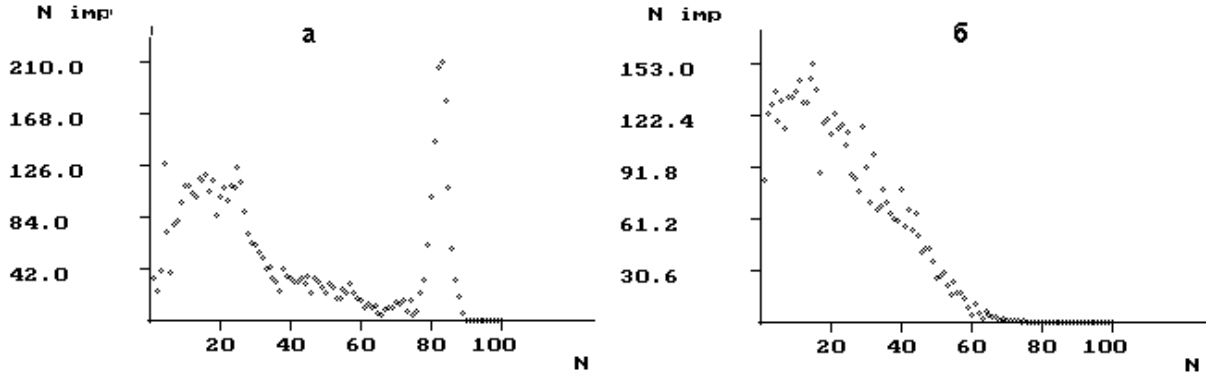

Figure 5. Pulses spectral distribution at the output of the photodetector: a)gamma-spectrometer; b) beta-spectrometer.

Table. Experimental and calculated values of scintillation gamma spectrometers sensitivity, designed for determination of ^{137}Cs in Marinelli vessel.

Scintillator	**Size, mm**	**Sensitivity, counts s^{-1} Bq**	
		measured	calculated
NaI(Tl)	∅ 63x63	0.022	0.025
CsI(Tl)	∅ 63x63	0.028	0.030
CWO	∅ 40x40	0.016	0.015
CWO	∅ 25x50	0.007	0.008
BGO	∅ 25x50	0.004	0.005

References

1. E.D.Cashwell, C.J.Everett, A practical manual on the Monte-Carlo method for random walk problems, Pergamon Press, N.-Y.,1959
2. Monte-Carlo method in radiation transfer problems, Ed. by G.I.Marchuk, Atomizdat, Moscow, 1967 (in Russian).
3. A.F.Accerman, M.Ya.Grudsky, V.V.Smirnov, Secondary electron emission from solids under gamma-ray irradiation, Energoatomizdat, Moscow, 1986 (in Russian).
4. A.F.Accerman, Simulation of trajectories of charged particles in matter, Energoatomizdat, Moscow, 1991 (in Russian).
5. V.K.Grishin, F.A.Zhivopiscev, V.V.Ivanov, Mathematical treatment and interpretation of physical experiment. Moscow State University Publ. House, 1988 (in Rusian).
6. N.G.Gusev, V.A.Klimanov, V.P.Mashkovich, A.P.Suvorov, Protection from ionizing radiation, Energoatomizdat, Moscow, 1989 (in Russian).
7. Yu.A.Tzirlin, Light collection in scintillator counters, Atomizdat, Moscow, 1975 (in Russian).
8. J.B.Birks, The theory and practice of scintillation counting, Pergamon Press, Oxford, 1964.
9. F.Ortiz, J.M.Los Arcos, A.Grau, L.Rodriguez, Nucl. Instr. Meth., **A312** (1992) 109.
10. J.Fraser-Mitchel, A.G.Wridth, Nucl. Inst. Meth., **A228** (1990) 429.

Optimization of scintillation light collection from $PbWO_4$ crystals

Ya. A. Berdnikov, O. Ya. Berdnikova ,V.F. Kosmach, V.M. Samsonov*, A.P. Shishlo

Saint-Petersburg State Technical University (Russia)
**Saint-Petersburg Nuclear Physics Institute (Russia)*

Abstract: The problems of increasing the light yield for crystal/photomultiplier system with long size lead tungstate scintillation $PbWO_4$ (PWO) were studied by using the ray tracing computer program. We have tested different shapes of crystals and geometry of the detector's optical system, different kinds of reflective materials, usage of reflecting covering at the top of crystal and the antireflection coating between the crystal and the photomultiplier input window. The improvement of uniformity of light collection was considered. The ray tracing program code "Light 3.0" is presented.

Keywords*:* simulation, light collection, tungstate crystal.

Introduction

In this work we consider the possibilities of increasing the light yield for scintillation crystals with high refraction index, that are planned to use for experiments in high-energy physics. The detectors should have good energy and space resolution and high radiation resistance for a reasonable price. The use of heavy scintillation crystals is thought to be one of the perspective options. We consider the lead tungstate crystals $PbWO_4$ (PWO afterwards).

This crystal has a high refraction index ($n \approx 2.2 \div 2.4$) that determines it's peculiar optical properties. One of the main problems with the use of these crystals is their low light yield, and we have to maximize the collection of the photons in the photomultiplier (PMT).

In this work we consider the probabilities of increasing the light collection using changing the geometry of the detector's optical system and different kinds of coating.

Analysis of the possibilities of increasing the light collection

Lets note some special things about the passage of light in a rectangular crystal with high refraction index. We assume $n_{crystal} = 2.2$ and isotropy for the PWO crystal in this section. First, the angle of incidence with the top/bottom side of the crystal doesn't change after reflecting from other sides. Second, some peculiarities are due to the relation between the refraction indices of crystal, outside media (air or vacuum) and the PMT glass. The rays that are not totally reflected on the top and the bottom sides cannot come out through the lateral sides (i.e. are totally reflected). There should exist the rays that are totally reflected on all the sides except the one, adjacent to the PMT.

Let's consider the different ranges of the angle between ray and the bottom side of crystal.

Range I: the rays that are totally reflected on the lateral sides. These rays can exit through the top and through the bottom sides. Most of them will exit through the bottom side, because the border crystal-PMT's glass is more transparent, than the border crystal-vacuum. The angle of incidence for this group is

$$0 \le \alpha_1 < \arcsin(1/n_{crystal}) \Rightarrow 0 \le \alpha_1 < 27^0$$

Range II: the rays that can get out through the PMT's glass only. The light yield is mostly due to these rays:

$$arcsin(1/n_{crystal}) < \alpha_2 < arcsin(n_{glass}/n_{crystal}) \Rightarrow 27^0 < \alpha_2 < 43^0$$

Range III: the rays that can not exit through any side. These rays are absorbed in the crystal:

$$arcsin(n_{glass}/n_{crystal}) < \alpha_3 < 90^0 - arcsin(n_{glass}/n_{crystal}) \Rightarrow 43^0 < \alpha_3 < 47^0 .$$

Range IV: the rays that exit through the lateral sides of the crystal:

$$90^0 - arcsin(n_{glass}/n_{crystal}) < \alpha_4 < 90^0 \Rightarrow 47^0 < \alpha_4 < 90^0$$

The rays from the ranges III and IV don't add to the light yield.

This analysis shows that the light collection can be increased by several means:

- Increasing the part of the rays from range I that enter the PMT by inserting antireflection films between the crystal and the PMT and by coating the top side of the crystal with metal reflecting film.
- Wrapping the lateral sides of the crystal with diffuse coatings or modifying the crystal shape to change the direction of rays III and IV.
- Changing the geometry of the optical system to allow rays of ranges III and IV going to the photocathode of PMT.

For two last cases all the analysis above becomes wrong, and special calculations (the ray tracing) should be made. We have worked out the special program "Light 2.0" for these calculations. The program was written on the C++ programming language. It has friendly Windows-interface. For calculations of complex optical system the next version of program "Light 3.0" was used.

The description of the model

To simulate the light collection process we used the Monte-Carlo method. We developed and programmed an algorithm that allows calculating the light collection index for an arbitrary optical system. The algorithm takes into account the polarization of light after the reflection and refraction on the borders of the media, there is a possibility to define any optical proprieties of the crystal, and also it takes into account the absorption of light in the crystal.

The light yield index K was calculated by

$$K = W'/W \qquad (1)$$

where W is the sum of energy of photons generated in the crystal, W' is one reaching the photocathode of PMT.

In the calculations we assumed, that:

- the refraction and the reflection of light is described by classical electrodynamics;
- the tracking of the light ray in the crystal was terminated, when it's intensity was 10^3 times less, than at the beginning (for Light 2.0 code);
- the crystal is optically isotropic;
- the photocathode is set right up to the glass of the PMT;
- the crystal, film, and glass surfaces are absolutely smooth;
- the coating covers the crystal without any air gaps;

Calculating K we took the average for 100,000 light rays (photons). The relative deviation of the resulting K was not greater than 0.1%.

The results of light collection processes simulation

In the beginning the different shapes of crystal and types of coating were considered. In this part we use a rectangular crystal 2x2x22 cm^3. In the calculations we took into account the dispersion of the refraction index with the wave length [1] (Fig. 1a). The spectral density of the produced light is shown in Fig. 1b. The absorption length was taken independently of the wavelength and is equal 2 m. One of 2x2cm sides of the crystal is adjacent to the input window of PMT. The glass of the input window has the refraction index 1.5. In some calculations an antireflection film was placed between the crystal and the PMT's glass.

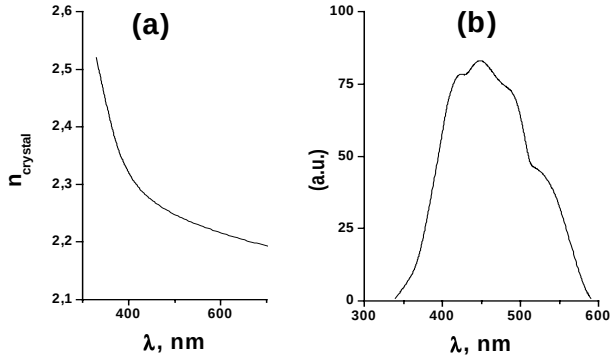

Fig. 1. Optical properties of the crystal. The refraction index (a) and spectral density distribution of produced light (b) versus the wavelength.

The results of calculations are shown in the Table 1 (Var. 1-7). The shapes of crystal are shown in Fig. 2. The maximal increase in light collection was got for variant 7 (approximately 50%), i.e. with significant deviation of the shape from rectangular and with inserting an antireflection film between the crystal and the PMT.

The relative increase in light collection index due to antireflection films depends upon exact conditions in which they are used. Using a film with a rectangular crystal increases K by 2% (var. 1 and 4). The film increases the light collection only for the rays from the range I. For a non-rectangular crystal the increase is about 5% (Var. 6 and 7), because in this case the conditions for light collection are better for all the rays.

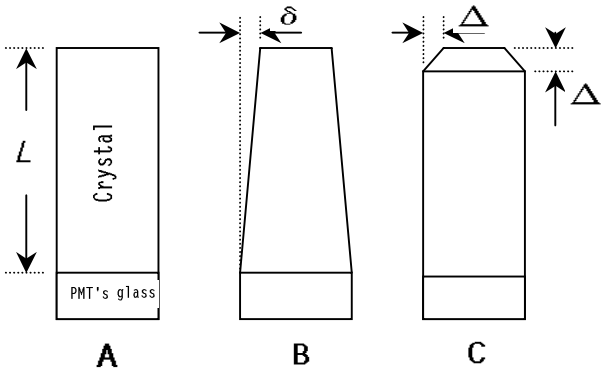

Fig. 2. The shape of crystal PWO. L = 220 mm, δ = 2.5 mm Δ = 10 mm

Table 1. Results of calculation of light collection coefficient K. $\varepsilon = 100\% \cdot (K_i - K_1)/K_1$.

Var. i	Shape	Description	K_i,%	ε,%
1	Fig. 2 A	No coating on the sides and no films.	17.76	-
2	Fig. 2 A	The top and lateral sides are coated with a mat film with albedo 0.98.	24.64	+39
3	Fig. 2 A	The topside of the crystal is coated with a metal (silver) film.	19.02	+7
4	Fig. 2 A	No coating. Between the crystal and the PMT there is a 53nm antireflection film with n=1.84.	18.15	+2
5	Fig. 2 B	No coating on the sides and no antireflection film.	22.60	+27
6	Fig. 2 C	No coating on the sides and no antireflection film.	25.57	+44
7	Fig. 2 C	No coating. Between the crystal and the PMT there is a 53nm antireflection film with n=1.84.	26.49	+49
8	Fig. 3 D	Special optical system for light collection is used.	21.78	
9	Fig. 3 E	-- // --	27.48	
10	Fig. 3 F	-- // --	32.27	

Quite a good result can be achieved with the diffuse coating - the light collection is increased by 39%. But we should note that the result depends strongly upon the albedo of coating. For the intermediate results we should note Var. 5. Even a slight deviation from rectangular shape results in a 25% increase of the light collection.

Our results for some variants are in satisfactory agreement with the experiment one [2]. For the crystal with diffuse reflector wrapping (MYLAR, MILLIPORE) light yield increases by 25-50% (our result is 39%).

In addition the different shapes of optical system of PMT detector presented in Fig 3. were examined (Table 1. Var. 8-10). The size of crystal is 23.8x23.8 mm^2 on the base and 20.5x20.5 mm^2 on the top and their length is 230 mm. The optical system with the maximal value K is showed in Fig. 3 (F). This system has very high uniformity of light collection in the volume of crystal. The results of calculation and experiment [3] are presented in Fig. 4.

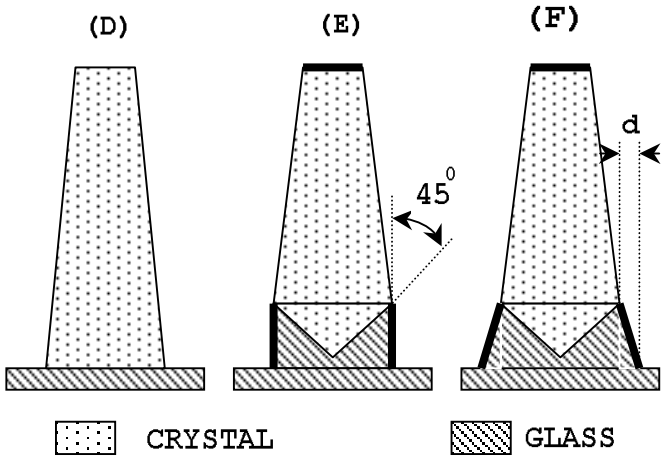

Fig. 3. Different shapes of the optical system of detector are shown. d=6.4 mm. Heavy lines mean the metal coating.

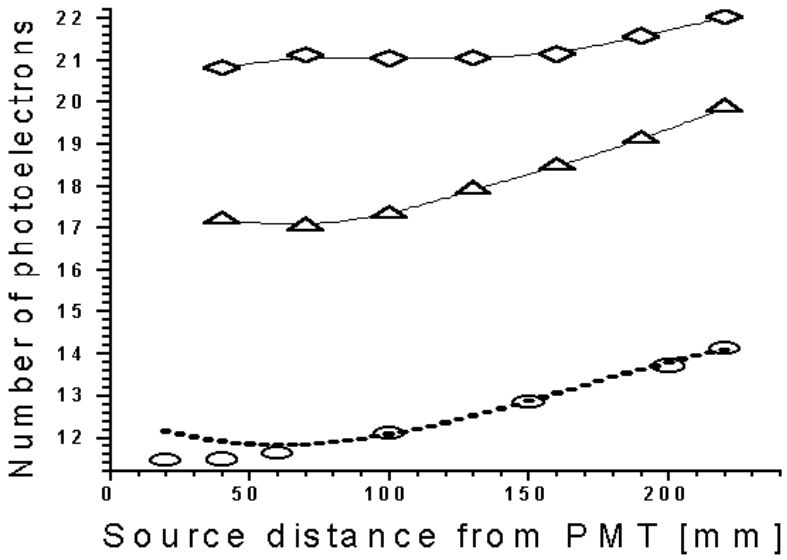

Fig. 4. The crystal response in photoelectrons at the total absorption peak is represented as a function of the source distance from the PMT. Point is used for results of the experiment [3], open circles, triangles and diamonds are the results of simulation for cases Fig. 3 D, E and F.

Conclusions

The results of light collection simulation for different shapes of crystal showed, that the maximum light collection index K is achieved with the change of the shape of the crystal from rectangular to the one, shown on Fig. 2.C. *K* increases by 44% if related to the rectangular crystal. Using an antireflection film between the crystal and the photomultiplier allows increasing K by extra 5%.

The best result will be if the special optical system of input window of PMT is used (Fig. 3. F). In the future we plan to optimize the crystal shape to get the maximal K.

We should note, that the calculation results describe a rather idealized crystal model (the basic simplifications are described above), and these results can change with taking into account the real properties of the crystal, the photomultiplier construction, the quality of the surfaces etc.

References

1. S.Baccaro, L.M.Barone, B.Borgia et.al.: ”Optical properties of lead tungstate ($PbWO_4$) crystal for LHC em-calorimeter”, CERN CMS TN/95-152, (1995).
2. G.Yu.Drobyshev, A.A.Fedorov, M.V.Korzhik et al.: ”Optimization of the lead-tungstate crystal/photodetector system for high-energy physics”, CERN CMS TN/94-313, (1994).
3. C.D'Ambrosio, C.Ercoli, S.Jaaskelainen et al.: "A HPMT based set-up to characterize scintillating crystals", CERN CMS EP/99-39, (1999).

Quality inspection of anisotropic scintillating crystals through measurement of interferometric fringe pattern parameters

N. Cocozzella[1], M. Lebeau[1], G. Majni[3], N. Paone[2], D. Rinaldi[3]

1) CERN division EP, 1211 Geneva 23, Switzerland
2) Dip. di Meccanica, Università di Ancona, via Brecce Bianche, 60131 Ancona Italy
3) INFM and Dip. di Scienze dei Materiali e della Terra, Università di Ancona, via Brecce Bianche, 60131 Ancona Italy

Abstract: The electromagnetic calorimeter of the CMS experiment at CERN requires more than 80'000 scintillating crystals to be assembled as radiation detectors. Quality inspection of crystals is necessary in order to prevent scintillating crystals from breaking because of residual stress. A quality control system based on optical inspection of interference fringe patterns has been developed. The measurement procedures have been theoretically studied, then a dedicated polariscope was built, in order to observe the crystals under imposed stresses or with residual internal stresses. The results are innovative, the photoelastic constant of PWO was measured and the procedure is applicable to mass production, not only to optimise the crystal processing but also to perform a quality inspection.

Keywords*:* Photoelasticity, Interference, Residual stress, Quality inspection

1. Introduction

Large dense crystals of $PbWO_4$ (PWO) suitable for this purpose are produced in the industry. It is very important to test the mechanical quality of the crystals quickly and by a non-destructive way, immediately after growth and mechanical processing phases.

Defects due to internal residual stress are the most important causes of breaking. The observation of unstressed crystals, by means of a polariscope [1], shows a symmetrical interference pattern due to the symmetry of the lattice. It is well known that a tensional state induces a lattice symmetry distortion.

In this case the interference pattern modifies its shape too (photoelasticity) [2]. Therefore the measurement of characteristic geometrical parameters of the interference fringe pattern offers a means for quality control of scintillating crystals.

Crystals with tetragonal lattice are defined as monoaxial because they have a single optical axis. Under load the interference pattern is modified as a function of the applied stress, and the crystal evolves from monoaxial to biaxial.

2. Interference in anisotropic stressed media

An optical anisotropic medium has different refraction indices along different directions, so when a ray of polarised light propagates through the medium it is divided into two rays: an ordinary ray and an extraordinary ray (see figure 1).

The ordinary ray is due to the ordinary refraction index, while the extraordinary ray is due to another refraction index, caused by anisotropy.

This effect, known in literature as birefringence [1] is observable by putting two crossed polarisers and a system of focusing lens, so the two rays are recombined and produce interference, because the optical paths are different

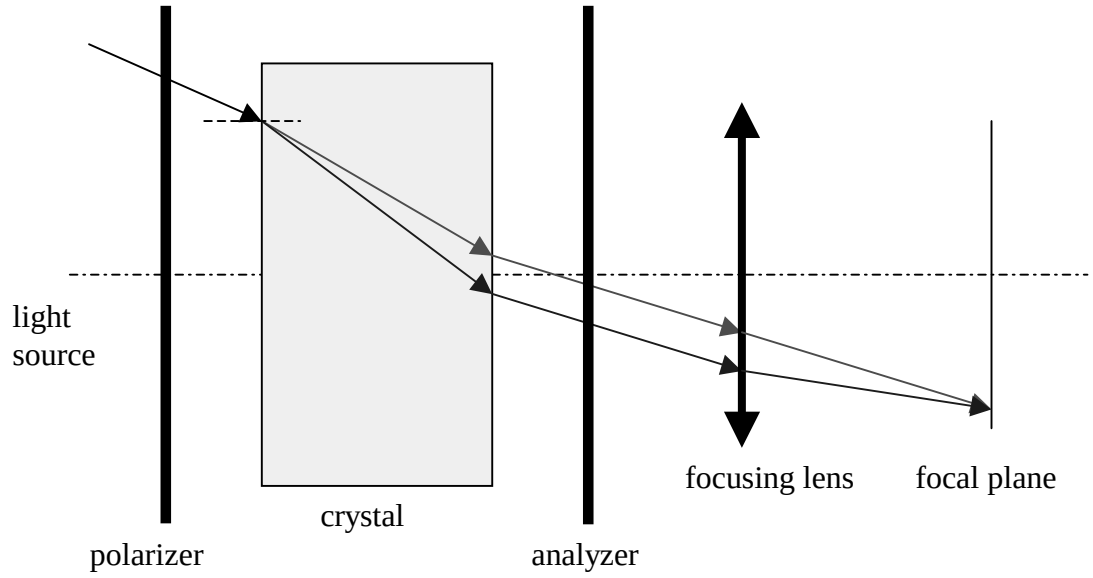

Figure 1. Birefringence in anisotropic medium

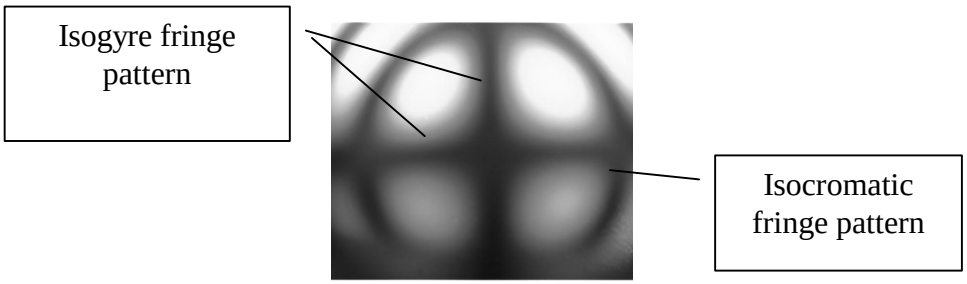

Figure 2. Interference fringe pattern for an anisotropic medium

This intensity can be plotted on a plane normal to the set-up axis, and we see that the phase difference, which only depends from the refraction index, generates the isochromatic fringe pattern, while we identify another interference figure in the shape of a cross, called isogyre, due to polarisation, and so independent from the refraction index (see figure 2).

If the medium is under stress, it modifies its refraction index as explained in the following equation (1) [4]:

$$\{\Delta n\} = [\pi] \bullet [S] \bullet \{t\} \qquad (1)$$

In (1) $\{t\}$ is the stress vector, $[S]$ is the compliance matrix, and $[\pi]$ is the piezo-optic matrix, which relates the strain in a variation of the refraction index.

In the case of PWO crystals the applied stress modifies the refraction indices. The refraction index ellipsoid modifies and so we find, in general, two circular sections, instead of one: these circular sections put in evidence two optical axes instead of one. See figure 3 as a theoretical example.

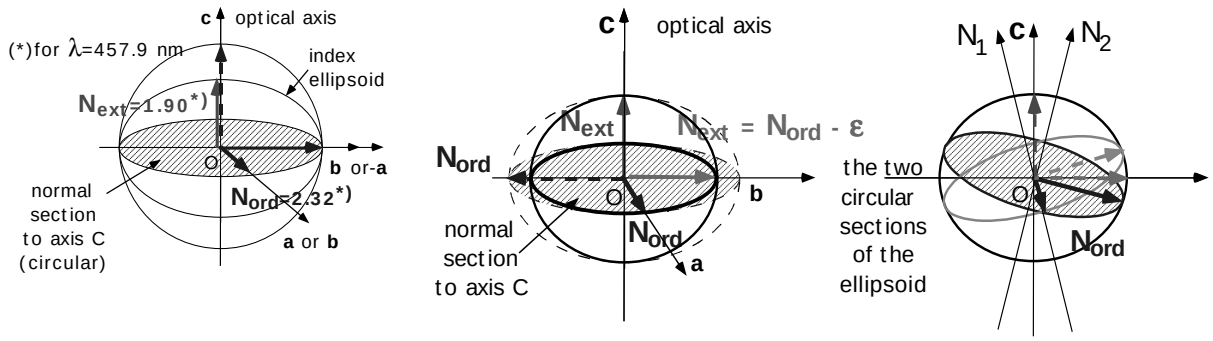

Figure 3. Effect of the stress on the refraction index of an anisotropic medium

If there is a change in the refraction index, there will be a change in the shape of the isochromatic fringe pattern: this deformation is obviously depending on the tensional state. Equation (1) allows predicting the interference fringe pattern of the crystal under mechanical load.

After putting in evidence the relationship between isochromatic fringe pattern and stress in a simple phenomenological way (because at present the π matrix is not known, at our best knowledge), we can perform a comparison between the predicted interference figures by a numerical way and the experimentally acquired photographs for the same load conditions.

Figure 4 illustrates this comparison in the case of bending load: at the left we have the simulation obtained by software, at the right we have an image acquired by a CCD camera, after loading the crystal under bending. The isochromatic is deformed from a circle into a pear-like shape: a good agreement between simulation and experiment is observed.

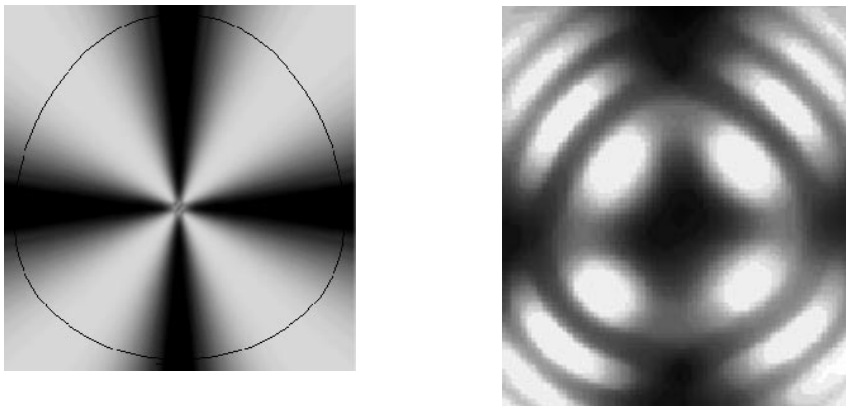

Figure 4. Comparison between a software simulation and a real fringe pattern deformation

3. Experimental set-up

To measure the internal stress, a dedicated plane polariscope was built, equipped with a mechanical loading device and a three-degrees of freedom support to move a CCD camera across a polar co-ordinate reference frame centred on the crystal.

The crystal is placed in the polariscope and loaded. Two loading devices are built to apply known stresses on the crystals. The two loading devices allow to load the crystals respectively under compression stress (figure 5) and under bending stress (figure 6). Then the measurement system is tested and calibrated.

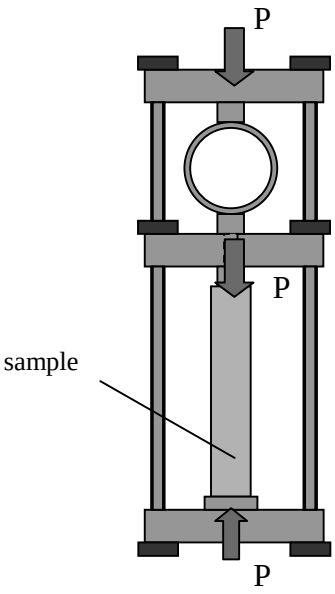

$$\sigma = \frac{P}{A}$$

Figure 5. Compression loading device

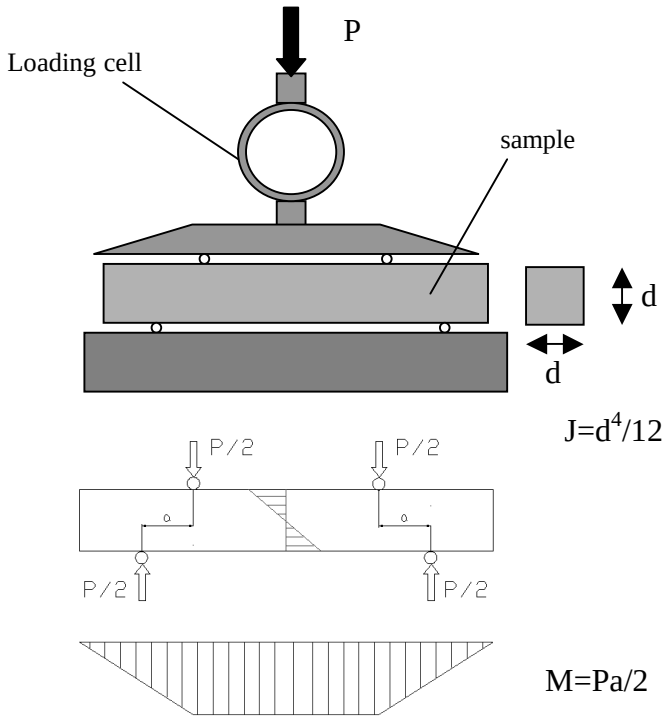

$$\sigma = \frac{Md}{2J} = \frac{3Pa}{d^3}$$

Figure 6. Bending loading device

4. Image analysis: measurement of photoelastic parameters

After digitising the picture, it is possible to measure some geometrical parameters:

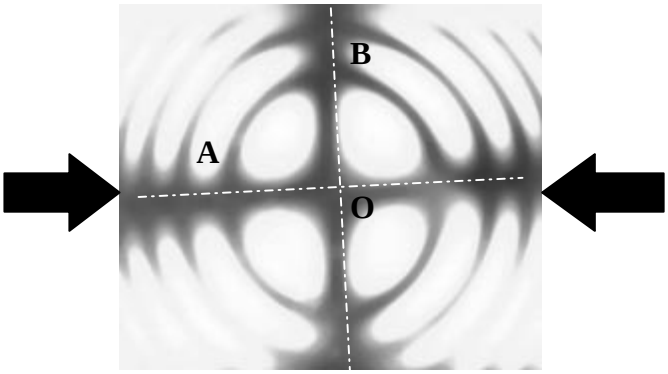

Figure 7. Sample under compression load

Taking as a reference figure 7:

1) Measure the length of semi-axis OB=b
2) Measure the length of semi-axis OA=a
3) Calculate the ratio between the axes and subtract 1 to obtain the elliptical ratio c:

$$c = \frac{b}{a} - 1 \qquad (2)$$

The photoelastic constant f_σ is the ratio of the elliptical ratio to the corresponding stress:

$$f_\sigma = \frac{c}{\sigma} \qquad (3)$$

It has not been previously measured to our knowledge.

We have experimentally measured the photoelastic constant by doing a series of loading with known stresses on a sample and analysing the deformation of the interference fringe pattern.

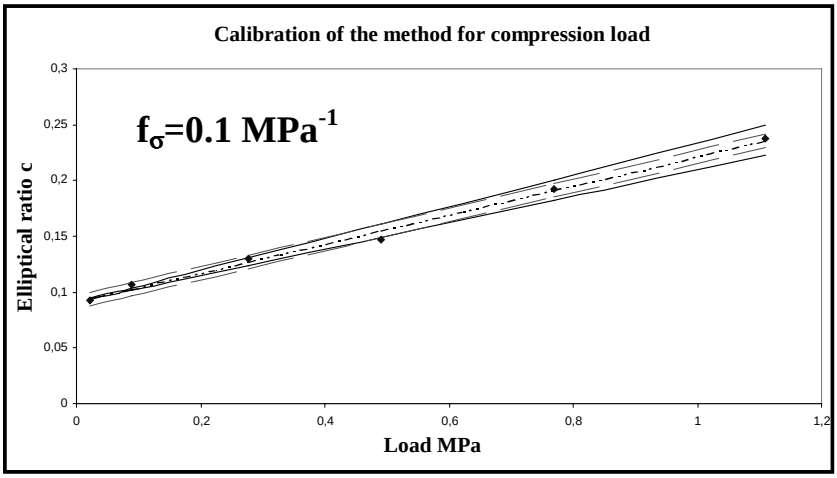

standard deviation on f_σ
$\pm 3s_f$=4%
standard deviation on c_o
$\pm 3s_b$=6%

Figure 8. Calibration of the method for compression load

Figure 8 shows the experimental results related to the applied load. We observe **a** linear behaviour as expected from the mathematical simulations.

The mentioned coefficient f_σ, the standard deviation on this coefficient (s_f), and the systematic error band (s_b) were calculated.

We have therefore experimentally measured the photoelastic constant of PWO**:**

f_σ=0.1MPa^{-1} with an offset of 0.08 MPa.

We interpret this offset as a residual internal tension.

5. Residual stress measurement

As an application some residual stress measurement were performed on a sample produced from a rod cut only on one side, inducing residual tension.

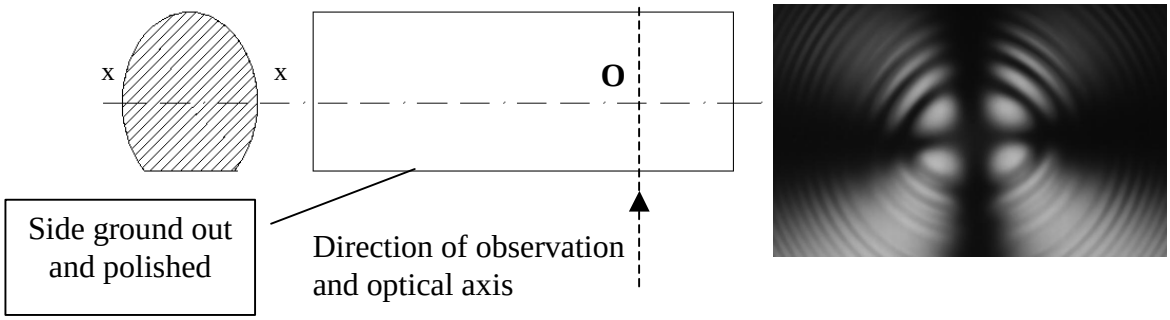

Figure 9. Residual stresses in a PWO crystal

Figure 9 represents the figure of interference at point O, revealing a tensional state of 1,67 MPa oriented along the axis x-x.

6. Conclusions

We have measured the photoelastic constant of PWO and we have developed a quality inspection procedure to prevent mechanical breaking of the crystals.

1. The photoelastic constant of PWO was determined and measured:

$$\mathbf{f_\sigma = 0.1\ MPa^{-1}}$$

2. A bench for residual stress inspection of crystals was built, for a contactless, non-destructive and quick procedure.
3. This method can be applied to any monoaxial transparent scintillating medium, of any size and material.
4. It is proposed for mass production inspection of the PWO crystals for the Electromagnetic Calorimeter of CMS at CERN-LHC.
5. It could be miniaturised for application to small size crystals used in medical applications.
6. With further developments of the model the piezo-optical matrix of PWO will be determined from specific conditions of observation

References

1. Born, M., Wolf, E., Principles of Optics, 6th edition, Cambridge University Press, New York 1980.
2. Wood, E., A., Crystals and Light, Dover, New York 1964.
3. Walhstrom, E., E., Optical crystallography, Wiley, New York, 1960.
4. Perelomova, N., V., and Tagieva, M., M., Problems in crystal physics with solution, Mir Publishers, Moscow.
5. Landau, Lifshitz, Théorie de l'élasticité, 1946 Editions de Moscou.
6. Rosenfeld, A., Kak, A., C., Digital picture processing, II edizion, Computer Science and Applied Mathematics.
7. Lebeau, M., Principles of mechanical processing of anisotropic scintillating crystals, CMS Note 1997/024, CERN, Geneva.
8. Baccaro, S., Barone, L., Borgia, B., Castelli, F., Cavallari, F., De Notaristefani, Diemoz, M., Faccini, R., Festinesi, A., Leonardi, E., Longo, E., Mattioli, M., Montecchi, M., Organtini, G., Paoletti, S., Valente E., Optical properties of Lead Tungstate ($PbWO_4$) crystal for LHC em-calorimeter, University of Rome 'La Sapienza', Physic Departement, internal note No. 1066, August 1995.
9. Ishii, M., Harada, K., Kobayashi, M., Usuki, Y., Yazawa, T., Mechanical properties of $PbWO_4$ scintillating crystals, Nuclear Instruments Meth. A376 (1996) 203-207.
10. Lebeau, M., Rinaldi, D., Photoelasticity for the inspection of mechanical stress in birefringent monoaxial crystals, Scint'97, International Conference on Inorganic Scintillators and their Applications, Shanghai, 22-25 September 1997.
11. Lebeau, M., Majni, G., Paone, N., Rinaldi, D., Photoelasticity for the investigation of internal stress in BGO scintillating Crystals, Nuclear Instruments Meth. A397 (1997) 317-322.
12. Kobelev, N., P., Soyfer, J., M., Elastic moduli of lead tungstate, Solid State Physics, 1996 vol. 39 N12 3589-3594 (in Russian)
13. Dorenbos, P., Van Eijk, C., Inorganic scintillators and their applications, Delft University press, 1995
14. Cocozzella, N., Quality control in scintillating crystals through interference fringe pattern analysis: theoretical study, design and construction of a test bench, Thesis, University of Ancona, March 1999 (in Italian).

Infrared scintillation in crystals

S.Belogurov[1], G.Bressi[2], D.Iannuzzi[2], G.Carugno[3], E.Conti[3], A.T.Meneguzzo[3]

[(1)]*I.T.E.P., B. Cheremushkinskaya 25, Moskow, Russia*
[(2)]*I.N.F.N. sez. di Pavia and Univ. di Pavia, v. U.Bassi, 6, Pavia, Italy*
[(3)]*I.N.F.N. sez. di Padova and Univ. di Padova, v. F.Marzolo, 8, Padova, Italy*

Abstract: We present experimental results on infrared scintillation in some crystals (CsI(Tl), Ge, CeF_3, BaF_2, PbF_2, PWO, Si, BGO,...). A chopped proton beam excited the samples. Radiation with wavelength within 1 and 15μm was detected by means of an infrared sensor. Infrared emission occurs in many crystals. CsI(Tl) showed the most promising characteristics. We therefore measured its infrared scintillation spectrum and yield. The spectrum present a wide and asymmetric peak at λ=(1.603±0.005)μm. The infrared scintillation yield is $(4.9\pm0.3)\cdot10^3$photons/MeV.

Keywords*:* scintillation, infrared, CsI(Tl)

Introduction

The systematic study of infrared (IR) scintillation has been started quite recently. Measurements were done in gaseous and liquid noble gases [1,2,3,4] where significant amount of IR light induced by ionizing particles was observed. The availability of IR detectors with high quantum efficiency and the positive results obtained with noble elements lead us to investigate scintillation properties of inorganic solid state samples in the wavelength range between 1 and 15μm. In the first part of this paper we report on experimental evidences of IR scintillation in crystals. The second set of measurements presented regards on spectrum analysis and yield evaluation in CsI(Tl).

First section of measurements: infrared scintillation in crystal samples

Experimental set up

The experimental apparatus is drawn in figure 1.

A 4 MeV proton beam, extracted from the Van der Graaf accelerator of Laboratori Nazionali di Legnaro, chopped in 400μs bunches by a rotating wheel, exited into air through a 10μm thick kapton window. The beam was collimated by a 2mm-diameter collimator, which was also used to monitor the beam intensity.

The crystal samples were placed in front of the window. On the opposite side of the crystal, a sensor detected the IR radiation. The distance between the sensor and the window was 23mm.

The IR detector was a HgCdTe sensor, $1mm^2$ area. It was sensitive in the wavelength region 1-15μm, with a quantum efficiency of about 65% between 1 and 12μm. To reduce the noise the detector was cooled down to liquid nitrogen temperature. Just in front of the detector a pure Si slice, 500μm thick, was placed to filter out the radiation with wavelength smaller than 1.2μm.

The HgCdTe signal was read by a current amplifier connected to a digital oscilloscope. Each measurement was obtained by averaging about 1000 tracks of the IR signals by means of the oscilloscope.

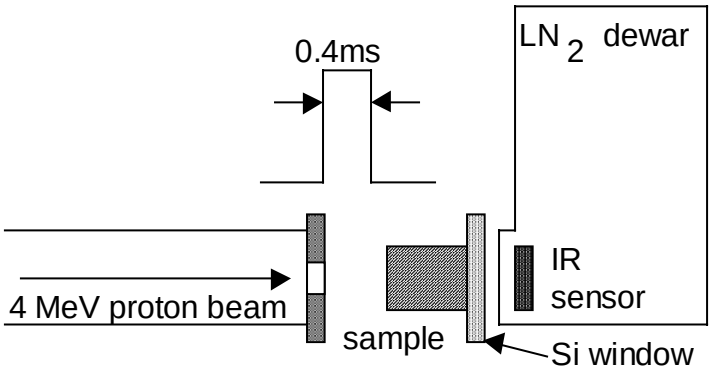

Figure 1: experimental apparatus used to study IR emission in crystals

In table 1 the list of the investigated crystals is reported. We chose materials transparent in the IR region. The quality of the bulk crystal was good for all the samples, except for NaI(Tl) which was probably damaged by humidity. The measure for that sample is poorly significant. The surfaces of the samples were optically polished, except for CsI(Tl) and sapphire. The surface of Ge crystal was oxided. The surfaces of PbF_2 and NaI(Tl) were bad due to roughness.

Taking into account the beam intensity variation and the energy lost in air, each sample absorbed the same amount of energy within 25%.

Experimental results and discussion

Fig.2 shows the detected IR signal obtained from some of the studied samples. Except for CsI(Tl), the y-scale is the same to allow a quick comparison of the signals.

Many samples present significant IR scintillation. It is interesting to underline that IR emission also occurs in materials which are not used as scintillators, such as Ge and Si.

For a correct comparison of the signal amplitude, light collection efficiency must be taken into account. The dominant factor to be considered is the solid angle view of the detector. Since the proton range in the crystals is very short (<100μm), we can assume that IR light generation is point-like and comes from the crystal face in front of the beam, opposite to the detector. The normalized IR signal amplitudes are reported in the 5th column of table 1. CsI(Tl) has the highest light yield. Ge is more than one order of magnitude below. CeF_3, BaF_2, NaI(Tl), PWO, PbF_2 show much lower amplitudes. Other crystals seem to be less interesting.

The time behavior of the light signals is quite different. For some samples (CsI(Tl), BaF_2, Al_2O_3) the light signals overlap the beam shape. Other crystals such as PbF_2, Ge, CeF_3 present long decay times . The decay times are well described by the formula:

$$V(t)=A\cdot\exp(-t/\tau_F)+B\cdot\exp(-t/\tau_S)+C$$

where τ_F and τ_S are the decay times of the fast and slow component respectively. The results of the interpolation are reported in table 1.

"Slow" crystals have τ_F of the order of some hundreds μs. For "fast" crystals (CsI(Tl), BaF_2, Al_2O_3) τ_F ranges between 60 and 90μs. This is just an upper limit since the average decay-time of the proton bunch as produced by the rotating wheel is about 80μs. For CsI(Tl) and Al_2O_3 the slow component in negligible. For BaF_2 the coefficient ratio *A/B* is 0.09.

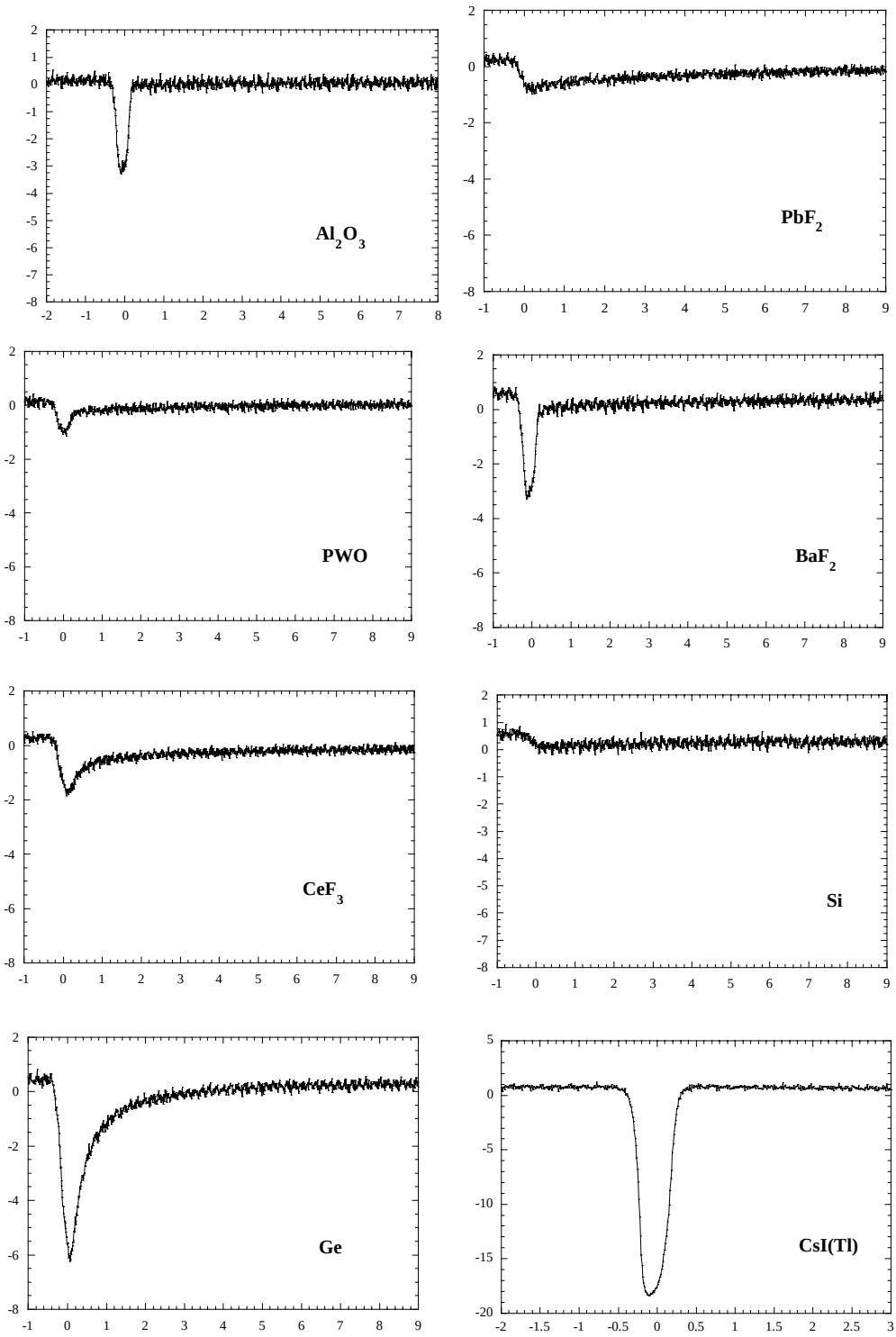

Figure 2: Examples of IR signals for some crystals. X-scale is in ms, Y-scale in mV

Table 1: List of the investigated samples. Details on the content of each column are reported in the text

Sample	Surface quality	Bulk quality	Length (mm)	IR signal (A.U.)	τ_F (µs)	τ_S (ms)
CsI(Tl)	good but not optically polished	ok	20	10.9	61±1	
Ge	oxided, not optically polished	ok	10	1.29	330±10	1.8±0.1
CeF_3	ok	ok	9.5	0.41	300±20	3.4±0.6
BaF_2	ok	ok	5	0.32	89±4	5.0±1.3
NaI(Tl)	bad	bad	23	0.3		
PWO	ok	ok	10.5	0.27	120±20	3.6±0.7
PbF_2	bad	ok	7.8	0.16	390±20	4.7±0.9
Al_2O_3	not optically polished	ok	0.8	0.075	72±3	
Si	ok	ok	0.5	0.01		2.6±0.6
BGO	ok	ok	19.8	<0.1		
ZnSe	ok	ok	3	0.015		
AgCl	ok	ok	1	0.02		
ThF_4	ok	ok	9.2	0.052		
AgBr	ok	ok	1	0.016		
GaAs(Zn)	ok	ok	0.3	0.005		
Quartz	ok	ok	0.9	<0.005		

From the measurements presented above, the following conclusions can be argued:

1) many crystals do emit IR radiation when irradiated with protons;
2) CsI(Tl) presents a very high yield compared to the other samples. Also Ge seems to be a good IR scintillator;
3) for almost all the samples, the decay part of the time response presents a double exponential shape. For CsI(Tl), BaF_2, Al_2O_3 the fast component is compatible with the bunch spread and the slow component is not relevant. The other samples show long decay times.

Second section of measurements: spectrum and light yield in CsI(Tl)

Experimental set up

An electron beam excited the CsI(Tl) crystal and its scintillation light was analyzed by a monochromator. The electrons were produced in bunches of 20ns with energy of 70 keV and were focused on the sample by a magnetic lens. A large area (diameter=5mm) InGaAs photodiode was placed close to the output slit of the monochromator. The photodiode was sensitive in the wavelength region from 0.9 to 1.7µm, with an average quantum efficiency of 0.76. It was biased in the reverse mode and read out by a charge amplifier connected to a digital oscilloscope. The CsI(Tl) face in front of the monochromator was polished with 0.3µm grain size optical polishing card. Signals were averaged over 50 samples for each position of the monochromator by means of the digital oscilloscope.

For the measurement of light yield the monochromator was removed and another InGaAs photodiode was used. It was sensitive over a wider spectral range up to 2.4µm. The

photodiode detected both the visible and the IR components of the scintillation. It was possible to insert a filter in front of the IR sensor, which transmitted light only between 1.25 and 1.75μm. Its average transmission was 84%.

Results and discussion

The IR scintillation spectrum in CsI(Tl) is shown in figure 3. The emission spectrum is corrected for efficiency of the detector and of the monochromator. The spectrum is quite wide and asymmetric, with a maximum at λ=(1.603±0.005)μm.

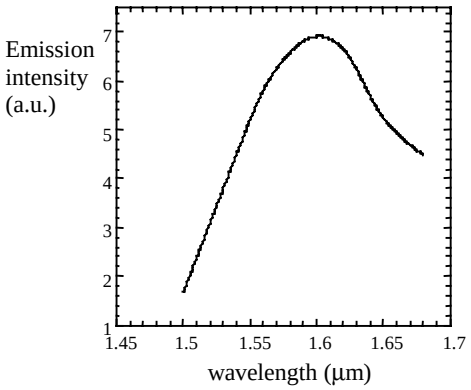

Figure 3: CsI(Tl) IR scintillation spectrum

The IR scintillation light yield (Y_{IR}) was estimated by the ratio of the pulse measured with (A_f) and without (A_{tot}) optical filter:

$$A_f / A_{tot} = (Y_{IR} \cdot T \cdot Q_{IR}) / (Y_{Vis} \cdot Q_{Vis} + Y_{IR} \cdot Q_{IR})$$

where Y_{Vis} is the known visible light yield, Q_{IR} and Q_{Vis} are respectively the mean quantum efficiency of the detector in the IR and visible region of the spectrum, and T is the mean transmittance of the optical filter. Putting $Y_{Vis}=(64.8\pm3.2)\cdot10^3$photons/MeV[5], we obtain: $Y_{IR}=(4.9\pm0.3)\cdot10^3$photons/MeV.

Conclusion

In this paper we reported about IR scintillation in crystal samples. To our knowledge this is the very first study on this topic. We believe that results obtained so far are very promising and we are working to clarify the origin of the IR scintillation in crystals and to find high yield and fast IR scintillators.

Acknowledgments

The authors thank Crystal Clear Collaboration and P.Leqoc for having provided some of the investigated samples. They also are grateful to Laboratori Nazionali di Legnaro staff. One of the author (SB) is grateful to Padova INFN section for financial support.

References

1. G.Carugno, Nucl. Instr. and Meth. **419** (1998) 617
2. G.Bressi *et al.*, submitted to Phys. Rev. A (Preprint DFPD99EI/36, Univ. di Padova)
3. S.Belogurov *et al.*, submitted to Nucl. Instr. and Meth. (Preprint DFPD99EI/33, Univ. di Padova)
4. G.Bressi *et al.*, submitted to Nucl. Instr. and Meth. (Preprint DFPD99EI/34, Univ. di Padova)
5. J.D.Valentine *et al.*, IEEE Trans. Nucl. Sci. **40** (1993) 1267

Influence of dopant ions on traps and recombination centres in lead tungstate

A. Vedda [(1)], M. Martini [(1)], F. Meinardi [(1)], M. Nikl [(2)], E. Mihokova [(2)], G.P. Pazzi [(3)], P. Fabeni[(3)], Y. Usuki [(4)], S. Baccaro [(5)]

[(1)] *Istituto Nazionale per la Fisica della Materia and Dipartimento di Scienza dei Materiali dell'Universita' di Milano-Bicocca, Via Cozzi 53, I-20125 Milano, (Italy)*
[(2)] *Institute of Physics, Academy of Sciences of the Czech Republic, Cukrovarnická 10, 162 53 Prague (Czech Republic)*
[(3)] *IROE del CNR, Via Panciatichi 64, 50127 Firenze, (Italy)*
[(4)] *Furukawa Co., Yoshima, Iwaki 970-11, Japan*
[(5)] *ENEA-INN/TEC, Via Anguillarese 301, 00060 S. Maria di Galeria, Roma, (Italy)*

Abstract: Traps and recombination centres in lead tungstate have been investigated by wavelength resolved Thermally Stimulated Luminescence (TSL) measurements after X-ray irradiation at 10 K and at 90 K. An undoped sample, and samples doped with aliovalent ions (Gd^{3+}, Nb^{5+}) have been considered. TSL structures at around 10-20 K, 50 K and 100 K are common features observed in all cases. Moreover, TSL peaks above 100 K are detected only in undoped and Nb^{5+}-doped crystals. The spectral composition of the emitted light reveals the existence of complex emission patterns strongly influenced by doping. The results are discussed on the basis of the possible role of the different dopant ions in the $PbWO_4$ lattice.

Keywords*:* lead tungstate, thermally stimulated luminescence, point defects

1. Introduction

In recent years the study of trap levels in $PbWO_4$ by Thermally Stimulated Luminescence (TSL) has been undertaken, due to their possible influence on the scintillation time decay and on the light yield of the material. Up to now, major attention has been given to TSL peaks above 100 K: in fact, it was found that trap levels occurring in the 150-250 K range and characterised by decay times at room temperature in the μs-ms time scales, strongly affect the scintillation process by giving rise to slow decay components at room temperature mostly related to the green emission band at 2.5 eV [1]. These trap levels appear to be related to point defects induced by the occurrence of Pb^{2+} deficiency in crystals grown by the Czochralski technique, as demonstrated by the role played by trivalent dopants (La^{3+}, Gd^{3+}) in lowering their intensity [2-4]. The proposal of a relation of the traps with oxygen vacancies has been put forth [5], but no electron centres directly related to those defects were found by EPR studies up to now. On the other hand, it was demonstrated that among extrinsic defects, $(MoO_4)^{3-}$ paramagnetic centres are associated to TSL traps evidenced in the 200 K region [6]. More recently, a correlation between a trap giving rise to a TSL peak at 50 K and a paramagnetic electron centre, namely an electron localized in a regular tungsten group $(WO_4)^{3-}$ [7,8], was established [9,10].

The emission spectra of the TSL were not extensively studied up to now [9,10]; however, the results concerning undoped and La^{3+}-doped crystals already put in evidence an influence of the spectral distribution of the TSL upon doping [10]. The aim of this work is to extend the picture of the wavelength resolved TSL properties of $PbWO_4$ in the 10-250 K temperature range by considering the effects of other aliovalent ions. By wavelength resolved measurements, the TSL emission spectra have been obtained on undoped crystals, as well as

on samples doped with Gd^{3+}, and Nb^{5+}: the results are discussed in comparison with those already obtained upon La^{3+} doping.

2. Experimental conditions

Crystals of undoped, Gd^{3+} and Nb^{5+} doped $PbWO_4$ were grown by Furukava Ltd (Iwaki, Japan) from 5N purity raw material. The doping levels in the melt were 135 ppm and 1350 ppm for Gd^{3+} and Nb^{5+} respectively. Taking into account the segregation coefficients of Gd^{3+}(~ 1.4) and Nb^{5+} (~ 0.4) dopants in the $PbWO_4$ lattice, expected true concentrations are about 170-190 at. ppm and 600-700 at. ppm in the crystal, respectively. TSL measurements in the 10-250 K range were performed following 10 K and 90 K X-ray irradiation (by a Philips 2274 X-ray tube operated at 20 kV). The TSL apparatus was a high sensitivity spectrometer measuring the TSL intensity both as a function of temperature and wavelength: the detector was a double stage microchannel plate followed by a diode array. The detection range was 200-800 nm and the spectral resolution was about 5 nm. A 0.1 K s^{-1} heating rate was used.

3. Results and Discussion

The 3D TSL measurements and contour plots of the TSL obtained after X-irradiation at 10 K are shown in Figs. 1, 2, and 3, for the undoped, Nb^{5+}- and Gd^{3+}-doped crystals respectively. Peaks at around 10-20 K are detected in all cases, whose low intensity is probably related to their closeness to the irradiation temperature. Another common feature of all samples is a strong TSL structure at around 50 K. Moreover, a further peak at 100 K is evidenced only in the case of the Gd^{3+}-doped sample. The spectral composition of the TSL signal in the 50 K region appears to be dependent upon doping: while only slightly different emissions are detected in the cases of undoped and Gd^{3+}-doped crystals (peaking at 430 and 440 nm at 50 K respectively), the spectrum of the Nb^{5+}-doped sample at 50 K is dominated by a distinct emission peaking at 480 nm. In the 100 K peak of the Gd^{3+}-doped crystal, emission at around 450 nm is observed.

In order to put in evidence the existence of higher temperature peaks, TSL measurements were also performed by irradiation at 90 K with a higher dose: no further structures were observed in the case of Gd^{3+}-doping, as only the 100 K peak already evidenced by the 10 K irradiation was detected. On the other hand, undoped $PbWO_4$ shows peaks at 90-100 K, 140-150 K and a composite structure in the 170-230 K region (Fig. 4). In the case of Nb^{5+}-doping, shown in Fig. 5, TSL emission is restricted below 200 K with peaks at 105 K and at 160-180 K.

At variance with what observed at 50 K, above 90 K the emission of the undoped sample is centred at 500 nm; emission at longer wavelength with respect to the 50 K region is observed in the case of Nb^{5+}-doping as well (λ_{max} = 580 nm and 540 nm at 105 K and at 170 K respectively). A slight low energy shift from the low T to the high T side of both the 105 and the 160-180 K structures is observed, which suggests the existence of different spectral components.

The intrinsic character of the traps responsible for TSL in the 10-20 K and 40-70 K region is put in evidence by their common presence in all investigated samples. Actually, it was recently demonstrated that the glow curve in this latter temperature range is composite, the dominant peak at 50 K being followed by minor structures at 55 and 67 K [10]. The thermal depths of these peaks turned out to be 48 meV, 65 meV and 104 meV respectively: very good agreement between the thermal depth of the principal peak at 50 K and the thermal ionisation energy of the $(WO_4)^{3-}$ paramagnetic electron centre [8] was found, leading to the identification of this trap state as responsible for the 50 K TSL peak. Moreover, the simultaneous presence of additional closely lying TSL peaks could suggest the existence of different variants of the $(WO_4)^{3-}$ centre.

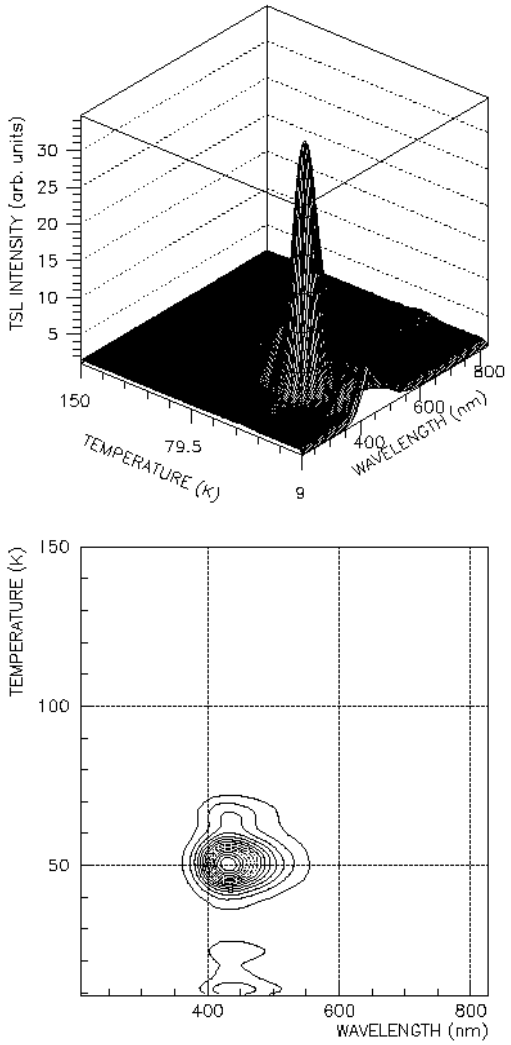

Fig. 1: 3D TSL measurement and contour plot of the TSL after X-ray irradiation at 10 K of undoped $PbWO_4$.

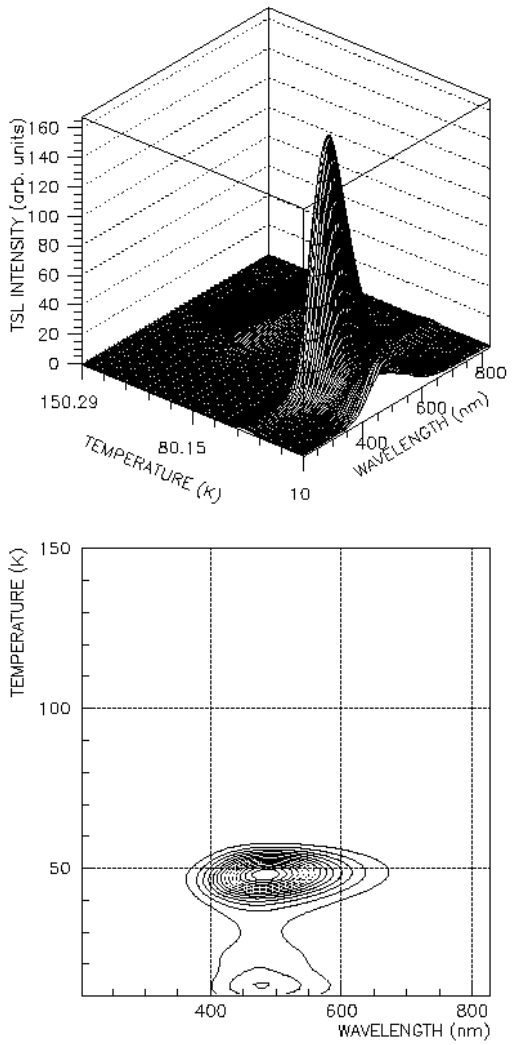

Fig. 2: 3D TSL measurement and contour plot of the TSL after X-ray irradiation at 10 K of Nb^{5+} -doped $PbWO_4$.

In spite of the similarity of the TSL peak positions in the considered samples, an influence of doping is noticed on the spectral composition of the emitted light. In undoped and Gd^{3+}-doped crystals, emission in the blue spectral region is observed, related to transition within a regular (WO_4) group [12]: really, a slight low energy shift of the emission is noticed in the case of the Gd^{3+}-doped sample, possibly suggesting the existence of an emission centre perturbed by the presence of the trivalent dopant. This is in accordance with what observed in the case of La^{3+}-doped samples, in which besides the regular 2.8 eV emission also one further band peaking at 2.6 eV was detected in a limited temperature range at around 60 K [10]. A stronger influence of the dopant on the TSL recombination centre is however detected in the case of Nb^{5+}-doping, as the emission peaks at 480 nm at 50 K: under the assumption that green emission is due to transitions within oxygen-vacancy-related WO_3 centres [13], and in agreement with the expected influence of such substitutional lower valence dopant ion in the lattice, this result calls for the existence of a high concentration of such centres which dominate the TSL emission also at very low temperatures. This is supported also by the high concentration of Nb^{5+} ions in the sample.

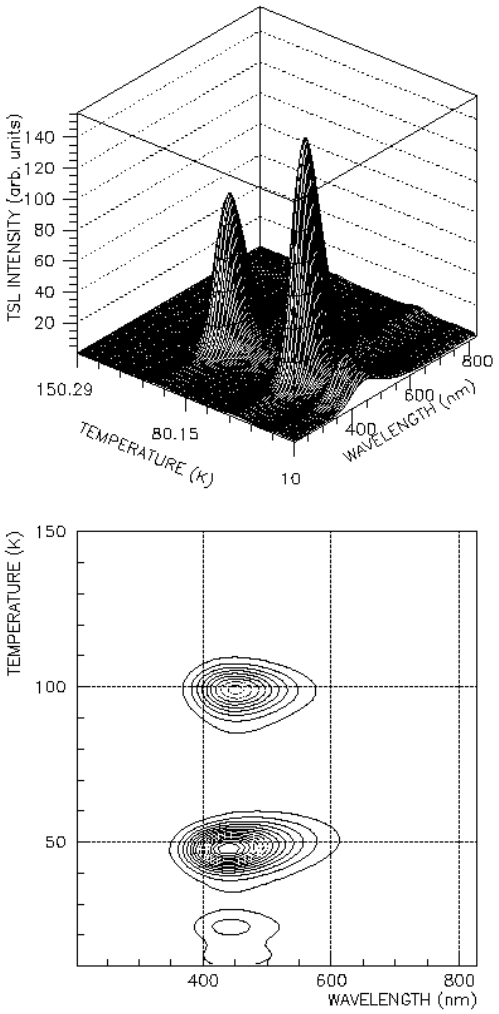

Fig. 3: 3D TSL measurement and contour plot of the TSL after x-ray irradiation at 10 K of Gd^{3+} - doped $PbWO_4$

At temperatures higher than 90 K, a strong influence of aliovalent ion doping on the TSL properties is observed. The undoped crystal display several TSL peaks above 100 K, which are not detected upon Gd^{3+}-doping. Moreover, the intensity of the 100 K structure is increased upon trivalent ion doping, as this peak was here observed in the undoped and Nb^{5+}-doped sample only after the strong x-irradiation at 90 K: as in the case of La^{3+}, such an increase can be explained by the occurrence of a higher concentration of traps or by an enhanced probability of charge capture in the absence of additional deeper states. Upon Nb^{5+} doping, suppression of TSL peaks is evidenced as well, but only for what concerns TSL structures in the 200 K region (Fig. 5). The different influence of substitutional Nb^{5+} dopant in the 150 and in the 200 K region leads to suggest a markedly different origin of trap states in these two temperature regions.

For what concerns the spectral composition of the TSL, at 100 K it turns out to be almost dominated by “regular lattice” blue emission in the trivalent ion doped sample. On the contrary, composite emission spectra extending in the green-red spectral region are observed in the undoped and Nb^{5+} -doped crystals; moreover, low energy emission is observed in these two latter cases at higher temperatures as well. Defect-related origins have been proposed both for green and red emission bands in $PbWO_4$ [13-16], and such defect states seem to operate as efficient recombination centres in TSL processes above 90 K.

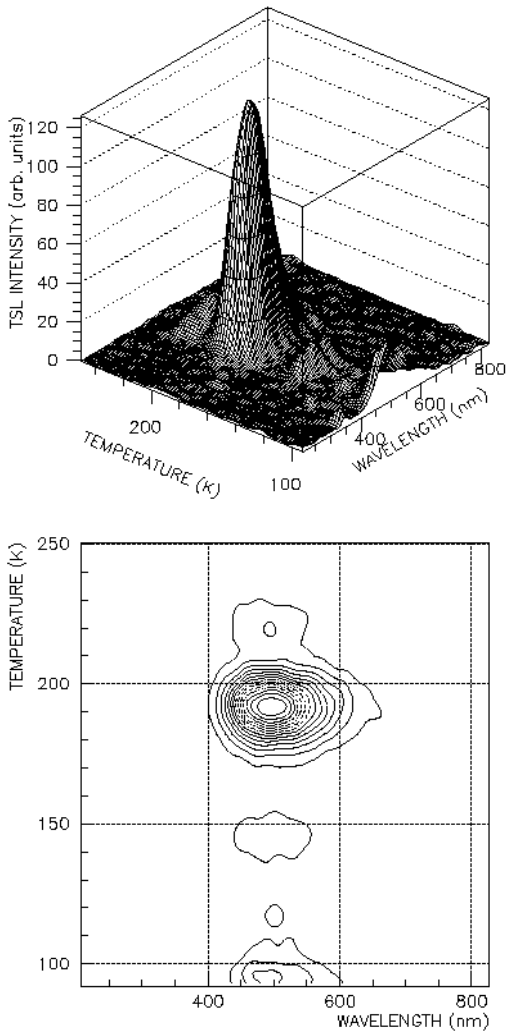

Fig. 4: 3D TSL measurement and contour plot of the TSL after X-ray irradiation at 90 K of undoped $PbWO_4$

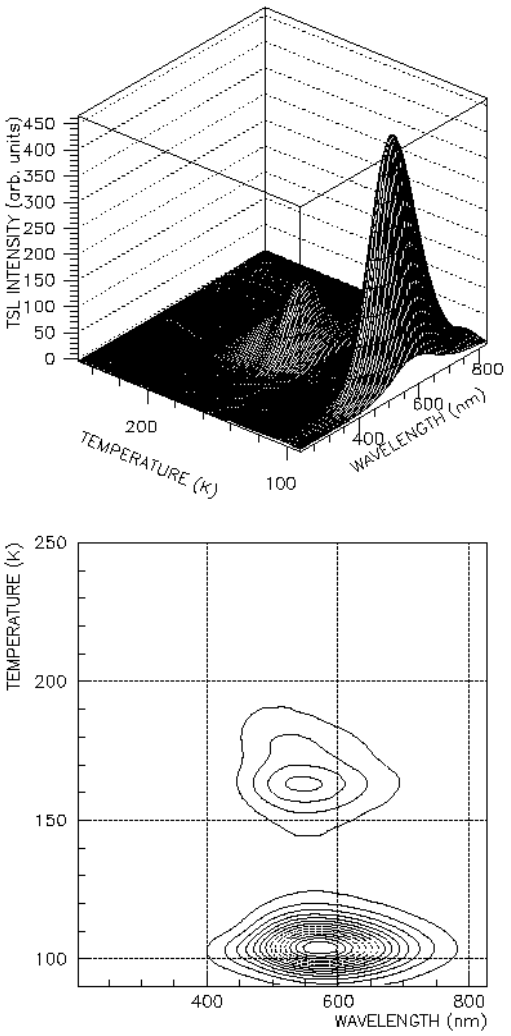

Fig. 5: 3D TSL measurement and contour plot of the TSL after X-ray irradiation at 90 K of Nb^{5+} -doped $PbWO_4$

Conclusions

In conclusion, the comparison between undoped, Gd^{3+} and Nb^{5+} ion doped crystals has allowed to put in evidence the complex role of these dopant ions on trap levels and recombination centres in an extended temperature range. The overall results demonstrate a higher efficiency of trivalent ion doping in reducing the concentration both of TSL traps above 100 K, and of defect-related emission centres.

References

1. M. Martini, G. Spinolo, A. Vedda, M. Nikl, K. Nitsch, V. Hamplova, P. Fabeni, G.P. Pazzi, I. Dafinei, P. Lecoq, Chem. Phys. Lett. **260** (1996) 418.
2. M.Nikl, P.Bohacek, K.Nitsch, E.Mihokova, M.Martini, A.Vedda, S.Croci, G.P.Pazzi, P.Fabeni, S.Baccaro, B.Borgia, I.Dafinei, M.Diemoz, G.Organtini, E.Auffray, P.Lecoq, M.Kobayashi, M.Ishii, Y.Usuki, Appl.Phys.Lett. **71** (1997) 3755.

3. S.Baccaro, P.Bohácek, B.Borgia, A.Cecilia, S.Croci, I.Dafinei, M.Diemoz, P.Fabeni, M.Ishii, M.Kobayashi, M.Martini, M.Montecchi, M.Nikl, K.Nitsch, G.Organtini, G.P.Pazzi, Y.Usuki, A.Vedda, Phys. Stat. Sol. (a) **164** (1997) R9.
4. S. Baccaro, P.Bohácek, B.Borgia, A.Cecilia, I.Dafinei, M.Diemoz, M.Ishii, O.Jarolimek, M.Kobayashi, M.Martini, M.Montecchi, M.Nikl, K.Nitsch, Y.Usuki, A.Vedda, Phys. Stat. Sol. (a) **160** (1997) R5.
5. M. Martini, E. Rosetta, G. Spinolo, A. Vedda, M. Nikl, K. Nitsch, I. Dafinei, P. Lecoq, J. of Lumin. **72-74** (1997) 689.
6. A. Hofstaetter, R. Oeder, A. Scharmann, D. Schwabe and B. Vitt, Phys. Stat. Sol. (b) **89** (1978) 375.
7. M. Bohm, F. Henecker, A. Hofstaetter, M. Luh, B.K. Meyer, A. Scharmann, O.V. Kondratiev, and M.V. Korzhik, Rad. Eff. and Defects in Solids, to be published.
8. V.V. Laguta, J. Rosa, M.I. Zaritskii, M. Nikl, Y. Usuki, J. Phys. Cond. Mat. **10** (1998) 7293.
9. M. Bohm, F. Henecker, A. Hofstaetter, M. Luh, B.K. Meyer, A. Scharmann, V. Metag, R. Novotny, O.V. Kondratiev, and M.V. Korzhik, Proceedings of the *"Workshop on Scheelite Tungstates"*, Oct. 12-14, 1998, Roma (Italy), to be published.
10. M. Martini, F. Meinardi, G. Spinolo, A. Vedda, M. Nikl. Y. Usuki, Phys. Rev. B, to be published.
11. M Springis, V. Tale, I. Tale, J. of Lumin. **72-74** (1997) 784.
12. W. Van Loo, Phys. Stat. Sol. (a) **27** (1975) 565.
13. R. Grasser, E. Pitt, A. Scharmann, G. Zimmerer, Phys. Stat. Sol. (b) **69** (1979) 359.
14. M.Kobayashi, M.Ishii, K.Harada, Y.Usuki, H.Okuno, H.Shimizu, T.Yazawa, NIM A **373** (1996) 333.
15. A.N. Annenkov, A.A. Fedorov, Ph. Galez, V.A. Kachanov, M.V. Korzhik, V.D. Ligun, J.M. Moreau, V.N. Nefedov, V.B. Pavlenko, J.-P.Peigneux, T.N. Timoshchenko and B. A. Zadneprovskii, Phys. Stat. Sol. (a) **156** (1996) 493.
16. M. Nikl K.Nitsch, S.Baccaro, A.Cecilia, M.Montecchi, B.Borgia, I.Dafinei, M.Diemoz, M.Martini, E.Rosetta, G.Spinolo, A.Vedda, M.Kobayashi, M.Ishii, Y.Usuki, O.Jarolimek, R.Uecker, J.Appl. Phys. **82** (1997) 5758.

Relaxation of electronic excitations in $PbWO_4$ and $CaWO_4$:Bi crystals

V. Nagirnyi[1], E. Feldbach[1], L. Jönsson[2], M. Kirm[1,3], A. Kotlov[1], G. Svensson[4], M. Åsberg-Dahlborg[4]

[1]*Institute of Physics, University of Tartu, Riia 142, 51014 Tartu, Estonia*
[2]*Physics Department, Lund University, Lund, Sweden*
[3]*II. Institute of Experimental Physics Hamburg University, Hamburg, Germany*
[4]*Department of Inorganic Chemistry, Chalmers University of Technology, Gothenburg, Sweden*

Abstract: Emission, excitation spectra of the main emission and those of the phosphorescence of $CaWO_4$:Bi and $PbWO_4$ crystals were studied using synchrotron radiation. It was shown that the relaxation of electronic excitations is characterized by a complicated cross-relaxation and charge transfer processes between cationic and anionic states in these systems.

Introduction

Despite extensive studies of $PbWO_4$ concerning its optical and scintillation properties, the nature of the excitonic states responsible for the light emission in this crystal is still under discussion. There are experimental and theoretical arguments in favor of both a cation exciton and an anion exciton model [1-4]. At present, many experimental data can be understood only taking into account an interplay between cation and anion sublattices, implying a complicated cross-relaxation between cationic and anionic excited states in $PbWO_4$ (see, e.g. [3]).

To investigate the processes of energy relaxation between cationic and anionic states it was interesting to compare $PbWO_4$ with $CaWO_4$:Bi. In the latter system, Bi^{3+}, occupying a cationic site in $CaWO_4$, has the same $6s^2$ electron configuration as Pb^{2+} in $PbWO_4$, and the energies of the first excited states of *6s6p* configuration in Pb^{2+} and Bi^{3+} ions are very close. As a comparison the peak energies of the emission and excitation bands of Pb^{2+} and Bi^{3+} ions in CaO are shown in Table 1.

Crystal	E_{em}, eV	E_{exc}, eV
CaO:Pb^{2+}	3.5	3.62
CaO:Bi^{3+}	3.3, 3.1	3.5

Table 1. The energies of the maxima of emission (E_{em}) and excitation (E_{exc}) bands in CaO:Pb and CaO:Bi [5,6].

The energy of the $6s^2 \rightarrow 6s6p$ electronic transition is expected to lie in the forbidden gap of $CaWO_4$ and therefore allows to investigate separately the processes of relaxation of electronic excitations under the excitation in cation impurity states and in the fundamental region.

Experimental

We studied the optical properties of $CaWO_4$:Bi crystals grown by the flux method at Chalmers University of Technology. During the growth Na^+ ions were introduced into the crystals to provide a local compensation of the Bi^{3+} extra charge. The investigated $PbWO_4$ crystals were of different origin (Bogoroditsk Techno-Chemical Plant, Russia, Furukawa Co., Japan, Institute of Physics, Prague, Czech Republic).

Reflection spectra as well as the excitation spectra of emission and phosphorescence of single $PbWO_4$ and $CaWO_4$:Bi crystals were studied in the region 3.5-30 eV at temperatures 8-300 K, using synchrotron radiation at the storage ring MAX I in Lund, Sweden. For comparison, a detailed spectroscopic study of the crystals was performed at the Institute of Physics, Tartu, using a conventional spectroscopic setup based on two double monochromators. Emission decay kinetics was investigated using the unique chopper at the SUPERLUMI station of HASYLAB at DESY, Germany [7].

Results and discussion

At 4.2 K, the excitation of a $CaWO_4$:Bi crystal in the fundamental absorption region ($E_{exc} \geq 5$ eV) produces an emission band which practically coincides with that of an undoped $CaWO_4$ crystal (Fig.1, curve 1). In the region 5–8 eV, where molecular oxyanionic excitons are directly created, the excitation spectrum of the main 2.88 eV emission (Fig. 2, curve 1) has practically the same shape as that of the intrinsic emission in pure $CaWO_4$ (Fig. 2, curve 2). However, the spectrum contains an additional low-energy excitation band peaking at 4.43 eV, which is caused by $6s^2 \rightarrow 6s6p$ electronic transitions in the Bi^{3+} ion. In [8] the shoulder at 4.15 eV in the excitation spectrum of $CaWO_4$:Bi powder at room temperature has been tentatively ascribed to $^1S_0 \rightarrow {}^3P_2$ transitions in the Bi^{3+} centre. However, this transition is known to be allowed only by vibronic interaction [9]. The intensity of corresponding absorption band should increase with temperature, and in a heavy Bi^{3+} ion, characterized by a strong spin-orbit interaction, one should expect it to be situated near the high energy C absorption band caused by $^1S_0 \rightarrow {}^1P_1$ transitions. In $CaWO_4$:Bi, the C absorption band is likely to be overlapped by the fundamental absorption of the crystal. Besides we observed a significant decrease of the 4.43 eV band intensity as the temperature was increased up to 295 K. In our opinion the 4.43 eV excitation band is connected with the transition to the lowest triplet excited state of Bi^{3+} ion ($^1S_0 \rightarrow {}^3P_1$ transition).

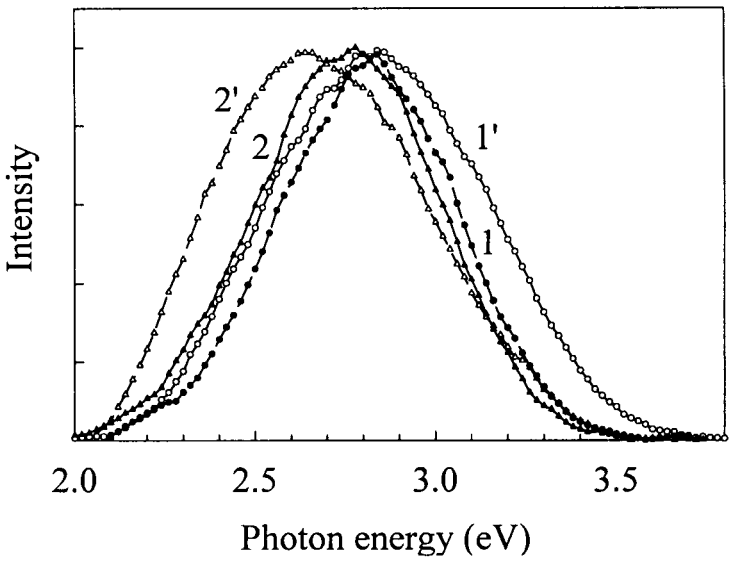

Fig. 1. Emission spectra of $CaWO_4$:Bi at excitation 5.3 eV (1, 1') and 4.43 eV (2, 2') at 8 K (1, 2) and 295 K (1', 2').

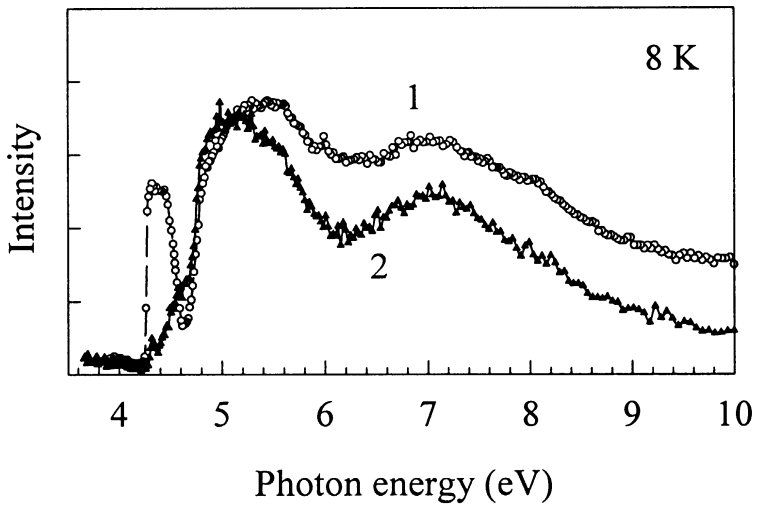

Fig. 2. Excitation spectra of the 2.9 eV emission in a $CaWO_4$:Bi (1) and pure $CaWO_4$ crystal (2) at 8 K.

This conclusion is supported by an asymmetric shape of this band with a typical for the A band double-peak structure at 4.2 K (see, e.g. [9]).

At 4.2 K, the emission spectrum of a $CaWO_4$:Bi crystal at the excitation in the impurity 4.43 eV band is only slightly shifted with respect to that at the direct optical creation of oxyanionic excitons at 5-8 eV (Fig. 1, curves 1,2) This fact leads to the suggestion that the oxyanionic complexes WO_4^{2-}, possibly perturbed by Bi^{3+} ions, rather than the triplet relaxed state of Bi^{3+} ion, might be responsible for the emission of $CaWO_4$:Bi even under the excitation of impurity states. Whereas under the excitation at 5-8 eV molecular excitons at regular WO_4 sites are mainly created. At room temperature the emission bands measured under the excitation in the impurity band and in the fundamental absorption region become more separated (curves 1', 2'). It may point to the different unharmonical effects in the relaxed excited states of regular and Bi^{3+}-perturbed WO_4^{2-} molecular ions.

In order to check the suggestion concerning the origin of the $CaWO_4$:Bi emission we studied the low temperature decay kinetics of the emission at the excitation in the fundamental absorption region and in the 4.43 eV band. The characteristic decay time of the triplet relaxed excited state of Bi^{3+} impurity centres in oxides and alkali halide crystals depends on which states of the triplet minimum are populated. It lies either in the nanosecond time scale if the emitting states are responsible for the emission, or in the millisecond scale if the metastable state is initially populated [10]. The decay time observed at the excitation in the impurity 4.43 eV band in $CaWO_4$:Bi was 30 μs at 8 K. This value does not agree with the decay times observed for Bi^{3+} centres in alkali halide and oxide crystals. It is closer to the decay time characteristic of WO_4^{2-} complexes in $CaWO_4$ (174 μs at 10 K [2]). This goes to prove further that the oxyanionic complexes are responsible for the emission at 4.43 eV excitation of $CaWO_4$:Bi. Thus we can conclude that although the Bi^{3+} states are responsible for the absorption at 4.43 eV, and this absorption band has a structure typical of the A absorption band of the mercury-like ions, the emission occurs from the electronic states of a WO_4^{2-} oxyanion molecule, perturbed by Bi^{3+} centre. This implies an effective energy transfer from bismuth to oxyanionic states during the relaxation of the luminescence centre.

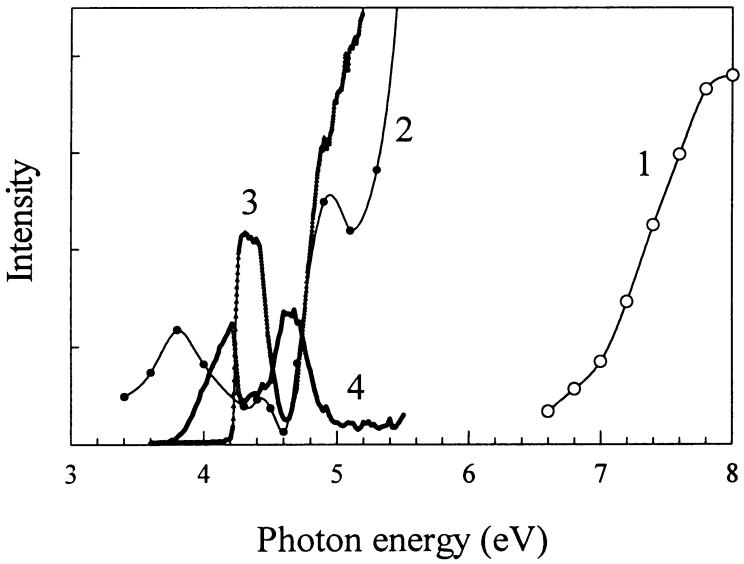

Fig. 3. Excitation spectrum of the TSL peak at 160 K in pure $CaWO_4$ at 80 K [3] (1) and excitation spectra of the phosphorescence (2), the 2.9 eV (3) and the 2.5 eV (4) emissions of $CaWO_4$:Bi at 4.2 K.

In order to establish whether the energy transfer from Bi^{3+} to WO_4^{2-} involves any charge transfer process we studied the excitation spectrum of phosphorescence in the region of the A absorption band of Bi^{3+} ions. The results of this study are shown in Fig. 3. It is known from the investigation of the excitation spectra of thermostimulated luminescence (TSL) that the creation of uncorrelated electron-hole pairs occurs in regular sites of a pure $CaWO_4$ crystal at the energies higher that 6.8 eV (Fig 3, curve 1) [3]. The excitation spectra of the phosphorescence in $CaWO_4$:Bi in the vicinity of the fundamental absorption edge and A absorption band of Bi^{3+} are shown in Fig. 3, curve 2. For comparison, the excitation spectra of the main blue emission (curve 3) as well as that of the

extrinsic green emission usually ascribed to oxygen-deficient WO_3 oxyanion complexes (curve 4) are depicted in the same figure. It is clear that the appearance of the phosphorescence at energies much lower than 6.8 eV is due to a short-range charge-transfer transitions in defective crystal sites, leading to the creation of correlated e-h pairs. The gap in the excitation spectrum of green emission at the energy ~4.4 eV reflects the competition in light absorption by Bi^{3+} ions and WO_3 complexes. A broad gap in the excitation spectrum of the phosphorescence is observed in the same energy region as the maximum of the A excitation band of Bi^{3+} ions and to the maximum of the excitation spectrum of the green emission, which indicates that neither Bi^{3+} ions, nor WO_3 complexes participate in the creation of correlated e-h pairs. That might mean that no charge is transferred in the process of the energy transfer from Bi^{3+} ion to WO_4^{2-} oxyanion at the excitation in the 4.43 eV band. Correspondingly, an effective energy transfer from bismuth to oxyanionic states involves a complicated cross-relaxation in the excited state of the luminescence centre. A clue to the reason of such a complicated cross-relaxation might be given by the recent theoretical band structure calculation performed for $PbWO_4$:Bi [11]. It has been shown that the Bi impurity band is situated in the forbidden gap in $PbWO_4$ and has a complicated structure involving also tungsten and oxygen states. Such a structure could promote a complicated branching during the relaxation in the Bi^{3+}-related luminescence centre, causing an energy transfer from Bi^{3+} to WO_4^{2-}. Similar processes are likely to occur in Bi-doped $CaWO_4$ crystal of the same scheelite type structure.

It is interesting to note that unlike the situation in a pure $CaWO_4$ crystal, the excitation spectrum of the phosphorescence in $CaWO_4$:Bi shows a sharp rise at energies higher than 5.3 eV. This phenomenon can stem from charge transfer processes from the impurity upper $^1P_1$ excited state situated in the low-energy part of the conduction band of $CaWO_4$:Bi.

The above discussed possibility of cross-relaxation between the excited states of a heavy mercury-like ion and WO_4^{2-} oxyanion may give an essential key to the understanding of the processes of electronic excitation relaxation in $PbWO_4$ crystals. The idea of possible complicated relaxation processes in a $PbWO_4$ crystal, involving both cationic and oxyanionic electronic states, has already been tentatively proposed in the literature [1, 3, 4]. In recent calculations of the band structure it was shown that there is an antibonding Pb6*s*-O2*p* σ^* hybrid state, situated close to the top of the valence band in $PbWO_4$ [11]. On the other hand, the calculations have shown that Pb related states are very diffuse in the conduction band and no density peculiarities are expected near the bottom of the conduction band [12]. Nevertheless, we believe that just like in a $CaWO_4$:Bi crystal, the cross-relaxation processes as well as charge transfer processes with the participation of both cationic and oxyanionic states play an important role in the relaxation of electronic excitations in $PbWO_4$ crystals. This can explain the very specific features observed in the emission decay kinetics [4], temperature dependence of emission intensity [4, 13] and in emission polarization properties in this crystal [14].

We found that charge transfer and recombination processes play an extremely important role in the relaxation of electronic excitations in $PbWO_4$. This is based on the investigation of an intense phosphorescence which may be effectively excited in the fundamental absorption region of $PbWO_4$ at $T<50$ K. Two well-known emission bands of the $PbWO_4$ crystal, the intrinsic blue emission at 2.9 eV and the extrinsic green emission at 2.5 eV, both contribute to the phosphorescence emission spectrum. The ratio of their intensities depends on the sample (Fig. 4). The investigation of the phosphorescence properties has been described in detail elsewhere [14]. Here we mention only its main features relevant for the subject of this paper. We found that the phosphorescence intensity constitutes up to 50% of the total emission intensity. It was shown that the phosphorescence has fast and slow decay stages. So, there is a

sequence of participating in recombination processes close and far separated pairs of electron and hole centres created due to charge transfer at the excitation by ultra-violet light.

The decay time is strongly temperature-dependent, indicating that recombination occurs due to the thermal release of one of the recombination partners. It was shown that this partner is a self-trapped electron localized in a regular oxyanionic site (WO_4^{3-} centre [15, 16]). In the most pure $PbWO_4$ crystals the intrinsic 2.9 eV band dominates in the phosphorescence emission spectrum (Fig. 4, curve 2). It means that the essential part of the phosphorescence originates from the recombination of released self-trapped electrons with holes in regular lattice sites or at the WO_4 complexes slightly perturbed by a defect in the cation sublattice. The polarization spectrum of the phosphorescence resembles that of the main emission. With all these data available we can draw the conclusion that charge transfer between cationic and anionic sublattices and recombination processes are the intrinsic features of the $PbWO_4$ the crystal, determining, to a large extent, its light emission properties.

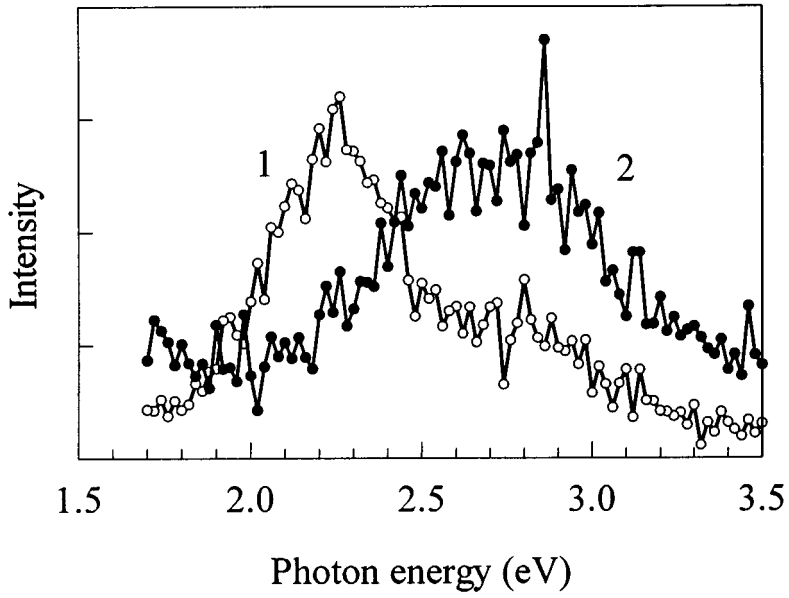

Fig. 4. Phosphorescence emission spectra of two different $PbWO_4$ crystals at 15 K.

It is worth mentioning that the excitation spectrum of the phosphorescence shows a sharp intensity increase at the excitation energy E>5 eV corresponding to the minimum energy needed for the creation of uncorrelated electron-hole pairs in $PbWO_4$ (Fig. 5, curve 1). This energy is obviously the minimum energy necessary for charge transfer between cationic and anionic sublattices, and it is surprisingly close to the energy of the sharp increase in phosphorescence efficiency at 5.2 eV in a $CaWO_4$:Bi crystal.

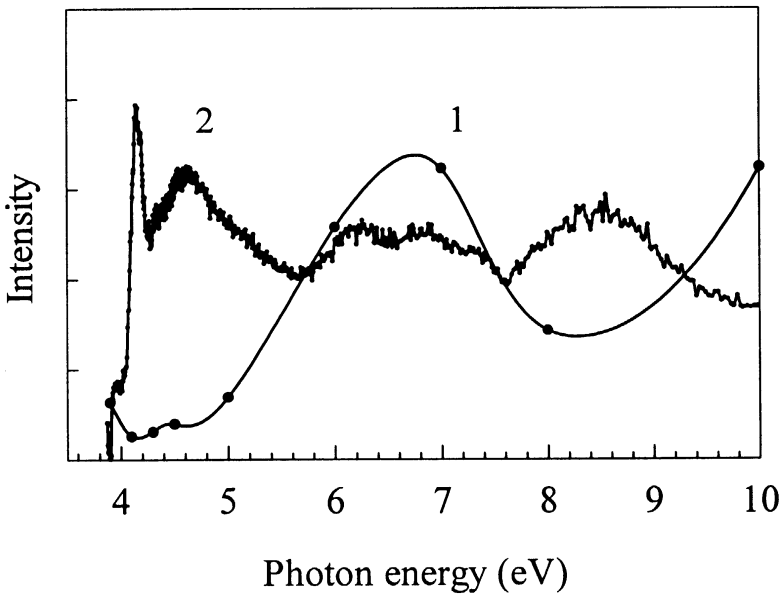

Fig. 5. Excitation spectrum of phosphorescence (1) and the 2.9 eV emission (2) of $PbWO_4$ at 8 and 15 K, respectively.

In conclusion, we would like to emphasize that a comparative study of $PbWO_4$ and $CaWO_4$:Bi gives the basis for understanding the relaxation processes in these systems. In our opinion their most explicit common feature is a remarkable interplay between cationic and oxyanionic states, including a complicated cross-relaxation and charge transfer processes in the excited states.

Acknowledgements

We are grateful to Prof. A. Lushchik and Acad. Ch. Lushchik for valuable discussion of the paper. This work was supported in part by the Estonian Science Foundation grant No. 3868. M. K. is grateful for the support from STINT Foundation (Sweden).

References

1. W. van Loo, *Phys. stat. sol. (a)*, **27**, 565 (1975).
2. M. J. Treadaway, R. C. Powell, *J. Chem. Phys.* **61**, 4003 (1974).
3. V. Mürk, M. Nikl, E. Mihokova, and K. Nitsch, *J. Phys.: Condens. Matter* **9**, 249 (1997).
4. D. Millers, S. Chernov, L. Grigorjeva, V.Pankratov, *Radiation Measurements*, **29**, 263 (1998).
5. A. E. Hughes, G. P. Pells, *Phys. stat. sol. (b)*, **71**, 707 (1975).
6. A. F. Ellervee, *Phys. stat. sol. (b)*, **82**, 91 (1977).
7. G. Zimmerer, *Nuclear Instruments and Methods in Physics Research A*, **308** 178 (1991).
8. R. B. Pode, S. J. Dhoble, *Phys. stat. sol. (b)*, **203**, 571 (1997).
9. V. Hizhnyakov, N. Kristoffel, Jahn-Teller mercuri-like impurities in ionic crystals. In *The dynamical Jahn-Teller effect in localized systems*, ed. by Yu. Perlin, M.Wagner, Elsevier Sci. Publishing, 1984, pp. 383-438.
10. Aceves, M. Barboza Flores, A. Maaroos, V. Nagirnyi, R. Perez Salas, T. Tsuboi, S. Zazubovich, V. Zepelin, *Phys. stat. sol. (b)*, **194**, 619 (1996).
11. R. T. Williams, Y. C. Zhang, Y. Abraham, N. A. W. Holzwarth, in *Proc. of SCINT99*, Moscow, August 16-20, 1999.
12. Y. Zhang, N. A. W. Holzwarth, R. T. Williams, *Phys. Rev. B*, **57**, 12738 (1998).
13. M. Nikl, P. Straková, K. Nitsch, V. Petří ek, V. Mú ka, O. Jarolímek, J. Novák, P. Fabeni, *Chem. Phys. Lett.*, **291**, 300 (1998).
14. E. Feldbach, L. Jönsson, M. Kirm, A. Kotlov, A. Lushchik, V. Nagirnyi, G. Svensson and M. Åsberg-Dahlborg, in *Proc. of ICL99*, Osaka, August 23-27, 1999.
15. V. V. Laguta, J. Rosa, M. I. Zaritskii, M. Nikl, Y. Usuki, *J. Phys.: Cond. Matter*, **10**, 7293 (1998).
16. M. Böhm, F. Henecker, A. Hofstaetter, M. Luh, B. K. Meyer, A. Scharmann, V. Metag, R. Novotny, O. V. Kondratiev, M. V. Korzhik, in *Proc. of the Intern. Workshop on Tungstate Crystals*, Rome, October 12-14, 1998 (Università degli Studi La Sapienza, Rome, 1999), pp. 141-145.

Influence of surface particularities on scintillation light yield of lead tungstate

Klassen N.[1], Shmurak S.[1], Sinitsyn V.[1], Red'kin B.[1], Rybchenko S.[1], Ille B.[2], Lebeau M.[3], Lecoq P.[3], Schneegans M.[4]

[1]*Institute of Solid State Physics RAS, 142432, Chernogolovka, Russia,*
[2]*IPNL, Lyon, France,*
[3]*CERN, Geneva, Switzerland,*
[4]*LAPP, Annecy, France*

Abstract: Anomalous decrease of scintillation light yield of lead tungstate with the increase of its length, proportional approximately to the logarithm of the length is accounted for the losses of the emitted light in the processes of multiple internal reflections at the surfaces of the crystal. These losses are connected with inhomogeneities of the crystalline structure in the subsurface layer, produced by mechanical stresses, structural transformations, chemical interaction with the ambient atmosphere. The ways for the light yield enhancement are proposed.

Lead tungstate ($PbWO_4$ – PWO) is rather promising material for scintillating registration of ionizing radiation due to its high density, short decay time of scintillations, convenient for photodiode registration spectral range of the light emission and comparatively low cost of production [1]. On the other hand, PWO has one very serious disadvantage, which is a significant obstacle for wide application of this material in radiation detectors. This is very low light yield of scintillations - even for the best samples of lead tungstate their light yield (*LY*) does not exceed 0.5 % of *LY* for CsI (Tl). Due to this reason up to now PWO as scintillator is used only for registration of particles with very high energy (LHC and several other accelerators). Wide usage of lead tungstate scintillators would be possible after sufficient increase of their *LY*.

In the case of long PWO crystals (23 cm) which are prepared for LHC calorimeter, rather a strange *LY* behavior has been observed: it decreased monotonously with elongation of the samples and it turned out, that for the best samples the decrease of the light yield was almost proportional to the logarithm of the length [2,3] and for the crystals with the length *L*=23 cm the light yield was about 20 - 30 % of the short ones. As it was shown by cutting of short samples from the long rods, the light emission ability of PWO is not changed with the increase of the length, so the observed fall down of the light yield should be attributed to deterioration of the collection of the emitted light by photodetectors in longer crystals [3]. For other well known scintillators - e.g., CsI (Tl) and BGO - this effect of essential decrease of the light yield as a function of the length was not observed. So the reasons of this fall down of the light collection as a function of the crystal's length could be found in particularities of optical and structural characteristics of PWO in comparison with CsI and BGO. These particularities distinguishing lead tungstate from other well-known scintillators do exist indeed. First of all observable losses of the transmitted light in the spectral region of scintillations (400 – 500 nm) are present even in the best PWO samples, achieving several percents of the total light flow [4]. On the other hand, slight deviations from stoichiometric composition, mechanical processing or thermal treatment of lead tungstate induce creation of local regions with different crystalline structures [3, 5–7]. In this paper we propose interpretation of the above mentioned decrease of the light yield of long PWO crystals as a result of the structural particularities localized in the vicinity of their surface.

In the case, when the losses of the light occur homogeneously in the volume of crystals, the *LY* dependence on the length is closer to exponential. It can be illustrated by a simplified model, when the emission point is situated at the axis of a cylindrically symmetrical crystal, when the photodetector is fixed to one of the end faces, whereas the opposite end face as well as the lateral face of the cylinder reflect the light perfectly. If the extinction of the light inside the crystal is described by coefficient α, the degree of the light penetration to the detector, when it achieves the end face, is described by the coefficient *K*, then the light yield of scintillations is described by the expression:

$$LY = \frac{K \times \exp(-\alpha L)}{1-(1-K)\times \exp(-2\alpha L)} \qquad (1)$$

The physical meaning of this expression can be understood easily: the nominator $K \times \exp(-\alpha L)$ corresponds to the relative intensity of the light, being emitted at the opposite end of the crystal and then achieving the photodetector just after the first contact with the detector face. $(1 - K)$ in the denominator describes the light flow, reflected from the detector back to the crystal; $\exp(-2\alpha L)$ corresponds to the light flow which passed after the reflection towards the opposite face, was reflects there and returned back to the detector face. Then the denominator as a whole describes relative losses of the light flow after passing the whole circle around the crystal. Then the unit, divided by this expression, will correspond the effective number of the light circulations inside the crystal until complete exhaustion. So the whole fraction corresponds to the product of the light flow, achieving the photodetector after a single contact, multiplied by the total number of these contacts. For weak losses of the light when the product αL is much less than unit this expression is transformed to the simplified form:

$$Y = \frac{K \times (1-\alpha L)}{K + 2\alpha L} = \frac{1-\alpha L}{1 + 2\alpha L / K} \qquad (2)$$

As it is seen clearly from the expressions (1) and (2), in the case of the volume light losses the light yield should decrease with the length of the crystal either exponentially or superlinearly. The experimental dependence of the light yield of real PWO crystals as a function of their length *L* described by P. Denes [2] is on the contrary sublinear and can be approximated by the logarithmic form. This means that the yield to the light losses of the parts of the crystal which are more and more distant from the scintillation point should decrease monotonously as a function of the distance. For the logarithmic dependence of the light yield the losses of the crystal element *dx*, separated from the scintillation point by the distance *x* , should be proportional to the ratio *dx/x*. This is not consistent with the model of usual absorption and scattering of the light homogeneously distributed in the volume of the crystals.

As it has been noticed earlier, the surfaces of lead tungstate crystals contain high concentration of various structural particularities, which are revealed either by X-Ray diffractometry or by optical microscopy [3, 5 - 8]. For example, mechanical processing of PWO crystals (cutting, lapping, polishing) results in creation of microscopical surface superstructure, consisting from parallel bands [8] (see Fig.1). Profilometric studies of PWO showed, that the amplitude of deviations of the surface from the perfect plane are much less, than the wavelength of the light, so these microscopical images at least partially should be attributed to local perturbations of the optical characteristics of the subsurface regions of the crystals. The existence of the local modifications of the optical properties of PWO crystals in the subsurface layer is confirmed by the studies of the excitation spectra of photoluminescence of lead tungstate [3, 5].

If we assume, that the main losses of the light, emitted in the scintillation process of PWO, are induced by the structural particularities localized in the vicinity of the surfaces of these crystals, we can obtain the analytical dependence of the light yield on the length, close to the experimental results, described above. The assumption about the particular role of the subsurface layer of lead tungstate crystals is confirmed by visual observations of light scattering: in the volume of high quality PWO elements scattering of the laser beam passing through the crystal is not seen, but at their surfaces it is rather strong. When a light beam, emitted from the point, situated at the axis of a crystalline rod, achieves its lateral surface, the losses of the light in the process of the internal reflection will be proportional to the intensity of the light flow. The latter will be inversely proportional to the square of the distance x between the emission point and the surface element under consideration. In this case the integration along the length of the crystal shows, that the light yield decrease with the length L should be inversely proportional to L. This decrease is too fast in comparison with the experimental dependence.

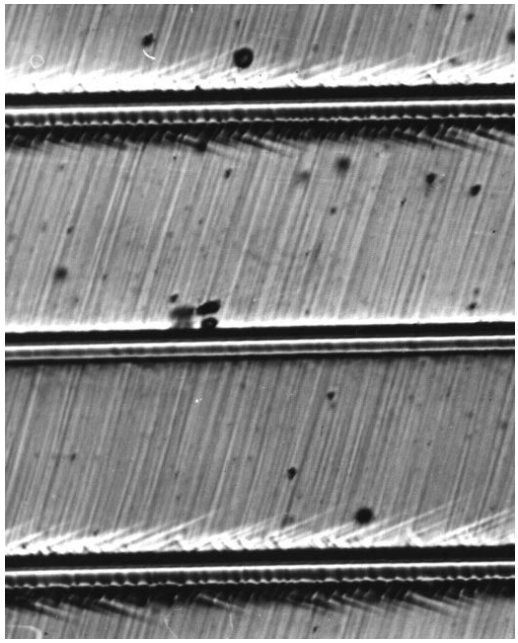

Fig.1. Reflection optical micrograph of lead tungstate surface after abrasive polishing and scratching by a diamond needle. Inclined parallel lines reveal structural inhomogeneities in the subsurface layer. The whole size of the picture corresponds to 1mm.

But the losses of the beam, which arrives to the surface element directly from the emission point, do not describe all the losses, induced by this element. Due to multiple internal reflections, taking place in the crystalline rod, which diameter is much less, than the length, a set of other light beams touch the surface element under consideration. The total number of these beams is approximately proportional to the ratio of the distance x between the emission point and the surface element to the radius of the crystal r. Resulting losses induced by the surface element situated at a distance x from the emission point will become proportional to dx/x, where dx is the width of the element in the direction along the axis of the crystal. It is clear, that integration along the axis of the crystal will show that the total losses of the emitted light should be proportional to the logarithm of the length, what is in better correspondence with the experimental results. Simple calculations, considering multiple reflections of the emitted light at the lateral surfaces of the crystalline rod, that the dependence of the losses D of the emitted light, induced by the surface particularities, are described approximately by the expression:

$$D \propto gt \times \ln(L/r) \qquad (3)$$

Here g is the coefficient of the extinction of the light in the subsurface layer, t – the thickness of this layer. This expression is in good qualitative correspondence with the experimental results. Taking into account multiple internal reflections of the emitted light, when the crystal works as macroscopic one-dimensional waveguide, we approach the situation of the light losses at the surface to one-dimensional case, described earlier [3].

But the measurements of the optical transmission of real PWO crystals in the spectral range, corresponding to the scintillation light, give for the light intensity decrement the values not more than 0.1. So it seems, that the product gt in (3) can not exceed this value and for real ratios L/r being not more than 10 the total damping of the light will not approach the value of 50–70 %, which is observed in the experiment. But for the case of tangent internal incidence of the light beams onto the surface the effective product gt can be much more, than for normal incidence, taking place during the measurements of the transmission. This is induced by the optical inhomogeneities that are present in the vicinity of the surface. On the one hand, possible increase of the refractive index in the subsurface layer can produce waveguiding effect and the light beam, touching the internal side of the surface will be captured partially by this waveguide. Hence it will pass in the subsurface layer more distance than in the case of a simple geometrical reflection and the effective value of the thickness t will be increased. On the other hand, inhomogeneities of the refractive index along the surface (they are seen distinctly at Fig. 1) will induce multiple partial reflections of the beams sliding in the directions almost parallel to the surface. By this way the so called distributed optical feedback is arranged resulting in the enhancement of the light intensity in the vicinity of the surface, increasing the effective probability of the optical transitions (what is equivalent to the growth of the extinction coefficient g). The two processes described above are capable to increase by an order of magnitude the effective losses of the light in the subsurface layer for tangent incidence of the light beams in comparison with the normal incidence, taking place in the measurements of usual optical transmission.

Considerations presented above demonstrate the ability of various structural particularities created at the vicinity of PWO surfaces to decrease LY by several times. So understanding of the nature of these particularities is an actual problem from the point of enhancement of the light yield of lead tungstate scintillations. One of the usual reasons for the creation of subsurface structural defects - mechanical stresses induced in the process of abrasive treatment of the crystals. These stresses can produce microcracks, filled with various contaminations, dislocations and other defects, which can modify local optical characteristics of the crystal in the vicinity of its surface. Additional possibility for creation of optical inhomogeneties especially actual for PWO - recrystallization of the subsurface layer, which can induce local misorientations of crystallographic directions. Lead tungstate is characterized by very high optical anisotropy [9], so these misorientations are capable to induce significant inhomogeneities of the refractive index.

Annealing and chemical polishing of lead tungstate surface eliminates partially the defects induced by abrasive treatment [3,5] and the light yield of scintillations is increased. But this increase is comparatively weak (10 – 15 %), so we should look for other reasons of creation of the surface structural particularities, additional to the residual stresses, induced in the process of abrasive treatment. One of these reasons - local structural transformations due to the possibility of the existence of several structural modifications of lead tungstate. These transformations can induce the band - like superstructure at the surface of PWO, observed by optical microscopy (Fig.1). In this case the structural modulation can be induced by the local stresses, which appear in the process of the transformation due to the differences of specific volumes of various phases. Creation of these stresses will retard the process of the transformation and it can proceed again only at some distance from the transformed region, where the stresses decrease. By this way transformed regions will be mixed with nontransformed ones.

Local structural transformations in the subsurface layer of lead tungstate can be created not only by the mechanical stresses, but as well by variations of stoichiometry and by other chemical processes, induced by the contact of the surface with ambient atmosphere. In addition to transformations of lead tungstate as a whole its partial decomposition to lead or tungate oxide can take place. For example, this decomposition can be provoked by interaction with atmosphere humidity. Either lead oxide or tungsten oxide will absorb the scintillation light very effectively, giving rise to severe *LY* decrease.

Considerations presented above show that the search for further optimization of the processing (and, may be, protective coating) of PWO surface can promise essential improvement of its scintillation light yield. Another way for sufficient *LY* increase is connected with the improvement of the optical connection between the crystal and the photodetector. It is seen clearly from expressions (1,2), where approaching of the coefficient *K* to 1 can increase *LY* sufficiently. Expression (2) demonstrates distinctly, that increase of *K* can weaken significantly the negative influence of the extinction, described by the factor α. The increase of *K* can be achieved by the development of a new way of optical connection of the crystal and the photodetector. For example, it can be the application of an intermediate substance with the refractive index, close to that of PWO (i.e. about 2.2). One of the possibilities to obtain such a substance is connected with preparation of a mixture of nanoscopical grains of optically dense material (e.g., titanium oxide with the refraction 2.8) and a polymer binding liquid. Anyway me can conclude, that the possibilities to improve the light yield of PWO crystals and to open wide field for applications of this material as scintillator are not exhausted.

This work was supported by the grant PICS 577 (RFFI - CNRS 98-02-22-022).

References

1. Lecoq P., in "Inorganic Scintillators and Their Applications", eds. P.Dorenbos and C.W.E. van Eijk, Proceedingsof SCINT 95, Delft 1995,p. 52 - 61.
2. Denes P., Report at CMS Collaboration Meeting, CERN, Geneva, 1995.
3. Klassen N.V., Shmurak S.Z., Red'kin B.S., Rybchenko S.I., Sinitzin V.V., in "Tungstate Crystals", eds. S.Baccaro, B.Borgia, I.Dafinei, E.Longo, Proceedings of the International Worshop on Tungstate Crystals, Rome 1998, p. 35 - 46.
4. Lecoq P., ibid., p. 23 - 32.
5. Klassen N.V., Shmurak S.Z., Shmyt'ko I.M., Red'kin B.S., Rybchenko S.I., Sinitzin V.V. et.al. in "Inorganic Scintillators and Their Applications", eds. P.Dorenbos and C.W.E. van Eijk, Proceedings of SCINT 95, Delft 1995, p. 475 - 482.
6. Korzhik M.V., ibid., p. 241 - 248.
7. Zhu R.-Y., in "Inorganic Scintillators and Their Applications", eds. Yin Zhiwen, Li Peijun, Feng Xiqi, Xue Zhilin, Proceedings of SCINT 97, Shanghai, 1997, p. 73 - 90. Yin Z.W., Li P.J., Feng J.M., ibid., p.191 - 194.
8. Melent'ev A.G., Klassen N.V., Kobelev N.P., Soifer Ya.M., Kristallografia, Vol. 42, 1997, p.1090 - 1095.
9. Lebeau M., Rinaldi D., in "Inorganic Scintillators and Their Applications", eds. Yin Zhiwen, Li Peijun, Feng Xiqi, Xue Zhilin, Proceedings of SCINT 1997, Shanghai 1997, p. 230 - 235.

Luminescence and Electronic Structure of Calcium and Lead Tungstates and Sulfates

I.A. Kamenskikh[1], M. Kirm[2], V.N. Kolobanov[1], V.V. Mikhailin[1], P.A. Orekhanov[1], I.N. Shpinkov[1], A.N. Vasil'ev[1], G. Zimmerer[2]

[1]*Physics Department, Moscow State University, 119899 Moscow, Russia*

[2]*II. Institute for Experimental Physics, University of Hamburg, Luruper Chausse 149, 22761 Hamburg, Germany*

Abstract: Reflectivity, luminescence emission and excitation spectra as well as nanosecond decay kinetics in the region of exciting photons 4 to 35 eV were measured for the pair of crystals $PbSO_4$ - $CaSO_4$ and compared to those of $PbWO_4$ –$CaWO_4$ studied previously in order to establish the role of lead states in these compounds potentially interesting as scintillators. A set of similar properties was observed: a sharp reflectivity peak at the energies lower than the first feature in the spectra of corresponding calcium compound (at 5.8 eV in $PbSO_4$ compared to 11.8 eV in $CaSO_4$, and at 4.25 eV in $PbWO_4$ compared to 6 eV in $CaWO_4$); fast nanosecond luminescence at RT with the excitation spectrum characteristic of the excitonic type mechanism of energy transfer; strong luminescence quenching with temperature resulting in the reduction of the yield by more than 2 orders of magnitude going from 10 K to RT. These properties are discussed in the assumption of the lead parentage of the states in the vicinity of the bandgap.

Keywords: lead sulfate, calcium sulfate, cation exciton

Introduction

Even after the extensive study of $PbWO_4$ luminescence and optical properties, which followed its nomination as a material for the calorimeter of Large Hadron Collider under construction in CERN, there is a diversity of opinions concerning the origin of its luminescence. Often its fast blue luminescence characterized at room temperature by a nanosecond decay time is attributed to the exciton or a center related to the complex anion [1], however, there are experimental facts that speak in favor of a different assignment. The first reflectivity peak of $PbWO_4$ was attributed in [2] to the exciton of the lead parentage and luminescence was also ascribed to it. Lead excited states were also considered as intermediate ones that transfer energy to the centers of WO_4^{2-} origin [3]. To obtain further information on the role of lead states in complex oxides, calcium and lead sulfates seem to be a promising pair of compounds since a large energy gap of ~ 10 eV between the occupied and free states of the sulfate group can assist in the separation between the lead and complex anion states. Moreover, in [4] lead sulfate was introduced as a promising material for high energy photon detection when a high counting rate combined with a high stopping power are required.

Here luminescent and optical properties of lead sulfate were extended to the VUV range and compared both to those of calcium sulfate and lead tungstate.

Experimental

$PbSO_4$ single crystal studied here was a natural occurring mineral anglesite kindly provided for these measurements by Fersman Mineralogical Institute. Synthetic $CaSO_4$ single crystals were grown in Tashkent State University. The samples studied were nominally pure crystals

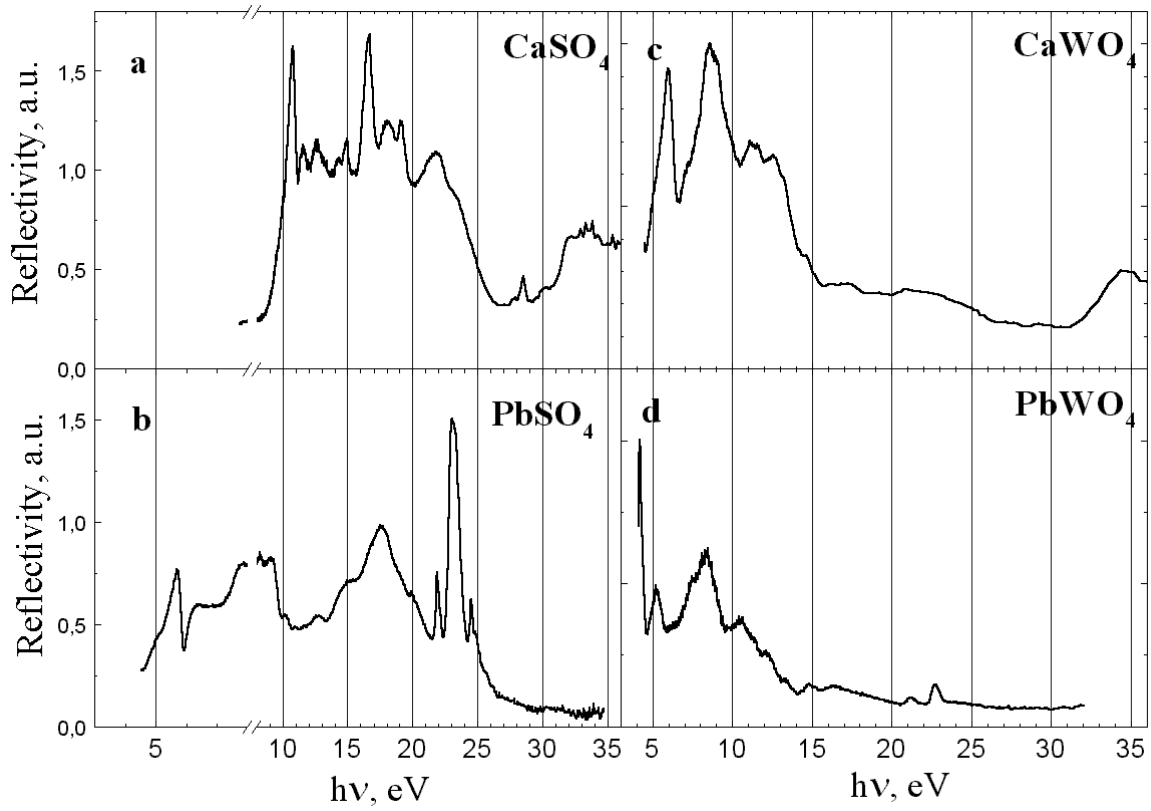

Figure 1. Reflectivity spectra of $CaSO_4$ (a), $PbSO_4$ (b), $CaWO_4$ (c) and $PbWO_4$ (d).

of $CaSO_4$ as well as doped by Eu and Mn. The measurements of the reflectivity and luminescence excitation spectra in the range 4 to 40 eV, of luminescence emission spectra and nanosecond luminescence kinetics in the temperature range 6 to 300 K have been performed at the SUPERLUMI station [5] of HASYLAB, DESY, Germany.

Results and Discussion

The reflectivity spectra of the pairs of crystals $CaSO_4$ - $PbSO_4$ and $CaWO_4$ – $PbWO_4$ are presented in Figure 1a-d. $CaSO_4$ is known as a wide bandgap insulator with the forbidden energy bandgap of the order of 10.5 eV [6]. The main features of the reflectivity spectrum (Figure 1a) can be identified in terms of molecular orbitals of the sulfate anion, for which the electronic configuration of the ground state is well established (see e.g. [7]). The first reflectivity peak at 10.8 eV can be assigned to the transitions from the antibonding 2p oxygen orbital t_1, the peak at 16.6 eV to the transitions from the $2t_2$.orbital formed by σ bonding of the sulfur 3p and oxygen 2p orbitals, other features are less pronounced. Substitution of Pb^{2+} ions for Ca^{2+} cations results in the narrowing of the forbidden energy bandgap both in case of $PbSO_4$ (Figure 1b) and $PbWO_4$ (Figure 1d). In $PbSO_4$ the first reflectivity peak is located at 5.8 eV and it has an anti-resonance profile. Such features are characteristic of isolated transitions. This statement is illustrated by Figure 2 where a simulated imaginary part of the dielectric permittivity ε_2 is plotted together with the reflectivity spectrum calculated using Krames-Krönig relations. The first candidate for this type of transitions would be $6s^2$ ($^1S_0$)$\rightarrow$ 6s6p ($^3P_1$) transition within the lead ion. Similar electronic structure in the vicinity of the bandgap is observed in lead halides (see [8] and references therein) where the highest lying occupied states and the lowest lying free states are of lead parentage. Lead ion is known to produce 4 absorption bands often noted as A, B, C, and D bands. However, in our case the

identification of higher-energy features of the reflectivity spectrum should be made with the account for the interaction with the states of the adjacent ions. Another interesting feature of $PbSO_4$ reflectivity spectrum is a high intensity peak at ~ 23 eV accompanied by a series of less pronounced peaks at lower and higher energies in the energy range 20 to 26 eV. Energy position of these features allows to attribute them to the lead core exciton formed by the transitions from the 5d core level of Pb^{2+}. Similar features were observed in many other lead compounds (see e.g. [9]), however in this case it has substantially higher intensity than for example in $PbWO_4$ (Figure 1d). Luminescence excitation spectra in the same region have deep minima corresponding to the maxima of the reflectivity. We can only speculate on the origin of such a high probability of these atomic-like transitions within lead ion in lead sulfate. One of the possible reasons is that in this compound 6p levels of lead do not overlap with the states of oxygen.

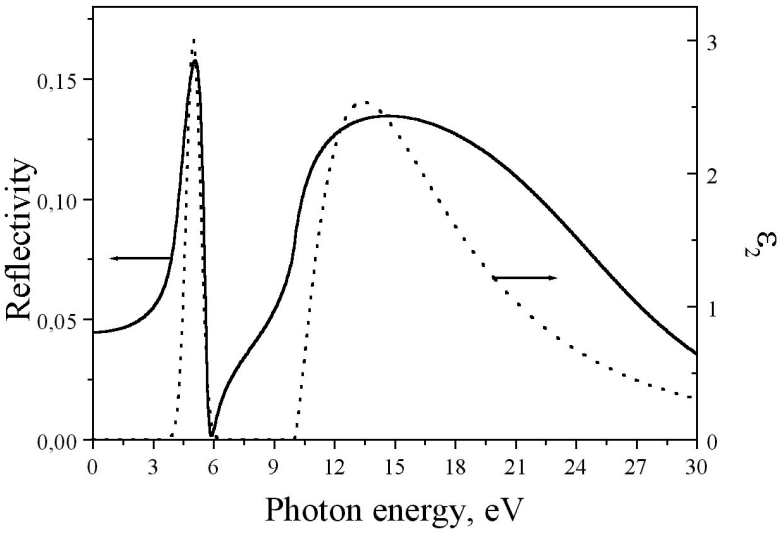

Figure 2. Simulated imaginary part of dielectric permittivity ε_2 and reflectivity spectrum R(hν) calculated from this data using Kramers-Krönig relations.

Figures 3 presents luminescence emission and excitation spectra of $CaSO_4$ and $PbSO_4$. In case of $CaSO_4$ two crystals were measured - a nominally pure one and that doped by Eu and Mn. The excitation spectrum of undoped $CaSO_4$ (Figure 1b) consists of a peak around 8 eV, at the energies below and above it the luminescence yield is almost zero. At ~ 16 eV luminescence yield starts to increase slowly again. The exact position of the first peak depends on the emission wavelength: for 270 nm emission it is at 7.7 eV and for 350 nm emission ~ at 8 eV. In both cases it is situated well below the fundamental absorption edge thus it is natural to attribute it to an intrinsic defect. It should be noted that in the luminescence excitation spectra of $CaSO_4$ doped with different trivalent rare earth ions this peak is also present. Among different defects observed in $CaSO_4$ [10] SO_3^- seems to be the most probable candidate for the recombination/luminescence center since there are at least 3 different types of them and they are common charge compensators in case of trivalent rare earth ions doping. At room temperature characteristic decay time of this luminescence is longer than a few microseconds. In the same figure excitation spectrum for Eu-emission in $CaSO_4$-Eu, Mn sample is presented providing an example of a different mechanism of the energy transfer to the luminescence center. The profile of the spectrum is typical of recombinational type of energy transfer to the emission center (consecutive capture of charge carriers): luminescence yield starts to increase at the energy of creation of separated electron-hole pairs with features superimposed that are anticorrelated with those of the reflectivity/absorption spectrum. At the energies exceeding 2 values of the forbidden energy bandgap a step-like increase of the yield due to the photon multiplication is observed.

In Figure 3c curve with asterisks presents the luminescence spectrum of $PbSO_4$ at RT (not corrected for the apparatus function). Down to 100 K it didn't depend on the excitation energy in the range 5 to 40 eV (with cooling down the halfwidth did decrease) and was similar to the luminescence spectrum observed in [4] at γ excitation at RT. At 6 K excitation with photon

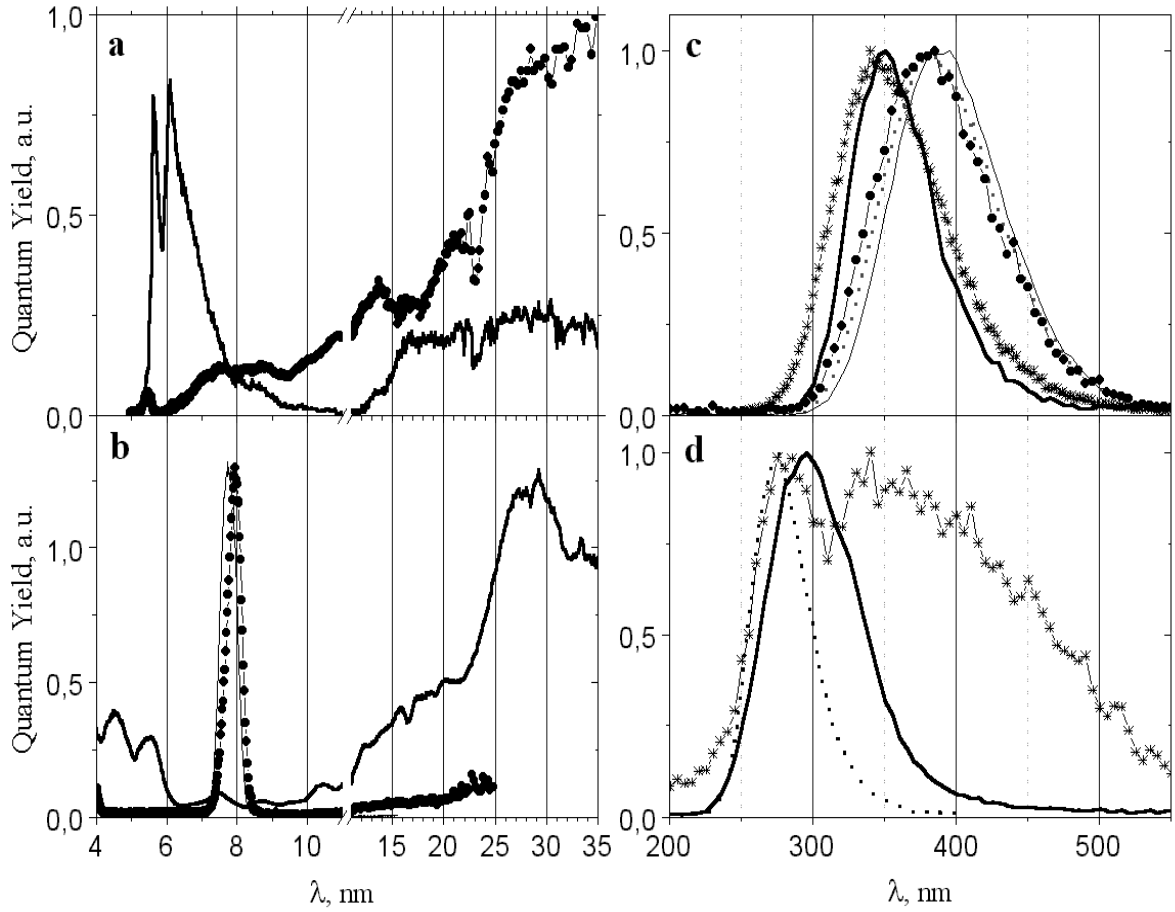

Figure 3. Luminescence excitation and emission spectra of $PbSO_4$ (a and c) and $CaSO_4$ (b and d). (a): 6K, emission 320 (solid curve) and 400 nm (circles); (c) emission spectra at RT for all the excitation energies – curve with asterisks; at 6 K, excitation 5.7 eV – solid curve, 7.7 eV – curve with circles, 10.8 eV – thin solid curve, 23 eV – dotted curve. (b): pure $CaSO_4$, 6 K, emission 270 nm - thin solid curve, 310 nm – curve with circles; CaSO4-Eu, Mn – thick solid curve; (d): pure $CaSO_4$, 6K, excitation 7.7 eV – dotted curve, excitation 8 eV – solid curve, excitation 20 eV – curve with asterisks.

energies larger than 7 eV resulted in the shift of the luminescence band towards longer wavelengths, the new position of the maximum was ~ 390 nm. Excitation in the energy range 5.8 – 7 eV produced a band peaking at 350 nm (shown with a thick solid curve in Figure 3c). Luminescence excitation spectra for 330 nm and 420 nm emission at 6 K are shown in Figure 3a. These are not 'as measured' spectra. Due to a substantial overlap of two luminescence bands it was not possible to measure their excitation spectra in pure form. Thus the solid curve of Figure 3a was obtained from the excitation spectrum measured for 330 nm emission by subtraction of the excitation spectrum measured at 420 nm multiplied by a coefficient which was chosen from the comparison of the luminescence spectra excited at different excitation energies. Similarly the curve with circles form Figure 3a was obtained by the subtraction of the contribution of the 330 nm emission from the excitation spectrum measured at 420 nm. Though the procedure is hard to justify strictly, the result provides evidence that at low temperatures the short wavelength luminescence band is excited mainly in the region 5.5 – 7 eV, further increase of its yield at ~ 12 eV can be attributed to the impact creation of lead excitons by hot photoelectrons. The band with the maximum at ~ 390 nm is excited in the energy region where separated electrons and holes are created. Slightly different profiles of the luminescence spectra measured at different excitation energies can be due to different contribution of the short wavelength band, which was checked by fitting the spectra with two

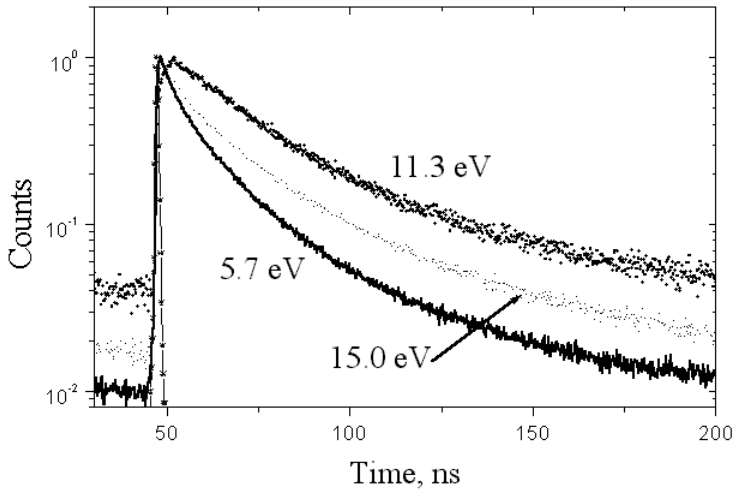

Figure 4. Energy dependence of PbSO4 luminescence kinetics at RT, 410 nm emission (excitation pulse is shown by the curve with asterisks).

gaussians. Thus at temperatures below 20 K (exact temperature limit to be verified) luminescence spectrum depends on whether the absorption of a photon resulted in the creation of an exciton or a separated electron-hole pair. The situation reminds that in alkali halides where at low temperatures σ and π excitons coexist (or on- and off-center excitons). In $PbSO_4$ as well the relaxation of adjacent ions can be different depending on whether a self-trapping of the exciton occurs or one of the charge carriers is self-trapped first and then recombine with another. In contrast to alkali halides in lead compounds electrons are known to self trap (for lead halides see [8] and references therein and for lead tungstate [11]). This may be the case for $PbSO_4$ as well (EPR studies are in progress). The absence of the longwavelength band at temperatures above 100 K can be due to low thermoactivation barrier for self-trapping. The fact that energy transfer mechanisms are different in different energy regions is illustrated by luminescence kinetics measured at RT (Figure 4). At RT luminescence of $PbSO_4$ is fast. Decay curves can be well fitted with 3 exponentials with characteristic times of the order of 5, 10 and 50 nanoseconds. In Figure 4 energy dependence of luminescence kinetics at RT is presented for 3 values of the excitation energy: 5.8, 11.3 and 15 eV. As discussed above 5.8 eV corresponds to the region of exciton creation, however, the decay is not single exponential. There can be several reasons for that such as surface losses or competing decay channels. 11.3 eV corresponds to the onset of transitions within the anion group. The emission spectrum remains unchanged at this excitation energy, thus, additional intermediate processes get involved in the energy transfer to the emission center. In the decay kinetics it manifests as a rise on region and addition of a slow component. At 15 eV the energy of the photoelectron becomes sufficient for the creation of a secondary exciton and we can see that the kinetics accelerates compared to 11.3 eV excitation.

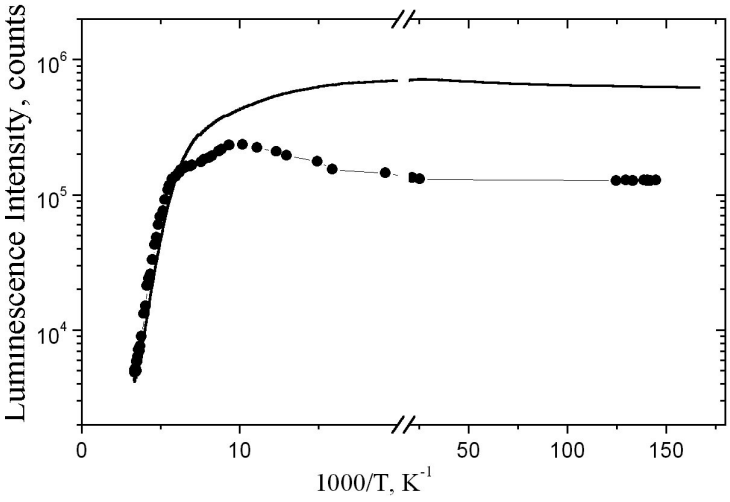

Figure 5. Temperature dependence of $PbSO_4$ luminescence intensity at 350 nm (curve with circles) and 410 nm (solid curve), excitation 15 eV.

Temperature dependence of the luminescence intensity excited at 15 eV is shown in Figure 5. As two luminescence bands substantially overlap, the temperature dependence was measured at two wavelengths – 350 and 410 nm. On logarithmic scale versus inverse temperature (1000/T, K^{-1}) both curves have a

linear part from ~ 150 to 300 K. Fitting the temperature dependence with a Mott function (ignoring the region between 150 and 60 K where the changes from one type of luminescence spectrum to the other one occur) gives the values of activation energy ~ 0.14 eV and frequency factor $\nu_0 = 2*10^{12}$ s^{-1}.

Summarizing, substitution of lead ions for calcium produces very similar effects in pairs of crystals $CaWO_4$ - $PbWO_4$ and $CaSO_4$ - $PbSO_4$:

(i) a blue emission band with a nanosecond decay time is observed both in $PbWO_4$ and in $PbSO_4$ at RT;

(ii) at RT fast luminescence of both lead compounds is strongly quenched, its intensity increases by ~ 2 orders of magnitude with cooling down to LNT, the decay time substantially increases;

(iii) along with the main emission band a longer wavelength one is observed both in lead tungstate and sulfate with a different profile of the excitation spectrum indicating a different mechanism of the energy transfer to the corresponding emission center;

(iv) an asymmetric isolated reflectivity peak at lower energies appears in lead compounds (at 4.25 eV in $PbWO_4$ and at 5.8 eV in $PbSO_4$) compared to the first peak in calcium compounds (at 6 eV in $CaWO_4$ and at 10.7 eV in $CaSO_4$.

It is concluded that in lead sulfate lead $^1S_0$ and $^3P_1$ states fall within the energy gap formed by the complex anion states; fast emission is attributed to the lead exciton.

Acknowledgements

The authors would like to thank M.I. Novgorodova, head of the Fersman Mineralogical Museum, RAS for providing the crystals of anglesite. Financial support of the DFG 436 RUS 113/437 grant is gratefully acknowledged.

References

1. W. Van Loo, Phys. Stat. Solidi (a) **27** (1979) 565.
2. A.N. Belsky et al., Chem. Phys.Lett. **243** (1995) 552.
3. D. Millers, L. Grigorieva, S. Chernov, A. Popov, P. Lecoq and E. Auffray, Phys. Stat. Solidi (b) **3** (1997) 585.
4. W.W. Moses, S.E. Derenzo, and P.J. Shlichta, IEEE Trans. Nucl. Sci. **NS-39** (1992)1190.
5. G. Zimmerer, Nucl. Instr. Meth. Phys. Res. **A308** (1991) 178.
6. A.N. Belsky, I.A. Kamenskikh, V.V. Mikhailin, I.N. Shpinkov, and A.N. Vasil‘ev, Physica Scripta **41** (1990) 530.
7. V.I. Nefedov, Yu.A. Buslaev, N.P. Sergushin et al., Izvestia AN SSSR, **38** (1974) 448.
8. R. Kink, T. Avarmaa, V. Kisand, A. Lohmus, I. Kink and I. Martinson, J. Phys.: Condens. Matter **10**, 693 (1997).
9. M. Kirm, V. Kolobanov, V. Mikhailin, D. Spassky and G. Zimmerer, Proc. Int. Worlshop on Tungstate Crystals, Roma, October 12-14, 1998, Università degli Studi La sapienza, p.149.
10. R. Huzimura and K. Atarashi, Phys. Stat. Sol. (a) **70** (1982) 649.
11. V.V. Laguta, J. Rosa, M.I. Zaritskii, M. Nikl and Y. Usuki, J. Phys.: Condens. Matter **10** (1998) 7293.

Scintillation Characteristics of Sb-doped $PbWO_4$ Crystals

H.F. Chen[1], C. Li, M. Shao[1], C.S. Shi[1], Z.M. Wang[1], C. Wu, Z.Z. Xu[1]
Q. Deng[2], J.Y. Liao[2], Z.W. Yin[2]

[1]*Department of Modern Physics, University of Science and Technology of China, Hefei, Anhui 230027, China*
[2]*Shanghai Institute of Ceramics, Shanghai 200050, China*

Abstract: This paper presents emission spectra, longitudinal transmission and light output for several Sb-doped $PbWO_4$ crystal samples. Scintillation decay kinetics was measured by using gate integration and single photon counting method with blue and green filters. Radiation hardness was measured by using ^{60}Co γ ray irradiation under different dose rates and different dose rate profiles. The light yield and radiation hardness of Sb doped $PbWO_4$ crystals are improved as compared to undoped crystals.

Keywords: lead tungstate, light yield, decay time, radiation hardness

1. Introduction

Lead tungstate, $PbWO_4$ (PWO), crystal is chosen by CMS experiment at CERN as the scintillation element for electromagnetic calorimeter (ECAL). To construct a precision ECAL, the PWO crystals are required to have good optical transmittance, adequate light yield (larger than 8 pe/MeV measured by a XP2262B PMT), fast decay time (at least 90% of scintillation light is emitted in less than 100 ns) and good radiation hardness (a loss of light yield less than a few percent in situ at LHC) [1].

The quality of PWO crystals depends on the purity of raw material, stoichiometry tuning and growth parameters. A complete suppression of impurities and structure defects in full size PWO crystals, however, is very difficult. Doping with trivalent or pentavalent ions is thus considered to be an effective alternative approach to compensate defects. We present here result of measurement on several Sb-doped PWO samples, which were grown by modified Bridgeman method at Shanghai Institute of Ceramics, Chinese Academy of Sciences.

2. Test result

2.1. Photoluminescence and transmission

The samples are Sb-doped, and was annealed in air. Typical photoluminescence spectrum, measured by a Hitachi 850 spectro-fluorometer with UV excitation, is shown in Fig.1. It is peaked at around 500 nm* and includes two components. Optical longitudinal transmission of SIC-294 and SIC-295, measured by using a Shimadzu MPC-2200 spectrophotometer, is shown in Fig.2. The transmission around 320-350 nm is improved as compared to undoped crystals, but still has significant absorption at 420 nm.

* The peak of radio luminescence is blue shifted as compared to photo luminescence, see reference [2] for the details.

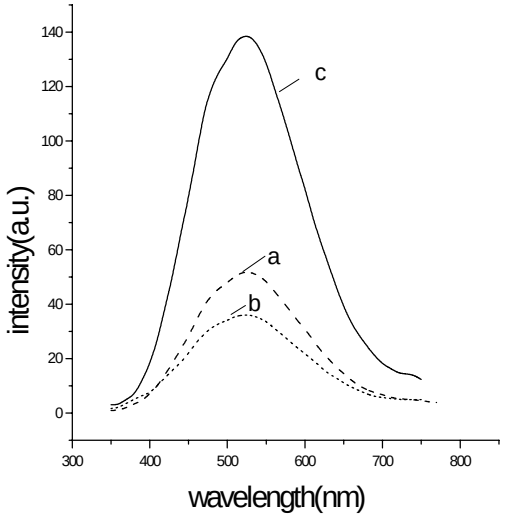

Fig.1: Emission spectra after air annealing
(a) PWO ($\lambda_{ex} = 310nm$);
(b) PWO:Sb(1000ppm) ($\lambda_{ex} = 303nm$);
(c)PWO:Sb(500ppm), La(100ppm)
($\lambda_{ex} = 303nm$)

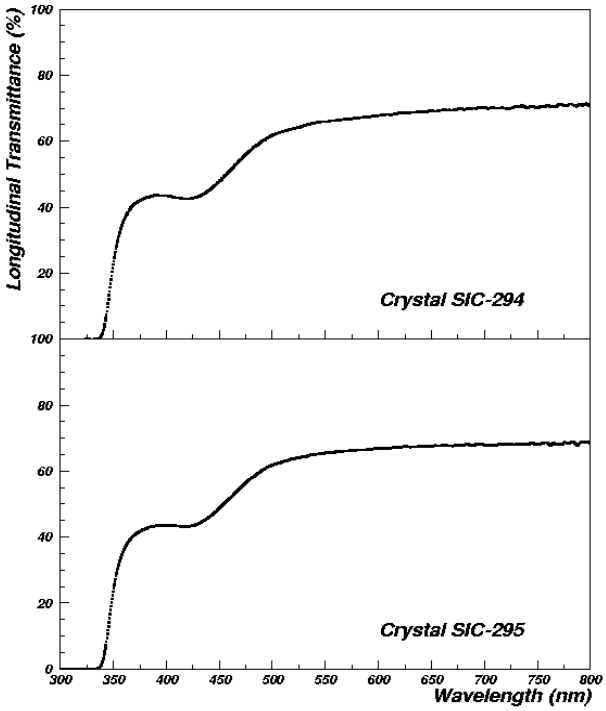

Fig.2: Longitudinal transmittance of crystal SIC-294,295

2.2. Light output and decay time

Light output was measured by using XP2262B PMT with silicon grease (n=1.5) coupling. Samples were excited by radioactive source. The photocurrent measured by PMT was integrated by using a LeCroy QVT 3001 with a gate width of 200 ns [3]. A special Roma fit method [4] was used to determine the light output.

Table 1 lists dimension of samples and their light output corrected to $18^{o}C$. The light output of Sb-doped samples is improved as compared to undoped crystals.

The scintillating decay kinetics was measured by two methods. One is to measure the light output with different gate widths. The ratio of light outputs between 100 ns and 1,000 ns gate is listed in Table 1.

Table 1: Light yield of samples

Sample No.	Size, mm	Light yield (pe/MeV)	LY(100ns)/ LY(1000ns) %
SIC-270	25×25×180	11.6	97
SIC-272	25×25×180	13.5	96
SIC-278	$22^2\times26^2\times230$	10.7	96
SIC-289	25×25×180	11.3	95
SIC-294	$22^2\times26^2\times230$	13.1	96
SIC-295	$22^2\times26^2\times230$	12.9	93

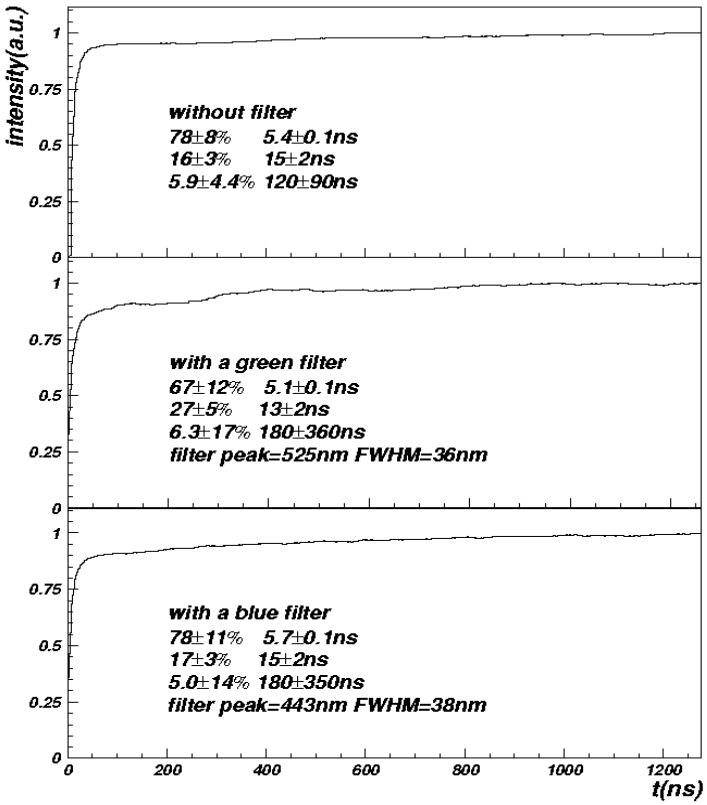

Fig.3: Decay time of crystal SIC-278

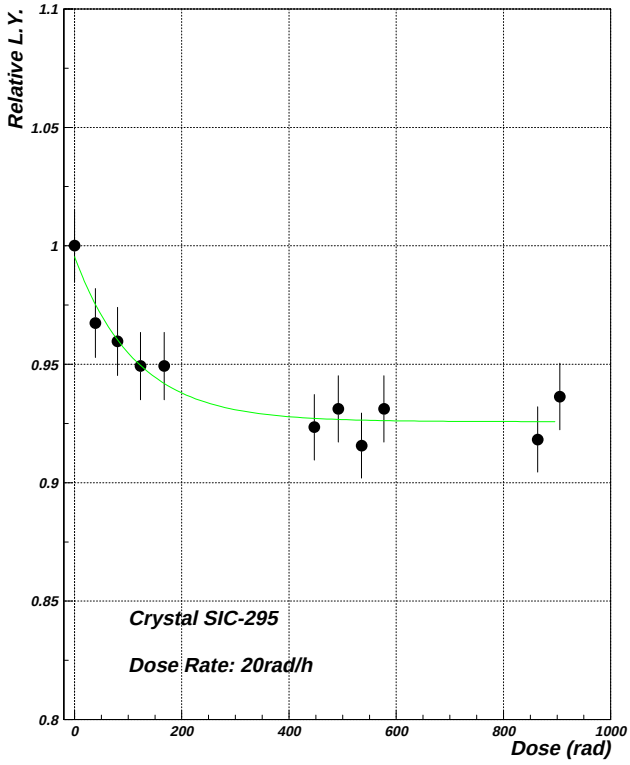

Fig.4: Light yield loss of SIC-295 during irradiation

Another method is to measure single photon counting spectrum [5] by using a blue filter ($\lambda = 443 \pm 16$), a green filter ($\lambda = 535 \pm 15$) and without filter. The decay kinetics can be fit to a sum of three exponentials. Fig. 3 shows the result for SIC-278 in the time range of 1,200 ns. The numerical results obtained by using these two methods are consistent.

2.3 Radiation hardness

The barrel crystals of CMS ECAL will be exposed to a dose rate from 15 to 30 rad/h at shower maximum *in situ* at LHC. It is required that the loss of crystal light output is less than a few percent with LHC dose profile. Samples were irradiated laterally at USTC by using a ^{60}Co source. This provides a uniform dose profile.

The room temperature was controlled at $18 \pm 1^{o}C$. Sample temperature was measured and used for light output corrections.

The top 18 cm length of full size samples was irradiated. The bottom 5 cm of the sample was shielded by 5 cm lead and 0.6 cm iron. The light output was measured when irradiation was interrupted. The cycle time for light yield measurements was about 40 minutes including 20 minutes of stabilization time for the PMT. The irradiation time was longer than 24 hours, so that light output of sample reached an equilibrium. Fig. 4 shows the degradation of the light output for sample 295. Results of all six samples are listed in Table 2.

It is not easy to exactly reproduce the LHC dose profile [5]. To simulate the longitudinal dose rate distribution we constructed a lead mask with different thickness as listed in Table 3.

The losses of light output of SIC-278 under irradiation with and without lead mask are shown in Fig.5. The ratio of the loss of light yield with mask to the 18cm lateral irradiation is about 1:1.5.

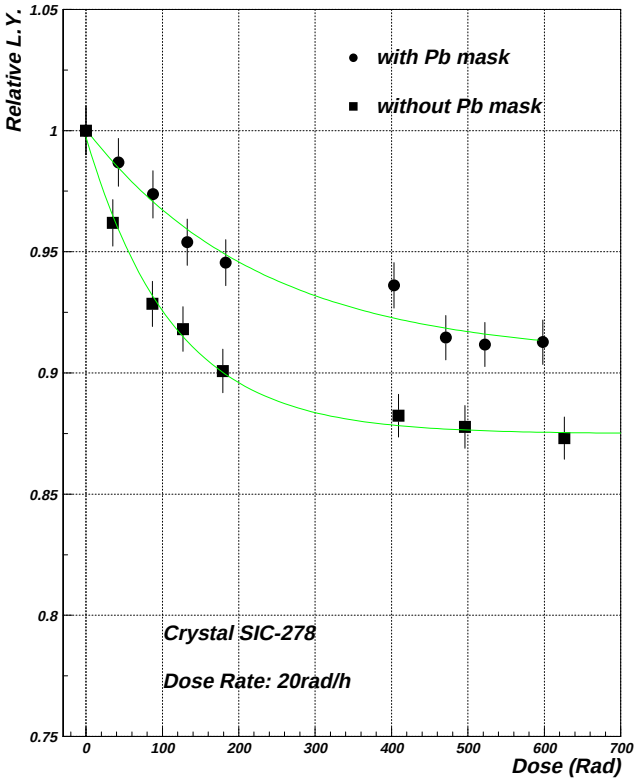

Fig.5: Light yield loss of SIC-278 under different dose distribution

Table 3: Lead mask thickness

Distance from the front face (cm)	0-1.5	1.5-5.5	5.5-9	9-15	15-21	21-23
Thickness of lead(mm)	8	0	11	28	48	55

3. Conclusion

Our result shows that Sb-doping improves PWO quality. Light output and decay kinetics of all samples are good enough for CMS. Significant improvement in radiation hardness is also found as compared to undoped crystals.

References

1. E. Auffray, M.Lebeau, P.Lecoq et al. ,CMS Note 98/038.
2. X.D. Qu , L.Y. Zhang, R.Y. Zhu, in these Proceedings.
3. Wu, T. Xu et al., Nucl. Instr. and Meth. **A 404** (1998) 311.
4. B. Borgia, M. Diemoz et al., Nucl. Instr. and Meth. **A 325** (1997) 69.
5. C. Wu, Z.M. Wang, Z.Z. Xu, Nucl. Instr. and Meth. **A 405** (1998) 176.
6. M. Huhtinen, CMS Note **98/055.**

Picosecond and nanosecond time-resolved study of luminescence and absorption of $CdWO_4$ and $PbWO_4$

Williams R.T[a]., Yochum H.M.[a], Ucer K.B[a]., Millers D.K.[b], Grigorjeva L.G.[b], Chernov S.[b]

[a]*Department of Physics, Wake Forest University, Winston-Salem, NC 27109 USA*
[b]*Institute of Solid State Physics, University of Latvia, LV-1063 Riga, LATVIA*

Abstract: Picosecond and nanosecond transient absorption and luminescence spectra were measured in $CdWO_4$ (stoichiometric, oxygen deficient, and Mo-doped) and $PbWO_4$ crystals (pure and La-doped) under 2.9 eV subpicosecond laser and nanosecond electron pulse excitation. The transient absorption band peaking below 1.3 eV in $PbWO_4$ is attributed to self-trapped electron. The intrinsic luminescence rise time is measured in both materials and found to match manifests of the self-trapped electron in $PbWO_4$ and to match decay of infrared absorption tentatively attributed to the electron polaron in $CdWO_4$. It is shown that the luminescence rise time is shorter for La-doped $PbWO_4$. The distance between trapped (or self-trapped) electrons and holes may play an important role in $CdWO_4$ and $PbWO_4$.

Keywords: $CdWO_4$, $PbWO_4$, luminescence center, transient absorption.

Introduction

A number of new scintillators were investigated during recent years by various authors and it was found that some tungstate crystals are very effective scintillators. $PbWO_4$ was chosen for use in high energy physics [1] and $CdWO_4$ is known as an x-ray scintillator for application in computed tomography [2].

It is generally assumed that the main luminescence in both materials is intrinsic and originates from electron transitions in regular tungstate groups. Thus, the luminescence is excitonic. Exciton creation is possible (i) by photons absorbed in an excitonic absorption band or (ii) via electron-hole recombination. Under ionizing radiation the second possibility is dominant. After electron-hole pair creation the charge carriers can be trapped as well as self-trapped and the exciton creation process will be complicated. The self-trapping of electrons was observed in $PbWO_4$ below 50 K [3], whereas the nature of holes is not clear. The recombinative formation of excitons in $PbWO_4$ at LNT is delayed relative to excitation [4], indicating some intermediate process taking place at times between electron-hole pair creation and exciton formation. We have not found previous publications of observations on self-trapped electrons and holes in $CdWO_4$. The present paper is devoted to study of time resolved luminescence and absorption in $PbWO_4$ and $CdWO_4$.

Experimental

Experiments were conducted using three setups: (1) The subpicosecond and picosecond time region was covered using laser pulse excitation. Absorption measurements were made with an optical multi channel analyzer system within 1.6-2.7 eV spectral region and by photodiode at 1.32 eV, while luminescence was measured with a Hamamatsu streak camera; (2) The nano- and microsecond region was covered using a pulsed electron beam as excitation source, and grating monochromator, PMT and storage oscilloscope for measurements. The

spectral region of the equipment was within 1.2-4.0 eV [5,6]; (3) Nitrogen laser pulses (3.67 eV) were used for luminescence excitation in some cases.

This equipment has time resolution of 10 ns and registration of luminescence was made through monochromator SPM-1 using PMT and time-correlating photon counting system. Setups(1) and (2) allow observation of transient absorption as well as luminescence.

Samples of monocrystalline $PbWO_4$ and $CdWO_4$ were studied. $PbWO_4$ samples were undoped and in some cases La-doped. $CdWO_4$ samples were undoped stoichiometric (Bicron) as well as oxygen deficient, and in some cases Mo-doped.

Results and discussion

$PbWO_4$. The blue luminescence peaking at 2.8 eV was observed in undoped $PbWO_4$ (Fig.1) under electron pulse irradiation at LNT. Decay kinetics of this luminescence are the same over all the spectrum.

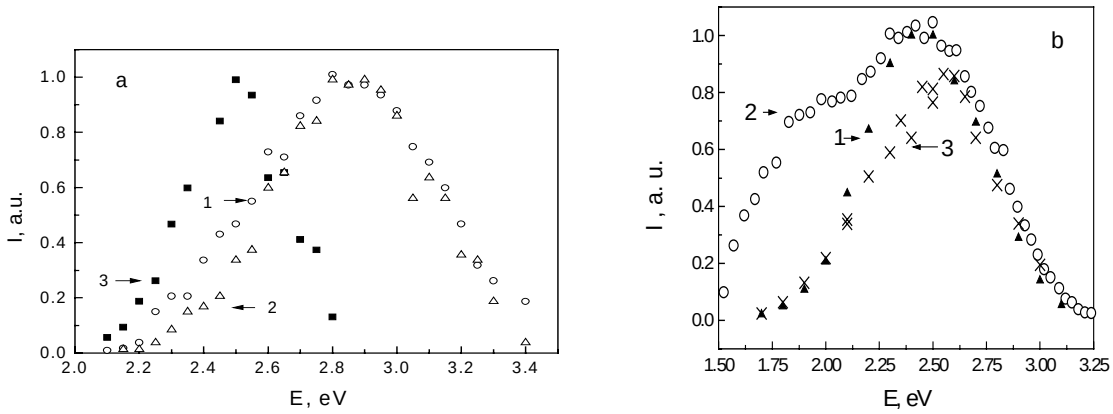

Fig.1. Normalized $PbWO_4$ and $CdWO_4$ luminescence spectra:
a) $PbWO_4$, undoped, at the end of irradiation pulse at RT (1), LNT (2) and delayed 100 ns at RT (3) respectively;
b) $CdWO_4$ at RT at the end of irradiation pulse for stoiciometric (1), oxygen deficient (2) and Mo-doped (3).

The luminescence spectrum of $PbWO_4$ at RT (Fig.1a) is more complicated and reveals two overlapping bands : besides the blue luminescence peaking at 2.8 eV, the green luminescence was observed. Decay of green luminescence is slower than that of blue and thus in delayed spectrum (Fig.1) green luminescence is dominant. The blue luminescence arises due to excited WO_4^{2-} complex [7] and green luminescence due to excited WO_3 complex [8]. The blue luminescence is excitonic, whereas the green luminescence can not be attributed to excitons bound or trapped at some defects, because the life-time of green luminescence is longer than that of blue.

The rise of blue luminescence is delayed relative to the excitation pulse - at LNT the intensity of luminescence rises during ~500 ns after the 10 ns electron beam pulse irradiation. The same result was obtained under band-to-band excitation by subpicosecond laser pulses and measurement by streak camera. The delayed luminescence rise is exponential showing 130 ns time constant at LNT. The time constant of luminescence rise depends on temperature and its Arhenius plot gives a straight line (Fig.2). The estimated activation energy is 0.043 eV, close to the measurement of 0.05 eV for self-trapped electron release [3]. Therefore the blue luminescence rise is limited by the electron release rate and migration of self-trapped

electrons. However the life-time of the self-trapped electron is ~10 μs at 50 K if it is estimated from extrapolation of temperature dependence from Fig.2, whereas ESR measurements [5] give this life-time as some minutes. The discrepancy in life-times is presumed to be due to the following:

EPR measurements were prepared on samples after long-time x-ray irradiation, during which accumulation of preferentially well separated electrons and holes takes place due to recombination of geminate pairs. In time resolved luminescence and absorption measurements all electrons and holes contribute. The main fraction of them are in geminate pairs in which distances between components are small, and this is the reason for the discrepancy of lifetimes mentioned above. The significance of electron-hole spacing in $PbWO_4$ was pointed out in [9] to account for different thresholds of photo-and thermostimulated luminescence excitation [10].

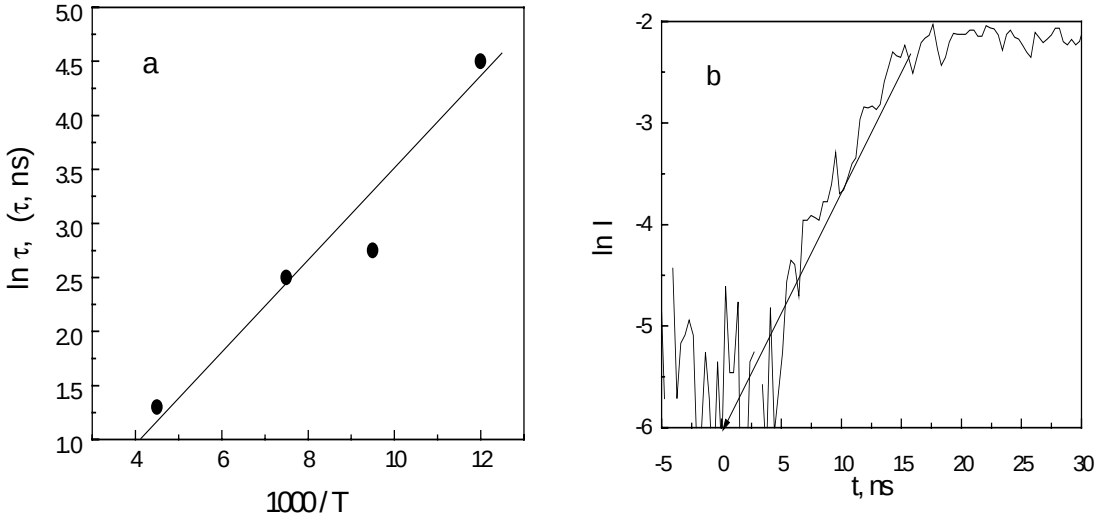

Fig.2. Luminescence delayed rise:
a) $PbWO_4$, rise-time temperature dependence;
b) $CdWO_4$ luminescence rise after subpicosecond band-to-band excitation at RT.

The blue luminescence in $PbWO_4$ is intrinsic, i.e. electron-hole recombination occurs at regular lattice sites. Thus, the mobility of holes must be low, suggesting possibly the holes are self-trapped at LNT in $PbWO_4$. This conclusion is supported by luminescence spectra measured at LNT and RT (Fig.1). The holes are mobile at RT and a fraction of them are trapped on WO_3 complex. Subsequent recombination of them with electrons gives the green luminescence. Since only the blue luminescence is observed at LNT, from sites generally considered to be perfect WO_4^{2-}, the holes at this temperature should be self-trapped. However, absence of an EPR signal makes it difficult to imagine the appropriate self-trapping configuration.

The transient absorption spectra (Fig.3) of $PbWO_4$ at LNT show at least three bands. Sloping up of optical density between 1.6-1.3 eV indicates that there is an absorption band peaking below 1.3 eV. The decay kinetics of this band is complicated at LNT.

One can draw out from the initial stage of the absorption kinetics an exponential component with the same time constant as that for the luminescence rise time. Thus, the center responsible for the absorption band peaking below 1.3 eV takes part in formation of the luminescence center excited state. Considering the fact that (a) other absorption bands are suggested to be from hole centers [11], (b) the activation energy for decay of the 1.3 eV

absorption matches that from self-trapped electron EPR, and (c) because of great similarity to a self-trapped electron absorption band observed recently in niobate crystals [12], we propose the band peaking below 1.3 eV is due to the self-trapped electron.

The luminescence and transient absorption in La-doped $PbWO_4$ are very similar to that for undoped $PbWO_4$. No additional luminescence band was observed. However the luminescence rise time at LNT in $PbWO_4$-La crystals is shorter and the decay of the absorption band peaking below 1.3 eV is faster.

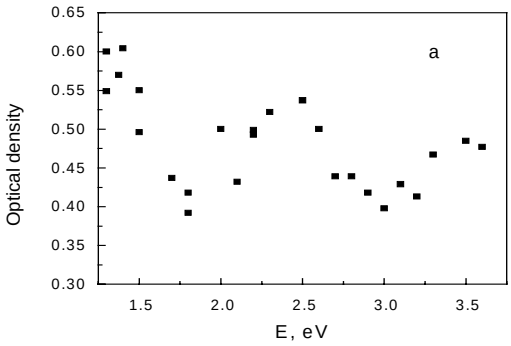

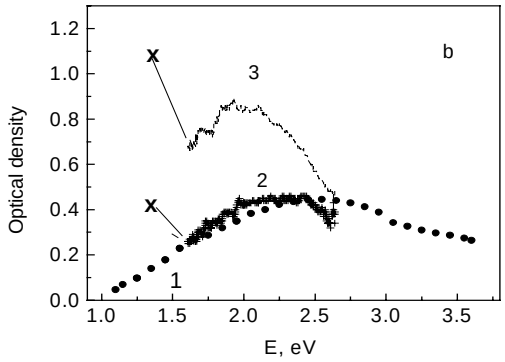

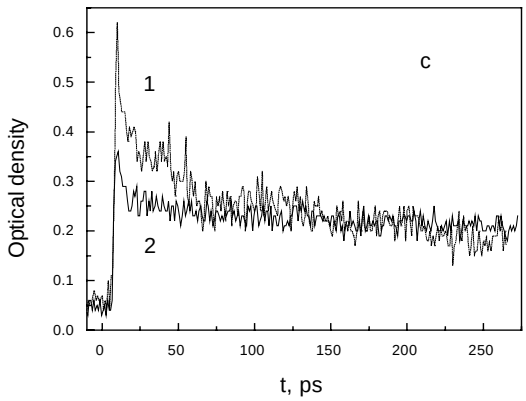

Fig.3. Transient absorption spectra and decay kinetics in $PbWO_4$ and $CdWO_4$.

a) Transient absorption spectra in $PbWO_4$ at the end of 10 ns electron beam pulse at LNT.

b) $CdWO_4$, absorption spectra at RT at the end of 10 ns electron beam pulse (1); under subpicosecond band-to-band excitation at 230 ps delay (2) and 3 ps delay (3) respectively.
Spectra 2 and 3 were measured by OMA, the X-point at 1.32 eV by the InGaAs photo-diode normalized to 2.5 eV signal.

c) $CdWO_4$ absorption decay kinetics at RT at 1.32 eV (1) and at 2.06 eV (2) after band-to-band excitation with subpicosecond pulses.

$CdWO_4$. The luminescence spectra of $CdWO_4$ crystals are shown in Fig.1b. One luminescence band peaking at ~2.5 eV is observed in undoped stoichiometric crystal. The oxygen deficient crystal shows an additional luminescence band peaking at ~2.0 eV. The luminescence at 2.5 eV is intrinsic [13], whereas the one at 2.0 eV comes from some oxygen deficient center [14]. The decay kinetics of luminescence excited by nitrogen laser pulses is

exponential and time constants are 15 μs and 26 μs for 2.5 eV and 2.0 eV bands respectively. Under pulsed electron beam irradiation, the luminescence decay kinetics reveal two time constants: 2 μs and 11 μs for the 2.5 eV band and 0.6 μs and 11.5 μs for the 2.0 eV band.

A delayed rise of luminescence intensity relative to excitation was observed for stoichiometric $CdWO_4$ (Fig.2.b) after band-to-band excitation with subpicosecond laser pulses at RT. The luminescence intensity rise was exponential with a time constant of ~4 ns at RT. The slow rise of this luminescence observed in the present work establishes that the formation of this exciton occurs via electron-hole recombination. Blasse et all showed that the 2.5 eV luminescence center is an exciton in anionic sublattice [13]. It seems that the 2.0 eV luminescence band is a defect emission similar to the green luminescence in $PbWO_4$. For clearing up the role of defects the luminescence of Mo-doped $CdWO_4$ crystal was studied. The luminescence spectrum of $CdWO_4$-Mo under pulsed electron beam irradiation is similar to that for stoichiometric undoped $CdWO_4$ crystal. The luminescence band shape is slightly different (Fig.1.b) and the luminescence decay in $CdWO_4$ - Mo crystal is faster than that in undoped $CdWO_4$. These differences probably are due to Mo influence on the exciton. The defect in the exciton environment lowers its symmetry and luminescence decay becomes faster.

The spectra of transient absorption induced by pulsed electron beam reveals a wide band peaking ~2.4 eV (Fig.3.b). The decay time of this band is the same as for luminescence [5]; therefore this absorption is attributed to the luminescence center excited state. The transient absorption spectra induced by subpicosecond laser pulses are different (Fig.3). These spectra show additional absorption at the long wave side of the spectrum. Relaxation of this absorption is fast, and absorption spectra at 230 ps delay is therefore similar to that induced by electron beam pulse. This fast relaxing absorption was due to some intermediate states taking place before the emitting state of the luminescence center is formed. It is pointed out, that at zero time delay, the absorption at 1.32 eV is approximately twice that at 2.06 eV, thus the optical density slopes up to the long wave side. We suggest that a strong transient absorption band is located at ≤1.32 eV. It is roughly estimated that absorption decay at 1.32 eV has a component with time constant between 3 and 4 ns. Thus this absorption decay time is very close to the delayed luminescence rise time. Consequently - the process of luminescence center formation in $CdWO_4$ is very similar to that in $PbWO_4$. In undoped $CdWO_4$, luminescence is intrinsic and arises via electron-hole recombination. One can conclude that at least one component - electron or hole - must be self-trapped. We can draw out some speculations from the results above. The transient absorption relaxation at 1.32 eV and 2.06 eV is different (Fig.3). Thus the absorption bands arise from different centers. If it is assumed that the absorption at 1.32 eV is due to the self-trapped electron by analogy to $PbWO_4$ discussed above, then the narrow absorption band at 2.0 eV as measured at 3 ps may be due to some hole state before the luminescence center excited state formation. The decay time of this absorption is long enough for its interpretation as due to some polaron state defect (trapped or possibly self-trapped) of the hole.

Acknowledgments

NRC Baltic State Twinning Grant; NSF DMR-9732023 and the Latvian Council for Science, grant #96.0662.

References

1. P.Lecoq. Scintillators and Their Application. Proc.Internat.Conf.”SCINT95”, Delft University Press, Delft, The Netherlands, August 28-September 1, 1995, p.52.
2. R.Deych, J.Dobbs, S.Marcovici, B.Tuval, Inorganic Scintillators and Their Application. Proc.Internat.Conf.”SCINT95”, Delft University Press, Delft, The Netherlands, August 28- September 1, 1995, p.86.
3. V.V. Laguta, J.Rosa, M.J.Zaritskii, M.Nikl, Y.Usuki, J.Phys.:Cond.Matter, **10** (1998) 7293.
4. D.Millers, S.Chernov, L.Grigorjeva, V.Pankratov, Rad.Measurements **29** (1998) 263.
5. L.Grigorjeva, R.Deych, D.Millers, S.Chernov, Rad.Measurements **29** (1998) 267.
6. E.D.Thoma, H.M.Yohum, R.T.Williams, Phys.Rev.**B56** (1997) 8001.
7. W.Van Loo, J.Solid State Chem. **14** (1975) 359.
8. J.A.Groening, G.Blasse, J.Sol.State Chem., **32** (1980) 9.
9. Y.C. Zhang, N.A.W. Holzwarth, R.T. Williams and M.Nikl,. In Proceedings of the Third International Conference on Excitonic Processes in Condensed Matter (EXCON’98), Editors R.T. Williams, W.M. Yen, PV 98-25 (The Electrochemical Society, Pennington, N.J., 1998) p.420-425.
10. V.Murk, M.Nikl, E.Mihokova, K.Nitsch, J.Phys.:Cond.Matter**. 9** (1997) 249.
11. M.Nikl, K.Nitsch, S.Baccaro, A.Cecilia et al. J.Appl.Phys. **82** (1997) 5758.
12. H.M.Yohum, K.B.Ucer, R.T.Williams, L.Grigorjeva, D.Millers, G.Corradi. To be published.
13. M.J.J.Lamers, G.Blasse, D.S.Robertson, Phys.Stat.Sol. A **63** (1981) 569.
14. D.Millers, L.Grigorjeva, S.Chernov. Acta Physica Polonica A. **95** (1999) 965.

Improvement in Scintillation Properties of $PbWO_4$ Crystals with Different Doping Ions

Li jianzhe, Chen gang, Ren shaoxia, Zhang ying, Chen xiaohong

Beijing Glass Research Institute, Beijing, P.R. China

Abstract: We have made significant improvement of $PbWO_4$ in light yield, radiation hardness and decay time by Sb, Y, and La-doping. It shows that doping Y, Sb+Y etc. are more promising methods to improve the scintillation property of PWO crystals. The results are discussed in this paper.

Introduction

When lead tungstate scintillating crystals are used as dense and fast radiators for γ-ray detectors in high radiation environment in future high energy accelerators such as LHC, the main problems were (1) radiation hardness is not yet satisfactory, (2) light yield is low. Our previous studies have shown that the complete suppression of the structure defects in full size PWO crystals is impossible just by means of stoichiometric tuning. When some impurities are removed from the raw materials, the origin of radiation damage is not related to the purity of the raw material but to structural defects produced during the growth process. These defets result from the leakage of lead (Vc(Pb)) and oxygen (Vo) and introduce local charge unbalance which easily traps electrons or holes and act as temporary color centres under irradiation[2]. So doping different ions to compensate charge and suppress the existing defects is necessary.

To compensate these vacancies, we doped some trivalent ions such as Sb^{3+}[1], Y^{3+} and La^{3+} [2] in PWO crystals respectively and made significant improvement of $PbWO_4$ in light yield, radiation hardness, transmittance and decay time.

Test Samples

The test samples are listed in Table 1. All the samples were grown by modified Bridgeman method in BGRI. The purity of raw materials (PbO and WO3) from the same source was 99.99%.

Table 1 The PbWO4 samples studied in this paper and their light yield.

ID	DOPANT	SIZE (MM)	L.Y.		
			L.Y. (200ns)	L.Y. (1000ns)	L.Y. (200/1000)
240	none	20*20*226	5.8		
340	La	20*20*143	11.4		
457	La	24*24*233	7.2	7.2	1.000
347	Sb	27*27*130	11.87	12.52	0.948
471	Y	24*24*230	16.91	16.85	1.003
473	Y	27*27*230	9.02	9.29	0.971
249	Sb, Y	24*24*230	13.56	13.81	0.982
511	Sb, Y	24*24*193	18.2		
459	Sb , La	20*20*230	12.87	13.01	0.989

T=18° Test by Institute of High Energy Phisics.

Measurement and results

1). Transmittance and decay time

It's well known that transmittance of PWO in the short wavelength region (320--450) is considerably improved by La-doping. But the different concentration of La along the crystal causes the shift of the transversal transmission edge (Fig.1).

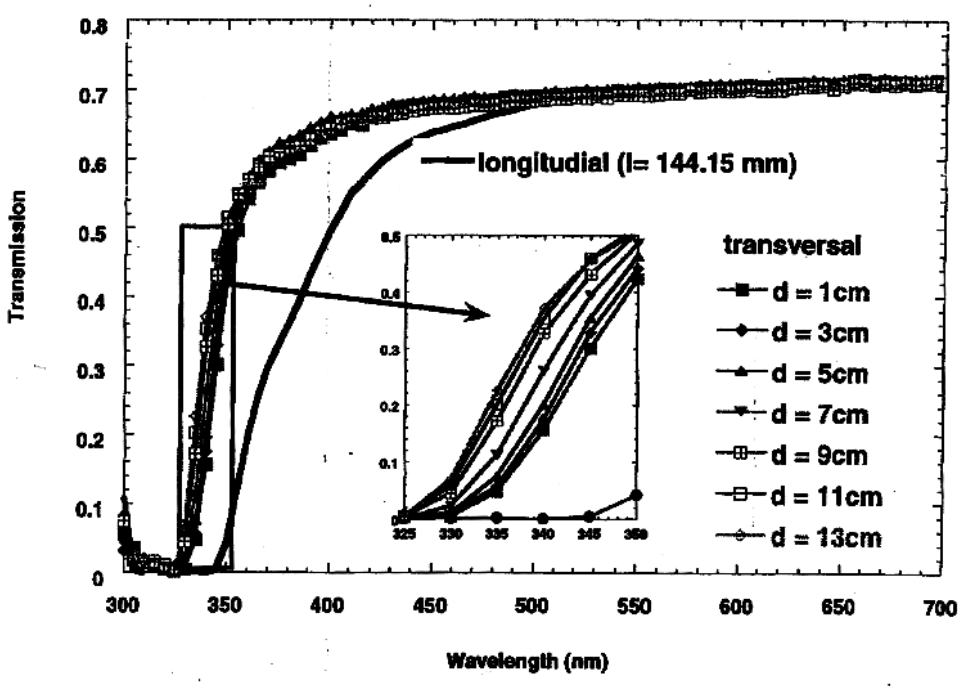

Fig.1 Optical transmission of the crystal no.340

Other trivalent ions (Sb^{3+}, Y^{3+}, Sb^{3+}+Y^{3+}, Sb^{3+}+La^{3+}) also give significant improvement in the transmittance in the short wavelength region. The problem is that absorption band around 420nm is induced by Sb-doping and the absorption band becomes more serious after annealing. The solution is co-doping of Sb+La (Fig.2--3). We also found that the decay time is shortened by doping these trivalent ions.

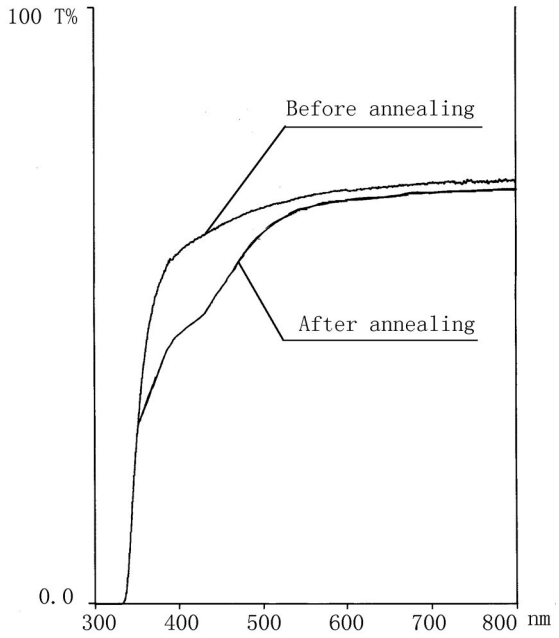

Fig.2 Longitudinal transmission of 347

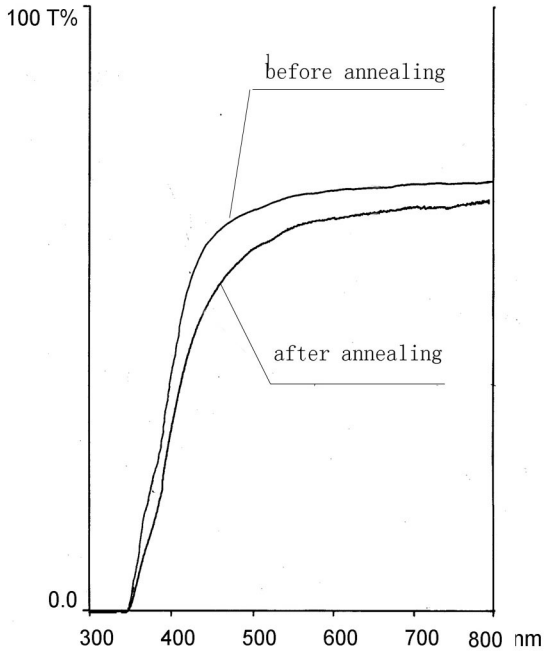

Fig.3 Longitudinal transmission of 459

2) Light yield and its homogeneity

From table 1 we can see that the PWO crystal's light yield is improved significantly by doping these trivalent ions since they can suppress the existing defects and improve the transmittance. The advantage of Y^{3+} is that its segregation coefficient is slightly below 1 and Y^{3+} can be distributed considerably uniformly along the crystal ingots [3]. Therefore, the L.Y. of Y-doped PWO crystal is very uniform such as sample 471. Although Sb^{3+}'s distribution along the ingots is not as good as that of Y^{3+}, the influence on L.Y. uniformity is not obvious (table 2). And the strong non-homogeneity of L.Y. along sample 459 is caused by non-uniform distribution of La in the ingot (table 3-4).

Table 2 The L.Y. tested from different position by IHEP: (T=20°)

ID	Dopant (wt ppm)	L.Y.(pe/Mev, 200ns) PMT on seed end	L.Y.(pe/Mev, 1000ns) PMT on seed end	L.Y.(pe/Mev, 200ns) PMT on top end	L.Y.(pe/Mev 1000ns)PMT on top end
249	Sb, Y	11.44	11.56	13.56	13.81
471	Y	11.94	12.03	13.31	13.37

Table 3 L.Y. of different part in sample 459 tested by ETH

Position of PMT	Position of source	L.Y.(pe/Mev)
Seed end	Top end	10
Seed end	5cm from top end	7.7
Seed end	12cm from top end	6.2
Opposite Seed end	Opposite top end	5.9

Table 4 GDMS analysis of sample 459

	Sb	La
Seed end	21ppm	130ppm
Top end	27ppm	15ppm

3) Radiation hardness

The samples 240 and 340 were irradiated with a high accumulated dose and high dose rate (table5). The results show that the radiation hardness is improved significantly by La-doping. But La-doped crystals have the problem of shorter recovery time [2] [3]. Other samples were irradiated at low dose rate around 20 rad/h. Such dose rate of exposure will be typical for barrel crystals of CMS electromagnetic calorimeter. The radiation hardnesses of sample 249 (co-doped with Y+Sb) and sample 471 (doped with Y) are satisfactory. The radiation hardnesses of samples 511 and 473 are not very good which may indicate that the doping concentration should be optimized. In addition, the light yield of Y-doping crystal rises after irradiation which is quite different from that of other trivalent ions doping crystals (table5).

Table 5 The radiation hardness of some samples

ID	dopant	Test by	Irradiation conditions:	LY after irra.
240	none	ETH	4Gy/h up to 54Gy	loss 100%
340	La	ETH	4Gy/h up to 54Gy	loss 5%
249	Sb, Y	IHEP	18.9Rad/h up to 530rad	loss 4.3%
511	Sb, Y	IHEP	18.9Rad/h up to 530rad	loss 12.7%
471	Y	USTC	20Rad/h up to 1000rad	rise 5%
473	Y	USTC	20Rad/h up to 1000rad	rise 13%

Summary and discussions

1) We have shown that doping PWO crystals with trivalent ions (Y, La, Sb) systematically improves several properties of this crystal.
2) Doping La or La+Sb can improve the radiation hardness of PWO crystals but La's non-uniform distribution in the long ingots indicates that they are not very good method to improve the scintillation properties of PWO crystals.
3) The radiation hardness of Y-doping crystal is very good and Y can suppress electron centers quite uniform along the crystal ingots. So Y-doping is a promising method to improve the scintillation properties of PWO crystals.
4) To resolve the problem of L.Y. rising in Y-doping PWO crystals after irradiation, doping with Y+Sb or Y+La are probably promising methods, but the concentration of Sb or La should be much less than that of Y. And we will do further study on these subjects.

References

1. Wang Shaohua, Shen Dingzhong, Ren Guohuao et al. Improvement of optical and scintillation performances of PbWO4 crystal by Sb2O3-doping. Shanghai Institute of Ceramics.
2. E.Auffray, P.lecoq, M.Korzhik, A.Annenkov, et al. Improvement of several properties of lead tungstate crystals with different doping ions. Nuclear Instruments and Methods in Physics Research ,1998:A 402:75-84
3. A.Annenkov, E.Auffray, A.Borisevich, et al. Suppression of the radiation damage in lead tungstate scintillation crystal. Submitted to Nuclear Instruments and Methods A

Measuring techniques for a large scale production of PWO scintillators

I. Dafinei[1], F. Cavallari[1], A. Cecilia[1], M. Diemoz[1], S. Guerra[1], E. Longo[1], G. Organtini[1], F. Pellegrino[1], S. Baccaro[2], M. Montecchi[2]

[1]I.N.F.N. Sezione di Roma e Dipartimento di Fisica, Università "La Sapienza", P-le A.Moro 2, 00185-Roma, Italy
[2]ENEA - INN - TEC, Casaccia, Via Anguillarese 301, 00060 S. Maria di Galeria (Rm), Italy

Abstract: Starting with 1999 the construction phase of the ECAL of the CMS has begun. Half of the barrel calorimeter [1] (modules type 2 and 3) will be assembled in the Regional Centre of INFN-ENEA Casaccia near Rome in Italy. Previous to the mounting procedures all the 30600 PWO crystals will be qualified for scintillation and radiation hardness characteristics by a specially built [2] Automatic Crystals Control System. The measuring techniques for light yield, light collection uniformity and radiation hardness characteristics of PWO crystals produced in Russia and China following the ECAL-CMS standards and measured in the INFN-ENEA Regional Centre will be discussed. Considerations on the properties of PWO scintillators produced in industrial quantities will also be made.

Keywords: $PbWO_4$, electromagnetic calorimetry, scintillators

Introduction

The electromagnetic calorimeter (ECAL), as a part of the Compact Muon Solenoid (CMS) detector will play an essential role in the search for the Higgs at the future experiments at LHC. The $PbWO_4$ crystal (PWO) was chosen for the construction of the barrel and the endcaps [1] of the ECAL mainly for its short radiation length (0.89 cm) and small Molière radius (2.19 cm). The relatively high radiation hardness of the material and the existing experience and production capacity in Russia and China were also important arguments for this choice. Given the large number of detector parts the production will take place in several Regional Centres, two for the barrel at CERN and INFN/ENEA near Rome, and one for endcaps under the responsibility of UK and Russian groups. Crystal supply is also distributed between Russian and Chinese producers. The strict requirements imposed on several parameters of the PWO scintillator as well as the distributed character of crystal production and assembling of detector parts, led the ECAL Collaboration to the definition of peculiar specification for the PWO crystals to be used for the ECAL detector construction [1, 3]. On the other hand it was stressed since the beginning of the study of $PbWO_4$ as a possible material for electromagnetic calorimetry, that PWO is a "tuneable" scintillator, its scintillating properties strongly depending on the growth and doping conditions. For the qualification of PWO crystals to be used in ECAL it was therefore compulsory to built measuring systems able to match two main constraints: high robustness in order to process several tenths of thousands of crystals in a relatively short time and high versatility in order to support modifications due to possible changes in the qualification procedure, as requested by the production experience. This work presents the automatic crystal control system (ACCOR) built at the ECAL-CMS Regional Centre in Rome, Italy. Based on measurements performed on PWO crystals produced in Russia and China following the ECAL-CMS standards, a discussion of the ACCOR technical parameters is made.

General considerations

When defining the parameters of interest and their related threshold values for PWO scintillators to be used in the ECAL of CMS one has to bare in mind the influence that these parameters might have upon the final energy resolution of the calorimeter. Thus the crucial issues are light yield (LY), light collection uniformity and radiation hardness. The correct geometry of crystals has to be added to the list due to the very high hermiticity imposed to the calorimeter. As a matter of fact geometry is the only parameter of interest that is directly measurable when one has to deal with several tens of crystals to be measured each day for several years spending a minimum amount of money and manpower. Strictly speaking, even the LY when measured with a photomultiplier (PM) on a classical bench (PWO crystal + PM) has to be corrected in a substantial way to give the LY of the scintillator in ECAL working conditions (PWO crystal + avalanche photodiode). Though not directly connected to the calorimeter resolution, the transparency of the crystal was chosen as one of the qualification parameters due to its influence on the light collection uniformity. More, the colour centres induced by gamma radiation in PWO are due to defects which modify the shape of the optical absorption edge of the crystal. This peculiarity makes possible the radiation hardness qualification of PWO crystals based on the shape of their transmission spectra [3]. The automatic crystal control system (ACCOR) built at the ECAL-CMS Regional Centre in Rome, Italy is able to give complete information on dimensions, transparency characteristics, light yield and light collection uniformity of the 2x17=34 types of ECAL standard geometry PWO crystals. Due to the fragility of PWO crystals in the work process of control and assembly the crystal handling is reduced to an unavoidable minimum. PWO crystals mounted on trays by groups of five (fig. 1) are measured in three successive steps: (i) dimensions, (ii) transmission and (iii) light yield, after a preliminary lecture of their identification barcode. At the beginning of an ACCOR run, the machine is fed with up to 7 trays mounted on a rack. Thus up to 35 crystals may be measured in a single run without human intervention. The trays are extracted from the rack and moved inside ACCOR by a set of pneumatic jacks and moving belts (fig.2). The measurements are performed inside of an air-conditioned dark room (working conditions: t=20±0.5 °C ; relative humidity 50±10%).

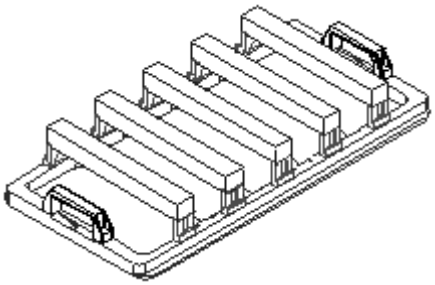

Fig. 1 Tray with 5 PWO crystals

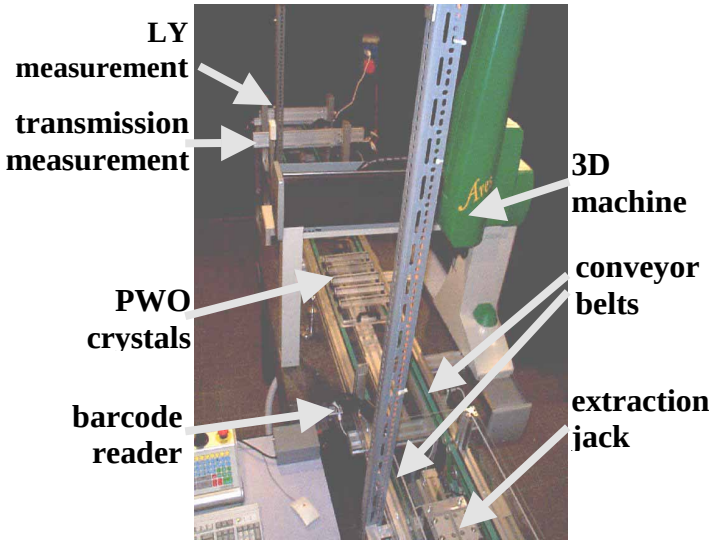

Fig. 2 ACCOR general view

Dimensions measurement

A commercially available 3D machine (model ARES700 AUTO delivered by Coord3 S.p.A.) is used for the measurement of the dimensions of PWO scintillators based on a protocol [3] defined by the ECAL Collaboration (9 points on the front and rear faces and 15 points on each lateral face are measured in order to reconstruct the shape of the crystal). The stability of the measurements was proven to be ±2μ. The five crystals of one tray are measured in 30 min.

Transmission measurement

Optical transmission of PWO crystals may be measured longitudinally (LT) and transversally (TT) with a single-beam diode array spectrometer (S2000 Ocean Optics) directly coupled to an integrating sphere (Labsphere Φ150mm). A Xe lamp LX175UV is used as UV-VIS light source. The lamp is equipped with a high pass filter (λ > 300 nm) in order to suppress the VUV emission of the lamp thus avoiding the Ozone contamination of the measuring room. The optical scheme of the set-up is given in fig. 3. The dark (***I**dark*) measurement is made at the beginning of each set of five crystals and reference measurements (***I**ref*) for LT and TT are made for each crystal. The transmission is calculated as:

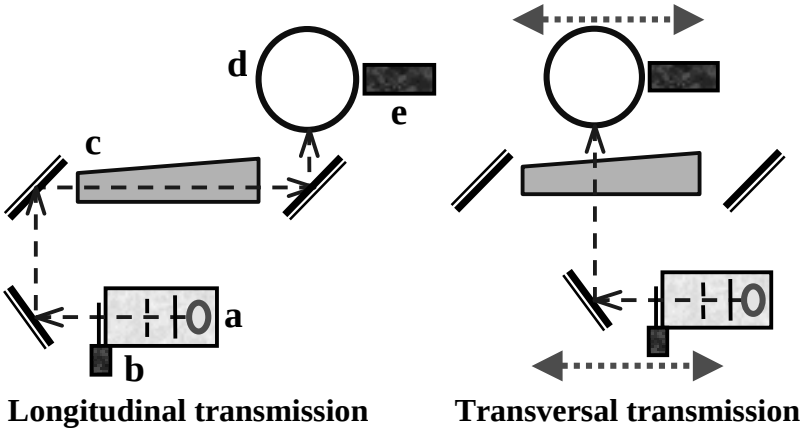

Fig.3 Optical scheme of the ACCOR spectrophotometer
a: Xe lamp and housing (note the Ozone suppressing filter and the pinhole for the beam diameter definition) ; b: shutter; c: PWO crystal; d: integrating sphere ; e: spectrophotometer. Dashed double arrows define the movement of the light spot along the PWO scintillator during the TT measurement.

$$T(\lambda) = 100 \cdot \frac{I_{meas} - I_{dark}}{I_{ref} - I_{dark}} (\%) \qquad (1)$$

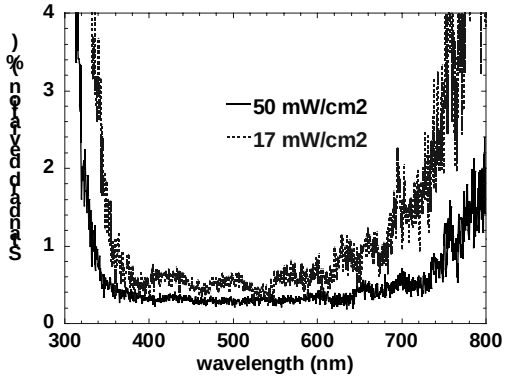

Fig.4 Spectrophotometer baseline fluctuations over 2 minutes in TT measurement configuration

A complete transmission measurement (LT and TT in 11 positions along the crystal) is made in approximately 100 seconds. The 12 transmission spectra are produced with a resolution of 1 nm in the 300 - 700 nm spectral range. The stability of the baseline during 2 minutes is better than 2% in the spectral range of interest (320 - 700 nm). As expected, the stability of the baseline is better for higher intensity values (fig. 4). Nevertheless the intensity cannot be raised indefinitely. The saturation of the CCD-diode array signal and the UV damage [4] of the crystal at high beam intensities have to be avoided. An optimum value of 50 mW/cm^2 was set for the light beam intensity. The systematic error due to the crystal positioning on the tray was also studied. 22 transmission measurements were casually made on ACCOR machine during one week on a PWO crystal which was removed from the tray after each measurement.

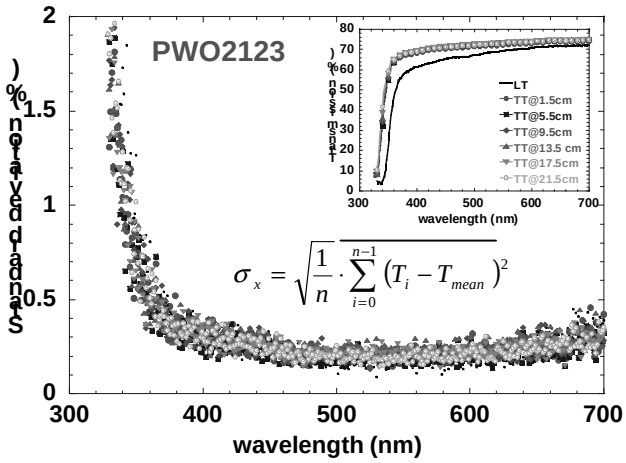

Fig.5 Reproducibility of the transmission measurements at ACCOR (LT and TT mean values for 23 runs are given in the sinset)

As fig. 5 shows, the results are reproducible in the limit of less than 2% standard deviation both for LT and TT spectra in the whole 320 - 700 nm spectral range. Global time for transmission measurement at ACCOR is approximately 20 minutes for 1 tray.

Light Yield

The light yield of the PWO scintillator is extracted in a classical way [2, 5] from the photo-peak position in the scintillation spectrum of a known gamma source. The Co^{60} source used in ACCOR is moved along the crystal thus obtaining the light collection uniformity characteristics for each crystal.

In spite of the relatively low LY of the PWO crystals, a careful analysis shown that it may be measured without optical coupling between the crystal and the PM, thanks to a precise description of the spectrum by means of an appropriate function [5]. In order to get the LY of the crystal from the Co^{60} spectrum measured by a CAMAC ADC a pedestal measurement and a calibration in ADC channels per photoelectrons is performed. The ADC calibration is obtained by means of a low intensity LED light pulses that produce the spectrum of 1 and 2 photoelectrons extraction [5].

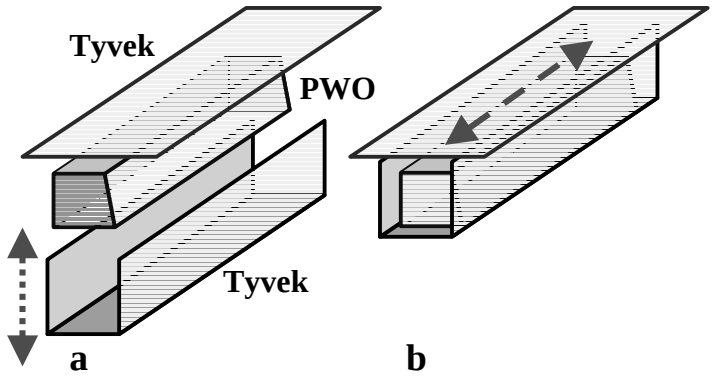

Fig. 6 LY and light collection uniformity measurement
a: at the arrival of the PWO crystal in measuring position; b: during the LY measurement. The PM is situated on the rear face of the crystal. The dashed double arrows represents the vertical movement of the lateral Tyvek wrapping and the horizontal movement of the Co^{60} source. The Tyvek screen on the front face of the crystal is not represented (see the text).

Measurements have shown that both pedestal and calibration are very stable in time and therefore there is no need to repeat them for each crystal. A wrapping of the PWO scintillator is obtained with Tyvek screens fixed at approximately 1mm near the front and upper faces of the crystal. A mobile Tyvek shape wraps the other three lateral faces of the crystal and is automatically removed when the LY measurement is finished and another crystal has to be positioned in front of the PM (fig.6). A distance of 5 mm between the rear face of the crystal and the PM is set in the LY measurement unit of ACCOR. Two different time gates (100ns and 1ms) are used in order to check for the existence of slow components in PWO crystal scintillation decay. The light collection uniformity (11 points along the crystal) is measured for the 5 crystals on a tray in approximately 30 min. Fig. 7 gives a typical Co^{60} spectrum obtained with a PWO scintillator in ACCOR.

Crystal qualification

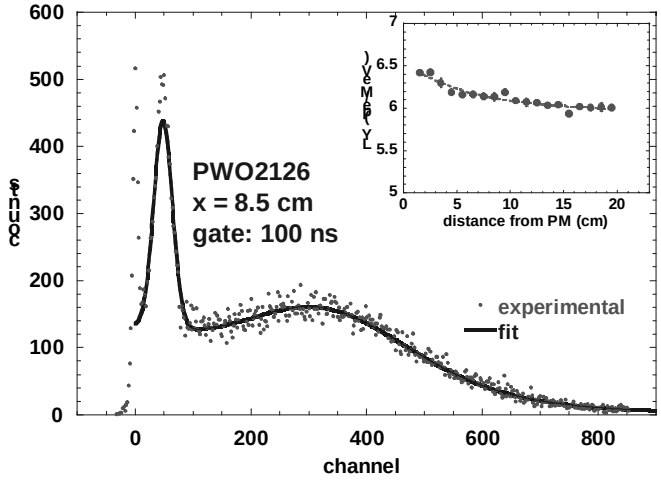

Fig.7 Typical Co60 spectrum and fit [5] obtained with a PWO scintillator in ACCOR. The light collection uniformity of the crystal is given in the inset

The geometry of the PWO crystals is directly measured so there is no problem to identify the crystals out of tolerances defined by ECAL Collaboration [3]. It is also straightforward to find a calibration factor between high energy beam tests results and data given by ACCOR measurements in order to define a limit of acceptability for PWO scintillators LY and light collection uniformity. More, transmission spectra may also give qualitative information on light collection uniformity especially in the case of crystals where a "core defect" is present. For obvious reasons instead, the gamma radiation hardness of PWO scintillators cannot be tested for all crystals in a direct way. As quoted above, transmission spectra (LT and TT) may carry, especially in the absorption cut off region precious information on the existence of defects responsible for a poor radiation hardness of the crystal. The solution adopted by the ECAL Collaboration [1, 2] was to find quality parameters (QP) based on transmission spectra characteristics which are correlated with the radiation hardness of the PWO crystals quantified by the induced absorption coefficient at 420 nm (μ_{420nm}), corresponding to the peak of PWO crystals emission spectrum. A problem is that crystals with optical dishomogeneities may give different spectra when measured with different spectrophotometers. Though not selective (they reduce the level of transmission on the whole spectrum) these dishomogeneities lead to different QP values from a spectrophotometer to another. In order to be independent on the device and to define an intercalibration procedure for each spectrophotometer involved in PWO scintillators qualification activities, a set (x_1, x_2, ... ,x_n) of QP having a good enough (say | r |>0.5) correlation with μ_{420nm} may be chosen. A function $F(x_1, x_2, ... ,x_n) = \mu_{420nm}$ can be then defined and a certain level of precision (say 10%) to this "fit" may be imposed:

$$\frac{1}{n}\cdot\sum_{i=1}^{n}\left|1-\frac{F_i}{\mu_i}\right|<0.1 \qquad (2)$$

where n is the number of crystals used for calibration (n>25)

The function F thus constructed will be then used as quality factor (Q) for the radiation hardness of PWO crystals. Among other qualities, ACCOR give transmission spectra, which allow any modification in the definition of the QP (1 nm resolution spectra in a large wavelength range extending from 320 to 700 nm). It will be therefore very simple to make the corresponding modification in PWO scintillators qualification protocol if the present criteria will have to be modified on the basis of preproduction experience. Recently we proposed to fit the PWO transmission spectrum with the function:

$$T(\lambda)=p_3\cdot\exp\{-\exp[-(\lambda-p_1)/p_2]\} \qquad (3)$$

Though based on the classical theory of light absorption i.e. not taking into account the absorption on defects nor the band structure of solids, it gives a good fit (errors on p_i coefficients < 0.2 %) of the PWO transmission spectra in the cut-off region both for Russian (Czochralski grown) and Chinese (Bridgman grown) crystals. Applying this fit to LT and TT spectra, new quality parameters may be found, having a stronger correlation with the radiation hardness of PWO crystals, thus making more reliable the qualification of PWO crystals for radiation hardness based on the shape of transmission spectra.

For what concerns the LY, a scale factor must be applied to the values obtained with ACCOR to take into account the absence of the optical coupling and the differences in quantum efficiency (QE) with respect to other devices. This factor is around 2 consistently with Monte Carlo calculations. A check on a representative set of PWO crystals has shown that, apart for measurements taken at the very ends of the crystals (near the PM), the shape of the uniformity curve obtained by ACCOR is in agreement with the one measured with optical coupling and different photomultipliers in other laboratories.

Conclusions

The automatic crystal control system (ACCOR) built at the ECAL-CMS Regional Centre in Rome, Italy is able to test the quality of PWO scintillators following the measurement protocol defined by the ECAL Collaboration. The measuring process is completely automatised and remote controllable. Up to 35 crystals may be characterised in a single run, which lasts approximately 10 h without human intervention. The measuring system is very robust and particularly versatile, the modular construction allowing future improvements or modifications in the measuring protocol. An exponential fit (3) to the shape of the transmission spectra is under study, to define new quality parameters that reliably qualify the PWO crystals for their radiation hardness.

References

1. CERN/LHCC 97-33, CMS TDR 4, 15 December 1997 *The Electromagnetic Calorimeter Project - Technical Design Report,*
2. G. Basti et al, CERN, CMS IN-1997/033 *A proposal for an Automatic Crystal Control System*
3. E. Auffray et al, CERN, CMS Note 98/038 *Specifications for lead tungstate crystals preproduction*
4. I. Dafinei et al, Proc. of the Int. Conf. on Inorg. Scintillators and Their Appl., SCINT'97, Sept. 22-25, 1997, Shanghai, China, *Colour centres production in PbWO4 crystals by UV light exposure*
5. B. Borgia et al, Nucl. Instr. and Meth., A 385 (1997) 69-73 *Precise determination of the light yield of scintillating crystals*

Radiation damage of Ce^{3+} (Tb^{3+})-doped phosphate and oxide scintillating glasses

S. Baccaro [1], A. Cecilia [2], R. Dall'Igna [3], M. Martini [4], J.M. Mares [5], E. Mihokova [5], M. Montecchi[1], M. Nikl [5], K. Nitsch [5], P. Polato [3], A. Vedda [4], G. Zanella [6], R. Zannoni [6]

[1] *ENEA, INN/TEC, via Anguillarese 401, 00050 S. Maria di Galeria, Rome, Italy*
[2] *INFN, Section of Rome, Piazzale A. Moro 5, Rome, Italy*
[3] *Stazione Sperimentale del Vetro, via Briati 10, 40141 Murano-Venezia, Italy*
[4] *INFM&Dept. of Material Sci., University of Milano, via Cozzi 44, Milano, Italy*
[5] *Institute of Physics AS CR, Cukrovanicka 10, 154 44, Prague, Czech Republic*
[6] *INFN&Dept. of Physics, University of Padova, via Marzolo 8, 44141 Padova, Italy*

Abstract: The effect of ^{60}Co irradiation (1-230 Gy) on the optical absorption spectra of selected phosphate and oxide-based scintillating glasses has been investigated by room temperature transmission measurements in the UV-VISIBLE range. Samples doped with rare earth ions (Ce^{3+}, Tb^{3+} as the emission centres, and Gd^{3+} as the constituent cation in some compositions) have been considered. Thermally Stimulated Luminescence (TSL) measurements following room temperature X-ray irradiation were also performed on the same samples. The results are discussed by taking into account the possible influence of different glasses composition on radiation induced point defects.

Introduction

Scintillators based on glass matrix are of great interest due to their lower production cost with respect to single crystal systems, easy shaping of elements [1]. In spite of the interest toward these materials, essential problems of glassy matrix exist and consist in the following:

- low transfer efficiency S, which is the reason for rather low light yield observed in glass scintillators with respect to single crystal systems [1, 2, 3],
- low radiation hardness [4].

Trivalent cerium and terbium are frequently used activators (with trivalent gadolinium as the constituent cation in some compositions) causing emission in the UV-blue and green-red spectral regions respectively.

The aim of this work is to study the dependence of oxide and phosphate glasses radiation hardness on the dopant (cerium or terbium) concentration and on the composition of the glass matrix. Furthermore, spectrally unresolved thermoluminescence (TSL) measurements were performed after X-ray irradiation at room temperature (RT) to obtain possible evidences about participation of TSL-related traps in radiation damage mechanism [5].

Experimental set-up and samples

Analysed samples are two groups of glasses based on oxide and phosphate matrices.

Oxide glasses: these samples are four oxide-based glasses produced in the Stazione Sperimentale del Vetro (Murano, Italy) with different percentage of Tb^{3+} and Gd^{3+}, as shown in Tab. I. One sample is doped by Ce^{3+} only as well (VNL6).

Tab. I: OXIDE-BASED SAMPLES

Sample denomination	Composition	Length (mm)
VNL21	oxides + 10%Tb^{3+} & 22% Gd^{3+}	15
VNL22	oxides + 25% Gd^{3+}	15
VNL23	oxides + 3% Tb^{3+} & 24% Gd^{3+}	15
VNL6	oxides + 4.5% Ce^{3+}	20

Phosphate glasses: these glasses are three phosphate-based samples produced in the Institute of Physics (Prague) with different percentage of Ce^{3+} and Gd^{3+}, as can be seen in Tab. II.

Tab. II: PHOSPHATE-BASED SAMPLES

Sample denomination	Composition	Length (mm)
VNL3	te + 25%$GdPO_4$ & 1%$CePO_4$	22
VNL4	hosphate + 25%$GdPO_4$	28
VNL5	hosphate + 1%$CePO_4$	40.5

For the optical transmission study, irradiations by a radioisotope ^{60}Co source were used (*Calliope* irradiation plant in ENEA, Casaccia, Italy) at doses between 1 and 230 Gy. The first irradiations were performed in the dosimetric point corresponding to a dose rate of 0.46 Gy/h, while the following tests were performed in the dosimetric point corresponding to 3.5 Gy/h. In fact, are not evident any recovery components in transmission spectra of samples after irradiation (until 7 days from the end of irradiation), hence we could assume the independence of irradiation effect from the dose rate. After irradiation, every sample was thermally bleached by heating for 2-3 hours at temperature of 240 °C for phosphates and 450 °C for oxides. Transmission measurements were performed by a Perkin Elmer spectrophotometer before and after irradiation (after 8 minutes from the stop of irradiation). The changes in the transmission of the glasses due to the irradiation were evaluated using the radiation induced coefficient defined as:

$$\mu = \left(\frac{1}{L} \right) \cdot \ln \left(\frac{T_0}{T} \right)$$

where L stands for the length of the sample, T_0 for the initial transmission and T for the transmission after irradiation. To compare optical properties of samples having different lengths, we calculated the optical density defined as:

$$\varepsilon = \frac{1}{L} \ln \left(\frac{100}{T(\%)} \right)$$

TLS measurements in the temperature range 20-300 °C were performed following irradiation of 1 Gy with a X-ray tube (Machlett OEG 50 operated at 32 KeV) at room temperature. The TSL signal was detected in the photon counting mode by an EMI9645 QB photomultiplier.

Experimental results and discussion

1- Oxide glasses doped with terbium

In Fig. 1 transmission curves of oxide-based glasses are reported. Transmission band-edge of samples containing respectively no Tb^{3+} and 3% of Tb^{3+} are characterised by a band-edge around 330 nm, while the sample containing the higher concentration of Tb^{3+} (10%) has a little knee around 330-380 nm (corresponding to a transmission value around 5%) with

significant increase in transmission located around 380 nm. The decrease of transmission in VNL21 sample can be explained by $^7F_6$—>$^5D_3$ (and higher states) absorption transitions of Tb^{3+} in the spectral region between 300-380 nm. In the other sample this effect is suppressed due to lower Tb^{3+} concentration and also lower initial transmission (VNL22) of a sample. In Fig. 2 we reported the radiation induced absorption coefficient of oxide samples after 230 Gy irradiation dose. At wavelengths higher than 460 nm, the radiation damage is lower for samples containing the higher concentration of Tb^{3+}, while at lower wavelengths radiation damage for VNL21 sample increases more steeply.

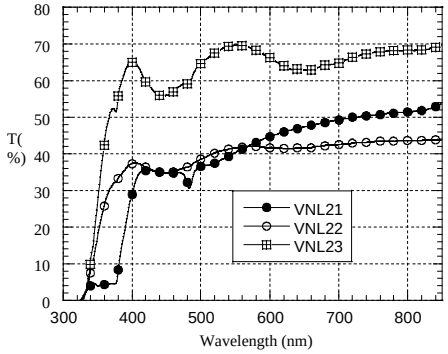

Fig. 1: Transmission curves of oxide samples

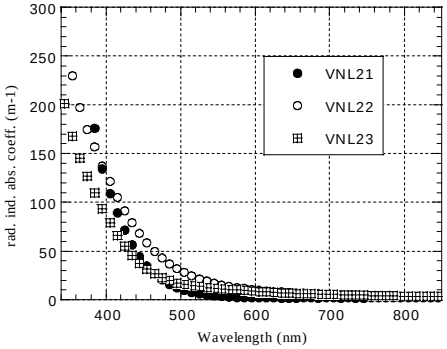

Fig. 2: Radiation induced absorption coefficient of oxide glasses after 230 Gy

Obviously the wavelengths of interests are the ones at which the Tb^{3+} doped glasses scintillate [1, 6] (482, 542, 585 and 621 nm), so that we reported the radiation absorption coefficients after 230 Gy irradiation dose for all samples and all indicated emission in Tab. III.

Tab. III: μ OF DOPED OXIDE GLASSES AT Tb^{3+} EMISSION WAVELENGTHS.

Sample	μ at λ = 482 nm	μ at λ = 542 nm	μ at λ = 585 nm	μ at λ = 621 nm
VNL21	16.70±1.50	3.89±1.05	2.23±0.94	1.73±0.89
VNL22	38.60±1.50	19.90±1.10	11.65±1.03	8.71±1.02
VNL23	20.61±0.80	12.00±0.64	9.41±0.64	7.87±0.67

The same samples underwent also TSL measurements in the temperature ranging from 25 °C to 300 °C. The results related to terbium doped oxide glasses are shown in Fig. 3 after X-irradiation. The glow curves display broad peaks extended in a wide temperature range in all the investigated samples. The intensity of the signals decreases by increasing the terbium content; this possibly indicates the existence of a competition process in carrier capture during irradiation between defects acting as trap levels and terbium luminescent centres.

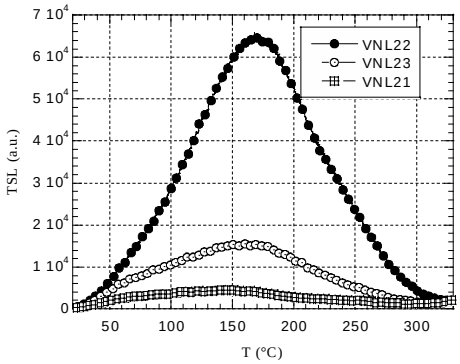

Fig. 3: TSL measurements on oxide samples

2- Phosphate-based glasses doped with cerium

In Fig. 4 the optical density (ε) curves of all phosphate samples are reported. It is evident that the sample containing only Gd^{3+} rare earth ion is characterised by a band-edge around 300 nm, while the other samples containing Ce^{3+} or both Ce^{3+}-Gd^{3+} ions are characterised by a slightly shifted band-edge (≈ 20 nm) towards the visible region of the spectrum. Irradiation induces a decrease in transmission proportional to the dose and that depends on the composition of the glasses. Samples doped (or co-doped) with Ce^{3+} show a decrease in transmission more accentuated in the UV region of the spectra (320-360 nm), while for the Gd^{3+} doped sample the decrease extends from 300 to 600 nm and is more pronounced around 500 nm. In Fig. 5 are given the radiation induced absorption spectra for all the irradiated samples after an irradiation dose of 68 Gy: it is evident that the shape and intensity of the radiation induced coefficient are sample dependent. Radiation induced absorption coefficient of samples containing Ce^{3+} is monotonically decreasing with the wavelength and it seems to improve as the ratio between the Ce^{3+} and Gd^{3+} concentrations is bigger. The Gd^{3+} doped sample has a rather structured extending from 310 to 650 nm and peaked around 500 nm. From the application point of view the wavelengths of interest are obviously the one at which the scintillator emits (350 nm for Ce^{3+} and 309 nm for Gd^{3+}); for this reason in Fig. 6 the radiation induced coefficients of samples at the proper scintillating wavelengths are reported.

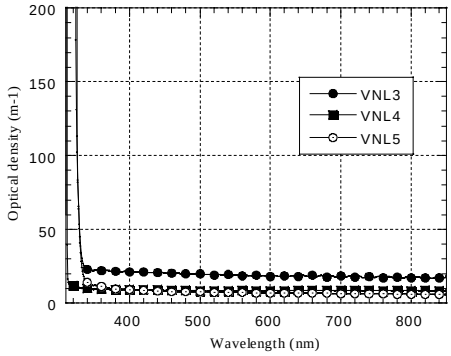

Fig. 4: Optical density of phosphate samples

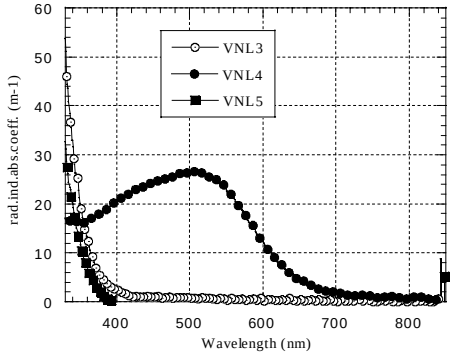

Fig. 5: Radiation induced absorption coefficient of phosphates after 68 Gy

It is evident from Fig. 6 that the Gd^{3+} doped sample is less resistant to radiation respect to samples containing Ce^{3+}, while the radiation coefficients of other samples are practically identical. These results were compared to TSL measurements performed in the temperature range between 25 °C and 300 °C; in the cases of cerium doped phosphate glasses (Fig. 7), the glow curves display broad TSL structures in the considered temperature range. The lower TSL signal of the sample containing both Gd^{3+} and Ce^{3+} ions could be preliminary explained by taking into account the efficient carrier capture operated by Gd^{3+} ions followed by energy transfer to Ce^{3+} sites. Higher efficiency of prompt recombination at luminescent centres could lower the probability of charge capture at TSL active traps.

3- The role of cerium in oxide and phosphate matrix

We have compared the results obtained at the samples VNL6 and VNL5 to get some more insight about the role of Ce^{3+} in oxide and phosphate matrices. When the optical density spectra are compared it is evident that Ce^{3+} doped phosphate has got a band-edge around 320 nm, while the other is characterised by a band-edge around 360 nm (Fig. 8). Such result can be explained by higher crystal field in oxide glasses, which shifts to lower energy the 4f-5d absorption transition of Ce^{3+} ion.

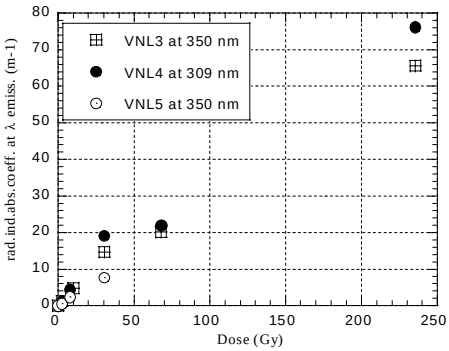

Fig. 6: Radiation induced absorption coefficient of phosphates at emission λ

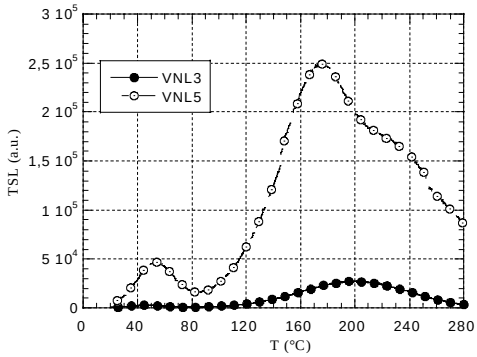

Fig. 7: TSL measurements on phosphate samples

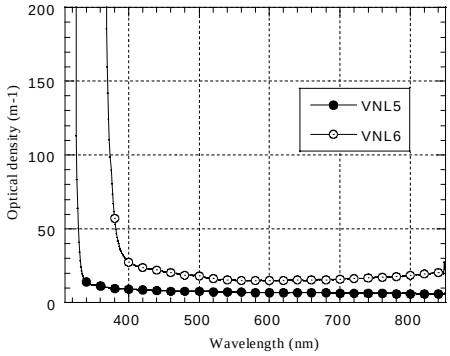

Fig. 8: Optical densities of Ce^{3+} doped oxide and phosphate

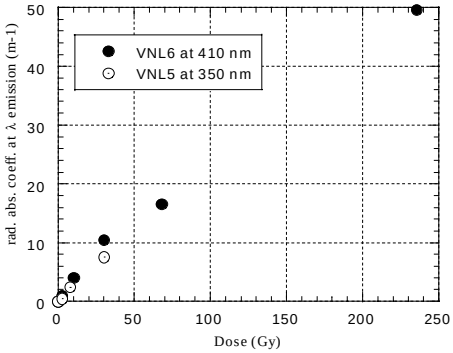

Fig. 9: Radiation induced absorption coefficient of Ce^{3+} doped phosphate and oxide glasses at proper emission wavelengths

The shape of radiation induced coefficient of both samples, the shape is approximately the same, with some shift towards the UV region in the phosphate sample. Comparing the radiation coefficient of both samples at the wavelengths of interest (350 nm for phosphates and 410 nm for oxides) one can conclude that the radiation hardness of phosphate and oxide samples under consideration is comparable (Fig. 9).

References:

1. S. Baccaro et al, Proceedings 5th ESG Conf. "Glass Science and Technology for the 21st Century", p. C1-23, C1-30 held in Prague, June 21-24, 1999.
2. E. Auffray et al, (CC collaboration), NIM**A380** (1996) 524.
3. M.J. Weber, Proc. of 5th Int. Conf. on Calorimetry in High Energy Physics, World Scientific, Singapore 1994, p.17.
4. P. Pavan, G. Zanella, R. Zannoni and P. Polato, NIM **B61** (1991) 487-490.
5. S. Baccaro et al, Proceedings 5th International Conf. on Inorganic Scintillator and Their Application, held in Moscow, August 16-20, 1999.
6. M. Bettinelli, G. Ingletto, P. Polato, G. Pozza, G. Zanella and R. Zannoni, Phys. Chem. Glasses **37**(1) (1996) 4-8.

Slow components of decay in Ce-doped fluoride crystals

E.A.Radzhabov, A.I.Nepomnyashikh

Vinogradov Institute of Geochemistry, Russian Academy of Sciences
Favorskii street 1a, P.O.Box 4019, 664033 Irkutsk, Russia

Abstract: Creation of spatially separated defects produced by 6-8 eV photons were investigated by means of thermoluminescence in alkaline-earth fluoride. Measuring the spectra of creation of thermoluminescence in BaF_2:Ce^{3+} we show that the production of thermoluminescence peaks related with self-trapped holes captured on F^- interstitials (H centers) observed above 6 eV, while weak TSL peak of self trapped holes observed by excitation above 7 eV.

The effect of photoionization on decay of Ce^{3+} luminescence was investigated in BaF_2, SrF_2, CaF_2 and CeF_3 in photon energy range 4-8 eV. Only single exponential Ce^{3+} luminescence decay was observed in 4-6 eV excitation region. The fast and slow decay times were observed above 6 eV excitation. We assume that above 6 eV excitation the Ce^{3+} luminescence decay controlled by tunnel recombination of trapped electron with hole centers.

Keywords: luminescence, decay, slow component, thermoluminescence, vacuum ultraviolet

Introduction

Dense fluoride crystals doped with Ce^{3+} are good materials for scintillators. Ce^{3+} ions in many crystals have a moderate decay time in few tens nanoseconds time scale and high light output. The obvious disadvantage of Ce-doped scintillators is slow components of decay time in microsecond time scale.

Obviously, slow components relate with recombination process of different types. We study that type of slow components, which belong to photoionization of Ce^{3+} ions by 6-9 eV photons in CaF_2, SrF_2, BaF_2 and CeF_3. Photoionization in Ce-doped alkaline-earth fluorides and oxides was goal of several investigations, commonly related with possibility of laser action of such crystals [1 , 2, 3].

Crystals	E_{em}, eV	τ_{rad}, ns	τ_{fast}, ns	τ_{slow}, μs
CaF_2:Ce^{3+}	3.63, 3.87	40	80	1.6
SrF_2:Ce^{3+}	3.78, 4.02	36	70	1.6
BaF_2:Ce^{3+}	3.83, 4.09	28	60	1.6
CeF_3	4.09, 4.3	15	20	1.5

Table 1. Emission bands and decay times observed in investigated crystals at 78 K. τ_{rad} – simple exponential decay times observed with 4-6 eV excitation photon energies, τ_{fast} and τ_{slow} were observed with 6-9 eV excitation photon energies.

The formation a color centers was found in CaF_2:Ce^{3+} due to optical pumping into the lowest 4f-5d band of Ce^{3+} ion with 308 nm excimer laser.

The color centers related with divalent cerium ions and initial value of created absorption quadratically depends on laser intensity pointing on two-step two-photon process [2]. Authors concluded that laser excitation results in the photoionization of the Ce^{3+} ion through 5d state. The electron is promoted to the CaF_2 conduction band where it has to be trapped by another trivalent cerium ion [2].

Later it was found that the 308 nm pumping of $CaF_2:Ce^{3+}$ at 80K leads only to move of F^- interstitial charge compensator from the (001) site to the (111) site [3]. Creation of color centers was observed in doubly doped $CaF_2:Ce^{3+},Na^+$ at 80K and in $CaF_2:Ce^{3+}$ at higher temperatures. Authors concluded that a mechanism involving production of self-trapped holes can account for the photochemical process. The initial step of mechanism can be represented as the transition from the valence band to the Ce^{3+}. Authors assumed that the first photon creates the Ce^{2+} center and hole on F^- interstitial (H center). Second photon absorbed by H-center caused spatial separation of defects [3].

Experimental details

The spectra in 4-10 eV region where measured with grating vacuum monochromator VMR2. Emission spectra were recorded using grating monochromator MDR2. In thermoluminescence studies the crystal was irradiated by light of VMF25 a 25W hydrogen discharge lamp dispersed by VMR2 monochromator a few minutes at 78K. The creation spectra were corrected on spectral response of monochromator and those of discharge lamp. Decay of photoluminescence was measured by single photon technique using CAMAC time-to-digital converters. Width of excitation pulse on half maximum was about 10 ns.

Excitation pulse decayed by hyperbolic law. To derive the real decay times we use convolution procedure.

Crystals were grown in vacuum with addition of 0.1 or 0.01 weight % of CeF_3 with taking measures to remove oxygen [4].

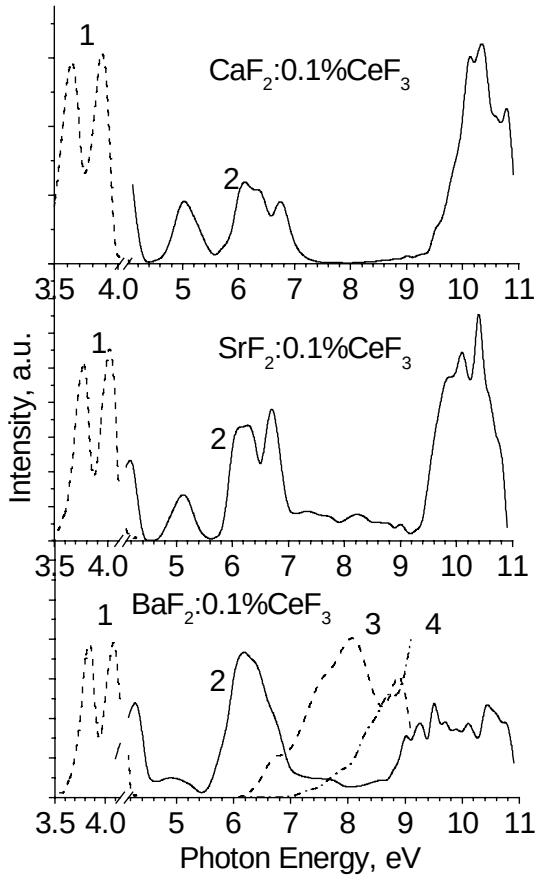

Fig. 1 Emission (1), excitation (2) and thermo-luminescence creation (3,4) spectra of BaF_2, SrF_2 and CaF_2 doped with 0.1 weight % of CeF_3. Emission spectra were measured at 78 K, excitation spectra were measured at 295 K. Thermoluminescence creation spectra were measured for 166 K (3) and 112 K (4) peak.

Results

Generally, photoionization means the delocalization of charge carrier– electron or hole from defect center.

Escaped electrons or holes can recombine back or can be trapped by some defects; holes very fast become self-trapped. So the photoionization can be investigated via the created defects. We study the ph otoionization of Ce^{3+} in several hosts using the radiative recombination of created defects - thermostimulated luminescence. Alternatively, some part of created defects may be involved into prompt recombinations. As a result the slow components in Ce^{3+} luminescence decay were observed.

Excitation and emission spectra

Two sharp emission bands of Ce^{3+} ion belong to transitions from lowest 5d state to spin-orbitally splitted 4f $^2F_{7/2}$, $^2F_{5/2}$ ground states (Table, Fig.1). The spectra where sufficiently the same at 78 K and 295 K. Excitation spectra consist of bands near 4.2 eV, 5 eV and group near 6.5 eV. The first two bands usually considered as 5d states splitted by crystal field. The last group of bands can be assumed as transition to 6s states (similar to excitation bands at 6.5-8.5 eV in LaF_3:Ce^{3+} [13]). While the charge transfer mechanism was not excluded for this photon energies [13].

The relative value of 5 eV excitation band decrease in a row from CaF_2 to BaF_2, while those of 6.5 eV group increase (see Fig.1). Similar behavior was seen in absorption spectra also. The excitation edge above 9 eV correlates with the edge of exciton absorption. The relative Ce^{3+} intensity within exciton and band-to-band transitions is decreased from CaF_2 to BaF_2. Evidently, the efficiency of transmittance of exciton energy to cerium is decreased in less compacted lattices. This effect cannot be explained by decrease in overlapping of exciton emission band, which is near 4 eV in all hosts, and Ce absorption. At seems the decreasing in effectiveness related with decreasing of exciton migration range in a row from CaF_2 to BaF_2.

There are also excitation shoulders in 7-9 eV region, which are less pronounced in CaF_2. Accordingly to this the thermoluminescence created in 7-9 eV region is less intensive in CaF_2.

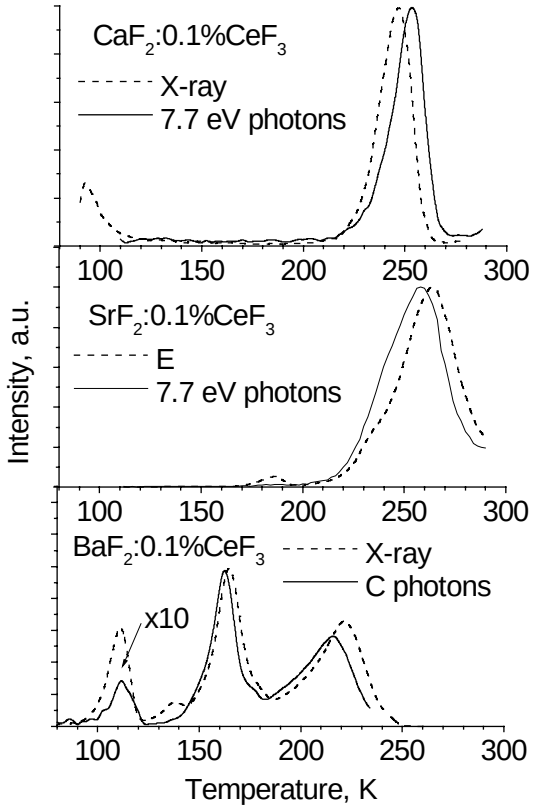

Fig.2. Thermoluminescence curves of alkaline-earth fluoride crystals doped with cerium stimulated by x-rays as well as by vacuum ultraviolet photons at 78K. Curves were normalized for comparison. Intensity of BaF_2 112 K peak stimulated by 7.7 eV photons was 10 times multiplied. Luminescence was measured in 3.87, 4.02, 4.09 eV Ce^{3+} bands for CaF_2, SrF_2 and BaF_2 respectively.

Thermoluminescence created by VUV photons

Several thermostimulated luminescence peak were observed in alkaline-earth fluorides when irradiated by photons with energy above 6 eV (Fig. 2). The glow curves in 140-300 K region created by VUV irradiation well coincide with those created by x-irradiation.

Low-temperature thermoluminescence peaks at 80-120 K are relatively much higher in X-ray irradiated samples.

Most extensively the thermoluminescence was investigated in BaF_2:Ce^{3+}. Three peaks at 112 K, 166 K and 220 K with comparable intensity were observed after x-irradiation (see Fig. 2). The relative intensity of 166 K and 220 K peaks was the same for all excitation energies of photons. These peaks were created by photon with energies above 6 eV. The

creation spectrum shows the maximum at 8 eV and then begins decrease (see Fig.2). Apart from this the 112 K peak was created above 7 eV and continuously increased up to 9 eV where exciton absorption edge begins. Similar behavior of thermoluminescence peaks was observed in BaF_2:0.01% CeF_3, while the relative peaks intensities and peak temperatures were slightly different.

Slow components in Ce^{3+} luminescence decay

At excitation by photons with energies lower than 6 eV the decay curve consist of single exponent with decay times listed in the Table. The decay times of both Ce^{3+} emission bands were equal. The decay times not changed down to 12 K, and designated as radiative decay times (τ_{rad} in Table). Above 6 eV excitation the decay curve consists of slow component and fast component, which become longer then τ_{rad} (see Table). The 0.4-3 μs part of decay curve is not well described by single slow component, the curve become more hyperbolic. The decay curves of not changed when temperature decreased to 78 K and to 12 K.

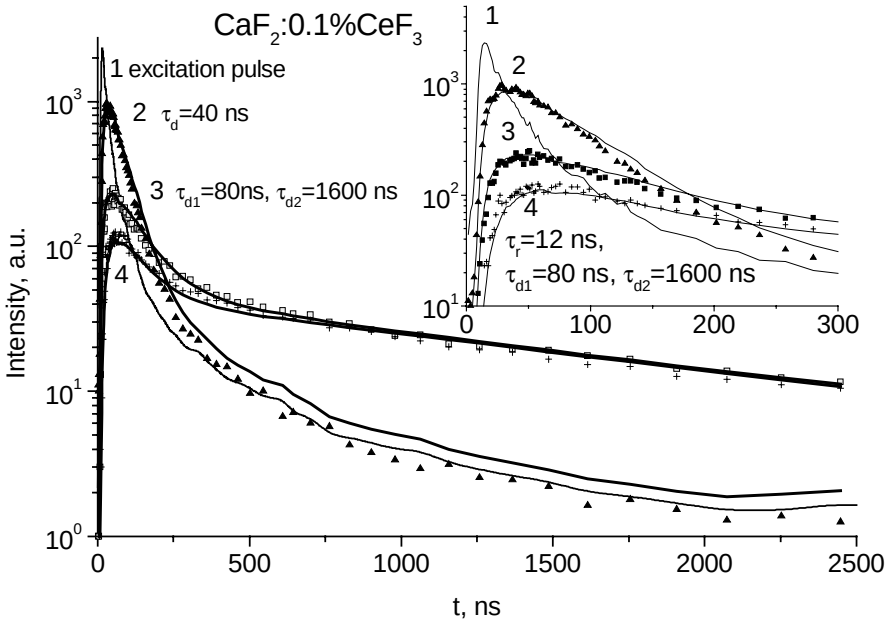

Fig.3. Decay of 3.87 eV Ce^{3+} luminescence in CaF_2:Ce. Curve 1 – excitation pulse, points on curve 2 – 4.3 eV excitation, points on curve 3 – 6.4 eV excitation, points on curve 4 – 7.2 eV excitation. Curves 2-4 were calculated using convolution of excitation pulse and shown exponential components. For curve 4 the 12 ns rise time are necessary to fit the experimental data.

Several CeF_3 crystals with different impurity levels have been investigated. The impurity level roughly can be monitored by ratio of 4.1 eV emission band to impurity perturbed 3.5 eV emission band [11]. Slow decay time was the same in several crystals with different impurity contamination. This points out that CeF_3 slow decay in microsecond time region depends on intrinsic defects.

Discussion

Thermoluminescence

X-irradiation of trivalent rare-earth ion (RE^{3+}) doped alkaline-earth fluorides at low temperature leads to creation of self-trapped holes of different kinds and electrons trapped on rare-earth ions – RE^{2+}. Several types of self-trapped holes captured near RE^{3+} ions designated as V_{kA} and on charge compensating F^- interstitials designated as V_H or H centers were observed [5]. Self trapped holes become mobile at 80-120 K in all alkaline-earth fluorides,

while some types of V_{kA} centers stable even at room temperatures [5]. Ce^{2+} and other RE^{2+} ions are stable below at least 400-500 K

The peak temperatures of the glow curves of CaF_2 were not characteristic of the particular rare earth, but instead were common to all the rare-earth ions [6]. Six or seven glow peaks were usually observed between 77 K and room temperature, and the temperature at which they occurred were identical for each ion to within a few degrees. Most also displayed a large glow peak at approximately 300 K. The centers proposed to be responsible for these effects involve different configuration of the F_2^- molecular ions [6]. Therefore, thermostimulated luminescence, which we observed in Ce^{3+} doped alkaline-earth fluorides below room temperature, related with delocalization of self-trapped holes and migration it to trapped electrons.

Recently two main thermoluminescence peak at 90 and 130-140 K in pure and RE^{3+} doped LaF_3 attributed to annealing of halogen defect sites, similar to the H and V_k centers in alkali halides [12].

Observation of thermostimulated luminescence after vacuum ultraviolet irradiation in alkaline-earth fluorides which is similar to those after x-ray irradiation means that ultraviolet photons create self-trapped holes as well as trapped electron centers. Within 6-7 eV excitation energies only hole centers of V_{kA}, H type created. Above 7 eV self-trapped holes are created additionally (see Fig. 1,2). Similar behavior was observed in BaF_2:0.01% CeF_3 also. At seems, by irradiation with 6-7 eV photons the electrons transfer from charge compensating F^- interstitials to Ce^{3+}, while above 7 eV zone holes created. So 1 eV can be considered as optical energy of V_k center binding on F^- interstitials. The thermal impurity stabilization energy for V_k centers in BaF_2:Tm^{3+} was estimated as 0.6 eV [5]. It is known that optical activation energy higher then thermal activation energy. Therefore both energies are in agreement.

The possibility of existence of Ce^{4+} ions in alkaline earth fluorides was discussed, but was not observed experimentally. Possibly the energy needed to transfer electron from Ce^{3+} to conduction band is too large mainly due to large ionization potential of Ce^{3+} ion. Observation of several types of self-trapped holes near RE^{3+} in x-ray irradiated alkaline-earth fluorides means that energetically the creation of pair self-trapped holes near rare-earth ion is more favorable than creation of RE^{4+}. This is a reason why transition from valence band to Ce^{3+} has a less energy than transitions from Ce^{3+} to conduction band.

Decay of luminescence

It is generally believed that excitation of Ce^{3+} ions in LaF_3 or CeF_3 crystals with energy above 6.5 eV lead to photoionization of cerium electron to conduction band [7]. Slow components of cerium luminescence related with electron escaping from some traps [7]. Our results show that photoionized charge carrier return to cerium by tunnel process. We assume that the irradiation of Ce-doped fluorides by photons with energy above 6 eV lead to transition of electrons from 2p F^- fluorine band to cerium level. Hole rapidly becomes self-trapped. The energy of recombination of electrons from Ce^{2+} with neighboring self-trapped holes is large enough to excite 4f-5d transition in Ce^{3+} ion. The recombination rate determines the fast and slow components of decay curve. Possibly the self-trapped holes captured on nearest interstitial give rise a fast decay component, while those captured on next nearest interstitial may give rise a slow component of decay.

Simple model

It is very attractive to explain the transitions between impurity levels and conduction and valence bands using simplified electrostatic model [9, 10]. The sum of photoionization and charge transfer thresholds of Ti^{3+} is found to give approximately the band gap energy of the

Al_2O_3host crystal [9]. The idea is rather simple: the charge transfer transition from conduction band to Ti^{4+} impurity level and photoionization transition from created Ti^{3+} to conduction band will lead to electron-hole pair. The sum of experimental values somewhat less then band gap energy [9]. In our case the transition energy from valence band to Ce^{3+} plus the transition energy from created Ce^{2+} to conduction band can be compared with band gap energy. The V_k centers creation threshold can be estimated as 7 eV in BaF_2 (see Fig. 1). The band gap of BaF_2 is equal 10.6 eV [5]. So the photoionization of Ce^{2+} can be estimated as less then 3.6 eV. Several weak absorption bands in near IR 0.88, 1.09, 1.49 eV and larger one near 2.5 eV were attributed to Ce^{2+} in CaF_2 [3]. The energy depth of Ln^{2+} against conduction bands can be estimated as f-s transition energy in free Ln^{2+} ion [10], that for Ce^{2+} gives 2.5 eV. Using 2.5 eV as photoionization threshold we obtain 7+2.5 = 9.5 eV, while the band gap equal 10.6 eV. So the rule [9] is valid in the case of BaF_2:Ce^{3+} within ~1 eV accuracy.

Conclusion

Photoionization in alkaline-earth fluoride crystals doped with Ce^{3+} ions by ultraviolet photons 6-10 eV begins with transition of electron from 2p F^- valence band to Ce^{3+} level. Followed tunnel recombination of Ce^{2+} electron with trapped hole in form V_k or H center leads to appearance fast and slow decay components of Ce^{3+} luminescence. Additionally several thermoluminescence peaks belonging to escaping of trapped holes are observed.

References

1. D. S. Hamilton, S. K. Gayen, .G. J. Pogatshnik, R. D. Ghen, W. J. Miniscaico, Phys. Rev. B: Cond. Matter **39** (1989) 8807
2. G. J. Pogatshnik and D. S. Hamilton, Phys. Rev. B: Cond. Matter **36** (1987) 8251
3. G.J. Hollinghworth and D.S. McClure, Phys. Rev. B: Cond. Matter **48** (1993) 13280
4. Crystals were grown by by P.Figura and V.Ivashechkin in our laboratory
5. Crystals with fluorite structure, edited by W. Hayes, Clarendon, Oxford, 1974
6. J.L. Merz and P.S. Pershan Phys.Rev. **162** (1967) 217
7. C. Pedrini, A.N. Belsky, A.N.Vasil'ev, et.al. Mat.Res.Soc.Symp.Proc. **348** (1994) 225
8. G.M.Williams, N.Edelstein, L.A.Boatner et.al. Phys.Rev.B **40** (1989) 4143
9. W. C. Wong, D. S. McClure, S.A. Basun, and M.R.Kokta Phys. Rev. B. **51** (1995) 5682 ; **51** (1995) 5693
10. A.J. Wojtowicz, Proc. Int.Conf. on Inorganic Scintillator and Their Applications, SCINT95, Delft Univ.press, The Netherlands 1996 p.95
11. A.J. Wojtowicz, M. Balcerzyk, E. Berman and A. Lempicki. Phys. Rev. B:Cond. Matter **49** (1994) 14880
12. B.Yang, P.D.Townsend, A.P.Rowlands Phys.Rev.B **57** (1998) 178
13. W.S.Heaps, L.R.Elias, W.M.Yen Phys.Rev.B **13** (1976) 94

Status of development of YAP-LuAP mixed scintillators. Optical, luminescence and light yield studies

A.N.Belsky[1,2], C.Dujardin[1], C.Pedrini[1], A.Petrosyan[3], W.Blanc[1], J.C.Gacon[1], E.Auffray[4], P.Lecoq[4]

[1]*Laboratoire de Physico-Chimie des Materiaux Luminescents, UMR 5620 CNRS, Université Claude Bernard Lyon-1, 69622 Villeurbanne, France*
[2]*Synchrotron Radiation Laboratory, Physics Faculty, Moscow State Lomonosov University, 119899 Moscow, Russia*
[3]*Institute for Physical Research, Armenian National Academy of Sciences, 378410 Ashtarak-2, Armenia*
[4]*CERN, 1211 Geneve-23, Switzerland*

Abstract: Optical absorption (in the range of 200 - 450 nm), luminescence emission and excitation spectra in the UV-VUV region and scintillation light yield (under ^{137}Cs, 662 keV excitation) of 3 series of $Lu_xY_{x-1}AlO_3$:Ce samples are presented. In addition to a regular shift of the cerium emission band and of the fundamental absorption edge of crystals upon x variation, an increase of luminescence yield under VUV and γ excitations for the intermediate x is observed. We explain this effect by a short-order clusterisation of mixed crystals.

Keywords: cerium, scintillators, orthoaluminates, mixed crystals, energy transfer

Introduction

Cerium doped $YAlO_3$ (YAP) is a well known fast scintillator (t ~ 20 ns) with a high light yield (~$2 \cdot 10^4$ photons/MeV), but has a low crystal density (5.5 g/cm^3). Cerium doped $LuAlO_3$ (LuAP) has a much higher crystal density (8.34 g/cm^3), but lower light yield [1,2]. Because both compounds have the same pseudo perovskite structure, elaboration of $Lu_xY_{x-1}AlO_3$ solid solution (LuYAP) doped by cerium is very attractive to improve the stopping power and to obtain a higher light yield. Furthermore, the crystal growth is easier when at least 20% of Y ions are incorporated into LuYAP and thermal stability of solid solution single crystals increases compared to that of LuAP [3].

The present paper reports on the optical, luminescence and scintillation properties of different $Lu_xY_{x-1}AlO_3$-Ce solid solutions grown by different techniques, with large variation of composition ($0 \le x \le 1$) and cerium concentration.

Fluorescence spectrum of all samples is composed of two overlapping emission bands centred near 360-370 nm at room temperature and originated from 5d-4f radiative transitions in Ce^{3+} ions. The position of the fluorescence maximum in mixed compounds slightly shifts from $LuAlO_3$ to $YAlO_3$ with x variation. Under direct excitation of cerium a fluorescence decay time is about of 20 ns.

Experimental details

The samples can be subdivided into three groups. The first one is a series of powder samples doped with 0.5% Ce^{3+} with x varying from 0 to 1.Single phase Ce-doped solid solution compounds have been prepared by melt quenching technique employing a Bridgman furnace. The advantage of powders is that it is possible to compare the samples containing the

same amount of cerium. It is more difficult in YAP and LuAP crystals because the cerium partition coefficients are different: k=0.6 in YAP and k=0.17 in LuAP. The second group is composed of two series of mixed single crystals grown by vertical Bridgman [3] ($1 \leq x \leq 0.3$) and Czochralski ($0 \leq x \leq 0.5$) methods. The third group of crystals, grown by vertical Bridgman method, contains a series of single crystals with the same composition (x = 0.5) but different cerium concentrations in the melt (0.4 – 0.6 at.%). The typical sizes of crystals are~5x5x10 mm^3. For all crystals, only one X-ray diffraction pattern is observed, and the lattice constant changes linearly with concentration of Lu (x).

Experimental set-ups used for optical, luminescence and light yield measurements were previously described [2,4].

Optical properties

The transmission of $Lu_xY_{x-1}AlO_3$-Ce crystals in the 200-450 nm region is governed by the cerium 4f-5d absorption transitions and by the absorption of intrinsic defects or impurities. The absorption spectrum of Ce^{3+} exhibits five bands peaking between 325 and 200 nm (Fig.1, a), which are the cause of the drop in transparency around 325 nm (Fig.1, b).

In some crystals, it was observed absorption at larger wavelengths which strongly overlaps the emission band. This could induce important light yield loss in bulk crystals. The profile of the transmission spectrum in the 325-400 nm region indicates the presence of at least two bands at 330 nm and 350 nm (Fig.1, b). These absorption bands are particularly intense in crystals grown by the Czochralski technique : YAP-Ce and mixed crystals containing a weak Lu concentration. The transmission increases with Lu concentration increases. Most of crystals grown by Bridgman and all crystals containing more than 30 % of Lu do not exhibit such bands. These bands were observed also in YAP-Ce crystals grown by Crytur Company. It was observed that under nearly identical growth conditions, the tendency for twinning and crack formation was increasing with the Y concentration in $Lu_xY_{x-1}AlO_3$-Ce mixed crystals [3].

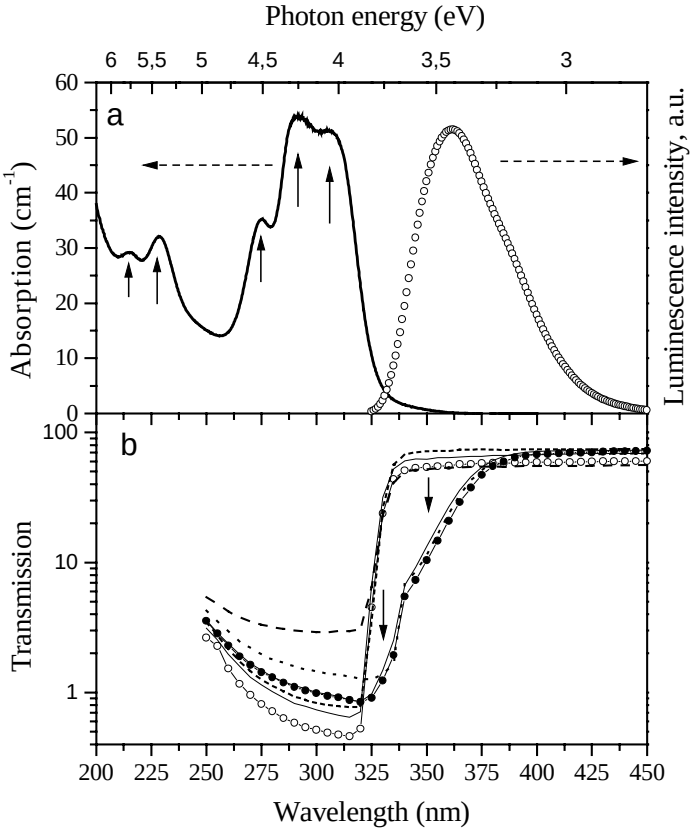

Fig.1 : a – absorption and emission spectra of LuAP-Ce; b – transmission spectra of different LuYAP-Ce crystals

The Czochralski technique may promote creation of large distortions, such as a dislocation, in comparison with the Bridgman technique. We assign the 330 nm and 350 nm absorption bands to intrinsic defects associated with dislocations and other macroscopic distortions in crystals. We can conclude that $Lu_xY_{x-1}AlO_3$-Ce large crystals will be of better optical quality than YAP-Ce large crystals.

Light yield

Light yield measurements of YAP-Ce and LuAP-Ce have been performed by several groups of different laboratories. In general, the light yield is found to be higher in YAP-Ce than in LuAP-Ce. But the results are rather dispersed due in a large part to the different experimental conditions and to different parameters: crystal geometry, concentration and spatial distribution of activator ions, optical quality of crystal volume and surface. Light yield is always found to be larger in YAP-Ce than in $Bi_4Ge_3O_{12}$ (BGO) and from some authors, 2-4 times larger.

The goal of the present study was not to determine absolute values of the light yield of LuYAP-Ce mixed crystals, but rather to study under the same experimental conditions the variation of its relative light yield in function of the relative concentration of Lu/Y, of cerium concentration and of crystal growth technique. Typical curves representing the scintillation pulse amplitude distribution are pictured in Fig.2 (the position of photopeak is indicated by an arrow).

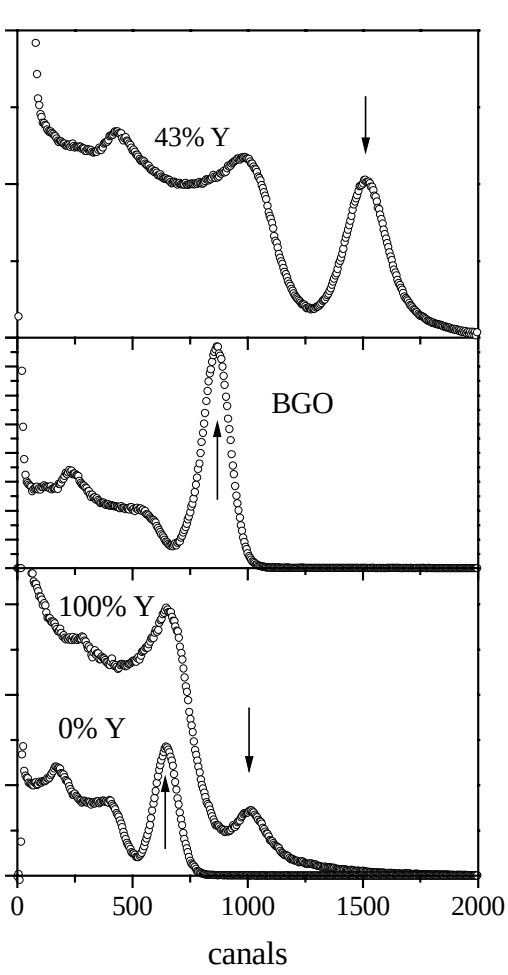

Fig.2 : Amplitude distribution of scintillation pulses under ^{137}Cs γ-ray excitation: YAP-Ce, LuAP-Ce (bottom pannel), BGO (middle pannel) and $Lu_{0.57}Y_{0.43}AlO_3$-Ce (top pannel)

The BGO photopeak is situated between the LuAP-Ce and YAP-Ce photopeaks, while the photopeak of mixed crystals is displaced towards larger channel numbers. It should by noted that our results, in comparison with the ones published by other groups [1], generally overestimate the light yield ratio BGO/(YAP-Ce) but the light yield ratio (LuAP-Ce)/(YAP-Ce) is the same.

Our measurements have been performed under 662 keV excitation of a ^{137}Cs source. The relative amplitude of the photopeak, which reflects the photoelectric effect, with respect to the spectrum due to the Compton diffusion, strongly depends on compounds and is determined by the ratio between the probability of photoelectric and Compton interaction at this energy. The ratio is larger for BGO and LuAP-Ce than for YAP-Ce and increases with the Lu/Y relative concentration in mixed crystals.

The relative photopeak position for three series of samples are shown in fig.3. The principal result of our study is the increase of the light yield for mixed crystals with intermediate Lu/Y concentration. Both series of crystals obtained by Czochralski and Bridgman techniques exhibit similar light yields for the same composition, indicating that the variation of the light yield is rather due to the change of composition and weakly influenced by the growth technique.

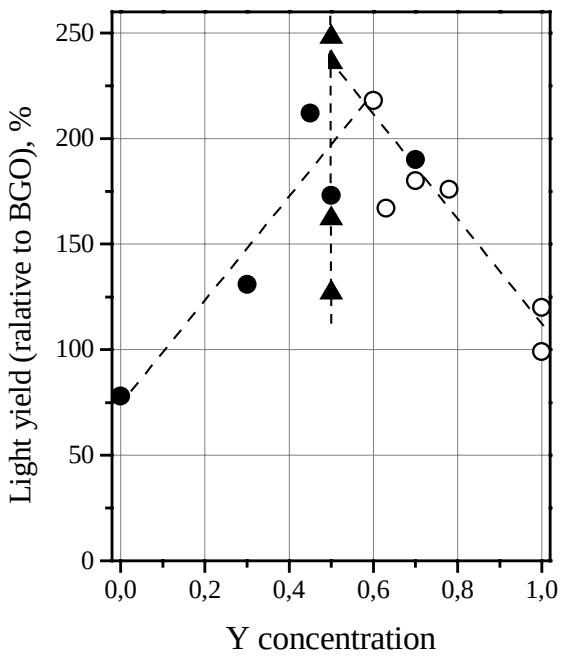

Fig.3 : Relative light yield of LuYAP-Ce single crystals grown by Czochralski (○) and Bridgman (● and ▲) techniques.

The main drawback of LuAP-Ce is the weak cerium segregation coefficient which limits the doping concentration and leads to inhomogeneities along the crystal. Data for the series of 3 samples of same composition of matrix ($Lu_{0.5}Y_{0.5}AlO_3$) and presenting a similar surface quality, but containing different cerium concentrations, are presented as black triangles in Fig.3. The nominal concentration increases from 0.2% Ce to 0.6%Ce. The best sample exhibiting a light yield of 2.5 times the one of BGO contains 0.45%Ce measured by the method of inductively coupled plasma-mass spectrometry.

Excitation spectra

The luminescence excitation spectra of a crystal near the fundamental absorption edge contains information about the energy transfer efficiency from the lattice to dopant ions. For the study of transfer mechanisms, $Lu_xY_{x-1}AlO_3$-Ce powders samples have been chosen since the real concentration of dopant ions is close of nominal concentration in powders.

Cerium luminescence excitation spectrum of $Lu_{0.7}Y_{0.3}AlO_3$-Ce powder is pictured in Fig.4 with a diagram of electronic transitions occurring under UV-VUV excitation. Cerium excitation in this compound is possible through three mechanisms [4]. A first process is the direct excitation of the 4f electron; it is dominant in region I (4-6 eV). Excitation and ionization of cerium can also arise from inelastic electron-electron scattering in the conduction band, but in the present case of low cerium concentration, the process is unlikely. A second mechanism occurs in region II (7.5 – 9.5 eV) near the absorption edge of the crystal. A photon creates a pair of bound electron-hole or a free exciton that can be localized in a state of self-trapped exciton. Its creation probability drops with increase of the photon excitation energy. Self-trapped exciton transfers efficiently its energy to cerium due to an important overlap between the Ce 4f-5d absorption spectrum and the emission band of self-trapped exciton. At photon excitation energy above 9 eV, the creation of separated electron-hole pairs is dominant.

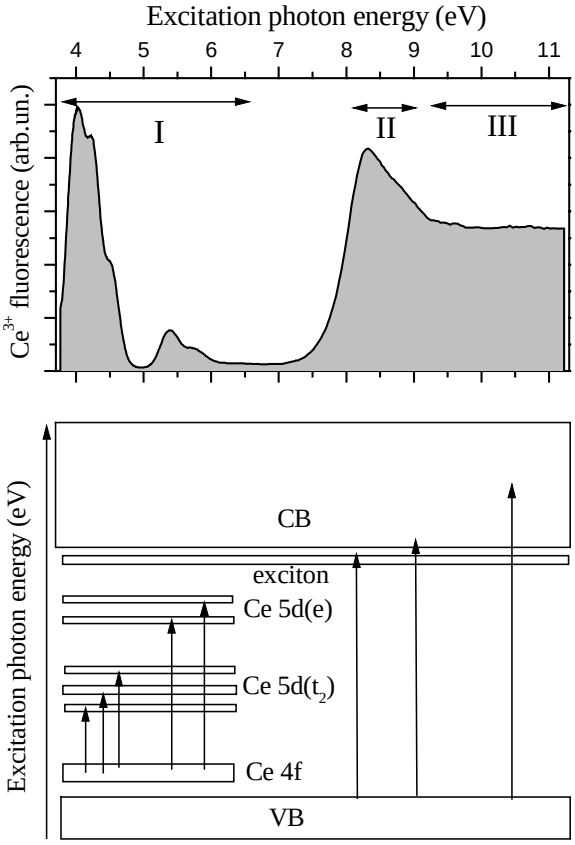

Fig.4: Energy levels diagram and luminescence excitation spectrum of $Lu_{0.7}Y_{0.3}AlO_3$-Ce

The main Ce excitation process occurring at higher excitation energy in region III (>9 eV) involves a sequential capture by Ce of hole and electron from separated electron-hole pair. The efficiency of this mechanism is stronger when the electron-hole distance in the pair is small.

It is reasonable to suppose that Ce excitation probability in region I is only proportional to the Ce concentration and does not (or weakly) depends on the solid solutions composition (Lu/Y). Cerium luminescence excitation spectra of $Lu_xY_{x-1}AlO_3$-Ce compounds (Fig.5) of various compositions (Y content varies from 0 to 100 %) were normalized to the intensity maximum in the region I. They have similar structure, but it is clearly observed some variations with the change of solid solution composition.

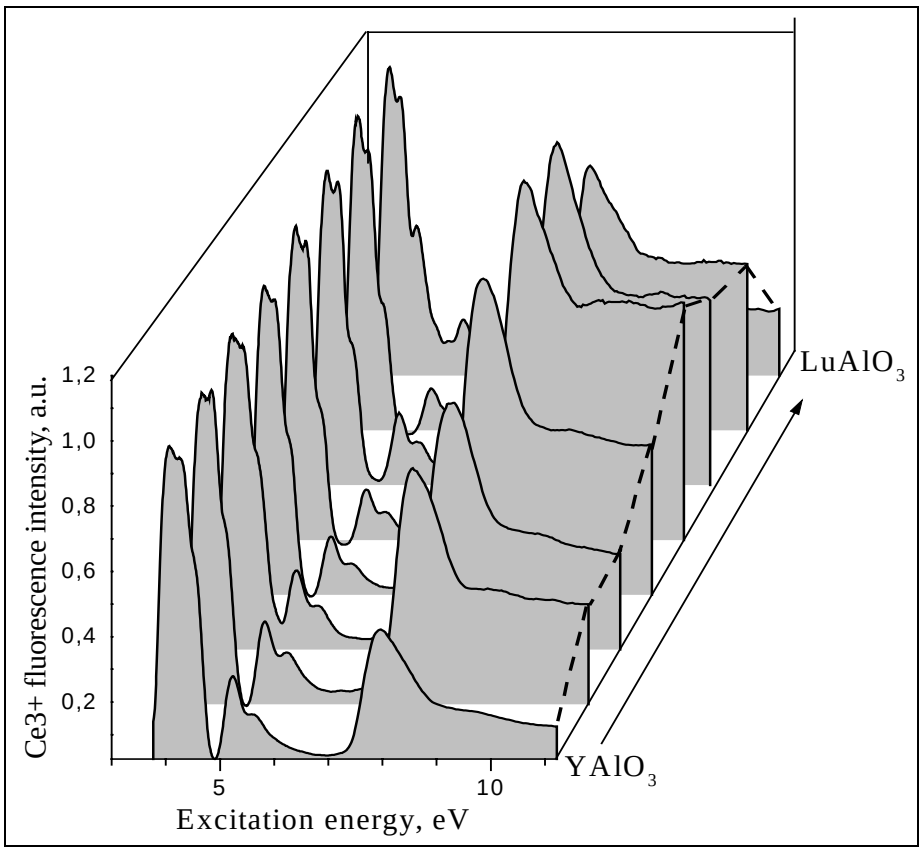

Fig.5 :Luminescence excitation spectra of (Lu,Y)AP-Ce solid solutions

In region I, the resolution of the spectra into 5 bands due to Ce 4f-5d transitions increases from YAP-Ce to LuAP-Ce. This effect is connected to the change of the average volume of the unit cell (from 203 $Å^3$ in YAP to the 198 $Å^3$ in LuAP) which leads to a variation of the crystal field strength.

But the more evident changes concern the excitation efficiencies in regions II and III with respect to that of region I. The ratios are pictured in Fig.6. Their composition dependence is similar to what was observed for the light yield in Fig.3. The excitation efficiency rapidly increases in the solid solution and reaches a maximum for compounds with compositions of 30-70 at. %Y, and the amplitude of the variation is around 200-300%.

Conclusion

The correlation between light yield and luminescence excitation measurements demonstrates that the increase of light yield is mainly due to the increase of energy transfer efficiency in (Lu,Y)AP-Ce solid solutions containing 30-70 at. % of yttrium.

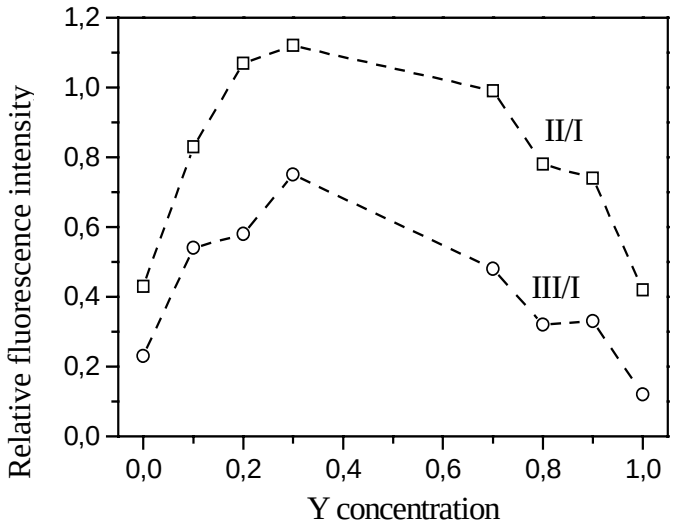

Fig.6 : Variation of excitation efficiency in the regions II and III relative to region I (for the details see text)

Increase of light yield and energy transfer efficiency at intermediate compositions of solid solutions have been previously observed in other ionic crystals and were related to the concentration dependence of short-order in solid solution components distribution . At some concentration values (usually 30-70 %) the creation of small clusters enriched by one of the components of mixed crystal is possible. Modulation of crystal potential by the boundaries of such clusters may decrease the diffusion length of secondary electrons and holes and promote the localization of electronic excitations. If the cluster size matches well with electron hole interaction radius, the probability of exciton formation and then of transfer efficiency from e-h pairs to cerium increase. These two phenomena lead to an increase of the energy transfer efficiency from the crystal lattice to dopant ions, and therefore to an increase of the light yield.

Acknowledgements

This work was performed in the frame of "Crystal Clear" collaboration with CERN and was supported in part by the NATO grant HTECH.LG 971230.

References

1. M. Moszynski, M. Kapusta, M. Mayhugh, D. Wolski, S.O. Flyckt, IEEE Trans. Nucl. Sci. 44 (1997) 183
2. C. Dujardin, C. Pedrini, W. Blanc, J.C. Gâcon, J. C. van't Spijker, O.W.V. Frijns, C.W.E. can Eijk, P. Doenbos, R. Chen, A. Fremout, F. Tallouf, S. Tavernier, P. Bruyndonckx and A.G. Petrosyan, J. of Phys.: Condens. Matter 10 (1998) 3061
3. A.G. Petrosyan, G.O. Shyrinyan, K.L. Ovanesyan, C. Pedrini, C. Dujardin, J. of Crystal Growth 198/199 (1999) 492
4. C. Dujardin, C. Pedrini, J.C. Gâcon, A.G. Petrosyan, A.N. Belsky, A.N. Vasil'ev, J. Phys.: Condens. Matter 9 (1997) 5229

VUV scintillators based on d-f transitions in rare earth ions

V.N. Makhov[1], J.Y. Gesland[2], N.M. Khaidukov[3], N.Yu. Kirikova[1], M. Kirm[4], J.C. Krupa[5], T.V. Ouvarova[6] and G. Zimmerer[4]

[1]*Lebedev Physical Institute, 117924 Moscow, Russia*
[2]*Universite du Maine, 72017 Le Mans, France*
[3]*Institute of General and Inorganic Chemistry, 117907 Moscow, Russia*
[4]*II.Institut für Experimentalphysik der Universität Hamburg, D-22761 Hamburg, Germany*
[5]*Institut de Physique Nucleaire, 91406 Orsay, France*
[6]*Institute of General Physics, 117942 Moscow, Russia*

Abstract: The study of spectral properties, decay kinetics and light output of VUV emission due to interconfiguration 5d-4f transitions in rare earth ions has been performed for several ternary fluoride crystals containing different concentrations of Nd^{3+}, Er^{3+} and Tm^{3+}. Strong concentration quenching was found in crystals highly doped with Er^{3+} which leads to nanosecond decay for both spin-allowed and spin-forbidden 5d - 4f transitions in Er^{3+}. This feature makes absolutely different decay properties of VUV emission for highly doped Er^{3+}- and Tm^{3+}-containing crystals. Neither Er^{3+}- or Tm^{3+}-containing materials studied here had better scintillation properties than those of BaF_2 with respect to their using as fast scintillators coupled with VUV sensitive vapours or photocathodes. Only some Nd^{3+}-doped crystals have simultaneously high light output and relatively good timing properties of VUV emission.

Keywords: Rare-earth ions, fluoride crystals, 5d-4f luminescence

Introduction

One of the most promising schemes of gamma-detectors for positron emission tomography (PET) is a combination of the fast dense scintillator and a multiwire proportional chamber filled with photosensitive vapour like TMAE, TEA, etc. [1-3] (or fast dense scintillator and solid photocathode like CsI). Since these vapours (or photocathodes) are sensitive to vacuum ultraviolet (VUV) radiation only it is necessary to use scintillators emitting in the VUV. Such a design of the detector could have very good time resolution and high radiation resistance but by now the principal characteristics of such devices are very far from those required for PET. The main problem of such detectors is their low efficiency caused by rather low light yield of the used scintillators (e.g. BaF_2) and small overlapping of the scintillation spectrum with absorption of photosensitive vapours or photocathods. The search for new VUV scintillators with higher light yield and the spectrum shifted to shorter wavelengths is necessary for improving the PET devices with detectors of this type.

Fluoride crystals, with their large forbidden gap, doped with trivalent rare earth (RE) ions (Ce^{3+}, Pr^{3+}, Nd^{3+}, Er^{3+}, Tm^{3+}, etc.) with parity-allowed interconfiguration 5d - 4f transitions, can provide an exceptional possibility for the production of emitting materials in the UV and VUV spectral range. As it was shown in [4] three RE ions Nd^{3+}, Er^{3+}, Tm^{3+} possess d-f emission in the VUV. So fluoride crystals doped with Nd^{3+}, Er^{3+}or Tm^{3+} can be considered as promising VUV scintillators for gamma-detectors which utilise VUV sensitive vapours or photocathods (see Fig.1).

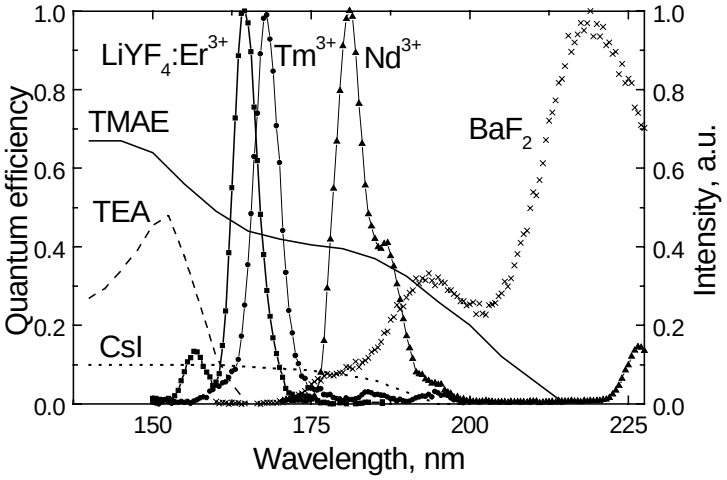

Fig.1. Quantum efficiency curves of TMAE and TEA vapours and of CsI solid photocathode (reproduced from Ref.[3]) and emission spectra of $LiYF_4$ doped with Er^{3+}, Tm^{3+} and Nd^{3+} and of BaF_2. All spectra are normalised with respect to their maxima.

Our recent studies of VUV emission of Er^{3+} and Tm^{3+} ions incorporated in some fluoride matrices have shown [5,6] that emission spectrum of these ions (due to 5d - 4f transitions) consists of two series of bands: fast emission bands (decay constant in the range from a few to tens nanoseconds for different crystals) and (or) slow ones (decay constant in the microsecond range) shifted to longer wavelengths. As it has been established in [7], the fast and slow components arise from spin-allowed (S-A) and spin-forbidden (S-F) 5d - 4f transitions, respectively.

The former originates from the higher-lying 5d state having the same value of spin as the ground state of 4f configuration, while the latter from lower-lying 5d state with different (higher by 1) value of spin than in the ground state of 4f configuration.

In the present paper the studies of spectral properties, decay kinetics and light outputs of VUV emission for several ternary fluoride crystals containing different concentrations of Nd^{3+}, Er^{3+} and Tm^{3+} ions (in particular for some stoichiometric compounds) have been performed.

Experimental

The spectral measurements were performed at the SUPERLUMI station [8] of HASYLAB at DESY under the excitation by synchrotron radiation (7-30 eV) from the DORIS storage ring. The measurements of luminescence spectra as well as the spectral selection of the bands for decay curves measurements were carried out with a 0.5 m Pouey-type secondary monochromator (with a resolution of about 1 nm) equipped with a solar-blind photomultiplier (for spectral measurements) and a microsphere plate detector (for decay curves measurements). The standard single-photon counting was used for time-resolved spectra and decay curve measurements (with time resolution of 0.1 ns).

The measurements of light outputs were performed under X-ray (1 keV) synchrotron radiation excitation at the S-60 electron accelerator of LPI. The VUV light detection was carried out with a 0.5 m Seya-Namioka analyzing monochromator and a solar-blind photomultiplier.

$LiErF_4$ and $LiTmF_4$ single crystals were grown by the Czochralski method as described in [9]. KF-based single crystals were grown with the technique of hydrothermal synthesis [10]. $LiYF_4:Er^{3+}$, $BaY_2F_8:Er^{3+}$, $BaY_2F_8:Tm^{3+}$, $BaEr_2F_8$ and $BaTm_2F_8$ single crystals were grown using the vertical Bridgeman method similar to that described in [11].

Results and discussion

The existence of slow S-F 5d - 4f transitions in Er^{3+}- and Tm^{3+}-doped crystals seems to make almost impossible the use of such crystals as fast VUV scintillators. However, our measurements have shown that highly doped (stoichiometric) Er^{3+}-containing compounds have nanosecond decay for all VUV emission bands.

Emission spectra and decay kinetics for $BaEr_2F_8$ and $BaTm_2F_8$ are shown in Figs. 2 and 3. In both spectra the band due to S-F transitions dominates (170 and 171 nm, respectively). However, decay characteristics of this band are absolutely different for these crystals: the decay constant for 170 nm band in $BaEr_2F_8$ is 4.8 ns while that for 171 nm band in $BaTm_2F_8$ is 265 ns (for weakly Er^{3+}- or Tm^{3+}-doped BaY_2F_8 the decay times of S-F luminescence are of the order of ~ 5 μs [6]). Similar results were obtained [12] for the S-F luminescence in the pair $KErF_4$ and $KTmF_4$ for which the decay constant for 167.5 nm band in $KErF_4$ was 9.2 ns while that for 170 nm band in $KTmF_4$ was 220 ns, and for $LiErF_4$ and $LiTmF_4$ where decay times of S-F luminescence were 4.4 and 203 ns, respectively.

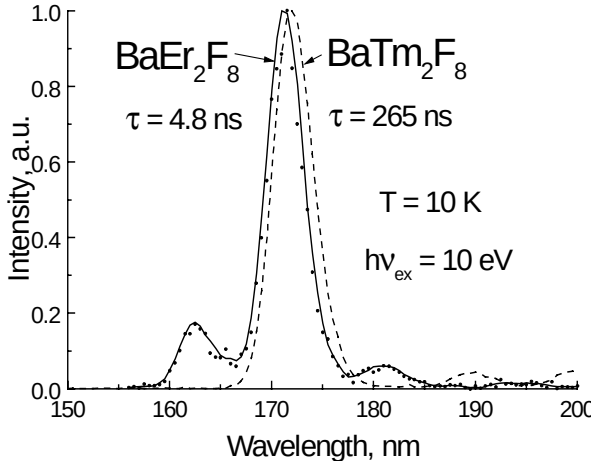

Fig.2. Emission spectra due to 5d-4f transitions in Er^{3+} and Tm^{3+} for $BaEr_2F_8$ and $BaTm_2F_8$.

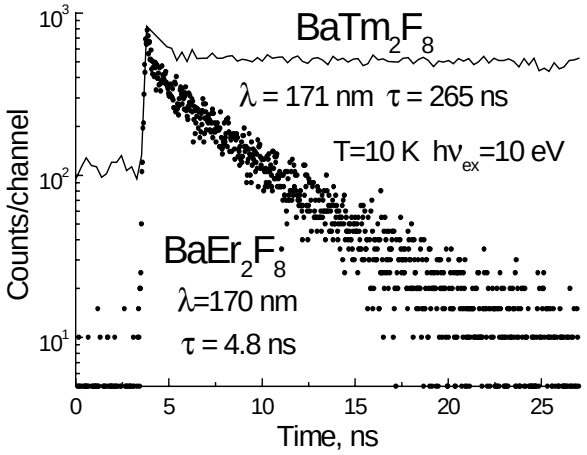

Fig.3. Decay kinetics of spin-forbidden 5d-4f luminescence of Er^{3+} and Tm^{3+} in $BaEr_2F_8$ and $BaTm_2F_8$.

The difference is due to different energy level schemes for high-lying 4f states of Er^{3+} and Tm^{3+} (see Fig.4). In case of Tm^{3+} no high-lying 4f levels exist with energies close to the energy of the lowest (emitting) 5d states, while in case of Er^{3+} the energy levels of some high-lying 4f states are very close to those of emitting 5d states and so the additional channel of non-radiative decay (resonance energy transfer 5d → 4f to neighbouring ions) leads to strong concentration quenching (shortening) of d - f emission, including S-F d - f luminescence.

The results of excitation spectra measurements for many fluoride matrices have shown that the quantum yield of Er^{3+} or Tm^{3+} d-f luminescence is extremely low in the region of fundamental absorption of the matrix till the energy of excitation reaches the threshold for processes of electronic excitations multiplication. This threshold lies at photon energy less than $2E_g$ (E_g is the band-gap) and the effect is much more pronounced at higher concentrations of Er^{3+} or Tm^{3+}. These features indicate that the mechanism of the energy transfer from the matrix to d-f luminescence is so-called impact mechanism of electronic excitations multiplication when fast photoelectrons excite directly (by impact) emission centers (Er^{3+} or Tm^{3+} ions) in the crystal. Since this mechanism is more efficient at higher concentrations of emission centers, in case of Er^{3+}-doped crystals the combined effect of concentration quenching and impact excitation results in relatively high quantum yield and fast decay of Er^{3+} d-f luminescence in highly doped (in particular, in stoichiometric) crystals. For example, for $LiY_{1-x}Er_xF_4$ series of single crystals the concentration quenching leads to the

decrease of the total quantum yield of d-f luminescence, however the quantum yield of the fast (S-A) component at high-energy excitation increases with concentration of Er^{3+}.

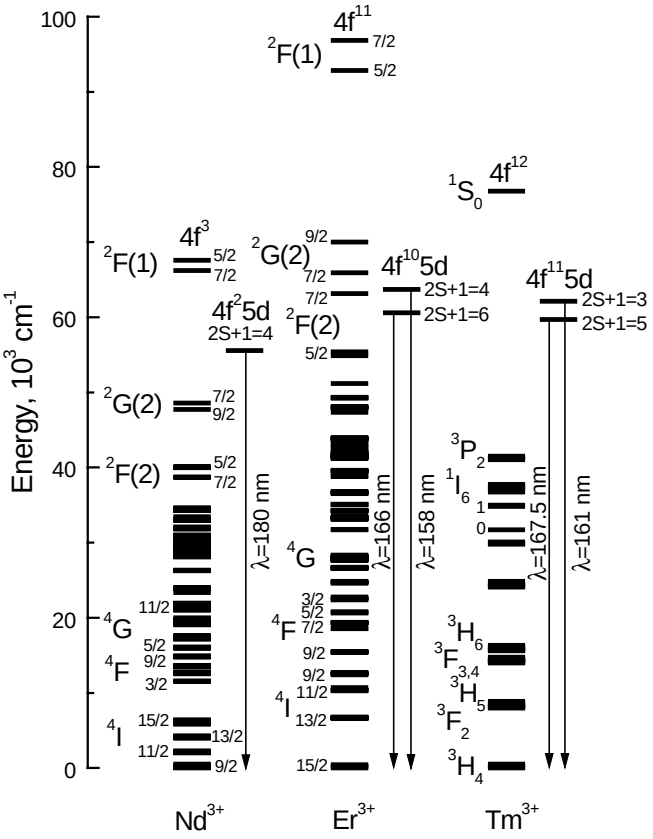

Fig.4. Energy level scheme of 4f configuration for Nd^{3+} in $LiYF_4$ [13], Er^{3+} in LaF_3 [14] and Tm^{3+} in $LiYF_4$.[15] and of 5d configuration (emitting states) for Nd^{3+}, Er^{3+} and Tm^{3+} in $LiYF_4$ (this work).

In weakly doped crystals the competition of the bands in the VUV emission spectrum of Er^{3+} or Tm^{3+} ion depends on the relative energy position of emitting levels for S-A and S-F transitions. If the energy gap between these levels is small enough, the phonon relaxation will exceed in rate the radiative decay of the higher-lying 5d state responsible for S-A transitions resulting in "pumping" the lower-lying 5d state responsible for S-F transitions, and accordingly, only slow S-F luminescence will be observable.

The estimation of light outputs of VUV emission expected at high energy irradiation for different compounds containing Er^{3+} or Tm^{3+} was made under excitation by X-rays with the energy 1 keV which exceeds the band-gap of the matrices by about two orders of magnitude. The results are shown in Table 1. In neither materials the light output (integrated in the range 150-200 nm) was larger than that of BaF_2 (integrated in the range 150 - 350 nm).

However the "overlap integral" $\int I(\lambda)\cdot Q(\lambda)\cdot d\lambda$, where $I(\lambda)$ is emission spectrum of the scintillator and $Q(\lambda)$ is quantum efficiency of photosensitive vapour (TMAE) or photocathode (CsI), for some Er^{3+}- or Tm^{3+}-containing crystals exceeds by several times that for BaF_2 (especially for CsI photocathode). Unfortunately this occurs only for crystals where slow decay dominates. Only in case of using TEA as photosensitive vapour the highly doped Er^{3+}-containing crystals will have good spectral overlapping of their main emission band at 158 nm with quantum efficiency curve of the vapour and will give good timing characteristics.

The reason of the low light output for d-f emission is poor efficiency of the main mechanism of the energy conversion (by impact excitation) from the fluoride matrix to d-f luminescence. Actually this means that in such systems the conventional recombination mechanism of the energy transfer doesn't work. This property is rather usual for d-f emission excitation in fluoride crystals doped with RE ions. However in many oxygen-containing matrices the recombination mechanism of the energy transfer is very efficient. Unfortunately this accompanies usually by considerable increase of the slow decay component. We found two oxygen-containing matrices doped with Nd^{3+}, namely YPO_4 and $LuPO_4$, where d-f emission of Nd^{3+} in the VUV (189 nm) is observed [16]. The light output of VUV emission for these materials is comparable with that of most efficient Ce-doped scintillators, but timing properties of VUV emission are not excellent to obtain a good time resolution.

Table 1. Comparison of light outputs for different fluoride crystals doped with Er^{3+} or Tm^{3+}.

Crystal	λ_{max}, nm	Light output rel. to BaF_2	Fraction of fast comp.	$\int I(\lambda)Q_{TMAE}d\lambda$ rel. to BaF_2	$\int I(\lambda)Q_{CsI}d\lambda$ rel. to BaF_2
$LiYF_4$:Er(5%)	166	24	6%	219	790
$LiYF_4$:Er(20%	166	11.4	17%	106	380
$LiErF_4$	158	1.3	100%	16	50
$LiYF_4$:Tm(1%	167.5	30	12%	268	940
BaY_2F_8:Er(5%	170	22.1	15%	196	665
BaY_2F_8:Er(20%)	170	19.6	16%	187	665
$BaEr_2F_8$	170	1.6	100%	15	45
BaY_2F_8:Tm(2%)	171	9.6	~0	83	265
$BaTm_2F_8$	171	1.7	~0	16	50
$KErF_4$	167.5	1.4	100%	18	50
$KTmF_4$	170	2.4	~0	20	60
ErF_3	158	1.0	100%	11	33
LaF_3:Nd(1%)	173	2.8	100%	33	100
BaF_2	220,19	100	100%	100	100

We found also one fluoride compound, K_2YF_5 doped with Nd^{3+}, in which the efficient recombination mechanism of energy conversion from the matrix to Nd^{3+} 5d-4f luminescence (185 nm) is observed (see Fig.5). From Fig.6 it is easily seen that it is possible to suppress considerably the fraction of the slow component by proper choice of the dopant concentration.

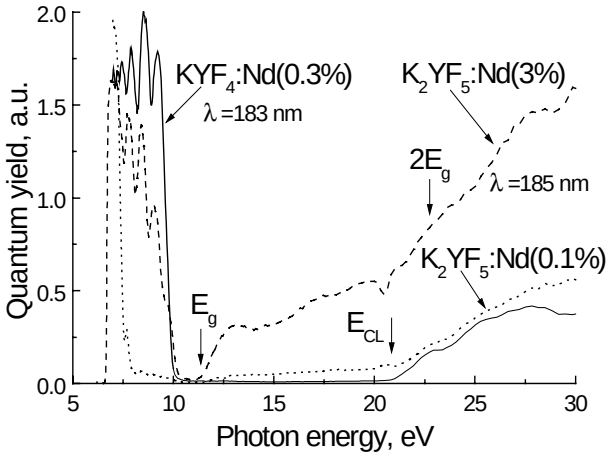

Fig.5. Excitation spectra of 5d-4f emission of Nd^{3+} doped into KYF_4 and K_2YF_5 crystals. E_g is the band-gap, E_{CL} is threshold energy for crossluminescence excitation.

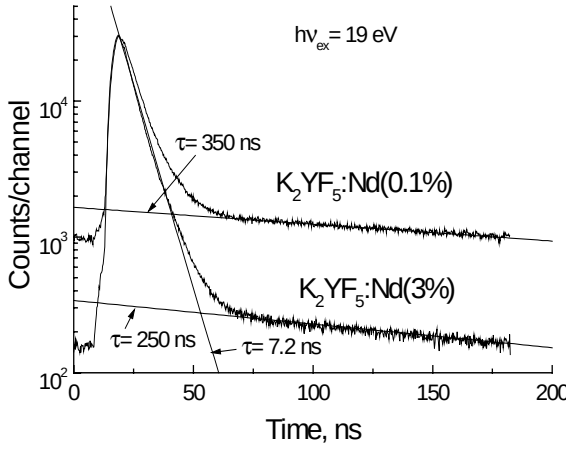

Fig.6. Decay kinetics of Nd^{3+} 5d-4f luminescence in K_2YF_5 for different concentration of Nd^{3+}. Excitation energy is 19 eV.

Conclusions

The spectral properties, decay kinetics and light outputs of VUV emission due to 5d-4f transitions in RE ions have been studied for more than 10 ternary fluoride compounds containing different concentrations of Nd^{3+}, Er^{3+} and Tm^{3+} ions.

It was found that decay properties of 5d - 4f emission for Er^{3+} and Tm^{3+} are strongly different in highly doped systems (stoichiometric compounds). This effect is due to different energy level schemes for high-lying states of 4f configuration in these ions. Strong concentration quenching in highly doped Er^{3+}-containing fluoride crystals leads to considerable shortening of the decay for both S-A and S-F 5d - 4f transitions. The combined effect of impact excitation and concentration quenching in such crystals can result in fast (nanosecond) decay of Er^{3+} VUV luminescence at still high light output.

Neither fluoride compounds doped with Er^{3+} or Tm^{3+} studied in this paper had light outputs larger than that of BaF_2. However, much better spectral overlapping of Er^{3+} or Tm^{3+} emission spectrum (due to d-f transitions) with quantum efficiency curves of photosensitive vapours (TMAE, TEA) and photocathodes (CsI) compared to the spectrum of BaF_2 can give some advantage of using Er^{3+}- or Tm^{3+}-containing crystals in gamma-detectors which utilise VUV sensitive vapours or photocathods. Nevertheless the wide band-gap crystals doped with Nd^{3+} are probably the most promising materials for fast VUV scintillators production.

Acknowledgements

The support of Graduiertenkolleg „Fields and localized atoms – Atoms and localized fields: Spectroscopy of localized atomic systems“ is gratefully acknowledged.

References

1. C.L.Woody and D.F.Anderson, Nucl. Instr. & Meth. A265 (1988) 291.
2. P.Schotanus, C.W.E. van Eijk and R.W.Hollander, Nucl. Instr. & Meth. A269 (1988) 377.
3. G.Charpak, V.Peskov, D.Scigocki and J.Valbis, Preprint CERN-EP/89-66, 1989.
4. K.H.Yang and J.A.DeLuca, Appl. Phys. Lett. **29** (1976) 499.
5. V.N.Makhov, N.Yu.Kirikova, J.Becker, M.Runne and G.Zimmerer, HASYLAB Annual Report 1996, Part I, p.273.
6. J.Becker, J.Y.Gesland, N.Yu.Kirikova, J.C.Krupa, V.N.Makhov, M.Runne, M.Queffelec, T.V.Uvarova and G.Zimmerer, J.Luminescence **78** (1998) 91.
7. R.T.Wegh, H.Donker and A.Meijerink, Phys.Rev. **B57** (1998) R2025.
8. G.Zimmerer, Nucl Instr. and Meth. **A308** (1991) 178.
9. M.Louis, E.Simoni, S.Hubert and J.Y.Gesland, Opt. Mater. **4** (1995) 657.
10. Y.Le Fur, N.M.Khaidukov and S.Aleonard, Acta Crystallogr. **C48** (1992) 978.
11. A.A.Kaminskii, T.V.Ouvarova, Izv. Akad. Nauk SSSR, ser. Neorg. Mat. **24** (1980) 2080.
12. J.Y.Gesland, N.M.Khaidukov, N.Yu.Kirikova, M.Kirm, J.C.Krupa, V.N.Makhov, M.Queffelec, T.V.Ouvarova and G.Zimmerer, J. Electron Spectroscopy and Related Phenomena **101-103** (1999) 579.
13. M.A.Couto dos Santos, P.Porcher, J.C.Krupa and J.Y.Gesland, J.Phys.: Condens. Matter **8** (1996) 4643.
14. W.T.Carnall, P.R.Fields and R.Sarup, J. Chem. Phys. **57** (1972) 43.
15. J.C.Krupa, unpublished.
16. J.Becker, J.Y.Gesland, N.Yu.Kirikova, J.C.Krupa, V.N.Makhov, M.Runne, M.Queffelec, T.V.Ouvarova and G.Zimmerer, J. Alloys and Compounds **275-277** (1998) 205.

Channels of Energy Losses in CeF_3 Crystals*

Chaoshu Shi[1,2], Jie Deng[2], Yaguang Wei[2], Guobin Zhang[2],
G. Zimmerer[3], J. Becker[3], Dingzhong Shen[4], Guanqin Hu[4]

[1]Phys. Dept., [2] NSRL,Univ. Of Sci. & Tech. Of China, Hefei, Anhui 230026, China
[3]Institüt für Experimental Physik der Universität Hamburg, Hamburg 22761, Germany
[4]Shanghai Institute of Ceramics,Shanghai 200050, China

Abstract: In this paper, the emission spectra in UV-VIS region at VUV, UV excitation and their temperature dependence in 6-453K as well as their excitation spectra (4-25eV) have been studied for CeF_3 crystals. These results show that a important way of losing energy is cascade energy transfer from regular Ce^{3+} to quenching centers via perturbed Ce^{3+} and defect centers in the CeF_3. Meanwhile, thermoluminescence of the CeF_3 above RT and corresponding trap effect are also discussed.

Keywords: CeF_3 crystal, Energy transfer, Luminescence, Excitation spectrum, Temperature dependence.

Introduction

Luminescence properties of CeF_3 crystals have been extensively studied in the last a few years [1-4]. Comparing with other scintillators, the CeF_3 is a very good candidate as Electromagnetic Calorimeters (ECAL) material used for further colliders, except that its density(6.16g/cm^3) is lower than that of $PbWO_4$ (8.28g/cm^3). It is also one of very excellent scintillators used for nuclear medicine such as positron emission tomography(PET). According to high energy excitation process in CeF_3 crystals, its light yield was estimated and can reach up to 7000-12000 photons/MeV [4], which is much higher than the measured experiment value(1500-4500 photons/MeV). In order to search the channel of losing energy in the crystals, we investigated its emission properties in the range of UV-VIS under different excitation and observed cascade energy transfer in it.

Experimental

The CeF_3 crystals were grown by Bridgman technique in high vacuum (10^{-5}-10^{-6}Torr). The original material was CeF_3 powder with purity 99.99%. The samples with the dimensions 10× 10×1 mm^3 were polished.

The emission and excitation spectra using Synchrotron Radiation Source and their temperature dependence were performed at SUPERLUMI station in HASYLAB of Germany. A setup including a GDM-1000 monochromator, IRO2W-cycle refrigerator made by Air Products company of US was used to measure fluorescence spectra in the 400-620nm range. Thermoluminescence of CeF_3 was recorded using QS-3500 Thermoluminescence Reader made by "HARSHAN" company.

* Supported by The National Nature Science Foundation of China under Grant No. 59372040 and 19774053

Results and Discussions

1. At 6K, under VUV excitation, the emission spectrum of CeF_3 crystals was a strong band with double peaks at 285nm and 301nm (Fig.1a), which originate from "spin-orbit" splitting of 4f ground states ($2F_{5/2}$,$2F_{7/2}$) in the transition of Ce^{3+}:5d 4f. With rising temperature, however, the double peaks were decreased and combined into one peak at 290nm. Meanwhile, the emission in the region of band tail (320-450nm) was obviously increased and appeared two bands peaked at 350 and 410nm (Fig.1b). As the temperature was being increased, variation tendency of both bands was the same, thus we only chose stronger one (350nm band) to discuss.

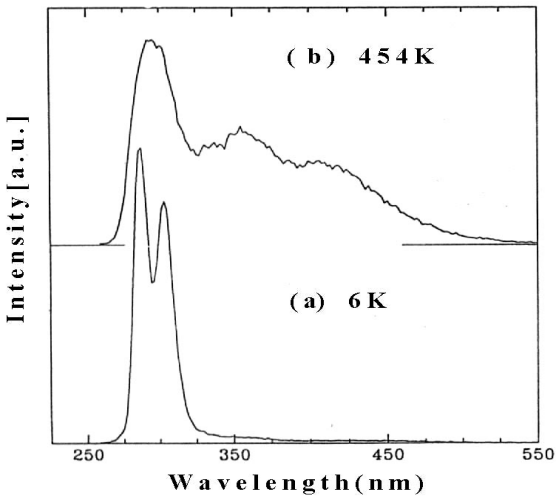

Fig. 1 Emission spectra of CeF_3 crystal under VUV excitation at 6K (a) and 454K (b)

The intensity ratio for the 290nm band to the 350nm band, I_{290}/I_{350}, was 55.0, 4.30, 3.75, 1.78 corresponding to temperature 6, 300, 420, 454K respectively [5].The temperature dependence of emission intensity shows that in CeF_3 there is energy transfer from 290nm band to 350nm band. The 290 and 350nm bands are assigned to intrinsic emissions from regular Ce^{3+} and perturbed Ce^{3+} in the crystal lattice respectively. The energy transfer can be also evidenced by their excitation spectra.

2. As shown in Fig.2a, the excitation spectrum of 290nm emission included four main excitation peaks at about 6.5, 7.9, 10.8, and 20.3eV corresponding to Ce^{3+}4f 5d, 4f→6s, F^- 2p→exciton state, and Ce^{3+}5p→5d transitions respectively [4, 6]. In the first excitation band there are five sub-bands at 4.9, 5.2, 5.5, 6.0 and 6.5eV which belong to stark components caused by crystal field splitting of Ce^{3+}-5d state [6]. Comparing with the excitation spectrum of 350nm emission (Fig.2b), in which there are very strong excitation peaks at 4.1eV (302.4nm) and 4.2eV (295.2nm), one can see that these strong excitation peaks just overlap 290nm emission band, and energy transfer from 290nm band (emitted by regular Ce^{3+}) to 350nm (emitted by perturbed Ce^{3+}) is quite efficient by means of radiation transfer way [7]. It is the first step of the cascade energy transfer in CeF_3.

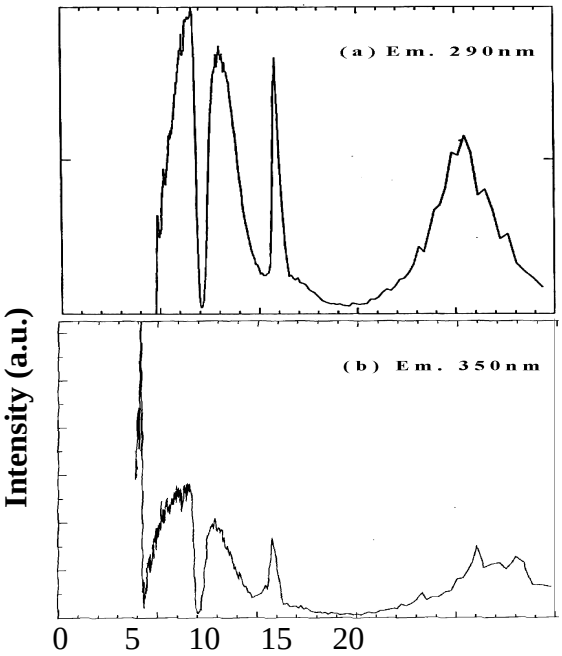

Fig. 2 At 6K excitation spectra of 290nm emission (a) and 350nm emission (b) from CeF_3.

3. The 350nm emission band is also excitation source of other emission bands centered at 470 and 535nm, as shown in Fig.3. These emission spectra were measured in the 33-230K range under excitation with UV-365 nm from high pressure mercury lamp [8]. The emissions in the visible range are ascribed to some defect centers (or impurity) and disappeared at RT due to temperature quenching or/and energy transfer to some quenching centers.
   According to these results mentioned above, we can conclude that in the CeF_3, there is energy transfer as follows (see Fig. 4):

   Regular Ce^{3+}→Perturbed Ce^{3+}→
   Defect centers→Quenching centers

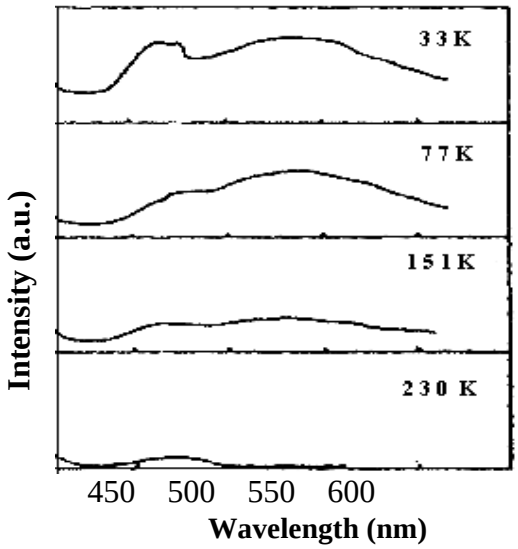

Fig. 3 Emission spectra of CeF_3 at low temperatures (33-230K) at 365nm excitation

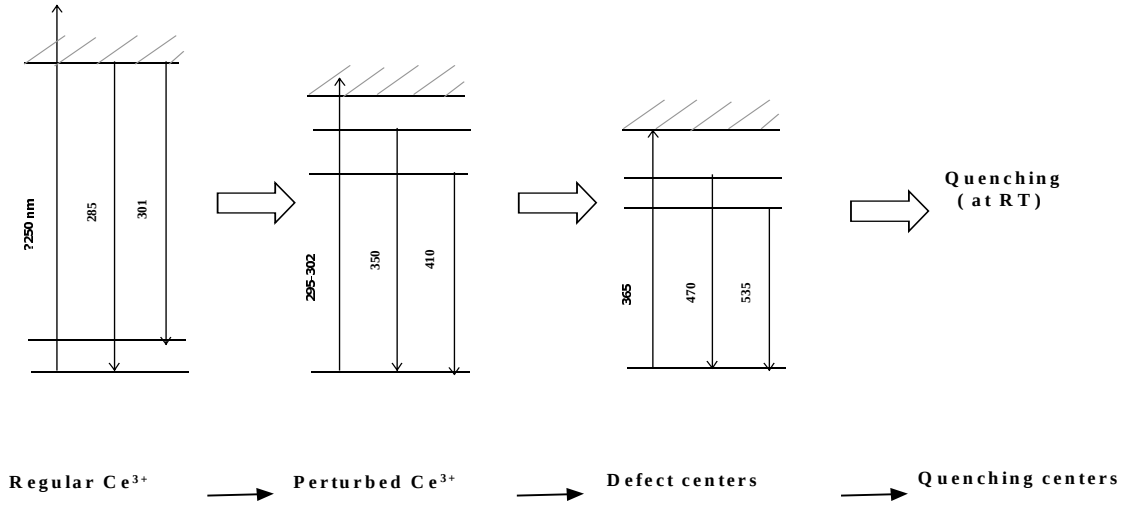

Fig. 4 Cascade Energy Transfer in Ce^{3+}

The cascade energy transfer process could be one of main reasons for decreasing luminescence efficiency.

4. What is the quenching center? Generally, quenching centers originate from some impurity or structure defects. For the CeF_3 crystal made by raw material with 4N or more purity, the quenching effect on luminescence is mainly caused by some structure defects, especially, various F^{--} vacancies. But the effect of trace impurity such as oxygen (which has absorption at~340nm) is also not rejected.

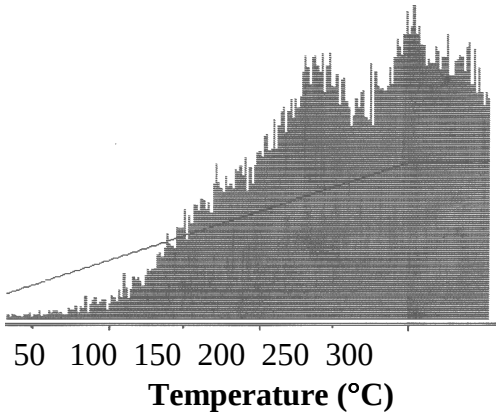

Fig. 5 Thermoluminescence of CeF_3 crystal above RT After X-ray excitation, the slope line in the figure gives the temperature range having linear temperature rising rate.

Thermoluminescence (TL) is one of efficient methods for studying defects in a crystal. Thus the TL of CeF_3 was researched in the 100-300K and 30-300°C (303-573K). After excitation with X-ray (50KV, 30mA, 2-min) at 100K, no TL signal was found below RT. However, after excitation with the same X-ray at RT, measured TL curve of CeF_3 as shown in Fig. 5. The TL peaks at near 240 and 300°C indicate that some deep traps with depth E~1eV exist in the CeF_3 crystal. When these deep traps captured free electrons in conduction band (CB) or free holes in valence band (VB), these trapped electrons or holes are very difficult to release into CB or VB and consequently to produce luminescence. In fact, such deep traps will become a kind of quenching centers.

Conclusions

In the CeF_3 crystals, there is cascade energy transfer, i.e regular Ce^{3+} can transfer energy to quenching centers via Ce^{3+} disturbed by defects and defect centers. It is one of important reasons decreasing luminescence efficiency of CeF_3 crystals. Maybe structure defects in the CeF_3 play a critical role in the cascade transfer. Thus decreasing defects and intercepting the cascade transfer is one of important methods for enhancing light yield.

References:

1. S. Anderson et al, Nucl. Instr. Meth. Phys. Res. A 332 (1993) 373
2. W.W. Moses, S.E. Derenzo, M.J. Weber, et al, J. Luminescence, Vol. 59 (1994) 89
3. E.Auffray, T.Beckers, J. Bourotte et al, Nucl. Instr. Meth. Phys. Res. A 378 (1996) 171
4. E.Auffray, T.Beckers, J. Bourotte et al, Nucl. Instr. Meth. Phys. Res. A 383 (1996) 367
5. Chaoshu Shi, Jie Deng, Xiaopu Lu, Chinese J. Lumin., Vol. 17 (1996) 66
6. Kun Wei, Changxin Guo, Jie Deng et al, J. Electron Spec. & Rel. Phen., Vol. 79 (1996) 83
7. M.Nikl, J.A.Mares, E.Mihokova et al, Solid State Communication, Vol. 87(3) (1993) 185
8. Chaoshu Shi, Mei Wang, M. Yin et al, Optronics & Laser (in Chinese) Vol. 6 (1995) 310

Spectroscopy of CsI(Tl) layers

N. Garnier [1] , C. Dujardin [1] , A.N. Belsky [1,2] , C. Pédrini [1] , J. P. Moy [3] ,
H. Wieczorek [4], P. Chevallier [5], A. Firsov [6]

[1] *Laboratoire de Physico-Chimie des Matériaux Luminescents, Unité Mixte de Recherche 5620 – Université Lyon 1, 69622 Villeurbanne, France*
[2] *SRL, Moscow State University, Physics Faculty, 119899 Moscow Russia*
[3] *Trixell, 460 Rue du Pommarin, ZI Centr'Alp 38430 Moirans, France*
[4] *PhilipsGmbH Research Laboratories, Weißhausstraße 2,D-52066 Aachen, Germany*
[5] *LURE, Bat 209D, Centre Universitaire Paris-Sud, 91405 Orsay, France*
[6] *IMP RAS, Laboratory of X-ray Optics and Technology, Chernogolovka, Russia*

Abstract: Emission and excitation spectra at ambient and low temperature of CsI(Tl) evaporated thin layers of "pillar-like" structure have been investigated. These luminescence properties and their thallium concentration dependence exhibit differences compared to single crystal. Spectroscopic results, light yield measurements and microluminescence analysis can be interpreted in terms of a dopant ion-bound exciton model involving two kinds of perturbed and non-perturbed thallium centers.

Keywords : CsI, thallium, layers, exciton.

Introduction

Spectroscopic properties of caesium iodide crystals doped with thallium are now well known. A large number of publications deal with the origin of its yellow emission and its high light output. It comes out from the more recent studies, that the centers emitting this fluorescence are of exciton-like nature and related to thallium ions as well [1-3]. These centers could be a host-exciton (the hole is in the valence band) with a thallium ion nearby, or a thallium-bound exciton (Tl^{2+} + e_{bound}) in which the hole is trapped in the thallium ion and the bound electron is delocalised in the neighbouring Cs^{+} ions, as for example it is sometimes the case in alkaline earth fluorides doped with divalent rare earth ions [4-6].

With the development of a new kind of X-ray flat panel detector built for radiographic and fluoroscopic measurements, a revival of interest for this material is happening [7,8]. Its growth by evaporation techniques on amorphous silicon photosensors leads to a pillar-like structure which increases spatial resolution while maintaining a strong X-ray absorption and high light output. As the growth technology of such layer is very different from bulk crystal growth, differences in the luminescence properties are observed [9]. We present data on luminescence properties of homogeneously doped CsI(Tl) layers, excitation and emission spectra under UV excitation at ambient and nitrogen temperatures, light yield measurements and spatially resolved excitation measurements along the needles of a particular sample. These results are analysed in terms of dopant thallium-bound exciton model [4].

Experimental

Spectroscopic and light yield measurements were performed on five homogeneously doped layers of different thallium concentrations given by the weight adding of thallium (from 6 to 500 mg) in the crucible.

Emission and excitation spectra were recorded under UV unfocalized excitation, using a xenon lamp, through a H10D Jobin Yvon monochromator, perpendicular to the layer on the top of the needles. The light emitted was analysed from the same side of the sample by a 9789B EMI photomultiplier through a H20 Jobin Yvon monochromator.

Light yield measurements were carried out using an americium source (59.6 keV) filtered with aluminium to avoid low energy X-ray emission and placed at 2 cm above the sample which was put on the window of a XP2020Q Philips photomultiplier without any contact grease.

Spatially resolved X-ray excitation measurements were performed on a particular sample voluntarily grown with inhomogeneous zones of thallium concentration.

The micro-focalized (25 μm) X-ray (14 keV) beam was obtained on the Microprobe line of the DCI storage ring of LURE in Orsay, using a Bragg-Fresnel multilayer focusing lens. Both X-ray fluorescence of thallium L_α and scintillation emission at different wavelengths were simultaneously recorded using a silicon detector for X-ray fluorescence and a 9789B EMI photomultiplier equipped with interferential filters for scintillation emissions.

Results and discussion

The emission spectra measured at room temperature under 310 nm excitation and at nitrogen temperature under 280, 305 and 330 nm excitations are presented in figure 1. These spectra are corrected for the transmission of monochromator and photomultiplier and normalised to the maximum of each curve. The spectra are identical for the different samples and so the results of only one are presented here.

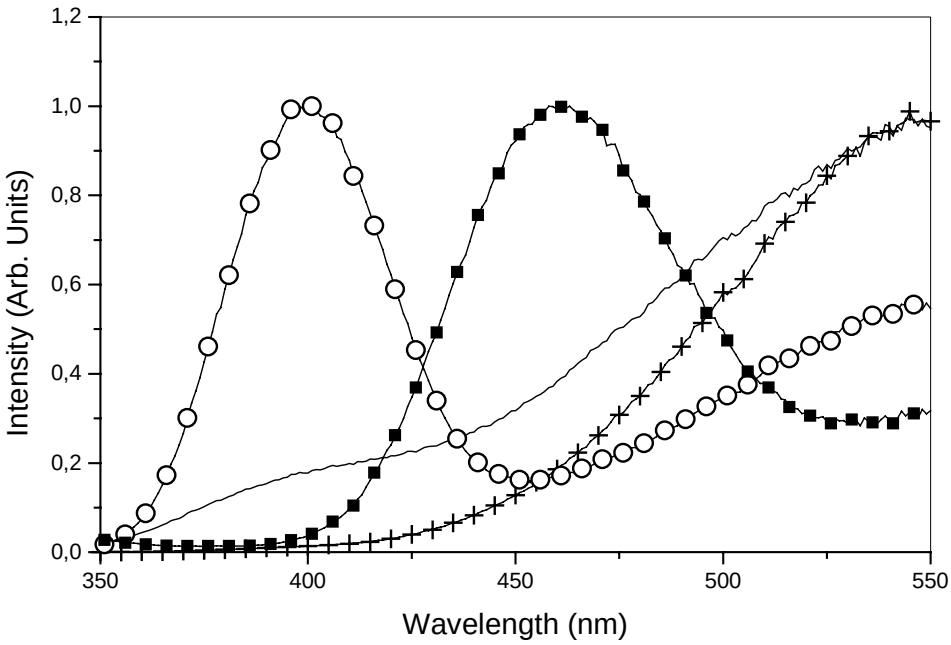

Fig 1 : Emission spectra of CsI(Tl) evaporated thin layers
- line : ambient temperature - 310 nm excitation
- cross : liquid nitrogen temperature - 280 nm excitation
- open circle : liquid nitrogen temperature - 305 nm excitation
- solid square : liquid nitrogen temperature - 330 nm excitation

Emission spectra of layers recorded at ambient temperature are very similar to those observed in single crystals with two bands centered on 400 and 550 nm. The emission spectra, observed at liquid nitrogen temperature show three bands with maxima at 400, 460 and around 550 nm. The UV (400 nm) emission band is clearly assigned to the emission of the triplet state of Tl^+. This band is composed of two emissions measured at 375 and 400 nm at liquid helium temperature [3,10] corresponding to emissions of triplet A_X and A_T of the Tl^+ , which cannot be resolved these at liquid nitrogen temperature. The two visible emission bands (460 and 550 nm) are identified as exciton-like luminescence, the 550 nm band is attributed to a strongly perturbed emitting center and the 460 nm to a weakly perturbed one. Because of the structure of the layer, we have the opportunity to isolate the 460 nm band ; its maximum is pointed at higher energy compared to measurements performed at 4.2 K on single crystals (around 490 nm in [10]) where this band presents a strong overlap with the 550 nm band.

Figure 2 shows the excitation spectra of emission centered at 400, 460 and 550 nm for the different thallium concentrated samples (one figure per sample) ; they are corrected for the excitation intensity given by the set lamp-monochromator and normalised to the maximum of each curve. For each set of spectra, the thallium content and the measured light yield, normalised to the maximum one, are indicated.

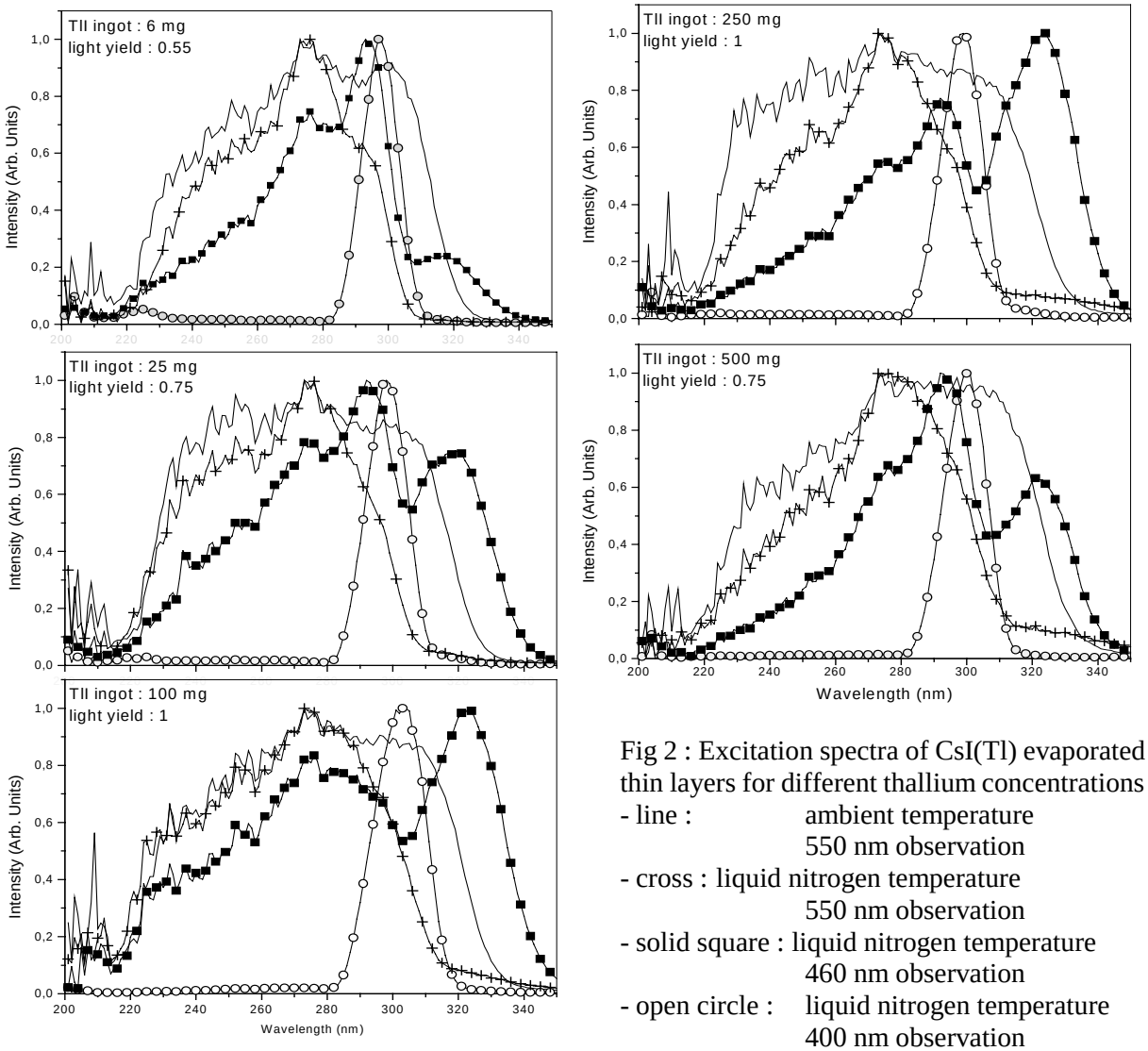

Fig 2 : Excitation spectra of CsI(Tl) evaporated thin layers for different thallium concentrations
- line : ambient temperature
550 nm observation
- cross : liquid nitrogen temperature
550 nm observation
- solid square : liquid nitrogen temperature
460 nm observation
- open circle : liquid nitrogen temperature
400 nm observation

The excitation spectra of the 400 and 550 nm bands in the UV domain are very similar to those observed in single crystals with a narrow excitation band peaked at 298 nm (A excitation band) for the 400 nm emission and a broad one with a complex structure from 220 to 300 nm for the 550 nm emission, including the different absorption bands at 238, 246, 257, 276 and 290 nm described by Masunaga [11]. We also observe the double structure of the A band with a maximum at 298 nm for the 400 nm excitation spectrum and with a maximum at 293 nm for the 460 nm excitation band.

The main difference with single crystal is the apparition of a very efficient excitation band peaked at 330 nm for the 460 nm emission. The intensity of this excitation band, has the same thallium concentration dependence as the light yield, increasing from 5 to 100 mg, being constant from 100 to 250 mg and decreasing from 250 to 500 mg of thallium iodide content in the crucible.

As it was observed in fluorite-structure crystals doped with rare earth ions such as BaF_2(Eu) [6], CaF_2, SrF_2, and BaF_2(Yb) [5], anomalous red shifted emission, very sensitive to temperature changes, is explained in a ion dopant-bound exciton model in which a hole is trapped by the impurity and the electron is delocalised among the neighbouring cations.

We can apply this model to CsI(Tl) and explain the two visible bands that are observed in alkali halides of bcc structure only, but not in alkali halides of fcc structure.

The visible fluorescences can be attributed to two different thallium-bound exciton centers, a strongly perturbed one emitting at 550 nm and a weakly perturbed one emitting at 460 nm.

While at T = 4.2 K, the weak 460 nm fluorescence band is hardly detected due to the overlap with the strong 550 nm emission band in single crystal, the former band is clearly observed in layer samples at liquid nitrogen temperature. This is consistent with the assumption that the layer growth technique induces much less constraints than the single crystal growth method.

With a growth by an evaporation technique, we avoid the phase transition from CsCl to NaCl structure above 900 K and the reverse transition, each one accompanied by a reduction of the specific volume of CsI and by inclusion of defects in the sample [12].

We can also suppose that the very small volume of each needle with empty space around permits a easier relaxation to stress in the material.

In weakly doped samples, the relative weakness of the 460 nm excitation band at 330 nm reflects the fact that most of the emitting centers are close to defects.

The number of thallium centers in regular sites (weakly perturbed) and the intensity of the 330 nm excitation band increase first with the thallium concentration, and then decrease for high thallium doping level since the emitting centers can be perturbed by neighbouring thallium ions.

The important point is that for the first time, the correlation of the light yield with the concentration of weakly perturbed centers is pointed out.

This is confirmed by results obtained from a X-ray micro-excitation along the needles of a particular inhomogeneously doped layer sample (figure 3). Such experiment allowed to detect, at a focused excitation point (25 μm), the X-ray fluorescence of thallium and the different fluorescences of the different emitting centers.

In highly doped regions of the needles, pointed out by a maximum in X-ray fluorescence of thallium, it is observed an excess of 550 nm fluorescence and a lack of 460 nm and other emissions, confirming the nature of the two emitting centers in CsI(Tl).

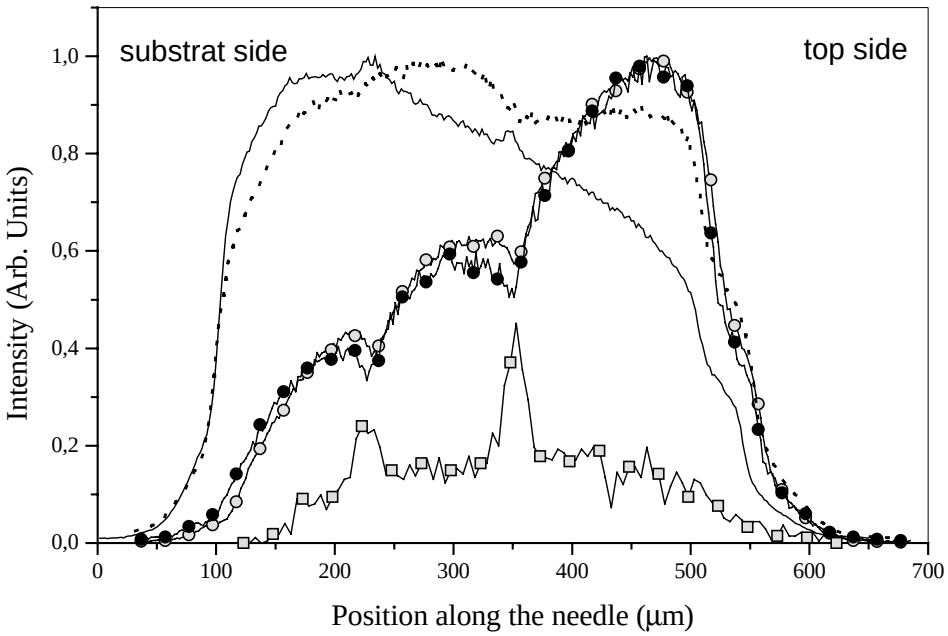

Fig 3 : Spatially resolved luminescence spectra at liquid nitrogen temperature of a particular inhomogeneously doped CsI(Tl) evaporated thin layer sample
- line : 550 nm emission band
- dot : 460 nm emission band
- open circle : 400 nm emission band
- solid circle : 300 nm emission band
- open square : X-ray fluorescence of Tl (10.26 keV)

The similar behaviour of the pure CsI emission around 300 nm and the Tl^+ emission at 400 nm is due to the overlap of the two emission bands at liquid nitrogen temperature under X-ray excitation.

We can also conclude from the general shape of the 550 nm emission along the needles that, as we reach the top of the needle, we observe a global decrease of the stress materialised by a decrease of the 550 nm emission.

Summary

The new method of growth of CsI(Tl), developed for the realisation of X-ray imaging flat panel detector, gives rise to a new CsI(Tl) structure exhibiting different spectroscopic properties and permitting to bring new features in the comprehension of scintillation process in such material.

It also permits to correlate the concentration of weakly perturbed emitting centers, assigned to weakly perturbed thallium-bound exciton emitting at 460 nm at liquid nitrogen temperature, with the light yield.

A more detailed paper is in preparation to describe these new features and the thallium bound exciton model.

References

1. J-M. Spaeth, W. Meise and K.S. Song, J. Phys. Condens. Matter **6** (1994) 3999
2. S.A. Chernov, A.I. Popov and L.E. Trinkler, Opt. and Spectr. **80** (1996) 661
3. M. Nikl, E. Mihokova, K. Polak, K. Nitsch, S. Zazubovich, V. Nagirnyi, V. Zepelin, A. Stolovich, G.P. Pazzi, P. Fabeni and L. Salvini, Materials Science Forum **239 - 241** (1997) 213
4. D.S. Mc Clure and C. Pedrini, Phys. Rev. B **32** (1985) 8465
5. B. Moine, B. Courtois and C. Pedrini, J. Phys. France **50** (1989) 2105
6. B. Moine, C. Pedrini and B. Courtois, J. of Lum. **50** (1991) 31
7. H. Wieczorek, G. Frings, P. Quadflieg, U. Schiebel, T.F.v. Bergen, F.M. Dreesen, M. Ligtenberg and T. Poorter, in: Proceedings of SCINT95 - Delft University of Technology (1995) 547
8. V.V. Nagarkar, T.K. Gupta, S. Miller, Y. Klugarman, M.R. Squillante and G. Entine, in Proceedings of IEEE Nuclear Science Symposium, San Francisco 1997, IEEE Trans. Nucl. Sci. **45** (1998) 492
9. A.N. Belsky, N. Garnier, C. Dujardin, C. Pedrini, B. Varrel, P. Chevallier and A. Firsov, The Electrochemical Society Proceedings **98-24** (1998) 195
10. V. Nagirnyi, S. Zazubovich, V. Zepelin, M. Nikl and G.P. Pazzi, Chem. Phys. Let. **227** (1994) 533
11. S. Masunaga, I. Morita and M. Ishiguro, J. Phys. Soc. Japan **21** (1966) 638
12. L.M. Shamovsky and A. Rogozhin in: Proceedings of SCINT95 - Delft University of Technology (1995) 487

Afterglow and Hysteresis in CsI:Tl

H. Wieczorek, M. Overdick

Philips GmbH Research Laboratories, Weißhausstraße 2, D-52066 Aachen, Germany

Abstract: CsI:Tl has always been known for long term afterglow and hysteresis effects, but few data are given in the literature. In this paper we present measurements on homogeneously doped CsI:Tl layers used in novel solid state X-ray detectors for medical imaging. Light yield enhancement after heavy X-ray irradiation as well as afterglow can be followed for some days. Both effects show a strong correlation with the thallium content, and the number of photons seen in the afterglow is equal to the difference of saturated and measured signal. Therefore we can explain both effects by deep trapping of X-ray generated carriers. Using a model that we previously developed to describe transient currents in amorphous silicon we are able to separate intrinsic and thallium related defect peaks. The microscopic nature of these defects is presently investigated.

Keywords: X-ray, afterglow, hysteresis, trapping, thallium centres

Introduction

Thallium doped caesium iodide (CsI:Tl) is a scintillator characterised by a high light output and a broad emission spectrum in the visible, well adapted to the optical absorption spectrum of amorphous silicon photosensors [1,2]. It is the material of choice for novel solid state X-ray sensors due to the possibility of large-area deposition at moderate temperature and due to its light-guiding structure and excellent spatial resolution [3]. We have shown before that digital dynamic X-ray imaging systems offer the required performance to replace film and image intensifier camera based systems in all practical cases [4].

CsI:Tl Layers

Polycrystalline layers of CsI:Tl with a thickness of up to 0.6 mm were produced by a special vacuum deposition technique so that a homogeneous doping level in the samples was ensured. Room temperature spectroscopic properties – absorption, excitation and emission spectra, decay times – are mostly comparable to single crystal literature data [5,6]. We see, however, an influence of the thallium concentration on the position and width of the excitation peaks, and the emission spectra of strongly doped layers are influenced by self-absorption in the short-wavelength part of the spectrum. A detailed description of the spectroscopy of CsI:Tl layers at ambient and low temperature and an interpretation in terms of a thallium ion bound exciton model can be found in another paper at this conference [7].

Afterglow

When afterglow in CsI:Tl crystals is described in the literature, measurement conditions are rarely mentioned. There is a large spread in the values given, as much as 0.3 – 5% after 5 s [8] or, much lower, 0.5 – 5% after 6 ms [9]. It is often assumed that afterglow is an intrinsic effect in CsI:Tl, but the detailed process is still unexplained. Oxygen-containing impurities, deformation of the crystals, and surface and volume structural defects are known to give an increased level of afterglow [8].

Fig. 1 shows the increase of the short term afterglow with the applied dose, measured under a dose rate of 11 μGy / s on a strongly doped sample with a photomultiplier and a low noise

current-voltage converter. In the time range between 10 ms and 1 s, the afterglow increases proportional to the applied X-ray dose and is saturated at 0.5 mGy. The saturated afterglow level is 2% of the stationary signal after 1 ms, a value which is independent of the dose rate used in the measurement, and roughly 1% after 10 ms. This saturation behaviour is characteristic of trapping effects. We assume that the short term afterglow is caused by structural or surface defects since it can be removed by annealing of the samples.

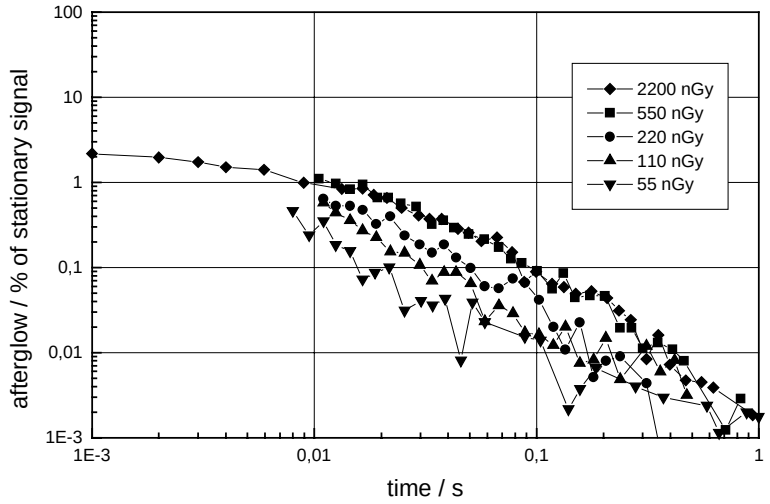

Fig. 1: Increase of short-term afterglow with applied X-ray dose.
Strongly doped sample, dose rate 11 µGy / s.

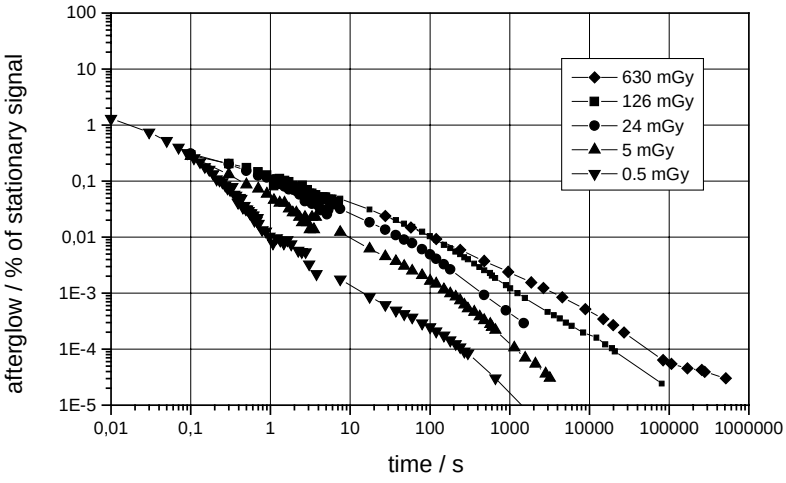

Fig. 2: Increase of long-term afterglow with applied X-ray dose.
Strongly doped sample, dose rate 5.25 mGy / s.

Measurements after application of a much higher X-ray dose show an additional long term effect. Fig. 2 shows the afterglow measured at a dose rate of 5.25 mGy / s with up to 630 mGy dose accumulated on a strongly doped sample. A Keithley picoammeter was used to follow the signal for a few days. The bottom curve, measured after application of 0.5 mGy, shows the saturated short term decay down to 0.01% after 1 s. The long term afterglow shows a strongly different time dependence with a much slower signal decay. It increases proportional to the applied dose before it is saturated at roughly 100 mGy. The residual signal level, 0.01% of the

stationary signal after 100 s, is partly influenced by the time needed for the application of the high X-ray dose. Some structure is seen in the afterglow curves even on a time scale of days.

Low-doped samples show a slightly different decay with a higher afterglow level in the left part and a lower level in the right part of the diagram, especially in the very long time range. We will show below that afterglow is mainly determined by thallium related defects since it is strongly correlated with the thallium content of the CsI:Tl layers.

Signal Hysteresis

Hysteresis in CsI:Tl was sometimes mentioned in connection with radiation damage but not yet explained. We found this phenomenon to be due to the same trapping effect as afterglow.

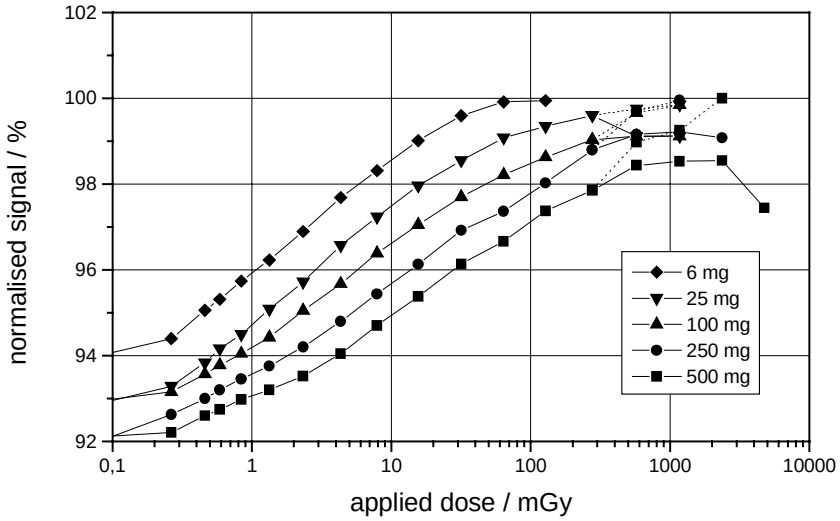

Fig. 3: Increase of light yield with applied X-ray dose, normalised values (see text). Dotted part of curves is corrected by an estimate for radiation damage.

Light yield measurements were done at low dose, alternating with high dose X-ray pulses of increasing duration, to measure the influence of the applied dose on the signal height. Fig. 3 shows the increase of the signal for differently doped samples, the doping level given by the thallium ingot in the crucible. The light yield increases steadily with the applied X-ray dose by up to 8%. Application of more than 500 mGy results in a reduction of the signal due to radiation damage. We normalised all curves to the saturated signal for strongly irradiated samples, including an estimate for radiation damage.

Low-doped samples show a clear saturation of the light yield at 100 mGy. In heavily doped layers the signal needs a much higher X-ray dose to increase and the saturation value is never reached due to radiation damage. In the view of a trapping model that we previously used to describe transient currents in amorphous silicon, this correlation of the hysteresis curves with the doping level is explained by a higher density-of-states for strongly doped samples [10,11]. The measured light yield enhancement is in fact a light yield reduction in virgin samples, caused by the capture of X-ray generated carriers in deep traps that stops them to contribute to the luminescence signal. When a certain fraction of the defects is filled by trapped charge, a quasi-equilibrium state without further charge trapping is established and the light yield is saturated. The enhanced light yield is stable for some hours before it starts decreasing to its initial value during a time span of days.

Trapping model

The total amount of charge that is trapped in virgin samples, the part of the signal that is missing before the light yield is saturated, can be determined by taking the integral over the difference between measured and saturated light yield in Fig. 3. We found that the trapped charge is proportional to the thallium doping level.

A quantitative estimate of the trapped charge density is achieved by calculation of the X-ray absorption in the sample, including fluorescence loss, and correction for the lower light output of low doped samples. The charge generation rate is calculated by comparison to the signal height calculated from solid state theory [12]. The light yield is stable when charge is trapped at roughly 0.01% of all Tl ions, independent of the doping level.

In the same way we can determine the trapped charge density from afterglow experiments by integration over the afterglow curve and comparison with the saturated light yield and the charge generation rate. If the trapping model is right, the amount of trapped charge calculated from signal hysteresis and afterglow must be equal. For low doped samples we find an excellent agreement, but for strongly doped layers only part of the charge trapped in the sample is emitted within the time range of the afterglow measurement so that the amount of charge measured in the afterglow seems to be lower than the charge stored in deep traps.

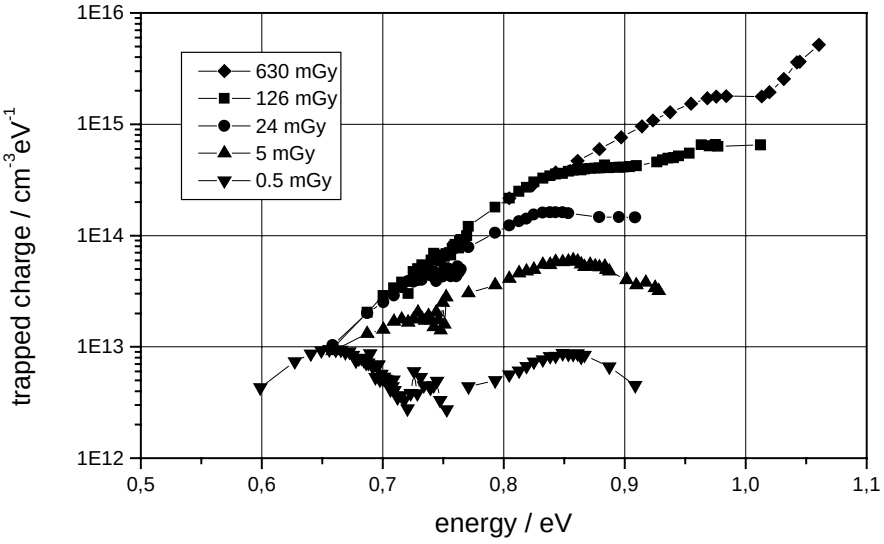

Fig. 4: Density of trapped charge derived from afterglow measurements shown in Fig. 2 for a strongly doped sample

The trapped charge density $n_t = I\,t\,/\,kTe$ is calculated from the photon current I seen in the afterglow assuming thermal emission from states at energy $E_t = kT\ ln\ \nu_0 t$ with $\nu_0 = 10^{12}\ s^{-1}$ [13]. Fig. 4 shows the occupation of deep traps for a strongly doped CsI:Tl layer. There are four different trapping centres at 0.65, 0.85, 0.95 and 1.05 eV or above. Only part of the latter peak can be seen within the afterglow measurement time. Fig. 5 shows that in a low doped sample the first two peaks are at slightly lower energy, 0.6 and 0.8 eV, respectively, but their occupation and absolute height are comparable to the curves shown in Fig. 4. The third peak at 0.95 eV is much smaller than in the strongly doped sample and the deep trap at above 1 eV is completely missing, indicating that these peaks are strongly related to the thallium ion.

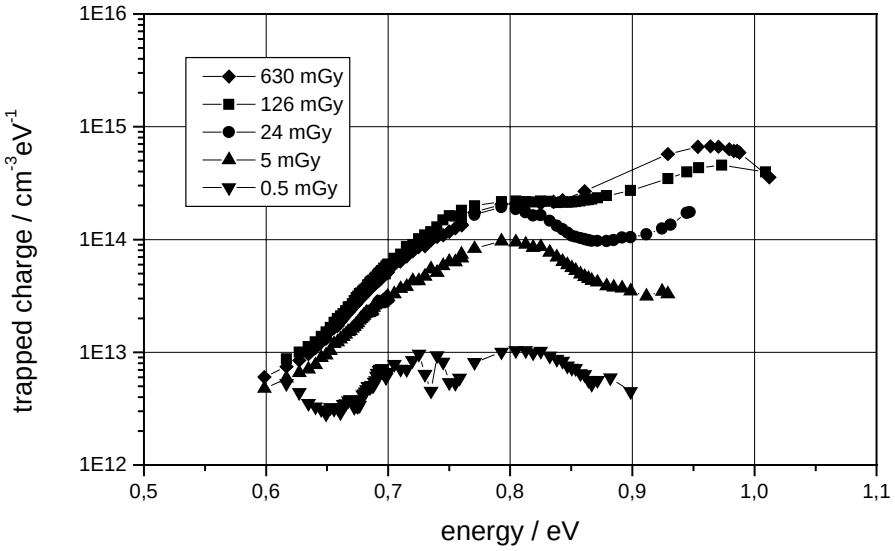

Fig. 5: Density of trapped charge, low-doped sample

From the comparison of low and strongly doped samples we find the following interpretation: There is a surface or structural defect peak at 0.6 - 0.65 eV, causing short term afterglow, which can be removed by annealing. The peak at 0.8 - 0.85 eV may be due to thallium ions at intrinsic defects since it is well comparable in low and strongly doped samples. The two peaks at 0.95 eV and above 1 eV must be due to other thallium states since their occupation increases strongly with the doping level. The interpretation of the nature of these defect peaks will further be supported by spectroscopic and thermoluminescence measurements [7].

Microscopic Model

Recent spectroscopic studies have led to a new model explaining the visible part of the CsI:Tl luminescence by thallium-disturbed off-centre excitons or by thallium-bound excitons [6,14]. Including our results on afterglow and signal hysteresis and comparing with literature data on other alkali halides [15,16], we get a microscopic model for luminescence and trapping:

In ionic halide crystals with a large band gap, free excitons are almost immediately self-trapped. In the normal CsI:Tl luminescence process, these self-trapped excitons recombine near a thallium ion, giving a pair of broad emission bands at 490 and 550 nm due to excitonic recombination and a second pair of emission bands at 375 and 400 nm which is caused by electronic transitions within the Tl^+ ion [6]. In a competing non-luminescent process the off-centre self-trapped exciton is split up, resulting in a distant F-H pair. The free electron in the F centre is captured by Tl^+ and the mobile H centre is deeply trapped at another thallium ion or some other defect, resulting in an iodine cluster at the impurity. When roughly 0.01% of the thallium ions are saturated with charge, there seems to be an equilibrium of trapping and recombination of trapped charge, and we get a stable light yield. The deeply trapped charge is set free when either electrons in Tl^0 or holes trapped near Tl^+ are thermally emitted and recombine, causing afterglow.

Summary

Though this is a simplifying trapping model which assumes the same attempt-to-escape frequency for different traps and neglects a number of possible processes like re-trapping or tunnelling recombination, it gives a quantitative description of luminescence, afterglow and

hysteresis effects. We have reduced the afterglow to a level which is low enough for application in solid state X-ray detectors. The microscopic nature of the deep traps, their spectroscopic properties, thermoluminescence effects, and the possible role of different kinds of weakly and strongly perturbed thallium centres are presently under investigation [7,17].

References

1. R.A. Street, I. Fujieda, R. Weisfield, S. Nelson, P. Nylen, Mat. Res. Soc. Symp. Proc. 258, 1145 (1992)
2. U. Schiebel, N. Conrads, N. Jung, M. Weibrecht, H. Wieczorek, T. Zaengel, M.J. Powell, I.D. French, C. Glasse: Medical Imaging 1994: Physics of Medical Imaging, SPIE 2163, 129 (1994)
3. H. Wieczorek, G. Frings, P. Quadflieg, U. Schiebel, T.F.v. Bergen, F.M. Dreesen, M. Ligtenberg, T. Poorter, in: Proceedings of SCINT95 – Delft University of Technology (1995), pp. 547-554
4. N. Jung, P.L. Alving, F. Busse, N. Conrads, H.J. Meulenbrugge, W. Rütten, U. Schiebel, M. Weibrecht, H. Wieczorek, Medical Imaging 1998: Physics of Medical Imaging, SPIE 3336, 396 (1998)
5. S. Masunaga, I. Morita, M. Ishiguro, J. Phys. Soc. of Japan 21, 638 (1966)
6. V. Nagirnyi, S. Zazubovich, V. Zepelin, M. Nikl, G.P. Pazzi, Chem. Physics Letters 227, 533 (1994)
7. N. Garnier, C. Dujardin, A. Belsky, C. Pédrini, J.P. Moy, H. Wieczorek, this conference
8. Ya.A. Zakharin, L.V. Kovaleva, L.L. Nagornaya, N.M. Naumenko, V.G. Protsenko, Yu.A. Tsirlin, L.N. Shpilinskaya, Iz. Akad. Nauk SSSR, Seriya Fizicheskaya 41, 1413 (1977)
9. G. Blasse, Chem. Mater. 6, 1465 (1994)
10. H. Wieczorek, W.Fuhs, phys. stat. sol. (a) 109, 245 (1988)
11. H. Wieczorek, Solid State Phenomena Vols. 44-46, pp. 957-972 (1995)
12. D.J. Robbins, J. Electrochem. Soc. 127, 2694 (1980)
13. W. Shockley, W.T. Read, Phys. Rev. 87, 835 (1952)
14. J.-M. Spaeth, W. Meise, K.S. Song, J. Phys. Condens. Matter 6, 3999 (1994)
15. N. Itoh, Adv. In Physics 31, 491 (1982)
16. K.S. Song, R.C. Baetzold, in: Defects in Insulating Materials, ed. O. Kanert, J.M: Spaeth, World Scientific, Singapore (1993), p. 69
17. D.S. McClure, C. Pédrini, Phys. Rev. B32, 8465 (1985)

Annealing Effect on Optical Emission Properties of Pure and Na-doped CsI Thin Films for X-ray Radiographic Application

Gyuseong Cho, Kyung Soo Lee, Do Kyung Kim and Koan Sik Joo*

Korea Advanced Institute of Science and Technology and
Myongji University, South Korea*

Abstract. Pure and Na-doped CsI film in thickness range from 100 to 400 □m has been thermally evaporated on glass substrate and its optical emission spectra at room temperature were investigated in view of several processing parameters, such as doping level, annealing temperature, and room temperature aging time. When 100 keV x-ray pulsed beam is irradiated, pure CsI thin film produces scintillation light of 310 nm peak attributed to the self-trapped exciton luminescence, but when it is annealed and quenched, another peak at 410 nm appeared because of iodine vacancy generation and both peak produce much light. In Na-doped CsI film case, a broad spectrum is observed and its light output increases as the annealing temperature increases up to 450 □C. This broad spectrum was considered as a sum of two peaks of which centers are at ~400 nm and ~450 nm due to Na+ and iodine vacancy color centers respectively. Light output measured in time after annealing degrades gradually and reaches to a saturation level in ~2 days. The equilibrium light output values is related to the doping level. This explains that the change of emission spectra as a function of aging time. So we can conclude that the annealing activates the dopants but also creates the iodine vacancies, and the iodine vacany peak at 450 nm disappears faster than the Na+ peak in CsI thin films.

CsI(Na) thin film, Annealing, Doping, Light Yield, Spectrum

Introduction

Recently columnar structured CsI thin film has attracted much attention in their application to the digital x-ray radiographic device, as a scintillating layer directly coupled onto pixel photo-diode array because of their higher light yield and more importantly because of their good light confining ability compared to the extended layer configuration of any phosphor such as an image intensifying screen.[1] The schematic configuration of pixel detector array and the columnar structure of CsI are shown in Figure 1. In order to fully absorb the X-rays, the film should have the appropriate thickness somewhere between 100 to 400 μm depending on the energy of x-ray. The CsI column has a diameter of 3 ~ 5 μm with a finite size of gap between them, which is thermodynamically determined in the optimum evaporation condition. So the geometric detection coverage is lower than the extended phosphor layer. One idea to overcome this weak point of columnar structure is to grow the larger size column and, if can, the same size as that of photo-diode element (~ 100 μm). Annealing of columnar CsI layer deposited onto patterned substrate had been tried to yield a larger light output without sacrificing the good spatial resolution as shown in Figure 2 (a).[2] As the result, the light output was a little improved but not much, probably because of polycrystalline structure of the congregated column. So we proposed the regrowth after making seed of thin monocrystalline layer onto patterned substrate as shown in the Figure 2 (b). In this paper, the effect of the annealing and aging of pure and Na-doped CsI thin scintillating films is described as a pre-study to develop the regrowth method

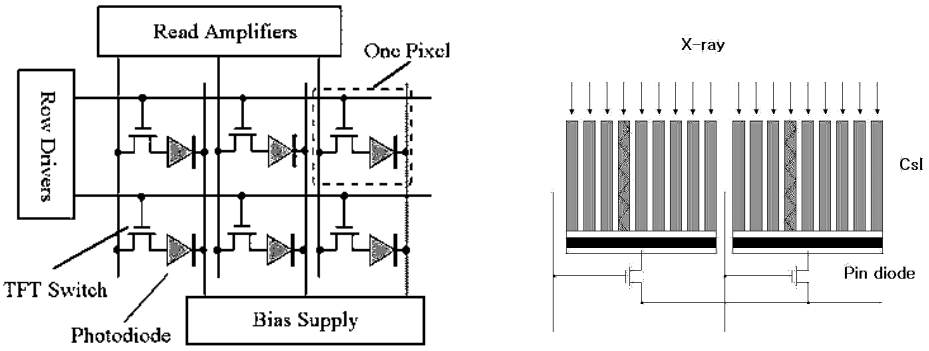

Figure 1. Schematics of X-ray pixel detector for radiographic application

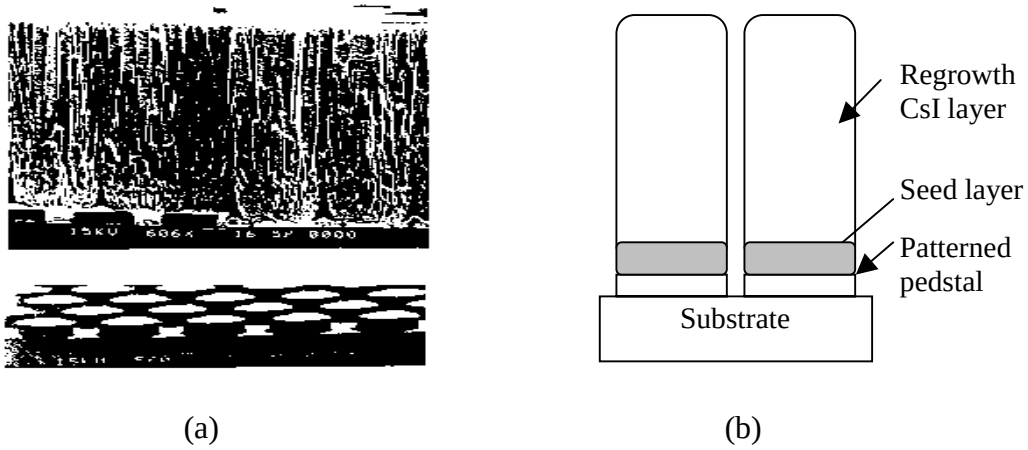

(a) (b)

Figure 2. (a) Congregated columns after annealing of CsI films deposited on the patterned substrate. (b) New proposal of making size controlled film by regrowth of CsI on thin monocrystal CsI layer on patterned substrate.

Experimental

A. Sample Preparation

The CsI and CsI(Na) scintillating thin film were grown on glass substrate by thermal evaporation method. Pure CsI were evaporated with 6N ultra pure powder (Aldlich Co.) In order to make Na-doped CsI film, we mixed powder of NaI and CsI with the various mole percent from 0.6 to 1.2 m/o in large quantity for accurate control of concentrations. We chose the Na doping first because its melting temperature, 651 °C is close to that of CsI, 621 °C so evaporation from a single boat preserves the concentration rate in film as the concentration in powder mixture. The evaporation conditions are as follows ; the temperature of quartz tube boat is 410°C, the temperature of 0.7 mm glass substrate is 110°C, the distance from boat to substrate is 4 cm and the pressure of environmental argon gas is 5 mtorr. The evaporation rate is around 0.7 ~ 1 μm/min. The annealing is done for two hours at temperature of 300°C, 375°C and 450°C. The quenching rate was 50 °C/min.

B. Measurements

The top view and cross-sectional view were examined by scanning electron microscope (SEM) before and after annealing. The light output from CsI films was measured by silicon pin photodiode (Hammamatsu S1790), the charge-sensitive preamplifier (Hammamatsu H4083) and an oscilloscope (Tektronics, TDS320), behind the substrate glass with a pulsed X-ray exposure of 5 msec and 100 kV (Dong-A X-ray, ERS-E). The relative light output

purely from CsI film was obtained by subtracting the pulse height in case with a black paper inserted between the film and photodiode from the pulse height without it to remove the signal contribution from interaction of x-ray with pin diode itself. The scintillation spectra were investigated with a optical fiber and monochrometer (Jovin Yvon, H10) attached with a photomultiplier (Hammamatsu R928). The schematics of these set-ups are shown in Figure 3. These signals were normalized with the film thickness.

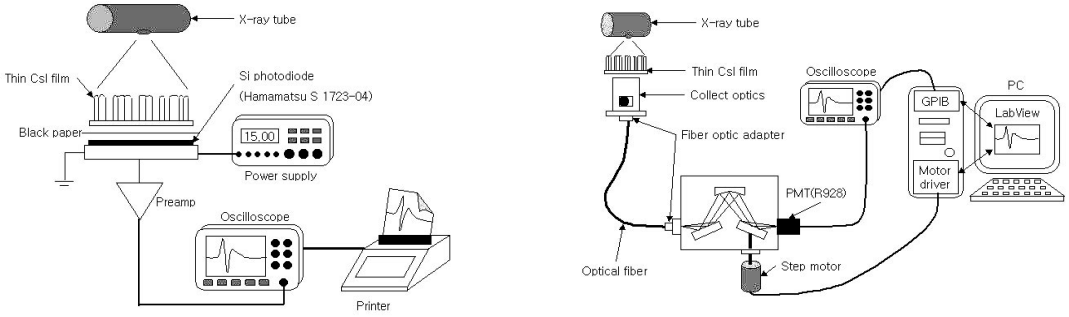

(a) (b)

Figure 3. Measurement set-up for (a) light yield using silicon p-i-n photodiode and (b) emission light spectrum using optical fiber coupled monochrometer from CsI thin films

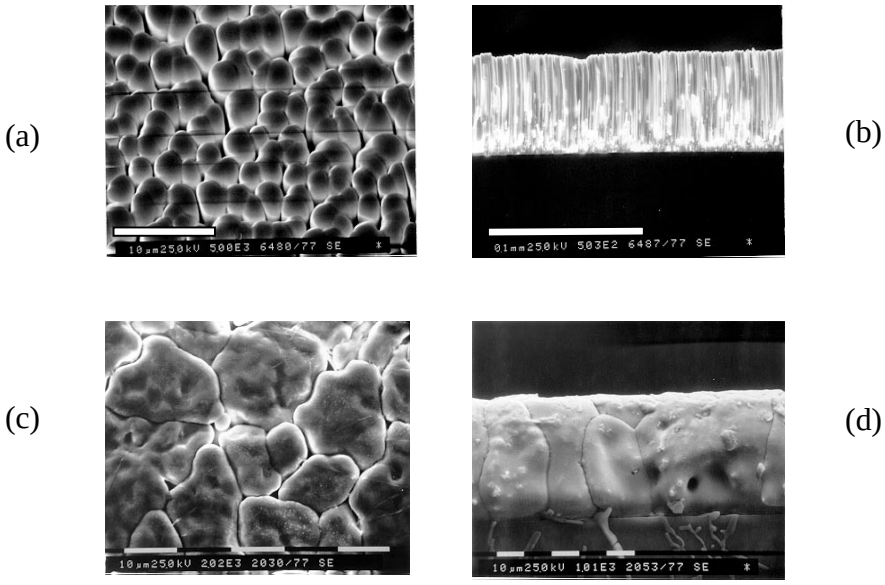

(a) (b)

(c) (d)

Figure 4. (a) Top view of columnar structure of CsI(Na) thin film, (b) Side view of columnar structure of CsI(Na) thin film, (c) Top view of annealed CsI(Na) thin film, and (d) Side view of annealed CsI(Na) thin film. The scale bar is 10 μm for figures (a), (b) and (d) and 100 μm for (b)

Results

A. Structure

The SEM micrographs of the top and cross-sectional view of deposited CsI layers before and after annealing are shown in Figure 4. Before annealing, the film clearly shows the columnar structure of which diameter is 3 ~ 5 μm. Since the height of practical film is more than 100 μm, the light collection efficiency is presumably small because of the big aspect

ratio. The Figure 4 (c) and (d) shows the congregated column or poly-crystal of grain size 20 to 30 μm. The annealed sample seems much translucent by visual inspection.

B. Emission Spectra

Figure 5 shows the emission spectra of pure CsI thin film when it is exposed 5 msec pulsed X-ray beam of 100 keV. The curve (a) is the spectrum as-deposited CsI and the peak at 310 nm can be ascribed to self-trapped exciton luminescence.[3, 4] Figure 5 (b) is the spectrum of annealed and quenched sample of which extra peak at 410 nm can certainly be attributed to the iodine vacancies that were generated during the quenching process.[5]

Figure 6 shows the emission spectra of Na-doped CsI thin film with different doping levels. The spectrum has a well known broad peak at 400 - 410 nm with a little knee at 450 nm and it is independent of doping level. The main peak is Na+ center which is physically a combination of Na and iodine vacancies, also knows as F_A center. The knee at 450 nm is due to additional peak at the same wavelength originated from iodine vacancies generated during the quenching process after annealing, and is reported by many authors.

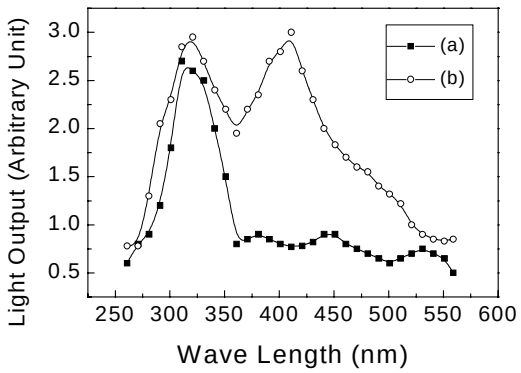

Figure 5. Emission spectra from (a) as-deposited CsI thin film and (b) annealed pure CsI thin film at 450°C for 2 hours

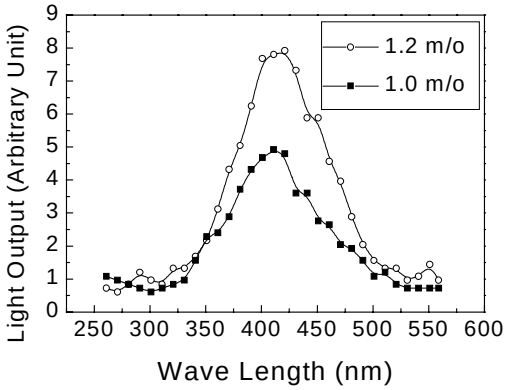

Figure 6. Emission spectra from CsI(Na) thin films annealed at 450°C with doping level of (a) 1.2 mole % and (b) 1.0 mole %.

C. Light Output

Figure 7 shows the relative light output from samples of different doping levels, and annealed at different temperatures. Each sample is annealed for 2 hours and measured within 30 minutes after quenching. As seen in the figure, annealing generally increases the light output for both undoped and Na-doped CsI thin film by producing additional longer wavelength peak due to iodine vacancies. However, the increase ratio of doped sample is much larger than the that of undoped one. This is due to that the coupling of the generated iodine vacancies to a nearby Na+ ions make activation centers. The increase rate of annealed sample at 450°C is 16.7. Figure 8 is the relative light output for a sample annealed at two different temperatures repeatedly. It is clear that the light output is closely associated the number of iodine vacancies in thin scintillating films and this is probably the quick transport of iodine atoms due to small grain size and large area of free surface in columnar structure.

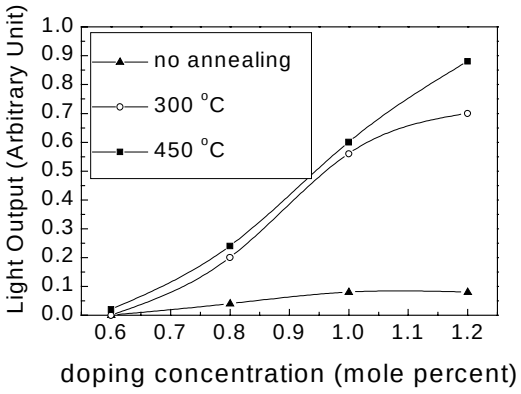

Figure 7. Light output from samples of different doping levels, annealed at different temperatures. Each sample is annealed for 2 hours and measured within 30 minutes.

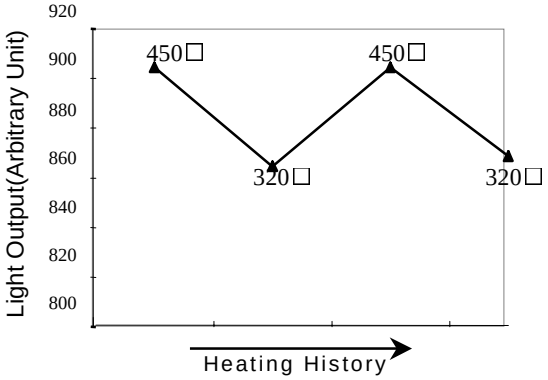

Figure 8. Light output after a repeated process of annealing at two different temperatures. X-axis only means the sequence of Measurements.

D. Aging Effect

The annealed sample shows the gradual degradation in light emission in hours. Figure 9 and 10 show the light output and the emission spectra as a function of aging time. The reduction of light output saturates in 50 hours and the equilibrium value of sample annealed at higher temperature is larger than the one annealed at lower temperature. From the Figure 10, we can see the spectrum change due to annealing into relatively broader shape with more clearly appearing two peaks at ~ 400 nm and ~ 450 nm from Na+ center and iodine vacancies respectively.

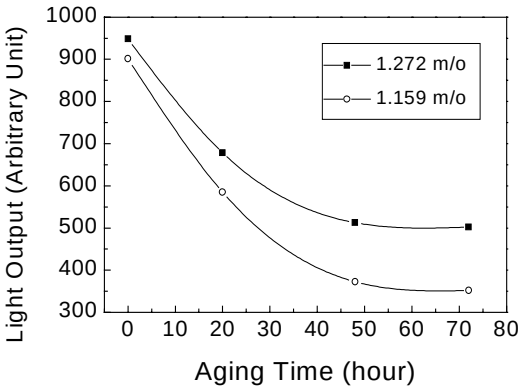

Figure 9. Degradation of light output as a function of aging time at room temperature after annealing at 450°C

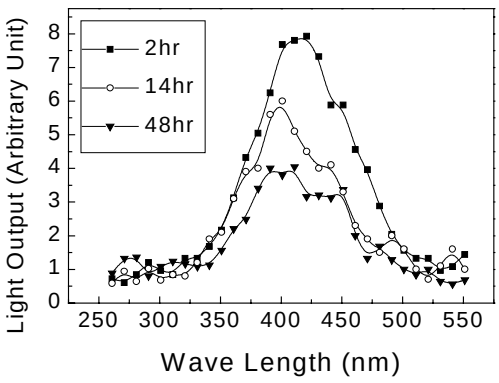

Figure 10. Degradation of light spectrum as function of aging time at room temperature after annealing at 450°C

Conclusion

We have investigated the annealing and aging effect on light yield and emission spectrum of pure and Na-doped CsI thin films. Annealing increases the light yield by creating iodine vacancies which has peak wavelength at 410 and 450 nm for pure and Na-doped CsI films. The higher annealing temperature is, larger the light output is. However the light output due to annealing gradually decrease in hours and reaches an equilibrium value in two days. Any way annealing process enhances the light output by activating Na dopants, but it certainly congregate several individual columns which make the light spread more wide. Also it is

noticed that the annealed sample shows more translucence compared to as-deposited film. Further study on thinner films on pixel-patterned substrate at different annealing condition, such as annealing temperature, duration time, quench speed will be tried to prepare the seed layer for regrowth method of making a large coverage scintillating film for x-ray radiographic application.

Acknowledgements

We would like to thank the President Moon in Dong-A X-ray Co. for donating the X-ray machine which make it possible to do this work and future research in this series. This work is sponsored by Korean Ministry of Commerce, Industry and Energy.

References

1. I. Fujieda, G. Cho, J. Drewery, T. Gee, T. Jing, S. N. Kaplan, V. Perez-Mendez, D. Wildermuth and R. A. Street, "X-ray and Charged Particle Detection with CsI(I) layer Coupled to a-Si:H Photodiode layers." IEEE Trans. Nucl. Sci. Vol. 38, No. 2, pp. 255-262, 1991
2. T. Jing, C. A. Goodman, J. Drewery, G. Cho, W. S. Hong, H. Lee, S. N. Kaplan, A. Mireshghi, V. Perez-Mendez, and D. Wildermuth, “Amorphous Silicon Pixel Layers with Cesium Iodide Converters for Medical X-ray Radiography,” IEEE Trans. Nucl. Sci., NS-41, pp. 903-909, 1994
3. B. K. Utts, S. E. Spagno, “An Investigation on the Characteristics of ‘Pure’ CsI Crystals,” IEEE Trans. Nucl. Eng. Num. 2, Vol. 37, pp. 177-182, April. 1990
4. D. Y. Smith, M. S. Malghani, “Configuration of the Self-Trapped Exciton in Alkali Halides,” Journal of Luminescence, 72&74, pp. 887-889, 1997
5. A. V. Gektin, N. V. Shiran, V. Ya. Serebryanyi, A. M. Kudin, and T. A. Charkina, “Role of Vacancy defects in CsI Luminescence” Opt. Spectrosc. 72(5), May 1992

Scintillating Crystals in Shanghai Institute of Ceramics, Chinese Academy of Sciences

Mao Yunqi and Yin Zhiwen

Shanghai Institute of Ceramics, Chinese Academy of Sciences
1295 Dingxi Road, 200050, Shanghai, China

Abstract: Since early eighties, the Shanghai Institute of Ceramics (SIC) started to work on inorganic scintillator crystals beginning with bismuth germanate ($Bi_4Ge_3O_{12}$, BGO) crystal for the construction of electromagnetic calorimeter in CERN-LEP3. Since then, a lot of oxide or halide crystals for different applications in experimental high energy physics and medical instrumentation were studied, developed and mass produced. Those include BaF_2, CeF_3, PbF_2, CsI and $PbWO_4$ crystals. In this paper, an overview of crystal growth, performance and applications of these crystals will be briefly presented.

Introduction

An integrated system of "fundamental research—growth technology research—mass production" has been established for the artificial crystal materials in SIC. The research objects include ferroelectric crystals, peizoelectric crystals, photoelectronic crystals, high-temperature semi-conductive crystals, scintillation crystals etc. Scintillating crystals are essential for radiation detection in a wide variety of applications. Scintillators irradiated by high energy particles or high energy radiation emit fluorescence light to proceed light to light transformation.

In recent years, there has been increasing interest in searching for new scintillation crystals for detectors used in high energy physics experiments, medical imaging, astrophysics, geophysics exploration, clandestine explosive finding and many other industrial applications. Among the most challenging uses of scintillator materials, especially for the inorganic crystal scintillators, is that in large, high-resolution calorimeters for high-energy physics experiments.

At the beginning of 80s. Classical inorganic scintillating crystals have been studied and developed in SIC. There were two kinds of inorganic scintillating crystals grown by SIC. One is oxide scintillating crystals such as $Bi_4Ge_3O_{12}$—BGO and $PbWO_4$. Another group is halides scintillating crystals such as CsI (TI), PbF_2, BaF_2 and CeF_3. Their growth technology, basic properties and main applications will be presented in this paper. The basic parameters of scintillators include density, radiation length, emission peak, optical transmission curve, light yield, decay time, radiation hardness and hygroscopicity. Fig.1 shows the procedure of growth technology for most scintillating crystals in SIC.

Bismuth Germanate $Bi_4Ge_3O_{12}$ (BGO) Crystal

Bismuth germanate $Bi_4Ge_3O_{12}$commonly abbreviated as BGO, is the crystalline form of an inorganic oxide with cubic eulytine structure, colourless, transparent and insoluble in water. When exposed to radiation of high-energy particles or other sources, such as gamma-rays, X-rays, it emits a green fluorescent light with a peak wavelength of 480 nm. With its high stopping power, high scintillation efficiency, good energy resolution and non-hygroscopic, BGO is a good scintillation material and is found a wide range of applications in high energy physics, nuclear physics, space physics, nuclear medicine, geological prospecting and other industries.

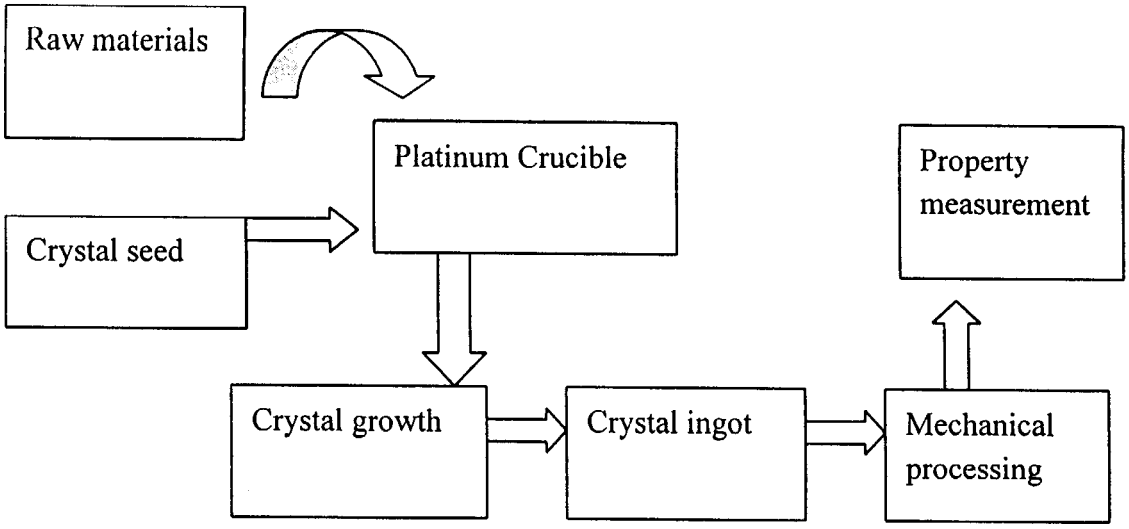

Fig.l. Growth technology for scintillatig crystals in SIC

Armed with the expertise of crystal growth accumulated in the past years, SIC has developed an unique technology for BGO growing and scaled up into quantity production in the R&D center of the institute. Now SIC become a world-wide famous BGO producer to meet the customer demands in crystal quality, quantity, cost effectiveness and delivery schedule. The boules up to 3"dia.×6"long or equivalent rectangular shape can be cultivated and crystal components with different shapes can also be provided as requested and its properties are tabulated in Table.1.

Application: Since the beginning of 1980s SIC had started R&D works on BGO crystal and then using bridgman technology for producing 11000 pcs, 12 tons large size high quality BGO crystals for L3 experiment in large electron-positron collider at CERN. Meanwhile, BGO crystals were selected for PET detector by GE company in USA; also act as scintillations material in γ-Spectrometer etc.

Table 1. Basic properties of BGO scintillation crystals grown by SIC

	BGO
Density (g/cm^3)	7.13
Radiation length (cm)	1.12
Emission peak (nm)	480
Light yield (%)#	7—10
Decay time (ns)	300
Radiation hardness (rad)	10^{4-5}
M.P.(O)	1050
Hygroscopicity	No

compared with the light yield of NaI: TI

$PbWO_4$ Crystal

Lead tungstate crystals ($PbWO_4$) has been chosen as first candidate scintillator crystal for the electro-magnetic calorimeter in the CMS detector which will be installed at the new CERN collider LHC in next century. This crystal has some special advantages-fast decay time, high density, short radiation length and good radiation hardness. However, it has also some shortages such as low light yield, containing slow components and not always stable in its radiation hardness. Table 2 shows the basic properties of PWO crystal grown by SIC and Fig.2 is its transmittance curve of PWO crystal (L=100 mm).

Table 2. Basic properties of PWO scintillation crystals grown by SIC

	PWO
Density (g/cm^3)	8.2
Radiation length (cm)	0.89
Emission peak (nm)	420/530
Light yield (%)#	0.5
Decay time (ns)	6/30
Radiation hardness (rad)	10^5
M.P.(C)	1123
Hygroscopicity	no

compared with the light yield of NaI: TI

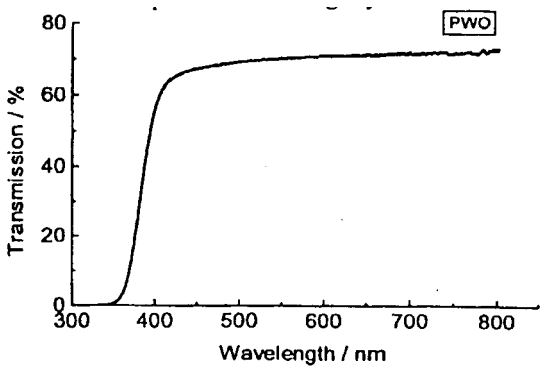

Fig.2. Transmittance curve of PWO crystal (L=100 mm)

Application: 86000 pcs PWO crystals, as electro-magnetic colorimeter, will be installed in the CMS experiment of Large Hadron Collide (LHC) at CERN and 36000 pcs crystals, as photo spectrometer, will be used in Alice experiment of Large Hadron Collider (LHC) at CERN.

CsI (TI) Crystal

CsI (TI) is a very important inorganic scintillation crystal. It has been chosen by KEK (National Laboratory for High Energy Physics, Japan) and SLAC (Stanford Linear Accelerator Center, USA) B-Factory experiments to construct the precision electromagnetic calorimeters. Detailed research on the scintillation property of CsI (TI) crystal has been studied widely. Table.3 shows its basic properties grown by SIC and Fig.3 is its light output against the radiation dosage (front-face irradiation).

Table 3. Basic properties of CsI (TI) scintillation crystals grown by SIC

	Cs(TI)	CsI
Density (g/cm^3)	4.53	4.53
Radiation length (cm)	1.86	1.86
Emission peak (nm)	550	305/400
Light yield (%)#	85	~4/~1
Decay time (ns)	1050	10/1000
Radiation hardness (rad)	10^3	10^{4-5}
M.P. (C)	621	621
Hygroscopicity	Slight	slight

compared with the light yield ofNaI:TI

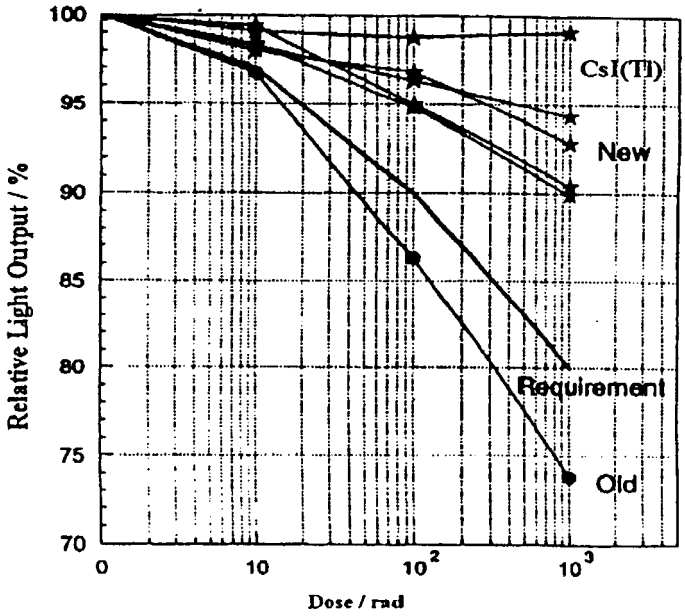

Fig.3. Light output of CsI (TI) crystal versus dose (front-face irradiation)

Application: It was used as electro-magnetic colorimeters for B-factory, Belle, KEK in Japan (total: 2100 pcs) and Babar, SLAC in USA (total: 2000 pcs). The crystal size is about $50^2 \times 300 \times 60^2$ mm^3.

PbF_2 Crystals

Lead fluoride (PbF_2) crystal was known to be a good Cherenkov radiator. Due to its very high density and good transmittance, this crystal is a very attractive candidate for use in heavy ion reactors where particle multiplicity is very high. Its main properties are listed in Table.4 Fig.4 shows its transmittance curves before and after irradiation as well as before and after annealing with 365 nm light ($30 \times 30 \times 200$ nm^3) in Fig.4. Table.5 shows the energy resolution of PbF_2 crystal produced by SIC.

Table 4. Basic properties of PbF_2 scintillation crystals grown by SIC

	PbF_2*
Density (g/cm^3)	7.7
Radiation length (cm)	0.95
Emission peak (nm)	—
Light yield (%)#	—
Decay time (ns)	—
Radiation hardness (rad)	10^3
M.P. (C)	822
Hygroscopicity	no

* Cherenkov radiator; # compared with the light yield ofNaI: TI

Table.5 Energy Resolution of PbF_2 Crystal Produced by SIC

Crystal Size (mm)	Energy (Mev)	Resolution (%)	Measurer
$30 \times 30 \times 185.4$	855	3.5	Mainz University, Germany
	734	3.7	
	450~705	$3.2/E^{1/2}$	

Application: Measure Mainz University, Germany, 1000 pcs for detector in heavy ion reator. Crystal size is $30 \times 30 \times 200$ mm^3.

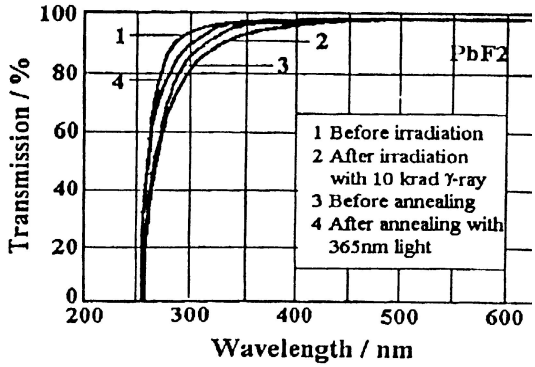

Fig.4. Transmittance curves of PbF_2 crystal before and after irradiation as well as before and after annealing with 365 nm light(30×30×200 mm)

BaF_2 Crystal

Barium fluoride (BaF_2) has long been used as transmissive medium due to its broad transmission spectrum. The discovery of the fast component of scintillation light from BaF_2 drew a considerable attention to the crystal. It is the fastest scintillator known so far and long been believed to be one of the most radiation resistant inorganic scintillators. In addition, this crystal has excellent time resolution, good detection deficiency. All these advantages make BaF_2 favorable for the applications in nuclear detection involving very high counting rates and severe radiation. Table.6 shows the basic properties of BaF_2 crystals grown by SIC. Fig.5. is its emission spectrum.

Table 6. Basic properties of BaF_2 scintillation crystals grown by SIC

	BaF_2
Density (g/cm^3)	4.89
Radiation length (cm)	2.03
Emission peak (nm)	220/310
Light yield (%)#	5/16
Decay time (ns)	0.6/620
Radiation hardness (rad)	10^{6-7}
M.P. (C)	1354
Hygroscopicity	no

compared with the light yield ofNaI: TI

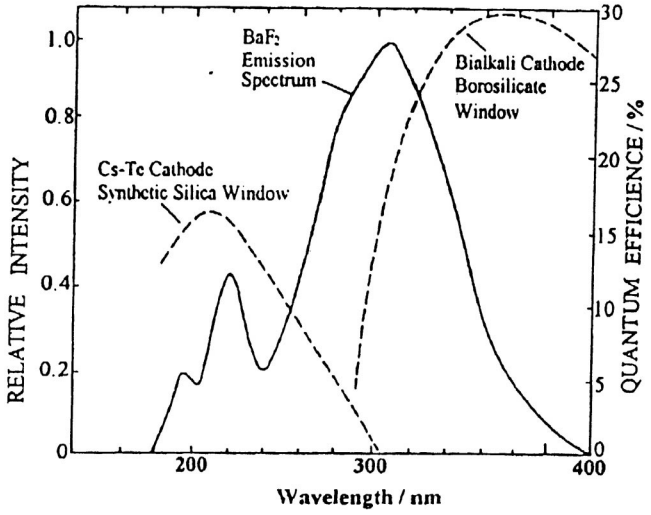

Fig.5. Emission spectrum of BaF_2 crystal

Application: It is selected by the high energy physics experiment in Brookheaven National Laboratory, USA (a dozen pcs of 350 mm long crystals) and PET experiment in the Radiation Instrumentation Lab. of Vrije University, Brussel, Belgium (Several hundreds pieces). And it is also selected as electromagnetic colorimeter for Superconducting Super Collider (SSC) in USA. But it is dropped.

Effect of annealing on optical and scintillation characteristics of PWO crystals grown by Bridgman method

M.Ishi[1], N.Senguttuvan[1], K.Tanji[1], T.Kittaka[1], Y.Usuki[2], M.Kobayashi[3], and M.Nik[4],

[1]SIT, Shonan Institute of Technology, Fujisawa 251-8511, Japan
[2]Furukawa Co., lwaki 970-11, Japan
[3]KEK, High Energy Accelerator Research Organization, Tsukuba 305-0801,
Japan Institute of Physics, Prague, Czech Republic

Abstract: In the present work evaporation rate of PWO (powdered crystal) and PbO (powder) in the temperature range of 700—1200°C was measured by means of thermogravimetric analysis (TG). The plot of logV Vs T^{-1} (T—temperature) was found to be linear and the temperature dependence of evaporation rate of PWO was found to be the same as that of PbO in the solid state. This shows that the crystals grown by the Czochralski method have Pb deficiency because of self-annealing. The optical transmittance and the excitation-emission spectra of the as grown and annealed PWO crystals grown by the Bridgman method were also measured. Annealing was performed in a temperature range of 500 C to 1000°C. The surface emission showed an extra stronger peak at 485 nm whose intensity decreased with annealing temperature. The transmittance was found to a have a small but consistent increase at about 350 nm with the annealing temperature.

Keywords: $PbWO_4$ Scintillator, Bridgman growth, luminescence, annealing

Introduction

$PbWO_4$ (PWO) scintillating crystals have a number of excellent properties compared with other well known inorganic crystal scintillators such as Nal:TI and BGO [1—3]. PWO is the most attractive for high-energy physics applications because of its high density (8.3 g/cm^3), short decay time (less than 10 ns for the most part of light output) and high radiation damage resistance (10^7 rad for undoped and 10^8 rad for La-doped PWO) [4, 5]. We have measured several of its properties and reported them elsewhere [6—8]. All our previous reports were based on the studies made on the Czochralski grown crystals. In the present investigation, we report the Bridgman growth and the subsequent annealing studies on single crystals of PWO.

$PbWO_4$ (PWO) single crystals are being grown by both Czochralski and Bridgman methods. In Czochralski method the crystals are self-annealed in air during growth. On the other hand the Bridgman grown crystals are prepared in semi-sealed platinum crucible and the crystal surface is closed by crucible wall and the molten material on top using the vertical alignment. As a result the crystals grown by the Czochralski method will have Pb deficiency because of self- annealing and the crystals grown by the Bridgman method will have oxygen deficiency because of the low oxygen vapor pressure of the growth atmosphere. These differences may lead to the differences in the scintillation characteristics of the Bridgman and Czochralski grown PWO crystals. In this paper results of the preliminary experiments on annealing and their subsequent effect on transmittance and emission are discussed.

Experimental

Single crystals of PWO were grown by the vertical Bridgman method. The detailed growth procedure has been discussed in our recent publication [9]. The grown crystals were cut and polished to a size of $10\times10\times20$ mm^3 for the annealing experiments. Evaporation rate of PWO

and PbO was measured by means of weight loss in thermogravimetric analysis using Rigaku 8078G2 thermal analyzer. The materials were taken in the powder form with a grain size between 250—850 μm in a container of 5×5 mm. In another set of experiments, all the samples were subjected to optical transmission and excitation-emission studies before annealing. To avoid any optical bleaching effect, the transmittance was measured prior to excitation-emission study. Transmittance was measured using a Hitachi U3210 spectrophotometer and excitation- emission using Hitachi F4500 instrument. Measurements were made after each annealing in air (oxygen rich) atmosphere at 500, 600, 700, 800, 900 and 1000°C for 1 h. Annealing in nitrogen atmosphere was carried out for temperatures of 600 and 1000°C. Emission was also recorded after polishing the surface of the sample annealed at 1000°C to about 0.5 mm.

Results and discussion

Evaporation rate

The thermogravimetric analysis was carried out on powdered PWO and PbO in air from room temperature to 1200°C. The evaporation rate, V, was calculated and it was plotted as logV VsT^{-1} (T—temperature). The plot is shown in Fig.1. As can be seen from the figure, the change in the evaporation rate of the powdered PWO crystal is smaller than PbO powder because of the larger surface area of the powder. At molten state the exposed surface area is only the cross section of the crucible containing the material. The evaporation rates of PbO and PWO at solid state are same. This experiment clearly shows that there will be PbO loss during Czochralski growth as a result of self-annealing.

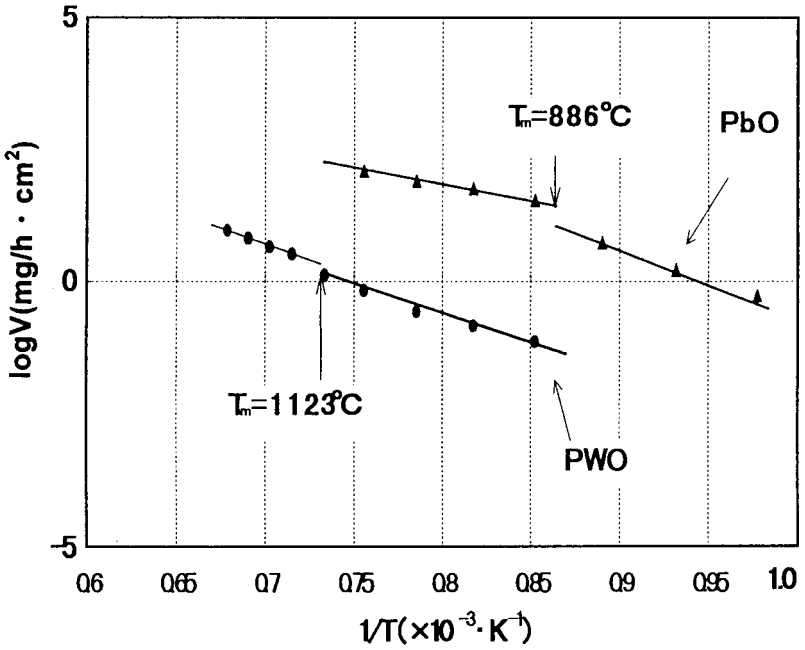

Fig.1. Weight loss by evaporation in air from solid and liquid

Transmittance studies

The crystals were grown using two different raw materials of different purity (4N and 3 times crystallized). The transmittance of the crystal of 10 mm thick is shown in Fig.2a. As can be seen from the figure 2a, the transmittance of the crystals grown from 4N pure raw material is shows absorption at 420 nm, which was noticed earlier and interpreted as a kind of color center, possibly related to O^- centers [10]. The transmittance is initially decreasing at 350 nm for annealing at 600°C and then increases for further annealing. The increase in transmittance at 350 nm is predominant when annealed at 1000°C. This result is in accordance with the

work of B.Han et al. [11]. Fig.2b shows the transmittance of crystals grown from three times crystallized raw material with enlarged scale.

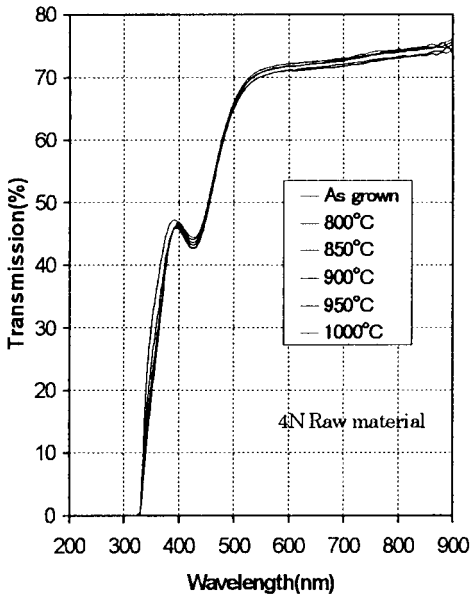

Fig.2a Effect of annealing on transmittance of PWO

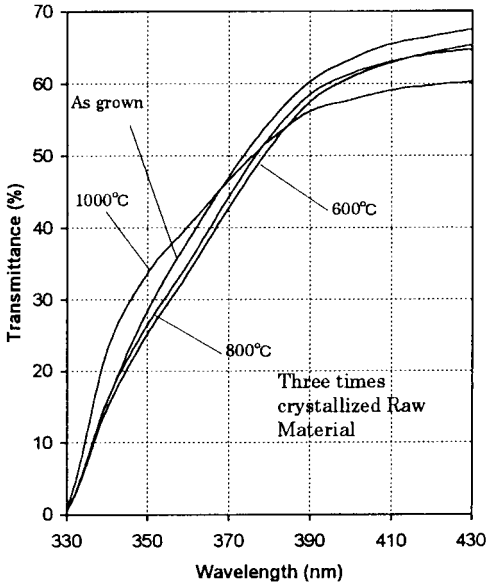

Fig.2b Effect of annealing on transmittance of PWO

Excitation-emission studies

The excitation-emission spectra showed blue emission from the surface of the as grown crystal. The same sample when annealed in air at different temperatures ranging from 500 to 800°C showed very strong green emission (Fig.3). The intensity of the green emission was maximum when annealed at 600°C and the further annealing at higher temperatures decreased the intensity. The emission pattern of the sample annealed at 1000°C is almost similar to that of the as grown crystal. But when annealed in nitrogen atmosphere, the green emission continued to appear even after annealing at 1000°C. The variation of the emission characteristics with respect to annealing temperature is shown in Fig.4.

From the above results we understood some surface phenomena taking place upon annealing at around 600—800°C. So in one experiment the annealed sample was polished to about 0.5 mm, i.e. the surface of 0.5 mm in thickness was removed by mechanical polishing. This (polished) surface did not show green emission. But when reannealed at 600°C the green emission reappeared on the same surface. The effect of polishing and reannealing on the green emission is shown Fig.5. This shows that the samples which are oxygen deficient have been supplied oxygen from the surrounding atmosphere. The thickness upto which oxygen diffused might be less than 0.5 mm as the emission reverted to the original pattern after polishing to about 0.5 mm. Further appearance of green emission from the reannealed samples confirms this mechanism of oxygen diffusion into the crystal upon annealing in air. But the disappearance of green emission upon annealing at higher temperature of 1000°C is due to the fact that all $W0_3$ ions have changed into WO_4 by oxygen diffusion and Pb evaporation. We also suggest that the as grown crystals would have very much oxygen deficiency, i.e., too much of $WO_{(3-x)}$ groups. Upon initial annealing at around 600 to 800 C these local $WO_{(3-x)}$ groups change to $W0_3$ centers. The green emission is supposed to originate from these WO_3 groups. Once they change into WO_4^{2-} molecules the green emission disappears. But the effect of nitrogen annealing is different. Upon annealing in nitrogen, a partial reconstruction of local oxygen deficiency, i.e., the transition from $WO_{(3-x)}$ (larger in number) towards WO_3 groups. These WO_3 are still present even after annealing at 1000°C and are responsible for the green emission. There seemed to be some anisotropy in the emission from different surfaces of the samples but the present work is limited not to include those results.

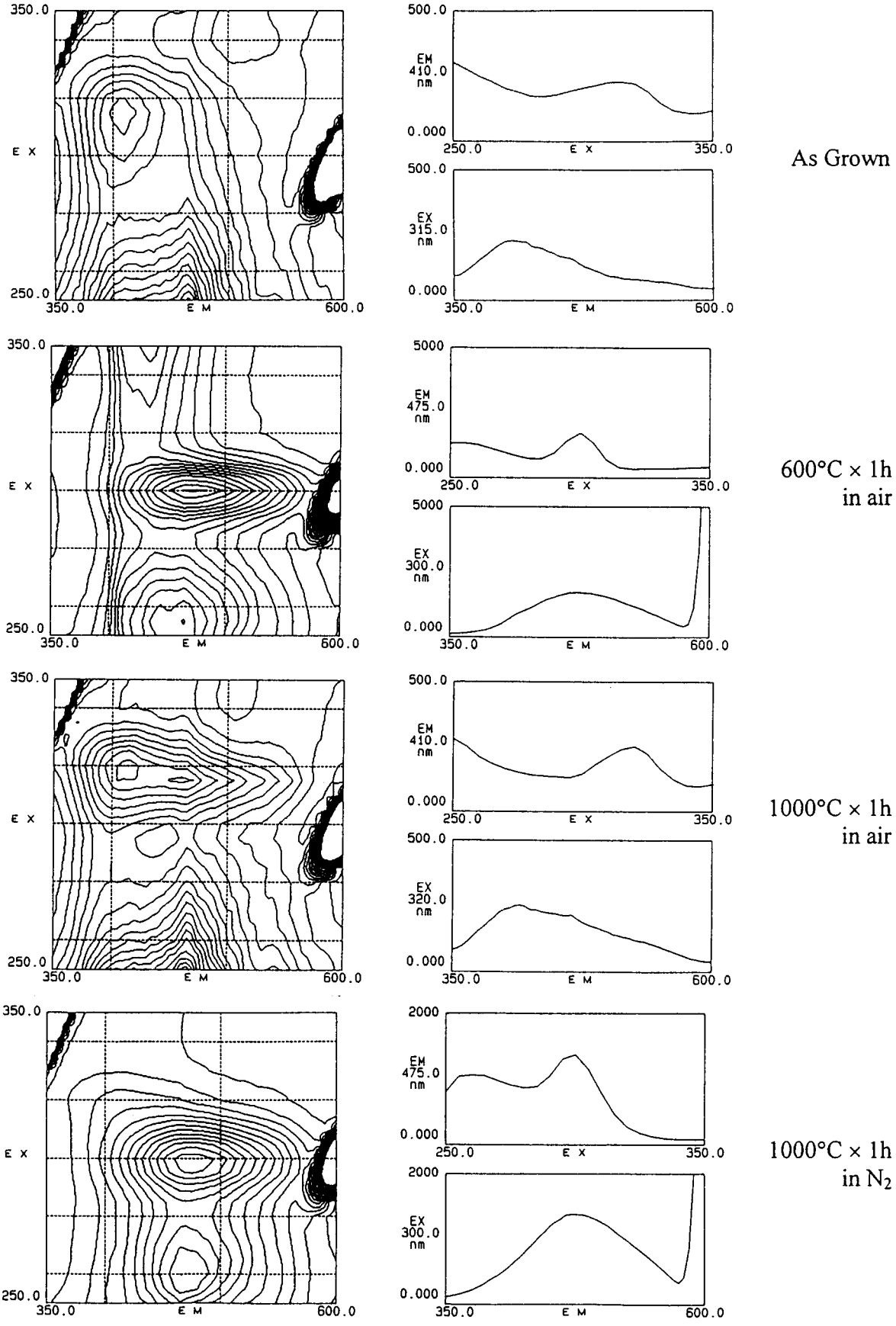

Fig.3 Excitation-emission spectra of PWO measured after annealing at different temperatures

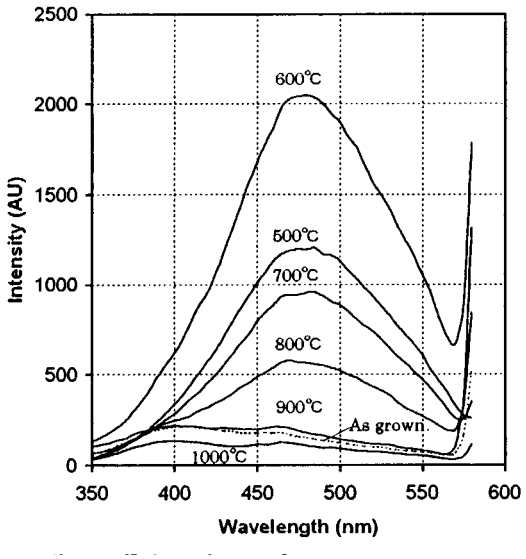

Fig.4. Effect of annealing temperaure on surface emission of PWO

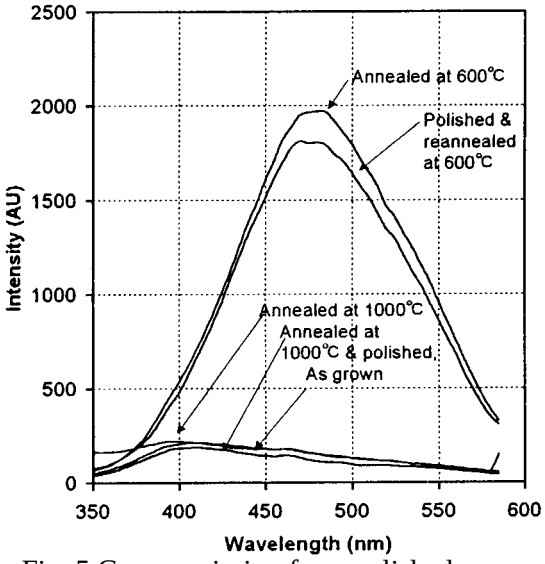

Fig. 5 Green emission from polished and reannealed surfaces of PWO

Summary

During Czochralski growth of PWO Pb evaporation is more predominant due to self annealing and there will not be any oxygen deficiency as the crystals are grown mostly in air. Pb vacancy is detrimental as it will enhance the radiation damage of the crystals upon irradiation. Hence we have recently suggested trivalent doping to improve Czochralski grown PWO crystals. On the other hand in the Bridgman growth there will be oxygen deficiency as the crystals are grown under low oxygen pressure in a closed crucible. The Pb evaporation is also contained as the growing crystal is surrounded by crucible along the surface and PWO melt on top. Still there may be a little Pb deficiency due to intrinsic stoichiometric defect. It is this difference between Czochralski and Bridgman growth of PWO which motivated the present work. The results are summarized in the following.

1. The evaporation of Pb from solid state has been confirmed by means of thermogravimetric analysis. This shows that there will Pb loss during Czochralski growth due to self annealing.

2. The transmittance of the PWO crystal upon annealing has two effects: increase in transmittance at 350 nm and decrease in it at 420 nm. The transmittance actually decreased at 350 nm initially upon annealing at 600°C and then it started increasing. This result has been clearly explained by B.Han et al.

3. As grown crystals showed blue emission from the surface and upon annealing at temperature range of 600—800°C it showed predominantly green emission with very high intensity. Further annealing at 1000°C reverted to blue emission. Following a generally accepted ascription of emission centers as WO_4 regular lattice group to the blue emission and oxygen deficient WO_3 group to the green emission components, the annealing induced changes can be expressed as follows:

(a) in air atmosphere:

$WO_{(3-x)} \rightarrow WO_3$ (by annealing at 600—800 C) $\rightarrow WO_3$ by annealing further at 1000°C)

(b) in N_2 atmosphere:

$WO_{(3-x)} \rightarrow WO_3$ (by annealing at 600) $\rightarrow WO_3$ (by annealing further at 1000°C)

4. The green emission disappeared upon polishing of annealed samples to about 0.5 mm. This shows that the diffusion of oxygen into the crystal is limited to athickness of less than

0.5 mm during annealing in the present study. The thickness of the diffusion layer may vary with annealing time and the temperature.

Reference

1. M.Kobayashi, M.Ishii, Y.Usuki, H.Yahagi, Nucl. Instr. and Meth. **A 333** (1993) 429.
2. M.Ishii, M.Kobayashi, Prog. Crystal Growth and Charact. **23** (1992) 245.
3. VG.Baryshevsky, M.V.Korzhik, V.I.Moroz, V.B.Pavienko, A.S.Lobko, A.A.Fyodorov, V.A.Kachanov, V.L.Solovjanov, B.I.Zadneprovsky, V.A.Nefyodov, P.V.Neiyodov, B.A.Dorogovin and I.L.Nagomaja, Nucl. Instr. and Meth. **A 322** (1992) 231.
4. M.Kobayashi, M.Ishii, Y.Usuki, Nucl. Instr. and Meth. **A 406** (1998) 442.
5. K.Hara, M.Ishii, M.Kobayashi, M.Niki, H.Takano, M.Tanaka, K.Tanji, Y.Usuki, Nucl. Instr. and Meth. **A 414** (1998) 325.
6. N.Senguttuvan, Premila Mohan, S.Moorthy Babu C.Subramanian, J. Crystal Growth, **183** (1998) 391.
7. Y.Usuki, M.Kobayashi, M.Ishii, Proc. Workshop on Scintillating crystals, Tsukuba, Japan (1997) 207.
8. M.Ishii, K.Harada, M.Kobayashi, Y.Usuki, T.Yazawa, Nucl. Instr. and Meth. **A 376** (1996) 203.
9. K.Tanji, M.Ishii, Y.Usuki, M.Kobayashi, K.Hara, H.Takano, N.Senguttuvan, *J.Crystal Growth* **204** (1999) 505.
10. M.Niki, K.Nitsch, J.Hybler, J.Chval, P.Reiche, Phys. Stat. Sol. (b) **197** (1996) K7.
11. B.Han, X.Feng, G.Hu, Y.Zhang, Z.Yin, "A study on the annealing effects and the radiation damage mechanisms of $PbWO_4$ single crystals", J. App. Phys. (to be published).

Characterization of Bridgman and Czochralski grown LuAP and LuYAP single crystals

A.G.Petrosyan[1], G.O.Shirinyan[1], K.L.Ovanesyan[1], T.I.Butaeva[1], C.Pedrini[2], C.Dujardin[2], A.Belsky[2]

[1]Institute for Physical Research, Armenian National Academy of Science, 378410 Ashtarak-2, Armenia
[2]Laboratoire de Physico-Chimie des Materiaux Luminescents, Unite Mixte de Recherche 5620 CNRS-Universite Lyon1, 69622 Villeurbanne, France

Abstract: Single crystals of Ce^{3+}-doped $(Lu,Y)AlO_3$ solid solutions of various composition in respect to Lu/Y ratio and Ce^{3+} concentration were grown using the vertical Bridgman and Czochralski processes. Growth conditions of solid solutions on the Lu-rich side were optimised towards high optical quality, high Ce concentration and good transmission properties in the range of Ce^{3+} emission.

Keywords: $LuAlO_3$-Ce, $(LuY)AlO_3$-Ce, Bridgman, Czochralski

Introduction

SCINT'95, SCINT'97, ICL'96 and the Crystal Clear collaboration meetings of recent years had placed considerable interest to $LuAlO_3$-Ce^{3+} and other dense perovskite-type scintillators for medical imaging applications (see many papers in [1-3]). At the present stage of development, good transmission properties in the range of Ce^{3+} emission and reasonably high doping levels are the major desirable goals towards increasing the light yield of thick samples. The mixed $(Lu,Y)AlO_3$-Ce^{3+} solid solution crystals are also in the list of materials of high current interest since they may possess a better combination of desired properties, especially if on the dense, Lu-rich side. Two major advantages of the solid solutions over $LuAlO_3$ have been recognised so far, i.e. (i) a higher value of the Ce^{3+} segregation coefficient and (ii) a higher thermal stability.

In the present work $LuAlO_3$-Ce^{3+} and $(Lu,Y)AlO_3$-Ce^{3+} solution crystals of various composition in terms of Lu/Y ratio and Ce concentration were grown by the vertical Bridgman and Czochralski techniques. Transmission properties near the optical edge and the level of Ce^{3+} doping have been found as the major parameters controlling the light yield in thick sample [4]. The light yields of around 200% of Bismuth Germanium Oxide (BGO) measured in the best crystals with still not very high Ce content suggest that further improvement of these materials is possible.

Crystallographic and physical properties

In many respects the two end-members ($LuAlO_3$ and $YAlO_3$) are similar or close in properties, such as the symmetry (space group D_{2h}^{16}, perovskite-type structure), unit cell parameters and melting points (Table 1), suggesting that solid solution single crystals can be easily grown in the whole range of concentrations. There are differences however, in densities, Ce incorporation, thermal expansion behaviour, tendency for twinning and in thermal stability. The expansion characteristics of the a-, b- and c-axes in $YAlO_3$ are monotone from room temperature to 800°C but with a strong anisotropy promoting twinning and cracking. In $LuAlO_3$, there are discontinuities for the a- and b-axes between

Table 1. Properties of end-member and solid solution single crystals in the $LuAlO_3$-$YAlO_3$ system (space group D_{2h}^{16})

	$YAlO_3$	$LuAlO_3$	$Lu_{1-x}Y_xAlO_3$	
			X=0,35	x=0,5
Unit cell parameters, Å	a=5,176 b=5,332 c=7,356	A=5,100 b=5,330 c=7,294	a=5,117 b=5,328 c=7,318	a=5,141 b=5,328 c=7,341
Unit cell volume, $Å^3$	203,5	197,9	199,5	201,1
Melting point, ^oC	1916	1900	~1900	~1900
Density, g/cm^3	5,35	8,34	7,35	6,88
Expansion thermal coefficients, 10^{-6}	9,5(a) 4,3(b) 10,8(c)	11,5(a) 5(b) 9,8(c)	not measured	not measured
Ce segregation coefficient	0,6	0,17	~0,32	~0,38
Thermal stability	High	Low	High	High
Tendency for twinning	High	Low	Low	Low

400 and 800^{o}C that may introduce additional strain during material cooling. Twinning is less pronounced, but crystal cracking is very common, especially if the crystallographic direction of growth is unfavourable. Thermal stability of the solid solutions even on the Lu-rich side ($x \geq 0,15$) increases strongly, as compared to $LuAlO_3$ [5]. The Ce segregation coefficient in the solid solutions is expected to increase with increasing the Y concentration.

The x-ray powder diffraction taken from the mixed crystals show a single set of reflections corresponding to the perovskite phase and a linear unit cell volume variation with x. The linewidths of reflections in the mixed crystals are broadened in respect to those in end-members that may be caused by larger local variations of the interplane distance values. Fig.1 shows the rocking curves for the (220) line taken from $LuAlO_3$ (a) and $Lu_{0,65}Y_{0,35}AlO_3$ (b) single crystals using DRON-4-07 diffractometer and CuK_α radiation. The linewidth ($\Delta\Theta$) in the mixed crystal is 18,65‘, which is noticably larger than that in the $LuAlO_3$ ($\Delta\Theta$ = 14,92’). The locations of the maximums in the two crystals are slightly dissimilar due to the difference in unit cell parameters (Table 1).

Different rare-earth coordinations of the rare-earth sites are possible in solid solutions at the same chemical composition. The third coordination sphere, which is composed of six rare-earth ions, may include both Lu and Y ions. If an equal distribution probability is assumed, the probabilities of simultaneous location of n ions of Lu (or Y) in this coordination sphere can be calculated using the theory of chances. Broad x-ray diffraction lines evidence for a higher lattice distortion in mixed crystals due to the presence of variously coordinated rare-earth sites giving rise to variations in the interplane distances.

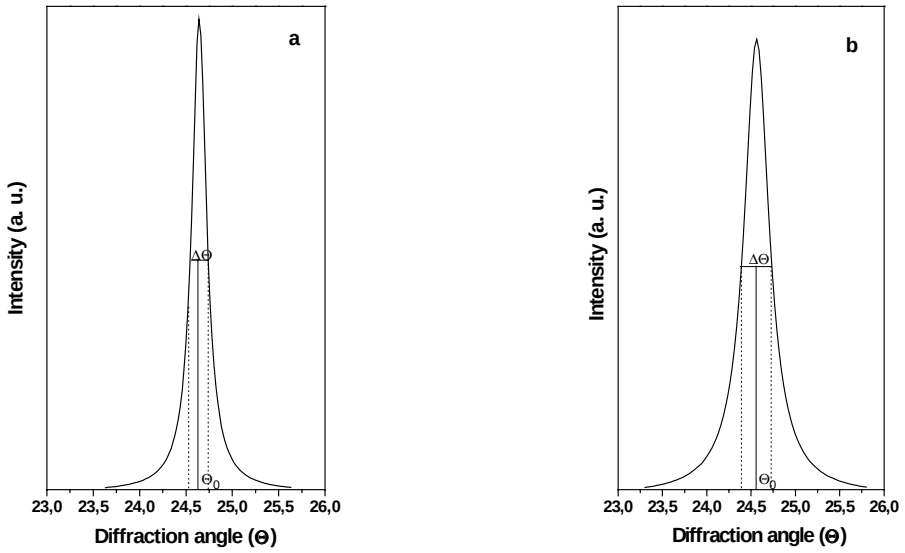

Fig.1. X-ray rocking spectra measured at (220) surfaces in orthoaluminate single crystals: (a) $LuAlO_3$, (b) $Lu_{0,65}Y_{0,35}AlO_3$.

Variable growth parameters

The quality of grown crystals depends on various factors and parameters. Growth rate, rotation rate (in Czochralski), temperature gradients must be optimised taking into accounts the Lu/Y ratio and initial Ce concentration in the melt. Empirical selection easily does this. The typical values of the growth rate are in between 1 and 4 mm/h depending on the dopant concentration. The axial temperature gradient may be as high as 50^oC/cm. Transparent and single phase crystals were grown under these conditions [5]. The maximum crystal sizes attempted by the Bridgman technique were 40-50 mm long, but for most of the present stage research it was sufficient to have smaller crystals to explore their potential before the costly and time-consuming step of growing large crystals.Good transmission properties near the optical edge are mandatory, because unwanted absorptions may overlap the Ce^{3+} emission band and result in large self-absorption of the emitted light [6]. Analyses of around twenty $LuAlO_3$-Ce and $(LuY)AlO_3$-Ce (Lu/Y=0,25÷5,6) variously Ce-doped (0,2÷1,5 at.% in the melt) single crystals grown by the vertical Bridgman or Czochralski processes had shown large scattering in the slope of the transmission edge, which could be steep or smooth depending on the density of as-grown color centers [7]. While there is no clear correlation with the Ce^{3+} content [6], the transmission profiles are strongly affected by the purity of starting oxides, growth atmosphere, residual oxygen amount and the purity of crucibles. The vacuum grown large crystals possess very good transmission properties near the optical edge however, growth of large crystals under high vacuum is complicated due to the stoichiometry offset. The most of recent effort was on Bridgman crystals of Lu/Y=1 and 1,85 compositions with doping levels in between 0,15 and 0,45 at.%. Growth conditions were optimized that provided for good and repeating transmission properties in most of the crystals from these two series. An important feature is that the transmission profiles vary inconsiderably when measured transversally at different points along the crystal length. Fig.2 shows the typical absorption spectra in a selected sample in terms of absorption coefficient in units of cm^{-1} against the wavelength. Effects of radiation induced transmission loss after exposing the crystal to high intensity ^{60}Co radiation source (total dose 1 Mrad, dose rate – 100 rad/sec) are also shown in the figure. Some further observations (to be discussed in details elsewhere) with

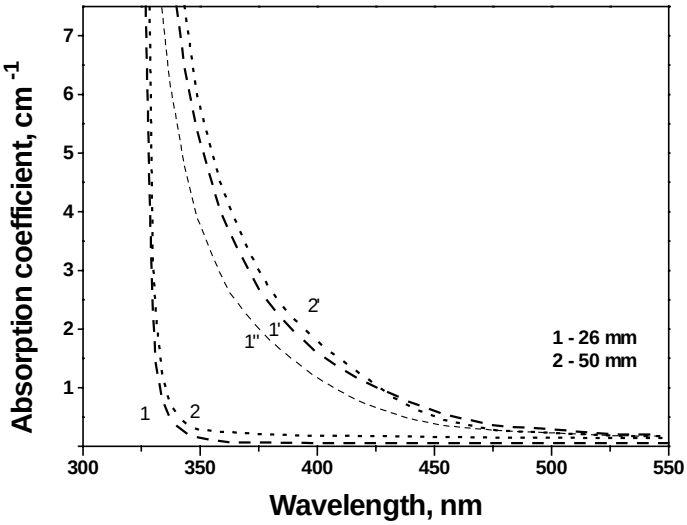

Fig.2. Absorption spectra in a $LuYAlO_3$-Ce (0,3 at.%, Lu/Y=1,85) single crystal measured transversally at different points from the top: 1, 2 – as-grown, 1', 2' – after gamma-ray irradiation (1 Mrad), 1'' – after 3 week long natural recovery.

regard to the radiation damage have been made, i.e. (1) crystals possessing a poor transmission near the optical edge are more resistant to radiation as compared to those with good transmission properties; such a behaviour is common for crystals of all compositions and grown by both methods, (2) increase of the Ce concentration results in a higher stability towards gamma-irradiation however, only a limited number of heavily doped crystals have been studied so far (a strong increase of $YAlO_3$-Pr stability towards shortwavelength (UV) radiation with increasing the Pr concentration was observed earlier in [8]), (3) after irradiation, a partial recovery of the transmission takes place in time when the sample is kept in the dark; further recovery is possible by bleaching the sample under visible light (similar or close behaviour was earlier reported for a $YAlO_3$-Ce crystal [9]).

The highest light yields were measured in samples with doping level above 0,3 at.% and possessing good transmission properties [4]. A high light yield was measured in thick samples (up to 20 mm long) as well. The maximum Ce content in the studied crystals was 0,5 at.% or lower, so that a higher light yield may be expected in more heavily doped crystals**.** Doping levels as high as 0,9 at.% were measured earlier in $LuAlO_3$-Ce [6], therefore it is realistic to increase the Ce concentration in the mixed crystals at least up to 1 at.%. In the Bridgman configuration, due to higher temperature gradients that can be experienced, it is easier to introduce higher Ce concentrations. The alternative is to cut the samples from the crystal last portions, which are heavily doped due to the normal freeze profile of the impurity distribution. For the presently available samples, the solid solution crystals of selected compositions grown so far by the vertical Bridgman and the Czochralski techniques (in most cases of roughly 5x5x5 cm^3 in size) show comparable results in terms of the light yield however; not all the compositions have been attempted by the Czochralski as yet. The Czochralski method provides for a more uniform Ce distribution over the length of grown crystals, since only a part of the initial melt is solidified, while the segregation effects are the same in both methods. The same applies to Lu/Y variation over the crystal length, which may result in a slight density variation from top to tail.

Conclusions

Many Ce^{3+}-doped $LuAlO_3$ and $(LuY)AlO_3$ single crystals were grown by the vertical Bridgman and Czochralski techniques. Consistent growth and satisfactory repeating properties of the crystals in terms of the crystalline quality and transmission properties near to the optical edge have been achieved, more particularly in crystals of Lu/Y=1 and 1,85 compositions and Ce doping levels in between 0,15 and 0,45 at.%. The growth method seems to be not strongly critical however, the two techniques possess complementary possibilities for materials further research and improvement.

Acknowledgements

This work was supported in part by NATO grant HTECH.LG.971230, Ministry of Science of Armenia (grant # 96-763) and Crystal Clear collaboration. I.Gambaryan performed gamma-irradiation using the Facility of the Institute for Physical Research.

References

1. Proc. International Conf. on Inorganic Scintillators and Their Applications SCINT'95, P.Dorenbos, C.W.E.van Eijk (Eds), Delft University Press, 1996.
2. Proc. Intern. Conf. Conf. on Inorganic Scintillators and Their Applications SCINT'97, Shanghai Institute of Ceramics, 1997.
3. Intern. Conference on Luminescence and Optical Spectroscopy of Condensed Matter, Conference Handbook, Institute of Physics of Czech Academy of Science, 1996.
4. A.Bel'sky, C.Dujardin, C.Pedrini, A.G.Petrosyan, W.Blanc, J.C.Gacon, E.Auffrey, P.Lecoq, this conference.
5. A.G.Petrosyan, G.O.Shirinyan, K.L.Ovanesyan, C.Pedrini, C.Dujardin, J.Crystal Growth 198/199 (1999) 492-496.
6. C.Dujardin, C.Pedrini, W.Blanc, J.C.Gacon, J.C.van't Spijker, O.W.V.Frijns, C.W.E.van Eijk, P.Dorenbos, R.Chen, A.Fremout, F.Tallouf, S.Tavernier, P.Bruyndonckx, and A.G.Petrosyan, J. Phys.: Condensed Matter 10 (1998) 3061.
7. A.G.Petrosyan, K.L.Ovanesyan, G.O.Shirinyan, T.I.Butaeva, C.Pedrini, C.Dujardin, A.Belsky, J.Crystal Growth (in press).
8. T.I.Butaeva, K.L.Ovanesyan, A.G.Petrosyan, Cryst. Res. Technol. 23 (1988) 849.
9. J.A.Kierstead, S.P.Stoll, C.L.Woody, Mat. Res. Soc. Symp. Proc. 348 (1994) 469.

Poster presentations

Influence of uniaxial stress and external electric field on luminescence of KI crystals under selective VUV excitation

M. Kirm[1], A. Lushchik[2], Ch. Lushchik[2], S. Vielhauer[1], and G. Zimmerer[1]

[1]*II. Institute of Experimental Physics, University of Hamburg, Luruper Chaussee 149 D-22761 Hamburg, Germany*
[2]*Institute of Physics, University of Tartu, Riia 142, EE-51014 Tartu, Estonia*

The excitation spectra of intrinsic and impurity emissions were studied for KI:Na (10 ppm) using VUV radiation of 10-18 eV. Photons create holes and hot conduction electrons, that produce secondary excitons ($h\nu_{ex} \geq 12.8$ eV) and secondary electron-hole pairs ($h\nu_{ex} \geq 13.8$ eV). The applied elastic uniaxial stress lowers the symmetry of the system, increasing the probability of the self-trapping and decreasing the energy transfer by excitons to the impurity centres. A shift of the threshold for the secondary exciton formation from 12.8 to 11.2 eV, is tentatively assigned to the processes of impact creation of secondary excitons by hot electrons that gain some additional energy due to an electric field.

Keywords: of multiplication excitations, uniaxial stress, electric field, KI.

Introduction

At low temperatures in some wide-gap ionic crystals (e.g. NaI and KI), the coexistence of free excitons (FE) and self-trapped excitons (STE), separated by an activation barrier between the states of FE and STE, has been shown experimentally and theoretically [1]. At the direct photocreation of FE in high purity KI crystals at 5 K, the narrow FE emission line at 5.83 eV is observed, nearly in resonance with exciton absorption. In KI:Na the creation of FE leads to an efficient excitation of broad-band emissions, peaking at 2.97 eV and 4.05 eV and corresponding to the π- and σ-emissions of excitations localised near Na^+. The emission bands of singlet and triplet STE (4.15 eV and 3.31 eV) are effectively excited by a formation of excitons as well as on a recombination of conduction band (c-band) electrons with relaxed self-trapped holes [1]. In KI the formation energy of an exciton with n=1 is E_e=5.83 eV and the onset of the direct band-to-band transition is E_g=6.31 eV [2]. The so-called E_x emission (3.0 eV) in nominally pure KI crystals can be easily suppressed by crystal doping with Li^+ ions [3] and it does not occur in the KI crystals grown from aqueous solution [4]. Therefore, the intrinsic origin of the E_x emission is doubtful. The hot photoelectrons, with energies somewhat larger than the direct formation energy of FE, create secondary excitons or secondary electron-hole (e-h) pairs. Such processes have been revealed in KI:Tl and KI:In at 300 K [5] as well as in KI at 80 K [6] and 8 K [7].

In the range of photon energies $h\nu_{ex}$ where the intrinsic processes of multiplication of electronic excitations (MEE) at 8 K with the creation of secondary excitons start, the following mechanisms must be considered: (i) an one-step processes with the formation of a two-electron excitation (two excitons or an electron-hole pair and an exciton); (ii) two-step process with the formation of a hole and a hot photoelectron which after some pathway in a lattice converts a part of the kinetic energy to the creation of a secondary exciton or an e-h pair (impact mechanism); (iii) two-step process with the formation of a hole and a hot photoelectron which after some pathway in a lattice participates in a nonradiative Auger transition to a lower state in a c-band with the simultaneous creation of a secondary electronic excitation (Auger mechanism). Secondary excitons can be also created in the recombination processes [5,8,9]. The electrons (e) in the c-band can recombine with free holes (h), with

metastable one-halide self-trapped holes (h_{s1}) and two-halide self-trapped holes (h_{s2}). The measurements of the excitation spectra for FE and STE in the energy range $2E_e < h\nu_{ex} < 3E_g$ are insufficient for separating the excitonic and e-h mechanisms of MEE. More precise investigation are needed.

Experimental investigation of MEE processes

The aim of the present study is to investigate the MEE processes and, in particular, the creation of secondary excitons in pure single crystals of KI and KI:Na using a spectral-kinetic method and applied external influences: the elastic uniaxial stress (EUS) and the electric field. In the region of the direct photocreation of excitons and e-h pairs in KI, the spectral-kinetic method [5,6,12], the elastic uniaxial stress [10,11] and the electric field [12,13,14] have been used earlier. The experiments were performed at the SUPERLUMI station of HASYLAB at DESY [15]. The intrinsic and impurity emissions (time-integrated as well as measured within a time window -length Δt, correlated with the excitation pulses of synchrotron radiation delayed by δt) were detected in the KI crystals excited by 5-30 eV photons at 8 K under the conditions of an applied elastic uniaxial stress (see also [10]) or an external electric field. The applied electric field strength was 5000 V/cm. The residual pressure in the experimental chamber was below $5 \cdot 10^{-10}$ mbar. The luminescence was analysed by a 0.5 m Czerny-Turner mounting monochromator equipped with a photomultiplier R2059 (used in studies with an applied EUS) or with a position sensitive detector (used in studies with an electric field).

Fig.1 reproduces a fragment of the intensity ratio spectrum (I_s/I_f) for slow (Δt = 140 ns, δt = 30 ns) and fast (Δt = 12 ns, δt = 1.3 ns) components of 4.15 eV emission detected through a monochromator in the energy range of 10-18 eV in KI:Na [10]. The value of I_s/I_f is practically constant in the range of 10 -12.5 eV, it rises sharply above $h\nu_{ex}$> 12.8 eV, reaches the maximum at 13.6 eV and then slowly decreases until 15.5 eV. The slow component of 4.15 eV is partly connected with an exciton-like σ-emission of Na^+ centres due to an interaction of mobile secondary excitons with Na^+ ions. Such a dependence of the intensity ratio of the exciton-like π-emission of Na^+ centres (2.97 eV) and STE σ-emission (4.15 eV) on $h\nu_{ex}$ was also described in [7]. The determined photon threshold energy (12.8 eV), where a sharp

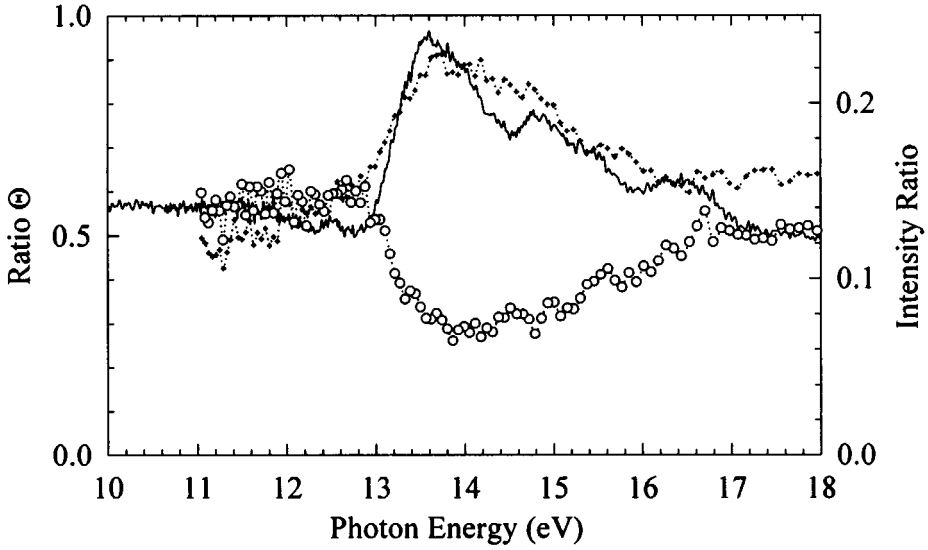

Figure 1. The intensity ratio spectrum (solid line) for slow and fast components of 4.15 eV emission in KI at 10 K. The spectra of $\Theta=(I^{st}-I^{unst})/I^{unst}$ for the 3.4 (+) and the 2.9 eV (o) emissions in stressed and unstressed KI:Na crystals at 10 K.

increase of the value I_s/I_f occurs (See fig. 1), slightly exceeds the sum of E_g+E_e=12.14 eV. In the case of a direct interband photoabsorption a part of the photon energy is transferred to a photohole. In the MEE region the creation process of secondary e-h pairs is clearly detected at $h\nu_{ex}$> 13.8 eV, above $2E_g$=12.6 eV. In KI as well in NaI and in other crystals (see [8,9]), the creation of spatially correlated electron and holes, that recombine with formation of mobile excitons before hole transition $h \rightarrow h_{s2}$, is observed at the irradiation by photons, the energy of which is somewhat larger than E_g.

Influence of elastic uniaxial stress and electric field on MEE

The applied elastic uniaxial stress ~ 1 kg/mm^2 causes an enhancement of the STE π-emission (3.31 eV) intensity and a decrease of the 2.97 eV emission of STE localised near Na^+ in KI:Na (20 ppm) at 8 K [10]. The effect of the EUS applied parallel to (100) illuminated surface of a crystal is interpreted as an increase of the self-trapping probability and a suppression of the energy transfer to the impurity centres by FE, before their self-trapping. That is consistent with the results of a theoretical work by Rashba, predicting a barrierless self-trapping of excitons in one and two dimensional lattice [1]. In Fig. 1 the spectra of the ratio $\Theta=(I^{st}-I^{unst})/I^{unst}$ for 2.9 eV and 3.4 eV emissions are also depicted in KI:Na. I^{st} and I^{unst} are the emission intensities in stressed and unstressed samples, respectively. The value of Θ for 3.4 eV STE π emission rises in the energy range of 12.8 - 16 eV and decreases for 2.97 eV emission, if compared to the regions of 11-12.8 eV and 16-18 eV, where the formation of an e-h or two e-h pairs occurs, respectively. At $h\nu_{ex}$> 16 eV, the value of Θ for the 3.4 eV π emission of STE is higher than that between 11 - 12.5 eV. The effect of a high local density of excitations becomes manifest in the energy range of 16-18 eV where one photon can create quartets of charge carriers. Moreover, the structures observable in the ratio spectrum of Θ are more dispersed than in those of the ratio of I_s/I_f. The piezoreflectance of KI at 120 K was investigated in [16]. In the reflection spectra of KI between 13 -16.5 eV the observed structures, corresponding to 5p (I^-) → 5d (I^-) interband transitions, were split into parallel and perpendicular components under the stress about 10 times as small as that used in our experiment.

Fig.2 depicts a scheme of the experiment with an external electric field (a) and the part (b) shows a typical time response of luminescence intensity in KI in the case of an applied positive field. All the spectra presented in the present paper were obtained only for the positive field (the mesh was held on a positive potential in regard to the sample). The thickness of the single crystals of KI was ~ 1 mm in these experiments. Fig. 3 presents the excitation spectrum for 3.2-3.4 eV emission (measured in such an energy interval using a position sensitive detector), as well as the relative enhancement of intensity ΔI/I for the same emission band in the electric field of 5000 V/cm in the energy range of 10 - 17 eV. For comparison the reflection spectrum, simultaneously recorded with excitation spectra, is presented. The value of ΔI/I is practically constant in the region of STE π- and σ-emission bands (see inset fig. 3.). A positive electric field applied perpendicularly to (100) illuminated surface of a crystal causes an enhancement of the intensity for the STE π-emission excited by the VUV radiation. Along the penetration direction (z coordinate) into the crystal, the applied electric field reduces differences between $n_h(z)$ and $n_e(z)$, corresponding to the distributions of the rapidly self-trapping holes and more mobile electrons, facilitating recombination of e and h_{s2} with the appearance of a more intense STE emission.

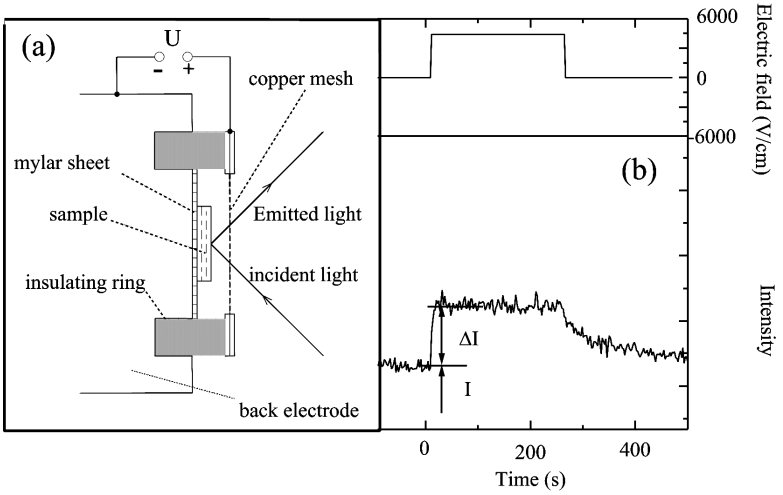

Figure 2. A scheme of experiment with an external electric field (a). A typical time response of luminescence (b) in KI at 10 K for the applied positive electric field.

At 8 K without an applied electric field, 12.5 eV and 16.5 eV photons create one or two e-h pairs, respectively. In the intermediate energy range of 12.8 - 13.5 eV, the creation of an e-h pair and a secondary exciton takes place (see Fig. 1). Photons of 13.5-15 eV cause the formation of spatially correlated electrons and holes (geminate e-h pairs). An applied electric field causes mainly two effects. It can destroy genetic e-h pairs (see also [14]). As a result, the electric field decreases the intensity of the π STE emission due to the recombination e and h_{s1} in the energy range of 13.5 -15 eV (the value ΔI/I decreases, Fig. 3.). The second effect is

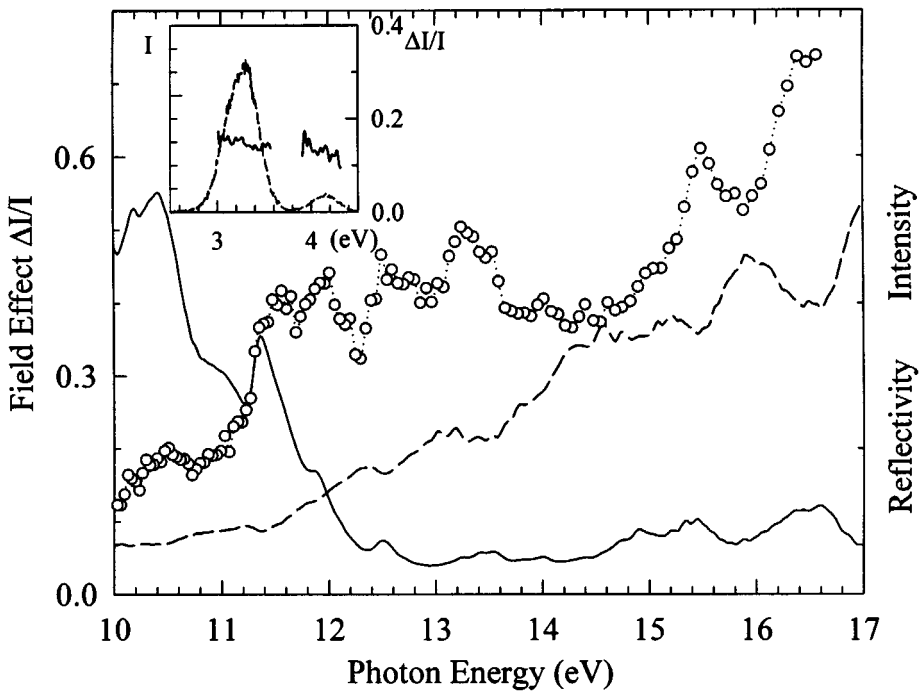

Figure 3. The reflection spectrum (solid line), the excitation spectrum of the STE π emission (3.2-3.4 eV, dashed line) and the relative field effect ΔI/I (open circles) in KI at 8 K. Inset shows the emission spectrum (dashed line) and the relative field effect ΔI/I (solid line) on emissions in KI at 8 K excited by 21 eV photons. The applied electric field strength was 5 kV/cm.

connected with a sharp rise of the relative electric field effect ΔI/I above $h\nu_{ex} \geq 11$ eV where its value reaches a level equal to that of at 15 eV. The threshold of the sharp increase for ΔI/I is observed at photon energies of about 2 eV lower than the thresholds in the ratio spectra of I_s/I_f for 4.15 eV emission and of Θ for 3.4 eV π emission of STE (see Fig. 1). A simple explanation for the sharp rise of the value ΔI/I between 11 and 12.8 eV where without any field only one e-h pair is formed, proceeds from the fact that at low temperatures the applied electric field with a strength of 5 kV/cm provides some additional energy to the c-band electrons sufficient for the creation of secondary excitons with n=1. Taking into account the results of the theoretical calculations for KI (see [17,18]), photons $h\nu_{ex} \geq 11$ eV are able to create c-band electrons with a kinetic energy of ~ 4 eV without any applied electric field. However, such a kinetic energy of the electrons is large enough for exciting In^+ centres in KI:In (see [19]) but too small for the impact creation of secondary excitons. The energy increase of hot photoelectrons from 4 eV to 6 eV by the applied electric field, opens a possibility for secondary exciton formation already by 11.5 eV photons. Taking into account the data about piezoreflectance for KI [16] the electron transitions 5p (I^-) → 3d (K^+) take place by 11-13 eV photons. The transitions 3d (K^+)→ 3s (K^+) are forbidden in the c-band. A strong electric field may increase the probability of these transitions and affect the possible Auger processes of exciton creation with a participation of hot photoelectrons in the c-band.

We investigated the influence of an electric field on intrinsic and impurity emission in KI in a wide energy range of 6-30 eV. A persuasive interpretation of the effects in this range will be performed in the future taking into account many circumstances. For example, in the energy range of 5.7-9 eV the value of the absorption coefficient is high ($5\cdot10^6$ - $3\cdot10^5$ cm^{-1}) and the nonradiative decay of electronic excitations near surface layer play an important role like other analogous phenomena (see [20]). The absorption coefficient is at least by an order of magnitude smaller in the spectral range of 10.5 - 18 eV, where our results were discussed. In spite of all complications, our investigations of the influence of an electric field provide important information about the elementary processes of MEE in wide-gap crystals.

Concluding remarks

On the basis of the experimental data we are in favour of the possible Auger and impact mechanisms for the creation of secondary excitations under MEE conditions. The recombination mechanisms for the creation of secondary excitons are also of importance. However, this does not rule out the occurrence of the two-electron excitation processes in KI. But the quantum efficiency of such processes is much lower due to the competition with one-electron excitations which are more likely to be created at the direct photoabsorption by VUV radiation. Two-electron excitations in ionic crystals were theoretically discussed in [21,22] and experimentally investigated in Xe and Kr cryocrystals [23]. The differences of the Auger and impact mechanisms in semiconductors were discussed earlier [24].

The creation of secondary excitons and spatially correlated electrons and holes was revealed using a set of experimental methods. These effects must be taken into account in the theory of optical spectra for wide-gap crystals (see also [25]).

Acknowledgements

This work was supported by the Estonian Science Foundation (grant 3868), the STINT Foundation (Sweden) and the Exchange Program between Tartu and Hamburg Universities.

References

1. Ch. B. Lushchik (Chapter 12) and E. I. Rashba (Chapter 12), in: “Excitons”, eds. E. I. Rashba and M. D. Sturge, North-Holland, Amsterdam (1982).

2. T. Tsujibashi, K. Toyoda, T. Hayashi, Sol. State Commun. **105** (1998) 681.
3. E.A. Vasil'chenko, Ch. B. Lushchik, K. Osmonaliev, Sov. Phys. Sol. State **28** (1986) 1113.
4. M. Itoh, J .Phys. Soc. Jpn. **64** (1995) 3097.
5. E. R. Ilmas, G. G. Liidya, Ch. B. Lushchik, Opt. Spectrosc. **18** (1965) 255, 359.
6. N. S. Rooze, Sov. Phys. Sol. State **17** (1975) 690.
7. A. Lushchik, E. Feldbach, R. Kink, Ch. Lushchik, M. Kirm, and I Martinson, Phys. Rev. **B 53** (1996) 5379.
8. A. N. Vasil'ev, V. V. Mikhailin, Izv. Acad. Nauk USSR Ser. Fiz. **49** (1985) 2044.
9. M. Kirm, E. Feldbach, R. Kink, A. Lushchik, Ch. Lushchik, In: "Excitonic Processes in Condensed Matter", ed. M. Schreiber, Dresden University Press, (1996) 179.
10. M. Kirm, A. Lushchik, Ch. Lushchik and E. Vasil'chenko, in "Physics and Chemistry of Luminescent Materials" eds. C.W. Struck, K.C. Mishra and B. DiBartolo, PV 98-24, The Electrochemical Society Proceedings Series, Pennington, NJ (1999) 267.
11. A. Bekeshev, E. Vasil'chenko, E.T. Sarmukhanov, K. Sh. Shunkeev, and A. A. Elango, Phys. Sol. State **36** (1994) 180.
12. V. P. Denks, Ch. B. Lushchik, and T. A. Soovik, Sov. Phys. Sol. State **11** (1969) 32.
13. T. Hayashi, S. Koshino, Y. Kawai, T. Okada, J .Phys. Soc. Jpn. **33** (1972) 1018.
14. V. P. Denks, V. I. Leiman , Sov. Phys. Sol. State **10** (1968) 1426.
15. G. Zimmerer, Nucl. Instr. And Meth. **A 308 (**1991**)** 178.
16. M. Miyabe,. K. Yagy, A. Yamada, Y. Aiura, T. Koide, T. Shidara, H. Kato and H. Fukutani, J .Phys. Soc. Jpn. **56** (1987) 378.
17. A. B. Kunz, J. Phys. Chem. Solids **31** (1970) 265.
18. Y. Onodera, M. Okazaki, and T. Inui, J .Phys. Soc. Jpn. **21** (1966) 2229.
19. E. Feldbach, M. Kamada, M. Kirm, A. Lushchik, Ch. Lushchik, and I. Martinson, Phys. Rev. **B 56** (1997) 13908.
20. V. P. Denks, P. L. Liblik, Trudy Inst. Fiz. Akad. Nauk Estonian SSR **40** (1972) 119.
21. D. L. Dexter, Phys. Rev. **126** (1962) 1962.
22. J. T, Devreese, A. B.Kunz, T. C. Collins, Sol. State Commun. **11** (1972) 673.
23. B. Steeg, E. Gminder, M. Kirm, V. Kisand, S. Vielhauer, G. Zimmerer, J. El. Spectr. Rel. Phen. **101-103** (1999) 879.
24. Yi Lu and Chin-Tang Sah, Phys. Rev B **52** (1995) 5657.
25. L. X. Benedict, E. L. Shirley, and R. B. Bohr, Phys.Rev. Lett. **80** (1998) 4514.

Luminescence excitation spectra and energy transfer in LiF-U,Cu and NaF-U,Cu scintillation crystals

V.A.Pustovarov[1], B.V.Shulgin[1], M.M.Kidibaev[2] and A.A.Zhamangulov[2]

[1] *Urals State Technical University, 620002, Ekaterinburg, Russia*
[2] *Issyk-Kuls State University, 722360, Karakol, Kyrgyz Republic*

Abstract. The time-resolved emission and luminescence excitation spectra as well as the reflection spectra of LiF and NaF sctintillation crystals codoped with uranium and copper have been studied using synchrotron radiation of X-ray (storage ring VEPP-3) and VUV (storage ring DORIS) regions by the use of the optical and luminescent time-resolved spectroscopy techniques over the energy region of 2-40 eV at temperatures 10,8 and 295 K. The spectral and decay kinetics parameters of the extrinsic luminescence and the energies of excited states of U^{6+}-ions were determined. The dominant role of the electron-hole mechanism of the energy transfer were established.

Keywords: time-resolved spectroscopy, excitation states, impurity center, energy transfer

Introduction

The LiF and NaF crystals doped by uranium salts are known for a long time as bright luminophores [1,2] and from recently as crystals for TLD and scintillation detectors of ionizing radiation. The model of luminescence centers for these crystals was offered and justified in Refs. [1,2]. This model is associated with the radiative transitions in the impurity U^{6+}-ions. The development of a techniques and methods of crystal growth with the coactivators in the Alybakov's Laboratory allowed us to obtain the crystals with an elevated scintillation (quantum) yield. It stimulates a further study of the electronic excitation relaxation processes with participation of the impurity centers in these crystals. The lowest energy of interband transitions E_g requires application of a VUV- spectroscopy technique with using of synchrotron radiation (SR) and imposes some known experimental difficulties. At the same time the application of VUV-excitation allows us to reveal the characteristics of the impurity centers in an undistorted kind, because the VUV-excitation does not create effectively a radiation-induced defects, that typical for alkali halide crystals at irradiation by X-rays or by electron beams.

In the present work the spectra and decay kinetics of luminescence as well as the luminescence excitation spectra with a time resolution (energy region 2-40 eV, T=10,8 and 295 K) of LiF and NaF crystals codoped with uranium and copper are investigated by the use of SR in X-ray and VUV ranges as well as of pulse electron beams.

Experimental details

The crystals were grown in air by Kyropolous method in Institute of Physics of Kyrgyz Republic and were certified by the absorption and EPR spectroscopy methods and by the Retherford's back scattering method. The samples were produced in the form of the polished plane-parallel plates ($10x10x1mm^3$). The measurements were carried out on the storage ring VEPP-3 (excitation by X-ray photons) [3] and on the SUPERLUMI station of HASYLAB (excitation by VUV photons) [4]. The excitation spectra were normalized to quantum intensities of SR falling into the crystal. The emission spectra were not corrected on spectral

sensitivity of the optical tract. The excitation spectra were measured for time-integrated (steady-state) luminescence as well as for the emission detected within time windows (length Δt_i) correlated with the excitation pulse of SR (delayed by δt_i). The delay δt and length Δt were equal to 2,2 and 8,2 ns for the fast component. The reflection spectra were measured at SR incidence angle of $17{,}5^0$.

Results and discussion

The luminescence spectra under X-ray excitation or selective VUV excitation show the structured 2,38 eV band (FWHM=130 meV) in LiF-U,Cu (the band-gap energy E_g is equal 14,2 eV [5], the energy of ground exciton state $Å_{n=1}$ is equal 12,82 eV) and the structured 2,23 eV band (FWHM=185 meV) in NaF-U,Cu (E_g=12,3 eV [6], $Å_{n=1}$=10,50 eV at T=295 K), see Fig.1. The availability of a structure depends on the concentration of activator.

According to EPR data and Refs. [1,2], these emission bands are due to U^{6+}-ions. The U^{6+}-ion substitutes a cation, the superfluous positive charge (+5) is compensated by means of a replacement of five environmental F^--ions by oxygen O^{2-} -ions [1]. According to Runciman [2], all six F^--ions are substituted by O^{2-} -ions and the indemnification of charge is executed by anion vacancy in the second coordination sphere.

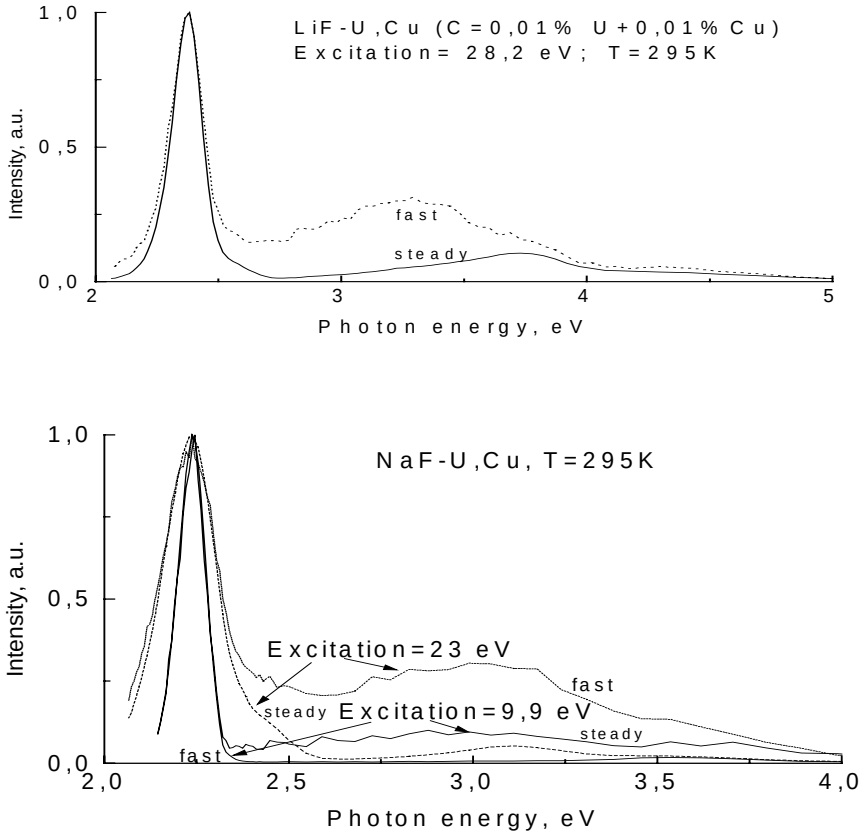

Figure 1. Time-resolved luminescence spectra of LiF-U,Cu and NaF-U,Cu crystals by selective VUV-excitation

The π-emission band of self-trapped excitons is not displayed even at T=10,8 K. Decay kinetics at $E_{exc}>E_g$ have fast (τ=1,6 ns) and slow ($\tau_{1/2}\approx$40 μs under electron beam excitation) components, Fig.2. The scintillation outputs (current registration) are equal to 137% for NaF-U,Ñu and 12,5% for LiF-U,Cu, relative to CsI-Tl crystals at T=295 K.

The U^{6+}-emission is not excited practically in the region of the Urbach tail of the fundamental absorption edge and in the n=1 exciton region at T=10-295 K, Fig.3,4. At the same time the U^{6+}-emission is excited effectively in both crystals over the region of the creation of electron-hole pairs. The electron-hole mechanism of energy transfer dominates. The appropriate recombination of holes with electrons located on impurity centers will form an excited states of impurity centers. Our EPR data and thermal activation spectroscopy data confirm this fact. The radiative intracenter transitions form the luminescence spectrum. The exciton mechanisms of energy transfer (the migration of nonrelaxed excitons or induced energy transfer from STE to impurity centers) will not be practically realized even at 10 K. At the same time the high-energy band on the fundamental absorption edge in luminescence excitation spectra of both crystals can correspond to creation of excitons directly beside U^{6+}-centers (by analogy with D-bands of Hg-like ions in alkali halide crystals).

In LiF-U,Cu crystals the known effect of photon multiplication is appreciable not obviously at energy $E>2E_g$, the maximum yield of 2.38 eV emission is reached in the energy region $E<E_g$ under intracenter excitation (10-12 eV), Fig.3. In LiF-U,Cu crystals the higher surface and migration energy losses take place. In difference from it in the NaF-U,Cu crystals the effect of photon multiplication is displayed clearly at $E_{exc}\geq 30$eV ($E\geq 2{,}5E_g$). The U^{6+}-emission yield is highest at photoexcitation in this energy region, Fig.4. Therefore we can expect that these crystals will have high scintillation efficiency.

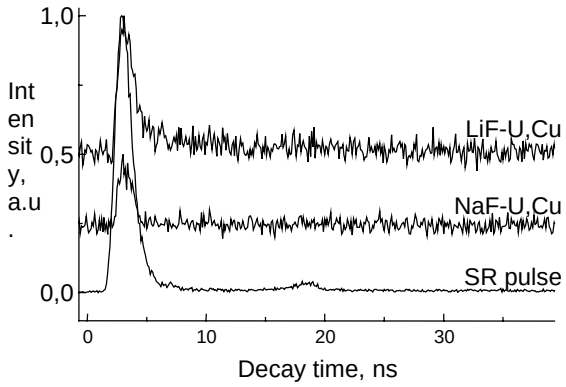

Figure 2. Decay kinetics of luminescence of LiF-U,Cu ($E_{emission}$=2,28 eV) and NaF-U,Cu crystals ($E_{emission}$=2,21 eV) by selective VUV- excitation E_{exc}=20 eV at 295 K

Acknowledgments

The authors would like to thank Dr. E.Zinin, Prof. G.Zimmerer and Dr. M.Kirm for help in the realization of SR-experiments.

References

1. 1. P.P.Feofilov, Optika i spektroskopia **7** (1959) 842.
2. 2. W.A.Runciman, J. Phys. at radium. **17** (1956) 645.
3. 3. V.A.Pustovarov, E.I.Zinin, A.L.Krymov, B.V.Shulgin, Review of Scientific Instrum. **63** (1992) 3521.
4. 4. G.Zimmerer, Nucl. Instr. and Methods in Phys. Res. **A308** (1991) 178.
5. 5. K.K.Rao, T.J.Moravec, J.C.Rife, R.N.Dexter, Phys. Rev. B: Solid State **12** (1975) 5937.
6. M.Kirm, A.Lushchik, B.Steeg, E.Vasil'chenko, S.Vielhauer and G.Zimmerer, Radiation
7. Effects and Defects in Solids (1999) (in press).

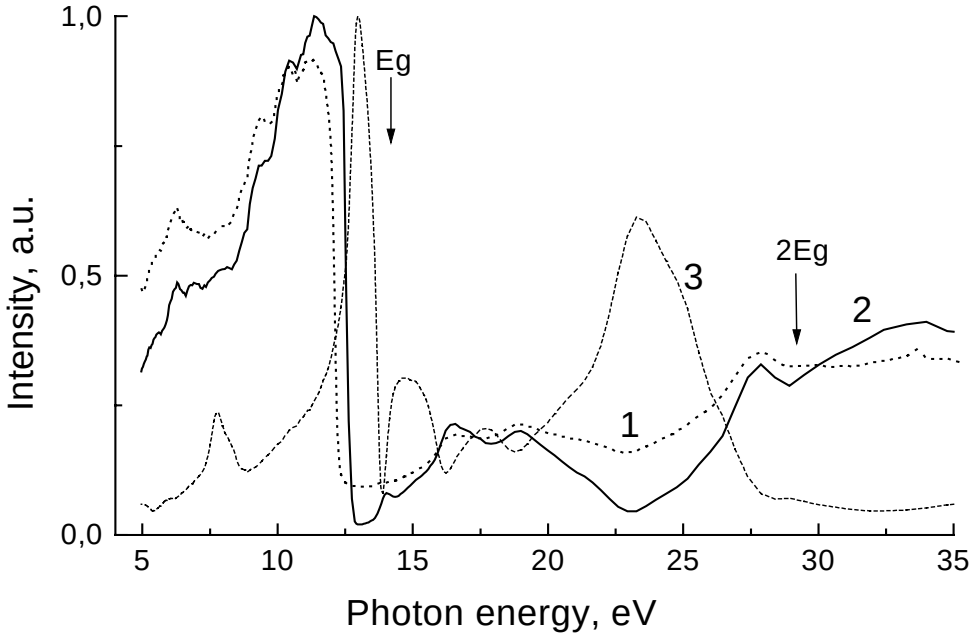

Figure 3. Luminescence excitation spectra ($E_{emission}$=2,28 eV) (1,2) and reflection spectrum (3) of LiF-U,Cu crystal (C=0,01mol.%U + 0,01 mol.%Cu) at 295K (1) and 10,8K (2,3)

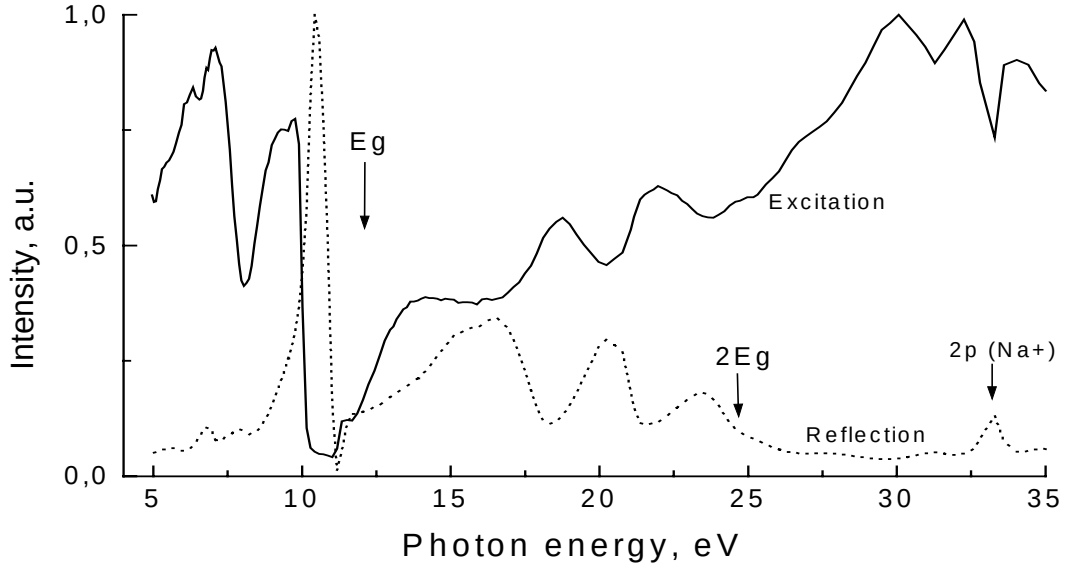

Figure 4. Luminescence excitation ($E_{emission}$=2,21 eV) and reflection spectra of NaF-U,Cu crystal (C=0,01mol.%U + 0,01 mol.%Cu) at 295 K

New features of self-trapped exciton luminescence in beryllium oxide

S.V. Gorbunov[1], K.V. Bautin[1], A.V. Kruzhalov[1] and V.Yu. Yakovlev[2]

[1]*Ural State Technical University, Mira St. 19, 620002, Ekaterinburg, Russia*
[2]*Tomsk Polytechnical University, Lenina St. 30, Tomsk, Russia*

Abstract: Time-resolved spectra, decay kinetics, degree of polarization of the luminescence and transient optical absorption induced by irradiation of BeO with electron pulses have been studied. It is found that the slowly decaying intrinsic luminescence band at 4.0 eV is associated with the splitting of the triplet excited states of self-trapped excitons.

Introduction

It is known that BeO crystals have intensive luminescence under electron beam and X-ray excitation. In BeO luminescence spectra two pairs of fastly and slowly decaying luminescence bands at 6.7, 4.9 and 4.4 eV related to two different types of singlet and triplet self-trapped excitons (STE) have been observed. The presence of two different types of STE can be due to a hexagonal structure of BeO crystals. In BeO wurtzite lattice there are two types of bonding, i. e. Be-O_{axial} and Be-$O_{non\text{-}axial}$, having different directions relative to the optical C-axis of the crystals. The analysis of luminescence polarization characteristics made it possible to assume that the axis of one of STE is almost parallel to Be-O_{axial} bond directed along C-axis, while the other STE axis is close to the direction of Be-$O_{non\text{-}axial}$ bond.

In the present work the results of research of time-resolved spectra, decay kinetics, degree of polarization of the luminescence and the transient optical absorption induced by BeO irradiation with electron pulses have been given. New data on the peculiarities of STE luminescence in non-cubic oxides have been obtained.

Experimental technique

We have be studied pure BeO crystals grown by the temperature gradient and Czochralski-Kyropoulos methods from a BeO solution in sodium tungstane melt. Total concentration of Li, B, Al, Mg and Zn impurities did not exceed 10-50 ppm. The mentioned impurities have been discovered by a laser-induced mass-spectrographic method. We measured the luminescence and the transient optical absorption induced by pulsed irradiation with an optical detection system consisting on a monochromator, a photomultiplier and storage oscilloscopes. Electron pulses with parameters (energy: 200 keV, duration: 10 ns, maximum fluence: 0.25 J/cm^2) were generated with a GIN-600 accelerator. Frank-Ritter and Raushan polarizers were used to analyze luminescence and transient optical absorption.

Experimental results and discussion

The decay kinetics of transient optical absorption of pure BeO crystals at 80 K in the range 3.6 eV may be described by the sum of three exponential components, Fig. 1. The decay time values of these components are equal to τ_1=340 μs, τ_2=7±0.3 ms and τ_3=450 ms. The first decay component of transient optical absorption with decay time 340 μs observed also in luminescence kinetics at 6.7 eV is due to radiative transitions from triplet STE state of the first type (further referred to as STE_1) [1]. The study of the dependence of optical density of two other components from electron fluence enabled us to determine the following

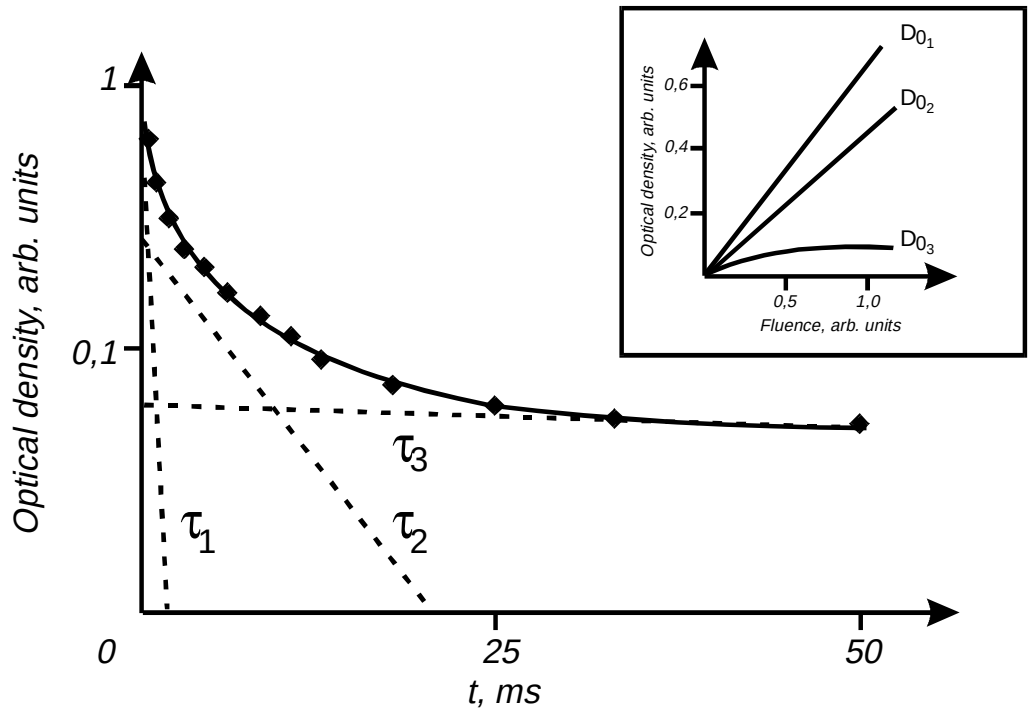

Figure 1. Decay kinetics of transient optical absorption at 3.6 eV in BeO crystals at 80 K. Optical density dependence on electron fluence shown in segment.

peculiarities of centres related to them. The intensity of optical absorption of STE_1 and centres with lifetime 7 ms grows linearly with the electron fluence increase, Fig. 1. A considerable contribution of the second component with τ=7 ms to the initial optical density amplitude (70% relative to the formed STE_1), independence of single-exponential character of the kinetics and the decay time on electron fluence, decrease of the optical absorption of this component when Zn and B impurities were added testifies to the intrinsic nature of centres related to the second component. On the other hand, the variation of values of the optical absorption of centres with characteristic decay time 450 ms from electron fluence is described by saturating dependence. It is indicative of the fact that these centres are the trapping centres related to the impurities or lattice defects.

For investigation of the nature of centres responsible for the component with decay time 7 ms we analyzed the transient optical spectra measured at 80 K with different time delay relative to an electron pulse and different polarization of probing light relative to optical axis **C** of BeO crystals, Fig. 2. In the absorption spectrum of the component 7.0 ms three bands at 2.6, 3.1, 3.7 eV are observed. A comparison with three-band structure of transient absorption spectra of STE of the first type showed that a short-wave 0.9 eV shift of a band at 1.7 eV of STE and an essential difference in polarization properties of all three bands are observed as well, Fig. 2.

When studying luminescence kinetics of BeO crystals an exponential component with decay time 7 ms coinciding with the same transient optical absorption component in its time-temperature properties was observed. In the luminescence spectrum of this component the band with a peak at 4.0 eV, whose intensity is three order less than such luminescence band at 4.9 eV due to radiative transitions from triplet state of STE of the second type (STE_2) was observed (Fig. 3).

Polarization properties of the luminescence in the vicinity of 4.0 eV band are likely to indicate the superposition of several bands. From the long-wave side of 4.0 eV band the polarization degree (P) is about +30%, whereas in the short-wave side P decreases to 0%. The intrinsic nature and slow decay time of luminescence at 4.0 eV enabled us to assume its

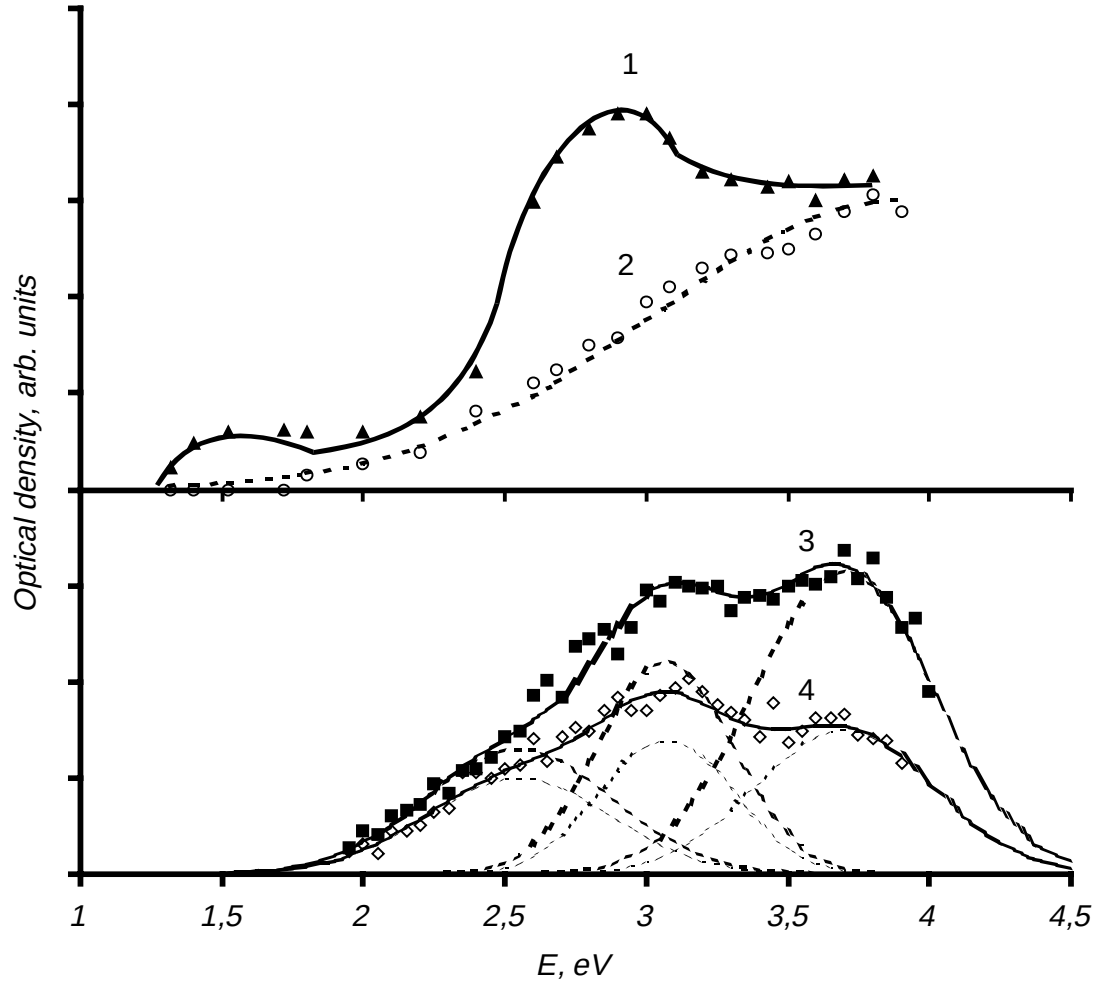

Figure 2. Polarized transient optical absorption spectra of BeO crystal taken 50ns (1, 2) and 5 ms (3, 4) after irradiation with electron pulse at 80 K. (1, 4) and (2, 3) denote the data measured with E perpendicular and E parallel C-axis, respectively

relation to the radiative transitions from STE triplet excited state. To support this hypothesis we studied temperature dependence of luminescence decay times at 6.7, 4.9 eV of both types of triplet STE and luminescence at 4.0 eV, Fig. 4. In the temperature range above 120 K the shortening of decay time of luminescence at 4.0 eV with the activation energy E_a=120 meV was observed. At T>160 K the lifetime of luminescence at 4.0 eV becomes invisible on the background of the component of decay kinetics of luminescence at 4.9 eV coinciding in decay time with the lifetime of luminescence at 6.7 eV and due to transitions between triplet excited states of two types of STE in BeO [1]. This process is characterized by the activation energy about 200 meV. The observed behaviour of luminescence at 4.0 eV and 4.9 eV is likely to indicate their relation with triplet states of one and the same center. An important feature of BeO crystalline structure is the low symmetry of anion positions (oxygen) - C_{3v} for axial sites (located on C axis) and C_s for non-axial sites.

According to calculations [2] and EPR studies of holes trapped near cation vacancies (V-type centres or monovalent impurity ions (centres of $[Li]^0$ type) BeO valent zone is formed from 2p oxygen states. In the crystalline field of C_{3v} or C_s symmetry a partial or complete splitting of p-states takes place. Earlier in [1] it was assumed that in BeO crystals STE have a hole component in the form of O^- ion. Term ^3P splitting into two states $^3A_1$ and ^3E in the C_{3v}

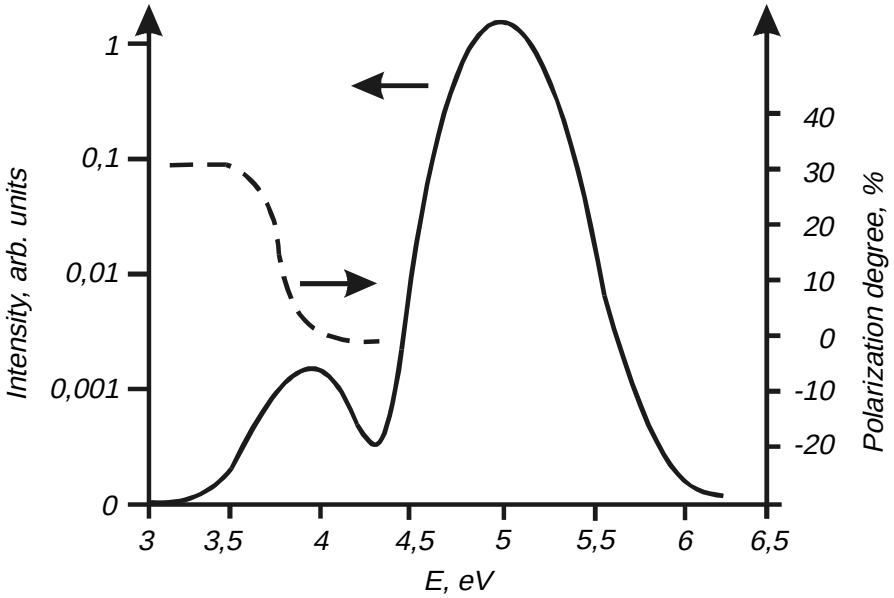

Figure 3. Luminescence spectra in BeO crystals. Dotted line showes the polarization degree

symmetry crystalline field corresponds to the triplet excited state of STE formed from such hole and s-electron. Thus, two bands of slowly decaying luminescence at 4.0 and 4.9 eV of STE in BeO can be attributed to radiative transitions from these states divided by the activation barrier 120 meV.

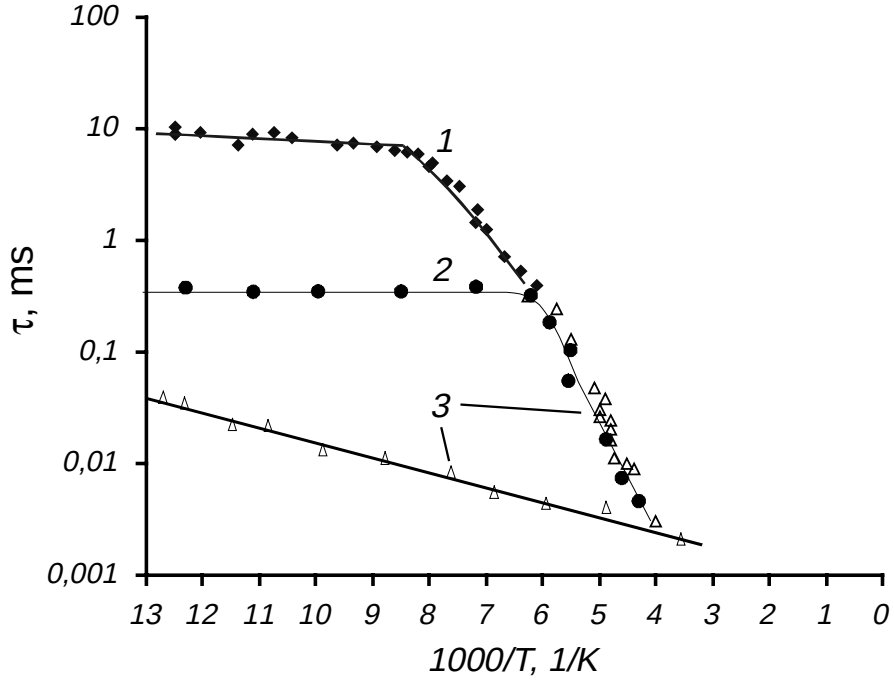

Figure 4. Temperature dependence of decay times of 4.0 eV (1), 6.7 eV (2) and 4.9 eV (3) luminescence

References

1. S.V. Gorbunov, S.V. Kudyakov, B.V. Shulgin, and V.Yu. Yakovlev, Radiation Effects and Defects in Solids **135** (1995) 269
2. V.A. Lobach, I.R. Rubin, and A.V. Kruzhalov, Fizika tverdogo tela **29** (1987) 2610

Excitonic emission of scheelite tungstates AWO_4 (A = Pb, Ca, Ba, Sr).

M. Nikl[1], P. Bohacek[1], E. Mihokova[1], M. Kobayashi[2], M. Ishii[3], Y. Usuki[4], V. Babin[5], A. Stolovich[5], S. Zazubovich[5], M.Bacci[6]

[1]*Institute of Physics AS CR, Cukrovarnicka 10, 162 53 Prague, Czech Republic*
[2]*KEK, IPNS, Tsukuba 305-0801, Japan*
[3]*Shonan Institute of Technology, Fujisawa 251-8511, Japan*
[4]Furukawa Co., Kamiyoshima, Yoshima, Iwaki 970-1153, Japan
[5]Institute of Physics, University of Tartu, Riia 142, 51014 Tartu, Estonia
[6]IROE del CNR, Via Panciatichi 64, 50 127 Florence, Italy

Abstract. Localized exciton emission spectra of four scheelite tungstate single crystals AWO_4 (A= Pb, Ca, Sr, Ba) were measured in a wide temperature range and their structure is discussed. Decay kinetics of $PbWO_4$ is presented in 0.35 – 300 K range and mathematical model is presented, which successfully approximates decay time and intensity temperature dependencies with a unique set of parameters. Beside usual thermal quenching also thermally induced exciton disintegration is considered, which was evidenced in earlier experiments.

Keywords: scheelite tungstates, luminescence, decay kinetics, exciton

Introduction

The scheelite tungstate crystals (AWO_4, A = Pb, Ca, Ba, Sr) show the excitonic luminescence, which is based on the radiative transition within tetrahedral $(WO_4)^{2-}$ group, where the exciton becomes autolocalised. Mainly $CaWO_4$ [1] and $PbWO_4$ [2] were studied in the past showing very similar excitonic emission spectra in the blue spectral region, while temperature dependencies of the emission intensity and decay kinetics were found markedly different. Renewed interest in $PbWO_4$ appeared recently due to its application in the future High Energy Physics detectors [3,4]. Recent detailed experimental and also theoretical studies revealed several interesting features of $PbWO_4$ excitonic emission. Namely, the "spread-eagle" shape of the blue emission was explained by the influence of the Jahn-Teller effect on the degenerated excited state of $(WO_4)^{2-}$ tetrahedron [5], co-existence of the I^{st} and II^{nd} order decay kinetics was noticed at room temperature (RT) [6] and explained by thermal disintegration of the excitonic state above 150 K [7] and recently the exciton binding energy was estimated about 0.1 eV [8]. Due to exciton instability in $PbWO_4$, intrinsic equilibrium between the exciton and electron-hole states is established above 200 K, which allows looking at $PbWO_4$ as a wide-gap semiconductor.

We have completed further experimental data related to the emission spectra and decay kinetics for four scheelite tungstate systems, which allows to make more general evaluation of the excitonic luminescence features related to $(WO_4)^{2-}$ complex anion group. Decay kinetics data were obtained for $PbWO_4$ case down to 0.35 K and detailed decay kinetics model is presented, which describes simultaneously temperature dependence of decay times and steady-state exciton emission intensity.

2. Experimental

Emission spectra and the decay curves were measured using Spectrofluorometer 199S (Edinburgh Instrument) modified for low temperature measurements. The spectra were

corrected for spectral dependence of the detection part sensitivity. Decay curves were measured using microsecond Xenon flashlamp excitation, photon counting detection with XP2233 photomultiplier and accumulation of data by multichannel analyzer running in a scaling mode. In a submicrosecond time scale the coaxial ns flashlamp was used and time-correlated single photon counting method was used to obtain the decay times down to 1 ns. To extract true decay times from the decay curves measured in ns time scale, common convolution-deconvolution technique was used. The decay kinetics below 4 K was measured using ^{3}He cryostat in Tartu laboratory, for further details see [9].

High purity AWO_4 (A=Pb, Ca, Ba, Sr) single crystals were prepared using Czochralski technique and starting materials with 5N purity. The GDMS and ICP chemical analyses confirmed close-to-6N purity of the crystals grown. From the crystal boules the plates about 7x7x1 mm were cut and polished for the optical experiments.

Experimental results and discussion

Emission spectra

Fig. 1 displays the emission spectra of AWO_4 (A=Pb, Ca, Sr, Ba) single crystals at 5 K. Despite the markedly different shapes corresponding to the different species one can notice some common features, namely the presence of a narrower central peak surrounded by two broad shoulders. Significant changes of the spectral shape for certain material are observed when the temperature is gradually increasing- as reported in Figs. 2 and 3 for $PbWO_4$ and $BaWO_4$, respectively. In particular, the intensity of high energy shoulder is increasing, while the intensity of low energy shoulder is strongly reduced. In the case of $BaWO_4$ (see Fig. 3) this trend ends up in the emission spectrum peaking around 370-380 nm at 200 K (central peak and low energy shoulder are visible very little).

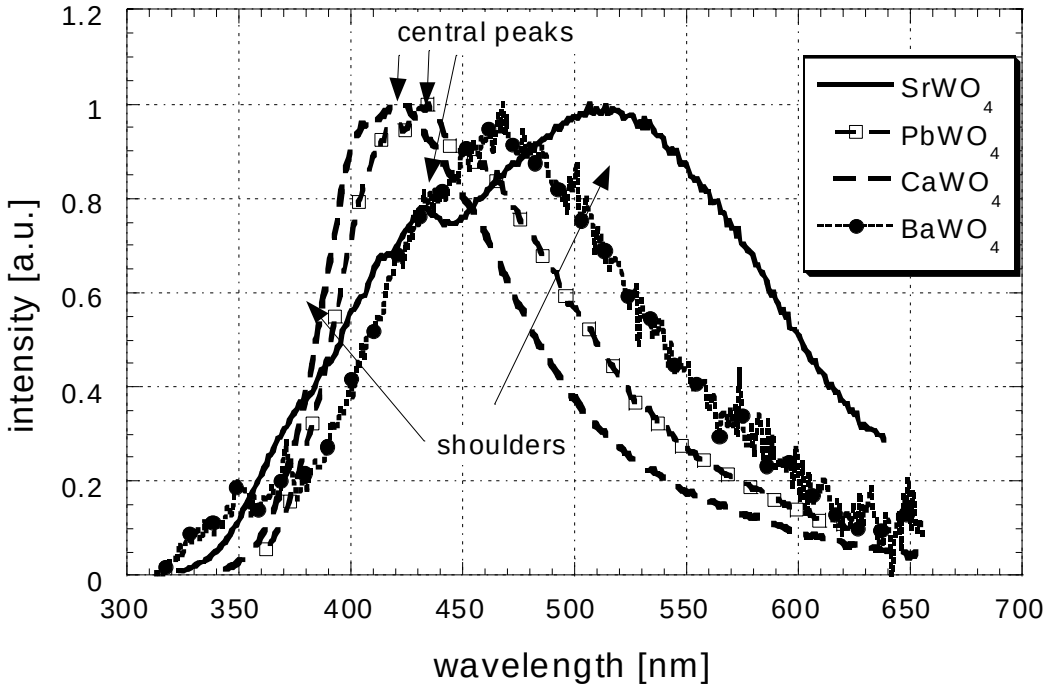

Fig. 1 Localized exciton emission in AWO_4 scheelite tungstates at 5 K under excitation in the exciton absorption region.

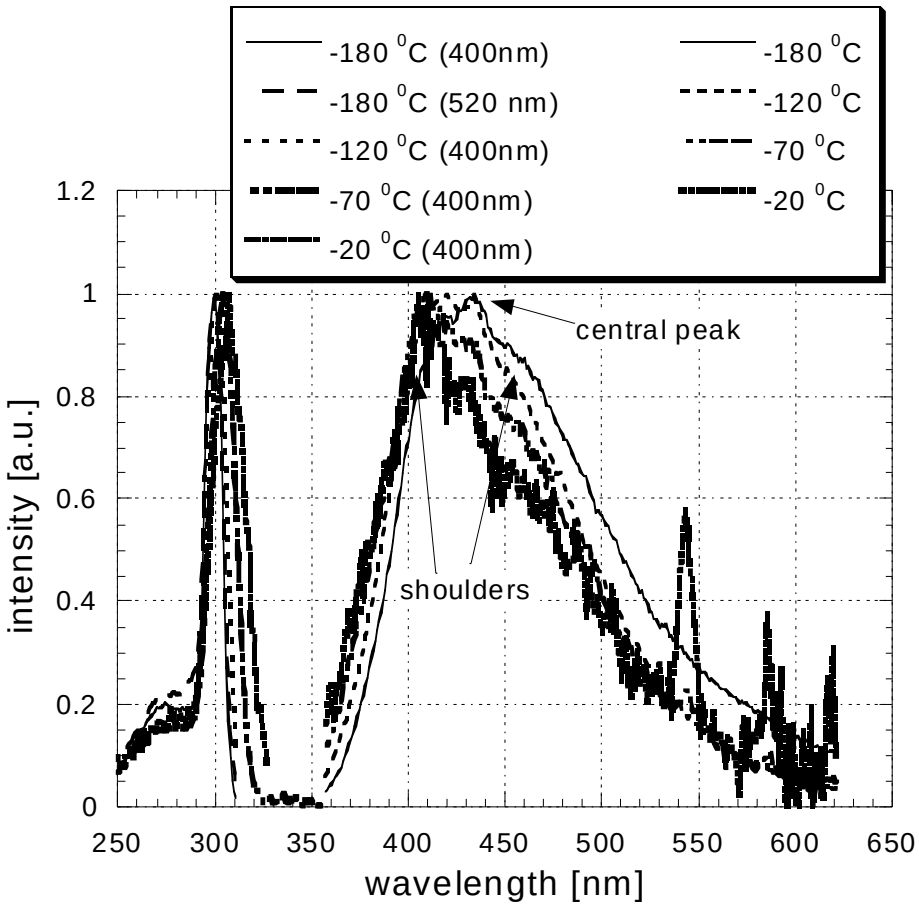

Fig. 2 Temperature dependence of $PbWO_4$ localized exciton emission under excitation in the exciton absorption region (290-300 nm). Corresponding excitation spectra (emission wavelength indicated in parenthesis) are also given, which reflect temperature development of the absorption edge.

Such triple-peak ("spread-eagle-shape") structure was calculated for the absorption spectra of the centres with the local cubic symmetry and threefold degenerated excited state [10]. In fact, the Jahn-Teller (JT) active vibrational modes of symmetry t_2 can produce a structured absorption band for $A_1 \rightarrow T_{1(2)}$. transitions [10]. Similar spectral shape was calculated as well for emission spectra in O_h symmetry [11] again due to the JT interaction of an electron in the triplet state with *e* and t_2 vibrational (JT active) modes.

It was determined that the lowest excited state of $(WO_4)^{2-}$ emitting centre in AWO_4 crystals consists of two lowest and closely lying triplet levels $^3T_1$ and $^3T_2$ [12,13]. As the local symmetry of the emitting centre is tetrahedral JT interaction with *e* and t_2 vibrational modes affects both triplet states. Preliminary calculations moreover show that (unlike Tl-like phosphors) the central tungsten gives only a small contribution to the JT coupling to *e* modes and no contribution at all to the JT coupling to t_2 modes. This is valid at least if possible contribution from 6p orbitals of W atom is neglected. As a result of that the main contribution to the JT coupling constants arises from molecular orbitals localized on the oxygen atoms.

From all the above mentioned one can make one of the following hypotheses about the origin of the structure of emission spectra and the temperature dependence of their shape for AWO_4 crystals:

- emission occurs from the lower lying triplet state splitted by JT interaction
- both triplet states affected by JT interaction give the contribution to observed emission

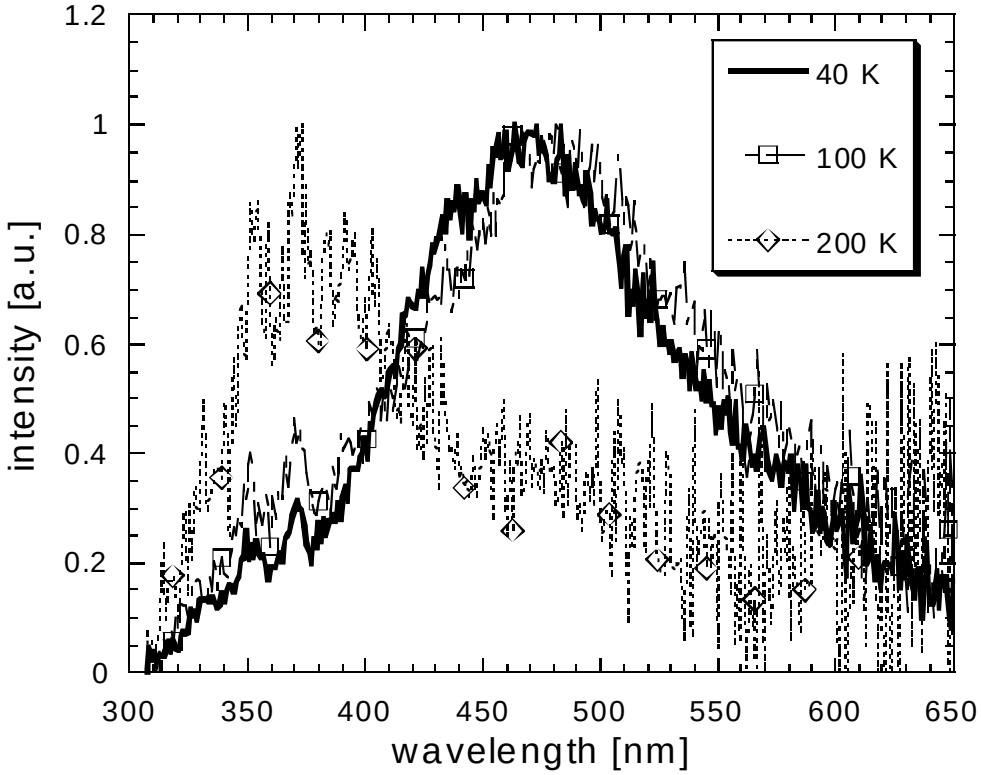

Fig. 3 Temperature dependence of the localized exciton emission in $BaWO_4$ under excitation in the exciton absorption region (260 nm)

- emission from one or both triplet states is moreover affected by the presence of the low symmetry local fields due to the fact that the symmetry of the emitting centre is not perfectly tetrahedral.

Decay kinetics

Decay kinetics of $CaWO_4$ and $PbWO_4$ was measured previously in ref. [1] and [2], respectively, down to the temperatures of a few K. Abrupt decrease of decay times at the lowest temperatures was observed in both cases. This suggests the presence of a pair of closely spaced energy levels involved in the excited state dynamics of $(WO_4)^{2-}$ centre. Essential difference between these two systems is observed above some 150 K, due to substantial shortening of $PbWO_4$ decay time and simultaneous intensity decrease. Such situation was explained by normal thermal quenching process, but recent measurements indicated presence of another delayed recombination processes in the decay kinetics [14] even under excitation in the exciton absorption peak. Thermally induced disintegration of the exciton excited state was proposed at $T > 150$ K based on the thermoluminescence excitation spectra [7] and finally relatively low binding energy of exciton was estimated (less then 0.1 eV in [8]), which strongly supports such hypothesis.

The main trouble in modeling excited state dynamics was met in [7] due to inconsistent temperature dependencies of the decay times and steady-state intensities measured at the undoped $PbWO_4$ sample. Also insufficient temperature interval was available for the decay kinetics measurements (above 4 K), which prevented reliable determination of the low temperature decay rates from the excited state levels. To separate delayed recombination components, which obscured the measurements of both the decay and emission intensity of the excitonic (blue) emission, two particular samples were used in this study. A sample showing comparable amount of the blue and green emission components was used taking advantage of the fact that all the recombination contributions are transferred to the green component due to efficient energy transfer via free charge carriers [15]. Consequently the

remaining blue emission component is almost free of recombination processes. Heavily La-doped $PbWO_4$ sample was used as a second choice, because in such a sample the recombination luminescence was severely suppressed [16] due to new nonradiative traps induced probably by the presence of La-dimers/small La aggregates. In Fig. 4, the decay times of the blue $PbWO_4$ emission are given in an extended temperature range (0.35 – 300 K) showing well defined low temperature plateau below 1 K. Furthermore, the steady-state intensity of the blue excitonic emission component above is given above 80 K (below this temperature it is practically constant). These experimental data were approximated by two excited state level model including also thermal quenching from both of them. Furthermore, another loss channel with activation energy 100 meV related to the exciton disintegration process was included (see the inset of Fig. 4).

The agreement between the experimental data and calculated curves is satisfactory for both the decay times and intensities using the same set of parameters summarized in Table 1. Thus, one can conclude that the dynamics of the prompt part of $PbWO_4$ excitonic luminescence can be successfully approximated within a simple two-excited state level model including intracentre thermal quenching and another loss channel based on thermally induced exciton disintegration. In the data approximation process essentially two cases were studied, namely with and without exciton disintegration simulated by a " thermal quenching-like" rate with the activation energy 100 meV and a free frequency factor. Just mentioned frequency factor value was determined about 1e9, which is about three orders below that related to the intracentre thermal quenching (see Table 1.). The presence of exciton disintegration process clearly helps to get a better fit of the experimental data around 150 K, while it induces essentially no change close to room temperature, where the intracentre thermal quenching is prevailing due to its dominant frequency factor value.

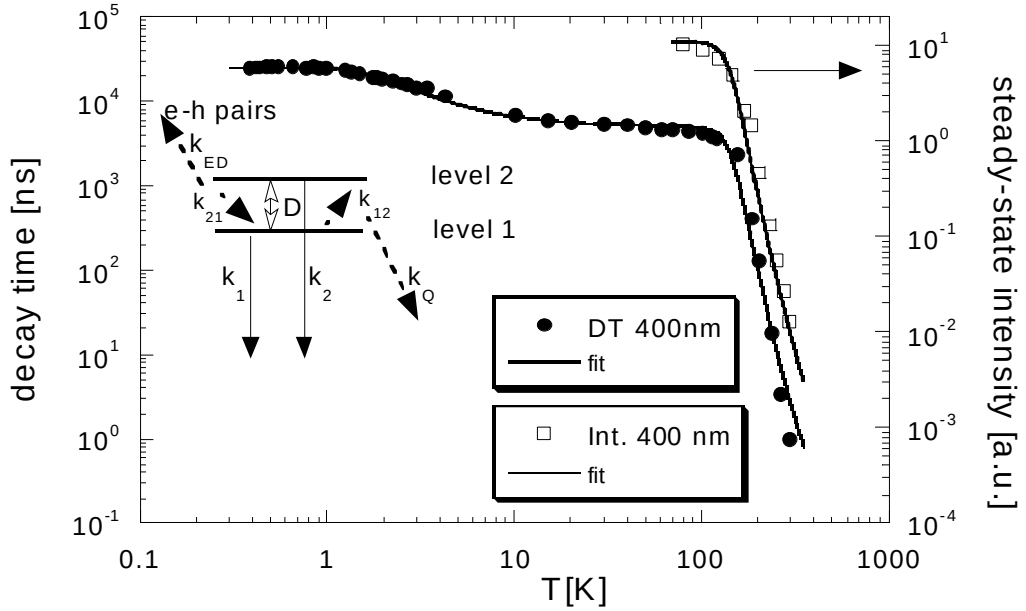

Fig. 4 Temperature dependence of the decay times and steady-state intensities related to the prompt part of the localized exciton emission in $PbWO_4$. Solid lines come from the model sketched in the figure with the parameters summarized in Table 1. The parameters k_1, k_2 stand for the radiative rates from excited state levels 1 and 2, respectively, k_{12} and k_{21} are the nonradiative rates interconnecting levels 1 and 2. Parameter D is the energetic separation between levels 1 and 2. Finally, k_Q stands for nonradiative quenching rate and k_{ED} for thermally induced exciton disintegration rate, where the latter is supposed to take place from the relaxed excite state. Both k_Q and k_{ED} are considered in a standard form $k_i=w_i\exp[-E_i/kT]$, where w_i and E_i stand for frequency factor and activation energy, respectively, see also [7].

Table 1. The summary of parameters used in the model calculation related to Fig. 4, parameter K is a "zero temperature" rate related to k_{12} and k_{21} parameters, while g is the ratio of degeneracies of the levels 1 and 2.

k_1	3.9e4 s	w_Q	1e12 s
k_2	3.7e5 s	E_Q	200 meV
K	5e5 s	w_{ED}	1e9 s
D	0.45 meV	E_{ED}	100 meV
g	1(2)		

References

1. M.Treadaway and R.C.Powell, J.Chem.Phys. **61** (1974) 4003.
2. W. van Loo, phys.stat.sol. (a) **27** (1975) 565 and **26** (1975) 227.
3. V.G. Baryshevski et al., NIM **A322**, 231 (1992).
4. M. Kobayashi, M.Ishii, Y.Usuki, H.Yahagi, NIM **A333**, 429 (1993).
5. K.Polak, M.Nikl, E.Mihokova, J.Lumin., **72-74** (1997) 781.
6. M.Martini et al, Chem. Phys. Lett., **260** (1996) 418.
7. V.Murk, M.Nikl, E.Mihokova, K.Nitsch, J.Phys.Cond.Mat. **9**, (1997) 249.
8. Y. C. Zhang, N. A. W. Holzwarth, R. T. Williams, and M. Nikl, Electrochemical Soc. Proc. Series, Pennington, NJ (1998), **PV 98-25**, p. 420 (Proc. of EXCON98, Nov 1-5, 1998, Boston, USA).
9. V. Nagirnyi et. al., J.Phys. Cond.Mat. **7**, (1995) 3637.
10. Y. Toyozawa and M.Inoue, J.Phys.Soc.Jap. **21** (1966) 1663.
11. M.Bacci, B.D. Bhattacharyya, A.Ranfagni, G.Viliani, Phys.Lett. **55A** (1976) 489.
12. C.J.Balhausen and A.D. Liehr, J.Mol. Spectrosc. **2** (1958) 342.
13. A. Annenkov et. al. Phys.stat.sol. (a) **170** (1998) 47.
14. M.Nikl et. al., phys.stat.sol. **195** (1996) 311.
15. M.Nikl et. al., Chem.Phys.Lett. **291** (1998) 300.
16. M.Nikl et al., Appl.Phys.Lett. **71** (1997) 3755.

Optical and Luminescent VUV-Spectroscopy of $La_2Be_2O_5$ Single Crystals

V.A.Pustovarov, A.V.Kruzhalov. V.L.Petrov, B.V.Shulgin, M.Kirm[1], G.Zimmerer[1] and E.I.Zinin[2]

Urals State Technical University, Experimental Physics Department
620002, Ekaterinburg, K-2, Russia
[1] II. Institut of Experimental Physics, Hamburg University, D22761 Hamburg, Germany
[2] Budker Institute of Nuclear Physics of Academy of Science, 630090, Novosibirsk, Russia

Abstract. The time-resolved emission spectra under excitation by synchrotron radiation of X-ray and VUV energy regions as well as by pulse electron beams, the time-resolved luminescence excitation spectra and reflection spectra, the decay kinetics of luminescence have been studied for pure and Ce-doped lanthanum beryllate crystals. The energy levels diagram and the energy gap was established. The excitonic states of the valence band are not displayed in spectra of the optical constants. The bifurcation of radiation relaxation of electron excitations is observed. The slow component in the luminescence spectra corresponds to emission of self-trapped excitons (STE), formed by a recombination pathways, the fast component can correspond to emission of relaxed metastable excitons from STE states.

Keywords: time-resolved spectroscopy, luminescence, excitonic states, oxide crystals, $La_2Be_2O_5$.

Introduction

The luminescence of triplet self-trapped excitons (STE) in the well-know alkali halide crystals is created by recombination pathway or directly through excitation of unrelaxed excitons [1]. At the same time for some complex oxide crystals, for oxides of metals of III group [2-4] the branching of radiative relaxation of electronic excitations (EE) takes place, in this case the direct optical creation of STE and their creation at recombination of electrons with holes give a different radiative states.

The lanthanum beryllate crystals used in laser and scintillation engineering. The significant interest to these crystals has occurred after observation in $La_2Be_2O_5$-Nd crystals of the effect of stimulation radiation [5]. The detailed spectroscopy researches of these doped crystals in the region $E<E_g$ were carried out in work [6]. In the fundamental absorption region the optical properties and efficiency of luminescence excitation were briefly investigated only in work [7]. At the same time the detailed research of EE structure and the processes of radiative relaxation permit to reveal in a considered context the characteristic features of EE in this class of oxides. On the one hand the motive of crystal structure of $La_2Be_2O_5$ crystals is similar with those of BeO crystals (deformed tetrahedrons BeO_4), for which in the optical spectra and in the processes of radiative relaxation of EE the excitonic states are expressed very brightly [8]. On the other hand for the compounds of transition d-metals (e. g., Sc_2O_3 [2,3], LaF_3 [9]) the manifestation of anion exciton states are completely away in optical spectra, that is determined by pd- genealogy of the top of the valence band (VB) and of the bottom of the conduction band (CB).

In the present work the reflection spectra, the time-resolved luminescence spectra and decay kinetics of luminescence under X-ray and selective VUV excitations as well as the

time-resolved luminescence excitation spectra are investigated in the range 5-35 eV at T= 295 and 10 K in pure and Ce^{3+} -doped $La_2Be_2O_5$ crystals.

Experimental details

The samples were grown by Dr.V.Matrosov, the Czochralski method was used. The crystalline structure (space symmetry group C^6_{2h} (C2/), z=4, parameters of elementary cell: a=7,5356A, b=7,3436A, c=7,4387A, β=$91^0$33') formed by deformed tetrahedrons BeO_4, in then inserted asymmetry the ions La^{3+} (the point group C_1), coordinated by ten oxygen ions [10]. The crystals were certificated by X-ray methods, the samples were produced in the form of polished plane-parallel plates (∅10-15 mm, h=1 mm). The measurements were carried out on the storage ring VEPP-3 (excitation by X-ray photons) [11] and on the SUPERLUMI station of HASYLAB (excitation by VUV photons) [12]. The excitation spectra were normalized to quantum intensities of synchrotron radiation (SR) falling into the crystal. The emission spectra in visible and UV region were analyzed by a B&M (Czerny-Turner sheme) secondary monochromator with a photomultiplier R2059 (Hamamatsu). The emission spectra were not corrected on spectral sensitivity of optical tract. The excitation spectra were measured for time-integrated (steady-state) luminescence as well as for the emission detected within time windows (length Δt_i) correlated with the excitation pulse of SR (delayed by δt_i). The delay δt and length Δt were equal to 2,2 and 8,2 ns for fast component, 23,5 and 111 ns for slow component respectively. The reflection spectra were measured at SR incidence angle of $17,5^0$.

Results and discussion

The reflection spectrum (RS) in the energy region 5-35 eV has two groups of bands at energy of 7-12 and 17-27 eV, Fig. 1. The analysis of the photoelectron spectra and the accounts of the electron structure executed for $La_2Be_2O_5$ in work [13], as well as the observed essential analogy with RS of LaF_3 [9] allow us to connect the low energy bands 7,0 and 10.4 eV with the transition of electrons from VB, formed by the 2p-states of oxygen, to CB,

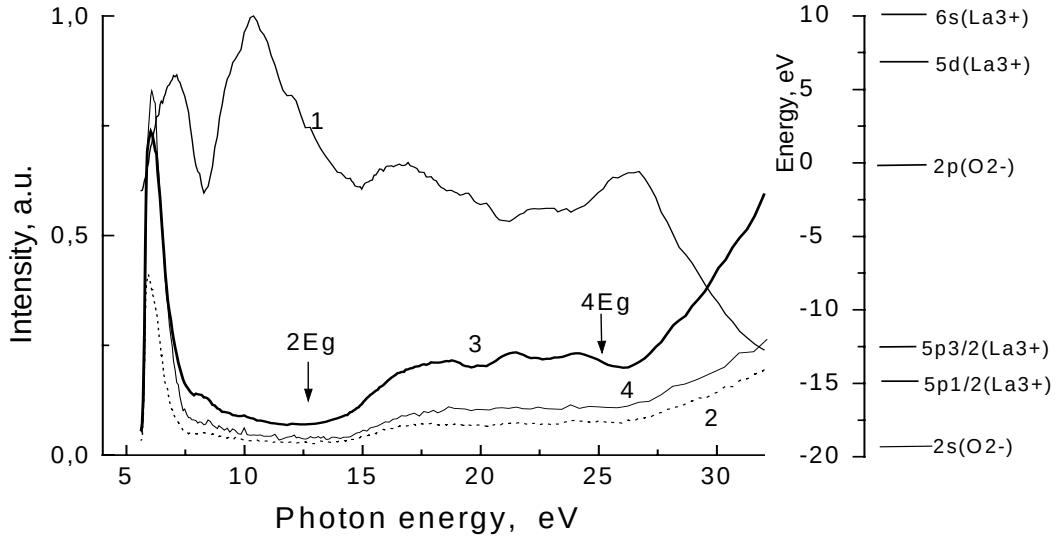

Figure 1. The reflection spectrum (1) and luminescence excitation spectra ($E_{emission}$=3,3 eV) of fast (2) and slow (3) components of decay kinetics of $La_2Be_2O_5$ crystals; the steady-state luminescence excitation spectra of Ce^{3+} centers ($E_{emission}$=2,7 eV) of $La_2Be_2O_5$-Ce (0,5 mol.%) crystals (4). T=10,8 K. To the right - the energy levels diagram of $La_2Be_2O_5$ crystals.

formed of 5d- and 6s-states of La^{3+}-ions. The manifestations of anion excitonic states in the region of longwavelength edge of fundamental absorption (LEFA) in RS do not take place. Therefore the band-gap energy E_g was determined on the basis of excitation spectra measurements, of low temperature thermostimulated luminescence and of the Urbach's rule (E_0=6,3 eV, σ_0=0,44, $\kappa_0=4x10^5$ cm^{-1}) [7]: at T=80 K E_g=6,2-6,5 eV. The bands in RS at energies higher more than 15 eV corresponds probablly to the transitions from 2p-states of oxygen to the higher states of CB. The structure at energies 19,4 and 20,3 eV corresponds to excitation of $5p_{3/2}$ $5p_{1/2}$ - levels of La^{3+} -ions (probablly it is a cation exciton). The transitions from 2s-levels of O^{2-} -ions form a peak 26,5 eV in RS. Fig.1 shows also the energy levels diagram.

The broad emission band ($_m$=3,34 eV, FWHM=0,82 eV, quantum yield η=0,5 at 80K) is observed in pure crystals at low temperature in the steady-state luminescence spectra under the X-ray, electron beam or photons (E>5,8 eV) excitations, Fig.2. The decay kinetics of this luminescence under the selective excitation by photons in the LEFA region or by photons with energy $E>E_g$ contains the fast (τ=1,7ns) and slow (microsecond time-range) components, Fig.3. The decay kinetics of slow component is nonexponential (under the electron beam pulse: $\tau_{1/2}$=8 μs at 80 K). The steady-state and slow luminescence spectra are identical.

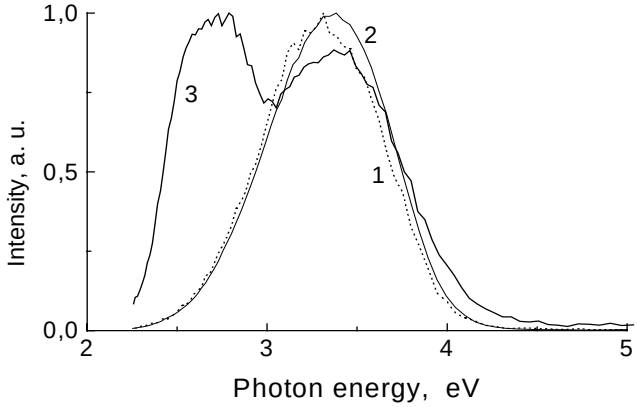

Figure 2. The fast (1), slow (2) and steady-state (3) luminescence spectra of $La_2Be_2O_5$ (1,2) and $La_2Be_2O_5$-Ce (0,5 mol.Vo) (3) crystals. $E_{excitation}$=6,2 eV, T=10,8 K.

The maximum of the fast luminescence spectrum has some shift to the low energy region ($_m$=3,30 eV, FWHM=0,78 eV), Fig.2. The luminescence excitation spectra (LES) of the fast and slow components have no bands at the energy less than LEFA. Both emissions are excited exclusively only in the LEFA region as well as in the region of a creation of the separated electron-hole pairs, Fig1. The luminescence excitation spectra of fast and slow components are different in the LEFA region. The maximum of the fast component LES ($_m$=5,94 eV, FWHM=0,78 eV) has a displacement to smaller energy with respect to a maximum of slow component LES ($_m$=6,05 eV, FWHM=1,02 eV). At $E>E_g$ the quantum yield of both emissions decreases. It is due to an increase of an absorption factor and losses of energy near the surface. The increase of both emissions is observed at the energy E>14 eV ($E>2E_g$). The region 19-21 eV corresponds to excitation of 5p levels of lanthanum ions, the RS and LES have an antibathic character. The second region of increase of quantum yield of fast, slow and steady-state emissions is observed in the energy E>4Eg, Fig.1. The effect of photon multiplication is displayed. The photoelectron spectral data [13] are specified, that the width of a valence band (E_v) is equal approximately 10 eV in $La_2Be_2O_5$ (as well as for the majority of oxide crystals $E_v>E_g$). This circumstance and availability of two thresholds of a quantum yield increase in the region $(2-4)E_g$ according to modern representations of the photon multiplication theory [14] allow us to conclude that the electron-hole mechanism of photon multiplication as a result of the nonelastic scattering of both hot photoelectrons and hot photoholes is realized in $La_2Be_2O_5$.

The emission spectrum of C^{3+}-doped $La_2Be_2O_5$ crystals has a broad intense band (E_{emiss}=2,66 eV, FWHM=0,4 eV, η= 0,4, τ=29 ns at 300 by direct selective 3,5-4,7 eV

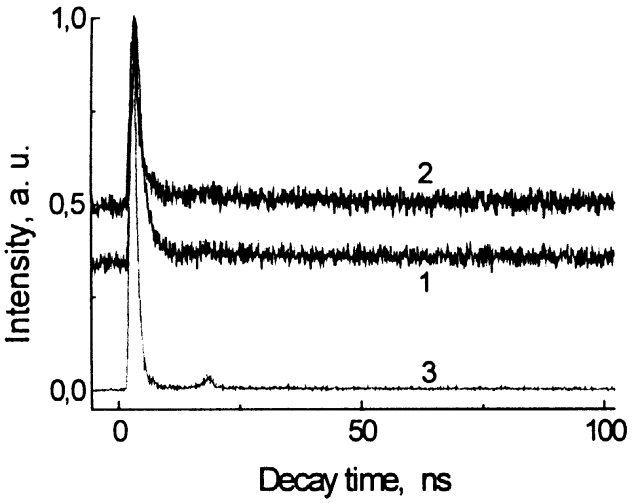

Figure 3. Decay kinetics of the luminescence ($E_{emission}$=3,3 eV) of $La_2Be_2O_5$ crystals, $E_{excitation}$=6,2 eV (1) and 21,4 eV (2), T=10,8 K. The exciting pulse of synchrotron radiation - (3).

photoexcitation (4f -5d transitions in C^{3+}-ions) and τ=38-45 ns, τ_{rise}=4-6 ns by pulse electron beam or X-ray excitations). The thermoactivation spectroscopy data of irradiated and thermochemical reduced crystals [7] show, that the excitation of C^{3+}-centers is due to the electronic recombination mechanism under excitation in the LEFA region or in $E>E_g$ energy region: ($Ce^{3+} + h^+ \rightarrow Ce^{4+}$; $Ce^{4+} + e^- \rightarrow (Ce^{3+})^* \rightarrow Ce^{3+} + h\nu$). All peculiarities in the LES of C^{3+}- centers (including the photon multiplication effect) correspond to the LES (emission 3,34 eV) of a pure crystal, Fig.1. However, it should be noted that the migration losses [15] (compared to emission 3,34 eV in pure crystal) at energy transfer to impurity centers are higher, and a narrow dip in LES of C^{3+}- emission at 7-14 eV confirms this fact. These parameters of Ce-emission and the brightly expressed effect of photon multiplication at energy $E>2E_g$ allows us to offer and use $La_2Be_2O_5$-Ce crystals as scintillation materials [16].

All set of the experimental data confirms the assumption [7] about intrinsic character of the 3,34 eV emission in the pure crystals $La_2Be_2O_5$. Availability of this emission in the spectrum of thermostimulated luminescence directly points to its recombination origin. A splitting of p-states of a valence band in a field of a low symmetry occurs in oxide crystals, therefore one of p-orbital appears as a nonbinding one [2]. The hole mass for a nonbinding p-orbital can be more higher than that for the other valence band, and because of this, there are prerequisitions for self-trapping of this hole. At the present time on the basis of a similarity between $La_2Be_2O_5$ and the binary or complex oxides (for example, $CaWO_4$ [4]) one can envisage that the 3,34 eV emission band in pure $La_2Be_2O_5$ is a result of recombination of electrons with self-trapped holes in the form of the O^- type polarons of a small radius.

The absence of excitonic manifestation in RS of $La_2Be_2O_5$ in the LEFA region as well as this for compounds of transition d-metals is determined by pd- genealogy of the valence band top and the conduction band bottom. In addition, the availability of the vacant 4f-levels can significantly shorten a life time of the 5d-states of La^{3+}-ions, as it was suggested in Ref.[9] for LaF_3, therefore the excitonic states should be metastable. At the same time, the value of the parameter σ_0=0,44 in the Urbach's rule for $La_2Be_2O_5$ points out on the strong exciton-phonon interaction and on the opportunity of self-trapping for excitons. The effective excitation of the fast 3,30 eV component in the LEFA region at lower energy than that for the maximum of LES for the 3,34 eV slow component points out on the bifurcation of an electronic excitation relaxation on different pathways, which is typical for various oxides [2-4]. On the basis of this, we believe, that the anion excitons in $La_2Be_2O_5$ are metastable. In this connection, they have no manifestations in RS, however, they manifest temselves in processes of the radiative relaxation. The radiative transitions from the relaxed STE's states can determine a spectrum of the fast 3,30 eV emission band. The allowed type of these transitions points out on the singlet character of STE. Though the LES (3,30 eV emission) does not correspond absolutly to the general tendency of formation of singlet STE in the well-know alkali halide crystals (primary excitation from the n=2 excitonic states [17]), it reflects a specific character of electronic excitation relaxation in $La_2Be_2O_5$ crystals.

References

1. Ch.Lushchik. Excitons. Nauka, Moskow, 1985.
2. A.I.Kuznetsov, V.N.Abramov, V.V.Murk and B.R.Namozov, Sov. Phys. Solid State **33** (1991) 2000.
3. V.Murk, O.Svinarenkov. Inorganic scintillators and their applications. Delft Univesity Press, Delft, The Nitherlands. (1995). P.227.
4. V.Murk, B.Namozov and N.Yaroshevich, Radiation Measurements **24** (1995) 371.
5. H.P.Jenssen, R.F.Begley, R.Webb, R.C.Moris, J. Appl. Phys. **47** (1976) 1496.
6. A..A.Kaminskii, Ngoc Tran, S.E.Sarkisov, V.N.Matrosov, M.I.Timoshechkin, Physica status solidi (a) **59** (1980) 121.
7. A.V.Kruzhalov, V.A.Pustovarov, A.A.Maslakov, V.L.Petrov and B.V.Shulgin, Optika i spektroskopiia **63** (1987) 457.
8. V.Yu. Ivanov, V.A. Pustovarov, A.V. Kruzhalov and B.V. Shulgin, Nucl. Instr. and Meth. in Phys. Res. **A282** (1989) 559.
9. C.G.Olson, D.W.Lynch and M.Piacentini, Phys. Rev. **B18** (1978) 5740.
10. L.A.Harris, R.Yakel, Acta Cryst. **B24** (1968) 672.
11. V.A.Pustovarov, E.I.Zinin, A.L.Krymov, B.V.Shulgin, Review of Scientific Instrum. **63** (1992) 3521.
12. G.Zimmerer, Nucl. Instr. and Methods in Phys. Res. **A308** (1991) 178.
13. T.A.Betenekova, A.V.Kruzhalov, N.M.Osipova, V.P.Palvanov, V.L.Petrov, I.N.Shabanova, Sov. Phys. Solid State **25** (1983) 175.
14. A.Lushchik, E.Feldbach, R.Kink, Ch.Lushchik, M.Kirm and I.Martinson. Phys. Rev. **B53** (1996) 5379.
15. A.N.Vasil'ev, V.V.Mikhailin and I.V.Ovchinnikova, Izvestia Akademii Nauk USSR, ser. fiz. **49** (1985) 2044.
16. L.V.Viktorov, A.V.Kruzhalov, A.A.Maslakov, V.L.Petrov, B.V.Shulgin and V.N.Matrosov, Copyright certificate USSR N921328. Bull. Izobretenii **14** (1982).
17. T.Matsumoto, M.Shirai and K. Kanno, J. Phys. Soc. Japan **64** (1995) 987.

Decay kinetics of d-f emission and thermoluminescence of $LiYF_4$ doped with rare earth ions (Ce^{3+}, Pr^{3+}, Nd^{3+})

N.Yu.Kirikova[1], A.N.Belsky[2], B.Chassigneux[3],
J.C.Krupa[3], V.N.Makhov[1] and M.Queffelec[3]

[1]*Lebedev Physical Institute, Leninsky Prospect 53, Moscow 117924, Russia*
[2]*Physics Department, Moscow State University, Moscow 117234, Russia*
[3] *Institut de Physique Nucleaire, 91406 Orsay Cedex, France*

Abstract. The energy, temperature and concentration dependencies of 5d - 4f emission decay kinetics were measured for series of powder samples of $LiYF_4$ doped with Ce^{3+}, Pr^{3+} and Nd^{3+}. It was found that decay curves have rise-on stage which starts at excitation energies a few eV higher than the fundamental absorption edge of the matrix and disappears at low enough temperatures and at high enough concentration of the dopant. The thermoluminescence of Ce^{3+}-, Pr^{3+}- and Nd^{3+}-doped and undoped $LiYF_4$ irradiated by monochromatised VUV synchrotron radiation has been studied in the temperature range 30-400 K. It was shown that the shallow traps with activation energy about 0.11 eV are responsible for the delayed charge transfer to emission centers in rare earth doped $LiYF_4$. The thermal release of this trap at 80 K corresponds well to thermally activated diffusion of self-trapped holes (V_k-centers).

Keywords: 5d-4f luminescence; Rare earth ions; Fluoride crystals;
Time–resolved spectroscopy; Thermoluminescence.

Introduction

Fluoride crystals doped with Ce^{3+}, Pr^{3+} or Nd^{3+} show fast emission with decay time of the order 10 ns which is caused by parity-allowed 5d → 4f transitions in rare earth ion. Due to this fact such crystals are extensively studied as promising fast scintillators for different applications [1]. The light yield and decay kinetics of the scintillation depend strongly on the dominant mechanism of the energy transfer from the matrix to the emission center. In particular, charge trapping processes can give considerable fraction of the slow component in scintillation kinetics (see, for example, [2-4]) that restricts time resolution of scintillators based on 5d → 4f luminescence in rare earth ions.

As it was reported in [2-4], at high energy excitation the decay kinetics of 5d → 4f emission of Ce^{3+}, Pr^{3+} and Nd^{3+} doped into $LiYF_4$ crystal is strongly non-exponential with considerably longer effective decay time than the lifetime for the 5d → 4f transition and with a distinct initial rising stage. It starts at excitation energies a few eV higher than the fundamental absorption edge of the matrix and disappears at low enough temperatures and at high enough concentration of the dopant. The model proposed in [2-4] for the explanation of this feature was based on the assumption of the existence of some traps which delay the charge transfer from the matrix to rare earth ions. However the problem under question what is the nature of the traps and which kind of carriers (holes or electrons) are captured on the traps. Thermoactivation spectroscopy is one of the most powerful technique for studies of traps and recombination centers in crystals.

Experiment

In the present work the decay kinetics and thermoluminescence (TL) of powder samples of Ce^{3+}-, Pr^{3+}- and Nd^{3+}-doped and undoped $LiYF_4$ irradiated by VUV synchrotron radiation (SR) has been studied in the temperature range 30-400 K. The measurements were carried out at station SA61 of SR source Super-ACO at LURE in Orsay. The 3-meter normal incidence monochromator was used for spectrally selective irradiation (in the range 5-30 eV) of samples mounted in a continuous flow helium cryostat. The TL was detected simultaneously by two channels equipped with photomultipliers and optical filters for spectral selection of different bands in the spectra of TL. The typical time of irradiation was 10 minutes and heating rate 0.1 K/s. Decay kinetics measurements were based on the single-photon-counting technique.

The powder samples of doped and undoped $LiYF_4$ were obtained by the high temperature diffusion technique. Mixtures of commercially available high purity fluorides and NH_4F, HF as agent, were heated in a platinum crucible contained in a nickel tube under argon gas circulation.

Results

The glow curves of doped and undoped $LiYF_4$ irradiated at 30 K by SR with different photon energies are shown in Figs.1-3. In case of Pr^{3+}- or Nd^{3+}-doped $LiYF_4$ one channel with UV filter detected 5d-4f luminescence of rare earth ion (two bands around 181and 230 nm for Nd^{3+}; two bands between 215 and 240 nm for Pr^{3+}). This channel could partly detect luminescence of self-trapped excitons (STE, the wide band centered at 290 nm [5]). Second channel with filter for visible spectral range detected 4f-4f luminescence of the doping ion (for Pr^{3+}- and Nd^{3+}-doped samples). In case of Ce^{3+}-doped $LiYF_4$ the 5d-4f luminescence of Ce^{3+} (the band around 300 nm) was detected via filter for visible light while 4f-4f luminescence of Ce^{3+} could not be detected by second channel because it is observed in the infra-red. Unfortunately we were not able to separate completely STE and 5d-4f luminescence due to their spectral overlapping.

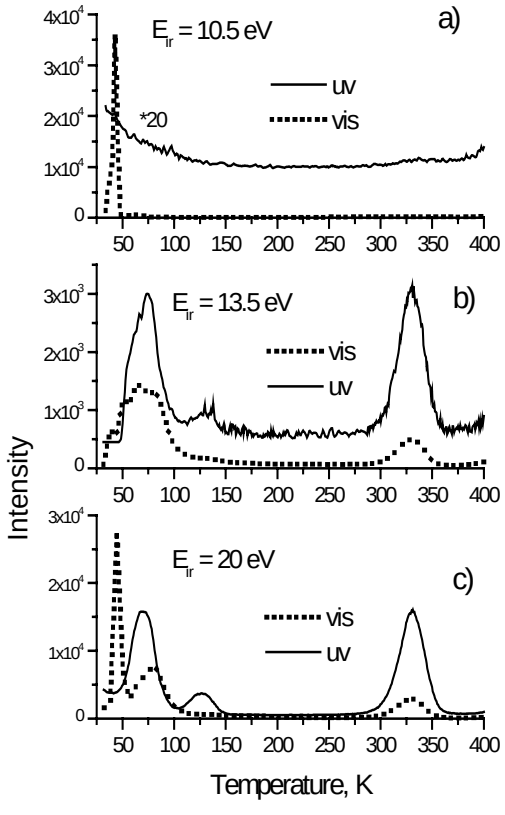

Fig .1. Thermoluminescence glow curves for $LiYF_4$:Pr^{3+}(1%), irradiated at 30 K by photons with energies: a) 10.5 eV; b) 13.5 eV; c) 20 eV.

The main features of the glow curves are as follows. "Pure" $LiYF_4$ has only two well pronounced peaks at 80 and 135 K. When UV emission is detected the strong and relatively wide peak at 70-80 K (probably it consists of two adjacent peaks) and the weak peak at about 130 K were observed for all doped $LiYF_4$ except for highly (5%) Pr^{3+}- doped sample. In the latter case, in this temperature range only very weak peak is observed at about 115K. The peak at about 80 K was also observed for $LiYF_4$:Pr^{3+}(1%) when visible emission was detected but the peak had slightly different shape than in case of UV emission detection. For $LiYF_4$:Nd^{3+}(1%)

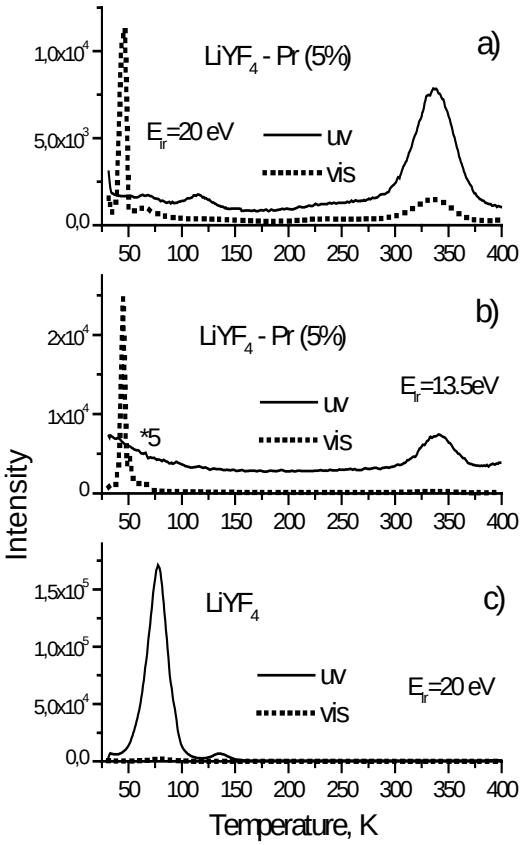

Fig.2. Thermoluminescence glow curves for $LiYF_4:Pr^{3+}$(5%), irradiated at 30 K by photons: a) 20 eV and b) 13.5 eV; c) for undoped $LiYF_4$, irradiated at 30 K by 20 eV photons .

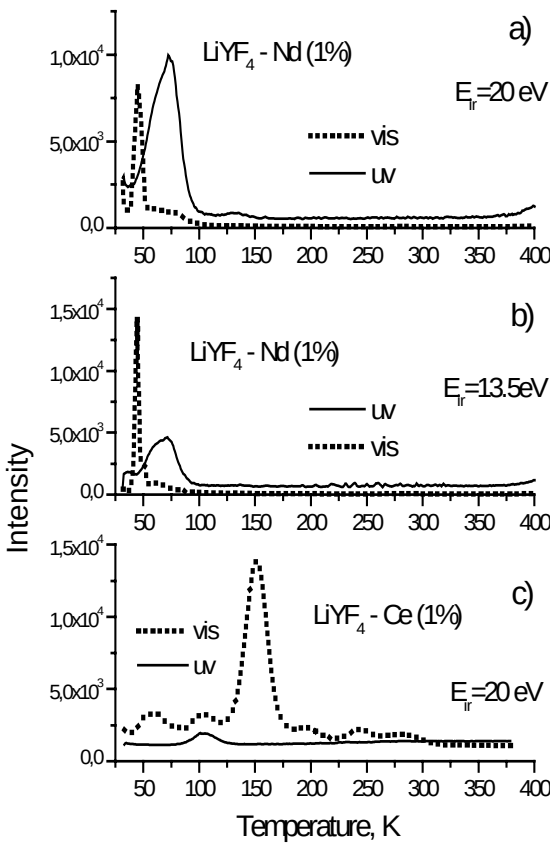

Fig.3. Thermoluminescence glow curves for $LiYF_4:Nd^{3+}$(1%), irradiated at 30 K by photons: a) 20 eV; b) 13.5 eV; c) for $LiYF_4:Ce^{3+}$(1%), irradiated by 20 eV.

sample the peak in this temperature range was very weak for visible emission. The strong peaks were observed at temperatures about 150 K in Ce^{3+}-doped $LiYF_4$, at about 330 K in Pr^{3+}-doped $LiYF_4$ and at higher than 400 K (we were not able to perform measurements at such a high temperature) in Nd^{3+}-doped $LiYF_4$ for both UV and visible emission. It was checked that the peak at 330 K in $LiYF_4:Pr^{3+}$ existed also if the sample was irradiated at 175 or 295 K. The narrow and strong peak at 45 K was detected for visible emission in all Nd^{3+}- and Pr^{3+}-doped $LiYF_4$. This peak was absent for undoped and Ce^{3+}-doped $LiYF_4$.

When doped $LiYF_4$ was irradiated by 13 eV photons the intensity of all peaks became considerably less than in case of irradiation by 20 eV photons. Irradiation by 10.5 eV photons created only one intense peak at 45 K (for visible emission) and no any other peaks at higher temperatures.

The depths of traps responsible for peaks in the glow curves at 80 K in undoped $LiYF_4$, 150 K in $LiYF_4:Ce^{3+}$ and 330 K in $LiYF_4:Pr^{3+}$ can be estimated by the well known formula [6]: $\varepsilon = 2.35 \cdot kT_m \cdot T_m/\Delta T_{1/2}$ where k is Boltzman constant, T_m is temperature at peak maximum, $\Delta T_{1/2}$ is half width at half maximum of the peak. The estimations give values of ε = 0.11, 0.44 and 1.4 eV respectively. The peak at 70-80 K in doped $LiYF_4$ is probably not a single peak, so the depth of this trap cannot be calculated. However it could be suggested that the main part of this peak corresponds to 80 K peak in undoped sample.

Decay curves of 5d → 4f emission for Pr^{3+} in $LiYF_4$ are presented in Figs.4,5. The behavior of Ce^{3+}, Pr^{3+} and Nd^{3+} decay kinetics is similar. It is mono-exponential (with $\tau \sim 35$ ns for Ce^{3+}, 18 ns for Pr^{3+} and 23 ns for Nd^{3+} in $LiYF_4$ at 300 K) at excitation in the spectral region of the direct 4f - 5d absorption and has a distinct rise-on stage at excitation in the intrinsic absorption region of the matrix (Fig.4), i.e. the delay in the energy transfer from the matrix to the emission centre is observed. The time profiles of Pr^{3+} emission have been measured at a number of temperatures between 200 and 350 K. In Fig.6 one can see the natural log of rise times found from fits of time profiles obtained under the 20 eV excitation versus inverse temperature. The rise-on stage in the kinetics disappears at high enough dopant concentrations (Fig.5) and τ of it grows strongly at lowering temperature (Fig.6).

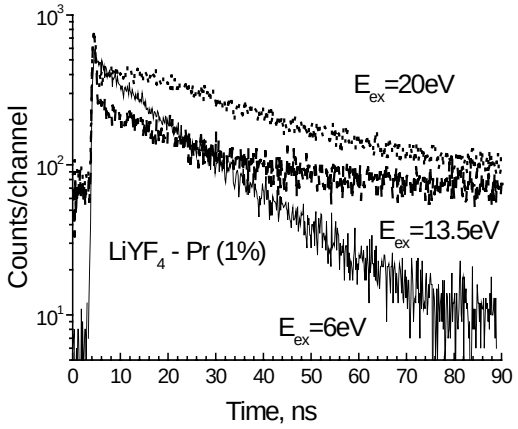

Fig.4. Decay curves of 5d → 4f emission of $LiYF_4:Pr^{3+}$(1%) measured at excitation photon energies: 6 eV, 13.5 eV, 20 eV.

Discussion

The peaks observed at 150 K in $LiYF_4:Ce^{3+}$, 330 K in $LiYF_4:Pr^{3+}$ and T > 400 K in $LiYF_4:Nd^{3+}$ are obviously due to thermally activated release of carriers from traps directly related to impurity ions themselves. The peak at 45 K can be due to the thermal motion of some defects in the lattice of crystal. If one supposes that the quality of studied samples is good enough, the traps for carriers responsible for the peak at 80 K in $LiYF_4$ should be of intrinsic nature. The peak has maximum intensity in "pure" crystal when only small part of carriers is captured by some impurity ions. This peak is situated at temperature which is characteristic for the thermally activated motion of self-trapped holes (STH) in $LiYF_4$ [7].

However, the exact nature of the trap responsible for the peak 80 K and the sign of carriers (hole or electron) captured on this trap are still unclear. As was mentioned before, one possible mechanism of delayed charge transfer to emission center could be hole self-trapping. In this case it is necessary to suggest that electrons are captured first on the emission center. For example, for Nd^{3+} ion the first stage of the process should be: $Nd^{3+} + e^- = Nd^{2+}$, and at temperatures higher than 80 K the holes diffuse through the crystal and recombine with electrons on the center: $Nd^{2+} + e^+ = (Nd^{3+})^* = Nd^{3+} + h\nu$. However, if for Nd^{3+} ion such mechanism is in principle possible, for Pr^{3+} and especially for Ce^{3+} ion which is a typical hole center, the electron capture at the first stage of recombination mechanism is practically impossible.

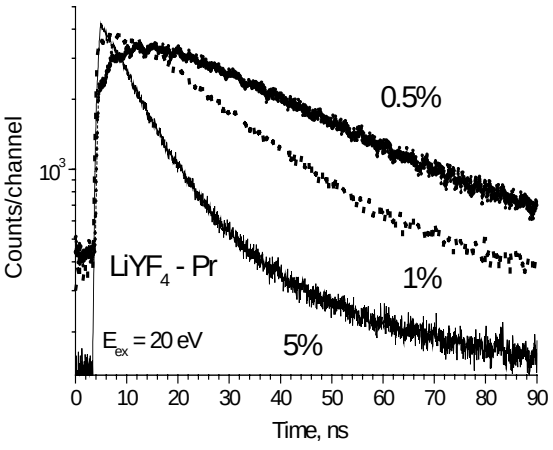

Fig.5. Concentration dependence of the $LiYF_4:Pr^{3+}$ 5d → 4f emission decay curves at 300 K. Excitation energy was 20 eV.

If one supposes that electron is captured at first not on emission center itself but at another defect situated near this center, e.g., on anion (fluorine) vacancy, forming F-center, then recombination of STH (thermally diffused along the crystal) with an electron at F-center can result in creation of STE. If the energy of STE is high enough (exceeds the energy of 5d-4f absorption in rare earth ion) the non-radiative energy transfer from STE to neighboring rare earth ion can occur. In case of Ce^{3+}- and probably Pr^{3+}-doped $LiYF_4$ such mechanism can explain the delay in the energy transfer from the matrix to emission centers. However this mechanism cannot work for Nd^{3+} because of the high energy of its 4f-5d absorption compared with the energy of STE emission in $LiYF_4$.

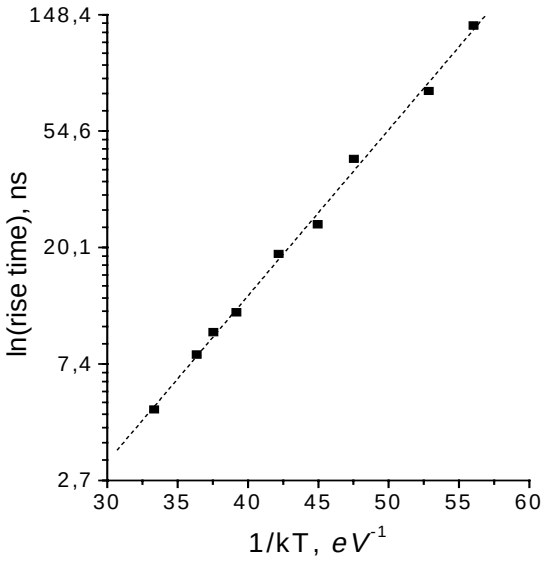

Fig.6. Rise time temperature dependence of Pr^{3+} 5d-4f emission under pulsed 20 eV excitation.

Thermal diffusion of STH can result also in its trapping by rare earth ion which did not capture any carriers during irradiation. In case of Ce^{3+} as an example the reaction would be: $Ce^{3+} + e^{+} = Ce^{4+}$. If F-center was created near this ion (as a result of electron capture by fluorine vacancy) the tunnel recombination of electron from this F-center with the hole on the ion will lead to the appearance of the excited state of the ion and correspondingly to the luminescence of the emission center: $Ce^{4+} + e^{-} = (Ce^{3+})^* = Ce^{3+} + h\nu$. Such process will have large enough yield if one supposes that many rare earth ions have fluorine vacancy in their neighbor, i.e. doping of $LiYF_4$ by light rare earth ions creates considerable distortion of the crystal lattice.

We estimated the value of the band-gap for $LiYF_4$ as $E_g \sim 12.5$ eV [8]. Irradiation by 20 eV corresponds to the creation of electron-hole pairs with high enough kinetic energy. So carriers in the pair become well separated and can be captured by different traps. This leads to the appearance of different intense peaks in glow curves and of the rise-on stage in decay profile (Fig.4). At photon energies $h\nu \geq E_g$ (13 eV) the direct recombination of electrons and holes on emission centers is dominant, so only small part of carriers will be captured by traps and the intensity of TL will be small. At high enough concentration of doping ions almost all carriers will be captured by these ions and so no peaks in the glow curve which are related to another traps (in particular, to thermally activated motion of STH) will be observed (compare glow curves for $LiYF_4$: 1%Pr^{3+} and $LiYF_4$: 5%Pr^{3+}). This explains the absence of rising stage in decay kinetics for highly doped crystals (Fig.5). Irradiation of the crystal by 10.5 eV photons, i.e. in the excitonic region (the first exciton peak in $LiYF_4$ is situated at 11.5 eV [8]) leads to the creation only of some defects in the lattice but no free carriers are created and captured on the traps.

If the delay in the energy transfer from the matrix to rare earth ions in $LiYF_4$ is due to thermal release of carriers from the traps the rise time in decay kinetics of 5d-4f emission should be determined by the trap lifetime τ which depends on temperature as $\tau \sim e^{\varepsilon/kT}$. If we take $\varepsilon = 0.11$ eV and a rise time at 300 K $\tau \sim 10$ ns (as is the case for Pr^{3+} in $LiYF_4$:1%Pr^{3+} (Fig.6)) then at 400 K the rise time will be about 3 ns and at 150 K $\tau > 1$ μs. These estimations are very close to experimental results on temperature dependence of Pr^{3+} 5d-4f luminescence decay kinetics in $LiYF_4$:1%Pr^{3+} (Fig.6). The rising stage in decay kinetics in

fact disappears at temperature T ~ 200 K (decay time at this temperature for Pr^{3+} 5d-4f luminescence in $LiYF_4$ is about 15 ns) but the fraction of the slow component becomes observable.

The activation energy value of nearly 0.14 eV obtained from the experimental rise time dependence curve agrees reasonably well with that of about 0.11 eV calculated using the glow curves. This is one more argument which supports our assumptions.

Thus the obtained results on TL studies of rare earth doped $LiYF_4$ are consistent with the model of carrier capture on some intrinsic traps (responsible for the peak 80 K in the glow curves) which was proposed for the explanation of non-exponential decay kinetics of 5d-4f luminescence of rare earth ions in this matrix.

Conclusions.

The measurements of TL glow curves after spectrally selective irradiation of samples by VUV radiation provide new information about the nature of carrier traps in wide band-gap materials. The TL of powder samples of undoped and Ce^{3+}-, Pr^{3+}- and Nd^{3+}-doped $LiYF_4$ irradiated by VUV SR has been studied in the temperature range 30-400 K. The results were analyzed on the basis of conventional models for the energy transfer and charge trapping in wide band-gap crystals. It was shown that the shallow traps with activation energy about 0.11 eV are responsible for the delayed charge transfer to emission centers observed in rare earth doped $LiYF_4$. The thermal release of this trap at 80 K corresponds well to thermally activated diffusion of STH (V_k-centers). However the additional studies are needed to find out the exact nature of the traps.

Acknowledgements

The support of the Federal Program “Integration“ and the Network 'Formation Recherche Pays Europe Centrale et Orientale' are gratefully acknowledged.

References

1. Proc. Int. Conf. SCINT’95, Delft, The Netherlands, Ed. by P.Dorenbos and C.W.E. van Eijk, Delft University Press, 1996.
2. A.N.Belsky, P.Chevallier, J.Y.Gesland, N.Yu.Kirikova, J.C.Krupa, V.N.Makhov, P.Martin, P.A.Orekhanov and M.Queffelec, J.Lumin. 72-74 (1997) 146.
3. I.H.Munro, C.Mythen, D.A.Shaw, I.A.Kamenskikh, N.Yu.Kirikova, V.N.Makhov, J.C.Krupa and M.Queffelec, Daresbury Laboratory Annual Report 1996-97, p.342.
4. J.C.Krupa, B.Chassigneux, M.Queffelec, N.Yu.Kirikova, V.N.Makhov, I.H.Munro, C.Mythen and D.A.Shaw, Daresbury Laboratory Annual Report 1997-98, p.368.
5. W.Hayes, M.Yamaga, D.J.Robbins and B.Cockayne, J.Phys.C: Solid State Phys. 13 (1980) L1011.
6. A.N.Vasil’ev and V.V.Mikhailin, Introduction in Solid State Spectroscopy, Moscow University Press, Moscow, 1987.
7. G.M.Renfro, L.E.Halliburton, W.A.Sibley and R.F.Belt, J.Phys.C: Solid State Phys. 13 (1980) 1941.
8. A.N.Belsky, P.Chevallier, J.Y.Gesland, N.Yu.Kirikova, J.C.Krupa, V.N.Makhov, P.Martin, V.V.Mikhailin and M.Queffelec, to be published.

Investigation of core-valence luminescence under the protons excitation

O.V.Rvaboukhin. V.Yu.Ivanov, A.V.Kruzhalov. F.G.Neshov

Urals State Technical University, Mira 19, 620002 Ekaterinbiirg, Russia

Abstract. Experimentally investigated ion luminescence of wide gap CsCl and BaF_2: crystals effected by protons of various energies. Under the action of 6.7 MeV protons 4.8. 5.2 eV bands in CsCl and 5.6 eV band in BaF_2 were registered, as a result of core-valence transitions.

Keywords: cross-luminescence

It's known that luminescence of visible region 4.8.-5.2 eV in CsCl and 5.6 eV in BaF_2 as a result of core-valence transitions (cross-luminescence) have a low ions excitation efficiency. We assume the existence of possibility of increasing cross-luminescence (CRL) yield by varying ion's types, energies and irradiation regimes. This work was performed at the Urals State Technical University cyclotron optic channel [1]. The possibility of FT excitation of CRL in wide gap crystals CsCl and BaF_2 were investigated. The protons with energies 0.7, 1, 3 and 6.7 MeV were used. Under the action of 6.7 MeV protons the 4.8.-5.2 eV in CsCl and 5.6 eV in BaF2 cross-luminescence were registered. There was no CRL (or it was too small) observed under the action of low energy H^+ (0.7 MeV) and CRL effected by 1 and 3 MeV protons appeared in a form of weak bands (see fig.1). Besides of CRL yield increasing we observed a gradually quenching of 4.1 eV luminescence of self-trapped excitons (STE) with increasing irradiation dose, and samples became blue colored (see fig.2).

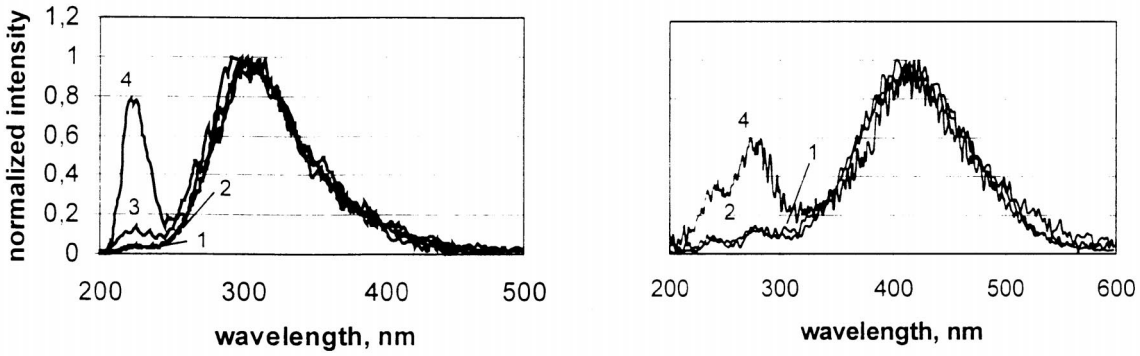

Figure 1. Luminescence spectra of BaF_2 (a) and CsCl (b) effected by protons with energies: 1—0.7 MeV, 2—1 MeV, 3—3 MeV and 4—6.7 MeV

According to existing beliefs, for increasing cross-luminescence probability it's necessary provide inverse occupancy of valence and core bands. Low energy ions interact, in general. with electrons of valence band and do not attain core band. That is decrease probability of inverse occupancy and consequently reduce CRL output. With the ion energy rise. effective ionization profile of internal electron K and L shells is increased. Electrons of upper shells including core electrons occupy hole vacancies of K or L shells providing demanded core band inverse occupancy. The same situation we have in case of high energy photon crossluminescence excitation. To analyze this situation we used correlation between E-ion energy and $\lambda \cdot M/m_e$, where λ is bonding energy of electron shell, Mision mass and m_e is

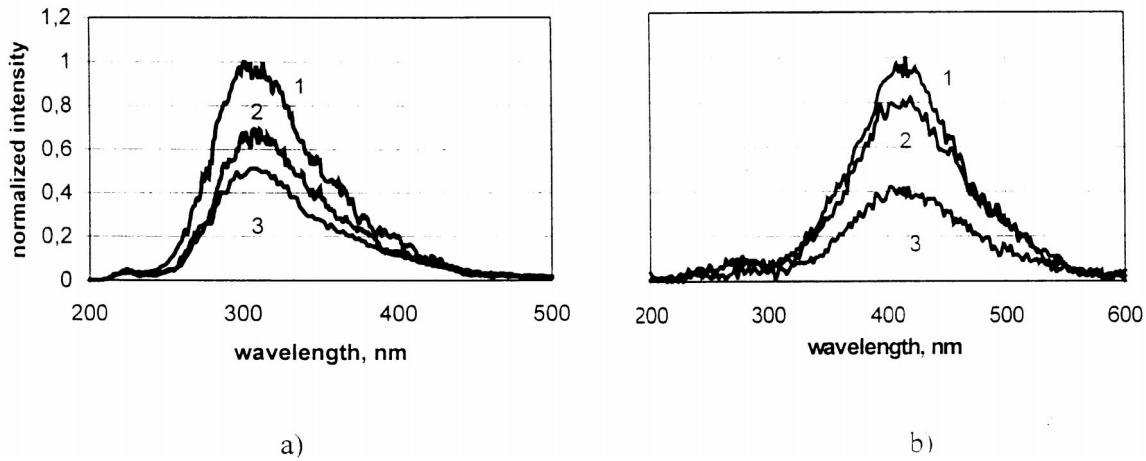

a) b)

Figure 2. Dose dependence of BaF_2 (a: 1—$2.6\times10^{14}sm^{-2}$, 2—$4.8\times10^{14}sm^{-2}$, 3—$8\times10^{14}sm^{-2}$) and CsCl (b: 1—$3.4\times10^{12}sm^{-2}$, 2—6.2×10^{13} sm^{-2}, 3—$4\times10^{14}sm^{-2}$) luminescence quenching under the action of 0.7 MeV protons.

electron mass [2]. When $E \propto \lambda \cdot M/m_e$ ionization profile has a rise proportionally to E^4 and inversely proportional to Z^{12}, where Z-atomic mass number. When $E \approx \lambda \cdot M/m_e$, ionization profile attains maximum and begins decrease. Bonding energy of electron K and L shells is correspondingly 36 and 5.7 keV for Cs, 37 and 6 keV for Ba [3]. From correlation between E and $\lambda \cdot M/m_e$ we can see that ionization profile have maximum under the action of 6.7 MeV protons. And this has to lead to increase of core band inverse occupancy and consequently CRL output.

As for radiation quenching of STE luminescence, it can be connected with effective formation of color centers during FT irradiation. Thus. the created secondary carriers trapped by color centers and consequently STE luminescence reduced.

References

1. O.V.Ryaboukhin, Solid State Detectors. Proceedings of symposium SSD-97, Ekaterinburg. 1998, p.163.
2. V.M.Kolyada, A.K.Zayichenko and R.V.Dmitrenko. X-ray-spectral analysis with ion excitation. Moscow, 1978.
3. A.A.Radtsig, B.M.Smirnov, Atom parameters and atomic ions: handbook, Energyatom Publish house, 1986.

Track effects in crossluminescence

R.A.Glukhov[1,2], C.Pedrini[2], A.N.Vasil'ev[1], A.M.Yakunin[1]

[1]*Synchrotron Radiation Laboratory, Physics Faculty, Lomonosov Moscow State University, 119899 Moscow, Russia*
[2]*LPCML, UMR 5620 CNRS, Université Claude Bernard Lyon-1, 69622 Villeurbanne, France*

Abstract: BaF_2 crossluminescence yield is calculated as a function of ionizing particle type and energy. The simulation is based on the model of interacting thermalized excitations (core holes, valence holes, electrons and self-trapped excitons) in the track region, with density of excitations depending on the particle energy and type.

Keywords: crossluminescence, BaF_2, ionizing particles

Introduction

Crossluminescence in BaF_2 and some other ionic crystals with heavy cations is excited well by high-energy photons and light particles (electrons, muons, etc.) but almost not excited by heavy particles (e.g. α-particles). Heavy particles excite only self-trapped exciton (STE) luminescence. The ratio of fast (crossluminescence, CL) and slow (STE emission) components of scintillator response has been shown by R. Novotny [1] to be applicable to discriminate the particle types.

This effect can be associated with the change of local density of excitations [2] in ionizing particle track in the following way. Crossluminescence is the radiation relaxation of an uppermost core hole located on a cation into a valence hole state. This type of relaxation has low probability (the rate is about 10^9 s^{-1}). If another excitation is located near the core hole, the Auger processes involving this excitation can occur, and in this case the core hole converts into the valence hole without photon emission [3]. The rate of this Auger relaxation strongly depends on distance between a core hole and an additional excitation [3–6]. It increases with the increase of the local density of excitations in the track, which in turn is proportional to stopping power. The excitation local density has a maximum in the core of the track and drops to zero with increase of the distance from the track axis. The relaxation length controls the distribution of excitations at the hot stage of relaxation and thermal diffusion of excitations. Therefore in case of heavy particles with high stopping power the density of electrons, valence holes and excitons in the interior of the track is enough for total quenching of crossluminescence from this region, and only core holes from the exterior part of the track can decay with photon emission.

The numerical simulation of the dynamics of track agrees with the described above picture. The calculations includes (i) the simulation of the track development due to the production of secondary excitations through the inelastic scattering, (ii) track evolution due to the cooling of hot excitations and their diffusion, and (iii) degradation of excitations with various radiative and non-radiative reactions between excitations. The results of simulation of crossluminescence and STE efficiencies and decays are presented for different particles.

Simulation procedure

Ionizing particle creates an excited track region in the crystal. We assume cylindrical symmetry for the track region, and therefore the problem can be solved in cylindrical coordinate system. This supposition can be approved for heavy particle tracks; for electrons this is only rough approximation (the structure of the track is much more complicated). The

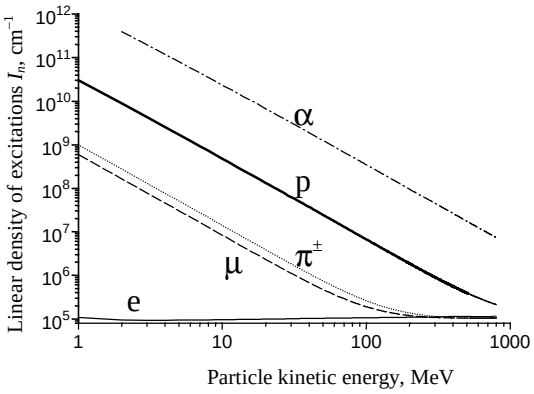

Figure 1. Number of electron-hole pairs for unit length I_n in the track of a particle as a function of its kinetic energy [7]

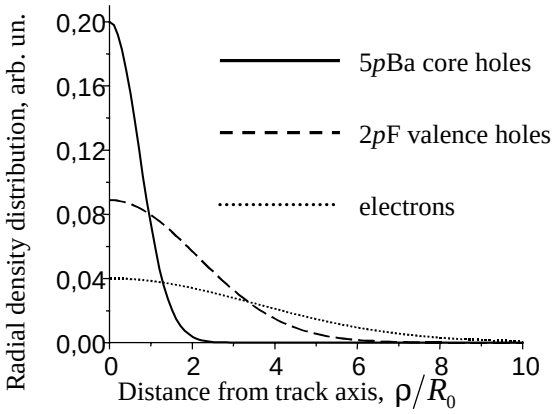

Figure 2. An example of radial distribution of the thermalised excitations across the track

energy deposit dE/dz as a function of particle kinetic energy E is directly connected with linear density of excitations $I_n(E)$ along the track (Fig. 1), if we suppose that the mean energy for creation of an electronic excitation in BaF_2 is about 30 eV. Since energy of the particle decreases along the track (the function $E(z)$ is easily calculated by integrating of dE/dz) we can calculate the dependence $I_n(z)$ on the distance from the track origin. For heavy particles the track length is much larger than its diameter. Therefore we can solve the problem for tracks with constant I_n regarding as a parameter and then average the results over the track.

After the inelastic scattering cascade (with characteristic time of 10^{-15}–10^{-14} s) and thermalization (with characteristic time of 10^{-12}–10^{-11} s) the track consists of electrons in the conduction band, holes in the fluorine valence band and holes in the barium uppermost core band. 2pF holes rapidly transfer to self-trapped states, and we'll not distinguish free holes from self-trapped holes. Electrons and holes are combined with creation of (self-trapped) exciton. The excitons are created during the hot stage of relaxation as well, but their concentration at this stage is negligible. Therefore we can describe the evolution of the track region using four concentrations: $n(\rho,t)$ for electrons, $p(\rho,t)$ for 2pF holes, $c(\rho,t)$ for 5pBa core holes and $s(\rho,t)$ for self-trapped excitons (STE), ρ is the distance from the track axis. The integrals of initial concentrations over the track cross-section $N(0)$ and $P(0)+C(0)$ are equal to $I_n(z)$. The ratio $C(0)/P(0) = 0.1$ is estimated from the CL quantum yield for γ-excitation. The initial distribution of thermalized excitations can be described by Gaussians with different dispersions. Initial distribution profiles for excitations before thermalization are the same, but thermalization is characterized by different diffusion coefficients (the highest for electrons, the lowest for core holes). We suppose that core holes does not migrate during the thermalization, so their space distribution does not changes during thermalization. The radial distributions for valence holes and electrons become broader after the thermalization. Typical distributions of excitations after thermalization are shown in Fig. 2. Since electrons and holes are charged, the electric field $E(\rho,t)$ should be taken into account. Only radial componenr of the field is important for cylindrical symmetry. Dimensionless variable ρ/R_0 is convenient for describing kinetics of electronic excitations in the presence of electric fields. ($R_0 = e^2/\varepsilon kT$ is the Onsager radius, equals to the distance at which Coulomb interaction between an electron and a hole is about thermal energy; here e is the electron charge, k is the Boltzman constant, T is temperature and ε is dielectric permittivity).

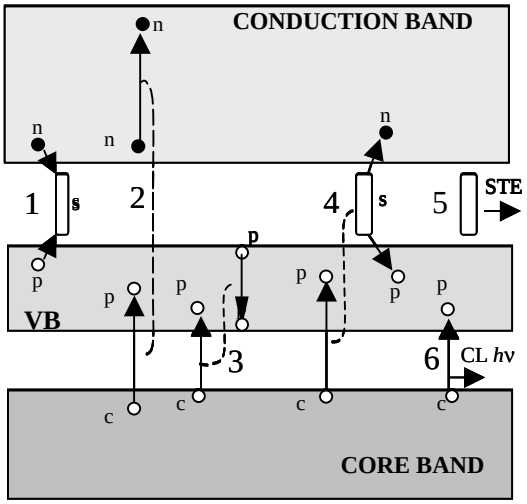

Figure 3. Relaxation processes of in CL crystals: creation of a self-trapped exciton (1), Auger relaxation of a core hole due to the interaction with an electron (2), with a hole (3), and an exciton (4), STE emission (5), and CL emission (6)

After thermalization of electronic excitations the concentration of them is controlled by a number of relaxation processes presented in Fig. 3: (1) $p+n\rightarrow s$, (2) $c+n\rightarrow p+n$, (3) $c+p\rightarrow 2p$, (4) $c+s\rightarrow 2p+n$, (5) $s\rightarrow h\nu_{STE}$, (6) $c\rightarrow p+h\nu_{CL}$. Processes 1 to 4 are bimolecular and are characterized by coefficients γ_{np}, γ_{cn}, γ_{cp}, and γ_{cs}, respectively. These coefficients can be estimated for charged pairs (1–3) using result for diffusion-control process: $\gamma_{\alpha\beta}=4\pi(D_\alpha+D_\beta)R_0$. The coefficient γ_{cs} is chosen as one tenth of γ_{cp}. Processes 5 and 6 are monomolecular and are characterized by coefficients $1/\tau_s$ and $1/\tau_c$, which are the inverse radiation times for STE emission and CL. During this final stage of relaxation excitations can diffuse through the crystal with diffusion coefficients D_α and mobility coefficients $\mu_\alpha=eD_\alpha/kT$.

Gathering all these terms, we can write the system of equations, which we use to simulate excited region evolution after thermalization of electronic excitations in a track created by a fast particle:

$$\frac{\partial p}{\partial t}=D_p\frac{\partial}{\partial\rho}\left(\frac{\partial p}{\partial\rho}-\frac{eE}{kT}p\right)-\gamma_{np}np+\gamma_{cn}cn+\gamma_{cp}cp+2\gamma_{cs}cs+\frac{c}{\tau_c}$$

$$\frac{\partial n}{\partial t}=D_n\frac{\partial}{\partial\rho}\left(\frac{\partial n}{\partial\rho}+\frac{eE}{kT}n\right)-\gamma_{np}np+\gamma_{cs}cs$$

$$\frac{\partial c}{\partial t}=D_c\frac{\partial}{\partial\rho}\left(\frac{\partial c}{\partial\rho}-\frac{eE}{kT}c\right)-\gamma_{cn}cn-\gamma_{cp}cp-\gamma_{cs}cs-\frac{c}{\tau_c}$$

$$\frac{\partial s}{\partial t}=D_s\frac{\partial^2 s}{\partial\rho^2}+\gamma_{np}np-\gamma_{cs}cs-\frac{s}{\tau_s}$$

$$\frac{\partial E}{\partial\rho}=\frac{4\pi e}{\varepsilon}(p+c-n)$$

The initial conditions for this system are the electron excitation distribution formed at the hot and thermal stages of the relaxation as described above. Boundary conditions are derived from the natural supposition that the number of electron excitations and the electric field at the infinity are equal to zero.

Some examples of the evaluation of excited region are displayed in Figure 4. Since processes 1 to 4 are bimolecular, their rates strongly depend on local concentration. This effect is illustrated by the right panel. The effect of transformation of excitations (from c to p) and creation of excitons in the track core is shown in the left panel.

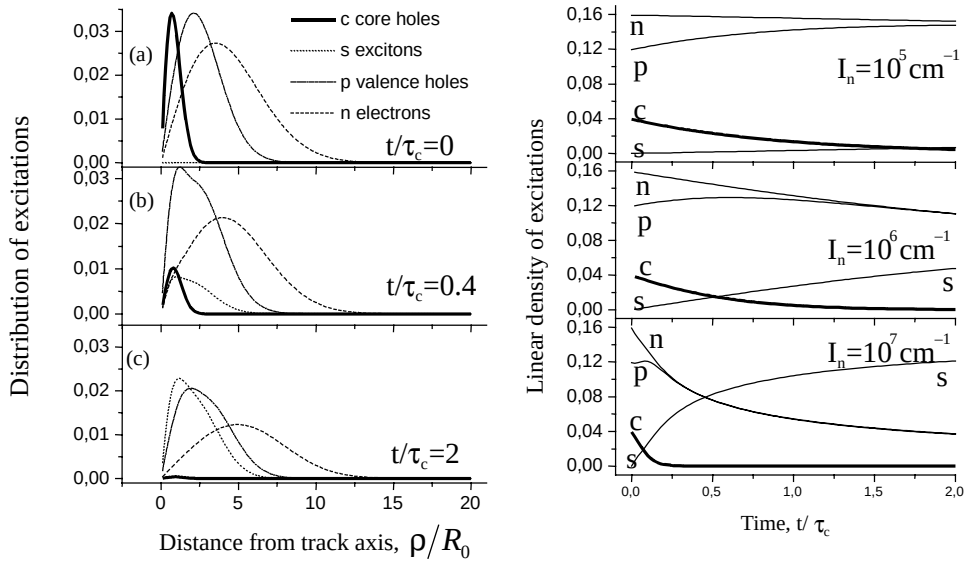

Figure 4. Evolution of the excited region after thermalization of the electronic excitations in the track created by a fast particle. Left panel: space evolution for I_n=10^6 cm^{-1}; right panel: temporal evolution of linear densities of excitations evolution for three various values of initial linear density of the electronic excitations in the track I_n

Since $I_n(z)$ is the known function of the distance along the axis, we can calculate the efficiency of CL produced by the track of ionizing particles with definite initial energies. Two examples of these calculations for various track diameters are presented in the Figure 5. These results are obtained for two values of track diameter. The values of track diameter and dispersions are chosen here only for estimation and should be evaluated more accurately in future calculations.

Since quantum yield for slow STE emission is proportional to particle energy (in contrary with CL, STE emission has no strong competition processes which quench luminescence), these curves can be used for the comparison with experimental data [1].

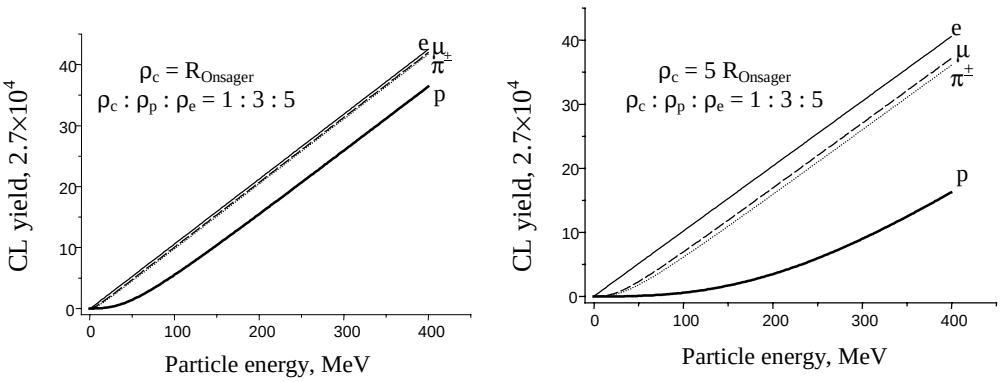

Figure 5. Crossluminescence yield versus particle energy for two values of track diameters

Conclusions

Presented simulation of track effects in crossluminescence excitation is an example of numerical study of evolution of excited region with several coexisting types of excitations with account for their interaction and electric fields induced by charge separation in the track region. The number of poorly estimated parameters allows us to achieve only qualitative fit of experimental data. Further simulation of the problem will be useful for obtaining more reliable information about track structure and evolution.

References

1. R. Novotny, Proc. Int. Conf. On Inorganic Scintillators and Their Applications, SCINT95, Delft University Press, The Netherlands, 1996, pp. 70–73.
2. A.N.Belsky, R.A.Glukhov, I.A.Kamenskikh, P.Martin, V.V.Mikhailin, I.H.Munro, C.Pedrini, D.A.Shaw, I.N.Shpinkov, A.N.Vasil'ev, Journal of Electron Spectroscopy and Related Phenomena, **79** (1996) 147–150.
3. A.N.Belsky, I.A.Kamenskikh, V.V.Mikhailin, A.N.Vasil'ev, Journal of Electron Spectroscopy and Related Phenomena, **79** (1996) 111–116.
4. R.A.Glukhov, M.Kamada, S.Kubota, E.Nakamura, S.Ohara, M.A.Terekhin, A.N.Vasil'ev, Proc. Int. Conf. on Inorganic Scintillators and Their Applications, SCINT95, Delft University Press, The Netherlands, 1996, pp. 204–207.
5. M.A.Terekhin, A.N.Vasil'ev, M.Kamada, E.Nakamura, S.Kubota, Phys. Rev., **B52** (1995) 3117–3121.
6. R.A.Glukhov, A.N.Vasil'ev, Materials Research Society Symposium Proceedings, **348** (1994) 387–392.
7. Review of Particle Physics, Phys. Rev **D54** (1996) 1.

Modification of crossluminescence spectra due to localization of core hole: tight-binding approximation

O.I.Baum, A.N.Vasil'ev

Synchrotron Radiation Laboratory, Physics Faculty, Lomonosov Moscow State University, 119899 Moscow, Russia

Abstract: Simulation of crossluminescence (CL) spectra for crystals with wide forbidden gap was performed for different crystal lattices. The model is based on the tight-binding approximation. Two cases are considered: without and with account for lattice relaxation. For the first model spectra are calculated for free and localized (one- or two-site) core hole states. Emission spectra were calculated for binary crossluminescent crystals with three crystal lattices (NaCl, CsCl and BaF_2 structures). The account for lattice relaxation was considered for one-site localized state using Green function method.

Keywords: crossluminescence

This work describes the simulation of crossluminescence (CL) spectra, which corresponds to the radiative transition of the hole from uppermost core band to valence one. This is a kind of intrinsic luminescence of pure alkali halides and alkali-earth halides with wide forbidden gap in case of forbidden Auger transition between these bands [1].

Until now there are still problems with explanation of the CL emission spectra. Moreover, the localization of the pre-emission state of the core hole does not confirm yet. The spectra have similar profiles in many systems. The width of the emission spectrum roughly equals to the width of the valence band.

In early crossluminescence investigations it was supposed that the CL emission spectrum corresponds to the density-of-states (DOS) of the valence band. Further investigations have shown that emission spectra of the majority of CL crystals are temperature dependent [2, 3]. However a number of problems relative to the details of spectra formation still remain unsolved.

In order to calculate spectra for such interband transitions without account for lattice relaxation we can consider both final and initial states as the superposition of states with definite wave-vector **k**. Therefore in this case we shall know (i) dispersion laws for holes both in valence and uppermost core bands, (ii) transition matrix elements and (iii) distribution of core holes over the Brillouin zone. These two bands are formed mainly by *p*-states of anions and cations, respectively. The simplest model, which can describe these bands in ionic crystals, is the tight-binding approximation with account for interaction only between the neighbor ions. Secular equations to determine these dispersion laws include interaction integrals for σ- and π-interactions of *p*-functions of ions. These secular equations depend only on parameters $W_\sigma^{ij} = \left\langle \psi_{\sigma\mathbf{a}}^i \middle| \hat{H}_1 \middle| \psi_{\sigma\mathbf{0}}^j \right\rangle$ and $W_\pi^{ij} = \left\langle \psi_{\pi\mathbf{a}}^i \middle| \hat{H}_1 \middle| \psi_{\pi\mathbf{0}}^j \right\rangle$, which are the energies of σ- and π-interactions of *p*-orbitals of atoms of types *i* and *j* (which can be *a* or *c* for anion and cation, respectively), centered on sites **a** or **0**, $\hat{H}_1$ is the crystal Hamiltonian minus ionic Hamiltonian. These parameters are supposed to satisfy the following relation: $W_\pi^{ij} = W_\sigma^{ij} / 8$ [4]. This ratio was validated by calculation of π and σ overlap integrals of hydrogen-type functions centered on different atoms of the same type (cations or anions).

Numerical values of these parameters were determined using the comparison of simulated density-of-states with experimental X-ray photoelectron spectra [2] and some known published calculated dispersion laws $E(\boldsymbol{k})$ along high-symmetry directions in the Brillouin zone.

Secular equations for dispersion curves $E(\boldsymbol{k})$ are 6×6 matrices for crystals with two ions in the cell and 9×9 matrix for barium fluoride. If we take into account only neighbor ions of the same type ($i=j$), these matrices are reduced to 3×3 ones. The advantage of this approach is the possibility of obtaining analytical solutions for several directions in Brillouin zone. The emission spectra are the integrals over Brillouin zone, which are calculated using Monte-Carlo method, and therefore the eigenvalues and eigenstates are evaluated numerically for randomly distributed points in the Brillouin zone.

Since the transitions occur between wave-functions of *p*-symmetry for both cases, special attention has been paid to the account for wave-vector dependence matrix elements $\left\langle \psi^a \middle| \mathbf{r} \middle| \psi^c \right\rangle$. Matrix elements for direct optical transitions between the valence and upper-core bands have been taken as constants [5]:

$$U_1 = \left\langle \psi^a_\sigma \middle| \mathbf{r}_\sigma \middle| \psi^c_\sigma \right\rangle,\ U_2 = \left\langle \psi^a_\sigma \middle| \mathbf{r}_\pi \middle| \psi^c_\pi \right\rangle,\ U_3 = \left\langle \psi^a_\pi \middle| \mathbf{r}_\sigma \middle| \psi^c_\pi \right\rangle,\ U_4 = \left\langle \psi^a_\pi \middle| \mathbf{r}_\pi \middle| \psi^c_\sigma \right\rangle.$$

The calculations of the emission spectra were realized for CsCl, RbF and BaF_2. For CsCl calculation based on hydrogen-like functions results in following relations: $U_2 = 0.226\ U_1$, $U_3 = -0.113\ U_1$, $U_4 = -0.451\ U_1$. The contribution of each component of matrix elements for transitions between cation and anion bands are shown in Fig. 1-b. Each curve has been normalized at the maximum in order to facilitate their comparison.

The distribution of core holes over the Brillouin zone is considered in two limit cases. The first one is the case of free core holes. After thermalization these holes are gathered at the top of the core band and are distributed over energy according to Boltzman distribution resulting in Gaussian distribution in **k**-space (factor F in Fig. 1-c). The second group of cases case is the one-site or two-site localization of a core hole. For one-site localization in real space results in the uniform distribution over the Brillouin zone ($F = 1$). Two-site localization (on sites separated by vector $\mathbf{R}_{loc}$) results in $F = \langle \mathrm{Cos}^2(\mathbf{kR}_{loc}) \rangle$ (see Fig. 1-c).

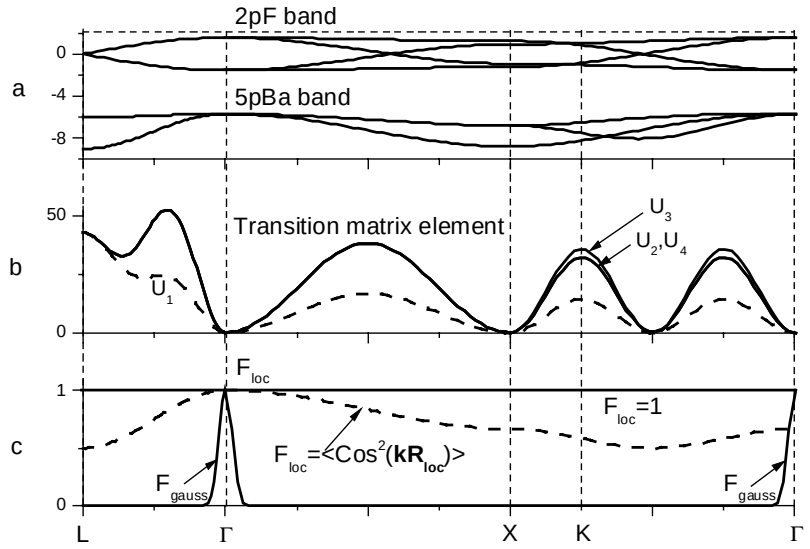

Fig. 1. a) Dispersion laws for BaF_2. b) Different components of matrix elements for transitions between cation and anion wave-functions. c) Distribution of core holes: free holes corresponds to $F=F_{Gauss}$; one-site self-trapping model, $F_{loc}=1$; two-site self-trapping model, $F_{loc}= \langle \mathrm{Cos}^2(\mathbf{kR}_{loc}) \rangle$.

Only the first case of free core holes is temperature dependent in these approximations. It results in sharp peaks, corresponding to transitions from the top point of the core band (Γ-point in case presented in Fig. 1). The reasonable width and structure of the emission spectrum can be observed only for almost flat branch at the top of the core band [6], so we consider that this case is not realized.

Figures 2 and 3 display simulated emission spectra for one- and two-site localization of core holes with or without account for dependence of transition matrix element on wave-vector.

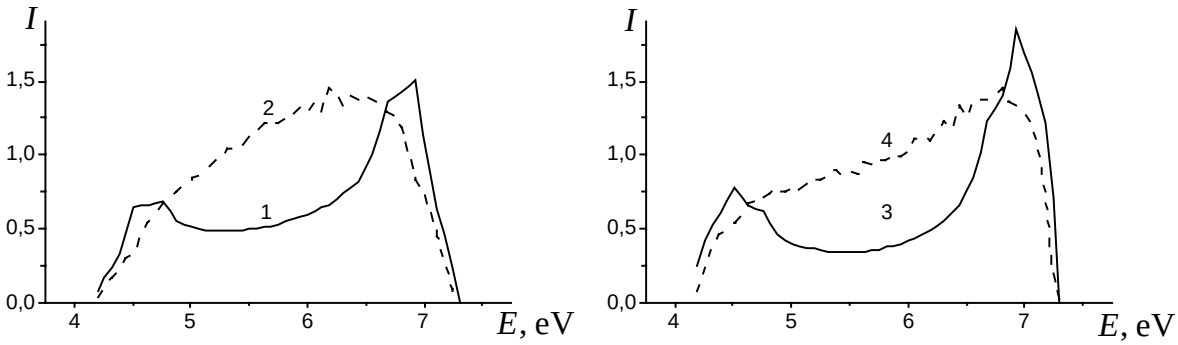

Fig. 2. Simulated emission spectra for BaF_2. Curves 1 and 2: one-site localization; curves 3 and 4: two-site localization. Solid curves correspond to constant matrix elements, dashed one, with account for wave-vector dependence of matrix elements.

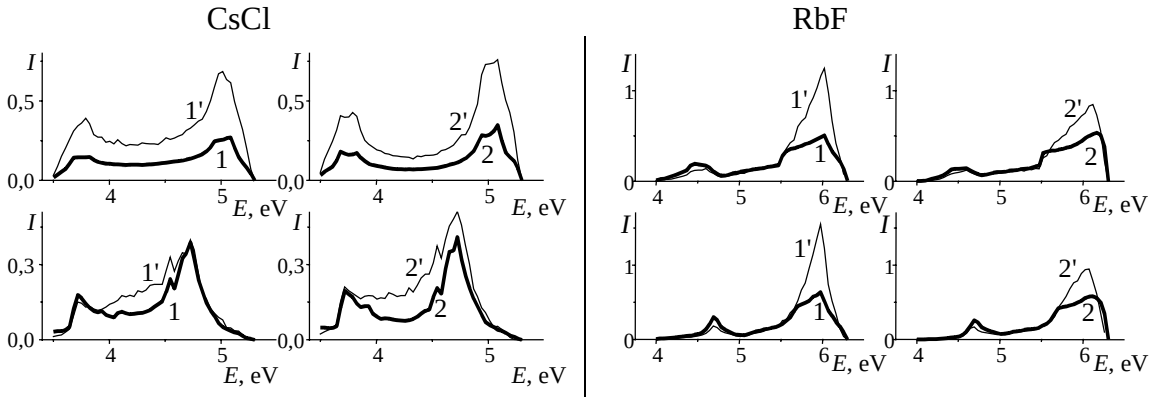

Fig.3. Simulated emission spectra of CsCl and RbF. Curves in bottom panels are calculated with account for anion-cation interaction in the Hamiltonian. Digits 1 and 2 designate one- and two-site self-trapping, respectively. The curves with primes mark spectra with account for matrix element dependence.

In general the account for transition matrix elements smoothes the van Hove singularities in spectra. For instance, wave-functions in Γ-point have the same symmetry, and therefore transitions in this point are forbidden, and transitions in the vicinity of Γ-point are significantly reduced (Fig. 1-b). In case of barium fluoride the account for the matrix element k-dependence results more dramatic change of CL spectra.

The account for anion-cation interaction in the Hamiltonian shifts positions of peaks but does not change the qualitative features of CL spectra (Fig. 3).

If we take lattice relaxation into account, the crystal translation symmetry is broken, and band approach should be modified. A localized core hole creates perturbation, which can be considered in frames of theory of defects. In this case it is convenient to describe CL with the help of Green functions [7, 8].

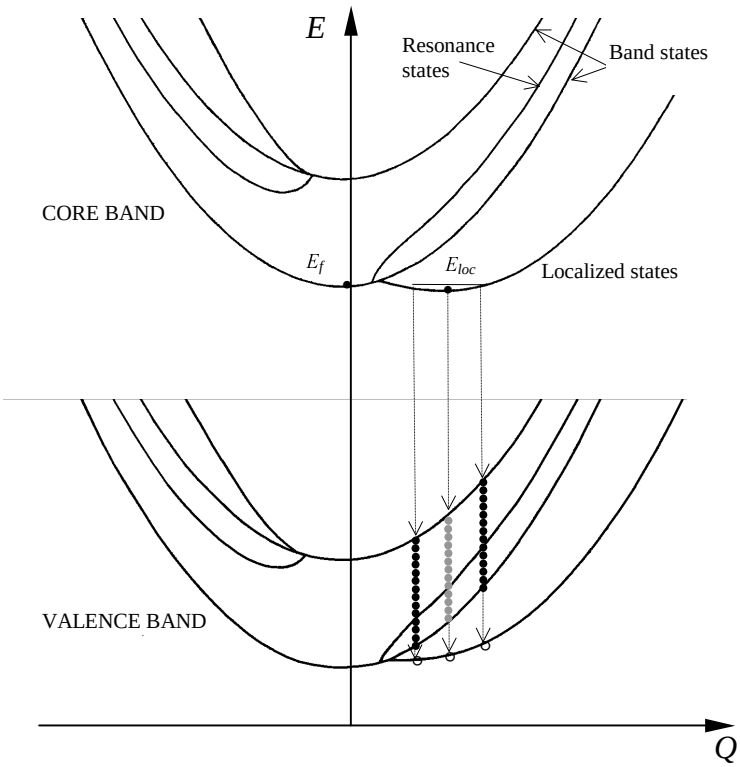

Fig.4. Configuration scheme of crystal band structure of in case of core hole localization. Scheme is plotted for total energy of system (system with core hole has higher energy than the system with valence hole, therefore the core band lies above the valence band in contrary with Fig. 1). Ratio of coupling factors is $\beta/\alpha = 0.7$.

Let us consider the scheme of a excited states for band excitations with account for localization of core states (Fig. 4). The system state is described by a configuration coordinate *Q*, which represents the lattice distortion around the core hole. The interaction of the core hole with lattice is characterized by coupling factors α. Coupling factor β corresponds to the interaction of the mode *Q* with holes in the valence band. There is an energy barrier between free and localized states for core holes [9]. If the values *Q* are small, the system is in a free state (at the bottom of core band in the vicinity of $Q = 0$). Under certain conditions, the localized states become more favorable: $E_{lok} < E_f$.

Emission spectra calculated in this model contain shallow part (transitions from the localized core hole state to band states of valence hole, which are represented by solid circles in Fig. 4) and sharp δ-lines in a low- or high-energy region (depending on the sign of β/α ratio). The resonance states (the curves that lie within the band boundaries) also modify the spectra. Fig. 4 shows that these three types of transitions are broaden differently with the increase of temperature, since the slopes of the curves corresponding to the final states are different.

Figure 5 presents CL spectra calculated for CsCl density of states. These CL spectra satisfy the «sum rule». The integrals of spectra remain constant for various β/α. The splitting of the localized states curve from the band states increases with the $|\beta/\alpha|$ ratio, and the probability of transitions to localized states of valence hole (see Fig. 4) increases. The analysis of results presented in Fig.5 allows us to conclude that ratio of coupling factors $|\beta/\alpha|$ in real systems is less than 0.4.

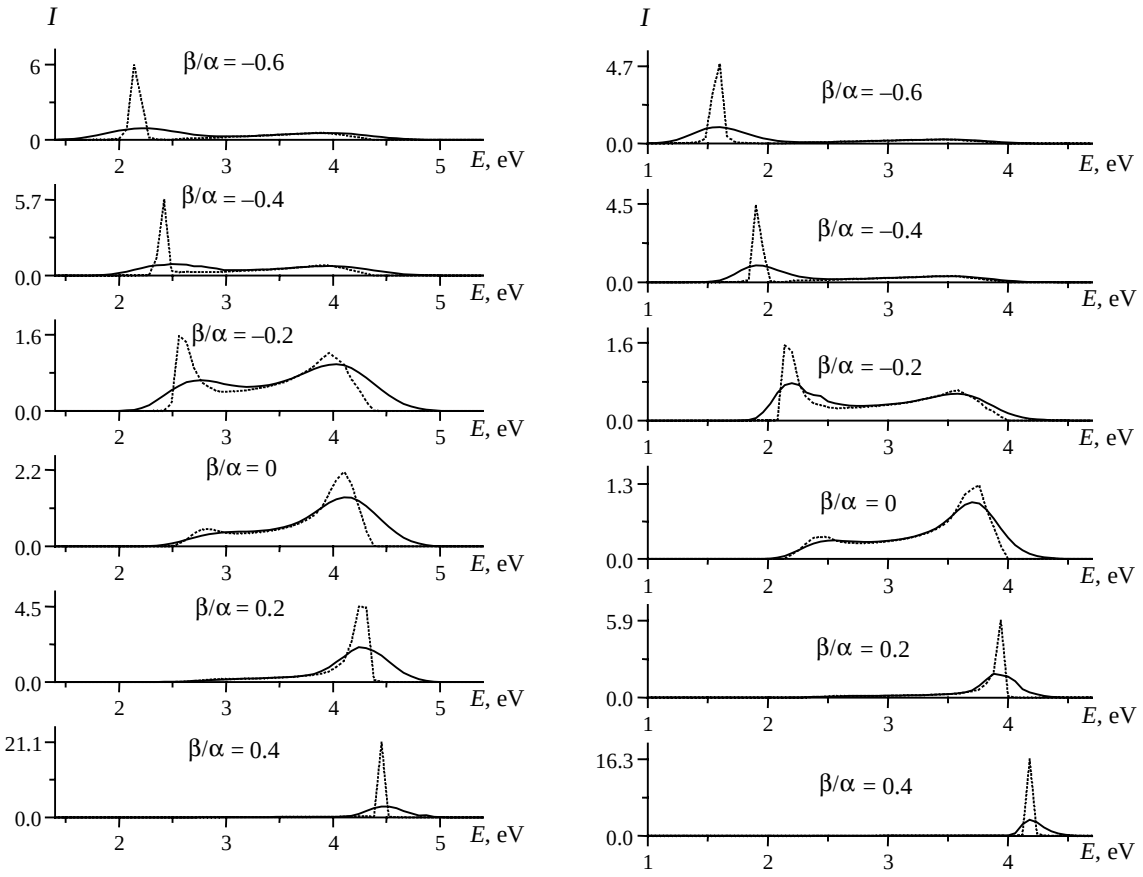

Fig.5. CL spectra in case of constant transition matrix elements at T=4K (dotted) and T=300K (solid). Left curves are plotted for $\left|E_{loc} - E_{free}\right| = 0.2$ eV; right ones, for $\left|E_{loc} - E_{free}\right| = 0.5$ eV.

References

1. Yu.M.Aleksandrov, V.N.Makhov, P.A.Rodny, T.I.Syreishchikova, M.N.Yakimenko, Fizika Tverdogo Tela, **26** (1984) 2865.
2. V.N.Makhov, Nucl. Instr. and Meth., **A 308** (1991) 187.
3. M.Itoh, M.Kamada, N.Ohno, Journal of the Physical Society of Japan, **66** (1997) 2502.
4. S.T.Pantelides, Phys. Rev. **B 11** (1975) 5082.
5. E.O.Kane, J. Phys. Chem. Solids. **1** (1956) 82.
6. A.N.Belsky, I.A.Kamenskikh, V.V.Mikhailin, A.N.Vasil'ev, J. of Electron Spectroscopy and Related Phenomena, **79** (1996) 111.
7. . .Stoneham, Theory of defects in solids, Vol.1, Clarendon Press, Oxford (1975).
8. Y.Kayanuma and A.Kotani, Journal of Electron Spectroscopy and Related Phenomena, **79** (1996) 219.
9. Y.Toyozawa, Prog.Theor.Phys., **26** (1961) 29.

Discrimination between Different Free Exciton Creation Processes in Solid Krypton

V. Kisand, E. Gminder, M. Kirm, B. Steeg, S. Vielhauer, and G. Zimmerer

II. Institute of Experimental Physics, University of Hamburg, Luruper Chaussee 149, D-22761 Hamburg, Germany

Abstract. Formation of free secondary excitons was investigated in solid krypton. Delayed electron-hole recombination and 'prompt' creation of secondary excitons were experimentally separated in time-resolved photoexcitation spectra. For the first time, clear anticorrelation between 'prompt' and delayed processes have been observed. Different thresholds corresponding to the creation of secondary excitons and secondary electron-hole pairs were detected in time-resolved excitation spectra. Two possibilities to explain the threshold for the 'prompt' processes are discussed: (i) inelastic scattering of the electrons in the framework of the multiple-parabolic-branch band model and (ii) creation of the electronic polaron complex. Comparison has been made between excitation spectra of krypton polycrystalline samples and krypton clusters.

Keywords: rare gas solids, krypton, free exciton, luminescence

Introduction

Due to their simple crystalline structure (monoatomic fcc) optical phonons are absent in rare gas crystals (RGC). All phonon-assisted relaxation processes are therefore slowed down, compared, e.g., to alkali halide crystals. Due to this unique property it is possible to discriminate between different relaxation processes in RGC on a nanosecond scale. As in solid Xe [1], Kr crystals exhibit strong self-trapped exciton (STE) luminescence (8.5 eV) as well as sample sensitive luminescence of free excitons (FE) (E_{ex}=10.12 eV) [2]. In the present work, the FE luminescence of solid krypton was used as a probe to study the relaxation- and recombination dynamics of electronic excitations up to 30 eV. Time-resolved FE excitation spectra and FE luminescence decay curves are presented and different FE creation processes are discussed.

Experimental set-up

The experiments were performed at the SUPERLUMI station of HASYLAB at DESY [3]. Selective photon excitation of 10 eV ≤ hν ≤ 35 eV with a resolution of Δλ=2.5 Å was used. Spectral- and time-resolved analysis of FE and STE luminescence was carried out with a high-flux VUV-monochromator (typical resolution Δλ=12 Å was used). At HASYLAB, the synchrotron radiation pulses have a FWHM of 130 ps. Due to the response of the detector (microsphere plate, El Mul) and the electronics used, the measured FWHM of the pulse was 400 ps.

Kr polycrystalline samples with a thickness of about 0.3 mm (an average growing rate 2 μm/min) were grown from gas phase near thermodynamic equilibrium conditions at 84 K. Finally, the crystals were slowly cooled down (about 1 K/min). For sample preparation krypton with highest commercially available purity (Spectra Gases Inc., 99.999 %) was used. During measurements, the pressure in the sample chamber was lower than $1 \cdot 10^{-9}$ mbar.

Decay of free excitons

FE decay curves, measured at 6 specific excitation energies, are presented in figure 1: 10.42 eV (in the exciton region), 11.59 eV (slightly below of the forbidden gap E_g=11.61 eV), 11.70 eV, 13.05 eV and 17.7 eV (in the band-to-band transition region, respectively 0.1 eV, 1.5 and 6.1 eV above the forbidden gap) and 23.4 eV (above threshold of 'prompt' secondary exciton creation). In the energy range of direct creation of excitons, with photoexcitation below E_g, the decay curves show a non-exponential behaviour. This was explained in terms of exciton-polariton transport to the sample/vacuum interface, including phonon scattering and transitions of FE into self trapped states [4].

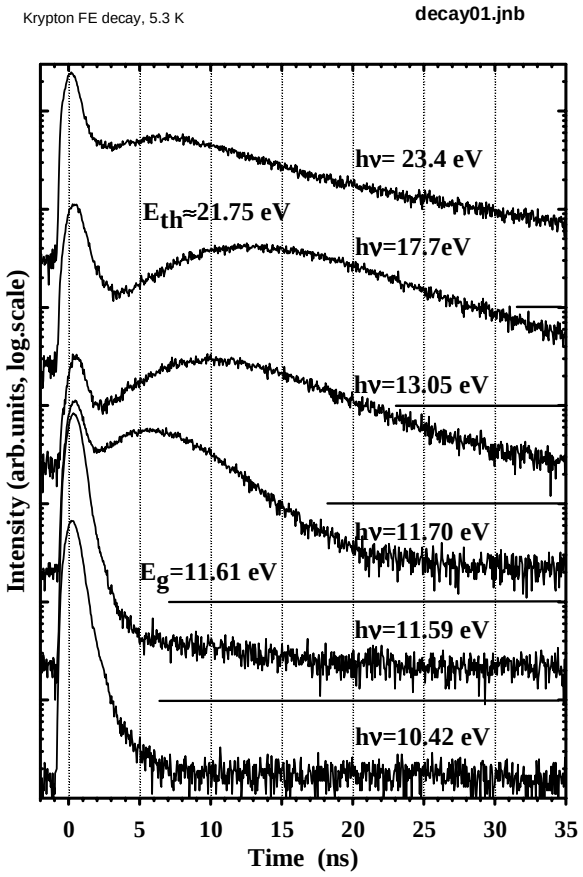

Figure 1. Decay curves of FE luminescence (E_{ex}=10.13 eV) at 6 specific excitation energies of solid Kr at 5 K. Time t=0 corresponds to the maximum of the excitation pulse.

Using primary excitation exceeding E_g, i.e. creating electron-hole pairs, the situation is more complicated. In that case the FE decay exhibits a 'prompt' component and a 'slow' component with a delayed maximum. It is important to note, that the 'prompt' part is superimposed to the rising part of the 'slow' component.

As Fig. 1 clearly demonstrates, the 'slow' component, caused by FE creation through electron-hole recombination, is responsible for the difference between decay curves excited below and above the forbidden gap. The microscopic process of FE creation via electron-hole recombination includes two aspects: (i) relaxation of hot electrons, and (ii) recombination of the relaxed electrons with the hole centres. It is quite natural to expect that by increasing of the excitation energy, electrons need more time to relax down to the bottom of conduction band and the maximum of the 'slow' component is more delayed. In the case of excitation by 11.7 eV photons (0.1 eV above E_g) the maximum is located about 6 ns from excitation pulse

but for 17.7 eV photons (6.1 eV above E_g), it is about 13 ns, respectively. Since all samples are in some degree 'unique', the shapes of slow component are slightly varing from sample to sample, but following the general trend discussed above. The 'slow' component in solid xenon was analysed in the case of small excess energies (≤ 1.4 eV above forbidden gap) in terms of a numerical model in more detail elsewhere [5].

For excitation energies above a threshold at E_{th}=21.75±0.2 eV, (will be discussed below), two excitations per one absorbed photon can be created. It means, that electrons in the conduction band have again low kinetic energy and the maximum of the 'slow' component moves back to shorter times. However, the shape of the 'slow' component above E_{th} is not so clear than following excitation directly above E_g for the following reasons: (i) due to the competition between secondary exciton and secondary electron-hole pair creation, and (ii) taking into account possible transitions at different points of Brillouin zone, the energy of electrons in the conduction band can be differently distributed.

Free exciton creation in the region of secondary excitations

Time-resolved excitation spectra of the FE luminescence of solid Kr were measured using time windows (length Δt) correlated with the excitation pulses (delayed by δt). Figure 2 shows FE excitation spectra measured in a short time window Δt=0.94 ns with delay δt=0 ns ('hot') and in a long time window Δt=32.5 ns with delay δt=7.2 ns ('long'). For comparison, the time-integrated FE excitation spectrum is also shown. Depending on the delay time and the window length, various processes dominate in the different time windows.

Immediate FE creation (δt=0, 'hot' window) is predominant in two regions: in the excitonic region ($h\nu<E_g$) and in the region above the threshold ($h\nu>E_{th}$=21.75±0.2 eV). This value of the threshold was determined in a special high-resolution experiment. In the excitonic region, direct creation of free excitons and their fast phonon-assisted relaxation to the lowest FE state occurs. The threshold at 21.75 eV can be explained (i) by the so-called process of multiplication of electronic excitations in the framework of multiple-parabolic-branch band model (secondary exciton creation via inelastic scattering of photo-electrons in a two step process) [6], or (ii) by simultaneous creation of a FE and a free electron-hole pair in a one-step process (electronic polaron complex) [7]. Both models predict a threshold at $E_{th}=E_g+E_{ex}$=21.73 eV which is in very good agreement with the experimentally observed value. For this threshold it is not possible to apply the 'classical' simple parabolic model [8] because, due to its limitations, it predicts an essentially higher threshold. A remarkable change in the shape of the decay curves correlates with this threshold as well (see figure 1). Similar thresholds with equivalent energy $E_{th}=E_g+E_{ex}$ were also observed in the case of solid xenon [1] and argon [9].

With longer delay δt, the contribution of 'slow' electron-hole recombination increases also in the time-resolved excitation spectrum. Eventually, for a delay of δt>7 ns, all possible FE creation mechanisms except electron-hole recombination are excluded. In the 'long' time-window (δt=7) the FE creation starts through electron-hole recombination exactly at the forbidden gap energy (clear step). The following increase of intensity in the 'long' window is caused by the shift of the maximum towards the time window.

The declining intensity in the 'long' time-window is correlated with creation of secondary FE above E_{th}=21.75 eV. The concomitant changes in the excitation spectra of 'hot' and 'long' time-windows corresponds to the competition between 'prompt' creation processes of secondary FE and creation of electron-hole pairs, which finally form FE in the recombination process. At threshold, the hot electrons in the conduction band lose their energy in the inelastic scattering event producing a free exciton and a low energy electron in the bottom of conduction band. With further increase of incident photon energy, hot photoelectrons are also

able to produce an additional electron-hole pair. As a result, the FE luminescence intensity rises in the ‘long’ time-window above 24 eV, corresponding to the threshold for two electron-hole pair creation ($2E_g$=23.2 eV), well established in alkali halides [8]. However, the threshold cannot be predicted by the simple parabolic model proposed in [8], rather the multiple-parabolic-band model has to be used for the threshold of secondary electron-hole pair creation as well.

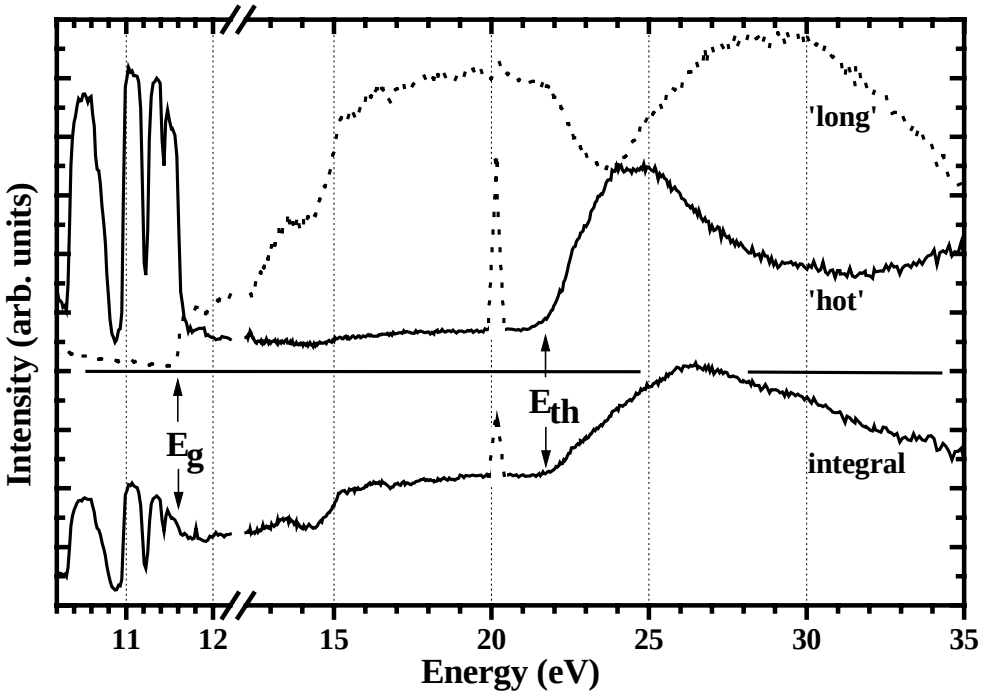

Figure 2. Time-integrated (bottom) and time-resolved excitation spectra of FE luminescence in ‘hot’ (top, solid line, δt=0 ns and Δt=0.94 ns) and ‘long’ time-window (top, dotted line, δt=7.2 ns, Δt=32.5 ns) of solid Kr at 5 K. Sharp peaks at 20 eV pronounced in hot and integral spectra are caused by higher order excitation.

The behaviour in the ‘long’ time-window is sample sensitive regarding to the amount of as-grown and radiation induced defects. The plateau extending over 16 to 22 eV and the minimum at 24 eV are not so well pronounced in each sample as shown in figure 2. Recently a similar anticorrelation between the ‘hot’ and ‘long’ time-window was also detected in the solid xenon [10]. The concomitant changes in spectra measured with δt=0 and δt=7 ns demonstrate clearly the power of time-resolved spectroscopy for monitoring various secondary exciton creation processes in RGC.

Comparison between krypton clusters and solid krypton

Spectrally- and time-integrated luminescence excitation spectra of krypton clusters were investigated recently by Karnbach [11]. Nevertheless, a comparison with our spectrally- and time-resolved data is very interesting. Figure 3 shows the FE ‘hot’ window (δt=0 ns, Δt≈0.94 ns) luminescence excitation spectrum for solid krypton, an excitation spectrum of the cluster (mean size N=34) luminescence and the electron mean free path of solid krypton [12].

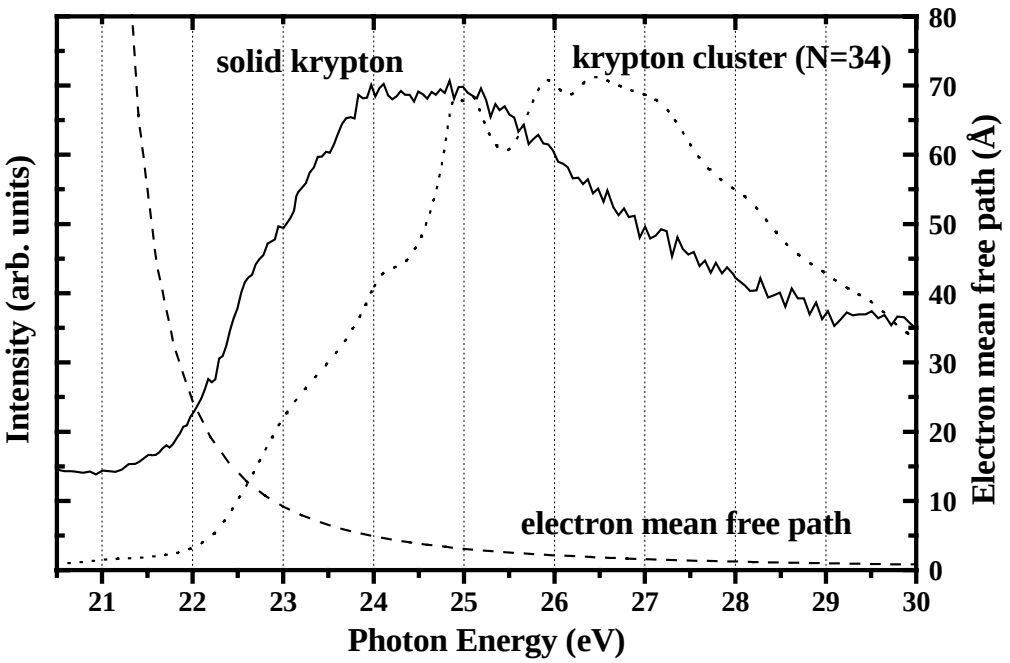

Figure 3. Excitation spectra (i) of FE luminescence in 'hot' window (δt=0 ns, $\Delta t \approx 0.94$ ns) for solid krypton at 5 K (solid line), (ii) spectrally- and time-integrated luminescence of krypton clusters (mean size N=34) (dotted line) [11], and the electron mean free path of solid krypton (dashed line) [12].

In the excitation spectra of the clusters, a threshold equivalent to $E_{th}=E_g+E_{ex}$ in the solid was observed, but especially in the case of small cluster it is shifted to higher energies. E.g. clusters with a mean size N=30 have a threshold at 22.3 eV. With increasing cluster size, the threshold moves to lower energies, until in the case of the cluster with a mean size of N=35000 it coincides with the threshold in solid krypton [11]. A similar shift was also observed for the maximum [11].

The peculiar behaviour of the excitation spectra of the clusters gives additional support to the presumption that above threshold at 21.75 eV the process of creation of secondary excitations is caused by the two step inelastic scattering. If the secondary excitation is created by an electron with sufficient kinetic energy, then the probability for this process rises if the electron mean free path decreases or the cluster diameter increases. The cluster excitation spectra demonstrate exactly such a behaviour. The creation of the electronic polaron complex (both excitations are created simultaneously) does not depend on the cluster size. Therefore comparison with cluster measurements affirms the presumption that threshold at 21.75 eV is caused by inelastic scattering of the electrons, that is possible as shown in the framework of the multiple-parabolic-branch band model. It is not excluded that both processes, two step inelastic scattering and creation of the electronic polaron complex participate in the formation of secondary excitation above threshold at 21.75 eV. However, this point needs additional theoretical investigation, especially concerning the *probability* of the creation of the electronic polaron complex by photoabsorption.

Acknowledgements

This work was supported by the Deutsche Forschungsgemeinschaft DFG (grant Zi 159/2).

References

1. B. Steeg, E. Gminder, M. Kirm, V. Kisand, S. Vielhauer, and G. Zimmerer, J. Electron Spectr. Rel. Phen., **101-103** (1999) 879-884.

2. V. Kisand, in “Excitonic Processes in Condensed Matter,” R.T. Williams and W.M.Yen, Editors, PV 98-25, p.385, The Electrocemical Society Proceedings Series, Pennington, NJ (1998).
3. G. Zimmerer, Nucl. Instr. Meth. Phys. Res. **A308**, 178 (1991).
4. D. Varding, I. Reimand, and G. Zimmerer, phys. stat. sol. (b), **185**, 301 (1994).
5. I. Reimand, E. Gminder, M. Kirm, V. Kisand, B. Steeg, D. Varding, and G. Zimmerer, phys. stat. sol. (b), **214** (1999), p.81.
6. A.N. Vasil’ev, Y. Fang, and V.V. Mikhailin, Phys. Rev. B, **60** (1999).
7. J.T. Devreese, A.B. Kunz, and T.C. Collins, Solid State Communic., **11**, 673 (1972).
8. A. Lushchik, E. Feldbach, R. Kink, Ch. Lushchik, M. Kirm, and I. Martinson, Phys. Rev. B 53, 5379 (1996).
9. G. Zimmerer, in “Excitonic Processes in Condensed Matter,” R.T. Williams and W.M.Yen, Editors, PV 98-25, p. 375, The Electrocemical Society Proceedings Series, Pennington, NJ (1998).
10. B. Steeg, PhD Thesis, The University of Hamburg (in preparation).
11. R. Karnbach, PhD Thesis, The University of Hamburg (1993).
12. N. Schwentner, Phys. Rev. B, **14,** 5490 (1976).

The rates of exciton and electron-hole impact production in wide-gap insulators

A.N.Vasil'ev[1], Y.Fang[2], V.V.Mikhailin[1,2]

[1]*Synchrotron Radiation Laboratory, Physics Faculty, Moscow State Lomonosov University, 119899 Moscow, Russia;* [2]Skobeltsyn Institute of Nuclear Physics, Moscow State Lomonosov University, 119899 Moscow, Russia

Introduction

Electron inelastic scattering of energetic electrons is of fundamental importance in the processes of interactions of high-energy quanta with condensed matter. This scattering results in impact production of secondary electronic excitations, which reveals in "photon multiplication" effect in luminescence excited by VUV photons [1], whereas cascade of such elementary acts determines total number of electronic excitations in scintillation process [2]. Threshold and rate are the most important characteristics of the production.

The simplest expressions for them with an allowance for energy and momentum conservation are obtained within the single-parabolic-branch band (SPBB) model of insulator for both conduction and valence bands. For electron-hole pair production, the threshold energy is [3]

$$E_{th}^{e-h} = (1+\mu)E_g, \quad (1)$$

where E_g is the gap, $\mu = m_e/(m_e + m_h)$, m_e and m_h are the effective masses of an electron and a hole, respectively, and the production rate near the threshold is [4]

$$W_{e-h}(E) \propto (E - E_{th}^{e-h})^2, \quad (2)$$

where E is the kinetic energy of the initial electron. For Wannier-Mott exciton production, the threshold is [5]:

$$E_{th}^{ex} = (1+\mu)E_{ex}, \quad (3)$$

where E_{ex} is the exciton energy for state $n=1$, and the production rate near the threshold will be obtained below as

$$W_{ex}(E) \propto \sqrt{E - E_{th}^{ex}}. \quad (4)$$

Beyond the SPBB model, theoretical researches were conducted in two directions: real-band Monte Carlo calculations and model-band analytic approaches. All these calculations were made for semiconductors. For impact production in wide-gap insulators, where the kinetic energy of the initial electron is about 10 eV, the SPBB model cannot be applied although it is valid for narrow-gap semiconductors. Moreover, the exciton effect in the threshold plays a crucial role in insulators. Recent experiment presented a vivid threshold for the secondary exciton production by a primary photoelectron after the absorption of photons in solid Xe [6]. The observed threshold energy is remarkably lower than that given by Eq. (3).

In this article we present a multiple-parabolic-branch band (MPBB) model for the conduction band and give analytic expressions for threshold energies and rates of production of e-h pairs and excitons by electron impact in wide-gap insulators. The analysis is based on the polarization approximation [5].

Multiple-parabolic-branch band model

In wide-gap insulators, conduction band at energies about 10 eV above its bottom can be described approximately as a set of free electron parabolic bands with effective mass $m_e = m_0$

shifted in wave-vector space by vectors $\boldsymbol{G}$ which are superposition of reciprocal lattice constants $\boldsymbol{b}_\mathbf{i}$ with integer coefficients: $\boldsymbol{G} = n_1\boldsymbol{b}_1 + n_2\boldsymbol{b}_2 + n_3\boldsymbol{b}_3$. This representation corresponds to extended Brillouin zones Ω_∞. When only the first Brillouin zone Ω_∞ is considered, $\boldsymbol{G}$ identifies the branch of the dispersion law. General form for dispersion laws is

$$E_e(\boldsymbol{k}) = \frac{\hbar^2\boldsymbol{k}^2}{2m_e}, \quad \boldsymbol{k} \in \Omega_\infty, \quad \text{or} \quad E_e^{\boldsymbol{G}}(\boldsymbol{k}) = \frac{\hbar^2(\boldsymbol{k}-\boldsymbol{G})^2}{2m_e}, \quad \boldsymbol{k} \in \Omega_B, \tag{5}$$

where the energy origin is at the bottom of the conduction band.

For simplicity, spherical effective mass m_h is used for holes in the valence band:

$$E_h(k) = \frac{\hbar^2 k^2}{2m_h} + E_g, \qquad \boldsymbol{k} \in \Omega_B \tag{6}$$

The width of such valence band is equal to $E_v = \hbar^2(k_{B,\max})^2 / 2m_h$, where $\boldsymbol{k_{B,max}}$ is the greatest distance between Γ-point and the boundary of the Brillouin zone. In this model the initial electron can be scattered not only from the same branch as in the SPBB model but also from branch $\boldsymbol{G}$ to branch $\boldsymbol{G}_1 \neq \boldsymbol{G}$, which is equivalent to the "umklapp" process. For electron energies less than $\hbar^2(k_{B,\min})^2 / 2m_e$, where $k_{\mathrm{B,min}}$ is the nearest distance between Γ-point and the boundary of the Brillouin zone, there is only one branch with $\boldsymbol{G} = 0$. Thus in the scattering threshold region the transition resulting in creation of secondary excitations from the only branch of the valence band can be restricted to the branch with $\mathbf{G} = 0$ in the conduction band.

Polarization approximation

We use the formulation of the polarization approximation given in Ref.5. This approach allows us to regard the scattering process as emission of virtual longitudinal photon followed by its absorption in the media. Since the absorption of such photon can be described in terms of energy loss function, we can take into account all processes contributed to $\mathrm{Im}[-\varepsilon^{-1}(\omega,\boldsymbol{q})]$, where $\varepsilon(\omega,\boldsymbol{q})$ is the dielectric function with account for spatial dispersion. In this approximation, the impact production rate for the initial electron with energy E is given as [5]

$$W_e(E) = \frac{V}{(2\pi)^3}\int d\omega \int_{\Omega_B} dq\, \mathrm{Im}\left[-\frac{1}{\varepsilon(\omega,q)}\right] |M_q^{ee}(E, E-\hbar\omega)\rho(E-\hbar\omega), \tag{7}$$

where $\hbar\omega$ and $\hbar\boldsymbol{q}$ are the energy and the momentum transfer (of virtual longitudinal photon), respectively. ρ is the electron density of states, and $M_q^{ee}(E, E-\hbar\omega)$ is the *e-e* interaction matrix element.

For impact production of the e-h pair without account of the interaction between their components, this expression can be deduced from Fermi's golden rule [7], but it is a more general expression which also describes the production of excitons and other secondary electron excitations. With this equation the e-e and e-h processes in impact production can be treated separately.

General expressions with the mpbb model

In the polarization approximation within the BPBB model e-e matrix element can be written as

$$M_q^{ee}(E, E-\hbar\omega) = \sum_Q M_q^{ee,\mathrm{SPBB}}(E, E-\hbar\omega), \tag{8}$$

with

$$M_q^{ee,SPBB}(E,E-\hbar\omega)=\frac{m_e^2e^2}{2\pi^2\varepsilon_0\hbar^4}\frac{1}{\rho(E)\rho(E-\hbar\omega)}\frac{1}{q^3}\Theta(\omega,|\boldsymbol{q}|,E),$$

$$\Theta(\omega,q,E)=\theta(\omega-\omega^-(E,q))-\theta(\omega-\omega^+(E,q))=\theta(q-q^-(E,\omega))-\theta(q-q^+(E,\omega)),$$

where the limits

$\hbar\omega^-=0$, $\hbar\omega^+(E,q)=E-(\hbar q-\sqrt{2m_eE})^2/2m_e$, and $\hbar q^\pm(E,\omega)=\sqrt{2m_eE}\pm\sqrt{2m_e(E-\hbar\omega)}$.

The limits for q are not dependent on Q and are the same as were given for SPBB model.

Inserting the above expressions with ρ determined by the dispersion law given by Eq. (5) into Eq. (7), we obtain

$$W_e(E)=\sum_{\boldsymbol{Q}}W_{\boldsymbol{Q}}(E)=\sum_{|\boldsymbol{Q}|}n_QW_{|\boldsymbol{Q}|}(E),$$

where n_Q is the number of nodes with same $\boldsymbol{Q}$ in the reciprocal space, and

$$W_Q(E)=\frac{e^2}{8\pi^3\varepsilon_0\hbar}\sqrt{\frac{m_e}{2E}}\int d\omega\int\frac{d\boldsymbol{q}}{|\boldsymbol{q}+\boldsymbol{Q}|^3}\,\mathrm{Im}\left(-\frac{1}{\varepsilon(\omega,\boldsymbol{q})}\right)|\Theta(\omega,|\boldsymbol{q}+\boldsymbol{Q}|,E). \tag{9}$$

When we take into account only the term with $\boldsymbol{Q}$=0, Eq. (9) is reduced to the well-known formula obtained within the SPBB model for the electron gas and for condensed matter and serves as a basic formula to treat the inelastic scattering of electron in condensed matter.

The expression for ε_2 in the case of Wannier-Mott exciton for $\boldsymbol{q}\neq 0$ can be obtained for non-degenerated bands. In this case, ε_2 is the function of $\hbar\omega-E_g-\hbar^2q^2/2(m_e+m_h)$ for energies $\hbar\omega$ less than $E_g+\hbar^2k_{B,\min}^2/2m_e$ (when only lowest band in the conduction band is taken into account). Assuming that $|\varepsilon|^2$ varies slower than ε_2, we can write a general expression for ε_2 for both exciton and e-h pair production as [7]

$$W_Q(E)=\frac{e^2}{4\pi^2\varepsilon_0}\frac{\sqrt{2m_e}}{3|\varepsilon|^2\hbar\mu}\frac{1}{\sqrt{E_QE}}\int d\omega\varepsilon_2(\omega,0)\left|\frac{\Delta_-^{3/2}\theta(\Delta_-)}{(\sqrt{E}+\mu\sqrt{E_Q})^2}-\frac{\Delta_+^{3/2}\theta(\Delta_+)}{(\sqrt{E}-\mu\sqrt{E_Q})^2}\right|, \tag{10}$$

where

$$\Delta_\pm=(\sqrt{E}\quad\mu\sqrt{E_Q})^2-(1+\mu)(\hbar\omega+\mu E_Q)$$

with $E_Q=\hbar^2Q^2/2m_e$. The expression for $\boldsymbol{Q}$=0 near the threshold can be reduced from Eq. (10) by taking the limit as follows

$$W_0(E)=\lim_{Q\to 0}W_Q(E)=\frac{\sqrt{2}e^2\sqrt{m_e}}{2\pi^2\varepsilon_0|\varepsilon|^2\hbar}\frac{1}{E}\int d\omega\varepsilon_2(\omega,0)\sqrt{E-(1+\mu)\hbar\omega}\,\theta(E-(1+\mu)\hbar\omega), \tag{11}$$

Thresholds

The threshold energy can be determined from the limits give by $\theta=0$ and $\varepsilon_2(\omega,0)=0$. So substituting $\hbar\omega=E_d$ ($E_d=E_g$ for *e-h* pair and $E_d=E_{ex}$ for exciton) into $\Delta_\pm=0$, we get lower and upper thresholds corresponding to Δ_- and Δ_+ as

$$E_{th,Q}^\pm=E_{th}^0\pm 2\mu\sqrt{E_Q}\sqrt{(1+\mu)(E_d+\mu E_Q)}+\mu(1+2\mu)E_Q, \tag{12}$$

where

$E_{th}^0=(1+\mu)E_d$

is the threshold for $Q=0$.

In comparison with the SPBB model, which is the special case here when Q=0, the threshold has two values (due to the transition to the other branch of the bands): the upper threshold is always larger than E_{th}^{0}, which has less effect on the rate in the threshold; while the lower threshold can be significantly lower than E_{th}^{0}. The lowest threshold $E_{th,Q}^{-} = E_d$ can be achieved if $\hbar Q = \sqrt{2m_e E_d}$. In this case, the vertical transition from the valence band to the conduction band like that in the photon-absorption becomes possible due to the transition of the initial electron from branch with $\hbar G = \sqrt{2m_e E_d}$ to the branch G = 0, allowing for the momentum conservation. The same reduction of the threshold was also obtained numerically and analytically for e-h pair production in silicon due to the multi-valley conduction band structure which is similar to the MPBB model here. For solid Xe the lower threshold versus Q calculated by Eq.(12) for exciton and e-h productions are plotted in Fig.1 with parameter of the fcc lattice constant a = 0.62 nm and the band parameters [6] E_{ex} = 8.359 eV, E_g =9.3 eV, $m_e = m_0$, $m_h = 2.1m_0$. The numbers in Fig.1 correspond to the transitions to the branch with G = 0 from different branches, which parameters and respective lower thresholds are shown in Tab.I.

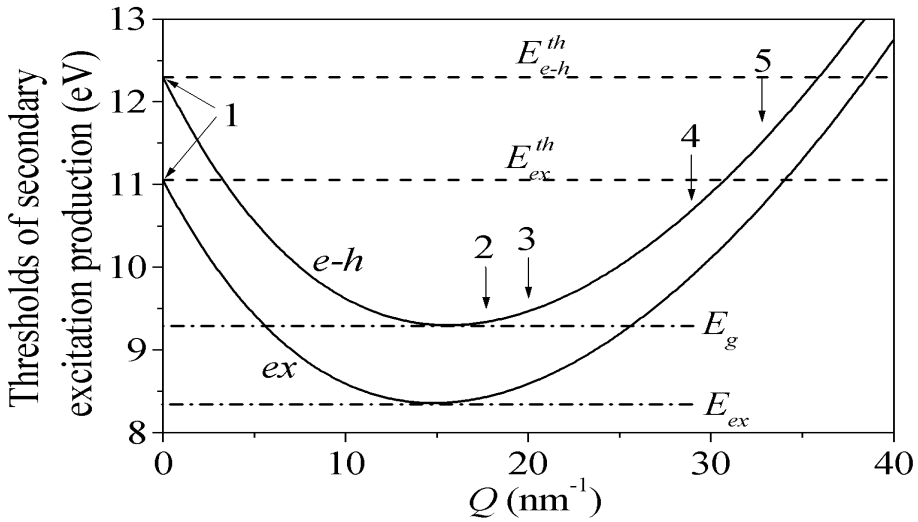

Fig.1 Lower thresholds of impact production of Wannier-Mott n=1 exciton and e-h pair vs Q for solid Xe calculated by Eq. (12) with parameters given in text and Tab.I.

Tab.I Multiple-branch parameters of solid Xe and associated lower thresholds for five different branches with the band structure parameters given in text.

	1	2	3	4	5
Q	0	$2\pi\sqrt{3}/a$	$4\pi/a$	$4\pi\sqrt{2}/a$	$2\pi\sqrt{11}/a$
n_Q	1	8	6	12	24
E_{th}^{ex}(eV)	11.06	8.43	8.62	9.84	10.95
E_{th}^{e-h}(eV)	12.30	9.33	9.49	10.64	11.72

The transition of the initial electron from the nearest branch with $Q = 2\pi\sqrt{3}/a$ has the lowest threshold for exciton production $E_{th}^{ex} = 8.43$ eV which is in good agreement with the threshold $E_{th}^{ex} = 8.45$ eV determined by the experiment [6].

Production rates near thresholds

If $\varepsilon_2(\omega,0)$ is determined, the production rate can be obtained using Eq. (10) and Eq. (11). Function ε_2 with $\boldsymbol{q}$ = 0 can be easily obtained from an experiment. $\varepsilon_2(\omega,\mathbf{q})$ can be determined [7] which results in ε_2 for three special cases:

For exciton n=1

$$\varepsilon_2(\omega,q) = C_\varepsilon 4\pi(\mathrm{Ry}^*)^{3/2}\delta\left[\hbar\omega - E_{ex} - \hbar^2q^2/2(m_e+m_h)\right];$$

For e-h pairs with interaction

$$\varepsilon_2(\omega,q) = C_\varepsilon 2\pi(\mathrm{Ry}^*)^{1/2}\theta\left[\hbar\omega - E_{ex} - \hbar^2q^2/2(m_e+m_h)\right];$$

For e-h pairs without interaction

$$\varepsilon_2(\omega,q) = C_\varepsilon\sqrt{\hbar\omega - E_{ex} - \hbar^2q^2/2(m_e+m_h)}\,\theta\left[\hbar\omega - E_{ex} - \hbar^2q^2/2(m_e+m_h)\right],$$

where

$$C_\varepsilon = \frac{e^2}{4\pi\varepsilon_0\hbar}\frac{1}{m_eE_g}\left(\frac{2m_em_h}{m_e+m_h}\right|^{3/2}.$$

Substituting these expressions for ε_2 into Eq. (10), we obtain the formula for rate of the impact production of secondary electron excitations as

$$W_Q(E) = \frac{\beta}{\tau_0}\frac{(\mathrm{Ry}^*)^{3-\alpha}}{|\varepsilon|^2E_gE^-_{th,Q}\sqrt{E_QE^-_{th,Q}}}\left(1+\mu\sqrt{\frac{E_Q}{E^-_{th,Q}}}\right)\left(E-E^-_{th,Q}\right)^\alpha\theta\left(E-E^-_{th,Q}\right). \quad (13)$$

The expression for Q=0 can be obtained by substituting the ε_2 expressions into Eq. (11) or taking the limit in Eq. (10) as

$$W_0(E) = \frac{\beta}{\tau_0}\frac{(\mathrm{Ry}^*)^{2-\alpha_0}}{|\varepsilon|^2E_gE}\left(E-E^0_{th}\right)^{\alpha_0}, \quad (14)$$

where

$$\tau_0 = \left(\frac{e^2}{4\pi\varepsilon_0}\right)^2\frac{m_e}{\hbar^3} = 4.14\times10^{16}\ \mathrm{s}^{-1},$$

and the parameters are shown in Tab.II. For e-h pair without interaction we obtain the Keldysh formula Eq. (2). For excitons, Eq. (14) corresponds to Eq. (4) mentioned in the Introduction.

Tab.II Parameters for Eqs. (13) and (14) for different types of secondary excitations.

	α	β	α_0	β_0
n = 1 exciton	1.5	$\frac{16(1-\mu)^{3/2}}{3\mu}$	0.5	$32(1-\mu)^{3/2}$
e-h pair with interaction	2.5	$\frac{16(1-\mu)^{3/2}}{15\mu(1+\mu)}$	1.5	$\frac{32(1-\mu)^{3/2}}{3(1+\mu)}$
e-h pair without interaction	3	$\frac{1}{12\mu}\left(\frac{1-\mu}{1+\mu}\right)^{3/2}$	2	$\left(\frac{1-\mu}{1+\mu}\right)^{3/2}$

Similar change of the softness for impact production rate of e-h pair in semiconductors from power 2 (given by SPBB model) to higher power (for the complicated conduction band structure) was obtained analytically (to power 3) and numerically. This softness is due to the anisotropy of the e-e transition processes with $Q \neq 0$ as well as the decrease of the density of possible final states for scattering process.

Strong inelastic scattering of electrons results in creation of excitations of two types: excitons in any bound states $(n = 1,...,\infty)$ and electron-hole pairs in continuum states. The yield of excitons in this scattering process

$$R(E) = W^{ex}(E)/\left[W^{ex}(E)+W^{e-h}(E)\right] \quad (15)$$

is plotted in Fig.2. The influence of phonon scattering [7] is also plotted.

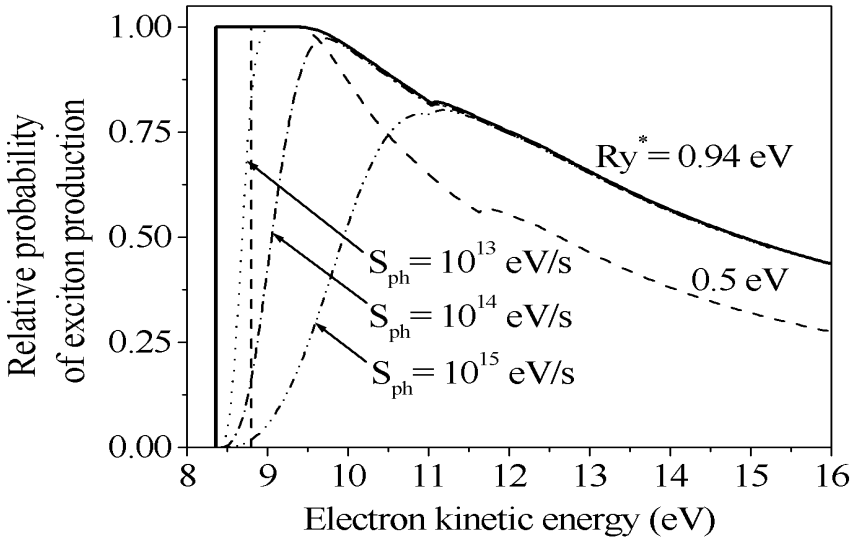

Fig.2 The yield of secondary excitons *R(E)* (given by Eq. (15) for solid Xe without phonon relaxation for two values of exciton bound energies (Ry*=0.94 eV and 0.5 eV) and the influence of phonon scattering, where S_{ph} is the rate of phonon relaxation.

Conclusion

The present study shows that simple multiple-branch dispersion law results in essential shift in threshold energy for production of secondary excitations. The rate of this inelastic scattering is slower than for SPBB model. The competition with other relaxation processes shifts the experimentally observed threshold to higher energies. The analysis uses polarization approximation and results in analytic formulae for rates of impact production of secondary excitations, both of electron-hole pairs and excitons. This information is of great importance for estimation of efficiency of energy conversion for scintillators.

Acknowledgments

The support of grants RFBR 97-02-17414, RFBR-DFG 96-02-00207G, Federal Program 2.1-535 and DFG No 436 RUS 113/437 are gratefully acknowledged. Authors would like to thank Prof. G.Zimmerer for fruitful discussion.

References

1. A. Lushchik, E. Feldbach, R. Kink, Ch. Lushchik, M. Kirm, and I. Martinson, Phys. Rev. B **53,** 5379 (1996).
2. V. V. Mikhailin, Nucl. Instr. Meth. B **97**, 530 (1995).
3. B. K. Ridley, *Quantum Processes in Semiconductors*, 3rd ed. (Oxford University Press, Oxford, 1993).
4. L. V. Keldysh, Sov. Phys. - JETP **10,** 509 (1960).
5. A. N. Vasil'ev, Nucl. Instr. Meth. B **107,** 165 (1996).
6. B. Steeg, M. Kirm, V. Kisand, S. Körding, S. Vielhauer, and G. Zimmerer, J. Low Temp. Phys. **111,** 739 (1998).
7. A. N. Vasil'ev, Y. Fang, and V. V. Mikhailin, Phys. Rev. B **60,** 5340 (1999).

VUV-Photoelectron spectroscopy of scintillation materials

A.N.Belsky[1,2], C.Dujardin[1], I.Kamenskikh[2], A.Philippov[2,3], C.Guillot[4], N.Barrett[4], G.Dujardin[5], L.Hellner[5], G.Comtet[6], and C.Pedrini[1]

[1]*LPCML, UMR 5620 CNRS, Université Claude Bernard Lyon-1, 69622 Villeurbanne, France*
[2]*SRL, Physics Faculty, Moscow State Lomonosov University, 119899 Moscow, Russia*
[3]*Russian Research Center "Kurtchatov Institute",123182 Moscow, Russia*
[4]*SRSIM/DRECAM/DRM, Centre d'Etude de Saclay, Saclay, France*
[5]*LPPM, Centre Universitaire Paris-Sud, 91405 Orsay, France*
[6]*LURE, bat.209D, Centre Universitaire Paris-Sud, 91405 Orsay, France*

Abstract. Photoemission of three scintillators CsI, $YAlO_3$:Ce and $LuAlO_3$:Ce has been investigated in the 40-200 eV excitation region. Comparison of the surface charge effect in these crystals and in the thin film of CsI has shown the importance of the surface photoconductivity for the local and integral compensation of such effect. The more efficient compensation observed for CsI from the I4d and Cs4d photoemission line profile analysis, is explained by the metallization of the surface. The non-radiative relaxation of excited 4d levels in CsI is dominated by the Auger relaxation. The resonant relaxation of bound electron and hole into a state with a hole in a upper level has been studied. The contribution of the Lu4f and 02p levels to the formation of the valence band has been evaluated using the difference of their photoionization cross sections. The Lu4f states are spread out in the whole band width.

Keywords: photoelectron spectroscopy, dielectric materials, core hole decay, Lu4f valence band,orthoaluminates of yttrium and lutetium, cesium iodide

Introduction

Photoelectron spectroscopy (PES) is an experimental powerful technique for studying the electronic properties of solids. During the last decade, the development of PES has been promoted by the use of synchrotron radiation as VUV photon excitation source. However, only a weak proportion of works on the electronic structure, the surface and the relaxation processes in solids using PES was devoted to insulating materials. This situation is due in a large part to the experimental difficulties for measuring the photoemission of insulators. But nowadays, the strong demand for new better scintillators gives a stimulus to careful studies of electronic properties of insulators. Furthermore, the development of numerical calculation of the electronic structure [1] and of the modeling of the relaxation processes of the electronic excitations [2] in insulators also stimulate studies of photoemission which bring information independent and complementary to luminescence spectroscopy.

Experiment

In the present paper are presented results of photoemission measurements of three scintillating materials. Pure and Tl-doped CsI are widely used in many applications. The samples were single crystals and thin films evaporated on Si(111) substrates. For surface studies, the sample consisted of around 3 monolayers prepared in situ on a Cu(111) substrate. The two other samples were $YAlO_3$ and $LuAlO_3$ single crystals. The experiment was carried out using the SA23 and SA73 beam lines of the storage ring SuperACO of LURE (Orsay, France). Before measurements, the samples were annealed and their surface cleaned, using Ar ionic bombardment and Auger spectroscopy control.

Surface charge problem

The kinetic energy of a photoelectron ejected from a conducting material after a photon absorption is determined by energy conservation rule $E_k^m = h\nu - E_b - W(1)$ where E_b is the electron binding energy, W is the electron work function. The absolute value of E_b can be measured relatively to the Fermi level, the position of which is known in metals. For insulators, two additional parameters must be involved : $E_k^d = E_k^m - E_g - V_{sc}(2)$where E_g is the bandgap of the crystal and V_{sc} is the surface positive charge potential. Furthermore, the Fermi level position cannot be measured in an insulator. The photoemission spectra are presented supposing $E_b = 0$ at the origin of the valence band photoemission.

Photoemission spectra of most bulk insulating crystals cannot be detected under excitation $h\nu \rangle\rangle E_g$. Photoelectrons are stopped by the surface charge potential created by photoemission (Fig. 1,I). Charge compensation is provided by a weak energy electron beam (flood gun). The photoelectron kinetic energy strongly varies with the energy of the compensation electrons in $YAlO_3$ (Fig. 1,II-V). The large shift of peaks (50 eV) is due to the decrease of the surface charge. It should be noted that the spectrum shifts without change of its shape (same bandwidth and same relative intensity of the lines), indicating a surprising good homogeneity of the surface charge, owing to the inhomogeneous distribution of the excitation photon beam. A complete surface charge compensation was not reached since the shift of the experimental spectrum relative to the calculated one using formula (2) is around 10 eV. The difficulty of a complete compensation is due to the strong increase of the number of secondary electrons with weak kinetic energy. The surface charge effect varies according to crystals. For example, for a same excitation energy, the photoemission spectrum of a CsI single crystal is detected without charge compensation with a shift of 70 eV [3]. Such a difference is due to the variation of the conductivity and, more especially, of the photoconductivity of crystals. For thin films of CsI (50-1000 nm), the shift is around 1 eV. These layers are made of micrometric sheets and it is supposed that the surface photoconductivity plays the major role in the local compensation (homogeneity of the photoelectron signal) and in the total compensation (stopping potential level). The surface charge compensation by the bulk photoconductivity has been observed in CaF_2 at the temperature T>500K under 21 eV excitation [4].

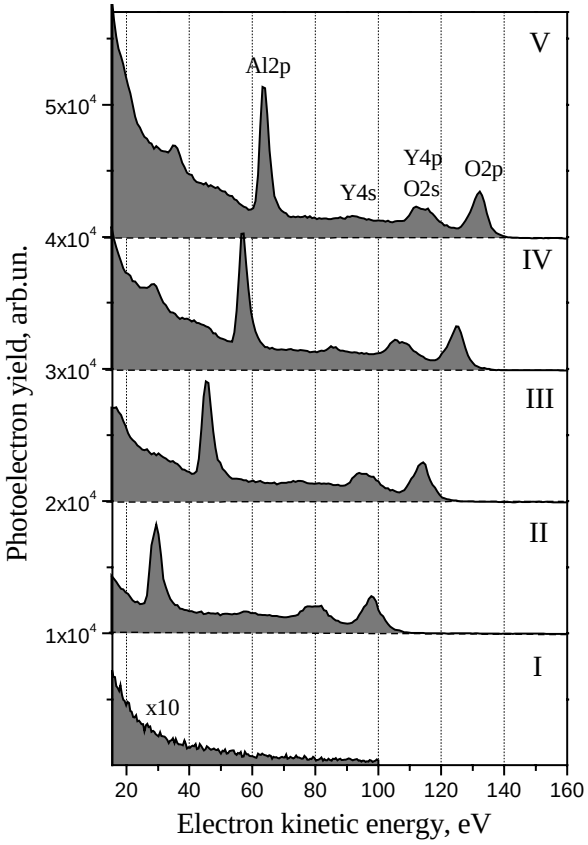

Fig.1: Photoemission of $YAlO_3$ single crystal measured at 160 eV excitation and various energies of charge compensation electrons: I- 0 eV, II- 2 eV, III- 4 eV, IV- 6 eV, and V- 8 eV.

Decay processes of 4d holes in CsI

Both Cs^+ and I^- ions have the Xe electronic configuration. Threshold energies of 4d levels are 55 eV and 79 eV for I^- and Cs^+, respectively [5]. Figure 2 shows photoemission spectra in function of the relative electron binding energy and of the photon excitation energy. The 4d level relaxation mainly occurs through Auger process and production of electrons excited in upper levels. The energy of Auger

electrons is constant for each channel of relaxation and reflects the energy difference between the electronic levels involved in the process. The Auger electron peaks are indicated in Figure 2. In the excitation region 50-120 eV, the variation of the photoemission peaks assigned to the electronic levels above 4d cannot be interpreted simply by the change of the photoionization probability of the relevant levels. The excitation spectra of photoemission yield for each level indicated in Figure 2 (so-called CIS spectra : Constant Initial State) are pictured in Figure 3. It is clearly observed a strong shift of the I5s and I5p (valence band) CIS spectra related to the Cs5p and Cs5s CIS spectra. These four spectra have a profile different to the total CsI absorption spectrum, but present some similarity with partial absorption of Cs4d and I4d. For example, the I5s CIS spectrum exhibits a sharp maximum at 55 eV which is correlated to the $4d^{10}(^1S_o) \rightarrow 4d^9 4f^1(^3P_1)$ transition energy of iodine clearly observed in the CsI absorption spectrum. The I5s CIS spectrum is maximum around 85 eV which is the energy of the giant absorption resonance of I4d. Cs5p and Cs5s CIS spectra reach their maximum at 95 eV and 105 eV, respectively.

The correlation of 5p and 5s CIS spectra with the 4d absorption of the same ion can be explained by the non-radiative transitions of a 4d electronic excitation (4d hole and bound electron) to an upper level electronic excitation with the creation of a hole in the level (for example 5p) and a more excited electron. As a result, the final state is the same as the one obtained after a direct photon absorption by 5p. Such Fano type transition requires a strong coupling between initial and final states, and therefore is really possible in the same ion. Same effects of 4d hole relaxation have been observed in BaF_2 [6]. But in CsI, we are dealing with two systems of close levels. The variation of the branching ratio of the $Cs5p_{3/2}$ and $Cs5p_{1/2}$ levels and the part increase of the Cs5p and Cs5s spectrum intensity in the region where the absorption is only due to the I4d level (below 80 eV), allow us to assume that similar but cross-transitions of 4d excitation do occur.

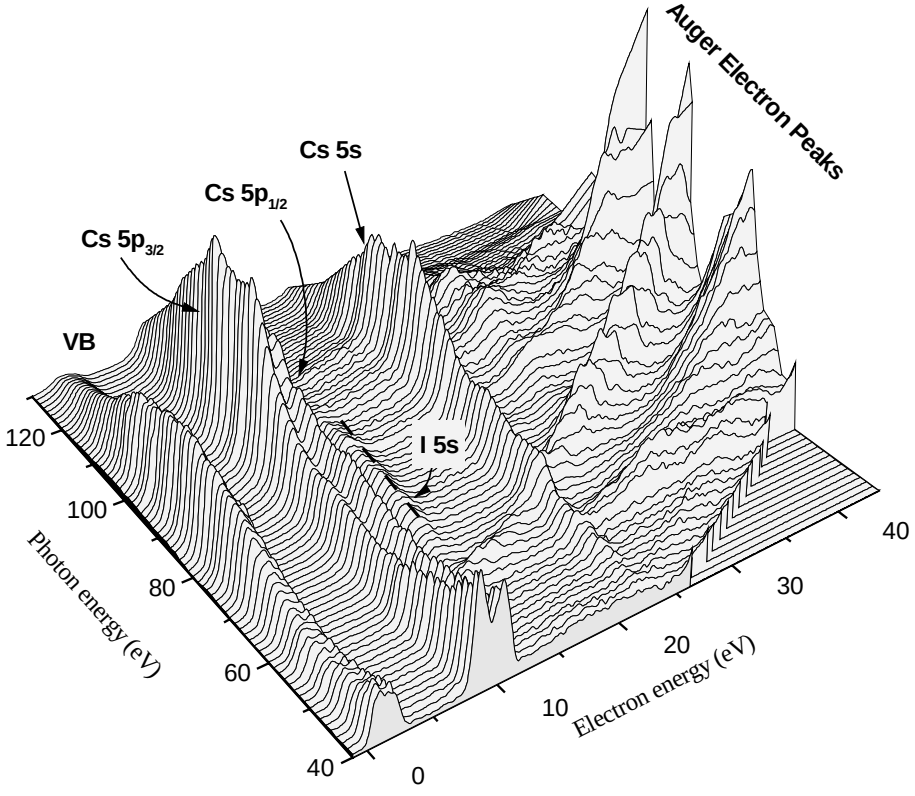

Fig.2: Series of photoemission spectra of CsI thin film (500 nm) in the excitation range 40 – 120 eV

The relaxation of Cs4d correlated hole and electron towards Cs5p and Cs5s states exhibit other peculiarities. The probability of such relaxation drops more rapidly than the absorption in the 100-130 eV region ; local resonances are detected in the continuum of the transitions, like peaks at 95 eV and 105 eV of the Cs5p CIS spectrum in the Cs5s CIS spectrum. These maxima well fit the local maxima of the absorption spectrum so that its structure in this region can be explained by Fano type resonances.

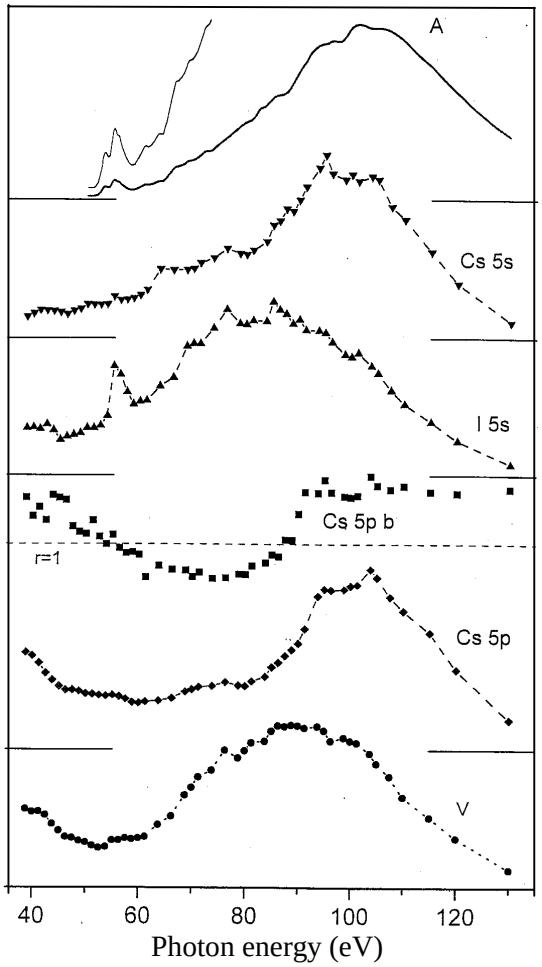

Fig.3: CIS photoelectron spectra for Cs5p, Cs5s, I5s and valence band (V)of CsI film. Branching ratio r of $Cs5p_{3/2}/Cs5p_{1/2}$ photoelectron peaks (Cs5p b) and CsI absorption spectrum [5]

Multiplication of electronic excitations

Secondary electrons under excitation hν >> E_g determine the total photoemission yield. Their number is proportional to the number of electron-hole pairs created by a photon in an insulator. The yield of e-h pairs is controlled by the electron-electron and electron-phonon interactions. The rising background in the low energy range of the photoemission spectra represents the secondary electron energy distribution. The threshold energy of the secondary electron contribution is $E_b=E_g$, for which the relevant electrons are photoelectrons ejected from the valence band and undergoing only one diffusion on the valence band electrons. The profile of threshold that looks like a continuous background, determines the e-h pair formation efficiency which is a very important parameter for scintillating materials. A same kind of threshold is found in the low energy part ($h\nu>2E_g$) of the luminescence excitation spectra. A combined analysis of photoluminescence and photoemission spectra can provide important information on the mechanisms of e-h pair creation. It should be noted that this threshold is most often hidden by the primary photoelectrons ejected from close core levels. For example, this threshold in CsI is hidden by the photoemission of Cs5p levels. In LuAP, the situation is favorable due to the increase of the Lu4f photoionization cross-section near 200 eV and the decrease of the O2s and Lu5p cross-sections.

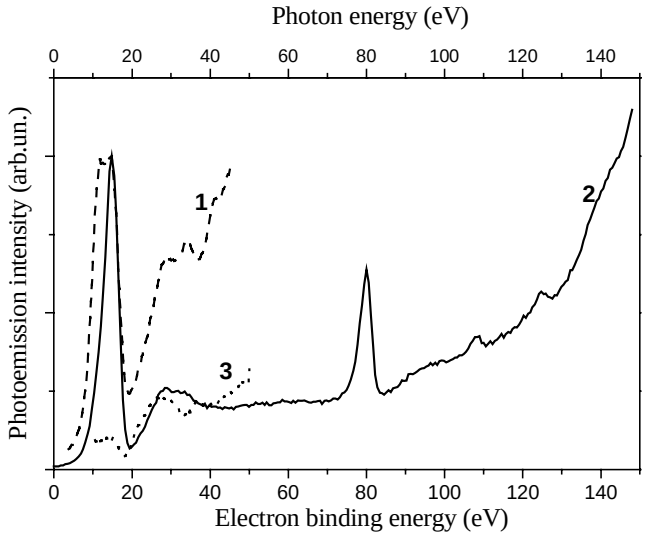

Fig.4: $LuAlO_3$ photoemission spectra (1- excitation 40 eV, 2 – 190 eV) and luminescence excitation spectrum of $LuAlO_3$-Ce (3)

Valence band of $LuAlO_3$

We took advantage of both the different excitation energy dependence of the Lu4f and O2p photoionization cross-sections and the weak wave

function overlap, to examine the profile of the band made of Lu4f and O2p. The cross-section curves of these levels cross at around 80 eV. The valence band photoemission spectra are represented in Fig. 5 Under 50 eV excitation, the absorption of O2p is dominant. The spectrum at 60 eV is almost unchanged ; these spectra represent the O2p contribution to the valence band consisting in two spin-orbit sub-levels. Above 70 eV excitation, it appears a narrow additional peak on the high energy side of the spectrum. Under 190 eV excitation, the contribution of O2p is negligible compared to the much larger photoionization cross-section of Lu4f. However, the peak is still broad, and in order to check the absence of any O2p contribution, it was proceeded to the following procedure. The dotted line curve is the result of the subtraction of "50 eV" and "100 eV" spectra, with a coefficient 0,57 which is the ratio of Lu4f/O2p photoionization cross-sections under 100 eV excitation. This curve nicely reproduces the photoemission band obtained under 190 eV excitation, demonstrating the only contribution of the Lu4f level to the valence band at this excitation energy. The width of the Lu4f level is about 10 eV, indicating that these states occupy the total width of the valence band. This result is very important for the interpretation of the valence band hole capture by Ce4f level in the scintillator $LuAlO_3$:Ce. It shows the possibility of direct Lu4f hole capture by Ce4f without passing through the intermediate 02p states.

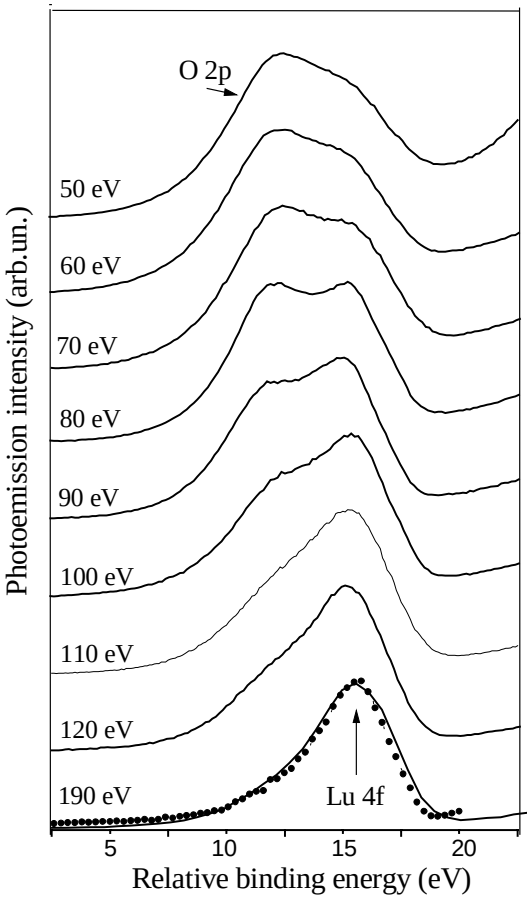

Fig.5: $LuAlO_3$ valance band spectra at different excitation The dotted line curve is the result of the subtraction of "50 eV" and "100 eV" spectra.)

Surface of CsI

The core state energies depend on the ion environment. The energy core level spectra are therefore different for an ion in the bulk and at the surface of the sample. The mean free path of an electron with energy 20-100 eV in a crystal is typically 0,5 nm. The variation of the excitation energy can point out the contribution of the surface states. In Fig. 6 are shown the results of a Cs4d and I4d photoemission spectrum analysis for CsI under 110 eV excitation. The shape of the I4d bands does not change with the excitation energy ; the bands are assigned to the two spin-orbit components of I4d and reflect the photoemission of I^- in the bulk. On the other hand, the profile of the Cs4d spectrum is more complex and changes with the excitation energy. It is possible to fit the spectrum by two pairs of bands separated by the same energy which characterizes the spin-orbit coupling. These two pairs of bands are attributed to the Cs^+ photoemission at the surface and in the bulk, respectively, as indicated in Fig. 6. This result can be interpreted as the effect of surface metallization of CsI.

Acknowledgments

This work was performed in the frame of "Crystal Clear" collaboration with CERN and was supported in part by the program "Réseau Formation-Recherche-Europe Centrale et Orientale", contract n° 150971C, of the French Ministry of Education and Science.

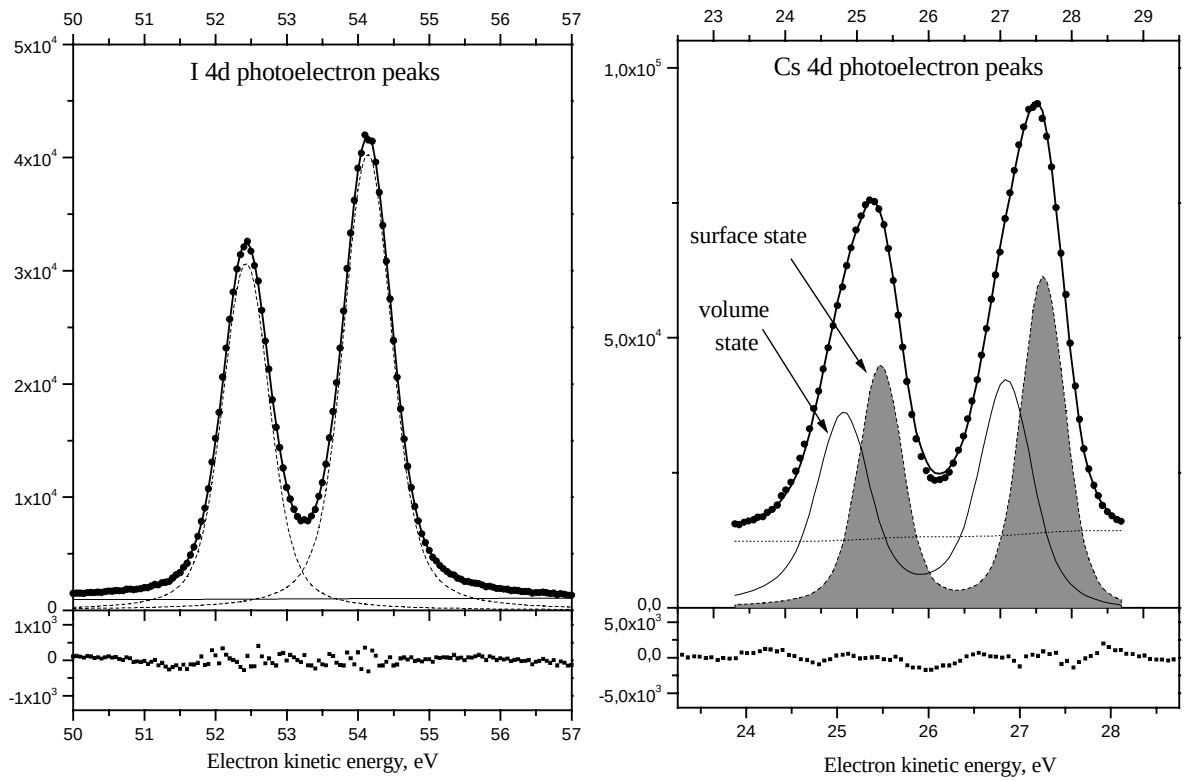

Fig.6: Photoemission spectrum (points) of I4d (left) and of Cs4d (right) of CsI.

References

1. Y. Zhang, N. A. W. Holszwarth, and R. T. Williams, Phys. Rev. B 57 (1998) 12738
2. R.A.Glukhov, A.N.Belsky, C.Pedrini, A.N.Vasil'ev, J. of Alloys and Compounds 275-77 (1998) 489
3. Belsky A. N., Comtet G., Dujardin G., Gektin A. V., Hellner L., Kamenskikh I. A., Martin P., Mikhailin V. V., Pedrini C., Vasil'ev A. N., Journal of Electron Spectroscopy and Related Phenomena 80 (1996) 109
4. M.Huisinga, V.E.Puchin, M.Reichling. NIM B141 (1998) 528
5. M.Cardona, R. Haensel, D. W. Lynch, and B. Sonntag. Phys. Rev. B 2 (1970) 1117
6. K. Ichikawa, O. Aita and K. Aoki. Phys. Rev. B 45 (1992) 3221

Scintillators on the base of single crystalline films of Al_2O_3-Y_2O_3 system oxides

[1]Yu. Zorenko, [1]V. Gorbenko, [1]I. Konstankevych, [1]M.Pashkovsky, [2]M.Globus, [2]B. Grinyov, [2]V.Tarasov, [3]P.Dorenbos, [3]C.W.E. van Eijk, [3]Edgar van Loef

[1]Institute of Applied Physics Lviv State University, 49 General Chuprynka Str., Lviv, 290044, Ukraine; [2]Institute for Single Crytals, 60 Lenin av., 310001, Kharkov, Ukraine; [3]Delft University of Technology, Faculty of Applied Physics, c/o IRI, Mekelweg 15, 2629 JB Delft, The Netherlands;

Abstract. Scintillation properties of single crystal films of Al_2O_3-Y_2O_3 oxide system grown by liquid phase epitaxy with the α-Al_2O_3, perovskite and garnet crystal structure for possible application in radioisotope monitoring have been investigated. Scintillators based on $Y_3Al_5O_{12}$:Ce SCF have been shown to have sufficient energy resolution of 8,3% and light yield of 0.4 with comparison to CsJ:Tl under irradiation by 5.15 MeV α-particles of ^{239}Pu. Absolute light yield of such SCF under ^{137}Cs source irradiation is equal to 12200 photons/MeV. It has been shown that SCF light yield can be increased by a factor of 1.45-1.5 in case of SCF on the basis of $YAlO_3$:Ce. The possibility of producing combined scintillators of the "phoswitch" type on the basis of "$Y_3Al_5O_{12}$:Ce ($Y_{3-x}Gd_xAl_5O_{12}$:Ce) SCF - $Y_3Al_5O_{12}$:Sc bulk crystal" for detection of the partial components of mixed ionizing fluxes is discussed.

Key words: oxides, single crystal films, scintillators, epitaxy, impurities.

Introduction

Progress achieved in the field of fabrication of single crystal films (SCF) of oxides by liquid phase epitaxy (LPE) needed for electronics and laser engineering opens an opportunity for producing series of film scintillation detectors on that basis [1]. Of all oxides suitable for this purpose, compounds like the Al_2O_3-Y_2O_3 system with α-Al_2O_3 leucosapphire, $YAlO_3$ perovskite and $Y_3Al_5O_{12}$ garnet structure attracts attention. Technology of producing the crystal with required dimensions is sufficiently developed, besides substrates of these compounds are commercially available and of relatively low cost.

The scintillators based on SCF can be applied for the following applications:

1. Radiation monitoring of α- and β- activities of radionuclides.

2. Detection of radiation with different penetrating ability by scintillators of the "phoswitch" type (SCF-scintillator on substrate-scintillator).

3. Detection of neutrons against radiation of other particles and quanta.

4. Biological monitoring by using X-ray detectors with screens on the basis of SCF with high spatial resolution [2,3].

In this paper, we study the principal possibility of fulfillment of the above mentioned applica-tions by means of manufacturing different types of scintillators on the basis of SCF of the Al_2O_3-Y_2O_3 compound system. It should be noted that this system allows wide modification of the composition and structure of crystallophosphors what makes it possible to produce on their basis a number of scintillators for detection of particles and low-energy quanta, in par-ticular those with various magnitude of effective atomic number z_{eff} from the range of 11- 60.

As activating impurities for these compounds Ce^{3+} ions are used, as a rule, that ensures large light yield of luminescence and high speed response (τ~20-70 ns) of the detectors. At the same time the LPE technology also enables to activate SCF of the studied oxides by mercury-like ions (Pb^{2+},Bi^{3+}) in the chosen concentration range.

Growth of scintillators on the basis of SCF

The growth of SCF of the investigated oxides was performed on the LPE standard equipment in the furnace with resistive heating using Pt-mounting from the overcooled melt solution (MS) based on $PbO:B_2O_3$ (1:10 mol/mol) fluxing agent, as well as crystal forming Al_2O_3, Y_2O_3 and R_2O_3 (R=Ce, Gd, Lu) oxides with total concentration of 9-12%. The purity of the initial component was 99,91… 99,99% with the content of transition metals of $3\cdot10^{-4}$-$3\cdot10^{-5}$ mol.%. Special attention should be given to the purity of the fluxing agent (up to 85-90 mass.% of MS): the most appropriate is using PbO of the yellow modification (Fe content not larger than $3\cdot10^{-4}$ mass.%) and powders of the undoped α-Al_2O_3, $YAlO_3$ and $Y_3Al_5O_{12}$ crystals as crystal forming components.

The wafers of undoped α-Al_2O_3, $YAlO_3$ and $Y_3Al_5O_{12}$ crystals with orientation perpendicular to the main crystallographic axes of crystals (for example, (111) or (100) for the case of garnet) and the thickness of 0.7-0.9 mm were used as substrates. In the case of manufacturing of the "phoswitch" detectors the wafers of $Y_3Al_5O_{12}$ and $Y_3Al_5O_{12}:Sc_x$ (x=0.15-0.2) crystals with the thickness of 2-5 mm were taken as substrates. The SCF thickness was determined by the type and energy of detecting particles or quantum, particular for detecting of α-activity of radionuclides (for example, ^{239}Pu) the thickness value did not exceed the particle path in a material (12-15 μm); whereas for the monitoring of β-activity (for example, $^{90}Sr+^{90}Y$ with the particle path untill 300-330 m) the thickness should be in the 50-70 μm range, mainly from the viewpoint of obtaining satisfactory structural quality of SCF. For X-ray detector screens [2,3] on the basis of $Y_3Al_5O_{12}$:Ce and $Lu_3Al_5O_{12}:Ce^{3+}$ the SCF thickness which determines the detector resolution can be chosen in the 1-5 μm (±0.1 μm) range. For the growth temperatures T_g from the 885-1050°C range the growth rate was 0.1-2.4 μm/min with a velocity of substrate rotation ω~80 rev./min.

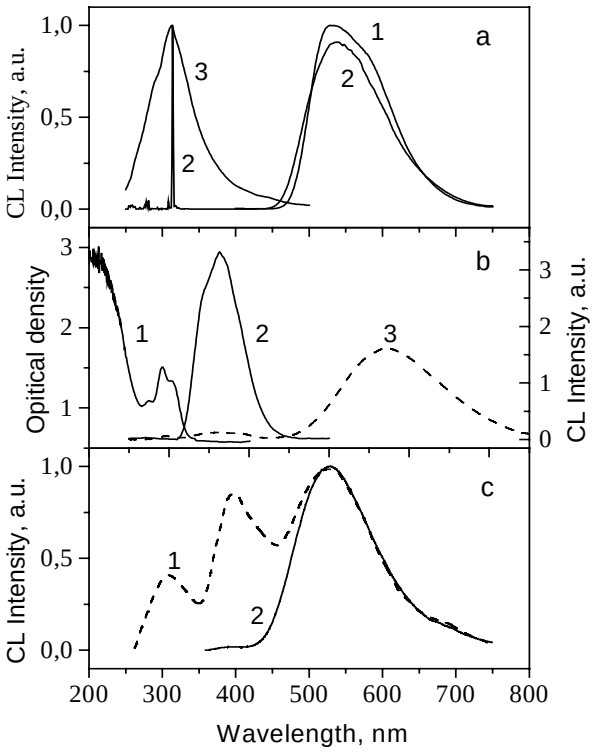

Fig. 1. a – Cathodoluminescent spectra (CL) of $Y_3Al_5O_{12}$:Ce SCF (1), $Y_{2.1}Gd_{0.9}Al_5O_{12}$:Ce SCF (2) and $Y_3Al_5O_{12}$:Sc bulk crystal (3); b - absorption spectra of $YAlO_3$:Ce SCF (1), CL spectra of $YAlO_3$:Ce SCF (2) and $YAlO_3$:Pb SCF (3); c – CL spectra of α-Al_2O_3:Ce SCF (1) and α-$Al_{1.8}In_{0.2}O_3$:Pb SCF (2).

The ratio between Y_2O_3+R_2O_3 and Al_2O_3 in MS is determined by the homogeneity region of the given oxide structural type. In particular, for the SCF on the basis of $Y_3Al_5O_{12}$ and

$YAlO_3$ this ratio was equal to 1:4 and 0.92-1.02:1, respectively. The 8.6 -10,4 mol.% (with respect to crystal forming components) concentration of doped impurity of CeO_2 has been chosen experimentally with the aim of SCF light yield optimization.

Detection of α-, β- radiation

Among all compounds of the Al_2O_3-Y_2O_3 oxides, the $Y_3Al_5O_{12}$:Ce SCF are the most prospective ones for monitoring of α- and β- irradiation. This scintillator type emitting in the visible spectral range (allowed transitions from the low term of $5d^1$ shell on the $^2F_{5/2,7/2}$ levels of the ground states of Ce^{3+} ions, λ_{max}=535 nm (Fig.1,curve 1)) possesses quite satisfactory scintillation characteristics under radiation detection both by photoelectric multiplier (PM) and photodiode (PD). In particular, Fig.2 presents an example of detecting the α-particles of together with the resistance to the action of an aggressive environment, temperature and irradiation makes prospective the application of such scintillators for radiation monitoring in a severe environment. For example, for analysis of radiation pollution of liquids or their vapours. The undoubted advantage of such scintillators in comparison with the analogs based on alkaline halide crystals and plastic materials consists in high temperature stability of emission (the quenching occurs only at T>200^{o}C).

It should be noted that the main factor limiting the light yield of the Ce containing detectors based on the Al_2O_3-Y_2O_3 SCF system, obtained from the MS on the basis of Pb-containing fluxing materials, is the presence within SCF of quenching centers connected with Pb and Fe ions as background impurities in the fluxing agent. Minimizing the influence of those impurities may be reached under growing SCF at the lowest degrees of MS overcooling, as well as by means of the use of perfectly pure components for MS and annealing of SCF in a reduced atmosphere [4]. This sample was used subsequently as standard one for estimation of light yield of other scintillators on the basis of SCF.

For further increase of light yield of the scintillators based on the Al_2O_3-Y_2O_3 SCF sys-tem we have investigated for the first time the possibility of growing the $YAlO_3$ SCF with perovskite structure (Z_{eff}=34) on undoped $YAlO_3$ substrates by the LPE technique. The preliminary obtained data are summed up in Fig.1, b. The absorption spectrum is seen from Fig.1, b, (curve 1) to consist of the superimposed bands with λ_{max}=276, 292 and 302 nm corresponding to the transition from the $^2F_{5/2,7/2}$ ground state on the terms of 5d- shell of Ce^{3+} ion. In the luminescence spectrum (Fig.1,b, curve 2) one observes the wide emission band consisting of the superimposed unresolved at 300 K bands with λ_{max}=364 and 346 nm to corresponding to the interconfiguration transition $5d^1$- $4f(^2F_{5/2,7/2})$ of Ce^{3+} ion in $YAlO_3$ with the decay time of the main component τ=30ns.

The measured scintillation characteristics carried out with an PM FEU-110 under excitation by α-particles of ^{239}Pu source show that $YAlO_3$ SCF samples of good optical and structural quality at the activator concentration of 9.6-10.4 mol.% in MS have a light yield which exceeds that of the $Y_3Al_5O_{12}$:Ce standard sample by a factor of 1.45-1.50.This fact points to the possibility of increase of light yield and resolution of the detecting units on the basis of the $YAlO_3$ SCF where as a light converter a PM with 350-450 nm spectral sensitivity range is used. Meanwhile, it is reasonable to use in the scintillator detectors on the basis of PD the $Y_3Al_5O_{12}$:Ce SCF which have the most long wavelength emission spectrum of all Ce-containing crystallophosphors on the basis of the Al_2O_3-Y_2O_3 compounds.

With this aim we have studied the luminescence characteristics of $YAlO_3$:Pb obtained by crystallization of $YAlO_3$ SCF at low growth temperatures. The luminescence spectrum of $YAlO_3$:Pb SCF (Fig. 1, a, curve 2) has characteristics of emission of mercury-like Pb^{2+} ion in SCF of the Al_2O_3-Y_2O_3 composition [4] two band shape with the maxima at 370 and 570 nm which correspond to the emission transition of the PbO_6^{10-} complexes. At increasing

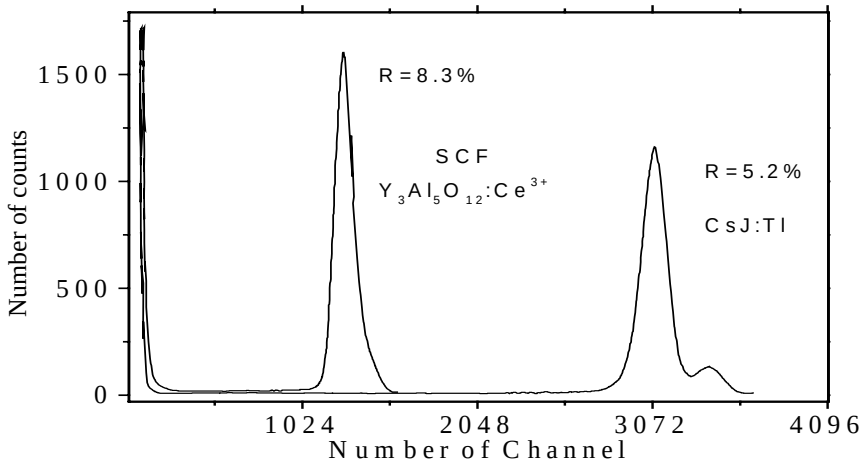

Fig. 2.Voltage distribution of output impulses for a single crystalline film $Y_3Al_5O_{12}:Ce^{3+}$, coupled with the photo-multiplier "Hamamatzu R1307", under irradiation by 5.15 MeV α-particles of Pu^{239} (the left-hand curve). For comparison, the corresponding distribution of impulses is given for a thin CsI:Tl plate (the right- hand curve).

the Pb ion concentration the band with λ_{max}=570 nm is dominant in the emission spectrum. The light yield of the SCF emission in this band when detecting the scintillations by PD is equal to 0.62 of corresponding value for a reference sample of the SCF $Y_3Al_5O_{12}$:Ce which has the similar emission spectrum. The decay time of the main component amounts to ~1.0-1.1 μs in the $YAlO_3$ SCF at 300K.

As continuation of these works we have studied the possibility of manufacturing SCF on the basis of α-Al_2O_3 for which Z_{eff}=11 that is close to the human body equivalence and have determined their scintillation characteristics. The ions of Ce^{3+} and Pb^{2+} (doping was performed directly by the MS component) were used as activators. The luminescence spectra of the α-Al_2O_3:Ce and α-Al_2O_3:Pb are plotted in Fig.1, c, curves 1 and 2, respectively. It should be noted that we have failed to reach the optimum degree of doping of the Al_2O_3 SCF by Ce^{3+} ions, that seems to result from the large difference in their ionic radii. Together with the luminescence band of Ce^{3+} with λ_{max}=396 nm, τ=50ns the emission spectrum bands of the mercury like Pb^{2+} ions with λ_{max}=310 and 526 nm appear in the emission of these SCF (Fig. 2, c, curve1). Increase in the segregation coefficient of the Pb ions in the α-Al_2O_3 SCF may be reached by introducing in the MS optically inactive ions with large ionic radius, for example, In. The luminescence spectrum of the $Al_{2-x}In_xO_3$:Pb SCF (x=0.1-0.3) is shown in Fig. 2, c, curve 2. It is seen that in the emission the long wavelength component with λ_{max}=526 nm corresponding to the radiative transition of the PbO_4^{6-} complexes is dominant one [7]. Under exciting the α-$Al_{2-x}In_xO_3$:Pb SCF by the ^{239}Pu source of α-particles the light yield in the scintillator unit with FEU-110 was equal to 0.3-0.4 comparison with $Y_3Al_5O_{12}$:Ce SCF standard sample and the decay time of the main component of 1.4-1.5 μs at 300 K.

Thus, the technology state we have achieved allows to obtain scintillators on the basis of SCF of the Al_2O_3-Y_2O_3 compounds doped by Ce with the light yield at exciting by ^{239}Pu source being not less 0.27-0.35 of that for NaJ:Tl; the light yield of SCF of the Y_2O_3 -Al_2O_3 system doped Pb ions is equal to 0.085-0.17 with respect to NaJ:Tl .

Detection of mixed ionizing fluxes

The LPE technology makes it possible producing the qualitatively new types of combined scintillators (CS) for the detection of components of mixed radiation fluxes. Such scintillators of the "phoswitch" type consist of one or two SCF for detecting α- , β-radiation and a bulk scintillator- substrate which is used for detection of X-ray and γ-radiation. The advantages of

these types of SC as compared with known analogs on the basis of alkaline halide crystals consist in their high chemical, thermal and radiation resistance, as well as in the approximate equality of the refraction coefficients of the SC parts what allows to practically avoid light loss at the scintillator interface. The possibility of specifying with high accuracy (±1 μm) the thickness equal to the α- or β-particles path length also enables to enhance the selectivity of detection of partial component of mixed radiation fluxes.

As a variant of producing the "phoswitch" scintillators on the basis of compounds of the Al_2O_3-Y_2O_3 system we have obtained and studied the $Y_3Al_5O_{12}$:Ce SCF - bulk crystal $Y_3Al_5O_{12}$: Sc CS. This SC may be used for monitoring of α-activity against β-, X-ray or γ-radiation depending on the substrate thickness in the 0.5-5 mm range. With the aim of increasing the light yield of the bulk component up to the value of 0.5 with respect to NaJ:Tl (using ^{137}Cs source) the $Y_3Al_5O_{12}$ substrate doping by Sc^{3+} impurities with concentration 0.15-0.2 per formula unit. The emission spectra of the $Y_3Al_5O_{12}$:Sc bulk crystal plotted in Fig. 1, a curve 3 consists of the wide peak in the UV range with λ_{max} =300 nm and τ≈0.8-0.9 μs. The light yield under exciting by γ-quanta of ^{137}Cs source (662 keV) is equal to 0.4-0.5 of that for NaJ:Tl in the given range of activator concentration. Separation of the signal from different components of CS can be performed by means of both selections with respect to τ and difference in the emission specta (Fig. 1, a).

The above mentioned type of the "phoswitch" scintillator has been also used for analysis of decomposition products of nuclei reactions with Z_{eff}≤25 in the wide energy range [5]. In this regard for the effective separation of n-γ or γ-p-α separation it is possible the use of CS with the three luminescent components, for example, $Y_3Al_5O_{12}$:Ce SCF - $Y_3Al_5O_{12}$:Pr (Nd) SCF - $Y_3Al_5O_{12}$:Sc bulk crystal with decay time equal to 70 ns, 30 ns (3.5 μs) and 0.8-0.9 μs, respectively.

The CS on the basis of the $(LuGd)_3Al_5O_{12}$:Ce SCF - $Y_3Al_5O_{12}$:Sc bulk crystal may be proposed as a type of construction of CS for detecting the warm neutrons. The SCF composition enables a replacement of Lu^{3+} up to one formula unit by Gd^{3+} ions without mismatching the SCF and substrate lattice constants. By taking this into account, the optimum thickness of the SCF for neutron absorption is about 30 μm. The $(LuGd)_3Al_5O_{12}$:Ce SCF emission spectra is shown in Fig. 1, a, curve 3. The shift of the maximum in the long wave length region as compared to the $Y_3Al_5O_{12}$:Ce^{3+} SCF makes it possible the use of detectors on the basis of photodiodes. The estimation of the light yield of SCF of this composition under exciting by ^{239}Pu source is equal to 0.5-0.6 with respect to the $Y_3Al_5O_{12}$:Ce SCF standard sample.

It should be noted that because of the low values of Z_{eff}=11-34 compounds on the basis of Al_2O_3-Y_2O_3 system may be used for detecting low energy quanta. In this regard construction of the "phoswitch"-scintillators on the basis of of oxides with large Z_{eff} is of interest. A possibility of producing such a CS on the basis of $CdWO_4$ compound has been considered by our in [6]. Carrying out the analogous works on $Bi_3Ge_4O_{12}$, by taking into account the high Z_{eff} value and cubic symmetry of unit cell, is also a prospective trend of investigation.

Acknowledgments

The work has been supported by INTAS-Ukraine under Grant No. 95/0166.

References

1. Yu.V.Zorenko, P.S.Malutenkov, N.I.Patsagan, I.V.Nazar, V.I.Gorbenko, M.M.Batenchuk, and M.V.Pashkovsky. Crystal Properties and Preparation, **36-38** (1991) 226.
2. .Koch, C.Raven, P.Spane, and A.Snigirev. J. Opt. Soc. Am. A. **15** (1998) 1940.

3. Yu.Zorenko, V.Gorbenko, I.Konstankevych, M.Batenchuk, M.Thoms. In Proceedings of SCINT'99, Moskow, Russia, 1999.
4. Yu.V.Zorenko, M.M.Batenchyk, V. I.Gorbenko, M.V.Pashkovsky, and I.V.Konstankevych. Zhurnal Pryklodnoj Spectroscopii, **67** (1999) 421.
5. V.V.Kamanin, A.Kugler, Y.G.Sobolev, A.S.Fomichev, S.Batsev, I.David, Yu.Zorenko. Commun. of the Joint Institute for Nuclear Research, Dubna, 1989.
6. Yu.Zorenko. Zhurnal Prykladnoj Spectroscopii, **65** (1998) 211.
7. Yu.Zorenko. Ukrainskyj Fizychnyj Zhurnal, **42** (1997) 559.

Emission Properties of Chloride Elpasolites

E.N. Mel'chakov[1], A.N. Mishin[1], B. Moine[2], C. Pedrini[2], S.V. Petrov[3], P.A. Rodnyi[1], A.V. Sidorenko[1]

[1]*Experimental Physics Department, St.Petersburg State Technical University, Polytechnicheskaya 29, 195251 St.Petersburg, Russian Federation*
[2]*Laboratoire de Physico-Chimie des Matériaux Luminescents, Université Claude Bernard Lyon 1, 43 boulevard du 11 Novembre 1918, 69622 Villeurbanne Cedex, France*
[3]*Institute for Physical Problems, Kosygina 2, 117973 Moscow, Russian Federation*

Abstract. Time-resolved emission spectra, luminescence excitation spectra, and decay curves of Cs-based elpasolite-structure chlorides measured under VUV and X-ray excitations are presented. The crystals offer two kinds of emission: intrinsic core-valence luminescence with decay constant about 2 ns and d-f and f-f transitions of rare-earth ions. The energy-band parameters of two crystals are estimated: $E_g \approx 8.6$ eV, $\Delta E_v \approx 2.6$ eV in $Cs_2NaLaCl_6$, and $E_g \approx 8.2$ eV, $\Delta E_v \approx 3.0$ eV in Cs_2KLaCl_6.

Keywords**:** core-valence luminescence, Ce^{3+}, Pr^{3+}, Gd^{3+} emission, VUV excitation, Cs-based chloride elpasolites

Introduction

There is great current interest in high energy physics, nuclear physics, and medicine in the development of new scintillation materials with high light output and short decay time. The essential feature required of scintillation materials is to be effective converter of high energy excitation to visible light, this is important also for cathode-ray phosphors, phosphors for X-ray intensifying screens and electron-pumped lasers. Reduction of the energy losses is very important in the devices transforming the high-energy excitation to visible light. Central to further progress in this field is the need for an understanding of the fundamental process, which follow the interaction of incident ionizing radiation with a scintillation material. Thus, the scintillation processes are considerable interest from a purely scientific point of view as well as for practice.

The allowed 5d $\rightarrow$ 4f transitions of Ce^{3+} and Pr^{3+} ions are the best for scintillator materials [1,2]. Shortest decay time (near 1 ns or less) is typical for core-valence luminescence (CVL), these are radiative hole transitions between upper core and valence bands of crystal [3]. Thus, materials with CVL-active cations (Cs, Rb, Ba) are required. The combination of CVL-active matrix with Ce, Pr, Gd-doping may lead to increasing of general emission intensity in complex halide compounds. The choice of crystals with CVL creates the additional channel for Ce-centres excitation enabling their recombination with core excitons and holes. Besides, ionic crystals with small band gap are desired and therefore chlorides are promising materials.

In the cubic elpasolites like $Cs_2NaLnCl_6$, the rare earth ions (Ln) occupy a centrosymmetric O_h site, and this is interesting for rare-earth spectroscopy [4,5,6] and for laser materials [1,7]. Considerably less attention has been paid to emission properties of the elpasolite-structure halides at high energy excitation [8]. In this work we extend our previous study of various halides to the chloride elpasolites Cs_2MLnCl_6 (M = Na, K, Rb, Cs, Ln = La, Ce, Pr, Gd) potentially useful for scintillators. In such crystals it is possible to observe CVL and emission of the rare-earth ions. Unlike the laser investigations, our interest here is with emission properties of the crystals under X-ray (30 keV) and VUV (10 - 140 eV) excitations.

Experimental

The Cs_2MLnCl_6 crystals have been prepared from the melts of proper mixtures of single crystalline CsCl, MCl and $LnCl_3$ compounds using the Bridgeman technique. Taking into account that the initial materials are hygroscopic, the preparation procedures have been performed in dry atmosphere.

For fast-emission measurements the subnanosecond (~ 0.6 ns) pulsed (repetition frequency 20 kHz) X-ray (40 kV) source has been used [9]. Energy of single X-ray pulse is about 10^{-8} J and such a pulse acts on a sample similar to high energy gamma quantum. A grating MDR-2 monochromator, FEU-71 photomultiplier and a single photon counting technique were used for the emission detection.

Luminescence excitation spectra were measured under selective VUV excitation in region 10 -140eV from SuperACO, synchrotron radiation source at LURE (Orsay, France). Measurements were performed in double-bunch mode of the synchrotron source operation. The pulse duration is 500ps and the repetition rate is 4MHz. Standard technique for time-resolved spectroscopy allowed the use of the time-gate option to separate the emission components of different decay rates. Emission was detected by fast photomultiplier tube through UV-VIS monochromator Jobin-Yvon D-10. Time resolution estimated is better then 100ps and spectral resolution is about 1 nm.

Results and discussion

Fig.1 shows the emission spectra of the pure $Cs_2NaLaCl_6$ and Cs_2KLaCl_6 crystals measured at pulsed X-ray excitation. Both crystals exhibit two emission bands 3.3 and 4.2 eV in Cs_2KLaCl_6, and 4.0 and 4.65 eV in $Cs_2NaLaCl_6$. The spectra in fig.1 are normalized, actually, relative energy efficiency of $Cs_2NaLaCl_6$ is 0.6% (as in CsCl) and it is slightly less in $Cs_2NaLaCl_6$. The excitation spectrum of Cs_2KLaCl_6 displays for both emission bands of double threshold 13.3 and 14.5 eV and a number of peaks: 14.2, 14.9, 15.8, 16.7, and 20.7 eV (fig.2). The similar threshold in $Cs_2NaLaCl_6$ is at 14 eV [10]. The decay curve of Cs_2KLaCl_6 (inset in fig.2) contains fast component 1.9 ns and slow component ~ 1 μs. The slow component belongs to excitonic luminescence, because the excitation spectrum of this emission exhibits a narrow peak at 7.55 eV. The basic decay component of $Cs_2NaLaCl_6$ is 2.0 ns. The luminescence intensity of the crystals shows thermal stability in range 80 to 400 K.

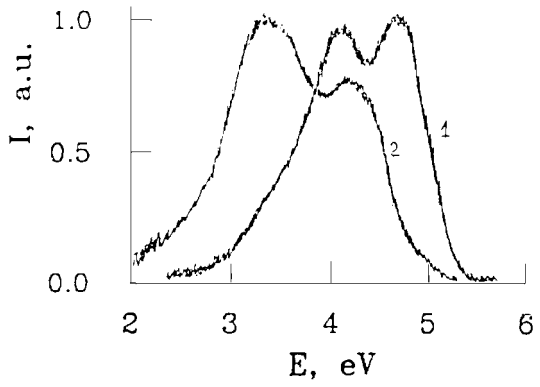

Fig.1. Pulsed X-ray excited spectra of 1- $Cs_2NaLaCl_6$, 2- Cs_2KLaCl_6, T = 300 K

The main decay constants, positions of the excitation thresholds and the luminescence bands point on CVL origin of the detected emission in $Cs_2NaLaCl_6$ and Cs_2KLaCl_6. The Cs^+ ions have 12-fold coordination in elpasolites, and the cluster model of core-valance 5pCs → 3pCl transitions predicts two or three CVL bands [11].

The obtained spectra allow us to determine parameters of energy bands in the crystals: valence band width ΔE_v and band gap E_g. In $Cs_2NaLaCl_6$: $E_g \approx 8.6$ eV, $\Delta E_v \approx 2.6$ eV , in Cs_2KLaCl_6: $E_g \approx 8.2$ eV, $\Delta E_v \approx 3.0$ eV. These data are in agreement with photoelectron emission spectra [12].

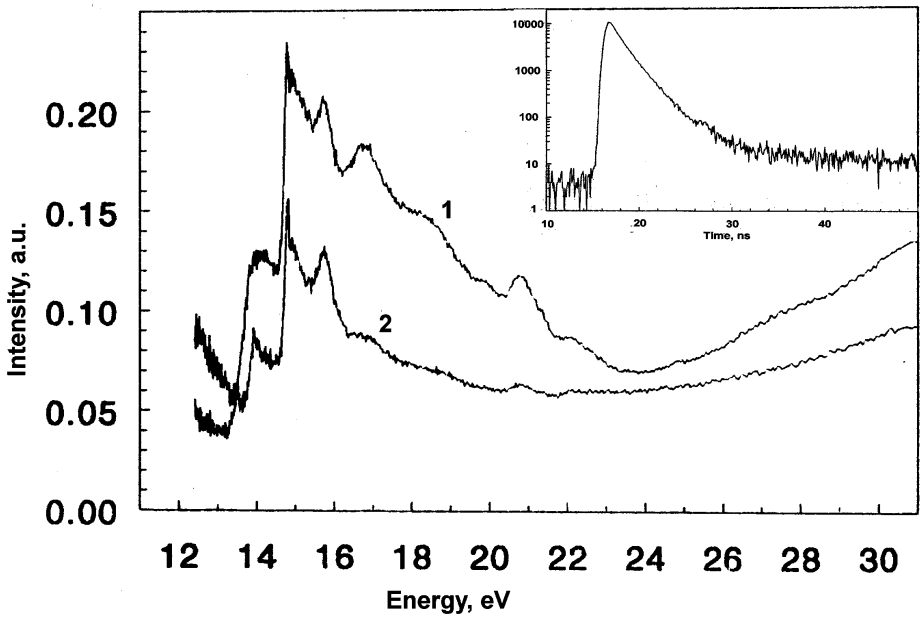

Fig.2. Excitation spectra of intrinsic luminescence of Cs_2KLaCl_6 measured through filters: 1 - UG5, 2 - UG3 at room temperature; inset – decay time curve of the luminescence.

The $Cs_2RbLaCl_6$ exhibits high emission yield at VUV excitation due to overlapping of the Cs and Rb core bands. In Cs_3LaCl_6 lattice, Cs ions occupy different sites to form two clusters [$CsCl_{12}$] and [$CsCl_6$] which responsible for CVL in this system. Correspondingly, two decay components (1.2 and 2.7 ns) of CVL have been detected.

It is known that an incorporation of Ce^{3+} ions in halides improves scintillation characteristics of crystals. Fig.3 presents X-ray-excited emission spectra of $Cs_2NaLaCl_6$:Ce(0.1 mol.%) and $Cs_2NaCeCl_6$ crystals. The 5d $\rightarrow$ 4f emission of Ce^{3+} ions (370 and 405nm bands) predominates in the crystals. Shot-wavelength CVL bands are detected only up to ~ 1 mol.% Ce. Maximum light output for $Cs_2NaCeCl_6$ is 12,000 photons/MeV. We have managed to approximate decay curve of $Cs_2NaCeCl_6$ by three decay constants: 1.89, 9.4 and 31.6 ns. Excitation spectrum exhibits typical for Ce^{3+} structure in range 5 to 8 eV. Besides, a threshold near 14 eV was detected, it means that core-valence transitions in $Cs_2NaCeCl_6$ take part in excitation of Ce^{3+} ions, like $CeCl_3$ [13]. In high-energy region the excitation spectrum of the fast emission exhibits a maximum near 80 eV (insert in fig.3). The maximum corresponds to position of 4d level of Cs, it means that holes from this level pass efficiently into upper 5pCs core band.

Conclusions

The $Cs_2NaLaCl_6$ and Cs_2KLaCl_6 crystals exhibit fast (~ 2 ns) and rather efficient emission under X-ray and VUV excitation. The emission characteristics point on its CVL origin. The energy-band parameters of the crystals are estimated: $E_g \approx 8.6$ eV, $\Delta E_v \approx 2.6$ eV in $Cs_2NaLaCl_6$, and $E_g \approx 8.2$ eV, $\Delta E_v \approx 3.0$ eV in Cs_2KLaCl_6.

Incorporation of Ce^{3+} ions improves the emission efficiency of the elpasolites. At high energy excitation, $Cs_2NaCeCl_6$ exhibits efficient d-f luminescence without CVL. The Pr and Gd ions influence slightly on intensity of CVL of host crystals. $Cs_2NaPrCl_6$ (weak d $\rightarrow$ f transitions) and $Cs_2NaGdCl_6$ (long decay time) offer not good scintillation properties. It seems reasonable to introduce a co-activator (Ce^{3+}) in $Cs_2NaGdCl_6$ as is done in $RbGd_2Br_7$ [14].

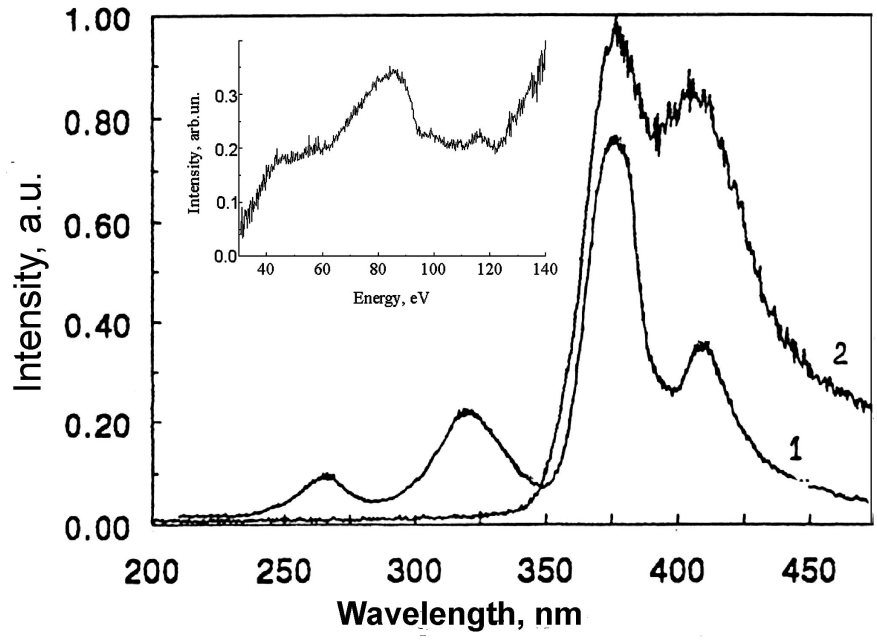

Fig.3. X-ray excited emission spectra of 1 - $Cs_2NaLaCl_6$:Ce (0.1 mol.%), 2 - $Cs_2NaCeCl_6$; inset – excitation spectrum of the emission around 320 nm, T = 300 K.

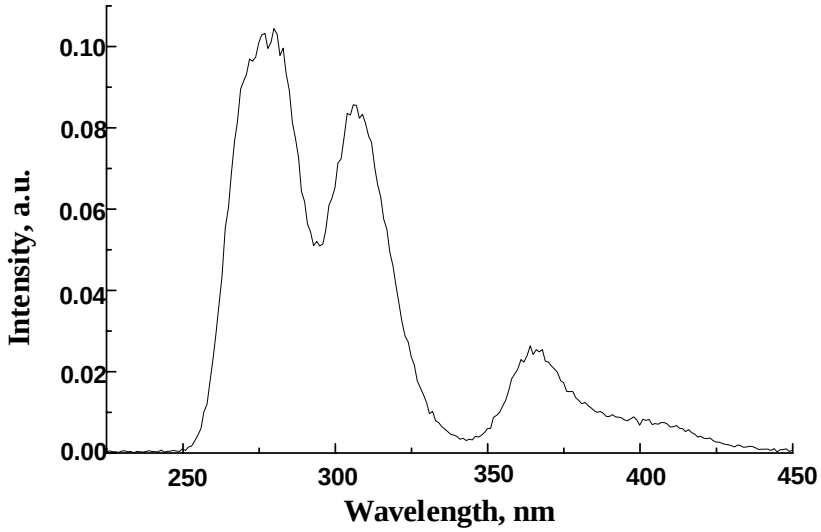

Fig. 4. Emission spectrum of $Cs_2NaPrCl_6$ at 100-eV excitation.

The emission spectrum of $Cs_2NaGdCl_6$ (fig.5) at 100-eV excitation exhibits a very intensive 315-nm band ($^6P \rightarrow {}^8S_{7/2}$ transitions of Gd^{3+}) with decay time of few milliseconds. The emission offers nearly the same intensity of CVL (255 and 275 nm bands) as in $Cs_2NaLaCl_6$, in remaining the spectrum in fig. 5 is similar to that at optical excitation [4].

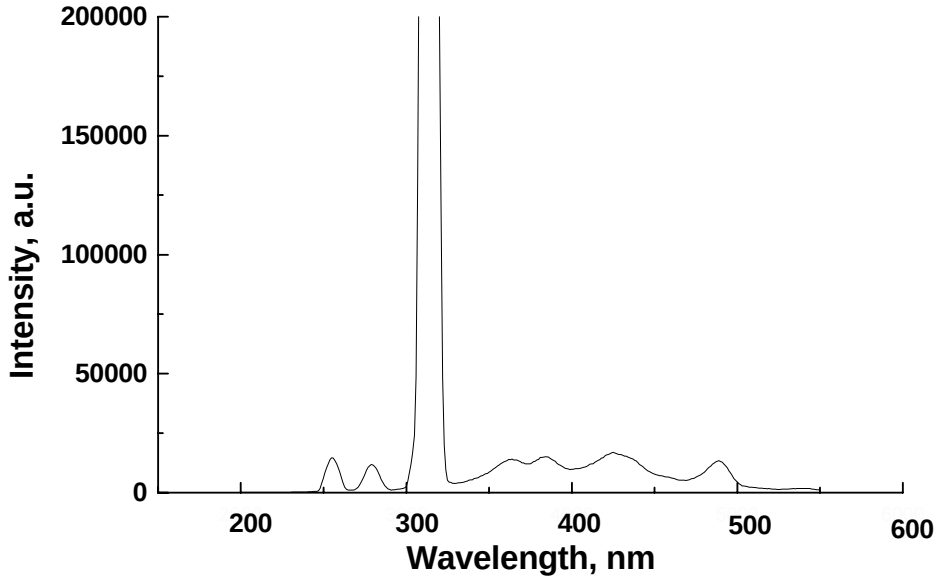

Fig.5. Emission spectrum of $Cs_2NaGdCl_6$ at 100-eV excitation.

References

1. B.F. Aull and H.P. Jenssen, Phys. Rev. B 34 (1986) 6640.
2. C.W.E. van Eijk, SPIE, 2706 (1996) 158.
3. P.A. Rodnyi, Sov. Phys. Solid State, 34 (1992) 1053.
4. A.J. de Vries and G. Blasse, J. Chem. Phys., 88 (1988) 7312.
5. M. Boauazaoui, B. Jacquier, C. Linares, and W. Strek, J. Phys.: Condens. Matter, 3 (1991) 921.
6. W. Ryba-Romanovski, G. Dominiak-Dzik, and S. Golab, J. Phys.: Condens. Matter, 6 (1994) 1593.
7. K.M. Murdoch, R. Cavellec, E. Simoni, M. Karbowiak, S. Hubert, and N.M. Edelstain, J. Chem. Phys., 108 (1998) 6353.
8. J.C. van't Spijker, P. Dorenbos, C.W.E. van Eijk, M.S. Wickleder, H.U. Gudel, and P.A. Rodnyi, J. Luminesc., 72-74 (1997) 786.
9. P.A. Rodnyi, B.R. Namozov, A.V. Rozhkov, and A.G. Ryzhkov, Patent RF, N2054739, 1996.
10. A.S. Voloshinovskii, V.B. Mikhailik, P.A. Rodnyi, I.P. Pashuk, O.T. Antonyak, and N.S. Pidzyrailo, Proc. of Int. Conf. "Inorganic Scintillators and Their Applications", eds. P. Dorenbos and C.W.E. van Eijk, Delft TU, (1995) 173.
11. A.S. Voloshinovskii, V.B. Mikhailik, P.A. Rodnyi, S.V. Syrotyuk, A.P. Shpak, and A.N. Yaresko, Phys. Solid State, 36 (1994) 1666.
12. I.H. Munro, S. Downes, P.A. Rodnyi, E.N. Mel'chakov, A.S. Voloshinovskii, and V.B.Mikhailik, Daresbury Annual Report 1994/1995, Daresbury Laboratory, Warrington, UK, (1995) 921.
13. A.S. Voloshinovskii, P.A. Rodnyi, O.T. Antonyak, N.S. Pidzyrailo, Phys. Solid State, 36 (1994) 339.
14. P. Dorenbos, J.C. van't Spijker, O.W.V. Frijns, C.W.E. van Eijk, K. Kramer, H.U. Gudel, and A. Ellens, Nucl. Instr. Meth. in Phys. Res., B132 (1997) 728.

GSO(Ce)-Based scintillator with energy resolution <10%

V.G.Bondar', V.P.Gavrilyuk, K.A.Katrunov, V.S.Kanevskii, E.V.Krivonosov, V.P.Martynov

Institute for Single Crystals, 60 Lenin ave., Kharkov, Ukraine

Abstract. Energy resolution 8.5% by γ-line 662 keV from ^{137}Cs was achieved by means of improvement of transparency and especially selected surface roughness of the cylindrical Gd_2SiO_5:Ce scintillator 27 mm in diameter and 90 mm long.

Key words: energy resolution, annealing, light collection

Introduction

It is known [1] that in case of registration of the scintillation light using photomultiplier energy resolution of the scintillation detector can be written as an expression: $R^2 = R_{in}^2 + R_{ph}^2 + R_{\tau}^2$, in which all the terms are statistically independent:

R_{in} is the value describing the dispersion of the light quantity which is formed in the process of radioluminescence and depends on the scintillator material;

R_{ph} is the value describing statistic variations of the number of photoelectrons knocked out from the photocathode by the scintillation photons; it is reversely proportional to the scintillator light output;

R_{τ} is the value corresponding to the nonuniformity of the light collection coefficient in different parts of the scintillator volume.

In this paper the authors made an attempt to improve energy resolution of GSO(Ce) detector owing to lowering the latter two terms by varying the bulk optical properties and reflection characteristics of the surface.

Annealing

It is difficult to get scintillators with high light output and energy resolution using a conventional growth method [2, 3]. A significant contribution to the deterioration of energy resolution is made by the nonuniformity of the light collection coefficient over the scintillator volume. This nonuniformity is explained by a significant absorption of the own luminescence due to the activator-vacancy complexes formed in the crystal growth process; the complexes are on the basis of cation vacancies of gadolinium and cerium ions. Decomposition of such complexes and the corresponding decrease of undesirable absorption is possible at annealing the crystals in the atmosphere with certain chemical potential. This has been already observed in oxide crystals doped with transitional ions [4].

The study was carried out with GSO(Ce) crystals (0.6 wt.% of Ce) 27 mm in diameter and 0.9 mm thick for measurements in the UV part of the spectrum; crystals 90 mm in length were taken for measurements in the region of λ>400 nm. The absorption spectra before and after annealing were registered on a spectral complex KSVU-23. The annealing was conducted in a furnace with a hermetic working space. Chemical potential of the atmosphere was about 40 kJ/mol. It is just this value corresponded to the best results. The annealing time was defined by the size of the samples, i.e. time of vacancy diffusion. Prior to measuring the spectra the end surfaces of the samples were polished to the roughness value R_z=0.05 μm. After annealing the transmission of the samples became better both in the region of radioluminescence (Fig.1) and in the UV part of the spectrum (Fig.2).

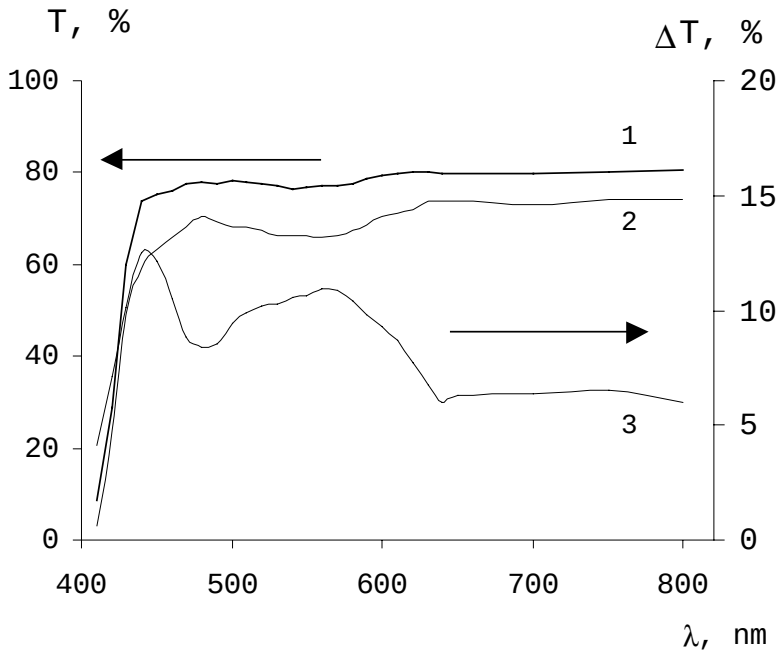

Fig.1 Transmission spectrum of GSO(Ce) crystal: 1– before annealing; 2 – after annealing; 3 – an extracted difference between the transmission spectra of the annealed and nonannealed samples.

This being so, the wavelength of the best transmission (λ=430 nm, Fig.1) practically coincides with the maximum of the luminescence spectrum [5]. The emergence of the well-structured band at λ=250 nm, a band near 200 nm as well as significant decrease of absorption at λ>210 nm (Fig.2) give evidence to a structural reconstruction of color centers in the UV part of the spectrum. Similar phenomena occur in high temperature oxides [6]; they are related to structural changes in activator-vacancy complexes. Improvement of transmission (in the long wavelength range) only in the wavelength range of luminescence of Ce activator ions confirms this point of view (Fig.1). A detailed study of the mechanism of structural reconstruction of activator-vacancy complexes under the effect of annealing in the controlled medium deviates from the theme of the present paper and requires special investigations.

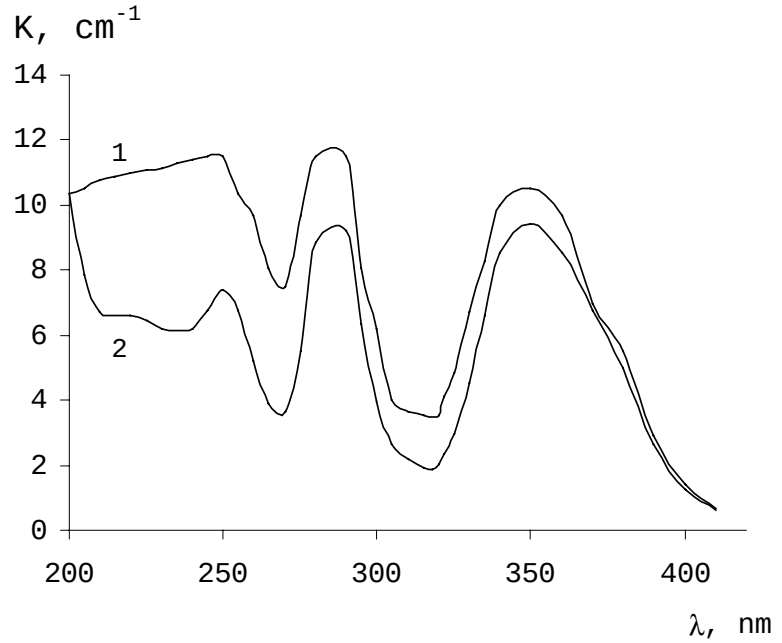

Fig.2 Absorption of GSO(Ce) samples: 1 - before thermal annealing; 2 - after thermal annealing.

Surface treatment of a scintillator

The effect of the scintillator transparency and character of its surface microrelief on energy resolution of the detector was studied using a numeric model of the light collection process [7]. This model is based on the method of Monte-Carlo, operating with the light beams as unit events. In the calculation of light scattering by the detector surface a conception of it being a smooth plane covered with randomly oriented grooves was used. This conception allowed to model the process of light collection in the detector which has no optical coupling between the reflecting coating and scintillator surface. The following values of GSO(Ce) characteristics were used for the calculation: refraction index n=1.9, light absorption coefficient in the luminescence band K=0.02…0.08 cm^{-1}. The output window (end) of the scintillator in the form of a cylinder was considered to have not a full coupling with the photoreceiver through the immersion medium with n=1.5. The coefficient of light reflection by the coating was R=0.85.

It is known [1, 7] that for achieving the best uniformity of the light collection coefficient τ over the length of the protruded cylinder all its surfaces are to be mirror smooth and the absorption coefficient should be minimal. Table 1 illustrates the degree of the effect of the scintillator transparency on resolution and light output of the detector.

Table 1. Calculated data on the mean light collection coefficient $\bar{\tau}$ and degree of its nonuniformity R_τ over the cylindrical scintillator ∅27×90 mm.

K, $см^{-1}$	0.08	0.06	0.04	0.03	0.02
$\bar{\tau}$	0.167	0.199	0.241	0.268	0.301
R_τ	32.6	20.1	9.6	6.2	4.7

The calculations show that there is no radial nonuniformity of τ at the given design of the detector. Deterioration of τ and R_τ is caused only by axial nonuniformity of τ (see Fig.3). The source of such deterioration is the increased absorption of the scintillation light. Thus, improvement of the scintillator transparency has a double effect: decrease of R_{ph} connected with the rise of $\bar{\tau}$ and light output; decrease of R_τ connected with the rise of the light collection coefficient from the parts of the scintillator remote from the photoreceiver.

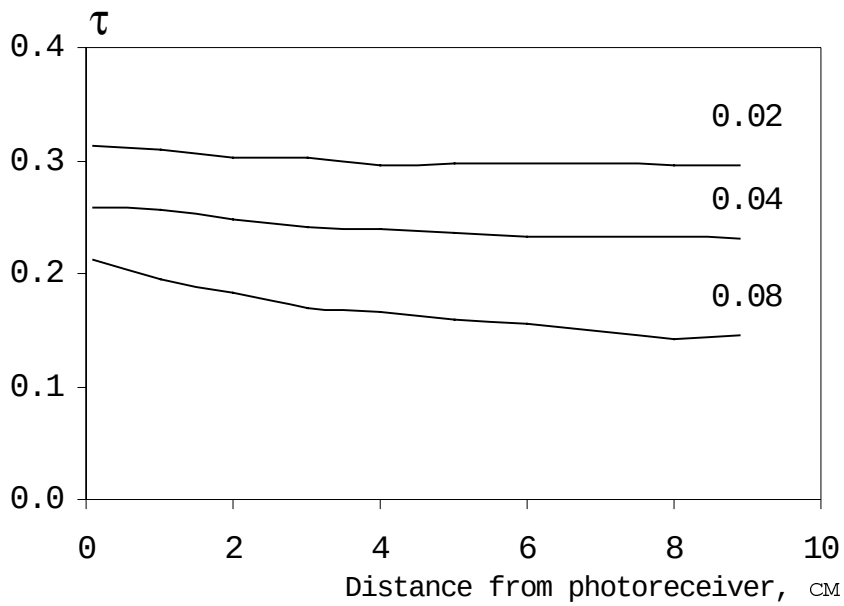

Fig.3 Calculated axial ditributions of the light collection coefficient over the length of the GSO(Ce) cylinder ∅27×90 mm. The numbers near the curves denote transparency of a scintillator K, cm^{-1}.

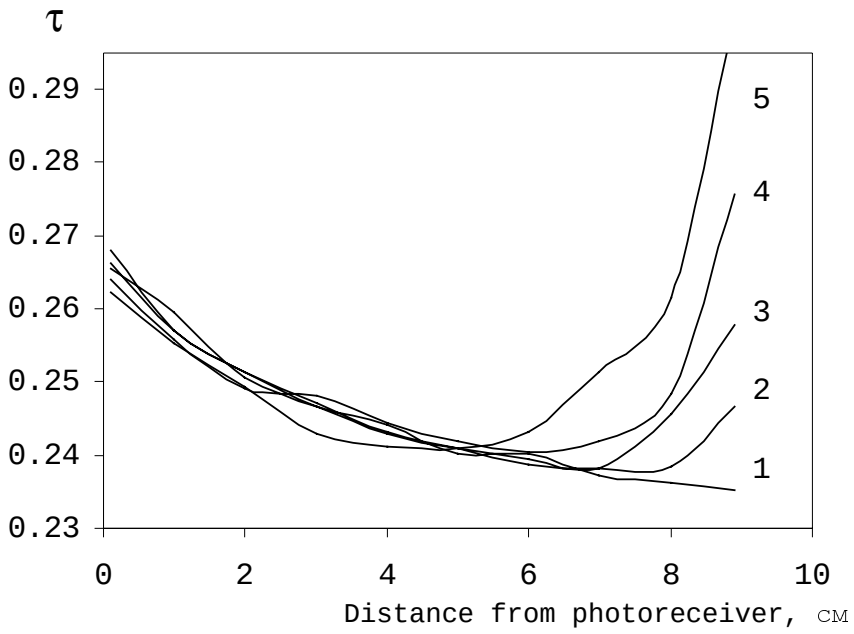

Fig.4. Calculated axial distributions of the light collection coefficient over the length of the GSO(Ce) cylinder ∅27×90 mm with different degree of roughness of the end opposite to the photoreceiver. The curves are enumerated in the order of the roughness degree increase: 1- polished end (R_z=0.05 μm); 5- maximum rough end.

There is one more way of improving the energy resolution of the detector. It is connected with the change of light collection conditions in the sample. At matting (making the upper end rough) the light collection coefficient becomes higher in the regions of the scintillator adjacent to this end. Its increase depends on the degree of the end roughness (Fig.4). As it is seen from the presented data there exists a certain degree of roughness at which deviation of τ from the mean value is minimal. This degree can be determined by experimental selection. Just this was done in this paper. With account of the calculated tendencies a series of measurements of the light output and energy resolution has been conducted. The results are given in Table 2.

Data on energy resolution of the sample given in Table 2 were obtained using a photomultiplier FEU-173. A sample treated according to the last line of the Table 2 and used with the Hamamatsu R1307 PM showed the energy resolution 8.5% on the line 662 keV.

Table 2. The effect of annealing and surface roughness on energy resolution of GSO(Ce) scintillator having the form of a cylinder, ∅27×90 mm by γ-line 662 keV from ^{137}Cs.

Sample treatment	Energy resolution R, %	
	Reflecting coating Tyvek	Reflecting coating fltoroplast film
Side surface-rough matting; both ends polished	24.4	23.8
Side surface and photosensitive end – polished, free end-rough grinding; the sample is annealed	13.8	13.1
Same surface roughness, except: free end – fine grinding; the sample is annealed	12.0	11.4

Conclusions

Increase of transparency of GSO(Ce) scintillation crystal by annealing in the atmosphere with the chemical potential ~40 kJ/mol and lowering of nonuniformity of the light collection coefficient with the help of mechanical treatment of the surface allows to achieve extremely high energy resolution of the detector. As a result of the change of surface and bulk characteristics of cylindrical Gd_2SiO_5:Ce scintillator with a diameter 27 mm and length 90 mm coupled with PM Hamamatsu R1307 the energy resolution 8.5% by γ-line 662 keV from ^{137}Cs was obtained.

References

1. Tsyrlin Yu.A., Globus M.E., Sysojeva E.P. Optimization of gamma-radiation detection by scintillating crystals. - .: Energoatomizdat, 1991. - 153 p.
2. T.Utsu and S.A.Kiyama, Journal of Crystal Growth, **109** (1991), 385.
3. Voloshin V.A., Korshin M.V., Kosmyna M.B., Preprint ISC-91-8, Institute for Single Crystals. Kharkov, 1991.
4. Kanevskii V.S., Krivonosov E.V., Litvinov L.A. and oth. J.Appl.Spectr., 1989, v.50, 4, P.651-654.
5. C.L.Melcher, J.S.Schweitzer, R.Utsu, S.A.Kiyama IEEE Transactions on nuclear science, v.37, 2, 1990, p.309-317.
6. Kanevskii V.S., Krivonosov E.V., Kvyatkovskii S.Ph. and oth. J.Appl.Spectr., 1989, v.51, 1, P.90-94.
7. Gavrilyuk V.P., Vinograd E.L., Grinyov B.V., Goriletsky V.I., Effect of surface conditions on the light collection in scintillation detectors // Functional Materials. – 1997. - 4, .4. - P.572-577.

Luminescence of $CsGd_2Cl_7:Ce^{3+}$ crystals

A. S. Voloshinovskii[1], V. B. Mikhailik[1], O. T. Antonyak[1], P. A. Rodnyi[2], P.Dorenbos [3], C. W. E. van Eijk[3], G. Zimmerer[4]

[1]*Lviv Franko State University, 8 Kirila i Mefodiya str., 290005, Lviv, Ukraine*
[2]*State Technical University, 29 Polytechnicheskaya str., 196251 St. Petersburg, Russian Federation*
[3]*Interfaculty Reactor Institute, Radiation Technology Group, Delft University of Technology, Mekelweg 15, 2629 JB Delft, The Netherlands*
[4]*II Institute of Experimental Physics, Hamburg University, Luruper Chaussee 1449, 22761, Hamburg, Germany*

Abstract. The luminescence parameters of Gd-based crystals are studied using synchrotron radiation in the energy range 4-30 eV. In $CsGd_2Cl_7$ - Ce^{3+} crystals, for range of fundamental absorption, the main contribution in Ce – emission is caused by recombination of electron-hole pairs with Ce^{3+} – ions. In crystal transparency the direct energy transfer from Gd^{3+} - ions to Ce^{3+} - ones is revealed. The luminescence excitation spectra features are explained from view of existence of two types excitons in crystal linked with the excitation of Cl^- - ions near Cs^+- or Gd^{3+} - ions.

Keywords: Gd-based compounds, high-energy relaxation, excitons

Introduction

The key requirements for scintillator materials in the most applications are high light output and short decay time [1]. The Ce^{3+} - ion is one of the most promising luminescence dopant in inorganic scintillators, due to relatively small intrinsic decay time (few tens of nanoseconds) of the parity-allowed 5d $\rightarrow$ 4f transitions. A number of Ce-doped oxides [2,3] and halides [4,5] have been studied as practicable scintillators. These investigations have revealed some regularities in process of energy transfer from the host lattice to Ce^{3+} - ions. The highest light output of Ce^{3+} - luminescence is usually achieved in Gd - and Lu - based crystals. Besides, among rare earth ions only Gd and Lu do not introduce in scintillator crystals electron or hole traps that would contribute to longer components in the scintillation pulse [1].

A feature of Gd-based crystals is well condition for migration of an electronic excitation over the Gd sublattice until it decays radiatively (~ 10ms) or transfers its energy to a luminescence centre [3]. For efficient energy transfer from Gd to Ce, the lowest 5d state of Ce must be situated just below the $^6P_{7/2}$ Gd - state. Position of the $^6P_{7/2}$ Gd - level depends very slightly on the type of the host crystal, while 5d - level of Ce is very sensitive to crystal field strength. Fluorides having weak crystal field cannot be convenient matrices for the Gd $\rightarrow$ Ce energy transfer. For instance, in $CsGd_2F_7$-Ce^{3+} the 5dCe-level is located higher than the $^6P_{7/2}$Gd - state and maximum light output of the crystal is only about 7 000 photons MeV^{-1} [4]. Besides, the wide-band-gap fluorides are not suitable system from the point of view of energy loss in the process of relaxation of electronic excitations in scintillators [1]. Quite recently a large light output (55 000 photons MeV^{-1}) has been observed in $RbGd_2Br_7$-Ce^{3+} crystal having good conditions for the Gd $\rightarrow$ Ce energy transfer [5]. A drawback of Rb-based crystals is intrinsic activity of ^{87}Rb isotope resulting background in pulse height spectra.

Relying on the above grounds, we undertake a study of $CsGd_2Cl_7$-Ce^{3+} crystal as a promising scintillator material. The luminescence characteristics of $CsGd_2Cl_7$-Ce^{3+} have been

measured at vacuum ultraviolet (VUV) excitation. Such a method is usually applied in the first stage of scintillator investigations to study the process of energy transfer from the low energy electron excitations to luminescence centres.

Experiment

The $CsGd_2Cl_7$ crystals were grown by the Bridgeman technique from previously anhydrous CsCl and $GdCl_3$ compounds. The $GdCl_3$ was dehydrated by heating in an atmosphere of chlorine created by thermal decomposition of NH_4Cl compound. The activation of crystals is implemented by adding of necessary amount of anhydrous $CeCl_3$ in raw material. The grown crystals had the well developed cleavage planes. The preparation of samples was carried out in a dry atmosphere in view of a hygroscopicity of $CsGd_2Cl_7$ crystals.

The luminescent study at high-energy excitation in 4 - 30 eV range was carried out on the set-up SUPERLUMI at HASYLAB. The instrumentation allowed us to measure the luminescence spectra and their excitation spectra with the use of time resolved spectroscopy methods in the interval 0,5 -500 ns.

Results and discussion

The luminescence spectra of $CsGd_2Cl_7$ and $CsGd_2Cl_7$-Ce (0,5 and 5 mol %) crystals are shown in fig. 1. The spectrum of $CsGd_2Cl_7$ crystal at T=9 K contains a reference band at 312 nm (the emission transition $^6P_j \rightarrow {}^8S_{7/2}$ in Gd^{3+} - ion) and broad band with a maximum at 435 nm. The last band can be attributed to luminescence of the self-trapped exciton. The additive of Ce- impurity to crystal leads to appearance of bands at 370 and 390 nm inherent for Ce- emission and yet to additional band at 430 nm (fig. 1, curve 2). The magnification of Ce- concentration up to 5 mol % leads to increase of intensity of Ce- luminescence bands (fig. 1, curve 3).

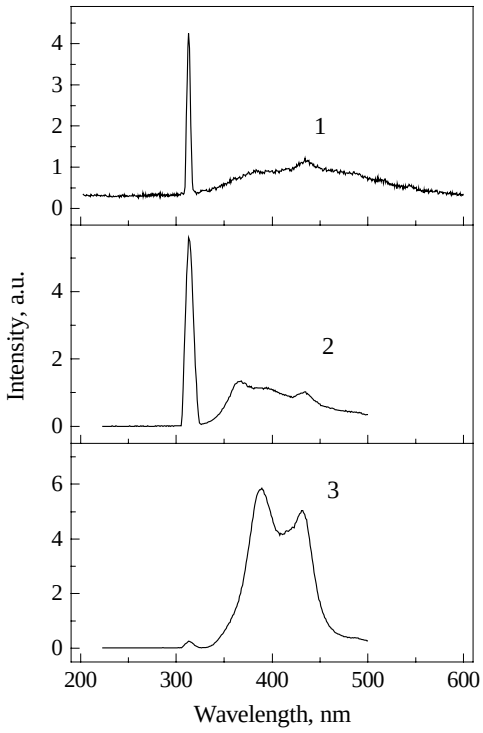

Fig.1. The luminescence spectra of Gd-based crystals excited at E=17 eV. 1 - $CsGd_2Cl_7$; 2 - $CsGd_2Cl_7$-Ce (0,5 mol %); 3 - $CsGd_2Cl_7$-Ce (5 mol %). T=9 K.

The excitation spectra of Ce-emission (fig. 2) clearly testify for energy excitation transfer from Gd^{3+}- ions to Ce^{3+}- centres. The decay time of Ce - emission (Ce - concentration C_{Ce} = 5 mol %) at the excitation within absorption bands of Gd (transitions $^8S_{7/2} \rightarrow {}^6P_j$, ^6I_j, ^6D_j) is equal to 28 ns (fig. 3). Such the time parameters indicate that the rate of excitation energy transfer from Gd^{3+} - ions to Ce^{3+}- ions surpasses the rate of the emission transitions, i.e. this quantity is approximately equal to 10^{-8} s^{-1}.

The excitation spectra of Gd - emission band (312 nm) in pure and Ce- activated $CsGd_2Cl_7$ crystals are displayed in fig. 4. The threshold of luminescence excitation is at the energy E=6,4 eV. After a sharp maximum at 7 eV the intensity of luminescence diminishes down to energy E=12 eV. Such the spectrum is typical for the exciton mechanism of luminescence excitation. The increase of luminescence output linked with effects of scattering of

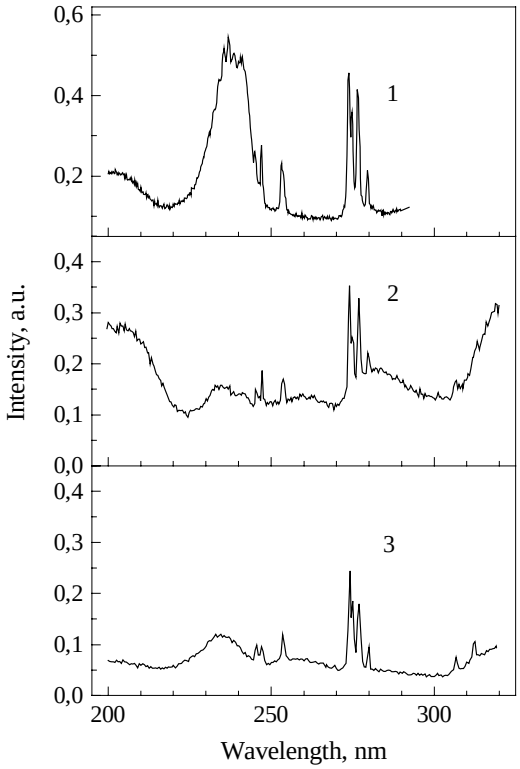

Fig.2. The excitation spectrum of Gd-emission (λ_{em}=312 nm) of $CsGd_2Cl_7$ crystal (curve 1) and Ce-emission (λ_{em}=375 nm) of $CsGd_2Cl_7$-Ce (0,5 mol %) (curve 2) and $CsGd_2Cl_7$-Ce (5 mol%) (curve 3) crystals in transparency region. T=9 K.

high-energy conduction band electrons on valence band electrons starts equally at the energy E=12,8 eV. In Ce - impurity crystals the luminescence output in the field of electron excitation multiplication is smaller. It is caused by capture of the part of high-energy electrons by impurity ions.

The shape of Ce - emission excitation spectrum differs essentially from that for Gd - luminescence. The intensity of luminescence excitation in the field of excitons creation (E=6,4 eV) is inappreciable. In the further the excitation spectrum is represented by curve with monotonically increasing intensity. On the excitation curve it is difficult to reveal the clear thresholds linked with the electron excitation multiplication. The view of luminescence excitation curve is characteristic of the case, when the luminescence is excited due to of recombination of electron - hole pairs with Ce - centres.

For explanation of the features of high-energy excitation of Gd^{3+}- and Ce^{3+} - ions we suppose that in $CsGd_2Cl_7$ crystal the excitons of two types can be realized. One type is interlinked with excitation of chlorine ions situated near Gd^{3+}- ions. Another type is stipulated by excitation of Cl^--ions situated near Cs^+-ions and could be considered as the usual self-trapped exciton such as V_k+e^-.

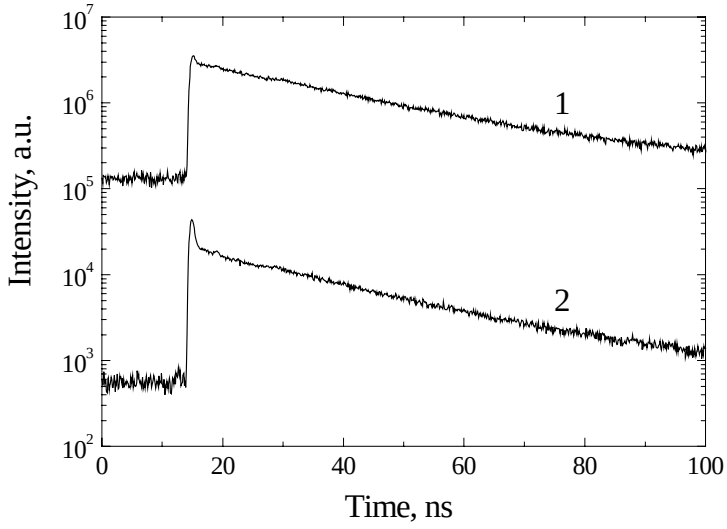

Fig.3. The decay time curves of Ce-emission in $CsGd_2Cl_7$-Ce (0,5 mol %) crystal at 275 nm excitation (1– T=300K; 2 – T=9K).

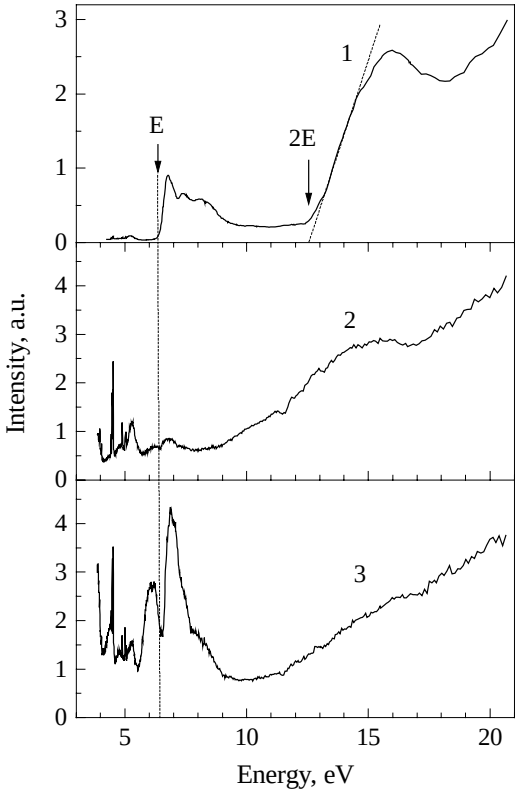

Fig.4. The luminescence excitation spectra of Gd-emission of $CsGd_2Cl_7$ (curve 1) and Ce-emission (curves 2,3) of $CsGd_2Cl_7$-Ce (0,5 mol %) crystal (curves 1, 2– T=300K; curve 3– T=9 K).

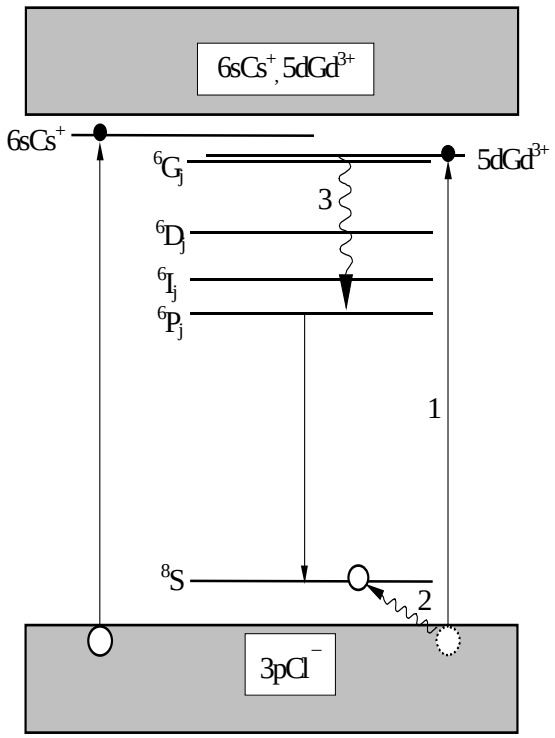

Fig.5. The supposed scheme of energy structure and transitions for exciton created by excitation of Cl^- - ion near Gd^{3+}- ion.

The supposed scheme of energy levels and transitions responsible for formation of excitons near Gd^{3+} - ions is shown in fig. 5. The transition 1 ($3pCl^- \rightarrow 5dGd^{3+}$) is responsible for formation of an exciton near Gd^{3+} - ions. In the further the exciton can undergo the peculiar self-trapping. The exciton relaxes and emits as Gd^{3+}- centre due to hole transition 2 and nonradiative transition 3 with overcoming activation barrier between 5d- and 4f- electron shells. At low temperature the existence of free exciton and its participation in transport of energy to Ce- impurity centres is possible. The latter can explain the increasing of Ce - luminescence output in the field of Gd - exciton formation at ~7 eV (see fig.4, curve 3).

Conclusions

The measurements of $CsGd_2Cl_7$-Ce luminescence excitation spectra allow us to mark out typical mechanisms of Ce-centres excitation. In the transparency region (E<6,4 eV), along with direct Ce excitation, the energy transfer from Gd - ions to Ce - ones occurs. The Gd→Ce energy transfer with transfer rate ~10^8 s^{-1} is observed at optical excitation of ^6P_j -, ^6I_j - and ^6D_j - levels of Gd^{3+} - ion. In the range of band-band transitions (E>6,5 eV) the recombination mechanism of Ce^{3+} centres excitation is observed. It is supposed that the existence of two types of excitons is responsible for peculiarities of Gd- and Ce-emission. One type is linked with the excitation of chlorine ions situated near Gd^{3+} ions, and the other type is caused by excitation of Cl^--ions situated near Cs^+-ions.

References

1. P.A. Rodnyi, Physical Processes in Inorganic Scintillators, CRC Press, NY, 1997.
2. C.L. Melcher and J.S. Schweitzer, Nucl. Instr. and Meth. A314 (1992) 212.
3. H. Suzuki, T.A. Tombrello, C.L. Melcher, C.A. Peterson, and J.S. Schweitzer, Nucl. Instr. and Meth. A346 (1994) 510.
4. D.R. Schaart, P. Dorenbos, C.W.E. van Eijk, R. Visser, C. Pedrini, B. Moine, and N. M. Khaidukov, J. Phys.: Condens. Matter 7 (1995) 3063.
5. P. Dorenbos, J.C. van't Spijker, O.W.V. Frijns, C.W.E. van Eijk, K. Kramer, H.U. Gudel, A. Ellens, Nucl. Instr. and Meth. B132 (1997) 728.

Coactivation induced phosphorescence of $BaAl_2O_4:Eu^{2+}$

S. Kh. Batygov, N. N. Vinogradova, Yu. K. Voronko,
L. N. Dmitruk, L. V. Moiseeva

General Physics Institute, Vavilov Street 38, Moscow 117947, Russia

Abstract. The X-ray excited luminescence of $BaAl_{2+x}O_{4+1.5x}:Eu^{2+}$ ($0 \le x \le 0.2$) phosphors coactivated with different trivalent rare earth ions was studied at 300 and 80 K. It was found that the intensity of intrinsic luminescence at 420 nm decreases while that of Eu^{2+} increases with an excess of Al_2O_3. The increase of Eu^{2+} luminescence with Al_2O_3 excess is explained by the increased Eu^{2+} incorporation in aluminate host. The afterglow enhancement induced by Al_2O_3 excess or by coactivation with some trivalent rare earth (Nd, Dy) was observed, analogous to that reported for $SrAl_2O_4:Eu^{2+}$ and $CaAl_2O_4:Eu^{2+}$. The long afterglow is ascribed to hole trapping at defect complexes containing Ba^{2+} vacancy. It is supposed that coactivator influences recombination rate by modifying the depth of the hole trap level of the defect. As hole released from the trap recombines with trapped electron the phosphorescence excitation of the Eu^{2+} ion acting as a hole trap must be indirect unlike the fluorescence that can be excited directly by electron recombination with Eu^{3+} ion, i.e. with hole trapped at Eu^{2+}.

Keywords: alkaline-earth aluminate phosphor, recombination luminescence, nonstoichiometry

Introduction

Alkaline earth aluminates MAl_2O_4 (M = Ca, Sr, Ba) doped with Eu^{2+} are known to be efficient phosphors [1-4]. Along with the fast fluorescence determined by the short decay time (<1 μs) of Eu^{2+} ions these phosphors exhibit a long (few seconds) phosphorescence at low level [2]. It was found that the luminescence efficiency of phosphors depends on stoichiometry. The brighter luminescence compared to the stoichiometric phosphor as well as the higher level of phosphorescence are observed in $SrAl_2O_4:Eu^{2+}$ containing excess of Al_2O_3 [3]. The hole trap formed by the Sr^{2+} vacancy was assumed to play role in the phosphorescence. A different model was proposed [4] based on the observation that some trivalent rare earth ions (Dy^{3+} or Nd^{3+}) added as an auxiliary activator into $SrAl_2O_4:Eu^{2+}$ or $CaAl_2O_4:Eu^{2+}$ cause very intense and long phosphorescence. The model assumed electron trapping by the Eu^{2+} ion and hole trapping by the Dy^{3+} or Nd^{3+} ion during excitation with subsequent recombination at Eu^{1+} of holes thermally released from Dy^{4+} or Nd^{4+}. In order to gain more information on the mechanisms of the recombination excitation of Eu^{2+} luminescence we have investigated in the present work the effect of nonstoichiometry and coactivators on the luminescence of the $BaAl_2O_4:Eu^{2+}$ phosphor.

Experimental

Samples of $BaAl_2O_4$ (BA), Eu^{2+}-activated as well as not activated were prepared by firing mixtures of $BaCO_3$, Al_2O_3 and Eu_2O_3 for 4-5 hours at 1300 ^{O}C in reducing atmosphere consisting of mixture of Ar and H_2. Oxides of Nd, Ce, Gd, Tb and Dy were used for coactivation. Stoichiometric samples as well samples containing up to 10% excess of Al_2O_3 were synthesized. The products were checked by X-ray analysis. The luminescence was excited with X-rays (W anode, 20 kV, 10 mA). Luminescence spectra in 300-650 nm range

and phosphorescence decay were measured with spectrometer KSVU-23 at room temperature and temperature of liquid nitrogen.

Results

The x-ray diffraction analysis has shown that samples enrichedzed with Al_2O_3 excess up to 10% contain a single phase with the same structure as the stoichiometric ones. Figure 1 and 2 give the luminescence spectra of the BA phosphor activated with 0.1% and 1% Eu. At room temperature the Eu^{2+} luminescence peaked at 500 nm depends on stoichiometry as well as on Eu^{3+} concentration. As in $SrAl_2O_4$:Eu [3], in BA phosphor with excess of Al_2O_3 the more intense Eu^{2+} luminescence is observed as compared with stoichiometric one. At liquid nitrogen temperature, the Eu^{2+} band shifts to 510 nm and a new broad band appears at 420 nm. Unlike Eu^{2+} band, the 420 nm band weakens with the Al_2O_3 excess. The intensities of Eu^{2+} and 420 nm bands in stoichiometric and Al_2O_3-rich samples with different Eu^{2+} concentrations are given in table 1.

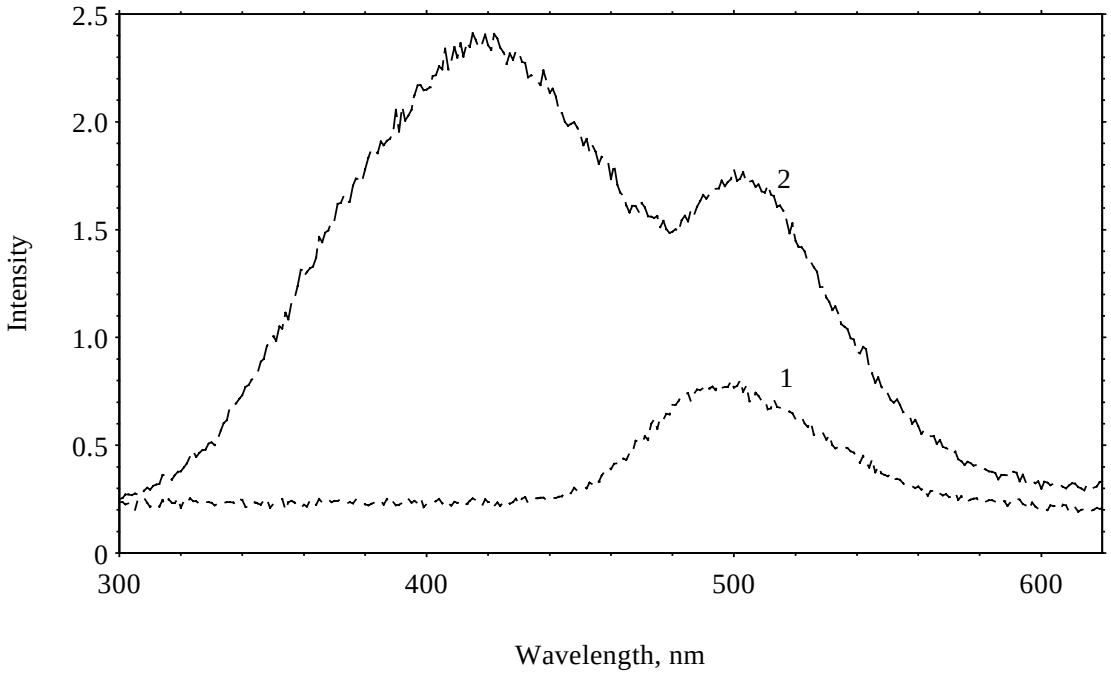

Figure 1. Luminescence spectra of $BaAl_2O_4$:0,1 at% Eu^{2+} at 300 K (1) and 80 K (2)

At 1%Eu the effect of nonstoichiometry on the Eu^{2+} luminescence intensity is less pronounced then in BA:0.1% Eu phosphor. Effects of nonstoichiometry and coactivation on the BA:1% Eu^{2+} phosphorescence are shown in figure 3.. The brightness and duration of the Eu^{2+} afterglow increase significantly with the Al_2O_3 excess and even more significantly with Nd^{3+} coactivation. In Nd^{3+}-coactivated phosphor excess of Al_2O_3 seems to shorten phosphorescence. The phosphorescence intensity of each sample in figure 3 is scaled to its steady-state luminescence level, so it is obvious that Al_2O_3 excess and Nd^{3+} coactivation increase the phosphorescence yield relative to fluorescence. Enhancement of Eu phosphorescence in nonstoichiometric and Nd-coactivated samples was observed at 80 K as well. Contrary to Eu^{2+}, the 420 nm band shows no afterglow.

Table 1. Relative intensities of intrinsic emission at 420 nm (80 K) and Eu^{2+} emission at 500 nm (300 K) in stoichiometric (Ba:Al=1:2) and nonstoichiometric (Ba:Al=1:2.2) samples

Emission band	Undoped		0.1% Eu		1% Eu	
	Ba:Al=1:2	Ba:Al=1:2.2	Ba:Al=1:2	Ba:Al=1:2.2	Ba:Al=1:2	Ba:Al=1:2.2
500 nm	-	-	0.8	2.0	2.1	2.2
420 nm	3.3	1.3	2.2	1.6	1.4	0.5

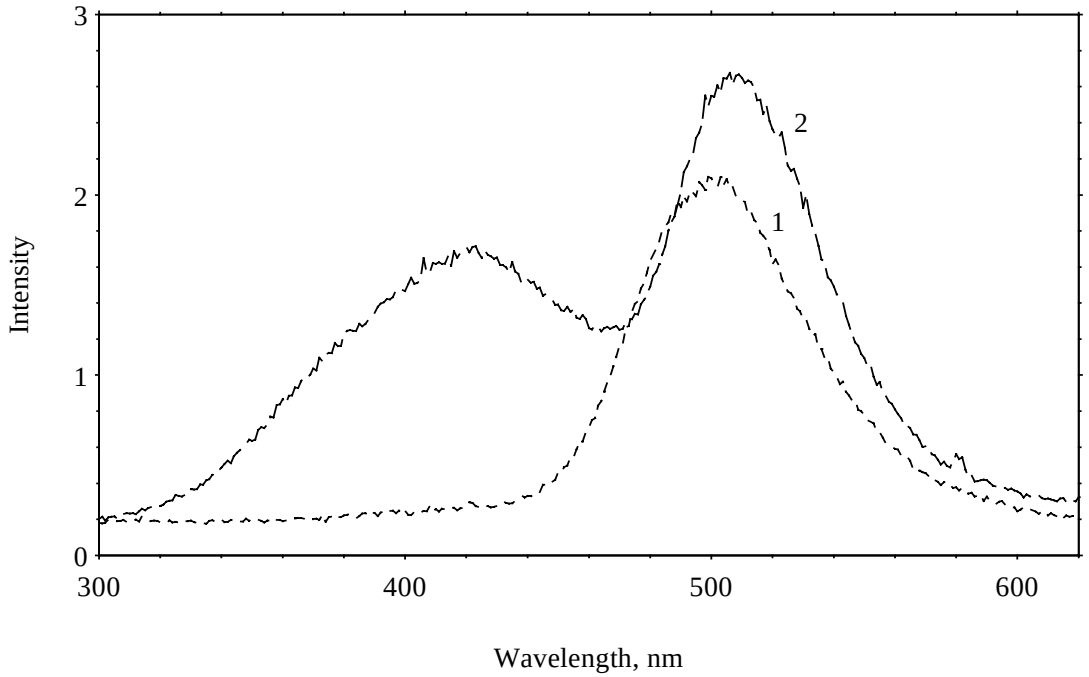

Figure 2. Luminescence spectra of $BaAl_{2.2}O_{4.3}$:0,1 at% Eu^{2+} at 300 K(1) and 80 K (2)

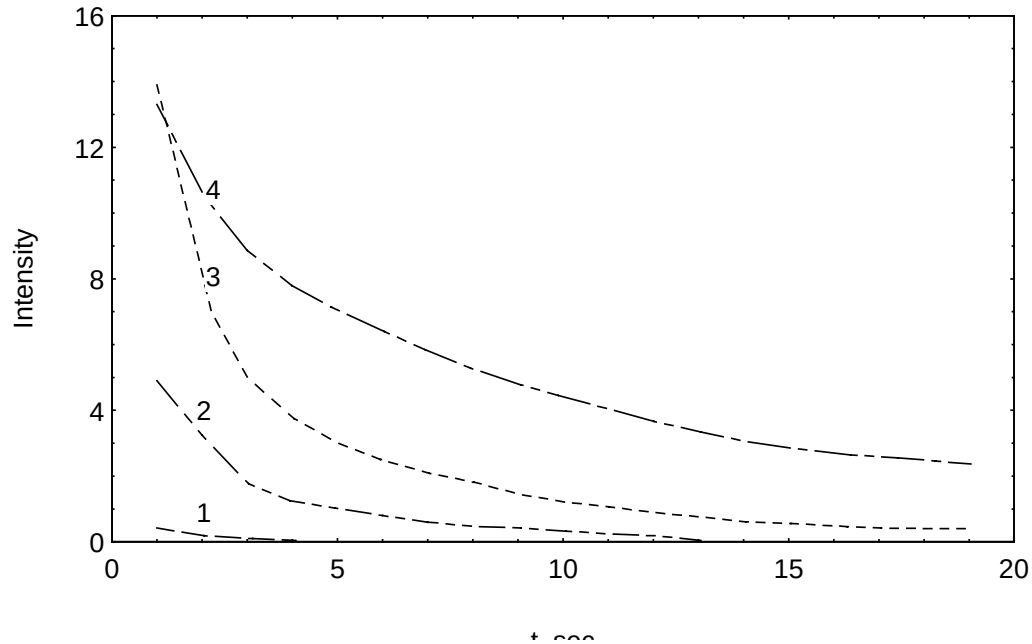

Figure 3. Eu^{2+} afterglow in $BaAl_2O_4$:1 at% Eu^{2+} (1), $BaAl_{2.2}O_{4.3}$:1 at% Eu^{2+} (2) $BaAl_2O_4$:1% Eu^{2+}, 1 at% Nd^{3+} (3), and $BaAl_{2.2}O_{4.3}$:1 at% Eu^{2+}, 1 at% Nd^{3+} (4)

Discussion

The 420 nm fluorescence band belongs probably to exciton bounded at some intrinsic defect. The Al_2O_3 excess may weaken the 420 nm band by reducing the concentration of this defect or/and by introducing more defects such as vacancies of Ba and O that reduces the intrinsic luminescence excitation efficiency due to competition between recombination centers. The later mechanism must weaken the Eu^{2+} luminescence as well. But for the Eu^{2+} the situation looks quite opposite - the Al_2O_3 excess induces the enhancement of Eu^{2+} luminescence. The increased Eu^{2+} luminescence intensity in nonstoichiometric phosphor can

be ascribed to higher activator incorporation in BA structure promoted by the excess of Al_2O_3 or/and to higher excitation efficiency. As for the phosphorescence, the most simple mechanism based on ionization of Eu^{2+} and electron trapping seems to be not appropriate. It is known that the Eu^{2+} ion readily oxidizes to Eu^{3+} and consequently acts as hole trap in different hosts. If Eu^{2+} in MAl_2O_4 is directly involved in recombination processes leading to phosphorescence it should be excited by the recombination of electron with Eu^{3+} formed by ionization of Eu^{2+}. However the photoconductivity measurements pointed to holes as the conducting species [3, 4], therefore the direct excitation of Eu^{2+} in phosphorescence is doubtful. Thus the variations in phosphorescence are to be connected with variations in depth and density of hole traps. The enhancement of phosphorescence with the excess of Al_2O_3, i.e. deficiency of BaO, in BA can be connected with hole traps introduced with Ba^{2+} vacancies (V_{Ba}) as it was proposed for Sr^{2+} vacancies in $SrAl_2O_4$ [3]. V_{Ba} having an effective negative charge must be an effective hole trap. The role of V_{Ba} can be assumed in Nd-coactivated phosphor too, since by coactivation with trivalent rare earth ion V_{Ba} must be created due to heterovalent substitution for Ba^{2+}. The model proposed in [4] seems to be less plausible since it presumes unusual valency states namely Eu^{1+} and Nd^{4+}. But the model with the single Ba^{2+} vacancy do not explain the observed difference between different coactivators. The complexes including V_{Ba} more probably play role in trapping processes. In nonstoichiometric BA the Al_2O_3 excess introduces vacancies of O^{2-} (V_O) equally with V_{Ba} and since both defects are doubly charged with opposite sign they tend to form amphoteric complexes acting as efficient traps for both holes and electrons. Depending on Al_2O_3 concentration the complexes can include one V_{Ba}-V_O pair or more. Trivalent coactivators substituting divalent barium have positive effective charge and shoud also form complexes with V_B and in that way influence the trap depth. The excitation of Eu^{2+} in this model takes place indirectly through the energy transfer from a center at which hole released from a trap recombines with captured electron. An oxygen vacancy may represented such center. The model implies a spatial correlation between Eu^{2+} ions and recombination centers.

References

1. G. Blasse, A. Bril, Philips Res. Reports 23 (1968) 201
2. F.C.Palilla, A.K.Levine, M.R.Tomkus, J. Electrochem. Soc. 115 (1968) 642
3. V. Abbruscato, J. Electrochem. Soc. 118 (1971) 930
4. T. Matsuzawa, Y. Aoki, N. Takeuchi, and Y. Murayama, J.Elektrochem.Soc. 143 (1996)

Improvements in the X-ray Characteristics of Gd_2O_2S:Pr Ceramic Scintillators

Ryouhei Nakamura and Mitsuru Ishii*

Hitachi Metals, Ltd., 5200 Mikajiri, Kumagaya-shi, Saitama 360-0843, Japan
**Shonan Institute of Technology, 1-Fujisawa, Kanagawa 251-8511, Japan*

Abstract. The image quality of X-ray CTs can be improved by using X-ray detectors with more sensitive, low afterglow scintillators. A Gd_2O_2S:Pr ceramic scintillator is already available commercially to fit that need. The present study investigated the effect of adding various rare earth and halogen elements to Gd_2O_2S:Pr ceramic scintillators to improve light output and afterglow. The 15% improvement of the light output was obtained by the Tb addition of 0.001 mole fraction. The light output increased by 7% and the afterglow decreased by 96% by F addition of 0.002-0.003 mole fraction.

Keywords : Gd_2O_2S:Pr, scintillator, X-ray CT, light output, afterglow

Introduction

X-ray CT (Computed Tomography) creates a cross-section image by photographically imaging the X-ray absorption coefficient in a particular part of the human body. The performance of an X-ray CT is strongly influenced by its X-ray detectors. Most X-ray CTs presently have Xe gas chamber detectors. However, Xe gas chamber detectors have low energy efficiency and sensitivity. A $CdWO_4$ single crystal scintillator grown by the Czochralski method exhibits an intrinsic luminescence by $(WO_4)^{2-}$ complexes and has low afterglow. However, solid state detectors consisting of the $CdWO_4$ scintillator with a Si photodiode are not sensitive enough to improve the quality of a CT. On the other hand, Gd_2O_2S:Pr ceramic scintillators sintered by hot isostatic pressing (HIP) have high light output and low afterglow, and solid state detectors made of the ceramic scintillators are available commercially [1-3].

Desirable properties in a X-ray CT scintillator are (1)high light output, (2)low afterglow, (3)low radiation damage, (4)high uniformity, (5)high machinability, and (6)chemical stability [4,5]. Rare earth and halogen elements were added to Gd_2O_2S:Pr ceramic scintillators in the present study to improve light output and afterglow. The results of that experiment are described in this paper.

Experimental Procedure

1) *Preparation of the Ceramic Scintillator*

A powder mixture was prepared by dry-mixing Gd_2O_3, Pr_6O_{11}, Na_2CO_3, $Li_2B_4O_7$, $K_3PO_4 \cdot 3H_2O$, S, lanthanoid oxide additives and pottasium halides. A $Ce(NO_3)_3 \cdot 6H_2O$ water solution was added to the powder mixture, and that mixture then was calcined at 1300 for 8h in an Al_2O_3 crucible with an Al_2O_3 cap. The calcined material was washed thoroughly with a 1N HCl solution and pure water. The average particle size of the Gd_2O_2S:Pr scintillator powder was 40 . Li_2GeF_6 (0.1wt%) was added to the scintillator powder as a sintering aid, and the powder was charged into a soft Fe capsule. The capsule then was sealed in a vacuum and the powder sintered, using a HIP apparatus, at 1300 for 2.5h under 1000atm pressure. The sintered ceramic scintillating material was sliced, to provide plate samples, and annealed in an Ar atmosphere containing O_2 gas.

2) *Evaluation Method*

The light output of the scintillator irradiated with X-rays generated from a W target (tube voltage ; 120kV, tube current ; 100mA) was measured using a PIN type of Si photodiode. The afterglow of the scintillator was obtained from the ratio of light output of the scintillator at 3ms, or 30ms after the X-ray irradiation was stopped, to the light output during X-ray irradiation. The light output of the scintillator was measured using X-ray CT. The luminescent decay constant was measured with a photomultiplier tube using □-rays (60KeV) from ^{241}Am.

Results and Discussion

1) *Effects on light output of rare earth ions*

Fig. 1 through 3 show the measured light output of samples to which nine kinds of lanthanoid elements were added. The relation between the content of added elements and the light output followed three patterns in the present study. Light output increased monotonically with the quantity of Tb addition; at a Tb content of 0.001 mole fraction, the relative light output was 115% of its normal value. When Eu or Yb were added, the light output decreased monotonically with the quantity of additive. On the other hand, when Dy, Nd, Sm, Ho, Er, or Tm were added, light output was greatest at a content of 0.0001 to 0.0002 mole fraction.

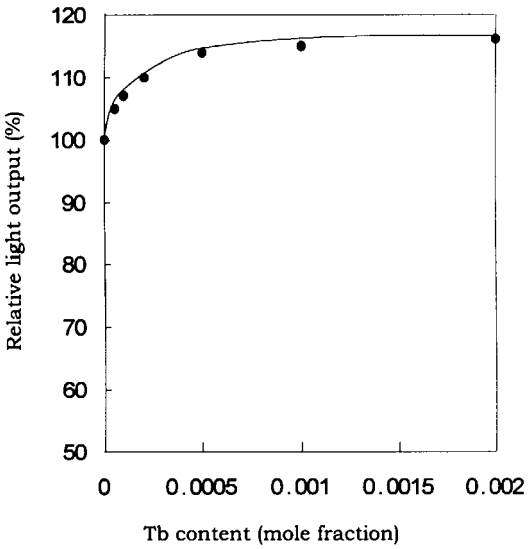

Fig.1 Relative light output of Gd_2O_2S:Pr doped with Tb.

The fluorescence intensity at 544nm, the main fluorescent wavelength of Gd_2O_2S:Tb, increased and that at 512nm, the main fluorescent wavelength of Gd_2O_2S:Pr, decreased (see Fig. 4). Apparently, part of the transition energy of the Gd_2O_2S:Pr was transmitted to the transition energy of the Gd_2O_2S:Tb (energy transfer) [6]. The increase in light output, attributed to the increased fluorescent intensity of the Gd_2O_2S:Tb, was suitable for the spectral sensitivity of a Si photodiode.

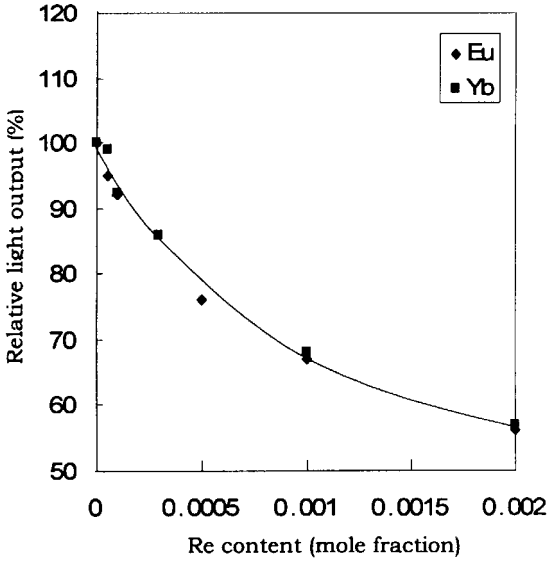

Fig.2 Relative light output of Gd_2O_2S:Pr doped with Eu or Yb.

The increased light output when a small quantity of Dy, Nd, Sm, Ho, Er, or Tm was added can be explained as energy transfer from Gd_2O_2S:Re (Re = Dy, Nd, Sm, Ho, Er, Tm) to Gd_2O_2S:Pr. These rare earth ions have many energy levels between the $^3P_0$ and $^3H_4$ levels of Pr^{3+} (the fluorescence at 512nm is caused by electronic transition between $^3P_0$ and $^3H_4$ levels of Pr^{3+}) [6]. When the quantities of these elements were increased in the present work, the probability of relaxation occurring was higher than that of fluorescence.

Accordingly, the fluorescent strength decreased with increases in the quantity of those elements, a phenomenon known as concentration quenching [7].

Results of measuring the afterglow are shown in Fig. 5. The afterglow increased with increasing quantities of Eu or Yb. Because the charge transfer state (CTS) energy of Eu^{3+} and Yb^{3+} is the lowest among all trivalent rare earth ions, these ions tend to capture an electron and become divalent easily. On the other hand, Pr^{3+} tends to lose an electron, easily becoming tetravalent[6]. The afterglow thus seems to increase because of an increase in electron and hole traps generated by electron transfer from Pr^{3+} to Eu^{3+} or Yb^{3+}. In the same way, the light output must decrease because of the capture of electrons and holes, which relates to fluorescence.

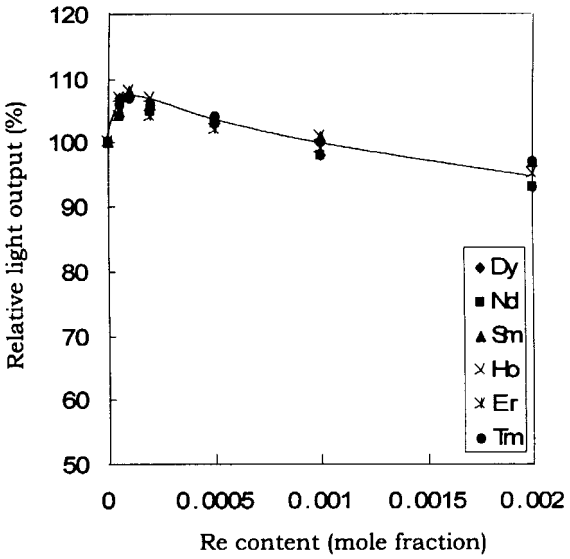

Fig.3 Relative light output of Gd_2O_2S:Pr doped with Dy, Nd, Sm, Ho, Er or Tm.

An f-f transition of Pr^{3+} doped into the Gd_2O_2S is allowed, whereas the f-f transition of Tb^{3+} is forbidden[6]. The fluorescent time constant for Tb^{3+} doped into the Gd_2O_2S therefore was much higher than that for Pr^{3+} doping. Additional quantities of Tb^{3+} element added to improve the light output thus must be kept to a minimum so as not to increase the fluorescent time constant and afterglow. No change was observed in the fluorescent time constant and afterglow in this study.

2) *Effects on light output and afterglow of halogen ions*

Fig. 6 and 7 show light output and afterglow of samples to which F^-, Cl^-, Br^-, or I^- ions were added. When F^-, Cl^-, or Br^- ions were added, whatever the additive is, light output showed maximum value at a mole fraction of 0.002-0.003. Relative light output were 107 % and 104 % for F^- and Cl^-, respectively. When I^- ions were added, light output increased slightly. On the other hand, afterglow at a mole fraction of 0.002-0.003 exhibited the minimum value as 4% for F^-, 6% for Cl^-, 13% for Br^- and 63% for I^-.

The F^- ions (ion radius 1.33Å) is probably substituted for O^{2-} ions (1.32 Å), Cl^- ions (1.81Å) and Br^- ions (1.96 Å) probably substituted for S^{2-} ions (1.74 Å) due to matching of ion radius. Then, F^-, Cl^-, or Br^- ions are charged in +1. If the intrinsic defects charge as minus in the neighborhood of F^-, Cl^- or Br^- ions, those ions compensate the charge of the defects. Accordingly, light output increases and afterglow decreases. Because of this mechanism, light output increased and afterglow decreased when F^-, Cl^- or Br^- ions were added at a mole fraction of 0.002-0.003. However, when

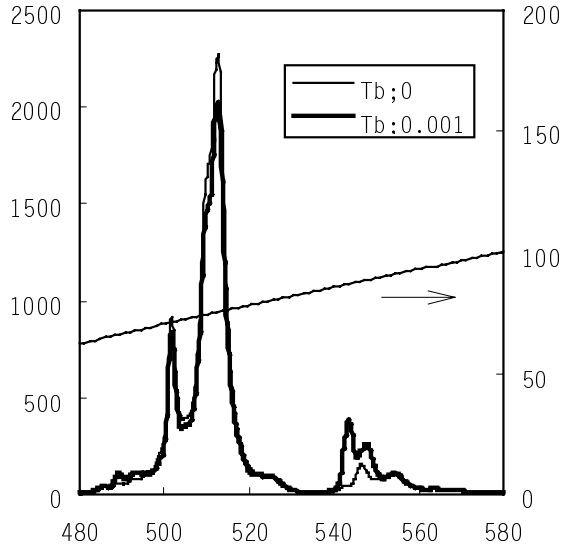

Fig.4 Luminescence spectra of Gd_2O_2S:Pr doped with Tb and typical sensitivity of Si photodiode.

F^-, Cl^- or Br^- ions were added over these amount, light output decreased and afterglow increased. Those F^-, Cl^-, or Br^- ions are charged in +1, and probably activates as electronic traps which makes afterglow degraded. Meanwhile degradation of afterglow for I^- ion adding was not significant, because I^- ions have a large ion radius (2.20Å) giving few crystallographic changes to the matrix.

3) *Characteristics of Gd_2O_2S:Pr with Tb and F elements*

Characteristics of Gd_2O_2S:Pr with the co-addition of Tb and F elements are shown in Table 1.

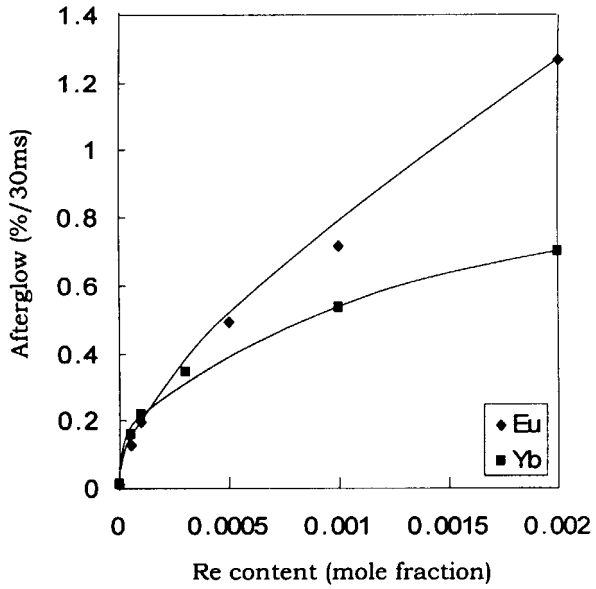

Fig.5 Relation between content of Eu or Yb and afterglow at 30ms after stopping X-ray.

Conclusions

The effect of various rare earth halogen elements on improving the light output and afterglow was investigated in the present study. The conclusions are as follows.

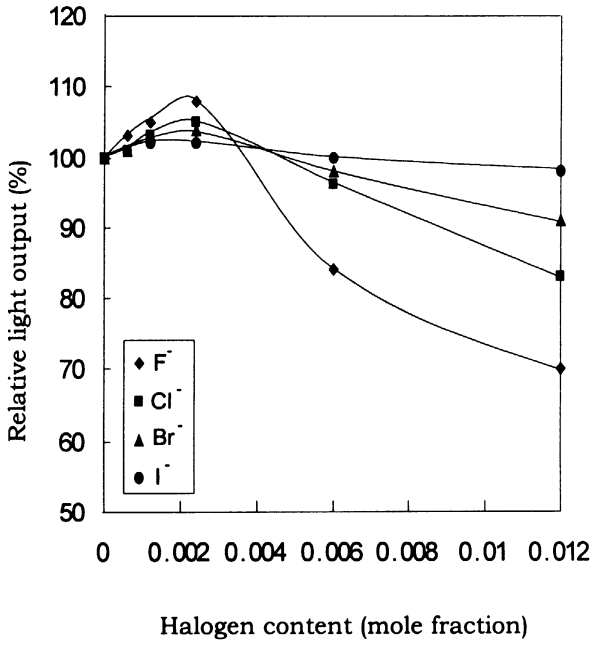

Fig.6 Relation between content of halogen ion and relative light output.

(1) Light output increased monotonically with the quantity of added Tb. When Tb was added in a 0.001 mole fraction, light output improved about 15%, and no change was observed in the fluorescent time constant and afterglow. Light output decreased monotonically with the quantity of added Eu or Yb. On the other hand, when Dy, Nd, Sm, Ho, Er, or Tm were added separately, light output improved slightly at a content of 0.0001 to 0.0002 mole fraction.

(2) Light ouput became maximum and afterglow became minimum by 0.002□0.003 mole fraction doping of F^-, Cl^-, or Br^-. Light output increased by 7% and afterglow decreased by 96% by F^- doping. Doping of I^- did not improve light output and afterglow significantly.

Table 1 Characteristics of Gd_2O_2S:Pr

Characteristics	Gd_2O_2S:Pr	$CdWO_4$
Relative light output	2.0	1.0
Peak Emission	510nm	540nm
Decay constant	3□s	5□s
Afterglow (at 30ms)	0.01%	0.001%
Radiation Damage (500R)	□2%	□2%

(3) Gd_2O_2S:Pr with the co-addition of Tb and F elements showed light output 2.0 times higher than that of $CdWO_4$. Afterglow and decay constant of this material sufficiently satisfy the requirements for high speed X-ray CT detecors.

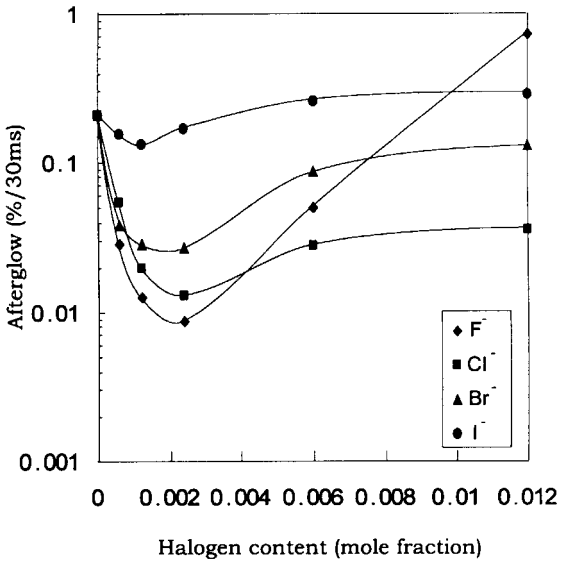

Fig.7 Relation between content of halogenion and afterglow.

References

1. Y. Ito, H. Yamada, M. Yoshida, H. Fujii, G. Toda, H. Takeuchi, and Y. Tsukuda, Jpn. J. Appl. Phys., **27**(1988) L1371.
2. M. Yoshida, M. Nakagawa, H. Fujii, F. Kawaguchi, H. Yamada, Y. Ito, H. Takeuchi, T. Hayakawa, and Y. Tsukuda, Jpn. J. Appl. Phys., **27**(1988) L1572.
3. H. Yamada, A. Suzuki, Y. Uchida, M. Yoshida, and H. Yamamoto, J.Electrochem. Soc., **136** (1989)2713.
4. C. D. Greskovich, D. Cusano, D. Hoffman, and R. J. Riedner, Am. Ceram. Soc. Bull., **71** (1992)1120.
5. C. Greskovich, and S. Duclos, Annu. Rev. Mater. Sci., **27** (1997)69.
6. S.Shionoya and W.M.Yen : Phosphor Handbook (CRC Press, 1999) p. 177-200.
7. S.Shionoya and W.M.Yen : Phosphor Handbook (CRC Press, 1999) p. 101-112.

$LuAlO_3$, $YAlO_3$ and $LaLuO_3$ structure analysis with neutron diffraction

[1]Galluci E., [1]Duiardin C., [1]Boudeulle M., [1]Pedrini C., [2]Petrosyan A.G., [3]Hansen T.

[1]*Laboratoire de Physico-Chimie des Matériaux Luminescents, Unité Mixte de Recherche 5620 CNRS- Université Lyoni, 69622 Villeurbanne, France*
[2]*Institute for Physical Research, Armenian National Academy of Science, 378410 Ashtarak-2, Armenia*
[3]*Institut Laue-Langevin, BP156F-38042 Grenoble*

Abstract. Neutron diffraction on $LuAlO_3$, $YAlO_3$ and $LaLuO_3$ powders has been performed. Structure refinements of results allow to establish the main crystal structure parameters and the coordination site of the metallic ion where the activator takes place.

Keywords: neutron diffraction, structure, $LuAlO_3$, $YAlO_3$, $LaLuO_3$

Introduction

Doped perovskite-like binary oxides are studied as scintillator materials and new phases are prepared continually in order to achieve better optical properties.

A reliable interpretation and prediction of light absorption and emission parameters by the crystals imply a complete knowledge of the activator site together with the coordination spheres and polyhedral linking within the matrix host.

In many cases, a rough description of the atomic structure is only available, based often upon old and approximate packing description of isotype material, of the orthorhombic "distorted perovskite" type. That is the reason why we undertook the crystal structure determination of $LuAlO_3$ and $YAlO_3$ on one hand, $LaLuO_3$ on the other hand, using neutron diffraction experiments, in order to get a possible way of comparison of their relative scintillating properties, when doped with cerium and praseodymium or any other rare earth.

Experimental

Powdered samples were prepared from single crystals grown using the standard Czochralski or Bridgman techniques, details of which have been given in references [1] and [2]. Stoechiometric mixtures of high-purity oxides were used to prepare the melts in Mo or Ir crucibles under Argon/Hydrogen atmosphere (LaLuO3, [3, 4] ; $YAlO_3$, [5, 6]; $LuAlO_3$, [7, 8]). The resulting crystals were optically transparent and free of light scattering as checked by optical microscopy. However some extra weak lines were detected in X-Ray diffraction patterns, indicating some domains of limited extension from other phase(s).

Neutron scattering measurements were performed on the D2B device at the ILL (Grenoble, France). Samples were mounted in a cylindrical vanadium can and data were recorded from 2θ = 0 to 160°, at λ = 1.5938Å at room temperature. Results were analysed with the GSAS program [9] using as starting structural model the unit cell parameters determined from refinement of personal X-Ray scattering data and atomic coordinates from [10] for $YAlO_3$ and $LuAlO_3$ and [11] for $LaLuO_3$. The final cycles of full-matrix leastsquared refinement for the three compounds consisted of 40 adjustable parameters (lattice parameters, positional and thermal parameters, scaling factor, zero shift, background parameters and Bragg-peak profile parameters, ...). Due to the poor quality of the observed profiles, anisotropic thermal factors

will not be considered in this paper. The reliability factors for $YAlO_3$ and $LuAlO_3$ are actually indeed rather poor, according to the required standards. However, as the structural data for $YAlO_3$ are very similar to the published ones [10], it is thought that crystal defects, like twins induced by grinding and other phases inclusions, which were occasionaly detected in such materials, together with some experimental misadjustment, would preclude any significant improvement.

The experimental and present structural data are summarized in the following three sets of figures and tables.

Results and discussion

All these perovskite-like orthorhombic structures were refined in space group Pnma (No.62), *Z* = 4, with the A-site cation (La, Y, Lu) situated on mirror planes (4(c), site symmetry Cs) and B-site cation (Lu, Al) situated on centres of inversion (4(b), Ci). Two oxygen positions, on mirror planes (4(c)) and general positions (8(d)) were considered.

For $LaLuO_3$, some substitution of lutetium by lanthanum was suspected, on the basis of density measurements. Such assumption could not be ascertained during structure refinnement.

The B-O6 octahedra have an almost regular cubic symmetry, with B-O distances consistent with the ionic radius of the element (Al^{3+}, Lu^{3+} according to reference [12].

As A-site are occupied by luminescent REE in substitution to the large cation of the binary oxides, the geometry and dimensions of this site play an important role in the crystal field approach.

The A-ion (La, Y, Lu) adopts a polyhedron volume larger than would be expected from the ionic radii, in order to minimize oxygen-ions repulsions within the coordination polyhedron [13]. The off-centre displacement within the polyhedron, allowing a better stabilization of A ion, should be noticed, with the smaller A-cation, lutetium, showing the larger shift when compared to yttrium and lanthanum.

While La-site in $LaLuO_3$ clearly exhibits a disorted 8-fold coordination, with four long La-O bonds, the description of Y and Lu environment in aluminates is much more complex. Height oxygen anions build a coordination shell swollen by a next oxygen and aluminium cations at quite the same (large) distances, in such a way that speaking of "9-fold coordination" as usual is rather ambiguous. The similarity of the polyhedron geometry, with Y ones somewhat larger, appears clearly related to cation radius, the electronic distribution being probably a second order parameter in coordination building.

Experimental results for $LaLuO_3$

Agreement factors: Rp = .0546 wRp = .0705 reduced $\chi^2 = 3.226$

Lattice parameters: a =6.0144(3) b = 8.3678(4) c= 5.8109(3) d_x = 8.219 g.cm^{-3}

Atomic parameters

Atom	Site	x	y	z	Uiso × 100
La	4(c)	.0500(3)	1/4	.5125(6)	.73(3)
Lu	4(a)	0	0	0	.82(7)
0	4(c)	.9475(6)	1/4	.1191(6)	.78(5)
0	8(d)	.3059(4)	.4361(3)	.8081(4)	1.23(6)

Interatomic distances

La-0	2.368(5) - 2.380(3)* - 2.510(4) - 2.783(4)* - 3.010(3)*
Lu-0	2.226(1)* - 2.203(2)* - 2.217(2)*
Lu-La	3.421(1)* - 3.534(2)* - 3.652(2)* - 3.914(1)*

* distances × 2

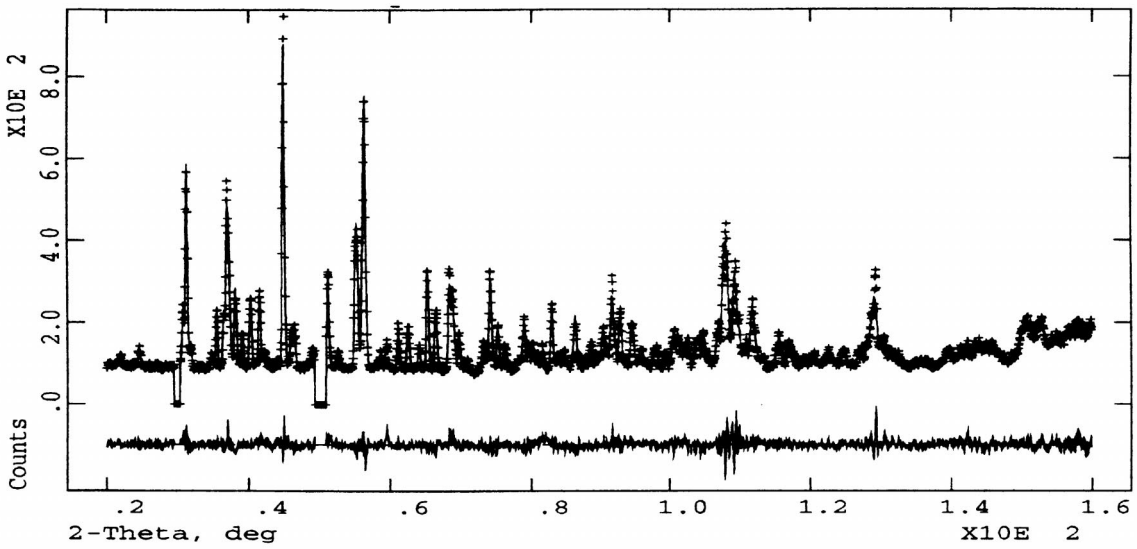

Fig.1-a. Observed neutron scattering, calculated and difference profiles for $LaLuO_3$

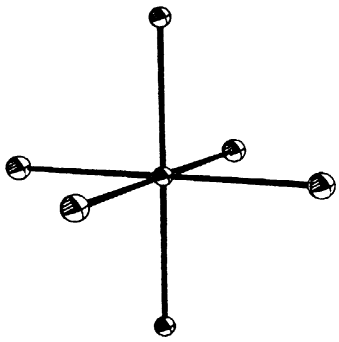

Fig.1-b—*Lu* coordination polyhedron

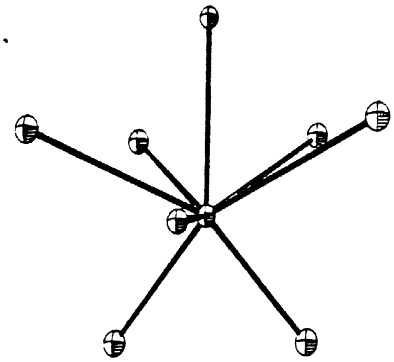

Fig.1-c—*La* coordination polyhedron

Experimental results for $YAlO_3$

Agreement factors: Rp = .1074 wRp = .1449 reduced $\chi^2 = 8.401$

Lattice parameters: a =5.3270(1) b = 7.3675(1) c= 5.1771(1) d_x = 5.358 g.cm^{-3}

Atomic parameters

Atom	Site	x	y	z	Uiso× 100
Y	4(c)	.0549(3)	1/4	.5135(3)	.07(3)
Al	4(a)	0	0	0	.35(6)
0	4(c)	.9776(3)	1/4	.866(4)	.13(5)
0	8(d)	.2942(2)	.4560(1)	.7956(3)	.32(4)

Interatomic distances

Y-O	2.248(2) - 2.280(1)*- 2.308(2) - 2.462(1)*- 2.571(1)*- {2.996(2)}
Al-O	1.899(6)* -1.910(1)* - 1.916(1)*
Al-Y	3.002(1)* -3.134(1)* - 3.247(1)* - 3.483(1)*

* distances ×2

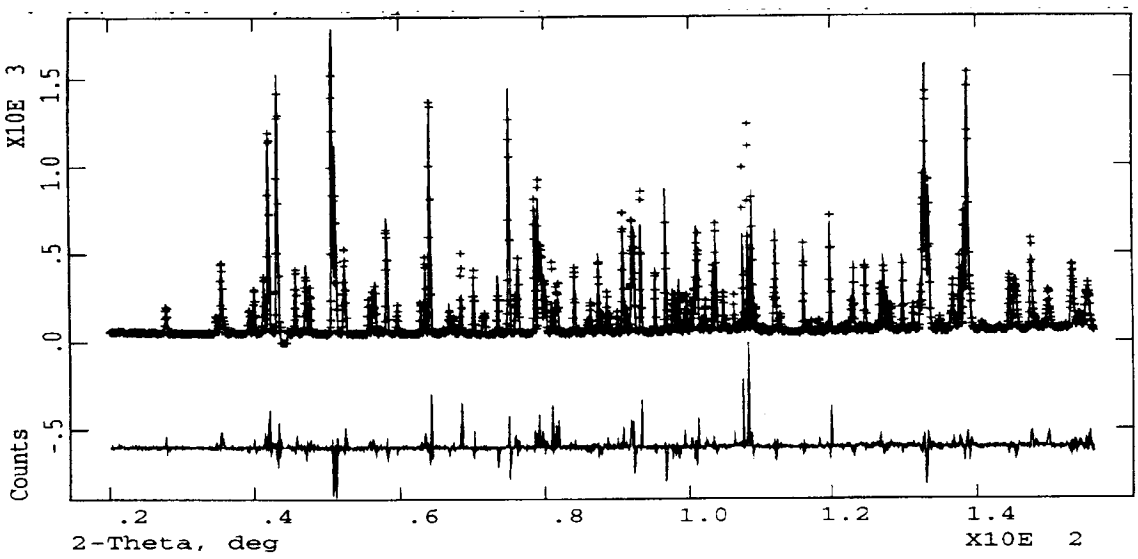

Fig.2.a. Observed neutron scattering, calculated and difference profiles for $YAlO_3$

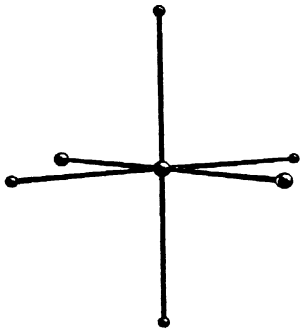

Fig.2-b—*Al* coordination polyhedron

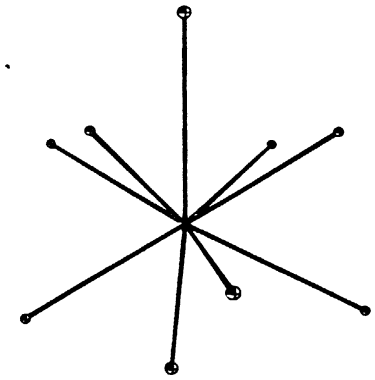

Fig.2-b—*Y* coordination polyhedron

Experimental results for $LuAlO_3$

Agreement factors:	Rp = .1367	wRp = .1821	reduced $\chi^2 = 23.99$	
Lattice parameters:	a=5.3323(1)	b=7.3059(2)	c=5.1071(1)	d_x = 8.344 g.cm^{-3}

Atomic parameters

Atom	Site	x	y	z	Uiso× 100
Lu		.0630(4)	1/4	.5163(4)	.45(5)
Al		0	0	0	.50(9)
0		.9714(4)	1/4	.0944(5)	.13(5)
0		.2972(3)	.4499(1)	.8003(3)	.32(4)

Interatomic distances

Lu-O	2.209(4) - 2.240(2)*- 2.249(3) - 2.407(2)*- 2.564(2)*- {2.993(4)}
Al-O	1.895(8)*-1.911(2)*-1.919(2)*
Lu-Al	2.961(1)* - 3.090(2)* - 3.225(2)* - 3.515(1)*

* distances × 2

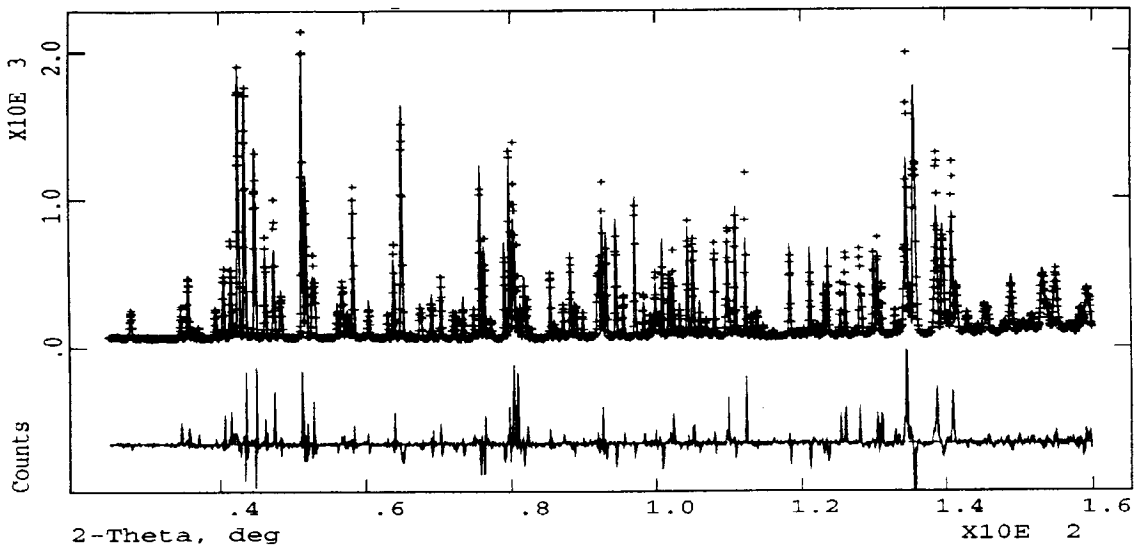

Fig.3-a. Observed neutron scattering, calculated and difference profiles for $LuAlO_3$

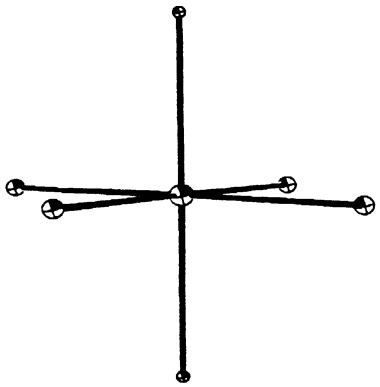

Fig.3-c—*Al* coordination polyhedron

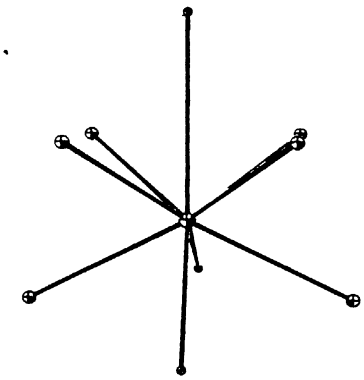

Fig.3-c—*Lu* coordination polyhedron

References

1. A.G.Petrosyan, J. Cryst. Growth, **139** (1994) 372.
2. A.G.Petrosyan and C.Pedrini, Proc. Int. Conf. on Inorganic Scintillators and Their Applications, SCINT'95 (The Netherlands: Delft University Press) pp.498—501.
3. K.L.Ovanesyan, A.G.Petrosyan, G.O.Shirinyan, C.Pedrini, L.Zhang, J.Crystal Growth **198/199** (1999) 497.
4. K.L.Ovanesyan, A.G.Petrosyan, G.O.Shirinyan, C.Pedrini, L.Zhang, Optical Materials **10** (1998)291.
5. T.I.Butaeva, K.L.Ovanesyan, A.G.Petrosyan, Cryst. Res. Technol. **23** (1988) 849.
6. C.Pedrini, D.Bouttet, C.Dujardin, B.Moine et al., Optical materials **3** (1994) 81.
7. C.Dujardin, C.Pedrini, J.C.Gacon, A.G.Petrosyan et al., J. Phys.: Condens. Matter **9** (1997) 5229.
8. A.G.Petrosyan, G.O.Shirinyan, C.Pedrini, C.Dujardin, K.L.Ovanesyan, R.G. Manucharyan, T.I.Butaeva, M.V.Derzyan, Cryst. Res. Technol. 33, **2** (1998), 239—246.
9. A.C.Larson, R.B.Von Dreele, General Structure Analysis System, LANSCE, MS-H805, Los Alamos National Laboratory.
10. J.Ranlov and K.Nielsen, J. Appl. Crystallogr. **28** (1995) 436.
11. Hk.Muller-Buschbaum and P.H.Graebner, Z.Anorg. Allg. Chem. **386** (1971) 158.
12. R.D.Shannon, Acta Cryst. **A32** (1976) 751.
13. N.W.Thomas, Acta Cryst. **B52** (1996) 16.

Scintillation Properties of $Lu_2Si_2O_7:Ce^{3+}$ (LPS) Crystals

D. Pauwels[1], N. Lemasson[1], B. Viana[1], A. Kahn-Harari[1]
E.V.D. van Loef[2], P. Dorenbos[2], C.W.E. van Eijk[2]

[1] *Laboratoire de Chimie Appliquée de l'Etat Solide, CNRS, UMR-7574, ENSCP*
11, Rue Pierre et Marie Curie, F-75231 Paris Cédex 05, France
[2] *Radiation Technology Group, Interfaculty Reactor Institute, Delft University of Technology*
c/o IRI, Mekelweg 15, 2629 JB Delft, The Netherlands

Abstract: We have characterized the γ– and X-ray scintillation properties of Ce^{3+} doped $Lu_2Si_2O_7$, a lutetium pyro-silicate (LPS) material. The rare earth ions are located in octahedral site with C_2 symmetry. This compound exhibits chemical stability and transparency in a wide optical range, and it presents a congruent melting which allows the elaboration of single crystals of good optical quality. The melting temperature is about 2000°C, slightly lower than for Lu_2SiO_5 (LSO). Two maxima at 305 nm and 355 nm are observed in the optical absorption spectrum. The emission spectrum of Ce^{3+} in LPS shows a broad band peaking at 380 nm, which is 40 nm shorter than in LSO. For nominal Ce^{3+} atomic concentrations in the range 0.005 - 0.01, the light yield varies in the range 13,000-23,000 ph/MeV under γ-ray excitation. The actual cerium concentration inside the crystal still needs to be determined. The scintillation decay time is around 30 ns and, in the first studies, no long component nor after-glow in the decay profile was observed.

Keywords: Silicate, Cerium, Scintillator

Material Preparation

The crystal growth of Eu^{3+} doped $Lu_2Si_2O_7$ was first reported in Ref. 1. $Lu_2Si_2O_7$ compound has a congruent melting [2]. In the present work, Ce^{3+} doped $Lu_2Si_2O_7$ is prepared by the floating zone technique which does not require large amounts of starting material. Polycrystalline starting material is prepared by solid state reaction between the constitutive oxides at 1500°C in a platinum crucible, under argon atmosphere.

The principle of this technique is described in Ref. 3. With the floating zone technique the crystal growth speed is 2 mm/h to limit the thermal gradient which is very strong. Such grown crystals are transparent, with approximate dimensions 5x2x1 mm^3 for the largest. Using X-ray diffraction, the samples were characterized and present the thorveitite structure and no parasitic phase. The lattice constants were refined; a = 6.765 Å, b = 8.839 Å, c = 4.715 Å, β = 101.96° and V = 275.9 $Å^3$. These values are similar to the unit cell constants of $Lu_2Si_2O_7$ [4], since the Ce^{3+} ratio is too low to affect the lattice constants.

One can also report the Z_{eff} value for the $Lu_2Si_2O_7$:Ce compound around 64.4 and a density of 6.23 g/cm^3.

Ce^{3+} Concentration

The Ce^{3+} and Lu^{3+} ions have rather different ionic radii, 1.01 Å and 0.86 Å respectively [5]. Thus, one expects the solubility of Ce^{3+} in the host crystal to be small. However the

knowledge of the Ce^{3+} content in the crystal is a required data to optimize the crystal growth and the scintillation light yield.

A first study was performed with crystals, synthesized by the floating zone process under various atmospheres (air , argon and vacuum). The results are gathered in table 1.

Table 1 : Relative Ce^{3+} concentration for different $Lu_2Si_2O_7$ crystals prepared by the floating zone process. (* the highest relative concentration is taken as 1)

Initial Ce^{3+} at. %	Preparation Atmosphere	Final relative Ce^{3+} concent.
1 %	air	0.54
1 %	argon	0.91
0.5 %	vacuum	0.54
0.5 %	vacuum + 12 hours of annealing under Ar/H_2 atmosphere	1*

These results have been deduced from the absorption measurements. One can conclude that Ce^{3+} concentration in the LPS structure is below 0.5% and that a large amount of the doping ions is not host by the matrix. Indeed this result is not surprising as the ionic radius greatly influence the solubility of the cerium. For instance in $Ce:Lu_2SiO_5$, at most 0.1% of the cerium ions can be introduced in the host lattice.

Furthermore, the Ce^{3+} concentration measured from the absorption measurements in the crystal annealed under Ar/H_2 atmosphere is much higher than in crystals synthesized under argon atmosphere. This could be explained considering that during the crystal growth, one part of the Ce(III) ions is oxidized in Ce(IV) state. It is known that some lanthanide trivalent ions (Ce^{3+}, Pr^{3+}, Tb^{3+}) have a tendency to become tetravalent inducing some charge transfer transition bands in the ultraviolet [6]. Such a CT band could be observed on the absorption spectrum (see figure 1). After annealing the crystal under Ar/H_2 atmosphere, the absorption band attributed to the O^{2-} and Ce^{4+} charge transfer decreases. Then, a Ce^{3+} absorption band can be detected around 305 nm (see in figure 2 the excitation measurements).

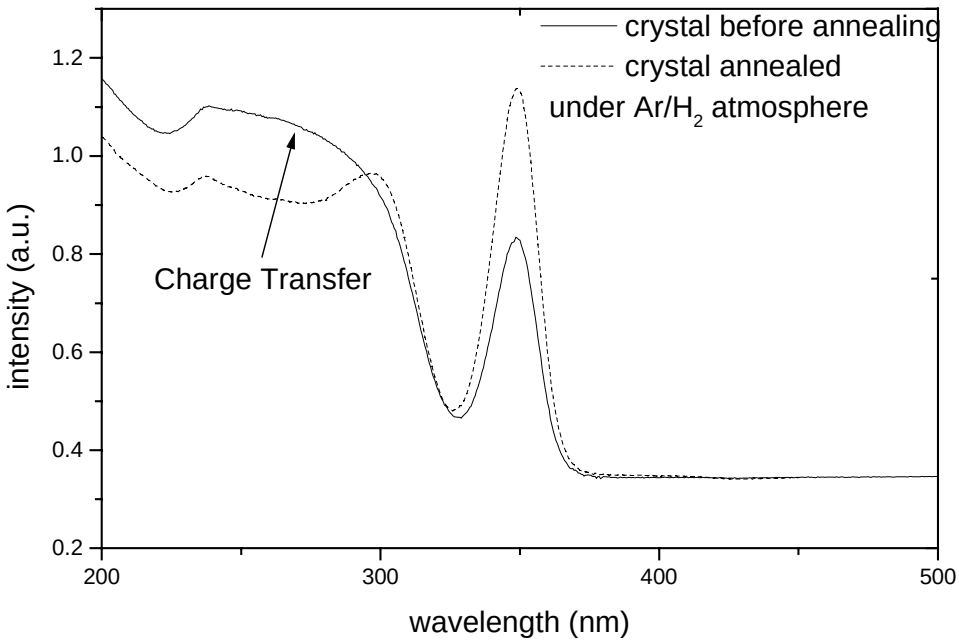

Figure 1: Absorption spectra of a crystal obtained by the floating zone technique. Plain: before and dashed: after annealing in Ar/H_2 atmosphere.

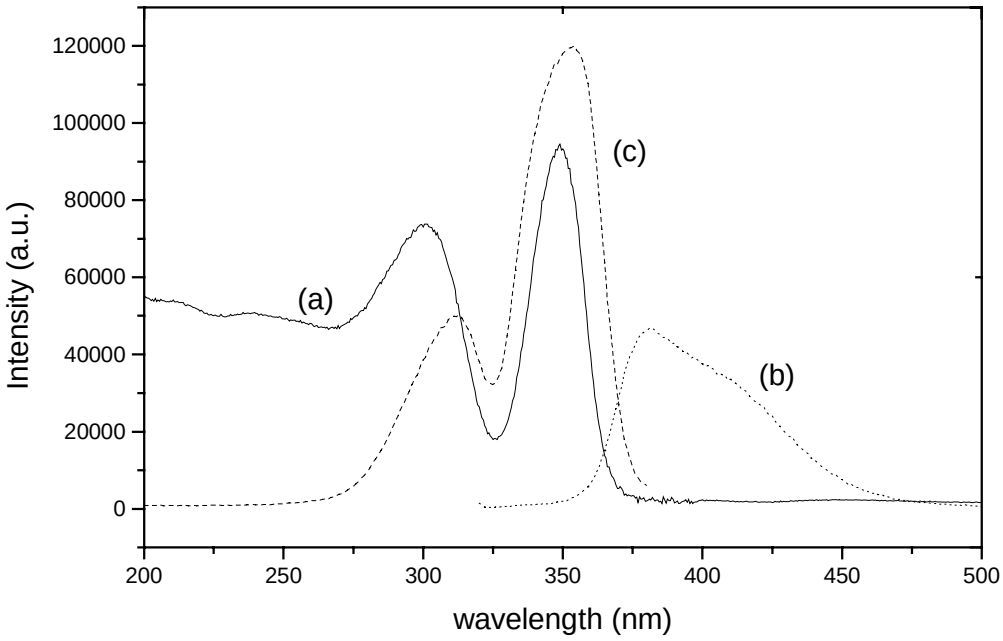

Figure 2: Optical characteristic of LPS:Ce single crystals: a) absorption spectrum b) emission spectrum c) fluorescence excitation spectrum (under a 400 nm emission wavelength)

One can expect that a single crystal grown by the Czochralski process (the melting point is about 2000°C), would not require any annealing, since the Czochralski enclosure is totally airtight and works in a reducing atmosphere to protect the iridium crucible.

Optical Properties

The absorption spectrum of Ce:$Lu_2Si_2O_7$ shows two broad bands peaking at 305 and 355 nm assigned to the 4*f* ->5*d* transitions. However, the band at the shortest wavelength is influenced at the higher energy position by the broad band previously ascribed to the charge transfer mechanisms (see part 1.2) and the exact position is difficult to determine. On the contrary two bands are clearly observed in the excitation spectrum and the maxima are at 313 nm and 355 nm. The crystallographic site of the rare earth ion is a distorted octahedron, thus it is likely that the 5*d* levels are split by the crystal field interaction into two components e_g and t_{2g}. VUV experiments are now necessary to complete the attribution and determine the energy level positions.

The Ce^{3+} luminescence in $Lu_2Si_2O_7$ consists in a broad band peaking at 380 nm. At low temperature, under laser excitation at 355 nm, two peaks appear on the emission spectrum at 380 nm and 415 nm respectively. The peaks are attributed to transitions from the lowest 5*d* energy level of the Ce^{3+} ions to the spin-orbit split $^2F_{7/2}$ and $^2F_{5/2}$ levels. The splitting energy value between the $^2F_{7/2}$ and $^2F_{5/2}$ levels is 2200 cm^{-1}. The Stokes shift for the Ce^{3+} doped $Lu_2Si_2O_7$, lutetium pyro-silicate is around 2000 cm^{-1}, a reasonable value for a luminescent ion slightly compressed in its crystallographic site [6].

Pulse Height Measurements

To study the behavior under γ excitation, pulse height measurements have been performed on crystals prepared by the floating zone technique under argon atmosphere, the size of these

crystals being approximately 1x1x0.5 mm^3. Two different light detectors have been used, an avalanche photodiode and a photomultiplier. The results are given in table 2 .

Table 2: Light yields obtained for several crystals (shaping time of 10 µs)

	Ce:LPS crystals (under floating zone)	γ-Sources	Photons/MeV
Ar atmoph.	1% (A)	^{241}Am	22020
Vacuum	0.5 % Ar/H_2 annealing (B)	^{137}Cs	13200
Vacuum	0.5 % Ar/H_2 annealing (B)	^{241}Am	19320
Vacuum	0.5% (C)	^{241}Am	16750
Vacuum	0.5% (C)	^{137}Cs	20720
Vacuum	0.5% (D)	^{137}Cs	21300
Vacuum	0.5% (D)	^{241}Am	18750

One can notice that the measured yield values are widely scattered (between 13000 to 22020 photons/MeV). These discrepancies could result from the shape of the different small crystals and from a variation of the Ce^{3+} concentration in these crystals. Indeed, Ce^{3+} concentration, in small crystals might be inhomogenous and, in that case, the light yields vary with the ratio of Ce^{3+} in the crystals. The energy resolution for the Ce:LPS estimated from the FWHM of the photo-peak is around 10 % (see Figure 3). For different shaping times ranging between 0.5 µs and 10 µs the resulting light yield is about the same. This indicates that the time response is fast.

In the future, the growth of larger crystals by the Czochralski method, associated with a chemical analysis will be developed to correlate the scintillation light yields results to the Ce^{3+} concentration.

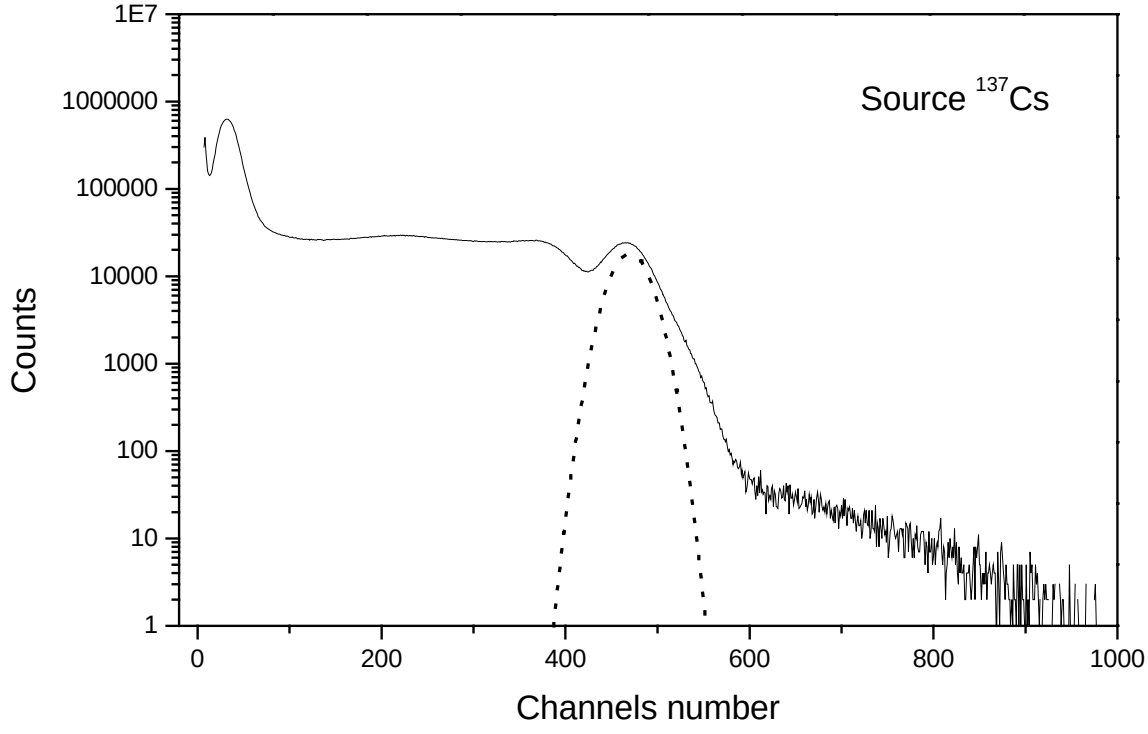

Figure 3: Pulse height spectrum of LPS:Ce

Decay Time Measurements

The scintillation decay time under γ-rays sources is about 30 ns and no long component or afterglow in the decay profile was observed. The radiative lifetime for an electric dipole allowed transition, can be expressed in the case of low symmetry as [7]:

$$\tau_{rad} = 1.5 \times 10^{-5} \frac{\lambda^2}{f \times n} = 30 \text{ ns}$$

where f is the oscillator strength, n the refractive index (around 1.75 [8]) and λ the emission wavelength.

The radiative value is in good agreement with the experimental Ce^{3+} lifetime obtained under laser excitation at 355 nm, τ_{exp} = 32 ± 5 ns (see Figure 4). No long component is observed in the Ce^{3+} decay profile.

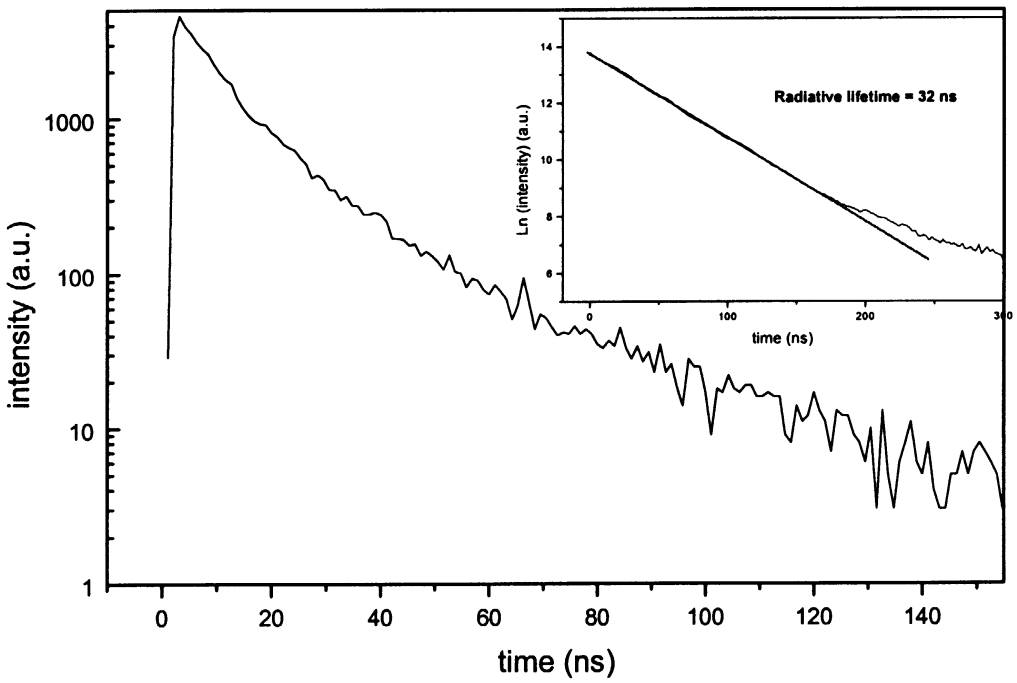

Figure 4: Scintillation decay of LPS:Ce. In inset is presented the fluorescence decay under 355 nm laser excitation

Conclusions

The light yields of LPS:Ce are in the range of others Lu-based scintillators while the Z_{eff} and density values are slightly lower than for others Ce^{3+} doped Lu-scintillators [see for instance Lu_2SiO_5:Ce, $LuAlO_3$: and Lu_2S_3:Ce values in Refs. 9-11].

The outstanding features of the LPS:Ce compound are the short decay time (30 ns without long component or afterglow process) and the crystal growth possibility. It makes this material an attractive new scintillator for detection of hard gamma rays. The growth of large crystals seems possible, if compared to LSO compound (Lu_2SiO_5), the LPS material exhibits a lower melting point. Furthermore only one type of site is offered to the cerium ions in the structure, and this should avoid parasitic energy transfer processes.

Further improvements are expected by optimizing the Ce^{3+} concentration. Crystal growth, by the Czochralski method, on this new promising scintillator, is now in progress and this material could occupy a good position in the lutetium based scintillator field.

References

1. F. Bretheau-Raynal, N. Tercier, B. Blanzat, M. Drifford, Mat. Res. Bull.; 15, 639 (1980)
2. A. NØrlund Christensen, Zeitschrift fur Kristallographie; 209, 7 (1994)
3. A. Revcolevski and R. Collongues, CR. Acad. Sci. Paris; 266, 1767 (1968)
4. F. Bertheau-Raynal, M. Lance, P. Charpin; J. Appl. Cryst. 14, 349 (1981)
5. R. D. Shannon, Acta. Cryst., 32, 751 (1976)
6. G. Blasse, B. C. Grabmaier, in Luminescent Materials, Springen-Verlag.
7. B. Henderson, G. F. Imbusch, "Optical spectroscopy of inorganic solids", Oxford (1989)
8. G. V. Anan'eva, V. E. Karapetyan, A. M. Korovkin, T.I. Merkylyaeva, I. A. Peschanskaya, I. R. Savinova, P. P. Feofilov, Izvestiya Akademii Nauk SSSr, Neorganicheskie Materialy, March , 8, 3, 349 (1982)
9. C. L. Melcher, J. S. Schweitzer, Nucl. Instr. and Meth. in Phys. Res., B134, 304 (1998)
10. M. Moszynski, D. Wolski, T. Ludziejewski, M. Kapusta, A. Lempicki, C. Brecher, D. Wisniewski, A. J. Wojtowicz, Nucl. Instr. and Meth. in Phys. Res., 385, 123 (1997)
11. J. C. van't Spijker, P. Dorenbos, C. P. Allier, C. W. L. van Eijk, A. R. H. F. Ettema, G. Huber, Nucl. Instr. and Meth. in Phys. Res., 134, 304 (1998)

Doped Rare – Earth Oxysulfides Luminescent Ceramics

Gorokhova E. I., Ananieva G.V., Demidenko V.A., Khristich O. A.,
Merkuliaeva T. I., Savostianov V. A.

Abstract. The report examines the particulars of formation under hot pressing conditions of polycrystalline materials based on yttrium, lanthanum oxysulfides with near X-ray structural density (residual porosity of < 0.1% vol.) and transparency in 0,32÷10μm range. The data presented demonstrate a rigid relation between structural, optical, and mechanical properties of ceramics and the conditions of hot pressing. It is shown that transparency of hexagonal doped oxysulfides of the rare-earth (at the substantial difference of refractive indices) is determined by the material's texturing in [001] direction. It is established that light output of first samples of x-ray luminescent ceramic screens is analogous to (and in some cases 1.5 times higher than) light output of Gd_2O_2S-Tb «Lanex Fine» powder screens by Kodak (at U=50kV): decay time is 560 ÷600μs.

Keywords: Rare-earth oxysulfides, hot pressing, ceramics

Doped oxysulfides based phosphors occupy a special niche among other luminophors since they offer the combination of features required for photo-, cathode-, x-rays logging. Their high: ability to absorb x-rays across wide energy spectrum, conversion efficiency and light output, the opportunity to control emission spectra and kinetics of damping, created demand for doped oxysulfides serving as matrices for the development of luminescent ceramics in Russia, Japan, Germany [1-4].

The first detailed examinations of the impact hot pressing factors have on the process of formation of transparent to its own radiation luminescent ceramics based on hexagonal matrix to which the rare-earth (RE) oxysulfides belong were being carried out by the authors since the end of the '80s while they were developing cathodeluminescent Y_2O_2S-Tb and La_2O_2S with various dopants [5-7]. That work's results were put into the foundation of a project aimed at creating x-ray luminescent converter screens based on Gd_2O_2S and other oxysulfides for up-to-date, general purpose radiodiagnostics equipment.

The starting materials for the ceramics were luminophors produced by standard manufacturing technique for oxysulfide luminophors, which implied a reaction between RE oxides and polysulfides of alkali metals in the presence of a mineralizer - lithium fluoride.

X-ray examinations of objects were carried on the DRON-2 diffractometer with copper anticathode and nickel filter within 10^0-125^0 of arc. For more precise measurement of cell parameters a system of planes (312), (223), (206) with large angles of reflection was selected. Texture along the (001) plane in the ceramic samples was evaluated by radiographic method [8]. The texture factor (F) was computed using 5 lines of reflection of RE oxysulfides from planes (001, 003, 101, 102, 110) characteristic of the texture.

The efficiency of conversion of x-ray excitation in the samples was evaluated on a radiospectroscopic unit that employed the point continuous excitation source REIS with energy of x-ray quanta up to 50 kV. Luminescence kinetics was investigated with a spectral kinetics unit, the excitation being provided by the LGI-502 nitrogen laser, and logging was by a multichannel time analyzer.

The powder luminophors utilized to obtain ceramics offered a characteristic grain shape: polyhedra, tabular and short-pillar. The crystal lattice parameters of the luminophors corresponded to those from ICPDS [10]. Varying the HP parameters of powders produced practically no effect on lattice parameters of polycrystalline samples.

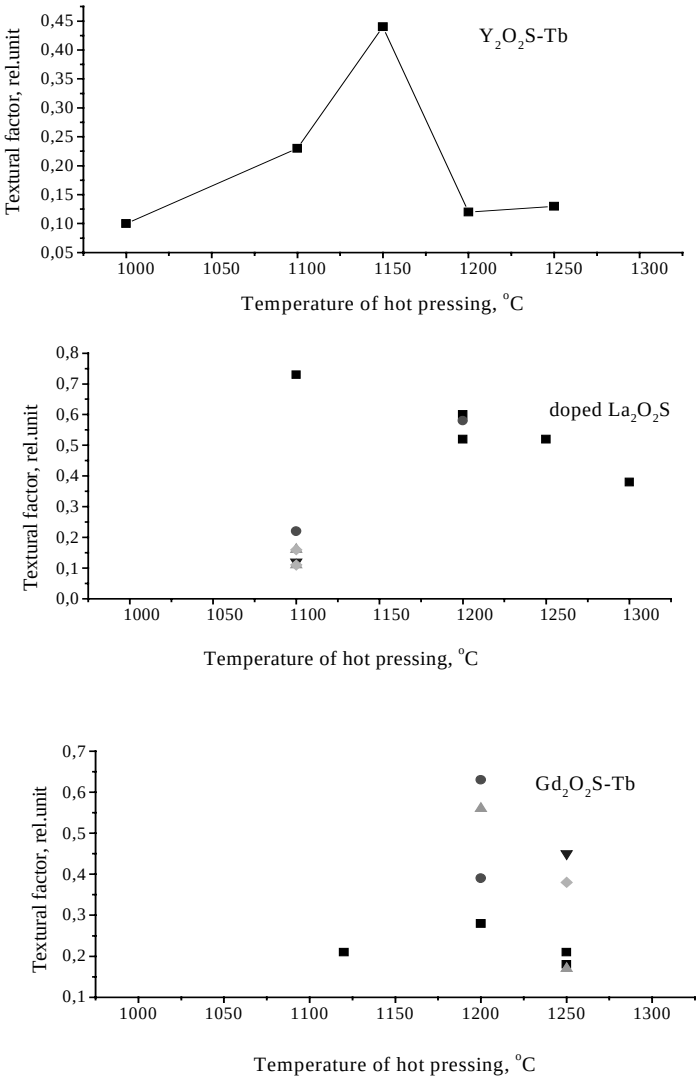

Fig. 1. The influence of hot pressing temperature on the texturing level of ceramics produced from Y_2O_2S-Tb, doped La_2O_2S, Gd_2O_2S -Tb based luminophors.

The x-ray structural investigation of the Y_2O_2S-Tb ceramics texture allowed to uncover a certain relation between texture and parameters of the technological process. It was found that the formation of texture in samples occurs along (001) plane, which for hexagonal crystals signifies a coincidence with the direction of the optical axis. This latter fact stands out as the decisive factor for obtaining a transparent polycrystalline material with substantial difference of refractive indices (∇n). For that reason a special attention was devoted to watching closely the degree of texturing in Y_2O_2S-Tb ceramics. The degree of texturing of ceramics plotted against HP temperature is displayed in Fig.1a. The formation of the highest texture in ceramics is observed at $1100 \div 1150^0$C pressing, at higher temperatures texture disappears, apparently due to decomposition of yittrium oxysulfide and liberation of Y_2O_3 [7]. Similar result is achieved by extending the process time from 60 to 90 min at 1150^0C. At the same time bringing up pressure from 200 to 250 MPa (maintaining same temperature) gives an increase in the degree of texturing of ceramics.

Results of the examination of microstructure of ceramics are presented in Fig. 2 (graph 1). While temperature of pressing rises from 1000 to 1150^0C, an increase in average grain size is observed (graph a), and the birth and growth of elongated grains (graph b). Further temperature increase brings about the disappearance of pole-like grains and degradation of grain cut. Raising the process pressure from 200 to 250 MPa ($T_{HP} = 1150^0$C) results in grain size growth on the average by a factor of 1.5. Extending time under pressure practically does not alter the structure of ceramics, while prolonging the exposure at 1150^0C (before applying pressure) makes elongated grains disappear and the structure to become more loose.

Microhardness of ceramics is changing in the same order as the parameters above (Fig. 2, graph 2): it grows along with growing temperature of pressing up to 1150^0C, and then falls away sharply. The textured samples, composed mainly of elongated and isometric clear-cut grains, have microhardness on the order of 800 kg/mm^2; ceramics with minimal grain texturing displays microhardness on the order of 300-400 kg/mm^2.

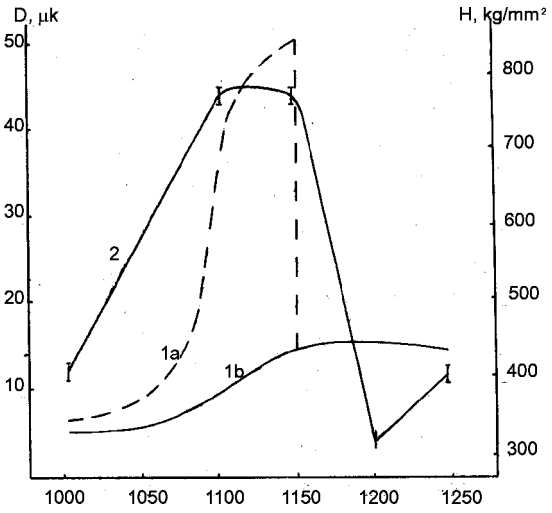

Fig.2 The dependence of grain size (graphs 1a,b) and microhardness (graph 2) of Y_2O_2S- Tb ceramics on temperature of hot pressing.

All data in Fig. 1 demonstrate a rigid subordination of properties of the ceramic samples to parameters of the HP process, and also their interdependence. For example, as transparency of hexagonal Y_2O_2S is determined by the material's texturing in [001] direction, then the impact of HP parameters on the level of transparency can be foretold on basis of the degree of texturing. Indeed, for samples with the greatest texturing, the transparency level is 55% at natural radiation wavelength of 0.55 μm (Fig. 3a). Transmittance of the samples with minimal value of "F" does not get over 10-20% in the IR. On the whole, transparency region for Y_2O_2S-Tb based ceramics is 0.32 - 8 μm. In production of lanthanum oxysulfide based doped ceramics connection between the factors of hot pressing and the form and predominant orientation of grains was also observable. By and large for La_2O_2S ceramics the pattern of changes in "F" value produced by temperature of the HT process is similar to Y_2O_2S ceramics in the > 1200^0C range; at lower temperatures the degree of texturing of doped La_2O_2S is different (Fig. 1b). And besides, in that matrix, side-by-side with texturing along pinacoid plane (001), a feebler texture also appears in rhombohedron (pyramid) plane (102) = (1012) which is at 45^0 to (001).

The greatest difference in behaviour of the aforementioned matrices is that in ceramic La_2O_2S samples no correlation is manifest between transparency, degree of texturing and grain forms. For example, some samples of doped La_2O_2S may exhibit intensive texturing and growth of elongated grains, while in others, with minimal texturing, both elongated and isometric grains might be growing. And transparency of the latter samples can be significantly higher than that of the first. The most transparent samples of doped La_2O_2S ceramics (Fig. 3b) were obtained at lower HP temperature than Y_2O_2S-Tb ceramics, which is due to different melting temperature of these matrices (2070 ± 30^0C for La_2O_2S [10] and 2120^0C for Y_2O_2S [11]) and the existence in La_2O_2S under plastic deformation of additional slip systems. The absence of connection between transparency and the degree of texturing in La_2O_2S ceramics is also explained by their physical or, more precisely, crystal optical properties: La_2O_2S exhibits very small anisotropy, and in 0.56 μm range it is absent altogether [10]. Microhardness of doped La_2O_2S ceramics with high transparency corresponds to monocrystal microhardness [10], and is 350÷400 kg/mm^2, which is twice as low as microhardness of Y_2O_2S.

The results of measuring such structurally-sensitive parameter as thermal linear expansion coefficient (TLEC) indicate that doped La_2O_2S ceramics features higher TLEC values than Y_2O_2S based ceramics: $9{,}7\times10^{-6}/^oC$ and $9{,}2\times10^{-6}/^oC$ correspondingly in the temperature range from 20 to 300^0C. This is due to dissimilarities of melting temperatures and lattice parameters of these materials: a = 4,047(2), c = 6,942(1), c/a = 1,715 for La_2O_2S-Tb ceramics and a = 3,781(1), c= 6,590(1) for Y_2O_2S-Tb ceramics.

The first experiments in hot pressing of terbium doped gadolinium oxysulfides based x-ray luminophors have demonstrated that the forming of transparent ceramics with density approaching x-ray structural density and corresponding ICPDS lattice parameters (a=3.848, c=6.666; c/a=1.731) is accompanied by changes in microstructure similar to those taking place in lanthanum and yittrium oxysulfides. As can be seen in Fig. 1c, the tendency toward texturing along (001) plane for Gd_2O_2S-Tb under certain conditions becomes stronger than

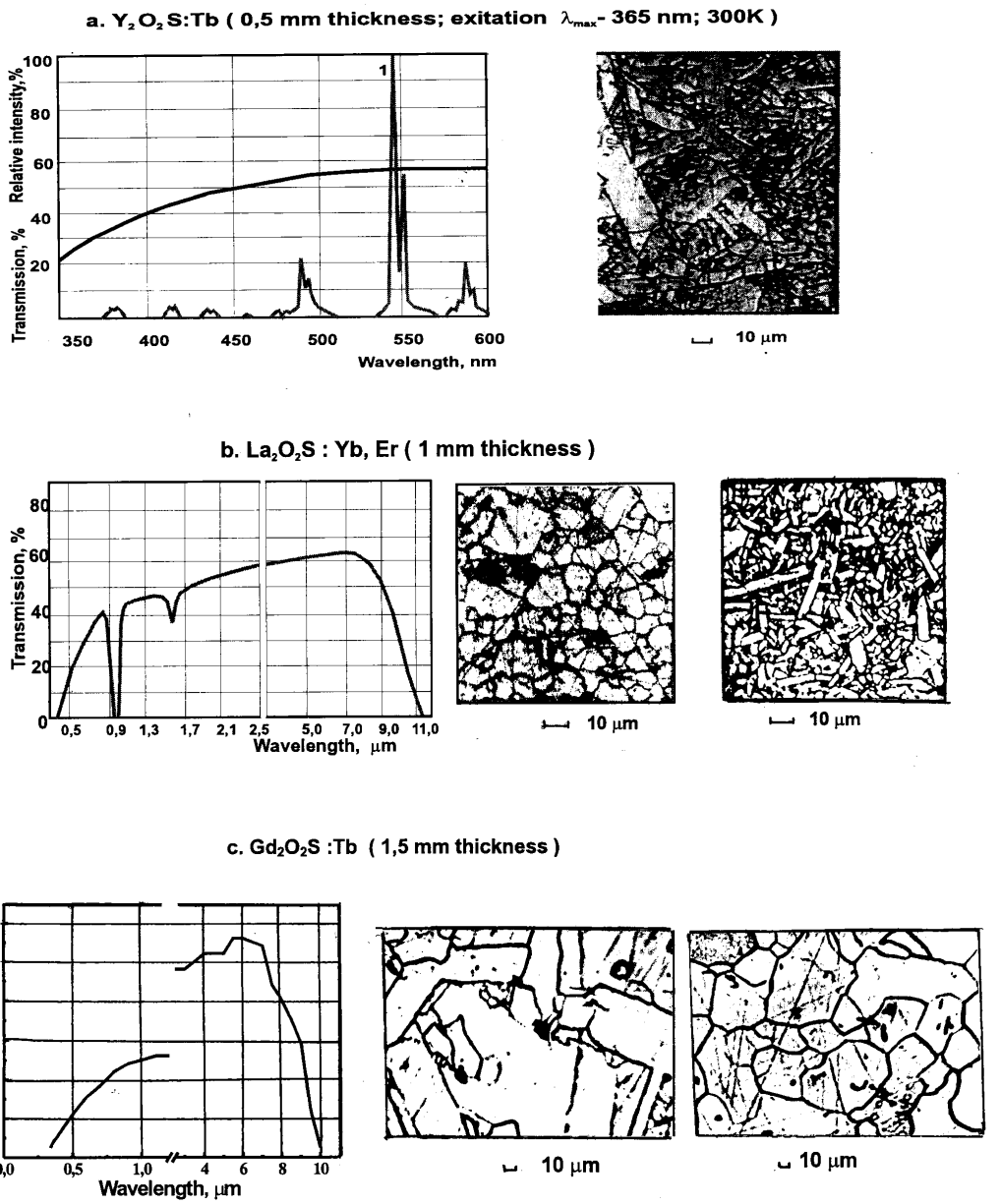

Fig.3. Transmittance, spectral emission (1) and microstructure of ceramics:
a - Y_2O_2S-Tb, b - La_2O_2S-Yb, Er, c - Gd_2O_2S-Tb.

with Y_2O_2S-Tb. The microstructure of Gd_2O_2S-Tb ceramics can be represented by both elongated and isometric grains. Fig.3c But unlike La_2O_2S, transparent Gd_2O_2S ceramics (Fig. 3c) can be achieved at certain degree of texturing, which is due to large difference of the refractive indexes of Gd_2O_2S 2.1-2.2 [12]. The value of microhardness of Gd_2O_2S-Tb ceramics correlates with the changing "F" value. At its highest it is 670 kg/mm^2.

The luminescence spectra of terbium doped oxysulfide ceramics are similar to powder luminophors spectra, and are characterized by line series in 385 to 600 nm range caused by transitions from $^5D_4$ and $^5D_3$ levels: for Y_2O_2S the share of luminescence from $^5D_3$ level in summary radiation is greater than for Gd_2O_2S-Tb and La_2O_2S-Tb.

Since Y_2O_2S-Tb ceramics was being developed as a cathodeluminescent material, we shall give some data on its cathodeluminescence light output. As was demonstrated by the research,

in through-transition measurements the value of this parameter greatly depends on the degree of transparency of ceramics. For that reason the most stable and high data were obtained with screens manufactured from textured samples. The light output of Y_2O_2S-Tb at 15 keV accelerating voltage is identical to that of a ZnS based screen [13] and is 5-7 cd/W. When switching to lower accelerating voltages (~ 5 keV), the light output of Y_2O_2S-Tb ceramics (2-3 cd/W) becomes higher than that of zinc sulfide luminescent ceramics, and approaches the powder luminophors level. Comparative studies of the resistance to permanent burnout of various types of cathodeluminescent screens (powder, ceramic, glass, and monocrystalline) have demonstrated that the best characteristics belong to ceramic screens, Y_2O_2S-Tb based screens in particular. In addition, like with other monolithic screens, ceramics offers enhanced electric strength.

The analysis of X-ray luminescence of the first experimental samples of Gd_2O_2S-Tb ceramics (1 mm thick) was conducted in comparison to a Kodak powder screen, the Lanex Fine (Gd_2O_2S-Tb). In addition, the evaluation of x-ray luminescence and samples of cathodeluminescent Y_2O_2S-Tb ceramics was carried out (on 0.5 mm thick samples). All the measuring was in through-transition mode. Accelerating voltage on the tube was 50 kV, current 50 μA, 1 mm thick Al filter was implemented, and registration was at λ - 543 nm. Under these excitation conditions the absorption of X-radiation in ceramic samples was 97÷100%, while in Kodak screen it was 38%. The luminescence intensity of ceramic samples proved higher than that of the powder screen: by a factor of ~ 2 for Gd_2O_2S-Tb, and 2.5 for Y_2O_2S-Tb. Greater relative intensity in yttrium samples compared to gadolinium is probably in connection with greater efficiency of ionizing radiation energy conversion into energy of excited state of terbium in Y_2O_2S resulting from the position shift of $^5D_4$ component into the low frequency area for that matrix compared to Gd_2O_2S and others in this homologous series [14]. The data obtained testify to the fact that thanks to higher x-ray image logging efficiency of ceramic screens it is possible to reduce substantially radiation exposure dose, thus providing for safe radiodiagnostic examination of a patient. The results of the investigation of luminescence kinetics have demonstrated that lifetime in Gd_2O_2S-Tb ceramics is 560-600 μs, and that in 3 ms the afterglow is 0.35% (with 10 Hz pulse train) (Fig.4). These data concur with similar characteristics of Gd_2O_2S-Tb powder screens from Kodak [15].

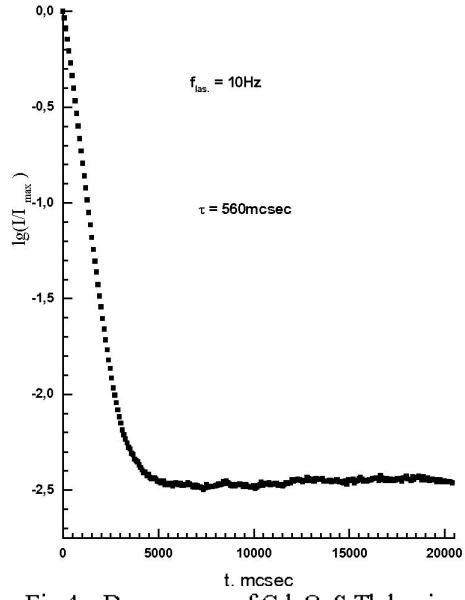

Fig.4 Decay curve of Gd_2O_2S-Tb luminescent ceramics (after nitrogen laser excitation with l = 337nm). Pulse 10nc, frequency -10 Hz.

In accordance with their kinetic characteristics terbium doped oxysulfides they can be employed as scanning screens for reading out standard TV signal (40 ms frames). Television scan standard can find use in practically any type of diagnostics, with the exception of computer tomography and coronography. The demand for wide dynamic range in computer tomography data logging requires the afterglow to be on the order of 1 μs while the investigation of heart blood supply dynamics - not greater than 1 ms. But for such application other dopants are to be introduced into Gd_2O_2S matrix [1÷4], which is what the authors intend to accomplish.

References

1. Y. Ito, H. Yamada, M. Yoshida, H. Fujii, G. Toda, Takeuchi, Y. Tsukuda, Hot Isostatic Pressed Gd_2O_2S: Pr, Ce, F Translucent Scintillator Ceramics for X-Ray Computed Tomography Detectors // Jpn. J. Appl. Phys. **V.27**, (1988) L1371
2. H. Yamada, A. Suzuki, Y. Uchida, M.Yoshida, H. Yamamoto , Scintillator Gd_2O_2S: Pr, Ce, F for X-Ray Computed Tomography // J. Electrochem. Soc. **V.136** (1989) 2713
3. W. Rossner, H. Bodinger, J. Leppert, B. Grabmaier ,The conversion of high energy radiation to visible light luminescent ceramics // IEEE Trans. Nucl. Sci. **Vol. 40** (1993) 376
4. G. Blasse, B. Grabmaier, Luminescent Materials // Berlin: Springer, 1994
5. E. Artukh, G. Ananieva, E. Gorokhova, T. Merkuliaeva, G. Novikova, O. Khristich, Crystal Lattice Parameters and Thermal Linear Expansion Coefficients of Doped Rare-Earth Oxysulfides Based Ceramics // OMP **Iss. 9 (**1992) 25
6. E. Gorokhova, L. Kinzhibalo, V. Kuprevich, T. Merkuliaeva, O. Khristich, Terbium Doped Yittrium Oxysulfide Based Luminescent Optical Ceramics // Rep. summ. of the VI All-Union Conference on Physics, Chemistry and Technology of Luminophors, Stavropol, VNIILuminophor, (1989) 104
7. G. Ananieva, E. Gorokhova, L. Kinzhibalo, V. Kuprevich, T. Merkuliaeva, O. Khristich, Terbium Doped Yittrium Oxysulfide Based Luminescent Optical Ceramics // Optical Journal, **V. 66** (1999) Iss. 5, 27
8. K. Matsuzaki, A. Inoue, T. Masumoto, Oriented structure in Dense Y, Ba_2Cu_3 oxides prepared by Press Forging // Jpn. J. Appl. Phys, **V.29 (**1990), N10, 1789
9. ICPDS- International Centre for Diffraction. Data USA, 1989
10. L. Sobon, K. Wickersheim, K. Buchanan and R. Alves, Growth and Properties of Lanthanum Oxysulfide Crystals, Journal of Applied Physics, **V.42 (**1971) 3049
11. Gmelin Handbook of Inorganic Chemistry. 8^{th} Edition. C 7 Sulfides, Oxide Sulfides, Alkali Thiometallafes. With 345 illustrations. System Number 39. Springer -Verlag Berlin- Heidelberg. New York. Tokyo, 1983
12. A. Gurvich, X-Ray Luminophors and X-Ray Screens. // M: Atomizdat, 1976
13. E. Gorokhova, V. Kuprevich, P. Vasiliev, Cathodeluminescent Composite Screen Based on Zincsulfide Luminescent Optical Ceramics. // Optical Journal, **Iss. 10** (1992) 59
14. T. Babkina, M. Gaiduk, N. Morozov, N. Soshin, Terbium Luminescence in Rare-Earth Oxysulfides. // (IRE of the Acad. of Sci. of the USSS Issue), (1978) 38
15. G. Mainprize, M. Yaffe. The effect of phosphor persistence on image quality in digital X-ray scanning systems. SPIE, **V.2708 (**1996) 85

New results on the scintillation properties of $RbGd_2Br_7$: Ce and comparison with three other well-known scintillators: NaI:Tl, CsI:Tl and Lu_2SiO_5:Ce

O. Guillot-Noël[1], J. C. van't Spijker[1], P. Dorenbos[1], C. W. E. van Eijk[1], K. W. Krämer[2] and H. U. Güdel[2]

[1]*Radiation Technology Group, Interfaculty Reactor Institute, Delft University of Technology, Mekelweg 15, 2629 JB Delft, The Netherlands*
[2]*Department of Chemistry and Biochemistry, University of Bern, Freiestrasse 3, 3000 Bern 9, Switzerland*

Abstract. In the present study, we investigated the scintillation properties of $RbGd_2Br_7$ crystals doped with Ce^{3+} concentrations of 0.11%, 2.05%, 4.1% and 9.8% under X-ray and γ-quantum excitation. The different measurements performed in this study are compared with the results obtained on the three following scintillators: NaI:Tl, CsI:Tl and Lu_2SiO_5:Ce.

Keywords: Scintillation crystals; γ-ray detection; Energy resolution; Time Resolution; nonproportionality; Rare-earth halides.

Introduction

The crystals of $RbGd_2Br_7$ with different Ce^{3+} concentration were grown by the Bridgman technique. $RbGd_2Br_7$ crystals are hygroscopic, therefore, they were sealed into small quartz ampoules with a ∅5x40 mm^3 size under nitrogen atmosphere.

X-ray induced emission spectra were recorded with an X-ray tube with a Cu anode operating at 35 kV and 25 mA, an EMI 9462 photomultiplier tube (PMT) and an ARC VM504 monochromator. Pulse height spectra were recorded with a Hamamatsu R1791 PMT. Light yields, expressed in photoelectrons per MeV (phe/MeV) were deduced from the measurements of the peak position of the photopeak compared with that of the single electron spectrum [1] and were converted into photons/MeV (ph/MeV) using the procedure described in [2]. The non-proportional responses were studied using different γ-ray sources to excite the compounds at energies between 1.332 MeV and 10 keV. Scintillation decay time spectra were recorded using the multi-hit method [3], employing XP2020Q PMTs as 'start' and 'stop' tubes and using γ-rays of a ^{137}Cs source. Time resolution experiments were carried out using a ^{22}Na source. The experiments are described in [4].

Results and discussion

The X-ray excited luminescence spectra of $RbGd_2Br_7$:Ce are shown in Fig. 1 together with those of NaI:Tl and Lu_2SiO_5:Ce crystals. The $RbGd_2Br_7$:Ce crystals show a Ce^{3+} 5d-4f emission band between 350 nm and 550 nm with a maximum peaking at 420 nm (Fig. 1), which is in the same wavelength range as the emission of NaI:Tl and Lu_2SiO_5:Ce. At very low concentration, 0.11% Ce, the broad emission band is composed of the two Ce^{3+} emissions but probably also of the self-trapped exciton (STE) luminescence peaking around 450 nm. For higher Ce^{3+} concentrations, the 5d-4f emissions are dominant and increase with the cerium concentration (Fig. 1). The narrow emission band seen around 313 nm (indicated by a star in Fig. 1) is due to the $4f^7$-$4f^7$ Gd^{3+} $^6P_{7/2} \rightarrow {}^8S_{7/2}$ transition.

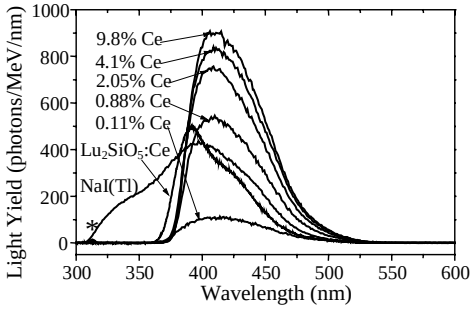

Fig. 1. X-ray induced emission spectra of $RbGd_2Br_7$ doped with 0.11%, 2.05%, 4.1% and 9.8% Ce^{3+}. The spectra of NaI:Tl and Lu_2SiO_5:Ce are also shown for comparison.

The decay time measurements in the first 2000 ns performed under γ-ray excitation on the $RbGd_2Br_7$:Ce crystals are gathered in Fig. 2 a) together with those of Lu_2SiO_5:Ce, NaI:Tl and CsI:Tl. The decay curves of $RbGd_2Br_7$:Ce are not single-exponential. The curves were fitted by assuming three exponential decay components. This assumption has no physical meaning but is used to characterize the decay curves. In Table 1, the three decay time components are presented as well as their contribution to the total light yield. The first component decreases from 101 ns to 43 ns when the cerium concentration increases from 0.11% to 9.8%. This short component represents the major contribution to the total light yield.

Table 1: Scintillation properties of some $RbGd_2Br_7$:Ce compounds under 662 keV γ-ray excitation: light yields, decay time components and energy resolution R. For the $RbGd_2Br_7$ compounds the R1791 PMTs, the detection efficiency is 0.240. The results are compared to those of NaI:Tl, CsI:Tl and Lu_2SiO_5:Ce.

Host	[Ce^{3+}] in %	Photon Yield in 10^3 ph/MeV (10 μs)	Decay time components Short(ns)/2nd(ns)/Long(μs) {% to the total light yield}			R %	Time Resolution FWHM in ps
$RbGd_2Br_7$	0.11	7.7±0.8	101±3 {45%}	510±50 {55%}	none {0%}	8.4	/
$RbGd_2Br_7$	2.05	47±5	57±2 {60%}	420±50 {36%}	~20 {4%}	4.1	/
$RbGd_2Br_7$	4.1	53±5	50±1 {60%}	440±30 {36%}	~25 {4%}	/	/
$RbGd_2Br_7$	9.8	56±6	43±1 {56%}	400±30 {40%}	~20 {4}	4.1	790±10
NaI:Tl		43 [5]	230 [8]	none	none	5.6 [10]	/
CsI:Tl		64 [6]	600 [9] {45%}	none {0%}	3.4 {55%}	4.34 [11]	/
Lu_2SiO_5	Ce	26 [7]	40 [7]	none	none	7.5 [12]	530±3

Another contribution, with a value around 450 ns, is also present for each concentration. For high concentrations, a long component appears with a value around 20-25 μs (Fig. 2 b)). For comparison, the decay spectra of Lu_2SiO_5:Ce, NaI:Tl and CsI:Tl are also presented Fig. 2 a). The Lu_2SiO_5:Ce spectrum is dominated by a very fast component of 40 ns. For NaI:Tl, the decay spectrum is dominated by a 230 ns decay component and for CsI:Tl, two components of 600 ns and 3.4 μs have been determined. Time resolution spectra were measured with $RbGd_2Br_7$:9.8% Ce, Lu_2SiO_5:Ce and BaF_2 crystals for an energy threshold set at E ≥ 511 keV. After correction for the contribution of the reference counter, we obtained a value (FWHM) of 790±10 ps, 530±3 ps and 300±4 ps for $RbGd_2Br_7$:9.8% Ce, Lu_2SiO_5:Ce and BaF_2, respectively (Table 1). For Lu_2SiO_5:Ce, a time resolution of 410 ps was reported in [15] using an XP2020Q PMT, a ^{60}Co source and an energy threshold at E > 100 keV. For NaI:Tl, 800 ps was reported in [16] with an XP2020 PMT, a ^{60}Co source and an energy threshold set at E > 100 keV. The $RbGd_2Br_7$:9.8% Ce compound has a good time resolution in the same range as that of NaI:Tl and 1.5 times worse than that of Lu_2SiO_5:Ce, which makes this compound suitable for fast timing applications.

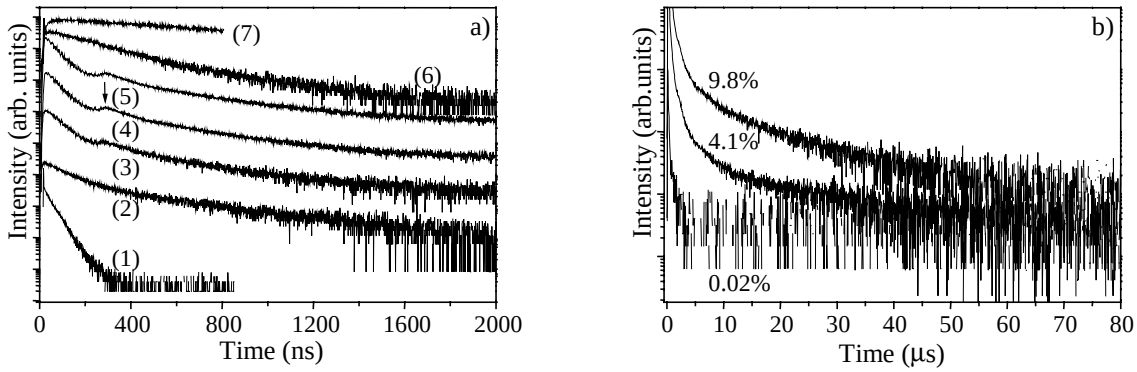

Fig. 2. a) Scintillation decay time spectra in the first 2000 ns of (1) Lu_2SiO_5:Ce, $RbGd_2Br_7$: (2) 0.11% Ce, (3) 2.05% Ce, (4) 4.1% Ce, (5) 9.8% Ce, (6) NaI:Tl from [13], and (7) CsI:Tl from [14]. The distortion near the arrow is caused by after pulses in the XP2020Q tube. b) Scintillation decay time spectra on a longer time scale for $RbGd_2Br_7$ with 0.02%, 4.1% and 9.8% Ce^{3+}.

Energy resolutions of 4.1% are reached for $RbGd_2Br_7$ with 2.05% and 9.8% Ce concentrations (Fig. 3), with a 7x4x2 mm^3 and 15x5x1 mm^3 size, respectively.

This energy resolution has never been achieved with any other scintillation detectors before. The 4.1% value is considerably better than the 5.6% and 7.5% of NaI:Tl and Lu_2SiO_5:Ce crystals (Table 1), respectively. The best energy resolution ever reported is 4.34% [11] for a CsI:Tl coupled to a silicon drift detector. A very good energy resolution of 4.38±0.11% has also been reported recently for YAP:Ce crystals [17].

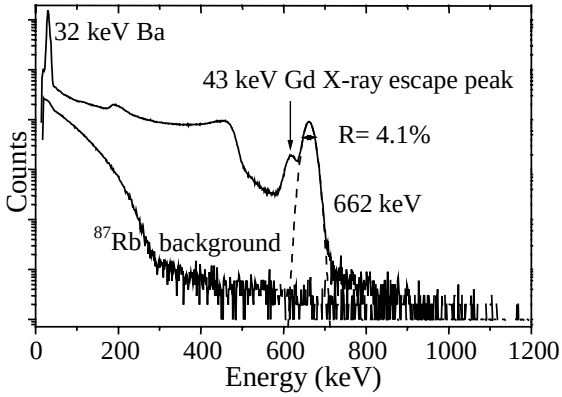

Fig.3. Pulse height spectra of $RbGd_2Br_7$:9.8% Ce recorded with γ-rays ^{137}Cs. The fit of the photopeak is indicated by dashed lines. The ^{87}Rb background is also shown

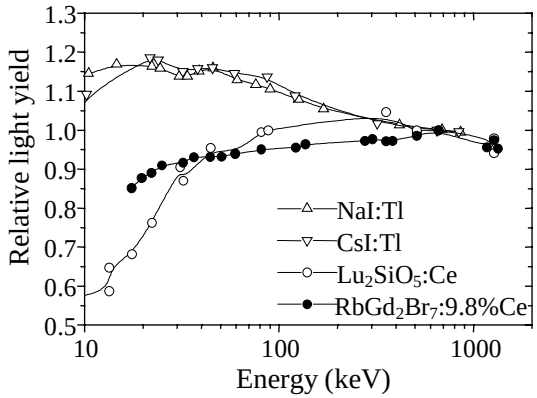

Fig.4. Response curve of $RbGd_2Br_7$ with 9.8% Ce^{3+}, Lu_2SiO_5:Ce from [18], NaI:Tl from [19] and CsI:Tl from [19].

Light yields (ph/MeV) are compiled in Table 1. $RbGd_2Br_7$:9.8% Ce shows the highest light yield of 56000±6000 ph/MeV. This number is higher than the 43000 ph/MeV of NaI:Tl [5]. Only CsI:Tl shows a higher light yield with 64000 ph/MeV, reported by Valentine et al. in [6]. Due to the presence of the radioactive isotope ^{87}Rb, scintillation pulses are generated intrinsically. The response curve of $RbGd_2Br_7$ with 9.8% Ce is shown Fig. 4 together with those of Lu_2SiO_5:Ce [18], NaI:Tl [19] and CsI:Tl [19]. The curves represent the relative light yield normalized to the light yield obtained at 662 keV with the ^{137}Cs source. The response of $RbGd_2Br_7$: 9.8% Ce is almost constant as function of excitation energy for γ-ray energies higher than 60 keV. The variation in the light yield is only 15 % in the range between 17.4 keV and 1.332 MeV. For Lu_2SiO_5:Ce, NaI:Tl and CsI:Tl, the variations are more pronounced in the same enrgy range with a nonproportionality of 40%, 20% and 20% respectively.

Conclusion

The study of the scintillator properties of $RbGd_2Br_7$ compounds doped with cerium ions, under X-ray and γ-quanta excitations, has shown very good results and this matrix presents a lot of advantages: a high photon yield of 56000±6000 ph/MeV, a main fast decay component of 43 ns, a good time resolution of 790 ps, a very good linearity in the energy response with only 15% variation in the range between 17.4 keV and 1.332 MeV and a very good energy resolution of 4.1%.

References

1. M. Bertolaccini, S. Cova, and C. Bussolatti, Proc. Nucl. Electr. Symp. Versailles, France, (1968)
2. L. H. Luthjens, P. Dorenbos, J. T. M. de Haas, A. Hummel, and C. W. E. van Eijk, Rad. Phys. and Chem. 55 (3) (1999) 255
3. W. W. Moses, Nucl. Instr. and Meth. A 336 (1993) 253
4. O. Guillot-Noel, J. C. van't Spijker, J. T. M. de Haas, P. Dorenbos, C. W. E. van Eijk, K. W. Krämer, and H. U. Güdel, IEEE Trans. Nucl. Sci, accepted (1999)
5. I. Holl, E. Lorenz and G. Mageras, IEEE Trans. Nucl. Sci. 35 (1988) 105
6. J. Valentine, D Wehe, G. Knoll, and C. Moss, IEEE Trans. Nucl. Sci. 40 (4, part 2) (1993) 1267
7. M. Moszyński, M. Kapusta, M. Mayhugh, D. Wolski, and S. O. Flyckt, IEEE Trans. Nucl. Sci. 44(3) (1997) 1052
8. D. R. Kinloch, W. Novak, P. Raby and I. Toepke, IEEE Trans. Nucl. Sci. 41 (1994) 752
9. P. Schotanus, R. Kamermans, and P. Dorenbos, IEEE Trans. Nucl. Sci. 37 (1990) 177
10. D.E. Persyk, T. E. Moi, IEEE Trans. Nucl. Sci. 25(1) (1978) 615
11. C. Fiorini, F. Perotti, Nucl. Instr. and Meth in Phys. Res. A 401 (1997) 104
12. C. L. Melcher, private communications, Sept. 1994
13. P. Dorenbos, J. C. van't Spijker, O. W. V. Frijns, C. W. E van Eijk, K. Krämer, H. U. Güdel, and A. Ellens, Nucl. Instrum. and Method in Phys. Res. B 132 (1997) 728
14. J. D. Valentine, W. W. Moses, S. E. Derenzo, D. K. Wehe, and G. F. Knoll, Nucl. Instrum. Method in Phys. Res. A 325 (1993) 147
15. T. Ludziejewski, K. Moszyńska, M. Moszyński, D. Wolski , W. Klamra, L. O. Norlin, E. Devitsin and V. Kozlov, 1994 IEEE Nucl. Sci. Symp. and Imag. Conf. , Norfolk, Virginia, USA 1, (1995) 299
16. M. Moszyński, C. Gresset, J. Vacher and R. Odru, Nucl. Inst. and Meth. 188 (1981) 403
17. M. Kapusta, M. Balcerzyk, M. Moszyński and J. Pawelke, Nucl. Instr. and Meth in Phys. Res. A 421(1999) 610
18. P. Dorenbos, J. T. M. de Haas, and C. W. E. van Eijk, IEEE Trans. Nucl. Sci. 42(6) (1995) 1
19. D. W. Aitken, B. L. Beron, G. Yenicay, and H. R. Zulliger, IEEE Trans. Nucl. Sci. NS-14 (1967) 468

Synthesis and scintillation properties of some dense X-ray phosphors

[1]Dujardin C., [1]Garcia-Murillo A., [1]Pedrini C., [1]Madej C.,
[1]Goutaudier C., [2]Koch A., [3]Petrosyan A.G., [3]K.L.Ovanesyan, [3]G.O.Shirinyan,[4]Weber M.J.

[1]Laboratoire de Physico-Chimie des Matériaux Luminescents, Unité Mixte de Recherche 5620 CNRS- Université Lyon1, 69622 Villeurbanne,France
[2]European Synchrotron Radiation Facility, BP 220, F-38043 Grenoble.
[3]Institute for Physical Research, Armenian National Academy of Science, 378410 Ashtarak-2, Armenia
[4]Lawrence Berkeley National Laboratory, Berkeley, CA 94720 USA

Abstract. Many ultra-dense lutetium or gadolinium based compounds doped with Eu^{3+} have been prepared. This paper reports on the major scintillation performances of these compounds. One of them (Lu_2O_3:Eu) is particularly promising and have been deposited on a screen. Performances of such a screen are presented.

Keywords: X-ray phosphors, Lu_2O_3:Eu

Introduction

X-ray phosphors have been developed since W.C.Roentgen discovered x-rays. Many systems are actually known and used in different devices for x-ray imaging systems. Nevertheless, detection technologies are improving their performance, and better x-ray converters would benefit image quality. For example, most of the x-ray phosphors have been developed for film radiography which are mainly green-blue sensitive. Actually, CCD camera as well as MOS technology which have good efficiency in the red range allow to obtain fast results without chemical processing. Requirements for such scintillation polycrystalline powders are:

-high effective atomic number (Z_{eff}) to obtain good stopping power of incident radiation

-good scintillation light yield

-afterglow must be avoided

-emission wavelength should match the maximum efficiency of the photodetector.

The most commonly used material for x-ray imaging systems is $Gd_2O_2S:Tb^{3+}$ (GOS). Its density is 7.34g/cm^3 (Z_{eff}=61.1) and its light yield is around 78000 photons/Mev depending on the granularity and preparation conditions. The major emission line is peaking at 547 nm (well-known $(4f^8)^5D_4 \rightarrow (4f^8)^7F_5$ green emission of Tb^{3+}). Most of the optical scintillation properties of this material are described in [1]. The time-constant of this emission line is in the ms range with low afterglow (0.1% if the initial signal within the 20ms after the x-ray beam obturation). For imaging with high spatial resolution thin powder phosphor layers are required because the spatial resolution is proportional to the thickness of the phosphor layer. If such a screen is used at high x-ray energies, the absorption and hence the image quality may be significantly reduced as a result of its thickness. Phosphors of higher density and higher effective atomic number than GOS improve the detector performance, under certain conditions even if the light yield is smaller. The purpose of this work was to find a polycrystalline materials having a better stopping power than GOS, and having other properties as good as GOS.

For the above applications research on very dense host materials doped essentially with Eu^{3+} (well-known very efficient luminescence) have been investigated. Synthesis, spectroscopic and scintillation properties of Lu_2O_3 , $LuTaO_4$, Lu_3TaO_7, $GdTaO_4$, Gd_3TaO_7 and $LiLu(WO_4)_2$ are presented.

Material preparation and experimental set-up

Europium-doped tantalates (Gd_3TaO_7, $GdTaO_4$, Lu_3TaO_7, $LuTaO_4$), oxides (Lu_2O_3, Gd_2O_3) and $LiLu(WO_4)_2$ tungstate were prepared by the solid state reaction technique. The mechanical mixed 3N to 4N purity oxide (except lithium carbonate) components were pressed into discs and fired in air with grinding and pressing procedures repeated at each successively higher temperatures. Tantalate compounds were also prepared by melting the mixed component oxides in Mo crucible under a reducing atmosphere with subsequent annealing in air. The germanate was prepared in sealed ampoules. The resulted materials were colorless and single phase. The lattice unit cell parameters measured by x-ray diffraction were close to those reported in [2,3].

Light yield have been measured by comparison with the light obtain with GOS from Riedel de Haen (RGS-N-Green). The x-ray source was operated at 15 kV, with Cu anode (the x-rays were mainly of 8 keV energy). The beam was collimated to 1 mm x 1.5 mm and illuminated the powder at 45° angle. The x-rays were mainly an energy of 8 keV. The powder has been deposited on aluminium plate; the thickness of the layer is 500 μm. With such a configuration, all the x-rays are absorbed. The signal was detected with a Si-photodiode perpendicular to the powder screen. The spectral response of the detector is 0.3 A/W at 550 nm and 0.35 A/W at 650nm.

	Zeff	ρ (g/cm^3)	$Z_{eff}^4.\rho$ (rel)	Structure	Space group	emission (nm)
Gd_2O_2S	61.1	7.34	1	hexagonal		547
Gd_2O_3	61.8	7.62/ 8.33	1.09/ 1.22	cubic/ monoclinic	Ia3 C2/m	611.2 614.9/623.2
Gd_3TaO_7	64.3	8.42	1.44	rhombic	D_2^5	612/615
Lu_2GeO_5	65	7.53	1.31	monoclinic	C_{2h}^6	611
$GdTaO_4$	66.3	8.83	1.7	monoclinic	P2/a	612.3/615.4
Lu_2O_3	68.8	9.42	2.11	cubic	Ia3	611.1
Lu_3TaO_7	68.9	9.49	2.09	cubic	O_h^5	612.3/615.4
$LiLu(WO_4)_2$	69.1	7.92	1.81	monoclinic	P2/n	609/broad 480
$LuTaO_4$	69.1	9.76	2.22	Monoclinic	P2/a	611.9

Table 1: Properties of the host materials and Eu^{3+} doped materials

Results

Neglecting the absorption edge, the x-ray absorption efficiency η_{abs} depends upon the effective number (Z_{eff}) and the density of the material such that: $\eta_{abs} \alpha Z_{eff}^4.\rho/E_x^3$ [4] (E_x is the x-ray energy). $Z_{eff}^4.\rho$ is reported in Table 1 relatively to GOS for comparison. Emission spectrum was recorded under 253nm excitation (charge transfer states of Eu^{3+}) . As expected, red emission lines due to the $^5D_0 \rightarrow {}^7F_J$ transitions of Eu^{3+} are observed. Major lines are listed in table 1. Spectroscopic behavior of $LuTaO_4$:Eu^{3+} have been studied by Blasse et al. [5]. For Lu_2O_3 and Gd_2O_3 doped with Eu^{3+} ref [6] and [7] give the main spectroscopic properties. The tungstate materials exhibit in addition to the Eu^{3+} lines a very broad band peaking at 480nm which is attributed to the $(WO_4)^{2-}$. The undoped materials give rise to the broad band alone.

Sample	LY
LiLu(WO4)2:5-10%Eu	2
Lu3TaO7:5%Eu	4
Lu2GeO5:5%Eu	6
Gd3TaO7:5%Eu	7
Lu2O3:25%Eu	9
LuTaO4:5%Eu	10
Gd2O3:0.1%Eu	10
Gd2O3:10%Eu	10
Lu2O3:0.05%Eu	11
Gd2O3:20%Eu	13
GdTaO4:1%Eu	14
GdTaO4:15%Eu	16
GdTaO4:3%Eu	16
Gd2O3:15%Eu	18
Gd2O3:0.5%Eu	19
Gd2O3:7%Eu	19
Gd2O3:3%Eu	20
Gd2O3:5%Eu	20
GdTaO4:10%Eu	22
GdTaO4:5%Eu	22
GdTaO4:1%Eu	22
GdTaO4:10%Eu	23
Lu2O3:0.25%Eu	24
Lu2O3:10%Eu	28
Lu2O3:0.5%Eu	33
Lu2O3:1.5%Eu	38
Lu2O3:2.5%Eu	46
Lu2O3:5%Eu	47
Gd2O2S:Tb (RGS-N)	100

Table 2: list of the mono-doped samples and their relative light output

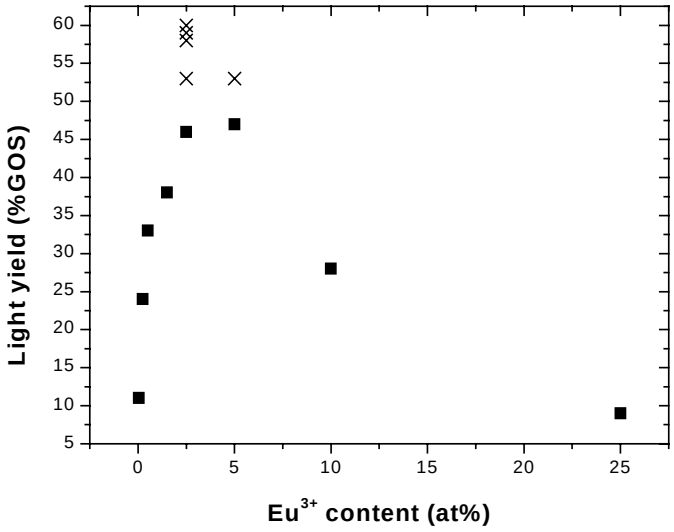

Figure 1: Light yield of Lu_2O_3 relative to GOS versus Eu^{3+} concentration. Squares indicate the single-doped materials, and crosses are Tb^{3+} co-doped compounds. The co-doping level is between 0.005 at. % and 0.1 at. %

The relative light yield was measured for many samples and listed in Table 2. The samples are sorted using the relative light yield value. For $GdTaO_4$, Gd_2O_3 (monoclinic) and Lu_2O_3, several concentrations have been tested. For Lu_2O_3, the variation of light yield versus the Eu^{3+} content (atomic %) is plotted in Figure 1. The two best single-doped samples are 2.5% and 5%. Extremely weak co-doping with Tb^{3+} (between 0.005 at. % and 0.1 at. %) improves the light yield significantly as shown in Figure 1 (crosses). The origin of this effect is under study using VUV synchrotron radiation. Since divalent europium and tetravalent terbium are also stable energy transfer from host materials to both ions may develop in different ways and then Tb^{3+} may capture remaining excitations and transfer its excitations to Eu^{3+} or give rise to the green luminescence. However, no green luminescence have been detected (Figure 2).

Screen test

Lu_2O_3:Eu,Tb already looks very promising although no optimization of the granularity or preparation conditions have been performed yet. Screens have been sedimented on 1 mm thick glass plates using this Lu_2O_3:Eu,Tb phosphor and the commercial Gd_2O_2S:Tb (RDS-N), 24 mg/cm^2 and 30 mg/cm^2 respectively. This deposition gave equal layer thickness of 50 µm and hence similar spatial resolution properties are expected. The screens have been characterized using an x-ray generator source with a Mo anode and 100-µm Zr filter operated at 30 kV, thus providing x-ray emission mainly at 18 keV. The spectral response is shown in Figure 2. The linespread function was measured to be 35 µm fwhm, in both cases. The non-uniformity is 14% rms for the Lu_2O_3 screen that is a factor of 2 higher than for the GOS screen when scanned with microscope optics of 1.2 µm pixel size at the screen. This non-uniformity is a result of the granularity. A larger pixel size would average and reduce these spatial variations.

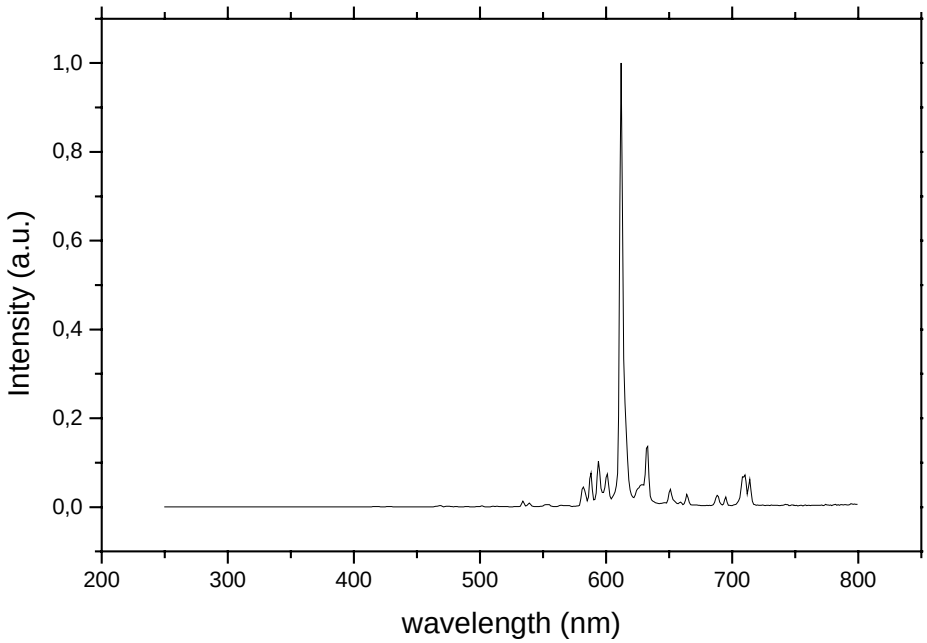

Figure 2: emission spectrum of Lu_2O_3:2.5%Eu^{3+}-0.005%Tb^{3+} under x-ray excitation. High voltage is 15kV, Cu-anode, 25µmCu, 50µm Al

The afterglow has also been studied at exposure levels of 10^6 ph/s/mm^2 (Fig. 3). The initial decay is slower than for GOS. After 1 s, a dynamic range of 10^3 is possible. For even higher dynamic range, GOS is limited by afterglow; Lu_2O_3:Eu decays further. The decay curves additionally depend on the exposure time. A reduction of the afterglow may be achieved with different co-doping without reducing the light yield. Radiation damage has been observed at high doses: 1% reduction in the signal response after an absorbed dose of 30 Gy for Lu_2O_3:Eu and 100 Gy for Gd_2O_2S:Tb. The material recovers partially at room. The red emission is better adapted to the spectral response of front side illuminated CCD's than the green emission of GOS. Even though the conversion efficiency is lower than for GOS, a typical front side illuminated CCD does register similar signal amplitude for the same number of absorbed

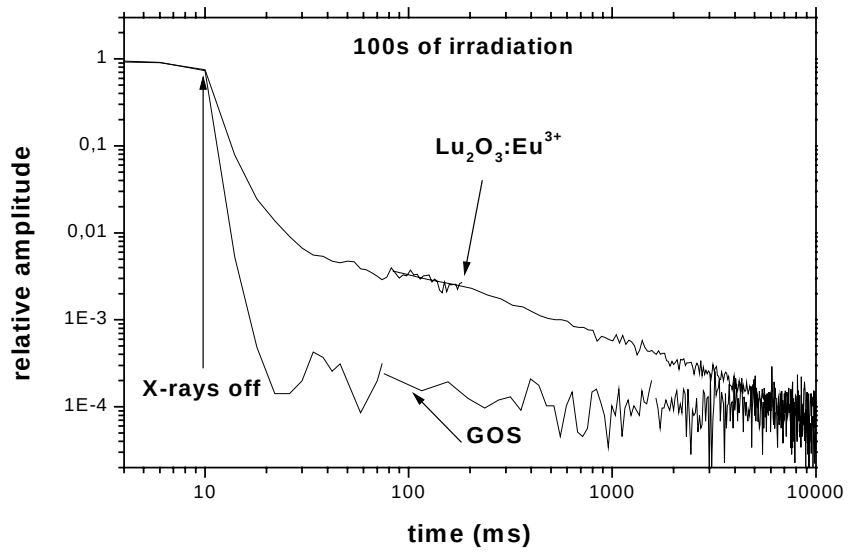

Figure 3 Afterglow measurement on GOS and Lu_2O_3:2.5%Eu^{3+}-0.005%Tb^{3+} under X-ray excitation

x-ray photons. The advantage compared to GOS is that the absorption of such a 50 µm thick screens is higher by 30% at 18 keV and 70% at 30 keV. In particular cases for which the x-ray shot noise dominates the detector performance, only the number of absorbed x-ray photons determines the signal-to-noise ratio and not the signal conversion efficiency of x-rays into an electronic signal.

Conclusion

Many very dense phosphors doped with Eu^{3+} ions have been synthetised and studied. Of these, Lu_2O_3:Eu gives the best light yield. Additional co-doping with Tb improves significantly the light yield. The material and screen properties of Lu_2O_3:Eu are sufficiently advanced so that a higher signal-to-noise ratio in X-ray imaging under typical medical imaging conditions can be achieved compared to Gd_2O_2S:Tb. Hence, lower doses to patients are expected with Lu_2O_3:Eu screens. Comparative tests on detectors in a routine working environment are planned.

References

1. L.H.Brixner, Material Chemistry and Physics, **16** (1987) 253-281
2. V.P. Sirotkin, A.A. Evdokimov, V.K. Trunov, J.Inorganic Chemestry (SSSR) 27 (1982) 1648
3. V.K.Trunov, L.N. Kinzhibalo, B.A. Efremov, V.G. Krongaus, Doklady AN SSSR 260 (1981) 103
4. M.Ishii and M.Kobayashi, Prog. Crystal Growth and Charac. 23, 245-311 (1991)
5. G.Blasse, G.J.Dirkden, L.H.Brixner and M.K.Crawford, Journal of Alloys and Compounds, 209 (1994) 1-6
6. A.Brill and W.L.Wanmaker, Journal of the Electrochemical Society,December 1964, Vol.11, No.12,1363-1368
7. G.Chen, R.G.Haire and J.R.Peterson, Applied Spectroscopy, Volume 46, Number 2,1992, 273-276

Scintillators with high Z_{eff} on the base of $Lu_3Al_5O_{12}$:Ce single crystalline films: growth, properties and applications

[1]Yu. Zorenko, [1]V. Gorbenko, [1]I. Konstankevych, [2]M. Batentschuk

[1]Institute of Applied Physics Lviv State University, 49 General Chuprynka Str., Lviv, 290044, Ukraine; [2]Institute for Material Science, Electronic Materials, University of Erlangen, Martensstrasse, 7, D-91058 Erlangen, Germany

Abstract. The paper examines the possibility of obtaining the scintillators with high Z_{eff} on the basis of $Lu_3Al_5O_{12}$:Ce single crystalline films (SCF) (Z_{eff} =59, ρ= 6.67 g/cm^3) doped with La^{3+}, Sc^{3+} and Y^{3+} ions for matching lattice parameters of SCF and $Y_3Al_5O_{12}$ (YAG) substrate. Peculiarities of growth of SCF by liquid phase epitaxy (LPE) and the role of La^{3+}, Sc^{3+} and antisite Lu^{3+}_{Al} defects in the processes of formation of the emission centers and in the dissipation processes of excitation energy are analyzed. Conversion efficiency of $(LaLuY)_3Al_5O_{12}$:Ce SCF is shown to be not lower than that of $Y_3Al_5O_{12}$:Ce what makes it possible to use them as screen of X-ray images with the spatial resolution of 0.75-1.0 μm. The possibility of "engineering" of emission spectra of the SCF, which overlapped with the spectral sensitivity of CCD X-ray detectors, is demonstrated. This can be reached via sensitizing of Ce^{3+} emission in $Y_3Al_5O_{12}$ SCF by Gd^{3+}, Tb^{3+} and Eu^{3+} ions.

Keywords: x-ray detector, single crystalline film, epitaxy, impurities, sensibilization.

Introduction

Sources of synchrotron radiation allow to visualize X-ray images of micron and submicron sizes when one uses scintillator screens in the form of single crystalline films (SCF) deposited by means of liquid phase epitaxy (LPE) on the surface of non-luminescent substrates. An example of the X-ray image detector with resolution R=1.3-1.5 μm with the screen on the basis of $Y_3Al_5O_{12}$:Ce -SCF of thickness h=5 μm has been described in [1]. The further increase of R can be achieved only by reducing SCF thickness that, in turn, requires obtaining the screens with maximum possible absorption coefficient of X-rays $\eta_{abs} \sim \rho Z_{eff}^4$, where Z_{eff} is the effective atomic number of SCF, and the conversion efficiency η not less than 2-5%.

Among the known garnet compounds the largest values of Z_{eff} =58.9 and ρ=6.67 g/cm^3 are characteristic to the $Lu_3Al_5O_{12}$:Ce garnet which refers to the number of efficient high response scintillators (λ_{max}=510 nm and τ=46 ns) with η=2.6 % [2]. This paper is dedicated to analysis of a possibility of producing the X-ray screens based on the $Lu_3Al_5O_{12}$:Ce SCF grown by LPE on $Y_3Al_5O_{12}$ substrates with relatively low prices, as well as to investigation of peculiarities of their optical, luminescent and scintillation characteristics.

Peculiarities of SCF manufacturing

We have studied the processes of obtaining the $Lu_3Al_5O_{12}$ based SCF on the $Y_3Al_5O_{12}$ substrates by doping the former by the La^{3+} and Sc^{3+} isoelectronic impurities (II) for reducing the mismatch between the SCF and substrate lattice parameters Δa≈0.093Å (compositions A and B in table 1, respectively). The La^{3+}ions are located exclusively in dodecahedral (*c*)-positions of the garnet lattice, whereas the Sc^{3+} ions at concentration x<0.3 per formula unit occupy (*c)*- and octahedral (*a*)-positions in 2:3 ratio, respectively [3]. At higher scandium concentrations predominantly Al^{3+}octahedral sites are replaced according to the nearly linear law [4].

The SCF of $Lu_3Al_5O_{12}$ were grown from the melt solution (MS) based on the $PbO:B_2O_3$ (10-12:1 mol/mol) fluxing agent and the Lu_2O_3 and Al_2O_3 oxides taken in 1:4 mol/mol ratio.

The $Y_3Al_5O_{12}$ wafer of (100) or (111) orientation with the diameter of 15-36 mm and the thickness ~0.7 mm were used as substrates.

Table 1. Content of crystal forming components (in mol. %) in MS for obtaining of SCF based on $(LuYLa)_3Al_5O_{12}$ (composition A) and $(LuSc)_3(AlSc)_5O_{12}$ (composition B).

	Composition A, mol. %					Composition , mol. %			
	Lu_2O_3	Y_2O_3	La_2O_3	Al_2O_3	CeO_2	Lu_2O_3	Sc_2O_3	Al_2O_3	CeO_2
1	18.42	0.63	8.23	72.72	-	19.02	6.74	74.21	-
2	18.27	0.90	8.17	72.66	-	18.39	9.80	71.81	-
3	17.78	0.88	7.95	70.69	2.70	17.81	9.49	69.50	3.16
4	17.19	0.85	7.68	68.33	5.95	16.95	9.03	66.14	7.85
5	16.63	0.83	7.43	66.14	8.97	15.99	8.52	62.38	13.09
6	16.22	0.80	7.25	64.49	11.24				

The $Lu_3Al_5O_{12}$ layers deposited on the $Y_3Al_5O_{12}$ substrates contain the Y impurities as a result of etching of the substrates during the initial stage of the epitaxial growth, and the concentration of these ions increases with the number of samples obtained. Due to this fact, for the effect connected with doping by Y^{3+} ions to be enhanced we have obtained series of the $Lu_3Al_5O_{12}$ SCF with La_2O_3/Y_2O_3 ratio equal to 13:1 and 9:1 mol/mol (compositions A1 and A2 in table 1). For each of the indicated in table 1 composition series of the SCF was obtained at various growth temperatures T_g in the 885-1040 ^{0}C range. The growth rate was 0.6-2.4 μm/min and the velocity of substrate rotation was ~80 rev./min.

The X-ray microanalysis of the composition of a number of SCF from the series A and B has been carried out for estimation of the segregation coefficients of different ions in the SCF on the basis of $Lu_3Al_5O_{12}$. For example, sample A6 had the com-position close to $Lu_{3.6}Y_{0.18}La_{0.035}Ce_{0.04}Al_{4.42}O_{12}$. This points to the possibility of localization of the significant part of the Lu^{3+} ions in the octahedral sites of the Al^{3+} ions what is, in particular, characteristic to the $Lu_3Al_5O_{12}$ crystal obtained from MS [5]. Obviously, this is promoted by SCF doped with Ce^{3+} and La^{3+} ions with much greater ionic radii than that of Lu^{3+}.

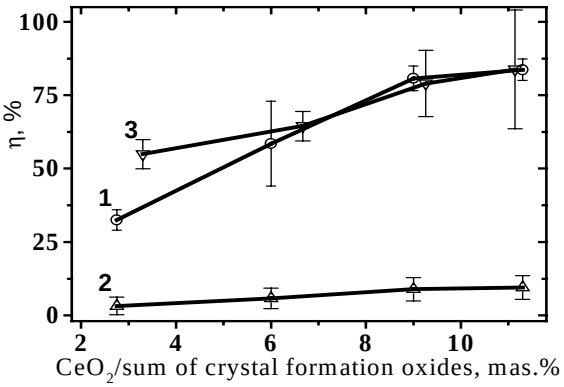

Fig. 1. Dependence of light output in $(LuYLa)_3Al_5O_{12}$:Ce (1), $(LuSc)_3(AlSc)_5O_{12}$:Ce (2) and $Y_3Al_5O_{12}$ (3) SCF series on relative concentration of activated impurity *CeO_2/sum of crystal formation oxides* in MS.

Fig.1 shows the dependencies of the light output η[1] in the SCF series of $(LaLuY)_3Al_5O_{12}$:Ce (curve 1) and $(LuSc)_3(AlS_C)_5O_{12}$:Ce (curve 2) compositions on the concentration of the CeO_2 impurity in MS as compared to the data for $Y_3Al_5O_{12}$:Ce [5]. The light output of the SCF of composition A (η_A) is observed as the activator concentration output increases under rising the activator concentration up to optimum

[1]The scintillation parameters of SCF have been measured during the excitation by α-particles of the ^{239}Pu in the scintillation unit on the basis of FEU-110 with reference to the standard scintillator of the $Y_3Al_5O_{12}$:Ce SCF with of the light output 10700 ph./MeV on the ^{137}Cs.

value ~9 mol.%, and the η_A approaches the value 0.85-0.87 of for the best samples of $Y_3Al_5O_{12}$:Ce composition. The dispersion of the η magnitudes in each SCF series is caused by differences in the ratio of the Ce^{3+} activator and quenching Pb^{2+} impurity concentrations in the given range of T_g.

An extraordinary feature of the $(LuSc)_3(AlSc)_5O_{12}$:Ce (B composition) is the appreciably lower value of the light output that amounts to not greater than 6.5 % of the optimum η in the range of optimum CeO_2 concentration in MS ~ 9 mol. % for the $Y_3Al_5O_{12}$ SCF (curve 2 in Fig 1). It should be noted that the analogous effect of Ce^{3+} luminescence quenching has been recently observed in $Lu_3Al_5O_{12}$:Ce [3] and $Y_3Al_5O_{12}$:Ce [7,8] doped with another II namely Ga^{3+}.

The optical and luminescent properties of the SCF

Absorption of the SCF of the studied compositions is caused by the $^1S_0$ $^3P_1$ transitions in the Pb^{2+} ions [4,9], whose doping presents the permanent factor in the SCF synthesis from the Pb-containing MS, as well as by the allowed electric dipole transitions with the E_n^1 and E_n^2 energies from the $^2F_{7/2}$ ground state of 4*f*-shell to the levels of the lower doublet of 5*d* shell of the Ce^{3+} ion [8] (Table 2). Varying the crystal field strength, which is proportional to the magnitude of $\Delta E_a=E_a^1-E_a^2$, results in the shift of the given bands of compositions A and B with respect to the similar bands for $Y_3Al_5O_{12}$:Ce^{3+} (table 2).

Table 2.The parameters of absorption and luminescence spectra of $(LuYLa)_3Al_5O_{12}$:Ce (A content), $(LuSc)_3(AlSc)_5O_{12}$:Ce (B content) and $Y_3Al_5O_{12}$:Ce SCF grown from Pb- containing MS

SCF content		Location of the absorption maxima, eV				Location of the emission maxima, eV			
		Ce^{3+}			Pb^{2+}	Ce^{3+}			Pb^{2+}
		$^2F_{7/2}\rightarrow 5d$ ($E_п^1$, $E_п^2$)		$\Delta E_п$	$^1S_0\rightarrow{}^3P_1$	$5d\rightarrow{}^2F_{7/2,5/2}$($E_л^1$, $E_л^2$)		$\Delta E_л$	yB(1,2)$\rightarrow{}^1A$
$Y_3Al_5O_{12}$:Ce		3.62	2.69	0.93	4.71	2.36	2.14	0.22	3.54 2.00
A	$(LuYLa)_3Al_5O_{12}$:Ce	3.60	2.75	0.85	4.74	2.435	2.265	0.17	3.73 2.07
B	$(LuSc)_3(AlSc)_5O_{12}$:Ce	3.54	2.80	0.74	4.805	2.46	2.29	0.17	3.055 2.17

The cathodoluminescent (CL) spectra of the SCF of compositions A and B are plotted in Fig. 2 and Fig. 3 respectively. As shown in Fig. 2a, the emission spectrum of the $Lu_3Al_5O_{12}$ SCF doped with La^{3+} and Y^{3+} (Fig. 2a, curves 1-2) in the UV spectral region consists of the superposition of the two bands with λ_{max}=267 nm (4.63 eV) and 284 nm (4.37 eV). At increase of Y concentration the intensity goes down without remarkably change in the ratio of the intensities of individual bands (curve 3). The above mentioned features of luminescence of the SCF of composition A may be explained by the formation the centers of radiative recombination in the bands with $h\nu_{max}$=4.63 and 4.67 eV as a product of the localization of the La^{3+} and Lu^{3+} II in the sites of the Lu^{3+} and Al^{3+} ions, respectively. The $La^{3+}{}_{Lu}$ ion similarly to $La^{3+}{}_{Y}$ in $Y_3Al_5O_{12}$:La [10] forms the split deep level. The latter acts as the localization centers for electrons and are formed due to large difference in non-Coulomb potential of the II which is proportional to the difference of the ionic radii $\Delta=R_{La}-R_{Lu}$=+0.195 Å. Recombination of the localized electrons with the free holes is the cause of luminescence band with $h\nu_{max}$=4.63 eV.

The anti-site $Lu^{3+}{}_{Al}$ defect (Lu in the octa-sites of Al^{3+}), which is inherent to structure of garnets obtained from MS, represents the analogy to the II and forms split level for localization ($\Delta=R_{Al}-R_{Lu}$=-0.33 Å [10]) of holes whose recombination whith free electrons is accompanied with luminescence in the 4.67 eV band. In the meantime, the concentration of such centers in SCF on the basis of $Lu_3Al_5O_{12}$ obtained from MS should be minimal [10,11]. The

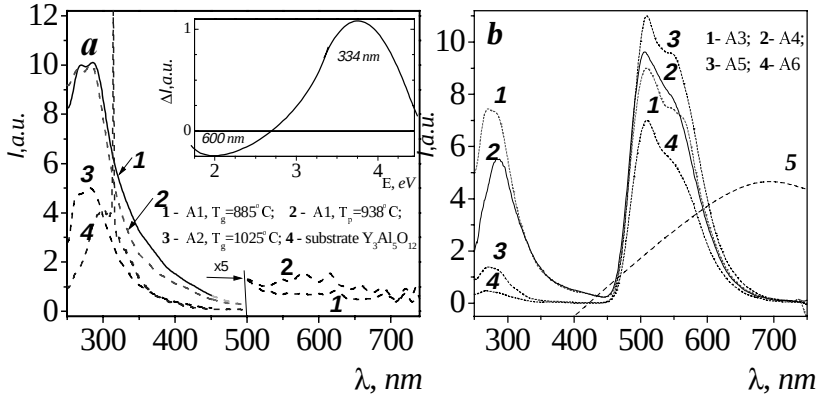

Fig. 2. CL spectra of $(LuYLa)_3Al_5O_{12}$ SCF (compositions A1, A2) (a) and $(LuYLa)_3Al_5O_{12}$:Ce (compositions A3-A6) (b). Spectrum of $Y_3Al_5O_{12}$ substrate (a, 4) and dependence of spectral sensitivity of CCD array of X-ray detector [1] are given for comparison. Insert - difference spectrum of SCF of Al composition obtained at T_g =885°C (1) and 938°C (2) which corresponds to Pb^{2+} ions emission.

intensity of the 4.37 eV band which is comparable with the emission of the $La^{3+}{}_{Lu}$ center can be explained only by significant increase of the $Lu^{3+}{}_{Al}$ center concentration because of the known "replacement" effect of ions with smaller ionic radius (Lu^{3+}) in octa-sites of garnet lattice [5] by ions with larger ionic radius (La^{3+}) with taking into acount the fact that Y^{3+} ions do not form split levels during substitution by Lu^{3+} as a result of small magnitude of R_{Lu}-R_Y=-0.04 Å [10].

The CL spectrum of the SCF (composition B) represents the superposition of the two bands with λ_{max}=290 nm (4.26 eV) and 324 nm (3.82 eV) (fig. 3, a, curves 1-3), with the ratio of their intensities being a function of the Sc concentration. For composition of Sc_2O_3 in MS equal to 7 mol.% (composition B1) the dominant is the 4.26 eV band, whereas at increasing the Sc_2O_3 concentration to 10 mol.% the main luminescence maximum shifts to the long wavelength range at the expense of the more intensive 3.83 eV component (Fig. 3,a, insert). The above mentioned behavior of the emission spectra in the SCF of composition B with growing Sc concentration is consistent mainly with the data for the $Y_3Al_5O_{12}$:Sc SCF [12]. This enables to interpret the bands with $h\nu_{max}$=4.26 and 3.82 eV as a recombination luminescence of the $Sc^{3+}{}_{Lu}$ and $Sc^{3+}{}_{Al}$ centers under substitution of the host Lu^{3+} and Al^{3+} ions by Sc respectively in the dodecahedral and octahedral positions of the garnet lattice.

Analysis of the differences in the emission spectra of the SCF of the A and B composition prepared at various T_g, that corresponds to the different concentration of the Pb impurities, allows to extract (Fig. 2, a and Fig. 3, a, inserts) the characteristic for the emission of mercury-like Pb^{2+} ions in garnets [4, 9], the doublet structure of the emission bands, as well as the location of their maxima (table 2). In the CL spectra of the SCF of composition A and B (Fig.2, b and Fig. 3, b) one can see the doublet emission band in the 450-700 nm region connected with the allowed $5d \rightarrow 4f(^2F_{5/2,7/2})$ transitions of the Ce^{3+} ions. Increase in the crystal field strength proportional to the difference of these transitions energy $\Delta E=E^1{}_e(^2F_{5/2})-E^2{}_e(^2F_{7/2})$ for the garnets of compositions A and B in comparison with $Y_3Al_5O_{12}$:Ce leads to the shift of Ce^{3+} emission bands at the short wave length range (table 2) and to the change in the SCF emission color.

Increasing activator concentration leads to the enhancement of the relative contribution of the Ce^{3+}ions emission in the SCF light output at corresponding reduction of UV luminescence intensity of the centers formed by II (Fig. 2, b and Fig. 3, b). This, to large extent, is characteristic to the SCF of composition A for which the luminescence is practically quenched in region of the

optimum CeO_2 concentration (>9 mol.%). For the SCF of composition B at the optimum CeO_2 concentration the intensity of the emission bands in the visible and UV regions are comparable that shows a strong competition between the Sc^{3+}_{Lu}, Sc^{3+}_{Al} and Ce^{3+} ions at intercepting the excitation energy and, obviously, is one of the causes of the low light output of luminescence.

Meanwhile, in our opinion, the main cause for the significant decrease of the $(LuSc)_3(AlSc)_5O_{12}$:Ce SCF light output is the presence of an effective channel of energy dissipation which is connected with the transitions between the allowed band extrema and activator levels.

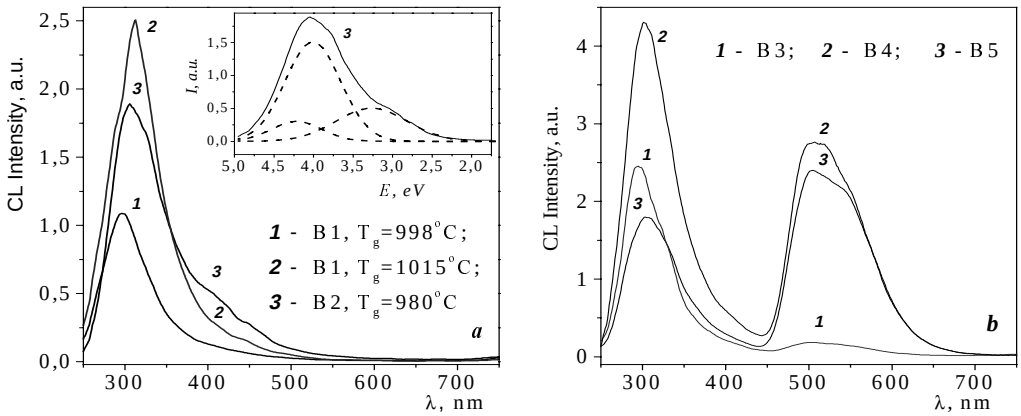

Fig. 3. CL spectra of $(LuSc)_3(AlSc)_5O_{12}$ (B1 and B2 contents) (a) and $(LuSc)_3(AlSc)_5O_{12}$:Ce (B3-B5 contents) (b)

Such a mechanism of quenching of luminescence of rare-earth ions with 4*f*-5*d* transitions we have earlier considered in $Y_3Al_{5-x}Ga_xO_{12}$:Ce;Pr [12, 13]. Apparently, as in the case of substitution by Ga, the consequence of large (~1.3 f. u.) degree of the substitution by Sc in the SCF of composition B lies in the narrowing of the garnet energy gap what results in increase of probability of non-radiative transitions between Ce^{3+} ion levels and band structure levels.

Appication of the scf based on $Lu_3Al_5O_{12}$

The emission spectrum of the $(LuLaY)_3Al_5O_{12}$:Ce (Fig. 2, b) overlaps considerably with the region of spectral sensitivity of Charge Coupled Devices (CCD) cameras used as radiation detectors [1] (Fig.2, curve5). The light output of the SCF of this composition while registering the radiation with a photodiode with spectral sensitivity close to sensitivity region of front-illuminated CCD [1] exceeds the $Y_3Al_5O_{12}:Ce^{3+}$ SCF light output by factor of 1.35-1.4. Estimated conversion efficiency value of ~7%, we have obtained for the SCF of this composition with ρ =6.6 g/cm^3, Z_{eff}=58 and in the range of CeO optimum concentration, shows increase of X-ray absorption coefficient by a factor of ~7 and 2.5 for the 5-17 and 18-60 keV energies, respectively for screens made on the basis of these SCF. This allows, according to the calculation following the procedure described in [1], to reach the resolution capability of X-ray detector not less than 0.75-1.0 μm at the SCF thickness ~1.0-2.0 μm and aperture of optical system ~1.0

As a continuation of these investigations, “engineering” of the SCF emission spectra matched with the range of CCD sensitivity is considered to be of practical importance. With this aim we have carried out preliminary study of the synthesis of SCF of $(LuGd)_3Al_5O_{12}$:Ce; $(LuGd)_3Al_5O_{12}$:Ce,Eu; $Lu_3Al_5O_{12}$:Ce,Tb and $Lu_3Al_5O_{12}$:Ce,Tb,Eu, as well as investigation of their luminescent and scintillation properties. By performing these works we have come to the possibility of shifting the Ce^{3+} ion emission in $Lu_3Al_5O_{12}$ SCF towards long wavelength range by doping with Gd^{3+} ions [7], as well as to increasing their light output by the means of sensibilization of Ce^{3+} ion emission by Gd^{3+} [7] and Tb^{3+} [14].

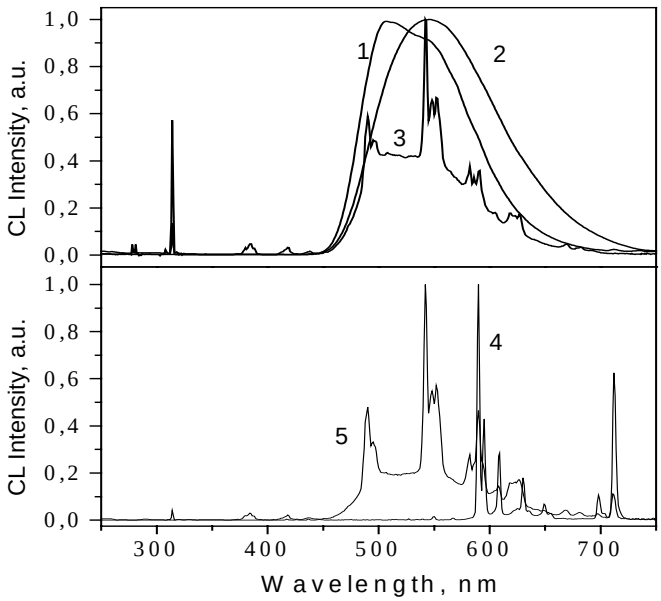

Fig. 4. Emission spectra of SCF $Lu_3Al_5O_{12}$:Ce (1), $(LuGd)_3Al_5O_{12}$:Ce (2), $Lu_3Al_5O_{12}$:Ce, Tb (3) $(LuGd)_3Al_5O_{12}$:Ce,Eu (4), $Lu_3Al_5O_{12}$:Ce, Tb, Eu (5). Light output of SCF 0.76 (1), 0.56 (2), 1.06 (3), 0.19 (4) and 0.26 (5) correspondingly.

Some results of these investiga-tions are presented in Fig. 4. The SCF samples of $Lu_3Al_5O_{12}$:Ce,Tb had the largest light output, which was by a factor of 1.45-1.5 higher with the Ce^{3+}/Tb^{3+} ratio of 1/5, than the analogous value for the reference $Y_3Al_5O_{12}$:Ce compound [1]. It should also be noted that introducing Eu^{3+} ions results in a noticeable decrease of the integral light output of SCF on the basis of $Lu_3Al_5O_{12}$:Ce.

Acknowledgments

The authors express their gratitude to S.Popovych for his help in measuring the SCF optical characteristics. The work was fulfilled due to support of INTAS-Ukraine porject under Grant No. 95-0166.

References

1. A.Koch, C.Raven, P.Spane, and A.Snigirev, J. Opt. Soc. Am. A., **15** (1998) 1940.
2. C.W.E. van Eijk, J.Andriessen, P.Dorenbos, a.a., Nucl. Instr. Meth. **A348** (1994) 546.
3. J.M.Robertson, and M.V.Tol, Thin Solid Films, **1-2** (1984) 221.
4. Yu.V.Zorenko, M.M.Batenchuk, V.I.Gorbenko, a. a., Zhurnal Pryklodnoi Spektroskopii, **67** (1999) 241.
5. M.Kh.Ashurov, Yu.K.Voron'ko, V.V.Osyko, a. a., Spectroscopy of Crystals, Nauka, Moscow, (1978) 71.
6. Yu.V.Zorenko, P.S.Malutenkov, N.I.Patsagan, a.a., Crystal Properties and Preparation, **36-38** (1991) 226.
7. 10. J.M.Robertson, M.V. van Tol, W.H., and G.Smith, Philips Journal of Research, **36** (1981) 15.
8. Yu.V.Zorenko, I.V.Nazar, L.N.Lymarenko, a.a., Optika i Spektroskopia, **80** (1996) 925.
9. G.B. Scott, and J.L. Page, J. Appl. Phys., **48** (1977) 1342.
10. Yu.V. Zorenko, Optika i Spektroskopia, **84,** (1998) 856.
11. Yu.V.Zorenko, M.V.Pashkovsky, M.M.Batenchuk, a. a., Optics and Spectroscopy, **80,** (1996) 776.
12. Ya.A.Valbis, L.G.Volzhenska, Yu.G.Dubov, a. a., Optika i Spektroskopia, **63,** (1987) 1058.
13. Yu.V. Zorenko, L.N. Limarenko, a.a., Zhurnal Prikladnoj Spektroskopii, **55** (1991) 774.
14. Yu.V. Zorenko, M.Batenchuk, M.Pashkovsky, a.a., Proc SPIE, **3358** (1998) 261.

Radiation damage factors of CsI(Tl) crystals

L.N.Shpilinskaya, D.I.Zosim, L.V.Kovaleva, A.M.Kudin, A.I.Mitichkin, T.A.Charkina

STC "Institute for Single Crystals "Lenin Ave 60, Kharkiv, 310001,Ukraine

Abstract. The light yield deterioration of CsI(Tl) crystals subjected to ionizing irradiation is found to be due to the increase of the scintillation light re-absorption caused by the formation of F-like color centers in the diffusion process. Those centers appear due to the formation of F ones stable at ambient temperature, the stabilization of the latter is realized effectively due to radiation-chemical transformations of CO_3^{2-} and OH^- ions.

Keywords: thallium-activated cesium iodide, color centers, radiation damage, re-absorption.

Introduction

The radiation-induced damage of CsI(Tl) scintillation crystals manifesting itself as the light yield degradation is due to the formation of color centers (CC) resulting in both transparency loss and the conversion efficiency reduction [1]. Since the absorption spectrum of formed CC overlaps the scintillation one, it is no doubt that the re-absorption contributes substantially to the light yield degradation. While the role of the conversion efficiency in the light yield loss remains still unclear. According to modern notions [2], the stable radiation-induced defects in alkali halide crystals (AHC) are due to formation of Frenkel type F-H pairs having the flying apart probability exceeding that of their mutual annihilation. In the presence of impurities, near-impurity (F,H) centers arise in crystals along with F,H pairs. In this case, it is not F center but H one that becomes localized near the impurity; that center transforms into H_A one and then a $(V_2)_A$ center arises due to the evolution of the latter. F_A centers can be obtained by the F band illumination of a crystal preliminary treated by ionizing radiation at temperatures close to the ambient one when the anion vacancy mobility is high enough. In the same time, the radiation-induced defect formation in crystals having a CsCl type lattice activated with mercury-like ions has been explained basing on a «vacancy type» mechanism. According to the latter, as a result of irradiation, electrons become localized on the activator ions under formation of A^o centers; those diffuse through anionic or cationic vacancies resulting in formation of paired A_2^o centers and more complex activator coagulations [3,4]. The available experimental data on the radiation resistance of mercury-like in activated CsCl type crystals, including CsI(Tl) ones doped additionally with anionic and cationic impurities cannot today be explained within the frame of the existing vacancy mechanism. In this work, the radiation-induced defect formation processes involving pre-radiation defects in CsI and CsI(Tl) crystals are discussed and an attempt is made to explain the radiation damage of crystals in the frame of a unified mechanism.

Experimental

The studies were carried out using samples made from CsI and CsI(Tl) crystals with different contents of thallium and molecular anions (MA) CO_3^{2-}, OH^-, SO_4^{2-}. Absorption spectra in UV, visible and IR regions were measured using SF-26 and UR-20 spectrophotometers. The light yield was measured on samples of 30 mm in diameter and different heights (5, 20, 60 and 90 mm). The light yield degradation was characterized as the (Lo-L)/Lo ratio where Lo and L are the light yield values prior to and after the irradiation, respectively. The re-absorption effect on the light yield reduction of irradiated crystals was estimated using the optical density change on 550 nm wavelength of ∅30 x 60 mm samples

measured with respect to a reference by the integrating sphere technique. The crystals were colored using a ^{60}Co gamma source, UV and daylight irradiation.

Radiation-stimulated change of the CsI(Tl) detector light yield

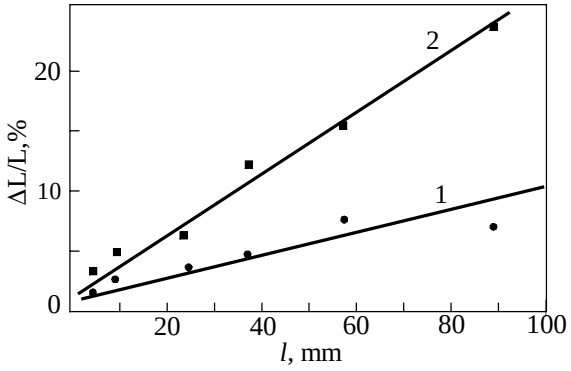

Fig. 1.The light yield degradation of ∅30 mm CsI(Tl) detector as a function of its length after 0,05 Mrad (1) and 0,5 Mrad (2)

To determine the effect of the scintillation efficiency reduction on the light yield degradation of irradiated crystals, the light yield of cylindrical detectors having different heights was measured prior to and after the irradiation.

It is seen from Fig.1 that the light yield degradation depends linearly on the detector height and can be approximated to zero thus evidencing that the conversion efficiency changes affect the light yield degradation only slightly. The re-absorption influence in the crystals was estimated from the optical density change in the 540 nm region corresponding the scintillation spectral maximum. The radiation-stimulated re-absorption increase is due to the presence of color centers in the crystals.

Color center formation in CsI(Tl) crystals

The color centers stable at ambient temperature and having the absorption bands in the activator absorption and emission region are known to be formed in CsI(Tl) crystals due to ionizing radiation and, in some cases, under the daylight action [5]. Fig. 2a presents the absorption spectra of gamma-irradiated CsI(Tl) crystal at different concentrations of Tl and CO_3^{2-}, OH^-, SO_4^{2-} molecular anions. The absorption bands are seen to increase in intensity as the Tl concentration rises. At the same Tl concentration, it is just crystals containing CO_3^{2-} ions as an additional impurity. In Fig. 3, the optical density variations of ∅30 x 60 mm CsI(Tl) crystals at the same irradiation dose are shown as functions of Tl and CO_3^{2-} ions. Neither new bands nor intensity increase of any bands as compared to non-irradiated samples are observed in absorption spectra of gamma-irradiated CsI(Tl) crystals doped additionally with SO_4^{2-} ions (Fig. 2,a) as well as with IO_3^- ones [5]. The Tl concentration being the same, the 430, 520, 560, 840, 975 nm bands intensities are higher in crystals with higher CO_3^{2-} ion content. According to [3], the absorption bands with maxima at 430 and 520 nm are due to Tl_2^o centers, weaker 390 and 465 nm bands, to Tl_2^+ ones while IR bands (840 and 975 nm), to more complex linear and three-dimensional associates of atomic thallium.

A high coloration intensity of CsI(Tl,CO_3) crystals can be attained irradiating them by UV and visible light, too; in both those cases, the absorption spectra are identical to those of gamma-irradiated crystals (Fig. 2,a,b). In contrast, CsI(Tl) crystals grown in vacuum using the Bridgman technique, having the activator concentration from $2\cdot10^{-5}$ to $5\cdot10^{-1}$ % and an additional SO_4^{2-} impurity are stable against light. A specific feature of CsI(Tl,CO_3) crystals colored by daylight consists in that at first the 355, 430, 520, 560, 840, 975 nm are appeared in the absorption spectrum and then, as the irradiation duration increases, the 390 and 465 nm ones arise (Fig. 2,b). The accumulation kinetics of color centers is of an usual character. As the irradiation duration grows, the intensity of all bands observed increases and then becomes saturated. A comparison of absorption spectra for crystals colored by gamma-irradiation (Fig.

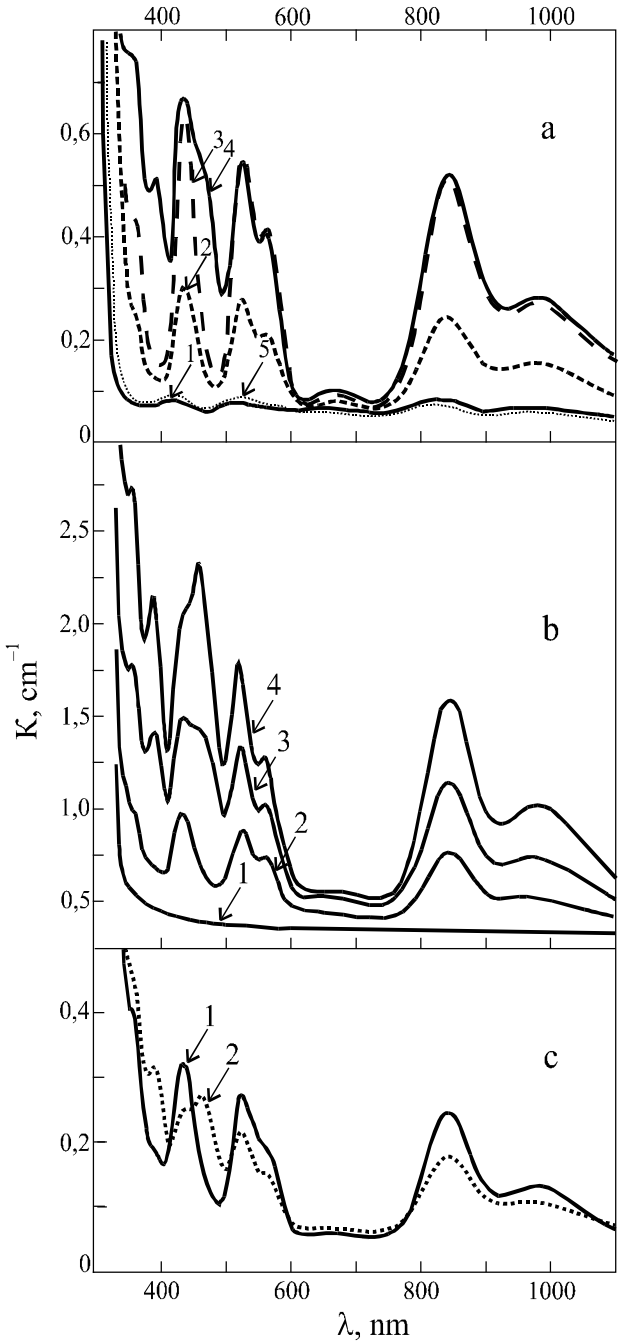

Fig. 2.

a) Absorption spectra γ-irradiated CI(Tl) crystal (0,01 Mrad). Concentrations (mol%)%: Tl - $1{,}1\cdot10^{-1}$ (1,2,4,5), $6\cdot10^{-2}$ (3); CO_3^{2-} - $6\cdot10^{-4}$ (3,4), $6\cdot10^{-5}$ (2), less then - $2\cdot10^{-5}$ (1,5); SO_4^{2-}-$1\cdot10^{-4}$ (5), less then - $2\cdot10^{-5}$ (1,2,3,4).
b) Absorption spectra of $CsI(Tl,CO_3)$ crystal prior to (1) and after (2,3,4) daylight irradiation during 3 hours (2), 9 days (3), 35 days (4). Concentrations (mol%): Tl - $6\cdot10^{-2}$, CO_3^{2-} - $6\cdot10^{-4}$.
c) $CI(Tl,CO_3)$ crystal absorption spectra immediately after γ-irradiated CI(Tl) crystal (0,01 Mrad) (1) and after the subsequent illumination by the filtered (436 nm) mercury lamp emission (2).

2,a) and by daylight (Fig. 2,b) shows that even at low Tl concentrations ($\leq10^{-2}$ %) intense 390 and 465 bands characteristic for Tl_2^+ centers appear in absorption spectra of daylight irradiated crystals. A similar effect can be observed if a crystal treated by ionizing radiation is illuminated by the light from the short-wavelength spectral region ($\lambda\leq430$ nm) (see Fig. 2,c).

Molecular anion transformations in the course of coloration

The appearance of bands due to activator type CC in the electron absorption spectra of colored $CsI(Tl,CO_3)$ crystals is accompanied by substantial changes in vibration spectra (Fig.4). As the intensity of bands typical for CC grows, that of CO_3^{2-} ion vibration bands decreases and a series of additional ones (593, 663, 745, 830, 947, 1223, 1315, 1679, 3318 cm^{-1}) ascribed to HCO_3^- ion appears. As in the case of $CsI(CO_3)$ crystals [6], the effect of HCO_3^- ion formation has a volume character. No changes were observed in vibration spectra of CsI and CsI(Tl) crystals containing SO_4^{2-} ions after gamma or daylight irradiation. A study of electron absorption spectra of isodose (10^3 rad) irradiated $CsI(SO_4)$ and $CsI(CO_3)$ crystals with the same MA content has shown that no F-absorption bands are observed in $CsI(SO_4)$ crystals in contrast to $CsI(CO_3)$ ones.

Discussion

The estimation of the re-absorption and of the scintillation efficiency reduction to the light yield degradation of gamma-colored CsI(Tl) crystals has shown that the light yield decrease is due to the transparency loss to the

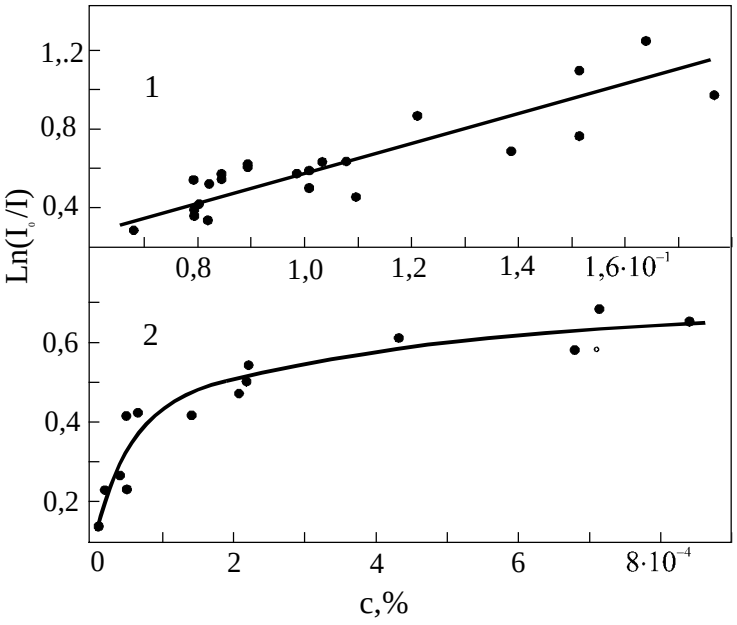

Fig.3. The optical density of γ-irradiated (^{60}Co, 0,5 Mrad) CsI(Tl,CO_3) crystals on the 540 nm wavelength as function of Tl(1) and CO_3^{2-}(2) concentration (mol%).

scintillation light. The CC formation under irradiation of CsI(Tl) has been found to be due both to Tl^+ and CO_3^{2-} ions. In spite of the Tl concentration differences in the crystals under study (almost by one decimal order), the optical density increase in the 540 nm band is defined mainly by CO_3^{2-} content and increases as the concentration of the latter grows (Fig. 3). Thus, the CO_3^{2-} ions contribute more significantly to the color center formation process. The comparison of 430, 520, 560, 840, 975 nm band intensities in absorption spectra of isodose irradiated CsI(Tl), CsI(Tl, CO_3) and CsI(Tl, SO_4) crystals has shown that, the SO_4^{2-} and CO_3^{2-} ion molar fractions being equal to each other, it is only the presence of CO_3^{2-} ions results in the intensity increase of the above-mentioned bands. Moreover, CsI(Tl, SO_4) crystals are not colored by daylight, as well as CsI(Tl) ones. Thus, the concentration of anionic vacancies compensating the excess charge of bivalent MA does not affect decisively the CC formation process. The diffusion possibility of Tl^o centers unstable at ambient temperature is also questionable. Due to decay of electron excitations, F or F_H centers are formed in CsI crystals activated with bivalent MA; those centers are decayed via a hole recombination process forming a scintillation pulse [7]. Unlike CsI(SO_4) crystals, F centers stable at ambient temperature are formed in CsI(CO_3) ones. According to [6], the F center stabilization is due to the presence of attendant hydroxyl impurity in crystals activated with CO_3^{2-} ions. Under ionizing irradiation, the interstitial hydrogen arises according to reaction (1); due to its diffusion, the reaction (2) occurs resulting in formation of the stable bicarbonate ion and F center. This is confirmed by vibration and electron absorption spectra (Fig. 2 and 4).

$$(OH^-)^* \rightarrow H^\circ_i + O^- \qquad (1)$$

$$H_i^\circ + CO_3^{2-} + V_a^+ \rightarrow HCO_3^- + F \qquad (2)$$

Along with the F center stabilization with HCO_3^- ions (Reaction 2), there are other stabilization possibilities involving hole centers of $(HI)^-_a$, $(HHI)^-_{aca}$ [8]. Thus, CC stable at ambient temperature arise in CsI and CsI(Tl) crystals in the course of radiation-chemical transformations involving OH^- and CO_3^{2-} ions. Irradiation of cation-doped AHC may result in formation not only F centers but also of F-like CC as F_A or F_{AA}.

Basing on the results obtained, absorption bands at 430, 520, 560, 840, 975 nm observed in irradiated CsI(Tl, CO_3) crystals can be attributed to F-like near-activator CC of F_{AA} type. The absence of photochemical transformations in CsI(CO_3) crystals in contrast to CsI(Tl, CO_3) ones points that the charge carrier delocalization occurs under involving thallium ions. In fact, CsI(Tl) crystals having the CO_3^{2-} ion content lower than its determination threshold ($2\cdot10^{-5}$ %) exhibit an appreciable phosphorescence though they are not colored by daylight while no essential afterglow is observed in CsI(CO_3) and CsI(OH) crystals. The emissionless decay of

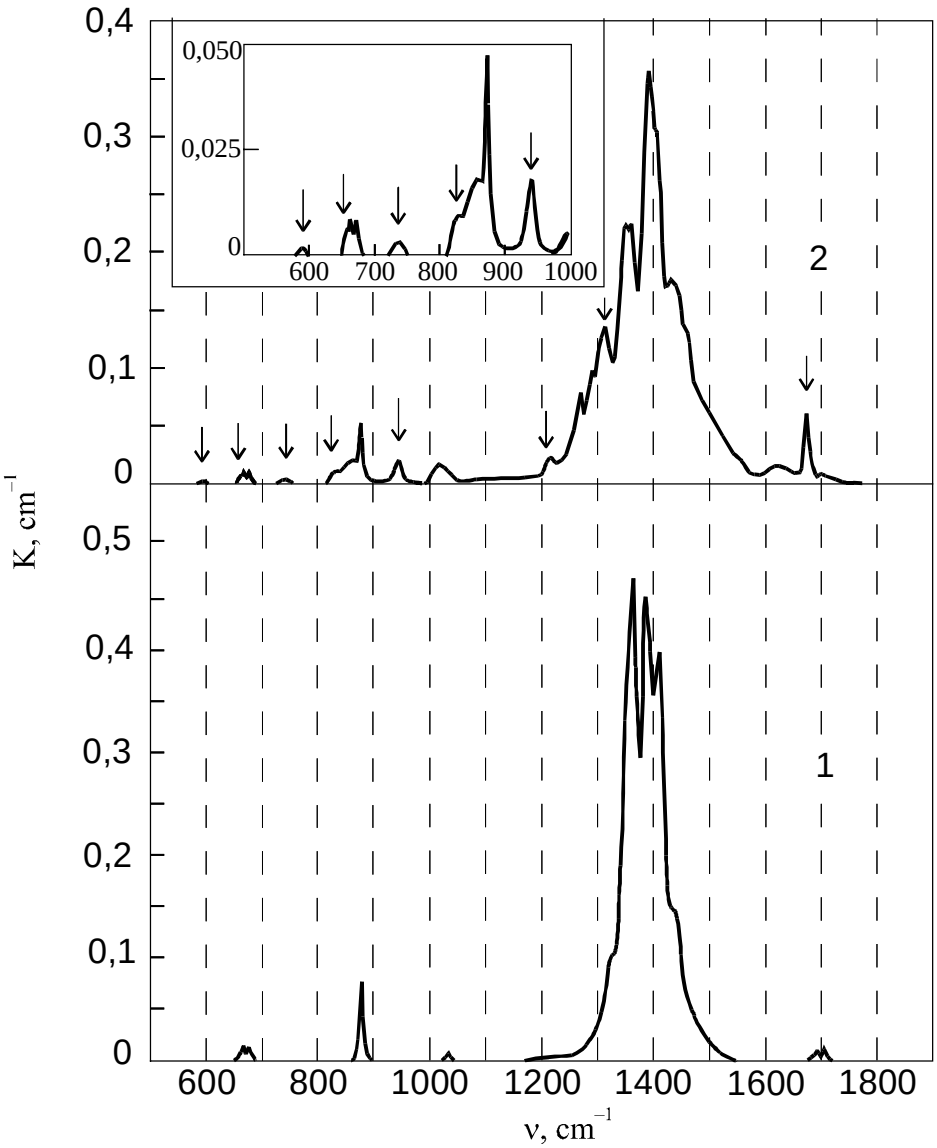

Fig. 3. IR absorption spectra CsI(Tl,CO_3) prior to (1) and after (2) daylight irradiation (bands typical for HCO_3^- - ions shown by arrows). The Tl and CO_3^{2-} ion concentration in the crystal are $6\cdot10^{-2}$ and $8\cdot10^{-4}$%, respectively.

electron excitations arising under daylight in CsI(Tl, CO_3) crystals containing additional OH^- ions results in the dissociation of the latter (reaction 1) thus giving an opportunity for the formation of F centers stabilized by HCO_3^- ions (reaction 2) and heteronuclear centers of V type. The diffusion of F centers in CsI crystals passing efficiently at ambient temperature in the presence of thallium results in formation not of F-aggregate CC but of those of [(Tl^+-Tl^+-V_a)+e] type which diffusion is hindered. It is transitions in an [(Tl^+-Tl^+)+e] center disturbed by an anionic vacancy that seem to be responsible for 430, 520, and 560 nm bands in the visible spectral region while long-wavelength bands 840 and 975 nm are associated with transitions in the F center disturbed by a (Tl^+-Tl^+) one. Basing on the conventional notation, the above centers can be designated as [Tl_2^+-V_a] with absorption bands 430, 520, 560 nm and [F-(Tl^+-Tl^+)] center with 840 and 975 bands. The model proposed makes it possible to explain the formation cause of [(Tl^+-Tl^+-V_a)+e] at the initial stage of the coloration by daylight. The appearance of 390 and 465 nm bands in the absorption spectrum at longer irradiation times is due to photoinduced discoloration of F_{AA} centers followed by the trapping of delocalized electrons by paired (Tl^+-Tl^+) activator centers under formation of Tl_2^+ ones responsible for 390 and 465 nm bands.

Conclusions

1. The predominant importance of re-absorption in the radiation resistance degradation of CsI(Tl) detectors has been established.

2. The increased scintillation light re-absorption in irradiated CsI(Tl) crystals is caused by formation of F-like activator color centers (F_{AA}) in the course of F center diffusion towards paired (Tl^{+}-Tl^{+}) centers.

3. The formation of stable F centers is possible under presence of CO_3^{2-} molecular anions and OH^- ions involved in radiation-chemical reactions in CsI and CsI(Tl) crystals.

4. The photochemical instability of CsI(Tl, CO_3) crystals is due to the emissionless decay of electron excitations causing the dissociation of attendant OH^- ions.

References

1. A.V. Gektin, M.E..Globus, Shepelev,N.V et al., Functional Materials, **4**, No. 4, (1997), 544.
2. Ch.B.Luschik, A.Ch.Luschik, Decay of Electronic Excitations with Defect Formation in Solids, Nauka, Moscow (1989).
3. A.K.Mednikov, V.I.Shtan`ko, in: Abstr. of 25th All-Union Confer. on Luminescence, Lvov (1978), p. 80.
4. L.P.Smolskaya, L.V.Kovaleva, V.N.Salomatov, et al.,in: Single Crystals, Production and Properties Thereof, No 8, VNIIM Publ., Kharkov (1982), pp. 11-17.
5. L.V.Kovaleva, L.L.Nagornaya, Ya.A.Zakharin et al., in: Growth and Properties of Crystals, No. 8, VNIIM Publ., Kharkov (1980), pp. 24-27.
6. B.V. Grinyov, L.N. Shpilinskaya, A.M. Kudin et al., Functional Materials, **4**, No. 4, (1997), 540.
7. V.I. Goriletsky, L.G. Eidelman, A.N.Panova et al., Nucl. Tracks. Radiat Meas., **V**21, No1, (1993), 109.
8. S.P.Sukhorebry, Radiation Defect Formation in Hydrogen-Containing Crystals, Master's Thes. Abstr. (Phys.-Math.), Lvov (1987).

Time-resolved spectroscopy of exciton states in undoped and doped CsI crystals

V.Babin[1], P.Fabeni[2], E.Mihokova[3], M.Nikl[3], A.Stolovitš[1], G.P.Pazzi[2], S.Zazubovich[1]

[1] *Institute of Physics, University of Tartu, Riia Str. 142, 51014 Tartu, Estonia*
[2] *IROE del CNR, Via Panciatichi 64, 50127 Florence, Italy*
[3] *Institute of Physics AS CR, Cukrovarnická 10, 16253 Prague, Czech Republic*

Abstract. Spectral and kinetic characteristics of exciton luminescence in undoped and doped CsI crystals have been studied at 0.36-300 K. The origin of the emission bands as well as the structure and parameters of exciton states have been determined. The processes resulting in the appearance of the exciton-like emissions under photo-excitation in the impurity-induced absorption bands and under excitation by the ionizing radiation are discussed.

Keywords: exciton luminescence, alkali halides

Introduction

Undoped CsI as well as CsI:Tl and CsI:Na crystals are well known and widely used as effective scintillating materials (see, e.g., [1]). Their luminescence characteristics were extensively studied for many years. However, only some years ago it was found that the visible emission of CsI:Tl arises from the radiative decay of an exciton localized near a Tl^+ ion [2, 3]. The origin of some emission bands observed in pure and doped CsI crystals as well as the processes occurring in doped CsI crystals under photo- and X-ray excitation are still under discussion. In many cases (except CsI:Tl), a detailed structure and parameters of the exciton states were not determined correctly, as the decay kinetics of exciton luminescence was studied only at the temperatures down to 4.2 K. Some essential details of the scintillation process were also unclear up to the latest time.

In this paper, the steady-state and time-resolved emission and excitation spectra as well as the decay kinetics of luminescence (see, e.g., Fig. 1) of the self-trapped excitons (STE) and of the excitons localized near impurity ions (Na^+, K^+) or various crystal structure defects were studied for undoped and doped CsI crystals of various origin at the temperatures down to 0.36 K under excitation by photons of the energy E_{exc}<6.2 eV. On the basis of the data obtained a conclusion was made on the origin of the ultraviolet (4.32 eV, 4.25 eV, 4.03 eV) emission bands overlapping with the 4.29 eV (σ) emission of the on-centre STE, which, according to [4], is responsible for a fast ultraviolet emission of CsI scintillator. The structure of the STE and various localized exciton states was determined and their parameters calculated from the temperature dependences of the luminescence decay times. The processes resulting in the appearance of the exciton-like emissions of doped CsI crystals under photoexcitation and under excitation by the ionizing radiation were compared. The crystals, set-ups and experimental procedures used were the same as those described in [2, 5-7].

Experimental Results

The low-temperature decay kinetics of the emissions studied was found to be characteristic of the emission arising from the triplet relaxed excited state. Similar to the 2.55 eV and 2.25 eV emission bands of CsI:Tl [2, 5], two types of the decay kinetic characteristics were observed:

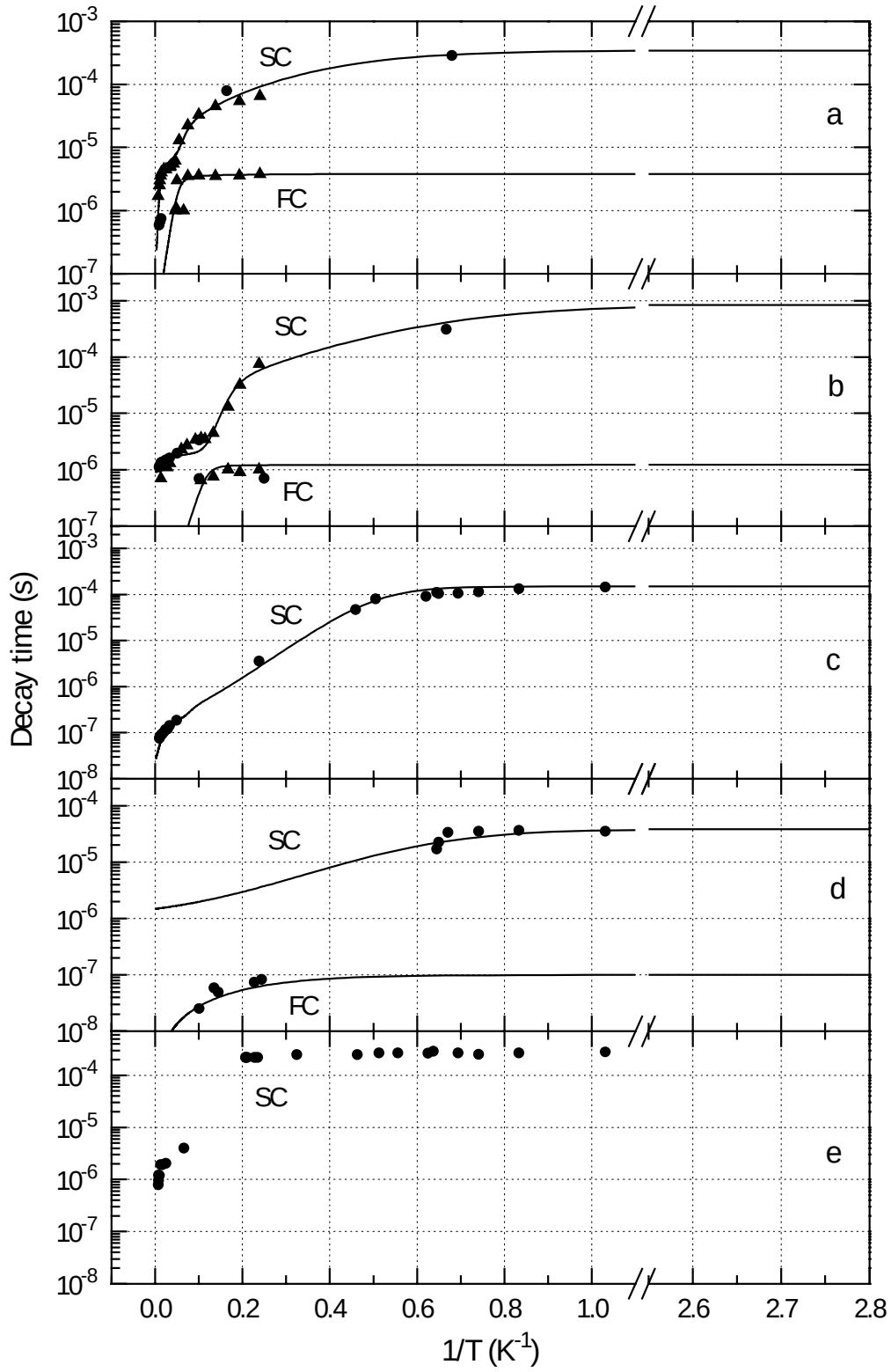

Fig. 1. Temperature dependences of the decay times $\tau(T^{-1})$ of the slow (SC) and fast (FC) components of the (a) 2.98 eV, (b) 3.32 eV, (c) 4.03 eV, (d) ~4.3 eV and (e) 3.0 eV exciton emissions (points). The corresponding $\tau(T^{-1})$ curves calculated with the parameters from Table 2 are shown by full lines.

(i) In most cases, two decay components, the fast (FC) and the slow (SC), are present. Temperature dependences of their decay times (τ_{FC} and τ_{SC}) are shown in Fig. 1, a-c (see also [8]). In this case, the low-temperature values of the decay times and their temperature

dependences are characteristic for the location of the metastable level of the triplet state *below* the emitting level. Indeed, at 0.36 K τ_{SC} is of the order of 10^2 μs and does not change up to 1 K. It means that at T<1 K the radiative transitions occur from the lower, metastable minimum of the triplet state. As the temperature rises, τ_{SC} decreases exponentially due to thermal transitions between the metastable and emitting levels and reaches the value of some μs at the temperatures where thermal equilibrium is established between these levels. In some systems, further increase of the temperature results in a second stage of the exponential decrease of τ_{SC} caused by the thermal transitions between the triplet and singlet states.

(ii) In the decay kinetics of the ~4.3 eV emission as well as of the wide 3.0 eV emission studied in [9], a slow components with much shorter decay time (40 and 46 μs, respectively) is observed at 0.36 K (Fig. 1, d-e). Such a decay kinetics is similar to that detected for the 2.25 eV emission of CsI:Tl arising from the strong off-centre configuration of an exciton localized near a Tl^+ ion. In case of CsI:Tl, the metastable minimum of the corresponding triplet exciton state was found to be located *above* the emitting minima [2, 5, 10]. Such a decay kinetics can be observed in CsI crystal also in case the emission is caused by the radiative decay of the metastable minimum of the on-centre exciton configuration.

Discussion

The analysis of the data obtained in the present paper and in [2, 5, 10] has shown that the decay kinetics of all the emission bands studied is similar to that of the triplet exciton luminescence of CsI crystal. It means that all these bands are of excitonic origin. The application of Kan'no [11] classification of exciton emissions along their relative Stokes shift $S_R=(E_{exc}-E_{em})/E_{exc}$ to the emissions studied allows to connect them with various exciton configurations (Table 1). The ultraviolet bands (S_R=0.23-0.27) arise from the on-centre configuration of the STE (4.29 eV) and localized excitons (4.32 eV, 4.25 eV, 4.03 eV).

Table 1. Characteristics of various exciton luminescence bands in CsI crystals

Crystal	Emission energy (halfwidth), eV	Excitation energy, eV	Relative Stokes shift	Exciton configuration
CsI	4.29 (0.28)	6.02-5.81	0.265	on-centre STE
	3.65 (0.31)			weak off-centre STE
CsI	4.03 (0.28)	5.5	0.27	on-centre
	~3.00 (~0.7)	5.5	0.45	strong off-centre
CsI	4.25 (0.41)	~5.75	~0.26	on-centre
	4.32 (0.33)	~5.75	~0.25	on-centre
CsI:Na	2.98 (0.33)	5.39	0.45	strong off-centre
CsI:K	3.32 (0.39)	5.65	0.41	weak off-centre
CsI:Tl	2.55 (0.35)	4.29	0.405	weak off-centre
	2.25 (0.35)	4.28	0.47	strong off-centre

The bands with S_R=0.35-0.40 arise from the weak off-centre configuration, and the bands with S_R=0.45-0.48, from the strong off-centre exciton configurations.

It is shown that the presence of the singlet state and the thermally stimulated triplet - singlet transitions are characteristics not only of the on-centre STE configuration [4] but also of the off-centre configurations of some localized excitons (see also [2]). It is also found that the reverse order of the emitting and metastable minima observed for the localized exciton in CsI:Tl may be the characteristic of some other localized excitons in CsI. According to [12], the reverse order of the metastable and emitting minima may be observed in the systems with a weak spin-orbit interaction (where the spin-spin interaction dominates) in case the hole is

shared almost equally between two halogen ions and the electron and hole components of exciton are well separated. These conditions are realized for a strong off-centre configuration of a localized exciton where the spin-orbit interaction is essentially supressed by the electron-phonon interaction and a defect stimulates more symmetric location of a hole between two halogen ions in the H centre. This is the case of the 2.25 eV emission of CsI:Tl and may be the case of the 3.0 eV emission of CsI both arising from the strong off-centre exciton configurations (Table 1), but not the case of the ultraviolet emissions arising from the on-centre exciton configuration. Most probably, the 40 μs-component of the ~4.3 eV emission is caused by the radiative decay of the metastable state of the on-centre exciton in CsI.

Taking into account these conclusions, the following parameters of the excited states responsible for the emission studied have been calculated by the method described in [6]: the probabilities of the radiative (γ_1, γ_2, γ_0) and nonradiative (p_2, p_0) transitions from the metastable (γ_1) and emitting (γ_2) levels of the triplet state and from the singlet state (γ_0, p_0) as well as energy distances between the metastable and emitting minima (δ) and between the triplet and singlet states ($\Delta E_{s\text{-}t}$) (see Table 2). At the calculations, it has been assumed that the 40 μs-component arises from the metastable level of the on-centre STE. For comparison, the parameters of the excited states responsible for the visible luminescence of exciton localized near Tl^+ ion are also shown. It is evident that the parameters of all the excited states studied are characteristic of excitons in CsI crystals.

Table 2. Parameters of the excited states responsible for the exciton emissions in CsI

Emission, eV	γ_1, 10^3 s^{-1}	γ_2, 10^6 s^{-1}	p_0, 10^6 s^{-1}	δ, meV	γ_0, 10^7 s^{-1}	$\Delta E_{s\text{-}t}$, meV	$p_{s\text{-}t}$, 10^8 s^{-1}
4.29 (σ)	26	1	9	0.7			
3.65 (π)	2.4	1.3	0.1	0.6	0.5	5.5	4
3.65 ($e+V_K$)	2.3	1.6	0.1	0.7	0.5	8	3
2.98 (ex Na^+)	2.9	0.25	0.013	0.5	0.2	9	1
					10	30	10
3.32 (ex K^+)	1.2	0.8	0.02	0.45	0.3	5	10
4.03	6.7	8	50	1.3	15	10	
2.55 (ex Tl^+)	2.4	~0.1	~0.1	0.6-0.7	0.3-1	12-14	0.1-1
2.25 (ex Tl^+)	~1.0	0.02	0.05-1	-0.6-0.8	2.0-4.0	35-37	1.4-1.5

The detailed study of the 4.32 eV, 4.25 eV and 4.03 eV emission bands located near the 4.29 eV emission of the STE and excited at 5.8-5.6 eV and 5.5 eV, respectively, carried out with the use of the uniaxial stress and the analysis of the published data has allowed us to conclude that these emissions are all connected with crystal structure defects [7]. The 4.25 eV and 4.32 eV emissions arise from the on-centre localized excitons connected with slightly expanded and stressed crystal regions, respectively. The 4.25 eV emission is often mixed with the 4.29 eV emission of the on-centre STE in CsI. It explains the fact that the intensity ratios of the ~4.3 eV emission and the 3.65 eV emission of the off-centre STE are strongly different in different publications (especially at T>20 K). The 4.03 eV emission as well as the wide 3.0 eV emission band both excited at 5.5 eV [9] arise from the exciton localized in some strongly distorted crystal regions (e.g., near large aggregates of vacancies) produced in the processes of crystal growth, long heating and slow cooling down, aggregation of the defects created by plastic deformation, etc.

On the basis of recent data, some conclusions can also be made on the processes occurring in doped CsI crystals under photoexcitation and under excitation by ionizing radiation. The photoexcitation of the crystals in the impurity-induced absorption bands results in the transfer of an electron to an impurity ion (A^+) from some mixed A^+ and I^- states located in the valence

band [7]. As a result, an electron centre (A^0) and the nonrelaxed hole in the valence band are created. Fast migration of the holes and their subsequent self-trapping results in the creation of V_K centres on different distances from A^0. A final result: an immediate radiative recombination of A^0 electrons with V_K centres, creation of stable (up to 60 K) $\{V_K\text{-}A^0\}$ pairs or unperturbed V_K centres in regular lattice sites, is determined by the energy (migration length) of optically created non-relaxed holes which, in its turn, depends on the position of the mixed A^+, I^- states with respect to the valence band top. In CsI:Tl, a fast recombination of Tl^0 electrons with close-lying V_K centres takes place resulting in the formation of an exciton near Tl^+ and the subsequent radiative decay of this exciton accompanied by the visible emission. The decay kinetics of this emission is exponential, and no components longer than 1 ms are detected at T<1 K [2]. The rise time of the visible emission is less than 50 ps, i.e., the relaxation processes resulting in the formation of the exciton-like state occur very quickly. Under the 5.5 eV excitation, the stable V_K centres are also created in CsI:Tl at 4.2 K. They are mainly located near A^0 but also in the regular lattice sites [13]. In CsI:Pb, unperturbed V_K centres (stable up to 90 K) are produced by photons of 5.7-4.4 eV energy [14].

The excitation of the crystals by ionizing radiation produces electrons and holes. According to [15], the correlated relaxation of associated electron-hole pairs occurs in KI and RbI. In the pure crystals they recombine, and the one-centre excitons are first created which transform into two-centre self-trapped excitons. Unlike this case, in the crystals containing the traps for electrons, the one-centre holes are first created. Basing on these data, we have suggested [13] that also in irradiated CsI, as soon as one component of the relaxing electron-hole pair (most probably, an electron) is trapped by A^+ ion, the second component (a hole) is immediately self-trapped near A^0 producing more or less close $\{V_K\text{-}A^0\}$ pair. The $\{e^-\text{-}V_K\}$ recombination in this pair leads to the formation of the exciton localized near A^+, whose radiative decay is accompanied by the intense luminescence of CsI:Na and CsI:Tl. Thus, the same impurity ion may take part in the process of trapping of an electron and a hole. Indeed, a relatively long scintillations rise time in CsI:Tl (about 40 ns at 300 K, see [13, 16]) can be explained by the process in the pairs, as the time of the STE creation in CsI is much shorter (~0.4 ps [17]). The temperature dependence of scintillations is well explained by the thermally stimulated migration of V_K towards A^0 in the $\{V_K\text{-}A^0\}$ pairs. This mechanism explains a large amount of spatially correlated $\{V_K\text{-}Tl^0\}$ and $\{V_K\text{-}Na^0\}$ pairs in CsI [18], small amount of Tl^{2+} and Tl^0 centres in the regular lattice site [3], temporal and temperature dependences of scintillations and high efficiency of these scintillators. The creation in this case of stable $\{V_K\text{-}A^0\}$ pairs explains the appearance of relatively slow afterglow which is absent under photoexcitation in the impurity-induced absorption bands.

Acknowledgements

The authors gratefuly acknowledge the financial support of NATO Linkage Grant OUTR.LG 960952 and Estonian Science Foundation Grant No. 3875.

References

1. P.A.Rodnyi, Physical Processes in Inorganic Scintillators, CRC Cleveland, USA, 1997
2. V.Nagirnyi, S.Zazubovich, V.Zepelin, M.Nikl, and G.P.Pazzi, Chem. Phys. Letters **227** (1994) 533
3. J.-M. Spaeth, W.Meise, and K.S.Song, J. Phys.: Condens. Matter **6** (1994) 3999
4. H.Nishimura, M.Sakata, T.Tsujimoto, and M.Nakayama, Phys. Rev. **B 51** (1995) 2167
5. V.Nagirnyi, A.Stolovich, S.Zazubovich, V.Zepelin, E.Mihokova, M.Nikl, G.P.Pazzi, and L.Salvini, J. Phys.: Condens. Matter 7 (1995) 3637
6. M.Nikl, J.Hlinka, E.Mihokova, K.Polak, P.Fabeni, and G.P.Pazzi, Phil. Mag. **B 67** (1993) 627
7. V.Babin, A.Elango, K.Kalder, and S.Zazubovich, Phys. Stat. Sol. (b) **212** (1999) 185

8. V.Babin, P.Fabeni, E.Mihokova, M.Nikl, A.Stolovits, G.P.Pazzi, and S.Zazubovich, Abstracts of SCINT'99, Moscow 1999
9. H.Lamatsch, J.Rossel, and E.Saurer, Phys. Stat. Sol. **41**, (1970) 605
10. V.Nagirnyi, A.Stolovich, S.Zazubovich, V.Zepelin, and G.P.Pazzi, Solid State Commun. **100** (1996) 621
11. K.Kan'no, K.Tanaka, and T.Hayashi, Rev. Solid State Sci. **4** (1990) 383
12. K.S.Song, C.H.Leung, and J.-M.Spaeth, J. Phys.: Condens. Matter **2** (1990) 6373
13. V.Babin, P.Fabeni, K.Kalder, M.Nikl, G.P.Pazzi, and S.Zazubovich, Rad. Measurements **29** (1998) 333
14. S.Zazubovich, R.Aceves, M.Barboza Flores, P.Fabeni, T.Karner, G.P.Pazzi, R.Perez Salas, and N.Jaanson, J. Phys.: Condens. Matter **9** (1997) 7249
15. S.Iwai, T.Tokizaki, A.Nakamura, K.Tanimura, N. Itoh, and A.Shluger, Phys. Rev. Letters **76** (1996) 1691
16. S.Chernov, A.Popov, and L.Trinkler, In: Proc. Int. Conf. "Inorganic Scintillators and Their Applications", eds. P.Dorenbos and C.W.E van Eijk, Delft University Press, Delft 1996, p. 439
17. M.Abdrakhmanov, S.Chernov, R.Deich, and V.Gavrilov, J. Lumin. **54** (1992) 197
18. S.Chernov, In: Proc. Int. Conf. "Excitonic Processes in Condensed Matter", ed. M.Schreiber, Dresden University Press, Dresden, 1996, p. 155

Photoinduced coloration of NaI(Tl) crystals: Effect of Lead Impurity trace concentrations

Shakhova K.V., Panova A.N., Goriletsky V.I., Gavrilyuk V.P., Kosinov N.N.

Institute for Single Crystals, NAS of Ukraine,
310001 Kharkov, Lenin ave. 60

Abstract. The photoirradiation effect on variation of absorption, luminescence and scintillation properties of large NaI(Tl) and NaI(Tl, Pb) crystals grown in ROST type units has been studied in the concentration ranges of (600—1200) ppm Tl and (0,01—0,05) ppm Pb. The presence of Pb trace concentrations in NaI(Tl) crystals has been found to result in the color center formation under visible light influence that manifests itself as changes in absorption spectra, a deterioration of the crystal transparency to the activator emission and of scintillation properties of detectors. The color centers formed in NaI(Tl, Pb) crystals develop in the thermoluminescence curve as peaks with maxima at 313 K and 343 K. Their degradation rate at room temperature defines the recovery kinetics of scintillation parameters of the colored detectors. The photocoloration mechanism is discussed for NaI(Tl) crystals containing the Pb impurity trace amounts.

Keywords: NaI(Tl) crystal, absorption, color centers, thermoluminescence

Introduction

It is known that color centers stable at room temperature can be formed in NaI(Tl) crystals due to action of radiation and visible light. This process is believed to be associated with the matrix photolysis stimulated by oxygen-containing impurities in the crystal [1]. In [2], the deterioration of the detector spectrometric performance due to irradiation is explained by formation of activator complex color centers responsible for the 340 K peak in thermoluminescence (TL) curve. The problem of NaI(Tl) crystals with photostable properties has been arosen in connection with growing of large crystals used in the medical instrument building as large-area detectors. Is some cases, the articles became colored even in the course of preparation. The representative samples of those crystals were found to exhibit different stability against the visible light independent of the activator concentration and the presence of oxygen-containing impurities being the melt hydrolysis products. This made it necessary to study additionally the NaI(Tl) crystal photocoloration causes with the aim to prepare detectors with scintillation parameters stable against the photoirradiation.

Experimental Procedures

The present investigation were carried out on commercially produced NaI(Tl) crystals. Large NaI(Tl) crystals were grown in a "Rost" type unit under the melt forced mixing, providing the uniform activator distribution in the crystal volume. The details of the crystal growth equipment developed and the growth conditions are given elsewhere[3]. Thallium concentration in the crystals, determined using the optical method, was 600 – 1200 ppm. The presence of impurities melt hydrolysis products was examined by IR spectroscopy. The lead impurity was not introduced into crystals intentionally but was present in some crystals, perhaps, as that introduced with the activator thallium iodide. The crystals employed for scintillation measurements had dimensions 30 mm diameter 63 mm height.

For optical absorption and luminescence measurements samples were cleaved from the ingots in a dry room (relative moisture 4 %) and packet in scalable containers. The samples were photoirradiated for 20 min using a mercury lamp provided by FS – 6 filter.

Absorption luminescence and scintillation properties were recorded using the standard units and setups.

Experimental Results

Fig. 1 presents typical dispersion dependencies of the absorption coefficient for a NaI(Tl) crystal containing 800 ppm Tl before (1) and after (2) the irradiation. The absorption spectrum of the crystal is seen to change substantially due to the light action. Namely, along with the 351 nm band disappearance, an appreciable absorption enhancement in the 320—900 nm range takes place expressed more clearly in the differential spectrum as a series of bands with poorly distinguishable maxima near 340, 410, 520, 580, 660, and 760 nm. Storage of the crystal in darkness at room temperature for a couple of weeks after irradiation leads to disappearance of the color centers (curve 3) and the initial absorption spectrum is recovered.

The position of 357 nm absorption band maximum characteristic for the initial sample coincides with that of the A band ($^1S0—^3P_1$) for NaI(Pb) crystals [4, 5]. The shorter-

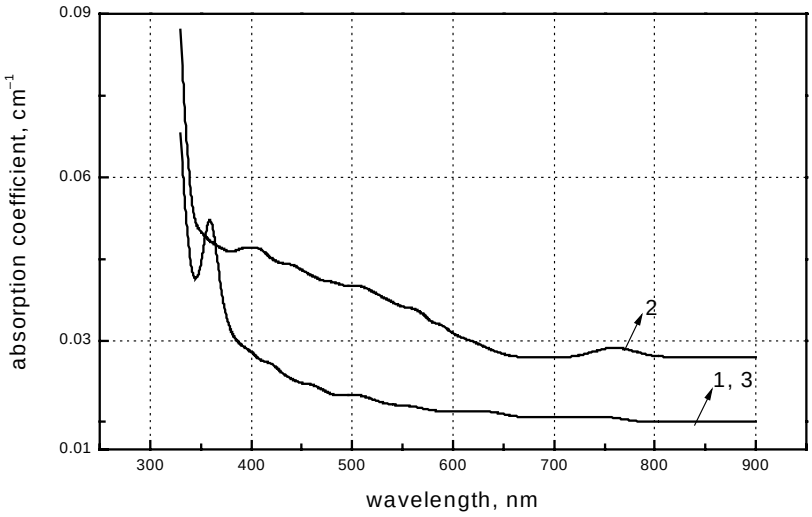

Fig. 1. Absorption spectra of NaI(Tl) crystal (800 ppm Tl) with traces of Pb before (1), after visible light coloration, (2) and after natural uncoloration (3)

wavelength B, C and D ones overlap with thallium absorption bands in NaI and thus are unobservable. However, the comparison of absorption spectra of a thin (t=0.1 cm) NaI(Tl) crystal before to and after the irradiation shows that the absorption in the B, C and D band regions is reduced due to the coloration.

The result obtained evidences that the lead impurity in NaI(Tl) crystals is involved into their photocoloration process. The Pb^{++} concentration estimation made according to [6] shows that the observed effect takes place in crystals containing trace Pb amounts (about 0,01 ppm). This is confirmed by the linear dependence of the relative (L/L_0) light yield of NaI(Tl) detectors of 30 x 63 mm size on the lead content therein (Fig. 2). At the Pb concentration of about 0,03 ppm, the light yield of those detectors is seen to be reduced by 50 %. Limiting lead content in the crystal which does not result in the light yield deterioration is less than 0,01 ppm.

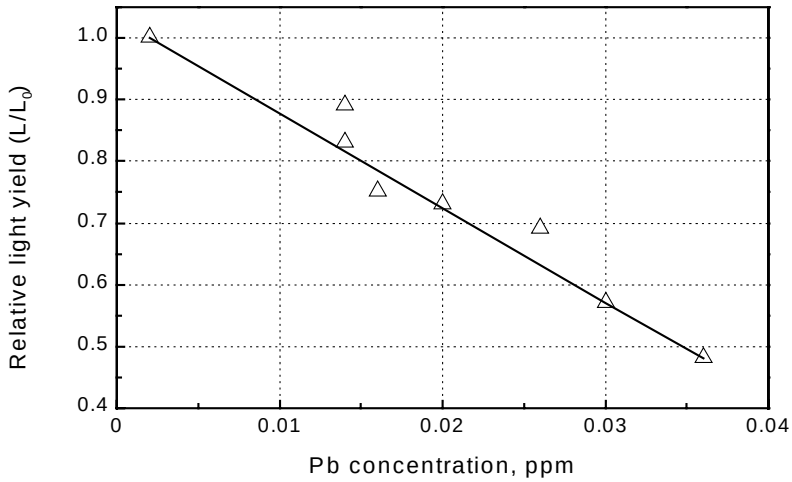

Fig. 2. Relative light yield of visible light colored NaI(Tl) crystals as function lead concentration

In some cases, the energy resolution of the detector is observed to be improved along with the light yield reduction. The light yield reduction of the detectors resulting from their photoirradiation can be due to deterioration both of the crystal transparency to the activator emission (what is obvious) and of the scintillation efficiency. However, the radioluminescence spectra measurements (^{137}Cs, 662 keV) made on 0.2 mm thick samples of NaI(Tl) evidence that the activator emission intensity is enhanced in a colored crystal (Fig. 3, curves 1, 2).

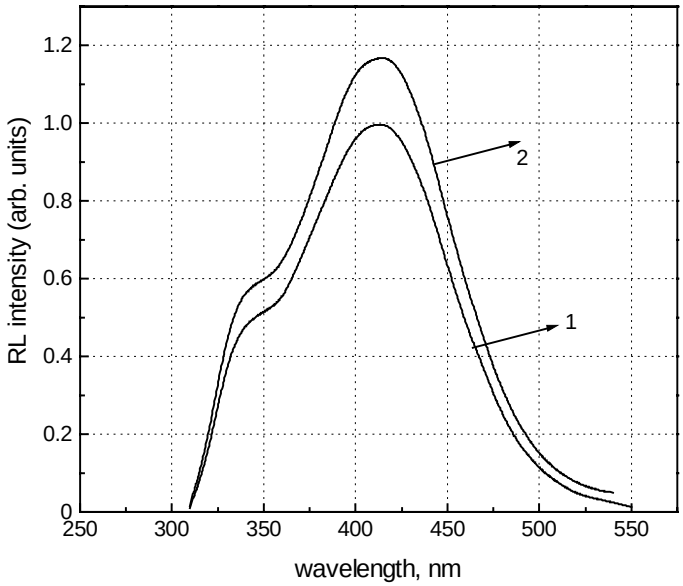

Fig. 3. Radioluminescence (^{137} Cs 662KeV) spectra of NaI(Tl), containing 800 ppm Tl (th=0,2 см) before (1) and after (2) coloration

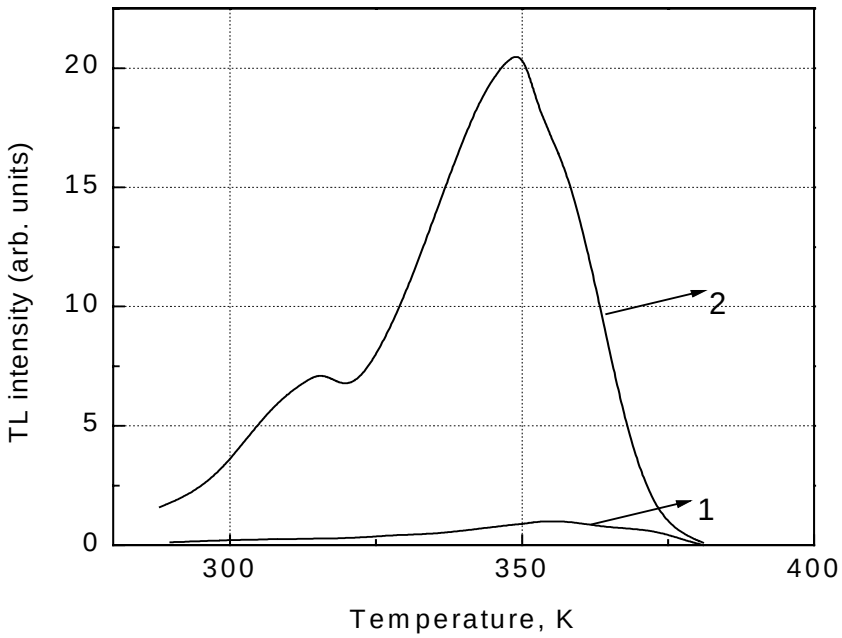

Fig . 4. TL curves for NaI(Tl) crystals, containing: (1) – 1200 ppm Tl and (2) – 1200 ppm Tl, 0,04 ppm Pb

Studies of the light yield recovery kinetics for colored detectors during their dark storage have shown that the process consists of two stages, namely, the fast and slow ones, thus pointing that at least two types of color centers differing in stability are formed due to the light action.

Fig. 4 shows the TL curves (1, 2) for NaI(Tl) crystals irradiated at 273 K having the same impurity composition (in anions) and the same activator content (1200 ppm of Tl) but different lead content. In the crystal 2, Pb concentration is 0,04 ppm. The samples were annealed in vacuum at 473 K for 2 hours before to measurements to decompose the possible high-temperature trapping centers [1]. The color centers arising in NaI(Tl) crystals in the presence of Pb impurity are seen to be observed on the TL curves peaks having maxima at 313 and 343 K. It is just the decomposition rate of those color centers at ambient temperature that defines the two-stage character of the scintillation parameter recovery for colored detectors.

Discussion and Conclusions

The experimental results presented above evidence that the lead impurity in NaI(Tl) crystals is involved directly into the color center formation under visible light action. Two competitive processes take place in this case. On the one hand, the scintillation efficiency of the crystal is enhanced slightly, since Pb^{++} absorption bands are absent in colored crystals, and thus, there is no competition with the activator for the exciting energy absorption. This is why an improved energy resolution is observed for some colored detectors. On the other hand, the color centers formed reduce the crystal transparency to the activator emission, thus worsening the detector scintillation parameters.

Consideration of the results obtained as well as of numerous works aimed at the study of properties of lead-activated alkali halide systems allows to suppose the following possible mechanisms of the NaI(Tl) crystal photocoloration. The intensity drop of the A band for $NaCl:PbCl_2$ and $KCl:PbCl_2$ crystals irradiated at room temperature observed if the impurity in

the crystal volume is in the dissociated state is explained by the electron color center formation (Pb^{++} Pb^{+}) [7]. In this case, it can be supposed, that the 313 K peak observed on the TL curve of NaI(Tl) crystals containing trace lead amounts is associated with the decomposition of electron color centers. Further studies are necessary to elucidate the nature of 343 K peak. Moreover, as it follows from [8], the presence of lead impurity in alkali halide crystals may stabilize the color centers formed due to irradiation, thus enhancing the formation efficiency of hole and electron centers.

At present, none of the described mechanisms can be preferred due to lack in experimental data. We suppose that the further studies of model NaI(Tl,Pb) crystals shall allow to state unambiguously the color center formation mechanism in this system.

Authors are thankful to S.P. Korsunova and Dr. V.V. Uglanova for their assistance and useful discussions.

References

1. Z. Baturicheva and N. Gurevich, Single Crystals Scintillators and Organic Luminofors No 5 pI, Kharkov ISC Pabl 1969, 257 (in Russian)
2. A.N. Panova, A.M. Kudin and A.V. Dolgopolova, Opt. i Spectros. **63** (1987) 444 (in Russian)
3. V.I. Goriletsky, V.A. Nemenov, L.G. Eidelman et al, J. Cryst. Growth **52** (1981) 509
4. S. Hashimoto and Y. Ohiwa, J. Phys. Soc. Jpn. **48** (1980) 1655
5. I. Baltog, L Marculescu, L Mihut et al, Phys. Stat. Sol. (a) **61** (1980) 573
6. G. Schulz and G. Breiter, Nucl. Instr. and Meth. **56** (1967) 179
7. J Pascual, F. Agullo – Lopez, Cryst. Latt. Def. **7** (1977) 161
8. G. Eqemberdiev, Trudy Inst. Fiziki AN Estonskoi SSR **51** (1980) 163 (in Russian)

Defect Luminescence of $LiBaF_3$ perovskites

M. Springis, P. Kulis, I. Tale, A. Veispals, H.-J. Fitting*

Institute of Solid State Physics, University of Latvia, 8 Kengaraga Str., LV-1063, Riga, Latvia
**Physics Department, Rostock University, Universitaetsplatz 3,D-18051, Rostock, Germany*

Abstract. Blue and red luminescence of intentionaly undoped $LiBaF_3$ crystals is studied. A broad, isotropic photoluminescence band centered at 410 nm can be excited with 210 nm – 275 nm light in as grown crystals. After X-irradiation at RT a new narrower, anisotropic luminescence band peaking at 425 nm appears having an additional excitation band at 290 nm. Furthermore, X-irradiation creates F- type centers and anisotropic centers with an absorption band at 630 nm and an luminescence band at 700 nm. No F- center luminescence is observed, all the others mentioned centers act as radiative recombination centers as well. It is speculated that the origin of the blue luminescence is due to oxygen defects and that the red luminescence is due to Fe impurities or complex structured defects.

Keywords: $LiBaF_3$, luminescence polarization, recombination, defect structure.

Introduction

$LiBaF_3$ crystals are a promising material for the ionizing radiation dosimetry and for their potential applicability in laser technology. In the case, that the stored radiation energy can be released as luminescence, it is necessary to have a suitable luminescence spectrum corresponding to the detector sensitivity, particularly in the blue region for the majority of photomultipliers and in the yellow- red spectral region for the photodiodes. The blue-green luminescence of Pb^{2+} or Ce^{3+} doped $LiBaF_3$ was investigated [1,2] and Eu^{2+} doped $LiBaF_3$ was studied for application as an X-ray storage phosphor [3]. Previous studies of pure $LiBaF_3$ crystals showed the presence of cross-luminescence with two emission maxima at 190 nm and 225 nm [4] and a broad self-trapped exciton emission band located near 300 nm [5].

Our aim was to investigate the blue photoluminescence, observed in most of the as grown $LiBaF_3$ crystals, and also possible luminescence centers, created by X-irradiation.

Results

As grown crystals

In most of the intentionaly non-purified and intentionaly non-doped as grown $LiBaF_3$ crystals we observe a broad blue luminescence band at 290 K (RT) intensity of which increases about 2 times when temperature is lowered to 90 K (Fig.1, circles). The blue photoluminescence excitation spectrum is complicated and involves several subbands in the spectral region from 200 nm to 280 nm (Fig.2, squares). Excitation in any subband results in the same broad luminescence band peaking at 410 nm. Measurements of azimuthal dependence of luminescence polarization (measurement method see, for example in [6]) show the polarization is nearly zero at any azimuthal angle (Fig.3a, circles; Fig.3b) indicating that the blue luminescence is isotropic. Intensity of the luminescence band at 410 nm changes slightly from sample to sample and only one sample treated with teflon shows no blue photoluminescence.

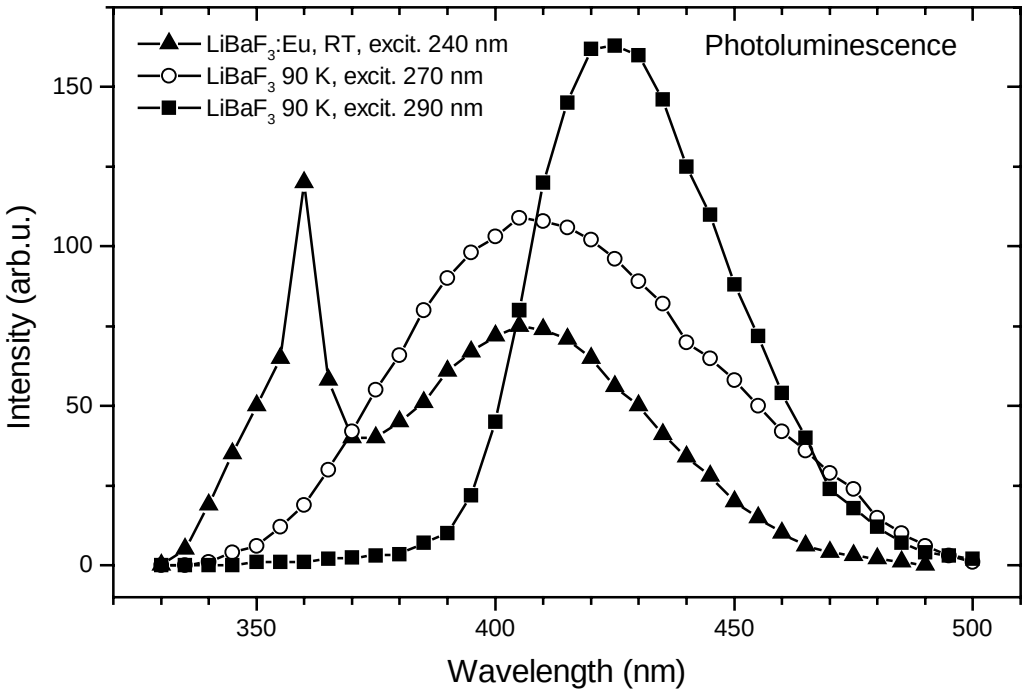

Fig.1. Blue photoluminescence of an undoped $LiBaF_3$ crystal at 90 K after X-irradiation at RT for 1h. For comparision: luminescence of Eu^{2+} in $LiBaF_3$ at RT is shown (triangles).

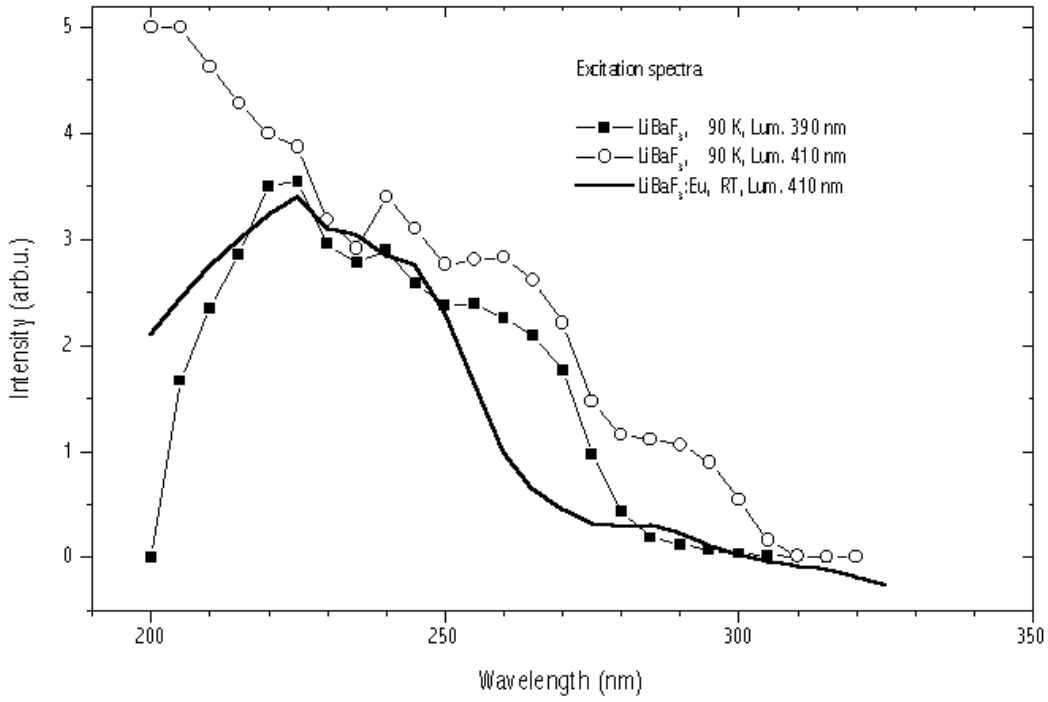

Fig.2. Excitation spectra of the blue luminescence of an undoped $LiBaF_3$ crystal at 90 K. For comparison the excitation spectrum of the Eu^{2+} luminescence at RT is presented (Bold line).

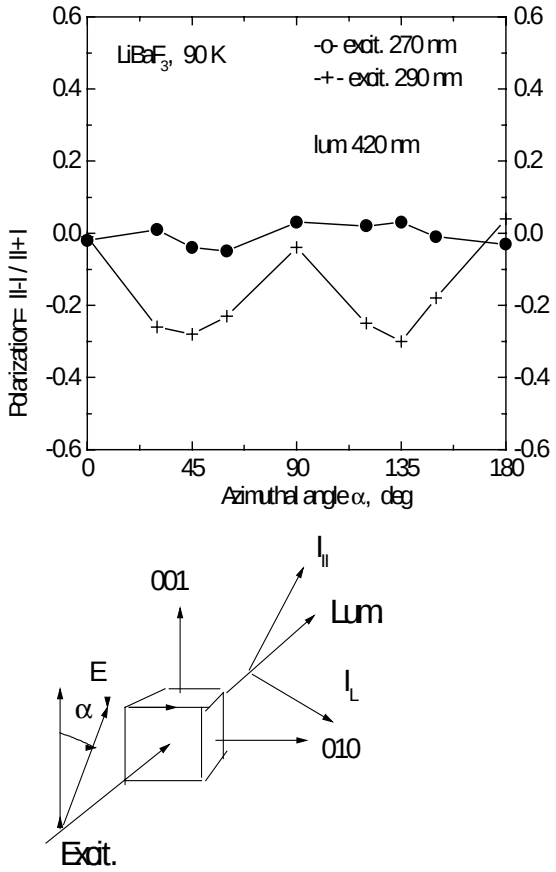

Fig.3a. Azimuthal dependence of polarization of the blue luminescence of $LiBaF_3$ crystal at 90 K under excitation with 270 nm light (circles) and with 290 nm light (crosses).
Fig.3b. Schematic illustration of the sample orientation with respect to the incident light electrical vector **E** and the emitted light electrical vectors $\mathbf{I_{II}}$ and $\mathbf{I_L}$, oriented parallel and perpendicular to the vector **E**.

X – irradiated crystals

X-irradiation of $LiBaF_3$ at 90 K as well as at RT decreases the intensity of the 410 nm luminescence and creates a new blue luminescence band centered at 425 nm (Fig.1, squares). The excitation spectra in the region from 220 nm to 280 nm are very similar for both the 425 nm luminescence band and for the 410 nm luminescence band. Nevertheless, the 425 nm luminescence band can be excited effectively with light having wavelength shorter than 220 nm and it has also an additional excitation band located at 290 nm (Fig.2, circles). Measurement of luminescence polarization under 290 nm excitation shows a significant azimuthal dependence (Fig.3a, crosses) indicating, that the luminescence is caused by an axial center, oriented in the <111> direction (C_3 symmetry). Generally the luminescence of an axial center can be π - polarized (dipol moment of optical transition oriented parallel to the center axis) or σ - polarized (dipol moment of optical transition oriented perpendicular to the center axis). Analysis of the azimuthal dependence of the luminescence polarization shows that the 290 nm light excites the σ - transition, but the 425 nm luminescence is caused by π - transition. The different optical transitions related to excitation and luminescence explain the large, more than 1 eV, Stokes shift.

Besides, X-irradiation at RT results in the creation of absorption bands, caused by F-type centers [7] and by centers with their band peaking at 630 nm. No luminescence of the F-centers was observed, whereas a strong luminescence band at 700 nm can be excited in 630 nm absorption band (see Fig.4 and Fig.5 respectively).

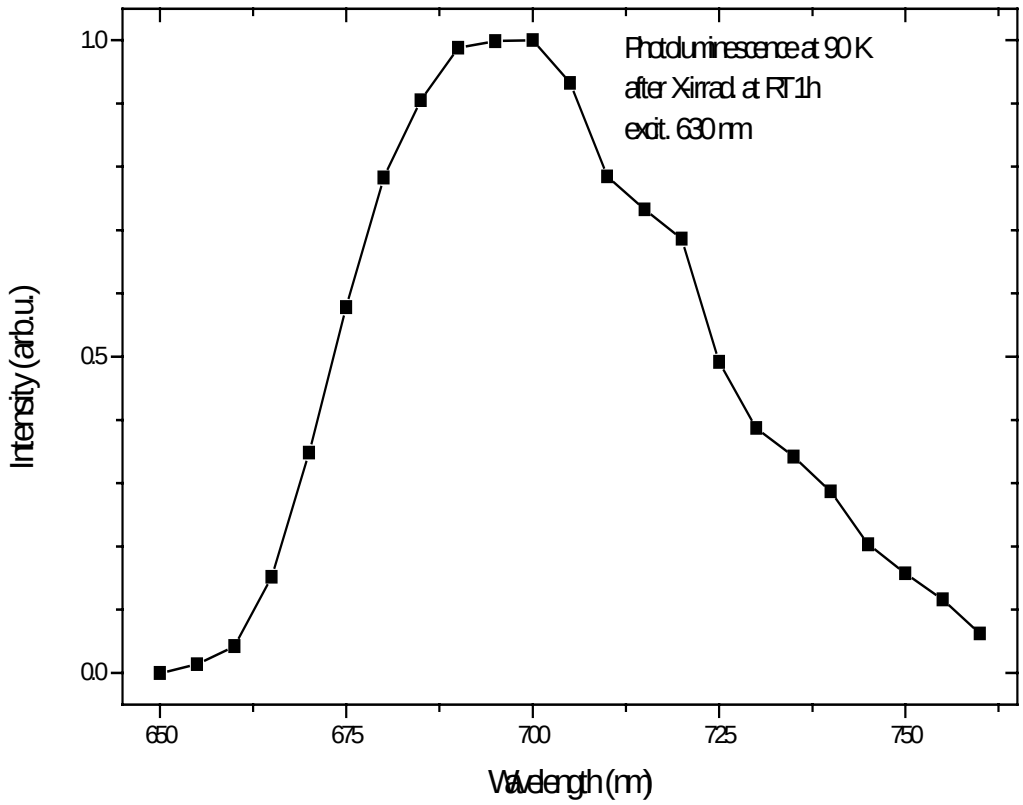

Fig.4. Red photoluminescence at 90 K of an undoped $LiBaF_3$ crystal, X-irradiated at RT for 1h.

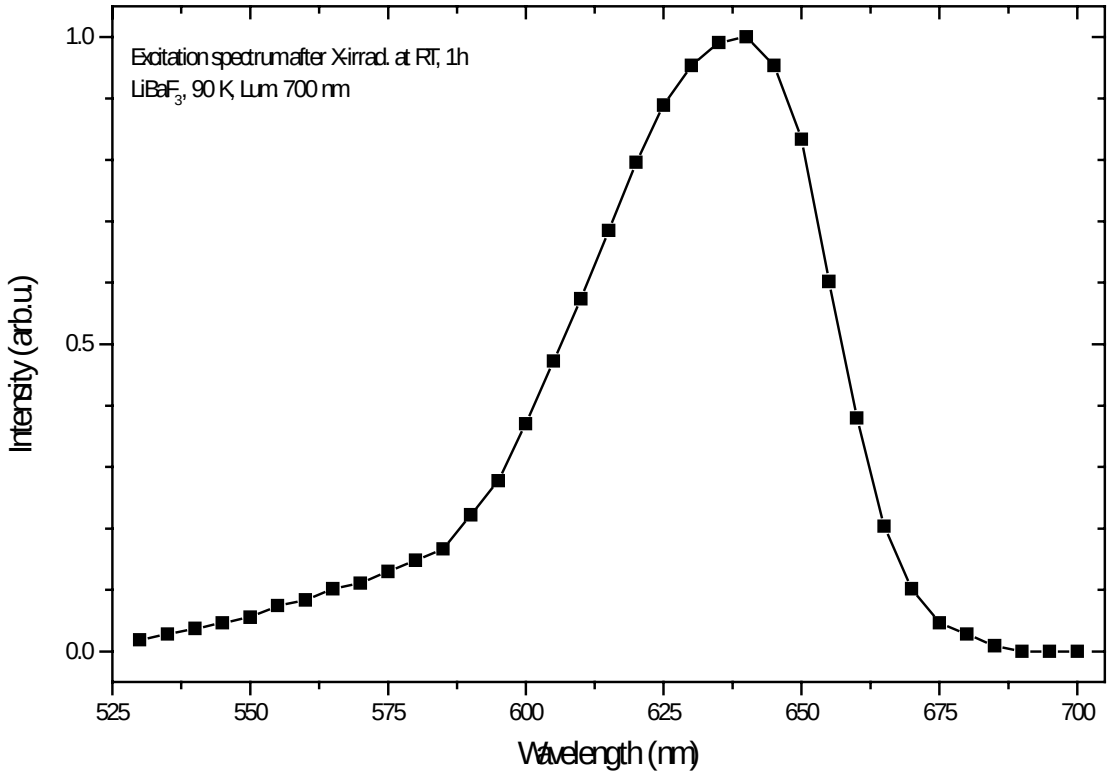

Fig.5. Excitation spectrum at 90 K of the red luminescence of an undoped $LiBaF_3$ crystal, X-irradiated at RT 1 for 1h.

Azimuthal dependence of red luminescence polarization shows that the red luminescence and its excitation are caused by π - π transitions in axial center, oriented in the <111> direction. Heating the crystal to 650 K completely destroys the red luminescence centers, while the 435 nm luminescence centers are only destroyed after heating the crystal to 900 K. Some correlation was observed between the intensity of the red luminescence and the Fe – impurity content in $LiBaF_3$ crystals. Moreover, the absorption at 630 nm saturates with X-irradiation doses faster than the F-center absorption.

All the mentioned emision bands are observed in thermostimulated luminescence spectra from 90 K to 500 K.

Discussion

The absence of blue luminescence in purified crystal suggests that the luminescence is probably due to impurity centers. It is well known that a widespread impurity in fluorides is oxygen. Difficulties to avoid oxygen indicate that nominaly undoped $LiBaF_3$ crystals are heavily contaminated with oxygen. Moreover, treatment with teflon helps to remove oxygen from fluoride crystal and really in such crystal no blue luminescence was observed. The spectral composition of blue luminescence and its excitation are very similar to those, caused by oxygen in other fluorides [8]. Therefore it maybe possible to assign the blue luminescence to oxygen. However, oxygen incorporated as O^{2-} in F^- site (non-cubic symetry!) needs a charge compensation. Thus a non-cubic center must be formed and an anisotropic luminescence is espected. Contrary to that an isotropic blue luminescence before X-irradiation was observed. Certainly, a π - σ - transition mixture is possibly causing an isotropic emision. After X-irradiation a complex axial center involving also oxygen maybe formed causing an anisotropic blue luminescence as observed. Another possibility is to assign the isotropic blue luminescence to a cation impurity, substituting Li or Ba which have cubic sites.

References

1. L. Prado et all., J. Phys. Chem. Sol. **57**, (1996) 413.
2. M. A. Dubinskii et all., J. Opt. Soc. Amer. **10**, (1997) 30.
3. C. T. Xia, C. S. Shi, Mat. Res. Bul. **32**, (1997) 107.
4. P. A. Rodnyi, M. A. Terrekhin, E. N. Melchakov, J. Luminescence **47**, (1991) 281.
5. M. J. Knitel, P. Dorenbos, J. T. M. de Haas, C. W. E. van Eijk, Rad. Meas. **24**, (1995) 361.
6. P. P. Feofilov, The Phys. Basis of Polarized Emission, Consult. Bureau, New York, 1961.
7. P. Kulis et all., Rad. Eff. and Def. In Solids (1999), in press.
8. P. W. M. Jacobs and S. H. Song, J. Phys. Chem. Sol. **41**, (1980) 437.

The Influence of Alkali Impurities on the BaFBr: Eu^{2+} Photostimulated Luminescence.

A. Shalaev and E. A. Radzhabov

Vinogradov Institute of Geochemistry, Academy of Sciences, Siberian Branch, Favorski Street 1a, PO Box 4019, 664033 Irkutsk, Russia. E-mail: alshal@igc.irk.ru

Abstract. The X-ray storage phosphor BaFBr:Eu^{2+} doped with alkali impurities (Na^+, K^+, Rb^+) gives a photostimulated spectrum shifted to lower photon energies. The photostimulation luminescence intensity considerably increases compared to BaFBr:Eu^{2+} upon room-temperature X-irradiation. This red-shift of the photostimulation spectrum is caused by formation of F_A centers on the Br^- sublattice as electron traps.

Keywords: BaFBr:Eu^{2+}, storage phosphors, photostimulated luminescence, F-center.

Introduction

Barium fluorobromine doped with Eu^{2+} is an important storage phosphor in which X-ray produced images are stable for long periods in the dark at room temperature. Currently it is widely applied for production of the imaging plates for radiography. Medical imaging plates are used in X-ray diagnostics, replacing conventional photographic film. This results in a greatly reduced X-ray dose for patients. The photostimulated luminescence (PSL) is excited usually by light with a He-Ne laser (633 nm) for the readout process. This gives the blue emission of Eu^{2+} at 390 nm. It is known that doping with some impurities (for example Ca^{2+}, Sr^{2+}) shifts the photostimulation spectrum towards the infrared region. This could allow the use of light-emitting diodes, instead of gas lasers, for the readout process [1,2]. This paper reports the redshift of photostimulation spectrum for BaFBr:Eu^{2+} crystals with alkali doping (Na^+, K^+, Rb^+).

Experimental

For the PSL measurements we prepared undoped BaFBr:Eu^{2+} crystals and those doped with varied concentrations of NaF, KF, RbF. The crystals were grown with the Shteber method in a graphite crucible in helium-fluorine atmosphere in order to reduce oxygen contamination. Stoichiometric mixtures of $BaBr_2$ and BaF_2 were used. All samples were doped with 0.1 mole % of Eu^{2+}.

For the PSL measurements the samples were irradiated with an X-ray source (30 kV, 10 mA) for 3 min. at room temperature. Low-energy X-rays were filtered out with an Al filter (thickness 1 mm). The excitation spectra were performed with a MDR12 grating monochromator and a halogen lamp. The light from a halogen lamp passed through an optical filter allowing only wavelengths longer then 500 nm to be transmitted. This was necessary to separate the stimulating light from Eu^{2+} emission. The UV luminescence was detected by a FEU106 photomultiplier through an optical filter appropriated for Eu^{2+} emission. The absorption spectra were measured in the visible and ultraviolet regions with a “Specord UV VIS” apparatus. For the absorption investigations, X-irradiation was carried out at RT (40kV, 40 mA, 20 min).

Figure 1 shows the PSL spectra of undoped BaFBr:Eu^{2+} and BaFBr:Eu^{2+} with alkali doping (2% K^+, 2%Rb^+ and 1.5%Na), X-irradiated at room temperature. In undoped BaFBr:Eu^{2+} the prominent peaks of the PSL spectrum at 2.18eV and 2.45eV were observed.

Upon 2% K and 2% Rb doping, the intensity of the PSL peak at 2.18 eV is increased by a factor of about 2. Moreover, in the case of 2% Rb doping the PSL peak was redshifted from 2.18 to 2.09 eV. Best results were obtained for sodium doping. Upon 1.5% Na doping the intensity of the PSL is increased by a factor of 12 in contrast to undoped samples; the PSL peak shifted to 2.06 eV.

The results for BaFBr:Eu^{2+} with various alkali doping are listed in table 1:

Table 1.

Storage phosphor	**PSL peak position** (ev)	**Redshift of PSL spectrum** (eV)	PSL intensity ratio of alkali doped to un-doped phosphors
BaFBr:0.1%Eu^{2+}:5%Na^{+}	2.06	0.08	13
BaFBr:0.1%Eu^{2+}:4%K^{+}	2.06	0.04	4
BaFBr:0.1%Eu^{2+}:2%Rb^{+}	2.09	0.06	2
BaFBr:0.1%Eu^{2+}	2.18	0	1

An increased impurity concentration leads to an increased PSL intensity. The largest PSL intensity is obtained for 5% NaF doping; the peak intensity is increased by a factor of 13.

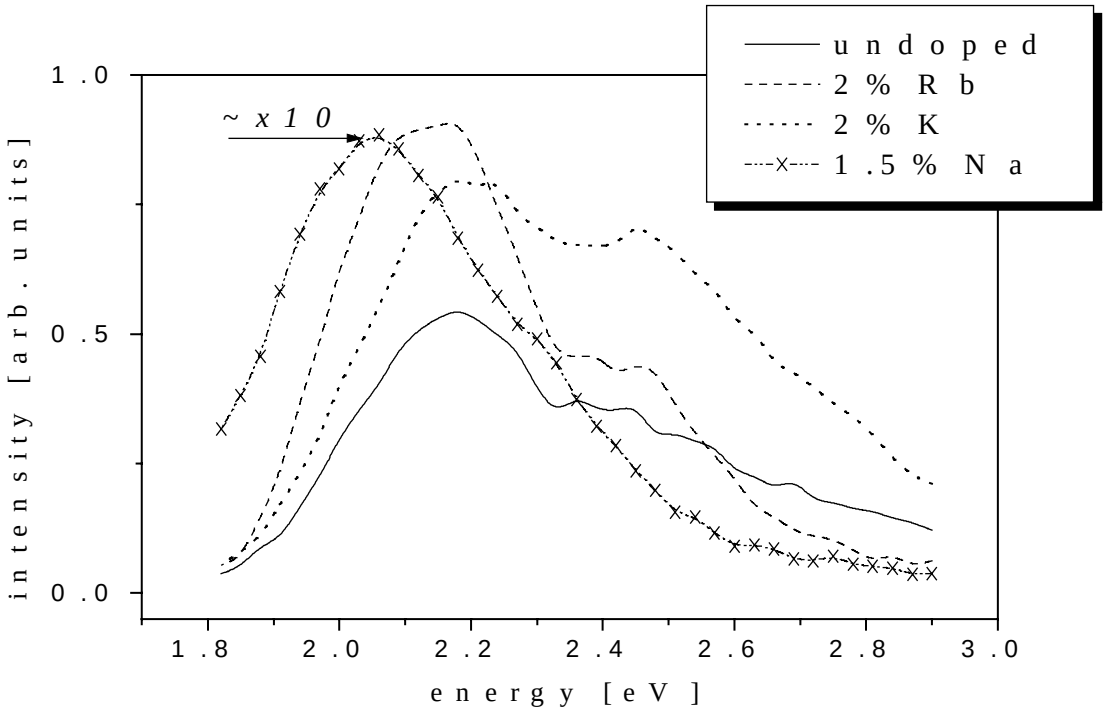

Fig1. PSL spectra of undoped BaFBr:Eu^{2+} and BaFBr:Eu^{2+} doped with various alkali ions (2%Rb, 2%K, 1.5%Na), X-irradiated at 300K. The PSL intensity of BaFBr:Eu^{2+}:1.5%Na (the curve with cross (x)) is scaled up by a factor of 10.

The absorption bands at 2.65 eV and 2.2 eV and excitation spectra (fig.2) appeared after X-irradiation of BaFBr:Eu^{2+}. They are ascribed to F(F^{-}) and F(Br^{-}) centers [3]. The doping with Na^{+} (or other alkali impurities) causes a shift of the PSL band at 1.98 eV to lower energies of about 1.9 eV. The absorption bands are shifted, as the PSL peak, to 1.99eV for BaFBr:Eu^{2+}:5%Na^{+} after X-irradiation at room temperature.

An increased impurity concentration leads to a decreased stimulation energy. The stimulation energy is the energy required for the readout of the active centers. The stored energy is released faster in BaFBr:Eu^{2+} with alkali doping then in undoped BaFBr:Eu^{2+}, by using the same intensity for the excitation light.

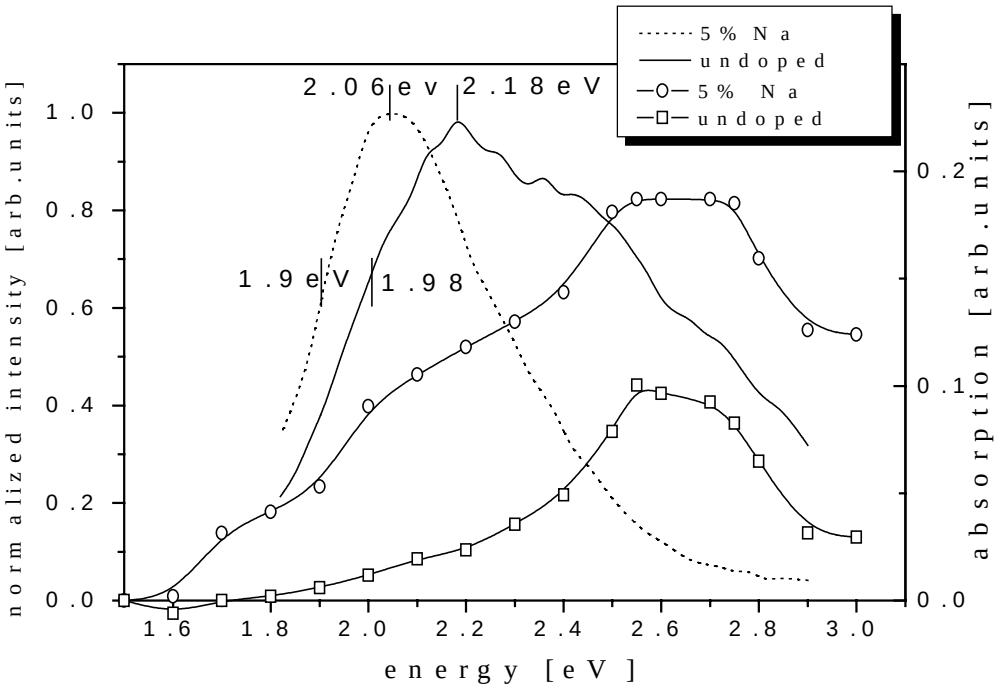

Fig.2. Normalized PSL spectra of BaFBr:Eu^{2+} and BaFBr:Eu^{2+}+5%NaF; absorption spectra (the curves with the squares and circles) of BaFBr:Eu^{2+} and BaFBr:Eu^{2+}+5% NaF. Spectra measured at room temperature.

Discussion

BaFBr:Eu^{2+} like PbFCl has matlockite structure: the fluorine layers and the double layers of bromine are separated by the barium layers. The doped Eu^{2+} ions replace Ba ions. The luminescence and storage mechanisms of BaFBr:Eu^{2+} phosphors have been the subject of several studies. But the exact mechanism of the PSL process is still not very clear. There are few models which describe the PSL process in BaFBr:Eu^{2+} [4,5]. All models identify F centers as electron traps. The electron excites to the conduction band leaving the holes in the valence band on X-irradiation of this material. The free electrons are trapped both by the fluorine or bromine anion vacancies making F (F^-) and F (Br^-) centers (the absorption peaks at 2.65 eV and 2.2 eV on fig.2, respectively). The F (F^-) centers do not play any role in the PSL process of BaFBr:Eu^{2+} [3]. The annihilation of F (Br^-) centers during photostimulation is radiative, since the electron-hole recombination in this case takes place near the Eu^{2+} sites. The above conclusions were derived in analogy to alkali halides. The substitution of Ba^{2+} ions by the small percentage of alkali impurities results in the generation of charge compensating Br^- vacancies caused by alkali doping of BaFBr:Eu^{2+}. The $F_A(Br^-)$ centers are produced by X-irradiation at room temperature. The optical absorption band at 2.2 eV of the $F_A(Br^-, Na^+)$ centers is broadened to lower energies, compared to the regular $F(Br^-)$ centers, by about 0.2 eV (fig.2). This is in agreement with the red shift of the PSL spectra of BaFBr:Eu^{2+}:Na. Apparently, the $F_A(Br^-, Na^+)$ centers dominate in the PSL spectrum at low energies (fig.2). Possibly the increase of photostimulated luminescence is due to the presence of charge compensating bromine vacancies that lead to the creation of more F centers. It is not clear why the sodium impurity leads to a better redshift than the potassium or the rubidium doping. One reason could be that the Na- ions have a smaller ionic radius (Na^+- 0.98A^o, K^+- 1.33A^o, Rb^+ - 1.49A^o [6]). The size of the Na-ion is smaller then the size of the replaced Ba-ion. Due to lattice relaxation the ions surrounding the $F_A(Br^-, Na^+)$-center move slightly inwards to the vacancy. Thus, they are reducing the diameter of the vacancy. That leads to a broadening of the absorption band of the $F(Br^-)$ center at 2.2 eV to 1.99 eV for the $F_A(Br^-, Na^+)$ centers.

In conclusion, the alkali doping leads to the formation of $F_A(Br^-)$ centers, a photostimulation redshift, and an intensity increase. The best results were obtained for sodium impurity, but the potassium and rubidium doping greatly improves the PSL properties of BaFBr:Eu^{2+} as storage phosphor too.

References

1. C. Dietze, T. Hangleiter, P. Willems, et. al., Appl. Phys. **80(2)** (1996) 1074-1078
2. S. Schweizer, P. Willems, P. J. R. Leblans, L. Struye, and J.-M. Spaeth, J.Appl.Phys.**79(8)** (1996) 4157-4165
3. A. R. Lakshmanan, Phys. Stat. Sol. **A 153** (1996) 3-27
4. F. H. Koschnik, J.-M. Spaeth, R. S. Eachus, W. G. McDugle, and R. H. D. Nuttal, Phys. Rev. Letters **67** (1991) 3571
5. H. H. Ruter, H. von Seggern, R. Reininger, and V. Saile, Phys. Rev. Letters **65** (1990) 2438
6. I. A. Parfianovich, E. E. Pensina, The electron color centers in the ionic crystals, ISU, Irkutsk, 1977

Detection of thermal and resonance neutrons using scintillators based on complex oxides

V.D. Ryzhikov, L.L. Nagornaya, S.F. Burachas, E.A. Danshin,
O.V. Zelenskaya, L.A. Litvinov, E.A. Losseva, V.V. Chernikov

STC for Radiation Instruments,
Concern «Institute for Single Crystals» of NAS Ukraine,
60 Lenin ave., 310001 Kharkov, Ukraine

Abstract. Spectra of pulse amplitudes of scintillation detector based on the complex oxides Gd_2SiO_5 and Lu_2SiO_5 (GSO and LSO) are presented in this paper. Comparative sensitivity studies were carried out for these scintillators. The possibility of the neutron detection by the products of the reactions of thermal and resonance neutron capture by gadolinium nuclei is shown. This is ensured by the detection of low energy gamma-radiation of the excited nuclei of Gd or Lu. With a purpose to reveal possible errors of measurements, the study of the effect of the induced gamma-radiation in the Gd or Lu-based scintillators is also presented. It appears as the result of crystal activation by neutrons.. The expediency of LSO application for the detection of thermal and resonance neutrons is also discussed.

Keywords: scintillator, silicates,thermal neutrons, resonance neutrons.

Introduction

The problem of spectrometry of thermal neutrons remains a question of present interest. It is known that a number of scintillation single crystals based on complex oxides are characterised, apart from high detection efficiency of gamma-quanta, by a large cross-section for thermal and over-thermal neutrons capture. Such single crystals include silicates and aluminates of rare earth elements, indium silicate, lead and cadmium tungstates, and some others.

In [2] were described the results of the study of $CdWO_4$ crystals intended for the detection of thermal and resonance neutrons. Low energy γ-quanta of the radiation trapping on the nuclei of tungsten and cadmium were used as nuclear reaction products.

Concerning silicates, Reeder [1] has shown that it is possible in principle to detect thermal neutrons using thin single crystals of gadolinium orthosilicate doped by cerium, Gd_2SiO_5:Ce . The measurements were conducted by usage of two-inch lead protected screen. The γ-peak (E_γ=77 keV) of the resonance neutron trapping on nuclei of ^{157}Gd, ($\sigma_{n,\gamma} = 2.5 \times 10^5$ barn) was observed in the pulse amplitude spectrum.

The possible use of $CdWO_4$ single crystals for thermal and resonamce neutrons detection was described in paper [2]. According that, neutrons can be detected using secondary gamma emission after neutron activation of tungstate and cadmium nuclei. LSO crystals have a light yield comparable with that of NaI(Tl). The lutetium nuclei have a large cross-section for thermal and resonance neutrons capture. However, the presence of a natural radioactive isotope, ^{176}Lu, and the high induced activity caused by the capture of neutrons may enhance the background. Therefore, the study of the influence of these factors on the detection sensitivity seems to be expedient.

The purpose of this work is to continue studying [1-3] the possibility of application of silicate scintillators such gadolinium and lutetium silicates doped with cerium (GSO and LSO) as for neutron detection. The investigations were carried out in the mixed field of ^{239}Pu

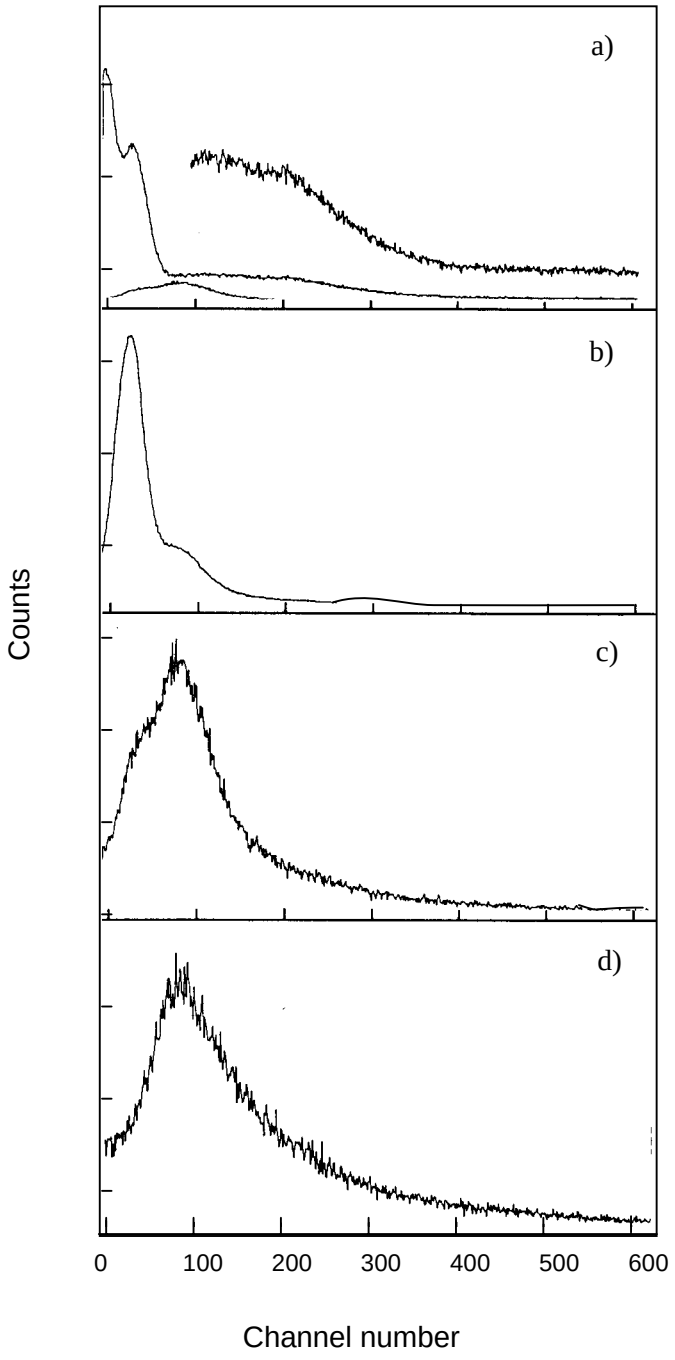

Figure 1: Pulse amplitude spectra from GSO crystals: a –calibration of the spectrometer ^{241}Am and ^{137}Cs; b – ^{239}Pu-Be are source of neutrons of a crystal without passive protection; c – passive protection 4 mm in thickness; d -passive protection 10 mm in thickness

- Be (α, nγ) - sourse of neutrons in the energy range of the most intense lines of internal conversion electrons (on-line) and in regime of induced radioactivity at excitation of nuclei with high cross-section of thermal neutrons trapping.

Experimental

The single crystals (dimensions 40×2 mm)of GSO and LSO were prepared by the Czochralski technique.

Irradiation of the crystals was carried out with a ^{239}Pu-Be source (10^5 neutrons/s). It was placed into a polyethylene sphere, 150 mm in diameter. The yield of the thermal neutrons at the surface of the sphere was 0.09 with respect to neutron source.

Activation of samples was carried out using a similar source of 5.0 10^6 neutrons/s in a paraffin container-moderator. The flux density of neutron source at the location of scintillator was 10^3 neutrons/s. GSO crystals were studied in the regimes of both induced radioactivity and on line. The intrinsic radiation background and induced activity of LSO crystals were studied. The conditions of optimisation of passive protection from γ-radiation of ^{239}Pu-Be were considered.

Results and discussion

The pulse amplitude spectra of GSO crystals are shown in Fig.1a-1d. They were registered under excitation of ^{137}Cs and ^{241}Am γ-sources and in the mixed field of gamma-neutron radiation from the ^{39}Pu-Be source. γ-lines of ^{137}Cs (E_γ = 662 keV), ^{137}Ba (33 keV) and ^{241}Am (59.6 keV) are distinctly seen in Fig 1a. Fig. 1b shows the spectrum of ^{241}Am measured without passive protection. The occurrence of ^{241}Am is explained by its accumulation as a result of ^{241}Pu decay. A peak of full absorption (FAP) at 96 keV is well pronounced in the spectrum of pulse amplitudes of GSO in the field of the neutron source, the spectrum being registered in the regime on line. According to Reeder [1] the γ-line of the thermal neutron capture with E_γ = 79 keV (^{158}Gd, $\sigma_{n,\gamma}$ = 2.5 10^5 barn) and E_γ = 89 keV (^{156}Gd, $\sigma_{n,\gamma}$ = 6.1 10^4 barn) makes the main contribution to this peak.

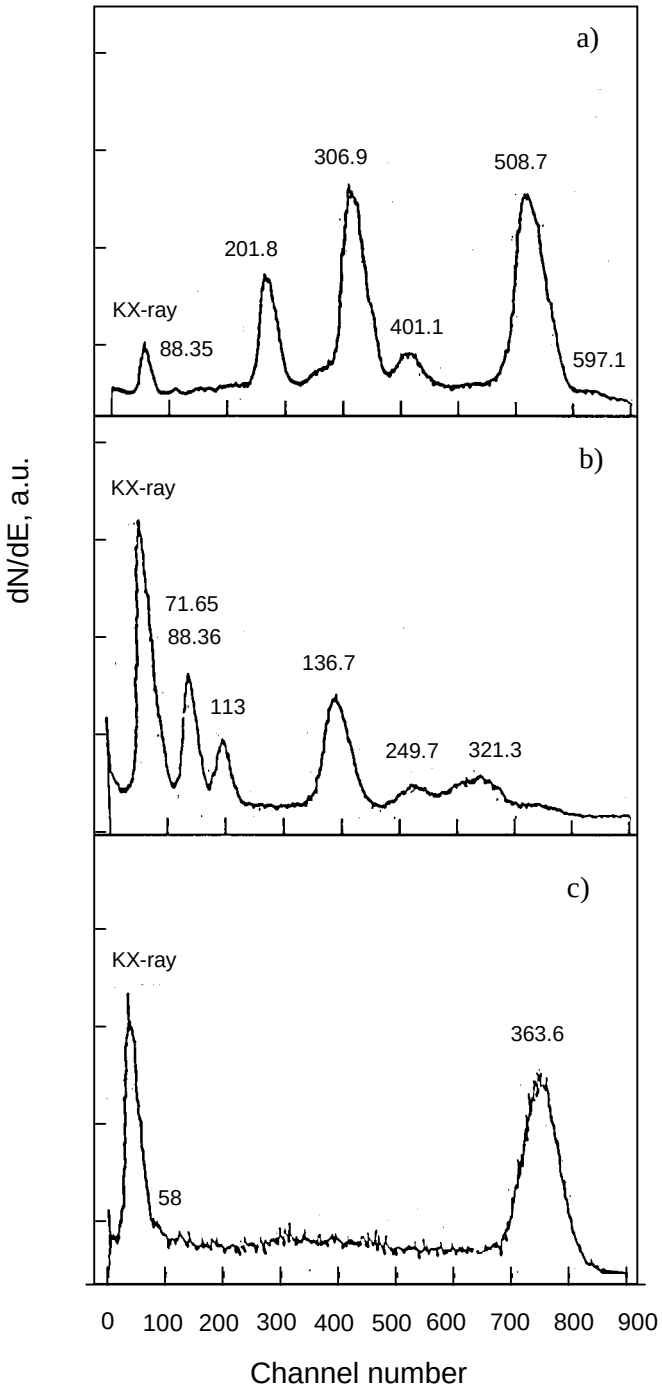

Figure 2: Pulse amplitude spectra from GSO and LSO crystals (maxima of peaks are given in keV): a – intrinsic radioactivity of LSO, ^{176}Lu; b – induced radioactivity of LSO, ^{176m}Lu and ^{177}Lu; c - induced radioactivity of GSO, ^{159}Gd.

However, regarding data of A.A. Harms and G. McCormack [4] the intensity E = 79 keV is 10 % and the intensity of lines of internal conversion electrons with E_ε = 71 keV and 78 keV caused by emission of this γ–line is 33.0 and 7.6 %, respectively. The intensity E_γ = 89 keV (^{156}Gd) makes 14 % and that of electrons of internal conversion with E_e = 81 keV and E_e = 88 keV makes 26.6 % and 6.2 % respectively. That means that the main contribution to FAP from thermal neutrons is made by internal conversion electrons. Deviations in FAP position are probably explained by the difference of energy scales of the spectrometer at calibration by electrons of internal conversion and γ-quanta.

The pulse amplitude spectra from the intrinsic and induced radioactivity of LSO and GSO scintillators are shown in Fig.2. The most distinctly seen are γ-lines of the natural radio-isotope ^{l76}Lu with E_γ = 88.35, 201.8, 306.9, 401.1 and 508.7 keV in the spectrum of LSO. FAP from γ-quanta ^{l77}Lu with E_γ = 71.65 keV and ^{l76m}Lu with E_γ = 88.36 keV are pronounced in the spectrum of the induced radioactivity of LSO (Fig.2b). Besides, FAP from the gamma-line of Lu with E_γ = 113, 208.4, 249.7 and 321.3 keV are also observed.

The pulse amplitude spectrum of ^{159}Gd, formed by the reaction ^{158}Gd (n,γ) → ^{l59}Gd is presented in Fig. 2c. The most intensive FAPs have the energies 363 keV and 58 keV, the latter coinciding with KX-quanta of Gd. The comparison of Fig.1 and 2 shows that GSO has advantage to LSO for the detection of thermal neutrons by the products of radiation trapping reactions, owing to its low intrinsic radioactive background and its low induced activity in a neutron flux.

The conducted investigations of GSO and CWO crystals [1-3] and the study of their characteristics in a flux of thermal neutrons confirm that the most promising at present crystals for practical applications in the spectrometry of thermal and resonance neutrons considered should be the above mentioned ones. Though for both crystals the energy of the

most intensive lines of γ-quanta of thermal neutrons radiation trapping lies in the close energy regions, the application of both crystals ensures the detection of resonance neutrons in the specified energy region. The low intrinsic radiation background of both crystals and their comparatively low neutron-induced activity favour this fact.

The results of the study of LSO allow to conclude that its application in on line regime will be impeded due to its high intrinsic radiation background and neutron-induced activity in the studied energy range.

Conclusions

The possibility of neutrons detection using the low energy γ-qanta produced by resonanse neutron radiation trapping reaction by gadolinium nuclei has been shown.

The pulse amplitude spectra of LSO scintillators from the intrinsic and induced radioactivity in neutron flow field have been studied. The authors marked the difficulties of using on line regime for LSO detection of thermal and resonance neutrons.

References

1. P.L. Reeder, «Neutron detection using GSO scintillator», Nucl. Instr. and Meth., A340 (1994) 371-378.
2. V.D. Ryzhikov, L. Nagornaya, V. Volkov et al, «Studies of cadmium tungstate single crystals for detection if thermal neutrons» in Proceeding of the International Conference on Inorganic Scintillators and their Applications, «SCINT'97», Shanghai, P.R. China, September 22-25, 1997, CAS, Shanghai Branch Press, 157-160.
3. V.D. Ryzhikov, S.F. Burachas, V.G. Volkov et al, «Neutron flux measurements using scintillator-photodiode-preamplifier system and new type scintillators» in Proceeding of the International Conference «Neutrons in Research and Industry», June 9-15, 1996, Crete, Greece, 586-595.
4. A.A. Harms and G. McCormack, «Isotopic conversion in gadolinium-exposure neutronimaging», Nucl. Instr. and Meth., 118 (1974) 583-587.

Point defects in beta-irradiated $Li_2B_4O_7$

E.F.Dolzhenkova V.N. Baumer, B.V. Grinyov, L.A.Grin',
M.F.Dubovik, A.V.Tolmachev, V.A.Tarasov

Institute for Single Crystals, NAS of Ukraine 310001, 60 Lenin ave., Kharkov, Ukraine

Abstract. Radiation-induced point defects were investigated in beta-irradiated $Li_2B_4O_7$ single crystals by thermostimulated methods in the temperature range 295-650K, optical absorption and X-ray analysis.

Keywords: Thermoluminescent dosimeters, lithium borate, beta-irradiation, point defect, thermostimulated luminescence, optical absorption, X-ray diffraction analysis

Introduction

Scintilation parameters of $Li_2B_4O_7$ (LTB) single crystals were described in [1]. Cu-doped LTB single crystal is known as an efficient material for high temperature dosimetry. Thermostimulated luminescence (TSL) glow curves of LTB samples irradiated with different gamma doses (from 0,5 up to 500 Gy) consist of three intense peaks at 433, 533 and 578K and some weak ones [2], but authers do not discribe the nature of the trap-centres. There are two intense TSL peaks at 423 and 458K, which are observed after irradiation by electron-beam with an energy of 4MeV ($F=5\ 10^{16} cm^{-2}$) and it is presumed that trapped-centres namely responsible for these peaks are oxygen vacancies in different-fold coordinations, from BO_3 triangles and BO_4 tetrahedra respectively [3,4]. Up to now there is no sufficient information about trapped-centers in LTB single crystals. In present study we identify and characterize dominant point defects induced in LTB by radiation.

Experimental

LTB single crystals were grown by Czochralski method. Main crystal parameters were analogous to those of perfect LTB crystals grown by Czochralski method [5]. Transparent samples 10x10x2 mm^3 were produced with optical c-axis along the 2mm dimension. Crystal samples were irradiated by radionuclide beta-source Sr-90:Yb-90 with activity 2 Ci (dose=7 10^5Gy). TSL was investigated within 290-650K temperature range, the sample heating rate was approximately 20K/min [6,7]. Three intense peaks at 414K, 473K, 548K and one weak peak at 365 K were observed on the TSL curve of LTB. This corresponds to the trap levels with activation energies of 0.83 eV, 0.96 eV, 1.0 eV and 0,73 eV respectively. Absorption spectra of additively colored crystals were measured by means of SPECORD M40 two-beam spectrophotometer at room temperature.

Results and discussion

LTB single crystals showed no optical absorption bands at wavelengthes 200-900 nm [7,8]. After irradiation the samples appears slightly yellowish in colour. Optical spectra show a weak absorption peak at 235 nm and a broad band in the range of 260-375 nm. It was determined that broad band consists of three individual bands peaking at 285 nm, 321 nm and 352 nm. The behaviour of the absorption spectra of the additively colored LTB crystals was examined in isochronal annealing experiment from 350 to 650 K at intervals of about 25K. The specimen was kept for 5 min at each annealing temperature and the optical absorption measurements were made at the same time. Absorption spectra of beta-irradiated single crystals after thermal annealing are shown in fig.1, too. It was found that radiation-induced

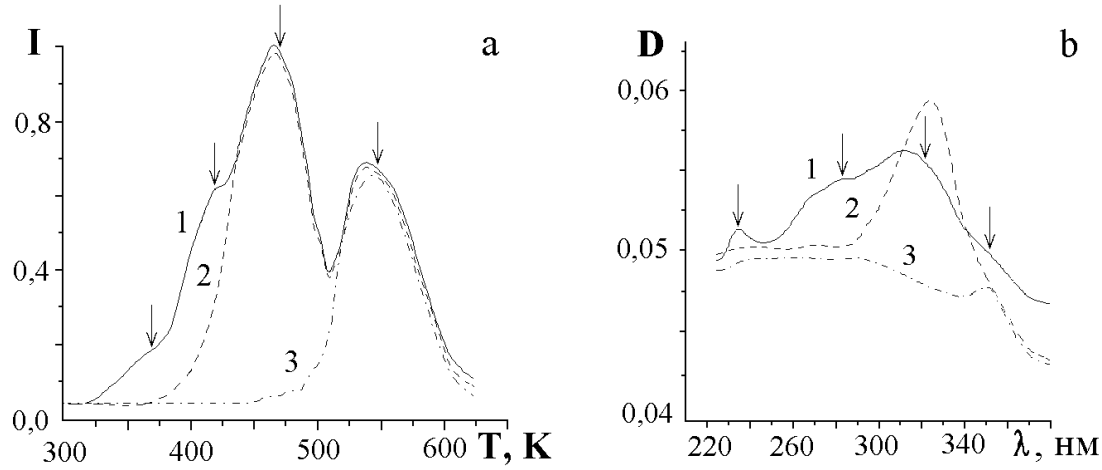

Fig.1.Thermoluminescence data (a) and absorption spectra (b) of additively colored $Li_2B_4O_7$ single crystals: 1-before thermal annealing and after thermal annealing at 2-414K and 3-565K. Gaussian maximum is pointed by an arrow.

peaks at 235 nm and 285 nm decay at 414 K, absorption bands at 321 nm and 352 nm decay at 565 and 630K. Comparison of thermal annealung results and TSL glow curve shows that the thermal decay of trapped-centres and the optical absorption bands absorption agrees well with the position of the dominant thermoluminescence peak.

Accourding to the calculations of F^+-center model in LiB_3O_5 single crystals, which is formed by electron trapped in an oxygen vacancy within (BO_4) groups one could expect optical absorption band at 320 nm [9]. Absorption peak at 345 nm is close to that of the F-center in irradiated gallium-gadolinium garnet single crystals[10]. Similar model of centres was found in alkali-borate glasses, in which an electron is trapped in an oxygen vacancy localized near alkali-ion [11]. So, in our reserch absorption bands at 321 nm and 352 nm could be ascribed to one (F^+-center) and two elecnrons (F-center) trapped in an oxygen vacancy, respectively.

Absorption bands at 235 and 285 nm could be assigned to main and additional levels of O^--center as in irradiated LiB_3O_5 single crystals [12]. Trapped hole could be localized on an oxygen-ion that bridges two borons: one three-coordinated and the other one four-coordinated, adjacent to the lithium vacancy.[13].

A serious support for the interpretation of the 321 and 352 nm absorption peaks as F^+- and F-center respectively, can be obtained from the data of thermal stability of centers in beta-irradiated LTB. During thermal annealing conversion $F \rightarrow F^+$ was found originating from hole cupture at F-centers thermally released from O^--centers. This leads to the amplitude increase of the 321 nm optical band due to F^+-center and noticeable decrease of the 352 nm absorption peak assigned to F-center, when absorption bands connected with hole-trapped centers disappeard. Similar regularities are characteristic for thermal annealing of neutron-irradiated BeO single crystals [14].

The most intense TSL peak is connected with the F^+-center decay. TSL spectra of LTB crystals consist of broad bands at 370-420 nm and at 550-650 nm.

X-ray diffraction data of beta-irradiated LTB single crystals were obtained using D500 “SIEMENS P3/PC” diffractomiter in Mo-Kα radiation with graphite monochromator. The date analysis was performed by means of the program SHELTXL-PLUS. The presence of different peaks with heights up to 0,7 e/A^3 near O(1), O(2), O(3) -ions in the D-pattern of the electron density for the irradiated samples is an evidence of possibility originating of oxygen vacancy in this sites. This O-ions bridges two boron atoms one three-coordinated and the other four-coordinated neighboring to Li-ion (fig.2). Site occupation factors calculaton shows

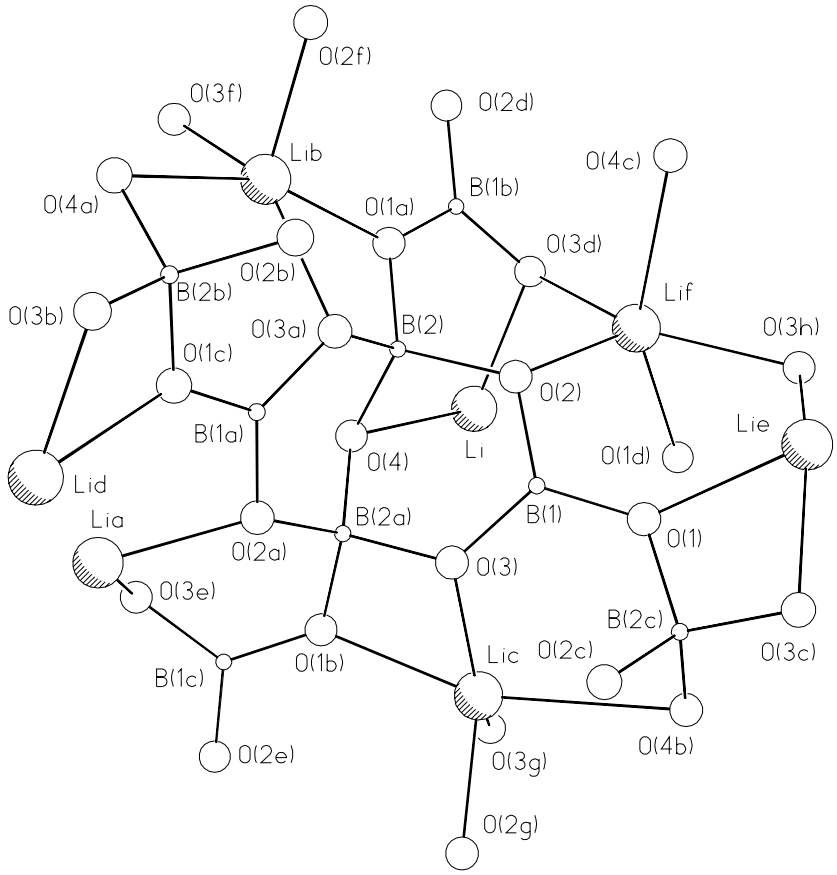

Fig.2.Structure of $Li_2B_4O_7$. The basic structural unit (B_4O_9) is marked by thick lines.

lack of O(1)- atom in their crystallographic position - K=0.986. These results allow to assume that O(1)-atom connected to the two neighbouring structural blocks (B_4O_9) is a preferential ones for vacancy originating. The hole-like center could be realized at O(1)-O(3)-atoms. Such a possibility is confirmed by the presence of Li-vacancy in irradiated LTB crystals (K=0.929).

References

1. E.L.Vinograd,Yi.T.Vyday,L.B.Zagariy et al.,Functional materials 1(1994)152.
2. Y.Kutomi,M.H.Kharita,S.A.Durrani,Radiat. Meas.24(1995)407.
3. Ya.V.Burak,B.N.Kopko,I.T.Lyseyko et al.,Neorg.Mater.25(1989)1226
4. S.F.Radaev,L.A.Muradyan,L.F.Malakhova et al.,Kristallografiya 34(1989)1400.
5. B.P.Nazarenko,E.F.Dolzhenkova,A.B.Levin et al.,Functional materials1(1994) 146.
6. .M.F.Dubovik,A.N.Shekhovtsov,L.A.Grin' et al.,IEEE International Fregency Control Symposium,Pasadena,USA,1998.
7. V.N.Baumer,L.A.Grin',E.F.Dolzhenkova et al.,Functional materials 6(1999)154.
8. O.T.Antonyak,Ya.V.Burak,I.T.Lyseiko et al.,Optica i Spectroscopiya 61(1986) 550.
9. A.V.Kuznetsov,A.B.Sobolev,I.N.Ogorodnicov,Fiz. Tverd. Tela 36(1994)3530.
10. V.G.Kostishin,L.M.Letiyk,O.E.Bugakova, Neorg.Mater.33(1997)853.
11. S.Arafa,A.Bishay, Phys.Chem.Glasses 10(1969)192.
12. I.N.Ogorodnikov,A.V.Porotnikov,A.V.Kruzhalov et al., Fiz. Tverd. Tela 40(1998) 2008.
13. I.N.Ogorodnikov,A.V.Porotnikov,S.V.Kudyakov et al., Fiz. Tverd. Tela 39(1997) 1535.
14. S.V.Gorbunov,K.N.Giniyatulin,A.V.Kruzhalov et al., Fiz. Tverd. Tela 28(1986) 606.

Nonproportionality and temporal response of ZnSe:Te scintillator studied by large area avalanche photodiodes and photomultipliers.

M. Balcerzyk[1], W. Klamra[2], M. Moszyński[1], M. Kapusta[1], and M. Szawlowski[3]

[1]*Soltan Institute for Nuclear Studies, 05-400 Otwock, Poland*
[2]*Royal Institute of Technology, Department of Physics, Frescati S-104 05 Stockholm, Sweden*
[3]*Advanced Photonix, Inc. 1240 Avenida Acaso, Camarillo, CA 93012, USA,*

Abstract*:* We have studied the scintillation properties of ZnSe:0.2%Te from STC Institute for Single Crystals, Kharkov, Ukraine. It is low-density crystal (5.42 g/cm^3). The emission length of the crystal is 610 nm. The luminescence pulse shape is single-exponential with 3 μs decay time constant. The light output is 28000 ± 1500 photons/MeV, comparable to LSO. The electron-hole yield is 26500 e-h pairs/MeV with Advanced Photonix Inc. ϕ16 mm Large Area Avalanche Photodiode (LAAPD). ZnSe(Te) has almost proportional light output vs. energy dependence at 5.9 keV reaching 85% of the light output per unit energy at 662 keV. The energy resolution for 662 keV γ line is 5.4% when measured with avalanche photodiode at gain 100 with excess noise factor equal to 2.16. The intrinsic energy resolution for 662 keV is 3,3%. We have observed also the increase of the values of *intrinsic* energy resolution with lowered shaping time constant. Intrinsic energy resolution accounts for effects connected with photoelectron- or electron-hole pair statistics. According to the contemporary models of intrinsic energy resolution such an effect should not be observed. Since attenuation length for 511 keV photons is 2.25 cm, the properties of ZnSe(Te) scintillator point toward its use as a low energy X-ray detector.

Keywords: ZnSe doped with Te, nonproportionality, X-ray detector, energy resolution

Introduction

The first report on use of ZnSe as X-ray detector was published by Ryzhikov *et al.* [1]. The first use of tellurium doped ZnSe as scintillator was reported by Vakulenko *et al.* [2]. The luminescence mechanism was reported by Ryzhikov *et al* [3] A more detailed bibliography can be found in Ref. [4]. ZnSe is low-density crystal (5.42 g/cm^3). The emission length of ZnSe:Te from ISC Kharkov, Ukraine is 610 nm. It is not suitable for photomultiplier (PMT) detection, therefore we decided to check ZnSe:Te properties by extended bialkali PMT with quantum efficiency (QE) of 4% at 610 nm and Large Area Avalanche Photodiodes (LAAPD) that have quantum efficiency of 90% at 610 nm. ZnSe has refractive index $n = 2.6$ [5] that neither matches refractive index of glass window of PMT nor n of silicon at that wavelength ($n = 3{,}87$ [6] and reflectance $R = 0.34$ [7]).Ryzhikov *et al.* reported light output L of ZnSe:Te as high as 80000 photons per MeV (ph/MeV) at X-ray excitation [8]. Dorenbos *et al.* [9] reported only 1300 photoelectrons per MeV (phe/MeV) measured with Hamamatsu R1017 PMT having 5% QE at 610 nm and 12000 e-h pairs per MeV with photodiode, both at 12 μs shaping time. ZnSe consists of light elements, i.e. zinc has K absorption line at 9.65 keV and selenium at 12.66 keV, namely both energies are below 20 keV, usual cutoff of energy for 70 kV peak voltage X-ray tube used in dental radiography. Since YAP:Ce ($YAlO_3$:Ce) contains only light elements in the above sense, we wanted to check nonproportionality, overall and intrinsic energy resolution of ZnSe:Te at wide range of energies to find whether it is also a proportional scintillator.

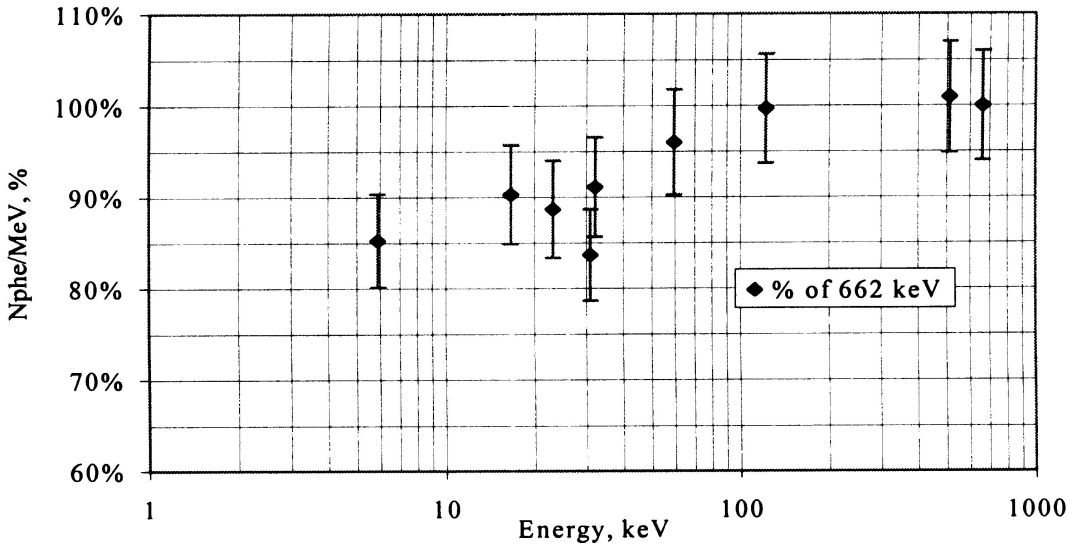

Fig. 1 Nonproportionality of light output of ZnSe(Te) in units of light output at 662 keV

We have previously observed [10] the increase of the values of *intrinsic* energy resolution with lowered shaping time constant for CsI(Tl). It has two exponential components of scintillation pulse shape (0.679 μs – 91% of light and 3.34 μs – 9% of light) [11]. We wanted to test that dependency for a system with only one exponential component of scintillation pulse shape, for which decay time constant is in the range of standard commercial spectroscopy amplifiers.

Experimental setup

We have used ZnSe:0.2%Te from STC Institute for Single Crystals, Kharkov, Ukraine. Two samples (1) 10x10x1 mm and (2) ∅10x5 mm were used. They were characterized as containing only fast (i.e. 1 - 3μs decay time constant) component of the luminescence (i.e. 1 - 3μs decay time constant). They were deep yellow and deep brown colors respectively. Sample (1) was polished on both large surfaces and sample (2) on one round surface, other being grounded only. Samples were glued to PMT or LAAPD with silicone grease of unknown refractive index – estimated around $n = 1.5$. For light output measurement and energy resolution measurement we have used ADIT 2" B51D01 PMT with extended bialkali photocathode. ADIT PMT has QE of 25% at 400 nm, 10% at 550 nm, 4% at 610 nm and 2% at 640 nm. We also used 16 mm diameter windowless LAAPD from Advanced Photonix. The rest of experimental setup consisted of preamplifier or charge sensitive EG&G ORTEC preamplifier model 142AH and Tennelec Spectroscopy Amplifier model 244 or EG&G ORTEC 672 Spectroscopy Amplifier. LAAPD has QE of 90% for 610 nm and 640 nm. Detailed technical characteristics of LAAPD can be found elsewhere [12]. PC-based multichannel analyzer Tukan, produced at SINS, was used to record energy spectra. For timing measurements we have used single photon counting with separated scintillators setup described elsewhere [13]. For start PMT (Photonis XP2020Q PMT) we have used NE111 plastic scintillator with trickled Cs-137 source, where NE111 plastic was excited by 625 keV K electron conversion [14]. Stop pulse was recorded by ADIT PMT from ZnSe:Te sample excited by 32 keV X-rays associated with electron conversion. 1/50 stop to start pulse count ratio requirement was fulfilled by diaphragm at stop PMT.

Results

Light output and proportionality

Light output of sample (1) was measured as 1280±40 phe/MeV at 10μs shaping time at 662 keV γ excitation from Cs-137 source. We have folded light emission spectrum at 610 nm published by manufacturer with standard ADIT QE curve. The calculation yields *L* 28800±1500 photons/MeV (ph/MeV). The measurement with LAAPD with QE of 90% at 610 nm yielded 26400±1500 e-h pairs/MeV, that is 29300±1700 ph/MeV. Note consistent results of *L* given in photons/MeV for PMT and LAAPD with refractive indices not matched.

Proportionality curve defined as photoelectron yield measured at specific energy of excitation to the photoelectron yield at 662 keV is shown in Fig. 1. ZnSe:Te is quite proportional scintillator down to 85%. Note a dip in proportionality curve at 30 keV, the K absorption line of Te (31.8 keV). The same unusual dip is observed for CaF_2:Eu 48.5 keV [15]. The value of dip (more then 5% in proportionality for ZnSe:Te) cannot be accounted by simple additional absorption of dopant of the heavy element.

Energy resolution

Intrinsic energy resolution *Dsc*, statistical contribution and noise contribution to overall energy resolution are defined elsewhere [16,17]. Overall and intrinsic energy resolution for ZnSe:Te (sample 1) is shown in Fig. 2 measured with ADIT PMT at 10 μs shaping time. We have used PMT to discard the influence of LAAPD noise. The tradeoff was much lower statistics in comparison to LAAPD measurement.

The intrinsic energy resolution grows with lowering energies with sudden change at ca. 30 keV. For 662 keV *Dsc* is 7.0±1.1% with overall resolution of 11.5±0.6%. The overall energy resolution for 662 keV γ line is 5.4% when measured with LAAPD at gain 100 with excess noise factor equal to 2.16. The intrinsic energy resolution measured with LAAPD for 662 keV is 3.3%.

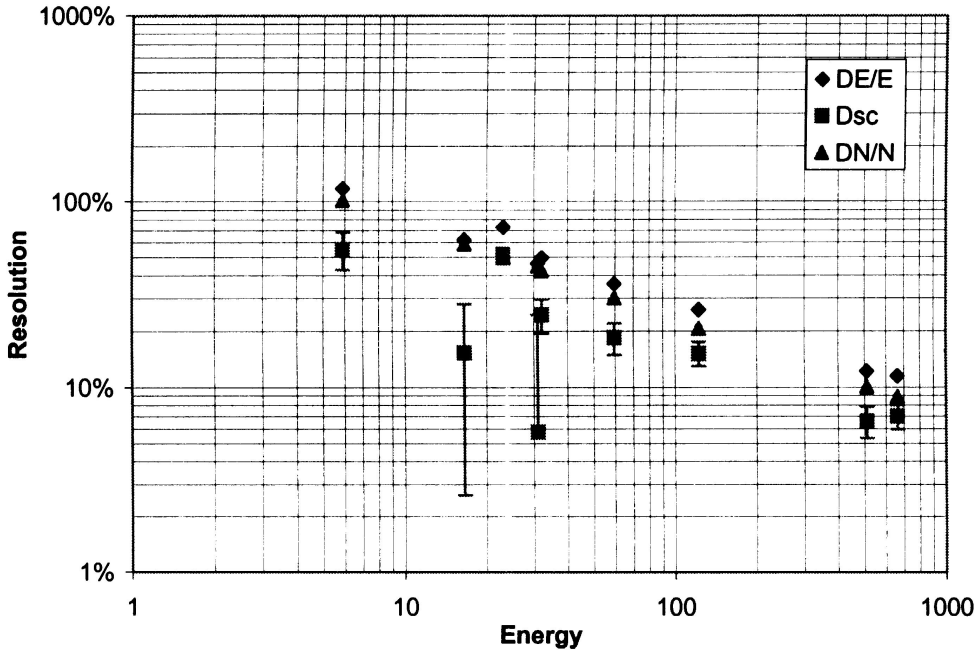

Fig. 2 Energy resolution of ZnSe: overall - diamonds, intrinsic - squares and statistical contribution - triangles for sample (1) measured with PMT

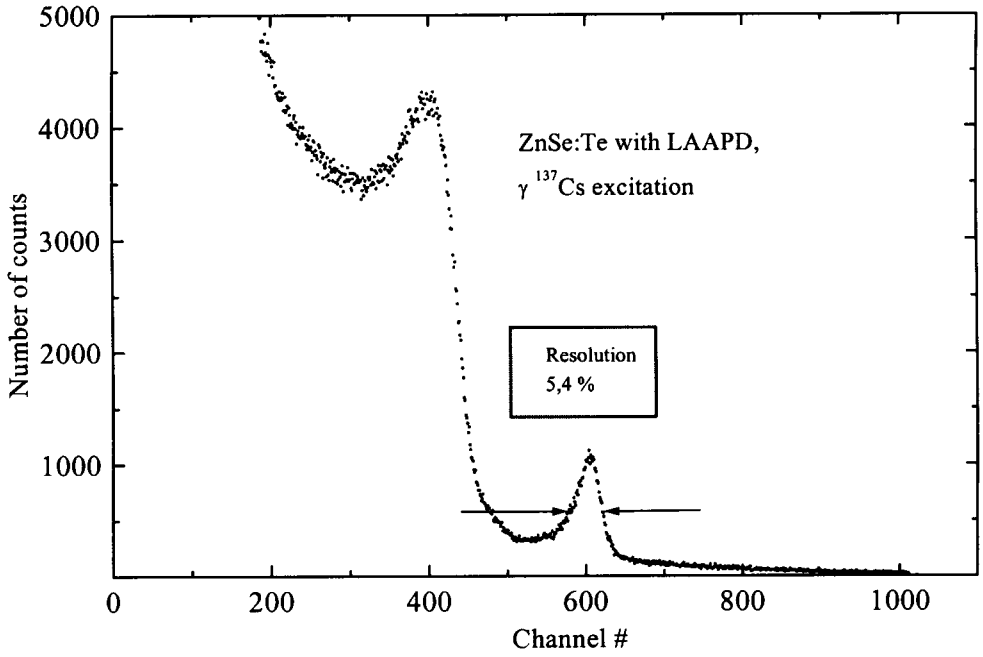

Fig. 3 Energy spectrum of ZnSe:Te excited with 662 keV from Cs-137 source and measured with LAAPD. Overall energy resolution was 5.4%

Shaping time dependencies

For the first time the peculiarity of intrinsic energy resolution dependence on shaping time of spectroscopy amplifier (i.e. the fraction of integrated light) was observed by Moszyński *et al.* [10] for CsI(Tl) for measurement with LAAPD and Fiorini [18] for CsI(Tl) attached to silicon drift chamber. Variation of *Dsc* for 662 keV γ excitation for ZnSe:Te is shown in for measurement with LAAPD at gain 100. The contribution of noise, statistics and overall resolution are also shown. Note that dependence on e-h pair (or photoelectron) statistics and LAAPD noise contribution are accounted by their respective contribution to overall energy resolution.

Scintillation pulse shape

We have measured scintillation pulse shapes of ZnSe:Te using Single Photon Counting (SPC) method. For sample (2) it consisted of dominating exponential decay with constant $\tau_1 = 2.7 \pm 0.1 \mu s$. There was also long time component with unidentified decay time constant. We did not check for correlation of decay time with wavelength of scintillation by means of SPC with monochromator in stop channel. However the reported [5] long time component of the luminescence at 640 nm should be observed by ADIT PMT, if that is present in that sample. Therefore we conclude that sample (2) contained mainly short time component of the luminescence with decay time constant $\tau_1 = 2.7 \pm 0.1 \mu s$.

Discussion

Since *L* (given in photons/MeV) measured with ADIT PMT *and* LAAPD exactly matches, we infer that for ZnSe:Te crystals with 610 nm scintillation wavelength the light output is limited to 28 000 ± 1900 photons/MeV. The use of ZnSe:Te at shaping times up to 12μs is limited to applications, where *L* of 28 000 ± 1900 photons/MeV is acceptable. The reported [8,19] light output of 80 000 photons/MeV is in ca. 2/3 connected with slow (i.e. $\tau_2 >> 10 \mu s$) luminescence at 640 nm.

When only light elements are stoichiometric constituents of a compound one expects such a scintillator to be proportional. That it does not *have* to be so, we report elsewhere [20] with

the cases of YSO:Ce (Y_2SiO_5:Ce) and YAG:Ce ($Y_3Al_5O_{12}$:Ce). Hence the case of ZnSe:Te gives the positive example with its almost flat and unit nonproportionality curve. Further research, must be done on small variations of nonproportionality curve at K absorption edges of *dopant* ion. As we already mentioned, these dips cannot be accounted by simple additional absorption. Calculations of electron response function are required to properly account for *dopant* presence. In lutetium containing crystals, cerium K line (40.4 keV) can be obscured by K line of Lu (63.3 keV) on nonproportionality curves. Therefore light-elements-containing scintillators are good examples for testing electron response calculations.

Shaping time dependence of intrinsic energy resolution did not find any explanation yet. After checking it for several scintillators and with several types of PMTs and LAAPD, we are convinced that it is not instrumental artifact. Further investigations are underway [21].

Acknowledgements

We acknowledge the help of D. Wolski and J. Kucharski in construction of the part of experimental setup. One of us (M.B.) acknowledges the support of "Legend Group" Advertising Agency in Warsaw, Poland in printing poster presentation of this communication. This work was supported in part by Polish Committee for Scientific Research (KBN) grants 8 T11E 025 15 and 8T 10C 005 15.

References

1. V.D. Ryzhikov, O.S. Shapiro, S.M. Ignatov, V.I.. „Afterglow of scintillation materials for X-ray tomography" Silin, Pribory i Tekhnika Eksperimenta, 29 (1986) 155
2. O.V. Vakulenko, A.N. Veretennikov, V.D. Ryzhikov, V.V. Chepelev, " Kinetic characteristics of the X-ray luminescence of ZnSe:Te at high levels of excitation." Zhurnal Tekhnicheskoi Fiziki 58 (1988) 632
3. V.D. Ryzhikov, V.I. Silin, N.G. Starzhinsky, "A new ZnSe/sub 1-x/Te/sub x/ scintillator: luminescence mechanism." Nuclear Tracks & Radiation Measurements 21 (1993) 53
4. http://www.ipj.gov.pl/~balcerzm/dowziecia/OVID_ZnSe_Te.htm
5. STC Institute for Single Crystals, Kharkov, Ukraine Product Catalog. See also http://mail.isc.kharkov.com/index.html
6. C.M. Herzinger, B. Johs, W.A. McGahan,. J.A. Woollam. W."Ellipsometric determination of optical constants for silicon and thermally grown silicon dioxide via a multi-sample, multi-wavelength, multi-angle investigation" Paulson, J. App. Phys. 83 (1998) 3323. See also D. E. Aspnes, A. A. Studna, Phys. Rev. B 27 (1983) 985
7. K. Navratil, J. Sik, J. Humlicek, S. Nespurek "Optical properties of thin films of poly(methyl-phenylsilylene)" Optical Materials 12 (1999) 105
8. V.D. Ryzhikov, Yu. A. Borodenko, S.N. Galkin, L.P. Galchinetskii, E.A. Danshin, K. A. Katrunov, E.M. Selegnev, V.I. Silin, SCINT95 Proceedings, (1996) 465
9. P. Schotanus, P. Dorenbos V.D.. "Detection of CdS(Te) and ZnSe(Te) scintillation light with silicon photodiodes" Ryzhikov IEEE Transactions on Nuclear Science, vol.39, no.4, Aug. 1992, pp.546-50.
10. M. Moszyński, M. Kapusta, J. Zalipska, M. Balcerzyk, D. Wolski, M. Szawlowski, W. Klamra; paper N9-1 presented at IEEE Nuclear Science Symposium 1998, Toronto, Canada and accepted for publication in IEEE Trans. Nucl. Sci. 46 (1999)
11. J.D. Valentine, D.K. Wehe, G.F. Knoll, C.E. Moss, IEEE Trans. Nucl. Sci 40 (1993) 1267
12. http://www.advancedphotonix.com/windowle.htm
13. L.M. Bollinger, G.E. Thomas, „Measurement of the time dependence of scintillation intensity by a delayed-coincidence method" Rev. Sci. Instr. 32, 1044 (1961)

14. M. Moszyński, B.Bengtson „Light pulse shapes from plastic scintillators” Nucl. Instr. Methods 142, 417 (1977).
15. D.W. Aitken, B.L. Beron, G. Yenicay, H.R. Zulliger, “The fluorescent response of NaI(Tl), CsI(Tl), CsI(Na) and CaF2(Eu) to X/rays and low energy gamma rays”, IEEE Trans. Nucl. Sci. NS-14 (1967) 468
16. M. Moszyński, M. Kapusta, D. Wolski, M. Szawlowski, W. Klamra, IEEE Trans. Nucl. Sci. 45 (1998) 472
17. P. Dorenbos, J.T.M de Haas, C.W.E. van Eijk “Non-proportionality in the scintillation response and the energy resolution obtainable with scintillation crystals.” IEEE Trans. Nucl. Sci. 42 (1995) 2190
18. Fiorini C. Longoni A. Perotti F. Labanti C. Lechner P. Struder L. IEEE Trans. Nucl. Sci. 44 (1997) 2553
19. V.D. Ryzhikov, L.P. Gal'chinetskii, E.A. Danshin, E.K. Lisetskaya, W.R. Lubimskii, S.N. Galkin, A.E. Filimonov, V.V. Chernikov. “Studies of effects of isovalent dopants on spectral-kinetic and scintillation characteristics of zinc selenide.” [Conference Paper] 1997 IEEE Nuclear Science Symposium Conference Record (Cat. No.97CH36135). IEEE. Part vol.1, 1997, pp.848-9 vol.1. New York, NY, USA.
20. M. Balcerzyk, M. Moszyński, M. Kapusta in this Proceedings
21. M. Balcerzyk, W. Klamra, M. Moszyński, M. Kapusta, M. Szawlowski in preparation

Heavy Oxide Scintillators: Bulk Crystals and Thin Films for Radiation Monitoring of Environment and Biological Objects

P. Dorenbos[1], C.W.E. van Eijk[1], E. van Loef[1], M.Globus[2], B. Grinyov[2], M.Ratner[2], V.Tarasov[2], Yu. Zorenko[3]

[1]Delft University of Technology, Delft, The Netherlands; [2] Institute for Single Crystals, Kharkov, Ukraine, [3] Institute of Applied Physics, Lviv State University, Lviv, Ukraine

Abstract. Operation characteristics of the apparatus for monitoring of environment are evaluated for different materials and sizes of the scintillation crystal in a broad range of γ-photon energies. The advantage of heavy scintillation crystals is quantitatively investigated. The possibilities of epitaxial growth of thin films with lutetium, their scintillation properties and spatial resolution are explored.

Keywords: heavy scintillators, radiation monitoring, luminescent films.

Introduction

For last years, the application field of heavy oxide scintillators was significantly broadened. Along with high energy physics, they received acceptance in radiation monitoring of environment and X-ray radiation imaging (in particular, for biologic objects) as luminescent screens. In view of this, the problem of optimization of the corresponding apparatus gains a complicated character since the choice of geometric parameters is interconnected with the choice of scintillation material. For solving such problem, it is helpful to estimate quantitatively the advantage of the use of heavy scintillators and to explore the properties of thin luminescent films grown from heavy materials.

The present paper is concerned with such investigations. In Sec. 2, operation characteristics of the apparatus for monitoring of environment are investigated in a broad range of γ-photon energy, the role and advantage of heavy scintillation elements being separated and examined. In Sec. 3, luminescence properties and spatial resolution of thin luminescent films are explored and the optimal version of growth method is proposed.

Use of heavy oxide scintillators for monitoring of environment

Detection and identification of radionuclide pollutions is at present an actual problem, especially for the regions of Ukraine and Belorussia adjacent with Chernobyl. This problem is usually solved with the use of scintillation detection systems (see, e.g. Refs. [1 - 6]) and encounters difficulties. A radionuclide pollution usually contains a number of different nuclides with overlapping energy spectra. A spectral line of a nuclide, overlapping with the lines of other nuclides, cannot be used for a reliable identification. For that aim one can use only a small number of the spectral lines, not overlapping with the lines of other nuclides. Unfortunately, for some nuclides (e.g. K-40) such spectral lines, suitable for identification, are rather weak, which hampers the identification of small amounts of nuclides.

The detection and identification of radionuclides is hampered also by a comparatively strong background activity. It limits from below the minimal detectable activity (MDA) which can be reliably identified with the use of a scintillation detector. The MDA (defined as the total activity of the examined sample expressed in the number of decays per second) is connected with the background activity N_{bac} (defined as the rate of counting background gamma-photons within the energy window) by the relation [1]

$$\mathrm{MDA} = (\beta/\eta)\,(N_{\mathrm{bac}}/t)^{1/2} \qquad (1)$$

Here η stands for the sensitivity defined as the ratio of the number of γ- photons, registered within the energy window near the complete absorption line, to the total number of γ- photons emitted by the sample; t is the exposition time; the numerical constant $\beta = 2$ corresponds to the confidence probability 95% . Eq. (1) allows for the Gaussian distribution of the number of emitted γ - photons with dispersion equal to the square root from their averaged number.

As seen from Eq. (1), MDA can be reduced via diminution of background activity and via enhancement of sensitivity η. In practice, background activity is lowered by a heavy protection shell, enclosing the detection system, and via counting gamma-particles within a narrow energy window near the spectral line of complete absorption (below the total window width is put equal to the trebled value of energy resolution).

To maximize sensitivity η, the substance to be examined is put into a vessel with a cavity for the scintillation crystal (Marinelli beaker). Such geometry provides the maximum averaged solid angle, subtended at the emission point by the scintillation crystal. To a reasonable extent, η can be increased via increasing the scintillation crystal size. A further enhancement of η can be achieved via using a heavy scintillator with a large section of complete absorption of γ-photons.

To calculate η for a limited set of most important nuclides, let us choose for the m-th nuclide the strongest radiation line (with the energy $E^{(m)}$) which does not overlap with the rest of the lines of the set. The detection sensitivity relative to the m-th nuclide, i.e. the number of the decays within its chosen line divided by the total number of the decays of the m-th nuclide, is

$$\eta^{(m)} = K_1^{(m)} K_2(E^{(m)})\, K_3(E^{(m)})\, K_4(E^{(m)}). \qquad (2)$$

Here $K_1^{(m)}$ stand for the ratio of the number of decays within the chosen line to the total number of decays of the m-th nuclide. $K_2(E)$ is the probability for a γ-photon, emitted in the sample with the energy E, to get onto the crystal surface without any energy losses caused by scattering in the sample (K_2 is averaged over the emission point position in the sample and the emission direction). K_3 is registration efficiency and K_4 is photofraction (the product K_3K_4 is the averaged probability for a γ-photon, got into the scintillation crystal, to be completely absorbed in the course of the subsequent interaction with the crystal). The coefficient $K_1^{(m)}$ is a nuclide characteristic, K_2 is mainly a geometric characteristic of the system sample – crystal, and K_3, K_4 are mainly related to the interaction of γ-photons with the crystal.

The optimization problem involves a large number of the detection system parameters: the shape and size of the sample under examination, the substance and size of the scintillation crystal, the crystal container material, the energy window width etc. An overlap of the radiation spectra of nuclides makes the problem essentially dependent on the set of the nuclides.

Earlier the optimization problem was solved by the Monte-Carlo calculation of the sensitivity η and MDA, only the final result being taken into account (see, e.g., [2-6]). The calculation can be made more informative if the stages of the detection process are traced. The first stage includes the γ-photon scattering inside the sample and terminates in their exit from the sample. The second stage is the interaction of γ-photons, escaped from the sample, with the crystal.

Such approach was realized in the Institute of Single Crystals via creating the library of source images. Each source is a sample of given shape and size containing a single (m-th)

nuclide. For definiteness, the samples of the shape of Marinelli beaker with the volume V are considered. The library includes the set of sources (V, m) with V= 250, 500, 1000 cm^3 and m=1,... m_{max}. Every source is presented in the library by the distribution function $\Phi(V, m \mid S, u, E)$ of γ-photons over the 5 variables: the surface point, S, of the γ-photon escape from the sample; the unit vector, u, and energy, E, of the γ-photon at the escape moment. For every source (given by V and m), the distribution function Φ is presented by a sufficient number (not less than 10^4) of γ-photons escaped from the sample.

The library of source images provides the possibility to investigate separately the influence of the source and scintillation crystal on the sensitivity and MDA. Besides, the library shortens the time, required for the simulation of the detection process, by two orders of magnitude.

Table 1. Characteristics of the successive stages of the detection process: K_1 – the contribution of the chosen spectral line to the total activity of each nuclide; K_2 – the fraction of emitted γ-photons got to the scintillation crystal (a characteristic of the source image); K_3 – registration efficiency; K_4 – photofraction; η – sensitivity; MDA – minimal detectable activity. The table relates to the Marinelli beaker of the volume 1000 cm^3 and scintillation crystal ∅ 63 × 63 mm.

Scintil-lation crystal	Nuclide to be exa-mined	Chosen line energy, MeV	K_1	K_2	K_3	K_4	$K_{234} \equiv K_2 K_3 K_4$	$\eta \times 10^2$	N_{bac} MDA / decays per second	
NaI(Tl)	Am-241	0.060	0.37	0.0650	0.864	0.992	0.0557	2.06	0.80	1.45
CWO					0.855	0.989	0.0550	2.03	0.89	1.55
BGO					0.842	0.989	0.0541	2.00	0.95	1.62
NaI(Tl)	Ra-226	0.609	0.495	0.0906	0.575	0.544	0.0283	1.40	1.40	2.81
CWO					0.775	0.776	0.0544	2.70	1.61	1.56
BGO					0.783	0.823	0.0584	2.89	1.72	1.51
NaI(Tl)	Cs-137	0.662	0.85	0.0959	0.560	0.543	0.0292	2.48	1.30	1.53
CWO					0.774	0.747	0.0554	4.171	1.50	0.87
BGO					0.767	0.807	0.0594	5.05	1.60	0.83
NaI(Tl)	Th-232	0.930	0.45	0.1045	0.509	0.450	0.0239	1.08	0.80	2.76
CWO					0.723	0.695	0.0525	2.36	0.92	1.35
BGO					0.719	0.765	0.0575	2.59	0.98	1.27
NaI(Tl)	K-40	1.460	0.105	0.1057	0.430	0.360	0.0164	0.172	0.48	13.4
CWO					0.670	0.635	0.0450	0.472	0.55	5.23
BGO					0.680	0.696	0.0500	0.525	0.59	4.88
NaI(Tl)	Ra-226	1.764	0.17	0.1110	0.421	0.339	0.0159	0.270	0.20	5.52
CWO					0.653	0.631	0.0436	0.741	0.23	2.05
BGO					0.660	0.653	0.0456	0.775	0.25	2.13
NaI(Tl)	Th-232	2.614	0.36	0.1233	0.364	0.346	0.0155	0.558	0.15	2.30
CWO					0.592	0.594	0.0434	0.156	0.17	0.88
BGO					0.573	0.646	0.0456	0.164	0.18	0.86

Table 2. The same for the Marinelli beaker of the volume 500 cm^3 and scintillation crystal $\varnothing\ 40 \times 40$ mm

Crystal	Nuclide to be examined	Chosen line energy (MeV)	K_1	K_2	K_3	K_4	$\eta \times 10^2$	N_{bac} MDA decays per second	
NaI(Tl)	Am-241	0.0596	0.37	0.0463	0.834	0.992	1.42	0.45	1.57
CWO					0.810	0.983	1.36	0.41	1.57
BGO					0.812	0.990	1.36	0.36	1.45
NaI(Tl)	Ra-226	0.609	0.495	0.0688	0.432	0.481	0.71	0.80	4.19
CWO					0.672	0.758	1.73	0.75	1.67
BGO					0.690	0.810	1.90	0.65	1.41
NaI(Tl)	Cs-137	0.662	0.85	0.0679	0.443	0.460	1.18	0.76	2.46
CWO					0.676	0.739	2.88	0.70	0.97
BGO					0.682	0.800	3.15	0.60	0.82
NaI(Tl)	Th-232	0.930	0.45	0.0729	0.372	0.360	0.44	0.47	5.19
CWO					0.606	0.666	1.32	0.43	1.65
BGO					0.601	0.720	1.42	0.37	1.43
NaI(Tl)	K-40	1.460	0.105	0.0769	0.306	0.267	0.066	0.25	25.2
CWO					0.530	0.547	0.245	0.23	6.52
BGO					0.530	0.607	0.260	0.20	5.73
NaI(Tl)	Ra-226	1.764	0.17	0.0806	0.290	0.264	0.100	0.12	11.5
CWO					0.505	0.520	0.36	0.11	3.07
BGO					0.480	0.585	0.38	0.090	2.63
NaI(Tl)	Th-232	2.614	0.36	0.0808	0.259	0.253	0.19	0.09	5.26
CWO					0.460	0.457	0.61	0.08	1.54
BGO					0.442	0.488	0.63	0.07	1.40

An example of calculation results is given in Tables 1 and 2 for heavy oxide crystals CWO, BGO and, for comparison, for the traditional scintillator NaI(Tl). The tables include 5 most widespread nuclides covering the spectral interval 0.06 to 2.6 MeV (the nuclides Ra-226 and Th-232 are presented in the table by two lines suitable for identification). Besides MDA, the tables give intermediate characteristics of the device: sensitivity η defined by Eq. (2), its constituent multipliers $K_1^{(m)}$, $K_2(E^{(m)})$, $K_3(E^{(m)})$, $K_4(E^{(m)})$, and background activity N_{bac}. These quantities were calculated by the Monte-Carlo method with the accuracy of the order of 3 %. The MDA values (the last column) agree with the corresponding experimental data with the accuracy 10 to 15 % (MDA is obtained experimentally with the same accuracy).

Tables 1 and 2 demonstrate an essential advantage of heavy crystals BGO and CWO as compared to NaI(Tl). Indeed, the application of heavy crystals instead of NaI(Tl) lowers MDA roughly by the factor of 2.5 for a crystal $\varnothing$ 63×63 mm or 3 to 4 for a crystal $\varnothing$40×40 mm.

Along with this conclusion, it is interesting to analyze the tables more in detail. The MDA values, given in the tables, vary in a broad interval from 0.8 to 25 decays per second. Let us trace the origin of such a great difference in MDA values.

First we shall restrict ourselves to Table 1 related to the scintillation crystals $\varnothing\ 63 \times 63$ mm. Sensitivity η, appearing in the MDA definition (1), is formed by two groups of multipliers: the coefficient K_1, which characterizes the nuclide activity distribution between its radiation lines, and the product $K_{234} = K_2\ K_3\ K_4$ related to the detection process. It can be seen from Table 1 that, as a rule, K_{234} rather weakly depends on energy, so that the difference

in sensitivity for various nuclides is mainly conditioned by the difference in K_1. The latter is to a large degree responsible also for the difference in MDA given in Table 1 for various nuclides. However, there is a general tendency to a slow decrease of MDA with increasing energy due to rather a fast decrease in background activity which overcompensates a weak diminution of the sensitivity multiplier K_{234} with increasing energy.

Now let us compare the versions of the device differing in sizes (Tables 1 and 2). The smaller device differs from the larger one by a less favorable detection geometry (the coefficient K_2 is less by about 30 %) and by a noticeably lower registration efficiency (the coefficients K_3 and K_4). As a result, the devices differ in sensitivity by the factor 2 or 3, which is somewhat compensated by a lower background activity in the case of the smaller device. As seen from Tables 1 and 2, where the MDA of the total volume of the sample is given, its values related to the smaller and larger devices differ roughly by the factor 1.10 to 2.2; correspondingly, the MDA values, related to the unit volume of the sample, differ by the factor of 2.2 to 4.5 (the difference is stronger for the lighter crystal NaI(Tl)).

Thin crystalline films of the heavy lutetium scintillator $Lu_3Al_5O_{12}$:Ce

The spatial resolution of X-ray screens, intended for microtomography, is limited by the thickness of luminescence coating and the grain size of the luminescence material. To achieve the micron or submicron resolution in the combination with a sufficient absorption of X-rays, it is necessary to grow luminescent micron-thick films with a high effective atomic number Z_{eff} on a non-luminescent substrate. For that purpose, single-crystal films with the heavy lutetium element (Z = 71) are perspective [7].

As a proper luminescence screen, a thin $Lu_3Al_5O_{12}$:Ce film on the $Y_3Al_5O_{12}$ substrate can be used. Such luminescence coating on the$Y_3Al_5O_{12}$ substrate was grown by the means of liquid-phase epitaxy on the base of a PbO-B_2O_3 containing flux. This method requires an approximate coincidence of the lattice constants of the film and substrate. For the system under consideration, this condition is not met: the lattice constant of the substrate exceeds that of the film by 0.093 A.

To diminish this difference, the luminescence material should be doped with proper large-radius isovalent impurity ions substituting small Lu ions in dodecahedral sites or Al ions in octahedral sites of the garnet lattice (the dope must produce no additional absorption in the spectral range of luminescence). For that purpose, two versions of a proper impurity have been examined: La_2O_3 and Sc_2O_3 (the compositions A and B, respectively). Each of them was added to melt in increasing amount until the coating of the substrate by the luminescence material has been observed. A stable epitaxial growth was achieved at the concentration of La_2O_3 and Sc_2O_3 equal to 8 and 10 mol. %, respectively. The substrate diameter was 15 to 36 mm, thickness about 0.7 mm, orientation (100) or (111). The purity of initial crystal ingradients was 99.990 to 99.999 mass %; the fluxing agent was prepared from PbO of yellow modification which contained , in particular, less than 3×10^{-4} mass % of the Fe group ions.

Along with the La_2O_3 or Sc_2O_3 impurity necessary for epitaxial growth, the luminescent impurity CeO_2 was introduced into the melt in different concentrations: 2.7 to 11.2 mol. % for the composition A and 3.2 to 13.1 mol. % for the composition B. For the composition A, light output was saturated at the CeO_2 concentration close to 9 mol. % and achieved 0.85 of the light output of the best $Y_3Al_5O_{12}$(Ce) samples under excitation by α-particles of the Pu-239 source. For the composition B, light output of the dope luminescence was found to be at least by an order of magnitude less. This can be connected with two channels of dissipation of the Ce^{3+} ion excitations: (1) through excitation of radiation recombination centers formed by Sc^{3+} ions in octa- and dodecahedron sites of the garnet lattice [8]; (2) through enhancement of nonradiative transitions between the excited Ce^{3+} state and the band top which nears the excited Ce^{3+} level with increasing Sc concentration [9].

Thus, the composition A ($Lu_3Al_5O_{12}$ doped with 8 mol. % of La_2O_3 and 9 mol. % of CeO_2 in melt) should be considered as an optimal version. Using the melt of this optimal composition, 10 to 12 samples can be grown simultaneously without a noticeable deterioration of luminescence properties (the relative straggling of light output does not exceed 8 %). Under such optimal conditions, the total weight of the melt amounts to about 1 kg, the substrates being 22 mm in diameter and the films 10 μm in thickness.

The samples of the composition A do not noticeably differ in luminescence properties from$Y_3Al_5O_{12}$(Ce) samples. The mentioned substitution of Lu ions in dodecahedral sites of the garnet lattice results in a slight (of about by 0.1 eV) red shift both of absorption and luminescence bands, so that the reabsorption degree is practically the same as for $Y_3Al_5O_{12}$Ce.

The conclusion follows that films of the optimal composition A, grown on the $Y_3Al_5O_{12}$ substrates, can be successfully used as X-ray screens. Being only slightly inferior to $Y_3Al_5O_{12}$ (Ce) samples in light output, they are distinguished by a great effective atomic number (58) and a high density (6.6 g/cm3). This provides the possibility to reduce the film thickness to about 1 μm and to achieve the spatial resolution of an X-ray detector in the interval 0.7 to 1 μm.

This work was supported by the Grant INTAS-UKRAINE 95/0166.

References

1. L. A. Currie, Analytical Chemistry **40** (1968) 586
2. Fraser-Mitchel, A.G. Wridth, Nuclear Instr. and Methods **228**, N 2, 3 (1990) 429
3. M. Rigetti, D. Hernandes, F. Spano, Nuclear Instr. and Methods **A280**, N3, (1989) 514
4. F. Ortiz, J.M. Los Acros, A. Grau, L. Rodriges, NIM **A312**, N 1,2 (1992) 109
5. R. De Leo, G. Erasmo, A. Pantaleo, Nuclear Instr. and Methods **129**, N3 (1975), 501
6. L. De Franceschi, F. Pagni, Nuclear Instr. and Methods **70**, N 3 (1969) 325
7. A. Koch, C. Raven, Proc. of the Intern. Conf. SCINT 97, ed. by Yin Zhiwen, Shanghai, P.R. China, 1997
8. Ya.Valbis, L.Volzhenska, Yu. Dubov, et al., Optika i Spektroskopiya **63** (1987) 1058.
9. Yu.V.Zorenko, M.V.Pashkovsky, M.M.Batenchuk, et al., Optika i Spektroskopiya **80** (1996) 776

Impurity and intrinsic defects dependent scintillation properties of $PbWO_4$ single crystals

L. Limarenko, M. Pashkovsky, Z. Moroz, Yu. Zorenko, I. Konstankevych

Institute of Applied Physics Lviv State University,
49 General Chuprynka Str., Lviv, 290044, Ukraine;

Abstract. The regularities of the formation the optical, luminescence and kinetic characteristics in dependence on technological conditions of PWO crystals growth both pure and doped with different type impurities are considered. The possibility of further improvement PWO scintillation parameters is discussed.

Key words: lead tungstate, scintillator, luminescence, doping, impurity, decay

Introduction

Due to its high density, short decay time and good radiation hardness $PbWO_4$ (PWO) was chosen as basic scintillation medium for the future high energy physics experiments at LHC (CERN) [1,2]. That is why lead tungstate crystals became a subject of intensive both technological and optical investigations withih last few years. The principal optical and luminescence properties of PWO crystals are under studies since 40-th [3-10]. Nevertheless until now no general conception about origin of the complex system of luminescence centres in PWO. The absence of unique model for the explanation of the energy transfer processes in excited lattice mainly connected with specific properties of PWO. These are the rather narrow region of homoheneity on the phase diagram $PbO\text{-}WO_3$, the existence of two congruently melting components (Pb_2WO_5 and $PbWO_4$) that undegro to polymorphic conversion at 887^oC, the evaporation of the crystal formative component with enough high partial pressures and the low stability of lead sublattice as result of flexibility of lead valency state [11-13]. So the relatively week variations in the conditions of growth, cooling and post-growth treatment and hence in the substructure of lattice defects induce significant changes in the most important characteristics of the PWO crystals and in parameter based on them scintillators.

A major part of the work described in this paper was therefore concerned with the comprehensive analysis the main properties of the PWO single crystals in functional dependence on growth conditions and thus the intrinsic defects of structure as well as on impurity-like defects which can affect PWO scintillation properties.

Result and discussion

PWO single crystals 15-20 mm in diameter and about 60 mm long were grown by Czochralski method in platinum crucible with HF heating. The raw charges were prepared by solid-phase high temperature synthesis of lead and tungsten oxides of the commercial purity. Undoped single crystals were grown in the oxygen atmosphere (p_{O_2}=1 atm) and in the air at other identical technological parameters. Doped PWO crystals were grown in oxygen atmosphere using the same purity raw components. Dopants Mo, Nb, Pr, Eu were introduced into the melt in the form of oxides. The samples for investigation were prepared in the form of discs (thickness of 5 or 10 mm) from the close to seed part of the ingots. All surfaces of the samples were polished. For the spectroscopic and kinetic measurements were used the generally accepted setups that ensured reliability of the results.

Optical and luminescence properties of undoped PWO single crystals

The X-ray luminescence spectra (XL) of all intentionally undoped PWO crystals at room temperature (RT) are presented by broad often nonelementary bands with emission in the energy region about 3.6-1.6 eV (Fig. 1, a). It can be seen that the position of the XL maximum and/or form of the spectral curve strongly depend on the growth conditions (in the complete technological cycle) and thus on the stoichiometric composition of the crystals and other types of the structural defects generated in the lattice. We believe that the growth of PWO crystals in the oxygen atmosphere using the modified working chamber (which secures optimal thermal conditions for crystallization process) allows to maintain the melt stability and in this way to ensure their composition close to stoichiometric one (i) and as result to obtain the colour-less crystals (possess the high transmission in the scintillation region) (ii) with preferentical contribution into light emission of the "blue" centres (iii) usually attributed to regular WO_4^{2-} groups [1-4, 8, 9]. (Fig. 1, a, curve 1). The insignificant distinction in the analyzed case on the oxygen con-tent in the gas environment at other identical regimes of the technological conditions (the growing in more weak oxidizing medium, i.e. in air atmosphere) leads to essential nonadequate optical characteristics: the PWO crystals were pale grey grey or yellow-green in colour. The formation of the intrinsic defects in cationic and anionic sublattices (creation of the (WO_3+F) irregular centres when stoichiometry shifts towards a greater PbO content [2,7,9]) accompanied by shift of the XL maximum toward the long wavelength region, i.e. the center of "green" luminescence began to play the considerable or major role in the light emission processes (the curves 2 and 3 in Fig. 1, a for pale grey and yellow-green samples respectively). At last, the yellow-orange PWO crystals were grown by mean melting rest which remained after previous growth (the necessary amounts of raw oxides were added). Such melt has an increased concentration of the background impurities which posses low segregation coefficients in PWO so it's possible the further disordering of the crystal structure in terms of impurity – like defects. These crystals emit in the band with two maximum: at 420 and ~520 nm (Fig. 1, a, curve 4). It should be noted that the bands of the additional absorption with $\lambda \approx 420$ nm ($k_3 \approx 0.5$ and $k_4 \approx 1$ cm^{-1} in maximum) were observed only in the spectra of last two yellow coloured crystals.

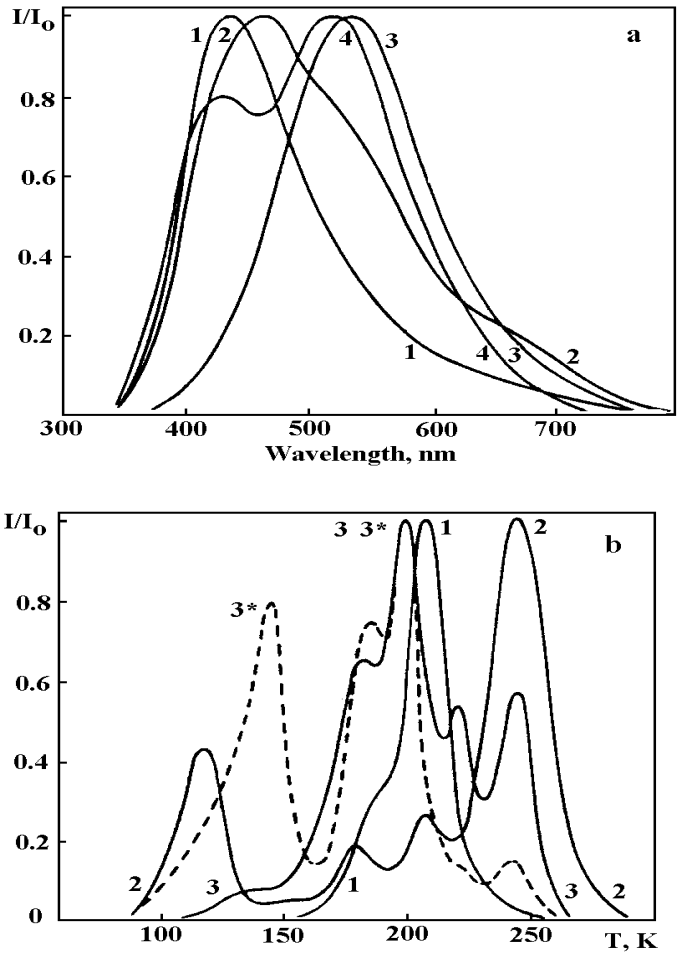

Fig. 1. X-ray excited emission spectra at RT (a) and spectra of thermoluminescence (b) of undoped $PbWO_4$ crystals grown in oxygen (1) and in air atmosphere (2, 3, 4).

The thermoluminescence (TSL) analysis was used for the establishment of the crystal lattice disorder degree in dependence on the PWO growth conditions. Fig. 1, b showes the glow curves for mentioned above types of PWO crystals. The number of TSL peaks in the ~90-

300 K region and their relative intensities strongly depend on type and concentration of the trap centres for charge carriers which form in the forbidden zone the system of the monoenergetic levels with the activation energy in the range ~0.3-0.5 eV. The TSL spectrum of colourless PWO sample is represented by peaks at ~190 and 210 K. The spectral composition of the light sum accumulated by traps correlates with "blue" emission at X-ray excitation. The generation of the intrinsic defects in PWO crystals grown in air is accompained by transformation their TSL spectra: the number of discrete peaks rises up to five and the redistribution in their relative intensities is observed (Fig. 1, b, curves 2, 3). The registration of TSL for grey coloured PWO sample using the wide band filter which transparent in the region >500 nm (i.e. the region of the "green" and "red" centres emission) gave the curve with peaks at ~180, 200, 230 and 250 K. The spectral composition of the intensive peaks at 200 and 230 K coinsides with the spectrum of the "green" optically active centres. At last, the post-growth treatment of yellow-orange PWO sample in the air at 1000^{o}C during 6 h transforms its TSL spectrum: supression of the peak at 245 K is accompanied by appearance of a new low temperature one (T=145 K) nontypical for the glow curves of investigated as-grown PWO crystals (Fig. 1, b, curve 3*). It should be noted that slow component in luminescence decay is very sensitive to the presence of traps which are stable at temperatures up to RT and active in the processes of energy transfer and storage [14].

Doped PWO crystals

The influence of doping PWO single crystals with ions that can effect (worse or improvement) optical, luminescence and kinetic characteristics of scintillators has been investigated.

The impurity of isovalent replasement (Mo^{6+}). We believe that the green component in PWO crystals emission may be caused by different type defects, specifically by residual molybdenum impurity presented in raw materials in concentration up to 10^{-3} mass.%. In order to verify the validity of this assumption we have grown the concentration series of PWO crystals (the level of melt doping was $5\cdot10^{-4}$-5.0 mass.% MoO_3). Only the crystals doped with 1.0 and 5.0 mass.% MoO_4 were slightly coloured in yellow. The spectra of optical absorption and X-ray excited luminescence at RT are shown in Fig. 2. a, b. Observed character of the spectral dependences evolution is typical for the solid solutions (apparently, limited in our case) of two compounds ($PbWO_4$ and $PbMoO_4$) with the identical character of the chemical bonds, adequate crystal structures (tetragonal), common cation (Pb^{2+}), equal ionic radii of W^{6+} and Mo^{6+} ($0.65\cdot10^{-10}$ m) and close dimensions of $[WO_4]^{2-}$ and $[MoO_4]^{2-}$ radicals ($2.57\cdot10^{-10}$ and $2.54\cdot10^{-10}$ m respectively) [15].

So, when increasing the impurity content from $5\cdot10^{-4}$ to 5.0 mass.% there occures, a shift in the X-ray luminescence maximum position from 420 nm (PWO) to about 500 nm (PWO–5.0 mass.% MoO_3) through the several "intermediate" stages (Fig. 2, b; curves 2-4). The analogical effect, i.e. shift in the position of absorption edge for the $PbWO_4$-$PbMoO_4$ system demonstrate the curves presented in Fig. 2, a. If the model is really correct then "pure" in practice emission caused by the transitions in the MoO_4^{2-} molecular complexes (Fig. 2, b; curves 5, 6) taking place under the circumstance of $n_2<<n_1$ (where $n_{1,2}$ denote the concentrations of the WO_4^{2-} and MoO_4^{2-} emission centres) may be explained by the nonradiative transfer of the excitation energy $WO_4^{2-}\rightarrow MoO_4^{2-}$ and higher efficiency of the MoO_4^{2-} centres in the processes of intercepting the excitation energy which migrate through disordered crystal lattice (smaller screening of MoO^{6+} nuclear in comparison with W^{6+} determines the greater covalency of Mo-O bond and thus the greater polarizability of MoO_4^{2-} anion [15]).

The impurities of heterovalent substitution (Li^{+}, Eu^{3+}, Pr^{3+}, Nb^{5+}). The intrinsic defects of a vacancy type with the necessity arise in the PWO lattice doped with the impurities of heterovalent substitution of the regular basis positions (Pb^{2+} and W^{6+}). In particular,

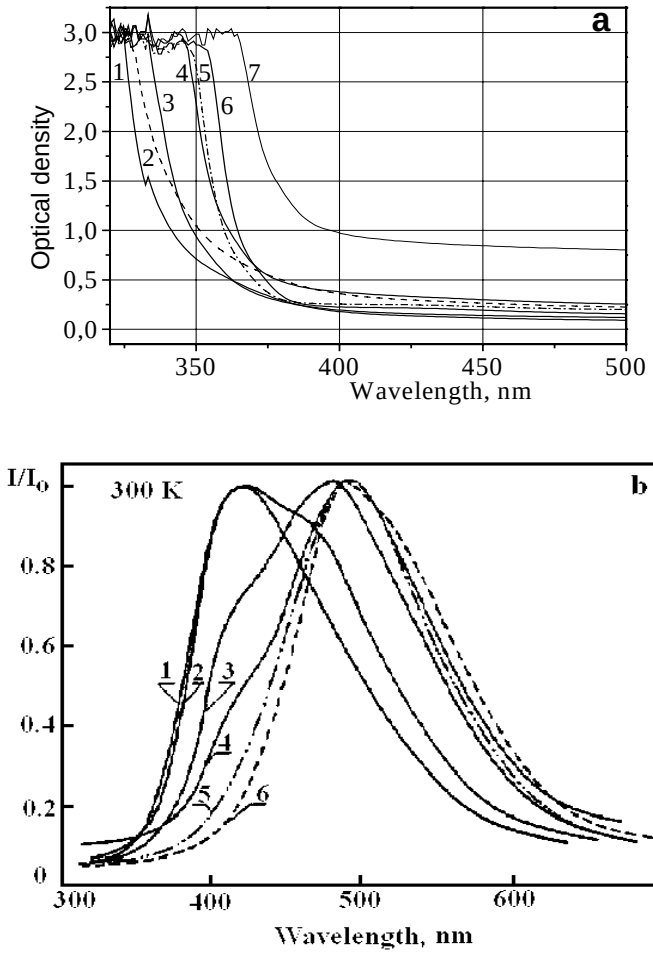

Fig. 2. The evolution of optical absorption (a) and X-ray excited emission (b) spectra in dependence on concentration Mo^{6+} in $PbWO_4$-$PbMoO_4$ system: a) 1 – $5\cdot10^{-4}$, 2 – $5\cdot10^{-3}$, 3 – $5\cdot10^{-2}$, 4 – $2\cdot10^{-1}$, 5 – $5\cdot10^{-1}$, 6 – 1 and 7 – 5 mass.%; b) 1 – pure PWO, 2 - 6 – PWO-Mo (2 – $5\cdot10^{-4}$, 3 – $5\cdot10^{-3}$,

introduction of singlevalent ions into Pb^{2+} sites and pentavalent ions into W^{6+} ones leads to generation of the oxygen vacancies. Doping with the trivalent elements is accompanied by arising of vacancies in the cationic sublattice. So doping purposely the PWO crystals with the impurities in the different charge states is an effective method for elucidation the role of intrinsic defects of the structure in the formation of PWO scintillation characteristics.

In order to perform a comparative analysis we have grown the serie of PWO crystals doped with Li^+, Eu^{3+}, Pr^{3+} and Nb^{5+} (raw oxides of the same purity specification for all crystals). The yellow colour of PWO-Pr^{3+} is caused by rather intensive bands of characteristic absorption in visible. In the spectra of extremally slightly coloured PWO-Li^+ crystals the weak absorption band with λ_{max}≈435 nm is observed. All other crystals at impurities concentration about $10^{-2} \div 10^{-3}$ mass.% were colourless. The X-ray luminescence spectra of the three single crystals, the pure one and those doped with Li^+ (10^{-2} mass.%) and Nb^{5+} ($5\cdot10^{-3}$ mass.%) are represented by the curves with λ_{max}≈425 nm which in fact coincide with each other (their intensities, half-widths are the same). The data derived for the crystals doped with Eu^{3+} ions represented important results related to the general problem of optimization of the scintillation parameters of PWO. It was established in particular, that the PWO-Eu^{3+} crystals are colourless and manifest a high structural quality and transmittance in the scintillation region if the impurity concentrations in the melt are less than 10^{-2} mass.% when compare with the undoped crystals. For both last crystals the X-ray luminescence spectra have maximum at λ_{max}~420 nm. It should be noted, that significant improvement of the PWO parameter (radiation hardness and optical transmission) have been reached by [16] for crystals doped with Y^{3+} and Gd^{3+} (the segregation coefficients 0,8 and 1,4, respectively). It was believed that such elements could compensate the Pb^{2+} deficiency, threby reducing the dencities of the (Pb^{3+}, O^-) defects.

Decay kinetic

It`s established that decay kinetics PWO crystals as optical and luminescence properties can vary in a broad range depending on the growth conditions, type and concentration intrinsic structural defects and, doping level with different impurities (Fig. 3, a, b). PWO

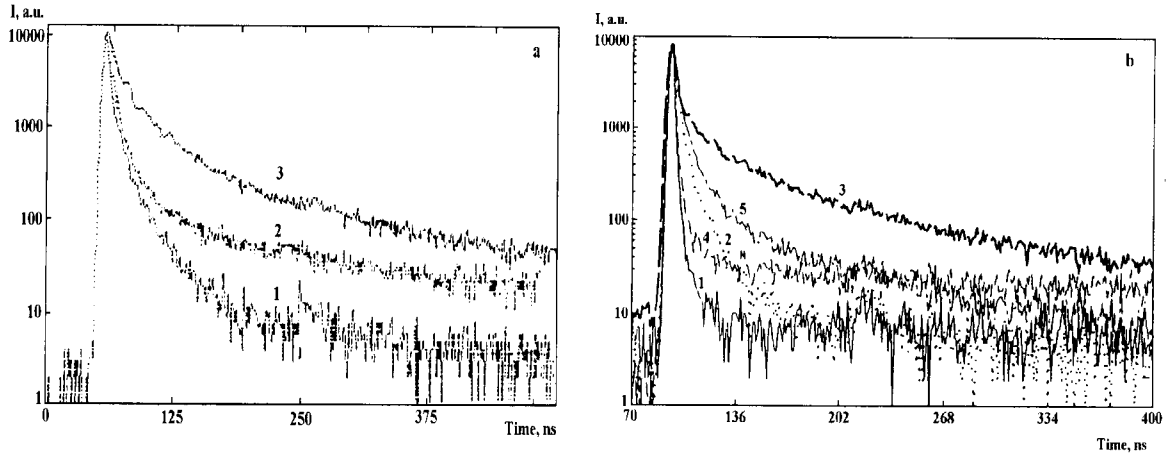

Fig. 3. X-ray decay kinetics of $PbWO_4$ crystals at RT.

luminescence kinetics at excitation (T=300 K) by pulse X-ray show exponential behavior in the initial part with τ_1, as fast component (usually 2-4 ns) and slower processes in the decay is present as well which can be fitted by another two exponents with decay times $\tau_2 \approx 18$-20 ns and $\tau_3 \geq 170$ ns (for the undoped PWO grown in the oxygen). However, scintilation decay can be extended to much longer time scale (for example, in the case of PWO-$5 \cdot 10^{-2}$ mass.% Pr_2O_3 we measured τ_1=1.16 (94%) and τ_2=3118 (6%) ns). From comparison results in Fig.3, a and related emission spectra in Fig.1, a it`s evident that colourless PWO samples have shorter decay times compared with yellow ones, i.e. the fast components in PWO scintillators mainly origin from "blue" emitting centres and only partly from "green" ones. The relative intensity of slow radiative decay components rises with increasing content of the "green" component in the emission spectra undoped yellow coloured crystals as well as PWO crystals with high concentration of Mo^{6+} impurity. In conclusion it should be noted that decay curve of PWO-Eu^{3+} is described by superposition of the two exponents with τ_1=0,5 and τ_2=4,5 ns (i.e. the "middle" and "slow" decay components are absent); the contribution of the ultra-fast component to the total light emission is equal to 87%.

Conclusions

The colourless PWO crystals possessed composition close to stoichiometric one with preferential contribution into light emission of “blue” centres may be grown by Czochralski method in oxygen atmosphere using raw material of commercial purity;

The spectral variability of luminescence in PWO single crystals may be explained by different character of structural disordering. In particular, the impurity content of the raw materials is a important factor which affects the formation of optical, luminescent and kinetic parameters of material. For example, the “green” component of emission may be caused by the residual Mo impurity;

The Eu impurity doesn’t change for the worse the main optical properties of PWO crystals (transparently, together with intensity and spectral content of the emission) turns out to be more effective in forming the kinetic parameters of scintillators when compare are with the Nb^{5+} impurity.

Acknowledgment

The work was supported by the Grant INTASS-Ukraine 95-0166.

References

1. P. Lecoq, Proc of the Int. Conf. SCINT'97, Shanghai, P. R. China, Sept. 22-26, 1997, SAS Shanghai Branch Press, 1997, 13
2. P. Lecoq, Proc of the Int. Conf. SCINT'95, Delft, The Netherlands, Aug. 28-Sept. 1, 1995, Delft Univ. Press, 1995, 52
3. F.A. Kröger, Some Aspects of the Luminescence of Solids, Elsevier, 1948
4. W. van Loo, Phys. Stat. Sol. (a), 27 (1975) 565
5. J.A. Grönink, G.Blasse, J. Solid State Chem., 39 (1980) 9
6. B. Reut Izvestiya AN SSSR, Ser. Phys., 49 (1987) 2032
7. M. Kobayashi, M. Ishii, Y. Usuki et. al. Nucl. Instrum. And Methods in Phys. Res., A333 (1993) 429
8. P. Lecoq, I. Dafinei, E. Auffray et. al. CERN-PRE. 1994
9. L.L. Nagornaja, V.D. Ryzhikov, U.Ya. Vostrikov et.al. Radiation Measur., 24 (1995) 375
10. M.V. Korzhik, V.B. Pavlenko, V.A. Katchanov et. al. Proc of the Int. Conf. SCINT'95, Delft, The Netherlands, Aug. 28-Sept. 1, 1995, Delft Univ. Press, 1995, 241
11. D.L. Alov, N.V. Klassen, N.N. Kolesnikov et.al. ibid, p.267
12. N.N. Klassen, S.Z. Shmurak, L.M. Shmut'ko et.al., ibid, p.475
13. L.L.Y. Chang, J. Amer. Ceram. Soc., 54 (1971) 357
14. G. Tamulaitis, S. Burachas, V.P. Martinov et.al. Phys. Stat. Solidi (a), 161 (1997) 538
15. V.V. Szherbina, Geochemistry (USSR), 10 (1965) 3
16. M. Kobayashi, Y. Usuki, M. Ishii, et. al. Proc of the Int. Workshop on Tungstate Crystals, Roma, October 12-14, 1998,

Effect of Gamma and Photoirradiation on Radiation Stability of Scintillators Based on $PbWO_4$ Single Crystals

L.Nagornaya, A.Apanasenko, Yu.Vostretsov, O.Zelenskaya, I.Tupitsyna, K.Katrunov, V.Ryzhikov

STC for Radiation Instruments, Concern "Institute for Single Crystals", 310001 Kharkov, Ukraine

Abstract. Radiation-optical properties are reported for single crystals $PbWO_4$ grown by Chochralski method in different atmospheres. The highest radiation stability was observed for lanthanum-doped samples grown in an inert media containing some oxygen. Doping with lanthanum was shown to decrease the concentration of deep traps responsible for the rate of transparency restoration of the initially pure samples. A possibility is shown of prediction of $PbWO_4$ radiation stability basing on photo-induced coloration and decoloration effects. The nature of doping effects upon radiation-optical properties of $PbWO_4$ is discussed.

Keywords: $PbWO_4$(PWO), monocrystals, absorption, gamma-irradiation, light output, defects

Introduction

The interest to the optical-radiation properties of the lead tungstate monocrystals (PWO) appeared last years because of a good perspective to apply it in high energy particles detectors. These crystals must have a good optical transmittance, the low induced absorption (IA) and afterglow level, have to be homogeneous along the length. In addition the crystals have to be cheap enough. These demands should be satisfied by a simple and efficient growth technology, which has not been evaluated yet through the lack of knowledge about relation between PWO optical properties and growth conditions. Especially it concern the influence of the air conditions on the optical-radiation properties of the PWO crystals. As a rule, the crystal growth conditions are not described in the papers. The measurements were carried out, in most cases , on individual samples. So the conclusions made could not be considered as a general. The purpose of this paper was to carry out systematic studies of influence of growth atmosphere upon radiation-optical characteristics and radiation defects of crystals PWO grown by Czochralski method under doping with some heterovalent impurities.

Objects and methods of study

Crystals PWO were grown by Czochralski method in vacuum or in an inert atmosphere (nitrogen, argon) with different oxygen content. Optical absorption of crystals before and after irradiation was studied using Specord UV-VIS and KSVU-23 spectrophotometers in the 300-600 nm range. Also measured were temperature stability of IA at T > 300 K, as well as photo-coloring. Samples for optical absorption measurements were prepared as cylinders 20 mm in diameter and 25-50 mm long with polished planar parallel ends. The samples were irradiated using an Co-60 source, Kharkov (T=300 K, dose rate 500 R/min). For photocoloration studies, samples were irradiated by a filtered hydrogen lamp light.

Results and discussion.

Results of optical transparency measurements for the crystals studied are presented in Fig.1. The highest initial transparency was noted for crystals grown under nitrogen. The crystals grown in air are characterized by a broad absorption in the region 420 nm.

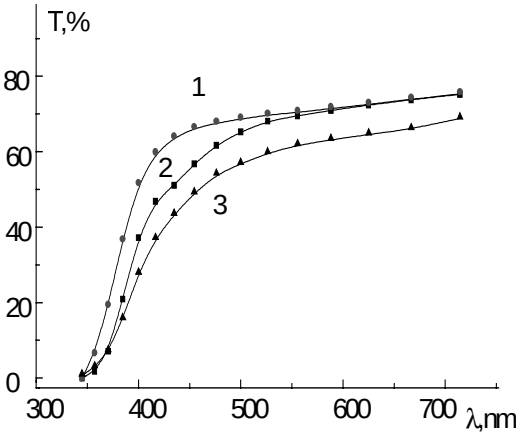

Fig.1. Transmission spectra of undoped PWO crystals grown in nitrogen (1), nitrogen with 19% oxygen (2) and in air (3).

According to Fig.1., the presense of the oxygen in the inert atmosphere leads to the extra absorption in the 375 nm and, especially, in the 420 nm region. However, transparency of such crystals is higher than of those grown in air. As noted in [1], this may be due to the influence of water vapor affecting PWO defectness. Effect of oxygen is possibly related to oxidation of the lattice sites of O^{2-} type located near the vacancies. Our measurement results as well as the literature data show that centers Pb^{3+} and O^{-} are initially present in the undoped PWO crystals grown by Czochralski method. Predominance of one or another type of centers depends upon crystal stoichiometry. Effects of doping of PWO strongly depends upon the type of the trivalent impurity. Yb-doped and La-doped PWO crystals have a very different optical characteristics and radiation hardness [2-4].

To study effects of dopants with different ionic radius upon optical transparency and radiation stability of $PbWO_4$, we have grown PWO crystals doped with La^{3+}, Fe^{3+}, Yb^{3+}. The results obtained are presented in Fig.2 (a,b), 3. According to our data, doping with ytterbium leads to a significant decrease in radiation stability. Strong absorption in the regions of 350 nm, 420 nm, 550 nm is observed after irradiation of the PWO crystals with Yb (Fig 2a) . Fe-doped PWO crystals also display a strong absorption in the 300-600 nm range (Fig.2b).

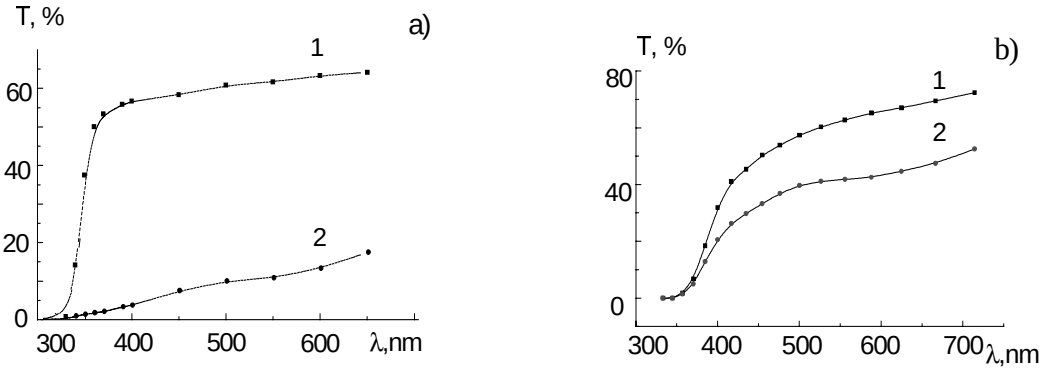

Fig.2. Transmission spectra of Yb (a) and Fe (b) doped PWO monocrystals before (1) and after (2) gamma-radiation.

In spite of it, doping with lanthanum (80 ppm) increases the transparency of PWO in the 350-370 nm region (Fig.3). The highest transparency (up to 80%) is observed with crystals grown in an inert atmosphere (nitrogen, argon). Somewhat lower transmittance of vacuum-grown samples is accompanied by a certain increase in absorbance in the 350-370 nm region

(which is lower than with nominally pure samples). The samples grown in air have the worse transparency. The absorption in these crystals is observed in all the wavelength range, and the 420 nm band is clearly manifested (Fig.3).

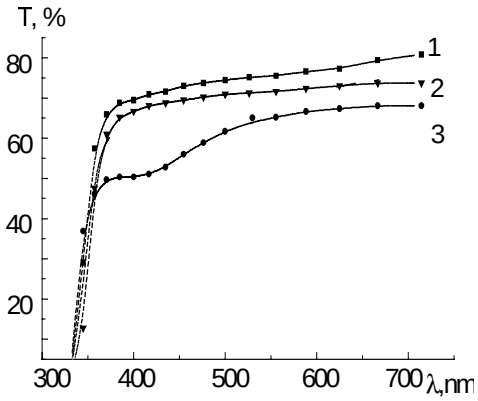

Fig.3. Optical transmission spectra of La -doped PWO crystals grown in argon (1) vacuum(2) and air (3) .

We assume, that the difference in acting Yb^{3+}, Fe^{3+} and La^{3+} impurities are explained by their ion radius. Perhaps, Yb^{3+} can substitute W^{6+} in the PWO lattice because their ion radiuses are close (0.81nm and 0.65nm, consequently). That gives the excess of oxygen vacancies, centers Pb^{3+} and O^{-}. In spite of it, La^{3+} substitudes Pb^{2+} and lead vacancies. (ion radius 1.04 nm and 1.26 nm, consequently [5]). This predicts the appearance of centers Pb^{3+} and O^{-}. La impurity is included in a lattice as La_2O_3, so La-doped PWO have less oxygen vacancies, then undoped.

Growth in oxygen-containing atmosphere, however, can lead to excess oxidation of lattice sites, which was really observed in our experiments as absorption at 420 nm. Probably, to grow high quality crystals in oxygen-containing atmosphere, higher concentration of lanthanum or optimisation of the growth atmosphere composition would be needed.

The results of the gamma-irradiation of the PWO crystals are presented in the Fig.4-6. The lowest IA was observed in samples grown in nitrogen. More sufficient IA was obtained after vacuum growth, and the crystals grown in air had the highest IA. As for initial optical absorption, IA appears to be lower when the crystal is grown in an inert atmosphere containing 19% oxygen than when it is grown in air. IA measurements were carried out one hour after the irradiation (Fig.4).

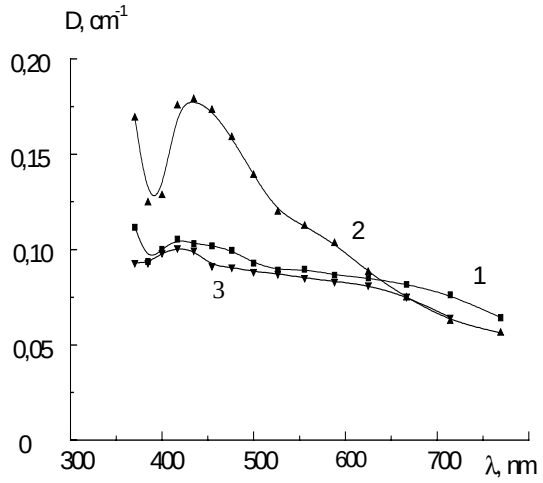

Fig.4. Induced absorption coefficient for undoped PWO crystals grown in nitrogen (1), air (2), vacuum (3).

La-doping of the PWO crystals leads to a significant decrease in radiation IA. The lowest IA values were found in crystals grown in an inert atmosphere (0.005 cm^{-1}) and in the air (0.015 cm^{-1} at 500 nm). Growth in vacuum gives crystals with high level of IA - about 0.025 cm^{-1} (Fig.5). One should note that gamma- radiation does not decrease the transparency in the 420 nm region in crystals where this absorption band is intrinsically strong - PWO[La] grown in air.

Moreover, in this region the crystal becomes more transparent after irradiation.It can be assumed that in such crystals after growth the most the oxygen ions located near to the defect sites are in the "absorbing" state (O^-), and the radiation cannot increase their concentration. On the contrary, after irradiation some of them can be transformed to O^{2-} state. That leads to the increase of the transparency by radiation.

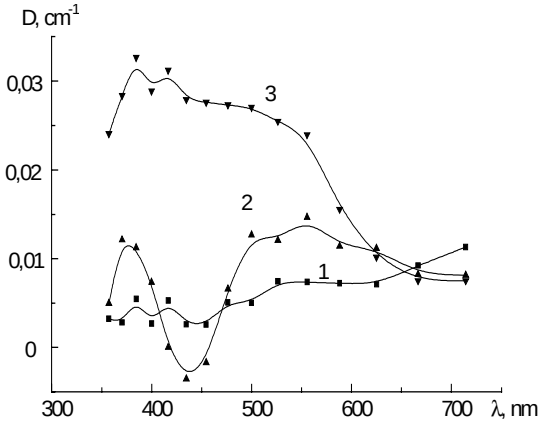

Fig.5. Induced absorption coefficient for the La-doped PWO crystals grown in argon (1), air (2) and vacuum (3) atmosphere.

Radiation stability of La-doped PWO crystals can be explained by the absence of unstable centers Pb^{2+} and O^{2-}, which are capable to pass over to the "absorbing" charge state, i.e., located close to the vacancies. This can be explained by low vacancy concentration due to their substitution with lanthanum, as well as excess oxygen in the lattice (see above). One should note that the effect of radiation transparency increase in the 420 nm region was described in [3] for crystals PWO doped with gadolinium. However, no data on growth condition have been presented.

Scintillation characteristics are directly connected with the optical transparency of scintillators. Measurements of light yield were carried out for crystals irradiated with high (10 kGy) and low (up to 1 kGy) doses. The light output of the irradiated undoped crystals (under excitation by a Cs-137 source, E=662 keV) could be measured only 5 hours after irradiation by 50 Gy due to strong phosphorescence. At the same time, crystals with lanthanum displayed practically no phosphorescence, and the measurements could be carried out in just one hour after irradiation.

The light output recover in the undoped and doped PWO crystals grown in different gas conditions and irradiated by the dose rate 4 Gy/min (dose 5kGy) are presented in Fig.6. Radiation-stimulated decreasing of the light output of nominally pure crystals grown in argon and in nitrogen was 35% and 40%, respectively. This is in an agreement with data on IA intensity of these crystals after irradiation (Fig.4). Similar light output decrease was observed in crystals grown in air (measurements 24 hours after irradiation). The recovery rate depends on grown conditions. For crystals PWO doped with lanthanum (growth in pure argon). The light output recovered reached 96% of the initial value during the first hour after the end of irradiation.

Very interesting results were obtained for lanthanum-containing PWO crystals grown in air. With initially low light output, an increase by 20-25% is observed after irradiation. This effect is explained by increasing of the crystal transparency in the maximum PMT sensitivity range (420 nm). When silicon photodiodes are used, the expected effect is less pronounced.

The creation of IA is explained by the capture the free carriers on traps during the recombination process. Recover of the initial charge state of the centers occurs as a result of thermal delocalization of these carriers from traps, which is observed as slow decreasing of IA with time constants depending upon the trap depth.

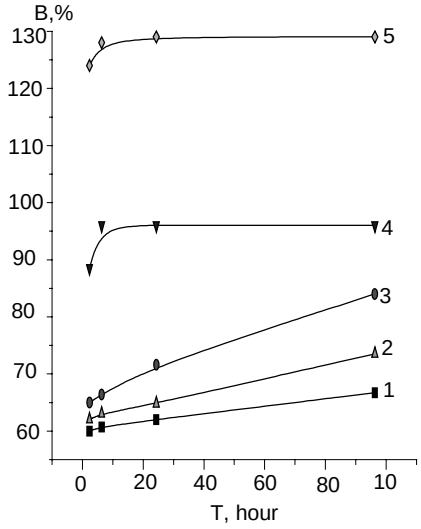

Fig.6. The light output recovering for γ-irradiated PWO crystals: N_2(1), air(2), Ar(3), La_2O_3+Ar (4), La_2O_3+ air(5)

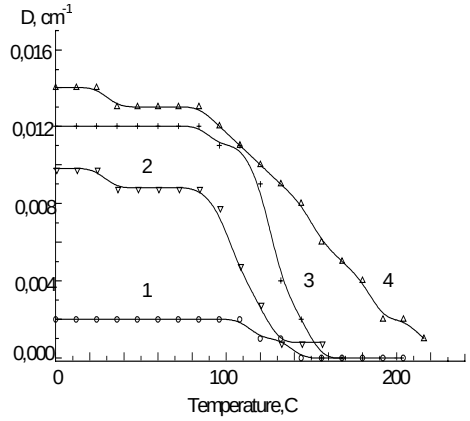

Fig 7. Induced absorption coefficient of PWO crystals during the heating: 1- PWO + N_2 + La, 2 - PWO + air + La, 3 - PWO + Ar, 4 - PWO + vacuum

We have carried out measurements of thermoactivation annealing of IA for PWO samples. The irradiation dose during IA measurements was 10 kGy. Heating rate from the room temperature to T=350 K was 0.2 K/s. The first stage of annealing is short enough for crystals grown in the inert atmosphere(about one hour). For crystals grown in air, it is longer (3-5 hours). Doping of PWO with lanthanum leads to considerably shorter times of recovery - up to tens of minutes (Fig.7). Annealing at room temperature, as a rule, does not lead to full recover of optical characteristics of PWO. Therefore we have measured IA under uniform heating of the irradiated crystals. The results obtained are presented in Fig.7. It can be seen that in undoped PWO samples the main annealing occurs at T=380-440 K. Samples containing lanthanum were annealed in a more narrow temperature range (370-400 K). This indicates that there are no deep traps in the lanthanum-doped crystals. These traps presents in the undoped crystals PWO and are responsible for more high-temperature stages of annealing and longer components of the IA fall at room temperatures. It can be assumed that doping with lanthanum suppresses the defects typical for undoped samples.

It was shown earlier that UV irradiation leads to the coloration of the PWO crystals which is similar to coloration after gamma-irradiation [6]. We investigated the effects of the light coloration of the undoped and La-doped PWO crystals grown in different gas conditions. It was established, that IA spectra is the same after gamma and light irradiation in all investigated PWO samples. Also the value of IA is the similar after gamma and light acting.

Analysis of the data shows that concentration of color centers is usually the highest in crystals grown in air. Crystals grown in argon and vacuum are colored by UV light in a similar way. Coloration of La-doped crystals growth in argon atmosphere is practically absent. Vacuum growth gives somewhat worse results. That coinsides with the results obtained after gamma irradiation.

Irradiation of colored crystals with light of wavelength in the region of IA spectrum leads to their rapid discoloration. The most efficient is 550 nm light. Similarity of effects of UV and gamma-radiation has been proven for crystals of different defectness. This is an additional confirmation of the similar nature of color centers in PWO induced by gamma- and photoirradiation. IA in PWO is related to re-charging of the pre-irradiation structural defects.

Conclusion

The highest transparency and radiation stability is obtained for PWO crystals that are doped with lanthanum and grown in an inert atmosphere containing some oxygen.

The recovery rate of transparency and light output depends upon composition and concentration of pre-radiation defects. Nominally pure crystals have three characteristic components on the recovery curve: 10-20 min, 3-5 hours and several days. The lowest value of the second constant (about one hour) is observed for crystals grown in the inert atmosphere, the highest - for those grown in air. Doping with lanthanum leads to substantially shorter recovery times of PWO transparency, which is characterized by only one constant - about one hour.

It is shown that photochromic effect is observed with formation of color centers which are identical to color centers induced by gamma-radiation.

Photoirradiation can be used for express prediction of radiation stability of crystals PWO.

References

1. Woody, J.A. C Kierstead, S.P. Stoll, R.Y. Zhu A Study the optical and Radiation damage propertes of Lead Tungstate Crystals. SCINT 95, P.278-285.
2. E. Affray, P.Lecog, A. Annenkov. Improvement of several properties of lead tungstate crystals with different doping ions.// .CMS NOTE 97-54, July 8, 1997. CMS CERN, CH-1211, GENEVA 23, Switzerland.
3. S. Baccaro, P. Bohacek, B. Borgia, Radiation Damage and Thermoluminescence of Gd-doped PbWO4.// Phys. Stat. Sol.(a), 164, R9, (1997).
4. A.Groenink, H.Binscha. J.Sol.Stat.Chem.,1979, V.29, P.227.
5. Гороновский. ркий срвоник о иии ./ . . . иинко . ив . ков к , 1987 .
6. I Daffini, B. Borgia, F. Cavollam Color Centers Production in PbWO4 Crystals by UV Light Exposure. SCINT-95.

Influence of technology conditions on luminescence parameters of large-size $PbWO_4$ crystals

I.M.Soljskii[1], A.V.Gectin[2], M.V.Korzhik[3],
R.V.Gamernyk[4], Z.A.Khapko[4], A.S.Voloshinovskii[4]

[1]*Institute for Materials, SCR "Carat", 290031, Lviv, Stryiska str., 202, Ukraine*
[2]*Institute for Single Crystals, Kharkiv, Ukraine*
[3]*Institute for Nuclear Problems, Minsk, Belarus*
[5]*Lviv Franko State University, 8 Kirilo i Mefodii str., 290005, Lviv, Ukraine*

Abstract. Samples of large-size $PbWO_4$ crystals 230 mm long and 80 mm diameter of great optical and scintillation homogeneity have been grown by the Czochralsky method under the different technological conditions. Dependence of photoluminescence and photocurrent within the green luminescence excitation band on polarization and direction of the light propagation have been investigated. It was revealed that maximal photocurrent and green photoluminescence intensity values had been observed with PWO crystal excitation in the Z-axis direction. Excitation with the linearly polarized light in this direction has resulted in the azimuthal dependence of photocurrent (photoluminescence) intensity at maxima alternation in 90°. This dependence correlates with orientation of Pb-O bond in crystal. It is assumed that complexes $[Pb^{2+}+WO_4^{-}]$ and $[Pb^{2+}+(WO_3+V_a)]$ are responsible for the green luminescence.

Keywords: photocurrent, luminescence centers, crystal growth

Introduction

Recently a lot of publications appeared which concern technology of lead tungstate (PWO) formation and physical processes occurring in it with UV-, X- and γ-quantum excitation. Radiation spectrum of such a crystal contains two main wide bands of luminescence: blue (λ_{max}=420 nm) and green (λ_{max}=500 nm). Their excitation spectra are separated rather well at the low temperatures (T≤100 K) and are overlapped highly on crystal heating up to the room temperature. Scintillation kinetics of the PWO crystal, besides fast component (nanosecond afterglow), also contains very slow one (several μs) connected mainly to the green luminescence [1].

Considering the severe requirements to the fast response these slow processes are undesirable on registering the high-energy particles. Therefore knowledge of the green luminescence nature can assist to choose the way to reduce the intensity and duration of the slow component.

In the present work spectral-kinetic and photoelectric characteristics of the large-size PWO crystals have been investigated with a view to consider and summarize the mechanisms of absorption and excitation relaxation in the green luminescence centers.

Experiment

PWO crystals have been grown by the Czochralsky method. Four large-size crystals (PWO1,…, PWO4) of 80 mm diameter and 230 mm long have been grown under the different technological conditions. The first crystal was grown from specially prepared mixture (mixture of PbO and WO_3). PWO2 crystal have been grown as follows. Necessary

amount of mixture was added to the melt remained after previous growing and recurrent growing has been performed. Further crystals were grown by repeating the same procedure. The grown crystals differed in defects level as evidenced by difference of their colour. The first PWO1 crystal practically was colourless. The next crystals were yellow, with maximal yellowness in PWO4 crystals. Samples for investigations were cut out of the central bulk part in the form of rectangular parallelepipeds of 8×8×5 mm^2 perpendicularly and in parallel to Z-axis of crystal.

Mercury lamp light and nitrogen laser radiation (λ_{rad}-337 nm) were used for excitation of photoluminescence (photoconductivity). For measuring the spectra of photoconductivity excitation, contacts were coated on the front and rear crystal faces (along light path).

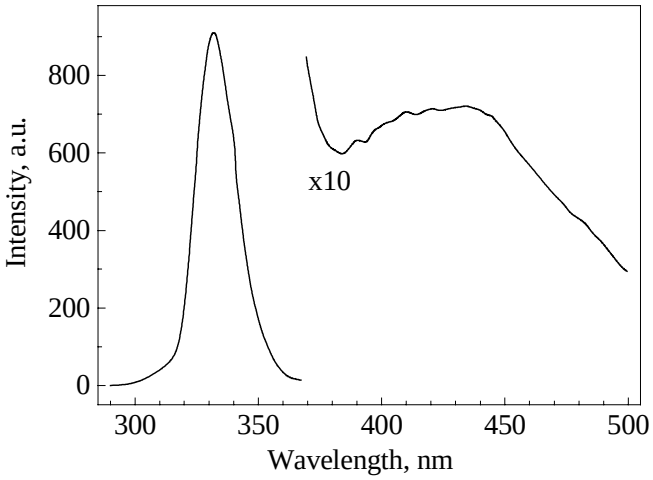

Fig. 1. Spectra of PWO crystal photoconductivity excitation measured at the room temperatures.

Photoconductivity excitation spectra of PWO crystal (fig. 1) were measured at the room temperatures. In all investigated crystals the intensive photocurrent band is observed in a vicinity 320 nm. In a number of PWO1,…, PWO4 crystals the half-width of this band is constant and only the intensity increases with the crystal defects occurrence. In the long-wave region of this spectrum one can observe weak band at 430 nm whose intensity practically is not changed in all the samples. Types of carrier produced in these photoconductivity bands have been defined by the photocurrent direction. In 320 nm band the electrons are as photo-excited carriers, and for 430 nm band the holes are.

Investigations of the oriented crystals excited within 320 nm band (λ_{exc}=313-337 nm) showed that propagation of the nonpolarized light along the optical axis contributed to photocurrent occurrence, and at the same time with excitation in direction being perpendicular to it under the same experiment the photocurrent was practically absent. Excitation with linearly polarized light revealed the azimuthal dependence of photocurrent value in the first case, with alternation of intensity maxima occurred in 90° (fig. 2). Different technological conditions for crystal production did not affect the qualitative picture of photoluminescence. On crystal exciting in the band of fundamental absorption (λ_{exc}=296 nm), the 420 nm luminescence band was observed with substantial longwave tail, and with excitation in the preedge region (λ_{exc}=337 nm) the wide luminescence band has maximum in 500 nm range. Intensity dependence of both luminescence bands on the crystal defects level has been discussed previously in work [2] so this problem will not be considered in given article.

It also turned out that the excitation along the optical axis (λ_{exc}=337 nm) created photoluminescence intensity in 3-4 times of the analogue one with the same crystal excited in the direction perpendicular to this axis. As with photoconductivity in the first case it was also observed the azimutal dependence of luminescence at the same repetition period of maxima.

Considered above the behaviour characteristics of photocurrent and photoluminescence are inherent only with crystal excited in preedge absorption ($313 \le \lambda_{exc} \le 337$ nm) and are absent on its excitation within fundamental absorption region ($\lambda \le 300$ nm).

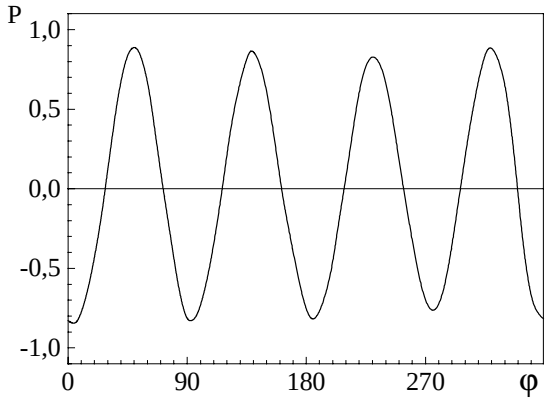

Fig. 2. The azimuthal dependence of photocurrent polarization degree for light propagated along the optical axis.

Discussion

Behaviour characteristics of photocurent and photoluminescence with excitation in the preedge absorption region can be due to PWO crystal structure. The 320 nm band (fig. 1) observed in the photoconductivity excitation spectrum appears in the region of defects absorption and correlates with the maximum position of the green luminescence excitation band. Previous articles [3, 4] showed that the optical absorption edge was not described by the Urbach's rule since it consists of two close bands: weak longwave and intensive (temperature dependent) shortwave ones. Green luminescence is effectively excited just at the longwave edge of fundamental absorption, and the excited state of the luminescence center was suggested to be considered as Pb^{3+}-WO_4^{3-}.

As far as electrons are photocurrent carriers in the 320 nm band it can be assumed that absorption center comprises lead ion which is able to change its valency ($Pb^{2+} \rightarrow Pb^{3+}$). On the basic of azimuthal dependence of photocurrent (photoluminescence) absorbing dipole is also stated to be oriented towards Pb-O, for Pb-O bond in this structure has 90° repetition period only in plane perpendicular to the optical axis. From calculations of the PWO crystals band structure given in article [5] it follows that the absorption edge may be formed by transitions in orbitals produced with Pb6s-states and 2p-oxygen. The presence of defect at the oxygen place results in WO_3-center occurrence, decrease of transition energy in Pb-O dipole and formation of local level in the forbidden region.

Transitions in this dipole produce the band of preedge absorption. Appearance of photoconductivity on crystal heating (T>150 K) adjust with thermal activation of electron into the conduction band revealed in [6].

This temperature dependence of excitation process of the green luminescence centers reveals itself in kinetic of decay time luminescence [7]. At the lower temperatures this emission is characterized by the monoexponential decay. But at the temperature as T>150° nonexponential millisecond decay component takes place. High intensity of the slow recombination processes in this luminescence band is due to thermal decay of the radiative center with the further restoring radiative recombination.

Existence of anion defects the electron and hole type in PWO crystal has been established by many authors. Trapping of electron with oxygen vacancy results in F^+-centers formation, and the hole localization on the oxygen ion produces O-centers [8]. Considering the existence of such defects in crystal, the process patterns of green luminescence excitation can be as follows:

$$Pb^{2+} + WO_4^{-} \rightarrow [\, Pb^{3+} + WO_4^{2-} \,]$$
$$Pb^{2+} + (\, WO_3 + V_a \,) \rightarrow (\, [\, Pb^{3+} + {}^{(}WO_3 + F^+ \,) \,] \,,$$

where V_a and F^+ are anion vacancy and F^+- center, respectively.

Conclusions

Investigation of the azimutal dependence for photoconductivity (photoluminescence) will allows to connect the absorption center responsive for green emission to dipole: lead with

defect at oxygen place. Occurrence of photoconductivity at T>150 K is due to the thermal electron activation from the excited state to conduction band.

References

1. M. Kobayashi, M. Ishii, Y. Usuki and H. Yahagi, Scintillation characteristics of $PbWO_4$ single crystals, Nucl. Instr. And Meth. **A 333** (1993) 429-433.
2. I. Sol'skyi, A. Gectin, M. Korzyk, Z. Khapko, A. Voloshinvskii, Spectral-kinetic parameters of large-size $PbWO_4$ crystals, Func. Matter. Vol.2, No.6 (1999)
3. W. Loo, Luminescence of lead molybdate and lead tungstate, Phys. Stat. Sol. (**a**) Vol.27 (1975) 565-574.
4. W. Loo, Luminescence of Lead Molybdate and Lead tungstate, Phys. Stat. Sol. (**a**) Vol.28 (1975) 565-574.
5. N.A.W. Holzwarth, Y. Zhang and R. Williams, Electronic Band structures of the scheelite tungstates and consequences for material properties, (privat comunication).
6. E.G. Reut, Photoconductivity and luminescence in crystal with scheelit structures, Solid state physics (in Russian), Vol.23, (1981) 2514-2516.
7. V. Murk, M. Nicl, E. Mihocova, A study of electron excitations in $CaWO_4$ and $PbWO_4$ single crystals, J. Phys. Condens. Matter. Vol.9 (1997) 249-256.

Study of optical properties of $PbWO_4$ crystals irradiated by gamma-quantums, fast neutron and 1 GeV protons.

V. Yevseyev ,V.Samsonov

St.Petersburg Nuclear Physics Institute Russian Academy of Sciences
188350 Gatchina, Leningrad district,RUSSIA

Abstract. The results of study effect of γ- Co^{60} , fast (1 MeV) reactor neutron and 1 GeV proton irradiation on optical properties of lead tungstate ($PbWO_4$) are presented. The peculiarities of radiation defect formation in $PbWO_4$ under these three type of irradiation are considered. It is shown that in crystals of lead tungstates essential role plays so-called subthreshold defect formation. The carried out comparative analysis of effect of gamma-rays, neutrons and protons on optical properties of PWO has shown , that the efficiency of defect formation increase at transition from gamma- to neutron – and further to proton irradiation.

Keywords**:** $PbWO_4$ **,** gamma-, neutron- and proton-iradiation, optical properties.

Introduction.

A known high radiation hardness of Lead Tungstate define its application as promising material in the EH-calorimeter of the CMS experiment at LHC.. At the same time it is necessary to note, that the given class of scintillators is not yet enough investigated from the point of view of a nature of radiation defects causing its radiation harness, but the available literary data on it carry faster descriptive character. Earlier in a number of works [1-3] the research of optical, emission, impurity and radiation properties of crystals $PbWO_4$ irradiated mainly by γ - quantums was carried out. However, for complete understanding of the specified properties and maintenance of radiation resistance of PWO it is necessary, alongside with γ- quantum to consider influence and of high energy particles - neutrons and protons.

In the given work the first results of comparable research of influence γ - quantum and high energy particles - neutrons and protons on heavy scintillators $PbWO_4$ are given.

Experimental.

The irradiation of samples $PbWO_4$ ($2x2x2cm^3$) by γ- Co^{60} was carried out at PNPI's installation "Researcher"(2000 Ci) with dozes 0,1…10 Mrad , by fast 1-MeV neutrons at PNPI's WWR-M reactor with fluences $7\cdot 10^{12}$ …. $1\cdot 10^{16}$ cm^{-2} and by 1-GeV protons at synchrocyclotron PNPI with fluences $1\cdot 10^{12}$ …$1\cdot 10^{14}$ cm^{-2}. The measurement of optical absorption in range wavelength 200-900 nm was performed at double-beam spectrometer Specord –M40.

Processes of radiation defect formation in heavy scintillators at an irradiation by γ- quantums, neutrons and high energy protons.

Irradiation by γ- quantums.

At an irradiation of crystalline substance with the gamma - quantum occurs displace of atom from a lattice site to interstitial and creation of defects such as Frenkel pairs (FP). As the probability of direct interaction of gamma - quantum with nucleus of atoms is small, the displace of atoms is connected with operation of fast electrons, originating as a result of a photoeffect, Compton-effect and formation of electron - positron pairs. At $E < 5$ eV the

Compton-effect prevails. At E> 5 MeV the essential role plays the derivation of electron-positron pairs. The contribution of photoelectrons in formation of radiation defects (RD) by knocking-out is insignificant.

Approximate estimations of number of the displaced atoms in PWO at energy γ- quantum 1,25 MeV give values N ~0,01 m^{-1} at threshold energy E_d = 100 eV.

The features of defect formation under irradiation by high energy particles.

The process defect formation by particles of high energies occurs in two stages. The first stage is connected to interaction of radiation with atoms of a crystal resulting to knocking-out of atoms from sites of a lattice. The second stage - interaction of primary knocked-out atoms with adjacent atoms of a crystal, with impurities and others inhomogeneous of a lattice.If energy colliding a particle E insignificantly exceeds threshold energy E_d, the simple defects – Frenkel pairs are created. Such defects will create in volume of a crystal at irradiation by γ-quantums ^{60}Co or by electron with energy ~ 10 eV. Rather complex there is a picture of radiation damage in that case, when is primary knocked atom receives energy E> > E_d, that is observed in case of an irradiation by high energy particles: fast neutrons , protons and electrons with energy > 10 eV. In this case the development of the cascade of atom - atom collisions at passing particles of high energies through substance, is accompanied by appearance of disordered regions (DR).

Irradiation by fast neutrons of reactor.

In contrast to γ- irradiation, the effect of fast neutrons on substance is characteristic by that because of absence of an electrical charge the neutrons cause damages of a crystalline lattice only in cases " frontal " collisions with a nucleus of lattice atom (elastic interaction). The primary knocked atom leaves the place in a lattice, therefore simultaneously occure a vacant site and atom in interstitial..

The occurred vacancies are united, derivating claster of vacancies and divacancies. Such congestions of defects in limited volume of a crystal (10-100), surrounded by a layer of a volume electrical charge - disordered regions - can essentially differ from the unbroken part of a crystal. DR, being macroscopic formation, can exhibit essential influence on optical properties of a material, resulting to light scattering, unselective absorption and /or to shift of edge of a fundamental absorption. Besides at collision of high -energy particle with atoms of a crystal in him there can be for short time $\tau \sim 10^{-6}$ s superhigh pressure about thousands atm. and high temperatures > 1000^{o} with the consequent fast cooling (so-called thermal wedges [4]). Therefore, at large flows of high-energy particles, the accumulation of the acts of local pressure and overheat inevitably results to radiation cracking of a crystal.

Irradiation by 1-GeV protons.

The nature of defects at high-energy proton irradiation is defined mainly by formation of group defects. At that a role of Coulomb, and also nuclear elastic and inelastic interactions in creation of group defects is various. So, in result of Coulomb collisions are created in main low-energy recoil atoms forming mostly point defects. The nuclear elastic and inelastic interactions result information of high-energy recoil atoms and fragment nuclei creating group defects. Thus, at an irradiation of PWO by protons of high energies it is possible to expect formation of defects of the 3-rd types: point defects, clusters of small sizes and DR.

The subthreshold defect formation.

In the crystals with ionic type of links (to which concerns $PbWO_4$) essential role plays so-called subthreshold defect formation , when the value of energy of colliding particle is less than threshold energy E_d of transfer of atom from a site of a lattice to interstitial (FP-creation). At subthreshold low energy mechanism of defect formation ,X-ray quantum or photoelectron displace atom from a site of a lattice not through of elastic interaction, but by excitation of an

electronic subsystem – ionization of deep K- atom shell with the consequent Auger-cascade of electron. The creation of simple defect - FP thus occurs with involvement of impurity atom , since Frenkel pair is born near to impurity, or is displaced itself impurity atom. On this basic it is possible to expect, that in crystal with ionic link the creation of FP is considerably facilitated in comparison with other crystals (for example, semiconductors) since in crystals with a wide forbidden gap and strong electron-phonon link energy of nonradiating recombination is great which can be comparable to energy of FP-formation.

Thus, the materials with ionic type of links are an example of crystals, which is characterized by effective subthreshold defect formation, connected, in particular, with involvement excitons [5]. The possible reason of the small contribution of cascades of nuclear displacements in a total number of RD is connected to active recombination of vacancies and superfluous atoms in the field of high density of both components of Frenkel-defects.

Experimental results.

In work the samples $PbWO_4$, undoped and specially doped by Niobium (Nb) from 4 up to 30 ppm size both 2 2 2 m^3 and 2 2 1 m^3 were used, grown up on- Czochralski at Bogoroditsc Technochemical plant (Tula district).

Effect of irradiation by gamma – quantums on optical properties of PWO –crystals.

The main results on a research of optical properties PWO irradiated with various dozes the gamma – quantum ^{60} , are reduced to the following:

1.With increase of a doze γ - radiation from 0,1 up to 10 rad is observed monotone degradation of optical transparency of crystals PWO through of them " colorings " at introduction of radiation defects - color centers and - as a consequence - decrease of optical transparency (λ) and optical absorption length L (λ).

2.In samples PWO irradiated with a maximum doze of gamma – quantum ^{60} 10 r d is observed effective annealing of RDs at 300

3.The positive influence on radiation resistance of Nb-doping PWO is marked which interferes with formation of color centers ;

4.The spectral dependence μ in a range of wavelengths 400-800 nm has nonmonotone character with extremums at 400 nm and 600-650 nm, , stipulated by a superpositions of absorption bands concerning to (WO_4) and F- center, accordingly .

Effect of irradiation by 1-GeV protons.

As a result of the carried out researches of optical properties PWO irradiated with protons is shown, that:

1. With growth of an irradiation doze is observed strong degradation of transparence coefficient T (λ) and optical an absorption length L (λ), and also shift of fundamental edge of an absorption in long wave part of a spectrum ;

2. The observable shift of fundamental edge of an absorption occurs sublinearly with a doze as Δ (λ) ~ $^{1/2}$;

3. The spectral dependence of proton-induced absorption coefficient $\mu_p(\lambda)$ has sort smoothly of falling down exponential dependence ;

4. The change of proton-induced absorption coefficient μ_p with a doze of an irradiation is described by degree dependence of a type μ_p ~ ^{n}, where n ~0,25 in an interval of dozes $1\cdot 10^{12}$ - $1{,}5\cdot 10^{13}$ m^{-2} and n ~0,9 in a range of dozes $1{,}5\cdot 10^{13}$ - $1{,}1\cdot 10^{14}$ cm^{-2} ;

5. From the analysis of spectral dependence (λ) for PWO with Nb and PWO without Nb is not revealed of noticeable influence Nb on radiation resistance of PWO to a proton irradiation. .

6. Proceeding from obtained experimental data on proton-induced absorption coefficient (absence on him of the absorption bands), and also judging from weaker than at the gamma- or neutron exposure radiation colouring of a crystal, is possible to believe, that at an irradiation of PWO by protons are entered not point defects, but clusters and DRs.

Effect of irradiation by fast neutrons of reactor.

From data on optical measurements follows, that:

1. With growth of doze irradiation of PWO samples without Nb occurs degradation of optical transmission (λ) and optical absorption length L(λ), and for λ= 400-700 nm this degradation is stronger, than for λ~ 300 nm ;

2. With rise of a doze has a place shift of fundamental edge of an absorption in short-wave area of spectrum and broadening of a forbidden gap PWO on 0,14 eV;

3. In the irradiated samples PWO doped and undoped by Nb s are observed annealing of radiation defects at = 300 and partial restoring of optical transparency of crystals;

4. The irradiation with maximum fluence $1\cdot 10^{16}$ cm^{-2}. results in strong loss of transparency of a crystal PWO through of an absorption of light by color centers , and through of scattering on macrodefects, arisen as a result of radiation cracking of PWO;

5. The spectral dependence of neutron-induced absorption coefficient $\mu_n(\lambda)$ has nonmonotone character with maximum at λ= 400 and 520 nm, stipulated by a superposition of the absorption bands concerning with (WO_4) - center and F- center;

6. The dose dependence of neutron-induced absorption coefficient $\mu_n(\ )$ in dose interval $7\cdot 10^{12}$ - $1\cdot 10^{16}$ cm^{-2} has sublinear character $\mu_n \sim$ ^{n}, where n ~ 0,4;

7. The spectral dependence of neutron-induced absorption coefficient $\mu_n(\lambda)$ has exponential character with a maximum at λ = 300 nm .

Summary.

It is shown, that the radiation damage of heavy scintillators PWO at γ- irradiation is stipulated by introduction of point defects such as Frenkel pairs , which components (the vacancies and interstitial) participate in formation of color centers , that results to degradation of optical transparency in the range of wavelengths 300-800 nm and deterioration of crystal light output.

The irradiation of PWO by fast neutrons results in formation as simple point defects (color centers) and DRs.

Is shown, that at large fluences of neutrons > $1\cdot 10^{15}$ cm^{-2} can take place radiation cracking of scintillators through formation in them of so-called thermal wedges (pressure of thousands atm., > 1000^o during $\tau\sim 10^{-6}$ s).

It is established, that the irradiation of PWO by protons with energy 1 GeV is accompanied by primary introduction of large defects of a type disordered regions.

In samples PWO, irradiated by protons, noticeable influence of doping by impurities - protectors on optical properties it is not revealed, that is indirect confirmation of low concentration in PWO point radiation defects.

The carried out comparative analysis of influence of three sorts of an irradiation on optical properties of PWO has shown, that the efficiency defect formation increases at transition from a gamma to neutron - and further to a proton irradiation.

References

1. E.Auffray et al.: CERN.- CMS TN/95, (1995) 123
2. R.Y.Zhu et al.:.NIM.**A376** , (1996) 319-334..
3. P.Lecoq et al.: NIM **A315**, (1992) 332-336.
4. J.W.Corbet, J.C.Bourgoin.: Point defects in solids. V.2, Pl. Press, N.Y, (1975).
5. A.I.Anselm ,L.G. Lang: Phys. St. Sol.(b), v.80,.691-695 (1977).

Lead tungstate scintillation crystals optimized for high-energy physics applications

S.Burachas[1], V.Bondar[1], B.Grinyov[1], K.Katrunov[1], V.Martinov[1], L.Nagornaya[1], V.Ryzhikov[1] *G.Tamulaitis*[2]

[1]*Concern "Institute for Single Crystals", pr. Lenina 60, Kharkov 310001, Ukraine*
[2]*Institute of Materials Science and Applied Research, Vilnius University, Naugarduko 24, Vilnius, Lithuania*

Abstract. Development of fabrication of lead tungstate (PWO) scintillation crystals grown by the Czochralski method is discussed. The optical and kinetic characteristics and radiation hardness of the crystals are compared with the standard specifications formulated to meet the needs of high-energy physics experiments. It is demonstrated that crystals fabricated by combining optimization of growth regimes and annealing conditions with La-doping can be produced without recrystallization within 60 h for the total period of melt preparation, growth, and annealing.

Keywords: PWO; Scintillation detectors; Radiation hardness; Optical absorption

Introduction

Recently, lead tungstate (PWO) considerably overran other scintillation crystals in certain applications for high-energy physics experiments. The increasing interest in the PWO scintillators is especially stimulated by their employment in the Large Hadron Calorimeter (LHC) project in CERN. The experience in production, characterization and application of PWO accumulated by several laboratories and research groups is summarized in specifications for PWO production, which have recently been prepared in CERN [1]. The specifications encompass the whole complex of characteristics including optical transmission, luminescence, radiation hardness, geometry etc. Therefore, it is of especial interest to compare the characteristics of our PWO crystals fabricated at Concern "Institute for Single Crystals", Kharkov, Ukraine, with these specifications.

Our concept of development of technology for PWO growth and subsequent thermal treatment was basically presented in [2] and it was aimed at fabrication of a colorless crystal with the luminescence spectrum peaked in the blue region (420-450 nm). Purity of the raw materials, conditions and regimes of synthesis, melt preparation, and crystal growth have been revealed as the main factors influencing the important characteristics of the PWO crystals. Crystal growth was monitored by the power consumed by the heater under automated maintaining of constant diameter of the growing crystal. Other important factors include annealing of the boule and block-shaped scintillation crystals, as well as composition and pressure of the atmosphere during the whole period from melt preparation to fabrication of the final scintillation crystal. The technological details are presented in [3,4] and the comparative analysis of the crystal characteristics is given in [5].

The present paper reports on further development of our technology in order to comply with the whole set of the specifications prepared at CERN [1].

Optimization of the growth and annealing technology without intentional doping

As demonstrated in [6], if the limit of the required response time is in the range up to 100 ns, the optimal peak position of the luminescence band can be red-shifted from 420 nm down to 450 nm. The crystals with this position of the luminescence peak have still no red

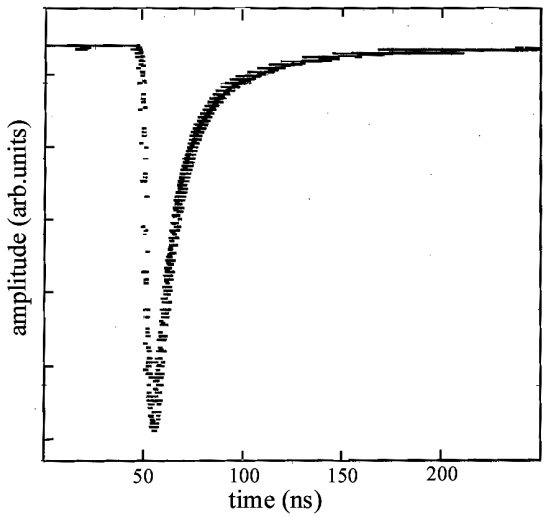

Fig. 1. Response kinetics of 6 PWO crystals compared with standard requirements (shadowed area).

component of the luminescence spectrum and do correspond to requirements for scintillator crystals. On the other hand, they have higher light yield, reaching up to 11-14 phe/MeV for 230 mm long crystals, than that of the crystals with extremely blue-shifted position of the luminescence band. Time evolution of response signal of 6 optimized scintillation crystals were measured at Paul Scherrer Institut (PSI) and are presented in Fig. 1. Note that no one of the decay curves proceed slower than the standard decay to accord the requirements for application (shadowed area in the figure 1).

Though having good light yield and temporal characteristics, the optimized samples had lower longitudinal transmission at 350 nm than that defined in the CERN specification (≥10%) [1]. The absorption in this spectral region is mainly caused by the absorption band peaked at 350-370 nm. The presence of this band is usually related with the Pb^{3+} centers [7]. However, the transmission of the crystals may be decreased not only by absorption centers, but also by light scattering centers. Inclusions of Pb_2WO_5, a small amount of which we identified by using X-ray phase analysis, may serve as such scattering centers. These inclusions may occur in congruentively melting composition for growing $PbWO_4$. It is worth noting that recrystallization does not ensure removal of the inclusions and, consequently, improvement of optical transmission of the crystals.

Insufficient radiation hardness was one of the drawbacks of these crystals. Irradiation of the scintillators up to the dose of 4.5 krad at the dose rate of 500 rad/min caused a decrease of the transmission by 5-20% of its initial value. We observed the photocromic effect also at lower irradiation intensities. In usual conditions the photocromic effect is rather small and can be unambiguously identified only after storing the sample in the darkness for 30-40 days. The photocromic effect was found to be strongly dependent on the content of impurities in the initial melt. We succeeded to trace two impurities, bismuth and tin, which considerably enhance the photocromic effect. Presence of bismuth and tin in the melt at concentrations of $5 \cdot 10^{-3}$ and 10^{-3} wt % , correspondingly, deteriorates the quality of the scintillator to the extent that they are unsuitable for any application.

Characteristics of La-doped crystals

It has been demonstrated that the radiation hardness may be improved by doping the PWO crystals by La [7,8]. Small amounts of La in PWO improve also the optical transmission and accelerate the luminescence decay [9,10]. So we also used La doping and got improved crystals without any additional adjustments of the growth technology optimized earlier for undoped crystals (see [3,4]).

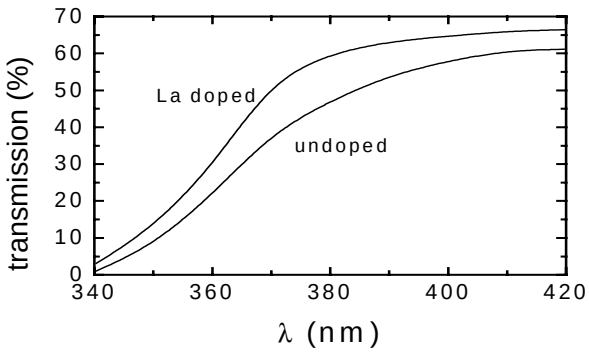

Fig.2.Optical transmission of undoped and La-doped PWO crystals.

First of all, the La-doped crystals have better transmission in the UV region (see Fig. 2). Since short-wave region of the emission band strongly overlaps with the

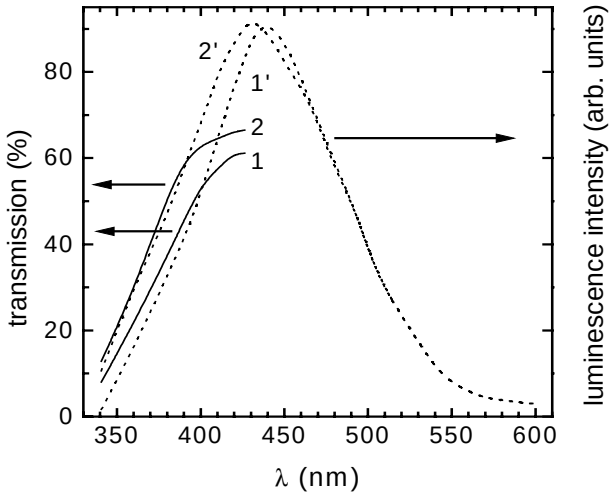

Fig. 3. Spectra of absorption (solid lines 1,2) and X-ray excited emission (dotted lines 1',2') of undoped (1,1') and La-doped (2,2') PWO crystals.

absorption edge of the crystal, reabsorption may be of considerable importance in formation of the final shape of the luminescence band as well as it may also influence the spectrally-integrated external luminescence yield. The situation is illustrated in Fig. 3, where absorption and emission spectra are compared for La-doped and undoped crystals. So the blue shift of the luminescence band in La-doped crystals seems to be caused just by decreasing reabsorption in the region 330-400 nm.

In order to control the radiation hardness of the PWO crystals we developed an express method without implementation of ionizing radiation. As it has been demonstrated in [11-13], UV irradiation causes formation of the same color centers as γ-radiation. So we established that the 30 min exposition of the crystal to UV radiation at 365 nm wavelength and $12.8 \cdot 10^{-2}$ mW/cm^2 intensity is approximately equivalent to the irradiation dose of 600 rad at the dose rate of 30 rad/min. The spectrum of the induced absorption in the region of interest is presented in Fig. 4. The induced absorption increases with decreasing wavelength, however, is still considerably lower than 1 m^{-1}. The value is lower than that specified by the CERN standard of $\leq$1.5 m^{-1} at the wavelength of 420 nm [1]. It is worth noting that the value induced absorption for our undoped crystals was usually in the range of 3-5 m^{-1}.

The transversal transmission of the La-doped crystal is presented in Fig. 5. In accordance with the specifications, 6 measurements every 4 cm along the crystal, the first one at 1.5 cm from the front face, were carried out. The dispersion of the transmission at the level of 50% was found to be 2.5 nm, i.e. less than the specified value of 6 nm. Consequently, the homogeneity of the crystal is sufficient for application.

The optimal level of the La doping seems to depend on peculiarities of the growth technology. In the samples grown by 3-times of recrystallization from the starting material the

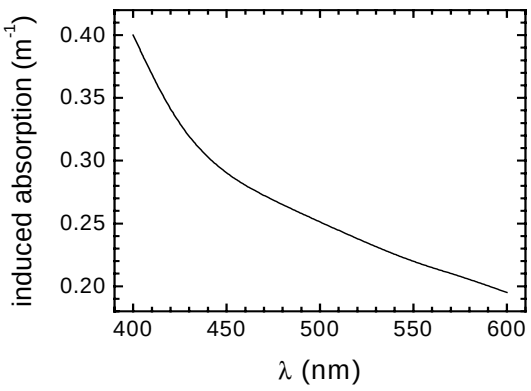

Fig. 4. Radiation-induced change of absorption after exposition of the La-doped PWO crystal to UV radiation at 365 nm wavelength and $12.8 \cdot 10^{-2}$ intensity for 30 min.

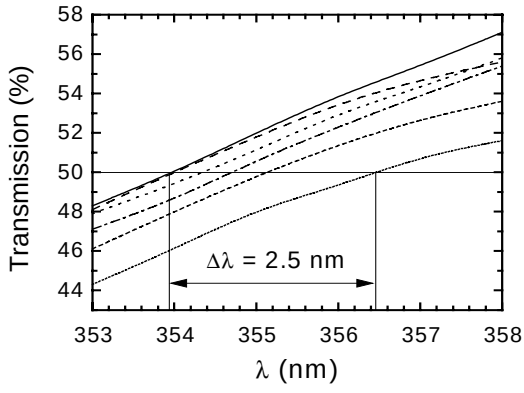

Fig. 5. Transmission of the La-doped PWO crystal in the vicinity of 50% measured at 6 points along the crystal to check the homogeneity of the crystal (see text for details).

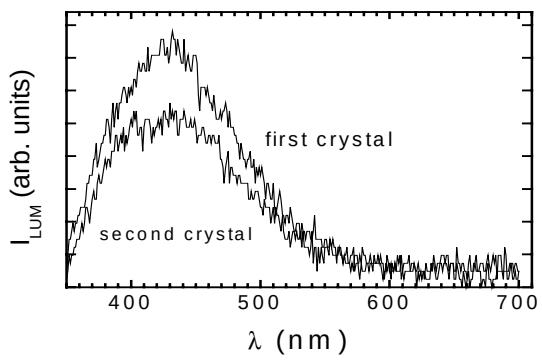

Fig. 6. Spectra of X-ray excited emission of two PWO samples grown subsequently by using the same melt.

optimal doping level was found to be ~ 80 at. ppm [14]. A slightly higher value of 100 at. ppm was shown to be optimal in our samples grown without recrystallization.

Furthermore, we carried out experiments to utilize the melt remained after growing one crystal for the growth of the next crystal. The second crystal was grown just after adding additional material into the melt. Though the light yield of the second crystal was slightly lower, all the characteristics important for PWO as a scintillator crystal were satisfactory. The luminescence of the first-grown and the second-grown crystals is compared in Fig. 6.

Conclusions

Optimization of melt preparation, thermal conditions, content and pressure of growth medium and other conditions in combination with La doping ensures fabrication of PWO crystals with a complex of properties corresponding the demands of application of these crystals in radiation detectors for high-energy physics experiments. The improved technology including the doping with La allows us to fabricate homogeneous 270 mm long crystals with diameter of 36 mm meeting all specifications without recrystallization. The whole cycle of crystal fabrication including melting, growth and thermal annealing is as short as 60 hours.

Acknowledgement

The work was financially supported by State Committee for Science and Intellectual Property, Ukraine.

References

1. E. Auffray, M. Lebeau, P. Lecoq, M. Schneegans. CMS Note 98/038, May 19, 1998
2. G.Tamulaitis, S.Buračas, V.P.Martinov, V.D.Ryzhikov, H.H.Gutbrod, V.I.Manko. phys. stat. sol. (a) 157 (1996)187
3. S.Burachas, V.Martynov, V.Ryzhikov, G.Tamulaitis, H.H.Gutbrod, V.I.Manko. J. Cryst. Growth. 186 (1998) 175
4. S.Burachas, V.Bondar, Yu.Borodenko, K.Katrunov, V.Martinov, L.Nagornaya, V.Ryzhikov, G.Tamulaitis, H.Gutbrod, V.Manko. J. Cryst. Growth 198/199 (1999) 881
5. G.Britwich, S.Burachas, Yu.Vostretsov, S.Kupstov, V.Martynov, L.Nagornaya, V.Polyakov, D.Renker, V.Ryzhikov. Proc. IEEE Nuclear Science Symp., Anaheim, USA, 3-9 November, 1996, Vol. 2, p. 763
6. G.Tamulaitis, S.Buračas, V.P.Martinov, V.D.Ryzhikov, H.H.Gutbrod, V.I.Manko, M.Terekhin. phys. stat. sol. (a) 161 (1997) 533
7. M.Kobayashi, Y.Usuki, M.Ishii, T.Yazawa, K.Hara, M.Tanaka, M.Nikl, S.Baccaro, A.Cecilia, M.Diemoz, I.Dafinei. Nucl. Instr. Meth. A 404 (1998) 149
8. S.Baccaro et al. phys. stat. sol. (a) 160 (1997) R5
9. M.Kobayashi, Y.Usuki, M.Ishii, T.Yazawa, K.Hara, M.Tanaka, M.Nikl, K.Nitsch. Nucl. Instr. Meth. A (to be published).
10. M.Nikl, P.Bohacek, K.Nitsch, E.Mihokova, M.Martini, A.Vedda, S.Croci, G.P.Pazzi, P.Fabeni, S.Baccaro, B.Borgia, I.Dafinei, M.Diemoz, G.Organtini, E.Auffray, P.Lecoq, M.Kobayashi, M.Ishii, Y.Usuki. Appl. Phys. Lett. 71 (1997) 3755

11. V.G.Bondar, S.F.Burachas, K.A.Katrunov, V.I.Man'ko, V.P.Martynov, V.D.Ryzhikov. Proc. SCINT-97, Shanghai, P.R.China, Sept. 22-25, 1997, p. 244
12. I.Dafinei, B.Borgia, F.Cavallari, M.Diemoz, E.Longo, S.Baccaro, A.Cecilia, M.Montecchi, G.Organtini, S.Salvatori, M.Nikl. ibid., p. 219
13. V.G.Bondar, S.F.Burachas, K.A.Katrunov, V.P.Martynov, V.D.Ryzhikov, V.I.Manko, H.H.Gutbrod, G.Tamulaitis. Nucl. Instr. Meth. A 411 (1998) 376
14. M.Kobayashi, Y.Usuki, M.Ishii, T.Yazawa, K.Hara, M.Tanaka, M.Nikl, S.Baccaro, A.Cecilia, M.Diemoz, I.Dafinei. Proc. SCINT-97, Shanghai, P.R.China, 1997, p. 167

On the Green Emission Centers in $PbWO_4$ Scintillator*

Yonghu Chen[1], Xiaoling Ye[2], Dongfang Zhou[2], Chaoshu Shi[1,2] Hongfang Chen[1]

Department of Physics, 2. NSRL, University of Science and Technology of China, Hefei 230026 People's Republic of China

Jingying Liao, Guanqin Hu

Shanghai Institute of Ceramics, Chinese Academy of Science, Shanghai 200050 People' Republic of China

Abstract. In this paper, cathodoluminescence, photoluminescence and their excitation spectra of $PbWO_4$ single crystals as grown and annealed in different atmosphere are analyzed and compared with each other. From the result that annealing in oxygen-abundant atmosphere leads to a great enhancement of green band in $PbWO_4$ luminescence, we conclude that the green emission is correlated with the decrease of oxygen vacancies V_O in $PbWO_4$ crystals. We suggest that the green emission originate from some localized excess oxygen defects, may be "$WO_4^{2-}+O_i$" (O_i means interstitial oxygen atom), which challenge the more prevailing view that assume the green centers be "WO_3+F" defects.

Keywords: Emission center, $PbWO_4$, Scintillator, Structural defect

Introduction

$PbWO_4$ single crystals (PWO) have been selected as scintillating material used to make precise Electromagnetic CALorimeter (ECAL) of the CMS experiments in a Large Hadron Collider (LHC) at CERN. It is also the most attractive candidate for the photon detectors of ALICE and COMPASS experiments.[1] Study on PWO have being extensively and systematically taken on an international scale for several years. However, as the luminescence mechanisms of PWO concerned about, there are still many problems to be unclear and argued about till now. Because PWO luminescence has an extraordinary structural peculiarity, that is, it would be significantly affected by the crystal growth condition and treatment process subsequently, it is very difficult to presume one model to explain all experimental results.[2] Fortunately, some common grounds have been reached and validated. For example, the blue emission in PWO luminescence is considered to connect with WO_4^{2-} group and be more intrinsic emission of PWO than the green and red emission which are linked with some structural defects in the crystals.[3]

In the present article, the green emission centers are discussed on the ground of annealing effect on PWO luminescence. Annealing in oxygen-abundant atmosphere has an effect of enormously increasing the green emission. So we relate the green emission to the decrease of oxygen vacancies V_O in PWO and suggest the green emission centers to be WO_4^{2-} groups with an interstitial oxygen atom O_i ($WO_4^{2-}+O_i$), or localized excess oxygen defects , instead of "WO_3+F" defects correlating with V_O.

Experimental

Used crystals in our experiments were polished slices with size $10x10x1mm^3$ cut from the big ingots grown by Bridgman method using raw materials WO_3 and PbO with 4N purity. The samples were annealed in air, oxygen or vacuum respectively. Their photoluminescence (PL) was measured with a fluorescence spectrophotometer (Hitachi 850) which has a Xe lamp as

excitation source. Cathodoluminescence (CL) was excited by electron beam with accelerative voltage 20KV and current density 10μA/cm^2.

Results and Discussion

In order to clearly show the effect of annealing in air on PWO luminescence, we make a comparison of UV-excited emission spectra between PWO before and after annealing in air and fit the spectra with three Gaussian subbands (shown respectively in Figure 1 and 2). The values of intensity in the two figures are comparable.

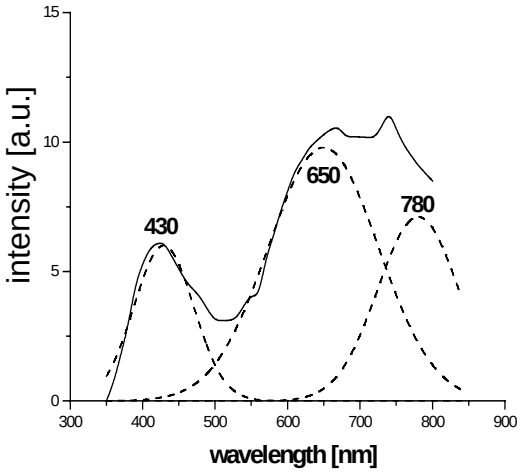

Fig. 1. The emission spectra (λ_{ex}=310nm) of PWO before air annealing and its components fit curve (dashed line).

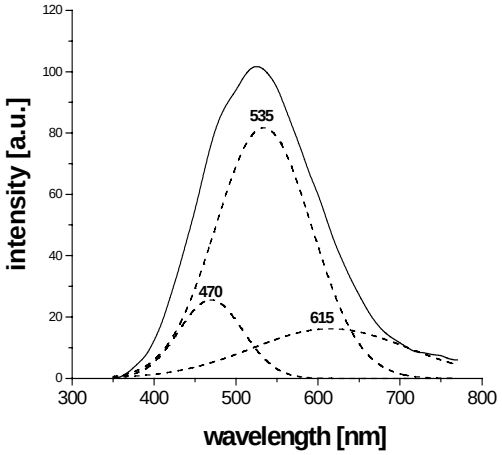

Fig. 2. The emission spectra (λ_{ex}=310nm) of PWO after air annealing and its components fit curve (dashed line).

The emission of PWO before air annealing is very weak, and except the intrinsic blue emission at 430nm, the most of luminescence befalls in a broad red band above 600nm. The three subbands peak at 430nm, 650nm and 780nm respectively. The broaden red band comprising of 650nm (red) and 780nm (infrared) subbands contributes 82% of the total light yield, while the contribution from green emission can be just ignored. After air annealing, the maximal intensity of emission increased nearly one magnitude, and the emission spectra peaks at 525nm (green) with a full width at half maximum (FWHM) of 170nm. Its three subbands center at 470nm, 535nm and 615nm respectively. The green subband offers up to 65% of the total light yield. So the increasing of the green emission is very significant.

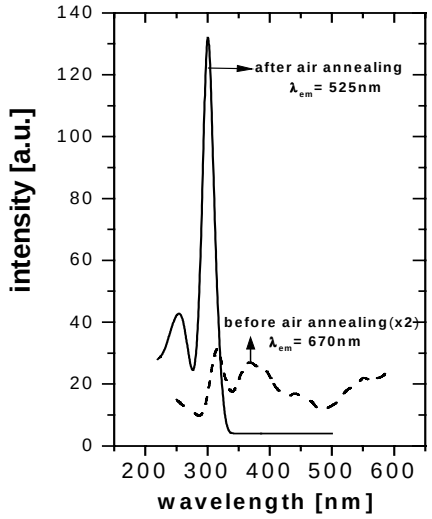

Fig. 3. The excitation spectra of PWO before and after air annealing.

Fig. 3 shows the excitation spectra of PWO photoluminescence before and after air annealing. The excitation spectra (λ_{em} =670nm) of PWO before air annealing have a main peak at 317nm. 370nm excitation

band with 50nm FWHM also has a large contribution to the red emission of PWO before air annealing. The excitation spectra (λ_{em} =525nm) of PWO after air annealing are dominated by a 303nm narrow excitation peak and a weaker 260nm excitation peak, and the long wavelength range beyond 303nm peak is perfectly flat. This result indicates that the peak around 310nm is corresponding to intrinsic state related to exciton excitation of PWO, while the excitation above 330nm more probably originate from the defects involving V_O.

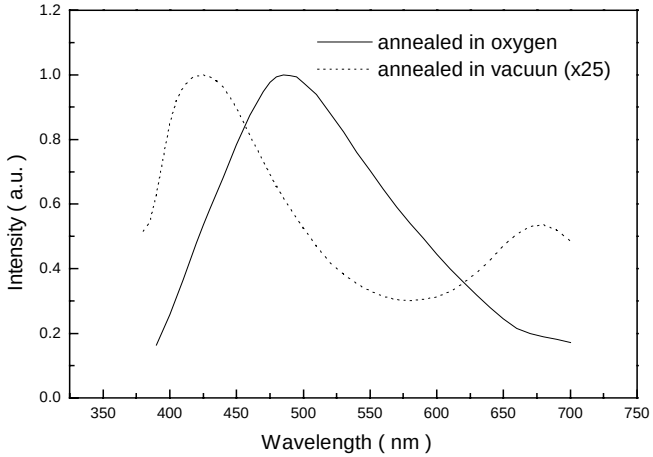

Fig. 4. Spectra of cathodoluminescence excited by electron beam with 20KV and 10μA/cm^2.

The major difference between cathodoluminescence and photoluminescence for same samples is the blue shift of emission peak in the former due to their different excitation mechanism. The CL spectra of two PWO samples annealed in oxygen and vacuum respectively are shown in Fig. 4. There are two bands centering at 425nm (blue) and 670nm (red) in the CL spectra of PWO annealed in vacuum, while for the sample annealed in oxygen, only one broad blue-green band peaking near 485nm. The emission for PWO annealed in oxygen is much stronger comparing with that annealed in vacuum, especially in the green band.

During preparation of PWO crystals, raw material PbO volatilizes more easily than WO_3,[4] so leaving lead vacancies V_{Pb} and oxygen vacancies V_O which are among the most important structural defects observed by other experiments. After annealing in vacuum, the V_O concentration must increase. These V_O in the crystal can capture electrons to form F^+ centers (V_O+e^-) or F centers (V_O+2e^-). Meanwhile, WO_4^{2-} changed into WO_3. According to the opinion of "WO_3+F" green centers[5], strong green emission should appear in vacuum-annealed samples rather than in O_2-annealed samples. But our results show only O_2-annealing or air-annealing (oxygen is abundant in air) lead to a remarkable increasing of the green emission. Therefore "WO_3+F" green centers are questionable.

The polarization measurements of the green components in PWO luminescence by Korzhik et al.[6] support the viewpoint that the green band originates from the centers with C_{3v} symmetry. While except the WO_3 group supposed by Korzhik has the C_{3v} symmetry, the center "WO_4^{2-}+O_i" also has the C_{3v} symmetry if only the interstitial oxygen O_i occupy one of any empty vertexes of the cubic which contains a WO_4^{2-} tetrahedron (Fig. 5). Actually WO_4^{2-} complex is not exactly a tetrahedron, and when an interstitial oxgen O_i adds to it, the stucture would be further changed, but it still has the C_{3v} symmetry. The unit cell of PWO has enough space to accommodate surplus oxygen due to its comparative low volume

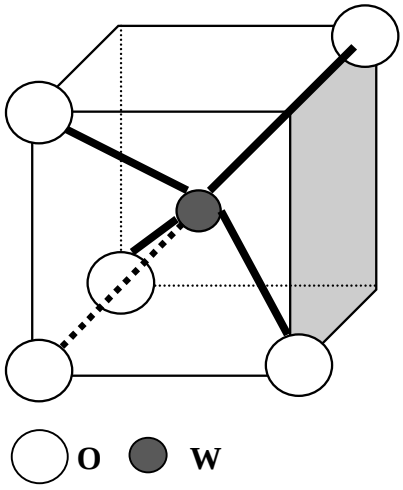

Fig. 5. The structure of "WO_4^{2-}+O_i"

occupation rate. So we suggest "$WO_4^{2-}+O_i$" as the green emission centers instead of "WO_3+F".

Above 400 , after only ten minutes' air-annealing, we can observe above-mentioned effect of annealing on PWO photoluminescence. On the other hand, UV-excited luminescence is affected by crystal surface where atmosphere of annealing has the most direct action. So we are more inclined to relate the green emission to "localized excess oxygen defects" when "$WO_4^{2-}+O_i$" centers are lack of other experimental evidence.

Conclusion

Annealing in O_2-abundant atmosphere leads to a significant increasing of the green emission in PWO luminescence. According to this, we conclude the green emission centers be some localized excess oxygen defects, maybe "$WO_4^{2-}+O_i$" centers, instead of "WO_3+F" defects involving the existence of V_O.

Reference

1. Lecoq et al., Nucl. Instrum. Methods Phys. Res. A 365, (1995) 291.
2. Annenkov A, Auffray E, Korzhik M et al. Phys. Stat. Sol. (a) 170, (1998) 47.
3. X. Feng, Z. Yin, Journal of Inorganic Materials, (in Chinese) 12 (4) , (1997) 449.
4. J. Liao et al., Journal of Inorganic Materials, (in Chinese) 12(4), (1997) 286.
5. M. V. Korzhik et al., Mat. Res. Soc. Symp. Proc., Vol. 348 (1994) 285.
6. M. V. Korzhik et al., Phys. Stat. Sol., (a) 154, (1996) 779.

Luminescence and transient absorption of doped PWO_4 scintillator crystals

D.Millers[a], S.Chernov[a], L.Grigorjeva[a] , V.Pankratov[a], M.Nikl[b], Y.Usuki[c]

[a]*Institute of Solid State Physics, University of Latvia, Kengaraga 8 Riga LV-1063, Latvia*
[b]*Institute of Physics, CAS, Cukrovarnicka 10, 16200 Prague, Czech Republic*
[c]Furukawa Ltd., 20, Kodate Kamiyoshima, Iwaki, Japan

Abstract. The transient absorption and luminescence under pulsed electron beam excitation were studied for undoped, La and Nb doped $PbWO_4$crystals. The absorption band at ~1.0 eV is suggested to be due self-trapped electrons and absorption band at 3.5 eV may be due to self-trapped holes. The formation of luminescence centers via electron-hole recombination is affected by La^{3+} and Nb^{5+} in doped crystals. The large fraction of electrons and holes are spatially correlated and undergoes thermostimulated recombination within these pairs. The distance between the electrons and holes play an important role in recombination process. The intrinsic luminescence arises in this recombination. Mechanism of La^{3+} influence on recombination processes is discussed.

Keywords: $PbWO_4$; $PbWO_4$- La^{3+}, Nb^{5+}; luminescence; transient absorption.

Introduction.

During recent years interest on scintillation properties of $PbWO_4$ (PWO) increases because PWO is a very good crystal for scintillators production for use in hight energy physics [1,2]. These scintillators will be used under radiation and thus their radiation hardness is critical important. The radiation hardness of PWO have been improved by doping with trivalent lanthanum (La^{3+}) as well as by pentavalent niobium (Nb^{5+}) [3-7]. However doping of PWO with La^{3+}or Nb^{5+} besides of improvement of radiation hardness caused some other very important changes of scintillation properties. Significant shortening of scintillation decay time was observed whereas scintillation yield decreases only a little [8-10]. Today there is more than one suggestion for role of La^{3+} dopand in enhancement of PWO radiation hardness [4,5,9,10], however the mechanism responsible for scintillation properties change is not clear. The study of luminescence center formation will help to understand the mechanism responsible for scintillation properties change by La^{3+} in PWO crystals. Study of both - transient absorption and luminescence spectra and kinetics within wide temperature region give a rich information on luminescence center formation [11,12] in undoped PWO crystals. Thus the similar study of PWO- La or PWO-Nb have been carried out in the present investigation.

Experimental

Experimental set-up includes the pulsed electron beam (10 ns, ~270 keV) source, optical channel for transient absorption as well as luminescence registration. The grating monochromator (MDR-2) was used for spectral measurements. Light signal was detected by photomultiplier tube, output signal was displayed on storage oscilloscope. The time resolution of equipment was ~20 ns. The experimental set-up is described more detailed elsewhere[13].

Results

The transient absorption spectra (TAS) of undoped PWO at 80 K reveals three bands peaking at 3.5 eV, 2.4 eV and ~1.0 eV (Fig.1.) The TAS measured at the end of irradiation pulse at ~80 K are very similar for undoped, La- and Nb-doped PWO. Whereas the TAS at RT are different for undoped and doped PWO crystals. Differences are more significant in delayed (50 ns after irradiation pulse) spectra.

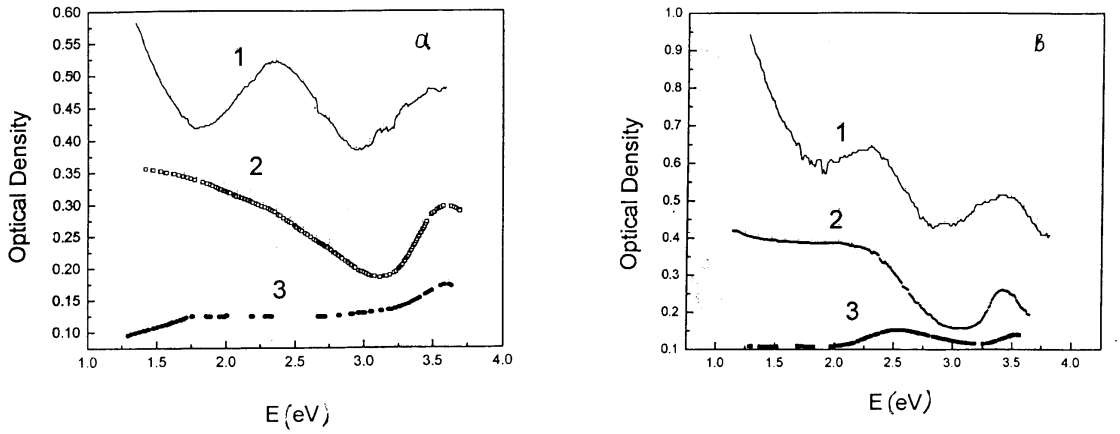

Fig.1. Transient absorption spectra of $PbWO_4$ crystal (a) and $PbWO_4$-La crystal (b) after electron pulse irradiation at 80 K (1) and 300 K (2,3). 1, 2 at 0 ns delay and 3 at 50 ns delay.

Two bands - at 3.5 eV and 2.4 eV - in TAS are in the same positions as observed in [14] for induced absorption of undoped PWO after steady state irradiation at RT. Four absorption bands (at 3.5 eV, 2.95 eV, 2.4 eV and 1.85 eV) is observed after steady state irradiation [14]. Two of these bands (at 3.5 eV and 2.95 eV) were ascribed to hole centers and two (at 2.4 eV and 1.85 eV) were suggested due to trapped electron centers [14].

The spectra of transient absorption at the short wavelength side shows only the band peaking at 3.5 eV, possibly the hole centers are responsible for this band. Since the ESR signals from hole centers in PWO were not observed up to day, nothing is known about structure of these centers [15].

The kinetics of transient absorption relaxation are quite complicated, they are different for different absorption bands and kinetics depends on crystal doping (Fig.2). For example, the kinetics of 1.0 eV band for pure PWO can be ascribed by three exponents at ~80 K: τ_1 = 80 ns, $\tau_2 \approx$ 600 ns and $\tau_3 \approx$ 4.3 μs, whereas kinetics of 3.5 eV band shows two exponents: $\tau_1 \approx$ 350 ns $\tau_2 \approx$ 4.7 μs. Different decay kinetics is an evidence that different defects (filled traps for electrons and holes) are responsible for transient absorption bands observed.

The relaxation kinetics of transient absorption at 80 K for doped PWO are somewhat similar to that for undoped PWO, however fast decay fraction of kinetics of 1.0 eV band shows exponent with τ= 30 ns and 35 ns for La- or Nb-doped PWO respectively, instead at 80 ns observed in undoped PWO.

The spectra of luminescence are the same for undoped PWO and PWO-La under irradiation pulse at ~80 K as well as at RT. These spectra shows one band peaking at ~2.9 eV (blue luminescence). This band is known to be intrinsic and arises due to electron transitions in WO^{2-}_4 complex.

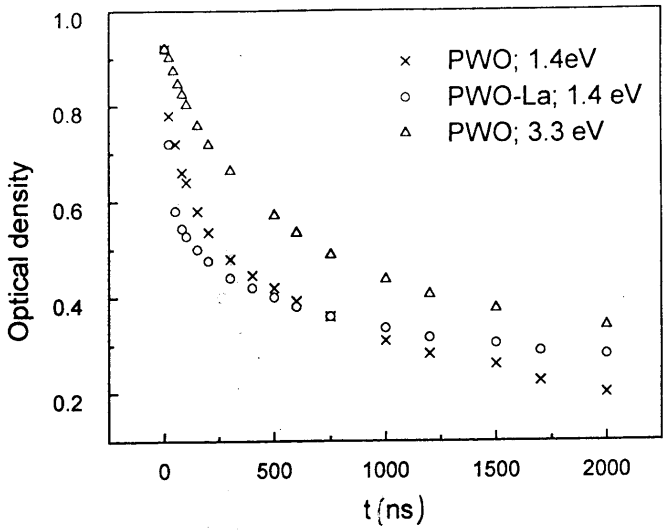

Fig.2. The decay kinetics of transient absorption at 80 K.

The kinetics of luminescence is very important characteristics for PWO. The rise of luminescence intensity after the irradiation pulse end was observed for undoped PWO at 80 K [12]. Thus the luminescence center excited state formation is delayed (delayed rise of luminescence) relative to excitation pulse. This delayed rise of luminescence is exponential and for undoped crystals used in the present study time constant is τ_r ~ 80 ns at 80 K. The rise of luminescence for PWO-La at ~ 80 K consists of two components - an initial prompt rise was followed by delayed (Fig.3). The prompt rise is close to 80% of luminescence total amplitude and following delayed rise is exponential with time constant τ_r ~ 30 ns for PWO-La and ~35 ns for PWO-Nb. One can point out that the rise times of luminescence for both undoped and doped PWO coincides with the faster relaxation times of transient absorption at 1.0 eV.

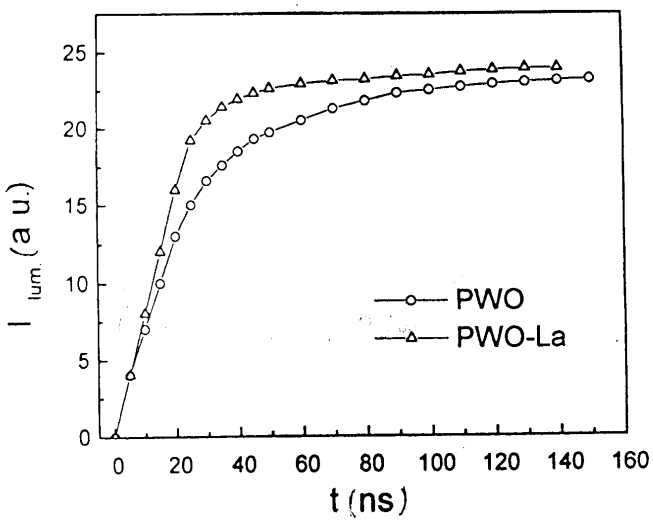

Fig.3. The luminescence rise PWO and PWO-La.

The study of luminescence yield dependence on temperature has been carried out. Since the decay kinetics are not exponential we use for analysis the luminescence half-life time (Δt). The luminescence amplitude I dependency on temperature was also measured and luminescence yield η was calculated as $\eta = I \cdot \Delta t$. The temperature dependencies of normalized luminescence yield η for undoped and La-doped PWO were shown at Fig.4. The

luminescence quenching for PWO-La was observed 30-40 K below than that for undoped PWO. The activation energy estimated is ~0.09 eV for PWO-La and ~0.15 eV for undoped PWO. The luminescence yields at RT are approximately the same for undoped and La-doped samples and this results coincides with results in paper [9]. Since the luminescence quenching for PWO-La take place at temperature below that for undoped PWO, it is suggested that a large fraction of electrons and holes are correlated and forms pairs. The distance between electron and hole within such pairs is small. Possibly the formation and recombination of these pairs occurs close to the dopant ion.

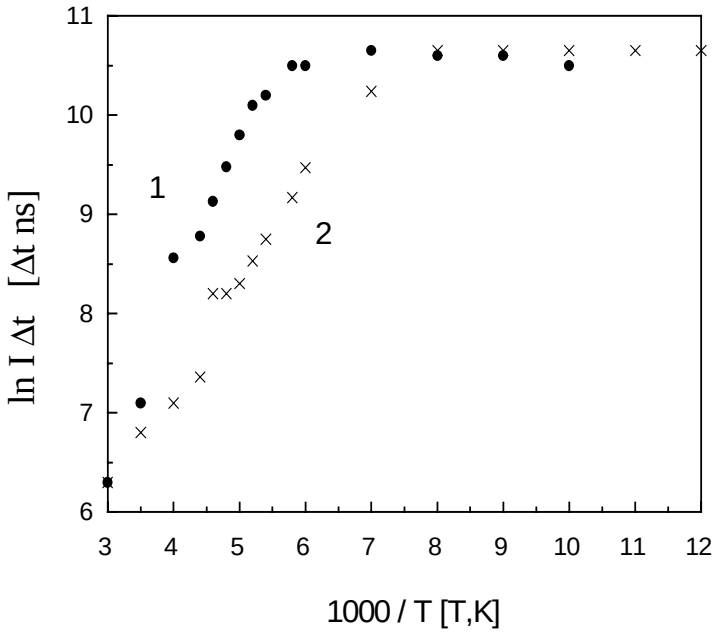

Fig.4. The temperature dependencies of normalized luminescence yield η for undoped PWO (1) and La-doped PWO (2).

The doping with La or Nb ions can affect the probability of nonradiative transitions in luminescence center or leads to the change of the probability of luminescence center excited state dissociation [16].

Discussion

The results obtained for undoped, Nb- and La-doped PWO gives information on processes of luminescence center formation and its radiative as well as nonradiative decay in both undoped and La-doped PWO. The time of luminescence center formation (<100 ns) at ~80 K for undoped PWO, estimated from delayed luminescence rise coincides with shorter relaxation time of transient absorption at 1.0 eV. Thus, the 1.0 eV absorption band is due to some shallow traps for electrons or holes. The charge carriers released from this trap participate in luminescence center formation. It is known that the most shallow trap in PWO was represented by self-trapped electron which is interpreted as WO^{3-}_4 complex, being stable below 50 K [17,18]. Thermostimulated luminescence at ~50 K shows the blue luminescence [19,20], thus the release of self-trapped electrons leads to the recombination with hole also trapped at regular lattice site (self-trapped hole). The activation energy estimated from temperature dependence of delayed luminescence rise time is ~0.04 eV for undoped PWO [12] and it is very close to activation energy of self-trapped electron thermal release (~0.05 eV) [17]. Thus, the thermal release (or destroying) of self-trapped electron followed by its radiative recombination with self-trapped hole is responsible for the delayed luminescence rise observed in our experiments. Such interpretation is supported by recent wavelength-resolved thermostimulated luminescence measurements [20]. We suggest the transient

absorption band at 1.0 eV, at least the short-lived part of this band, is due to self-trapped electrons. The appropriate candidate for self-trapped holes absorption seems to be 3.5 eV band. We suggest the self-trapped hole forms the core of the luminescence center. Thus, trapping of electron by hole and formation of luminescence center excited state do not affect the core. This is the reason why in 3.5 eV absorption fast relaxation is not observed similar to that at 1.0 eV.

The extrapolation of temperature dependence of probability for thermal release of self-trapped electron to 80 K from [17] gives a long lifetime for self trapped electron which is some orders longer than observed in our experiments delayed luminescence rise times at ~80 K. We suggest this discrepancy is because in [17] only a stable and spatially well separated fraction of self-trapped electrons and holes is observed. We can assume that a large fraction of electrons and holes created by irradiation were not spatially well separated and forms geminate pairs (the electron and the hole created in the processes of the absorption of the single photon or in the same event of inelastic electron-electron scattering [21]). Relaxation of these geminate pairs leads to self-trapping of electrons and holes within a short distances between them and interaction within these pairs results in increase of probability for thermal release of self-trapped electron as well as enhances the probability of recombination with geminate self-trapping hole. Thus, the life time of self-trapped electrons is reduced. Similar effect is known for undoped and doped alkali halides [22,23]. Thus we suggest a significant fraction of luminescence in our experiments is due to the electron-hole recombination within geminate pairs.

Similar conclusion on separation of electrons and holes in PWO and $CaWO_4$ was suggested in [24] on basis on photostimulated and thermoluminescence study.

The experimental results show that La- and Nb-ions significantly affects to luminescence center formation process. The luminescence rise and decay times are considerably shorter in doped PWO [6,8,9]. The contribution of short-lived luminescence component ($\tau \approx 2$-4 ns) is larger in La- and Nb-doped PWO [6,8,9]. The influence of La- an Nb-ions on PWO luminescence can be well understood if we assume the mentioned above - the initial spatial separation of electrons and holes is important for their recombination rate. The recombination of self-trapped electron-hole pair can be stimulated if the pairs is in dopants Coulomb field as well as dopant may suppress in some way the spatial separation of the electrons and holes. The recombination can be speed up by both these possibilities It is important that in La- and Nb-ion doped PWO the prompt component is ~80% from luminescence pulse amplitude and the relative intensity of short-lived component of scintillation decay is approximately 80% [9,10].

Conclusions

Comparison of luminescence kinetics and transient absorption decay kinetics allow to propose, that the absorption band at 1.0 eV is due to self-trapped electron, 3.5 eV absorption band possibly due to self-trapped hole.

The recombinative formation of luminescence centers involves thermal release of self-trapped electron within geminate electron-hole pair.

In PWO-La and PWO-Nb the dopant either stimulates the radiative recombination within geminate pair of self-trapped electron and hole, either decreases the spatial separation of electrons and holes within geminate pairs.

Acknowledgement

This work was supported by a joint project Crystal Clear Collaboration (CERN) and Latvian Council of Science (grants #96/0662)

References

1. 1.P. Lecoq, I. Dafinei, E. Auffray, M.. Schneegans, M.V. Korzik, O.V. Missevitch, V.B. Pavlenko, A.A. Fedorov, A.N. Annenkov, V.L. Kostylev. Nucl. Instrum. Methods Phys. Res. **A365** (1995) 291.
2. 2.R.J. Zhu, D.A. Ma, H.B. Newman, C.L. Woody, J.A. Kirstead, S.P. Stoll, P.W. Levy, Nucl. Instrum. Methods Phys. Res. **A376** (1996) 319.
3. 3.A.N.Annenkov et al. Phys. Stat. Sol.(a), **156** (1996) 493.
4. 4.S.Baccaro et al. Phys.Stat.Sol.(a), **160** (1997) R5.
5. A. Annenkov, E. Auffray, M. Korzik, P. Lecoq, J.P. Peigneux, Phys. Stat. Sol.(a), **170** (1998) 47.
6. M. Kobayashi, Y. Usuki et al., Nucl. Instrum. Methods Phys. Res. **A404** (1998) 149.
7. E. Auffray et al. Nucl. Instrum. Methods Phys. Res. **A402** (1998) 75.
8. M. Nikl et. al., Appl. Phys. Letters **71** (1997) 3755.
9. M. Kobayashi, Y. Usuki et al., Nucl. Instrum. Methods Phys. Res. **A399** (1997) 261.
10. M. Kobayashi et al., Proceedings at the Intern. Workshop on Tungstate Crystals, Roma (1998) 163.
11. D. Millers, S. Chernov, L. Grigorjeva, A. Popov, E. Auffray, I. Dafinnei, P. Lecoq, M. Schneegan, J. Lumin. **72-74** (1997) 693.
12. D. Millers, L. Grigorjeva, S. Chernov, A. Popov, P. Lecoq, E. Auffray. Phys. Stat. Sol.(b), **203** (1997) 585.
13. D. Millers, E. Kotomin, L. Grigorjeva, R. Eglitis, J. Lumin. **55** (1993) 243.
14. M. Nikl et al., J. Appl. Phys. **82** (1997) 5758.
15. M Bohm et al., Proc. Int. Workshop in Tungstate Crystals, Roma, 12-14 Oct. (1998) 141
16. M. Nikl et al., Chem. Phys. Letters **291** (1998) 300.
17. V.V. Laguta, J. Rosa, M.J. Zaritskii, M. Nikl, Y. Usuki. J. Phys. Cond.Matter**, 10** (1998) 7293.
18. M. Bohm, F. Henecker, A. Hoffstaetter, M. Luh, B.K. Mayer, A. Scharmann, D.V. Kondratiev, M.V. Korzik. Rad. Eff. Def. Solids (in press).
19. M. Springis, V. Tale, I.T ale, J. Luminesc. **72-74** (1997) 784.
20. M. Martini, F. Meinardi, G. Spinolo, A. Vedda, M. Nikl, Y. Usuki, Phys. Rev. B **60** (1999) 4653.
21. A.N. Belskiy, I.P. Kamenskikh, V.V. Mikhailin, I.N. Spinsov, A.N. Vasil`ev, Phys. Scripta **41** (1990) 530
22. S. Iwai, T. Tokizaki, A. Nakamura, T. Shibata, A. Schluger, N. Itoh, J. Luminesc. **60-62** (1994) 720.
23. S. Chernov, J. Lumin. **72-74** (1997) 751.
24. Y.C. Zhang, N.A.. Holzwarth, R.T. Williams, M. Nikl, Proc. Intern. Conf. Excitonic Processes in Cond. Matter. EXCON'98, 98-251 (1998) 420.

Thermally stimulated luminescence properties of lead tungstate crystals

M. Böhm, A. Hofstaetter, M. Luh, B.K. Meyer, A. Scharmann

1st Physics Institute, University of Giessen, Germany

M.V. Korzhik, O.V. Kondratiev, A.E. Borisevich

Institute for Nuclear Problems, Minsk, Belarus

V.V. Laguta

Institute for Problems of Materials Science, Kiev, Ukraine

P.Lecoq, E.Auffray-Hillemans

CERN, Geneva, Switzerland

Abstract. In this study we systemized Thermo-Stimulated Luminescence (TSL) properties of synthetic lead tungstate crystals obtained at different technological conditions. The combination of TSL, Thermo-Stimulated Current (TSC) and Electron Paramagnetic Resonance (EPR) measurements performed by us during several years formed a good basis to identify thermo-stimulated processes in the material. Undoped crystals as well as specimen doped by Nb, La, Lu, Y, Mo, Eu ions and combinations of those have been investigated. Out of the multitude of samples we took typical representatives of each sort. Concentration of doping in the melt was at the level of 50-100ppm. Trap parameters of the centers detected through TSL have been numerically calculated from the equation for a kinetic of arbitrary order. An annihilation time τ (Table 1) of the traps allows to distinguish its influence on the room temperature scintillation. The contribution of the traps detected to slow scintillation components, afterglow and radiation damage in the material will be discussed.

Introduction

The mass production of lead tungstate (PWO) scintillation elements with parameters specified for the CMS experiment at CERN has already started, nevertheless systematic investigations are still necessary for a better understanding of this compound. In that context we studied systematically the properties of thermally stimulated luminescence (TSL) emitted by a variety of synthetic lead tungstate crystals grown under different technological conditions. The combination of TSL, thermally stimulated conductivity (TSC) and electron paramagnetic resonance (EPR) measurements performed by us during several years provide a good basis to identify thermally stimulated processes in the material. Lead tungstate has an exceptional position in the tungstate family with Scheelite structure. The characteristic hole defects [1] have never been observed in this crystal since the structure of valence and conduction bands differs substantially from that of other tungstates [2]. PWO is very sensitive to the conditions during synthesis. This shows up e.g. by an ordering of defects in a superstructure brought about by lead deficiency in the crystal [3].

For nominally undoped lead tungstate crystals these can generally be grouped into bands near 50, 100 and 180 to 230 K [4-9] (glow peaks occasionally found at temperatures below 50 K will not be discussed here). The intensity of the first group is weakly sensitive to crystal

growth conditions whereas all other bands depend in their intensities strongly on melt stoechiometry and the atmosphere used during crystal growth [9,10].

Doping the crystal with stable trivalent rare earth (La, Lu, Gd) and Y ions with concentration of some tens of ppm increases the intensity of the second group and completely suppresses the last one [8,11].

After the X-irradiation filling traps responsible for TSL several characteristic electron centers can be observed in lead tungstate by EPR. One of them occurs in all crystals since it is an intrinsic defect. An additional electron autolocalized at an anionic WO_4^{2-} complex via a Jahn- Teller distortion creating a WO_4^{3-} center [5, 6, 12]. This rather shallow trap gets emptied near 50 K with an activation energy of 50 meV and frequency factors in the range of 10^3 to 10^4 s^{-1} [12]. The electrons released partly recombine radiatively, partly are caught by deeper traps. One of them is a WO_4^{3-} electron center disturbed by a nearby three-valent impurity ion like La, Lu or Y [5]. It decays near 97 K. Other deep electron traps are provided by $(MoO_4)^{2-}$ and $(CrO_4)^{2-}$ complexes replacing tungstate groups while preserving the regular lattice symmetry. They are stable up to nearly [9, 13] respectively above room temperature. MoO_4^{3-} gives rise to green luminescence and slow decay of scintillations [13].

Further paramagnetic centers created by ionizing radiation are connected with impurity ions on Pb sites accompanied by oxygen vacancies in the neighbourhood. The stability of these centers ranges from 160 K to well above room temperature. Finally oxygen vacancies, isolated or their associations, have to be taken into account as trapping sites, such centers, however, were not yet observed by means of EPR in lead tungstate crystals.

Experimental results

All crystals investigated have been grown within PWO crystal R&D performed by the Bogoroditsk Techno-Chemical Plant (BTCP, Russia). Details of the crystal growth are described elsewhere [15]. Beside undoped crystals such doped by Nb, La, Lu, Y, Y+Mo and Eu ions have been studied, concentration of doping in the melt being at the level of 50-100ppm. One undoped (Un1) and all doped crystals have been grown following the standard procedure developed at BTCP. A second undoped crystal (Un2) was grown from the same raw materials in open atmosphere with a pulling rate higher than 20 mm/h in order to minimize losses of oxygen from the melt.

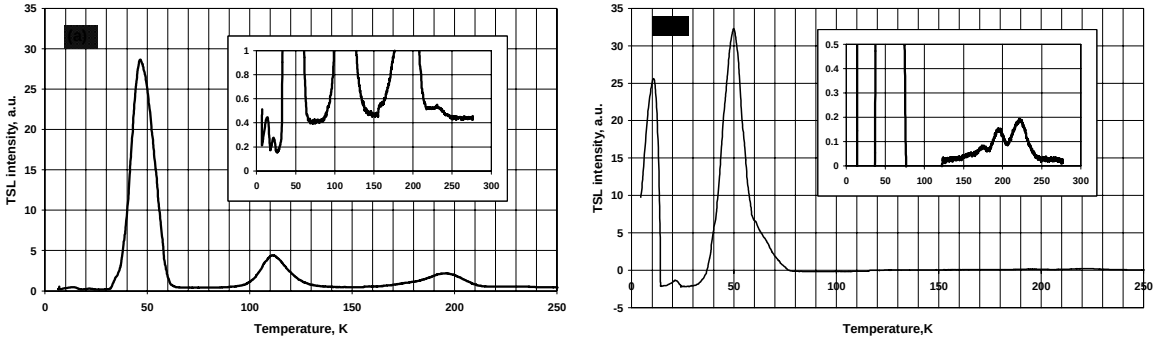

Fig.1. Glow spectra of Un1(a) and Un2(b) samples measured in integral luminescence regime.

Figs.1a and 1b show TSL spectra of samples Un1 and Un2. For Un1 prominent glow peaks near 50 K, 100 K and 200 K are observed, the latter revealing a small shoulder at 230 K. Sample Un2 grown in oxygen rich atmosphere is characterized by an absence of the band in the region of 100 K and a strong suppression of the peaks near 200 K with exception of the 230 K emission. In addition the band near 50K has a long range temperature shoulder in Un2

due to the existence of a small peak near 65 K. Such a shoulder is also detected unsystematically in doped samples. A shift from the blue to the green region found for the maximum of the luminescence emitted throughout the sharp intense 50 K glow peak as shown in Fig.2 indicates that this peak consists in both samples of at least two sub-bands.

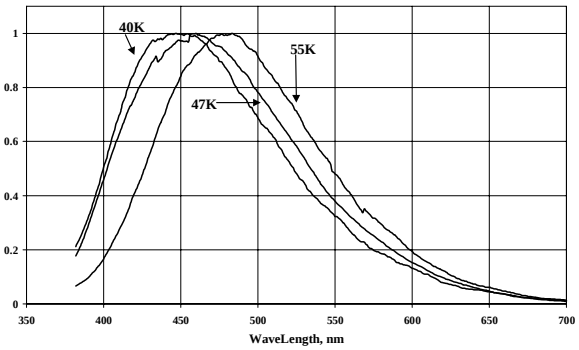

Fig.2 Temperature dependence of the spectral distribution of the luminescence emitted within the TSL peak in the vicinity of 50 K.

TSL spectra of crystals doped by Nb, La, Y and Y+Mo are presented in Figs. 3(a-d). As was mentioned earlier [11] Nb doping does not change TSL spectra comparing to undoped Un1 crystal, whereas a new band appears near T = 75 K in the samples doped with trivalent ions. There also the peaks near 180 K are suppressed and the intensity of the band near 100 K is increased by 3-5 times.

Codoping Y and Mo inverts the intensity ratio of the two bands near 50 and 100 K. This seems to reflect the fact that a higher concentration of $(MoO_4)^{2-}$ traps effectively competes with the $(WO_4)^{3-}$ center [6]. The group of bands between 180 and 230 K is not completely quenched in this crystal, in contrast to pure Y doping.

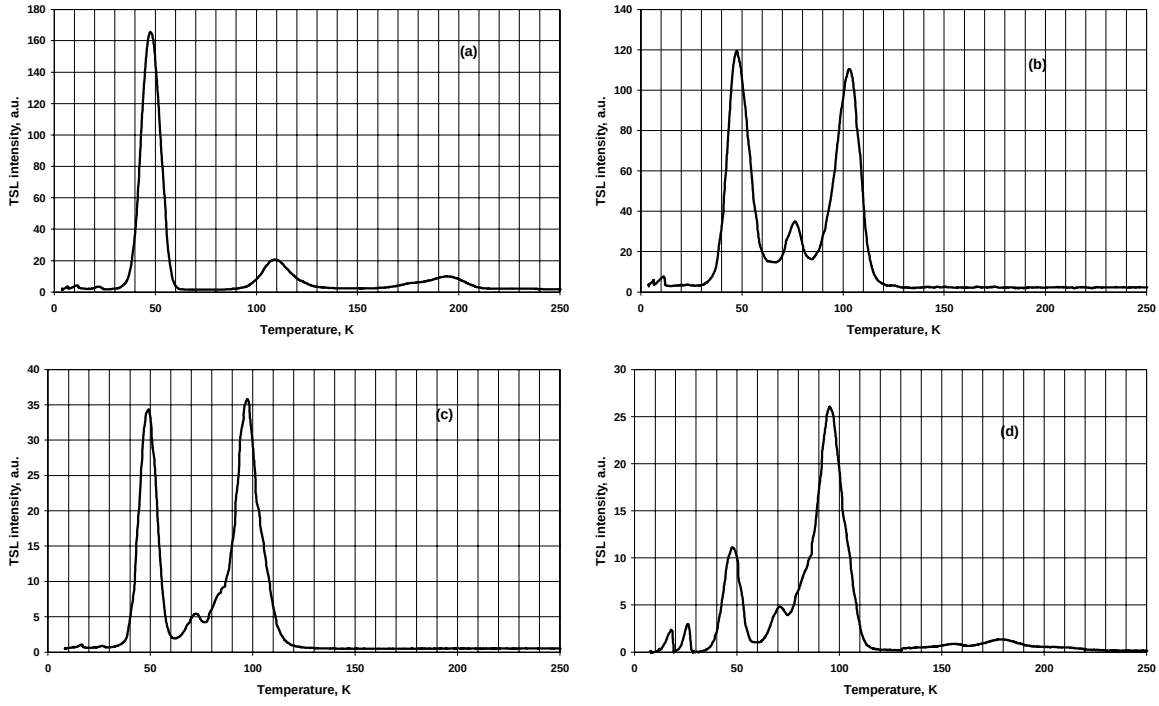

Fig.3. Glow spectra of the crystals doped with Nb(a), La(b), Y(c) and Y+Mo(d) measured in integral luminescence regime.

A special annealing technique, the method of partial activation, was applied to PWO:La and PWO:Nb in order to resolve the structure of the band in the vicinity of 100 K. Results of the measurements for the two crystals with and without partial annealing are given in Figs. 4(a, b). A shift of the maximum of several Kelvin is observed in both samples after partial activation of the band.

Trap parameters of the various centers showing up in TSL have been numerically calculated from the following equation for a kinetic process of arbitrary order [16]:

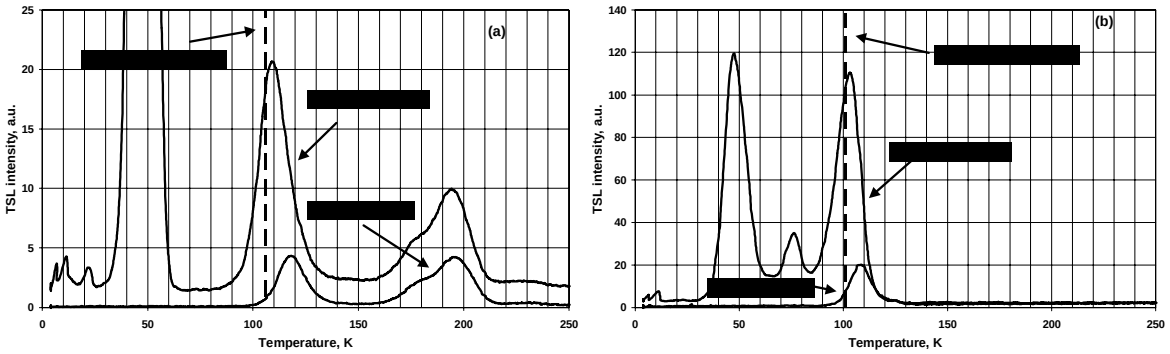

Fig.4 Glow spectra of the Nb (a) and La (b) doped crystals measured integral luminescence regime with and without partial annealing.

$$\frac{dN}{dt} = \frac{SN^{\gamma}}{N_0^{\gamma-1}} \exp(-E/kT)$$

Here N_0 is a concentration of traps, N the concentration of populated traps at time t, S a frequency factor, γ the order of the kinetic, E the thermal activation energy and T the temperature. Parameters S, γ and E have been varied and their values determined from the best fit to the bands measured, taking into account in some cases also a doublet structure. An annihilation time τ of the traps which allows to distinguish its influence on the room temperature scintillation properties has been evaluated from the equation with fixed parameters determined from the appropriate fit to the respective TSL curves. As an example fitting results for crystal Un.1 and their correspondence to the experimental data are shown in Figs. 5(a-c).

All parameters determined in this way for the crystals studied are summarized in Table1 together with wavelength and energy of the emission maxima.

The TSL peak in the vicinity of 50 K consists of two strongly overlapping bands with maxima near 47 and 50K. The high temperature part is caused by a trap with an activation energy of 50 meV whereas the lower peak is due to a 70meV trap. The 50 meV trap center dominates in all samples; in Un2 its fraction is more than 99%. The kinetic order of the band varies from 1.1 in undoped and Nb crystals to an average value of 1.35 in samples doped with trivalent ions. This higher value seems to reflect the retrapping of carriers at the disturbed $(WO_4)^{3-}$ -X^{3+} traps (cf. above). We did not find a correspondence of the 70 meV center to any paramagnetic species. So the origin of this trap is not clear until now, as well as that causing the shoulder in Un2 having the same activation energy of about 70 meV.

To the peak near 75 K appearing in RE doped crystals contributes only one trap with an activation energy of appr. 130 meV. The carriers trapped there are released via the conduction band with a kinetic order of about 1.5. Obviously this trap is created by trivalent rear earth ions but we did not observed paramagnetic centers correlated with corresponding peak.

The peaks in the vicinity of 100 K are not easy to fit since there again several centers can contribute. Results from the partial activation of the band show that at least two traps are involved in the emission. In this way two centers with activation energies 200 to 220 (γ=1.5-1.7) and 270 meV (γ=1.7-2.2) were found to be involved in the TSL emission near 100 K. In addition in samples doped with Y and Y+Mo a third center with an activation energy of 120 meV and nearly first order kinetic results from the fitting procedure

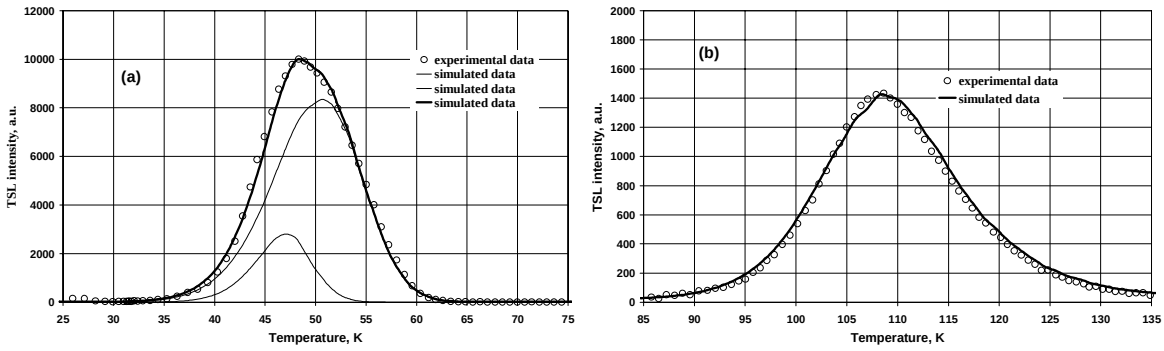

Fig.5 Comparison of the experimental TSL spectrum and results of fitting for sample Un1.

Bands in the vicinity of 200 K are well fitted in the samples where they exist. Two low temperature peaks (near 170 resp. 190 K) appear due to traps with thermal activation energies of 400 and 500 meV and kinetics close to first order, the weak 230 K peak overlapping with those mentioned above is due to a trap with E = 490 meV and $\gamma = 1$.

In all crystals both peaks near 50 and 100 K are accompanied by thermally stimulated conductivity. Fig. 6 shows TSC spectra of Y and Y+Nb doped samples. As usual they are shifted to higher temperatures compared to TSL peaks. A weak TSC peak near 75 K is also detected in RE doped samples. Systematic occurrence of other TSC peaks was not observed.

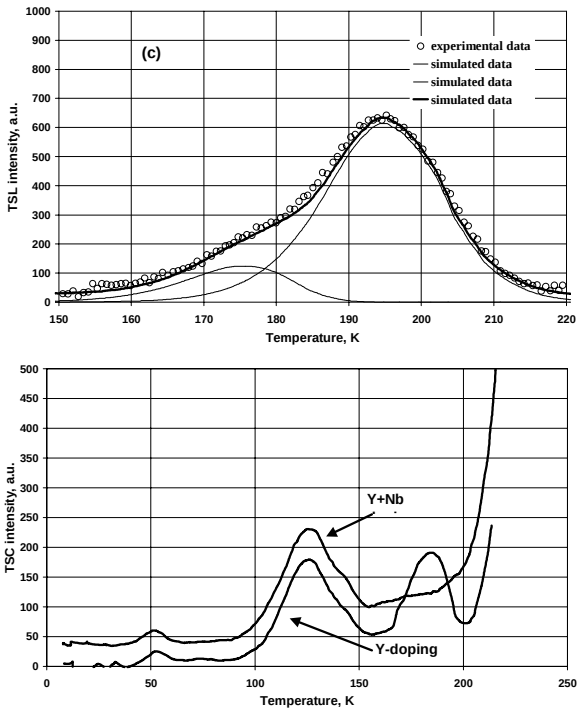

Fig.6 Thermally stimulated current measured in Nb doped and Nb+Y doped samples.

Discussion

From the data obtained one can infer the existence of a variety of traps in PWO with approximate activation energies of 50, 70, 130, 200, 270, 400, 490 and 500 meV. The origin of the 50 meV and the 200 (190) meV traps is clear from the EPR results mentioned above. The first one is the intrinsic $(WO_4)^{3-}$ center. The second trap is the disturbed $(WO_4)^{3-}$ -X^{3+} center (X = La, Lu, Y) as founded in [18].

Other trap centers did not show paramagnetic properties so their origin interpretation needs of an additional argumentation. As basis for that one has to take WO_3 into consideration [17]. At the first glance it is unlikely to have various different traps related to oxygen vacancies within the anionic complexes. All bonds of the tungstate tetrahedra in a $PbWO_4$ crystal with pure scheelite have the same length and all tetrahedra are equivalent. This situation, however, changes significantly if the structural peculiarity of synthetic stolzite is taken into account. The new structure found for Pb-deficient synthetic stolzite, $Pb_{7.5}W_8O_{32}$, is a superstructure of a scheelite type [3]. The presence of such superstructure was observed in crystals grown with lead deficiency as well as in crystals grown from stoechiometric raw materials when the ratio

of free surface to volume is relatively large. One can conclude that crystals grown in such conditions are a solid solution of two components, namely a pure scheelite and a scheelite type structure. The superstructure appears due to partial deficiency of lead in one (Pb3) of the four lead sites. This induces displacements of atoms surrounding the deficient site distorting the tungstate tetrahedra, increasing anion-cation distances from 1.79Å found in $PbWO_4$ to 1.84 - 1.94 Å for the tetrahedron surrounding W(1) and decreasing them to values close to 1.68Å within W(2-4) tetrahedra. Thus, in addition to the ordinary scheelite tetrahedra there are two additional types of tungstate tetrahedra with different dimensions. We attribute to oxygen vacancies V_o in these tetrahedra the trap centers with thermal activation energies of 210-220 and 270 meV. The drastic fall in concentration of these traps as revealed by the strong suppression of TSL intensity near 100 K in sample Un2 strongly supports such interpretation. Finally, the increase in intensity of the of TSL peaks connected to these traps is clearly correlated with the increasing number of crystallization processes [7,10] or otherwise with increase of the fraction of scheelite type structure in the solid solution. The 70 meV trap we suppose to be related to such vacancies in regular scheelite tetrahedra.

The group of peaks in the vicinity of 200 K has been attributed to divacancy centers localized in the same polyhedron [11]. This is in good agreement with the three sorts of tungstate tetrahedra mentioned above. From the analysis of the TSL intensities in the respective bands we conclude that the 400 and 500 meV traps are due to distorted superstructure tetrahedra and that the 490 meV trap is related to an ordinary tetrahedron. We do not exclude that the structure of this group of peaks can be more complicated by the overlapping with the weak wide peak generated by $(MoO_4)^{3-}$ centers [4] since we never observed lead tungstate crystals without Mo traces.

Following this interpretation it seems to be possible to describe also uncontradictory the changes of TSL spectra in doped crystals. From one hand an activation of crystals with stable trivalent impurities results in a strong suppression of the 400, 490 and 500 meV traps. Such ions localized at Pb sites introduce in the crystal an extra positive uncompensated charge and will thus compete with the creation of V_o vacancies. This causes a decrease in their (normalized) concentration N and therefore drastically decreases the amount of di-vacancies since the probability to create such defects is proportional to N^2. In addition the dopant ions occupy empty lead sites in the lattice and so suppress the superstructure fraction with its distorted tetrahedra in the crystal. On the other hand trivalent ions create the 130-200 meV traps at the release of which the retrapping of carriers by V_o centers is occured. Such retrapping is at the origin of the TSL peaks intensity increase in the vicinity of 100-110K when crystals are doped with mentioned ions.

Finally we want to note that both single and di-vacancy centers are occupied by paired electrons. Due to the relatively narrow band gap of the crystal the $F(V_o+2e)$ and the di-vacancy centers are rather shallow and their ionized states (or F^+ centers) have virtual levels in the conduction band.

The most serious problem preventing a full understanding of the TSL mechanism in PWO remains the open question for the recombination partners for the carriers released from the centers discussed above. The wide spread in the maximum energies of TSL emissions even for peaks related to traps with the same activation energy (cf. Table 1) shows that these until now unknown species significantly influence the thermally stimulated processes.

Table. 1 Parameters of the traps in different lead tungstate crystals

Group	Crystal	Fraction, %	T_{max}, K	E, meV	S	γ	τ, sec	λ_{em} (E_{em}), nm (eV)
10-30K	PWO:Y+Mo		17	9.5	$7.0\cdot10^{1}$	1.0	$9.0\cdot10^{-2}$	401 (3.08)
			25	29	$8.0\cdot10^{4}$	1.0	$3.8\cdot10^{-5}$	434 (2.86)
	Un. 1	17.7%	47	70	$2.0\cdot10^{6}$	1.2	$8.3\cdot10^{-6}$	458(2.71)
		82.3%	51	50	$4.0\cdot10^{3}$	1.1	$1.8\cdot10^{-3}$	
	Un. 2	99%	51	52	$6.0\cdot10^{3}$	1.1	$1.3\cdot10^{-3}$	
		Shoulder	61	70	$2.0\cdot10^{4}$	1.5	$9.7\cdot10^{-4}$	
	PWO:Nb	38.0%	48	79	$1.5\cdot10^{7}$	1.4	$1.7\cdot10^{-6}$	449 (2.76)
		62.0%	52	58	$2.4\cdot10^{4}$	1.1	$4.1\cdot10^{-4}$	473 (2.62)
	PWO:La	17.3%	48	72	$2.0\cdot10^{6}$	1.2	$9.0\cdot10^{-6}$	448 (2.77)
		82.7%	50	51	$5.0\cdot10^{3}$	1.5	$1.9\cdot10^{-3}$	444 (2.79)
	PWO:Y	9.4%	47	69	$2.0\cdot10^{6}$	1.2	$8.0\cdot10^{-6}$	477 (2.60)
		90.6%	49	55	$2.0\cdot10^{4}$	1.4	$5.1\cdot10^{-4}$	484 (2.56)
	PWO:Y+Mo	28.3%	45	67	$2.0\cdot10^{6}$	1.5	$8.6\cdot10^{-6}$	456 (2.72)
		71.7%	49	54	$2.0\cdot10^{4}$	1.2	$4.5\cdot10^{-4}$	468 (2.65)
	PWO:Eu	27.6%	46	70	$2.8\cdot10^{6}$	1.2	$6.0\cdot10^{-6}$	475 (2.61)
		72.4%	50	57	$2.4\cdot10^{4}$	1.3	$4.4\cdot10^{-4}$	468 (2.65)
75K	PWO:La		75	135	$1.0\cdot10^{8}$	1.6	$2.8\cdot10^{-6}$	448 (2.77)
	PWO:Y		75	131	$1.0\cdot10^{8}$	1.6	$2.6\cdot10^{-6}$	
100-110K								
	Un. 1		105	230	$6.7\cdot10^{9}$	2.2	$2.2\cdot10^{-6}$	500 (2.48)
	PWO:Nb		103	210	$7.5\cdot10^{8}$	2.3	$9.2\cdot10^{-6}$	498 (2.49)
	PWO:La		97	190	$2.9\cdot10^{8}$	1.35	$6.4\cdot10^{-6}$	443 (2.80)
	PWO:Y	56.0%	97	190	$2.9\cdot10^{8}$	1.3	$6.4\cdot10^{-6}$	463 (2.68)
		44.0%	102	120	$2.0\cdot10^{4}$	1.1	$5.4\cdot10^{-3}$	461 (2.69)
	PWO:Y+Mo	54.0%	94	190	$2.9\cdot10^{8}$	1.5	$6.9\cdot10^{-6}$	477 (2.60)
		46.0%	100	120	$2.0\cdot10^{4}$	1.1	$5.4\cdot10^{-3}$	470 (2.64)
Using annealing technique								
	PWO:Nb	17.5%	103	220	$1.5\cdot10^{9}$	1.5	$3.6\cdot10^{-6}$	498 (2.49)
		72.5%	114	270	$9.0\cdot10^{10}$	2.2	$7.3\cdot10^{-7}$	504 (2.46)
	PWO:La	43.0%	95	200	$2.0\cdot10^{9}$	1.7	$1.9\cdot10^{-6}$	453 (2.74)
		57.0%	104	270	$1.0\cdot10^{13}$	1.6	$4.7\cdot10^{-9}$	444 (2.79)
180-200K								
	Un. 1		172	400	$2.0\cdot10^{10}$	1.1	$3.1\cdot10^{-4}$	
			190	500	$9.0\cdot10^{11}$	1.4	$5.0\cdot10^{-4}$	473
	PWO:Nb		174	400	$2.0\cdot10^{10}$	1.1	$3.1\cdot10^{-4}$	477
			190	500	$9.0\cdot10^{11}$	1.4	$5.0\cdot10^{-4}$	482
230K	Un. 1		226	490	$2.0\cdot10^{9}$	1.0	$9.0\cdot10^{-2}$	
	PWO:Nb		226	490	$2.0\cdot10^{9}$	1.0	$9.0\cdot10^{-2}$	

References

1. A. Hofstaetter, A. Sharmann, D. Shwabe, B. Vitt, Z.Physic B 30(1998)305
2. Y. Zhang, N. A. W. Holzwarth, R. T. Williams, Phys.Rev.57(1998)12737
3. J.M.Moreau, Ph.Galez, R.E.Gladyshevski, J.P.Peigneux, and M.V.Korzhik, J.Allows and Comp., 284(1999)104
4. A.Hofstaetter, R.Oeder, A.Sharmann, D.Shwabe, B.Vitt, phys.stat.sol. (b) 89(1978)375
5. M.Bohm, F.Henecker, A.Hofstaetter, M.Luh, B.K.Meyer, A.Sharmann, O.V.Kondratiev and M.V.Korzhik, "Electron Traps in the Scintillator Material PbWO4 and Their Correlation to the Thermally Stimulated Luminescence" EURODIM98 Interant. Conf. Keele University (England) 5-11 July, 1998, 1998.
6. M.Bohm, F.Henecker, A.Hofstaetter, M.Luh, B.K.Meyer, A.Sharmann, V.Metag, R.Novotny, O.V.Kondratiev, M.V.Korzhik, "Shallow electron traps in the scintillator material PbWO4 correlation to the thermally stimulated luminescence" Precented at PWO Workshop, Roma, 11-14 October, 1998.
7. M.Korzhik, A.Borisevich, and O. V.Kondratiev Proc. SPIE 2667(1996)105
8. M.Nikl, P.Bonacek, K.Nitsch,, E.Mihokova, M.Martini, A.Vedda, P.Croci, G.P.Pazzi, P.Fabeni, S.Baccaro, B.Borgia, I.Dafinei, M.Diemoz, G.Organtini, A.Auffray, P.Lecoq, M.Kobayashi, Y.Usuki, Applied Phys.Lett. 71(1977)3755
9. A.N.Annenkov, E.Auffray, A.E.Borisevich, G.Yu.Drobishev, A.A.Fedorov, O.V.Kondratiev, M.V.Korzhik, P.Lecoq, V.D.Ligun, O.V.Missevitch, V.B.Pavlenko, J-P.Peigneux, Yu.D.Prokoshkin, A.V.Singovski, R.F.Zouevski, NIM A 403(1998)302
10. A.N.Belski, S.M.Klimov, V.V.Mikhailin, A.N.vasiliev, E.Auffray, P.Lecoq, C.Pedrini, M.V.Korzhik, A.N.Annenkov, P.Chevallier, P.Martin, and J.S.Krupa, Chem. Phys. Lett.277(1997)65
11. A.Annekov, E.Auffray, M.Korzhik, P.Lecoq, J.-P. Peigneux, phys.stat.sol. (a), 170(1998) 47
12. V.V.Laguta, J.Rosa, M.I.Zaritski, M.Nikl, Y.Usuki, J.Phys.: Condensed Matter 10(1998) 7293
13. M.Bohm, A.E.Borisevich, G.Yu.Drobishev, A.Hofstaetter, O.V.Kondratiev, M.V.Korzhik, M.Luh, B.K.Meuer, J.P.Peigneux, A.Sharmann, phys.stat.sol. (a) 167(1998) 243
14. M.Nikl, K.Nitsch, A.Cecila, M.Martini, M.Montecchi, A.Vedda, P.Croci, E.Risetta, G.Spinolo, S.Baccaro, B.Borgia, I.Dafinei, M.Diemoz, M.Kobayashi, Y.Usuki, M.Ishi, O.Jarolimek, P.Reiche, J. Applied Phys.. 82(1977)5758
15. A.Annenkov, A.N.Kostylev, V.D.Liogun, M.V.Korzhik and P.Lecoq Inorgani Scintillators and Their Applications, Ed. Yin Zhiwen, li peijun, Feng XIQI, Xue Zhilin, Shanghai, September 1997 (p.362)
16. Analysis of the Thermally Stimulated Processes. Chen R., Kirsh Y. Pergamon Press, 1973
17. M.V.Korzhik, V.B.Pavlenko, T.N.Timochenko, V.A.Kachanov, A.V.Singovski, A.N.Annenkov, V.D.Ligun, I.M.Solski, J.P.Peigneux, phys.stat.sol. (a) 154 (1996) 779
18. A.Hofstaetter , V.V.Laguta, et al. Proc. Scint99, to be published

Study on Macroscopic Defect of $PbWO_4$ Crystals Grown by Bridgeman Method

Zheng Lianrong Chen gang Ren shaoxia Li jianzhe Sun guoli Wei jin Yu hongzhi

Beijing Glass Research Institute, Beijing, P.R. China

Introduction

$PbWO_4$ Scintillating crystal has attracted much more interest in recent years as one of the promising candidates for dense, fast and radiation-hard materials for high quality γ-ray detectors in high radiation environment in future high energy accelerators such as LHC. But some properties of PWO crystals such as transmittance, light yield and radiation hardness are not satisfactory due to the gas babbles, solid inclusions and crack etc. in PWO crystals grown by Bridgeman method. We studied these defects carefully and found some way to reduce them.

Crystal growth

The crystals were grew by modified Bridgeman method designed by ourselves in BGRI. The purity of raw materials (PbO and WO_3) from the same source was 99.99%. The crystals are grown in Platinum crucible in the air and the growth speed is 0.4 --1.0mm/day. After improvement in the growth technology, we have got full size (230mm) qualified PWO crystals.

Observation of the crystals' macroscopic defect

The crystals mainly crack at the two positions: 1) Transversely crack at the joint of seed and the bottom of the crystal. The sheets are usually 20--30mm in length and 1--2mm in breadth. The cleavage planes are sunken with kelly inclusions. After analysis by electron probe microanalyser, we found that the inclusions are mainly made from Pb, W and Sb (Fig.1). 2) Transversely crack at the top of the crystals. These sheets are usually 30mm in length. The color of the top of the crystals is usually brown.

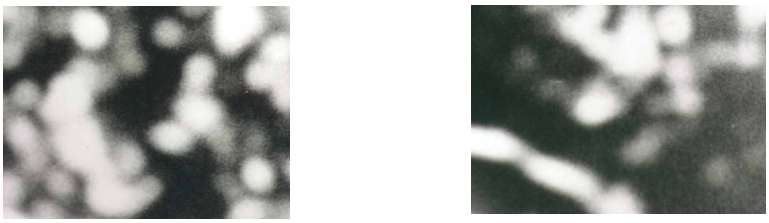

Fig.1 Inclusions image magnified 3000 times by electron probe microanalyser)

We analysed the two kind of sheets by GDMS and found little difference in their composition (table 1)

Results and discussion:

When the interface are stable, the maximum growth speed of the crystal is

$$f_{max} = ks(\partial T / \partial Z)_S / \ L \qquad (1)$$

$(\partial T / \partial Z)_S$:temperature gradient in the crystal near the interface. Ks: thermal conductivity of the crystal. ; density of the crystal. L: latent heat.

There is the most part of the crucible and crystal in the high temperature area and only small part of them in the low temperature area at the initial stage of the crystals growth. We can deduce from formula (1) that the latent heat of crystallization can't diffuse quickly during this period, which lead to the solid-liquid interface descend. So the temperature gradient become smaller and the f_{max} decrease. At the same time, the growth interface is not stable because the crucible's falling speed is faster then $f_{max,}$ which result in the structure defect and cracking of the PWO crystal. Moreover, the air current is unstable at the initial stage of the crystals growth and then cause the temperature fluctuation near the crystal, which increase the crystal's cracking intention. The growth interface will become more unstable when the rough air becomes strong. Therefore, growth terrace appear on the growth interface. When the terrace move faster than the growth interface, inclusions are captured.

At the later period of crystal's growth, there is only small part of the crucible and crystals in the high temperature area. So the latent heat of crystallization can diffuse quickly and the growth interface becomes protruding. However, the impurities concentration increase, the temperature gradient become smaller and the growth speed becomes faster which result in supercooling. So the structure defect and cracking of the PWO crystal increase during this period.

Measures

1). Improving the technology of raw material's pretreatment and make the raw material access to optimal stoichiometry tuning.
2). Using oriented and high quality seed crystals
3). Improving the furnace's structure to get more suitable temperature field.
4). Improving the technology of crystal growth, adjust the crucible's falling speed during the initial and later stage of crystal growth.

After adopting these measures, we have gotten some full size crystals with little macro-defect and crack. And their transmittance, L.Y. and radiation hardness are improved correspondingly.

Reference

1. P.Lecoq, I.Dafinei, E.Auffray, et al. Lead tungstate scintillators for LHC EM calorimeter. Nuclear Instruments and Methods in Physics Research ,1995:A 365:291-298
2. M.Nikl, J.Rosa, K.Nitsch, et al. Optical and EPR study of point defects in $PbWO_4$ single crystals. Proc. of ICDIM 96, 1996

Optical anisotropy effects in lead tungstate crystals

R. Chipaux[1], M. Géléoc[1,2]

[1]*CEA/DSM/DAPNIA/SED, CE-Saclay, 91191 Gif sur Yvette cedex, France*
[2]*now at CEA/DCC/DPE/SLCS, CE-Saclay, 91191 Gif sur Yvette cedex, France*

Abstract. The anisotropic crystal structure of lead tungstate leads to strong consequences in its optical properties and their characterization. Beyond the variation of surface reflections due to the birefringence of the material, we report the observation that part of the bulk light absorption is sensitive to the light polarization direction. This variable part varies with the quality of the crystal, and is clearly related to internal structural defects. Irradiation experiments with gamma rays or fast neutrons confirm the recent improvement of the short term resistance of this scintillator. Its long term behaviour remains identical, and acceptable for the use in high energy electromagnetic calorimetry. A polarization direction dependant induced absorption is observed, specially after high levels of radiation. Ray tracing programs in development for the simulation of the light yield in lead tungstate should take into account all these anisotropic effects.

Keywords : Lead tungstate, radiation dammage, birefringence, refractive index

Introduction

Lead tungstate, the scintillating material foreseen for the electromagnetic calorimeter of the CMS experiment in project at the Large Hadron Collider [1], has an anisotropic crystal structure, scheelite type, $I4_1/a$, for the stoichiometric $PbWO_4$. This anisotropy has important consequences in crystal growth, machining, etc., as reported in [2] ; it induces also directly optical birefringence, which complicates optical characterizations. It has also indirect consequences in the optical transmission properties of the material : as shown in section 3, both initial and radiation induced absorptions are sensitive to the light polarization direction.

Refractive index

New measurements of the lead tungstate refractive index have been recently published by S. Baccaro and co-workers [3]. Compared to their previous published data [4] only little change is found for the ordinary index, but the accuracy of extraordinary index values is greatly improved. Thus the numerical formulæ proposed in a previous note [5] should be considered as inaccurate, especially for the extraordinary index.

Results of fit based on the new data are presented in table 1 for the Cauchy formula :

$$n = \sum_{i=0}^{m_c} \frac{n_{c_i}}{\lambda^{2i}} = n_{c_0}\left(1 - \frac{\lambda_{c_1}^2}{\lambda^2}\left(1 - \frac{\lambda_{c_2}^2}{\lambda^2}\left(1 - \cdots\right)\right)\right) \qquad (1)$$

and in table 2 for the Sellmeier law :

$$n^2 - 1 = \sum_{i=0}^{m_s} \frac{n_{s_i}^2}{1 - \frac{\lambda_{s_i}^2}{\lambda^2}} \qquad (2)$$

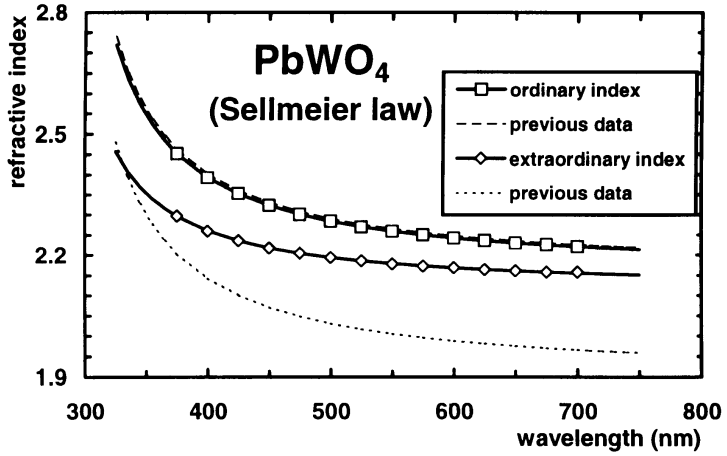

Figure 1 : Ordinary and extraordinary indices of $PbWO_4$ as function of wavelength : data [3] and fit to a one term Sellmeier law ; comparison with the previous data [4,5].

Figure 1 represents the data and its fit by the Sellmeier law, compared to the previous results.

We would recommend the use of the following expressions, derived from the parameters shown in tables 1 and 2, where wavelengths λ are in nanometer :

$$n_o = \sqrt{3.5325 + \frac{1.19198}{1 - 73053\lambda^{-2}}} \pm 0.01 \qquad (3)$$

$$n_e = \sqrt{3.7834 + \frac{0.73754}{1 - 71073\lambda^{-2}}} \pm 0.02 \qquad (4)$$

Table 1 : $PbWO_4$ index fits : parameters of the five terms Cauchy formula.

	n_{c_0}	$\lambda_{c_1}^2$ (nm^2)	$\lambda_{c_2}^2$ (nm^2)	$\lambda_{c_3}^2$ (nm^2)	$\lambda_{c_4}^2$ (nm^2)
Ordinary index	2.1941	-7405.9	-177418	69434	170104
Extraordinary index	2.1480	5038.0	889480	142481	66245

Table 2 : $PbWO_4$ index fits : parameters of the two terms Sellmeier law ($\lambda_{s_0} = 0$).

	n_{s_0}	n_{s_1}	λ_{s_1} (nm)
Ordinary index	1.5914	1.0918	270.28
Extraordinary index	1.6683	0.8588	266.60

This negative birefringence implies to take some precautions in optical transmission measurement. The intensity of the Fresnel reflections on the surface will depend on the orientation of the optical axis of the measured crystal and on the direction and polarization of the light beam. For example, at 450 nm, in the case of light beams polarized perpendicularly and parallel to the optical axis, the difference in measured transmission due to this effect is 3.6 %. Taking into account this effect allowed us to put in evidence some dependencies of the optical absorption in lead tungstate with the light polarization direction, as shown in the next section.

In the recent Russian $PbWO_4$ crystals, as indicated in [2], the optical axis is parallel to the small faces and to one of the lateral faces of the crystal. It is easy to determine visually the faces traversed by the optical axis, and thus to orient the crystal in longitudinal transmission

measurement in order to have, for example, the optical axis vertical. In that geometry, the light beam is perpendicular to the optical axis, and does not split in two distinct rays, and the Fresnel reflections are easily determined for any polarization state of the light beam. The simplest method would be to use linearly polarized light, either parallel or perpendicular to the optical axis and to calculate the reflections using respectively the ordinary or the extraordinary index.

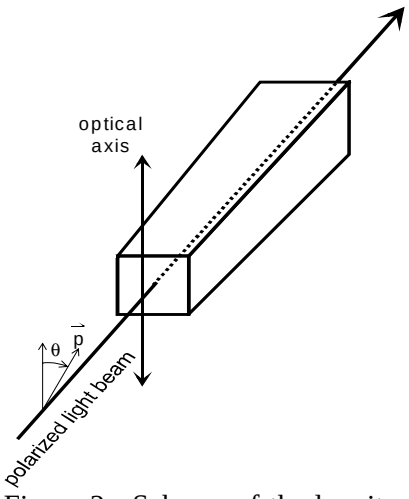

Figure 2 : Scheme of the longitudinal transmission measurements.

Optical absorption

Variation with the direction of light polarization

We have performed longitudinal light transmission measurement on several Russian crystals. In this study, both sample and reference beams were polarized by UV visible linear sheet polarizers [6].

We have varied the angle θ between the direction of polarization and the optical axis from 0° to 180° (see figure 2).

An example of the set of data obtained is shown for one crystal on figure 3.

As in figure 4, we report the variations of the transmission at each wavelength and compare them to the ones that would have been induced by the modulation of the Fresnel reflections alone starting from the maximum of transmission, (*i.e.* for a direction of polarization perpendicular to the optical axis).

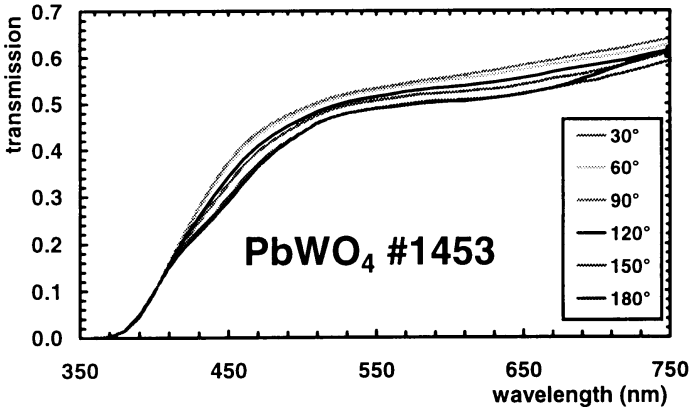

Figure 3: Longitudinal optical transmissions *versus* wavelength for crystal #1453 for different directions of the light polarization. The angle is the angle θ between the directions of light polarization and optical axis.

The amplitude of the modulation can not be always explained by the Fresnel reflections, (see for example figure 4), which indicates that part of the absorption is polarization dependent.

After correction from the reflections, we can extract the intrinsic absorption coefficient $\mu(\theta)$, which, at the first order in θ can be written as :

$$\mu(\theta) = \mu_0 + \mu_\theta \sin^2(\theta - \theta_0) \tag{5}$$

μ_0 is given by the maximal transmission, μ_θ and θ_0 by the amplitude and the phase of the sinusoid, corrected of the reflections. In this treatment, multiple reflections have been neglected. In all crystals, the phase of the sinusoid is independent of the wavelength, and nearly

equal to 0°. The difference with 0° can be due to systematic errors caused by disorientation of the polarizer, and to little deviation of the optical axis from its ideal direction. This deviation is always below 10°, and confirm the orientation of the optical axis indicated in [2].

Figure 5 shows the variation of μ_0 and μ_θ with the wavelength. In every case, μ_θ is positive, indicating that the bulk absorption is greater when the light is polarized along the optical axis. In crystals #1453 and #1694, two bands can be observed in μ_θ, a rather sharp around 450 nm and a smaller and broader one around 650 nm. At 450 nm μ_θ can be as high as one half of μ_0. In crystals like #1695 and #1854, μ_θ is negligible above 400 nm. In crystal, #1699, no clear feature is observed in the μ_θ spectrum. In this crystal μ_θ remains almost equal to one half of μ_0 at every wavelength.

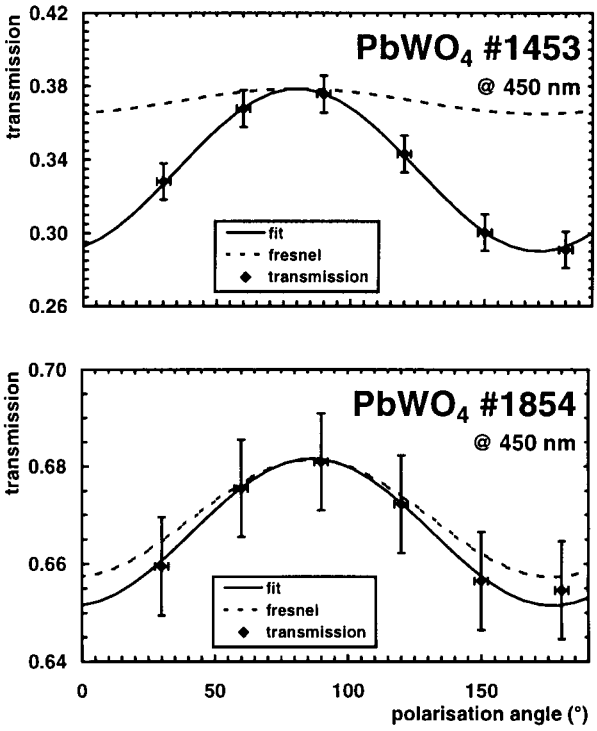

Figure 4 : Transmission *versus* polarization direction for crystals #1453 and #1854 at 450 nm. Solid line : first order sinusoidal fit of the data, dashed line : modulation due to Fresnel reflections.

Variation after irradiation

We have investigated the behaviour of the lanthanum doped crystal #1854 under irradiation. In a first experiment it received a gamma dose of 25 Gy at a rate of 0.5 Gy h^{-1} in

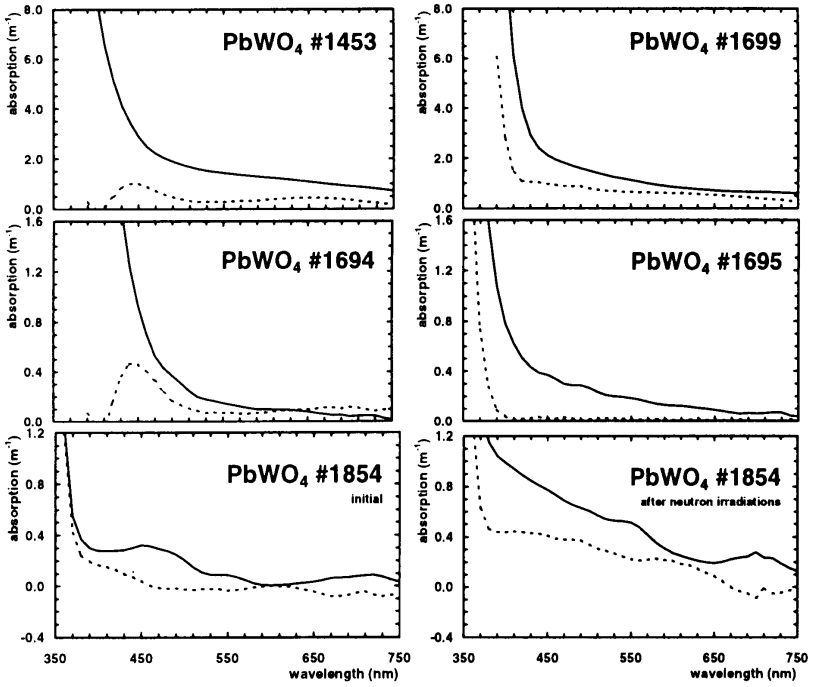

Figure 5 : Attenuation coefficients μ_0 (solid line) and μ_θ (dashed line) *versus* wavelength for crystals #1453, #1694, #1695, #1699 and #1854. Notice the differences in scale between crystals.

our ^{60}Co irradiation facility Cocase, then in a second one it received in the reactor Ulysse a cumulated fast neutron fluence of $2\ 10^{14}$ fast neutrons cm^{-2} in three steps summarised in table 3. After annealing, a second neutron irradiation at the same fluence ($2\ 10^{14}$ fast neutrons cm^{-2}) was performed. Details on the irradiation facilities have been previously published [7,8]. Transmission measurements have been performed longitudinally with light polarized linearly, parallel to the crystal optical axis (ordinary ray), or perpendicularly (extraordinary ray), after a delay of at least one week after irradiation, caused by the induced radioactivity.

The low rate gamma irradiation does not induce large degradation in the transparency as shown in figure 6. For the ordinary ray, the induced absorption coefficient remains less than 0.1 m^{-1}. These data are typical for recent rad-hard crystals. Even more, for the extraordinary ray, a small, but significant improvement is observed around 460 nm. A similar behaviour has been observed previously around 420 nm in Gd and La doped $PbWO_4$ samples [9].

After annealing during 6 hours at 200° C, the initial state is practically recovered (see figure 6).

Table 3 : Neutron irradiation conditions.

	fast neutrons (E > 100 keV) (cm^{-2})	epithermal neutrons (1 eV < E < 100 keV) (cm^{-2})	thermal neutrons (E < 1 eV) (cm^{-2})	Ionising dose (Gy)
		annealing (200°C, 8h)		
Step 1	$1\ 10^{12}$	$3.3\ 10^{12}$	$2.9\ 10^{12}$	125
Step 2	$2\ 10^{13}$	$6.7\ 10^{13}$	$5.8\ 10^{13}$	2 500
Step 3	$2\ 10^{14}$	$6.7\ 10^{14}$	$5.8\ 10^{14}$	25 000
		annealing (200°C, 8h)		
Step 4	$2\ 10^{14}$	$6.7\ 10^{14}$	$5.8\ 10^{14}$	25 000
		annealing (200°C, 8h)		

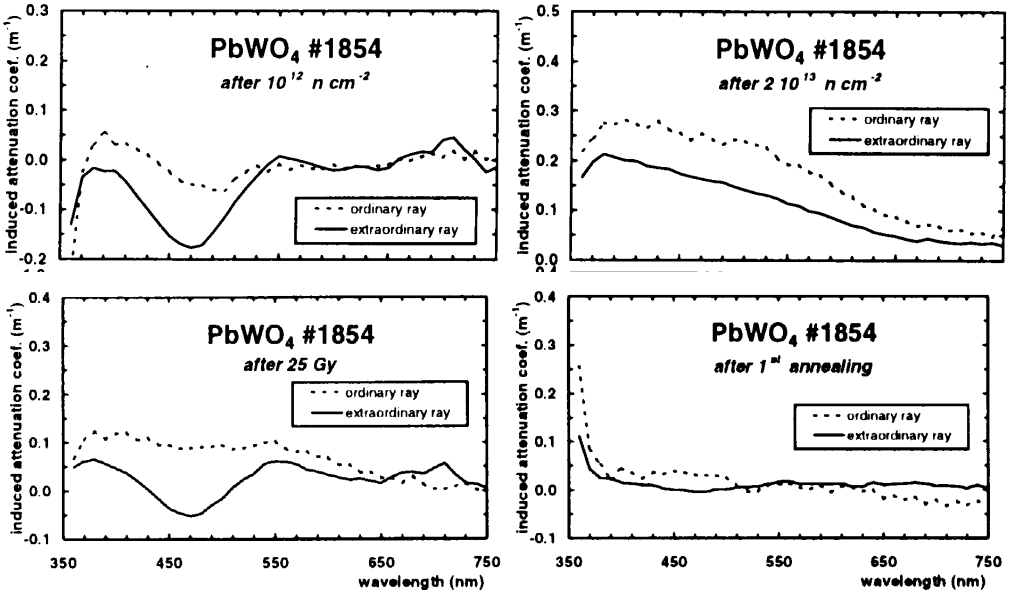

Figure 6: Induced absorption coefficients in crystal #1854 *versus* wavelength for the ordinary and extraordinary rays, after 25 Gy irradiation (left), and annealing (right).

The first neutron irradiation gives results comparable to the gamma irradiation. Higher fluence induces absorption coefficients which remains less than 1 m^{-1} after 2 10^{14} fast neutrons cm^{-2}, but are very different for ordinary and extraordinary rays as shown in figure 7. As the initial absorption in the poorest crystals, the induced absorption is higher for the ordinary ray, that is when the light is polarized along the optical axis. A band centred around 520 nm is clearly seen. After annealing the crystal recovered almost its initial transparency. The second neutron irradiation to 2 10^{14} fast neutrons cm^{-2} induced similar damage.

Conclusion

This study points out the cares that should be taken to perform precise optical absorption characterization of lead tungstate crystals. Strong dependence of absorption on light polarization direction are observed, for the initial absorption in absorbing crystals, as well as for the induced absorption under radiation in recent, optimised crystals. This behaviour, coupled with the band shape of this absorption, strongly suggests the influence of anisotropic structural defects, such as lead or oxygen vacancy, already invoked for the explanation of radiation resistance variation in these crystals.

However, this absorption dependence takes amplitudes and shapes which depend deeply on the crystal quality and should not be related to one unique type of defect but is rather be a general feature of lead tungstate, besides not astonishing in such strongly anisotropic material.

On a practical point of view, the importance of this effect may imply to incorporate absorption anisotropy (as well as optical anisotropy) in the ray tracing programs, such as LITRANI [10], developed to describe the detector evolution and simulate its ageing.

Finally the neutron irradiation reported here confirm the early reported [8] long term behaviour of lead tungstate in the CMS calorimeter, with induced absorption lower than 1 m^{-1} after doses equivalent to 10 years of operation, and the improvement of it's short term radiation resistance.

Acknowledgements

This work was made in the frame of the CMS ECAL monitoring development project, under the head and with the constant support of J.-P. Pansart and J. Rander. We would like to thanks E. Auffray and P. Lecoq, CERN, wo provided us with up to date crystals. We are indebted, for the neutron irradiation, to J. Safieh, G. Dauphin and the operating team of the Ulysse reactor.

References

[1] CMS collaboration : “The Compact Muon Solenoid — Technical Proposal”, CERN/LHCC 94–38, LHCC/P1 (1994) ; “The Electromagnetic Calorimeter Project — Technical Design Report”, CERN/LHCC 97–33, CMS TDR 4 (1997).

[2] M. Lebeau and D. Rinaldi, in : Proc. Int. Conf. on Inorganic Scintillators and their Applications, SCINT 97, Z.W. Yin, P.J. Li, X.Q. Feng and Z.L. Xue eds., CAS Shanghai Branch Press, 1998, p. 230–235.

[3] S. Baccaro et al., Nucl. Instr. and Meth. in Phys. Res. A 385 (1997) 209–214.

[4] S. Baccaro et al., in : Proc. Int. Conf. on Inorganic Scintillators and their Applications, SCINT 95, P. Dorenbos and C.W.E. van Eick eds., Delft University Press, 1996, p. 293–295.

[5] R. Chipaux, “Numerical formulæ for the refractive index of lead tungstate”, CMS–TN/95–184 (1995).

[6] Ealing UV-visible linear polarizers, ref. 23–2363.

[7] R. Chipaux, J.-L. Faure, P. Rebourgeard, G. Dauphin and J. Safieh, Nucl. Instr. and Meth. in Phys. Res. A 345 (1994) 440–444.

[8] R. Chipaux et al., in : Scintillator and Phosphor Materials, M.J. Weber, P. Lecoq, R.C. Ruchti, C. Woody, W.M. Yen and R.-Y. Zhu eds., Mat. Res. Soc. Symp. Proc., vol. 358, 1994, p. 481–486 ;
R. Chipaux and O. Tozon, in : Proc. Int. Conf. on Inorganic Scintillators and their Applications, SCINT 95, P. Dorenbos and C.W.E. van Eick eds., Delft University Press, 1996, p. 274–277.

[9] S. Baccaro et al., Phys. Stat. Sol. (a) 160 (1997) R5 ;
S. Baccaro et al., Phys. Stat. Sol. (a) 164 (1997) R9.

[10] F.-X. Gentit, “LITRANI”,
http://www-dapnia.cea.fr/Spp/Experiences/CMS/cristal/index.htm,
see also : F.-X. Gentit, “The Monte-Carlo program Cristal”, CMS–TN/1996–143 (1996).

Determination of the crystal structure of lead tungstate by neutron diffraction

A. Cousson[1], W. Paulus[1], R. Chipaux[2]

[1]*CEA/DSM/DRECAM/LLB, CE-Saclay, 91191 Gif sur Yvette cedex, France*
[2]*CEA/DSM/DAPNIA/SED, CE-Saclay, 91191 Gif sur Yvette cedex, France*

Abstract. The crystal structure of lead tungstate, $PbWO_4$, is tetragonal, scheelite type, space group $I4_1/a$. This compound, du to the difference in the vapour pressure of the two raw oxides, WO_3 and PbO, used in the crystal growth, is frequently subjected to lead deficiency. It has been reported by one group that lead vacancies can order in a crystal structure derived from the scheelite type, but of lower symmetry and described by the space group *P4*/*nnc* or $P\bar{4}$.

We report here on neutron diffraction measurements performed on three different single crystals, two of them being presented to us as possibly presenting the lead deficient phase. Our measurements do not show any indication of structural distortion, even at 70 K for one of the samples. The existence of a lead deficient structure remains unconfirmed.

Keywords : Lead tungstate, crystal structure, neutron diffraction

Introduction

Lead tungstate, $PbWO_4$, occurs in nature as tetragonal stolzite, of scheelite type [i] and monoclinic raspite [ii]. The common form for the industrial crystals used in particle detection is the scheelite type, space group $I4_1/a$. Following X-ray diffraction studies on lead deficient crystals, a distortion of this structure, described by the space group *P4*/*nnc*, has been described by Moreau *et al.* [iii]. The corresponding composition is $Pb_7W_8O_{(32-x)}$. Further neutron diffraction investigation on powdered samples leads the same authors to a third tetragonal structure, space group $P\bar{4}$, with the composition $Pb_{7.5}W_8O_{32}$ [iv]. However these distorted lead deficient structures have not been observed elsewhere, even in precise studies around stoichiometry [v].

It is largely admitted that non-stoichiometry, especially lead vacancies, has a large influence on the spectroscopic and optical properties of lead tungstate and on its behaviour under radiation [vi]. The existence of a specific crystal structure for lead deficient $PbWO_4$ is a key point in the interpretation of the properties of lead tungstate, for example the occurrence of a second maximum of radiation resistance when lead content decreases (the first being at exact stoichiometry) [vi].

A structural transition has also been suggested in lead tungstate at 220 K [vii], but no indication on the character of this transition has been reported.

Thus the confirmation, or not, of the existence of the phase $Pb_7W_8O_{(32-x)}$ $Pb_{7.5}W_8O_{32}$ would be of great importance.

Experimental

To clarify the problem, we have undertaken neutron diffraction measurements on single crystals. This technique is particularly adapted to observe small displacements of oxygen atoms. Three lead tungstate samples, about 10 mm^3, were measured. The first sample comes

from the early crystals synthesised in 1994. The two last are issued from the crystals grown for CMS R&D at Bogoroditsk, and were presented to us as possibly presenting the distorted tetragonal structure.

Data collection was performed on the 5C2 neutron four-circle diffractometer installed at the hot source beamline of the reactor Orphée, Saclay (France). All samples were measured at room temperature. One of them was also tested at 120 and 70 K.

Results

Table 1 report the refinement results and parameters. In all cases, the quality of the crystal was found excellent. The diffraction patterns were examined in the *P* cell, to check about reflections forbidden in the scheelite symmetry. No reflection peak, with $I > 3\sigma(I)$, was observed that could not be interpreted in the $I4_1/a$ space group.

	space group	a (Å)	c (Å)	wavelength (Å)	reflections measured	independent reflections	R	Rw	goodness of fit
sample 1 293 K	$I4_1/a$	5.456	12.02	1.1056 (Ge 311)	450	385	2.04 %	1.91 %	0.9222
sample 2 (CMS #1655) 293 K	$I4_1/a$	5.46(1)	12.04(2)	0.8305 (Cu 220)	196	176	1.96 %	2.11 %	1.0868
sample 3 (CMS #1830) 293 K	$I4_1/a$	5.46(1)	12.05(2)	0.8305 (Cu 220)	463	401	2.80 %	2.71 %	1.0002
sample 3 (CMS #1830) 120 K	$I4_1/a$	5.46(1)	12.01(2)	0.8305 (Cu 220)	406	328	3.33 %	3.19 %	1.0949
sample 3 (CMS #1830) 70 K	$I4_1/a$	5.46(1)	12.01(2)	0.8305 (Cu 220)	404	337	3.15 %	2.94 %	1.0587

Table 1 : Results and parameters of the structure refinements for lead tungstate samples measured at LLB.

Conclusion

No deviation from the scheelite structure has been observed in the samples measured. No phase transition has been observed above 70 K. The crystal structure of the single crystals studied in this work is undoubtedly of the scheelite type. Up to now, the existence of a specific crystal structure for lead deficient $PbWO_4$, such as $Pb_7W_8O_{(32-x)}$. or $Pb_{7.5}W_8O_{32}$ remains to be confirmed.

Acknowledgements

This work was initiated following exchanges within the CMS and Crystal Clear collaborations and stimulated by numerous discussions with P. Lecoq, J.-P. Peigneux, and J.-M. Moreau.

References

1. P.W. Richter, G.J. Kriger and C.W.F.T. Pistorius, Acta Crystallogr., **B32** (1976) 928.
2. T. Fujita, I. Kawada and K. Kato, Acta Crystallogr., **B33** (1977) 162.
3. J.-M. Moreau, Ph. Galez, J.-P. Peigneux and M.V. Korzhik, J. Alloys and Compounds, **238** (1996) 46.
4. J.-M. Moreau, Ph. Galez, R.E. Gladyshevskii, J.-P. Peigneux and M.V. Korzhik, J. Alloys and Compounds, **284** (1999) 104.
5. P. Bohacek *et al.*, "Stoichiometry and radiation damage of PWO crystals grown from melts of different composition", *in* Tungstate Crystals, Proc. Int. Workshop on Tungstate Crystals, Roma, 12-14 October 1998, pp 57–60 ; J. Sykora, M. Husák, O. Jarolímek, A. Strejc, D. Sedmidubsky, "The crystallographical study of compounds originating in the PbO–WO_3 system", *ibid.*, pp 95–97.
6. A. Annenkov *et al*., Phys. Stat. Sol. (a), **170** (1998) 47.
7. N.V. Klassen, S.Z. Shmurak, B.S. Red'kin, S.I. Rybchenko, V.V. Sinitzin, "Processing technology and scintillation performance of PWO", *in* Tungstate Crystals, Proc. Int. Workshop on Tungstate Crystals, Roma, 12-14 October 1998, pp 35–46.

Light collection in the CMS lead tungstate crystals : relation between monitoring and calibration variations

R. Chipaux

CEA/DSM/DAPNIA/SED, CE-Saclay, 91191 Gif sur Yvette cedex, France

Abstract. The ageing of scintillating crystals under radiation leads to a deterioration of their transparency, thus of their effective light yield and their calibration. The link between the transparency variation, as measured by a fibre optic monitoring system, and the calibration variation is not trivial.

A model describing the light collection process is proposed. It helps to understand the parameters, which govern this correlation, mainly absorption length and light back-reflection or diffusion characteristics. This model describes well the results of numerical qualitative simulations of light collection in lead tungstate crystals. It also explains the differences between calibration and monitoring variations observed in test beam.

Important slopes could be obtained when the crystal ends have a different behaviour for monitoring and scintillation lights, like in the case of bare surfaces. As anticipated, the correlation slope tends toward one, when absorption is low and both monitoring and scintillation lights are well contained in the crystal, and thus independently of the geometry (front or back) of the monitoring light injection.

Keywords : Scintillator detector, light yield, ageing, ray tracing.

Introduction

In scintillation detectors exposed to radiation, like in the CMS lead tungstate electromagnetic calorimeter [1], the light collection efficiency will vary along time, because of the modification of the scintillating material transparency. In CMS, for example, maintaining the energy resolution of the instrument will require : – a calibration with physical events of known energy, at a time scale of a few weeks ; – a continuous monitoring of the optical properties of the crystals by a fibre optic monitoring system, to interpolate calibration corrections during that time [2]. However, the correlation between variation of crystal transparency, as measured by the monitoring system, and variation of the calibration parameters of the same crystal is not trivial [2].

We have proposed a model describing the light collection process in transparent materials. This model is detailed in [3] and we will focus here on its main qualitative results, namely on the correlation monitoring/calibration.

Modelisation and simulation

We recall here the main results of the model. See [3] for details. Both monitoring and scintillation lights can be decomposed in a direct part, coming directly to the photodetector, (indexed *d*), a "back" part (for scintillation light), (indexed *b*) and a "multiple turn" part. The variation of monitoring and scintillating light yield efficiencies (respectively $C_m(t,\lambda)$ and $C_s(t,\lambda,z)$) can be expressed as function of a few numbers of parameters, namely the optical absorption coefficient $\mu(t,\lambda)$, effective reflection coefficients *k* (respectively k_m and k_s), and effective path coefficients *b*. In the model, the effect of light absorption in the material,

represented by $\mu(t,\lambda)$, is disconnected from other sources of light loss, which are associated to the coefficients *k*.

With these hypothesis, the light collection efficiency for monitoring light, $C_m(t,\lambda)$, can be written as :

$$C_m(t,\lambda) = \frac{C_{m_D} \exp\left(-b_{m_d}\mu(t,\lambda)L\right)}{1-k_m^2 \exp\left(-2b_m\mu(t,\lambda)L\right)} \tag{1}$$

where *L* is the length of the scintillator.

In case of monitoring light is injected from the back of the crystal, *i.e.* from the side of the photo detector, $2\,b_m$ should naturally replace b_m in this equation.

And the efficiency for scintillation light, $C_s(t,\lambda,z)$, can be written as :

$$C_s(t,\lambda,z) = \frac{C_{s_D} \exp\left(-b_{s_d}\mu(t,\lambda)(L-z)\right) + C_{s_B} \exp\left(-b_{s_b}\mu(t,\lambda)(L+z)\right)}{1-k_s^2 \exp\left(-2b_s\mu(t,\lambda)L\right)} \tag{2}$$

As shown in [3], this model agrees with the simulations performed assuming perfectly polished materials. For a "uniformized" scintillator, *i.e.* for a scintillation detector in which the light yield has been voluntary homogenised in *z*, (for example by depolishing one lateral face, as foreseen in the CMS calorimeter), one can nevertheless presume that the same arguments can be used. In that case, the effective reflection coefficients *k* would represents the global result of end and lateral surfaces reflections, or more generally the quality of light confinement in the crystal.

To obtain the variation of the detector calibration coefficients $S_s(t,E_0)$, $C_s(t,\lambda,z)$ should be convoluted with the energy density and the photodetector quantum efficiency, and then integrated over *z* and λ. (One assumes that other elements, such as quantum efficiency, gain, etc. are constant). For small variations, (*i.e.* low induced absorption), it is reasonable to write the total scintillation efficiency by the same equation using mean parameters : $\overline{\mu}$ (absorption coefficient at the wavelength of the effective maximum of emission) and $\overline{z}_{sh}$ (mean position of the energy deposited) :

$$S_s(t) = \frac{S_{s_D} \exp\left(-{}^{sh}b_{s_d}\overline{\mu}(t)(L-\overline{z}_{sh})\right) + S_{s_B} \exp\left(-{}^{sh}b_{s_b}\overline{\mu}(t)(L+\overline{z}_{sh})\right)}{1-{}^{sh}k_s^2 \exp\left(-2\,{}^{sh}b_s\overline{\mu}(t)L\right)} \tag{3}$$

Correlation

In high absorption materials, *i.e.* when $\mu^{-1}(t,\lambda) = \Lambda(t,\lambda) \le L$, the relative variations of the efficiencies ($\mathrm{d}S_m/(S_m\,\mathrm{d}\mu)$ and $\mathrm{d}S_s/(S_s\,\mathrm{d}\mu)$), (and thus the correlation slope $(\mathrm{d}S_s/S_s)/(\mathrm{d}S_m/S_m)$, which is the parameter that will be used to correct the calibration coefficients from the monitoring data), are governed by the direct light variation, so by the effective paths : $b_{m_d}L$ and $b_{s_d}(L-\overline{z}_{sh})$. b_{m_d} is related to the angular aperture of the optic fibre injecting the monitoring light ; b_{s_d} is related to the angular aperture of the photodetector. They are close together, and the main difference comes from the two lengths L and $L-\overline{z}_{sh}$. The correlation slope is given by $b_{s_d}(L-\overline{z}_{sh})/b_{m_d}L$.

On the contrary, in low absorption materials the effective reflection parameters k_m and k_s play a crucial role. If the containment is poor for both types of light, (k_m and k_s near 0), the correlation slope remains equal to $b_{s_d}(L-\overline{z}_{sh})/b_{m_d}L$, as shown in figure 1 for scintillator's

absorbing ends. If the containment is efficient, (k_m and k_s near 1), the relative variations tend to equilibrate, and the correlation slope approaches 1. This is the case in figure 1 for reflective and diffusive ends. In these conditions, the geometry of monitoring light injection (from the front or the back of the scintillator) is relatively secondary.

They are cases for which a notable difference exists in containment between scintillation light and monitoring light. In the very simple example of bare polished materials, the monitoring light is only partially reflected at the detector's ends, when part of the scintillation light is in total reflection on every surfaces including ends (obviously at the exception, to be able to be detected, of the photodetector surface). This induces high correlation slope. It can reach 2, 3 or even more, as shown in figure 1 for refractive ends. This could explain, at least qualitatively, the values of slope observed in test beam, and their dispersion [4]. As seen in the figure, the slope is very sensitive to the initial absorption length, or correlatively, to the quality of the light confinement, and both parameters can vary sensibly among the crystals tested.

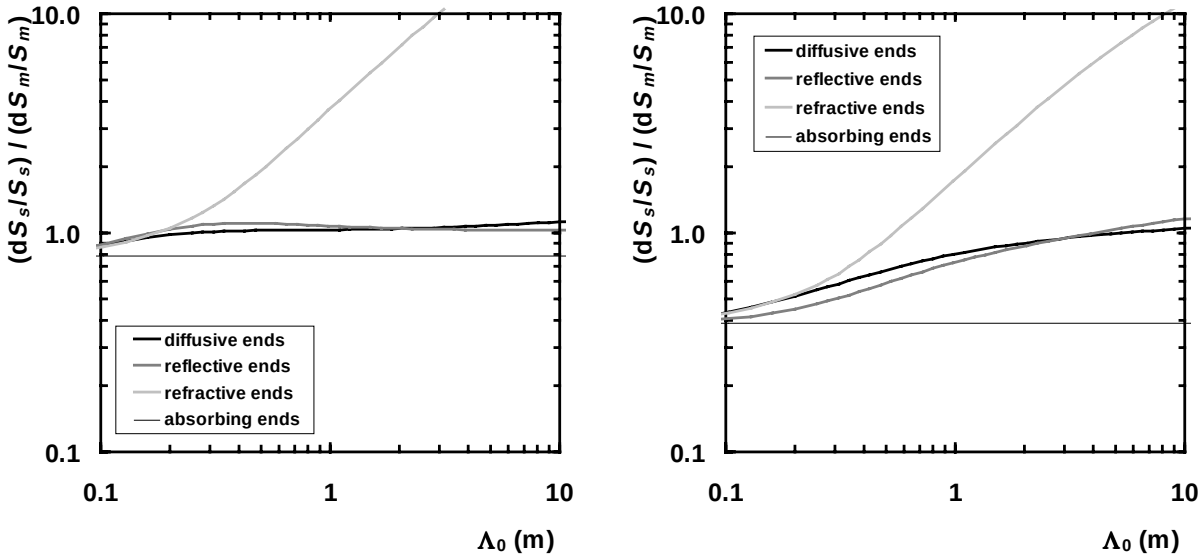

Figure 1 : Variation of the slope of the correlation between scintillation light and monitoring light variations (*i.e.* $(\mathrm{d}S_s/S_s)/(\mathrm{d}S_m/S_m)\big|_{\Lambda=\Lambda_0}$) as a function of the initial absorption length Λ_0, for various types of treatment of the scintillator's ends : fully absorbing ; bare (refractive) ; covered by a perfect specular reflector (reflective) or by a perfect diffuser (diffusive).

Simulations have been made for a 50 GeV electron shower in a tapered crystal with perfect surfaces (without chamfers), assuming the same absorption variation for scintillation and monitoring lights.

On right, monitoring light is injected through the front of the scintillator (CMS ECAL geometry), on left through the back.

Conclusion

This model, based on a limited number of parameters related to physical quantities – absorption length, mean path lengths, reflection transmission (or light confinement) coefficients –, points out the two regimes for scintillation/monitoring correlation. In high absorption materials, the signals are due to the direct light, and the correlation will be dominated by the difference of the optical path lengths. We may predict in that case values of correlation slope less than one, because of the longer path for the monitoring light. In low absorption materials, an increase of absorption affects overall the indirect light, and the correlation is dominated by

the quality of light containment, and by its eventual difference between monitoring and scintillation lights. This may lead to important correlation slopes, especially in bare, polished, materials. In order to keep the slope near the optimal value of one, highly reflexive, either diffusive or specular, coatings should be used. This not only increases the light yields, but also should uniformize their relative variations.

Acknowledgements

This work was in the frame of the CMS ECAL monitoring development project, under the head and with the constant support of J.-P. Pansart and J. Rander.

References

1. CMS collaboration :
   "The Compact Muon Solenoid — Technical Proposal", CERN/LHCC 94–38, LHCC/P1 (1994) ;
   "The Electromagnetic Calorimeter Project — Technical Design Report", CERN/LHCC 97–33, CMS TDR 4 (1997).
2. P. Verrecchia, Nuclear Physics B (Proc. Suppl.), **61B** (1998) 71-76 ; P. Bonamy et al., "The ECAL Calibration : Use of the light monitoring system. Version 2.0", CMS NOTE-1998/013 (1998).
3. R. Chipaux and M. Géléoc, "Modelisation and simulation of the light collection in the CMS lead tungstate crystals", CMS NOTE-1998/091 (1998), submitted to Nucl. Inst. and Meth. A.
4. P. Verrecchia, personal communication.

Spectral-luminescent properties of molibden doped $PbWO_4$ crystals

B.I. Zadneprovski, V.A. Nefedov, I.S. Bykov, E.V. Polyansky

All-Russia Research Institute of Mineral Materials Synthesis, Institutskaya St. 1, Alexandrov, Vladimir Region, 601600 Russia

Abstract. Single crystals of $Pb(WO_4)_{1-x}(MoO_4)_x$ have been grown with x=0-0,1. Their transmission spectras and x-ray luminescence have been studied depending on the content of molibden addition and vacuum annealing. Light emission has also been measured and preliminary data of scintillation kinetics have been obtained. It is evident that molibden introduction in small quantities intensifies the green luminescence and increases the light yield. Time constants of glow are increasing. The obtained results are now under discussion

Keywords. Lead tungstate, molibden, x-ray luminescence, transmission spectra, light yield**.**

Introduction

It is now well established that $PbWO_4$ single crystals are candidate scintillators for precision electromagnetic calorimetry of high-energy particles [1]. Many advantages of $PbWO_4$ in comparison with other crystal scintillators are defined now [2]. However a quantum output of luminescence of growing $PbWO_4$ crystals is rather small. So, in spite of technology success in the production of such scintillator, the search of ways of pointed $PbWO_4$ characteristic increasing remains actual.

Still in earlier investigations on $PbWO_4$ there was defined the presence of two basic glow centres types (blue and green) and a possible transfer of excitation energy from the first to the second was supposed [3]. Results of studies of sheelite-like solid solutions $Ca(WO_4)_{1-x}(MoO_4)_x$ [4] and $NaBi(WO_4)_{2-2x}(MoO_4)_{2x}$ [5] luminescence point the possibility of such transfer intensity by the way of a certain amount of $(MoO_4)^{2-}$ groups introduction in initial tungstates. It is supposed to be a result of speed transfer increasing without temperature activation [5]. Dissolving of lead molibdate $PbMoO_4$ in the tungstate $PbWO_4$ is also accompanied by the formation of solid solutions of the pointed type [6]. Taking into account the given above postulations and possibility to intensity $PbWO_4$ emission by use of its green component we have grown single crystals of $Pb(WO_4)_{1-x}(MoO_4)_x$ with x equal to 0-0,1. Its phase composition, transmission and x-ray luminescence spectras are studied; a technical light yield is measured and the effect of influence the pointed above characteristics of vacuum annealing of crystals is defined.

Experimental procedure

The crystals for the investigation have been grown by Chohralski method in Pt-crucible under air atmosphere. The mechanical mixture of preliminary grown crystals $PbWO_4$ and $PbMoO_4$ as a charge is used for the manufacturing of doped crystals. The ratio of components corresponded to $Pb(WO_4)_{1-x}(MoO_4)_x$ within x=0; 0,0125; 0,025; 0,05; 0,1; 1,0. Crystals with length of 60-70 mm and diameter of 14-16 mm were obtained. Samples for measuring were manufactured in the type of cylinder with the diameter and length of 12 mm; the end faces were polished. The samples have been annealed under 0,1-0,3 Pa vacuum at 900°C for 24 hours.

X-diffraction studies of crystals were made with the use of CuK_α-radiation and registration accurancy of reflection angles not worth than ±0,005°. The transmission spectras have been taken by ″Specord-M40″ in the nearest UV and in the visible regions (300-900 nm). The luminescence spectras have been registered in the range 350-700 nm under the excitation MoK_α-radiation and monochromator resolution of ±0,5 nm. The light yield of samples has been measured relatively comparison sample $Bi_4Ge_3O_{12}$ on line ^{137}Cs (The method is given in [7]). All measurements have been taken before and after annealing the samples at room temperature.

Results and discussion

The grown $Pb(WO_4)_{1-x}(MoO_4)_x$ crystals look like the same initial $PbWO_4$. They are transparent and have a yellow color of medium intensity. There is no visual admixture influence the color and brightness. During the vacuum annealing the behaviour of doped crystals is analogical $PbWO_4$; it means that samples are completely discolored. X-ray diffraction studies have also shown that molibden doping and annealing bring no new lines and do not change reflection intensity. In all cases the diffraction pictures corresponded to the known tetragonal β-phase of $PbWO_4$. At the same time together with the addition and increasing of molibden admixture content the diffraction pictures stably shows the increasing shift of lines in the region of big angles of reflection (for the composition x=0,1 shift 0,03°). With the annealing a shift of the same type takes place in the direction of smaller angles. Values of attendant changes of lattice constants and density are given in the table 1.

Table 1. Lattice constants and density of the crystals before/after annealing.

Composition	$\mathbf{a}_0$, Å	$\mathbf{c}_0$, Å	ρ, g/cm^3
$PbWO_4$	5,465 / 5,470	12,059/12,061	8,10 / 8,08
$Pb(WO_4)_{0,9}(MoO_4)_{0,1}$	5,461 / 5,465	12,056/12,059	7,94 / 7,93
$PbMoO_4$	5,424 / -*	12,047/ -	6,67 / -

*) Dates on annealing of $PbMoO_4$ crystals are not reported.

It's clear, that fixed character of structure changes depending on composition is a consequence of tungstem and molibden isomorphism in their compounds and accordingly a full mixture in the system of $PbWO_4$-$PbMoO_4$ [6]. At the same time the decreasing of lattice constants and density is as natural result with due regard for smaller values of pointed above characteristics for solutionable $PbMoO_4$ than for $PbWO_4$ matrix. A certain increase of cell dimension annealing may result of relaxation of compressive stresses. It is evident both in pure $PbWO_4$ and doped crystals. According to [8] the source of such stresses may be extrastoichiometric interstitial oxigen, caught by crystal during growth (or annealing) under the air.

In transmission spectras of crystals the addition of molibden is accompanied (within a small concentration of admixture) by a sharp shift of absorption edge to the long waves region and the subsequent more smooth shift as the content of admixture is increasing (Fig. 1a, table 2). This is followed by weakening and narrowing of the absorption band in the region 375-500 nm (λ_{max}=425 nm) usual in the coloured $PbWO_4$ crystals. Absorption coefficient in the band maximum is decreasing correlating with admixture quantity of molibden. Annealing both doped and pure $PbWO_4$ has practically no effect on the absorption edge position but eliminates the band almost completely (Fig. 1b, table 2). Absorption coefficient at λ=425 nm of the annealed samples do not differ greatly and have no correlations with composition.

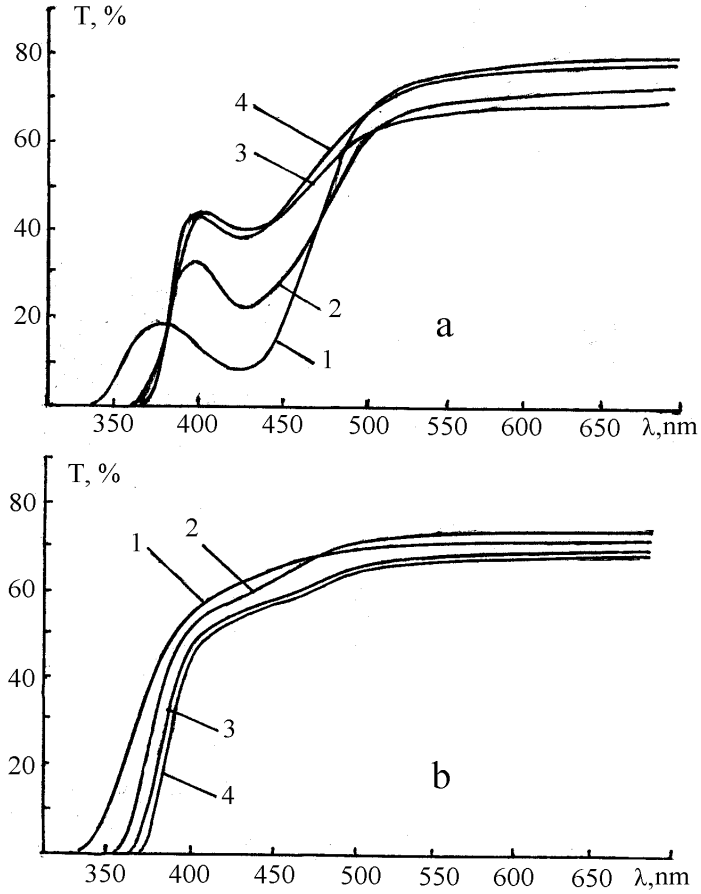

Fig. 1. Tranmission spectra of $Pb(WO_4)_{1-x}(MoO_4)_x$ crystals taken before (a) and after (b) annealing: 1 - x=0; 2 – 0,0125; 3 – 0,05; 4 – 0,1.

In x-ray luminescence spectras of $Pb(WO_4)_{1-x}(MoO_4)_x$ crystals with $x \leq 0{,}025$ there appears one band and with x=0,05 and 0,1 appears an additional band of 530 nm (Fig. 2a). No naturally determined link of spectra maximum position with the composition is traced before annealing (table 2). At the same time such dependence for the luminescence intensity is evident, it means sharp increasing within small contents of $(MoO_4)^{2-}$ ($x \cong 0{,}0125$) and decreasing within the next increasing of doping. Annealing of both pure and doped $PbWO_4$ crystals shifts their spectra peaks to the short wave region (Fig.2b, table 2). After the annealing a tendency of emission maximum shift in the green luminescence region within the increasing of molibden content is perfect traced. The band of 530 nm in spectras of corresponding samples is preserved. The intensity of luminescence after annealing is decreasing evidently but as it were before it the emission of crystals with admixture of molibden is higher than pure $PbWO_4$.

Doped crystals exceed $PbWO_4$ on light yield (table 2). The light yield dependence on molibden content corresponds to x-ray luminescence intensity. It is evident before and after the annealing. And what is more, the more increasing takes place within small quantities of admixture. Preliminary measuring of scintillation kinetics in the crystals $Pb(WO_4)_{1-x}(MoO_4)_x$ (x=0,0125 and 0,025; annealing) showed two time components: τ_1=10-14 ns (share 20-25%) and τ_2=50-70 ns (75-80%). For the initial $PbWO_4$ after the annealing the following was fixed: τ_1=2,0-2,2 ns (28%); τ_2=6,9-7,9 ns (48%) and τ_3=29-34 ns (24%).

Analizing the achieved results it is possible to note the following. Jumping type of absorption edge shift and sharp emission intensify within small contents of molibden essentially differs from the further with increasing of change doping of these characteristics. It testifies about its different behavour in $PbWO_4$ depending on admixture concentration. As a

reason of such difference it is possible to point the transfer from statistic division of molibden ions in $PbWO_4$ matrix to some its structural regulating. The appearence in spectras the luminescence of crystals beginning with compositions of **x**≅0,05 of the band 530 nm and corresponding the maximum of emission $PbMoO_4$ confirms the possibility of such phenomenon.

Table 2. Characteristics of transmission and x-ray luminescence spectras, light yield of crystals depending on composition before/after annealing.

X	λ_0, nm	k_{425nm}, cm^{-1}	λ_{max}, nm	I_{max}, per-units	**C,% BGO**
0	337,8/336,0	2,23/0,46	512/490	0,39/0,08	2,4/3,8
0,0125	362,6/363,0	1,65/0,42	509/493	0,85/0,168	4,6/12,1
0,025	363,9/364,2	1,54/0,51	510/500	0,76/0,167	4,1/8,3
0,05	366,5/366,0	0,86/0,48	506/500	0,72/0,155	3,0/8,1
0,10	369,0/369,0	0,81/0,49	512/502	0,42/0,158	4,5/6,3
1,00	396,8/ -	-	530/ -	0,0063/ -	-

x – is a content of $(MoO_4)^{2-}$; λ_0 – absorption edge position; k_{425nm} – is a coefficient of absorption within λ=425nm; λ_{max} - and I_{max} - is an x-ray luminescence lengthwave maximum and its intensity; C – is a light yield within E_γ=662 keV.

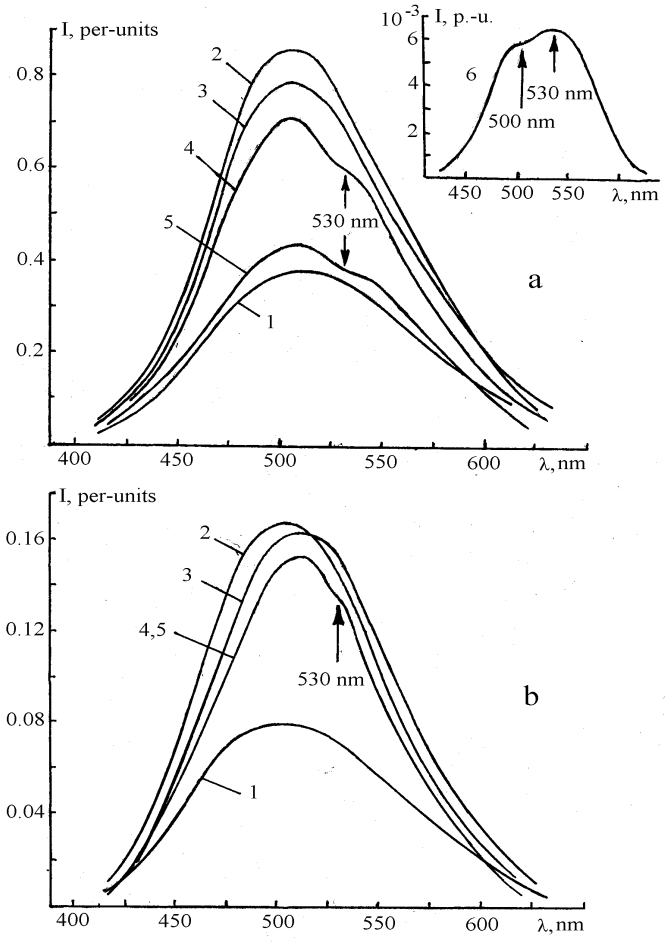

Fig. 2. X-ray luminescence spectra of crystals $Pb(WO_4)_{1-x}(MoO_4)_x$ taked before (a) and after (b) annealing: 1 – x=0; 2 – 0,0125; 3 – 0,025; 4 – 0,05; 5 – 0,10; 6 – $PbMoO_4$.

From comparison of luminescence spectras of $PbWO_4$ and $PbMoO_4$ (Fig. 2a, sp.1, 6) it is clear that the addition of molibden and the in- creasing of its content must be fol- lowed by the shift of spectra maxi- mum in green region and the uniform decreasing of its intensity. The first moment is really takes place (the most distinctly after an- nealing). The second is evident on- ly on the background of common essential increasing of emissiom yield. As the intensity of $PbMoO_4$ luminescence is much lower than $PbWO_4$ it is difficult to suppose the possibility of creation of additional centres of green luminescence in such a big quantity on the $(MoO_4)^{2-}$ groups, espessially in intervals of small concentrations ($\mathbf{x}\leq 0{,}025$). It is possible that small quantities of such centres appeares only within the contents of molibdate groups of $\mathbf{x}\geq 0{,}05$, and it is showed by the appearance of the band of 530 nm. Nealy the same character of change during the annealing of luminescence spectras of pure and doped crystals also confirm that small additions of molibden do not create centres of green light in some quantity differi from taking place in molibden-free $PbWO_4$.

Taking into considerations these reasons the explanation of achieved results doesn't look very discrepant on the base of presentations [5] about the role of admixtural molecular ions $(MoO_4)^{2-}$ in sheelite type of solid solutions $Me(WO_4)_{1-x}(MoO_4)_x$, as the intensification of excitation energy transfer from blue into green centres of emission. In our case it is a transfer between own blue and green centres of $PbWO_4$ matrix. Its competitive character and the possibility of two processes of excitation: direct and through the condition of competitive centre of blue luminescence [9], bring to redistribution of intensity between bands. Then, in limits of model of centres interaction [9], it is possible to imagine the intensification of the green emission of $PbWO_4$ as a result of creation on the base of additional anions $(MoO_4)^{2-}$ of additional "quick" chanels of transfer and increasing the energy share of excitational condition of blue centres to the transferring one to the green centres and lightening through its emission.

Conclusion

The autors consider, that the achieved results make some different idea about the admixture of molibden in $PbWO_4$, usually considering as nondesirable in this scintillator. It is evident, that molibden in definite concentrations can play the role of off-beat activator of own centres of green light $PbWO_4$. Probably it is provided with the way of crystals doping. The effect of intensification of $PbWO_4$ emission may be the decisive for some technique spheres of radiation and high energy particles registration .

In conclusion authors appreciate the help of Drs. Kozlov V.A. and Devitsyn E.G. (FIRAN, Moscow) during the scintillation measurings and useful discussion of achieved results.

References

1. P. Lecoq, Proc. Conf. Inorg. Scint. and their Appl., SCINT'95, Delft Netherlands, 1995, 52.
2. M. V. Korzhik, Proc. Conf. Inorg. Scint. and their Appl., SCINT'95, Delft, Netherlands, 1995, 241.
3. W. Van Loo, Phys. stat. sol. (a), **27** (1975) 565; **28** (1975) 227.
4. A. M. Gurvith, Introduction in physikal chemistry crystalline phosphors, High school, Moscov, 1971 (in Russian).
5. Sh. Effendiev et al., Sol. stat. phys., **36** (1994) 3171 (in Russian).
6. V. M. Nagiev et al., Sol. stat. phys., **24** (1982) 2872 (in Russian).
7. M. V. Belov et al., Preprint of Lebedev Physical Inst. Russian Acad. Sci., Moscov, 1995, №29.
8. B. I. Zadneprovski et al., Inorg. Mater., **35** (1999) 295.
9. A. N. Belski et al., Proc. of the Intern. Workshop on Tungstate Cryst., Rome, 1998, 115.

Optical properties of cadmium and zinc tungstate single crystals

V.N. Kolobanov[(1)], V.V. Mikhailin[(1)], I.N. Shpinkov[(1)], D.A. Spassky[(1)],
M. Kirm[(2)], G. Zimmerer[(2)] and V.N. Makhov[(3)],

[(1)]Synchrotron Radiation Laboratory, Moscow State University, 119899 Moscow, Russia
[(2)]II Institut fur Experimentalphysik der Universitat Hamburg, D-22761 Hamburg, Germany
[(3)]Lebedev Physical Institute, 117924 Moscow, Russia

Introduction

An interest to cadmium and zinc tungstate single crystals is due to their wide application in scintillation detectors, in particular, for X-ray tomography [1]. Both crystals belong to the same crystallographic type of monoclinic tungstates with the C^4_{2h} space group.

In the present paper the reflection and luminescence excitation spectra for $CdWO_4$ and $ZnWO_4$ single crystals have been studied in the photon energy range 3.5 – 30 eV. With the use of Kramers-Krönig relations the optical functions (the imaginary and the real part of the dielectric constant ε_1 ε_2, absorption coefficient α, the energy loss function $\mathrm{Im}(1/\varepsilon)$) of the crystals were calculated. The processes of electronic excitations multiplication (EEM) are discussed in the framework of diffusion model of near-surface losses.

Experimental

The measurements of reflection and excitation spectra have been performed at the SUPERLUMI setup with the use of synchrotron radiation (SR) from the DORIS storage ring at DESY (Hamburg, Germany) [2]. The measurements were carried out under ultrahigh vacuum conditions (10^{-9} torr) at both room temperature (RT) and 10 K (LHT). The incidence angle for SR was 17.5^0. The spectra of cadmium tungstate were measured for freshly cleaved surface of the crystal while those of zinc tungstate for the polished sample. The crystals were grown by the Czochralski method. During the procedure of treating the measured spectra the influence of scattered light and high orders of diffraction was taken into consideration. It should be mentioned that when making measurements of reflection spectra the orientation of polarization vector of SR with respect to the crystallographic axes of the crystals was not taken into account. As was shown recently [3], the polarized reflection spectra of tungstates have considerable differences in the fundamental absorption region of the crystals. This is just that factor which can account for the discrepancy of the spectra obtained for tungstates by different authors with the use of highly polarized SR [4].

Results and discussion

Reflection spectra and calculation of optical functions

The reflection and absorption spectra of cadmium tungstate and zinc tungstate crystals are presented in Fig.1. The absorption spectra were calculated from measured reflection spectra with the use of Kramers-Krönig relations. For the approximation of reflection spectra into the region of transparency of the crystals the data on refraction index were taken from [1]. In the high energy region the reflection coefficient was approximated as $R \sim \omega^{-4}$.

The first low-energy peak in the reflection spectrum of $CdWO_4$ is shifted with temperature from 4.30 eV at LHT to 4.20 eV at RT, what is the characteristic feature for the exciton peak at the fundamental absorption edge of the crystal. Apparently, exciton is created on the oxy-anion complex WO_6^{6-}, because both the top of the valence band and the bottom of the conduction band are formed mainly from the orbitals of WO_6^{6-} complex [5, 6].

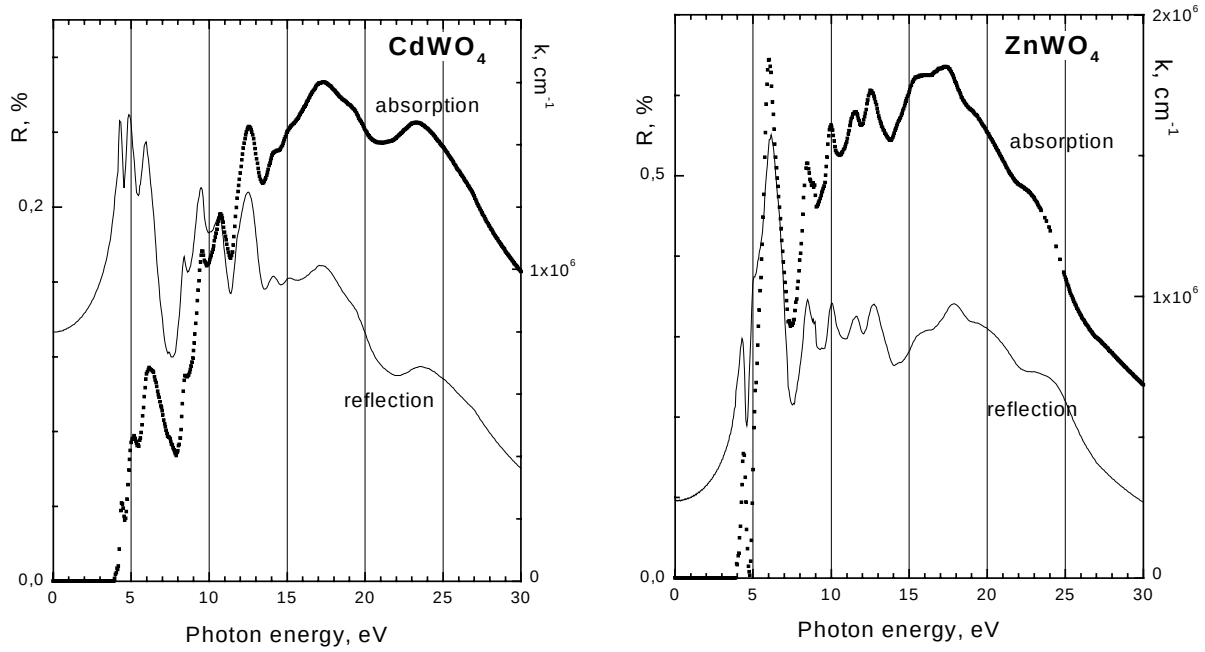

Fig1. Reflectivity (solid line) at 10K and calculated absorption spectra (dotted line) for $CdWO_4$ and $ZnWO_4$.

Table.1 Positions of reflection peaks (in eV) assigned to the same transitions in zinc and cadmium tungstate crystals.

	1	2	3	4	5	6	7	8	9	10	11
$ZnWO_4$	4.32	5.2	6.15	8.5	10.1	11.6	12.8	16	18	20	24.0
$CdWO_4$	4.3	4.9	5.95	8.4	9.5	10.7	12.5	15.1	17.3	19.2	23.6

The next peak at 5.15 eV corresponds to interband transitions and its energy position does not depend on temperature. The width of the bandgap for $CdWO_4$, estimated as the beginning of the rise of reflection coefficient after the excitonic peak, is E_g = 4.55 eV. Similar consideration for $ZnWO_4$ crystal gives the estimation of the bandgap for this crystal as being E_g = 4.65 eV.

The obvious similarity is observed in the structure of reflection spectra for these two crystals. It should be mentioned that the structure of reflection spectra for these crystals in the studied energy region is much more rich in peculiarities than that for calcium and lead tungstates [7, 8]. The difference can be due to different space symmetry group of crystals under consideration, mainly monoclinic-type structure (tungstanite) for $ZnWO_4$ and $CdWO_4$; tetragonal-type structure (scheelite) for $PbWO_4$ and $CaWO_4$. The calculations of relative contribution of atomic orbitals (AO) of central atom and of ligands to molecular orbitals (MO), and of the energy positions of MO for WO_6^{6-} and WO_4^{2-} - complexes were performed in [5, 6, 9]. The number of MO forming the valence band in the case of octahedral complex WO_6^{6-} will be higher than in the case of tetrahedral complex WO_4^{2-}. As a result the structure of MO for WO_6^{6-} - complex can become more rich than that for WO_4^{2-} - complex, that leads to more complicated structure of reflection and absorption spectra.

In accordance with data from [5, 6], the bottom of the valence band WO_6^{6-} is formed by $1a_{1g}$, $1e_g$, $1t_{1u}$, which consist mainly of s(σ) - orbitals of ligands. The remaining part of the valence band is formed mainly by - orbitals of ligands. The central atom contributes

only to $1e_g$, $2e_g$ and $1t_{2g}$ orbitals of valence band (13, 27 and 25 % respectively). The conduction band in the case of octahedral oxy-anion complex consists of $2t_{2g}$, $3e_g$, $4t_{1u}$ and $3a_{1g}$, which are formed mainly by of the central atom. Thus, the orbital $3a_{1g}$ is formed mainly (near 95-98%) by 6s W, and $4t_{1u}$ – by 6 W. MO at the bottom of conduction band $2t_{2g}$ and $3e_g$ consist of mainly (60-70 %) 5d states of W and the remaining part of 2p states of oxygen.

The cation Cd^{2+} has the outmost filled electronic shell $4d^{10}$, and Zn^{2+} $3d^{10}$. In unexcited state (configuration nd^{10}; n=3 for Zn^{2+} and n=4 for Cd^{2+}) these ions have the only energy term $^1S_0$. After the electron transition from the nd level into the excited state (configuration $nd^9(n+1)s$), the transitions from the ground term $^1S_0$ to terms $^1D_2$ and $^3D_{1,2,3}$ (the same for both ions) of excited configuration are possible in principle. The energies of these transitions are 10.36, 10.03, 9.84 and 9.68 eV for Zn^{2+}, and 11.03, 10.7, 10.22 and 9.98 eV for Cd^{2+} [10]. The transitions on the cation $^1S_0$ – $^1D_2$, $^3D_{1,2,3}$ are dipole-forbidden in accordance with the selection rules, and so the transitions with charge transfer from cation to anion have more probability. The contribution of cation electronic states into combined interband density of states (into the formation of energy bands) does not exceed 25 %. Taking into account the similarity of outermost electron shells for both cations, one should expect for these crystals the remarkable similarity of absorption (reflection) spectra, which are formed mainly by transitions in WO_6^{6-} complex.

Thus, the first group of peaks in reflection spectra at 4-14 eV includes anion exciton at the edge of fundamental absorption and interband transitions from 2p( ), 2 ( ) of oxygen and small fraction of d states of tungsten and of the cation in the valence band to $2t_{2g}$ and $3e_g$ orbitals forming the bottom of conduction band. The second group of reflection peaks at 15-25 eV is typical for both tungstanites and scheelites [3,7]. In accordance with the model of MO, the reflection peaks can be due to electronic transitions between MO a_{1g}, t_{1u} ($1a_1$, $1t_2$ in the case of tetrahedral complex) and the bottom of conduction band which consists of MO t_{2g}, e_g ($4t_2$, 2e – orbitals in the case of tetrahedral complex). Orbitals a_{1g}, t_{1u} ($1a_1$, $1t_2$) form the bottom of the valence band and consist mainly of 2s(σ) levels of oxygen. The transitions from these orbitals form the most high-energy absorption peaks, in particular the peak at 23.5 eV.

Electronic excitations multiplication

The luminescence of cadmium and zinc tungstates is characterized by intense wide- band emission peaked at 480-490 nm [11] which is typical for tungstate crystals. In Fig.2 the luminescence excitation spectra measured for $CdWO_4$ (λ_{emis} = 480 nm) and $ZnWO_4$ (λ_{emis} = 490 nm) at 10 K are presented. The first peak at 4.2 eV in the spectra of $CdWO_4$ and $ZnWO_4$ corresponds to the sharp increase of luminescence intensity in the region of the Urbach tail of fundamental absorption, when incident radiation is completely absorbed in the volume of the crystal. Further increase of absorption coefficient leads to the decrease of the depth of the light penetration into the crystal and accordingly to the rise of the non-radiative decay of electronic excitations at the surface defects. As a result, maxima in absorption (reflection) spectra of $CdWO_4$ and $ZnWO_4$ manifest as the dips in luminescence excitation spectra.

In the energy region higher than 11 eV the increase of luminescence yield is observed for both crystals, which can be related to the effect of EEM. However two more effects can give the considerable contribution to the rise of luminescence yield: the decrease of near-surface losses due to the increase of the light penetration depth, and increase of the fraction of absorbed light caused by the decrease of reflection coefficient. For the estimation of the role of EEM in forming the shape of excitation spectra it is necessary to take into account the influence of several factors leading to changes of luminescence quantum yield.

The fraction of the light absorbed by the crystal as well as the near-surface losses factor can be taken into account in accordance with simple diffusion theory [12]. The luminescence excitation spectrum can be given by:

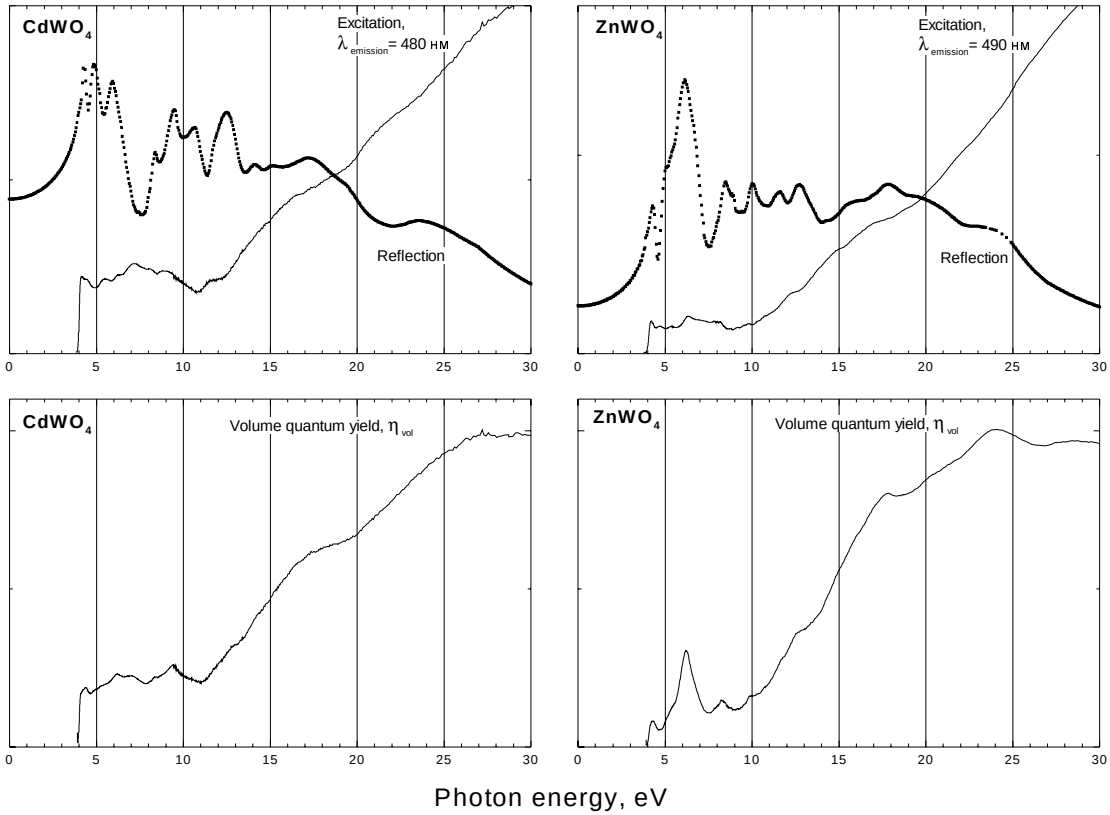

Fig.2. Luminescence excitation spectra and reflection spectra (above), volume quantum yield spectra (below) calculated by formula (1) for $CdWO_4$ and $ZnWO_4$.

$$\eta_{экс}(h\nu) = \frac{(1 - R(h\nu)) * (1 - \exp(-K(h\nu) * d)}{1 + K(h\nu) * L} * \eta_{vol} \qquad (1)$$

where η_{vol} is volume quantum yield, R reflection coefficient, K absorption coefficient, L diffusion length, and d crystal thickness. The diffusion length parameter depends on the value of lifetime τ of EE responsible for the emission $L=(D\tau)^{1/2}$, D – diffusion coefficient.

The parameter η_{vol} is luminescence quantum yield, which is determined by volume processes. This parameter contains information on EEM as well as on migration losses, which determine mainly the luminescence quantum yield in the region between the edge of fundamental absorption and the threshold of EEM. In Fig.2 the dependence $\eta_{vol}(h\nu)$ is presented which was calculated for $CdWO_4$ by formula (1) for L = 50 Å. In the energy region 4-11 eV the volume quantum yield fluctuates near the constant value that is characteristic for the recombination luminescence type in case of the lack of concurring processes [12]. The fluctuations can be due to migration losses when transferring energy of excitation to luminescence centers, to changes with energy of electronic excitations diffusion length, and to some inaccuracy of calculations by Kramers-Krönig relations.

In the energy region $h\nu$ >11 eV the rise of $\eta_{vol}(h\nu)$ is seen for $CdWO_4$ which is caused by the beginning of EEM. At further increase of excitation energy the electrons from the deep levels of the valence band begin to participate in the EEM processes. The increase of $\eta_{vol}(h\nu)$ exhausts at excitation energy corresponding to the participation in the EEM processes of electrons from the bottom of the valence band. Therefore the stop of the increase of $\eta_{vol}(h\nu)$ at 17 eV can be considered as the finish of electron-hole pairs doubling in the $CdWO_4$ crystal.

Further rise of the volume luminescence quantum yield, starting from 19-20 eV, is due to the next step of the multiplication of electron-hole pairs under the excitation of one photoelectron. The increase of $\eta_{vol}(h\nu)$ stops again at 25-26 eV in accordance with the same mechanism described before. The difference between photon energies corresponding to the beginning and to the end of the increase of the volume quantum yield can be used for the estimation of the valance band width. From the data on doubling and tripling of electronic excitations the valance band width of $CdWO_4$ can be estimated as being not higher than 5-6 eV.

Conclusions

As a result of studies performed for $CdWO_4$ and $ZnWO_4$ crystals it has been established the qualitative similarity of the structure and energy positions of the peaks in reflection spectra of studied crystals in the energy region 4-30 eV. The main structure in absorption (reflection) spectra of $CdWO_4$ and $ZnWO_4$ crystals in the energy region 4-30 eV corresponds to transitions with the participation of WO_6^{6-} - complex. The first peak in reflection spectra of $CdWO_4$ and $ZnWO_4$ at 4.3 eV corresponds to the creation of exciton on the oxy-anion complex. The width of the bandgap has been determined for cadmium tungstate as E_g = 4.55 eV and for zinc tungstate E_g = 4.65 eV. The estimation of the valance band width was made for both crystals: $E_v \leq 6$. For both studied crystals the effect of EEM is observed at photon energies $h\nu \geq 11$ eV.

Acknowledgements

The support of grants Deutsche Forschungsgemeinschaft DFG No 436 RUS 113/437, RFBR-DFG 96-02-00207G, RFBR 97-02-17414, Integration Federal Program 2.1-535 is gratefully acknowledged.

References

1. Victorov L.V., Skorikov V.M., Zhukov V. ., Shulgin B.V. Inorganic materials (in Russian) Vol.27 10 (1991) . 2005
2. Zimmerer G. Nuclear Instruments and Methods in Physics Research A 308 (1991) p.178
3. Kolobanov V., Kamenskikh I., Mikhailin V., Shpinkov I., Spassky D., Zadneprovsky B., Patkin L., Kirm M. and Zimmerer G., HASYLAB Annual Report 1999, part I, p.301.
4. Kolobanov V.N., Mikhailin V.V., Spassky D.A. Preprint, MSU 1998, 1
5. van Oosterhout A.B., The Journal of Chemical Physics, vol.67, 6 (1977) p.2412
6. Zhukov V.P., Gubanov V.A. and Anisimov V.I., Optics and spectroscopy (in Russian), vol.46, 1 (1979) p.85
7. Kolobanov V.N., Kirm M., Makhov V.N., Mikhailin V.V., Spassky D.A., Vielhauer S., Zimmerer G., HASYLAB Annual Report 1998, Part I, p.371.
8. Belsky A.N., Kamenskikh I.A., Kolobanov V.N, Mikhailin V.V., Orekhanov P.A., Shpinkov I.N., Vasil'ev A.N., Proceedings of the International Workshop on Tungstate Crystals, Roma – October 12-14, 1998 p.115
9. Kebabcioglu R., Muller A., Chem. Phys. Letters, vol.8, 1 (1974) p.59
10. Moore C.E. 1950 Atomic Energy Levels NSRDS-NBS 35, p. 61, 128
11. Ovechkin A.E., Ryzhikov V.D., Tamulaitis G. and Zukauskas A., Phys. Stat. Sol. (a) **103** (1987) p.285
12. Vasil'ev A.N., Mikhailin V.V. Introduction in solid state spectroscopy, Moscow University Press, Moscow 1987

Influence of admixture defects on scintillation and optical characteristics of cadmium tungstate single crystals

L.Nagornaya, I.Tupitsyna, A.Apanasenko, O.Zelenskaya

STC RI of Concern "Institute for single crystals" NAS of Ukraine, 60 Lenin Ave., 310001, Kharkov, Ukraine

Abstract. In this paper, effects of admixtures from groups I-V were studied on optical and spectrometric characteristics, as well as on afterglow, of cadmium tungstate crystals. It has been shown that the light output of $CdWO_4$ crystals containing isovalent dopants, e.g., Ca, Ba, Zn, etc., is, in fact, at the same level and even higher than that of the undoped crystals. Admixtures, which affect scintillation parameters the most significantly, are admixtures with non-compensated charge. The light output for such crystals is reduced up to 5 times . Such crystals become colored, and afterglow increases by more than two orders of magnitude.

Keywords: cadmium tungstate, admixture defects**,** scintillation characteristics

Introduction

Highly efficient scintillators based on cadmium tungstate ($CdWO_4$) single crystals are widely used in computer X-ray tomography, radiation monitoring devices and spectrometric instruments for detection of ionizing radiation. This makes preparation of $CdWO_4$ (CWO) crystals with high scintillation characteristics an important problem. It is known, that admixtures can significantly affect properties of CWO crystals[1-5, 8]. In this paper, effects of admixtures from groups I-V were studied on optical and spectrometric characteristics, as well as on afterglow, of cadmium tungstate crystals.

Experimental

The investigated crystals were grown by the Czochralski method using platinum crucibles with high-frequency heating in oxygen-containing atmosphere. The dopant ions were entered into a melt in form of oxides in an amount $10^{-4} \div 10^{-1}$ % mass. The dopant concentration in the crystals was evaluated by X-ray fluorescence. The samples were shaped as cylinders with dimension ∅15×15 mm ^{3} and ∅15×1 mm ^{3} , their surfaces being polished. In this paper, we studied optical transmittance, X-ray luminescence (XRL), thermally stimulated luminescence (TSL), thermally stimulated conductivity (TSC) and scintillation characteristics, as well as on afterglow of cadmium tungstate crystals containing admixtures from I-V groups.

The transmission spectra were measured by a Hitachi-330 spectrophotometer. XRL, TSL and TSC were measured in the temperature range between 85 and 350 K in the process of cooling or heating a sample by using stationary or pulsed 200-keV X-ray radiation (a RUP-200-005 and an MIRA-2D X-ray generator, respectively). The heating rate during TSL measurements was 0.2 K/c. The light output was measured under excitation by a Cs-137 source ($E\gamma$ =662 keV), using photomultiplier FEU-110, with an integration constant of the recording system of 12.0 mcs.

Results and discussion

Scintillation characteristics and afterglow

Table 1 shows the values of light output and energy resolution of CWO crystal samples measured under irradiation with Cs-137 (662 keV), as well as afterglow.

Table 1. Light output and afterglow of CWO single crystals with admixture defects .

N	Impurities	Quantity in malt, mass. %	Light yield , %	Energy resolution, %	Afterglow 20 ms after excitation ,%
1.	undoped		100	9.5	<0.01÷0.02
2.	CdO	10^{-1}	98	10.0	-
3.	Li	$2,5\times10^{-2}$	102	10.0	<0,02
4.	Li	$2,5\times10^{-1}$	95	11.5	<0,02
5.	Na	1×10^{-3}	106	10.0	<0,02
6.	Na	1×10^{-2}	99	12.0	<0,02
7.	Ag	5×10^{-2}	49	27.3	<0,02
8.	Ag	5×10^{-3}	61	28.5	<0,02
9.	Ag	5×10^{-4}	89	14.0	<0,02
10.	K	5×10^{-2}	49	28.5	<0,02
11.	Mg	2×10^{-2}	94	13.2	0.2
12.	Ba	5×10^{-2}	102	10.8	<0,02
13.	Sr	5×10^{-2}	104	10.0	<0.02
14.	Ca	1×10^{-1}	101	10.3	<0,02
15.	Zn	1×10^{-1}	100	10.7	<0,02
16.	Y	3×10^{-2}	20	39.4	0,6
17.	Ce	5×10^{-2}	15	-	0,2
18.	Nb	3×10^{-2}	8	20.5	0,1
19.	Nb	3×10^{-3}	45	13.0	0,05
20.	Sm	1×10^{-1}	65	31.4	1.2
21.	Zr	3×10^{-3}	98	11.4	0.6
22.	Hf	3×10^{-2}	47	25.6	0,05
23.	Hf	3×10^{-3}	90	15.3	<0,02
24.	Hf	3×10^{-4}	90	13.1	<0,02
25.	Pb	2×10^{-3}	78	14.0	<0,02
26.	Pb	2×10^{-2}	77	22.0	<0,02
27.	Pb	2×10^{-1}	64	28.5	<0,02
28.	Cr	5×10^{-3}	39	-	<0,02
29.	Cr	2.5×10^{-2}	20	-	<0,02
30.	Mo	5×10^{-2}	38	18.8	0,05
31.	Mo	5×10^{-1}	35	-	0,1
32.	Ni	2×10^{-3}	100	14.4	<0,02
33.	Ni	2×10^{-2}	61	21.1	<0,02
34.	Ta	3×10^{-2}	74	13.5	<0,02
35.	Bi	$2,5\times10^{-1}$	48	15,2	1.8
36.	Bi	$2,5\times10^{-2}$	60	30.9	0,6
37.	Bi/6Li	$2,5\times10^{-2}$	95	10.6	0.2
38.	Gd	5×10^{-2}	49	12.8	1.2
39.	Fe	5×10^{-4}	98	17.0	0.03
40.	Fe/55Li	5×10^{-4}	99	11.0	0.03
41.	Fe	5×10^{-3}	41	34.2	-
42.	Fe/5Li	5×10^{-3}	41	32.4	-
43.	Ho	$2,5\times10^{-3}$	45	30.7	0.6
44.	Ho (after annealing)	$2,5\times10^{-3}$	40	25.4	0.2
45.	Eu	$2,5\times10^{-3}$	51	20.8	0,8
46.	Eu (after annealing)	$2,5\times10^{-3}$	45	17.3	0.3

It has been shown that the light output of CWO crystals containing isovalent dopants, e.g., Ca, Ba, Zn, etc., is, in fact, at the same level and even higher than that of the undoped crystals. These admixtures do not significantly affect afterglow and transmittance as well. The univalent impurities of the type Me^{+}= Li, Na do not produce any significant effect on the

scintillation characteristics. It has been established that the influence of Me^{3+} dopants upon the light yield is the strongest (light yield becomes 2-3 times lower) at concentrations of 5×10^{-3} - 5×10^{-2} % mass. This is related to the formation of color centers, which are intricate complexes including the dopant atom and intrinsic defects which compensate the surplus positive charge. Admixtures of Mg, Zr and, especially, trivalent Y, Ce, Sm, Bi, Ho, Eu worsen the afterglow, which is related to the formation of trapping centers. Thus, for Bi-containing crystals with concentrations above 10^{-1}% mass. the afterglow can reach 2-3%. Introduction of Li as a compensator of the excess charged Bi^{3+} and annealing in the oxygen-containing atmosphere of crystals containing Ho and Eu improve the afterglow and light output by 2 times and more.

Basing on our studies, requirements have been formulated to the purity of the initial raw material. The CWO samples for tomography had light output of ~40% with respect to NaI(Tl) and afterglow of <0.01% in 20 ms after excitation; with samples made for spectrometry, energy resolution was <10% over Cs-137 line (662 keV). All these samples had improved radiation stability.

It is known, that the change of afterglow and light output connected with appropriate change of optical transmittance and TSL of the samples. Therefore we performed the investigations of these characteristics of CWO crystals

Optical transmittance

Studies of transmission spectra of CWO crystals (nominally pure and doped with various admixtures) have shown that introduction of dopant leads to a decrease in optical transparency with higher dopant concentration in all the spectrum. Besides this, in crystals containing Na, Li, Pb, Ca, Fe, Zn, Ta, Ag, Sr, Ba, Bi the intensity of the band observed in nominally pure CWO in the region of 350-440 nm is enhanced . In samples containing Ag a band at 400-620 nm appears, and the samples are of pink color, with Cr band is at 355-700 nm (red color), with Ce - 255-620 nm, brown coloration. For crystals doped with Mn and the absorption edge is significantly shifted towards the long-wavelength region (~ 380 nm). Introduction of Mg, Bi, Hf gives rise to strong absorption bands with maximum at 345, 360, 340 nm, respectively, and half-width ~20 nm. Y, Gd colors CWO samples into grayish-blue, and in absorption spectra a strong broad band is observed in the region of 360-800 nm. Absorption spectrum of samples containing Sm has a characteristic structure with absorption bands at 365, 380, 392, 408, 420, 455, 465, 472 nm, while samples containing Ni display bands at 480 and 520 nm. The presence of Ho is reflected in optical absorption spectra as narrow bands in the region of 362 nm, 450-465 nm, 540-550 nm. It is impossible to avoid the resence the impurities in CWO crystals. So we carried out the experiments aimed at increasing the transparency of doped CWO crystals. Thus, for example, introduction of Li compensating the

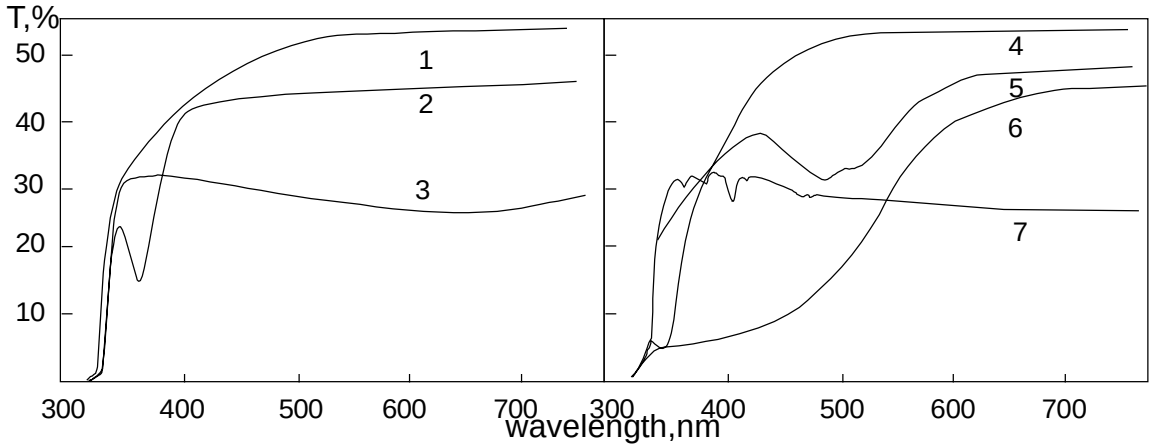

Fig.1. Transmission curves of CWO crystals: 1-nominally pure, 2- doped with Bi, 3-doped with Gd, 4-doped with Mg, 5-doped with Ni, 6-doped with Ce, 7-doped with Sm

excess charge of i^{3+} and Fe^{3+} leads to higher transparency. Besides this, annealing in oxygen-containing atmosphere of crystals doped with trivalent admixtures, which have grayish-blue color, allows to discolor these samples and to increase their light output.

Thermally stimulated luminescence

TSL glow curves of nominally pure crystals and of those doped with Ba and Pb have weak peaks in the region of 100÷250 . For crystals doped with Na and Y, the intensity of low-temperature peaks is increased. A noticeable increase in the accumulated light is observed for crystals doped with Mo, Bi, Sm, Ho, Nd, Eu (Fig.2). TSL spectrum of CWO: samples includes two bands with maxima at 460-500 and 600-700 nm, the contribution from which is different for different peaks. TSL of the CWO: sample is composed of two peaks with different spectral composition: $_{max}$=130-140 (510-515 nm) and $_{max}$=230 (540 nm). After annealing in oxygen-containing atmosphere the intensity of the low temperature TSL peak is decreasing.

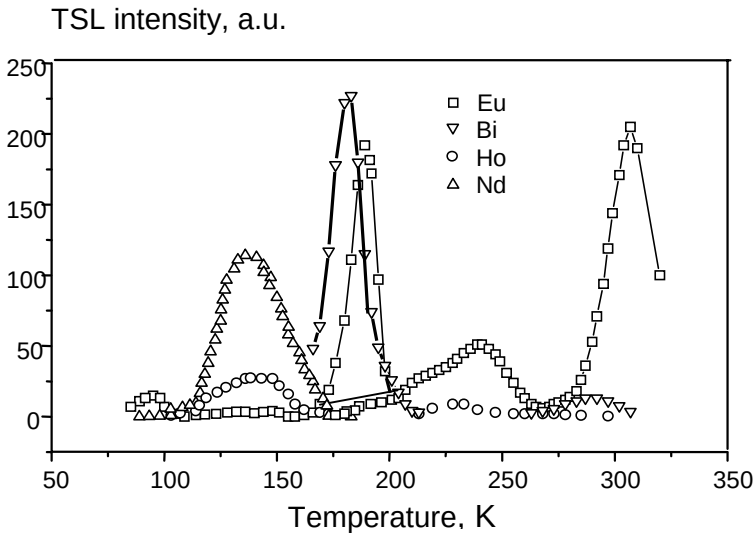

Fig.2. Curves of the TSL of CWO crystals doped with Eu, Bi , Ho , Nd

Conductivity of the non-annealed sample rises with temperature exponentially at >130 . The annealing removes this effect.

Studies of "red" (600-700 nm) component of TSL and TSC of Fe-doped crystals have shown that when concentration of this dopant is increased up to 10^{-3} % mass., intensity of TSL and TSC falls to the noise level (Fig. 3.). Such behavior is not typical for other dopants studied, when peak intensity increased with higher dopant concentration. Thus, increase of the response time in Fe-doped CWO crystals cannot be related to light accumulation.

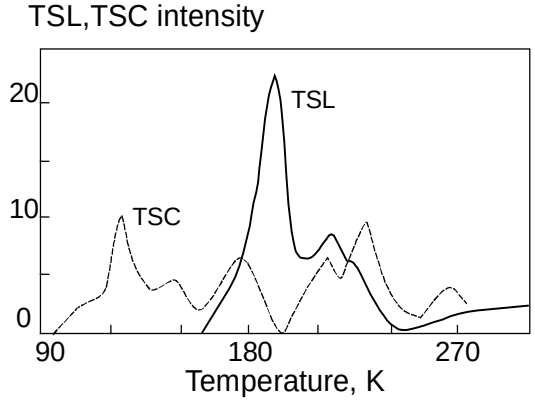

Fig.3. Curves of the TSL and TSC (λ>600 nm) of CWO crystals doped with Fe (5×10^{-4} % mass)

Conclusions

It has been established that most isovalent dopants do not lead to the formation of color centers that lower the light output and enhance the afterglow. However, some isovalent dopants favor the formation of radiation defects under X-ray irradiation, which leads to a decrease in light output.

It is shown that heterovalent dopants with non-compensated charge strongly decrease the light output and increase afterglow of CWO crystals. However, these dopants do not decrease the radiation stability, and in certain cases the radiation stability is even improved.

Basing on our studies, requirements have been formulated to the purity of the initial raw material. The CWO samples for tomography had light output of ~40% with respect to NaI(Tl) and afterglow of <0.01% in 20 ms after excitation; with samples made for spectrometry, energy resolution was <10% over Cs-137 line (662 keV). All these samples had improved radiation stability.

Acknowledgements

The authors are very grateful to Prof. M. Pashkovsky for helpful discussion and Z. Moroz for help in the growth of the crystals.

References

1. M.Batenchuk, Z.Moroz, L.Limarenko, et.al."Impurities role in the formation of optical-luminescent and scintillation properties of tungstate single crystals", International Workshop on Tungstate Crystals, Roma, October 12-14, 1998
2. M.Pashkovsky, L.Limarenko, A.Nosenko, et.al., Visnik Lvivskogo Universiteta, **3(11) (**1968) 48.
3. L.Limarenko, M.Pashkovsky, Phizichna electronika, **V.1 No1** (1969),82
4. S.Nedelko, M. Krisuk, A.Opanasenko, et.al, Jurnal prikladnoi spectroskopii, **V.65 No1** (1997) 55
5. I.Kushnirenko, Z.Moroz, L.Nagornaya, et.al.,Ukrainskii phizicheskii jurnal, **37** (1992) 976
6. D.R.Kinloch,W.Novak, P.Raby et.al. "New Developments in Cadmium Tungstate", Proseeding IEEE93, San Francisco, October 30-November1993,**V.1,** P.661-663
7. Melcher C.L.,IEEE Transaction on Nuclear Science, **V.63 No1**(1989) 1188
8. M.Kobayashi, M.Ishii, Y.Usuki, NIM **A349** (1994) 407

Influence of molybdenum ions impurities on the optical properties of lead tungstate single crystals

S.G. Nedilko, O.V. Chukova, P.I. Korenjuk, M.S. Nedilko,
Z.T. Moroz*, M.V. Pashkovskyi*

Faculty of Physics, Taras Shevchenko Kyiv University
6, acad. Glushkova Ave., 252650, Kyiv, UKRAINE
** Faculty of Physics, Ivan Franko Lviv State University, Lviv, UKRAINE*

Abstract. Absorption, x-ray and photoluminescence, excitation and Raman spectra of lead tungstate single crystals synthesised with the adding of MoO_3 oxide impurity to the bench were carried out. The additional "green" emission of these crystals was shown to caused by radiation transitions in MoO_4^{2-} molecular anions formed on the place of tungstate groups of lead tugstate crystals. The conclusion was made, that "green" emission of "pure" lead tugstate crystals is not concerned with a presence of uncontrolled impurities of molybdate molecular groups.

Keywords: scintillation, lead, tungstate, crystal, doped, molybdenum

Inroduction

Investigation of $PbWO_4$ (PWO) lead tungstate single crystals doped with various impurities draws great attention in the last years. Study of such impure crystals have the double aim. First, it is a task to change both mechanical and spectral-luminescent characteristics of these crystals in the preferable direction, second, it is attempting to solve by such a way question about nature of own luminescence of PWO crystals [1-5]. In particularly, molybdenum ions (Mo) are used as such an impurity [6-9]. Investigation of PWO crystals doped with Mo ions impurities is also important because accordingly to the one of hypotheses the Mo ions oxide groups such as Mo $_4^{2-}$ or Mo $_4^{3-}$ are responsible for the exhibition of the "green" luminescence of PWO crystals. But, there are not enough available experimental and theoretical data yet to motivate structure of the centers of own and impurity emission of PWO-Mo crystals. This work is one more step on the way of solving this problem.

Experiment

Photoluminescence (PL) and excitation spectra were studied at the equipment included the registering -12 and excitation M -4 double monochromators. Raman scattering was investigated using triple monochromator Coderg T-800. X-rays spectra and kinetic were obtained by Dr. A.S.Voloshinovskyi, Lviv State University.

Crystals were grown by Chokhralsky's method in the platinum crucibles under inductive heating in the oxygen atmosphere and pressure 1 atm. The bench for synthesis were mixture of oxides in stoichiometric relationship. Content of ironlike impurities in PbO and WO_3 trade oxides did not exceed 10^{-4} --10^{-3} mas. %. "Pure", not specially doped, PWO crystals were boundary representative of series of crystals obtained from the bench with content of Mo $_3$ oxide varied in = 10^{-4} -- 10^{-1} mas. % region. Samples for investigation were rectangle parallelepiped with the dimensions 10 10 5 mm.

Experimental results

Contribution of the «green» component of emission band with peak position $\lambda_m \sim 490$ -- 520 nm increases in the x-ray luminescence (XRL) spectra respectively to increasing of Mo $_3$

content in the bench. This band dominates in the XRL spectra for both stationary and pulse excitation for crystals with the $\geq 5 \cdot 10^{-2}$ mas. % (see Fig.1 and also [9]). The λ_m for momentary XRL spectra at room temperature change from 489 to 492 nm with t_d delay time increasing from 20 ns to 10 μs (Fig.1, curve 1, 3). XRL spectra obtained at stationary excitation exhibit the further shift of λ_m to the long wave length region, especially at the temperature decreasing from room to 77 K, when the λ_m = 516 nm (Fig.1, curve 5). The XRL decay curve can be divided on the beginning region with $\tau \cong 5$ ns and region of slow decay with $\tau \cong 2{,}7$ μs (Fig.1, curve 1).

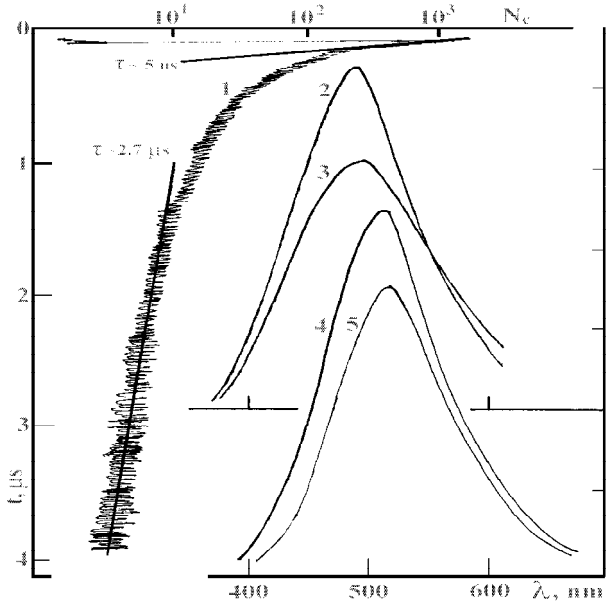

Fig. 1. Decay curve (1) and XRL spectra (2-5) of PWO-Mo crystal ($C=5 \cdot 10^{-2}$ mas. %) at the pulse (2, 3) and stationary excitation (4, 5). T = 300 (1-4) and 77 K (5); t_d = 20 ns (2) and 10 μs (3)

The PL spectra of PWO-Mo crystals are the same. PL is excited in the broad asymmetric band with the maximum λ_m^{ex} = 340 nm (Fig. 2a). Two short wave length components in the 350 -- 460 and 440 -- 520 nm regions superimposed on this PL band at the short wave length excitation (λ_m^{ex} = 297 nm) that leads increasing of the short wave length wing of emission spectra. (Arrows on Fig.2 show excitation and registration wave length value at the recording of PL and excitation spectra respectively.) Decay of «green» PL at λ^{ex} = 337,1 nm excitation (practically in maximum of excitation band) is described by exponent with $\tau \cong$ 65 ns at room temperature and $\tau \cong$ 16,0 μs at 77 K.

Discussion

There is a possibility to discuss the noted data on basis of its comparison with the spectral and kinetics properties of "pure" PWO crystals synthesized from initial compounds of the same bench as for PWO-Mo crystals. One can see, the "green" PL (λ_m = 520 nm) of "pure" PWO crystals is excited in the 275 – 350 nm band with λ_m^{ex} = 316 nm and their "blue" PL in the 265 – 305 nm band with λ_m^{ex} = 297 nm (Fig. 2b). Thus, "green" emission of of PWO-Mo crystals is similar to "green" band of "pure" PWO crystals only by position of emission band. These bands are excited in the different regions.

The "green" emission of PWO and PWO-Mo crystals are different also by decay time at the both photo and x-ray excitation. So, the "green" PL of PWO crystals decays with $\tau \cong$ 20 ns at room temperature and with $\tau \cong$ 6,0 μs at = 77 (excitation λ^{ex} = 337,1 nm). XRL of PWO crystals (integral spectral registration) has $\tau \cong$ 4,5 -- 20 ns and $\tau \cong$ 1,0 μs at room temperature and = 77 respectively [7]. Therefore, the "green" emission of PWO-Mo crystals decay slower than "blue-green" own luminescence of PWO matrix, that also is a cause of the long wave length shifting of time resolved XRL spectra (Fig. 1). Changing of shape of PL spectra dependently on λ^{ex} also shows that own "blue-green" emission of PWO matrix exhibits in the short wave length region of luminescence spectra of PWO-Mo crystals (Fig. 2a). Obviously, the initial region of decay curve of XRL with $\tau \cong$ 5 ns (Fig. 1) is responsible to the decay of this emission. The "green" XRL of PWO-Mo crystals decays with

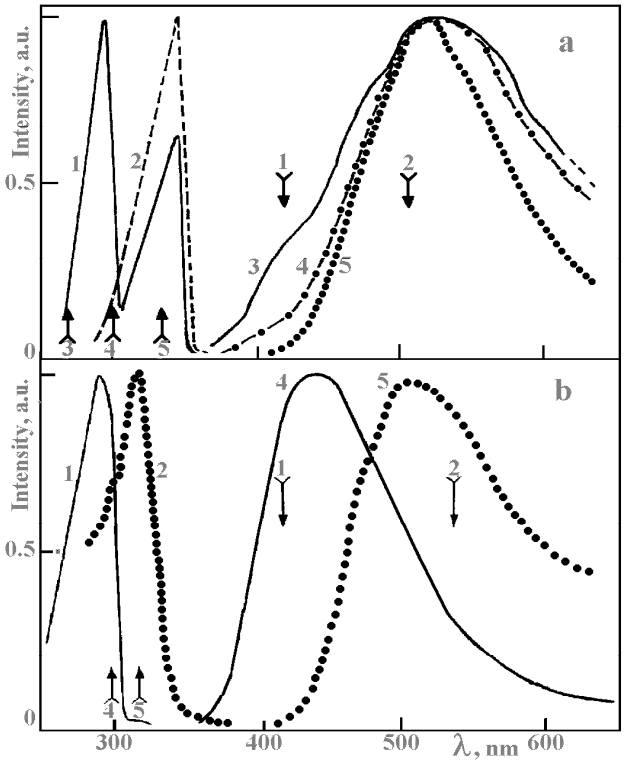

Fig. 2. Excitation spectra (1, 2) and PL spectra (3-5) of PWO-Mo (a) and PWO crystals(б); T = 4,2 K

$\tau \cong 2{,}7$ μs. Thus, we have to do conclusion about different origin of the"green" emission in the cases of PWO and PWO-Mo crystals.

Intensity of the "green" luminescence of PWO-Mo crystals is proportional to the Mo ions content, then it must be connected with the centers formed on the basis of Mo^{6+} ions. Placement of these ions on the W^{6+} lattice's sites is the most probable, because they have equal charges and near ion radii. The nearest neighborhood of M^{6+} ion in the lattice is four oxygen ions, thus, really, the Mo $_4^{2-}$ molecular group is formed when the Mo^{6+} ion takes W^{6+} place. Formation of such a group have no obstructions from the crystallochemical point of view, because structures of lead tungstates and lead molybdates crystal lattices also are identical. Therefore, the "green" luminescence of PWO-Mo crystals is connected with Mo $_4^{2-}$ molecular anion (MA). This conclusion agrees with the similarity of spectral and kinetic parameters of described here emission to the characteristics of compounds, luminescence centers of which are formed on the basis of Mo $_4^{2-}$ M : $PbMoO_4$ crystals [10-12], Cs_2SO_4 crystals with Mo $_4^{2-}$ impurities [13], alkali halide crystals (AHC) with Mo $_4^{2-}$ impurities [14]. Mentioned above affirmation also agrees with the results of Raman investigations.

We had established, that Raman spectra of PWO-Mo crystals contain lines with peak positions 869 and 738 m^{-1}, intensities of which are proportional to both the Mo $_3$ oxide concentration in the bench and intensity of the "green" luminescence. These lines obviously are exhibitions of ν_1 and ν_3 modes of Mo $_4^{2-}$ anions. (Frequencies of the relevant inner modes of Mo $_4^{2-}$ M are equal 869 and 766 and 743 m^{-1} [15].) Thus, Mo impurity is really included in the PWO lattice as a Mo^{6+} ion that forms together with the nearest oxygen ions the Mo $_4^{2-}$ molecular group. The last is a core of emission center.

Are the excitation of "green" luminescence as well as absorption edge caused by the radiation transitions only in the Mo $_4^{2-}$ M or no? The further analysis shows that likely no. Really, absorption of hydrated Mo $_4^{2-}$ aqua ion is characterized by two bands with maximums positions ν_m (in cm^{-1}) and absorption coefficients in the band maximum k_m (in l/mol·cm) are 43500, 6600 and 48000, 12200 for long wave length and short wave length bands respectively (Fig. 3). Absorption spectra of impurity Mo $_4^{2-}$ ions in Cs_2SO_4 crystals, where Mo $_4^{2-}$ ion replaces SO_4^{2-} sulphate group have the same shape and band positions (Fig. 3 [13]).

Position symmetry of anion group in the Cs_2SO_4 crystal is $_s$, that leads removal of degeneration took place for tetrahedral Mo $_4^{2-}$ ion in an aqua. But, connected with the symmetry decreasing splitting of the electron energy levels does not lead radical changes in the absorption of Mo $_4^{2-}$ group (Fig. 3). Noted sentence is also correct for the case of Mo $_4^{2-}$ MA impurity in the AHC, although in AHC MA undergo more distinctive deformation as for case of their placement in Cs_2SO_4 crystals. This is confirmed by Raman data concerning inner modes of Mo $_4^{2-}$ group. Really, tetrahedral MA of X $_4^{2-}$ type have 9 inner modes of $\nu_1(\ _1)$,

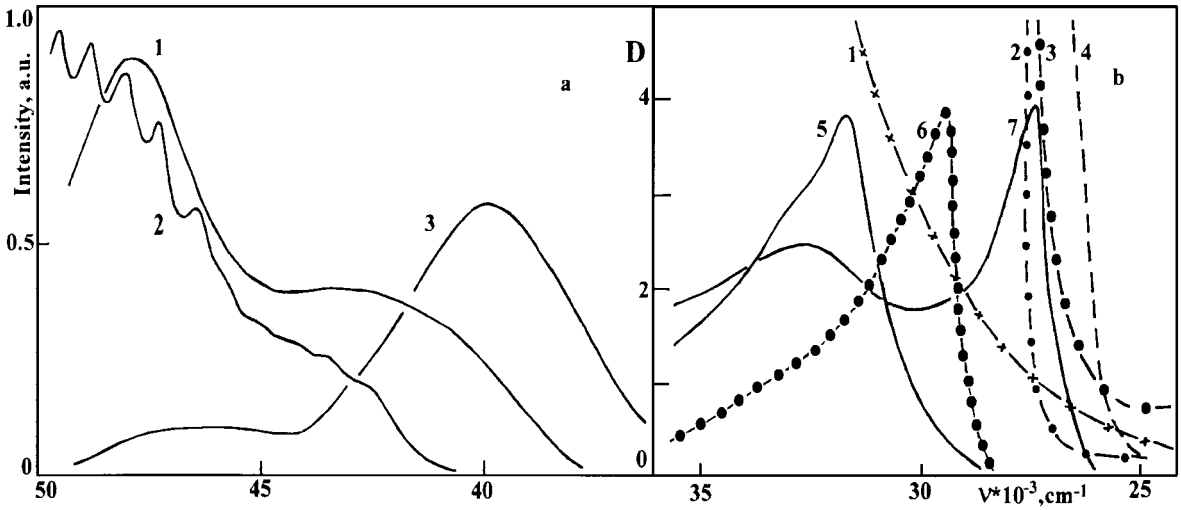

Fig. 3. Absorption and excitation spectra of "isolated" MoO_4^{2-} ions (a) and PWO, PWO-Mo and $PbMoO_4$ crystals (b)

a) absorption of Cs_2MoO_4 aqueous solution (1) ($T=T_{room}$), Cs_2SO_4- Cs_2MoO_4 crystals (2) (T=77 K) [13] and excitation spectra of MoO_4^{2-} ions in CsCl crystals (T = 4,2 K) (3);

б) absorption (1-4) and excitation spectra (5-7) of PWO (1, 5), $PbMoO_4$ (2, 4, 7) [10] and PWO-Mo crystals (3, 6); T = 4,2 (1-3, 5, 6), 77 (7) and 300 K (4)

$\nu_2(E)$, $\nu_3(F_2)$ and $\nu_4(F_2)$ type, the most intensity Raman lines of which are corresponded to symmetry $\nu_1(\ _1)$ mode and antisymmetry $\nu_3(F_2)$ mode. Value of splitting of $\nu_3(F_2)$ mode in crystal field is an indicator of degree of $\ _4^{2-}$ MA deformation. So, four bands in the regions: ν_1 = 898-900, ν_3 = 838-842 and ν_4 = 318-320 m^{-1} [16] are observed for aqua ion ($_d$ symmetry of MA). Accordingly to Raman data, $\nu_1 \cong 897$ m^{-1} for Cs_2SO_4 crystal. Mo $\ _4^{2-}$ M placement in AHC leads splitting of $\nu_3(F_2)$ mode to three components with the frequencies 876, 855 and 927 m^{-1} [14]. But, as it was mentioned already, the electron-vibration absorption spectra in this case are the similar to that, which are observed for aqua ion and for Cs_2SO_4 - Mo $\ _4^{2-}$ crystals. It must be noted here, that PL of emission centers formed by Mo $\ _4^{2-}$ ions in AHC excited, in general, on the long wave length absorption edge ($\nu_m^{ex} \cong 40$ 000 cm^{-1}). In the series of our works concerning investigation of spectral-luminescent properties of luminescence centers formed by MA of $\ _4^{n-}$ (X = Cr, V, Mo) type in various matrices we have assumed that MA of $\ _4^{n-}$ type form in crystals complex emission centers, including besides MA, core of the center, also lattice's defects: anion vacancy trapped electron, or cation of M^{2+} (M = , etc.) type. Precisely formation of such complex centers by molecular anions is a cause of shifting of absorption and excitation bands of unassociated in complexes MA of $\ _4^{n-}$ type to long wave length region. We have tendency to consider that the same case takes place also for centers of the "green" luminescence formed by impurity Mo ions in PWO crystals. So, Mo $\ _4^{2-}$ molecular group is a core of emission center that must also contain Pb^{2+} cations in the case of PWO crystals. Thus, excitation band of "green" luminescence of PWO-Mo crystals is caused by transitions in the complex Pb^{2+}Mo $\ _4^{2-}$ center, components of which are connected by the covalent interaction in a common electron system. These assumptions agree with the fact that PWO-Mo crystals are intermediate by the position of absorption band of the "green" emission in comparison with the correspondent characteristics of $PbMoO_4$ crystals and "pure" PWO crystals.

As for, are Mo $\ _4^{2-}$ ions included in the lattice separately as "isolated", or do they form aggregates, microinclusions of $PbMoO_4$ crystals [9], this moment now is not the main for studying nature of "green" emission. Even if the $PbMoO_4$ crystallites are forming in the PWO-Mo crystals, then question, - can anyone of Mo $\ _4^{2-}$ M be an emission center or only some of them, - is open. But, the fact that excitation spectra of PWO-Mo crystals are

noticeable different from the excitation spectra of $PbMoO_4$ crystals (Fig. 3) evidences that including of Mo_4^{2-} ions in PWO lattice as «isolated» is more reliable.

Conclusions

Impurity molybdenum ions are included in the lead tungstate crystal lattice as ions those replace W^{6+} ions of $PbWO_4$ crystal lattice and formed in $PbWO_4$ matrix Mo_4^{2-} molecular groups.

Centers of the "green" luminescence of lead tungstate single crystals doped with molybdenum ions must be consider as complex formations, with Mo_4^{2-} molecular anions as cores.

The "green" luminescence of "pure" lead tungstate crystals is not connected with the presence of uncontrolled Mo^{6+} ion impurities in the crystal composition.

References

1. N.V. Klassen, S.Z. Shmurak, B.S. Red'kin *et all*, Tungstate crystals. Proc. Intern. Workshop, Rome-Oct. 12-14, 1998, Universita degli Studi *La Sapienza* (1999) 35
2. A.N. Belsky, I.A. Kamenskikh, V.N. Kolobanov *et all*, Tungstate crystals. Proc. Intern. Workshop, Rome-Oct. 12-14, 1998, Universita degli Studi *La Sapienza* (1999) 117
3. M. Nikl, Tungstate crystals. Proc. Intern. Workshop, Rome-Oct. 12-14, 1998, Universita degli Studi *La Sapienza* (1999) 129
4. M.V. Korzhik, Proc. Intern. Conf. SCINT'95, Delft, The Netherland (1996) 241
5. M. Bohm, F. Henecker, A. Hofstaetter *et all*. Tungstate crystals. Proc. Intern. Workshop, Rome-Oct. 12-14, 1998, Universita degli Studi *La Sapienza* (1999) 141
6. M. Kobayashi, M. Ishii, K. Harada, Proc. Intern. Conf. SCINT'95, Delft, The Netherland (1996) 286
7. S.G. Nedelko, . . Voloshinovskii, M. . Krisjuk et all, Proc. Intern. Conf. SCINT'95, Delft, The Netherland (1996) 263
8. S.G. Nedelko, M.A. risjuk, Handbook of Intern. Conf. on Luminesc. and Opt. Spectroscopy of Condensed Matter, Prague, Czech Republic (1996) P9-25
9. M. Batenchuk, I. Konstankevyh, L. Limarenko et all, Tungstate crystals. Proc. Intern. Workshop, Rome-Oct. 12-14, 1998, Universita degli Studi *La Sapienza* (1999) 49
10. W. van Loo, Phys. Stat. Sol (a). **27 (**1975) 565
11. J.A. Groenink, G. Blasse, J. Sol. State Chem. 32 (1980) 9
12. Z.G. Reut, Izv. AN SSSR. Ser. fiz. (*in Russian*) **49** (1985) 2032
13. R. Borromei, G. Ingletto, L.Di. Sipio, Chem. Phys. Letters **82** (1982) 288
14. M.U. Bely, V.V. Bojko, Yu.D. Glinka, Izv. AN SSSR. Ser. fiz. (*in Russian*) **53** (1989) 1778
15. R.K. Khanna, W.S. Brower, B.R. Guscott et all, J. of Research of NBS. Phys. and Chem. **72a** (1965) 81
16. I.Ya. Kushnirenko, S.G. Nedilko, Yu.O. Pervak, Visnik Kyiv. Univ. (*in Russian*) (1979)

Characteristic Features of Automated Growth of Large Scintillation Alkali Halide Single Crystals Free of Oxygen-Containing Impurities

B.G.Zaslavsky, V.S.Suzdal, A.M.Kudin, S.I.Vasetsky, L.N.Shpilinskaya, T.A.Charkina, J.A.Nesterenko, A.I.Mitichkin, L.V.Kovaleva, V.N.Zviagintsev

STC "Institute for Single Crystals", Lenin Avenue 60, Kharkiv 310001, Ukraine

Abstract. Influence of some oxygen-containing impurities on the spectrometric characteristics and radiation resistance of CsI(Tl) crystals has been studied. Borate-ions are shown to be no less dangerous impurity comparing to carbonate-, sulphate- and hydroxide-ions. The content of borate ions in the trace amount causes the crystal colouring under gamma-rays and light output becomes less. A method has been suggested so that the melt should be purified from impurities right when crystals are pulled therefrom automatically. Grown from the purified melt the crystals do not contain any absorption band in the IR-spectrum, which is characteristic of borate-, carbonate-, and sulphate-ions, and possess a higher radiation resistance.

Keywords: Automated pulling; Oxygen-containing impurities; Melt purification; Radiation resistance.

Introduction

Developments in high-energy physics stimulated modern automatically controlled processes of growing scintillation alkali-halide single crystals. Institute for Single Crystals of National Academy of Sciences of Ukraine has elaborated and mastered to use in industrial production highly-efficient methods of pulling the melt onto a seed and feeding it with melted [1] and powdery [2] initial raw material. The methods are so productive that they will soon replace the Stockbarger-Bridgman crystal growing method that appears to be out-of-date for its low productivity. Controlling the crystallization rate with feeding rate transducer [1] and melt level transducer [2] makes it possible to maintain the cross-section of a growing crystal with accuracy up to 1% even if very big ingots (over 500mm in diameter) are being grown.

However, crystal quality does not depend only on crystallization rate stability but also on the purity of raw material. Since the above methods suggest that the crystals weighing several hundreds kilograms should be pulled from the melt while the melt is being fed in the crucible, impurities will be distributed in the crystals according to Pfann equation [3] for zone melting. This means that the methods indeed solve the task of homogeneously distributing the activator along the ingot. However, to obtain the crystals having minimum quantity of harmful impurities (including oxygen) along their length, one should use a very pure raw material. For a number of applications and high energy physics, in particular, scintillators should allow a very homogeneous light output along their length and resist to radiation rather well. For example, inhomogeneity of the light going out of the truncated CsI(Tl) pyramids, over 300mm long, which is required for the calorimeter of the Stanford accelerator, should not exceed 6%. The requirement for radiation resistance is determined as no more than 20% worsening of light output when a scintillator is exposed to gamma-irradiation dose 10^4 rad. Sulphates, carbonates, hydroxides, nitrates and other oxygen-containing impurities are always present in the initial raw material and sometimes their quantity exceeds the limits specified in standards. Cleaning the raw material from impurities additionally is not always effective but always makes the material to cost much more.

Analysis shows that the sodium- and cesium iodides produced by various companies and graded as "specially pure products" contain, however, approximately the same amount of oxygen impurities. This points to the fact that the raw material purification methods applied during raw material synthesis have reached their limit. Manufacturers do not always control how much oxygen-containing impurities alkali-halide salts have. Meanwhile, our research has shown that if CsI crystals contain carbonate- and sulphate ions as much as $3 \cdot 10^{-5}$ mass %, the blue luminescence component gets much more intensive making use of these crystals impossible as fast scintillators. As shown in [4, 5], stability of the spectrometric features of CsI(Tl) crystals to be irradiated depends on both activator concentration and the concentration of oxygen-containing impurities. For example, the content of BO_2-ions in the trace amount causes the intensive colouring of crystals under irradiation and releases much less light. So, development of scintillation crystals growing processes to obtain crystals having oxygen-containing impurities as less as possible is a rather topical task to accomplish.

Experiment and discussion of results

CsI(Tl) crystals, 200 to 450mm in diameter and 350 to 450mm high, were grown by means of automated pulling from the melt available in a conic crucible while the melt was being fed [1]. The ingots grown were then cut into blanks along the growth axis which truncated pyramids over 300mm long were made from. To make scintillators, selection of crystals was performed to satisfy the following requirements. Inhomogeneity of thallium distribution along the ingot centre line must not exceed 10%. Total content of carbonate- and sulphate ions must not exceed $2 \cdot 10^{-4}$ mass %. Concentration of the activator was measured every 10mm. The optical method was used to determine transparency at the fall-off in A-absorption band of the activator. The calibration curve was plotted according to the samples in which known thallium concentration has been found by the polarographic method. Oxygen-containing impurities in different parts of the ingot were determined with the help of IR-spectroscopy. The light output was measured for both medium-size surveillance specimens ∅25 x 25mm and ready-made scintillators shaped as truncated pyramids 306 to 327mm high. The radiation resistance of the crystals was determined by an original technique based on measuring the optical density $\ln(I_O/I)$ by the Tailor method [6]. Samples ∅30 x 60 mm that had been cut out of different parts of a boule were used. Their relative optical density $\ln(I_O/I)$ in the wavelength of λ = 550 nm was determined before and after irradiation by $5 \cdot 10^5$ rad. CsI standard with absorption coefficient κ_{550}=0.005 cm^{-1} was used to compare. By numerical value of radiation resistance (RR) we mean the value of deviation $\Delta \ln(I_O/I)$ that is determined to be ≥0. It has been experimentally found that if $\Delta \ln(I_O/I) < 1.1$, the change in ready-made product light output $\Delta L/L < 20\%$ after being exposed to dose 10^4 rad.

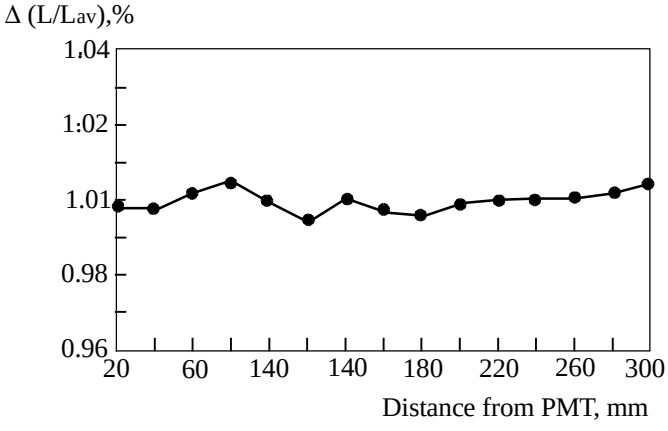

Fig.1. Relative change of light output ($\Delta L/L_{av}$, %) along the pyramid axis

To provide for uniformity in the light output it is necessary first of all to assure activator distribution all over the crystal as homogeneous as possible. The necessary distribution can be ensured if the growth rate and diameter of a growing crystal are kept constant [7]. Table 1 shows examples of thallium distribution along the growth centerline for three crystals. Deviation in the activator concentration from the average value most often does not exceed ±5% in the boule cylindrical part 30 mm long.

Such a high homogeneity in distributing the activator and a good transparency of the crystal (0.01cm^{-1} on wavelength 550nm) make it possible to attain a high uniformity of the light output (~1%) along the scintillator axis comparatively easy. Fig.1 shows an example how the light output is distributed along the axis of a pyramid.

The radiation damage of crystals is caused by deterioration in their transparency that takes place as a result of color center formation after the crystals have been irradiated [8]. The color centers are linked to impurity-induced defects and structural defects in the crystal lattice. Some authors [9] believe that after irradiation conversion efficiency η degrades too. Comparison of changes in the light output after irradiation for crystals of different length shows that the change in η may be disregarded if exposure doses are about 10^4 rad. It is the impurity composition of crystals that affects their radiation resistance exclusively much. Such doped ions as CO_3^{2-}, OH^- and SO_4^{2-} are known to considerably reduce the radiation resistance of CsI(Tl) crystals [4]. The mechanism of forming stable radiation-induced defects with CO_3^{2-} and OH^- ions is described in detail in [10]. As shown in [5] and confirmed herein, BO_2^- ions are harmful that much too. Fig.2 shows how CsI(Tl) crystal radiation resistance depends on the content of borate ions.

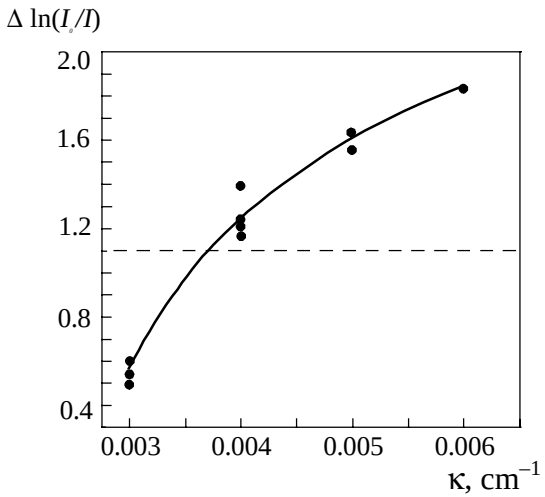

Fig.2. Dependence of optical density change $\Delta\ln(I_O/I)$ from the content BO_2^--ions in CsI(Tl) crystals at isodose radiation 0,5 Mrad.

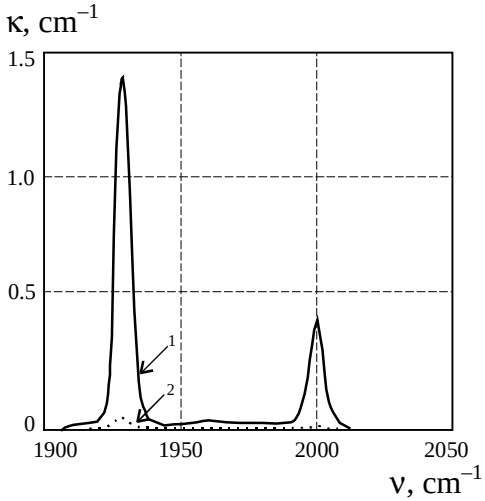

Fig.3. Absorbtion coefficient (κ_{1930}) in ν_3-variation BO_2^--ions in CsI(Tl) crystals, grown with the treatment of melt (2) and without it (1).

Since presently we have no independent and reliable method to determine the amount of BO_2^- in alkali-halide crystals at the level of $1\cdot10^{-5}$ - $1\cdot10^{-4}$ mass %, the borate-ions content was controlled according to the absorption in 1930 cm^{-1} band which is characteristic of valent ν_3-variation. The IR-absorption spectrum in ν_3-variation of BO_2^--ion in crystal is given in Fig.3. Need for purification the melt from borates has emerged in connection with processing of crystal machining wastes (small pieces, chip cuttings). This mainly concerns those rejected scintillators whose surfaces have undergone grinding and polishing with boron-containing abrasive materials. Since CsI(Tl) crystals are very easy to be colored at the presence of borate ion traces and boron is available enough in the environment, the undesirable quantity of this impurity may get in the growth installation feeder when it is charged with raw material.

Table 1 gives quantities of C_{Tl} activator and impurities by CO_3^{2-}, SO_4^{2-} and BO_2^- as well as radiation resistance values for the crystals that have been grown from both ordinary salt and salt mixed with industrial wastes.

Table 1. Impurities distributed in height of the crystals and the crystals radiation resistance.

H (mm)	Impurities content in crystals grown from different raw material											
	Salt				100% wastes				wastes treated Ti			
	Tl $\times 10^{-2}$ mass. %	SO_4^{2-} $\times 10^{-5}$ mass. %	BO_2^- κ, cm^{-1}	RR	Tl $\times 10^{-2}$ mass. %	SO_4^{2-} $\times 10^{-5}$ mass. %	BO_2^- κ, cm^{-1} (*)	RR	Tl $\times 10^{-2}$ mass %	SO_4^{2-} $\times 10^{-5}$ mass %	BO_2^- κ, cm^{-1}	RR
10	9.5	1,5	–	0.7	7.7	1,5	0.005	1.6	7.0	–	–	
50	9.6	1,9			8.7	1,9	0.005		7.2	–	–	0.72
100	9.4				9.8				8.2	–	–	
150	9.7			0.75	9.9				8.3	–	–	
200	9.6	2,3	–		9.7	2,3	0.005	1.65	8.2	–	–	079
250	9.8				9.8				8.5	–	–	
300	9.8				9.9				8.2	–	–	
350	9.9	2,7	–	0.8	9.9	2,3	0.006	1.8	8.4	–	–	0.83

*) The borate-ions content is expressed in terms of absorption coefficient (K_{1930}) in 1930 cm^{-1} band.

From the data of Table 1, it follows that the crystals grown from wastes contain a higher concentration of borate-ions and are not resistant to radiation $\Delta \ln(I_O/I) > 1.1$, whereas those grown from the ordinary fine crystalline raw material containing no borate impurities, easily withstand the radiation resistance test $\Delta \ln(I_O/I) < 1.1$).

The idea of purifying the melted alkali metal halogenides from oxygen-containing impurities immediately when pulled [11] is that these impurities should be converted into insoluble compounds. The calculation of isobar-isotherm potentials (ΔG^o_T) in the relevant chemical reactions shows that titanium is the most adequate metal for these purposes. As an example we would like to specify the values of ΔG^o_T and temperature coefficient for some reactions with insoluble TiO_2 being formed.

$$Ti + 0.5Cs_2SO_4 \leftrightarrow TiO_2 + 0.5Cs_2S \qquad \Delta G^O_T = -403.4 + 9{,}3\cdot 10^{-3}T$$

$$Ti + Cs_2CO_3 \leftrightarrow TiO_2 + Cs_2O + C \qquad \Delta G^O_T = -142.3 + 105{,}8\cdot 10^{-3}T$$

$$Ti + 1.33CsBO_2 \leftrightarrow TiO_2 + 0.67Cs_2O + 1.33\ B \qquad \Delta G^O_T = -851.1 + 45{,}9\cdot 10^{-3}T$$

It should be noted that aluminium can be used for purification of melting salts too, however low temperature of aluminium melting could cause certain problems when the metal is used to purify alkali-halide salts in a platinum ware. Contacting directly, the aluminium will dissolve the platinum. However, it may certainly be used for melt purification in ceramic or quartz-ware.

Our experience shows that metal titanium should be preferably used to purify the melted, automatically pulled out, alkali-halide salts. A high melting temperature of this metal (1725°C) and its chemical activity as well as structural features of the make-up and feeder system [1] make it possible to treat the melt immediately in the process of crystal growth

without any complication. The X-ray phase analysis has shown that the powder that is formed and deposited on the feeder bottom is a mixture of TiO_2 (modification of rutile and anatase) and Ti_2O_3. The data of Table 1 and curve 2 (Fig.3) show that small quantity of titanium added to the melt enables to get rid of sulfate and borate impurities. This method of purification has been comprehensively evaluated in growing large-size, alkali metal iodide-based single crystals, 400mm in diameter, such as CsI(Tl), CsI(Na) and NaI(Tl). In the grown crystals, there was no titanium detected by chemical analysis methods.

Conclusion

The suggested method of purifying melted alkali metal halogenides be means of treating them with the metals forming low-soluble oxides is not only simple and highly effective but also universal. At present, one can be sure to state that the method makes it possible to decrease the quantity of CO_3^{2-}, SO_4^{2-},OH^-, NO_3^- and BO_2^- ions in alkali-metal iodide-based crystals to the concentrations that are beyond the threshold of sensitivity inherent in chemical and optical methods of determination. This method of purification may turn out to be preferable for obtaining fast scintillators-inactivated CsI crystals for which presence of any above-mentioned impurity amounting to $3 \cdot 10^{-5}$ mass % is inadmissible. For the time being, CsI scintillators having the low-intensive blue component are usually grown by repeatedly re-crystallising the melt, which is the main reason for their high cost. We do not see any substantial difficulties for using this method to purify the melt in growing optical crystal such as KBr, KCl, NaCl whose transmittance in the IR-area is deteriorated by oxygen-containing impurities.

It should be noted that the purification could be applied not only to automated pulling with melt feeding but also to the ordinary Kyropolous method. However, in the latter case, the melt is to be prepared beforehand. The process of preparation must cover melt treatment with a metal to subsequently let oxides settle down. The final phase of melt preparation should include filtering the melt from deposited oxides and other insoluble impurities.

Acknowledgements

The authors are thankful to Dr. V.F.Tkachenko for performing x-ray phase analysis and identification of products resulting from chemical interaction of titanium with oxygen-containing impurities in cesium iodide melts.

References

1. B.G.Zaslavsky, J. Crystal Growth 200 (1999) 476.
2. V.I.Goriletsky, L.G.Eidelman et al., J.Crystal Growth 128 (1993) 1059.
3. V.G.Pfann, Zonnaya Plavka (Zone Melting) (Mir, Moskow) (1960) 37 (Russian ed.)
4. L.V.Kovaleva, L.L.Nagornaya, Y.A.Zakharin et al., Rost i Svoystva Kristallov (Institute for Single Crystals, Kharkov) 6 (1980) 24.
5. L.V.Kovaleva, L.N.Shpilinskaya, A.M.Kudin, et al., Functional Materials 5 (4) (1998) 484.
6. Taylor A.H. J.Opt. Soc. Amer. 4 (1920) 9.
7. B.G. Zaslavsky, Functional Materials 5 (4) (1998) 499.
8. R.Y.Zhu, IEE Trans. Nucl. Sci., 44 (3) (1997) 468.
9. A.V.Gektin, N.V.Shiran, Proc. Int. Conf. on Inorganic Scintillators and Their Application, Shanghai, China (1997) 115.
10. B.V.Grinyov, L.N.Shpilinskaya, A.M.Kudin, et al., Functional Materials 4 (4) (1997) 540.
11. B.G.Zaslavsky, B.V.Grinyov, V.S.Suzdal, et al., J. Crystal Growth 198/199 (1999) 856.

Manufacturing of scintillation elements by plastical deformation

N. V. Klassen, S. Z. Shmurak, A. P. Ivanov, S. I. Makhonin (1),
A. A. Rogojin, A. E. Bakhur, A. O. Nikitin. (2)

(1) Institute of Solid State Physics, Chernogolovka, Russia
(2) All-Russia Institute for Mineral Resources, Moscow, Russia

Abstract. Plastical deformation was applied for manufacturing of scintillation elements in several ways. Big diameter and superthin slices were produced from CsI smaller ingots. These slices were used in the model of simplified alpha - particles spectrometer, which demonstrated satisfactory parameters and due to much lower price in comparison with semiconductor spectrometers can obtain rather wide field of applications. Deformation polishing improves by many times antihumidity resistance of hydroscopic materials. Local plastical deformation at the interface between two crystalline pieces has been used for optical and mechanical connection of separate parts of scintillators. By this way manufacturing of scintillators with sufficiently increased length can be made. Plastical deformation of ZnS scintillators with as-grown structural inhomogeneities resulted in essential improvement of their optical homogeneity.

Keywords: scintillators, plastic deformation, alpha-spectrometry.

The plastical deformation of various crystals, which are applied for scintillation detectors, is a well known phenomenon, which can take place in a wide set of situations, when the crystals are subjected to mechanical stresses (growth and subsequent cooling, annealing, cutting, grinding, lapping, gluing, etc.). In these situations the deformation is not controlled and as usual its influence on scintillation performance is harmful, because a lot of structural defects are introduced into the crystal, deteriorating their scintillation characteristics (the light yield, afterglow, energy resolution, etc.) [1]. So many efforts are applied usually for minimization of negative consequences of the plastical deformation during the preparation of scintillation elements. On the other hand, detailed studies of the plastical deformation in dielectrical and semiconducting crystals, being produced in the Institute of Solid State Physics (ISSP) in Chernogolovka for many years, showed, that controlled application of the plastical deformation can bring a lot of positive results for manufacturing of crystalline scintillation elements.

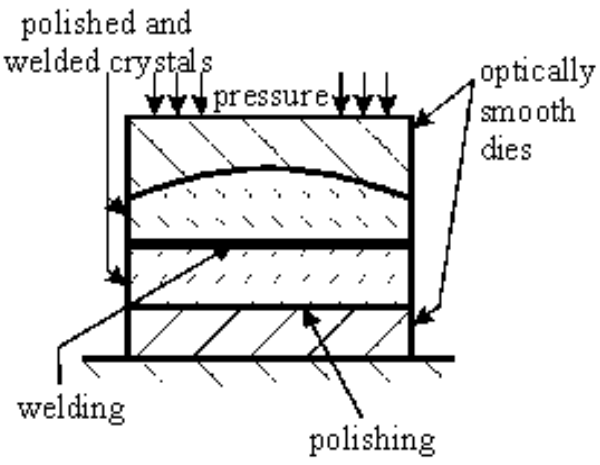

Fig. 1. Deformation polishing and welding.

Surfaces of any crystalline elements are subjected to the influence of mechanical stresses and corresponding plastical deformation most frequently. ISSP specialists developed the so called deformation polishing of surfaces of various crystals, which is alternative to the well known abrasive polishing [1]. The main idea of deformation polishing consists in flattening of the surface under processing by compression with optically

smooth die from a hard material until the surface of the crystal will become the replica of the die's surface (see Fig.1). This method is applied successfully in the production of optical and scintillation elements from alkali halides - e.g., from KCl, NaCl, CsI, etc. The surface roughness under deformation polishing does not exceed 5 nm, so the crystal does not need any finishing treatment under the compression. The method of deformation polishing has a set of significant advantages in comparison with traditional abrasive treatment of surfaces. It needs much less labor efforts and lower qualification of technicians. Wastes of abrasive materials and of materials subjected to polishimg are decreased by many times, so the profits either from economical or from ecological points of view are obvious, especially for processing of toxically materials (e.g., containing widely used in radiation detectors Tl, Se, Pb, Hg, etc.). Abrasive processing induces most frequently tensile stresses in the subsurface layer of the crystal, what results in creation of microcracks and other kinds of microcavities. Due to this fact the mechanical strength of this layer is lower, than in the volume. On the contrary deformation polishing generates compressive stresses, microcracks are not created and our measurements showed, that the mechanical strength of the subsurface layer in this case is several times bigger, than in the volume.

It turned out, that deformation polishing increases by many times the chemical resistance of the surface. For example, optical and scintillation elements from hygroscopic alkali halides, including CsI(Na) after deformation polishing can be kept at open air with usual humidity during several years without any change in surface transparency whereas the same materials after abrasive polishing become opaque in one-two weeks. Hence in contrast to abrasively polished crystals alkali halide elements after deformation polishing does need any antihumidity precautions like protection coatings, air drying, etc. One of the explanations of the antihygroscopic effect of deformation polishing is connected with much better smoothness of the surface, which does not contain microcracks and microsteps, which are appropriate to abrasively polished surfaces and work as absorption centers for molecules of water from the ambient atmosphere.

During the process of deformation polishing the die and the crystal are not shifted with respect to each other, thus limitations for the complexity of the geometry of the surface under processing do not exist in contrast to the process of abrasive polishing, where these limitations are rather rigid. For example, deformation polishing has been applied in ISSP for manufacturing of position sensitive detectors consisting from arrays of small CsI(Tl) elements, produced during one cycle from a single CsI(Tl) crystals (as it is shown schematically in Fig.2).

Generally speaking, Fig. 2 illustrates the situation, when the plastical deformation penetrates into more deep regions of crystals in comparison with compression flattening of the surface, when the plastical deformation can be localized in the subsurfaces layers. Another example, when sufficient transformation of the crystal geometry occurs during manufacturing of ready elements from crystalline ingots, deals with production of thin CsI(Tl) slices (0.3 - 0.6 mm) with comparatively big

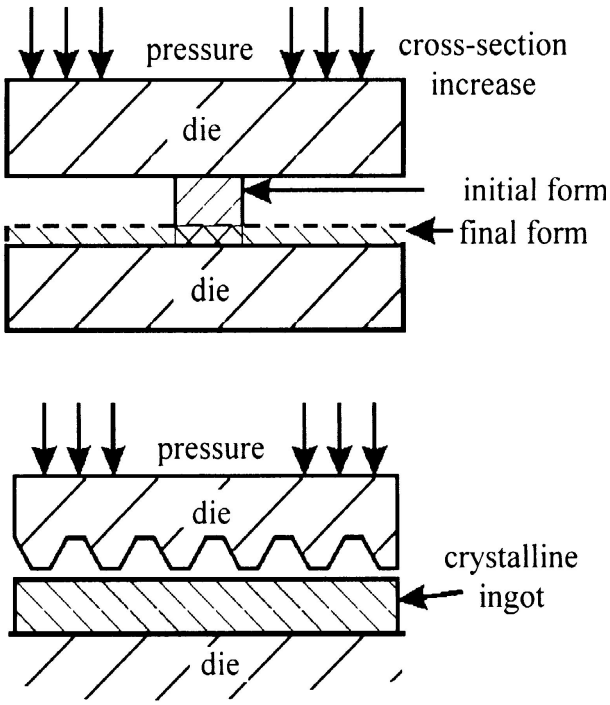

Fig. 2. Deformation shaping of scintillators and optics.

diameter (60 - 80 mm) from much smaller single crystalline ingots. This kind of thin slices can be applied effectively either for position sensitive scintillation X-Ray and gamma - detectors or for economic scintillation alpha - spectrometers. We studied experimentally the possibility of constructing of this kind of spectrometers, based on combination of thin layer CsI(Tl) slice with photoelectronic multiplier, connected with multichannel analyzer or ADC-plate, installed into a computer.

Fig. 3. Thin CsI(Tl) slices made by plastical deformation.

Alpha - spectrometric method with preliminary radiochemical preparation of a sample and using of isotope indicators ^{242}Pu, ^{236}Pu, ^{243}Am, ^{232}U is one of the most sensitive and accurate techniques for determination of such high - toxical radio - emitting nuclides as $^{239+240}$Pu, ^{238}Pu, ^{241}Am, ^{234}U, ^{238}U, ^{232}Th, ^{230}Th, ^{228}Th, ^{210}Po in environment objects. As measuring tools standard alpha - spectrometers are applied usually, based on semiconductor detectors or pulsed ionizing chambers with gas filling, for example, EURISYS MEASURES (France) — IN 114, Aladin; EG&G ORTEC (Germany) — Octete PC; CANBERRA (USA) —Analyst; DOZA (Russia) — Progress - Alpha.

But the cost of the above mentioned devices is rather high - several tens of thousands USD, so not every laboratory is capable to buy them. On the other hand the problem of reliable measurements of the content of radio-emitting nuclides in natural objects (soil, water, etc.) every year becomes more and more actual due either to wreck throw-outs from Atomic Power Plants and nuclear - fuel cycle enterprises or to increasing strictness of the requirements to the radiation safety of the environment. Our studies showed, that much less expensive scintillation alpha - spectrometer can be designed using described above combination of plastically - thinned CsI(Tl) slices (see Fig. 3) and photomultipliers. The effectiveness of alpha - particles registration by means of such a device is not worse, than the effectiveness of ionizing chambers (ε= 0.47 - 0.48), but the energy resolution (about 200 KeV) (see Fig. 4) is significantly worse in comparison with modern alpha - spectrometers with semiconductor detectors or ionizing chambers (30 - 50 KeV). But if one uses radiochemical methods of selective extraction of radionuclides developed in VIMS and corresponding programme software, enabling to consider mutual overlapping of analytical picks, this resolution is quite sufficient for reliable determination various radionuclides such as ^{210}Po (Fig. 4), ^{234}U, ^{238}U (Fig. 5a), $^{239+240}$Pu (Fig. 5b), ^{232}Th, ^{230}Th, ^{228}Th.

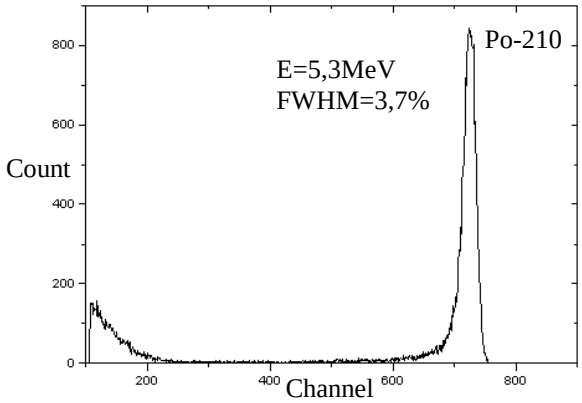

Fig. 4. Scintillation spectrum of the specimen prepared of the soil sample with extracted Po-210.

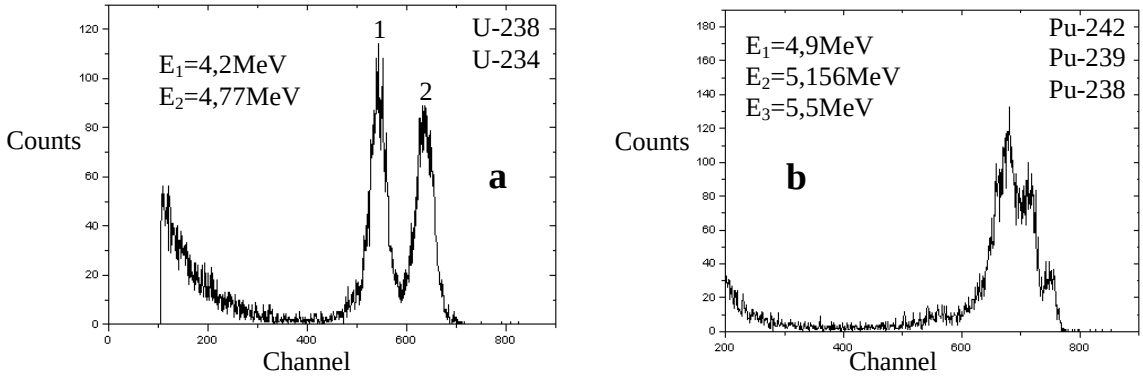

Fig. 5. Scintillation spectrum of the specimen prepared of the soil sample with extracted isotopes of Uranium (a) and Plutonium (b).

Differing from spectrometers with semiconductor detectors or ionizing chambers the scintillation spectrometer does not need vacuum or gas filling in a working volume. It is compact, simple in construction and service, works reliably. Estimated cost of such a detector device is at least one order lower, than that of alpha - spectrometers with semiconductor detectors or ionizing chambers. Hence alpha - spectrometry will be able for usage of routine mass analyses in the most of laboratories for ecological and radiation control, nature resources studies, etc.

It should be emphasized, that the plastical transformation of ingots from small to big diameter is much more effective method for manufacturing of thin CsI slices, than traditional combination of cutting and abrasive lapping and polishing processes. The content of internal structural defects, introduced into the crystal during the process of manufacturing, in the process of plastical transformation is significantly lower. It needs much less labor efforts, because after deformation processing the quality of the slice's surface is rather high and it does not require any additional treatment. The mechanical strength of the slice is bigger by several times in comparison with the abrasive procedure, what is essential for next manipulations with such a thin and big diameter plate.

One of the severe obstacles for wide scale application of plastical polishing and geometry transformation procedures consists in the uncontrolled connection between the dies and the surfaces subjected to processing. Generally speaking, this connection can result from three phenomena: physical adhesion between the materials of the die and the crystal due to interatomic forces of Van-der-Waals character, chemical reactions between them and, at last, mixing of the materials of the die and the crystal induced by the pulses of the release of the elastic energy which takes place in the intermediate region between the contacting surfaces. The first two processes can be removed by a proper choice of the die's material and the

lubricant of the die. The elimination of the third process is more difficult, because on the one hand the plastical deformation is necessary component of the technological procedure, but on the other hand the same deformation induces the pulses of the energy release. So the search for the optimal relation between the temperature, the stress, the duration and some other parameters which govern the process of deformation treatment is the main component of the development of this technology for any definite material.

On the other hand, we have used the process of local release of the elastic energy occurring in the interface between the two contacting surfaces for the development of a new kind of connection between optically transparent materials [2,3]. Due to the fact, that the plastical deformation plays a significant role in this process and the behavior of the contacting materials in the intermediate layer is melt-like, this kind of connection can be called "deformation welding". The process of deformation welding differs significantly from thermodiffusion connection of optically transparent crystals, described earlier [4]. In thermodiffusion process the local plastical deformation in the interface is minimized and the connection takes place due to thermally activated diffusion between the contacting materials, pressed to each other by comparatively weak stresses, which are not sufficient to induce the plastical deformation. In this case preliminary fine polishing of the surfaces being connected up to the state of the optical contact is necessary. The high vacuum is necessary as well. In our case neither fine preliminary polishing nor any vacuum pumping are needed. The whole process can proceed at the open air and the necessary contacting between the surfaces as well as the energy needed for welding are produced by the local plastical deformation of the interfaces.

ISSP specialists have tested successfully deformation welding for wide set of optically transparent crystals: alkali halides, fluorides (CaF_2, BaF_2, PbF_2, CeF_3), lead tungstate and some others. In all the cases perfect optical contact and strong mechanical connection have been achieved. For scintillating crystals the process of deformation welding has a lot of promising applications. First of all, in many cases manufacturing of the elements with increased length can be made more effectively by deformation welding, than by increase of the dimensions of as-grown crystals. Moreover, the welded scintillating elements can have higher quality, than the as-grown ones. This is due to inevitable changes of the crystal properties along its length during the procedure of the growth. Concerning the scintillation parameters this means that at one end the light yield, decay time and other characteristics can differ from their values at the opposite end. This fact will deteriorate the energy resolution and other parameters of the detector. In the case of welding the long scintillation element can be accumulated from several parts, which can be preliminary selected and have exactly identical characteristics.

For high density scintillators the optical connection of the crystal with the photodetector is problematic due to essential steps of the refraction indexes between the scintillator and the polymer glue, which is usually applied. But if one uses sufficiently plastical solid material for the "gluing" of the scintillator and the photodiode by means of deformation welding, the problem of too big difference between the refractive indexes of the crystal and the glue can be eliminated, because in contrast to polymers there is a wide set of optically transparent plastical crystals with rather high optical t refractions which can be used as "solid glue".

In addition to transformations of geometry of crystals the plastical deformation can be used for transformations of internal atomic structure of scintillators. For example, zinc sulfide (ZnS) is a well known scintillator, but its application is limited by structural inhomogeneities, which are present usually in single crystals of ZnS due to its polymorphism (at the room temperature melt grown zinc sulfide exists in an intermediate structure, being a mixture of cubic and hexagonal atomic configurations). These inhomogeneities induce additional light scattering and optical absorption, retard radiative recombination by means of internal electrical fields, etc. Regulated plastical deformation of ZnS single crystals transforms them

to the stable cubic structure, eliminating the most part of structural inhomogeneities [5]. The concentration of stacking faults was decreased by many times, the broadening of X-Ray reflections at diffractograms was eliminated, the intensity of photoluminescence was increased and the spectral width of the light emission bands became lower. Thus the crystal as a whole became much more perfect.

References

1. N. V. Klassen, “Dependence of Scintillators’ Optical Properties on Intrinsic Structural Defects”, in “Scintillator and Phosphor Materials”, ed. M.Weber et. al., p. 247, San – Francisco, 1994.
2. N. V. Klassen, V. V. Sinitzin, S. Z. Shmurak, et. al. “Deformation and Thermal Treatment Application to Heavy Scintillators Production”, in “Heavy Scintillators for Scientific and Industrial Applications”, ed. F.D. Notaristefani, P. Lecoq, M. Schneeegans, p. 587, Frontieeres Editions, France, 1992.
3. N. V. Klassen, S. Z. Shmurak, et. al., “Deformation Welding of Scintillating Materials”,, in “Scintillator and Phosphor Materials”, ed. M. Weber et. Al., p. 551, San – Francisco, 1994.
4. N. V. Klassen, S. I. Makhonin, Yu. A. Ossipyan, “Application of Plastical Deformation Deformation in Production of Solid State Optical Elements”, in “Materialovedenie” (“Materials Science Transactions”), № 2, 1997, “Mashinostroenie”, Moscow.
5. V. R. Regel, E. A. Ctepantzov, A. V. Tovmasian, “On Solid State Reactions, Taking Place at Crystalline Boundaries during Thermocompression Connection”, Izvestia Acad, Sciences, USSR, phys, series, 1986, v. 50, p. 472
6. M. P. Kulakov, S. Z. Shmurak, Phys. Stat. Sol. (a), v. 59, p. 147, 1980

A Non-Vacuum Growth Technique for Cubic PbF_2 Crystal with Strong Cherenkov Radiation Effect

Dingzhong Shen, Guohao Ren and Shaohua Wang

Shanghai Institute of Ceramics, Chinese Academy of Sciences
1295 Dingxi RD. 200050, Shanghai, P.R.China
dzshen@online.sh.cn

Abstract. A non-vacuum growth technique for pure PbF_2 crystals was reported in this paper. It used a kind of chemical as a scavenger to deprive the oxygen impurities in the raw materials and growth system and realized the growth of PbF_2 crystals under non-vacuum condition. By means of spectrophotometer, it was found that the transmission of the crystal dependents on the doping amount of the scavenger, the purity of the raw materials, as well as the later processing method. The PbF_2 crystals grown with this method are characterized by short absorption edge of 250nm, good energy resolution of $3.2\%/\sqrt{E}$, as well as very weak radiation damage.

Key words: lead fluoride, crystal growth, non-vacuum, Cherenkov effect

Introduction

When charged particles move uniformly and pass through a transparent material, and if its velocity is faster than that of light which travels within the material, the material will emit a weak visible light along a definite direction. This light is called Cherenkov radiation. The detector for collection of Cherenkov light emitted by the secondary particles of the electromagnetic showers is referred to as a Cherenkov shower counter. It is a very important detection device in high-energy physics experiment. Total-absorption electromagnetic shower calorimetry asks Cherekov radiator: 1) short radiation length, 2) no fluorescence, 3) high refractive index, 4) transparent, especially in UV region. To satisfy the above requirements, Willianms [1] and Dalley [2] suggested that in the experiment to detect high-energy γ-rays, electrons, and positrons, the ideal material for such a detector would be a "transparent lead brick". A near approximation of this is cubic lead fluoride crystal. The most outstanding properties of PbF_2 are its high density ($7.7g/cm^3$), short radiation length (0.93cm), large average atomic number as well as good transmission extending to UV. Its light output is sufficient to have a good electromagnetic energy resolution.

However, for a long time, the problems on the crystal growing techniques have not been resolved and the grown crystals can not meet the needs for application either in size or in their properties. Since PbF_2 crystals are easy to be contaminated by oxygen at high temperature, they are usually grown with vacuum method. However, the vacuum method not only costs very high, but also can not deoxidize effectively, so that there are always some needle-like defects and absorption of UV light in PbF_2 crystals. These defects greatly decrease the transmission and Cherenkov radiation intensity of the crystals. So, it is necessary to look for a new method for deoxidization in addition to purification of the raw materials.

Since the number of Cherenkov photons (dN) having a wavelength between λ and dλ is given by[3] $dN \propto \lambda/d\lambda^2$, the high transmittance in the short wavelength region is an important characteristic in order to collect many Cherenkov photons by photomultiplier. So, the transmission, especially at short wavelengths, is mainly used as a criterion to evaluate the crystal quality in this paper.

Experiment

The raw material used for growing cubic PbF_2 crystals is orthorhombic PbF_2 powder, which was synthesized by combining $PbCO_3$ with HF at high temperature:

$$PbCO_3 + HF \rightarrow PbF_2 + CO_2 + H_2O$$

The products were put in vacuum oven and heated to about 120°C for a few hours. The components CO_2 and H_2O in system were vaporized. According to X-ray diffraction (XRD) analysis, the produced lead fluoride powder was orthorhombic PbF_2 (Fig. 1).

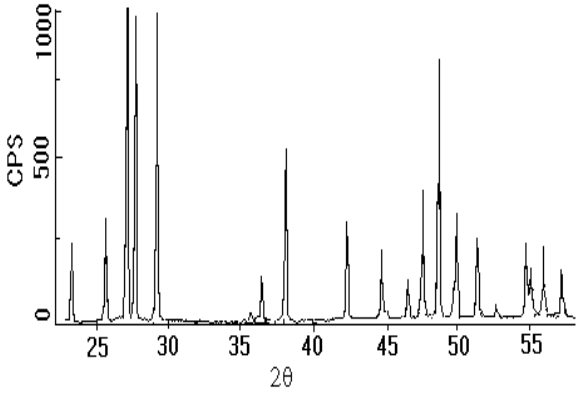

Fig. 1 XRD pattern of orthorhombic lead fluoride.

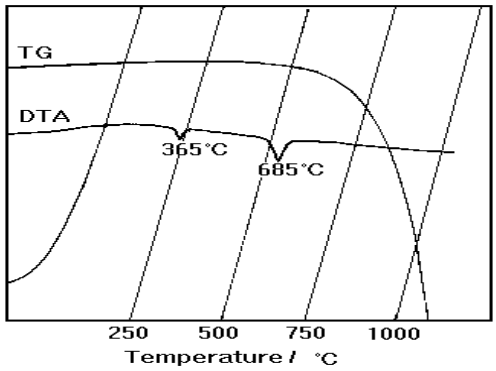

Fig. 2 DTA and TG curves of orthorhombic PbF_2

The DTA and TG curves of the raw materials were measured by NETSCH STA429 differential thermal analyzer. In the DTA curve (Fig. 2), there are two endothermal valleys: one is at 365°C, the other is at 685°C. The former corresponds to the phase transition of orthorhombic to cubic, and the latter corresponds to the melting of cubic PbF_2 crystal.

The crystals were grown by modified Bridgman method under non-vacuum condition. In this method, a chemical that can scavenge oxygen impurities, such as O^{2-}, OH^-, and doesn't cause any harmful effects on the crystal properties and growth equipment was used. Both PbF_2 powder and the scavenger were mixed thoroughly and then put into platinum crucible (Fig. 3). The temperature of furnace was controlled and kept to be above the melting point (822°C) of lead fluoride by a computer during whole growing process. The temperature gradient near the solid and liquid interface was about 40°C/cm and the descent rate of crucible was 1cm/hr.

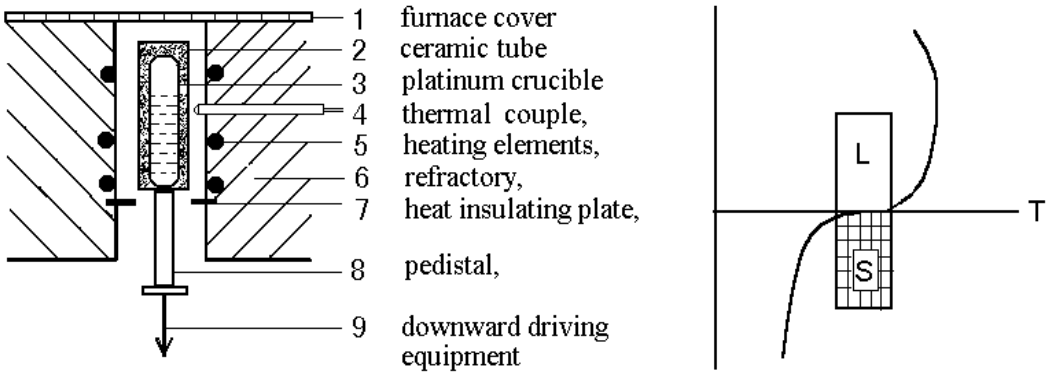

Fig. 3 Schematic diagram of furnace structure (left) and temperature curve (right)

The as gown crystals were colorless and transparent. After cutting, grinding and polishing, the ingot was processed into various samples with different size, the largest sample with the dimension of 30×30×300mm.

The starting materials and sample obtained at various stages were examined by X-ray diffraction (XRD). The impurities in raw materials were analyzed by atomic absorption spectrometry (AAS). The transmission of PbF_2 crystal was measured by Shimadzu UV-2501PC Spectrophotometer.

Results and discussion

Transmission and absorption edge

The optical transmission versus wavelength for a crystal was measured both transversly and along the longitudinal axis (Fig. 4 left). All curves are not corrected for absorption and reflection losses. As shown in Fig. 4 left, the intensity of the transmitted light at wavelength longer than 400nm is over 80%, then gradually decreases to 75% around 300nm and cut off at about 245nm. Compared with other published results where the absorption edge was reported at 280nm[4], the absorption edge of our PbF_2 crystals shifts about 30nm forward short wavelength. Based on energy band theory, the energy gap of PbF_2 crystals is 5.84eV[5] corresponding to 212nm. The fact that the absorption edge of our PbF_2 crystal is more closed to the theoretical one than other producer's indicates that the non-vacuum method is superior to vacuum one for growing PbF_2 crystals.

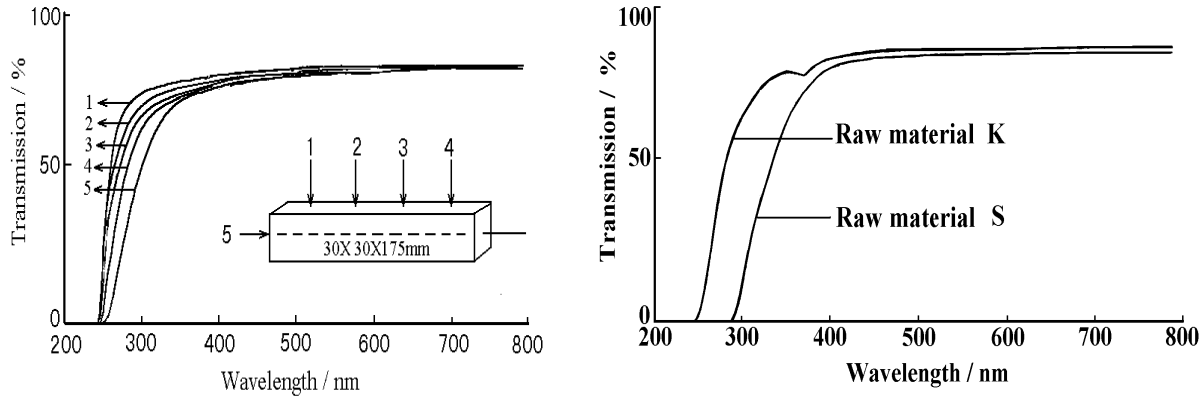

Fig. 4 Transmission varies with the spatial position of the crystal (left) and the raw materials (right)

The transverse transmission varies with position of the crystals: it decreases from the beginning to the finishing end (which grown late in the growing process). This effect is rather stronger for light with shorter wavelength. There are at least two factors that are responsible for the phenomena: one is impurities usually accumulated at the later stage, the other is some micro defects often appeared in the late grown part, such as scattering centers, needle-like defects and so on.

On the other hand, the transmission is strongly dependent on the kind of the raw materials. As shown in Fig. 4 right, the grown PbF_2 crystals from different starting materials have different transmission curves, especially the cut off edge. However, it is difficult to identify which elements cause the deference of transmission among different raw materials. Based on the chemical analysis results, impurities in the raw materials are suggested to be responsible for the decrease of transmission at shorter wavelengths.

Transmission and doping amount

Scavenger plays a key role in the non-vacuum growth of lead fluoride crystals. Without scavenger, it is impossible to grow lead fluoride crystals within atmosphere. However, the doping amount of scavenger is also an important factor. If the doping amount is too low to deprive oxygen impurities from the raw materials and the growth system, the grown crystal

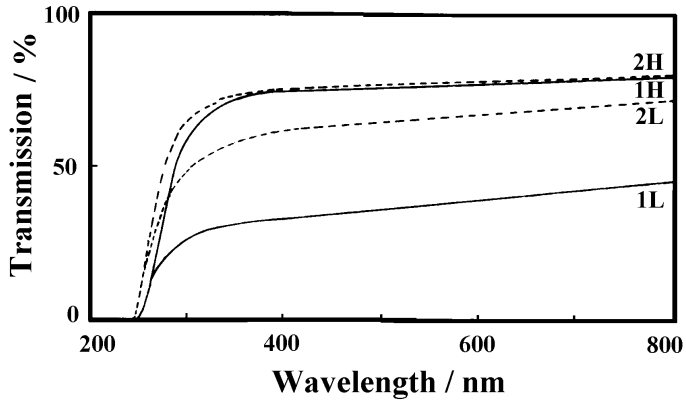

Fig. 5 Dependence of the transmission of PbF_2 crystals on the doping amount of scavenger (1/2: raw materials; H/L: doping amount of scavenger is High or Low)

will be contaminated by oxygen. As shown in Fig. 5, no matter for raw material No.1 or No.2, when the doping amount increases from 1 wt.‰ to 2 wt.‰, the transmission of the crystals increase greatly. It is worth to say, the cut off edge of the crystal keeps constant for the same raw material, no matter its transmission increases or decreases. When the doping amount is less 1 wt.‰, there will appear a lot of needle-like defects. According to our observation with optical microscope, these defects are slip lines related with oxygen. When the doping amount increases to 2 wt.‰, these slip lines disappear and the transmission rises. But if the doping amount of scavenger is too high, the grown crystals will become easy to crack.

Energy resolution

The energy resolution of 9 pieces of PbF_2 crystals with size of 30×30×166mm was tested in Mainz university of Germany. With direct electron beam on the crystals at low rate, an energy resolution of 3.5% at 855MeV was determined, and at 450MeV and 705MeV, the value is: $\sigma / E = 3.2\% / \sqrt{E}$

With scattered particles from liquid hydrogen target and for elastic electrons at 734MeV, an energy resolution of 3.7% was obtained (Table 1). Woody et al have measured the energy resolution of PbF_2 crystal supplied by Optovac and obtained a resolution of $\sigma/E=5.95\%/\sqrt{E}$ for the 3×3 array and $\sigma/E=5.70\%/\sqrt{E}$ for the 5×5 array from 1-3 GeV. Compared with these test results, our $3.2\%/\sqrt{E}$ represents the best energy resolution measured with PbF_2 so far.

Table 1. Energy resolution of lead fluoride crystals grown with non-vacuum method

Crystal Size(mm)	Energy(MeV)	855	734	450 705
30×30×166	Resolution(%)	3.5	3.7	$3.2/\sqrt{E}$

Radiation hardness

Radiation hardness is one of the key considerations in choosing materials for detectors in high-rate environments. To study the irradiation of PbF_2 crystals, a 166mm long sample was irradiated by photons from a ^{60}Co source with a dose of 10 krad. Fig. 6 shows the transmission of the sample before irradiation (curve 1) and after irradiation (curve 2). All these curves in

Fig. 6 was corrected for reflection losses and thickness. When the irradiated crystal was annealed with 365nm filtered light for a few minutes, the transmission can recover completely at longer wavelength, and only little residual damage was remained at very short wavelengths below 280nm (curve 4). Even though, it is clear that the radiation hardness has been greatly improved over that grown by vacuum method in the past.

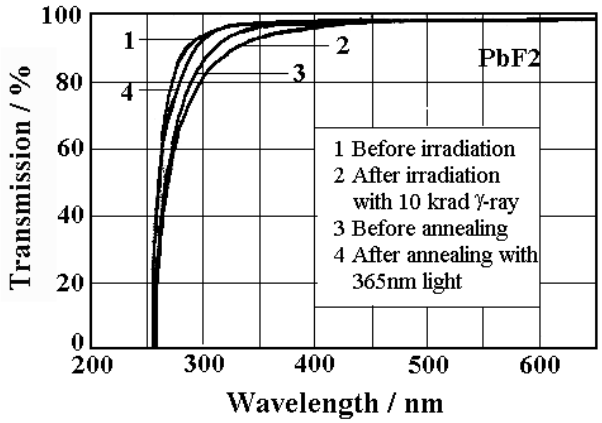

Fig. 6 Transmission of PbF_2 crystals before and after irradiation with 10 krad γ-rays as well as before and after annealing with 365nm filtered light

References

1. W. S. C. Williams and Caplan, A lead fluoride total-absorption spectrometer for high-energy electron and photons, Nature, 1957, **17**(4571): 1185-1186
2. E. B. Dally and R. Hofstadter, High energy γ-ray detector with good resolution, The Review of Scientific Instruments, 1968, **39**: 658-659
3. YOSHIO YOSHIMURA and AKIHIRO MAKI, New lead glasses for Cherenkov counters, Nuclear Instruments & Methods in Physics Research, 1975, **126**: 541-547
4. D. F. Anderson, et al, Lead fluoride: An ultra-compact Cherenkov radiator for EM calorimetry, Nuclear Instruments and Methods in Physics Research, 1990, **A290**: 385-389
5. Paul R. Findley, et al., Phys. Rev. B, 1983, **28:**4761-4767
6. C. L. Woody, et al., A study on the use of lead fluoride for electromagnetic calorimetry, IEEE Transaction on nuclear science, 1993, **40**: 546-551

Synthesis and scintillation properties of several borate oxides

[1]Lebbou O., [1]Dujardin C., [1]Goutaudier C., [1]Cohen-Adad M.T.,
[1]Pedrini C., [1]Moine B., [1,2]Belsky A.N.

[1]Laboratoire de Physico-Chimie des Matériaux Luminescents, Unité Mixte de Recherche 5620 CNRS- Université Lyon1, 69622 Villeurbanne Cedex
[2]Synchrotron Radiation Laboratory, Physics Faculty, Moscow State University, 118998 Moscow, Russia

Abstract. $LnAl_3(BO_3)_4$ (Ln=Gd, Y or Lu) powders doped with Ce^{3+} have been prepared and analyzed. Main chemical and fluorescence properties are given. Cerium ion exhibits in these materials a 25 ns fluorescence in the ultra violet range (maximum at 340 and 365 nm).

Keywords: borates, cerium

Introduction

Recent works on $LuBO_3$ doped with Ce^{3+} have shown very promising scintillation properties. The measured light yield on powders is between 24000 and 27000 photons / Mev [1,2,3]. The decay time of cerium under UV excitation is nearly 30 ns. Unfortunately, all crystal growth attempts of reasonable size crystals failed for two major reasons: phase transition between the calcite and the vaterite structure induces severe damage in the crystal during the cooling procedure, and the low evaporation temperature of boron changes two much the stoechiometry of the melt. Other boron systems (aluminates for example) may be obtained in crystal form.

The purpose of this contribution is to present preliminary chemical, optical as well as scintillation properties of $LnAl_3(BO_3)_4$ (Ln=Gd, Y or Lu) doped with Ce^{3+}.

Material preparation and analysis

The samples were synthesized by means of solid state reaction. In the preparation of mixture, a small excess of H_3BO_3 was used to compensate the volatilization of B_2O_3 during heating.

Several grinding and firing cycles were needed to obtain complete reaction and well crystallized specimens.

The nominal composition was calculated through the weight losses during each thermal treatment. The purity of the samples was controlled by X-ray diffraction.

$LnAl_3(BO_3)_4$ with Ln = Gd, Y or Lu is isostructural of the huntite $Mg_3Ca(CO_3)_4$ [4] which is rhombohedral double – carbonate based on a deformation of the NaCl face centered cube. It belongs to the space group R32.

In a such structure :

- boron atoms are three- fold coordinated and isolated groups form superposed layers parallel to the hexagonal base. In two successive layers, borate groups are disposed in 180° rotation.
- each Al atom is inside an octahedral formed by six oxygen belonging to borate groups.
- Ln is located into a right trigonal prism formed by six oxygen belonging to borate groups.

Nuclear magnetic resonance has been performed and spectra point out the three – fold coordination number of B atoms [5] and show a unique Ln and Al site. ATD-TG experiments indicate that $GdAl_3(BO_3)_4$ has a congruent melting point near 1254°C (figure 1a, 1b, 1c). At the exact stoechiometry $GdAl_3(BO_3)_4$, a only one thermal effect is observed corresponding to the congruent melting point of the compound and showing the lack of possible structure change. When B_2O_3 content changes, a second thermal effect appears before the melting of mixture traducing phenomena which cannot be attributed to a decomposition of $GdAl_3(BO_3)_4$ before melting. This second effect corresponds to the crossing of more complex equilibrium field. Between 1209 °C and 1241 °C for 58.3% of $BO_{1.5}$ and between 1222 °C and 1242 °C for 49% of $B0_{1.5}$, the only present phase is liquid + solid $GdAl_3(BO_3)_4$. When temperature is higher than 1241 °C or 1242 °C, the mixture is liquid. The decrease of the melting temperature with the change of $BO_{1.5}$ content confirms the congruent melting of $GdAl_3(BO_3)_4$. The characteristic parameters of $LnAl_3(BO_3)_4$ are given in the table I.

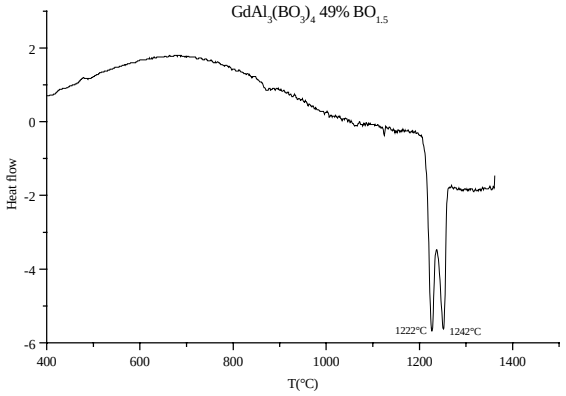

(a)

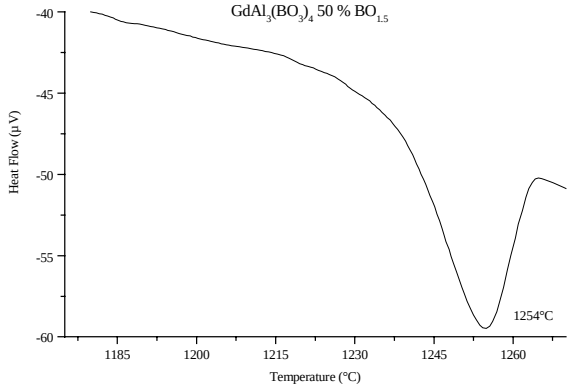

(b)

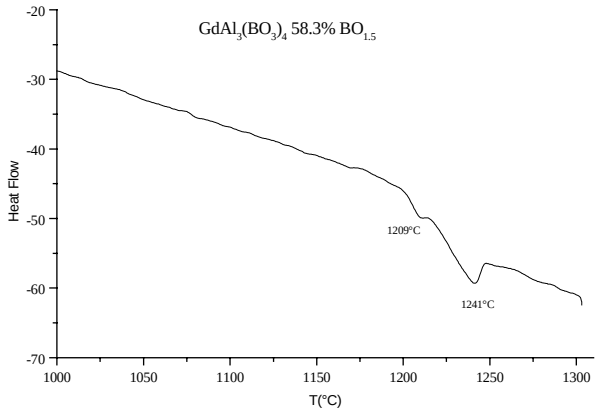

(c

figure 1: Change of melting point of $GdAl_3(BO_3)_4$ with composition

Spectroscopic and scintillation properties

The Ce^{3+} is well-known to exhibit fast UV fluorescence resulting from the 5d → 4f radiative recombination. In $LnAl_3(BO_3)_4$ (Ln=Gd, Y or Lu) under UV excitation (4.6 eV, 270 nm), the emission spectrum is composed of two bands extending from 2.9 to 3.8 eV (325 to 425 nm).

Table I: Characteristic parameters of $LnAl_3(BO_3)_4$

Formula	Ionic radius (Å)	Melting point (°C)	Lattice parameter (Å)	Density (g/cm^3)
$LuAl_3(BO_3)_4$	0.861	1272	a=9.243 c=7.199	4.593
$YAl_3(BO_3)_4$	0.900	1265	a=9.268 c=7.238	3.755
$GdAl_3(BO_3)_4$	0.938	1254	a= 9.294 c=7.254	4.346

The splitting is 0.26 eV. The excitation spectra exhibit five bands resulting from the splitting of the 5d orbital under the D_3 site symmetry as observed in the Eu^{3+} doped Y based material [6]. All the results are presented in figure 2 and major emission and excitation band positions are reported in table 2. For the Y materials, results are in good agreement with reference [7]. All these positions are obtained with a fitting procedure using gaussian functions. Under 320 nm excitation, the decay time of the Ce^{3+} emission is around 25 ns for the three compounds. After normalization of the excitation band peaking around 3.8 eV, the relative amplitude of the two bands (4.6 and 4.9eV) decreases with the Stokes shift (0.2, 0.18, 0.17) from Gd, Y to Lu compounds. But the energy difference between the second state (~ 4.5eV) and the emission band varies in the opposite direction (0.83, 0.89, 0.95 eV) from Gd to Lu based powder. This different behavior is explained by the different evolution of the ionic radii difference between the activator (Ce^{3+} r= 1.14 Å) and the Ln^{3+} ion (r_{Gd}= 1.08 Å, r_Y= 1.015 Å, r_{Lu}= 0.97 Å). These value are for 8-fold coordinate ions. The evolution of the relative amplitude may be explained by non-radiative processes [8]. Thermal dependence of these excitation spectra as well as kinetics studies are in progress.

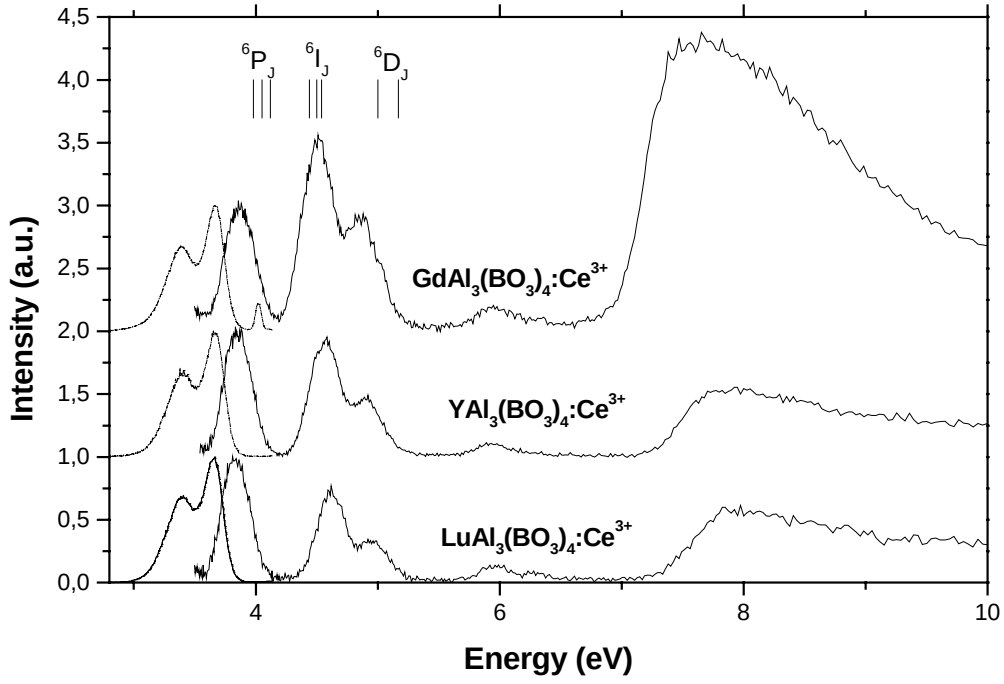

Figure 2.dashed line: emission spectra at room temperature using 4.6 eV excitation (270 nm). Solid lines: excitation spectra with a 380 nm filter (3.26 eV). Positions of the Gd^{3+} excited states are also reported.

Table 2: Peak positions (eV) of Ce^{3+} emission and excitation bands.

Ln	Ce emission	Ce excitation	Fund. abs. edge	STE emi.
Lu	3.66,3.40	3.83,4.61,4.96,5.94,6.2	~ 7.3	~ 4.13
Y	3.67,3.41	3.85,4.56,4.91,5.91,6.2	~ 7.3	~ 4.13
Gd	3.67,3.40	3.87,4.50,4.87,5.92,6.2	~ 6.9	no

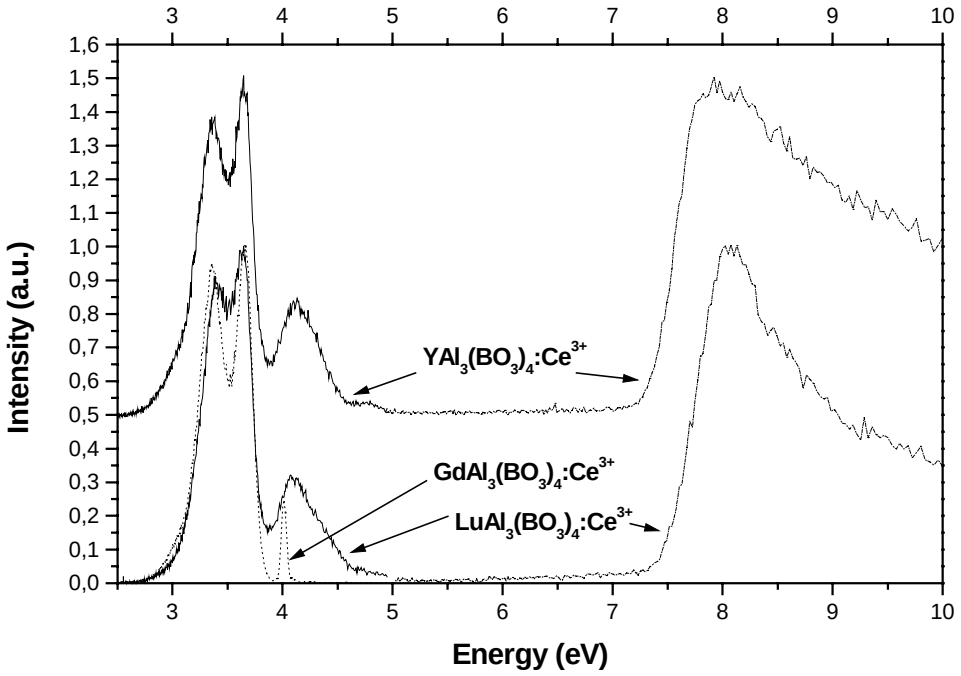

Figure 3.Solid and dot curves: emission spectra at room temperature under X-ray excitation (40 kV). Dashed line: excitation spectra with a 300nm filter (4.13eV)

Under X-ray excitation, additional emission band around 4.13 eV (300 nm) appears for Y and Lu aluminate borates. This emission is due to self-trapped exciton (STE) as observed in many compounds. Excitation band of this emission are presented in figure 3. This emission does not match completely with the Ce^{3+} excitation bands, which is not very favorable for radiative transfer to Ce^{3+}. The Gd compound does not exhibit such band but the 310nm Gd^{3+} due to ^6P_J to $^8S_{7/2}$ radiative recombination. In such situation, only Gd^{3+} to Ce^{3+} transfer occurs since the Ce^{3+} emission does not overlap the lowest Gd^{3+} state. We are in the situation defined as group III in reference [9]. In addition this compound exhibits a higher excitonic transfer to Ce^{3+} than for the other materials. It means that a very efficient non radiative transfer from STE to Gd^{3+} occurs which then transfer to Ce^{3+}. Change in the emission spectra shape under X-ray or UV excitation may be due to a reabsorption process from Ce^{3+}. Penetration depth of X-rays (high voltage 40 kV) is higher than for UV in powders. The excitation band strongly overlaps the emission and emission from Ce^{3+} perturbed centers appear as a shoulder in the low energy part of the emission spectrum under X-ray excitation.

Conclusion

In the view of crystal growth attempt, ATD-TG measurements have been performed. These experiments indicate that $GdAl_3(BO_3)_4$ has a congruent melting point at about 1254°C. Similar measurements on Lu and Y based compounds are actually in progress. First spectroscopic results on cerium doped $LnAl_3(BO_3)_4$ are given. Cerium emission under UV excitation occurs between 325 nm and 425 nm with a decay time of 25 ns. Under X-ray STE emission at 300 nm appears except in the Gd-based compound. It is remarkable that excitonic excitation band for Gd compounds as well as excitations with slightly higher energy is very intense relatively to the first Ce^{3+} excitation band in comparison of the two other compounds. The light yield should be better for this compounds. Careful light yield of these powders will be performed, but first feeling suggest that intensity of the emission spectra under x-ray excitation looks similar to $LuBO_3:Ce^{3+}$.

References

1. C.W.E. van Eijk, Proceeding of the International Conference on Inorganic Scintillators and Their Applications, Shangai, PR China, September 22-25,1997, p3
2. L.Zhang et.al., Proceeding of the International Conference on Inorganic Scintillators and Their Applications, Shangai, PR China, September 22-25,1997, p303
3. W.W.Moses et al., Proceeding of the International Conference on Inorganic Scintillators and Their Applications, Shangai, PR China, September 22-25,1997, p358
4. L. Graf and W. F. Bradley, Acta Cryst. (1962).15, 238
5. P. S. Marchetti, D. Kwon, W. R. Schmidt, L. V. Interrante and G. E. Maciel, Chem. Mater. (1991), 3, 482-486
6. F.Kellendonk, G.Blasse, Phys.Stat.Sol. (b), **108**, 541 (1981)
7. M.J.Knitel, New Inorganic Scintillators and Storage Phosphors for Detection of Thermal Neutrons, 1998 p77
8. G.Blasse, A.Brill, The Journal of Chemical Physics, Vol. 47, n°12 (1967)
9. P.Dorenbos, J.C.van't Spijker, C.W.E. van Eijk, Proceeding of the International Conference on Inorganic Scintillators and Their Applications, Shangai, PR China, September 22-25,1997, p307

The application of skull melting process for refractory scintillators production

E.E. Lomonova, S.Ch.Batygov, M.A. Borik, L.N. Dmitruk, Yu.K. Voron'ko, V.V. Osiko.

General Physics Institute, Vavilov Street,38, Moscow 117942, Russia

Abstract. Large amount of scintillating crystals will be needed in near future for medical diagnostics and for high energy physics. It is important to develop more economical processes which provide cheaper crystals. This requirement can be satisfied by using «skull» melting process, which means direct RF-heating of the melt in a water cooled container with subsequent crystallization. It can be applied to the great variety of different chemical compounds. Then in some cases large scale crystallisation can be accomplished. As a result large amounts of single crystals (some tens of kilograms) can be grown in one run.

Keywords: single crystal growth, fast scintillators, refractory oxides, skull melting.

Introduction.

Single crystals of refractory oxides play an important role in modern material science and technology. They can be used as active media in lasers, in non-linear optics, as essential components in microelectronic devices ea. At present some refractory oxide single crystals are interesting as fast bright scintillators. Most of these materials have melting points of about 1500ºC, though some of them are 2000ºC or even higher.

The single crystals of refractory oxide compounds are grown by conventional crucible technique (Chohralsky, direct crystallization), which uses heated crucibles fabricated of noble metals such as iridium. Large amount of scintillating crystals will be needed in near future for medical diagnostics and for high energy physics. By this reason it is important to develop more economical processes which provide cheaper crystals. This requirement can be satisfied by using skull melting process, which means direct RF-heating of the melt in a water cooled container with subsequent crystallisation.

The radio frequency heating technique has been applied to metals since the beginning of the twentieth century. In the mid -1960s it was used to melt oxide dielectric materials both in France and the Soviet Union [1-2]. This technique is used to produce refractory ceramic materials, to prepare complex oxide components in the melt, to make glass and to grow crystals.

A possible method of melting of dielectric materials has been proved in principle by French researchers. One of their most important results was the melting of dielectrics in a cold container. At the same time, a group of Soviet scientist develop this technique for producing refractory single crystals from the melt. A review paper on rf melting in cold crucible was published in 1978. At present this technique attracts growing attention.

Growth of single crystals by direct radio frequency melting in a cold container.

At room temperature electric resistivities of dielectric materials are 10^{-4}-10^{14} ohm.cm. However their electric resistivities decrease to 0,01-100 ohmxcm at temperature close to their melting point and then their conductivity's increase during the melting. As result the melt can directly absorbs the rf field energy effectively.

The procedure of skull melting and crystallisation of refractory oxides consists of four steps (fig 1).

1. Local heating of the material from room temperature up to that of melting, which can be achieved directly by RF-heating, (so - called melt seeding); after local melting the seeding melt drop becomes able to absorb RF energy independently and grow in volume.
2. Melting of the charge with subsequent pouring the initial power material into crucible until the desired volume of the melt is reached.
3. Establishment of optimal electrical parameters of RF-generator and heat equilibrium conditions in the melt and solid shell(skull) system.
4. Crystallisation of the melt.

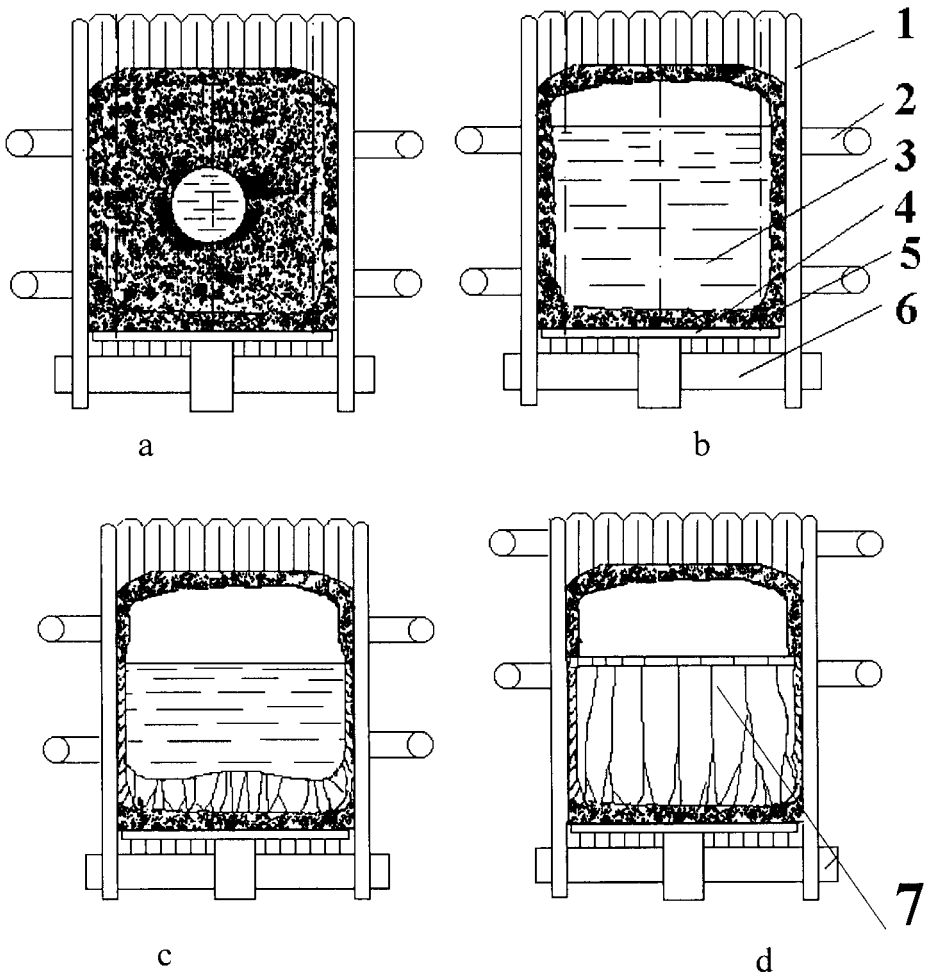

Fig. I. Illustration of the initial melting(a), melt-solid equilibrium(b), and direct crystallisation (c-d) in the cold container. (1)-water-cooled tubing; (2)- RF coil water, (3)- melt (4)-cooled bottom (5)- solid shell, (6)-insulating bottom of micalex, (7)-crystals.

As usually small portion of the metal, which forms the oxide, is incorporated in the charge in order to initiate the seed melting process. The pieces of seed metal absorb RF-energy and are rapidly heated. Additional heat is provided due to exothermic oxidation of the metal. The overheated metal melts surrounding charge, which begins to absorb RF energy independently(fig 1.a). The rest metal oxidises in air atmosphere and admix itself to the charge without any contamination of the melt.

When the volume of the melt reached desired level it is necessary to achieve thermal and spatial equilibrium between melt and solid polycrystalline shell or skull (fig.1b). Phase equilibrium means that the temperature of any point of the interface is equal to the melting temperature, and does not change in the course of time. The single crystal can be grown by

different methods. One of the most simplest method is direct crystallisation of the melt by pulling down of the cold crucible relatively inductor of RF-generator (fig. 1c-d). The cold container and the installation «Kristal -403» for melting and direct crystallisation of refractory materials are shown in fig 2.

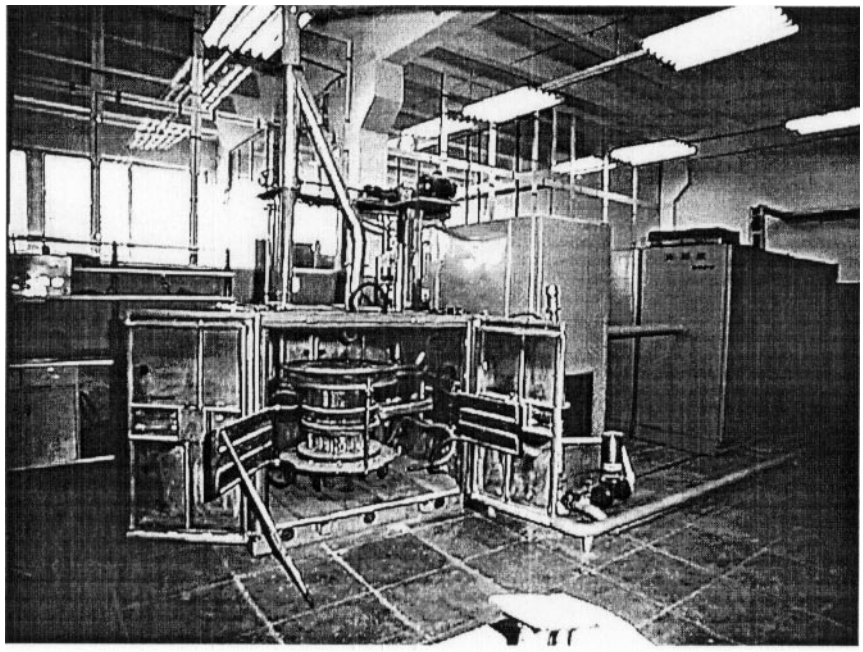

Fig.2. The installation «Kristal -403» for melting and direct crystallisation of refractory materials.

The obvious advantage of the skull melting and crystallisation are as follows:

1.The temperature of the process is not limited and may reach 3000^0C or higher.

2.There is no contact of the melt with the crucible material; this provides high «purity» of the process and give possibility of growing of chemical active compounds is possible.

3.Freedom of choosing any gas atmosphere.

Therefore skull melting can be applied to the great variety of different chemical compounds. Opportunity of the effective screening of new scintillating compounds appears.

Then in some cases large scale crystallisation can be accomplished. As a result large amounts of single crystals (some tens of kilograms) can be grown in one run. The crystallisation equipment which is available at present can simultaneously melt from 0,5 up to 120 kg of charge (table 1).

Table 1. Commercially available installation for CZ and PSZ skull melting and crystallization.

Commercially available installation	«Crystal 401»	«Crystal 403»	«Crystal 405»
Total electrical power, kW	100	250	250
Power of oscillations, kW	60	160	160
Frequency of oscillations, MHz	5.28	1.76	1.76
Crucible diameter, m	0.2	0.4	0.5
Crucible height, m	0.3	0.7	1.0
Productivity, $kg.h^{-1}$	0.3-0.5	2-3	4-5

A great number of simple and complicated individual oxide and solid solution single crystals have been grown by skull melting (table 2). Most of these oxides can be activated successfully with rare earth and transition metals and show an effective luminescence in ultraviolet, visible and infrared regions of spectra.

Table 2. Single crystals grown from a cold crucible [2].

Compounds	T_m[a], °C	Growth	Growth conditions				Crystal
		method	RF power, kW	frequency, MHz	Crucible diameter, mm	Gas medium	size, mm
Al_2O_3	2046	CZ,DZ	-	-	80	-	d=10-35 l=160; 1=1-3
$BaTiO_3$	1618	DC	60	5.28	80, 120	air	5x510
$BaWO_4$	1490	DC	60	5.28	80, 120	air	5x5x10
$Bi_{12}GeO_{20}$	930	CZ	5	1-10	-	-	d=20, l=70-80
$CaTiO_3$	1970	DC	60	5.28	80, 120	air	5x5x10
$CaWO_4$	1560	DC	60	5.28	80, 120	air	5x5x10
CeO_2	2700	DC	60	5.28	50-80	air	vol=1-3cm^3
CoO	1805	DC	60	5.28	50-80	air	vol=1-3cm^3
Er_2O_3	2400	DC	-	-	-	-	l=1-3
$ErCrO_3$	2300	DC	60	5.28	80, 120	air	1x1x10
Fe_3O_4	1560	DC	60, 20	5.28, 3	50-80 60, 85	air $CO-CO_2$	vol=1-3cm^3 l=2
Fe_3O_4-$FeTiO_4$	-	DC	20	3	60, 85	$CO-CO_2$	l=10
Gd_2O_3	2395	DC	-	-	-	-	l=1-3
$LaCrO_3$	2430	DC	60	5.28	80, 120	air	1x1x10
Ln_2NiO_4(Ln-La, Pr, or Nd)	-	DC	20	3	60, 85	$CO-CO_2$	4x4x6
$Ln_2Ti_2O_7$(Ln-Sc, Y, La, Nd, Sm, Eu, Dy, Tb, Gd, Ho, Er, or Yb)	1600-1900	DC, CZ	60	5.28	80, 120	air	l=2-12 d=3, l=8
$M_{1-x}O$(M-Mn, Co, Fe, or Ni)	2000	DC	20	3	60, 85	$CO-CO_2$	l=10
$MnZnFe_2O_4$	-	CZ[d]	-	-	-	-	d=10-17, l=100
Nd_2O_3	2300	DC	60	5.28	50-80	air	l=1,5
$Nd_3Ga_5O_{12}$	-	CZ	100, 75	1-7, 7-10kHz	80	-	d=35, l=92
Pr_2O_3	2250	DC	60	5.28	50-80	air	l=1,5
Sc_2O_3	2405	DC	-	-	-	-	l=1-2
$Sc_2Zr_2O_7$	2700	DC	-	-	-	-	l=1-2
$SrTiO_3$	1910	DZ CZ	60	5.28	80, 120 130	air	5x5x10 d=15, l=30
TiO_2	1855	DC	60	5.28	50-80	air	vol=1-3cm^3
Y_2O_3	2410	DC	-	-	-	-	l=1-3
$Y_3Al_5O_{12}$	1930	DC	-	-	-	-	l=1-3
$YCrO_3$	2290	DC	60	5.28	80, 120	air	1x1x10
$ZrO_2(HfO_2)$-MgO,CaO, SrO, Sc_2O_3, Y_2O_3,Ln_2O_3	2700-3000	DC	20, 60, 160	0,44, 1.76, 5.28	50-500	air	~0,5-5kg
Si	1470	CZ	-	250-470kHz	31, 75	Ar	d=15-25

[a]T_m=melting point;
[b]CZ=Czochralski method, DZ=directional crystallisation;
[c]l=length, d=diameter;
[d]Czochralski method with radiation heating

For example this technique was most successfully applied to growth of a new class of single crystals -cubic solid solution based ZrO_2 -fianites (fig.3). The technology and applications of fianite crystals is currently develop. Crystals size and optical homogeneity have been shown to depend on the melt composition and crystallisation conditions.

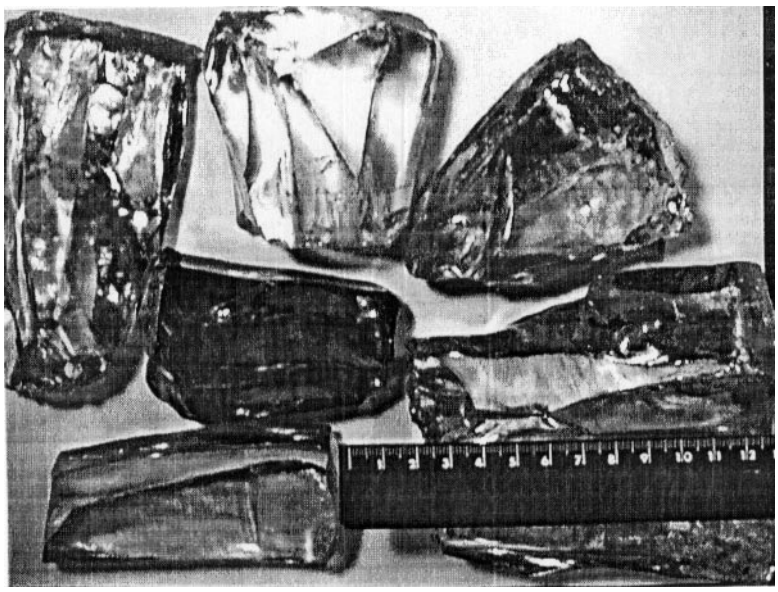

Fig 3. The -cubic solid solution based ZrO_2 single crystals -fianites

We can suppose that some oxide single crystals doped with rare earth elements (for example Ce^{3+}) as well as some single crystal oxide solid solutions (for example $ZrO_2(HfO_2)$ - CaO (MgO, Y_2O_3) can be used as perspective fast scintillates. The production of such single crystals will be economically more effective in comparison with the production of refractory scintillators with crucible techniques.

Conclusion.

Up to now the skull melting technique was not used to produce scintillating single crystals. However on the basis of our experience it is possible to consider the skull melting as very perspective technique for industrial production of the refractory scintillators as well as for search of new high density, fast scintillators.

References

1. 1.Aleksandrov V.I., Osiko V.V., Prochorov A.M., Tatarintsev V.M., Synthesis and Crystal Growth of refractory Materials by RF Melting in a cold Container. Curr.Top.Mater.Sci., 1, 421-480, 1978.
2. 2.Osiko V.V., Borik M.A., Lomonova E.E. Crucible-Free Methods of Growing Oxide Crystals From the Melt.,Ann.Rev.Mater.Sci. 17, 101-122, 1987

Growth and luminescence of LaB_3O_6 single crystals: pure and doped by Ce.

A.N.Shekhovtsov, M.F.Dubovik, A.V.Tolmachev, B.V.Grinyov, T.I.Korshikova, M.V.Dobrotvorskaya, E.F.Dolzhenkova, V.N.Baumer.

Institute for Single Crystals, NAS of Ukraine, 310001, 60 Lenin Ave., Kharkov, Ukraine.

Abstract. In present paper pure and doped by Ce LaB_3O_6 single crystals were grown in air atmosphere by the Czochralski technique from melt in the platinum crucibles. Absorption, X-ray and thermoluminescence spectra of pure and doped by Ce LaB_3O_6 single crystal are investigated. The thermoactivating parameters are calculated. Energy band structure of the LaB_3O_6 single crystal was determined by the XPS method.

Keywords: crystal growth, luminescence, borate compound.

Introduction

During recent years, search for new materials for registration of different types of radiation is being intensively carried out. Inorganic scintillators, namely borate compounds, find a wide application in different regions of science and industrial. LaB_3O_6 is one of the more interesting borate compounds [1], but all data about optical and scintillation properties of this single crystal were obtained on powder or polycrystalline samples. Authors of this paper made endeavour of growth of LaB_3O_6 single crystals by the Czochralski method and briefly described some optical properties of this crystal.

Experimental

LaB_3O_6 crystals belong to C2/c space group. Up to now LaB_3O_6 single crystals of small size have always been grown by solution-melt method and by hydrothermal method [2]. To grow these single crystals we used Czochralski method. The growth was carried out in growing installation with ohmic heating. The temperature was controlled by precision temperature regulator which provided the possibility of changing the temperature according to linear law with little speeds and the temperature maintain in the working zone with an accuracy of 1^oC.

The LaB_3O_6 charge of stoichiometric composition was synthesized according to ceramic technique. Activator inserted into the charge in amount 0,5 at.% Ce. The charge was loaded in a platinum crucible with a diameter 30 mm. Preliminary experiments shown the possibility of stable growth in this system. Large single crystals LaB_3O_6 were obtained on the melt surface by spontaneous crystallization with a cooling rate 30 ºC/h (Fig.1). The largest faces to be the (101) plane. We initially performed crystallization on platinum wire, and than on an oriented seed. Numerous growth runs have here to for been made to determine optimum growth condition. Single crystals up to about 8 mm in diameter and 15 mm in length were grown from the melt under conditions of crystal pulling rate of 0,7 mm/h and rotation rates of 20 $min^{-1.}$. An axial temperature gradient over the melt surface did not exceed 15 ^{0}C/cm. Obtained single crystals thermally annealed in the growing installation after separating from the melt and than slowly cooled with a furnace to the room temperature.

Crystals were transparent and possessed large regions free of any optical inhomogeneity. The phase body composition was checked by X-ray phase analysis method. The X-ray phase analysis data have shown that there is about 10 % $LaBO_3$ phase.

Main crystal data (a=9.946(1), b=8.163(1), c=6.4965(5) A, β=127.06(1), V=420.9 A, Z=4, d_{cal} =4.219 g/cm^3, F(000)=480, μ(CuKα)=78.16 mm^{-1}) were determined using powder SIEMENCE D500 diffractometer (CuKα radiation, graphite monochromator on the diffracted beam) and refined by Rietveld full profile analysis in the 2Θ range from 10 to 161^0. Atomic coordinates were refined using FULLPROF program package (full matrix, thermal anisotropy parameters for La atoms and isotropic ones for B,O atoms). Analysis of Ce-substituted samples do not revealed extra peaks in the difference Fourier map. This fact allows to assume that cerium atoms substitute lanthanum ones in their crystallographic position.

Our crystals were cleavage along (101) plane under mechanical deformation. Investigation by optical microscope reveals surfaces of nearly absolute cleavage.

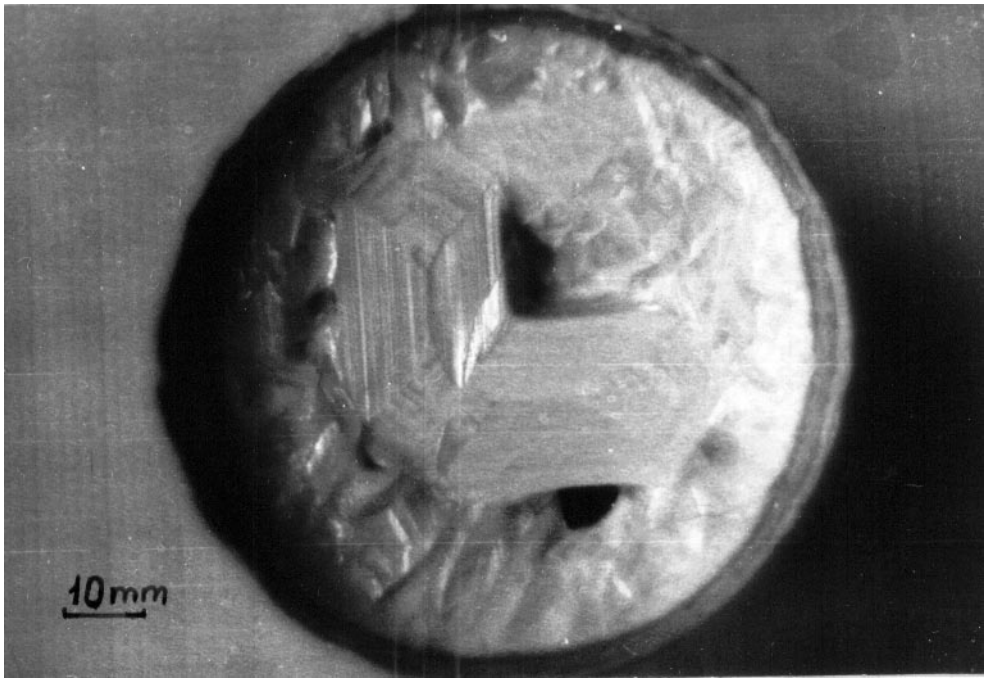

Fig.1. Morphology of LaB_3O_6 single crystals grown by spontaneous crystallization. The growth surface parallel to the (101) plane.

To carry out measurements, 4×4×1 mm transparent polished samples were made. X-ray luminescence was measured using the automated unit SDL-2 (produced by LOMO). Thermoluminescence was investigated within 290-600 K temperature range, the sample heating rate equaling 20 K/min. The absorption spectrum was measured by means of SPECORD M40 two-beam spectrophotometer. KRATOS automated equipment was used for measurement of X-ray photoelectron spectra.

Results and discussion

Shown in Fig.1 is the absorption spectrum of undoped LaB_3O_6 single crystal. The absorption spectrum of undoped LaB_3O_6 single crystal has one band with a maximum at 250 nm. The analysis of the absorption spectrum of the undoped crystal allows to conclude that peak at 250 nm appropriates to the edge of intrinsic absorption. This magnitude is typical for metaborates of rare-earth compounds [3]. The absorption of 4f-5d cerium states in LaB_3O_6:Ce was not observed due to a low concentration of Ce.

The luminescence spectra of pure LaB_3O_6 single crystal and doped by Ce at 290K were obtained in 300-450 nm region under the X-ray excitation (Fig.3.). The X-ray luminescence spectrum of pure LaB_3O_6 single crystal (Fig.3, curve 1) is characterized by the presence of the one wide peak at 342 nm. This peak, seemingly, correspondences to the emission relaxation

of autolocalized excitons, which takes place into oxide crystals [4]. The introduction of Ce additives, even in low concentrations, leads up to the strength quenching of the X-ray luminescence of LaB_3O_6 single crystal and shift of peak (Fig.3, curve 2) in 360 nm region. The excited state of Ce^{3+} disposes in all likelihood near of the bottom of conduction band and following recombination on ground state of Ce^{3+} takes place.

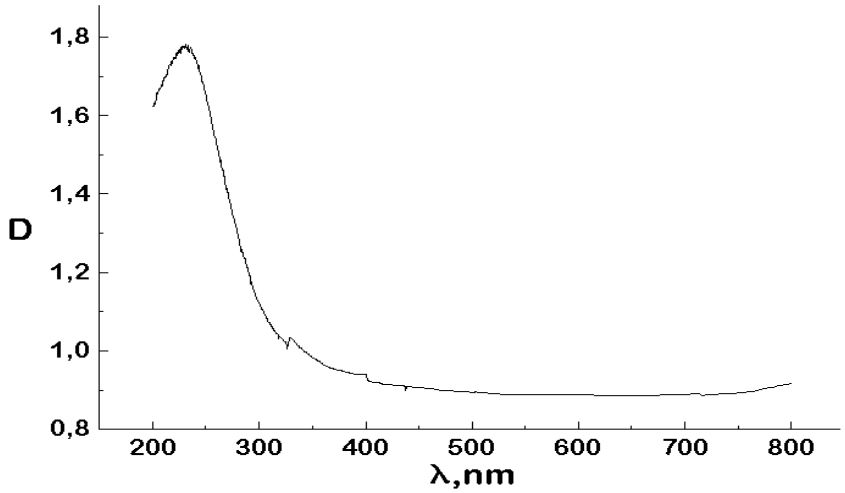

Fig.2. Absorption spectrum of undoped LaB_3O_6 single crystals.

Color centers in LaB_3O_6 single crystals are created under the ionizing radiation. Fig.4 presents

Table.

Activation energy, eV	Frequency factor, sec^{-1}	Light time, sec
0.82	~10^8	~59

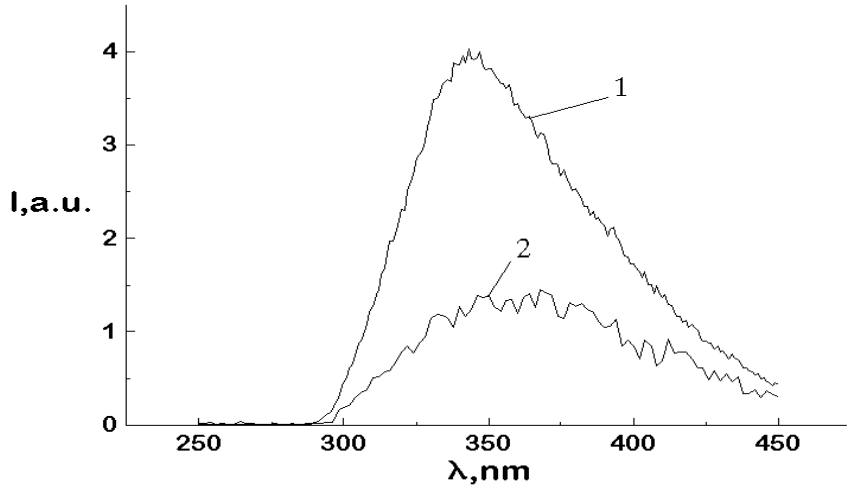

Fig.3. X-ray luminescence spectrum: 1-pure LaB_3O_6 single crystal, 2- LaB_3O_6 single crystal doped by Ce. The luminescence intensity of LaB_3O_6:Ce increased in ten times.

the thermostimulated luminescence curve of pure single crystals, irradiated with $3*10^3$ R dose. It known [5], that one of the possible types of the radiation defects in borate crystals are boron atoms in the interstices of crystal lattice. Therefore, this peak can be connected with emission relaxation of such radiation defects. The thermoactivating parameters are calculated according to [6] and presented in the Table. The activation of LaB_3O_6 single crystals by Ce^{3+} lead up to disappearance of peak on the thermostimulated luminescence curve. This fact can be connected, seemingly, with changing of charge state of $Ce^{3+} \rightarrow Ce^{4+}$ after irradiation and following $Ce^{4+} \rightarrow Ce^{3+}$ restoration after heating.

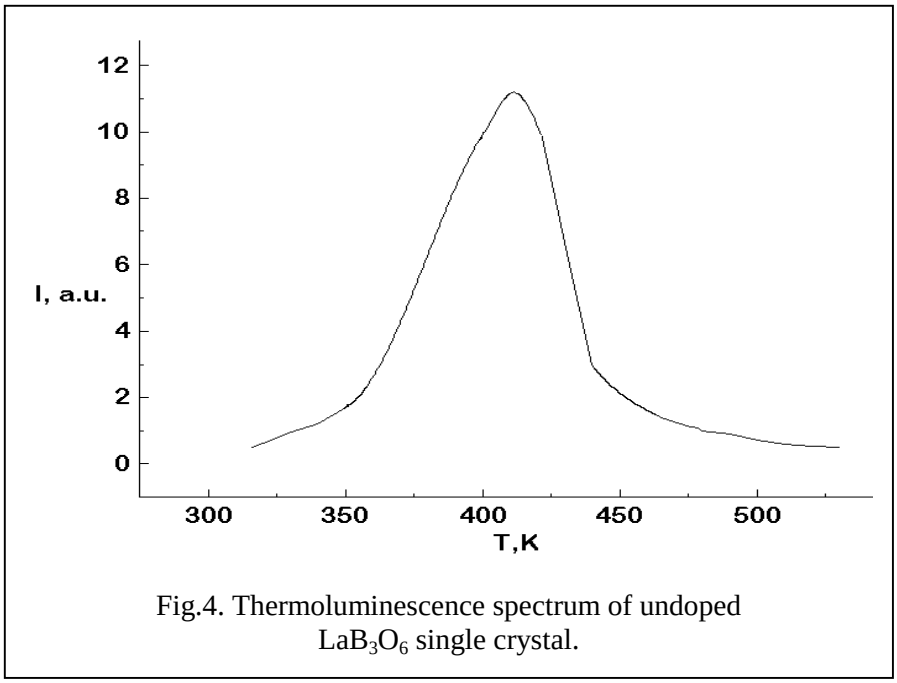

Fig.4. Thermoluminescence spectrum of undoped LaB_3O_6 single crystal.

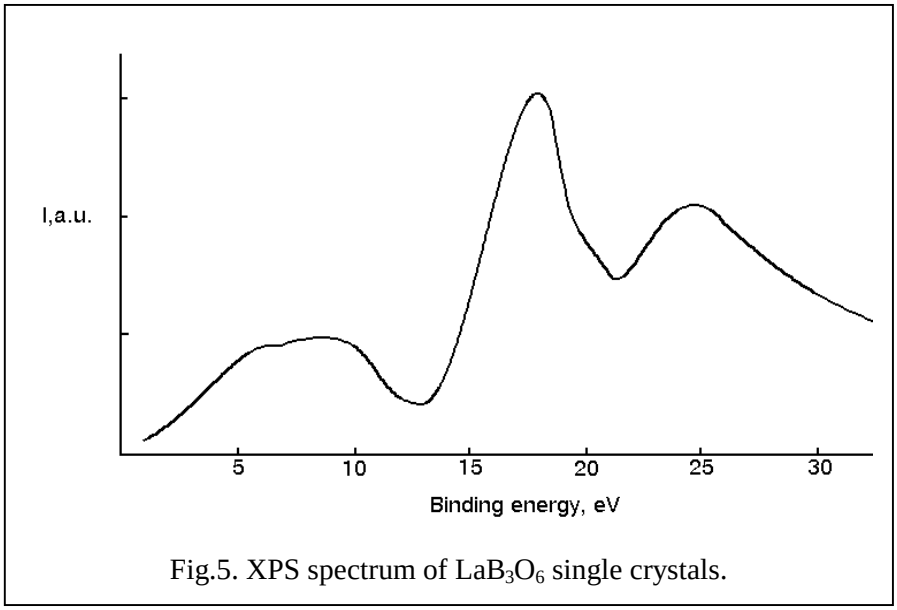

Fig.5. XPS spectrum of LaB_3O_6 single crystals.

The experimental data about basic electron states, which determine valence band and close core levels are defined. The XPS spectrum of LaB_3O_6 single crystals is shown in Fig.5. The valence band consist of the one wide peak with width about 5 eV. It can characterized valence band width. The maximum at 18 eV correspondence to the 5p states of lanthanum. There is a wide maximum at 26 eV appropriating to the 2s states of oxygen.

Conclusions

It were shown next results: pure and doped by Ce LaB_3O_6 single crystals were grown by the Czochralski technique; the edge of intrinsic absorption of the pure LaB_3O_6 single crystal disposes about 250 nm; intensive X-ray luminescence peak at 342 nm and peak at 0.82 eV on thermoluminescence curve were observed; introduction of cerium leads up to strength quenching of X-ray luminescence and disappearance of peak on the thermostimulated luminescence curve of LaB_3O_6 single crystal; energy band structure of LaB_3O_6 single crystal was determined by the XPS method

References

1. M.J.Knitel, X.E.Yu, P.Dorenbos, C.W.E.van Eijk, Procceding of SCINT97 (1998) 318.
2. V.I.Pakhomov, G.B.Silnitskaya, A.V.Medvedev, B.F.Dzhurinskiy, Neorganicheskie Materialy 8 (1972) 1259; 5 (1969) 1661 (in Russian).
3. V.G.Karabutov, N.N.Morozov, A.S.Pronin, B.F.Dzhurinskiy, Neorganicheskie Materialy, 14 (1978) 2021 (in Russian).
4. A.I.Kuznetsov, V.N.Abramov, B.R.Namozov, T.B.Uybo, Trudy Instituta Fiziki AN Estonskoj SSR 53 (1982) 83 (in Russian).
5. A.Yi.Kuznetsov, A.B.Sobolev, I.N.Ogorodnikov, A.V.Kruzhalov, Solid State Physics 36 (1994) 3530.
6. R.Chen, Journal of Electrochemical Society 116-9 (1969) 1254.

Interaction of melt with gas atmosphere at growing scintillation oxide crystals by the czochralski method

V.P.Martynov

Scientific Research Organization "SELDI". 1st entry, Gosprom, 5 Svobody sq., 310022 Kharkov, Ukraine

Abstract. Experimental study of structure-sensitive properties of oxide melts have been carried out. They confirmed the fact of inner structure transformation. The resulting effect of the factors that influence the inner structure defines the coordination of clusters of crystal-forming components and the ability of the melt to a monophase crystallization. |The redox potential of the gas atmosphere has an effect on the direction and degree of structural transformations, stoichiometric disordering of the oxide melts, nature of formation of various defects in crystals (light scattering centers-LSC, color centers-CC etc.).

Keywords: inner structure, cluster, coordination, stoichiometry, melt

Introduction

A specific application of oxide scintillators in high energy physics as detectors of ionizing radiation, tomographic and introscopic devices requires usage of a big number of crystals with a minimal spread of optical and spectral-luminescent characteristics. Obviously, with the increase of production the vulnerability of the crystal growth methods and probability of typical structure defects formation in them become higher. The structure defects include: light scattering centers (LSC). stoichiometric disordering (SD), color centers (CC) and have a negative influence on working characteristics of scintillators. Usually the origin of these defects is considered separately with the attention focused on particular problems of the developed growth methods. It is assumed, for example, that formation of LSC is mainly connected with the growth from the overcooled melt [I], SD is the result of evaporation of some crystal forming cation [2]. Formation of CC is related to the change of valence of the crystal forming cations or dopants, which were purposefully or uncontrolled way introduced into crystals [3].

The author considers the nature of these defects' formation to be common and connected with the variation of the inner structure in the melts due to their incongruent evaporation and thermochemical dissociation (association). With this. a significant effect on the degree and direction of these processes has a redox potential (ROP) of the growth gas medium (GM) which predefines the thermochemical activity of oxygen and its deficit or excess in the oxide melts [4]. The resulting effect of the factors having influence on the inner structure of melts defines the coordination of clusters of the crystal forming components; those, depending on their structure can be able or unable to a monophase crystallization.

Results and discussion

Experimental study of structure-sensitive properties of melts, interaction of the system GM-melt, origin of LSC, SD, CC, was carried out on the oxide melts and crystals: $Y_3Al_5O_{12}$ (YAG), $YalO_3$ (YAP), Gd_2SiO_5 (GSO), $PbWO_4$ (PWO), $CdWO_4$ (CWO). The structure transformation process was registered by the variation of the structure-sensitive properties - viscosity and indirectly- by the loss of the melt mass (due to evaporation) depending on pressure and GM composition. In particular. Fig.1 shows the variation of isotherms of YAG

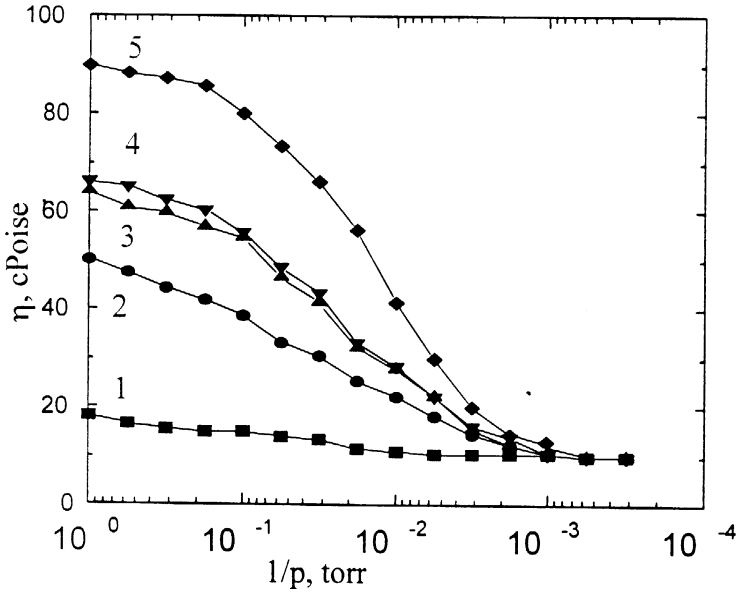

Fig.1. Dependence of isotherms of the YAG melt viscosity on composition and pressure of the gas medium. 1—Ar(H), 2—Ar(O), 3—N_2(O), 4—Ar, 5—N_2.

melt viscosity (η) as a function of gas medium composition and its pressure [5]. In the nitrogen atmosphere the melt viscosity is 90 cPoise. in argon having ~2 vol.% of hydrogen it goes down to 20 cPoise. Introduction of oxygen to the gas medium (to 1.5 vol.%) also decreases the melt viscosity. With a decrease of GM pressure a sharp drop of the viscosity in the range of $5x10^{-2}...5x10^{-2}$ torr is observed. This gives evidence to the beginning of structural transformations in the melt. The latter are caused by its deeper dissociation due to which an intensive incongruent evaporation ofpseudogas suboxides begins.

The loss of the melt mass (YAG, YAP, PWO and CWO) at first becomes smaller as the GM pressure is decreased (Fig.2), the intensity of the upgoing gas flow which carry the evaporation products from the melt surface being weakened. With a further decrease of the GM pressure the loss of the melt mass begins to grow abruptly at certain for each melt values of pressure depending o their thermochemical stability. This testifies to the beginning of thermochemical dissociation in these melts as a result of which PWO and CWO melts inclined to the incongruent evaporation begin to decompose. Thus, the results of the experiments confirm the occurrence of structural transformations in the oxide melts. They can be suppressed or activated as the redox potential of the GM varies.

Structural transformations in the oxide melts predefine the ratio of clusters of the crystal forming components near crystallization front, coordinated same way as in the crystallizing material. All other structural formations are the intrinsic impurities; they are rejected by the crystallization pressure of the growth surface till their concentration does not exceed the critical one. With the increase of concentration the intrinsic impurity is built into the crystal incoherently thus forming LSC. Basing on the experimental data it was found the role of the intrinsic impurities in YAG and YAP melts can be played by the monomer clusters $[AlO_4]^{5-}$ and

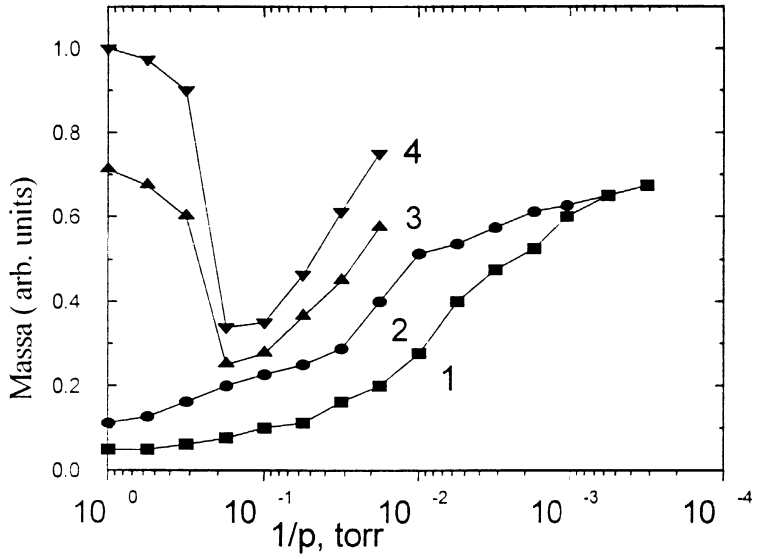

Fig.2. Melt mass losses (relative units) as a function of pressure of the gas medium. 1—YAP, 2—YAG, 3—PWO, 4—CWO.

$[AlO_6]^{9-}$, respectively [6] or polyanions of the type $[Al_nO_9(3n+1)]^{(3n+2)-}$. This is explained by the difference of monomer coordination with respect to the corresponding crystals or their polymerization as a result of melts' association. In the CWO melt the intrinsic impurity is a part of cations Cd2+ coordinated probably by the dodecahedron motive. In the PWO melt the role of the intrinsic impurities play octahedral clusters [W06J contra-indicated for the structure of sheelite.

While in a binary oxide system crystallized can be more than one compound: YAP, YAG (Y_2O_3—Al_2O_3), PWO, Pb_2WO_5 (PbO-WO_3) the intrinsic impurities are condensed in the crystals in the form of LSC, structurally similar to the accompanying compounds in the state diagram. In the system CdO—WO_3 there is only one compound (CWO) and LSC in crystals are identified with the phases having an excess of some cation. Varying the redox potential of the gas atmosphere can destabilize foreign clusters initiating the formation of LSC in crystals. In particular, it should be increased for YAP melt and decreased for other ones. It is noteworthy that destabilization of anionic cadmium polyhedrons not coinciding in coordination with the crystal structure at other equal conditions leads to the rise of cadmium content in crystals despite its predominant evaporation from melt in the growth process.

Usually the stoichiometric disordering is evaluated by the ratio of crystal forming cations. However, an important and sometimes decisive significance has their stoichiometry by oxygen. Oxygen content in the melt in the growth proces depends on the redox potential of GM, provided the melt and GM are in the equilibrium state. Under real conditions practically all oxide melts being overheated or owing to their physico-chemical properties use to evaporate and due to this fact their subsurface layer enriched with pseudogas evaporation products starts to work as the energy barrier, hindering the diffusion of GM oxygen to the melt volume. This being so, a mass exchange proceeds in the system melt-GM in the direction melt $\rightarrow$GM and the equality of chemical potentials is established between oxygen of GM and the melt suface. As a result a deficit of oxygen occurs in the melt volume. The direction of mass exchange can vary oppositely if an associated (overcooled) melt will contact GM. Its subsurface layer now cannot impede the diffusion of GM oxygen to the melt volume. As a result, the oxygen deficit in the associated melt is replenished, equilibrium and equality of chemical potentials of oxygen in GM and melt volume are established corresponding to the fixed temperature of the melt.

A reversibility of mass transfer in the system GM-melt and melt stoichiometry disordering by oxygen are quite real in the process of crystal growth. Since a specific feature of the Czochralski method is such that the melt is subjected to a multiple overcooling and overheating and as the redox potential does not practically change one can state that the crystal grown by the Czochralski method is not uniform in the stoichiometric composition by oxygen. This is confirmed by episodically appearing local coloration of the upper and lower parts of PWO crystals, which due to specific character of this method are grown from the associated melt with an elevated content of oxygen.

The absence of the methods for controlling stoichiometric disordering of oxide crystals by oxygen does not allow evaluating it quantitatively. But we have noticed a significant difference in the lattice parameters of the colored PWO grown in air in the absence of melt overheating and those colorless and grown in the inert medium containing ~0.3vol.% of oxygen. The colored sample had a = b = 5.4612 (4), c = 12.045 (1), the colorless one had a = b = 5.4606(6), c = 12.0437(10) Å.

The majority of the oxide scintillation crystals require limitation of oxygen content in GM during their growth. This concerns Ce-doped scintillators and crystals (PWO, CWO) in which possible is variation ofactivator ions' or crystal forming cations' valence which results in the CC formation. Limitation of oxygen content is necessary from the side of both its maximum permissible level in GM and minimum one (at least regarding PWO). The latter while

approaching stoichiometry by oxygen acquire coloration due to the change of lead cations' valence ($Pb^{2+} \rightarrow Pb^{3+}$). When having a deficit of oxygen it becomes colored due to a partial reduction of the crvstal forming cations. Somewhat different in the mechanism of CC formation are CWO scintillators in which , besides the effect ofGM oxygen, coloration can appear as a result of stoichiometry disordering by cations depending n the redox potential of GM. The negative influence of CC is manifested basically in case of their localization in the region of the spectra of the intrinsic luminescence. Particularly, for GSO the CC absorption coincides with the spectral part λ=440 nm and can reach the value K≤10-1 $^2cm^{-1}$. In PWO crystals the CC absorption coincides with the maximum of the luminescence spectrum (~ 430 nm).

Formation of color centers as a result of stoichiometric disordering by oxygen has a reversible character. Annealing at a lowered pressure of the gas medium can bleach the colored crystals. Specifically, annealing of GSO in high vacuum (~$5x10^{-5}$ torr.) at a corresponding selection of the regimes allows to decrease absorption in them down to K≤10-1 $^2cm^{-1}$.. This extends their application field as bulk detectors of full absorption. CC in PWO are eliminated at premelting temperatures and partial oxygen pressure Po_2~10^{-5} atm.

The reversibility of coloration allows to optimize optical quality of scintillation crystals. Besides, solved are the problems connected with the Ce-doped crystals (YAP, GSO) for which desirable is the increase of the redox potential ofGM with the purpose to restrict the number of LSC (YAP) and make higher the mechanical strength of GSO (but in this case CC will appear in them). After annealing the cintillator blanks that had been subjected to the main types of mechanical treatment CC disappear and optical quality of crystals is on the level of initially colorless samples.

Conclusions

The results of the carried out investigations confirm the importance of the role of the gas medium in the process of crystal formation. The effect of its redox potential on the inner structure of melts predefines a common origin of defects in oxide scintillation crystals. Stoichiometric disordering of oxide scintillators by oxygen is a necessary condition of their workability and reversibility of their coloration is an important factor in the technique of growing scintillators with the improved quality.

References

1. S.Burachas, V.Martynov, V.Ryzhikov, G.Tamulaitis, H.H.Gutbrod, V.I.Manko, J. Crystal Growth. 186, (1998), 175—180.
2. L.Nagornaya, S.Burachas, Yu.Vostretsov, V.Martynov, V.Ryzhikov, J. Crystal Growth, 198/199. (1999), 877—880.
3. M.Kobayashi, Y.Usuki, M.Ishii, T.Yazawa, K.Hara, M.Tanaka, M.Niki, S.Baccaro, A.Cecilia, M.Diemoz, I.Dafinei, Proceedings of the International Conference on Inorganik Scintilators and Their Applications, SCINT 97, Shanghai, P.R. China, September 22—25. (1997), 167—170.
4. J.A.Novokhatski, "Gasy v oxidnykh rasplavakh", Metallurgiya, Moskva, (19750, 132—138. (Rus.)
5. V.P.Martynov, V.A.Voloshin, G.V.Voloshma, Sb. "Vyraschivaniye, issledovaniye i primeneniye kristallov", VNII Monokristallov, Kharkov, N15, (1985), 7—17. (Rus.)
6. V.P.Martynov, Sb. "Tolucheniye i svoistva kristallov" VNII Monokristallov, Kharkov, N17, (1986), 158—168. (Rus.)

Luminescence properties of $ScPO_4$ single crystals

Anatoly N. Trukhin[a] and Lynn A. Boatner[b]

[a]*University of Latvia, Solid State Physics Institute, 8 Kengaraga St., LV-1063, Riga, Latvia*
[b]*Solid State Division, Oak Ridge National Laboratory. Oak-Ridge, TN. 37831, USA*

Abstract. Flux-grown $ScPO_4$ single crystals exhibit a number of luminescence bands in their x-ray-excited luminescence spectra - including sharp lines arising from rare-earth elements plus a number of broad bands at 5.6 eV, 4.4 eV, and 3 eV. The band at 5.6 eV was attributed to a self-trapped exciton (STE) [1], and it could be excited at 7 eV and higher energies. This luminescence is strongly polarised (P = 70 %) along the optical axes of the crystal and exhibits a kinetic decay time constant that varies from several ns at room temperature to ~10 μs at 60 K and up to ~1 ms at 10 K. It is assumed that the STE is localized on the Sc ions. The band at 3 eV can be excited in the range of the $ScPO_4$ crystal transparency (decay time = 3 to 4 μs.) This band is attributed to a lead impurity that creates different luminescence centers. At high temperatures, the band at 4.4 eV is dominant in the x-ray-excited TSL and afterglow spectra. Its intensity increases with irradiation time beginning at zero at the initial irradiation time.

Keywords: Scandium orthophosphate, self-trapped exciton, luminescence.

Introduction

Scandium orthophosphate is a material with a number of promising applications due to its resistance to radiation, high chemical durability, hardness, and good optical properties. The material has potential applications in thermoluminescence dosimetry and frequency control and as an optical material and laser host. In particular, $ScPO_4$ in both pure and doped forms, is a promising phosphor/scintillator due to the rich nature of its luminescence spectra under ionizing radiation. Therefore, we have characterised the luminescence and related properties of $ScPO_4$ in a series of experimental investigations.

The $ScPO_4$ crystal structure was determined in Ref. [1]. It can be viewed as consisting of eightfold-coordinated Sc ions with four oxygens at a short distance (0.2153 nm) and with four additional oxygen ions at a somewhat longer distance (0.2260 nm). Each of these discrete lengths are tetrahedrally oriented orthogonal to each other. Therefore, it can be assumed that the Sc ions form bonds with the oxygen ions through two sets of d orbitals ($d\gamma$ and d_ε) that are each tetrahedral and orthogonal to one another. The phosphorus ion is fourfold-coordinated with oxygen ions in a slightly distorted tetrahedron. Each unit cell contains four molecules. The structure is tetragonal zircon-type with unit cell parameters: a = 0.6574 nm and b = 0.5791 nm.

A combination of optical and photoelectric methods has previously been used by Trukhin [2] to investigate SiO_2, GeO_2, $AlPO_4$ and $GaPO_4$ crystals and to study their intrinsic properties. In the case of Sc-containing crystals, similar investigations were reported in Ref. [3] for Sc_2O_3 where it was shown that the intrinsic absorption edge of scandium oxide is determined by the d states of scandium, and no exciton states were found.

Single crystal of $ScPO_4$ were grown using a flux method [4] in tightly covered platinum crucibles containing lead pyrophosphate as the flux [1]. After soaking for 16 h at 1360 ^oC, the crucibles were cooled at a rate of 1 ^oC/h to 900 ^oC and then directly to room temperature. The $Pb_2P_2O_7$ flux was then dissolved in boiling HNO_3. A series of $ScPO_4$ crystals from nominally

pure to deliberately doped with Cu, Yb, Fe, V, Eu, Mn, and Tm with a doping level of about 1 wt % were studied. The crystals were of different dimensions not exceeding ~80 mm^2. Samples of desired thickness were cleaved with the use of a sharp chisel. All of the resulting sample plates were parallel to the optical axis, whose direction was determined by the use of a polarising microscope. The degree of polarization of the x-ray-excited luminescence was determined by the use of an analyser containing 8 silica glass plates of 1 mm thickness and maintaining the Brewster angle with respect to the luminescence beam.

Results

The measured absorption spectra for different samples are presented in Fig. 1. It can be seen that, in spite of essential differences in absorption value, in the range of optical

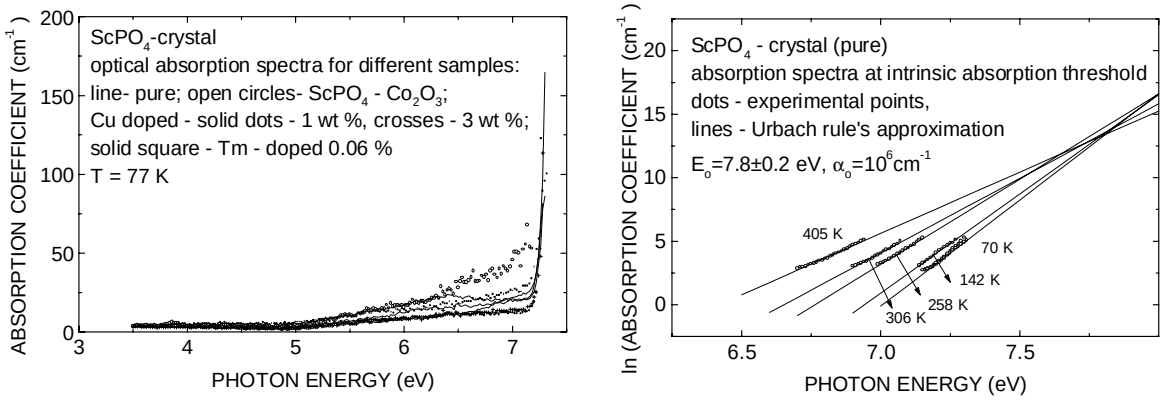

Fig.1. $ScPO_4$ crystal optical absorption spectra (left) and Urbach rule 's approximation (right).

transparency, the cut-off of transparency took place in the same energy range. Therefore, it was concluded that this represents the intrinsic absorption threshold, and attempts were made to check the correspondence of this threshold to the Urbach rule by measuring the absorption spectra in the range of the threshold using the thinnest samples at different temperatures. In Fig.1 (right) these data are presented in semilogarithmic coordinates, and it is apparent that there is good correspondence to the Urbach rule in the form corresponding to the model introduced by Toyozawa [7] for the case of strong exciton-phonon interactions. The equations expressing the Urbach rule are:

$$\alpha = \alpha_0 \exp [- \sigma (E_0 - E)/kT], \quad \sigma = \sigma_0 (2kT/\hbar\omega) \tanh(\hbar\omega/2kT) \qquad (1)$$

The crossing point E_0 = 7.75±0.05 eV is located below the maximum of the broad structureless absorption band at 8.8 eV, whose position was estimated from the reflectivity spectra (not presented). Values of the parameter σ_0 = 0.63 and the crossing-point position both correspond to Toyozawa's criterion of a strong exciton-phonon interaction [7]. The value of $\hbar\omega$ = 70 meV may correspond to the range of optical phonons of $ScPO_4$. According to the theory [7], this may reflect the equality of the electron and hole effective mass involved in the exciton creation. It is significant that the Urbach's-rule parameters do not depend on impurities (See Fig.5) within experimental error.

The presently available single-crystal $ScPO_4$ samples exhibit a number of luminescence bands in the range available to our apparatus. In Fig. 2 (left), the x-ray-excited luminescence spectra obtained at different temperatures are presented. The outstanding questions are: (1.) What is the nature of a given luminescence band - intrinsic or extrinsic? and (2.) By what processes is the luminescence excited?

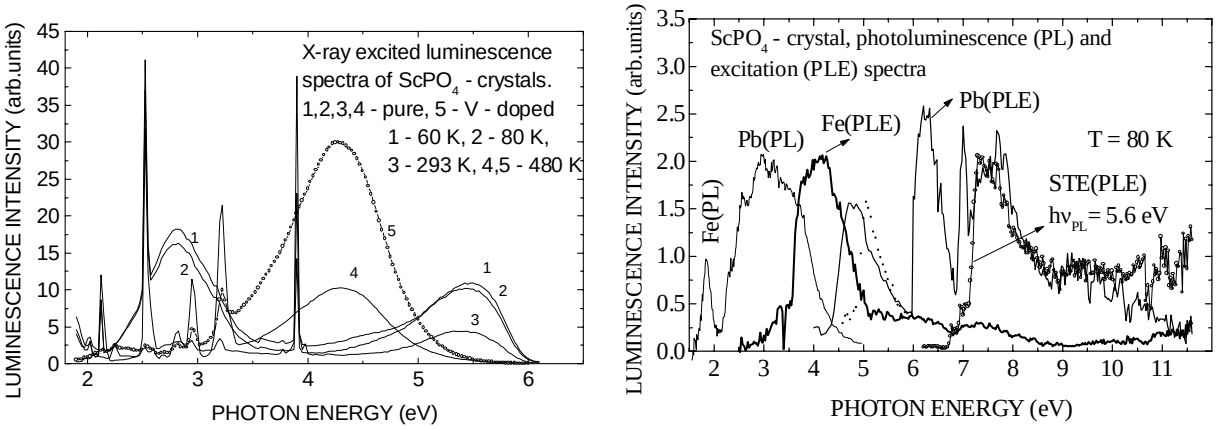

Fig.2. $ScPO_4$ single-crystal luminescence spectra: (left) x-ray excited spectra; (right) - photoluminescence). Fe - luminescence of the iron center; Pb - assumed to be lead-related luminescence. Points at 5 eV correspond to the 3.5 eV sub-band excitation spectrum, but the line at 2.8 eV is a sub-band of the Pb-labelled curves. STE – self-trapped exciton luminescence [12].

In Fig.2, several sharp lines are seen that apparently belong to rare-earth elements, and these will not be considered further in this preliminary report. Primary attention here will be paid to an examination of the host materials' luminescence properties. The first consideration for the host-material luminescence would be excitation in only the intrinsic absorption range. The candidates for the intrinsic effects are the two bands at 5.6 eV and at 4.4 eV. In Fig.2 (right), the excitation spectra for the luminescence band at 5.6 eV are compared with the excitation spectra of other bands. This band can only be excited in the intrinsic range. Other luminescence bands shown in the figure have excitation bands below 6.9 eV. These exist in the "as-received" crystals and, therefore, can be ascribed to extrinsic luminescence centers. Now let us consider the other data for the 5.6 eV band. These are: the temperature dependence of the photoluminescence (PL) intensity, the PL decay time constant, and the luminescence polarization (Fig.3). The dependencies can be divided into three ranges: First, a range at 10 K, second a range at 40 to 270 K, and a third range at 270 to 400 K. In the first range, τ increases whereas the intensity decreases. This effect requires further study since a self-consistent explanation is not apparent at this time. In the second and third ranges, there is a good correspondence between $\tau(T)$, I(T), and P(T); and these ranges differ in the estimated activation energy. The third range is the range of the 5.6 eV-band thermal quenching. The activation energy for thermal quenching is estimated to be 0.22 eV. From the second temperature range, we estimate an activation energy of about 0.02 eV. In the following, we argue that the thermally activated reorientation of self-trapped excitons (STE) leads to a loss of polarization, decreasing the STE life time and a lost of amplitude due to interactions with defects. The degree of polarisation at 60 K is 70 to 10 % and the electric field vector of the luminescence is parallel to the optical **c** axe of the $ScPO_4$ crystal. The 5.6 eV band cannot be excited in a pure electron-hole recombination process since it was not observed in the thermo-stimulated luminescence. This provides good evidence for the excitonic nature of this luminescence band. In Fig.4 (right), the thermoluminescence curves are presented, and in Fig.4 (left), the thermoluminescence spectra are presented and compared to the x-ray-excited spectra. Together with the thermoluminescence studies, the thermo-stimulated electric depolarisation of the x-ray-excited sample has been obtained (not shown). For all of the TSL peaks, we observed peaks in the depolarisation current. Therefore, the thesis of electron-hole recombination is valid. In the thermoluminescence spectra, broad bands at 3.4 and 4.4 eV as well as sharp lines are present.

The broad band at 3 eV that is visible in the PL and that was excited in the range of optical transparency of the $ScPO_4$ crystal (excitation at 5 eV with two sub-bands) falls into two bands that exhibit: different temperature dependencies of their intensity, separated excitation

bands (Fig. 2), and different roles in thermostimulated luminescence. The low-energy sub-band is not seen in the TSL spectra. However, they may belong to the same impurity (probably lead), which creates luminescence centers of different types. The band at 3 can be excited in the range of the $ScPO_4$ crystal transparency. It life time (τ) is about 3 - 4 μs for excitation in this range. Ther is a correlation between τ of this band and that of 5.6 eV band for excitation in the intrinsic absorption range by either photons or x-rays (Fig.3). This effect is accounted for by overlapping of the 5.6 eV band with the excitation band of the blue luminescence. Therefore, 5.6 eV luminescence excites the centers responsible for luminescence at 3 eV. The same effect was observed for the red luminescence of an iron impurity in $ScPO_4$ crystals. (Fig.2).

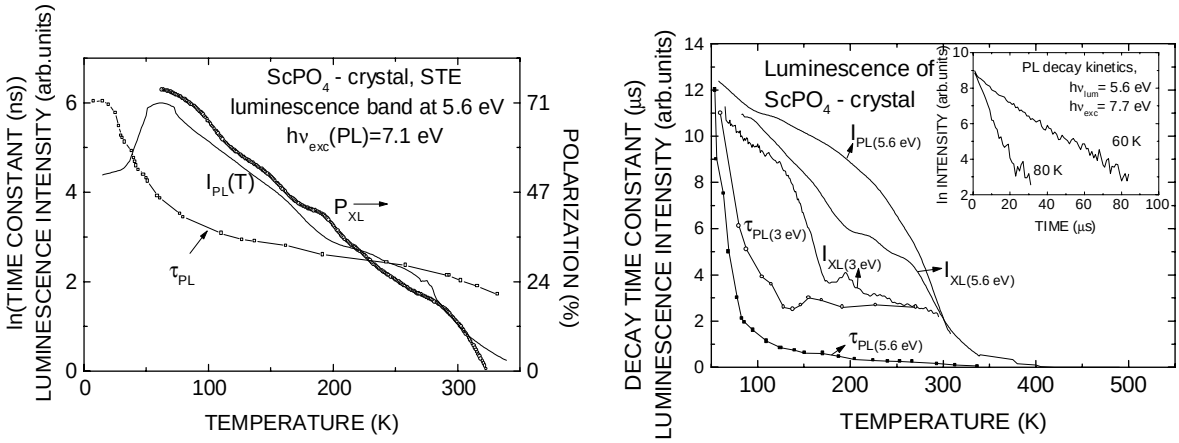

Fig.3.Temperature dependencies for different luminescence band intensities and decay time constants as well as the 5.6 eV band polarisation in $ScPO_4$ crystals. In insertion PL decay kinetics.

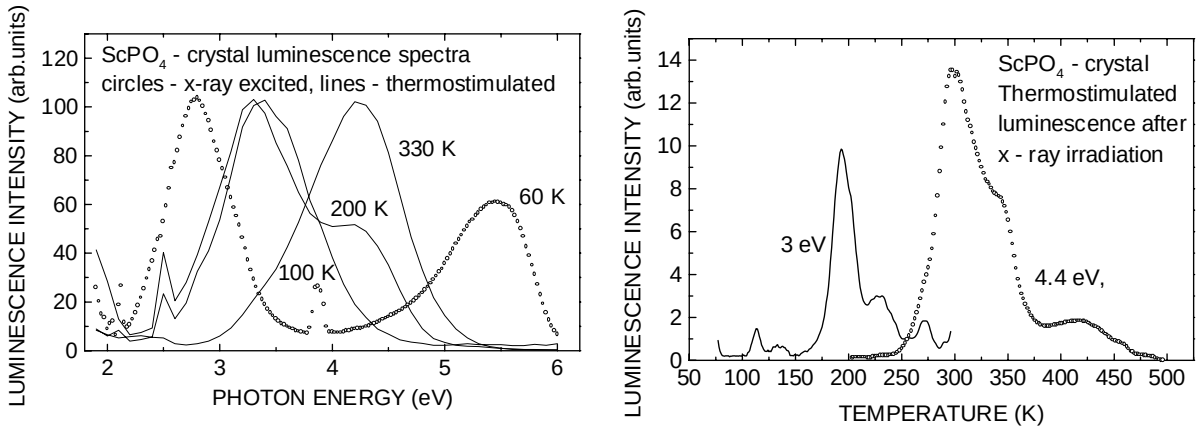

Fig.4. Thermostimulated luminescence (TSL) curves (right) and TSL luminescence spectra (left) for $ScPO_4$ crystal. (Monochromator slits were fully open).

At high temperature, the luminescence at 4.4 eV becomes dominant in the x-ray-excited and TSL spectra (Fig.4) as well as in the afterglow. The TSL and afterglow with the 4.4 eV band can be excited in the intrinsic range of the $ScPO_4$ crystal, however the excitation transparency range gives only TSL, and we did not observe the afterglow. So, below optical gap this luminescence is not excited directly.

The luminescence intensity increases with the time of irradiation almost from zero at the initial time. The kinetics of this increase depend on the temperature. For room temperature, they are slow - increasing with saturation in one hour under x-rays. At higher temperatures (510K), this increase takes place in few minutes followed by a decrease (Fig.5). Such kinetics correspond to complex processes, showing that accumulation is necessary for observation.

The polarization is: P = - 14 % with respect to optical axes of the crystal. The polarisation degree and orientation are independent of the conditions of observation (x-ray or TSL or afterglow in the time range of tens of minutes). The afterglow time dependence is changed with a change of the temperature from $t^{-0.3}$ at 330 K to t^{-2} at 510 K. A sample that was deliberately doped with vanadium exhibited the most predominant band at 4.4 eV at high temperature (480 K) in the PL, x-ray excited luminescence, and TSL. Impurities such as Eu^{3+} and Mn^{2+} reduce the luminescence band at 4.4 eV but it does not disappear in samples not deliberately doped with vanadium.

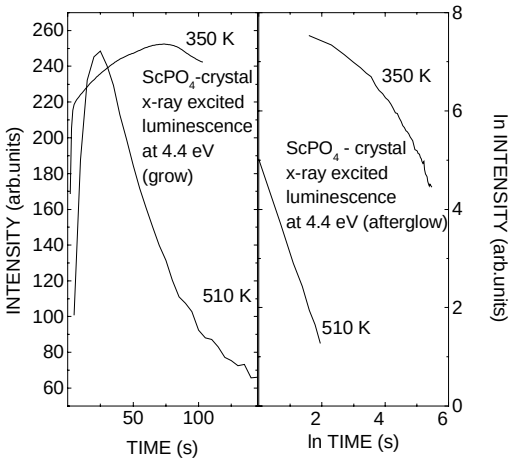

Fig.5. Kinetics of 4.4 eV luminescence band in $ScPO_4$ crystal.

Impurities can play a competitive role with respect to charge carrier trapping.

Discussion

There is a small shift between the position of the intrinsic absorption threshold and the photoconductivity threshold, and thus, we can conclude that there is exciton creation by light in this energy range (See Fig.6). This is in agreement with the observation of the host-material luminescence band at 5.6 eV, which is excitable in the intrinsic absorption range only and cannot be excited in a pure electron-hole recombination process such as TSL. The Stoke's shift for this band is about 1 eV, therefore it can be ascribed to a self- trapped exciton (STE). A transfer through hopping mobility was not verified because of the very effective mechanism of energy transfer through ultraviolet luminescence reabsorption by, for example, iron and lead centers.

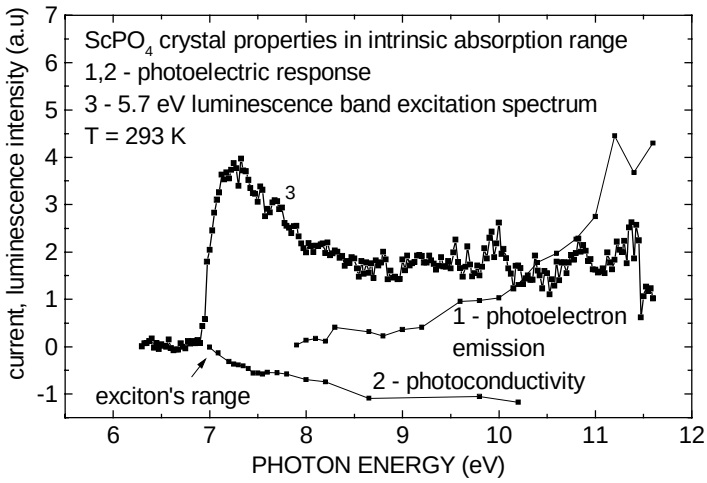

Fig.6 Intrinsic properties of $ScPO_4$ crystal [12]

Measurements of the degree of polarization of the luminescence band at 5.6 eV and its temperature dependence show that the orientation of the STE can be changed by temperature.

We can determine that the energy gap in $ScPO_4$ crystal has a value of 7.2 eV at 293 K from the data shown in Fig.6. The lack of STE luminescence in TSL shows that there is no charge-carrier self-trapping or, if such process self-trapping or, if such process exist, there is no creation of a STE from the recombination of a free carriers or there is a sufficiently high barrier for charge-carrier self-trapping.

The stability of the intrinsic absorption-tail position, in spite of a vanadium impurity substitution for phosphorus, suggests that scandium states are responsible for the tail. In

previously studied $AlPO_4$ and $GaPO_4$ crystals [8], the tail positions differ in each case. Therefore the PO_4 energetic states should be higher. The d orbital of Sc can be responsible for lowest excited states of the $ScPO_4$ crystal. This is consistent with the point that the STE is localised on Sc ions since its luminescence parameters correspond well with those reported for the Sc-impurity luminescence in Al_2O_3 [11].

The growth of $ScPO_4$ crystals with the use of a lead-containing material assures some contamination with lead in the final samples. We have ascribed the broad luminescence band to lead impurities because of the similarity with the luminescence of lead oxide glasses as well as with the luminescence of lead phosphates [10]. There are at least two types of luminescence centers to participate in different recombination processes. One with a band at 2.8 eV is not seen in the afterglow at 80 K (it cannot participate in the TSL peak at 200 K because it is thermally quenched at that temperature). Only centers responsible for the sub-band at 3.4 eV participate in the recombination processes. If we also assume that, in the case of $ScPO_4$ crystals, the Pb^{++} ions are the origin of all these centers, then different surroundings of these ions would give different trapping capabilities for the charge carriers.

Finally we comment on the nature of the luminescence band at 4.4 eV that appears only in the electron-hole recombination process. It is detectable from RT to 550 K. The fact that it can be excited in the range of transparency of the $ScPO_4$ crystal by the creation of a TSL peak at 480 K shows the extrinsic nature of this luminescence. Also, the correlation with the vanadium impurity supports this point of view. However this band is seen in all of the available samples regardless of their purity. It can be excited with a high energetic yield by continuous excitation with a high-density electron beam. This band belongs to an anisotropic defect, which cannot be excited directly in range of the crystal's transparency. Therefore, it exist only under high-energy excitation.

This work was supported by the grants 96.0665 of the Scientific Society of Latvia

References

1. Milligan W.O., Mullica D.F., Boatner L.A., Inorganica Chimica Acta, **60** (1982) 39.
2. Trukhin A.N., Non-Crystalline Solids. **149** (1992) 32.
3. Abramov V.N., Ermoshkin A.N., Kuznetsov A.I., Sov. Sol. St. Phys. **25** (1983) 1703.
4. Feigelson R.S., J. Am. Ceram. Soc. **47** (1964) 257.
5. Trukhin A.N., Phys. Stat. Sol. b **86** (1978) 67.
6. Huggett C.R., Teegarden K., Phys. Rev.B **141**(1966) 797.
7. Y.A. Toyozawa, Techn. Report. ISSP A1(1964) 119.
8. Trukhin A.N., Solid State Communications. **90** (1994) 761.
9. Trukhin A.N., J. Non-Crystalline Solids **189** (1995) 1.
10. Blasse G. and Dirksen G.J., Materials Chemistry and Physics. **12** (1985) 551.
11. B.R. Namozov, V.V. Murk, R.I. Zakhartchenya, M.P. Korobkov, Solid State Phys. (Russian) **40** (1998) 653.
12. Trukhin A.N., L.A. Boatner, Proceedings of the 13 IC on Defects in Insulating Crystals. - Wake Forest University: TTP, Materials Science Forum. **239 -241** (1996) 573.

Optical and spectral properties of the crystals A_2ZnJ_4: Mn^{2+} (A = Cs, Rb).

M.S. Pidzyrailo, O.M. Berdychevsky, V.V. Vistovsky, I.P. Pashuk

Ivan Franko State University, 8 Kyryla i Mefodia Street, 290005, Lviv, Ukraine
e-mail: OM.misc@ames.lviv.ua

Abstract. Reflection, emission and excitation spectra of the crystals A_2ZnJ_4: Mn^{2+} (A = Cs, Rb) are reported. Measurements were carried out in the temperature range of 77 – 300 K. From the reflection spectra band gaps and the exciton positions were defined. Emission spectrum in both cases consist of the green single band approximately at 18300 cm^{-1}. A detail analysis with the assignment of excitation bands to the electronic transitions in Mn^{2+} impurity are given. Calculations were carried out using Tanabe – Sugano and Curie formalism. Also were defined a parameters B, C and Dq for the crystals Cs_2ZnJ_4:Mn^{2+} and Rb_2ZnJ_4:Mn^{2+} in tetrahedral coordination.

Keywords: crystals, emission spectrum, excitation spectrum, impurity

Introduction.

A_2BX_4 crystals have received considerable attention in the recent years . It was stipulated by that fact, that they serves as a convenient objects for the examination of a broad circle of the physical phenomena (ferro – and segnetoelectrical properties, phase transitions, effects of the vibrionic interaction etc.).

Crystals A_2ZnJ_4 (A = Cs, Rb) belong to the β - K_2SO_4 -like structure (space group $D^{16}_{2h} = P_{nma}$), the elementary cell parameters for the Cs_2ZnJ_4 are a=8.29, b=14.45, c=10.84 Å at 293 K [1]. Three phase transitions take place in the crystal at 96, 108 and 120 K [2].

In the previous papers a birefringence [3] and Raman scattering [4] of the Cs_2ZnJ_4 crystal was studied. It was shown, that the tetrahedral complex of ZnJ_4 leads to the appearance of three times degenerate vibration modes $\nu_3(F2)\approx170$ cm^{-1} and $\nu_4(F2)\approx62$ cm^{-1}, one twice degenerate vibration mode $\nu_2(E)\approx44$ cm^{-1} and one fully symmetrical mode $\nu_1(A1)\approx1220$ cm^{-1}. An interesting feature of the Raman spectra of Cs_2ZnJ_4 crystal is a high temperature sensitivity of it low frequencies region (below 90 cm^{-1}).

Optical spectra of the crystals with transition – metal impurities (in particularly Mn^{2+}) have a complex character. Therefore, as a subject of great interest may be the studying of impurity energy levels, crystal field parameters and influence of the different factors (temperature, stress etc.).

In this work we present our results on reflection, emission and excitation spectra measurements for the crystals Cs_2ZnJ_4 and Rb_2ZnJ_4 with the Mn^{2+} impurities , which were carried out in the temperature range of 77 - 300 K.

Experimental details

Halide compounds with the general formula of $A_mB_nX_l$, (where A – alcali ion, B – alcali-earth ion, X - halogen) in most cases has an ionic bonding type [5]. Hence, the basic principles of their structure are determined by the general rules of ionic crystals arramgement.

Crystals $Cs_2ZnJ_4:Mn^{2+}$ and $Rb_2ZnJ_4:Mn^{2+}$ were grown by the Bridgeman - Stockbarger method in a quartz crucibles from the equimolar initial raw materials, which was preliminary refined by the zone melting method. Concentration of the Mn^{2+} ions in both cases approximately was $1.2*10^{-3}$ mol/%. Samples with a satisfactory quality we obtain with the growth speed of 8 mm/h.

The measurements of reflection, emission and excitation luminescence spectra were carried out at set-up mounted on a foundation of MDR – 6 monochromator in the temperature range of 77 - 300 K.

Results and discussions

Reflection spectra.

Reflection spectra of both crystals at 77 K consist of two distinct excitonic peaks (Fig 1a, 1b, dotted line), which positions are shown in Table 1. With the increasing of the temperature to 293 K, reflection peaks shift to the low energy side (approx. 0.056 eV). Using known equations for the positions, binding energy and radius of the exciton [6]:

$$E_n = E_g - \frac{F}{n^2}, \qquad F = \frac{\mu}{m}\left|\frac{R}{\varepsilon^2}\right., \qquad r_n = R\varepsilon n^2 \left.\frac{m}{\mu}\right|$$

where E_g – band gap of the crystal, E_n – position of the excitonic peak, μ - reduced effective mass of the hole and electron, ε - dielectric constant, m – electron mass, R – Ridberg constant. With the assumption, that the effective mass of the electron and hole are equal, we defined a E_g, F and r_1 parameters for both crystals (see Table 1). For the excited states excitonic radii are much large, then a lattice constant.

Table 1. Parameters of the excitons and band gaps of the crystals Cs_2ZnJ_4 and Rb_2ZnJ_4.

Parameter	$Cs_2ZnJ_4:Mn$	$Rb_2ZnJ_4:Mn$
E_1, eV	4.854	4.992
E_2, eV	5.245	5.336
E_g, eV	5.375	5.474
F, eV	0.521	0.482
r_1, Å	3.7	3.874

Emission spectra.

Under excitation of the doped crystals with the blue or ultraviolet radiation the emission spectra consists of the single band at 18285 cm^{-1} (ΔH = 967 cm^{-1}) for the crystal $Cs_2ZnJ_4:Mn^{2+}$ and 18309 cm^{-1} for the crystal $Rb_2ZnJ_4:Mn^{2+}$ (fig 1a, 1b, open circles). With the increasing of the temperature to 293 K peak position shifts to the lower energy side, and a halfwidth increase proportionally to $\sqrt{T}$. In limits of studied impurity concentrations ($2.5*10^{-5}$ mol/% - $1.2*10^{-3}$ mol/%) peak positions of the emission bands, and also their halfwidth remained invariable. In the $Cs_2CdJ_4:Mn^{2+}$, which have the same structure type, two emission bands are observed at 18471 and 13865 cm^{-1} [7]. The latter, most probably, is due to the other type of local symmetry of Mn^{2+} impurity, since their measurements were conducted with a highly activated samples. In the crystals CsI:Mn with the increasing of Mn^{2+} concentration (0.1 – 20 mol/%) different types of the impurities centers is appeared, and the emission spectrum shifts to the high energy side [8]. Identical energy position of the emission bands lead us to the conclusion, that the Mn^{2+} ions in the both crystals substitute Zn^{2+} ions.

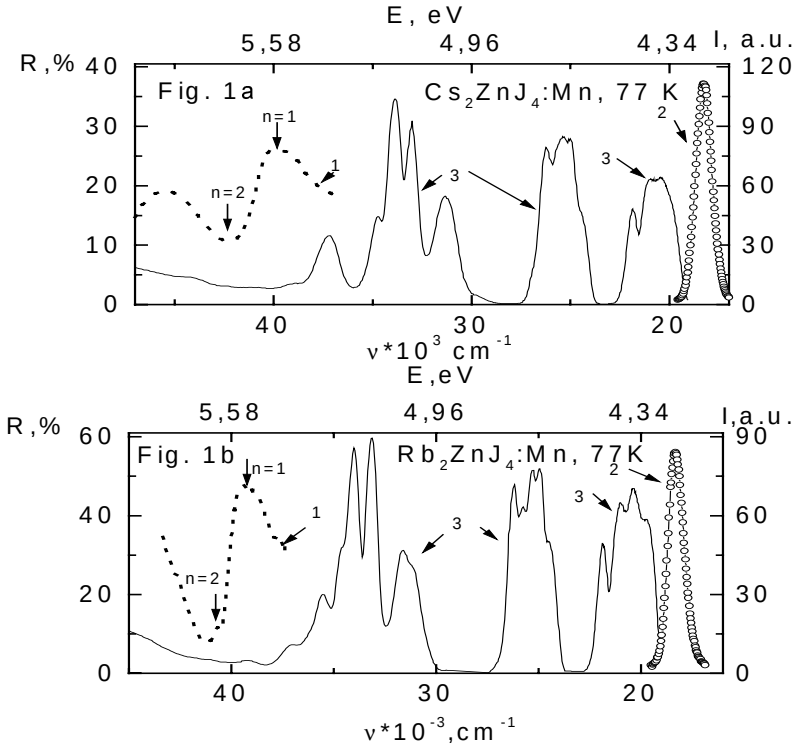

Fig.1. Reflection spectra (1, dotted line), emission spectra (2, open circle) and excitation spectra (3, solid line) of the crystals $Cs_2ZnJ_4:Mn^{2+}$ (fig. 1a) and $Rb_2ZnJ_4:Mn^{2+}$ (fig 1b) at 77 K.

Excitation spectra.

The excitation spectra (fig. 1a, 1b, solid line) of the crystals $Cs_2ZnJ_4:Mn^{2+}$ and $Rb_2ZnJ_4:Mn^{2+}$ at 77 K consist of the broad bands at 20900, 25700 cm^{-1} and a fine structure in the high frequency region ($\nu > 29000$ cm^{-1}).

Broad bands at 20900 and 25700 cm^{-1} have a complex character for both cases. As a result of the decomposition of these bands into gaussian components we show, that the bands 20900 and 257010 cm^{-1} consists of four and six component respectively (see table 2). Positions of the excitation band in our crystals are close to the absorption bands in the crystal $[(CH_3)_4N]_2MnBr_4$ [9], where Mn^{2+} impurity also has a tetrahedral coordination.

A large number of the excitation bands make it possible to implement their assignment to the corresponding electronic transition in Mn^{2+} impurity. Because a manganese ion surrounded by four J^- ions and has a tetrahedral coordination, we made a calculations of electronic level energy as a function of crystal field strength under assumption of cubic site symmetry. The results of our calculation are shown in Table 2. Tree`s correction factor α were taken equal to the value of 76 cm^{-1}.

The bands in the excitation spectra have been assigned using corresponding Tanabe-Sugano diagram (fig. 3). Best fitting between observed and calculated frequencies we obtain for Dq=325 cm^{-1} ($Cs_2ZnJ_4:Mn^{2+}$) and Dq=351 cm^{-1} ($Rb_2ZnJ_4:Mn^{2+}$), which are very close to the Dq value for $[(CH_3)_4N]_2MnBr_4$ [9].

The ground level of Mn^{2+} ion is $^6A_1(^6S_1)$. Low energy absorption bands in a crystals with Mn^{2+} impurity are due to the transitions from $^6A_1(^6S_1)$ to quaternary term ^4G ($^4T_1$,$^4T_2$,^4E,$^4A_1$ levels). Tanabe-Sugano diagram was constructed under assumption of the degeneracy of the ^4E and $^4A_1$ levels. From the experimental results we can see that this levels consists of two sublevels ($\Delta\nu$=774 and 778 respectively); and a splitting value is much large than for the crystals MnF_2 ($\Delta\nu$=310 cm^{-1}) and $CsF_2:Mn$ ($\Delta\nu$=400 cm^{-1}) [11]. Possibly, it may be due to the strong overlapping of ligand electronic levels.

Taking into account a covalence factor β [12], we used equations from [11] for constructions of modified Sugano diagram. Our observed values of the energy levels of ^4G term are in good agreement with calculated for both cases, when covalence factor are equal to 11%.

Our calculation shows that ^4D terms are decomposed into two states $^4T_2$ and ^4E and the term ^4P are not decomposed at all. At the same time our excitation measurements of the 25700 cm^{-1} band shows, that this band consist at least of six components. From comparison of the

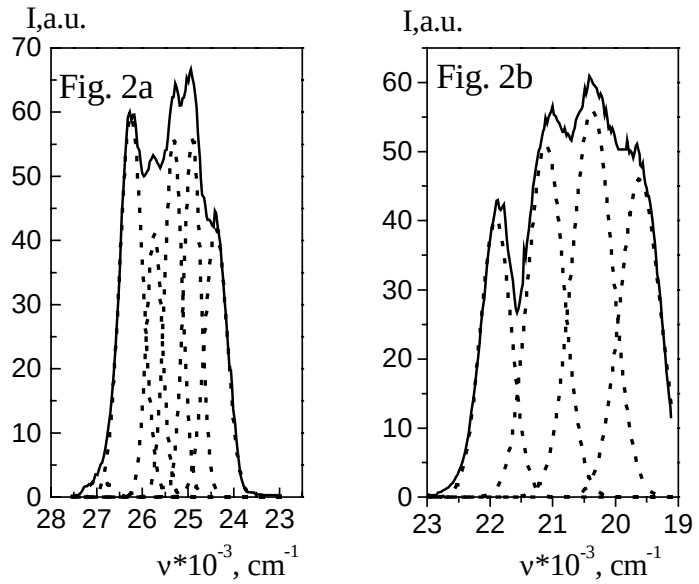

Fig. 2. Gauss decomposition of the excitation bands 25700 cm^{-1} (fig. 2a) and 20900 cm^{-1} (fig. 2b), in the case of Rb_2ZnJ_4, 77 K.

calculated values of term frequencies ^4D and ^4P with experimental data follows, that the term ^4P is decomposed into two levels, and term ^4D - into three levels. Five levels were observed by the authors [14] in the case of Zn_2SiO_4:Mn. They suppose, that level $^4T_2$ (^4D) splits into three components, and level ^{4} – into two components. Nevertheless, it seems, that the magnitude of splitting of these levels are under influenced of two factors: a spin - orbit interaction and presence of covalence of a crystal.

In both crystals in the high frequency region excitation bands are observed at $\nu > 35000$ $^{-1}$, which are close to first excitonic reflection peak. Therefore, it most probable, that they should be assigned to absorption of a near impurity exciton, which also confirmed by their strong temperature dependency.

Table 2. Assignment of the electronic transition and energy level position in the crystals $Cs_2ZnJ_4:Mn^{2+}$ and $Rb_2ZnJ_4:Mn^{2+}$, 77 K

Cs_2ZnJ_4:Mn				Rb_2ZnJ_4:Mn			
Observed		Transition from $^6A_1(^6S)$ to:	Calcu-lated	Observed		Transition from $^6A_1(^6S)$ to:	Calculated
Position	Halfwidth			Position	Halfwidth		
19834	317	$^4T_1(^4G)$	19485	19608	320	$^4T_1(^4G)$	19248
20488	324	$^4T_2(^4G)$	20694	20375	323	$^4T_2(^4G)$	20622
21133	278	$^4E(^4G)$	21133	21109	289	$^4E(^4G)$	21109
21907	274	$^4A_1(^4G)$	21908	21907	245	$^4A_1(^4G)$	21907
24400	274	$^4T_2{}^1(^4D)$	24780	24392	246	$^4T_2{}^1(^4D)$	24719
24916	201	$^4T_2{}^2(^4D)$		24908	186	$^4T_2{}^2(^4D)$	
25311	229	$^4E(^4D)$	25311	25319	189	$^4E(^4D)$	25319
25722	246	$^4T_1{}^1(^4P)$	26119	25739	177	$^4T_1{}^1(^4P)$	26313
26295	269	$^4T_1{}^2(^4P)$		26247	250	$^4T_1{}^2(^4P)$	
26908	228			26940	219		
30998	363	$^2T_2(^2I)$	29046	31054	363	$^2T_2(^2I)$	28597
31578	363	$^2T_1(^2I)$	30009	31820	347	$^2T_1(^2I)$	29770
33030	314	$^4A_2(^4F)$	34560	33151	283	$^4A_2(^4F)$	34569
33877	366	$^4T_1(^4F)$	34736	34006	244	$^4T_1(^4F)$	34776
34700	403	$^4T_2(^4F)$	35486	34611	259	$^4T_2(^4F)$	35636
37216	564			35498	427		
				36821	731		
B,cm^{-1}	638			639			
C,cm^{-1}	2801			2798			
Dq,cm^{-1}	325			351			

Conclusions

1. From the reflection spectra of the crystals Cs_2ZnJ_4 and Rb_2ZnJ_4 excitonic parameters and band gaps are defined.

2. Preliminary assignment of the excitation bands of the crystals $Cs_2ZnJ_4:Mn^{2+}$ and $Rb_2ZnJ_4:Mn^{2+}$ with the respect electronic transition was made.

3. Calculations of the energy levels in tetrahedral field of the Mn^{2+} impurity in the crystals Cs_2ZnJ_4 and Rb_2ZnJ_4 are not exactly coincide with the experimental value. If we consider, that the covalence factor is 11%, situation became a little better for both cases.

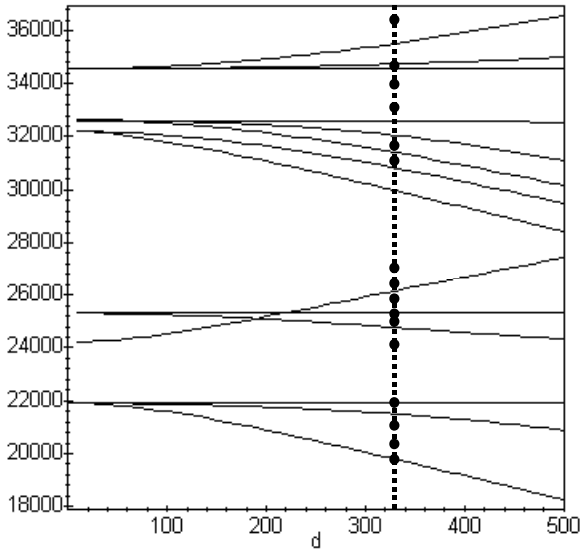

Fig. 3. The Sugano diagram for the Cs_2ZnJ_4: Mn crystal. Points: observed frequencies, line: Dq=325 cm^{-1}.

References

1. K. Gesi J. Phys. Soc. Japan. v.50, No. 11. (1981) 3535
2. J.J. Melero at al., Solid state commun. - 1995. - v.95, No.4. - pp. 201
3. S.V. Melnikova, S.V. Primak FTT T.34 No.7 (1992) 2137
4. O.P. Lamba, S. Sinka, Solid State Commun. Vol. 57, No. 5, (1986) 365 37
5. . . Alexandrov, “Phase transitions in the ABX_3 compounds”, Nauka, Novosibirsk, 1981
6. R. Nox, “The excitons”, Myr, Moscov, 1966
7. . . Bolesta, U.M. Furgala, Ukr. Phys. J., Vol. 36 No.11 (1991) 1654
8. A. Stevens, Phillips Res. Repts 32, (1977) 77
9. L. Dubicki, at al., Colloq. Int. C.N.R.S., No. 225 (1977) 217
10. M.S. Pidzyrailo at al., Lviv University Bulletin - Physics, Vol. 31 (1998) 75
11. T. Martin at al, Molecular Physics, Vol. 32, No. 2, (1972) 217
12. B. Ghosh, R. Mukherjee, Phys. Status Solidi (B), 102, (1980), 89
13. D. Curie, C. Barthou, B. Canny, J. Chem. Phys., Vol. 61 No. 8 (1974) 3048
14. D.T. Palumbo and J.J. Brown, J. Electrochem. Soc. 117, 1184 (1970)

Effect of impurities on the radiation hardness of the scintillating fluorohafnate glasses

L. N. Dmitruk[1], S. H. Batygov[1], V. A. Balashov[1], N. N. Vinogradova[1], L. N. Moiseeva[1], E. G. Devitsin[2], V. A. Kozlov[2], U. N. Efimov[3], V.D. Fedorov[3]

[1]*General Physics Institute, Vavilov Street 38, Moscow 117947, Russia*
[2]*Lebedev Physical Institute, Leninski prospect 53, Moscow 117924, Russia*
[3]*All Russian Chemical Technology Institute, Kashirskoe shosse 31, Moscow, Russia*

Abstract. The effect of some cations, oxygen and chlorine, as well as glass melting atmosphere, on the radiation hardness under γ-irradiation of glasses in HfF_4-BaF_2-CeF_3-AlF_3-NaF-InF_3 system was studied. Melting in the mildly oxidizing atmosphere and using the sublimated HfF_4 with low oxygen content allowed us to improve the radiation hardness. An increase in the radiation hardness of the glass doped with some heterovalent cations of highest valency (Ce^{4+}, Fe^{3+}, Cr^{3+}) in comparison with undoped glasses was observed.

Keywords: fluoride glass, scintillator, radiation hardness.

Introduction

Scintillating HfF_4-based glasses, doped with Ce^{3+}, are attractive as scintillator for sensors because of the small decay time, large density, and small cost of production, compared to single crystal scintillators. A relatively poor radiation hardness in comparison with single crystal scintillators is a disadvantage of such glass [1, 2]. It is well known that cation and anion impurities can strongly affect the radiation hardness of solids. The synthesis atmosphere, particularly in the presence of heterovalent cations, is another important factor determining radiation hardness.

In the present work the effect of cation (Fe, Cr, Ni, Zr) and anion impurities (oxygen, chlorine) on the radiation hardness of scintillating fluorogafnate glasses doped with $Ce^{3+}$was studied. The most stable compositions in the HfF_4-BaF_2-CeF_3-AlF_3-NaF-InF_3 system, which allowed preparation of large size glass without crystallization, were chosen for investigation.

Experimental

The compositions of the fluorogafnate glasses in HfF_4-BaF_2-CeF_3-AlF_3-NaF-InF_3 system (HBCeANI) are given in Table 1.

Table 1. Compositions of glasses (mol.%)

HfF_4	BaF_2	CeF_3	AlF_3	NaF	InF_3
51.5	20	5	2.5	20	1
61.5	15	5	2.5	15	1
48	20	5	4	22	1
57	33	5	4	-	1
57	34	8	-	-	1

Typical content of transition metals in the raw fluorides was $5 \cdot 10^{-3}$ to 10^{-2} %, and the oxygen concentration was $5 \cdot 10^{-2}$ to 10^{-1} %. The concentration of FeF_3, CrF_3, NiF_2, CeF_4, CeO_2, HfO_2 dopants added in the batches varied from 0.1 to 0.3 wt.%.

In order to ensure identical melting condition, series of glasses doped with different additives and undoped glass as control were prepared simultaneously in several sockets of carbon boat covered with glass carbon. The glasses were melted at 840-860°C for 60 min and then cooled to 620 °C. Then the boat was removed from the furnace and quenched at a fixed cooling rate. The glasses were melted in Ar, Ar+5 vol % H_2, Ar+3 vol %Cl_2 and Ar+ 0.1 vol %Cl_2 atmospheres.

Samples for optical absorption spectroscopy were prepared by polishing glasses to plates 5 mm thick and 6 mm diameter. The samples prepared were measured before and after γ-irradiation using Specord M 40 Spectrometer in the range 250-780 nm.

In order to characterize the radiation damage, the radiation induced absorption coefficient μ(λ) after γ-irradiation (^{60}Co source) was defined, $\mu(\lambda) = (1/d)\ln(T_o(\lambda)/T(\lambda))$, where d is the sample thickness, T_o the optical transmission before irradiation, T the optical transmission after irradiation. Light yield was estimated by comparing the ^{137}Cs photo peak obtained from the glass sample with that obtained from a standard CeF_3 crystal of same dimensions.

Results

The effect of glass melting atmosphere on radiation hardness is shown in Figs.1 and 2.

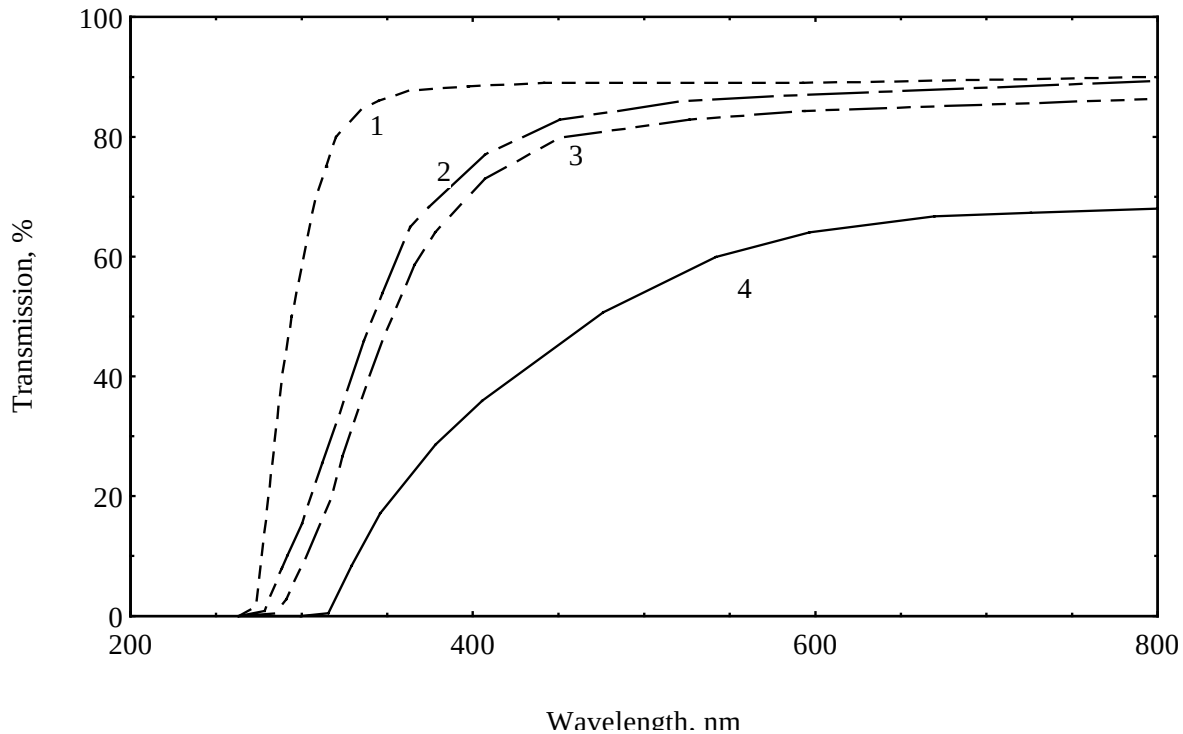

Fig 1.Transmission spectra of 51,5HfF_4 20BaF_2 5CeF_3 2,5AlF_3 20NaF-InF_3 glass melted under Ar and (Ar+H_2) atmosphere: 1- Ar atmosphere, before γ-irradiation; 2- Ar atmosphere, after γ-irradiation with 5 10^5 rad dose; 3- Ar atmosphere, after γ-irradiation with 10^7 rad dose; 4- (Ar+5%H_2) atmosphere, after γ-irradiation with 5 10^5 rad dose

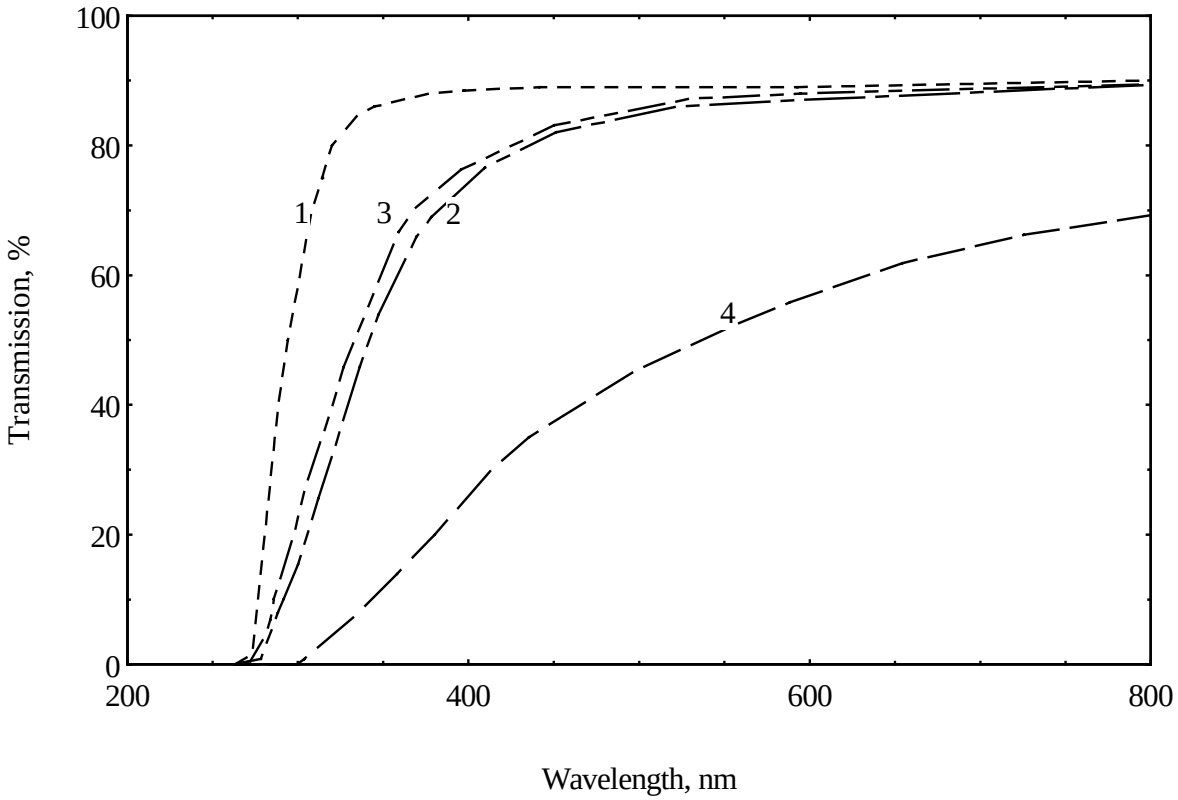

Fig 2.Transmission spectra of 51,5HfF_4 20BaF_2 5CeF_3 2,5AlF_3 20NaF-InF_3 glasses melted under (Ar+Cl_2) atmosphere: 1- glass melted under (Ar+0,1%Cl_2) atmosphere, before γ-irradiation; 2- Ar atmosphere , after γ-irradiation with 5 10^5 rad dose; 3- (Ar+0,1%Cl_2) atmosphere ,after γ-irradiation with 5 10^5 rad dose; 4- (Ar+3%Cl_2) atmosphere ,after γ-irradiation with 5 10^5 rad dose

Strong radiation damage took place for glass melted in reducing atmosphere as well as for that melted in atmosphere with high chlorine concentration. Transmission spectra of glass melted in Ar and Ar with a low chlorine concentration were similar. In latter case, slightly increased transmission after γ-irradiation was observed.

The transmission spectra of HBCANI glasses doped with transition metal fluorides and oxides before and after γ-irradiation are shown in Fig.3 and Fig.4 in comparison with undoped HBCANI glasses melted in argon atmosphere. Some glasses were prepared from batch containing HfF_4 purified by sublimation. This treatment moves off oxygen and transition metals. The transmission spectra of these glasses are shown in Fig.5.

Radiation induced absorption coefficients of some glasses and light yields under γ-excitation are given in Table 2.

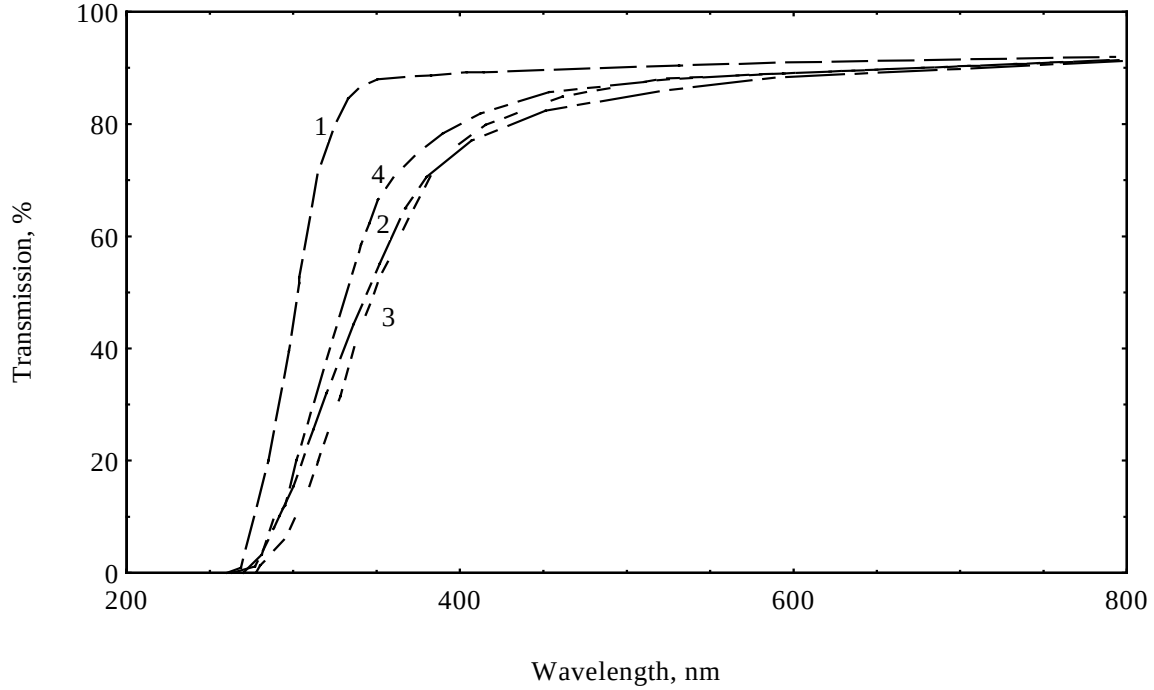

Fig 3.Transmission spectra of $51{,}5HfF_4\ 20BaF_2\ 5CeF_3\ 2{,}5AlF_3\ 20NaF\text{-}InF_3$ glasses doped with CeO_2 and CeF_4 melted under Ar: 1- glass doped with 0,3% CeF_4, before γ-irradiation; 2-undoped glass, after γ-irradiation with 5 10^5 rad dose, 3- glass doped with 0,2% CeO_2, after γ-irradiation with 5 10^5 rad dose; 4- glass doped with 0,3% CeF_4, after γ-irradiation with 5 10^5 rad dose;

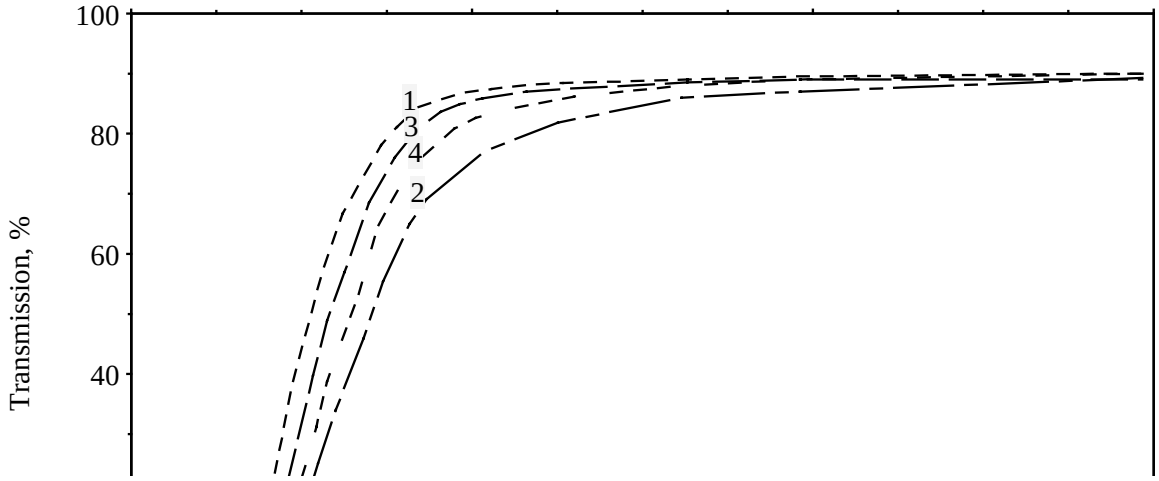

Fig 4.Transmission spectra of $51{,}5HfF_4\ 20BaF_2\ 5CeF_3\ 2{,}5AlF_3\ 20NaF\text{-}InF_3$ glasses doped with FeF_3 melted under Ar: 1- glass doped with 0,2% FeF_3 ,before γ-irradiation; 2- undoped glass after γ-irradiation with 10^7 rad dose; 3 - glass doped with 0,2% FeF_3, after γ-irradiation with 10^7 rad dose 4-glass doped with 0,2% FeF_3, after γ-irradiation with 10^7 rad dose

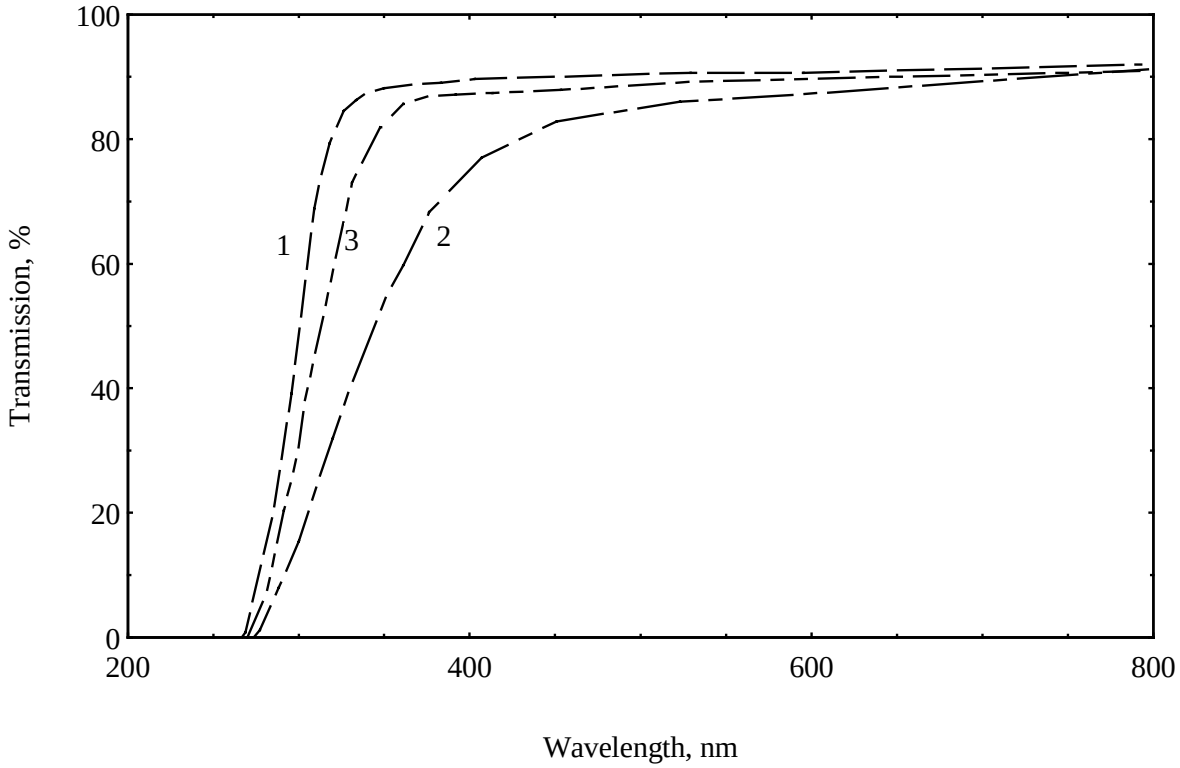

Fig 5.Transmission spectra of 51,5HfF_4 20BaF_2 5CeF_3 2,5AlF_3 20NaF-InF_3 glasses prepared from batch contained sublimated HfF_4 (Ar atmosphere): 1- undoped glass, before γ-irradiation; 2- undoped glass, after γ-irradiation with 10^7 rad dose;; 4- glass doped with 0,3% CeF_4, after γ-irradiation with 10^7 rad dose

Table2 Radiation induced absorption coefficients and light yields of glasses.

Additives, wt%	Melting atmosphere	μ, cm^{-1}, After $5\cdot10^5$ rad		μ, cm^{-1}, after $1\cdot10^7$ rad		Light yield, %NaI(Tl)
		at 325 nm	at 360 nm	at 325 nm	at 360 nm	
Base composition without additives	Ar	1,34	0,66	1,60	0,77	0.52
"	Ar+5%H_2	3,60	2,53	-	-	0.75
"	Ar+3%Cl_2	4,72	3,3	-	-	0.50
"	Ar+0.1%Cl_2	1,15	0,36	1,34	0,68	0.54
0.2CeO_2	Ar	1,65	0,80	2,02	1,05	0.52
0.3CeF_4	"	0,78	0,32	1,19	0,60	0.48
0.1FeF_3	"	0,55	0,12	0,74	0,28	0.44
0.1CrF_3	"	0,70	0,16	01,02	0,36	0.43
3.0ZrF_4		1,30	0,60	1,52	0,73	
5ZrF_4	"	1,42	0,71	1,64	0,80	0.46
Purified HfF_4 without additives	"	0,65	0,15	0,85	0,35	0.56
Purified HfF_4 +0.3CeF_4	"	0,21	0,049	0,35	0,54	0.53
Purified HfF_4 +0.1FeF_3	"	0,19	0,042	0,30	0,048	0.48

On the basis of the experimental data obtained it is possible to make the next conclusions:

-The glass composition does not effect substantially on the radiation hardness. All glasses presented in Table 1 show similar behavior.

-The spectra of glasses melted under different atmospheres show no evidence of any absorption in UV and visible range before irradiation with the exception glasses doped with Ni^{2+} and Cr^{3+} which show characteristic absorption bands;

-The glass melting atmosphere strongly influences the radiation hardness of the fluorohafnate glasses. Regardless of the glass composition and doping, the radiation hardness decreases when reducing atmosphere is used;

-There was a strong fall of radiation hardness of glass melted in argon with high chlorine concentration; however, at low chlorine concentration a little increase of the radiation resistance in comparison with glass melted in neutral atmosphere was observed;

-The glasses doped with oxides show lower radiation hardness in comparison with control;

-The radiation hardness of the glasses doped with CeF_4, FeF_3, CrF_3 is higher than that of control;

-The NiF_2, ZrF_4 impurities did not influence radiation hardness;

-The glasses prepared under neutral or mildly oxidizing atmosphere from the batch contained the sublimated HfF_4 and doped with CeF_4 or FeF_3 have the best radiation hardness;

-The light yield of glasses doped with transition metals is lower than that of undoped glasses;

-Reducing atmosphere leads to increase of light yield.

Discussion

Reducing atmosphere of glass melting results in increased filling of local states above the valence band giving rise to higher concentration and higher depth of hole traps. Reducing atmosphere can also promote the formation of Hf^{3+} and structure defects, e.g. fluorine vacancies acting as electron traps. All this may lead to the observed increase of radiation-induced coloration of glasses melted in reducing atmosphere. The effect of oxygen and chlorine on coloration of irradiated glasses can be explained by introduction with these impurities defects acting as hole traps. The formation of coloration centers in the fluorozirconate glasses under ionizing radiation was studied in [3-6]. The stable holes centers connected with O and Cl as well as Zr^{3+} ions resulting from trapping electrons were found. Similar defects should be formed in fluorohafnate glasses due to similarity of the compositions and properties of the fluorozirconate and fluorohafnate glasses. Decrease of the radiation damage of the glasses prepared from batch containing high purity HfF_4 is in accordance with the role of the oxygen defects in coloration. The Cl impurity also enhances coloration due to formation of hole traps. The observed improvement of the radiation hardness of the glasses melted at low chlorine concentration can be explained if one assumes the low absorption by center Cl_F^0 formed by trapping hole at Cl^- as compared with some other hole center forming in the absence of F. At low Cl concentration, the formation of that hole centers is inhibited by Cl^- competition in hole trapping. If the simultaneously formed electron centers also have relatively low absorption the resulting coloration will be lower then in Cl-free glass. Increase of overall concentration of electron and hole centers at higher Cl concentrations leads in the end to increased radiation damage.

It is known that the glasses often contain reduced ions Zr^{3+}(Hf^{3+}) [7,8]. As a result, fluorine vacancies may appear elsewhere in glass network. The effect of heterovalent cations with highest valency (Fe^{3+}, Cr^{3+}, Ce^{4+}) on radiation damage of the glasses melted under

neutral atmosphere may be explained by decreasing of the Hf^{3+} ions and fluorine vacancies due to the oxidizing effect of these impurities. Also the valency of the heterovalent impurity cations may change depending on glass melting conditions. For example both Fe^{3+} and Fe^{2+} ions are usually present in the glasses melted under neutral atmosphere [9]. Reducing atmosphere reduces these impurities in the melt to low valency and the effect of doping disappears.

The clearing up of the optimum gas atmosphere of glass melting as well as optimum concentration of the above mentioned heterovalent cations may be a promising approach to improve the radiation hardness of glass in future. Another approach is the shift of the luminescence peak to a longer wavelengths. In some cases the fluorohafnate glasses show fast scintillation (decay time less than 10 ns) at 360 nm in the absence of Ce ions [10]. At this wavelength the induced absorption coefficient is considerably less than that at wavelenght of Ce luminescent peak (Table 2).

References

1. L.Dmitruk, E.Devitsin, V.Kozlov in Proc. 9th Int. Symp. on Non-Oxide Glasses, Hangzhou, China (1994) p.90.
2. P.R.Hobson, D.C.Imrie, T.Price, S.Salih, K.W.Bell, .M.Brown, D.J.A.Cockerill, P.S.Flower, G.H.Grayer, B.W. Kennedy, A.L.Lintern, M.Sproston, K.J.McKinlay, J.M. Parker, D. Bowen, T. Cliff, R. Hannay, R. Smith, J. Non-Cryst Solids **213&214** (1997) 147-151.
3. A. Abgrall, M. Poulain, G. Boisde, V. Cardin, G. Mase, Proc. SPIE. Vol. 618 Infrared Optical Material IV(1986), 63.
4. D.L.Griscom, P. Hart, J.M. Jewell, J.T. Kohli and J.E. Shelby. J. Non Cryst. Sol. 1988, 103, 300.
5. P.E. Fisanich, L.T Halliburton, L.N. Feuerhelm, S.M.Sibley, Journ.of non-crystalline solids, vol.70,pp.37-44,1985
6. R. Gases, D.L. Griscom, D.C. Tran, Journ.of non-crystalline solids, vol.72, pp.51-63, 1985
7. A.Bruce et. el. Proc. 7th Int. Symp. on Non-Oxide Glasses, Rennes, France 1990, 333-343.
8. D. R. MacFarlane, P.J. Newman, J.D. Cashion and A. Edgar Proc. 11th Int. Symp. on Non-Oxide Glasses. Sheffild, UK, (1998), 33-37.
9. P.W. France, S. F. Carter, J.M. Parker, Phys. Chem. Glasses, **27** (1986) 32-10.
10. S.Batygov, L.Dmitruk, L.Moiseeva, N.Vinogradova, L.Popov, Extended Abstracts of 11th Int. Symp.on Non-Oxide Glasses, September 1998, Sheffield, UK ,pp.252-255.

Magnetic resonance investigations on oxygen-related luminescence centres in A1N: Y_2O_3 ceramics

S.Schweizer[1], U.Rogulis[1], J.-M.Spaeth[1], L.Trinkler[2], and B. Berzina[2]

[1]*University of Paderborn, Warburger Str. 100, D-33098 Paderborn, Germany*
[2]*Institute of Solid State Physics, University of Latvia, 8 Kengaraga Street, LV-1063 Riga, Latvia*

Abstract. The structure of oxygen-related luminescence centres in nominally undoped and Y_2O_3 doped A1N ceramics were investigated by electron paramagnetic resonance (EPR), electron nuclear double resonance (ENDOR) and optically-detected EPR. The photoluminescence detected EPR lines having *g* values of 1.990 and 2.008 were assigned to a recombination between neighbouring donor and acceptor pairs. The two EPR lines at $g = 1.987$ and $g = 2.003$ detected via the recombination luminescence in the afterglow are due to a recombination between the same *distant* donor and acceptor pairs. The donor was previously speculated to be an electron trapped on an oxygen impurity which substitutes a nitrogen on a regular lattice site. The defect structure of the acceptor was established by ENDOR as a hole trapped on an O_N-v_{Al} complex (v_{Al} = Al vacancy). The measured superhyperfine interaction is caused by two equivalent ^{27}Al nuclei both having $a = \pm 29.6$ MHz and one ^{27}Al nucleus having $a = \pm 27.0$ MHz.

Keywords: Magnetic resonance, oxygen-related luminescence, A1N: Y_2O_3 ceramics

Introduction

The high thermoluminescence sensitivity to radiation of A1N Y_2O_3 ceramics which have been proposed for application as dosimetric material [1] encouraged the study of radiation defect centres in these ceramics. A1N crystallises in the wurtzite structure and has a band gap of 6.2 eV [2]. It is usually contaminated with oxygen. The optical properties of oxygen-related defects in A1N have been studied by several authors, e.g. [3—5]. Excitation of A1N with photon energies higher than 4.0 eV leads to a broad oxygen-related luminescence band in a spectral range between 310 and 380 nm. Irradiation of A1N with ultraviolet (UV) light or X-rays results not only in luminescence, but also in storage of radiation energy. The stored energy can be released either by thermal or by optical stimulation [6, 7]. Electron paramagnetic resonance (EPR) data of A1N have been discussed e.g. as oxygen-related defects [8] or as an electron trapped on a N vacancy [9]. EPR detected in red and infrared photo luminescence of A1N single crystals showed resonances of $S = 1/2$ and $S = 1$ systems [10]. In this article we present an investigation of the defect structure of oxygen-related luminescence centres in A1N: Y_2O_3 ceramics with magnetic resonance methods.

Experiment

Sample preparation

A1N: Y_2O_3 ceramics were sintered at 1785°C for 2 hours from fine grain A1N and Y_2O_3 powders produced by plasma synthesis [11]. The A1N powders, which were kept in an organic solvent, contained ≤ 1 ppm uncontrolled impurities such as Cr, Fe, Ni, Zn, and Zr whereas the Y_2O_3 powders were contaminated ≤ 1 ppm by Zr, Eu, Tb, Yb, and Lu. The oxygen content in A1N grains of Y_2O_3 doped A1N ceramics was determined to be approximately 0.15 mol%. In undoped A1N ceramics the oxygen content was estimated to be significantly higher, namely in the range of 0.7 mol%.

Spectroscopy

Prior to electron paramagnetic resonance (EPR) and electron nuclear double resonance (ENDOR) investigations the samples were X-irradiated (tungsten anode, 50 kV, 30 mA) for several hours at room temperature (RT). The EPR and ENDOR measurements were performed with a computer-controlled, custom-built EPR/ENDOR spectrometer.

Optically-detected EPR (ODEPR) spectra were recorded with a computer-controlled, custombuilt spectrometer working at 25 GHz (K-band), at 72 GHz (V-band) or at 93 GHz (W-band). All ODEPR spectra were measured at 1.5 K using a photomultiplier in a spectral range of 200—800 nm. In the case of photoluminescence detected EPR (PL-EPR) investigations the samples were excited in the ultraviolet (UV) spectral range with a deuterium lamp and a subsequent 240 nm interference filter at 1.5 K. The PL-EPR was detected either in the integral luminescence for wavelengths higher than 300 nm or in different spectral ranges using edge filters. The recombination luminescence detected EPR (RL-EPR) measurements where the EPR is measured in the afterglow luminescence were performed either following an excitation with a deuterium lamp (240 nm interference filter, 1-2 hours) or irradiation with a mobile X-ray tube (tungsten anode, 60 kV, 15 mA) at 4.2 K or at RT. The RL-EPR was detected either in the integral luminescence or using edge filters.

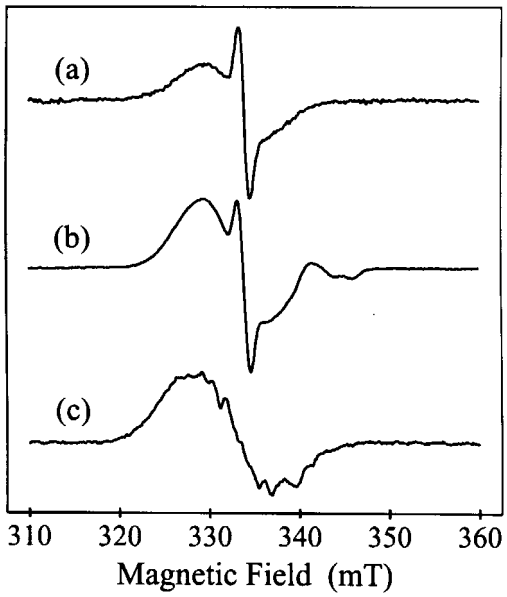

Figure 1. EPR spectrum of (a) undoped A1N ceramic, (b) A1N: Y_2O_3 (3.8 mol%), and (c) A1N: Y_2O_3 (9.6 mol%). All spectra were measured in X-band (9.31 GHz) at T = 6 K after X-irradiation at RT.

Experimental results

EPR and ENDOR

The EPR spectrum of undoped A1N ceramic shows after X-irradiation at room temperature a superposition of two structureless lines (figure 1(a)), one with g = 2.004±0.001 and a linewidth (full width at half maximum) of approximately 9 mT, which is very similar to the EPR line found in neutron-irradiated A1N ceramic [9], and one having g = 1.999±0.001 and a linewidth of 1.6—1.7 mT which was not observed in neutron-irradiated A1N ceramic. In the EPR spectrum of an A1N: Y_2O_3 (3.8 mol%) ceramic (figure 1(b)) additional resonances with g values between 1.96 and 1.98 could be detected. The ratio between the two EPR lines at g = 1.999 and g = 2.004 has changed in favour of the broad line at g = 2.004. The narrow EPR at g = 1.999 line has disappeared in the spectrum of the A1N: Y_2O_3 (9.6 mol%) ceramic (figure 1(c)), which shows a new structured line with g = 1.999. Storing the X-irradiated A1N

samples in the dark at RT for several days led to an simultaneous decrease of the broad EPR line and the narrow one. In A1N: Y_2O_3 (3.8 mol%) ceramic the resonances having g values between g = 1.96 and g = 1.98 remained unchanged whereas in A1N: Y_2O_3 (9.6 mol%) the structured line with g = 1.999 showed the same decay as the other two lines. After annealing up to 500°C for a few minutes all EPR signals have disappeared.

The ENDOR spectrum of A1N: Y_2O_3 (3.8 mol%) (figure 2(a)), measured at 333.4 mT, shows two lines at 10 and 18 MHz which are separated by approximately twice the Larmor frequency of ^{27}Al at the applied magnetic field. This indicates that these resonances are due to ^{27}Al interactions [12]. ENDOR-induced EPR on these lines showed that they belong to the

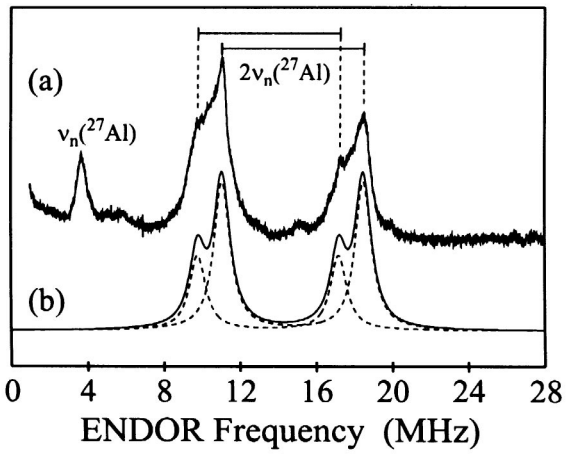

Figure 2. (a) ENDOR spectrum of A1N: Y_2O_3 (3.8 mol%) ceramic, measured in X-band (9.29 GHz) at B = 333.4 mT and T = 7 K after X-irradiation at RT. (b) Calculated ENDOR spectrum of a S = 1/2 system interacting with two equivalent ^{27}Al having an isotropic shf interaction of a = ±29.6 MHz and one ^{27}Al having a = ±27.0 MHz. The dashed lines indicate the two different ^{27}Al shf interactions.

broad EPR line at 2.004. The double structure of these lines can be understood by assuming a S = 1/2 system interacting with two equivalent ^{27}Al having an isotropic shf interaction of a = ±29.6 MHz and one ^{27}Al having a = ±27.0 MHz. The anisotropic shf interaction and the quadrupole interaction of ^{27}Al nuclei (nuclear spin of 5/2) are not resolved and below 1 MHz. The resonance at 3.70 MHz is due to the Larmor frequency of free ^{27}Al.

Optically-detected EPR

Figure 3(a), spectrum (1), shows a PL-EPR spectrum of undoped A1N ceramic in K-band (24 GHz). Only one line at approximately g = 2.00 having a linewidth of 21 mT could be detected. In W-band (93 GHz) we could observe two EPR lines (figure 3(b), spectrum (1)). One with g = 1.990±0.005 and a linewidth of 17 mT, and one with g = 2.008±0.005 and a linewidth of 12mT. No further resonances could be detected. The PL-EPR spectrum of A1N: Y_2O_3 (3.8 mol%) ceramic yielded the same resonances but with lower intensities. The line intensity ratio of the two lines did not change upon varying the spectral range of detection. In the A1N: Y_2O_3 (9.6 mol%) ceramic we did not find any EPR line.

After UV or X-ray excitation at 4.2 K all investigated ceramics showed an afterglow for several hours. RL-EPR of undoped A1N ceramic yielded in K-band only one EPR line at g = 1.995 with a linewidth of 17 mT (figure 3(a), spectrum (2)) whereas in W-band two lines could be detected (figure 3(b), spectrum (2)): one with g = 1.987±0.005 and a linewidth of 10 mT, and one with g = 2.003±0.005 and a linewidth of 14 mT (note, that the lines are saturation broadened). The RL-EPR spectra depend on the Y_2O_3 doping level: the EPR line at g = 2.003 is present for all doping levels whereas the resonance at g = 1.987 vanishes with higher Y_2O_3 concentration. The intensity ratio of the two lines did not change upon varying

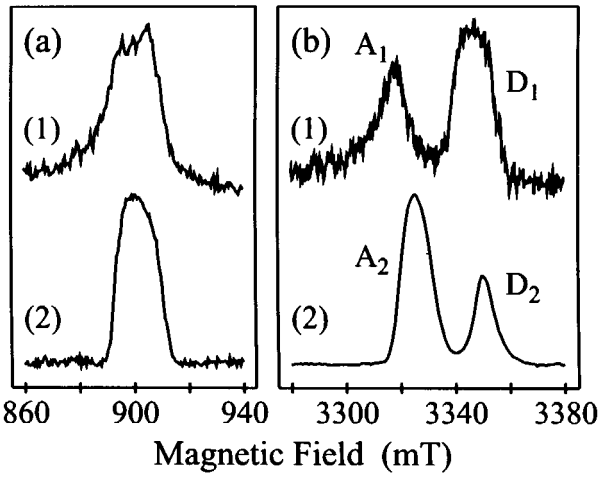

Figure 3. UV excited PL-EPR and RL-EPR spectra of undoped A1N ceramic detected in the integral luminescence, (a) K-band spectra: (1) PL-EPR, (2) RL-EPR; (b) W-band spectra: (1) PL-EPR, (2) RL-EPR

the spectral range of detection from 300 to 700 nm. The RL-EPR could also be detected after excitation at 4.2 K and subsequent annealing up to 300 K as well as after X-irradiation at RT.

Discussion

The two RL-EPR lines at g = 1.987 and at g = 2.003, respectively, belong to two defects with S = 1/2 each. This was established by RL-EPR investigations at different microwave frequencies (figure 3). We assigned the RL to a recombination of distant donors and acceptors. Since the g value of the line at g = 1.987 (labelled D_2 in figure 3) is smaller than 2, it must be assigned to a donor [12], whereas the line at g = 2.003 (labelled A_2) must be assigned to an acceptor.

Since the spectral characteristics of the PL is very similar to that of the RL, the two PL-EPR lines at g = 1.990 (labelled D1 in figure 3) and at g = 2.008 (labelled A_1), respectively, which belong also to defects with S = 1/2, should be caused by similar donor and acceptor pairs as those causing the RL-EPR. The donor was previously speculated to be an electron trapped on an oxygen which substitutes a nitrogen, i.e. $(O_N)^-$ [4, 5]. Therefore, we assign the donors detected by PL- and RL-EPR to $(O_N)^-$ centres. The fact that the g values of the donor and the acceptor are shifted somewhat in PL-EPR compared to RL-EPR as well as the changes in the EPR linewidths can be understood by a significantly different coupling between the donors and acceptors in PL. PL is in contrast to RL mainly caused by a recombination of exchange coupled neighbouring donors and acceptors, while the RL is the recombination between distant donors and acceptors.

The conventional EPR line at g = 2.004±0.001 having a linewidth of approximately 9 mT is within experimental error identical to the RL-EPR line at g = 2.003±0.005 which has a linewidth of about 10 mT (for low microwave power). The ENDOR spectrum, measured on this EPR line, showed the presence of a shf interaction with two equivalent ^{27}Al nuclei having a = ±29.6 MHz and one ^{27}Al having a = ±27.0 MHz. This indicates that our defect has three ^{27}Al nuclei as nearest neighbours which is in agreement with the model of an O_N-v_{Al} complex for A_2 discussed in the literature [4, 5]. The intensity of the structureless EPR line at g = 1.999 changes upon the Y_2O_3 doping level. Since the oxygen content in A1N ceramics is reduced by Y_2O_3 doping this line is probably also due to an oxygen-related defect centre. The nature of the other observed resonances is still an open question.

References

1. L.Trinkler, P.Christensen, N.A.Larsen, and B.Berzina, Radiation Measurements **29** (1998), 341.
2. S.Loughin, R.H.French, W.Y.Ching, Y.N.Xu, and G.A.Slack, Appl. Phys. Lett. **63** (1993), 1182.
3. S.J.Pacesova and L.Jastrabik, phys. stat. sol. (b) **93** (1979), K111.
4. R.A.Youngman and J.H.Harris, Journal of American Ceramic Society **73** (1990), 3238.
5. T.Mattila and R.M.Nieminen, Phys. Rev. B **55** (1997), 9571.
6. B.Berzina, L.Trinkler, E.Palcevskis, and J.Sils, Materials Science Forum **239—241** (1996), 145.
7. L.Trinkler, A.J.J.Bos, A.J.M.Winkelman, P.Christensen, N.Agersnap Larsen, B.Berzina, Radiation Protection Dosimetry **84** (1999), 207.
8. G.E.Archangelskii, M.V.Fock, S.I.Pacesova, and L.Jastrabik, phys. stat. sol. (b) **108** (1981), K117.
9. K.Atobe, M.Honda, N.Fukuoka, M.Okada, and M.Nakagawa, Japanese Journal of Applied Physics **29** (1990), 150.
10. P.W.Mason, H.Przybylinska, G.D.Watkins, W.J.Choyke, G.A.Slack, Phys. Rev. B **59** (1999), 1937.
11. E.Palcevskis, L.Jakobsen, L.Trinkler, and U.Ulmanis, Proc. Euro Ceramics V. Key Engineering Materials **132—136** (1997), 185.
12. J.-M.Spaeth, J.R.Niklas, and B.H.Bartram, Structural Analysis of Point Defects in Solids, Springer Series in Solid State Sciences **43**, Springer Verlag, Berlin, 1992.

Scintillation Properties of Monolithic Polycrystalline ZnS-Te

Gorokhova E.I.*
Tiurin G.P.**., Permogorov S. A.***, Khristich O. A.*

** S.I. Vavilov GOI, St. Petersburg, Russia*
*** «V.G. Khlopin Radium Institute» NPO, St. Petersburg, Russia*
**** A.F. Ioffe Physical Technical Institute, St. Petersburg, Russia*

Abstract. The experimental data of monolithic polycrystalline transparent ZnS -Te capasity of efficient ionizing radiation to light conversion and of its quick response. Is was established that when subjected to 3,5 MeV alpha particles radiation, the ZnS – Te polycrystal as compared to CsI – Tl crystal features 1.6 times greater pulse amplitude and almost 6 times quicker response. It was noted that the ZnS – Te polycrystal displays low gamma quanta sensitivity, which is important for the detection of charged particles accompanied by gamma quanta background. ZnS-Te can be looked at as a rather promising scintillation detector material for experimental nuclear physics applications - detection and counting of charged particles at the wide energy range, including high energy charged particles of the cosmic origin.

Keywords: detection of ionizing radiation, transparent polycrystalline ZnS-Te, scintillation properties.

Success in nuclear radiation research strongly depends on the efficiency of the scintillation detector of ionizing radiation and on its response time [1]. That explains the interest of the designers in expanding their inventory of scintillating materials and upgrading the qualities of those already known. The experiments studying the effects of charged particles on monolithic polycrystalline ZnS-Te which were obtained by the authors as early as the beginning of the ‘90s as a cathode luminescence screen [2] permitted us to estimate that material’s capacity of efficient conversion of ionizing radiation to light, combined with the fast response. This report presents the results of that research work.

Investigation of transmission spectra in the ZnS-Te test samples disclosed that their transparency window is no different from that of the non-doped ZnS, and extends from 0.36 to 15 μm. Fig.1 presents a fragment of the transmission spectra of ZnS-Te samples optimal in terms of composition and manufacturing conditions. The density of those samples corresponds to the x-ray structural density - 4.09 g/cm^3. The average grain size varies depending on the composition and conditions of manufacture from 50 to 200 μm. The microhardness is near to that of ZnS monocrystals, and is 190± kg/mm^2.

Investigation of the luminescence spectra of polycrystalline ZnS-Te samples was carried out using excitation by an unfocused nitrogen laser beam at T = 80 and 300 K. The spectra obtained feature intensive luminescence bands in blue part of the spectrum, corresponding to recombination of excitons bound at single atoms or closely located pairs of the isoelectronic Te dopant. A close correlation was observed between the Te content in the mixture and the Te dopant concentration in the sample. Luminescence spectrum of the most efficient ZnS-Te samples is displayed in Fig.1.

The study of scintillation properties of ZnS-Te was carried out in Russia (at the “V. G. Khlopin Radium Institute “ NPO) and in Finland (at the University of Iyvaskyla, Physical Department, Accelerator Laboratory) using irradiation by different radiation sources: alpha particles (^{241}Am, standard ^{233}U, ^{238}Pu, ^{239}Pu isotopes mix), the ^{252}Cf spontaneous fission

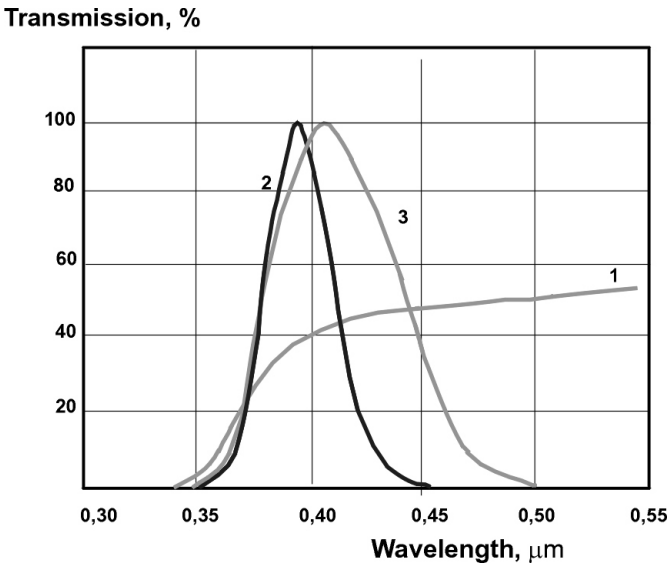

Fig.1 A fragment of the transmission spectrum (1) and the emission spectrum (2,3) of doped monolithic polycrystalline ZnS. Excitation be the LGI-21 nitrogen laser.
2 - T=77K; 3 - T=300K. (1 mm thick sample).

fragments, gamma quanta (^{60}Co) and by different (C, S, Fe, Xe) ion beams. The scintillating material was positioned upon the entrance window of the photomultiplier (FEU-30) through the optical grease, at 1 cm distance from the was watched using the digital oscilloscope, Le-Croy-9310, which featured 300 MHz frequency range and allowed to register 1 ns rise time pulses.

The data obtained was compared to characteristics of the monocrystalline CsI-Tl tested under analogous conditions. The thickness of the samples compared was 4 mm. Fig.2 depicts the pulse shapes at photomultiplier output when the ZnS-Te and CsI-Tl scintillators were irradiated by ^{241}Am source 5.3 Mev α-particles. The oscillogrammes illustrate that an ZnS-Te based scintillator compared to a CsI-Tl crystal delivers 1.6 times greater pulse amplitude along with approximately 6 times faster rise and fall time of the output signal. At the same time it was found that the ZnS-Te parameters in time domain could be controlled: changing the Te content in the polycrystal enables to vary afterglow time between 5 and 250 ns. It is necessary to note however that with shorter afterglow the decrease in pulse amplitude was observed.

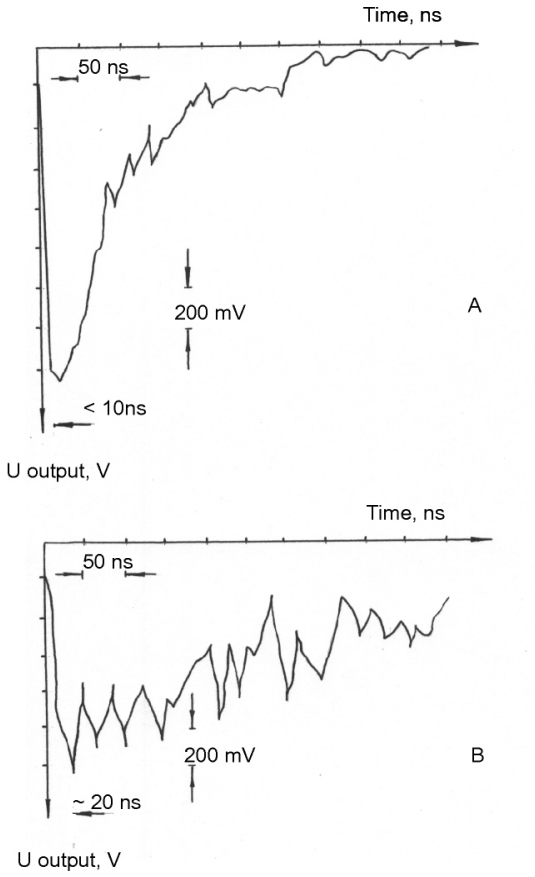

Fig 2 . The photomultiplier output pulse shapes when irradiating the doped monolithic polycrystalline ZnS based (a) and monocrystalline CsI-Tl based (b) scintillators by ^{241}Am
Sourse a-particles (5.3 Mev).

The research revealed low sensitivity of ZnS-Te to γ-quanta. For example, when being irradiated by γ-quanta from a ^{60}Co source there were practically no pulses observed at the photomultiplier output, while the same radiation when applied to a CsI-Tl crystal yielded significant pulse amplitudes, comparable to pulse amplitude produced by α-particles radiation. This particular property of the scintillator could be most helpful when making use of it in registering charged particles against the background of γ-quanta. Calculations demonstrate that with thickness of 4 mm the energy with which a particle would «shoot through» an ZnS-Te based scintillator will be 40 Mev for protons, 120 Mev for α-particles. It follows that creating the scintillators with greater thickness would allow to implement them for the detection of higher energy protons and α-particles, the task which is quite actual at the moment. The

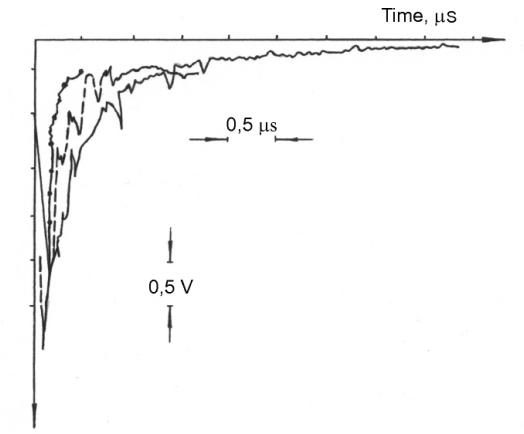

Fig 3. Various pulse shapes when irradiating the doped monolithic polycrystalline ZnS based scintillator by the flux of ^{252}Cf spontaneous fission fragments.

matter of energy resolution demands additional consideration, but low light flash rise time allows to use this scintillator for the spectrometry of charged particles by their time of flight. The low light flash fall time makes it possible to work at higher flux intensities of charged particles. It was observed when irradiating the scintillator by the ^{252}Cf fission fragments that the pulses of the same amplitude displayed different fall times (Fig.3). That allows to suggest that this scintillator could be used in particle identification by charge (Z-identification), for which purpose sufficiently thin scintillator layers could be employed.

Fig.4 demonstrates the dependencies between the pulse amplitude at spectrometric channel output for the CsI-Tl and ZnS-Te scintillation detectors and the energy of the registered particles, obtained when the detectors were irradiated by the monoenergetic flux of different ions. For the ZnS-Te scintillators, in contrast to the CsI-Tl ones, a linear relationship is observed between the light flash energy and the energy of the particles being registered across the wide span of their atomic masses, which allows to look forward to a certain simplification of the procedure of energy calibration for a scintillation detector when employing ZnS-Te.

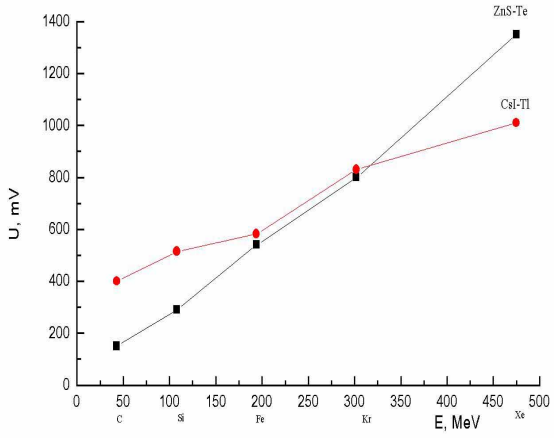

Fig.4 Dependencies of the pulse amplitudes at spectrometric channel output for the CsI-Tl based and ZnS-Te based scintillation detectors on the energy of the registered particles, obtained when irradiating the detectors by a flux of monoenergetical ion beams.

The table reflects basic properties of the ZnS-Te based scintillator in comparison to similar characteristics of wide known scintillators [3].The collation with its powder* zinc sulfide analog (ZnS-Ag) demonstrates that ZnS-Te offers high transmittance within its own emission band (see Fig.1, graph 1), comparable with that of the monocrystalline ZnS (i.e. approaching the theoretically possible), and remarkable parameters in time domain. In terms of response and light output, ZnS-Te surpasses not only CsI-Tl, but also CaF-Eu.

When compared to NaI-Tl, ZnS-Te displays higher service ratings (strength, no hygroscopicity, etc.), although it lags slightly behind in light output.

Altogether, taking the properties achieved in their entirety, the transparent monolithic polycrystalline ZnS-Te can be looked at as a rather promising scintillation detector material for experimental nuclear physics applications - detection and counting of charged particles at the wide energy range, including high energy charged particles of the cosmic origin.

The physical properties of ZnS-Te and some other known scintillators [3]

Properties	ZnS-Ag (powder)	NaI-Tl (mono-crystal)	CsI-Tl (mono-crystal)	CaF-Eu (mono-crystal)	ZnS-Te (poly-crystal)
Emission maximum (nm)	450	415	550	435	410
Light output, % rel. to NaI-Tl	130	100	45÷50	20	80
Decay time (ns)	300÷10000	230	600÷1000	940	200÷250
Mechanical behaviour	fragile	fragile, laminate	soft, plastic deform	mechanically strong	mechanically strong
Hygroscopicity	no	yes	yes	no	no
Optical quality	opaque	transparent	transparent	transparent	transparent

*In addition, direct experimental assessment of the properties was carried out (under the same conditions as ZnS-Te) for the luminescent optical ceramics ZnS-Ag, Cl, created by the authors at the end of the ‘70s [4, 5]. The tests run on the 0.4 to 1.0 mm thick samples have indicated that the ZnS-Ag, Cl ceramics is similar in light output to ZnS-Te, and in damping time - to ZnS-Ag powder. But in contrast to the latter, the ZnS-Ag, Cl ceramics is transparent in the optical spectrum (transmittance within its own emission band, with λ_{max} - 470, is 15÷30%, depending on thickness), offers high radiation strength and mechanical strength. Preliminary result obtained is the evidence of advisability of considering the possibilities for employing the ZnS-Ag, Cl luminescent optical ceramics in α-particles registration scintillator capacity.

References

1. G. Blasse. Scintillator Materials. American Chemical Society, Vol.6, Iss 9, (1994) 1465.
2. E. I. Gorokhova, L. N. Kinzhibalo, S. A. Permogorov, L. N. Tenishev, O. A. Khistich. Abstr. International Conf. Luminophor - 92 187.
3. HARSHAW/QS Scintillation Detector Catalog. Saint-Gobain, Ceramiques Industriells, (1992) 111.
4. F. K. Volynets, , E. I. Gorokhova et all., Izobretenie 515352 (1972).
5. Gorokhova E.I., Kuprevich V.V., Vasiliev P.J. Cathodeluminescent Composite Screen Based on Zincsulfide Luminescent Optical Ceramics. Optical Journal. (1992). - Iss. 10 59.

Small-grained Detector of Ionizing Radiation Based on ZnSe(Te)

V.G.Volkov, V.P.Gavrilyuk, L.P.Gal'chinetskii, B.V.Grinyov, E.A.Danshin,
K.A.Katrunov, V.Z.Kvitnitskaya, V.D.Ryzhikov.

Institute for Single Crystals, 60 Lenin ave., 310001 Kharkov, Ukraine

Abstract. A highly efficient ZnSe(Te) scintillation detector combined with Si-photodiode has been developed. A conglomerate made up of ZnSe(Te) grains is used as a scintillator. Optimal shape of the grains, reflecting cover and disperse environment type are selected to improve light collection within the detector using numerical simulation. Various shapes of light guides have been considered to maximize light output of the detector.

Keywords: small-grained scintillator, γ-,β-radiation, light transducer

Introduction

Scintillators based on ZnSe(Te) in combination with silicon photodiode are distinguished by their high scintillation efficiency η (18%) [1] and good spectral matching coefficient F = 91% . This makes them very promising for detection of beta- and low energy gamma-radiation. Single crystalline plates ZnSe(Te) in combination with PMT -110 have energy resolution of ≅ 9% for conversion electrons ^{137}Cs [2]. In addition, crystals ZnSe(Te) are non-hygroscopic and have high radiation stability (up to 10^8 rad). Electron back scattering coefficient *k* in ZnSe(Te) is 40-50%.

The present-day preparation techniques of scintillation crystals ZnSe(Te) do not allow to obtain plates larger than 4 cm in diameter. Improvement of detector sensitivity can be achieved not only by increasing its area, but also by creation of optimum conditions of light collection in the scintillator.

One of the possible ways to increase the detector area is to make a detector in the form of a conglomerate of small grains of ZnSe(Te) combined into a single "small-grained" ("small-crystalline") scintillator. The area of such scintillator is practically unlimited from the point of view of technology of its preparation. In this case the problem of optimum light collection conditions becomes vital. The ways of its solution involve optimization of the grain size, the use of additional reflective coatings and transparent disperse medium in which the grains are installed.

In this paper we report a small-grained scintillator based on ZnSe(Te). Its thickness is 0.15-0.2 cm, which corresponds to 90% absorption of 50 keV γ-ray radiation or 2.4 MeV beta-radiation [3]. The grain size was chosen to correspond to the scintillator thickness (single-layer packing). Multilayer structures with particle size smaller than the scintillator thickness have low output efficiency of intrinsic radiation due to light losses on the grain boundaries.

Calculation of optimum light collection conditions in a ZnSe grain

Using Monte-Carlo (MC) method, calculations of optimum light collection conditions in the small-grained ZnSe(Te) scintillator were carried out. The MC procedures for calculation of light collection in scintillation detectors have been described in detail [4]. For the calculations, we assumed that grain sides were mirror-smooth (cleavage surfaces). Two limiting cases were considered of the location of scintillation flashed inside the grain: a) high penetrating ability of the detected radiation – the flashes are uniformly distributed inside the crystal; b) low penetrating ability of the detected radiation, which is completely absorbed by

the thin layer adjacent to the crystal surface (the layer thickness is small as compared with characteristic dimensions of the crystal). For intermediate values of penetrating ability the light collection τ is between these limiting cases.

Several shapes of ZnSe(Te) grains, which are easily obtainable practically, have been considered: parallelogram, parallelogram with rounded upper side, tetrahedral pyramid, trihedral and hexahedral prisms, and a hemisphere. In Table 1 calculated values τ are presented for grains of these shapes, both without additional reflective coating and for two cases of reflective coatings. These cases were: a) diffusely scattering coating without optical contact with crystal surface and reflection coefficient R=0.9, which is realized with Teflon reflectors (reflector 1); b) reflective coating in optical contact with the crystal surface, R=0.9 (reflector 2), which corresponds to covering of the crystal surface with MgO powder.

Table 1. Light collection coefficients of ZnSe(Te) grains of different shapes and types of reflective coating

Shape grain	without reflector	reflector 1	reflector 2	without reflector	reflector 1	reflector 2
	the flashes uniformly distributed inside a grain			the flashes absorbed by the thin layer adjacent to the grain surface		
Tetrahedral pyramid	0,600	0,815	0,590	0,668	0,836	0,599
Hemisphere	0,437	0,508	0,536	0,627	0,656	0,548
Trihedral prism (pattern 1)*	0,357	0,447	0,484	0,378	0,461	0,470
Trihedral prisms (pattern 2)*	0,147	0,177	0,263	0,146	0,180	0,256
Hexahedral prism (pattern 1)*	0,202	0,258	0,190	0,221	0,264	0,193
Hexahedral prism (pattern 2)*	0,145	0,172	0,395	0,147	0,171	0,412
Parallelogram with rounded upper side **	0,339	0,410	0,297	0,371	0,432	0,296
Parallelogram	0,144	0,173	0,258	0,145	0,175	0,259

*pattern 1 corresponds to the case when one of the sides of the prism is the output window; pattern 2 – when the output window is the prism bottom.

**grain has a shape of parallelogram; the side opposing the output window is a part of cylindrical surface with r=0.17 cm.

Calculation results accounting for effects of the adhesive composition with n=1.5 and absorption coefficient α=0.05 cm^{-1} upon light transmission from the output window to the light sensitive surface of the silicon photodiode with n=4 showed that 68% of the total light passed through the output window of the scintillator are reflected from the boundary “crystal-adhesive”; 6.7% are reflected from the boundary “adhesive – photodiode surface”; 0.3% are absorbed in the bulk of adhesive, and only 25% interact with the light-sensitive surface of the photodiode. For adhesives with n=1.6 this value increases up to 30%, and with n=1.8 – even 40%. Filling with adhesive of the space above the output window leads to a decrease in τ with higher filling levels.

It can be concluded from these results:

- maximum τ value for a single crystalline grain of ZnSe(Te) is reached when it is pyramid-shaped with side inclination angle to the base 60^o;

-light collection for all the considered crystal shapes is improved in the presence of light-reflecting coating, degree of this improvement is substantially different with different shapes;

-filling the space between grains with an optical adhesive leads to a decrease in the light output;

-the fraction of intrinsic radiation that interacts with the sensitive surface of the photodiode substantially increases with higher n of the adhesive ensuring the optical contact between the detector output window and the photodiode;

-application of the reflective coating onto the grain surface favors rise in integral light output of the small-grained scintillator.

Efficiency of a small-grained ZnSe(Te) scintillator

Accounting for the results of computer calculations aimed at optimization of light collection conditions 4 samples of small-grained ZnSe(Te) scintillator were prepared, 3.5 cm in diameter and 0.15 cm thick:

sample 1 – formed of several layers of grains of arbitrary size and shape, without reflective coating, in the matrix of an optically transparent polymer medium; it was located inside a metal container with output window of quartz glass;

sample 2 – formed of one layer of grains of the optimized sizes and shapes in the matrix of an optically transparent polymer medium; covered with a special housing, without reflective coating and quartz glass;

sample 3 – same as sample 2, but the grains are covered with light-reflective composition;

sample 4 - a single-crystalline ZnSe(Te) plate.

The efficiency of the detectors was determined by measurement of the output signal by the pulse method in the counting mode. Intrinsic radiation was detected with silicon p-i-n photodiodes S3590 Hamamatsu. ^{137}Cs was used as ionizing radiation source. This nuclide, alongside with 662 keV gamma-radiation, does also emit internal conversion electrons. We determined both total number of countings (I_{total}) and the number of counts corresponding to gamma-radiation only (I_γ). In the latter case, an aluminum disc was installed between the source and detector to cut off beta-radiation. The difference $I_\beta = I_{total} - I_\gamma$ characterizes beta-efficiency of the detector, and the value $\kappa = I_\beta / I_{total}$ - its relative sensitivity to beta-radiation. X-ray sensitivity of the detector was determined by detection of the radiation from a RUP-100 X-ray source at 100 kV voltage on tube (effective energy of quanta ~70 keV). As photoreceiver a PD-288 silicon photodiode with light sensitive area of 1 cm^2 was used. The light output of the sample 1 was taken equal to 1. The measurement results are presented in Table 2.

Table 2. Efficiency of ZnSe(Te) small-grained scintillators for detection of beta- and gamma-radiation of ^{137}Cs and X-ray radiation

Sample	Number of countings			X-ray sensitivity, arb. Units	κ
	I_{total}	I_γ, E=665 кe	I_β, E=512 кe		
1	1900	1700	200	1,0	0,1
2	3500	1700	1800	1,31	0,5
3	4600	2700	1900	1,75	0,4
4	2700	2400	300	-	0,09

The following conclusions could be made:

-the best sensitivity, both with ^{137}Cs and 70 keV X-ray sources, was observed for sample 3;

-efficiency of sample 2 as compared with sample 1 is practically the same for gamma-radiation. At the same time, sample 2 is much more efficient for detection of beta-radiation. This can be explained by different penetrating ability of gamma- and beta-radiation in the scintillator material. Scintillation flashes caused by gamma-radiation of ^{137}Cs (E=665 keV) are distributed practically uniformly over the detector volume, while flashes due to beta-radiation (E=512 keV) appear in a thin layer near the surface. In the case of multilayer location of grains across the scintillator (sample 1), the scintillation light is substantially attenuated at the grain boundaries.

-the use of reflective coating on grain surfaces (sample 3) significantly improve the detector efficiency for gamma-radiation, sensitivity to beta-radiation remains practically unchanged. This is due to absorption of conversion electrons by the reflective coating on the grains;

-efficiency of the single crystalline plate of ZnSe(Te) is much lower for beta-radiation as compared with samples 2 and 3. For gamma-radiation, this difference is not so significant. This can be explained by non-smooth character of the scintillator surface, due to which electrons can be partially absorbed by adjacent grains. This means that effective coefficient of electrons back scattering from such surface is lower than for the smooth surface of the single crystalline plate. Consequently, the efficiency of the scintillator with respect to beta-radiation is higher.

Calculation of the optimum shape of light transducers.

To increase the output signal of the detector, the area of the substrate upon which scintillator grains are placed should be increased. The limit for such an increase is related to small light sensitive area of Si-photodiodes. Thus, there is a need to use a light transducer to concentrate the scintillation light on the photoreceiver.

Transmission coefficients were calculated for different types of light transducers using MC method. The reflection of light from the transducer surface, upon which scintillator grains were located, was considered as reflection from the boundary between media with refraction indexes of 1.5 and 2.57 respectively (light transducer – a ZnSe(Te) grain). If a light beam enters the grain, probability of its coming back to the transducer was taken as 0.6 (the value of light collection coefficient for the pyramid-shaped grain with the angle between the side and the base 60^o). The direction of a light beam having entered the transducer was considered as evenly distributed in space (isotropic source).

The transducer efficiency can be characterized by the relationship

$$P = \tau S_2/S_1 \qquad (1)$$

where S_2 is the area occupied by scintillator grains,

S_1 is the area of the transducer output window connected to the photoreceiver.

It shows how many times the signal from small-grained scintillator with light transducer is stronger than that in the case when scintillator grains are applied directly upon the transducer.

The optimum shape for light transducer is wedge-like (Fig.1a).

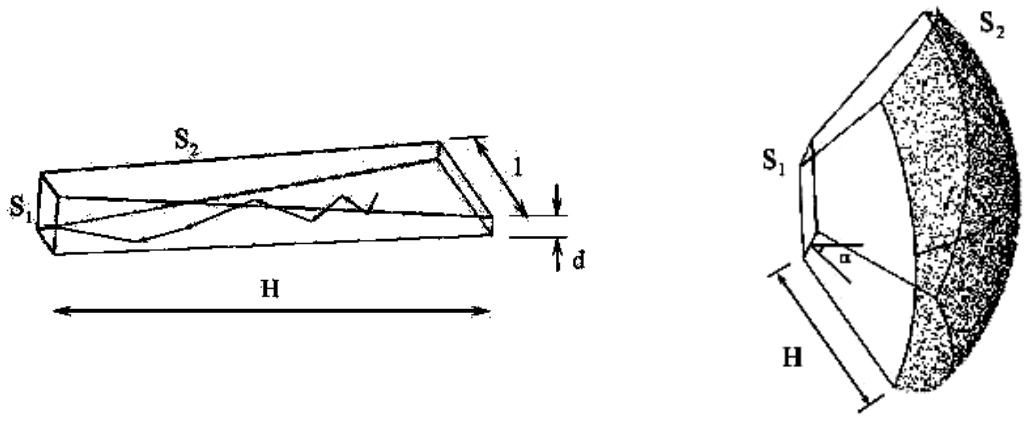

a b

Fig.1. Concentrating light transducers. S_1 – area coupled with the photoreceiver; S_2 – area covered with scintillator grains; a – wedge-like transducer (counting mode); b - transducer with spherical input surface (spectrometry).

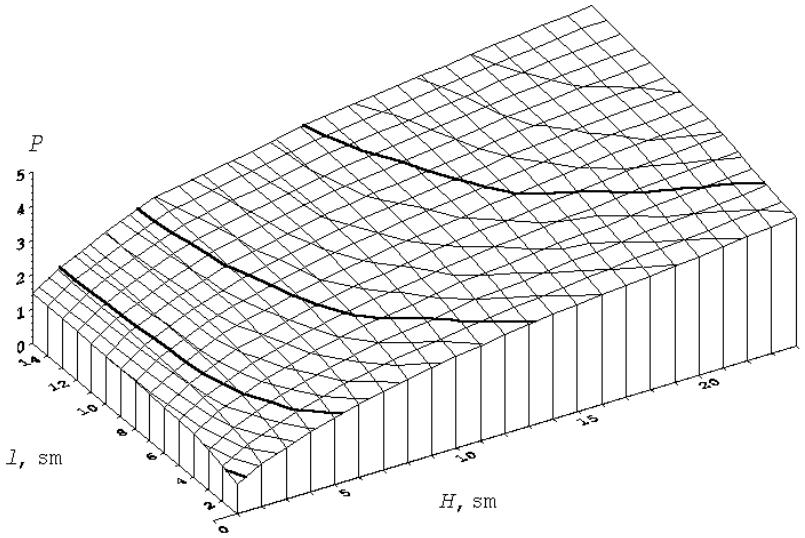

Fig.2. Efficiency P of the wedge-shaped light transducer as function of its dimensions – length *H* and width at the end opposite to the transducer *l*. Dimensions of the output window S_1 = 1×1 cm.

Scintillator grains are applied onto the surface of the wedge of large area. The back end of the wedge is light-sensitive (coupled with a photodiode). Optimization of the design consists in choosing wedge length *H* and its width at the far end (from the output window) *l* to ensure the highest efficiency P as defined by (1). Fig.2 shows calculated two-dimensional dependence of efficiency P upon the said geometrical factors. It is important that value of S_1 is practically not limited and should be related only with conditions of specific detector application.

To use a small-grained detector for spectrometry, the light transducer design should ensure equality of τ in different points of S_1. Analysis of different transducer shapes from this point of view showed that the optimum design is concentric in shape with input window in the form of spherical surface element (Fig.1b). Calculation of τ for such transducer (2 cm length, inclination angle of the sides to the output window 30^o) results in a contribution of ~2% of non-uniformity τ to the energy resolution. Such detectors, as for their total light output (P=1.17), are worse than detectors with wedge-shaped transducers (P=1.8 for S_2=10 cm^2), but are promising for spectrometric applications.

Conclusions

1. Using light collection model, optimum grain shape was determined for ZnSe(Te) scintillator, and calculations have been made of the effects of reflective coatings and parameters of the transparent matrix of the small-grained scintillator upon its sensitivity.

2. Accounting for the results of modeling, small-grained scintillators were prepared, which were much more sensitive than detectors made of single crystalline plates of the same material.

3. Optimum design of the concentrating light transducer for efficient light collection from the small-grained scintillator of large area onto light sensitive area of the photodiode for operation both in the current mode (wedge-shaped transducer) and in the spectrometric mode (transducer with spherical surface) has been calculated.

4. The results obtained allow to produce highly efficient detectors of beta-, X-ray and soft gamma radiation on the basis of small-crystalline ZnSe(Te) scintillators.

Acknowledgements

The authors are grateful to Yu.A.Borodenko and R.A.Govorova for preparation of the sample 1.

References

1. Katrunov K.A., Galchinetskii L.P., Ryzhikov V.D. et.al. Determination of conversion efficiency of X-ray luminophores by measurement of radiation power, Atomnaya Energiya, v.76, No.5 (1994), p.428-431.
2. Ryzhikov V.D, Borodenko Yu.A., Galkin S.N.et.al. Scintillation crystals ZnSe(Te): preparation, propeties, applications.- Proc.Int.Conference «Inorganic Scintillators and their Applications», August 28-September 1, 1995, Delft, The Netherlands. – P.465-468.
3. Ryzhikov V.D., Sokhin V.P. Optimization of scintillator thickness during detection of X-ray and gamma-radiation in a broad energy range. Pribory i Tekhnika Eksp., No.5 (1988), p.177-181.
4. Gavrilyuk V.P., Vinograd E.L., Grinyov B.V., Goriletsky V.I., Effect of surface conditions on the light collection in scintillation detectors, Functional Materials, vol.4, .4 (1997), P.572-577.

Luminosity monitor of the HERMES experiment at DESY

Th.Benisch[1], S.Bernreuther[1], E.Devitsin[2], V.Kozlov[2], S.Potashov[2],
K.Rith[1], A.Terkulov[2], Ch.Weiskopf[1]

[1]*Physikalisches Institut, Universität Erlangen-Nürnberg,*
91058 Erlangen, Germany
[2]*Lebedev Physical Institute, 117924 Moscow, Russia*

Abstract. A detector, consisting of two calorimeters with $NaBi(WO_4)_2$ radiation hard crystals as a radiator, readout by photomultipliers, which use the Bhabha scattering and the annihilation of the beam positron and the target atom electron to measure the luminosity of the HERMES experiment at DESY, is described. Properties of the monitor, measured in a test beam, and its performance in the experiment are presented.

Keywords: high-energy, calorimeter, radiation-hard, crystal

Introduction

The HERMES experiment is a second generation polarized deep inelastic scattering experiment to study the spin structure of the nucleon. It is being run at the HERA storage ring at DESY. The HERMES apparatus is based on a forward spectrometer with an internal gas target in the HERA lepton ring. A complete description of the spectrometer can be found in [1]. The HERMES internal gas target is described in [2].

The luminosity measurement is based on the elastic scattering of beam positrons from target gas electrons $e^+e^-\rightarrow e^+e^-$ (Bhabha scattering) [3] and annihilation into photon pairs $e^+e^-\rightarrow\gamma\gamma$ [4]. The cross sections are known precisely, including radiative corrections, e.g. $e^+e^-\rightarrow e^+e^-\gamma$, $e^+e^-\rightarrow e^+e^-\gamma\gamma\gamma$[5].

The scattered particles exit the beam pipe at z = 7.2 m and are detected in coincidence by two small calorimeters (see fig.1) with a horizontal acceptance of 4.6 to 8.9 mrad, which is limited by the size of the beam aperture in the magnet shielding plate. For a beam energy of 27.5 *GeV* the symmetric scattering angle is 6.1 mrad and both scattered particles have half of the beam energy.

Detector design

Due to the high radiation background in the region very near to the beam the calorimeter consists of Cherenkov crystals of $NaBi(WO_4)_2$ (NBW) [6], which has a high radiation hardness on the order of 7×10^5Gy. To further minimize radiation damage, the calorimeters are moved away from the beam pipe exit window by about 20 cm in the horizontal direction for beam injection and before dumping. The properties of NBW are summarized in Table 1:

The luminosity monitor (LUMI) consists of two calorimeters each containing 12 NBW crystals of size 22×22×200 mm covered with 25 μm thick aluminized mylar foil. The accuracy of crystal dimensions are 50 μm in transverse and 200 μm in longitudinal direction. Photomultipliers (PM) Hamamatsu R4125Q (19 mm in diameter) with synthetic silica window and bialkali photocathode (15 mm in diameter) was chosen as a photodetector.

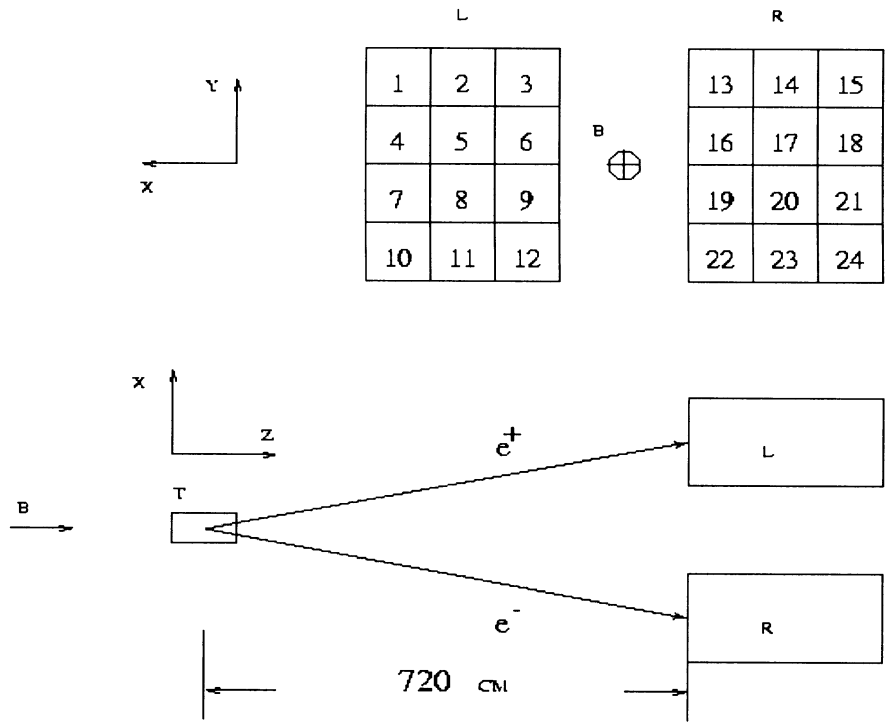

Fig.1 Schematic front and top view of the HERMES luminosity monitor. B - electron beam; T - gas target; L and R - left and right calorimeters of the monitor.

Table 1: properties of NBW crystal.

	unit	
density	g/cm^3	7.57
index of refraction		2.15
radiation length	cm	1.03
Moliere radius	cm	2.38
critical energy	MeV	9.75
optical transparency	nm	>380
radiation hardness	Gy	$\sim 7\times10^5$
hygroscopic		no

The PMs were coupled to the crystals by Rhodorsil optical grease (n=1.41). The crystals and the photomultipliers are situated in a metal frame, serving as a magnetic and light shielding. Each crystal receives laser light pulses to monitor gains via optical fibers coming from the HERMES gain monitoring system.

Trigger and data acquisition system

The trigger is used to separate physical events from background. The Bhabha and annihilation events have high energy deposition in both calorimeters. Therefore a trigger signal is produced in case of a coincidence of events in both detectors exceeding the threshold of about 5 *GeV*. Since most of background events have a high energy deposition only in one detector, a rather pure selection of useful events is maintained. For absolute energy calibration of the calorimeters the elastic scattered positron on the target nucleon is used, which deposits the energy around that of the beam (27.5 *GeV*). To detect these events an additional trigger

sensitive to such signal in one detector is in operation. The trigger scheme allows to process events of 100-200 Hz trigger rate without affecting the dead time of the main HERMES data acquisition system.

Properties measured in test beam

Prior to installation in the experiment both calorimeters were tested in the DESY test beam by electrons with energy between 1 and 6 *GeV*.

Energy resolution

The energy resolution of a calorimeter can be parameterized the following form (the terms are summed quadratically) [7]

$$\sigma/E=a/E\oplus b/\sqrt{E}\oplus c. \quad (1)$$

Fig.2 shows the measured resolution versus energy for a single crystal and the full matrix. Table 2 gives parameters of the fits shown in this figure.

Table 2: Energy resolution fit parameters.

matrix	a	b	c
1×1	3.3±2.3	11.1±0.5	1.0±1.8
3×3	4.3±0.8	9.3±0.4	0.3±1.4

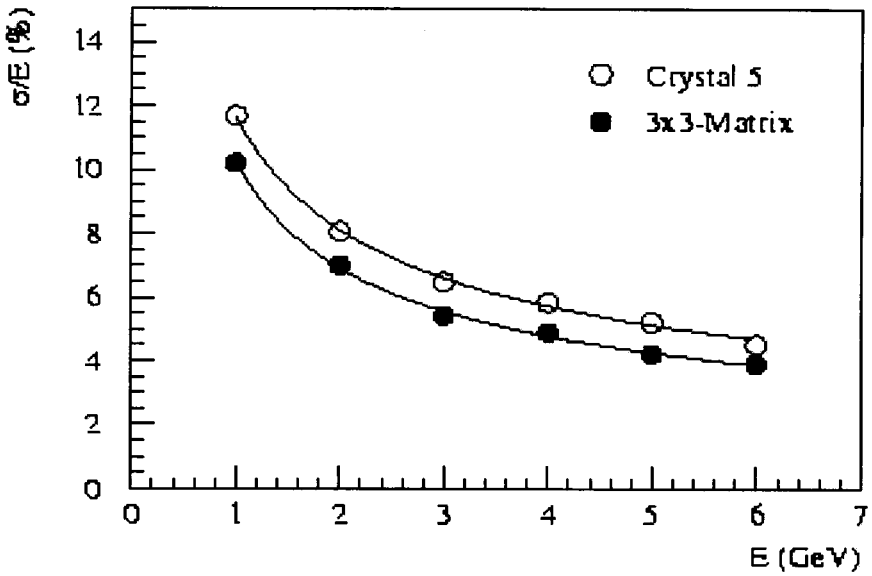

Fig.2 Measured energy resolution of a 3x3 matrix and a single crystal.

Spatial parameters of a shower.

Since the detector's lateral cell size (22×22 mm) is comparable to the Moliere radius of NBW crystal (23.8 mm), an electromagnetic shower evolves in several crystals and therefore the electron impact point can be reconstructed with good resolution.

To reconstruct the incident particle coordinate the two-column asymmetry η is used:

$$\eta=(A_R-A_L)/(A_R+A_L), \quad (2)$$

where A_R and A_L are pedestal subtracted amplitudes in adjacent to the incidence point (left and right) columns of crystals. Shooting the test beam at different points along a transverse to the crystals axis *x*, we have obtained a number of data points, which were parameterized by the following function [8]:

$$\eta=x/|x|\{1-\exp(-|x|/b_2)+2a_1b_1[\exp(-|x|/b_2)-\exp(-|x|/b_1)]\}, \quad (3)$$

where a_i and b_i are so called shower parameters. The extracted values are specified in Table 3. The parameter a_2 related to the other ones by equation (4):

$$2a_1b_1+2a_2b_2=1. \quad (4)$$

Table 3: Shower parameters

$a_1(mm^{-1})$	$a_2(mm^{-1})$	$b_1(mm)$	$b_2(mm)$
0.144±0.001	0.0055±0.0003	2.76±0.03	19.0±0.4

To reconstruct the coordinates of the incident particle equation (3) is numerically inverted. Depending on the distance from the crystal edge different resolution can be achieved. An application of the method to Monte Carlo shows that the best spatial resolution (0.5 mm) is obtained for particles hitting the border between two crystals. This method is used to reconstruct experimental events. See reconstructed impact points of the Bhabha and annihilation events in Fig.3.

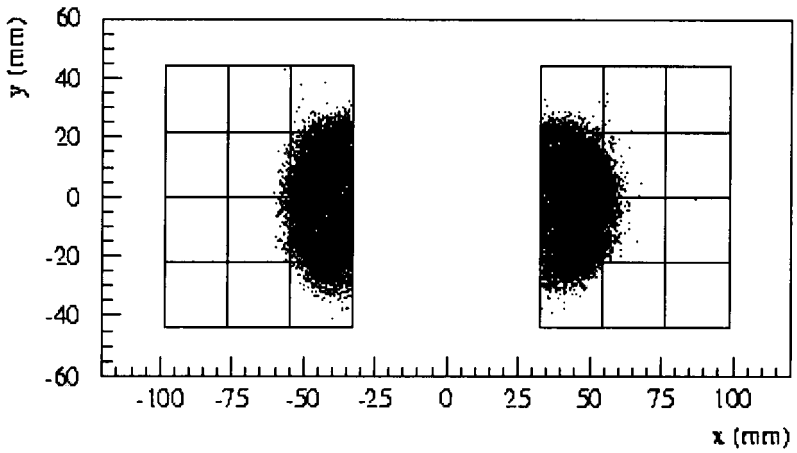

Fig.3 Reconstructed impact points of Bhabha and annihilation events.

Energy Calibration

The initial calibration of the detector was performed at the test beam described above. During the experiment calibration factors of the LUMI monitor determined in the test beam may change with time (due to instabilities in e.g. photomultiplier gains, NBW crystal transmission of light, readout electronics etc.) therefore it should be recalibrated periodically to make a correct energy measurement.

The calibration procedure consists of a periodic (about once in a week) determination of the gain factor set c_i and of ADC mean pedestal set P_i. The calibration algorithm is performed by a minimization iteration procedure for which events from the elastic scattering of positrons on the target nucleus are used. Because most of the events have shower leakage from the LUMI detector the first step is to reconstruct total energy using the measured deposited energy. The following functional is minimized in the procedure (valid within the accuracy of the detector experimental resolution):

$$[c_i(A\_i-P\_i)]=E_0, \quad (5)$$

where E_0 is the energy of the beam particle (27.5 *GeV*). The accuracy reached by such procedure is better that 0.5%.

Luminosity measurement

As mentioned above the luminosity measurement is based on the combination of elastic scattering of beam positrons from target gas electrons (Bhabha scattering) [3] and annihilation into photon pairs [4]. By measuring the event rates R of this process with the cross section, σ theoretically exactly known, the luminosity is determined by:

$$L = R / \int \varepsilon (d\sigma / d\Omega) d\Omega \qquad (6)$$

where ε is the detector efficiency and the integration is performed over the detector acceptance region. Though, analytically the calculation is hard to carry out, it is easier to use for this purpose a Monte-Carlo simulation, where the detector properties can be accurately described.

We separate relative and absolute luminosities in the following way. Relative luminosity R is the corrected event rate which is used for weighting different target spin states during extraction of spin dependent structure functions g_1 and g_2 as well as structure function ratio F_2^n/F_2^p. No absolute normalization is needed here. However, for measuring absolute cross-sections and structure functions the absolute luminosity L (see Eq.(6)) is needed.

Background and systematics of the luminosity measurement are stipulated by the following sources: geometrical acceptance uncertainty, theoretical cross-section uncertainty, beam position variation, background (the Bhabha scattering and e^+e^--annihilation on the HERA beam rest gas, the bremsstrahlung on the target and rest gas and accidental coincidences), rate corrections due to photomultiplier gain drop, absolute energy calibration, instability of the trigger electronics (amplifier, linear adder and discriminators). If quadratically added all the sources of the systematic error on the absolute luminosity (where error on the acceptance dominates) yield 6.3-6.4%. Since the absolute normalization does not matter in determination of the relative luminosity, the uncertainty on the integrated cross-section over the detector acceptance does not enter in its systematic error. For this reason it is much smaller and when summed up reaches between 0.9 and 1.5%.

References

1. HERMES Collaboration, *The HERMES Spectrometer*, DESY 98-057; e-print hep-ex/9806008, Nucl. Instr. and Methods A.417(1998)230.
2. HERMES Collaboration, *The HERMES Internal Gas Target*, to be submitted to Nucl. Instr. and Methods A.
3. H.J.Bhabha, Proc.Roy.Soc.(London) A154(1935)195.
4. L.D.Landau, E.M.Lifshitz., *Quantum Electrodynamics*, Moscow, 1989.
5. F.A.Berends and A.Böm, in High Energy Electron-Positron Physics, eds. A.Ali and P.Söding, World Scientific Publishing, Singapore, p.27.
6. G.I.Britvich et al., Nucl. Instr. Meth. A321 (1992) 64; A.V.Antipov et al., Nucl. Instr. Meth. A327 (1993) 346; V.Samsonov, Proc. of the «Crystal 2000» International Workshop, Chamonix, France, 1992, eds. P.Lecoq et al. (Ed.Frontieres, 1993) p.383.
7. R-Y.Zhu, *Limits to the Precision of Electromagnetic Calorimeters*. Proceedings of the first International Conference on Calorimetry in High Energy Physics, Fermi National Accelerator Laboratory, Batavia, Illinois, October 29 - November 1, 1990, eds. D.F. Anderson et al., World Scientific (1991)25.
8. D.P.Barber et al., Nucl. Instr. Meth. A329(1993)79.

Scintillation Assemblies Based on NaI(Tl) Crystals with α-radiation Reference Sources

V.R.Lyubynskiy, N.N.Smirnov, E.P.Sysoeva, E.V.Sysoeva, L.S.Zubenko

Dept. of Alkali Halide Crystals of NTK "Institute for Single Crystals" of National Academy of Sciences of Ukraine, Kharkov, Ukraine

Abstract. The scintillation assemblies on the base of the NaI(Tl) crystals with the α-radiation reference source are developed and investigated. Alpha-radiation source (^{239}Pu, ^{238}Pu or ^{241}Am) as a plate by 1 mm thickness was built-in inside assembly. It was placed on a flat end face of a crystal, opposite PMT. To improving scintillation performances the collimator and special crystal form were used. With this goal optimization of concentration was provided also. The assemblies based on ∅ 63x63 mm NaI(Tl) and PMT "Hamamatsu" R1307 with energy resolution (4-5)% for α-radiation and (6-7)% for γ- radiation ^{137}Cs and γ-equivalent (3.0-3.5) MeV were obtained.

Keywords: Scintillation assembly, stabilization, reference source, alpha-radiation.

Introduction

The problem of the scintillation spectrometer gain stabilization occurred almost with it appearance and it wasn't solving finally at present. Analysis of the problem shows that the most efficient and convenient way of the solving is the using of the light flash as reference signal for stabilization system, for example, [1-3]. A number of types of reference light sources on the base of light-emitting diodes (LED's) and α- or γ- radioactive sources are known. Under using LED whole measuring path is stabilized except the detector. So far as temperature dependencies of light yield of the crystal and LED are significantly different, stabilization with LED become don't efficient enough. The most successful and adequate to using conditions is the source, in which light flashes, arising from detector irradiated by α-particle from radioactive source built-in, are used [3]. Different ways of radioactive source placing inside of detector are known. One of earliest and successful solution was activating the host crystal with radioactive impurity or lodging of the small doping crystal in undeep well on the entrance window of the host crystal. This way don't use widely because of having technological hardness only (difficulties with radiation safety). Applied sources, lodging at entrance and output windows of the detector, are widely used. In the latter case the detectors are almost unsuitable for solving of ecology monitoring problem, because of low γ-equivalent. To improve this performance the complex detectors are used. In such detectors light flashes are produced by the thin NaI(Tl) crystal with applied α-radiation source. This crystal is optically connected with bulk CsI(Tl) crystal. Such design proved a very high γ-equivalent (up to 5 MeV), but because of difference temperature dependencies of NaI(Tl) and CsI(Tl) light yield so stabilization may be insufficient. Under design stabilization system with reference α-source should be note, that for alkali-halide crystals the temperature dependencies of light yield under α- and γ- excitation may be rather different [4-6]. This difference is especially noticeably CsI(Tl) crystals. For NaI(Tl) crystals light yield at α- and γ- excitation rather same in wide temperature range (from minus 20 ^{0}C to 60 ^{0}C) [7]. Thus, the most perspective for creating stabilization systems are detectors based on the NaI(Tl) crystals with reference sources.

Experimental

The characteristics of the scintillation assemblies on the base of the NaI(Tl) crystals with the α-radiation reference source are investigated. As scintillator was chosen crystallized NaI(Tl), because of having rather high γ-equivalent and practically absence of temperature dependence of signals at α- and γ-excitation. Alpha-radiation source (^{239}Pu, ^{238}Pu or ^{241}Am) as a plate by 1 mm thickness was built-in inside assembly. It was placed on a flat end face of a crystal, opposite PMT. The scintillation parameters were measured on the spectrometer consisting of a photoelectron multiplier tube model FEU-183 or FEU-176, charge sensitive preamplifier model PUG-1K, pulse amplifier model BUS2-97, amplitude analyzer model AMA-03F and high voltage power model BNV-30-01. PMT "Hamamatsu" model R1307 and R1306 were used in assembly also. A radionuclide ^{137}Cs was used as source of γ-radiation.

Results and discussion

The base characteristics of scintillation assembly with reference source are energy resolution at α- (R_α) and γ- (R_γ) excitation and γ-equivalent ($C_{\alpha/\gamma}$), that is the position of the α-radiation peak in γ-radiation scale.

For improving R_α between the source radiation surface and the end face of a crystal the teflon collimator was placed. Number, size and spacing of the holes was chosen as that, which gives the best R_α supplying needed counting rate in α-peak (30-50 c^{-1}).

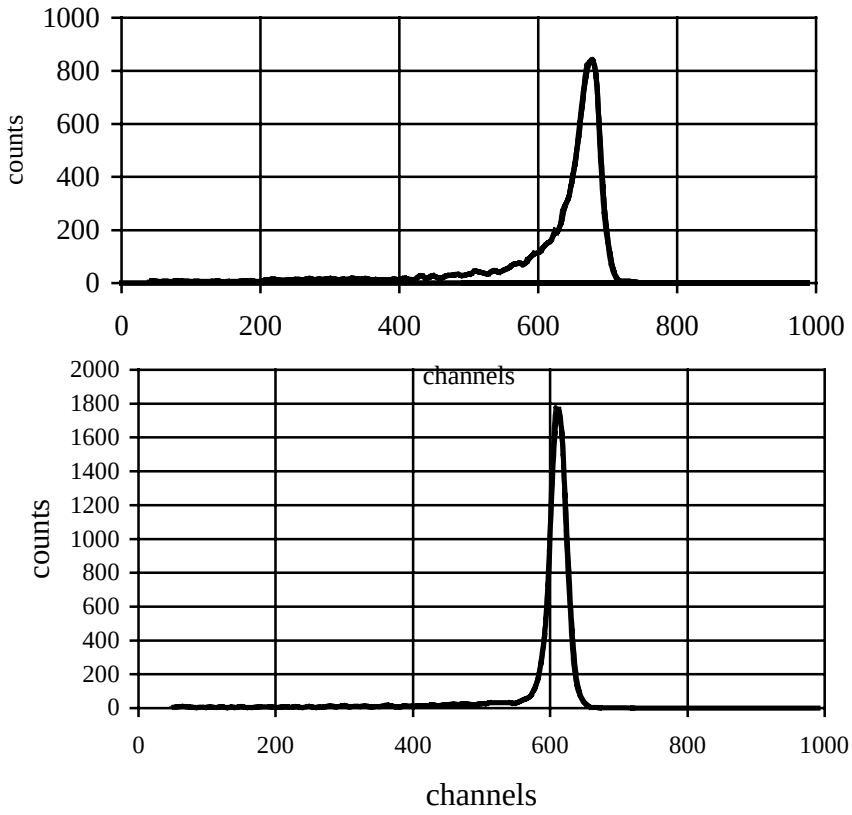

Fig.1. Spectrum of reference α-source ^{238}Pu without (a) and with (b) the collimator.

As far as absorption of α-particles is happen in thin (10 μ or 30 mg/cm^2) layer of material, a very important role has a treatment of crystal surface. It must be polished well and it must be dried so that, there wasn't "dead layer" which absorb radiation but without convert its energy in light energy [8]. Alpha-particles get onto crystal surface under different angles and their paths in surface layer are different, which lead to different energy looses and, at last, to distortion of energy spectrum. Collimator with uniformly distributed apertures directs a flow of α-particles from source so that they drop on the crystal surface perpendicularly. In this case they loose equal energy in crystal and spectrum shape become significantly better. Fig.1 shows spectra from the reference source ^{238}Pu with ∅63x63 mm NaI(Tl) with and without collimator. As one can see from the fig.1, when the special collimator is using, the shape of spectrum and energy resolution become significantly better (from 6-7% to 4-5%).

There were used a few factors to receive high γ-equivalent. Light yield of the NaI(Tl) crystal depends on concentration of the activator. These dependencies are different for α- and γ-excitation. It was necessary to pick up optimum concentration ensuring on the one hand high γ-equivalent and the good spectrometric characteristics on the other. Our research has shown that the most convenient for reference detectors are crystals with higher than usual for spectrometric crystals activator content. NaI(Tl) crystals, grown by Stockbarger methods, were investigated. ∅ 40x40 mm crystals were cutting out from different parts of bulk grown with activator content in raw from 0.1 to 1 %. Crystals were packed with ^{241}Am α-source without collimator. Then their scintillation characteristics were measured. After that chemical analyze of activator content was made. The fig.2 shows concentration dependencies or light yield under α - and γ -excitation, fig.3 shows the same dependence for γ- equivalent, fig.4 – for energy resolution.

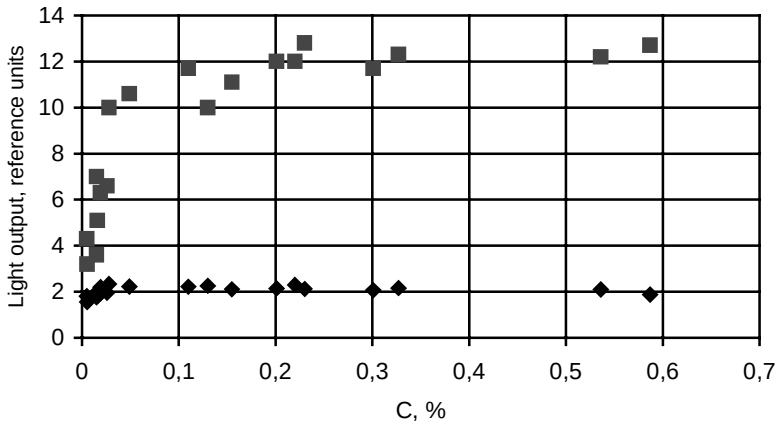

Fig.2. Concentration dependencies of light output of ∅ 40x40 mm NaI(Tl) crystals at α- (⊙) and γ- (♦) excitation.

As its seen from fig.2, light yield under γ-excitation much more early get out on plateau then under α- excitation, so γ-equivalent (see fig.3) grows with concentration of thallium to big concentration. But as one can see from fig.4 growing of activator concentration don't have influence almost on resolution under α- excitation, it is leads to significant deterioration of resolution under γ- excitation. This is caused by with appearance of complex thallium centers, competed with general luminescence centers in energy absorption of primary excitation [9].

So, need to choose optimal activator concentration, provided for a maximum γ-equivalent and good spectrometric properties. Such concentration is from 0,05 to 0,1% in the bulk, which is corresponded 0,6% in raw.

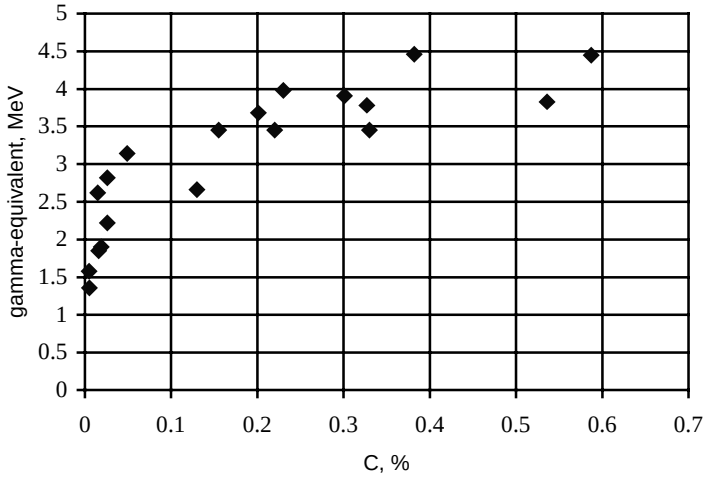

Fig.3. Concentration dependence of γ-equivalent of ∅ 40x40 mm NaI(Tl) crystals.

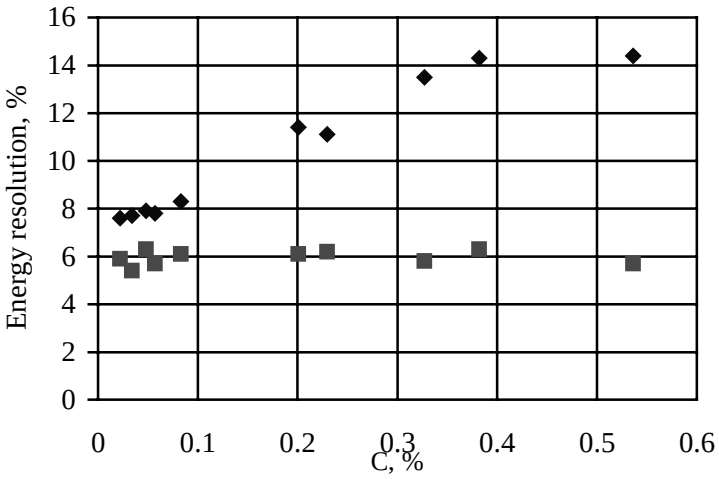

Fig.4. Concentration dependencies of energy resolution of ∅ 40x40 mm NaI(Tl) crystals at α- (⊙) and γ- (♦) excitation.

The research of the different dopants influence on the properties of the single crystals NaI(Tl) was made. On the base of the research dopants, increasing γ-equivalent, was proposed. The possibility that by changing shape of the crystal this characteristic may increase was considered. Some of detector geometry (for example with using dome-shaped top of the crystal with special treatment of its surface) were shown good results, but it would have to refuse because of technological difficulties.

Table shows the result of research. It is working out the technology of the producing scintillation assemblies with reference α-source on the base of NaI(Tl) ∅40x40mm and ∅63x63 mm crystals with following parameters:

Table

Sizes of crystal, mm	∅63x63		∅40x40	
PMT	Hamamatsu R1307	FEU-182, 183	Hamamatsu R1306	FEU-176
R_{α}, %	3 – 4	4 – 5	3 – 4	3.5 – 4.5
R_{γ}, %	6 – 7	7 – 8	6 – 7	6.5 – 7.5
$C_{\alpha/\gamma}$, MeV	3.0 – 3.5	3.0 – 3.5	3.0 – 3.5	3.0 – 3.5

Fig.5 shows the spectrum of γ-radiation ^{137}Cs for assembly based on ∅63x63 mm NaI(Tl) crystal and PMT "Hamamatsu" R1307 with built-in α-radioactive source ^{238}Pu.

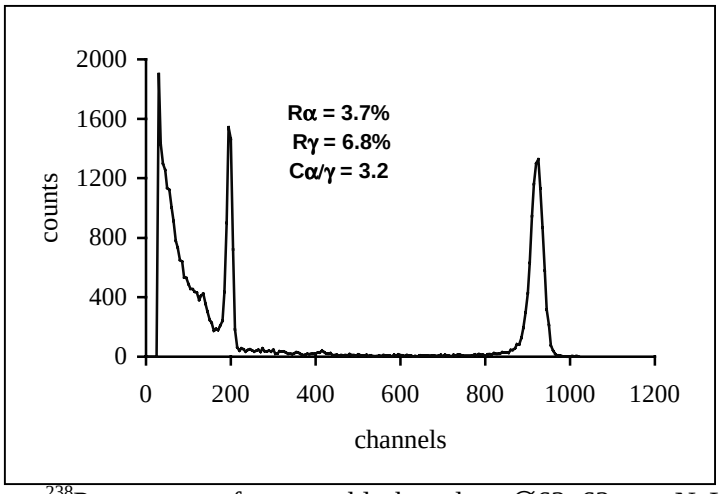

Fig.5. ^{137}Cs + ^{238}Pu spectrum for assembly based on ∅63x63 mm NaI(Tl) crystal and PMT "Hamamatsu" R1307 with built-in α-radioactive source.

Conclusion

The most perspective for creating stabilization systems are detectors and assemblies based on the NaI(Tl) crystals with built-in reference α-source. To improving scintillation performances the collimator and special crystal form could be used. Optimum concentration for high γ-equivalent with good spectrometric was found. The assemblies based on ∅ 63x63 mm NaI(Tl) and PMT "Hamamatsu" R1307 with energy resolution (4-5)% for α-radiation and (6-7)% for γ- radiation ^{137}Cs and γ-equivalent (3.0-3.5) MeV were obtained.

References:

1. Scintillation detectors Harshaw QS, Catalogue "Saint-Gobain aramiques Industrielles", March, 1992.
2. Bicron Corporation, Catalogue, 1993.
3. O.P.Sobornov, I.A.Lebedev, O.P.Shchtglov, "Pribory i tekhika eksperimenta", **№ 3** (1988) 62 – 64 (in russian).
4. J.B.Birks, The Theory and Practice of Scintillation Counting, Pergamon Press, Oxford, 1964, p. 513.
5. R.B.Murray, A.Meyer, Phys. Rev. **122** (1961) 815-826.
6. F.S.Eby, W.K.Jentcke, Phys. Rev. **86** (1954) 911-920
7. E.V.Sysoeva, V.A.Tarasov, O.V.Zelenskaya, V.F.Sulyga, "Nuclear and Methods in Phys.Res.", **A414** (1998) 274 –278.
8. L.B.Zagarij, Yu.T.Vydaj, Yu.A.Tsyrlin, Opticheskie i scintillyacionnye materialy, Kharkov, **№ 9** (1982) 88-91. (in russian).
9. A.N.Panova, Izvestiya AN SSSR, ser. fiz., **49** (1985) 1994-1998.

Scintillation blocks of high sensitivity for detection of gamma-radiation based on cadmium tungstate

[1]V.Nekrasov, [1]Yu.Borodenko, [1]E.Selegenev, [1]L.Piven, [2]I.Solsky, [3]Yu.Zorenko, [3]L.Limarenko, [3]Z.Moroz, [3]M.Pashkovsky

[1]Sientific Research Organization "SELDI", P.O.Box 108, Kharkiv, 310022, Ukraine;
[2]Research Production Association "Carat", 202 Stryjska Str., Lviv, 290031, Ukraine;
[3]Institute of Applied Physics Lviv State University, 49 General Chuprynka Str., Lviv, 29044, Ukraine

Abstract. Technological process has been developed for growth of cadmium tungstate (CWO) single crystals by Czochralski method using "Physiterm" (France) installations. Growth of CWO crystals (diameter 60-65 mm, length of cylindrical part up to 150 mm) is ensured by the specially developed heating unit and programmed variation of rotation rate. On the basis of ∅63×63 mm CWO crystals a detection block has been developed, comprising PMT, amplifier-shaper, high voltage converter inside a common housing. The detection block has following technical characteristics: amplitude resolution (over ^{137}Cs line) – not less then 9% - 12%; sensitivity, using ancillaries of the Marinelle vessel type – 0.037 pulses/s. The spectrometric detection block developed on the basis of ∅63×63 mm CWO scintillator is highly efficient for detection of gamma-quanta, and, as for the whole complex of characteristics, are superior to the existing analogs.

Key words: Scintillator, scintiblock, spectrometry, gamma-radiation, PMT.

Introduction

Detection blocks of ionizing radiation are widely used in equipment for nuclear physics. There blocks normally comprise scintillator single crystal NaI(Tl) and PMT. Alongside with all positive technical characteristics, NaI(Tl)-based scintillators have an important disadvantage – they are hygroscopic. This causes certain problems in course of their operation. However, until recently all other scintillators had been significantly inferior to single crystals NaI(Tl) as for their technical-economical characteristics and, consequently, could not be competitive. Recent achievements in the field of materials science have resulted in the development of a whole class of new scintillators, in particular, $CdWO_4$.

Scintillators based on $CdWO_4$ are non-hygroscopic, with density of ~7.9 g/cm^3 and effective atomic number 65. This allows to obtain, provided the size is the same detection efficiency 4-5 times higher than with NaI(Tl). In addition, $CdWO_4$-based scintillators have much weaker dependence of light output on temperature than other scintillators [1].

As disadvantages of $CdWO_4$-based scintillators, one can note their relatively low light output (~35% with respect to NaI(Tl)), high decay time (6-7 μs), as well as technical problems which did not allow to grow sufficiently large and uniform single crystals $CdWO_4$.

Results and consideration

The present work was aimed at the development of technological process of growing large-sized single crystals $CdWO_4$ and creation, on the basis of these crystals, of a high sensitivity spectrometric detection block which would be superior, as for its technical characteristics, to all the known analogs.

The $CdWO_4$ (CWO) single crystals have been grown in air atmosphere by Czochralski technique using the growth equipment "Physiterm" firm, France with HF-heating from platinum crucible. The powders of tungsten oxide WO_3 and cadmium carbonate $CdCO_3$ of 99,99 industrial marks have been used as initial materials for the charge preparation.

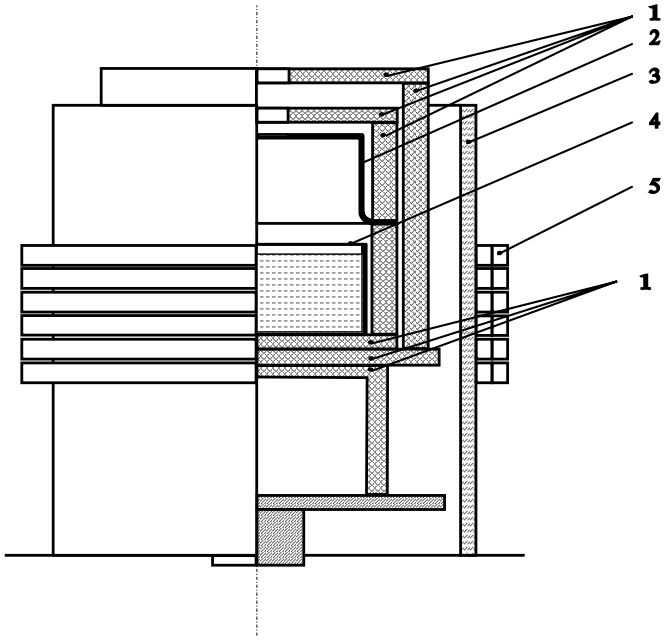

Fig.1 Construction of furnace

1. alumina plates and cylinders,
2. Pt-screen,
3. quartz cylinder,
4. Pt-crucible,
5. inductor.

The stoichiometric mixture of the powders was pressed into tabloids and subjected to solid phase synthesis at temperature 1000 EC. The charge melting in the crucible was carried out under conditions with ensured the minimum overheating.

The thermal unit represented in fig. 1 has been designed and manufactured for the crystals grown. The availability of the active platinum thermal screen under condition of corresponding thermal insulation using the corundum permits to create the necessary temperature gradients in the working volume. The charge of the axial temperature gradient in the grown cycle is corrected by means of alteration of the crystal rotation rate.

The growth of CWO single crystals have been realized in two following stages. Primary CWO crystals were grown using the charge after synthesis and their chemical analysis has been carried out. In dependence on analysis result the composition correction was reached by addition of $CdCO_3$ in quantity about 0.5-1.1 mas.%. Subsequently the primary produced single crystals were used as raw material for the growth of the crystals with required perfection.

The geometrical sizes of the grown CWO crystals are following: the diameter about 65 mm and length of the cylindrical part up to 120 mm.

To achieve the CWO scintillation parameters within the bounds of possibility it's extremely important to establish the interconnection between optical and light technical characteristics and type and concentration of the structural imperfections (intrinsic defects, back-ground impurities) which create the optically-active centres and dependent on charge composition, gas medium in the working chamber and thermodynamic conditions of the CWO crystals growth. With the purpose of determination such interconnection we investigated the optical characteristics and light yield of the scintillation elements obtained from CWO crystals that were grown from the different charge types, both preliminary recrystallized and prepared by method of solid-phase synthesis using the $CdCO_3$ and WO_4 components. The variable parameter of the technological cycles is a quality of CdO addition for the evaporation correction of this oxide (which possesses the high partial pressure) in the growth process.

The absorption spectra (AS) of CWO single crystal grown from the recrystallized raw materials with different values of CdO excess are presented in fig. 2, curves 1-3. The crystal prepared from the charge without CdO additio (fig. 2, curve 1) are characterized by noticeable yellowish-green color. The intensity of absorption is decreased with the rise of concentration

of the CdO addition (curves 2-3) so with CdO component excess of the order of 1.0-1.1 mas.% the grown CWO crystals are practically colorless in the volume of the cylindrical part (length up to 120 mm).

The spectra of additional absorption (AA) (fig. 2, insert, curves 1-2) with were obtained by means of substraction of the 1-3 curves are presented by two distinctive bands at 365-370 nm and at 540-560 nm (with low intensity) on the background of noticeably increase AA in the region of CWO absorption edge. For interpretation of the origin this AA it should be taken into consideration that the segregation coefficient for iron impurity is k~0.2, hence it follows that in the twice crystallized CWO the concentration of the undesirable impurity is minimum (about 10-5 w.%). Consequently the presence of structural defects, specifically connected

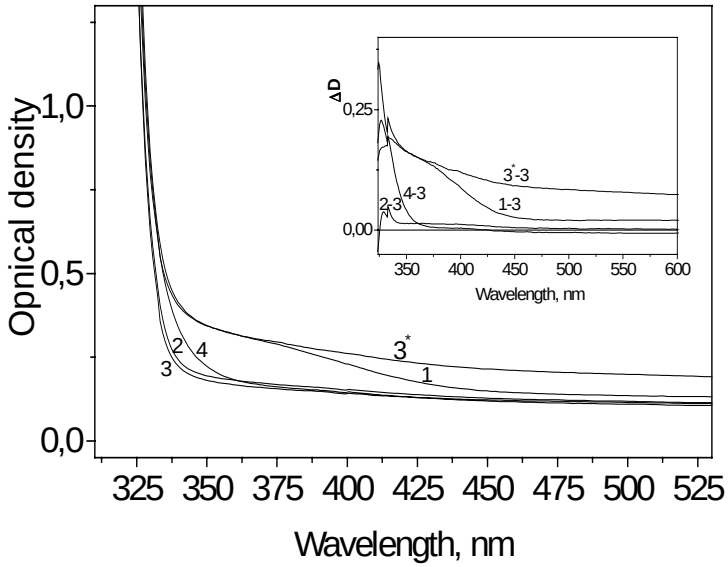

Fig.2 Absorption spectrum of CWO crystals obtained from recrystallizated blend with various values of CdO admixtures (1 – without admixture, 2 – 1.0 mas. % , 3 – 1.1 mas.%); from the blent based on $CdCO_3$ and WO_3 with admixture 1.1 mas.% CdO (4). 3^* - absorption spectrum of sample №3 annealed at T=600 K during 3 hrs.

with loss of certain quantity of CdO as more volatilirable component in the melt, may be the most possible reason for AA in the CWO scintillation region. In such case quite after first crystallization process we obtained the charge with components ratio Cd/W<1 for which the some concentrations of Cd vacancies (V_{Cd}^{2-}) and oxygen vacancies (V_O^{2+}) as well as their associates under condition of rather high defects concentration are characteristic. In our-opinion just V_{Cd} and V_O centres are responsible for the AA bands in CWO crystals spectra at 365-370 nm and 540-560 nm that doesn't at variance with the results and interpretation [1,2,3] in whole.

It should be noted that the presence of optically active centres connected with the crystal lattice defects significantly affects the scintillation parameters of CWO crystals (Table 1). From presented in table data it can be seen that with increase of CdO excess in the melt and resulted decrease of AA, the light yield of the samples rises at γ-excitation (^{60}Co, E=1.02 MeV) as well as at -particles excitation (^{239}Pu, E=5.5 MeV). The maximum value of light yield about 36.5% relatively NaJ:Tl (4.4 a.u.l.y.) is achieved for the CWO single crystals that were grown from the melt with the CdO excess of 1.0-1.1 mas.% (table 1).

Table 1. Light output of CWO crystals obtained from recrystallizated blend in dependence on CdO content

	Value of CdO admixture, mas.%	Light output of samples			
		in ^{60}Co τ= 2μs, %	in ^{60}Co τ= 5μs, %	in ^{239}Pu τ= 5μs, %	in ^{60}Co relatively to NaI:Tl (4.4), %
1	0.0	68	73	83	26.4
2	1.0	90.5	95	90	34.7
3	1.1		100	100	36.5
4*	1.1		87	90	

The crystal 4* is obtained from raw material based on $CdCO_3$ and WO_3 without previous recrystallization.

The samples was shaped in the form of parallelepiped of 10×10×20 dimension.

With the aim of choice of the optimal technological variants for the raw materials preparation we also produced the CWO crystals using the charge on the base of $CdCO_3$ and WO3 components with the $CdCO_3$ excess (in the re-calculation for CdO) about 1.1 mas.%. The absorption spectrum of the element prepared from such crystal is presented in fig. 2. The single crystal possessed the rather intensive yellowish color which correlates with AA spectrum (insert in fig. 2) consisted in band at 336 nm and wide, without structure, band in visible.

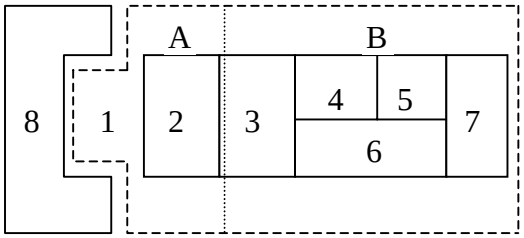

Fig.3 Circuit diagram of detector unit
A – scintiblock
1. Detector based on CWO
2. PMT
B – Electron subunit
3. PMT switcher
4. Amplifier-shaper
5. Differential detector based on PIC-processor
6. High voltage transformer
7. Connection center with peripheral equipment
8. Measuring cuvette (Marinelli vessel).

In taking into account the results for (1-3) crystals we assume that for the last type crystal (4) it's very possible the ratio Cd/W>1. In this case it's necessary to consider the possible affect on AA of the background iron impurity in two valent states (Fe^{3+} and Fe^{2+}) with bands of charge transfer at 370 and 460 nm [4] and also possibility of F-centers creation which connected with generated anionic vacancies [2,3] with AA at $_{max}$>500 nm. The light yield of such crystals is equal 0.87-0.9 relatively sample 3 (table 1).

The described above results permit to conclude that the optimal condition, from the standpoint of achievement of maximum possible values of optical transparency and light yield, is the growth of CWO crystals using the recrystallized charge with composition correction shifted to CdO excess of about 1.0-1.1 mas.%.

Basing on the obtained single crystals $CdWO_4$, a technological process gas been developed for fabrication of detection blocks ∅63×63 mm.

As for its design, the detection block comprises a scintillator, a PMT and an electronic subblock placed into a common duralumin housing (Fig. 3)

Table 2. The main parameters of the $CdWO_4$-based detection block.

	Parameter	Value
		CdWO
1.	Energy range, MeV*	0.06-3
2.	Sensitivity, pulse/s/Bk On ^{137}Cs on ^{40}K	 ≥0,037 ≥0,034
3.	Energy resolution on ^{137}Cs, %	9 - 12
4.	Output pulse parameters - pulse height, mV/keV - duration on 0,5 pulse height, μs	 3 15
5.	In-set temperature sensor, mV/°C	2
6.	Supply voltage, V	+12
7.	Consumed current, mA	≤140
8.	Dimensions of crystal , mm	∅63×63
9.	Dimensions of detector, mm	90 360

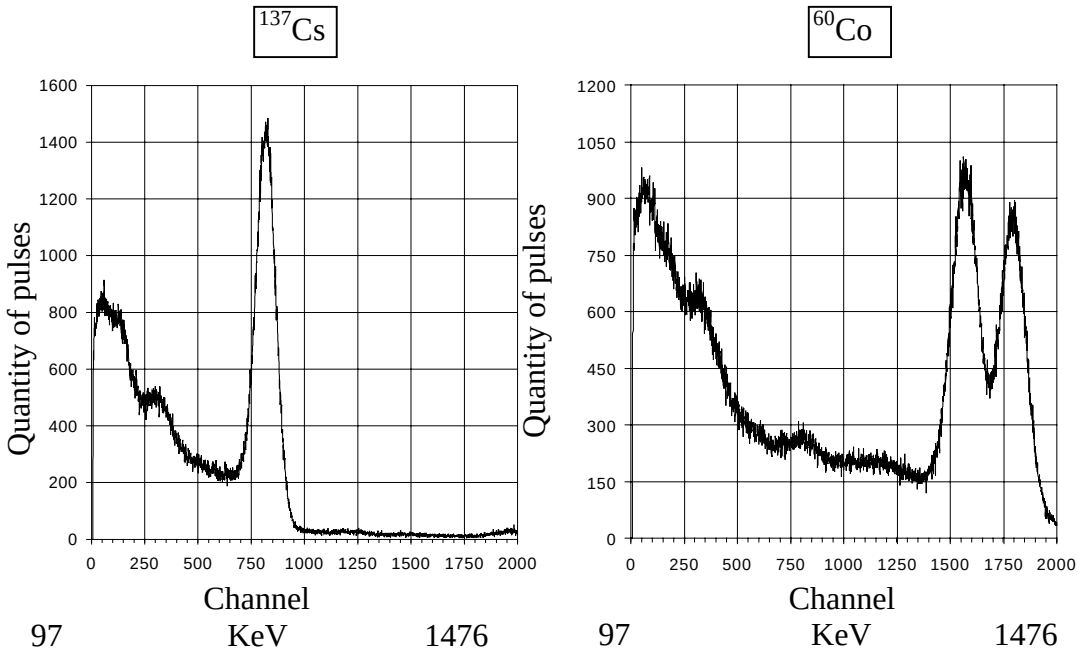

Fig.4. Spectrum of ^{137}Cs and ^{60}Co.

Long decay time of $CdWO_4$ demanded the development of a specially designed electronic subblock. thud, for formation of formation of optimum (bell-shaped) output pulse, which is required for operation of the spectral analyzer, the three-stage amplifier-shaper uses active filters, and the built-in threshold amplifier with adjustable detection threshold of signal amplitudes allows to expand the detected amplitude range. This enables to carry out precision measurements using standard spectral analyzers.

The detection blocks can be equipped with electronic subblocks comprising, alongside with amplifiers shapers, stabilized controlled high-voltage transformers for PMT power supply and three-channel differential discriminators for selected radionuclide windows (e.g., ^{137}Cs or ^{40}K) matched to microprocessors. The microprocessor with a built-in analog-to-digit converter allows to carry out statistical processing of the detected amplitudes according to a pre-set algorithm, both in selected “windows” or in the whole range of detected amplitudes,

and to make corrections of energy-dependent sensitivity. This makes the detection block a self-contained remote dosimetric devise ensuring the requires processing of signals.

The main parameters of the $CdWO_4$-based detection blocks of ∅63×63 mm size are presented in Table 2 and Fig.4.

Conclusions

From these data it is clearly seen that the ∅63×63 mm $CdWO_4$-based detection blocks are, as for the whole complex of their characteristics, superior to the known analogs and can be used as part of equipment for nuclear physics, allowing to solve a number of problems which could not be treated using the existing analogs.

References

1. Prospect Harshow
2. L.N. Limarenko, A.E. Nosenko, M.V. Pashkovsky, Vlijanie strukturnyh defektov na fizicheskie svojstva volframatov, Lvov, Vyshcha shkola, 1978,-160s.
3. M.M.Batenchuk, Avtoref. diss. Kand. fis.-mat. n. Lvov, 1985, -12 s.
4. A.E.Ovechkin, Kharkov, 1988, -12c.
5. L.Limarenko, Yu.Zorchenko, M.Pashkovsky, Rol' sobstvennyh defektov i primesej v formirovanii opticheskih harakteristik monokristallov CdWO4 i ZnWO4, J. Prikl. Spektr., 1996, t.64, #3,s.415-421

Chemical Impurity Study on the Polyaniline by the positron Annihilation

Kiyong Nam, Changhee Lee, Koansik Joo*, Gyuseong Cho**

Neutron Physics Div., KAERI, Yusong,Taejon 305-600,
** Dept.of Physics, Myong Ji Univ. Yongin, Kyonggi 449-728,*
*** Dept. of Nuclear Engineering, KAIST, Yusong, Taejon,*
305-701, Republic of Korea.

Abstract. We have measured the effect of the sizes and kinds of scintillators on the time resolution of the fast coincidence system. Two pairs BaF_2 scintillation detectors with different sizes and one pair plastic scintillation detector were used in the measurement. After calibrating TAC (time to amplitude converter), it was obtained that the time resolution of plastic scintillation system was better than others as 298 ps when measured ^{60}Co for ^{22}Na energy window. In addition to that, we recognized that the resolution was dependent of the length of delay line on the CFD (constant fraction discriminator) panel, neglecting the size of scintillators.

We prepared three kinds of Polyaniline and used the fast coincidence system for Positron Annihilation Spectroscopy to measure positron lifetime. That is, positron lifetime in solid state of Polyaniline was measured as a function of three distinctive conductivities. We obtained the result that the lifetime of positron decrease with increase of Polyaniline conductivity.

Keywords: Polyaniline, Positron annihilation, time resolution

Introduction

In the field of radiation detection, many methods of measurement have been developed and advanced for the respective purposes keeping face with the enhancement of measurement instruments. Especially, coincidence method, a kind of the radiation detection methods, may be indispensable to investigate on the information such as energy structure, decay constant, and half lifetime, etc. of radioisotopes. We have set up such a fast time coincidence system to study on the time resolution, with scintillation detectors changing, and then compared the time resolutions for the respective detector.

The time resolution of coincidence system means a measure how fast the system sensitively handles and responds to the two time signals between start and stop signals. So, the information on the time resolution of the system is important and necessary to the analysis of time spectrum.

In the present, we studied which factors affect, or contribute to time resolution of the system. To study the factors, we first set the fast coincidence system, which is composed of radiation detection and electronic parts, respectively. We measured each resolution with respect to the size and kind of scintillation detectors, and according to the lengths of delay line for external signal delay. After optimizing the coincidence system, it applied to the Positron Annihilation Spectroscopy.

Experiment

A. Positron Source Sampling

A radiation source, ^{22}Na prepared as shown in Figure 1. A ^{22}Na source in ^{22}NaCl solution was deposited on kapton foil and sandwiched it by the foils, after evaporating. Radioactivity was about 35 μCi. Radioisotope ^{22}Na, which have half lifetime of 2.6 years, emits γ-rays having energy of 1.27 MeV and positrons having maximum energy of 0.56 MeV [1].

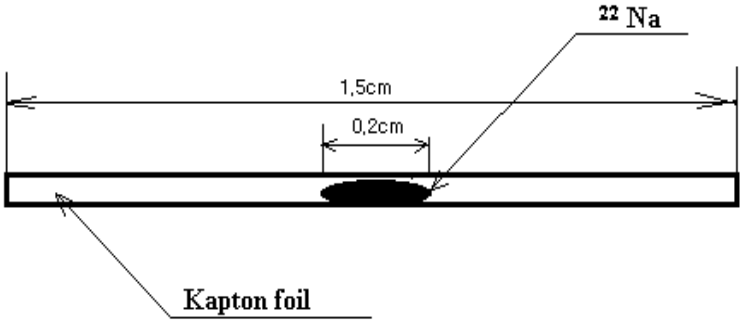

Figure 1: Sampling scheme of ^{22}Na positron source.

B. Composition of Fast Coincidence System

Scintillation detector part was consisted of scintillators and PMT (photo multiplier tube) with Base. We used two kinds of crystals as scintillators, i.e., BaF_2, and Plastic scintillators, which adhered onto each of PMT windows. Two pairs of the cylindrical-typed BaF_2 scintillators with the size of 2″×20mm and 1″×10mm and one pair of plastic with 2″×2″ were used in measurement, respectively. The plastic scintillation detector was composed of Model 2M2PP, BICRON co., and RCA Model 8550, Canberra co. as PMT with Base (Model 2107). In case of that of BaF_2, it adhered onto window of PMT XP2020Q constructed by Philips co. and 265 ORTEC co. as a base. As a time signal generator, we used two constant fraction differential discriminator (CFD 583), made by EG&G ORTEC corp. The constructed detection part was connected to electronic part as shown in Figure 2, which is a typical fast coincidence system.

Energy windows on CFD were set to 1.27 MeV photons as a start signal, and to 511 keV annihilation photons as a sop signal. The detection of γ-rays with energy of 1.27 MeV imply the sign for positron creation in the radiation source, and that of 511 keV γ-rays mean the sign of positron annihilation resulted from the interaction with an electron in material. We obtained the time spectrum on multi-channel analyzer corresponding to the time intervals between start and stop signals.

We measured the prompt curve from ^{60}Co source on the above determined energy windows of ^{22}Na. Prior to finding time resolution, we calibrated time per channel on MCA, with correspondence to variations of several delay-switches on the panel of delay module (Model 425A). The calibrated values were obtained as 24.4~25 ps per channel, which is equal to the inverse value, for example, of the slope in Figure 3. Figure 2: Block diagram of Fast coincidence system.

The lengths of delay line that make external delay of signal on CFD583 have also taken into considerations as a factor to affect on time resolution. The length was determined by the rising time properties of anode signal output from Base (Model 2107). Following is an equation (1) for me [2].

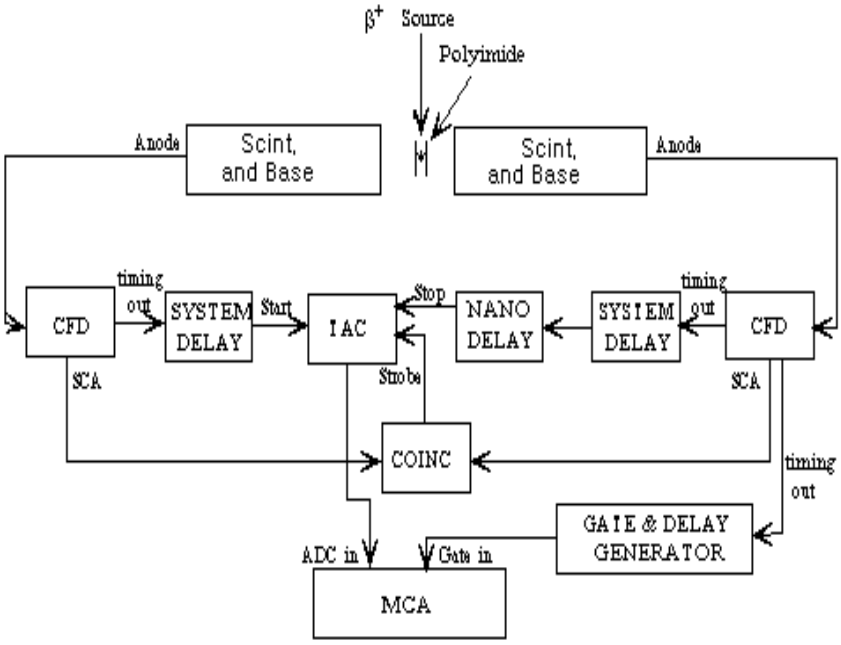

Figure 2 : Fast coincidence block scheme

$$Td(Ext.) \cong 1.1\ tr - 0.7\ ns \qquad (1)$$

Where tr is the 10 % to 90% rise time of the anode pulse. A value of 0.7 in equation (1) is internal delay value of CFD583. To optimize the system, suitable delay line length was selected to connect between two 'CFD external delay' and then controlled by adjusting of walk potentiometer so that the bipolar constant fraction signals for all amplitudes cross through the baseline approximately at the same time. Five clipped cables with different length have used to the delay connector on the panel of CFD583.

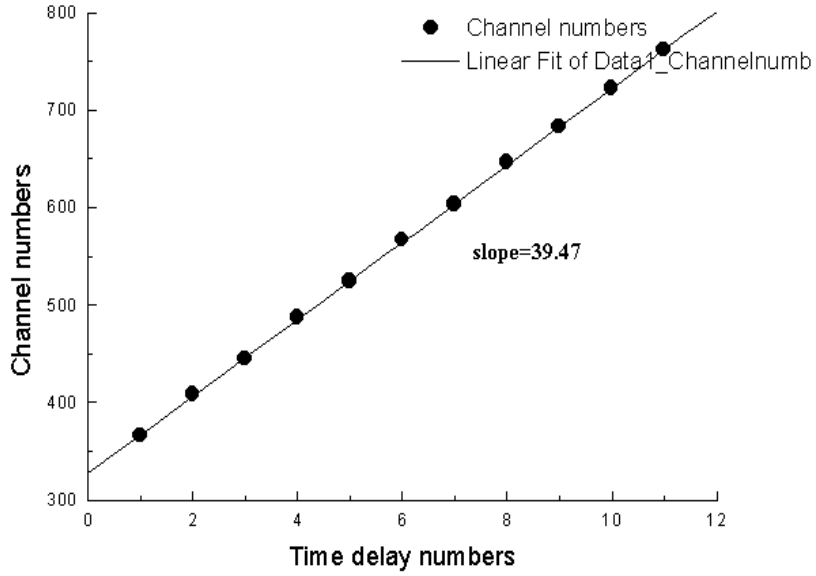

Figure 3: A Fitting graph of TAC calibration data.

Results and discussion

Table 1 accounts for the contribution of the length of cable to the time resolution. The relationship of clipped delay line length to the FWHM (full width at half maximum) was measured and summarized in Table 1.

It can realize from Table 1 that the time resolution sensitively responds to the clipping cable length which determined from equation (1). In general, the external delay lines on CFD, which is time marking unit, were necessary to compensate as much as time during pulse raise from the anode output of PMT [3]. The clipped length of cable compensates the pulse raising time. According to the length, the convergence of zero crossing point becomes to sharper or broader so that the CFD may generate false signals. Therefore, I suggest that the measuring of raising time be important as well as the length of clipping cable.

Table 2 accounts for the contribution of the size and kind of scintillators. In case of using plastic scintillators, the resolution has a good value. Among the same kind, but different size of BaF2 scintillators, the result in Table 1 shows that the thinner the thickness of scintillators, the better the time resolution. That shows agreement with the general fact.

Table 1. The values of time resolution with correspondence to the clipped length of delay line cables

Clipped length (cm)	Time Resolution (ps)
47	302
60	300
86	324
94	323
155	390

Table 2. Time resolution for several scintillators.

Scintillators	Size	ps/channel	FWHM	Time Resolution
BaF2	2″×20mm	24.4	15.1	368 ps
BaF2	1″×10mm	24.6	15.3	320 ps
Plastic	2″×2″mm	25.3	11.6	298 ps

As shown in Table 2, time resolution of the plastic scintillation detector was better, but worse in energy resolution than that of BaF_2. Since the energy resolution of the plastic scintillators is bad, and so it can detect only the Compton peaks of 1.27 MeV and of 511 keV. We employed BaF_2 scintillation detector rather than the plastic for measuring the positron lifetime, since the difference in time resolution between two detectors was relatively small, moreover it was rough to definite and calculate the ranges of the two Compton peaks. Referring to the result of Table 2, we finally used delay cable with lengths of 60 cm to the system.

Thereafter, we controlled the window width by adjustment of upper and lower discriminator levels on the panel of CFD583. There were no differences on the time resolution, except for coincidence count rates. It just shows that the wider the width of windows, the more the coincidence counts. Coincidence count rate of the system was about 25 cps (counts per second). Figure 4 shows the example of the prompt curve to measure time resolution.

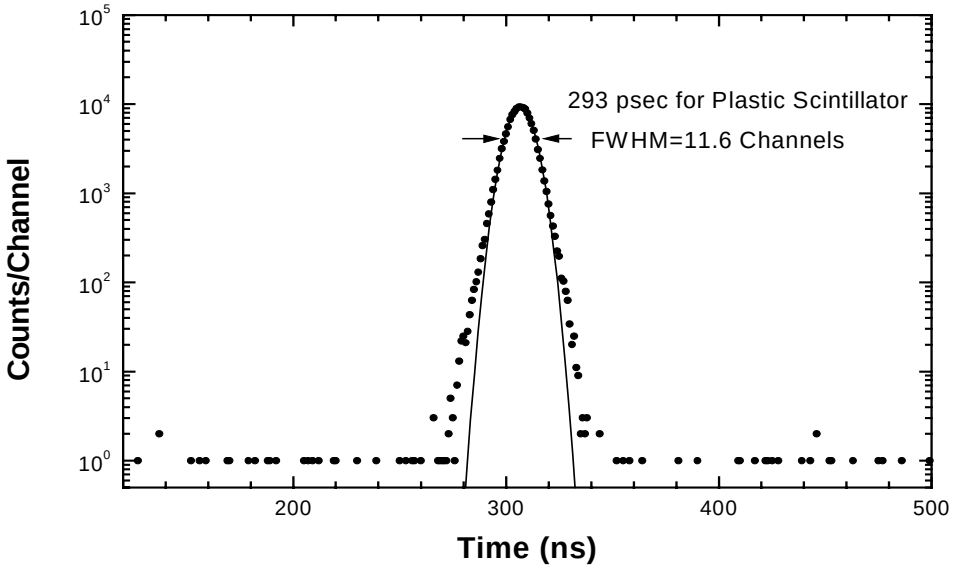

Figure 4: Fitting graph of the prompt curve to measure time resolution.

A. The Conductive Polyaniline Samples

A Polyaniline is a sort of polymer, which have the property of electric conductivity. We are supplied Polyaniline to have three distinctive conductivity from department of Chemistry in Myong Ji University.

The sample can be obtained by the reaction of oxidation-polymerization. The chemical dopants (HCl) and its concentration can control a conductivity of the material. We prepared the three film-typed polyanilines with different conductivity. Conductivity of the sample 1 was ~5 S/cm (pH=0 HCl) which have the range between metals and semiconductors. The sample 2 was ~10-3 S/cm (Ph=2.5) sample which is comparable with that of Si or Ge, and the sample 3 was ~10-7 S/cm (pH=4.9) which is in the low conductive range of the semiconductor.We have applied the fast coincidence system into the positron annihilation Spectroscopy. We obtained the positron lifetimes as a function of the conductivity of

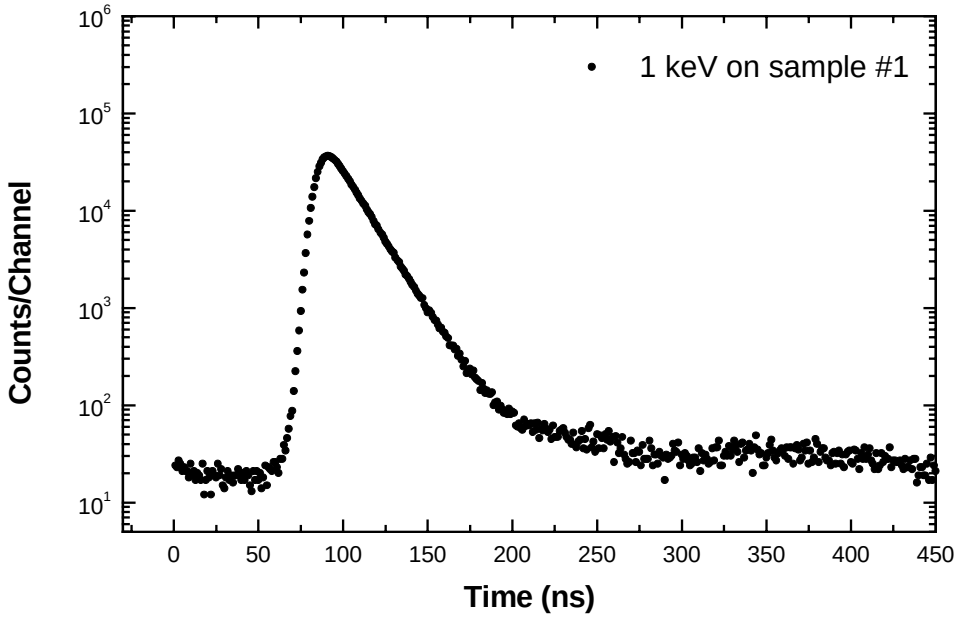

Figure 5: Positron lifetime spectrum for Polyaniline.

Polyaniline. In addition to that, we also measured the samples as a function of the variation of positron energy, which was done at ETL (Electrotechnical Laboratory). That gives us the information on the depth profile.Figure 5 shows one of the positron lifetime spectra for Polyaniline. The spectrum commonly may include several lifetime components that is information on the Polyaniline. We used PAFITT-88 as a analyzing program to deconvolute the lifetime components [4].

Incident positron energy was fixed by several values, that is, 0.5, 1, 5, and 15 keV. Table 3 represents all the positron lifetimes as a function of incident energy for respective conductivity. The τ_1 is a bulk lifetime component in the solid state Polyaniline and τ_2 is resulted from positronium produced in the material. I_1 and I_2 is relative intensities of τ_1 and τ_2, respectively.

Table 3. The positron lifetime as function of incident energy for each of conductivity.

Sample 1 : 5 S/cm (pH=0)				
keV	τ1(ps)	τ2(ns)	I1(%)	I2(%)
0.5	378	4.3	97.3	207
1	383	4.0	98.8	1.2
5	388	5.6	98.4	1.6
15	387	2.1	98.4	1.6

Sample 2 : 10-3 S/cm (pH=2.5)				
keV	τ1(ps)	τ2(ns)	I1(%)	I2(%)
0.5	369	3.1	96.0	4.0
1	382	3.6	98.6	1.4
5	381	3.82	98.5	1.5
15	375	2.1	98.5	1.5

Sample 3 : 10-7 S/cm (pH=4.9)				
keV	τ1(ps)	τ2(ns)	I1(%)	I2(%)
0.5	360	3.9	96.7	3.3
1	364	3.2	98.6	1.4
5	367	4.7	98.6	1.4
15	369	2.2	98.7	1.3

The atomic model of Postitronium (Ps) is very similar to that of Hydrogen. The lifetime of ortho-Positronium (*o*-Ps) is typically about 1 to 10 ns resulted from pick-off annihilation. It can be produced in the kind of molecule materials, not in the metal for the high density of electron. However, Ps can be produced on the surface, or at the interface of materials [5]. As shown in Table 3, we conformed that Positronium be produced in all materials of Polyaniline, although the intensity was lower than that of bulk. Figure 6 represents the results as a function of conductivity as well as that of incident positron energy.

Figure 6 shows that the higher the conductivity of the Polyaniline, the longer the bulk lifetime. It implies that the size of open space volume in the material be expanded with respect to the increasing of conductivity. We guess that the reason of longer positron lifetime in high conductivity be resulted from the increased dopants concentration. We also realize that the bulk lifetime increase with the incident positron energy from Figure 6. We guess that the reason be resulted from the longer thermalization process, since the higher the incident energy, the longer the time that necessary to thermalization of positron.

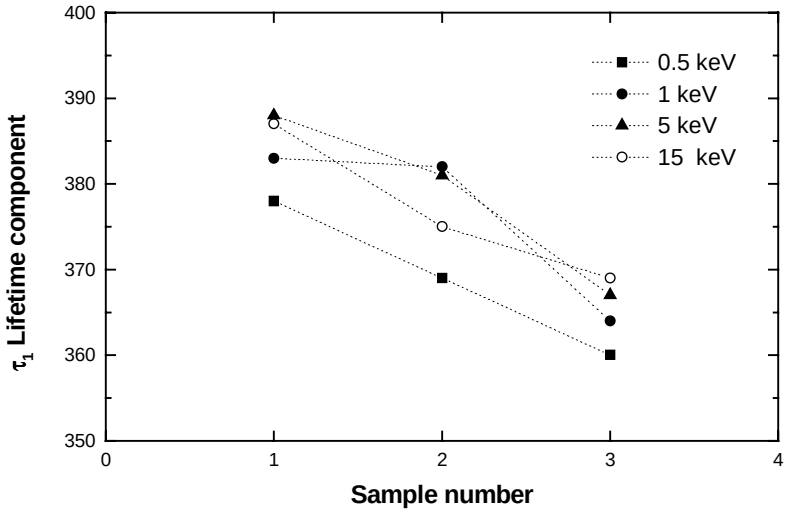

Figure 6: Positron life times as a function of conductivity and of incident energy of positrons.

Conclusions

We investigated that what factors affect on the time resolution. It found that the resolution sensitively vary with the clipping delay line cable. We also understood that in case of using plastic scintillators, the resolution has a good value and realized that among the same kind, but different size of BaF2 scintillators, the thinner the thickness of scintillators, the better the time resolution.

We conformed that Positronium be produced in all materials of Polyaniline. It realized that the bulk lifetime increase with the incident positron energy. We suggested the reason like that the higher the incident energy, the longer the time that necessary to thermalization of positron.

Acknowledgments

We would like to thank to Dr. R. Suzuki. We are indebted to him to allow us the utilizing of monoenergetic positron acceleration system.

References

1. J. Legrand, F. Lagoutine, and N. Coursol, Table de Radionucleides, LMN, Vol. II(1975) 3
2. Model 583 Constant Fraction Differential Discriminator Operating and Service Manual, EG&G ORTEC
3. N. Tsoulfanidis, Measurement and Detection of Radiation, 1976.
4. P. Kirkegaard, N. J. Pedersen, and M. Eldrup, PATFIT-88, Riso National Laboratory, 1989
5. Dupasquier, P. Hautojärvi, and M. J. Manninen, et al., Positrons in Solids, 1st Ed., Vol. XII, (1979)19

A Study On Point Defects In Lead Tungstate With Positron Annihilation

Gu Mu, Tang Xuefeng, Tong Hongyong, Liang Ling, Chen Lingyan
Department of Physics, Tongji University, Shanghai 200092, P. R. China

Liao Jingying, Shen Dingzhong, Yin Zhiwen
Laboratory of Functional Inorganic Materials, Chinese Academy of Science, Shanghai 200050, P. R. China

Wang Jingcheng, Xu Weixin
Shanghai Key Laboratory of Metal-Functional Materials, Shanghai 200940, P. R. China

Abstract: This paper presents a study on point defects in Lead Tungstate ($PbWO_4$) by using positron annihilation lifetime. The measurement were carried out for the cases of untreated, vacuum-annealed, oxygen-annealed and La-doped $PbWO_4$ crystals. It was found that the components of τ_2 which reflect the positron annihilation in point defects, for each case are different from each other. Some tentative models for the defects were discussed.

Keywords: $PbWO_4$ crystal, positron annihilation, lead vacancy, oxygen vacancy

Introduction

$PbWO_4$ has been regarded as one of the most promising scintillation crystal, and has been chosen for electromagnetic calorimeter of compact muon solenoid (CMS) at larger hadron collider (LHC) at CERN because of its fast luminescence, high density and low cost [1-3]. Therefore, a lot of work has been done recently in order to improve its performance on luminescence and radiation hardness for application. It was found that the luminescence and radiation hardness of the crystal are strongly modified by defects because the properties are very sensitive to the syntheses of crystal growth, dopants, annealing condition and etc. [4-8]. But the exact nature is not clear. Positron annihilation technique is an effective method to study defects in crystals. In this paper, the positron annihilation lifetimes were measured for the cases of untreated, vacuum-annealed, oxygen-annealed and La-doped $PbWO_4$. Some tentative models for the defects were discussed.

Experimental Procedure

The samples in table I were provided by Shanghai Institute of Ceramic (SIC). All samples were grown by Modified Bridgman technique with 4N raw materials and then were processed to rectangular films with their faces polished to optical grade. The first sample was untreated; the second and third ones had been annealed at vacuum and oxygen circumstances, respectively; and the last one was La-doped.

The positron annihilation lifetimes were measured with an Ortec fast-fast coincidence apparatus [9]. The time resolution of the apparatus can be described by a two-Gauss function with full width at half maximum (FWHM) and percentage of counts (PC) at 226.3ps, 86.1 % and 355.8ps, 13.9 %, respectively.

Each lifetime spectrum was accumulated to the counts exceeding 10^6.The positron source used in our experiment was ^{22}NaCI, which was covered with mylar films. In order to eliminate the effect of the film as well as the source itself, the positron annihilation lifetime of

perfect monocrystalline silicon had been measured. Comparing with the spectra between ours and the standard position annihilation lifetime of perfect monocrystalline silicon, we deduced that the contribution of the film and source itself could be described by two exponential components with lifetimes τ and PC at 390.0 ps, 6.1% and 1600.0 ps, 1.2%. They would be treated as a background in the spectra analysis.

Table 1 $PbWO_4$ sample

Sample	*Annealing*	*Dimension,* (mm^3)	*Remarks*
SIC-1		12×12×12	
SIC-2	Vacuum (950° 24h)	12×12×12	
SIC-3	Oxygen (950°C, 24h)	12×12×12	
SIC-4		12×12×12	La:400 ppm

Results and Discussion

The positron annihilation lifetimes were decomposed into two exponential components with POSITRON FIT-EXTENDED program [10]. The results are shown in table 2.

Table 2 Results of Positron Annihilation in $PbWO_4$ Crystals

Samples	$\tau_1(ps)$	$\tau_2(ps)$	$I_1(\%)$	$I_2(\%)$	$\kappa(ps^{-1})$	χ^2
SIC-1	183.0	363.6	82.2	17.8	0.048	1.135
SIC-2	195.8	441.5	89.7	10.3	0.029	1.234
SIC-3	164.3	324.5	62.7	37.3	0.112	1.176
SIC-4	171.2	345.6	66.5	33.5	0.099	1.281

where, τ_2 and I_2 are the lifetime and percentage of intensity of the second component which reflects to the positron annihilation in defects in $PbWO_4$ crystal; κ is the positron capture rate, which is defined as $\kappa = I_2(\tau_1^{-1} - \tau_2^{-1})$ [II]; τ_1 and I_1 are the lifetime and percentage of intensity of the first component, where τ_1 is defined as $\tau_1 = 1/(\lambda_f + \kappa)$ and λ_f is the free positron annihilation constant of the perfect $PbWO_4$ lattice.

The raw material used for $PbWO_4$ crystal growth is the mixture of PbO and $W0_3$ in stoichiometry. From the previous studies [9,12-14], we know that PbO is easier to volatilize than $W0_3$ during crystal growing. Therefore it can be deduced that the main defects in $PbWO_4$ are Pb vacancy (V_{Pb}) and O vacancy (V_O), which may exist individual or in the form of V_{Pb}-V_O complex. The second component of the positron annihilation lifetime of the untreated $PbWO_4$ crystal is supposed to result from the defects of V_{Pb} and V_{Pb}-V_O, which can act as positron traps.

The lifetime τ_2 of oxygen-annealed sample is equal to 324.5 ps which is shorter than that of the untreated one but similar to the lifetime of V_{Pb} in $PbTiO_3$ [15]. It seems reasonable to assume that the second component of the positron annihilation lifetime of the oxygen-annealed sample is induced by V_{Pb} as well. The V_O may be compensated by oxygen incorporated during oxygen annealing and the main defect left in the crystal is V_{Pb} As far as the case for vacuum annealing is concerned, the situation is in reverse to that of oxygen annealing. The lifetime τ_2 is longer and the intensity I_2 is lower than that of the untreated sample. The results can be explained by oxygen vacancy. Vacuum annealing may result in oxygen diffusion out of the crystal and lead to more oxygen vacancies left in the crystal. Therefore it becomes more favorable for V_{Pb} to be associated with V_o. As we know that Vo presents positive charge, so it can reduce the positron capture ability of the associated $V_{Pb.}$

Comparing the positron annihilation lifetime of the La-doped $PbWO_4$ with that of the untreated one, we found that the tendency of the change on the spectrum of the La-doped crystal towards to the case of the oxygen-annealed sample. It is suggested that the change is created by V_{Pb} which may be introduced by La^{3+} ion. La dopants were incorporated into the crystal by adulterating raw material with La_2O_3 powder. The La_2O_3 can replace two Pb ions and two O ions at normal lattice sites and yields an extra O^{2-} ion. The extra O^{2-} ion can compensate the V_O which has been discussed above. The valence of La^{3+} substitution is higher than that of Pb^{2+} and the local charge balance can be achieved by V_{Pb} . So La^{3+} doping can not only compensate the V_O but also introduce V_{Pb}. This hypothesis can be further supported by the work [16-17].

Conclusion

Point defects in Lead Tungstate ($PbWO_4$) have been studied by using positron annihilation lifetime. Some tentative models for the defects have been discussed for the cases of untreated, vacuum-annealed, oxygen-annealed and La-doped $PbWO_4$ crystals. It is supposed that the main defects in untreated $PbWO_4$ are Pb vacancy (V_{Pb}) and O vacancy (V_O), which can exist individual or in the form of Y_{Pb}-V_O complex. The V_O can be compensated by oxygen that will diffuse into the crystal during oxygen annealing, and the main defect in oxygen- annealed sample is V_{Pb}. The case of vacuum annealing is in reverse to that of oxygen annealing. The oxygen will diffuse out of the crystal during vacuum annealing to result in more oxygen vacancies in the crystal. Therefore V_{Pb} become much favorable to be associated with V_O, and the concentration of the individual V_{Pb} decrease. When the crystal is doped with La, the V_O will be suppressed by the extra O^{2+} and meanwhile the V_{Pb} will be introduced by La^{3+} ions.

This work was supported by National Natural Science Foundation of China, Science & Technology Development Foundation of Shanghai Colleges and Universities, Key Subject Development Foundation of Shanghai Educational Commission, Research Foundations of Key Laboratory of Functional Inorganic Materials, Chinese Academy of Science and Shanghai Key Laboratory of Metal-Functional Materials.

References

1. Compact Muon Solenoid Technical Proposal, CERN/LHCC **94-38,** LHCC/PI, 1994;
2. R.Y. Zhu, D.H. Ma, and C.L. Woody, A Study on the Properties of Lead Tungstate Crystals, CALT-**68-1973**,1995;
3. I. Dafinei, and et al.. Mat. Res. Soc. Symp. Proc. **348** (1994) 98
4. J.Y. Liao, B.F. Shen, P.F. Shao, and et al., Journal of Inorganic Materials (in Chinese) **12** (1997) 286
5. C.L. Woody, J.A. Kierstead, S.P. Stoll, and et al., IEEE Trans. on Nucl. Sci. **43** (1996) 1585
6. M. Kobayashi, M. Ishii, Y. Usuki, and et al., Nucl. Instr. and Meth. **A406** (1998) 442
7. E. Auffray, P. Lecoq, M. V. Korzhik, and et al., Nucl. Instr. and Meth. A**402** (1998) 75
8. S. Baccaro, B. Borgia, A. Cavallari, and et al.. Journal of Luminescence **72-74** (1997) 748
9. J.L. Qi, M. Gu, X.F. Tang, and et al., to be published on Nuclear Science and Technology (in Chinese)
10. P. Kirkeqard, and M. Eldrup, Comp. Phys. Corn. **7** (1974) 401
11. W. Brandt, Appl. Phys. **5** (1974) I
12. B.M. Epelbaum, K. Inaba, S. Uda, et al.. Journal of Crystal Growth **178** (1997) 426
13. J.M. Moreau, Ph Galez, J. P. Peigneux, and et al., J Alloys and Comp. **238** (1996) 46
14. Z.W. Yin, P.J. Li, and J.W. Fen, Proc SCINF97 4 (1997) 191
15. Y.J. He, W.Z. Yu, J.J. Xiong, and et al., Proc of ICPA-7, World Sci. Pub, (1985) 687
16. B.G. Han, X.Q. Feng, G.Q. Hu, and et al.. Journal of Applied Physics **84** (1998) 2831
17. R.Y. Zhu, Q. Deng, H. Newman, and et al., IEEE Trans. on Nucl. Sci. **45** (1998) 686

Fluoride systems NaF-(R,Y)F_3 as a new class of scintillators and active media for UV and VUV lasers

S. P. Chernov[1], D.N. Karimov[2], T.V. Ouvarova[2], E.O. Yankovskaya[2]

1 Physics Department, Moscow State University, 119899 Moscow, Russia
2 General Physics Institute, 117334 Moscow, Russia

Abstract: The results of the spectroscopic study of a new material NYF:Ce^{3+} in the UV and VUV regions are presented. Luminescence emission and excitation spectra as well as absorption spectra have been measured. The transparency region of the nominally pure matrix has been determined. The medium is expected to provide fast scintillating materials and is a promising matrix for tunable generation in the region 310-360 nm. The possibility of extending to shorter wavelength region by doping with other rare earth elements is discussed.

Keywords: NYF:Ce^{3+}, fast scintillator, active media

Introduction

Cerium doped insulating crystals are known as efficient scintillators. Some of them can also be considered as laser media. There is a variety of solid state lasers for infrared and visible regions, however the works on solid state lasers for the ultraviolet (UV) region are scarce, while those for the vacuum ultraviolet (VUV) are practically absent. One of the main reasons precluding from the development of solid state lasers for the UV and VUV spectral ranges is a limited number of available matrices meeting the requirements of high transparency in the short wavelength range which can be successfully doped by triply charged rare earth ions (TR^{3+}). From this point of view fluoride matrices transparent in the VUV are the most promising. By now the generation has been achieved on the 5d $\rightarrow$4f transitions in the Ce3+ ion in the following matrices: $LiYF_4$ [I], $LiLuF_4$ [2], $LiCaAlF_6$ [3], $LiSrAlF_6$ [3], LaF_3 [4] and on the transitions in Nd^{3+} ion in the matrix of LaF_3 [5].

Here we present the first results of the study of crystalline systems NaF-RF_3 (R= Y, Gd - Lu) represented by the compound $Na_{0.5-x}R_{0.5+x}F_{2+2x}$ (NRF) in the range of intermediate concentrations of TR^{3+}. These compounds are solid solutions with a disordered fluorite crystal structure [6]. Congruent melting, low melting point (around 1000 C), wide ranges of homogeneity make these compounds technologically favorable for obtaining uniform single crystals without cellular distribution of components [7]. The most attractive matrices for the UV and VUV region seem to be those of NRF with R= Y, Lu, Tm and Er due to the position of the d configuration of the free ions of these TR^{3+} [8], which allows to expect their fundamental absorption edge to be a at quite high energy when determined by the 4f $\rightarrow$5d transitions.

Here we present the results for the crystal of $Na_{0.4}Y_{0.6}F_{2.2}$ (NYF) which from the matrices mentioned above is expected to be the most transparent in the VUV region.

Samples and Measurements

Single crystals of NYF and NYF:Ce^{3+} were grown by the vertical crystallization in a carbon heating site, in the fluorine atmosphere created by the thermal decomposition of tephlon. Multicellular carbon crucibles were used with the growth rate of 3 – 5 mm/hour.

Purification of the raw materials (NaF of the 99.999 purity, yttrium and cerium fluorides of high purity with the contents of transition metals less than 10 –4 mass% from oxygen has been achieved by preliminary fluoridation of their melts. Thus grown crystals were 10 to 12mm in diameter and 30 to 50 mm in length. The crystals were free from scattering inclusions.

High isomorphous capacity of the NYF matrix allows to introduce up to 30 at.% of TR^{3+} of cerium subgroup with the distribution coefficient K=0.85, TR^{3+} of the yttrium subgroup can be introduced up to the total substitution for Y with K=1 [9]. A wide achievable range of TR^{3+} concentration is a very attractive property of these matrices.

The samples studied were plates with parallel sides of 1 to 3 mm width with polished surfaces cut of the middle part of the crystal. The transmittance was measured using the photometer "Specord UV-VIS" and a monochromator VMR2 with the inverse linear dispersion of 1.66 nm/mm. For the VUV measurements a specialized hydrogen lamp was used as a light source and a PMT 38 with sodium sallicylate screen for the detection of the transmitted radiation. For the measurements of the luminescence spectra at RT a spectrograph ISP-30 was used with a Hg lamp as a source. Luminescence was detected using a photofilm RF-3 and then analysed using a microdensitometer IFO-451.

Results and Discussion

The growth of optical crystals for the short wavelength region presents additional requirements to the purity of the materials since most of the impurities absorb in the UV and VUV spectral ranges. First of all we have studied the undoped matrix NYF.

The spectra of the samples 2 and 3 cut of the same crystal (with the thickness of 1 and 3 mm respectively) and 1 (1 mm thick) after re-crystallization are shown in fig. 1a and 1b (a – short wavelength edge, b – infrared edge).

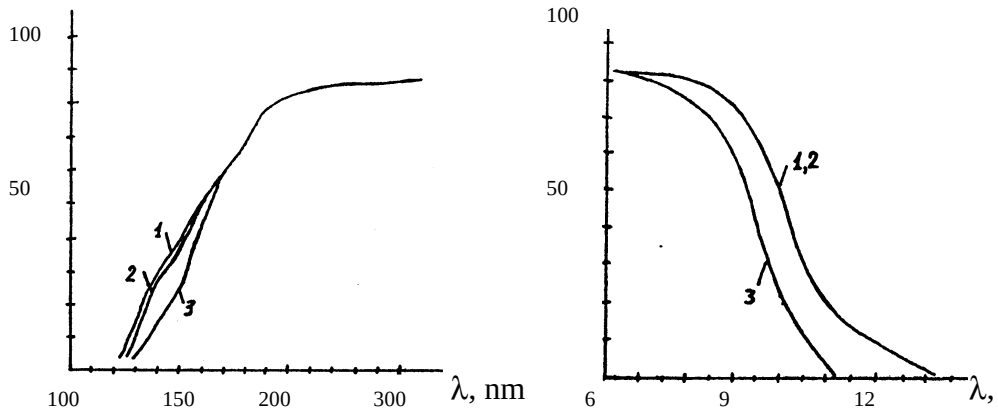

Fig. 1. Transmission spectra of the undoped samples of $Na_{0.4}Y_{0.6}F_{2.2}$ in the UV and VUV spectral ranges (a) and in the IR region (b): 1 – sample after re-crystallization of 1 mm thickness; 2,3 – samples of the thickness 1 and 3 mm grown from the raw material.

Comparison of the curves 2 and 3 demonstrates that there is a substantial absorption in the region 130-160 nm (curve 3) probably due to the absorption of oxygen impurity. Similar absorption was observed in LiF doped with oxygen [10]. To improve the transparency of the material in the VUV region a conventional method of purification by multiple re-crystallization was applied which helps to get read of some of the impurities including oxygen. As can be seen from Fig. 1 (curve 1) in the wavelength region < 160 nm the

transparency of the crystal after re-crystallization improved by 2 to 3% on average, the short wavelength edge shifted towards shorter wavelength to 127.2 nm with transparency level of 5 %. The modest effect of the treatment can be due to high solubility of oxygen in the crystal structure of NYF and its weak segregation in the crystallization process (the distribution coefficient is close to unity). Thus deep purification of the material from oxygen impurity should be performed at the initial stage of charge preparation.

Hence the matrix studied has a transparency comparable to such conventional VUV material as LaF_3 (λ_{edge} = 125 nm [12]), however, its isomorphous capacity is much higher. High purity of the raw material relative to the admixture of oxygen as well as other anion impurities can result in a decrease of the observed absorption and possibly in the shift of λ_{edge} towards shorter wavelengths.

Absorption spectra of a concentration series of single crystals of NYF:Ce^{3+} comprise 3 absorption bands, 2 shorter wavelength ones are substantially overlapped (Fig. 2). The corresponding position of the bands is summarized in Table 1.

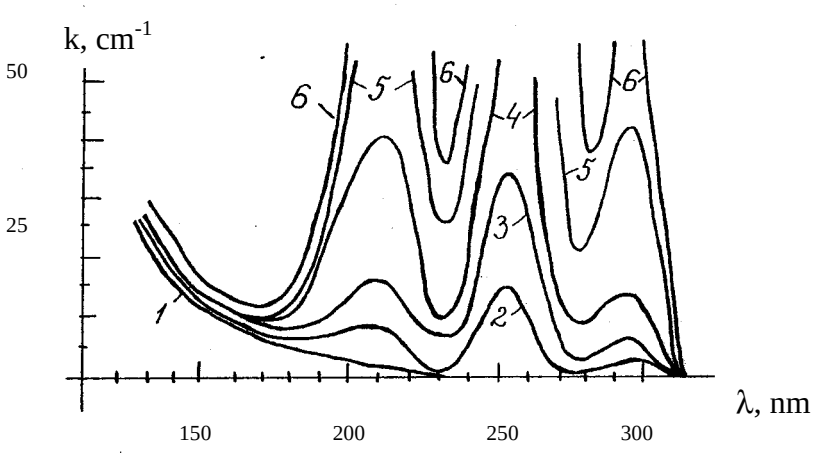

Fig. 2. Spectra of the f → d transitions in the Ce^{3+} ion in the NYF single crystal for different concentrations of Ce^{3+}, (mol.%): 1 – pure matrix; 2 – 0.05; 3 – 0.1; 4 – 0.25; 5 – 0.5; 6 – 1.0.

Table 1. Peaks in the absorption spectra of NYF:Ce^{3+}

λ_{max}, nm	ν_{max}, 10^3 cm^{-1}	$\Delta\nu$, 10^3 cm^{-1}	k, cm^{-1}
294	34,0	2,3	3,1
254	39,4	4,2	15,7
211	47,3	9,4	8,2

λ_{max} и ν_{max} stand for the wavelength and wave number of the absorption bands, respectively; $\Delta\nu$ is the halfwidth of the bands; k –the absorption coefficient in the maximum of the band. The concentration of Ce^{3+} in the sample was 0.05 mol.%. High values of the absorption coefficient and halfwidth of the observed bands allow to attribute these features to the allowed 4f – 5d transitions in the Ce- ion. The oscillator strength of the bands are characterized by the values of the order of 10^{-2} also indicating that they are due to allowed transitions. The position of the first maximum of the d-configuration in the NYF matrix is by 15740 cm^{-1} lower than in the free ion of Ce^{3+} [13]. Quantitative analysis of the splitting of the d-state in the spectrum requires detailed information on the crystal field in the site occupied by the cerium ion. However, a large variety of optical centers formed by Ce^{3+} (due to structural disorder) makes this a difficult task. Similar profiles of the absorption spectra of Ce^{3+} were observed in the single crystals of $LiYF_4$ (YLF) and $LiLuF_4$ (LLF) [1,2,14]. The

absorption bands in NYF:Ce are shifted towards longer wavelengths by 1300 cm^{-1} on average compared to YLF:Ce indicative of a stronger crystal field of NYF.

Fig.3 demonstrates the concentration dependence of the absorption coefficient in the maximum of the weakest (294 nm) absorption band. As it can be seen from the figure, the dependence is almost linear confirming the assignment of this band to the transitions in the Ce^{3+} ion. Higher concentrations of Ce^{3+} were not studied due to high absorption in all the bands (above 50 cm^{-1}).

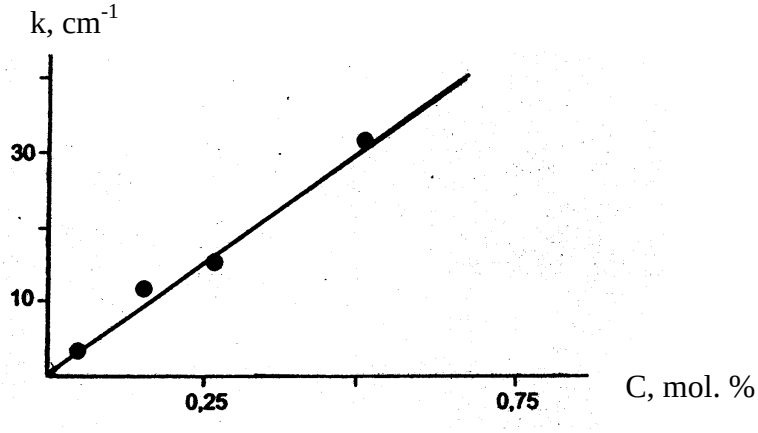

Figure 3. The dependence of the absorption coefficient in the maximum of the band with λ_{max} = 294 nm on the cerium concentration in NYF:Ce^{3+}.

The luminescence spectrum of a single crystal of NYF:Ce^{3+} (cerium concentration of the order of 1 mol.%) excited by not dispersed emission of a Hg lamp is shown in fig. 4.

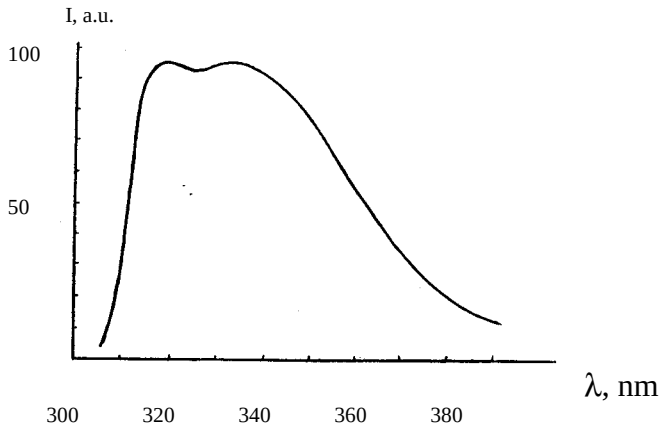

Figure 4. The luminescence spectrum of a single crystal of NYF:Ce^{3+}.

The spectrum consists of two not resolved bands with the maxima at 318 nm (31450 cm^{-1}) and 333 nm (30030 cm^{-1}) with a total halfwidth of 4550 cm^{-1}. The double structure of the luminescence band is due to the transition from the lowest level of d-state to the ground state of Ce^{3+} ion split by spin-orbit interaction into the sublevels $^2F_{5/2}$ and $^2F_{7/2}$ [1-2, 15,16]. According to the spectrum the separation between the sublevels $^2F_{5/2}$ and $^2F_{7/2}$ is of the order of 1920 cm^{-1}. The Stocks shift between the maximum of the lowest level of the d-state and the short wavelength luminescence band is of the order of 2550 cm^{-1}. The characteristic decay time of the bands is about 20 ns (at the limit of time resolution of the detection system).

In the preliminary measurements the excitation spectra were similar to the absorption ones.

Conclusions

Presented results of the investigations of a new wide bandgap crystal NYF:Ce^{3+} demonstrate its potential for the application as a scintillator as well as for obtaining laser generation. Large width of the luminescence bands is favorable for obtaining tunable generation in the range 310-360 nm with ultra short pulses. Doping with other TR^{3+} with a higher energy of the excited d-state than that of Ce^{3+}, such as Pr^{3+}, Nd^{3+}, Tm^{3+}, Er^{3+} [17, 18] would allow to reach even shorter wavelength range. Wide transparency region of a new fluoride matrix NYF together with its relatively high radiation stability (about 10^4 Gr[19]) make it a promising material for VUV optics.

References

1. Ehrlich D.J., Moulton P.F., Osgood R.M., Optics Letters **4** (1979) 184.
2. Dubinskii M.A., Semashko A.K., Naumov S.L. et al., Laser Physics **4** (1994) 480.
3. Marshall C.D., Speth J.A., Payne S.A. et al., J. Opt. Soc. Am. **B11** (1994) 2054.
4. Ehrlich D.J., Moulton P.P., Osgood R.M., Opt. Lett. **5** (1980) 339.
5. Waynant R.W., Klein P.H., Appl. Phys. Lett. **46** (1985) 14.
6. Sobolev B.P., Crystal Growth **18** (1990) 233 (in Russ.).
7. Fedorov P.P., Turkina T.M., Melashina V.A. et al., Crystal Growth **17** (1988) 198 (in Russ.).
8. Dieke G.H., Crosswhite H.M., Applied Optics **2** (1963) 675.
9. Zamoryanskaya M.V., Petrova M.A., Semenova T.S., Inorganic Materials **34** (1998) 752 (in Russ.).
10. Smushkov I.V., Soyfer L.M., Chubenko A.I. et al., J. Applied Spectroscopy **7** (1967) 87 (in Russ.).
11. Fedorov P.P., Sobolev B.P., Belov S.F., Izv. AN SSSR, Inorganic Maretials 15 (1979) 816 (in Russ.).
12. 0uvarova T.V., Chernov S.P., Mikhailin V.V. et.al, The 9 national conference on coherent and nonlinear optics dedicated to the memory of academician R.V. Khokhlov. Digest of reports, 13-16 June 1978, Leningrad.- .: 1978.- part 1.- p.8.
13. Lang R.L., Canad. J. Res. A. **14** (1936) 127.
14. Apayev R.A., Eremin M.V., Naumov A.K., Optica and Spectroscopy **84** (1998) 816 (in Russ.).
15. Kaplyansky A.A., Medvedev V.N., Feofilov P.P., Optics and Spectroscopy **14** (1963) 664.
16. Kaminsky A.A., Ouvarova T.V., Kochubey et al., Quantum Electronics 16 (1989) 513 (in Russ.).
17. Ivanova O.N., Ouvarova T.V., Chernov S.P., DAN SSSR **283** (1985) 1339 (in Russ.).
18. Chernov S.P., Mikhailin V.V., Ouvarova T.V., Phys. State Sol.(a) **88** (1985) 169.
19. Vasil'chenko V.G., Motin Yu.D., Krechko Yu.A. et al., Inorganic Materials 29 (1993) 739 (in Russ.).

Author Index

A

Alves, H. 128
Ananieva, G. V. 517
Andriessen, J. 224, 254
Annenkov, A.N. 201, 212
Antonyak, O. T. 492
Apanasenko, A. 589, 653
Åsberg-Dahlborg, M. 315
Assmann, S. 70
Auffray, E. 201, 212, 363, 619
Babin, V. 429, 544

B

Baccaro, S. 137, 309, 106, 346, 352
Bakhur, A.E. 668
Balashov, V.A. 708
Balcerzyk, M. 167, 571
Barrett N. 470
Batentschuk, M. 532
Batygov, S.H. 497, 684, 708
Baum O.I. 453
Baumer, V.N. 568
Bautin, K.V. 425
Beck, R. 181
Becker, J. 375
BELLE calorimeter collaboration 186
Belogurov, S. 304
Belsky, A.N. 277, 363, 379, 408, 440, 470, 679,
Benisch, Th. 730
Berdnikov, Ya.A. 293
Berdnikova, O.Ya. 293
Berdychevsky, O.M. 703
Bernreuther, S. 730
Berzina, B. 715
Bilyi, M. U. 260
Blanc, W. 277, 363
Boatner, L. A. 697
Boehm, M. 619
Bohacek, P. 137, 429
Böhm, M. 128
Bondar, V.G. 487, 604
Borik, M.A. 684
Borisevich, A. 619
Borodenko, Ju.A. 740
Boudeulle, M. 506
Bourgeois, S. 277
Bressi, G. 304
Burachas, S.F. 564, 604
Butaeva, T.I. 408
Bykov, I.S. 643

C

Carugno, G. 304
Cavallari, F. 346
Cecilia, A. 106, 137, 346, 352
Charkina, T.A. 538, 663
Chen, G. 342, 627
Chen, H. 609
Chen, H.F. 332
Chen, X. 342
Chen, Y. 609
Chernikov, V.V. 564
Chernov, S. P 756
Chernov, S. P. 336, 613
Chevallier, P. 379
Chiba, M. 137
Chipaux, R. 629, 636, 639
Cho, G. 391, 746
Cocozzella, N. 298
Cohen-Adad, M.T. 679
Comtet, G. 470
Conti, E. 304
Cousson, A. 636

D

Dafinei, I. 346
Dall'Igna, R. 106, 352
Danshin, E.A. 564, 724
Davies, G. 201
Demidenko, V. A. 517
Deng, J. 375
Deng, Q. 206, 332
Derenzo, S. E. 53
Devitsin, E.G. 708, 730
Diemoz, M. 137, 346
Dmitruk, L.N. 497, 684, 708
Dobrotvorskaya, M.V. 689
Dolzhenkova, E.F. 568, 689
Dorenbos, P. 272, 282, 476, 492, 511, 523, 577,
Döring, W. 181
Drobychev, G.Yu. 212
Dubovik, M.F. 568, 689
Dujardin, C. 277, 363, 379, 408, 470, 506, 527, 679
Dujardin G. 470

E

Efimov, Uy.N. 708
Egranov, A.V. 113
Evdokimov, V.A. 212

F

Fabeni, P. 309, 106, 544
Fang, Y. 464
Fedorov, A.A. 212
Fedorov, V.D. 708
Feldbach, E. 315
Ferrand, B. 157
Firsov, A. 379
Fitting, H.-J. 236, 555
Fouassier, C. 277

G

Gâcon, J. C. 277, 363
Gal'chinetskii, L.P. 724
Galluci, E. 506
Gamernyk, R. V. 595
Garcia-Murillo, A. 527
Garnier, N. 379,
Gavrilyuk, V.P. 487, 550, 724,
Gektin, A.V. 230, 79, 595
Géléoc, M. 629
Gendner, N. 195
Gesland, J.Y. 369
Globus, M.E. 476, 577,
Glukhov R.A. 448
Gminder, E. 458
Gorbenko, V. 476, 532
Gorbunov, S.V. 425
Goriletsky, V.I. 550,
Gorokhova, E. I. 517, 720
Goutaudier, C. 527, 679
Grigorjeva, L.G. 336, 613
Grin', L.A. 568
Grinyov, B.V. 476, 568, 577, 604, 689, 724,
Güdel, H. U. 282, 523
Guerra, S. 346
Guillot, C. 470
Guillot-Noël, O. 282, 523
Guillot-Noël, O.

H

Hansen, T. 506
Hara, K. 137
Hejny, V. 181
Hellner, L. 470
Hizhnyi, Yu. A. 260
Hofmann, D.M. 128
Hofstaetter, A. 181, 128, 619
Holm, U. 195
Holzwarth, N. A. W. 118
Hu, G. 375

I

Iannuzzi, D. 304
Ille, B. 321
Inagaki, T. 191
Isaenko, L.I 242
Ishii, M. 137, 402, 429, 501
Ivanov, A.P. 668
Ivanov, V.Yu. 266, 446
Ivashechkin, V.F. 113
Ivashkin, A.P. 113

J

Jansons, J. 236
Johnson, K. F. 195
Jönsson, L. 315
Joo, K. S. 391, 746,

K

Kahn-Harari, A. 511
Kamenskikh, I.A. 277, 326, 470,
Kanda, Y. 191
Kanevskii, V.S. 487
Kapusta, M. 167, 571
Karimov, D.N. 756
Katrunov, K.A. 487, 589, 604, 724,
Khaidukov, N.M. 369
Khapko, Z. A. 595
Khristich, O. A. 517, 720
Kidibaev, M.M. 421,
Kim, D. K. 391
Kirikova, N.Yu. 369, 440,
Kirm, M. 242, 266, 33, 315, 326, 369, 415, 435, 458, 648
Kisand, V. 458
Kittaka, T. 402
Klamra, W. 571
Klassen, N.V. 321, 668
Klintenberg, M. 53
Kobayashi, M. 137, 402, 429
Koch, A. 157, 527
Kolobanov, V.N. 326, 648
Komar, V.K. 230
Kondratiev, O.V. 128, 619

Konstankevych, I. 476, 532, 583, 740
Korenuk, P.I. 658
Korol, Yu.L. 248, 254
Korshikova, T.I. 689
Kortov, V.S. 61
Korzhik, M.V. 181, 201, 212, 97, 128, 595, 619
Kosmach, V.F. 293
Kostylev, V.L. 212
Kotlov, A. 315
Kovaleva, L.V. 538, 663
Kozlov, V.A. 708, 730
Krämer, K. W. 282, 523
Krivonosov, E.V. 487
Krupa, J.C. 369, 440
Kruzhalov, A.V 242, 266, 425, 435, 446
Kudenko, Yu.G. 113
Kudin, A.M. 538, 663
Kulipanov, G.N. 266
Kulis, P. 236, 555
Kutmy, V.E.
Kuznetsov, A.Yu. 248, 254
Kvitnitskaya, V.Z. 724

L

Labiche, J. C. 157
Laguta, V.V. 128, 619
Lebbou, O. 679
Lebeau, M. 298, 321
Lecoq, P. 3, 201, 212, 321, 363, 619
Lee, Ch. 746
Lee, K. S. 391
Lemasson, N. 511
Li, C. 332
Li, J. 342
Liao, J.Y. 332
Limarenko, L. 583, 740
Liogun, V. 619
Litvinov, L.A. 564
Lomonova, E.E. 684
Longo, E. 346
Loseva, E.A. 564
Ludwig, W. 157
Luh, M. 128, 619
Lushchik, A. 33, 415
Lushchik, Ch. 33, 415
Lyubynskiy, V.R. 735

M

Madej, C. 527
Majni, G. 298
Makhonin, S.I. 668
Makhov, V.N. 369, 440, 648
Mao Y. Q. 397
Marcos, R. 201
Mares, J.A. 106, 352
Marsman, M. 224
Martini, M. 137, 309, 106, 352
Martynov V.P. 487, 604, 693
Matsumoto Y. 191
Meinardi, F. 106, 309
Mel'chakov, E.N. 482
Meneguzzo, A.T. 304
Mengesha, W. 173
Merkuliaeva, T. I. 517
Metag V. 181, 128
Meyer, B.K. 128, 619
Meyer-Larsen, A. 195
Mihokova, E. 309, 106, 352, 429, 544
Mikhailik, V. B. 218, 492
Mikhailin, V.V. 326, 464, 648
Millers, D.K. 336, 613
Minami, K. 191
Mineev O.V. 113
Mishin, A.N. 482
Missevitch, O.V. 212
Mitichkin, A.I. 538
Moine, B. 482, 679
Moiseeva, L. 497, 708
Montecchi, M. 352, 346, 352
Morino, R. 201
Moroz, Z. 583, 658, 740
Moses, W. 11
Moszyński, M. 167, 571
Moy, J. P. 379

N

Nagirnyi, V. 315
Nagornaya, L. 564, 589, 604, 653
Nakamura, R. 501
Nam, K. 746
Nedilko, S. G. 260, 658,
Nefedov, V.A. 643
Nekrasov, V.V. 740
Nepomnyashchikh, A.I. 113, 357
Neshov, F.G. 446
Nesterenko, Y.A. 663
Nesterenko, Yu. 230
Nikitin, A.O. 668
Nikl, M. 137, 309, 106, 352, 402, 429, 544, 613

Nitsch, K. 106, 352
Novotny, R. 181, 128

O

Ogorodnikov, I.N. 242, 266
Orekhanov, P.A. 326
Organtini, G. 346
Osiko, V.V. 684
Oskine, A.V. 212
Ouvarova, T. V. 369, 756
Ovanesyan, K.L. 408
Overdick, M. 385

P

Pankratov, V. 613
Panov, V.V. 212
Panova, A.N. 550
Paone, N. 298
Pashkovsky, M. 476, 583, 658, 740
Pashuk, I.P. 703
Paulus, W. 636
Pauwels, D. 511
Pazzi, G. P. 309, 106, 544
Pédrini, C. 277, 89, 363, 379, 408, 448, 470, 482, 506, 527, 679
Peigneux, J.-P. 212
Pellegrino, F. 346
Permogorov, S. A. 720
Petrosyan, A.G. 363, 408, 506, 527
Petrov, S.V. 482
Petrov, V.L. 435
Philippov A. 470
Pidzyrailo, M.S. 703
Piven', L. 740
Polato, P. 106, 352
Polyansky, E.V. 643
Potashov, S.Yu. 730
Pustovarov, V.A. 242, 266, 421, 435
Q
Qu, X.D. 147
Queffelec, M. 440

R

Radzhabov, E. A. 113, 357, 560
Ratner, M. 577,
Red'kin, B.S. 321,
Ren Sh. 342, 627
Ren, G. H. 674
Rinaldi, D. 298
Rith, K. 730
Rodnyi, P. A. 218, 482, 492
Rogojin, A.A. 668,
Rogulis, U. 70, 236, 715
Romanov, N.G. 128
Ryaboukhin, O.V. 446
Rybchenko, S.I. 321,
Ryzhikov, V.D. 564, 589, 604, 724,

S

Samsonov, V.M. 293, 599
Savostianov V. A. 517
Scharmann, A. 128, 619
Schneegans, M. 201, 212, 321
Schweizer, S. 70, 715
Selegenev, E.M. 740
Sempere, P. 201
Senguttuvan, N. 137, 402
Shakhova, K.V. 550
Shalaev, A. 560
Shao, M. 332
Shekhovtsov, A.N. 689
Shen, D. Z. 375, 674
Shi, C.S. 332, 375, 609
Shiran, N.V. 230
Shirinyan, G.O. 408
Shishlo, A.P. 293
Shmurak, S.Z. 321, 668
Shpilinskaya, L.N. 538, 663
Shpinkov, I.N. 326, 648
Shulgin, B.V. 421, 435
Shwartz, B.A. 186,
Sidorenko, A.V. 482
Sinitsyn, V.V. 321
Smirnov, N.N. 735
Sobolev, A.B. 248, 254
Solsky, I.M. 595, 740
Spaeth, J.-M. 70, 715
Spassky D. 648
Springis, M. 236, 555
Steeg, B. 458
Ströher, H. 181
Stolovich, A. 429, 544
Sun, G. 627
Suzdal, V.S. 663
Svensson, G. 315
Sysoeva, E.P. 288, 735
Szawlowski, M. 571

T

Takano, H. 137
Tale, I. 236, 555
Tale, V. 236
Tamulaitis, G. 604

Tanji, K. 137, 402
Tarasov,V.A. 288, 476, 568, 577, 735
Terkulov, A. 730
Thies, S. 195
Tolmachev, A.V. 568, 689
Trinkler, L. 715
Trukhin, A. N. 697
Tupitsina, I. 653
Turin, G. P. 720

U

Ucer, K.B. 336
Usuki, Y. 137, 309, 402, 429, 613

V

Valentine, J.D. 173
van Eijk, C. W. E. 22, 218, 224, 282, 476, 492, 511, 523, 577
van Loef, E.V.D. 282, 476, 511, 577
van‘t Spijker, J. C. 523
Varaksin, A.N. 248
Vasetsky, S.I. 663
Vasil'ev, A.N. 43, 326, 448, 453, 464
Vedda, A. 137, 309, 106, 128, 352
Veispals, A. 236, 555
Viana, B. 511
Vielhauer, S. 415, 458
Vinogradova, N.N. 497, 708
Vistovsky, V.V. 703
Volkov, V.G. 724
Voloshinovskii, A.S . 218, 492, 595
Voronko, Yu.K. 497, 684
Voronova, V.V. 230
Vostretsov, Yu. 589

W

Wang, S. H. 674
Wang, Z.M. 332
Watterich, A. 128
Weber, M. J. 53, 527
Wei, J. 627
Wei, Y. 375
Weiskopf, Ch. 730
Wieczorek, H. 379, 385
Williams, R. T. 118, 336
Wu, C. 332

X

Xu, Z.Z. 332

Y

Yakovlev, V.Yu. 425
Yakunin A.M. 448
Yan, D.S. 206
Yankovskaya, E.O. 756
Ye, X. 609
Yevseyev, V. 599
Yin, Z.W. 206, 332, 397
Yochum, H.M. 336
Yonas A. 118
Yoshimura, Y. 191
Yu, H. 627

Z

Zadneprovski, B.I. 643
Zanella, G. 106, 352
Zannoni, R. 106, 352
Zaslavsky, B.G. 663
Zazubovich, S. 429, 544,
Zelenskaya, O.V. 564, 288, 653
Zhamangulov, A.A. 421
Zhang, G. 375
Zhang, L.Y. 147
Zhang, Y. C. 118
Zhang, Y. 342
Zheng, L. 627
Zhicol, O.A. 689
Zhou, D. 609
Zhu, R.Y. 147
Zimmerer, G. 492, 648, 369, 415, 375, 326, 458, 242, 266, 435, 218,
Zinin, E.I. 266, 435
Zorenko, Yu. 577, 476, 740, 583, 532
Zosim, D.I. 538
Zouevski, R.F. 212
Zubenko L.S. 735

Subject Index

5d-4f luminescence 272, 369, 440

A

A1N: Y2O3 ceramics 715

Ab initio molecular dynamics 224

Absorption 550, 589

ABX_3 structures 79

Active media 756

Afterglow 385, 501

Ageing 639

Alkali halides 33, 544

Alkaline-earth 497

Alpha-radiation 735

Alpha-spectrometry 668

Aluminate phosphor 497

Anisotropy 266, 629

Annealing 402, 487

Automated pulling 663

B

Band-structure 260, 336, 453, 689

Beta-irradiation 568

Beta-radiation 724

Birefringence 629

Borate compound 679, 689

Bridgman method 206, 402, 408

C

Calculation 260

Calorimeter 147, 181, 186, 190, 191, 195, 201, 212, 298, 346, 397, 730

Calorimetry 369, 629

CCD 157

Ceramics 517, 715

Certification 212

Cherenkov effect 674

Chloride elpasolites 482

Cluster 248, 254, 693

Collection 293, 321, 487, 636, 639

Color center 97,147, 230, 236, 446, 538, 550, 589, 599, 643, 693

Coloration 538, 550

Combined detector 564

Coordination 693

Core hole decay 470

Core-valence luminescence 218, 482

Cross-luminescence 113, 446

Crystal Clear Collaboration 3

Crystal doping 97

Crystal field depression 272

Crystal field 224, 425

Crystal growth 191, 595, 674, 689

Crystal structure 97, 636

Cs-based chloride elpasolites 482

Czochralski 408

D

Decay 33, 43, 79, 106, 113, 137, 186, 195, 212, 218, 236, 248, 266, 277, 282, 304, 309, 315, 326, 332, 336, 342, 357, 369, 415, 421, 425, 429, 435, 440, 448, 458, 482, 492, 497, 511, 517, 544, 568, 571, 583, 595, 613, 679, 697, 708

Decay kinetics 106, 266, 277, 315, 369, 425, 429, 435, 440, 544, 613

Decay time 332

Defect centres 128

Defect structure 555

Defects 53, 61, 70, 118, 128, 206, 342, 375, 391, 464, 544, 555, 568, 589, 595, 599, 609, 627, 629, 653, 668, 674, 715

Detection of ionizing radiation 720

Detection system 288

Detector 3, 22, 128, 167, 181, 186, 195, 218, 288, 379, 458, 476, 487, 527, 532, 555, 571, 668, 720, 724, 730, 735

D-f transitions 369

Dielectric materials 470

Diffusion-Controlled-Tunneling Luminescence 236

Doping 137, 583, 658

Dosimetry 79

E

Efficiency 11, 33, 43, 79, 106, 157, 186, 315, 352, 363, 425, 446, 464, 476, 487, 517, 532, 538, 564, 577, 599, 663, 720, 724, 740

Electric field 415

Electromagnetic Calorimetry 181, 186, 346

Electron spin resonance 61

Electronic excitations 33, 43, 315, 415, 458, 464, 492

Electronic structure 43, 118, 167, 248, 254, 260

Embedded cluster method 53

Emission 113, 218, 482

Emission centres 106, 315, 352, 583, 609

Emission spectrum 703

Energy losses 230

Energy resolution 11, 167, 173, 186, 195, 282, 476, 487, 523, 571, 653, 668, 674, 735, 740

Energy storage 79

Energy transfer 97, 106, 363, 375, 421

Energy transfer 33, 43, 106, 230, 272, 282, 315, 326, 375, 408, 421, 440, 492, 595, 648

Epitaxy 476, 532

EPR 236, 421, 619, 715

ESS 22

Excitation density 33

Excitation spectra 33, 218, 230, 242, 266, 282, 315, 326, 336, 363, 375, 421, 435, 458, 482, 492, 544, 555, 595, 609, 703

Exciton emission 113, 544

Excitons 33, 43, 53, 266, 315, 379, 415, 429, 435, 448, 458, 464, 492, 544, 689

F

Fast scintillators 3, 113, 440, 663, 684

F-centers 538, 560

Fluorescence 89

Fluoride crystals 369, 440

Fluoride glass 708

Fluorides 277

G

Gamma -detection 282, 523

Gamma detector 167

Gamma-irradiation 589, 599

Gamma-radiation 724, 740

Gamma-ray detection 22

Gd-based compounds 492

Glasses 3, 70, 106, 352, 708

Growth 97, 167, 191, 206, 298, 321, 336, 363, 375, 379, 397, 402, 408, 425, 487, 511, 532, 583, 589, 595, 604, 627, 663, 674, 679, 740

H

Halogenide scintillators 79

Hartree-Fock 224

Heavy scintillators 577

High energy physics 3, 79

High-energy relaxation 492

Hole diffusion 53

Hole-self-trapping 236

Hot pressing 517

Hysteresis 385

I

Impurities 79, 97, 118, 425, 421, 476, 532, 560, 583, 604, 658, 674, 697, 703, 740

Infrared scintillation 304

Interference 298

Ionizing radiation 97, 128, 288, 476, 555, 589, 697, 720

L

Lanthanides 272

Lattice relaxation 53, 224, 248, 453

Layers 157, 379, 385, 391, 527

Lead vacancy 752

Light collection 157, 186, 288, 293, 346, 487, 639, 724

Light output 501, 589

Light transducer 724

Light yield 97, 206, 212, 332, 639, 643

Luminescence centers 33, 242, 336, 375, 408, 415, 492, 555, 595, 613, 643, 697

Luminescence polarization 555

Luminescent films 577

M

Magnetic resonance 70, 128, 715

Mass production 619

Medical Imaging 3, 11, 79

Melt purification 663

Microscopy 157

Microtomography 157

Mixed crystals 363

Molecular anions 538

Monitoring 147

Monte Carlo method 288

Multiplication of excitations 33, 415

N

N-arena 22

Neutron detection 22, 242

Neutron diffraction 506, 636

Neutron- iradiation 599

Neutron-gamma discrimination 218

Neutrons 106, 218, 352, 564, 599, 629

Nonproportionality 167, 173, 523, 571

Nonstoichiometry 497

O

Optical absorption 61, 70, 224, 260, 425, 458, 511, 560, 568, 599, 604

Optical properties 201, 260, 293, 511, 599, 604, 629, 648, 658, 697

Optical transmission 212

Oxides, 61, 97, 248, 425, 476, 492, 564, 653

Oxygen vacancy 752

Oxygen-containing impurities 385, 663

Oxygen-related luminescence 715

P

Perovskite 79, 97, 363, 408, 476, 482

PET 11

Photocurrent 595

Photoelasticity 298

Photoelectron spectroscopy 470

Photon Detection 181

Photostimulated luminescence 560

Planar X-Ray 11

Plastic deformation 668

Point defects 97, 118, 309, 568, 583, 599, 740

Polyaniline 746

Positron annihilation 746, 752

Prompt excitation 53

Proton-iradiation 599

Q

Quality inspection 298

Quantum mechanical calculations 53

Quenching 43, 53, 113, 375, 391, 446, 448, 689, 697

R

Radiation damage 79, 128, 137, 147, 342, 352, 538, 619, 629, 636, 697, 708

Radiation defects 538, 599

Radiation hardness 97, 137, 186, 201, 206, 212, 332, 342, 346, 604, 627, 663, 674, 708, 730

Radiation monitoring 577, 653

Radiation resistance 663

Radiation stability 195, 589, 724

Rare gas solids 458

Rare-earth halides 523

Rare-earth ion 113, 254, 369, 440

Rare-earth oxysulfides 517

Rare-earth trihalides 282

Ray tracing 639

Re-absorption 538

Recombination 33, 106, 128, 236, 242, 282, 309, 352, 357, 385, 435, 458, 492, 497, 532, 555, 613, 697

Reference source 735

Refractive index 629

Refractory oxides 684

Relaxation 248

Residual stress 298

Resonance neutrons 564

S

Scattering, 22, 43, 70, 288, 321, 421, 448, 458, 464, 648, 674, 730

Scintillating glasses 106, 352

Scintillation glasses 106

Scintillation mechanisms 53, 277

Scintillation spectrometer 288

Self-trapped excitons 230, 236, 242, 266, 415, 421, 425, 435, 446, 544, 697

Sensibilization 532

Simulation 293

Single crystal film 476, 532

Skull melting 684

Slow component 357

Small-crystalline detector 724

Small-grained scintillator 724

SNS 22

SPECT 11

Spectra simulation 288

Spectrometry 740

Stabilization 735

Stoichiometry 693

Stokes shift 224

Storage phosphors 61, 560

Synchrotron radiation 242, 266, 277, 315, 415, 421, 435, 440, 482

T

Tagged Photons 181

Temperature dependence 375

Thallium centres 379, 385

Thermal neutrons 564

Thermal quenching 53

Thermoluminescence 61, 106, 137, 230, 309, 336, 352, 357, 440, 550, 568, 689, 715

Thermoluminescent dosimeter 230, 568

Thermostimulated exoelectron emission 61

Thin films 470, 577

Time resolution 523, 746

Time-resolved spectroscopy 242, 266, 421, 435, 440, 458, 595

TOF 22

Track effects 43

Transient absorption 336, 613

Transmission spectra 643

Trap centers 70

Trapping 385

U

Uniaxial stress 415
Uniformity 212

V

Valence band 470
VUV scintillator 369
VUV spectroscopy 33, 357, 482
VUV-Photoelectron spectroscopy 470

W

Wide-gap insulators 464

X

X-ray CT 11, 501
X-ray detector 532, 571
X-ray diffraction analysis 568
X-ray imaging 11, 157
X-ray luminescence 643
X-ray phosphors 527
X-ray storage phosphor 70

Material Index

Al_2O_3 33, 61
AlN:Y_2O_3 715
$BaAl_2O_4:Eu^{2+}$ 497
BaF_2 357, 397, 446, 453, 304
BaF_2-LaF_3 113
$BaFBr:Eu^{2+}$ 70, 560
$BaLiF_3$:Ce 218
$BaWO_4$ 429
BeO 266, 61, 425
$Bi_4Ge_3O_{12}$ 304, 577,
CaF_2 357
$CaSO_4$ 326
$CaWO_4$ 118, 326, 429
$CaWO_4$:Bi 315
$CdWO_4$ 260, 118, 336, 577, 648, 653, 693, 740
Ce^{3+} 272, 89, 352
Ce^{4+} 89
CeF_3 191, 248, 89, 357, 375, 397, 304
Cs_2KlaCl_6 482
$Cs_2LiLaCl_6$ 218
Cs_2LiYCl_6 218
$Cs_2NaLaCl_6$ 482
$Cs_2RbLaCl_6$ 482
$Cs_2ZnJ_4:Mn^{2+}$ 703
Cs_3LaCl_6 482
CsBr Ga^+ 70
CsCl 446, 453
$CsGd_2Cl_7:Ce^{3+}$ 492
CsI 391, 397, 470
CsI:Na 544
CsI:Tl 186, 167, 379, 385, 523, 538, 544, 304, 663, 668
CWO 564
$Gd(BO_2)_{22}$ 679
Gd_2O_2S 517
Gd_2O_2S:Pr 501
$Gd_2O_2S:Tb^{3+}$ 527
Gd_2SiO_5 693
$Gd_3(GaSc_6)_5O_{12}$ 693
Gd_3BO_6 679
Ge 304
GSO 89, 564
GSO:Ce 167, 487
HfF_4-BaF_2-CeF_3-AlF_3-NaF 708
HfO_2 Y_2O_3 684
KBr 33
KCl 33
KI 33, 415
Kr 458
$La_2Be_2O_5$ 435
LaB_3O_6 689
$LaCl_3$ 282
LaF_3 277
$LaLuO_3$ 506
$Li_2B_4O_7$ 568
LiB_3O_5 242
$LiBaF_3$ 230, 236, 555
$LiBaF_3:Ce^{3+}$ 224
LiF:U,Cu 421
$LiLuF_4$ 277
$LiYF_4$ 277, 440
$LnAl_3(BO_3)_{181}$ (Ln=Gd or Lu) 679
LSO 89
LSO:Ce 167
$Lu_2Si_2O_7:Ce^{3+}$ 511
Lu_2SiO_5 248
Lu_2SiO_5:Ce 523
$Lu_3Al_5O_{12}$ 476
$Lu_3Al_5O_{12}$:Ce 532, 577
Lu_3BO_6 679
LuAG:Ce 167
$LuAlO_3$ 470, 506
$LuAlO_3:Ce^{3+}$ 408
LuAP 89
LuAP:Ce 167
$LuBr_3$ 282
$LuCl_3$ 282
LuF_3 277
$LuPO_4$ 89
$Lu_xY_{x-1}AlO_3$:Ce 363, 408
MgO 33, 61
$Na_{0,4}Y_{0,6}F_{22}$ (NYF) 756
$NaBi(WO_4)_{11}$ 730
NaCl 33, 453
NaF:U,Cu 421
NaI:Tl 167, 523, 550, 735
NBWO 564
Nd^{3+} 272
$NF(RY)F_3$ [R = (Ce – Lu)] 756
$NYF:Ce^{3+}$ 756

$Pb(WO_4)_{3-x}(MoO_4)_X$ 643
PbF_2 397, 304, 674
$PbMoO_4$ 260
$PbSO_4$ 326
$PbWO_4$ 181, 195, 201, 206, 260, 293, 298, 309, 315, 321, 97, 118, 128, 137, 147, 326, 336, 342, 346, 397, 402, 429, 304, 583, 589, 595, 599, 604, 609, 613, 619, 627, 629, 636, 639, 658, 693
$PbWO_4$ (Sb) 332
Pr^{3+} 272
$Rb_2ZnJ_4:Mn^{2+}$ 703
RbBr Ga^+ 70
$RbGd_2Br_7$:Ce 523
RE_2SiO_5 97
$REAlO_3$ 97
$ScPO_4$ 697
Si 304
SrF_2 248, 357
$SrWO_4$ 429
Tb^{3+} 352
Xe 464
Y_2O_2S 517
Y_2O_3 33
Y_2SiO_5 , 693
$Y_3Al_5O_{12}$ 476, 693
YAG 89
YAG:Ce 167
$YAlO_3$ 470, 506, 693
YAP 89
YAP:Ce 167
YSO:Ce 167
ZnS:Te 720
ZnSe:Te 167, 571, 724,
$ZnWO_4$ 648